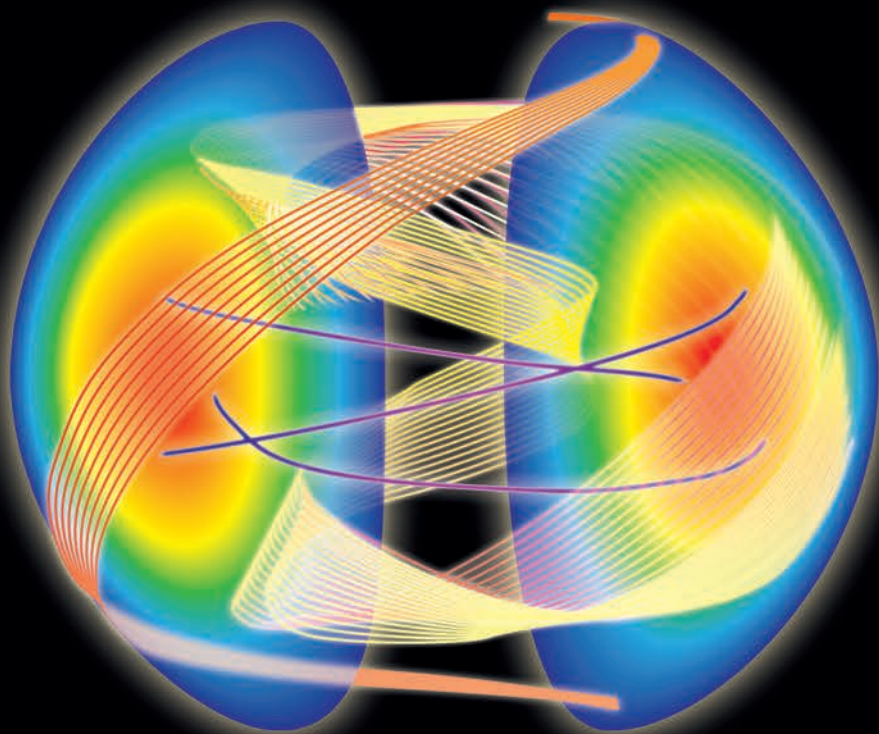


# FUSION PHYSICS



**IAEA**

International Atomic Energy Agency

**Edited by:**  
**Mitsuru Kikuchi**  
**Karl Lackner**  
**Minh Quang Tran**

# FUSION PHYSICS

The following States are Members of the International Atomic Energy Agency:

AFGHANISTAN	GHANA	NIGERIA
ALBANIA	GREECE	NORWAY
ALGERIA	GUATEMALA	OMAN
ANGOLA	HAITI	PAKISTAN
ARGENTINA	HOLY SEE	PALAU
ARMENIA	HONDURAS	PANAMA
AUSTRALIA	HUNGARY	PAPUA NEW GUINEA
AUSTRIA	ICELAND	PARAGUAY
AZERBAIJAN	INDIA	PERU
BAHRAIN	INDONESIA	PHILIPPINES
BANGLADESH	IRAN, ISLAMIC REPUBLIC OF	POLAND
BELARUS	IRAQ	PORTUGAL
BELGIUM	IRELAND	QATAR
BELIZE	ISRAEL	REPUBLIC OF MOLDOVA
BENIN	ITALY	ROMANIA
BOLIVIA	JAMAICA	RUSSIAN FEDERATION
BOSNIA AND HERZEGOVINA	JAPAN	RWANDA
BOTSWANA	JORDAN	SAUDI ARABIA
BRAZIL	KAZAKHSTAN	SENEGAL
BULGARIA	KENYA	SERBIA
BURKINA FASO	KOREA, REPUBLIC OF	SEYCHELLES
BURUNDI	KUWAIT	SIERRA LEONE
CAMBODIA	KYRGYZSTAN	SINGAPORE
CAMEROON	LAO PEOPLE'S DEMOCRATIC REPUBLIC	SLOVAKIA
CANADA	LATVIA	SLOVENIA
CENTRAL AFRICAN REPUBLIC	LEBANON	SOUTH AFRICA
CHAD	LESOTHO	SPAIN
CHILE	LIBERIA	SRI LANKA
CHINA	LIBYA	SUDAN
COLOMBIA	LIECHTENSTEIN	SWEDEN
CONGO	LITHUANIA	SWITZERLAND
COSTA RICA	LUXEMBOURG	SYRIAN ARAB REPUBLIC
CÔTE D'IVOIRE	MADAGASCAR	TAJIKISTAN
CROATIA	MALAWI	THAILAND
CUBA	MALAYSIA	THE FORMER YUGOSLAV REPUBLIC OF MACEDONIA
CYPRUS	MALI	TUNISIA
CZECH REPUBLIC	MALTA	TURKEY
DEMOCRATIC REPUBLIC OF THE CONGO	MARSHALL ISLANDS	UGANDA
DENMARK	MAURITANIA	UKRAINE
DOMINICA	MAURITIUS	UNITED ARAB EMIRATES
DOMINICAN REPUBLIC	MEXICO	UNITED KINGDOM OF GREAT BRITAIN AND NORTHERN IRELAND
ECUADOR	MONACO	UNITED REPUBLIC OF TANZANIA
EGYPT	MONGOLIA	UNITED STATES OF AMERICA
EL SALVADOR	MONTENEGRO	URUGUAY
ERITREA	MOROCCO	UZBEKISTAN
ESTONIA	MOZAMBIQUE	VENEZUELA
ETHIOPIA	MYANMAR	VIETNAM
FINLAND	NAMIBIA	YEMEN
FRANCE	NEPAL	ZAMBIA
GABON	NETHERLANDS	ZIMBABWE
GEORGIA	NEW ZEALAND	
GERMANY	NICARAGUA	
	NIGER	

The Agency's Statute was approved on 23 October 1956 by the Conference on the Statute of the IAEA held at United Nations Headquarters, New York; it entered into force on 29 July 1957. The Headquarters of the Agency are situated in Vienna. Its principal objective is "to accelerate and enlarge the contribution of atomic energy to peace, health and prosperity throughout the world".

# FUSION PHYSICS

EDITED BY:  
MITSURU KIKUCHI  
KARL LACKNER  
MINH QUANG TRAN

INTERNATIONAL ATOMIC ENERGY AGENCY  
VIENNA, 2012

## COPYRIGHT NOTICE

All IAEA scientific and technical publications are protected by the terms of the Universal Copyright Convention as adopted in 1952 (Berne) and as revised in 1972 (Paris). The copyright has since been extended by the World Intellectual Property Organization (Geneva) to include electronic and virtual intellectual property. Permission to use whole or parts of texts contained in IAEA publications in printed or electronic form must be obtained and is usually subject to royalty agreements. Proposals for non-commercial reproductions and translations are welcomed and considered on a case-by-case basis. Enquiries should be addressed to the IAEA Publishing Section at:

Marketing and Sales Unit, Publishing Section  
International Atomic Energy Agency  
Vienna International Centre  
PO Box 100  
1400 Vienna, Austria  
fax: +43 1 2600 29302  
tel.: +43 1 2600 22417  
email: [sales.publications@iaea.org](mailto:sales.publications@iaea.org)  
<http://www.iaea.org/books>

© IAEA, 2012

Printed by the IAEA in Austria  
September 2012  
STI/PUB/1562

### **IAEA Library Cataloguing in Publication Data**

Fusion physics. — Vienna : International Atomic Energy Agency, 2012.

p. ; 24 cm.

STI/PUB/1562

ISBN 978-92-0-130410-0

Includes bibliographical references.

1. Nuclear fusion. 2. International Thermonuclear Experimental Reactor (Project). 3. Controlled fusion — International cooperation. 4. Tokamaks — International cooperation. I. International Atomic Energy Agency.

IAEAL

12-00774

## FOREWORD

Recreating the energy production process of the Sun — nuclear fusion — on Earth in a controlled fashion is one of the greatest challenges of this century. If achieved at affordable costs, energy supply security would be greatly enhanced and environmental degradation from fossil fuels greatly diminished. *Fusion Physics* describes the last fifty years or so of physics and research in innovative technologies to achieve controlled thermonuclear fusion for energy production.

The International Atomic Energy Agency (IAEA) has been involved since its establishment in 1957 in fusion research. It has been the driving force behind the biennial conferences on Plasma Physics and Controlled Thermonuclear Fusion, today known as the Fusion Energy Conference. Hosted by several Member States, this biennial conference provides a global forum for exchange of the latest achievements in fusion research against the backdrop of the requirements for a net energy producing fusion device and, eventually, a fusion power plant. The scientific and technological knowledge compiled during this series of conferences, as well as by the IAEA Nuclear Fusion journal, is immense and will surely continue to grow in the future. It has led to the establishment of the International Thermonuclear Experimental Reactor (ITER), which represents the biggest experiment in energy production ever envisaged by humankind.

The IAEA also would like to thank the editors of the book, M. Kikuchi, K. Lackner and Minh Quang Tran, for preparing this comprehensive manuscript on fusion, including magnetic and inertial fusion concepts. They have selected a prominent group of contributors, many of whom have provided seminal scientific contributions to important developments in the field. The IAEA also conveys its gratitude to the authors for their long standing cooperation. Their work is highly appreciated, and this present compendium will help to raise awareness of the opportunities offered by fusion and the path towards a demonstration fusion power plant.

## PREFACE

In 1958, during the second Conference on Peaceful Uses of Nuclear Energy in Geneva, nuclear fusion research was declassified. At this time the basis of nuclear fusion science and technology was confined to a few books and monographs written by ‘pioneers’.

After this event, the tradition to periodically exchange the latest discoveries in fusion research development was established by the International Atomic Energy Agency (IAEA) through its series of Fusion Energy Conferences (IAEA FECs). It was natural that in 2008 the 22nd IAEA FEC came back to the same location in Geneva, the Palais des Nations, to celebrate the fiftieth anniversary of the declassification.

The progress over the past half century has been immense. We are now in the building phase of the International Thermonuclear Experimental Reactor (ITER) with the prospect of having 500 MW of fusion power in the second half of the 2020s and starting studies for the step beyond ITER, a demonstration reactor (usually referred to as the DEMO power plant). A new generation of scientists and engineers is needed to build and exploit ITER and accompanying fusion devices, and to prepare the next step beyond ITER. Master and PhD programmes have been set up in many universities worldwide to train what is usually referred to as the “ITER Generation of Scientists”. Compared to 1958, the growth of the field of nuclear fusion has led to a multiplicity of specialized subfields, each having its own textbooks.

The occasion of the 2008 IAEA FEC prompted us to propose to the IAEA International Fusion Research Council (IFRC) to sponsor a tutorial book for post-graduate students. Our aim is to provide an introduction to nuclear fusion, its status and perspectives. Specialized chapters are devoted to the main concepts under R&D (magnetic and inertial confinement) together with the physics as well as the technology basis. With the strong support and under the guidance of the IFRC, we have invited international experts to contribute to the project. Our vision of the book was shared by all contacted colleagues, who enthusiastically accepted this difficult tutorial task.

It is our hope that the material presented will allow post-graduate level students to become familiar with the topics of their studies. More advanced researchers will also find materials on topics adjacent to their field of specialization. The progress in nuclear fusion research is such that it has become impossible to cover in detail all the key issues: this book is not intended to replace specialized monographs or review articles.

The book starts with an introduction to the case for the development of fusion as an energy source, followed by chapters on the physics of confinement, equilibrium and stability of tokamaks. Diagnostics, heating and current drive by neutral beams and radiofrequency waves, and plasma-wall interactions

are described in detail. While the tokamak is currently the leading concept for the realization of nuclear fusion, it is important to note that other concepts (helical confinement concepts and, in a broader sense, other magnetic configurations) have also received wide interest worldwide. Last but not least, inertial confinement fusion is one of the important lines of research, which naturally finds its place in the book. The later part of the book is oriented towards ITER and fusion technology.

The realization of this book would not have been possible without the enthusiastic commitment of all authors, who took upon themselves the task of sharing their vast knowledge with the ITER generation in parallel with their research duties. We would like to wholeheartedly thank them for their dedication. Our responsibility has also included careful reading of the contributed manuscripts. That was done with the help of a few colleagues, whose contribution is gratefully acknowledged.

Last but not least, our appreciation also goes to the IAEA and its staff, which provided an unfailing support and encouragement. We would like to particularly thank G. Mank, R. Kamendje, R. Kaiser and T. Desai, whose support throughout this endeavour has rendered the publication of this volume possible. We also would like to acknowledge the very useful contribution of B. Gulejova, whose professional expertise has helped solve a multitude of editorial issues.

Mitsuru Kikuchi

Karl Lackner

Minh Quang Tran

December 2011

## **EDITORIAL NOTE**

*Although great care has been taken to maintain the accuracy of information contained in this publication, neither the IAEA nor its Member States assume any responsibility for consequences which may arise from its use.*

*The mention of names of specific companies or products (whether or not indicated as registered) does not imply any intention to infringe proprietary rights, nor should it be construed as an endorsement or recommendation on the part of the IAEA.*

*The authors are responsible for having obtained the necessary permission for the IAEA to reproduce, translate or use material from sources already protected by copyrights.*

*Material prepared by authors who are in contractual relation with governments is copyrighted by the IAEA, as publisher, only to the extent permitted by the appropriate national regulations.*

*This publication has been prepared from the original material as submitted by the authors. The views expressed do not necessarily reflect those of the IAEA, the governments of the nominating Member States or the nominating organizations.*

*The IAEA has no responsibility for the persistence or accuracy of URLs for external or third party Internet web sites referred to in this book and does not guarantee that any content on such web sites is, or will remain, accurate or appropriate.*

# CONTENTS

## CHAPTER 1 THE CASE FOR FUSION

1.1.	INTRODUCTION.....	1
1.2.	ENERGY SCENARIOS .....	3
1.2.1.	Near term energy scenario.....	5
1.2.2.	Long term energy scenario and the role of fusion .....	7
1.3.	FUSION BASICS.....	14
1.3.1.	What is fusion? .....	14
1.3.2.	Fusion power gain $Q$ .....	17
1.3.3.	Fusion reactions.....	20
1.3.4.	Fusion fuels .....	23
1.3.5.	Direct conversion to electricity.....	26
1.4.	APPROACHES TO FUSION.....	26
1.4.1.	Magnetic confinement fusion.....	27
1.4.1.1.	Progress in tokamak based magnetic confinement fusion research.....	32
1.4.2.	Inertial confinement fusion .....	35
1.4.2.1.	Progress in inertial confinement fusion research.....	38
1.5.	SOCIOECONOMIC PERSPECTIVES .....	40
1.5.1.	Environment, safety and non-proliferation .....	40
1.5.1.1.	Emissions in normal operation .....	40
1.5.1.2.	Possible accidents.....	41
1.5.1.3.	Waste.....	41
1.5.2.	Cost comparison with other sources of energy.....	42
1.5.2.1.	Direct costs of fusion power production.....	42
1.5.2.2.	External costs of fusion power production.....	45
1.5.3.	Public acceptance of fusion .....	46
1.5.4.	Spin-offs of fusion research .....	47
1.6.	CONCLUSION.....	51

## CHAPTER 2 PHYSICS OF CONFINEMENT

2.1.	INTRODUCTION AND OVERVIEW .....	59
2.2.	NEOCLASSICAL TRANSPORT .....	63
2.2.1.	Introduction .....	63

2.2.2.	Toroidal magnetic configuration .....	65
2.2.3.	Guiding centre motion.....	66
2.2.4.	The drift kinetic equation .....	71
2.2.5.	Bootstrap current .....	75
2.2.6.	Magnetic field ripple .....	78
2.2.7.	Transport in a stochastic field .....	82
2.3.	TURBULENT TRANSPORT.....	83
2.3.1.	Introduction .....	83
2.3.2.	Examples of basic microinstabilities .....	86
2.3.2.1.	Electron drift instabilities .....	86
2.3.2.2.	Ion temperature gradient instabilities .....	89
2.3.3.	Non-linear gyrokinetic equations for tokamak turbulence .....	91
2.3.4.	Kinetic description of microinstabilities .....	95
2.3.4.1.	Linear onset condition for ion temperature gradient mode ..	96
2.3.4.2.	Electron temperature gradient instability.....	99
2.3.4.3.	Trapped particle instabilities .....	99
2.3.5.	Spatial structure of microturbulence.....	103
2.3.5.1.	Role of magnetic shear: Sheared slab geometry .....	104
2.3.5.2.	Role of toroidal geometry: Ballooning representation .....	106
2.3.5.3.	Role of zonal flow shear .....	108
2.3.6.	Different channels of turbulence transport .....	110
2.3.6.1.	Ion thermal transport .....	111
2.3.6.2.	Electron thermal transport .....	113
2.3.6.3.	Particle transport .....	114
2.3.6.4.	Momentum transport .....	116
2.3.7.	Physics of transport barriers.....	118
2.4.	GLOBAL ENERGY CONFINEMENT SCALING STUDIES .....	123
2.4.1.	Introduction .....	123
2.4.2.	Energy confinement scalings: Dimensional parameters .....	124
2.4.2.1.	Ohmic and L-mode plasma confinement trends.....	124
2.4.2.2.	H-mode confinement trends and scalings.....	128
2.4.2.3.	Advanced statistical methods and error analysis.....	133
2.4.3.	Dimensionless analysis .....	136
2.4.3.1.	Basics .....	136
2.4.3.2.	Scalings .....	139
2.4.4.	L-H threshold scalings .....	140
2.4.5.	Implications relative to theoretical models .....	144
2.5.	LOCAL TRANSPORT.....	145
2.5.1.	Basics.....	145
2.5.2.	Models.....	147
2.5.2.1.	Neutral beam models.....	147

2.5.2.2.	Neutral transport.....	149
2.5.2.3.	RF heating and current drive models.....	150
2.5.2.4.	Current drive models .....	152
2.5.3.	Perturbative transport .....	155
2.5.4.	Profile stiffness .....	160
2.5.5.	Transport barriers.....	163
2.5.5.1.	Core.....	163
2.5.5.2.	Edge.....	169
2.5.6.	Comparison with theoretical models.....	173
2.6.	TURBULENCE MEASUREMENTS .....	176
2.6.1.	Measurement techniques.....	177
2.6.1.1.	Probe techniques.....	177
2.6.1.2.	Electromagnetic wave scattering.....	178
2.6.1.3.	Electromagnetic wave reflectometry .....	179
2.6.1.4.	Electromagnetic wave Doppler backscattering (DBS).....	180
2.6.1.5.	Phase contrast imaging (PCI).....	181
2.6.1.6.	Heavy ion beam probe (HIBP) .....	181
2.6.1.7.	Beam emission spectroscopy (BES).....	182
2.6.1.8.	High frequency charge exchange spectroscopy (HF CHERS).....	183
2.6.1.9.	Correlated electron cyclotron emission (CECE).....	183
2.6.1.10.	Analysis techniques .....	184
2.6.2.	Experimental results .....	185
2.6.2.1.	Wavenumber spectra.....	185
2.6.2.2.	Frequency spectra.....	187
2.6.2.3.	Radial profiles .....	189
2.6.3.3.	Ion and electron temperature fluctuations.....	191
2.6.3.4.	Zonal flows and geodesic acoustic modes.....	192
2.6.3.5.	Core turbulence suppression .....	194
2.6.3.6.	Evidence for non-local effects .....	195

## CHAPTER 3

### EQUILIBRIUM AND MACROSCOPIC STABILITY OF TOKAMAKS

3.1.	INTRODUCTION.....	225
3.1.1.	Basic tokamak configuration.....	227
3.1.2.	Timescales of tokamak dynamics .....	228
3.2.	TOKAMAK EQUILIBRIUM.....	230
3.2.1.	The straight cylinder.....	231
3.2.2.	Toroidal plasma equilibrium .....	232
3.2.2.1.	The large aspect ratio approximation .....	234

3.2.2.2.	Formulations of the Grad–Shafranov equation .....	236
3.2.2.3.	Dimensionless parameters characterizing the plasma equilibrium.....	239
3.2.2.4.	Shaping of plasma cross-section and the tokamak poloidal field system.....	242
3.2.2.5.	Axisymmetric stability of tokamak equilibria .....	244
3.3.	THEORY OF MACROSCOPIC INSTABILITIES IN TOKAMAKS.....	246
3.3.1.	One-fluid MHD stability theory .....	246
3.3.1.1.	Ideal MHD stability .....	246
3.3.1.2.	Effects of dissipation on linear stability of global modes.....	269
3.3.1.3.	Finite amplitude perturbations .....	281
3.3.2.	Extensions to the MHD model .....	287
3.3.2.1.	Introduction .....	287
3.3.2.2.	Derivation example: reduced (low frequency) MHD.....	291
3.3.2.3.	Derivation example: two-fluid equations.....	296
3.3.2.4.	Relation to kinetic models.....	299
3.3.2.5.	Qualitative two-fluid effects on MHD instabilities.....	300
3.3.3.	Energetic particle physics and kinetic MHD .....	302
3.3.3.1.	Introduction .....	302
3.3.3.2.	Models .....	303
3.3.3.3.	Global modes in toroidal geometry.....	306
3.4.	EXPERIMENTAL OBSERVATIONS OF MHD MODES .....	316
3.4.1.	Internal kink modes .....	317
3.4.2.	Classical tearing modes.....	322
3.4.3.	Neoclassical tearing modes (NTMs).....	325
3.4.4.	Edge localized modes (ELMs).....	327
3.4.5.	Ideal pressure limiting modes.....	331
3.4.6.	Wall effects on MHD modes.....	334
3.4.7.	Alfvén and energetic particle modes (EPMs).....	337
3.5.	DISRUPTIVE INSTABILITIES.....	342
3.5.1.	Introduction .....	342
3.5.2.	Classification by causes.....	343
3.5.2.1.	Density limit disruptions.....	343
3.5.2.2.	Beta limit.....	344
3.5.2.3.	Limit on $q$ .....	344
3.5.3.	Phases of disruptions .....	345
3.5.3.1.	Thermal quench .....	345
3.5.3.2.	Current quench.....	347
3.5.4.	Damage potential.....	349
3.5.4.1.	Heat pulse .....	349
3.5.4.2.	Electromagnetic forces.....	350

3.5.4.3.	Runaway generation .....	352
3.5.5.	Mitigation methods .....	353

## CHAPTER 4

### PLASMA DIAGNOSTICS

4.1.	INTRODUCTION.....	360
4.2.	PASSIVE DIAGNOSTIC METHODS .....	362
4.2.1.	Magnetic measurements .....	362
4.2.2.	Electrical probes (Langmuir probes).....	368
4.2.2.1.	Introduction to electrical probes.....	368
4.2.2.2.	Langmuir probes.....	368
4.2.3.	Visible and UV spectroscopy.....	375
4.2.4.	Bolometry .....	378
4.2.4.1.	Thermal devices.....	378
4.2.4.2.	AXUV detectors .....	382
4.2.5.	Methods based on electron cyclotron emission measurements.....	384
4.2.6.	Passive neutral particle analysis.....	393
4.2.7.	Methods based on X ray radiation .....	400
4.2.7.1.	Soft X ray radiation .....	400
4.2.7.2.	High resolution X ray spectroscopy.....	404
4.2.8.	Experimental nuclear physics methods.....	412
4.2.8.1.	Neutrons, charged fusion products, hard X rays .....	412
4.2.8.2.	Gamma ray spectrometry.....	421
4.3.	ACTIVE DIAGNOSTIC METHODS.....	426
4.3.1.	Probing by laser beams .....	426
4.3.1.1.	Thomson scattering.....	426
4.3.1.2.	Laser induced fluorescence technique.....	432
4.3.2.	Probing by particles .....	435
4.3.2.1.	Diagnostic neutral beams for plasma studies in magnetic fusion devices.....	435
4.3.2.2.	Active charge exchange recombination spectroscopy diagnostic .....	438
4.3.2.3.	Motional Stark effect .....	443
4.3.2.4.	Active charge exchange and Rutherford scattering .....	445
4.3.2.5.	Heavy ion beam probe diagnostics .....	449
4.3.3.	Probing by microwaves and laser beam: interferometry, polarimetry, reflectometry .....	452
4.3.3.1.	Introduction .....	452
4.3.3.2.	Interferometry and polarimetry.....	454
4.3.3.3.	Plasma reflectometry for electron concentration profile measurements.....	473

4.3.3.4.	Application of reflectometry to density fluctuation measurements.....	482
4.4.	ENGINEERING PROBLEMS.....	485
4.4.1.	Changing of mechanical properties.....	486
4.4.2.	Changing in electrical properties.....	486
4.4.3.	Changes in optical properties.....	487
4.5.	CONCLUSION.....	489

## CHAPTER 5

### PLASMA HEATING AND CURRENT DRIVE BY NEUTRAL BEAM AND ALPHA PARTICLES

5.1.	HEATING AND CURRENT DRIVE PHYSICS BY NEUTRAL BEAM AND ALPHA PARTICLES .....	535
5.1.1.	Basic processes of neutral beam injection.....	535
5.1.2.	Physics of ionization of injected neutral beam .....	537
5.1.3.	Multi-step ionization and Lorenz ionization.....	540
5.1.4.	Energy transfer to electrons and ions by neutral beam injection .....	543
5.1.5.	Energetic particle orbits on the axisymmetric magnetic surfaces .....	546
5.1.6.	Fast ion behaviour and high temperature production with NB injection .....	549
5.1.7.	Physics of neutral beam current drive: fast ion distribution function.....	551
5.1.7.1.	Rayleigh–Ritz method.....	553
5.1.8.	Physics of neutral beam current drive: shielding current and NBCD efficiency.....	554
5.1.9.	Experimental observation of beam-driven current .....	558
5.1.10.	Physics of ripple loss of fast ions: banana drift and ripple trapped losses.....	560
5.1.11.	Physics of particle trajectories in non-axisymmetric fields.....	563
5.1.12.	Alpha heating.....	565
5.1.13.	D-T experiments in large tokamaks (TFTR and JET).....	568
5.2.	NEUTRAL BEAM HEATING.....	571
5.2.1.	Introduction .....	571
5.2.2.	Ion source.....	575
5.2.2.1.	Plasma generator .....	575
5.2.2.2.	Multicusp source .....	576
5.2.2.3.	Radiofrequency plasma source .....	578
5.2.3.	Extraction and acceleration .....	579
5.2.3.1.	Child–Langmuir Law .....	579
5.2.3.2.	Multi-stage acceleration.....	581
5.2.3.3.	Beamlet steering.....	582
5.2.4.	Positive-ion-based NBI.....	584

5.2.5.	Negative ion source .....	587
5.2.5.1.	Negative ion production.....	588
5.2.5.2.	Advantages of volume production .....	590
5.2.5.3.	Caesium seeding.....	592
5.2.6.	Negative ion extraction/acceleration .....	594
5.2.7.	Negative-ion-based NBI .....	595
5.2.7.1.	N-NBI for JT-60 .....	595
5.2.7.2.	N-NBI for LHD .....	596
5.2.7.3.	N-NBI for ITER.....	597
5.2.8.	MV power supply.....	599
5.2.9.	Remarks on future NBI technology .....	600

## CHAPTER 6

### RADIOFREQUENCY WAVES, HEATING AND CURRENT DRIVE IN MAGNETICALLY CONFINED PLASMAS

6.1.	INTRODUCTION.....	609
6.2.	THEORY OF RF WAVE PROPAGATION IN A MAGNETIZED PLASMA .....	611
6.2.1.	Electron cyclotron waves.....	620
6.2.2.	Lower hybrid wave propagation and accessibility.....	624
6.2.3.	Ion cyclotron wave propagation and accessibility .....	630
6.2.4.	ICRF wave absorption in a hot plasma .....	633
6.2.4.1.	Absorption on electrons .....	634
6.2.4.2.	Absorption of ICRF waves on ion cyclotron harmonics .....	635
6.2.4.3.	Minority ion cyclotron absorption .....	637
6.2.5.	Quasi-linear absorption of ICRF waves on ions .....	638
6.2.6.	Quasi-linear absorption on electrons.....	642
6.2.6.1.	Lower hybrid current drive.....	642
6.2.6.2.	Electron cyclotron current drive.....	645
6.2.6.3.	Current drive by the fast ICRF waves .....	647
6.2.7.	Wave propagation in toroidal geometry, geometric optics .....	648
6.2.7.1.	Geometric optics and the ray equations .....	649
6.2.7.2.	Modifications to wave accessibility and absorption in toroidal geometry.....	651
6.2.7.3.	Numerical simulations of lower hybrid current drive using coupled Fokker–Planck and ray tracing calculations ..	652
6.2.8.	Wave propagation in toroidal geometry, full-wave treatment .....	653
6.2.8.1.	Full-wave simulations of minority heating in the ICRF .....	653
6.2.8.2.	Full-wave simulations of mode conversion in the ICRF .....	656
6.2.8.3.	Full-wave simulations of lower hybrid waves .....	657

6.3.	EXPERIMENTAL RESULTS ON RF HEATING AND CURRENT DRIVE.....	658
6.3.1.	ICRF heating and current drive experiments.....	659
6.3.2.	ICRF antenna and transmission line design.....	666
6.3.2.1.	ICRF transmission line architecture .....	666
6.3.2.2.	ICRF source technology.....	667
6.3.2.3.	ICRF transmission line design.....	669
6.3.2.4.	ICRF wave launchers .....	671
6.3.3.	Lower hybrid heating and current drive experiments .....	677
6.3.4.	Lower hybrid wave launchers.....	682
6.3.4.1.	RF coupling theory.....	685
6.3.4.2.	Numerical coupling codes .....	687
6.3.4.3.	Evolution of LH launchers in tokamaks .....	690
6.3.5.	Applications of electron cyclotron heating and current drive.....	694
6.3.5.1.	Wave propagation and absorption experiments.....	695
6.3.5.2.	Electron cyclotron current drive (ECCD) experiments.....	703
6.3.6.	Electron cyclotron transmission line and antenna design.....	710
6.4.	GYROTRONS FOR ECR HEATING AND CURRENT DRIVE .....	714
6.4.1.	Introduction to gyrotrons .....	714
6.4.2.	Physical principles of the gyrotron .....	716
6.4.3.	Overview of gyrotron theory.....	717
6.4.4.	Engineering features of the gyrotron.....	722
6.4.4.1.	Electron gun and beam tunnel.....	722
6.4.4.2.	Gyrotron cavity .....	723
6.4.4.3.	Internal mode converter (IMC).....	723
6.4.4.4.	Phase correcting mirrors and output window .....	724
6.4.4.5.	Depressed collector.....	724
6.4.4.6.	Auxiliary components .....	726
6.4.5.	State of the art gyrotrons.....	726
6.4.6.	Prospects and future directions.....	730
6.4.6.1.	Multi-megawatt gyrotrons .....	730
6.4.6.2.	Frequency tuneable gyrotrons.....	731
6.4.6.3.	Improvement of gyrotron efficiency .....	732
6.4.6.4.	Gyrotrons for DEMO.....	732

## CHAPTER 7

### PLASMA–WALL INTERACTIONS

7.1.	INTRODUCTION.....	756
7.2.	BASIC PHYSICAL PROCESSES AND UNDERLYING THEORY .....	758
7.2.1.	Basic concepts.....	758

7.2.1.1.	Boundary layer.....	758
7.2.1.2.	The plasma sheath.....	760
7.2.1.3.	The scrape-off layer.....	762
7.2.2.	Recycling.....	764
7.2.3.	Atomic and molecular processes.....	767
7.2.4.	Erosion processes.....	772
7.2.4.1.	Physical sputtering.....	772
7.2.4.2.	Chemical sputtering.....	774
7.2.4.3.	Arcing.....	777
7.3.	DEVELOPMENT OF PLASMA FACING MATERIALS.....	779
7.3.1.	Carbon containing materials.....	779
7.3.2.	Beryllium.....	782
7.3.3.	High-Z materials.....	784
7.3.4.	Mixed materials.....	784
7.4.	PRESENT PROGRESS OF PLASMA–WALL INTERACTIONS IN TOKAMAKS.....	786
7.4.1.	Wall conditioning.....	786
7.4.1.1.	Surface cleaning.....	787
7.4.1.2.	Plasma assisted coating of thin films.....	789
7.4.2.	Impurities and dusts.....	791
7.4.2.1.	Impurities.....	791
7.4.2.2.	Dusts.....	793
7.4.3.	Erosion and re-deposition.....	794
7.4.3.1.	Divertor erosion and re-deposition.....	794
7.4.3.2.	Limiter erosion and re-deposition.....	795
7.4.3.3.	Main chamber wall erosion and re-deposition.....	795
7.4.4.	Hydrogen isotope retention and removal.....	796
7.5.	CONTROL OF PLASMA–WALL INTERACTIONS.....	798
7.5.1.	Divertors.....	798
7.5.1.1.	Introduction.....	798
7.5.1.2.	Divertor operation regimes.....	799
7.5.1.3.	Effect of divertor geometry.....	806
7.5.2.	Particle transport in the divertor SOL.....	810
7.5.2.1.	Plasma flow and drift effects.....	810
7.5.2.2.	Recent advances on cross-field particle transport.....	819
7.5.3.	Energy deposition.....	823
7.5.3.1.	Steady state power load on the divertor.....	823
7.5.3.2.	Transient energy deposition during ELMs.....	827
7.5.3.3.	Active control of peak heat fluxes.....	831

7.6.	ISSUES OF PLASMA–WALL INTERACTIONS FOR NEXT STEP TOKAMAKS .....	831
7.6.1.	Power handling and particle exhaust .....	832
7.6.2.	Transient heat loads .....	833
7.6.3.	Material migration .....	835
7.6.4.	Control of in-vessel tritium inventory .....	835
7.6.5.	Integrated PWI issues for steady state operation .....	836

## CHAPTER 8

### HELICAL CONFINEMENT CONCEPTS

8.1.	INTRODUCTION .....	847
8.2.	HELICAL CONFINEMENT CONCEPTS .....	849
8.2.1.	Production of 3-D toroidal flux surfaces .....	849
8.2.2.	Helical confinement devices .....	852
8.2.2.1.	Classical stellarators .....	853
8.2.2.2.	Torsatrons/Heliotrons .....	855
8.2.2.3.	Heliacs .....	858
8.2.2.4.	Modular stellarators .....	859
8.3.	THE PHYSICS OF HELICAL SYSTEMS .....	861
8.3.1.	Heating and particle–wave interaction .....	861
8.3.1.1.	Electron cyclotron heating and current drive .....	861
8.3.1.2.	Electron Bernstein wave heating in stellarators .....	866
8.3.1.3.	Ion cyclotron heating in helical systems .....	868
8.3.2.	Plasma equilibrium .....	870
8.3.2.1.	Basic equilibrium properties .....	870
8.3.2.2.	Optimized stellarators .....	871
8.3.2.3.	Computation of 3-D equilibria .....	873
8.3.2.4.	Experimental equilibrium identification .....	874
8.3.3.	Plasma stability .....	877
8.3.3.1.	Introduction and theoretical background .....	877
8.3.3.2.	Ballooning modes .....	881
8.3.3.3.	Global pressure driven modes .....	882
8.3.3.4.	Energetic particle driven Alfvén instabilities .....	885
8.3.4.	Bounce-averaged particle orbits .....	894
8.3.5.	Neoclassical transport models .....	896
8.3.5.1.	Neoclassical modelling .....	896
8.3.5.2.	Classical and advanced stellarator configurations .....	898
8.3.5.3.	Radial electric field .....	899
8.3.5.4.	Bootstrap current .....	900
8.3.5.5.	Parallel resistivity .....	900

8.3.5.6.	Optimization of neoclassical transport.....	901
8.3.6.	3-D features of transport and confinement .....	903
8.3.6.1.	Role of neoclassical transport .....	904
8.3.6.2.	Characterization of turbulent transport .....	906
8.3.6.3.	Particle transport.....	909
8.3.6.4.	Electron temperature evolution.....	911
8.3.6.5.	Isotopic effect .....	912
8.3.6.6.	Magnetic configuration effects on confinement .....	913
8.3.6.7.	Improved confinement regimes .....	915
8.3.6.8.	Impurity transport.....	918
8.3.7.	Boundary layer and divertor physics.....	923
8.3.7.1.	Island divertor concepts .....	923
8.3.7.2.	Transport features of helical SOLs .....	924
8.3.7.3.	Detachment regime .....	928
8.4.	OPERATIONAL LIMITS .....	930
8.4.1.	Density limit .....	930
8.4.2.	Beta limit .....	933
8.5.	STELLARATOR OPTIMIZATION .....	936
8.5.1.	Equilibrium.....	936
8.5.2.	Particle drift.....	936
8.5.3.	Stability .....	938
8.5.4.	Integrated optimization concepts .....	938
8.6.	HELICAL REACTOR CONCEPTS.....	941
8.6.1.	Heliotron reactors .....	941
8.6.2.	Modular stellarator reactors .....	942
8.6.2.1.	US compact stellarator power plant study (SPPS).....	943
8.6.2.2.	The Helias reactor .....	944
8.6.3.	Concluding remarks.....	945

## CHAPTER 9

### THE BROADER SPECTRUM OF MAGNETIC CONFIGURATIONS FOR FUSION

9.1.	INTRODUCTION.....	958
9.2.	REVERSED FIELD PINCH: TOROIDAL CONFINEMENT AT WEAK MAGNETIC FIELD .....	959
9.2.1.	The configuration: ideal MHD equilibrium and stability .....	961
9.2.1.1.	Current driven instability.....	964
9.2.1.2.	Pressure driven instability.....	964
9.2.2.	Reversal of magnetic field: minimum energy state and reconnection ....	965
9.2.2.1.	Minimum energy state.....	965

9.2.2.2.	Standard model of RFP dynamics: non-linear tearing modes and magnetic reconnection .....	967
9.2.3.	Confinement: effects of magnetic stochasticity.....	972
9.2.4.	Improved confinement .....	976
9.2.4.1.	Eliminating the free energy source .....	976
9.2.4.2.	Single helicity states .....	979
9.2.5.	Beta limits in the RFP .....	982
9.2.6.	Resistive wall instabilities and their control .....	984
9.2.6.1.	Characteristics of resistive wall instabilities in the RFP.....	984
9.2.6.2.	Feedback suppression of resistive wall instabilities .....	985
9.2.7.	Sustaining the plasma .....	986
9.3.	COMPACT TORI: ELIMINATING THE HOLE IN THE TORUS.....	990
9.3.1.	Spheromaks .....	990
9.3.1.1.	Magnetic surfaces.....	990
9.3.1.2.	Spheromak formation.....	991
9.3.1.3.	Sustainment phase and helicity injection.....	994
9.3.1.4.	Current amplification.....	997
9.3.1.5.	Regular versus stochastic magnetic field.....	998
9.3.1.6.	Spheromak: a flexible configuration.....	998
9.3.2.	Field reversed configuration (FRC).....	1000
9.3.2.1.	Field geometry .....	1000
9.3.2.2.	FRC formation .....	1002
9.3.2.3.	FRC equilibrium.....	1003
9.3.2.4.	Plasma rotation and stability .....	1005
9.3.2.5.	Steady state FRCs.....	1006
9.4.	OPEN CONFINEMENT SYSTEMS.....	1008
9.4.1.	Confining a plasma on the open field lines .....	1008
9.4.2.	Mirror confinement.....	1008
9.4.3.	Role of ion collisions.....	1010
9.4.4.	Electron axial confinement.....	1011
9.4.5.	Velocity-space microinstabilities.....	1012
9.4.6.	MHD stability .....	1014
9.4.7.	Suppression of end losses .....	1015
9.4.7.1.	Tandem mirrors.....	1015
9.4.7.2.	Plasma rotation .....	1018
9.4.7.3.	Gas-dynamic trap .....	1019
9.5.	OTHER FUSION CONFIGURATIONS: A BROAD RANGE OF IDEAS.....	1020
9.5.1.	Levitated dipoles .....	1020
9.5.2.	Cusps .....	1022
9.5.3.	Magneto-electrostatic confinement and electrostatic confinement.....	1023

9.5.4.	Pinches .....	1023
9.5.5.	Magnetized target fusion .....	1024
9.5.6.	Other concepts .....	1025
9.6.	SUMMARY .....	1026

## CHAPTER 10

### INERTIAL FUSION ENERGY

10.1.	BRIEF HISTORY .....	1043
10.2.	INTRODUCTION .....	1044
10.3.	BASIC CONCEPT OF INERTIAL FUSION ENERGY .....	1044
10.4.	REQUIREMENT ON FUSION GAIN .....	1046
10.5.	IMPLOSION CONCEPT .....	1048
10.5.1.	Why compression? .....	1048
10.5.2.	Gain scaling of implosion ignition .....	1050
10.6.	IMPLOSION PHYSICS .....	1051
10.6.1.	Ablative acceleration and laser-throughout plasma interaction in direct drive implosion .....	1053
10.6.2.	Classical absorption .....	1054
10.6.3.	Collective laser plasma interactions .....	1055
10.6.3.1.	Resonant mode conversion .....	1056
10.6.3.2.	Density profile modifications .....	1058
10.6.3.3.	Electron-ion decay and oscillating two stream instabilities .....	1058
10.6.3.4.	Two-plasmon decay instability .....	1059
10.6.3.5.	Stimulated Raman scattering .....	1060
10.6.3.6.	Stimulated Brillouin scattering .....	1061
10.6.3.7.	Filamentation instability: self-focusing .....	1062
10.7.	ABLATION PRESSURE AND DIRECT DRIVE IMPLOSION HYDRODYNAMICS .....	1063
10.7.1.	Ablation pressure .....	1063
10.7.2.	Rocket model and hydrodynamic efficiency .....	1065
10.7.3.	Implosion non-uniformity and stability .....	1065
10.7.4.	Implosion instabilities .....	1068
10.8.	FAST IGNITION: PRESENT STATUS AND FUTURE PROSPECTS ...	1069
10.8.1.	Why fast ignition? .....	1069
10.8.2.	Ignition conditions .....	1070
10.8.3.	Fast ignition integrated experiments .....	1074
10.8.3.1.	Direct plasma heating .....	1074
10.8.3.2.	Cone-shell target .....	1076



# CHAPTER 1

## THE CASE FOR FUSION

**P.K. Kaw, I. Bandyopadhyay**  
Institute for Plasma Research,  
Bhat, Gandhinagar, Gujarat, India

### 1.1. INTRODUCTION

Humans do not live by bread alone. Physically we are puny creatures with limited prowess, but with unlimited dreams. We see a mountain and want to move it to carve out a path for ourselves. We see a river and want to tame it so that it irrigates our fields. We see a star and want to fly to its planets to secure a future for our progeny. For all this, we need a genie who will do our bidding at a flip of our fingers. Energy is such a genie. Modern humans need energy and lots of it to live a life of comfort. In fact, the quality of life in different regions of the world can be directly correlated with the per capita use of energy [1.1–1.5]. In this regard, the human development index (HDI) of various countries based on various reports by the United Nations Development Programme (UNDP) [1.6] (Fig. 1.1), which is a parameter measuring the quality of life in a given part of the world, is directly determined by the amount of per capita electricity consumption. Most of the developing world (~5 billion people) is crawling up the UN curve of HDI versus per capita electricity consumption, from abysmally low values of today towards the average of the whole world and eventually towards the average of the developed world. This translates into a massive energy hunger for the globe as a whole. It has been estimated that by the year 2050, the global electricity demand will go up by a factor of up to 3 in a high growth scenario [1.7–1.9]. The requirements beyond 2050 go up even higher.

How is humankind going to produce the vast amount of energy it needs? In the absence of any new developments, the workhorse is likely to be based on fossil fuels. On the other hand, the use of fossil fuels as the major source of energy over the last century has led to significant global warming through the emission of greenhouse gases. Also, the fossil fuel reserves have started depleting with only coal, the largest emitter of CO<sub>2</sub>, having the potential to last a few hundred years. Oil and gas reserves have already started dwindling and would last a few tens of years by various estimates; political and military conflicts for control of oil and gas have already dominated the world energy scenario over the last decade. Deployment of conventional fission based nuclear power, on the other hand, has faced serious public opposition due to concerns of proliferation, radioactive hazardous wastes, the potential for catastrophic Chernobyl like disasters, etc., all

politically and technically soluble problems and yet a matter of concern even today. Alternative clean energy resources such as solar and wind, though having the potential to become a major source of energy, yet have to significantly address issues of energy density (which makes them unsuitable for large urban industrial complexes), efficiency and cost of production before they can become a viable alternative. Thus the human race is at a critical juncture today, when we need to quickly develop a viable alternative source of clean energy with easy global accessibility which can lead to sustainable development.

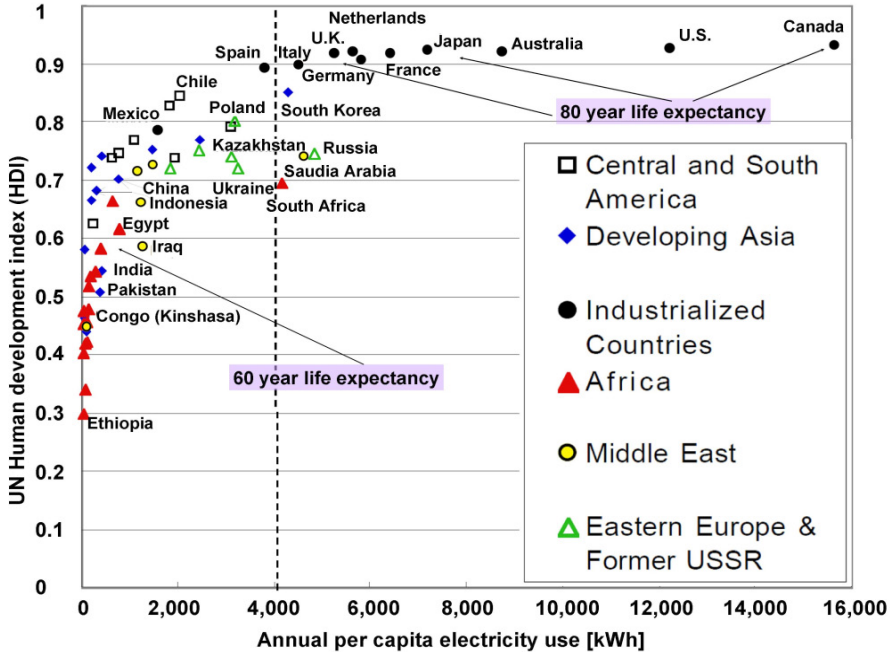


FIG. 1.1. United Nations human development index as a function of per capita energy use in kWh (60 countries, 1997). Electricity consumption increases with human development. Courtesy of Ref. [1.1].

It takes considerable time to develop new energy technologies and even more time for them to be established as an alternate energy source in a cost effective, safe and environmentally friendly way. Thus it is not too early to start now. In this chapter we shall present a case for rapid development and deployment of energy produced by nuclear fusion, an advanced nuclear technology with none of the concerns of proliferation or accident scenarios of conventional fission reactors and minimal radioactive wastes. Nuclear fusion research has seen a remarkable progress since it started in a major way about 50 years ago and it has culminated in the start of construction of the first experimental fusion reactor called ITER [1.10] in a wonderful cooperation involving in effect more than

half of the world's humanity. This is particularly gratifying because finally the world is coming to realize that global problems have to be solved by burying national differences and working together to find technical solutions to difficult problems. The world of today is a highly interconnected web where the engine of industrial growth in one region is fuelled by investments from another region and the economic ills and stagnation of one region directly influence the prosperity in another region. Hence this cooperation in nuclear fusion research may become a model for the technical solution of other global problems in the future.

In Section 1.2 we give a brief description of the energy needs of the developing and the developed world to bring out with clarity the magnitudes of energy requirements in the near term (say up to the year 2050) and in the longer term (for the rest of the century), the methods which are likely to be employed in the absence of any new technologies, the consequences for our environment and how we might benefit in the long term by the use of non-fossil fuel sources of energy. We also argue that for fulfilling the demand of centralized industrial and urban centres, it will be necessary to promote the growth of CO<sub>2</sub> free nuclear energy sources to about 40% of the total demand. Among advanced nuclear technologies, a special place is filled by nuclear fusion because of its merits such as easy, universal and almost unlimited access to the basic fuel, reduced and more benign wastes, better safety features and the promise suggested by recent technical developments in the field. Many of these features are detailed in the subsequent sections. Thus in Section 1.3 we discuss the basic fusion process itself, including the merits of fusion, the fusion reactions likely to be exploited and the possibility of using advanced fuels. In Section 1.4 the basic approaches to fusion have been summarized, with the bulk of the discussion on magnetic confinement and the tokamak concept. A discussion is also provided for the inertial fusion energy concept and the two large experiments, namely the US based National Ignition Facility (NIF) [1.11] and the Laser Mega Joule (LMJ) [1.12] experiment of France. In Section 1.5 we discuss the various socioeconomic issues of relevance to the public acceptability of fusion, such as the costs, safety issues and spin-offs, and in the final section we conclude our discussion.

### 1.2. ENERGY SCENARIOS

The main energy resource for the world in the past few centuries has been fossil fuels. Analysis carried out by the World Energy Council (WEC) [1.13], the International Energy Agency (IEA) [1.14] and other international organizations in 1996 estimated that the fossil fuel resource lives based on reserves of coal, natural gas and petroleum (using present technologies) were 231, 63 and 44 years respectively [1.15]. Furthermore, the resource lives based on *total* resource base including non-conventional oil resources such as oil shale, tar sand and heavy oil, or gas resources such as shale gas from the Devonian period, tar sand gas,

underground aquifers, coal bed methane, methane hydrate and deep layer gas (using evolving technologies) may be a few hundred years. Thus if we so desire, fossil fuel resources may last us a hundred years or so. However, it is worth noting that the fossil fuel wealth which has been created by millions of years of geological evolution on the Earth, and which may be needed for sundry reasons (other than burning) by our grandchildren and their progeny, will have been squandered away in about 300 years of modern human civilization.

Furthermore, the massive use of fossil fuels for energy production during the past century has started seriously degrading our environment. Greenhouse gases are causing a significant warming of the planet with all the associated consequences. Massive use of coal has also made phenomena like smog and acid rain a common predicament of our major urban centres. If we increase the consumption of fossil fuels by a factor of three, the consequences for the global environment are likely to be staggering. In view of the above discussion, it is unlikely that the use of fossil fuels for energy production will have an unfettered growth in spite of the needs.

On the other hand, present day fission based nuclear energy, although it plays an important supportive role (or even dominant role in countries such as France), has associated safety, radioactive waste disposal and proliferation issues. Similarly, power plants based on renewable resources such as wind or solar, while already growing at a significant pace, will continue to play only a supportive role because of the low energy density and lack of suitability to power urban industrial complexes.

Thus, although we may be able to somehow satisfy our energy needs in the short term, what is the remedy for long term energy needs and who is going to take up the challenge? Fortunately, of late there is a growing recognition among governments around the world of the possible disastrous consequences of uncontrolled global warming [1.16] and the need for supporting the development of new energy technologies. Many governments have set a target of not allowing a temperature rise of more than 2°C. This would need reduction of carbon emissions by about 80% over the next half a century [1.17]. It is important to note that there are starkly contrasting requirements on the energy chain, with the ever increasing global demand on the one hand and the environmental and social concerns on the other. Furthermore, energy systems leading to sustainable development of the entire human race must address the needs of the present without compromising those of future generations. Hence we must look for alternative energy resources which neither stress the ecosystem beyond the present level, nor totally exhaust the already dwindling fuel reserves to prevent future generations from their use for various applications. The new energy resources must be developed well in time, taking into account the following:

- They must be based on efficient and clean energy conversion processes with widespread public acceptance and involvement.

- They must lead to sustainable development of the entire world, so must be based on virtually inexhaustible resources, available globally without having to depend on resources from politically unstable regions.
- They must be sufficiently energy dense, capable of driving large scale industries, without requiring very large scale, widely distributed installations.

### 1.2.1. Near term energy scenario

In the near term, specifically over the next 20–30 years, several of the already available non-fossil energy sources which are continuously being improved for better efficiency, wider availability and reduced pollution are likely to be increasingly used to supplement the fossil fuel energy sources so as to fulfil the global energy demand as well as possibly address environmental concerns. Two such sources immediately come to mind. One is solar energy and the other is nuclear energy.

Solar energy is renewable and is hence an obvious candidate for sustainable development. Solar energy may be utilized through solar photovoltaic methods (solar cells) or through solar thermal methods (hot water for residential purposes, commercial use or electricity production) or through biofuel cultivation. In all these cases, the basic problem is the low flux of solar energy on the Earth's surface, which makes it difficult to plan massive energy hungry industrialized urban centres running on solar energy. Nevertheless, solar energy technologies have seen remarkable development of late with the advent of nanotechnology. New plastic materials made of specially designed nanoparticles of polymer called quantum dots can convert the invisible infrared spectrum of the solar energy into electric energy. Conventional solar panels, including plastic solar cells, use the visible part of the energy, whereas about 50% of the Sun's energy actually lies in the infrared spectrum [1.18]. Scientists from Spectrolab, a subsidiary of Boeing, have recently reported [1.19] development of multijunction solar cells with an efficiency of more than 40%, a new world record for solar photovoltaic cells. This greatly surpasses today's industry average of 12–18% efficiencies and the best available solar cells with 22% efficiency. The Spectrolab scientists also predict that concentrator solar cells could achieve efficiencies of more than 45% or even 50% in the future, with theoretical efficiencies being about 58% in cells with more than three junctions.

Even though the early use of solar photovoltaic methods was mostly ranging from small individual appliances such as calculators to powering remote homes not connected to grids, of late a number of medium sized solar photovoltaic power plants have been installed, mainly in Europe and the USA. For example, Spain has several power stations producing tens of megawatts, the largest being the 60 MW (85 GW·h) Parque Fotovoltaico Olmedilla de Alarcón, while the 14 MW (30 GW·h) Nellice Airforce base photovoltaic station is the largest in the

USA [1.20]. Several large photovoltaic power stations are also being constructed, the largest being the 550 MW Topaz Solar Farm in California. Japan, one of the largest markets of solar energy, intends to increase its residential electric energy consumption from solar to 50% by 2030 from the present level of a fraction of one per cent [1.21]. In the USA, the goal is to meet 10% of US peak generation capacity by 2030, which would be the energy equivalent of about 180 million barrels of oil at that time [1.22].

Thus, while solar photovoltaic is gradually establishing itself as an alternative energy source, it is likely to play only a supportive role for several generations. It still has to address several issues: it lacks the energy density of other conventional large power plants, for example nuclear reactors, and so cannot be deployed in large urban industrial complexes (it needs large scale deployment). The stability of a grid with significant photovoltaic contribution, especially in winter without enough sunlight, or during night time, has not been fully studied. The high investment cost and maintainability are still issues to be resolved, as are the problems with generation of toxic wastes in the manufacturing of photovoltaic panels and their ultimate disposal.

Biofuel technologies such as the production of ethanol or biodiesel either from sugar or starch rich vegetation or from biological wastes on the other hand have also experienced significant development over the years. Biofuels are being used routinely in many countries now, mixed with conventional fuels such as petrol or diesel to be used as primary automobile fuels. Newer generation biofuels such as algae oils or *oilgae* [1.23], conversion of vegetable oils or biodiesel into gasoline or genetically engineered plants consuming more carbon than is released from combustion of the biofuels they produce are also becoming significant. While biofuels are likely to play a supportive role in primary fuels, they have been plagued with issues such as altering food prices as crop cultivation is reoriented from food to fuel production, or adding significantly to greenhouse emission, soil erosion, deforestation and desertification. In some developing countries the use of biofuels has contributed to arid lands, expansion of deserts, general losses of biodiversity and instability in food prices. Hence it is highly unlikely that biofuels will become a dominant primary energy source for electricity production.

The nuclear energy option based on nuclear fission, on the other hand, is a valuable one which is already being exploited at ~25% average level in the developed world. Countries such as France are even using a much higher (~78%) percentage of nuclear energy. Naturally fissile materials such as  $^{235}\text{U}$  will perhaps get exhausted in a few hundred years, but as one masters the use of fissile materials such as  $^{239}\text{Pu}$  and  $^{233}\text{U}$ , which can be bred from fissile materials like  $^{238}\text{U}$  and  $^{232}\text{Th}$ , fission can supply the world with energy for several thousand years. Even though nuclear energy plants can readily fulfil the needs of centralized industrial centres, wider exploitation has been curtailed because of fears of nuclear proliferation and lack of safety. This has prevented free access to nuclear

technologies. Furthermore, there are worries about the need for great care in the handling of nuclear waste. Most of these problems have technical solutions but may have significant economic and other political and social implications. Thus it is uncertain as to how much of the energy needs can be satisfied by utilization of nuclear fission power.

Thus over the next 20–30 years, the world energy scenario is likely to remain more or less the same with fossil fuels remaining the workhorse, but oil and gas gradually becoming more scarce and expensive. Conventional nuclear reactors will increase their share of energy sources, especially in emerging economies such as India, while alternative sources like solar photovoltaic and biofuels are expected to play a more significant supportive role, especially in developed economies. However, new energy technologies take significant time to establish and hence the seeds of alternative energy sources to serve the world in the long term for sustainable development need to be sown now.

### **1.2.2. Long term energy scenario and the role of fusion**

There have been several detailed attempts at developing scenarios for electricity demand and supply on both a regional as well as a global basis. Some of the most recent comprehensive ones are the studies being carried out [1.24–1.29] by the International Institute for Applied Systems Analysis (IIASA) [1.30] under the auspices of the World Energy Council (WEC) [1.13] and also the studies by the Intergovernmental Panel on Climate Change (IPCC) [1.31]. The main objective of these studies has been to estimate the upper range of future electricity supply to be assured by the existing power generating capacities along with an estimate of additional power supply capacities generated by prospective technologies. Another objective of these studies has been to determine a region-wise breakup of the possible development paths of power generation systems, especially in a scenario of fast depleting fossil fuel reserves. They also include estimates of the respective share in total installed capacities and maximum electricity supply of each technology or fuel type, including advanced energy technologies, such as thermonuclear fusion.

However, one of the problems with such studies is that they all naturally have to assume a set of likely prevailing scenarios with underlying assumptions, for example regarding population, economic and industrial growth, new technology developments, the availability of primary energy resources and a host of other factors. As a result, the predictions from these models differ somewhat depending on the underlying factors in a given scenario. For example, the IIASA–WEC study [1.32] on eleven different world regions describes three alternative cases of future economic development and energy consumption trends that further divide into six different scenarios, and quantifies their implications. Figure 1.2 shows the projected world energy consumption until the year 2100. Case “A”

corresponds to a scenario of remarkable technological improvements leading to rapid economic growth and consequently resulting in the highest energy demand. Case “B” corresponds to a more realistic and less spectacular growth scenario where technology improvements are also moderate, and consequently results in lower energy consumption. Case “C” is driven by ecological considerations for the future, though it allows for significant technological progress, especially in areas related to alternative (non-fossil) energy resources, and relies on extensive international cooperation focused on environmental protection and equitable economic growth. Consequently, the projected energy consumption in case “C” is the lowest among all scenarios.

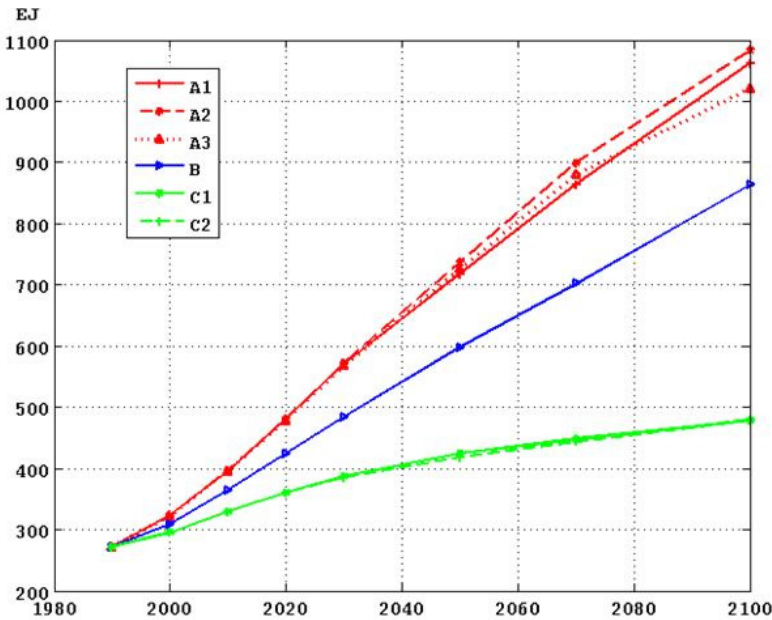


FIG. 1.2. World Final Energy Consumption until the year 2100 in the IIASA–WEC Study “Global Energy Perspectives”. Plotted using the data from Ref. [1.32].

On the other hand, Fig. 1.3 shows past usage and projections from the IIASA–WEC analysis [1.30] of the total primary energy consumption in different regions of the world. Thus we see, as is well documented in many recent studies, that while the technologically advanced OECD nations show a steady saturation or small growth over this century (or even a slight decrease in North America in the later part of this century), the developing nations in South and Central Asia, such as India and China, or the Middle East nations, show a spectacular growth (up to tenfold) in primary energy consumption. In fact, it is expected that by the end of the century final energy consumption in these developing countries will be more than three times higher than in the industrialized OECD and Former Soviet

Union countries. This projection is very real, as is evident from the economies of India and China, which are already showing sustained, close to double digit, growth rates and have the potential to grow even faster throughout the coming few decades. Such sustained growth in the developing world is going to put an enormous demand on primary energy resources, which, simply stated, cannot be sustained by the ever dwindling and potentially environment degrading reserves of fossil fuels.

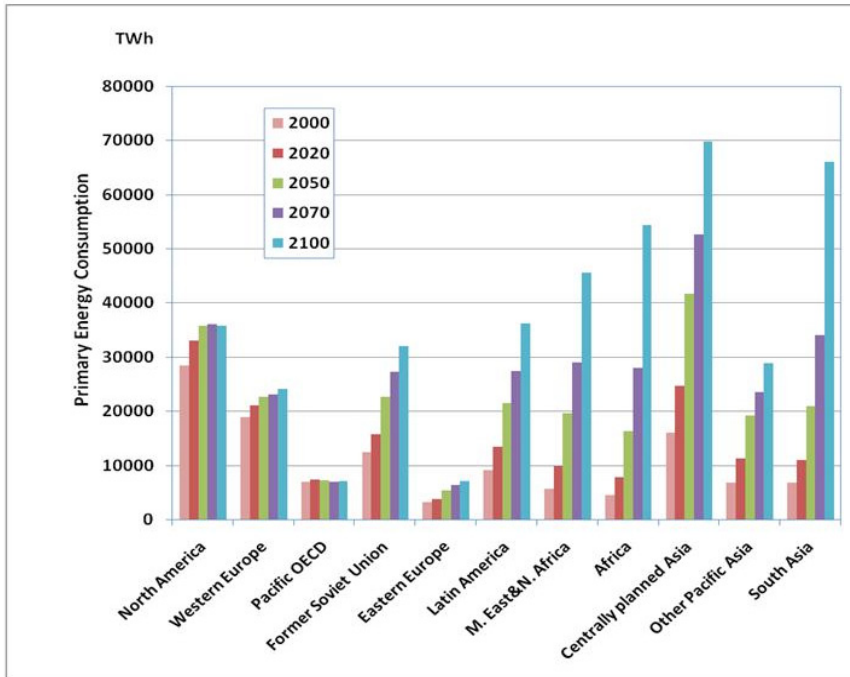


FIG. 1.3. Region-wise primary energy consumption in IIASA-WEC scenario B. Plotted using the data from Ref. [1.32].

In spite of differences in the predictions on the global energy scenario, there is one factor generally common to all of them: they all envisage a gradual shift away from fossil fuel sources by the end of the 21st century. Figure 1.4 shows the past actual use of various energy resources and the projections till the end of this century by the IIASA-WEC scenario B model [1.30]. Important to note in this projection is the substantially growing dependence on non-fossil-fuel resources, for example nuclear and renewables, in the second half of this century, simultaneous with gradual reduction in the dependence on oil and gas. It is important to note that, in this model, the contribution of coal remains more or less constant at the present day value.

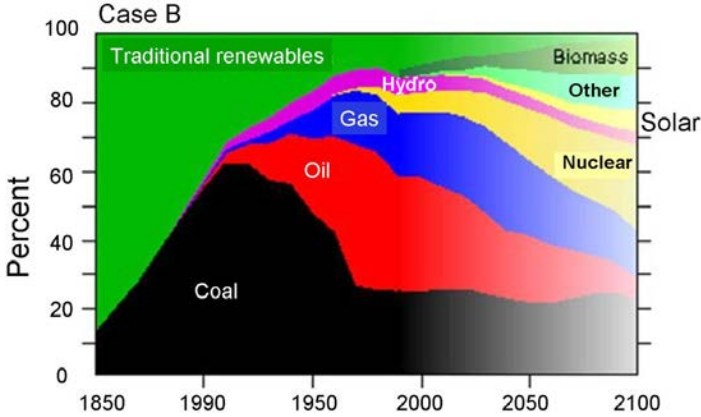


FIG. 1.4. Evolution of primary energy shares, historical development from 1850 to 1990 and projections till 2100, for Case B. Plotted using the data from Ref. [1.32].

However, on the other hand, even though coal will be available in the world for slightly over 150 years, the prospect of countries such as India and China being forced to rely on coal for their energy demand would be disastrous to the environment of the whole Earth, as is clear from the recent discussions on the mounting evidence of an incipient global warming. The world is already experiencing a steady rise in temperature (Fig. 1.5) [1.33] and its effects are already showing in global climate changes caused by changes in flow patterns in global ocean currents, as well as depleting ice layers in the polar and Himalayan regions. Even though, as some argue, there may be uncertainties in long time predictions of climate, it would be foolhardy to assume that the uncertainties would necessarily lead to a favourable situation.

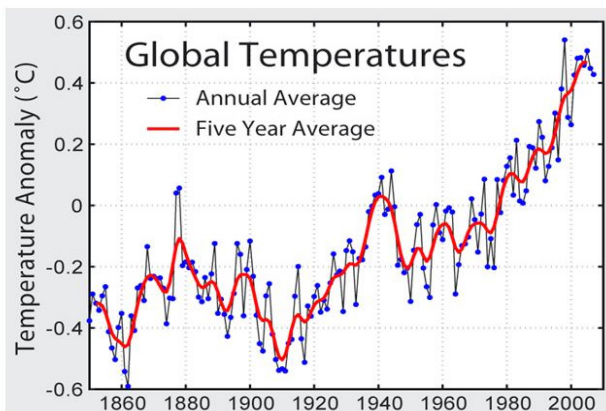


FIG. 1.5. Global average temperature over the last one and a half centuries showing a more or less steady increase over the last fifty years or so. The fluctuations and their cycles can be correlated with various events such as solar cycles [1.33].

However, as we look at nuclear energy as an important primary energy resource, it is important, in view of the uncertainties involved in a very wide acceptance of the utilization of fission power, that we do not put all our nuclear eggs in one basket. We must also look at all advanced nuclear energy technologies. Fusion is one such option. Thus, if one aims at restricting CO<sub>2</sub> emission levels to within 450 parts per million (ppm) (the pre-industrial level being about 280 ppm), as the constraint tightens, the use of coal diminishes and the contribution from other sources increases, with fission and fusion power together playing a dominant role (see Fig. 1.6).

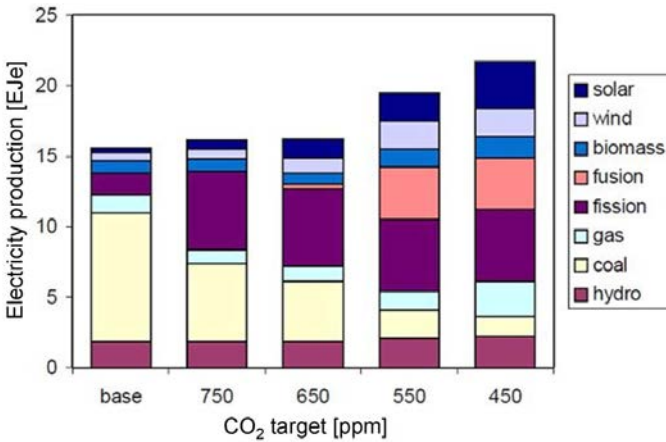


FIG. 1.6. Projections for CO<sub>2</sub> emission constrained energy scenarios in Western Europe in 2100 with a large role of nuclear fusion [1.34]. (1 exajoule-electric (EJe) ~ 277.7 terawatt-hours (TW·h).)

Let us now consider for example the specific case of India. From 1981 to 2000, its GDP has grown at an average rate of 6% and since 2000, because of opening up of the economy through policy decisions, at a faster rate of close to 8%. It has the potential to grow at about 5% even as far as 2050. The ratio of its growth of electricity generation to GDP growth over the past decades has been a steady factor of about 1.2. The total electricity generated in 2002 was about 638 TW·h, of which about 66.7% was through coal and lignite, 19.6% through oil and gas and only about 3% through nuclear. Projections by the Department of Atomic Energy [1.35] predict the electricity production to go up to about 8000 TW·h by 2050, still 47% of which is likely to be resourced from coal. This scenario is very challenging and barely sustainable as this would mean the total carbon emission in India would jump from a level of about 300 metric tonnes of carbon (MtC) today to about 2100 MtC by 2050 (which is about 30% of the global carbon emissions in 2000). By a much more conservative estimate using the ANSWER/MARKAL model [1.36], the total electricity production in India

will increase to about 3000 TW·h by 2050 and about 4300 TW·h by 2100 (which still implies a carbon emission from India by 2100 of about a quarter of the global emission level). A scenario in which the global atmospheric CO<sub>2</sub> concentration is restricted to be within 550 ppm is shown in Fig. 1.7. By this model, the restricted emission scenario can be achieved if fusion starts playing a dominant role beyond 2060 with a share of about 10% by the turn of this century, with about 430 TW·h of fusion electricity produced in India from about 67 GW of installed capacity.

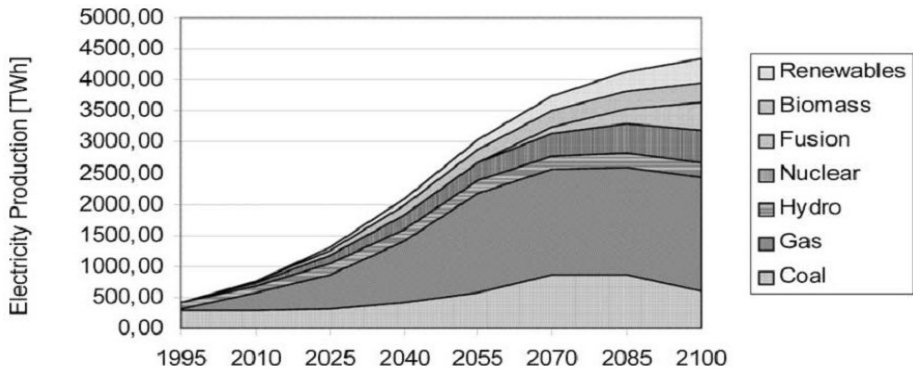


FIG. 1.7. Projections of dependence on different primary energy resources in India with global CO<sub>2</sub> emission restricted to 550 ppm by the year 2100, with India contributing only 7.5% of the global emissions. Reprinted from Ref. [1.36]. Copyright (2010), with permission from Elsevier.

These models show that fusion power is likely to give us a wonderful opportunity to provide a viable and credible solution to the long term sustainable energy needs of the world. It has none of the CO<sub>2</sub> emission problems of fossil fuels. The amount of CO<sub>2</sub> emission in the entire life cycle of fusion reactors (through manufacturing processes of some reactor components), as shown in Fig. 1.8 [1.37], can be up to a factor of 45 times less than that of coal based reactors of the same capacity. It is somewhat more than the CO<sub>2</sub> emission from a comparable fission based nuclear reactor. Thus fusion power, in a way similar to fission power, can alleviate the already deteriorating climatic conditions and prospects of global warming that the world is facing today. In contrast to the renewables, it is energy dense and can therefore be used for satisfying the needs of urban industrial complexes. On the other hand, compared to the conventional fission based nuclear power plants, it has the prospect of considerably reduced long lived radioactive emission problems and inherent operational safety. The biological hazard potential of fission plants (defined in terms of the ratio of the amount of radioactive material in a reactor to the allowed level of concentration in the atmosphere) is several orders of magnitude higher than that predicted for fusion reactors. Some of the common radioactive waste materials in fission reactors, such as <sup>131</sup>I, <sup>90</sup>Sr or <sup>137</sup>Cs, are highly toxic and hazardous, especially

the latter two, which have half-lives of about 30 years, which is long enough to require their absolute containment for hundreds of years. On the other hand, the main radioactive fuel in a fusion reactor, tritium, can easily be discharged from our bodies through metabolism. It is a weak (18.6 keV maximum energy) beta emitter whose radiation can easily be absorbed by a thin sheet of paper [1.37]. As a result, the allowable concentration level of tritium in the atmosphere is 500 times higher than that for  $^{131}\text{I}$ . However, the main potential problems of radioactivity in fusion reactors will be from neutron activated reactor components. Fusion reactors are being designed with carefully chosen low activity materials so as to require containment of less than one hundred years after decommissioning of the reactors. Thus fusion power is likely to get much more social acceptance when it becomes commercial. Moreover, the resources are plentiful to the extent that they are virtually inexhaustible and easily accessible to the entire cross-section of the world population.

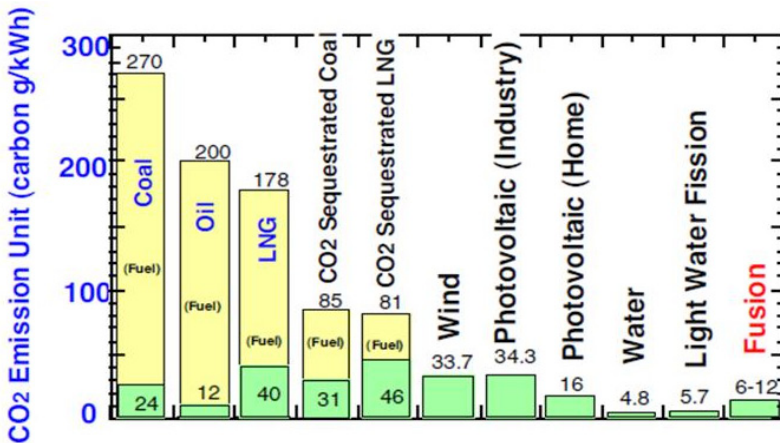


FIG. 1.8. CO<sub>2</sub> emission level of power reactors based on various fuel resources in their entire life cycle, showing fusion reactors as the third lowest CO<sub>2</sub> emitter after hydro and fission reactors [1.37].

It is satisfying to note therefore that the tremendous amount of research and development over the last about 50 years in the field of fusion science and technology has reached a critical stage today. Scientists from some of the world's major nations, namely, China, the whole of the European Union, India, Japan, the Republic of Korea, the Russian Federation and the USA, which together account for more than half of the world's population, have come together to build ITER, the first experimental thermonuclear reactor which will produce energy ten times greater than the input auxiliary heating power. Various countries have national programmes to build demonstration reactors or DEMO (for example in the EU [1.38, 1.39], Japan [1.40], the USA [1.41] and India [1.42]) — some as early as

in 2030, but most likely by 2050 — which will actually supply electricity to the grid.<sup>1</sup>

In conclusion then, in the short term of the next 30–40 years, the world energy scenario is likely to be still dominated by gradually depleting fossil fuels, with nuclear fission and renewables taking a gradually increasing share. During this time fusion energy will establish itself through experiments like ITER and demonstration power plants like DEMO. In the long term, towards the end of this century, however, fusion power is likely to become commercial and play an increasingly dominant role in the world energy scenario.

### 1.3. FUSION BASICS

#### 1.3.1. What is fusion?

The brightest example of fusion around us is provided by the stars and the Sun, which have been burning brilliantly for billions of years using this option. In contrast to nuclear fission, where heavy nuclei like uranium are fragmented and release energy, in fusion one starts with light elements and brings them together so that they may fuse to form heavier elements. The resulting heavier elements have slightly less mass than the fusing elements and this mass difference results in the release of energy. As an example, when deuterium and tritium nuclei (which are the two heavier isotopes of hydrogen with mass numbers 2 and 3 respectively) are brought together, they fuse and form a helium nucleus and a neutron; the mass difference is released as 17.6 MeV of energy. Energy comes out in the form of the kinetic energies of the product nuclei, from which it may be trapped and used for electricity production. For fusion to occur, one has to bring the protons or heavier reactant nuclei (which are positively charged and naturally repulsive) close enough to overcome the electrostatic repulsion, so that the nuclear strong force (a very short range force), which binds the nucleons together in a nucleus, helps them fuse by a quantum mechanical tunnelling process. This is possible when the nuclei are heated to very high *thermonuclear temperatures*, when the kinetic energy of the thermal particles is enough to help

---

<sup>1</sup> However, the 14 MeV neutron fluence in ITER at about 0.5 dpa/a (displacement per atom per year) will be much less than that of DEMO (~20 dpa/a) or other future fusions reactors. Because of this, ITER will not be able to test reactor relevant first wall materials with high neutron irradiation doses. Furthermore, neutron fluxes of pressurized water fission reactors are about 100 times lower than they would be in fusion reactors, and have lower neutron energies. So fission reactors also cannot be used to fully test fusion reactor materials. To specifically address the materials issue, therefore, the International Fusion Materials Irradiation Facility (IFMIF) [1.43] is being launched in a collaboration between Japan, the EU, the Russian Federation and the USA. IFMIF will have an accelerator based D-Li neutron source with fluence of up to 20 dpa/a.

## THE CASE FOR FUSION

them overcome the electrostatic repulsion and come close enough to fuse. For the case of deuterium and tritium nuclei, this requires that a mixture of D-T nuclei be heated to a temperature of the order of  $\sim 10$  keV (i.e.  $\sim 100$  million  $^{\circ}\text{C}$ ); the resulting process is known as thermonuclear fusion.

The energy released through a fusion reaction is much larger than that in chemical reactions, because the binding energy that holds the nucleons in a nucleus together is far greater than the energy that binds atoms and molecules together through electronic linkages. For example, the ionization energy of a hydrogen atom (energy required to strip the single electron from a hydrogen atom) is 13.6 eV — less than one millionth of the 17.6 MeV released in the D-T reaction. Fusion reactions also have an energy density (energy released per unit mass of the reactants) much larger than fission reactions, even though individual fission reactions involving very heavy nuclei are generally much more energetic than individual fusion reactions. Only in direct conversion of mass into energy, for example through matter–antimatter collisions, could more energy per unit of mass than in the fusion reactions be released.

A slow thermonuclear fusion of protons is what mainly powers the Sun and the stars, the tremendous gravitational energy due to the very large mass holding the fusing protons together against the de-confining tendency due to thermal expansion. Uncontrolled fusion reactions in the form of thermonuclear explosions using deuterium and tritium, where the plasma is unconfined, have already been achieved on Earth. Thus there is no doubt that thermonuclear fusion works and produces lots of energy. As it is impossible to produce astronomical masses on the surface of the Earth, the biggest challenge for scientists is achieving fusion in a controlled manner in a confined plasma, which can then be used for electricity production or any other useful application. Controlled thermonuclear fusion research, aimed at converting fusion energy into electric energy, has been carried out around the world for more than 50 years. In spite of the tremendous scientific and technological needs of this field, fusion research has seen a remarkable and steady progress, comparable to some of the fastest growing technical challenges in modern science and technology, such as developments in semiconductor chip manufacture and accelerator research. Tokamak based fusion experiments based on the magnetic confinement fusion concept have also doubled the characteristic confinement parameter, the so called triple product (which we shall describe in detail later), once every couple of years and have already achieved the so called break-even condition where the output energy produced as a result of the fusion reaction is equal to the input energy spent in achieving the reaction. This has culminated in commencement of construction of the ITER device which will produce about ten times more power than the input heating power; ITER is slated to start operations in about a decade from now.

What are the merits of fusion energy, should we succeed in exploiting it? First of all its fuel is plentiful. Deuterium is found mixed up (1 part in 6000) as

heavy water (D<sub>2</sub>O) in natural water. It is virtually inexhaustible. Tritium does not exist naturally because it has too many neutrons and is therefore unstable to beta decay, with a half-life of about 12.6 years. It has to be bred from lithium, which is widely available in the Earth's crust and also in the oceans. Pure deuterium fusion is also possible, although the conditions required for its successful exploitation are more stringent (because of weaker fusion cross-sections) and are therefore likely to be met only in second generation fusion reactors. The fuel is therefore virtually inexhaustible and is likely to last several tens of thousands of years.<sup>2</sup>

Secondly, fusion fuel is readily accessible from everywhere. This gives tremendous energy security to all nations and is to be contrasted with the politically inflammable uneven distribution of fossil fuels such as oil (6% of the nations own more than 66% of the oil wealth of the world).

Thirdly, there are limited radioactive waste problems. None of the fusion reaction products are radioactive in the first place. Fusion neutrons can induce radioactivity but that can be minimized by a clever choice of structural and other materials so that only short lived radioactivity is produced. There is also the prospect of using advanced fuels such as proton–boron which produce essentially neutron-less fusion and hence no radioactivity.

Fourthly, the fusion reaction is inherently safe. There is no danger of runaway reactions, criticality or a meltdown. At a given instant of time the total inventory of fusion materials in the device is just enough to produce the power for a few seconds. This is to be contrasted with fission reactors, where the inventory stored at a given instant is enough to cause a major explosion.

Lastly, there are no dangers of proliferation or of a terrorist group or fringe group running away with key materials which may be put together to form a crude device. The fusion reaction is so difficult to initiate that it needs a major technical establishment such as a magnetic fusion reactor or a laser fusion reactor or an atomic fission device to create conditions under which fusion may be initiated. It is thus completely free from such misuse.

---

<sup>2</sup> It is worth mentioning here that a D-T based 1 GW(e) fusion reactor will burn about 37 kg of D and 56 kg of T annually. It is to be noted that while the D inventory is not an issue, tritium has to be bred in the fusion reactor itself from lithium and cannot be stored indefinitely as it is radioactive with a half-life of 12.6 years. It is to be noted that the accumulated yield of T by all of CANDU's fission reactors will be only about 30 kg in 2025 after more than 40 years of operation. However, with stringent inventory control, and by achieving even a modest net tritium breeding ratio of 1.01 in a fusion reactor, it is possible to achieve a doubling time (the time when one fusion reactor can produce enough excess T to support a second reactor) of less than 5 years [1.44–1.46].

### 1.3.2. Fusion power gain $Q$

Now let us examine the conditions which a reactor successfully giving fusion energy output must satisfy. We first note that we have to invest energy in raising the temperature of the D-T mixture to about 100 million °C. This converts the gas mixture into a plasma, which radiates mainly through bremsstrahlung radiation because of electron–ion and electron–electron encounters. Secondly, if the D-T plasma is diluted by some impurities which are not fully ionized, there is some radiative power loss associated with impurity radiations which cools the electrons and through them the D-T mixture because the electrons and ions are in near thermal equilibrium. In addition to this, if the plasma is confined by magnetic fields, it radiates by synchrotron radiation. The power required to maintain the plasma at 100 million °C is thus related to the power required to sustain the plasma temperature against thermal conduction/convection losses plus the radiative power losses of the above three varieties.

The net power output of a fusion power reactor can be measured in terms of the steady state fusion power gain or the  $Q$  factor defined as the ratio of the fusion power output to the input power, i.e. the auxiliary power supplied from outside to sustain the reaction:  $Q = P_{output} / P_{input} = P_{fusion} / P_{aux}$ . Thus, for fusion power to be successful, the minimum criterion for a fusion power plant is  $Q > 1$ . The state  $Q = 1$  is known as the *break-even* condition, when fusion output power just equals the auxiliary input power. On the other hand, the thermonuclear fusion plasma can also be confined in an ignited state when  $P_{aux} \rightarrow 0$  or  $Q \rightarrow \infty$ , which happens for the D-T fusion reaction, for example, when the output alpha particles from the fusion reaction lose all of their energy in keeping the thermonuclear plasma hot and thus the alpha power accounts for the transport and radiation losses. In such a scenario, the fusion reaction is completely self-sustained by the alpha power and no external heating power is required. Now, the net heating power in the plasma can be obtained through the power balance:

$$P_{heat} = P_{aux} + P_{\alpha} - P_{Br} = P_{trans} + dW_p / dt \quad (1.1)$$

where  $P_{\alpha}$  and  $P_{Br}$  are the power in the alpha particles and bremsstrahlung losses respectively and are given by:

$$P_{\alpha} = n_D n_T \langle \sigma v \rangle E_{\alpha} V_p = n_e^2 \langle \sigma v \rangle E_{\alpha} V_p / 4 \quad (1.2)$$

$$P_{Br} = C_B T^{1/2} n_e^2 V_p \quad (1.3)$$

where it is assumed that  $n_D = n_T = n_e$  for a 50/50 D-T mix,  $\langle \sigma v \rangle$  is the average collision cross-section of the reactants,  $E_{\alpha}$  is the energy carried by the alpha particles (3.5 MeV) and  $V_p$  is the plasma volume.  $P_{trans}$  is the total power

lost through various transport processes and  $dW_p / dt$  is the power required to increase the internal (kinetic) energy of the plasma, with  $W_p = 3n_e k_B T_e V_p$ ,  $k_B$  being the Boltzmann constant. The last term  $dW_p / dt$  in Eq. (1.1) is applicable only in transient cases. The transport losses are related to the total energy content through the energy confinement time  $\tau_E$ , defined as:

$$\tau_E = W_p / (P_{heat} - dW_p / dt) \quad (1.4)$$

Thus the power balance equation Eq. (1.1) can be written in terms of the energy confinement time  $\tau_E$  and the fusion gain  $Q$  (note that  $P_{fusion} = 5P_\alpha$ ) as:

$$n_e^2 \langle \sigma v \rangle E_\alpha \left( \frac{Q+5}{4Q} \right) - C_B T_e^{1/2} n_e^2 = \frac{3n_e k_B T_e}{\tau_E} + \frac{d}{dt} (3n_e k_B T_e) \quad (1.5)$$

Thus for a steady state condition, i.e.  $d/dt = 0$ , Eq. (1.5) yields for the very important product of density times energy confinement time:

$$n_e \tau_E = \frac{3k_B T_e}{\frac{\langle \sigma v \rangle E_\alpha (Q+5)}{4Q} - C_B T_e^{1/2}} \quad (1.6)$$

Thus the break-even condition  $Q = 1$  leads to the critical minimum condition for a fusion plasma, usually known as the Lawson criterion [1.47]. Equation (1.6) gets slightly modified as follows if the conversion efficiencies of input power sources ( $\eta_{in}$ ) and that of output thermal energy to electric energy ( $\eta_{out}$ ) are considered [1.48]:

$$n_e \tau_E = \frac{3(1 - \eta_{in} \eta_{out}) k_B T_e}{\eta_{in} \eta_{out} \frac{\langle \sigma v \rangle E_\alpha (Q+5)}{4Q} - C_B (1 - \eta_{in} \eta_{out}) T_e^{1/2}} \quad (1.7)$$

Typically one can assume  $\eta_{in} \eta_{out} \sim 1/3$  and then the optimum temperature for break-even for a 50/50 D-T plasma occurs at  $T_e \sim 15$  keV; thereby the Lawson criterion for the break-even condition becomes:

$$n_e \tau_E = 10^{20} \text{ s} \cdot \text{m}^{-3} \quad (1.8)$$

If one wants to consider the fusion reaction for a range of temperatures, one has to use the variation of the fusion cross-section with temperature. Roughly speaking, the fusion rate  $\langle \sigma v \rangle$  varies with temperature as  $T_e^2$  and hence the Lawson criterion for a D-T plasma at  $T_e = 15$  keV may be rewritten in the form:

$$n_e T_e \tau_E > 1.5 \times 10^{21} \text{ keV} \cdot \text{s} \cdot \text{m}^{-3} \quad (1.9)$$

For the D-D reaction, the cross-section for fusion is smaller than that for D-T and the fusion energy yield per reaction is also less, so that the critical condition is a temperature of 400 million °C and an  $n_e \tau_E$  product given by  $n_e \tau_E > 10^{22} \text{ s} \cdot \text{m}^{-3}$ .

Lawson also gave the minimum temperature required for a fusion reactor, which is the threshold temperature at which the fusion power density just exceeds the bremsstrahlung radiation. Thus, we see from Fig. 1.9 that the minimum temperature for D-T reactions is  $T > 3\text{keV}$ , and for D-D reactions,  $T > 20\text{keV}$ .

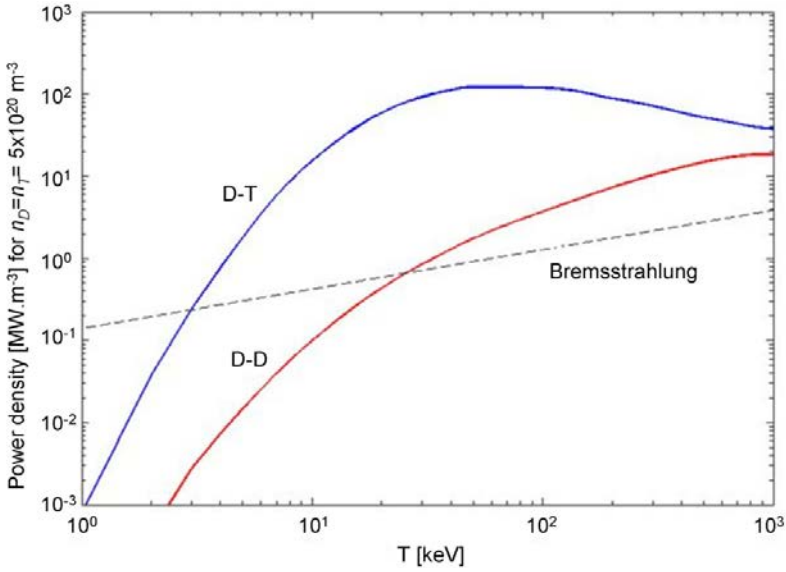


FIG. 1.9. Power density for a density of  $n_D = n_T = 5 \times 10^{20} \text{ m}^{-3}$  (plotted with data from Ref. [1.49], p. 45).

We can also see from Eq. (1.6) that the ignition criterion ( $Q \rightarrow \infty$ ) becomes:

$$n_e \tau_E = \frac{3k_B T_e}{\langle \sigma v \rangle E_\alpha / 4 - C_B T_e^{1/2}} \quad (1.10)$$

When the plasma attains the ignited state, no external heating is required and the fusion reaction is self-sustained through the energy of the fusion products till the plasma burns up all the fuel as long as the necessary condition for ignition is maintained. For ignition, the optimum temperature for a 50/50 D-T fuel at  $n_e = 10^{20} \text{ m}^{-3}$  is  $T_e = 30 \text{ keV}$

$$n_e T_e \tau_E > 8.1 \times 10^{21} \text{ keV} \cdot \text{s} \cdot \text{m}^{-3} \quad (1.11)$$

Here of course we have assumed that most of the radiated energy is in the form of bremsstrahlung radiation (true for fusion plasmas at  $\sim 10\text{--}20$  keV) and thus  $P_{rad, \min} = P_{Br}$ ; otherwise there are terms like  $-C_{cy} B^2 T_e / n_e$  also for cyclotron radiation in the denominator in Eqs (1.6) and (1.10) which we have neglected here.

### 1.3.3. Fusion reactions

The most convenient, though not necessarily most efficient fusion reaction to carry out in present day magnetic fusion devices like tokamaks is that between deuterium (D) and tritium (T) (Fig. 1.10), both isotopes of hydrogen, one with one neutron and the other with two neutrons in their nucleus respectively (normal hydrogen has only one proton and no neutron in its nucleus). The D-T fusion is most conveniently achievable because the collision cross-section of the D-T fusion reactions is the highest and occurs at the lowest temperature.

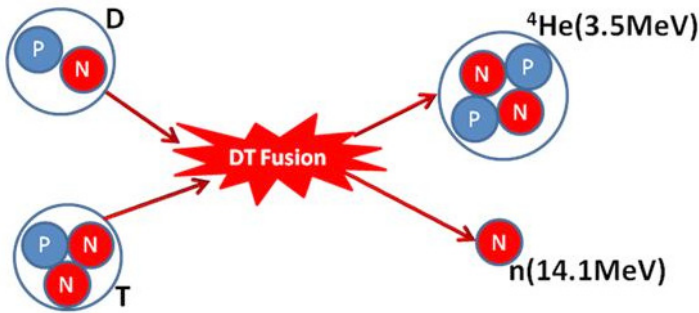


FIG. 1.10. Schematic of a D-T fusion reaction.

The reasons for this can be visualized in the following way. In a nucleus, the protons and the neutrons are bound together by the nuclear strong force, which is of very short range; as a result the binding is primarily between immediately neighbouring nucleons. Thus the nucleons which are completely surrounded by neighbouring nucleons, for example those in the interior of a nucleus, are more strongly bound than those on the surface. Thus the nuclear *binding energy* is the energy required to separate the nucleons. Its magnitude is given by the Einstein formula  $\Delta E = \Delta m c^2$ , where  $\Delta m$  is the small mass difference between the nucleus and the sum total of constituent nucleon masses and  $c$  is the speed of light. Since for the smaller nuclei, the ratio of their volume to surface area is small, for them the binding energy per nucleon due to the strong force is generally smaller than that of the large sized nuclei. This is because for the large sized nuclei, the interior nucleons are *more completely* surrounded by neighbouring nucleons and the binding energy per nucleon approaches a limiting value corresponding to that

## THE CASE FOR FUSION

of a fully surrounded nucleon. On the other hand, the electrostatic force between protons is long range and follows the *inverse square law*. Thus to add a proton to a nucleus, one has to overcome the so called *Coulomb barrier* experienced by the approaching proton due to the repulsive electrostatic force from all other protons already within the nucleus. As these two forces oppose each other in a nucleus, the net resulting binding energy per nucleon generally increases with the size of the nucleus, up to the nuclei of the elements iron and nickel. Beyond these nuclei, the binding energy per nucleon starts decreasing for heavier nuclei, until it becomes negative for very heavy ones, which are then naturally unstable, fissile and radioactive. Thus  $^{56}\text{Fe}$ , the most common isotope of iron with 26 protons and 30 neutrons, is one of the most stable nuclei with a binding energy of 8.790 MeV/nucleon and is formed as the end product of most fusion and fission chain reactions. This is the reason why  $^{56}\text{Fe}$  is the most abundant element in the universe and is found at the core of the Sun and the stars.<sup>3</sup>

As the deuterium and the tritium nuclei have the lowest binding energy per nucleon, the kinetic energy required for them to have the highest probability for fusion to occur is the lowest. This is represented by the collision cross-section curves, which are plotted in Fig. 1.11 for the D-T reaction as well as for some of the other common fusion reactions. In this figure, the kinetic energy of the reacting particles increases from left to right, while the vertical axis (in barns) represents the probability of a collision between two particles with that kinetic energy resulting in a fusion reaction. Thus the D-T reaction has the largest cross-section at about 100 keV, while for the other reactions, the peak probability occurs at much higher temperature as also they have much lower probability; for example, the p- $^{11}\text{B}$  reactions have the largest cross-section, of about 1.2 barns (about 5 times less than the peak D-T cross-section) at 642 keV.

---

<sup>3</sup> Although technically  $^{62}\text{Ni}$  is slightly more stable with a binding energy of 8.794 MeV/nucleon it is less abundant than  $^{56}\text{Fe}$  as it is not the natural end product of the fusion and fission chain reactions.

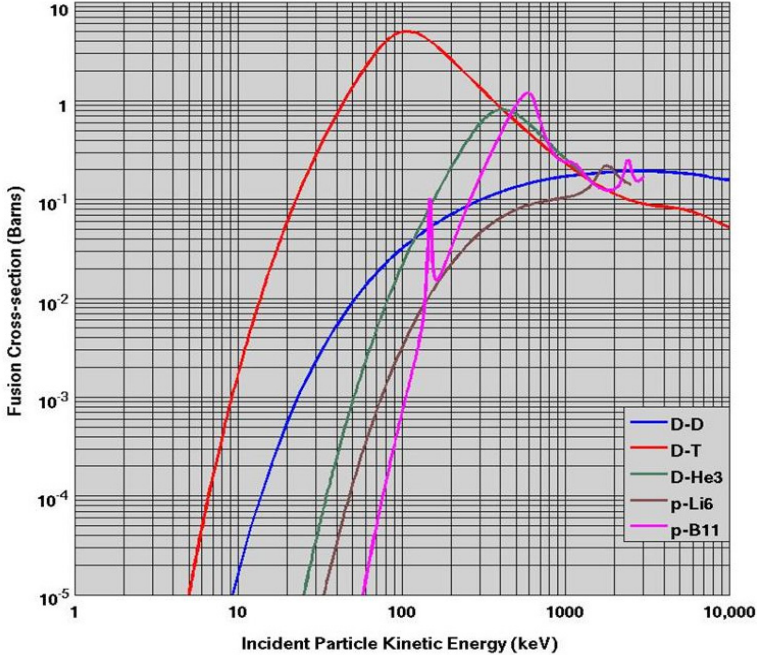


FIG. 1.11. Fusion cross-sections of various fusion reactions as a function of kinetic energy of an incident  $D$  or  $p$  on a stationary target. The data for the  $D$ - $D$ ,  $D$ - $T$ ,  $D$ - $He^3$  and  $p$ - $Li^6$  curves are taken from the ENDF B-VII database [1.50] for incident deuterium/proton, while that for  $p$ - $^{11}B$  is taken from Ref. [1.51]. The curve for  $D$ - $D$  represents a sum over the cross-sections of the reaction branches.

TABLE 1.1. LIST OF THE MOST FAVOURABLE FUSION REACTIONS

1.	$D + T$	$\rightarrow$	$^4He$ (3.5 MeV) + $n$ (14.1 MeV)
2.	$D + D$	$\rightarrow$	$T$ (1.01 MeV) + $p$ (3.02 MeV) (50%)
		$\rightarrow$	$^3He$ (0.82 MeV) + $n$ (2.45 MeV) (50%)
3.	$D + ^3He$	$\rightarrow$	$^4He$ (3.6 MeV) + $p$ (14.7 MeV)
4.	$T + T$	$\rightarrow$	$^4He + 2 n + 11.3$ MeV
5.	$^3He + ^3He$	$\rightarrow$	$^4He + 2 p$
6.	$^3He + T$	$\rightarrow$	$^4He + p + n + 12.1$ MeV (51%)
		$\rightarrow$	$^4He$ (4.8 MeV) + $D$ (9.5 MeV) (43%)
		$\rightarrow$	$^4He$ (0.5 MeV) + $n$ (1.9 MeV) + $p$ (11.9 MeV) (6%)
7.	$D + ^6Li$	$\rightarrow$	$2 ^4He + 22.4$ MeV
8.	$p + ^6Li$	$\rightarrow$	$^4He$ (1.7 MeV) + $^3He$ (2.3 MeV)
9.	$^3He + ^6Li$	$\rightarrow$	$2 ^4He + p + 16.9$ MeV
10.	$p + ^{11}B$	$\rightarrow$	$3 ^4He + 8.7$ MeV

### 1.3.4. Fusion fuels

The D-T reaction is not necessarily the most desirable fusion reaction as one of its major disadvantages is the production of a 14.1 MeV neutron in each reaction. The neutrons get absorbed in the surrounding fusion chamber (for example in tokamaks in the surrounding mostly metallic structures such as blankets and vessels). The effect of neutron activation on metals is roughly that they become hardened, brittle, as well as radioactive. This has two important effects: first, it becomes necessary to use low activation materials inside the vacuum chambers of fusion devices, and second, the lifespan of the machine components surrounding the fusion plasma gets seriously limited. Thus, even though the first generation of fusion devices will depend on D-T reactions because of the ease of achieving them, future devices may use more efficient reactions resulting in less neutron activation. Table 1.1 contains a list of fusion reactions that are most favourable.

Any of the above reactions can in principle be the basis of future fusion reactors for power production. However, the level of difficulty in achieving them depends on several factors. In the first generation tokamak based fusion reactors like ITER, a mixture of D-T particles is confined in a magnetic trap and heated to high energies (about 10–20 keV mean), where the particles have a distribution of kinetic energy (called a Maxwellian distribution), with a small fraction of them attaining 40 keV and fusing.

In addition to the temperature and cross-section of the reactions, one must also consider the total energy of the fusion products  $E_{fus}$ , the energy carried by the resultant charged particles  $E_{ch}$  and the atomic number  $Z$  of the non-hydrogenic reactant. One interesting case is the D-D reaction, which has two branches, one resulting in a T and a proton, the other in a  $^3\text{He}$  and a neutron, both branches having a 50/50 probability. The T can further undergo a D-T reaction and the  $^3\text{He}$  can undergo a D- $^3\text{He}$  reaction. However, while the T in fact gets completely burnt up in a deuterium plasma and adds its energy further to the reaction chain, the optimum temperature for D- $^3\text{He}$  reactions is much higher than that of D-D reactions and is not expected to contribute to the overall fusion energy. Thus one can calculate the overall D-D fusion energy as  $E_{fus} = 12.5$  MeV and the energy in charged particles as  $E_{ch} = 4.2$  MeV.

Another important parameter in the fusion reactions is the *neutronicity* of the reaction, which is measured as  $(E_{fus} - E_{ch}) / E_{fus}$ , the fraction of the fusion energy released through neutrons. Neutronicity is an important indicator of the magnitude of the problems associated with neutrons, such as radiation damage, biological shielding, remote handling and safety. The higher the neutronicity, the more complex are the problems associated with neutron generation. In Table 1.2 some of the important parameters for the four most important fusion reactions are tabulated. For the D-D and D-T reactions the neutronicity is easy to calculate,

while for the last two reactions, where this calculation would give zero, the values quoted are rough estimates based on side reactions that produce neutrons in a plasma in thermal equilibrium. Sometimes, even though the main reaction may not produce neutrons, one of the chain reactions involving one or more constituents of the fuel or resulting ions may produce neutrons. A fusion reaction is considered aneutronic if the overall neutron energy from all possible chains is less than 1% of the fusion energy.

TABLE 1.2. SOME IMPORTANT PARAMETERS OF THE FOUR MOST IMPORTANT FUSION REACTIONS

Fuel	Z	$E_{fus}$ [MeV]	$E_{ch}$ [MeV]	Neutronicity	$\langle\sigma v\rangle/T^2$	$2/(Z+1)$	Reactivity	Lawson criterion	Power density [W.m <sup>-3</sup> kPa <sup>-2</sup> ]
D-T	1	17.6	3.5	0.80	$1.24\times 10^{-24}$	1	1	1	34
D-D	1	12.5	4.2	0.66	$1.28\times 10^{-26}$	2	48	30	0.5
D- <sup>3</sup> He	2	18.3	18.3	~ 0.05	$2.24\times 10^{-26}$	2/3	83	16	0.43
p- <sup>11</sup> B	5	8.7	8.7	~ 0.001	$3.01\times 10^{-27}$	1/3	1240	500	0.014

A unique aspect of the D-D reaction is that there is only one reactant, which is an important factor when calculating the reaction rate. In any of these four reactions, the reactants should also be mixed in the optimal proportions. This is the case when each reactant ion plus its associated electrons accounts for half the pressure. Assuming that the total pressure is fixed, this means that the density of the non-hydrogenic ion is smaller than that of the hydrogenic ion by a factor  $2/(Z+1)$ . Therefore the rate for these reactions is reduced by the same factor, on top of the differences in the values of  $\langle\sigma v\rangle/T_e^2$ . On the other hand, because the D-D reaction has only one reactant, the rate is twice as high. Thus for non-hydrogenic fuels, due to the fact that they require more electrons, which account for nearly half the pressure without having any role in the fusion reaction, the reaction rates are lower by a factor of  $2/(Z+1)$ . It is usually a good assumption that the electron temperature will be nearly equal to the ion temperature. However, in certain modes of operations, for example in tokamaks, there is a possibility that the electrons could be maintained at a substantially lower temperature than the ions. In such a case, known as the so called *hot ion mode*, there is no reduction due to the charge number. Thus for D-D reactions, as any particle can react with any other particle, there is a net gain by a factor of 2.

Thus in Table 1.2 the values for *reactivity* are found by dividing  $1.24 \times 10^{-24}$  by the product of  $\langle \sigma v \rangle / T_e^2$  and  $2/(Z+1)$ . The *reactivity* is indicative of the factor by which the other reactions occur more slowly than the D-T reaction under comparable conditions. The Lawson criterion values are the reactivity weighted with  $E_{ch}$  and give an indication of how much more difficult it is to achieve ignition with these reactions, relative to the difficulty for the D-T reaction. The last column in Table 1.2 gives the fusion power density achieved in the different reactions. Thus we see that even though the D-T reaction has the highest fusion power density as also it is the easiest to achieve, it also has the highest neutronicity. Thus D-T reactions need the maximum amount of neutron shielding, have to necessarily use low activation materials and suffer from lifetime issues for critical machine components.

On the other hand, the so called advanced fuels like D-<sup>3</sup>He or p-<sup>11</sup>B have the great advantage of being very low in neutronicity. In the p-<sup>11</sup>B reactions, for example, small amounts of neutrons and gamma radiations are indeed generated through intermediate chains in the p-<sup>11</sup>B fusion as also X rays through bremsstrahlung radiation. However, with careful design and selection of fuel concentrations, it would be possible to limit the overall neutron energy to less than 0.2% and both neutron as well as X ray and gamma doses to acceptable levels of occupational doses through moderate amounts of shielding.

Similarly, the D-<sup>3</sup>He reactions also directly produce no neutrons; however, as the optimum temperature for these reactions is more than 50 keV, the ensuing D-D reactions (half of them) produce a triton and a proton, with the other half producing a <sup>3</sup>He and a 2.45 MeV neutron. Further, the resulting D-T reactions produce the 14.1 MeV neutrons. Although the D-D reactions can be reduced by optimally selecting the D fuel concentration, overall neutron energy in D-<sup>3</sup>He reactions cannot be reduced to below several per cent, because of which D-<sup>3</sup>He reactions cannot be considered as aneutronic.

However, the major problem for advanced fuels is that one needs to heat the fusion plasma to much higher  $\beta$  (thus higher  $n$  and  $T$ ) values compared to the D-T plasmas, as also much higher confinement times so as to achieve a high enough Lawson factor. This may pose the major road block for fusion reactors based on advanced fuels, unless novel concepts and designs for stable configurations emerge to make that possible. Moreover, since most of the energy in D-T fusion is extracted from the neutrons that are captured in the surrounding blankets, it has the advantage that one has to extract heat volumetrically from the reactor blankets. On the contrary, to have reactors based on the low (or zero) neutronicity fusion reactions, one has to extract very large amounts of surface heat — heat that is conducted to the divertor targets by the plasma particles. Of course at the high temperatures of these fusion reactions, a significant amount of the plasma energy is also radiated out through synchrotron radiation in the microwave range and it should be possible to develop technologies to trap this

microwave radiation and convert it into electricity. The X rays emitted through bremsstrahlung radiation, on the other hand, can be absorbed in layers of metal foils. Nevertheless, the divertor targets for the aneutronic reactions would have to bear an unprecedented amount of heat load, and great strides in ultra-high heat flux material development and very significant R&D in other related technologies will be necessary. However, not enough research has gone into exploring these avenues to totally rule out advanced fuel based fusion devices in the future. Thus, even though initial fusion reactors will be based on D-T fusion because it is easily achieved, future fusion devices may use more innovative fuels.

### 1.3.5. Direct conversion to electricity

Since many of the fusion reactions give energy to charged particles, it is possible to convert fusion energy directly to electricity through various methods such as induction effects or through electrostatic effects decelerating charged particles in an electric field. It is true that in the first generation of D-T reaction based fusion reactors, as 80% of the fusion energy goes into the neutrons, electricity generation will have to be mostly through conventional steam turbines using the heat generated by the neutron absorption. However, in future fusion devices based mainly on aneutronic fusion like  $p\text{-}^{11}\text{B}$ , it would be possible to convert about 80% of the charged particle energy directly into electricity. The fraction of fusion energy which goes into the charged particles also gets released in the form of microwave radiation through synchrotron radiation and X rays through bremsstrahlung radiation. The microwaves can be used either to drive a current in the plasma itself (as required in the case of tokamaks) [1.52, 1.53] or suitable technology can be evolved to capture the microwave energy and convert it into electricity. The X ray energy can also in principle be converted into electricity through photoelectric effects by making the rays pass through arrays of conducting foils. However, due to deep penetration of the X rays, this might need many layers of metallic foils to absorb all the energy and would require clever reactor designs [1.54].

## 1.4. APPROACHES TO FUSION

To achieve fusion on Earth, one has to create a plasma of the fusion reactants of sufficiently high temperature and density, and also hold it confined for a sufficiently long time away from any surrounding material walls. There are two main approaches for achieving this: magnetic confinement and inertial confinement. Magnetic confinement fusion is the more developed of the two approaches and is presently the most promising path to developing future fusion reactors based on this concept, especially as they can confine the plasma in a steady state for long durations. The ITER device, presently under construction at

Cadarache in France, will be the first fusion reactor producing 500 MW of fusion power, 10 times more than the input auxiliary heating power. It would also have plasma discharges of 3000 s duration in the non-inductive phase of operations, a first step to steady state operations.

The inertial confinement fusion (ICF) approach, on the other hand, works primarily in a pulsed fashion, achieving thermonuclear fusion through micro-explosions of reactant targets induced by high power laser or particle beams at a high repetition rate. The two largest ICF experiments in the world presently are the National Ignition Facility (NIF) at the Lawrence Livermore National Laboratory in the USA, which was commissioned in March 2009, and the Laser Megajoule (LMJ) facility in France, scheduled for construction completion in 2014. Both these facilities are designed to achieve ignition conditions. However, given the rather limited driver conversion efficiency ( $\sim 10\%$ ) of the lasers and the conversion efficiency of  $\sim 35\text{--}40\%$  of fusion to electric power needed for power production, ICF facilities would need a fusion gain of about 100–200 for net power production. Hence, ICF reactor systems for power generation seem to be more challenging.

#### 1.4.1. Magnetic confinement fusion

In magnetic confinement fusion, one utilizes the electromagnetic properties of the charged plasma particles to trap them away from material walls in a specifically designed magnetic field configuration called a *magnetic bottle*. This exploits the ability of a steady magnetic field to dramatically restrain the motion of the charged particles in a plasma across the magnetic lines of force, while allowing them to move freely along them. Research and development in the area of magnetic confinement fusion has given rise to a variety of confinement configuration concepts.

The most successful way of trapping the plasma particles along the magnetic field lines has been achieved by magnetic confinement fusion based on the tokamak concept. In a tokamak, the plasma is formed in the shape of a torus or a doughnut, through a specially designed magnetic field configuration. Such a configuration can be formed, for example, as shown schematically in Fig. 1.12, by turning around a solenoidal set of ring-like coils, in the form of a torus, thus forming a *toroidal* magnetic field. However, a purely toroidal magnetic field cannot confine the plasma particles as the curvature of the field lines produces opposite particle drifts for the ions and the electrons, leading to a charge separation; the consequent electric field leads to a rapid loss of the plasma to the walls. To prevent the charge separation, one needs an additional component of the magnetic field turning around on the minor cross-section of the torus — the *poloidal* magnetic field. The poloidal magnetic field in tokamaks is formed by passing a toroidal current in the plasma itself. The resultants of the toroidal and

poloidal magnetic field lines spiral infinitely around the torus in nested toroidal surfaces forming globally closed *magnetic flux surfaces*. The pitch of the field lines is defined as the safety factor  $q$ , so called because of its immense importance in determining MHD plasma stability. Such a toroidal plasma configuration under toroidal and poloidal magnetic fields, however, experiences a hoop force, trying to expand the plasma torus radially outward. To achieve radial equilibrium, one has to provide vertical magnetic fields through vertical field coils, which are typical current carrying rings concentric with the torus.

The combination of the toroidal and poloidal magnetic fields leads to the concept of toroidal magnetic bottles in which one can confine the hot plasma far away from material walls in a stable way for long durations. In these nested magnetic surfaces, the hot plasma in the core is thermally insulated from the colder plasma near the edge. The charged particles can move across the magnetic surfaces only by collisions with other charged particles or through turbulence. However, they typically cover a distance millions of times the length of the vessel before they reach the material walls and are lost. Detailed reviews of tokamaks as well as other toroidal magnetic confinement configurations can be found in several publications [1.55–1.59].

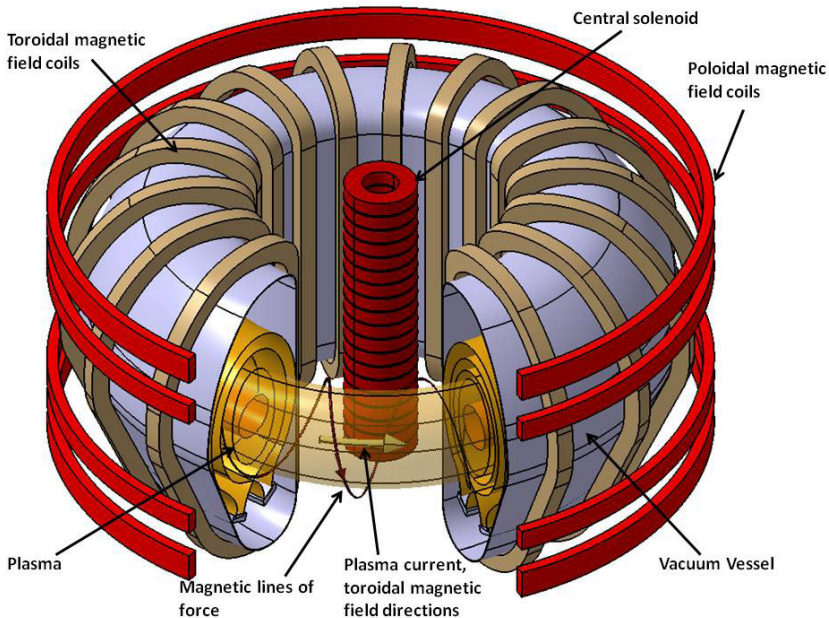


FIG. 1.12. Schematic of a tokamak.

The plasma current in most tokamaks is driven inductively through transformer action. The primary of a “central solenoid” is placed concentrically

at the centre of the torus, with the plasma itself (being made of charged particles) acting as the secondary. However, inductive effects being inherently transient in nature, such tokamak plasma current drive is also transient. Steady state tokamak discharges can be achieved by driving plasma current non-inductively by several means. Injection of high power energetic neutral particle beams and/or of radiofrequency waves at characteristic resonant frequencies, imparting momentum selectively to the ions or electrons, has so far proved very successful in driving currents in tokamak-like devices. A significant part of the plasma current (theoretically 100%) can also be driven by the self-generated *bootstrap current* — the name given to a current produced by radial diffusion in the plasma itself in the presence of density gradients through momentum exchange between trapped and passing particles. Since the plasma pressure profile peaks around the tokamak centre and the bootstrap current is proportional to the radial gradient of pressure, the bootstrap current is also necessarily off-axis and zero at the centre. Hence some additional current drive is still required to drive the current at the plasma centre in largely bootstrap current driven devices. Future advanced tokamaks are being designed in which most of the plasma current will be bootstrap driven, so as to minimize the energy spent in auxiliary current drive.

In magnetic confinement configurations, the magnetic forces have to act against the plasma pressure to confine the plasma. The maximum magnetic forces that one can apply today in such configurations are limited by technological constraints: the maximum magnetic field strength achieved today in cryogenically cooled superconducting coils is about 16 T (on the surface of the conductor), although in future, development of high Tc superconductors holds the promise to exceed this limit. The plasma pressure, on the other hand, is proportional to the product of the density and the temperature. The magnetic field applies a magnetic pressure on the plasma and the ratio of the plasma pressure to the magnetic pressure is generally referred to as the plasma beta ( $\beta = \langle nT \rangle / (B^2 / 2\mu_0)$ ,  $B$  being the magnetic field strength,  $n$  and  $T$  being the plasma density and temperature). The plasma  $\beta$  has great importance regarding the stability of magnetically confined plasmas. The maximum  $\beta$  values achieved in magnetic fusion plasmas are around a few per cent, implying that the plasma pressure is always much smaller than the magnetic field pressure. Since the temperature required for achieving fusion reaction is fixed ( $T \sim 10$  keV), and the plasma pressure must be low, the plasma density must fall in a certain range — which is less than one billionth of solid density. The Lawson criterion, on the other hand, requires a confinement time of the order of a few seconds. (On the timescale of single particle motion in the confining magnetic field, one second is a very long time!)

The magnitude of achieved  $\beta$  is essentially limited by the efficiency of the means by which one heats the plasma to high temperatures and/or by the *efficiency* of the magnetic bottle — how well it is able to retain the thermal energy

that the plasma is fed with. The plasma can be heated by Joule heating by driving internal plasma currents (ohmic heating as in tokamaks, reversed field pinches, etc.), which is, however, limited to temperatures of up to about 1 keV. This is because, as the plasma resistivity decreases with increasing temperature, ohmic heating becomes ineffective. Further heating to fusion relevant temperatures of tens of keV is possible by either injecting high energy neutral particle beams of isotopes of hydrogen (NBI) across magnetic fields, or by injecting high power radiofrequency (RF) waves with frequencies which resonate with natural plasma frequencies such as the ion cyclotron (ICRF), electron cyclotron (ECRF) or lower hybrid (LHRF) frequencies. However, even though all these auxiliary techniques have been successful in heating the plasma to fusion relevant temperatures, auxiliary heating has also led to significant degradation of the energy confinement. This happens because the confinement is largely determined by turbulent processes in plasmas, which are significantly amplified by the heating processes. The energy confinement time, which is dependent on several machine and plasma parameters, crucially increases with increase in the plasma major radius, i.e. the machine size. This has necessitated the construction of very large devices like ITER to achieve  $Q > 1$  operation, almost twice as large as any of the existing tokamaks.

However, over the past few decades, rapid strides have been made in the improvement of plasma confinement in tokamaks by either shaping of the plasma poloidal cross-section or operating the tokamaks in novel regimes of parameter space. For example, with the aim of achieving higher  $\beta$  and higher plasma current in tokamaks, it has been found that the optimum configuration is to have a non-circular plasma configuration, typically a D-shaped one, characterized by an *elongation* and a *triangularity*. Such a D-shaped plasma cross-section is provided by suitably shaping the poloidal magnetic field configuration by an additional set of poloidal field (PF) coils, which are also concentric with the torus. Moreover, it has been found that the energy confinement time critically depends on the plasma properties near the edge region of the tokamak plasma, and hence the edge region in tokamaks has to be handled with care. In the next subsection we will see evidence of the tremendous improvement in the confinement properties of tokamak plasmas by a careful control of the plasma edge. In the first generation of tokamaks, the plasma edge used to be *limited* where the outermost boundary is restricted by a material *limiter* schematically shown in Fig. 1.13, with which the plasma is in contact. However, in such configurations, a considerable amount of impurity is released into the plasma due to erosion of the material limiter caused by bombardment of the hot plasma particles on it, which leads to large impurity radiation losses. A much better configuration in terms of energy and particle exhaust was achieved when the plasma cross-sections became *diverted*, where the outermost magnetic field flux lines are opened up to make them strike on a chosen *divertor target*. In this configuration, the divertor bears most

of the thermal loads carried by the plasma particles transporting across the last closed magnetic flux surface, which then flow along the open field lines on to the divertor target. One can reduce the energy of the impinging particles by suitably maintaining the density in the *divertor region*, i.e. the region close to the divertor target, shown schematically in Fig. 1.13. Even though modern tokamaks use divertor targets, the plasma is still initiated from a limited configuration and then gradually brought to a divertor configuration through plasma shaping by changing appropriately the poloidal field coil currents. Strong pumping of the exhaust from the divertor region can prevent the impurities from going back to the plasma. Thus the deleterious effects of the impurities in plasma confinement could be reduced in such configurations. Divertors are also very efficient in removing the helium ash from the plasma.

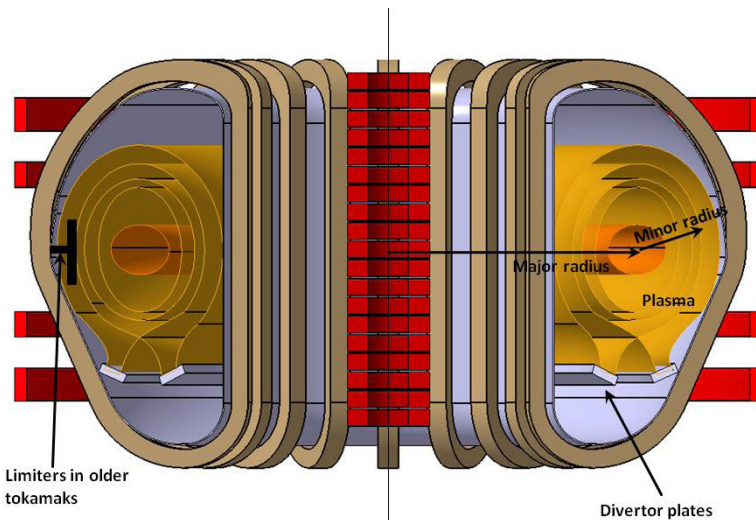


FIG. 1.13. Vertical cut section of the tokamak schematic shown in Fig. 1.12, showing the major tokamak components and parameters.

However, tokamak plasmas are subject to various kinds of instabilities and perform reliably only when operated within certain boundaries in the parameter space, for example below certain density or current limits. Close to or above these limits, the plasma current generally suffers sudden disruption due to internal plasma instabilities. This leads to large induced currents and undesirable electromagnetic forces on the surrounding machine components. However, many methods have now been found to increase the domain of reliable operation of tokamaks, avoiding plasma disruptions.

In this context, it is worth mentioning the significant progress in research with the other major toroidal confinement concept, namely the *stellarator*. In stellarators, depicted schematically in Fig. 1.14, the poloidal magnetic field is

produced by careful profiling of the magnetic field topology through complex non-planar toroidal field coils. The stellarator is toroidally non-axisymmetric (helical), and closed toroidal magnetic surfaces are formed in three dimensions by fields entirely produced by the externally wound coils. Thus there is no need to drive plasma currents in stellarators, which eliminates the danger of macroscopic disruptive instabilities and makes them very attractive for reactor concepts. Work on large stellarators such as LHD in Japan [1.60] and Wendelstein-7X [1.61] in Germany and on innovative stellarator concepts in the USA are especially encouraging since stellarators form the most advanced toroidal confinement concept after tokamaks. Some of the major shortcomings of stellarators are the complex technology of large coils producing 3-D magnetic configurations, poorer (than tokamak) particle confinement properties due to large deviations of particle orbits from 3-D flux surfaces, the associated intense neo-classical transport of the plasma and alpha particles and the as yet relatively insufficient database on the turbulent flux of heat and particles.

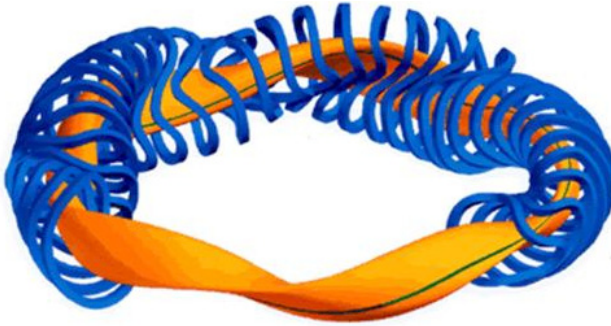


FIG. 1.14. Schematic of stellarator magnetic field coils and plasma configuration (courtesy of Ref. [1.62]).

#### 1.4.1.1. Progress in tokamak based magnetic confinement fusion research

Overall, tokamak based magnetic confinement fusion has registered impressive progress in key areas of reactor relevance in the last 10–15 years. Significant improvement of the transport properties, operating density and stability of the tokamak plasmas have been achieved in this period. A number of improved confinement regimes were discovered; as a result, the fusion triple product  $nT\tau_E$  and  $Q_{DT}$  equivalent have increased to about  $1.5 \times 10^{21}$  keV·s·m<sup>-3</sup> and about 1.25 respectively in separate plasma discharges in JT-60U. Many D-T experiments have been conducted on JET and TFTR, which has produced fusion

## THE CASE FOR FUSION

powers of 16 MW and 11 MW respectively in these two machines (see Fig. 1.15), with the JET device achieving<sup>4</sup>  $Q_{DT} \sim 1$  in 50/50 D-T operations.

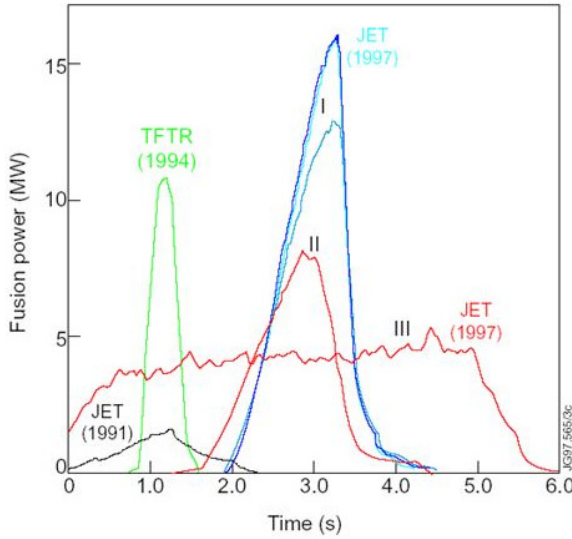


FIG. 1.15. Fusion power produced in JET and TFTR experiments [1.63].

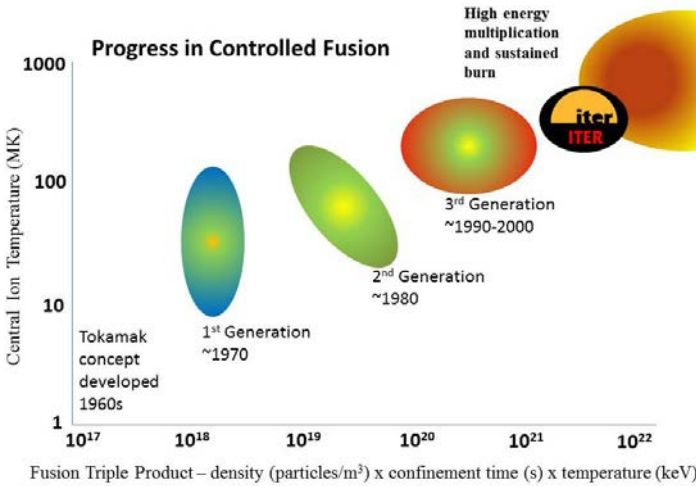


FIG. 1.16. Progress in achieved central ion temperature and fusion triple product.

<sup>4</sup> The JET 16MW discharge actually achieved a maximum  $Q_{DT}$  of 0.64. However, this was in a transient discharge, which in steady state conditions would indeed amount to about unity if one takes into account the factor of  $dW/dt$  in the fusion gain calculation ( $Q_{DT} = P_{fusion} / (P_{aux} - dW/dt)$ ).

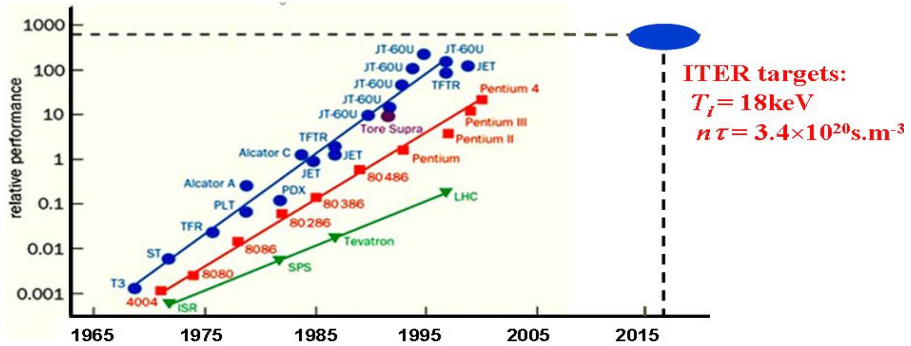


FIG. 1.17. Development of tokamak based fusion research measured in terms of the fusion product of fuel density times energy confinement time ( $n\tau$ ) as compared to semiconductor chip development (Moore's Law) as well as that of accelerator research. Courtesy of J.B. Lister (CRPP-EPFL, Lausanne, Switzerland), and also Ref. [1.64].

It is worth considering here the progress of magnetic confinement fusion research over the last about half a century depicted in Fig. 1.16 in terms of the fusion triple product achieved in various tokamak devices. Since the start of tokamak experiments in the 1960s, this product has increased by more than three orders of magnitude. In fact the progress of magnetic confinement fusion research based on the tokamak concept has been faster than the Moore's Law (Fig. 1.17) which is traditionally applied as a measure of development of semiconductor chips.

Thus, tokamaks are today the most advanced of the toroidal confinement systems, which makes them the most promising candidate for the first generation of fusion reactors. This has culminated in the start of construction of the ITER device (Fig. 1.18) based on the tokamak concept. Scientists and engineers from the European Union, China, India, Japan, the Republic of Korea, the Russian Federation and the USA have come together in an unprecedented international collaboration to build the ITER device at Cadarache, in the south of France. ITER is aimed at demonstrating the scientific and technical feasibility of fusion reactors and intends to operate largely at  $Q = 10$  conditions, while the possibility of achieving controlled ignition operating conditions is also foreseen. It is to be noted here that it is not essential for fusion reactors to operate at ignition conditions. Considering that reactors would have an overall energy efficiency (ratio of final electric energy pumped to the grid to the fusion energy produced in the devices) of about 35%, operation with  $Q$  between 20 and 40 would be sufficient for fusion reactors to be a viable energy option.

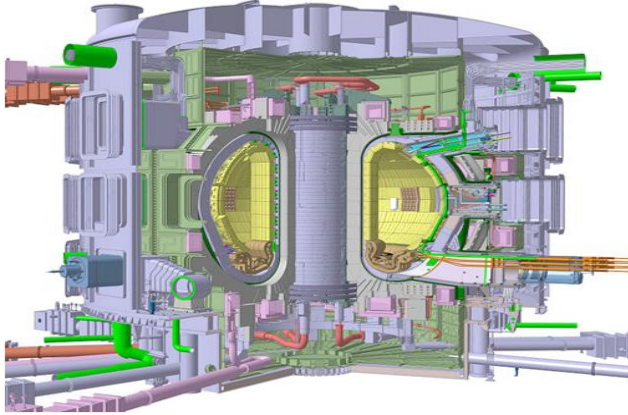


FIG. 1.18. Schematic of the ITER tokamak [1.10].

### 1.4.2. Inertial confinement fusion

Inertial fusion is a completely different approach to a fusion reactor. If a pellet of solid fusion fuel is compressed to very high densities and a portion of it is heated to the temperatures required for ignition, it is possible to generate net fusion power before the pellet blows itself apart in a micro-explosion. In this approach confinement is not achieved by external fields, but by the inertia of the hot fuel that keeps it together for a finite time (hence the name inertial confinement). Compression is accomplished by heating just the surface of a spherical hollow shell target uniformly from all sides, whereby the intense heating of the surface creates an inward implosion of the fuel as the surface layer ablates and explodes outward. The driver of the compression process can be either a giant laser pulse or a pulsed heavy ion beam from a particle accelerator.

Let us first consider here a few elementary aspects of inertial fusion; details may be obtained in Refs [1.65, 1.66]. In order to reuse the containment chamber of the micro-explosion again and again, the typical fusion output energy must be about 100 MJ; if this is repeated with a frequency of a few Hz, we have a fusion reactor of several hundreds of MW fusion power. Working out the size of a typical D-T fusion pellet at cryogenic (solid) densities and fusion temperatures ( $\sim 10$  keV) which would produce this much fusion energy by complete burning, we get a pellet radius of about 1 mm. The typical disassembly time of the pellet is the time it takes a rarefaction sound wave to travel from the surface of the pellet to its interior and is of the order of a fraction of a nanosecond in a D-T plasma at fusion temperatures. The gain factor

$$G = \eta_c \times f_b \times \left( \frac{E_f}{E_{in}} \right) \quad (1.12)$$

depends on the coupling efficiency ( $\eta_c$ ), the fractional burn ratio ( $f_b$ ) and the ratio of the maximum fusion energy output ( $E_f$ ) to the input energy content ( $E_{in}$ ) and can be maximized by optimizing each of these ratios. Its desirable value is given by the condition of low circulating electric power ( $\sim 25\%$ ) in the reactor, giving  $\eta_d \times G > 10$  (or  $G = 70-200$  for a 5–15% driver efficiency  $\eta_d$ ). The fractional burn ratio of the pellet is determined by the ratio of fusion reaction time and the disassembly time and is given by

$$f_b = \frac{\rho R}{(H_f + \rho R)} \quad (1.13)$$

where  $\rho$  is the fuel density and  $H_f = (8m_f c_s) / \langle \sigma v \rangle$ , where  $c_s$  is the sound speed given by  $c_s = \sqrt{2k_B T / m_f}$  and  $m_f$  is the average mass of the fuel ions (for an equimolar D-T plasma,  $m_f = 2.5m_p$ ,  $m_p$  being the proton mass) [1.66]. Thus the factor  $\rho R$  of the pellet determines the fractional burn ratio. For inertial fusion, the basic ignition condition is attained by heating a fuel with a  $\rho R$  of about  $4 \text{ kg}\cdot\text{m}^{-2}$  to a minimum temperature of about 5 keV, corresponding to a fractional burn of about 3.5%. However, ignition alone is inadequate for inertial fusion, which must additionally overcome a factor of  $\sim 10$  in hydrodynamic coupling efficiency and another factor of  $\sim 10$  in driver efficiency. To overcome these inefficiencies, ICF capsule implosions will require a global fuel  $\rho R$  of approximately  $30 \text{ kg}\cdot\text{m}^{-2}$ , resulting in a fractional burn of about 30%. This  $\rho R$  criterion in inertial fusion is like the Lawson criterion in magnetic fusion. It can obviously be achieved by having either a low density, large radius configuration, or a high density, small radius configuration. Simple estimates can be made that show that the required driver energy scales approximately as the inverse of the square of the fuel density. Therefore, in order to minimize the driver size required for inertial fusion, compression of the D-T fuel to very high densities (about  $200-400 \text{ g}\cdot\text{cm}^{-3}$  of D-T density for a mm size pellet, which is about 1000–2000 times the normal solid density) will be required. It also turns out that energetically it takes an order of magnitude less energy to compress the fuel to the required densities (where matter is degenerate) than it takes to bring the whole assembly to fusion ignition temperatures. The strategy which is therefore adopted is one where the entire matter is compressed to required densities but only a small hot spot is heated to ignition temperatures. The size of the hot spot is chosen in such a manner that the alpha particles produced in the hot spot can come out and heat neighbouring layers of the fuel, leading to the propagation of a burn wave producing fusion reactions throughout the whole fuel.

Schematically the four important phases associated with a pellet implosion are as follows: as the driver energy impinges on the initially solid matter of the capsule, this material is transformed into a plasma with a temperature of

the order of a few keV, the capsule is ablated and the heated plasma expands outward with a velocity of about  $100\text{--}1000\text{ km}\cdot\text{s}^{-1}$ . As a reaction, the remaining portion of the spherical capsule is accelerated to about  $300\text{--}500\text{ km}\cdot\text{s}^{-1}$  towards the centre, compressing and heating (via mechanical work) the thermonuclear fuel. If, at the culmination of the implosion, specific conditions associated with the compressed fuel configuration are attained, thermonuclear ignition at the centre and subsequent propagation of a “thermonuclear burn wave” to the whole fuel will occur, leading to large burnup. The final density achieved by the fuel during a capsule implosion depends on: (1) the external driving pressure, which must reach  $10^8\text{ atm}$ ; (2) the resistance of the target matter to compression (low isentrope should be kept); and (3) the development of hydrodynamic instabilities and asymmetry during the implosion process. The external pressure is determined by the ablated material and the incident driver energy flux. Although compression is energetically attractive and reduces the driver size required for efficient fuel burnup, high gain also requires a high temperature region (referred to as the hot spot) for ignition to occur. The hot spots form during the final stages of the inertial confinement fusion capsule implosion, provided that hydrodynamic instabilities do not mix them with the surrounding cold fuel. For D-T fuel, the capsule can be considered as transparent to the  $14.6\text{ MeV}$  neutrons produced in the fusion reaction (especially near the time of ignition). Therefore, the self-heating of the hot spot is done predominantly by the alpha particles released from the D-T reactions and by the work by the implosion. For effective self-heating, the areal density of the hot spot must be comparable to the alpha particle range, which turns out to be  $0.3\text{ g}\cdot\text{cm}^{-2}$  at a temperature of  $10\text{ keV}$ . The formation of a hot spot within the cold main fuel is the key scientific issue for inertial fusion. A crucial requirement for the generation of the central hot spot is a high degree of symmetry of the spherical implosion, which demands uniform irradiation and control of certain hydrodynamic instabilities.

Another concept in inertial fusion systems, which has been quite active during the last decade or so, is the heavy ion accelerator driven inertial fusion system. In this concept the laser driver is replaced by a heavy ion beam, which can be produced with a much higher electrical efficiency and is also excellent at heating solid density plasmas by classical Coulomb collisions. It also tries to eliminate a major concern about neutron contamination of final focusing optics in laser driven configurations by the use of magnets in accelerator driven configurations. Earlier concerns were related to transport of the beams over significant distances, problems due to space charge effects, etc. The recent focus of these experiments is towards reduction of target chamber size and hence the cost of the experiments, for example by the use of “liquid protected” target designs allowing highly compact target chambers. The compact target chambers allow focusing magnets to be placed closer to the target, resulting in reduced focal spot size and hence a smaller driver, which finally results in a large cost reduction.

It is instructive to make a comparison between fusion plasmas in magnetic confinement systems and those encountered in inertial fusion energy systems. Inertial fusion plasmas produce energy in a pulsed manner whereas magnetic confinement plasmas are essentially steady state. This is why the fusion gain in inertial fusion is expressed in terms of ratio of total fusion energy release to input consumed energy (and not as a ratio of output to input power). In magnetic confinement fusion, the particle densities are very small,  $\sim 5 \times 10^{20} \text{ m}^{-3}$  in fusion grade devices. In comparison, air density at atmospheric pressure is about  $5 \times 10^{25} \text{ m}^{-3}$ . Thus, the plasma in a magnetic confinement device is like a vacuum for all practical purposes! This is understandable. In magnetic fusion the plasma pressure is contained by a ten times larger magnetic pressure and since the containment fields are limited to a few tesla by the present technology limits of superconducting magnets, the plasma pressure is limited to 10 atm and the plasma density to near high vacuum densities of the order of  $5 \times 10^{20} \text{ m}^{-3}$ . On the other hand, the ICF plasma produces enormous pressures of the order of  $10^{12}$  atm and particle densities of the order of  $5 \times 10^{31} \text{ m}^{-3}$ . In magnetic confinement, particle and energy confinement times have to be in the range of 1–10 s, which is indeed a very long time compared to single particle gyration times in a magnetic field. It is determined by many complicated factors such as geometry and turbulent processes in the plasma and is often impossible to predict or even determine empirically. On the contrary in inertial fusion, the confinement times required are very small, of the order of a fraction of a nanosecond, and are essentially guaranteed by virtue of inertia.

#### *1.4.2.1. Progress in inertial confinement fusion research*

The results of ICF experiments performed over the last two decades have formed the basis for the design of the ignition experiments National Ignition Facility (NIF) and Laser Megajoule (LMJ).

NIF, currently in operation at the University of California's Lawrence Livermore National Laboratory, is a stadium sized facility containing a 192 beam, 1.8 MJ, 500 TW, 351 nm laser system together with a 10 m diameter target chamber with nearly 100 experimental diagnostics. NIF is being built by the Department of Energy, United States National Nuclear Security Administration, and when completed will be the world's largest laser experimental system, providing a national centre to study inertial confinement fusion and the physics of matter at extreme energy densities and pressures. NIF's 192 laser beams will compress fusion targets to conditions where they will ignite and burn, liberating more energy than required to initiate the fusion reactions. NIF experiments will allow the study of physical processes at temperatures approaching 100 million K and 100 billion times atmospheric pressure.

NIF was fully commissioned in March 2009 when its 192 laser beams delivered a record of 1.1 MJ of laser energy in the target chamber. By December 2008 the NIF team had already delivered 1.005 MJ of  $1\omega$  infrared and 626 kJ of  $3\omega$  ultraviolet energy to the target chamber. (NIF's main laser produces laser light in the infrared range of frequencies, which is commonly known as  $1\omega$ . The final optics assembly of NIF converts this laser frequency to green light ( $2\omega$ ) and finally to ultraviolet ( $3\omega$ ). The ultraviolet laser light has the maximum efficiency in compressing NIF's fuel capsules.) In these commissioning activities, 540 kJ of  $3\omega$  energy was produced in 96 beams — exceeding the project completion energy criterion. During this commissioning process, 207 TW of laser beam power has been injected into the Target Chamber Center in a 2 ns pulse in 96 beams, meeting the 200 TW peak power requirement.

The LMJ facility under construction in France is the largest inertial confinement fusion facility being built outside the USA and is designed to deliver on target 1.8 MJ and 550 TW of 350 nm ultraviolet light. Completion of the LMJ facility is expected in 2014 (originally 2008) and the system will be able to deliver 600 shots per year. The target chamber will be 10 m in diameter and a (cryogenic) high precision target holder is being developed. A prototype experiment (Ligne d'Integration Laser, LIL) consists of a group of 8 laser beamlines (out of 240 for LMJ) and a 4 m diameter target chamber. It started to operate in 2002. First results have been obtained on one beamline of LIL with pulses of 18 kJ at 1053 nm and 7 kJ of ultraviolet, shaped as a 20 ns prepulse followed by a 3 ns main pulse, all in accordance with the expectations. The LMJ experiment is complemented by vigorous efforts in numerical simulation, increasing the present computational capability by a factor of 20.

However, as mentioned before, due to the poor driver efficiency (conversion from electric to laser energy), conventional ICF experiments would need very large fusion gains ( $\sim 100$ ) to be attractive for power generation. Nevertheless, a more recent development of the 'fast ignition' concept has the promise to dramatically reduce the incident laser power requirement, which has again made ICF experiments interesting for power generation. In this approach, the heating and compression phases of the implosion are decoupled — the target is first compressed in the conventional way using a driver laser system, and then when the imploding target reaches maximum density, a second ultra-short pulse ultra-high power petawatt (PW) laser delivers a single pulse focused on one side of the core, starting the ignition process. A number of experiments are currently under way to explore the fast ignition concept, the most prominent being the GEKKO XII facility in Japan and the proposed HiPER facility of the EU. If the fast ignition approach becomes successful, it could dramatically reduce the total energy required to be delivered at the target. For example, whereas NIF uses 192 ultraviolet laser beams of a total energy of 1.8 MJ, the driver of the proposed

HiPER facility would be 200 kJ and the heater 70 kJ, yet the predicted fusion gain in HiPER is even higher than in NIF.

## 1.5. SOCIOECONOMIC PERSPECTIVES

We now turn to certain socioeconomic issues which are relevant to the acceptability of developing thermonuclear fusion as an alternative energy source of the future. These issues are related to public perception of the environmental impact of the normally operating reactor as well as a reactor subject to potential accident scenarios, cost comparison with other energy alternatives and spin-offs to other fields of interest.

### 1.5.1. Environment, safety and non-proliferation

#### *1.5.1.1. Emissions in normal operation*

The safe confinement of fusion reactor inventories and the minimization of releases during normal operation, possible accidents, decommissioning and storage of waste, are major objectives in fusion power plant design. Besides tritium, the other source of radioactivity in the plant is the intense flux of fusion neutrons penetrating into the material surrounding the plasma and causing activation. Fusion power stations will have an extremely low density of fuel inventory inside the chamber holding the fusing plasma; hence their power production stops a few seconds after fuelling is stopped. Fusion reactors are not associated with any greenhouse gases and they would have low levels of residual power density arising from the decay of neutron activated materials in their structure after the termination of burn. These favourable generic features lead to substantial safety and environmental advantages, but the full exploitation of these advantages will depend upon the details of design and materials selection. A number of reactor studies have been carried out, especially in the EU, the USA and Japan. They generally differ substantially in their gross power, major radii, aspect ratio and power density, etc., although detailed safety and environmental analyses have been performed for most of them. The foundations of all the analyses of safety and environmental impacts were based on detailed and comprehensive calculations of neutronics, activation and derived quantities.

Three confinement barriers are foreseen: vacuum vessel, cryostat and outer building. Small fractions of the radioactive materials are released during normal operation. The amounts depend strongly on design characteristics such as cooling medium, choice of structural materials and blanket design. Several studies on normal operation doses to the general public have been performed. According to one such study, presented in detail in Ref. [1.67], the releases during normal operation for two different plant models are summarized in Table 1.3. The

expected doses to the most exposed individuals of the public would stay well below the internationally recommended limits [1.42] and amount to less than 1% of the naturally occurring dose rate.

TABLE 1.3. DOSES TO THE PUBLIC DUE TO NORMAL OPERATION EFFLUENTS FOR TWO DIFFERENT FUSION PLANT MODELS

	Model 1	Model 2
<b>Doses to the most exposed public from gaseous effluents</b> [ $\mu\text{Sv}$ per year]	<b>0.28</b>	<b>0.003</b>
<b>Doses to the most exposed public from liquid effluents</b> [ $\mu\text{Sv}$ per year]	<b>0.95</b>	<b>0.11</b>

*1.5.1.2. Possible accidents*

Detailed accident scenarios have been analysed in which different methods (bottom-up and top-down) are applied to guarantee a complete list of the accident sequences. Reactivity excursions are for several reasons not possible in a fusion power plant. Therefore, the most severe accidents are typically related to failures of the cooling system or confinement systems. Even without any cooling, temperatures in the structural materials will stay well below the melting temperature and keep the confinement barriers intact. During the most severe internal accident in a fusion plant the expected dose to the most exposed individuals of the public would stay in the range of the annually occurring natural radiation ( $\sim 1 \mu\text{Sv}$ ) [1.67–1.70].

As a worst case scenario it was assumed that the complete vulnerable tritium inventory (roughly 1 kg) of the fusion plant is released at ground level. The initiator of such an accident could only be very energetic outside events such as an airplane crash on the plant. Even if the worst weather conditions are assumed, only a very small area, most likely within the perimeter of the site, would have to be evacuated [1.34, 1.68, 1.69].

*1.5.1.3. Waste*

All the radioactive material produced in a fusion plant is neutron induced. Detailed analysis of the amount and composition of the fusion power waste has been performed [1.15, 1.71, 1.72]. The time evolution of the radiotoxicity of the waste is shown in Fig. 1.19. The plant model assumed is based on available materials. The figure shows a rapid decrease in radiotoxicity once the plant is

shut down. The time evolution of the fusion waste is compared with the time evolution of the waste from a PWR fission plant and with the radiotoxicity of ash in a coal-fired power plant. The radiotoxicity of the waste of fission plants hardly changes on the timescale of a few hundred years.

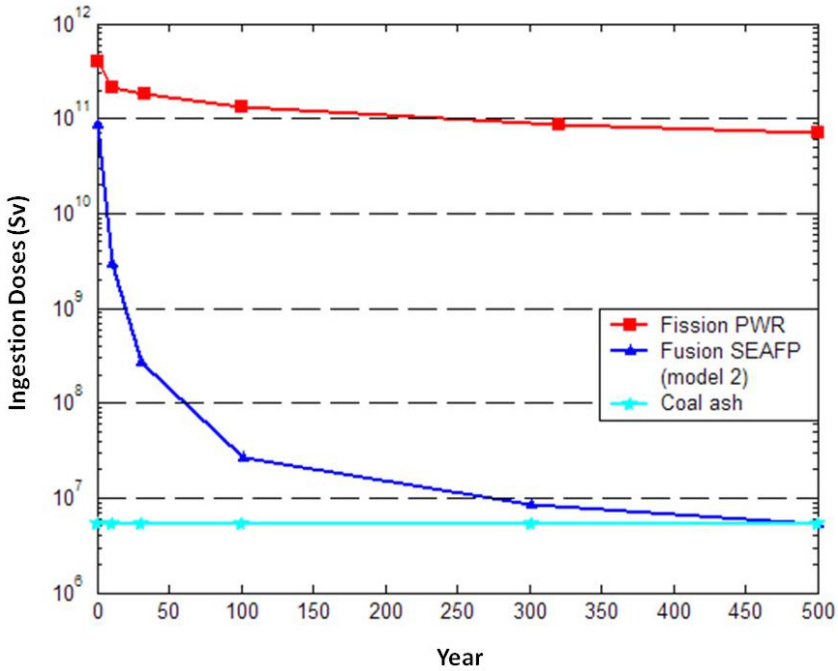


FIG. 1.19. Development of radiotoxicity for a fusion plant, a fission plant and the ash of a coal plant. It is assumed that all the plants produce the same quantity of electricity. The volume of coal ash is of course 2–3 orders higher [1.71].

### 1.5.2. Cost comparison with other sources of energy

Power production technologies based on fusion belong to the class with low ‘external’ costs, comparable with solar and wind based technologies. In the last decade, several models have been developed to estimate the cost of power produced by fusion based technology. Like any other conventional source of energy, a fusion power source would involve two kinds of costs.

#### 1.5.2.1. Direct costs of fusion power production

The ‘direct’ costs comprise the contributions from constructing, fuelling, operating and disposing of the power plants. The estimation of direct costs

requires a deep understanding of fusion physics and technology, hence this work is generally performed by fusion experts. However, the economic methodology and calculations applied by them are standard, as recommended by several international agencies, and have been verified by non-fusion experts. On the other hand, the external costs have mainly been estimated by non-fusion experts. One such estimate has been carried out by EFDA-SERF [1.69], derived by a computer model, dividing the plant into about eighty systems that are individually costed. This costing model was benchmarked against the costs of the proposed large fusion experiment ITER, which have been derived in very detailed studies, mainly conducted by industry, and in independent, parallel efforts by the ITER Parties. The total capital cost, including that of interest rates during construction, was combined with estimated replacement costs, other operating costs, payments into a decommissioning fund and assumptions on availability, to obtain the cost of electricity. This was done in a standard manner, the ‘levelized cost’ methodology, which is used for example in OECD and IAEA studies. Figure 1.20 shows the breakdown of the cost of electricity resulting from a typical set of assumptions. The prediction of the absolute cost of fusion generated electricity in more than fifty years from now requires in particular a realistic assessment of the uncertainties. A large number of calculations were therefore carried out, covering ranges of assumptions for the key physics and technology parameters affecting the economic performance of a power plant.

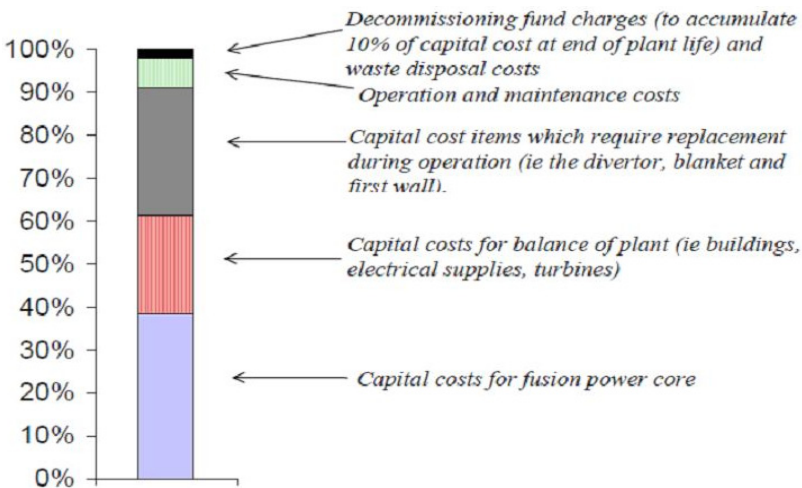


FIG. 1.20. Composition of the cost of electricity from a fusion power plant. Fuel costs, which are very small, are included under operation and maintenance. Reprinted from Ref. [1.69]. Copyright (2010), with permission from Elsevier.

There have been several estimates of the cost of electricity (CoE) of fusion electricity. The major cost of a fusion power plant is the cost of construction as

the fuel cost would be negligible in comparison. The target cost of construction according to these estimates is about 2200–3750 euro/kW(e) (kW(e) = kilowatts electrical), while the target normalized CoE (ratio of cost of fusion electricity to the cost of electricity of a coal plant of the same power capacity) is about 0.7–1.5 [1.37]. Thus even though the expected maximum target direct cost of fusion electricity is about 50% greater than those of coal (without emission abatement costs) or fission, it becomes competitive with ‘clean coal’ when emission abatement costs are included. Renewables vary greatly in their cost prospects, their range, and their capability to contribute to baseload power production. Fusion electricity is found to be competitive in production costs with typical renewables, but can provide, in contrast to most of the latter, steady baseload power without additional energy storage costs. However, it should be noted that current projections may not be adequately dealing with certain realities which influence real costs; these are: likely availability of fusion power plants affecting real costs, likely political decision making influencing real schedules, likely economic and regulatory environments strongly affecting introduction of fusion energy, etc.

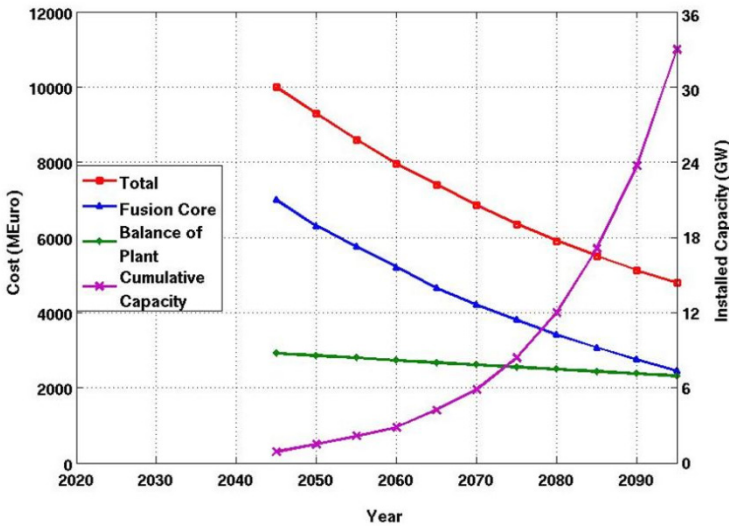


FIG. 1.21. Learning curve for fusion power (for 1 GW(e) plants). (Figure adapted from Ref. [1.71] assuming first commercial fusion power plant around 2045.)

Moreover, the collective construction and operation experience is expected to lead to considerable cost reduction owing to accumulated learning processes [1.34, 1.71]. Learning curves describe the correlation between the cost reductions and the cumulated installed capacity. The slope of the curve — the so-called progress ratio — gives the cost reduction for a doubling of the capacity. A

progress ratio of 0.8 is assumed for the novel components in the fusion core. This ratio is well within the values generally experienced in industry; possible physics progress is also included. Figure 1.21 shows the expected cost development with time [1.71, 1.73]. Thus, the cost evolution of the total fusion plant suggests that the initial cost of fusion powered electricity would be relatively high, mainly because of the high cost of construction of the reactors. However, with continued effort to develop more cost effective technologies and accumulative learning, it is likely to come down in the early part of this century to within the target cost, making the cost of fusion electricity close to those from other conventional sources and hence affordable.

### *1.5.2.2. External costs of fusion power production*

The direct costs of electricity generation, calculated as described above, do not include costs such as those associated with environmental damage or adverse impacts upon health. In the case of some present sources of electricity, these 'external' costs are substantial.

A methodology for evaluating, in a standardized way, the external costs of electricity generation by different fuel cycles had been previously developed for the European Commission in the framework of the 'ExternE' project, which involved more than 40 different European institutes from nine countries [1.74].

The ExternE methodology is a bottom-up methodology, with a sitespecific approach, considering the effects of an additional fuel cycle located in a specific place. It assesses the entire life, fuel cycle and closure of a power plant. This includes materials manufacturing, construction, operation of the plant, dismantling, site restoration and disposal of waste. At each stage, factors such as hazardous chemical or radioactive emissions, road accidents, occupational accidents, accidents at the plant exposing the public to risks, and occupational exposure to hazards are considered. Even effects such as the destruction of visual amenity are evaluated. The adverse effects are quantified in monetary terms and summed to produce an estimate of the total external costs. This implies that goods which are usually neither traded nor priced need to be valued. The approach involves, evidently, significant uncertainties in such issues as the impact of CO<sub>2</sub> emissions on climate and the dose-response relationships, and raises controversies in the economic valuation of adverse health effects and deaths. It also poses the question of how to cost, at the moment of power generation, health consequences arising in the relatively distant future. For the present studies, such costs were attributed in full as if arising at the moment of power generation, without any discounting, taking a social, rather than a commercial, viewpoint.

Under the Joule III programme of the European Union, the ExternE project had generated a large set of comparable and validated results, covering more than 60 individual power plant cases, for 15 countries and 12 different fuel

cycles. A wide range of technologies had been analysed, including fossil fuels, fission power and renewables. Under the SERF1 and SERF2 programmes this methodology was extended to include fusion, evaluating the externalities for a hypothetical power plant situated at Lauffen, a city in the vicinity of Stuttgart, Germany. The fusion specific data were initially taken from the results of the European Safety and Environmental Assessment of Fusion Power (SEAFP), for the two power station concepts studied in SEAFP [1.70], and later updated to include a further power plant model of favourable characteristics. The main conclusions of the studies [1.34, 1.70] are summarized in Fig. 1.22, which shows the calculated external costs, per kilowatt-hour of electricity generated, of electricity from coal, gas, fission, biomass, photovoltaics, wind and fusion [1.9]. All the numbers shown are subject to significant uncertainty. Because the external costs associated with global climate change are particularly uncertain, these are displayed separately.

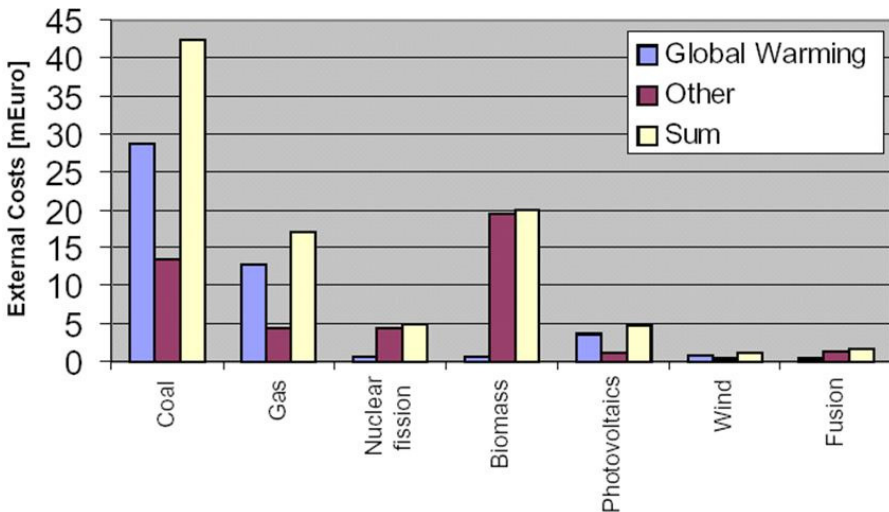


FIG. 1.22. External costs per kWh of energy production. Taken from Ref. [1.34], drawn using the data from Ref. [1.75].

### 1.5.3. Public acceptance of fusion

Sociological studies within SERF also investigated “Fusion and the public opinion”. With large scale commercial applications some 50 years in the future, fusion energy production and the associated benefits and risks are not yet a matter of public debate. Empirical sociological studies were therefore either restricted to groups with above-average prior knowledge of fusion (structured interviews with science journalists, environmental journalists, fusion and fission

experts, members of environmental movements), or worked with focus groups, which received introductory briefings from both fusion advocates and critics. Both approaches showed differing expectations for the future energy mix (with everybody wishing for an increasing role for renewables), but also a rather broad agreement for a continuation of research into the fusion option.

What industries will most pay attention to in the future is being conscious about the global environment. In this context, fusion waste management can be one of the most important aspects in accordance with this trend. Recent studies in this field have focused on a minimization of the radiotoxicity and a reduction of the volume of the radioactive components, attempting to find a solution by introducing the concept of ‘clearance’ and recycling under regulatory control and by improving the purity of materials. A study indicates that reinforced neutron shielding can clear massive structural components located outside the shield from regulatory control, leading to a dramatic reduction of radioactive waste as shown in Fig. 1.23 [1.76]. This kind of concept can improve public acceptance of fusion in a practical way.

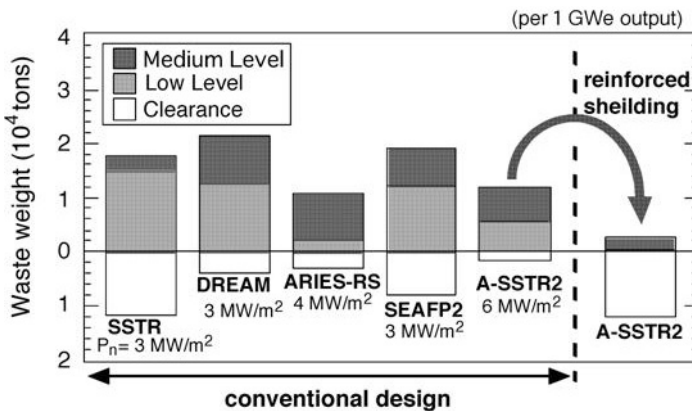


FIG. 1.23. Comparison of waste weight per 1 GW(e) output for fusion reactors and the impact of reinforced neutron shielding (courtesy of Ref. [1.76]).

#### 1.5.4. Spin-offs of fusion research

One of the important aspects of investment in fusion science and technologies is the role of R&D spin-offs. The role, proper analysis and projection of spin-offs and estimation of the rate of societal return involved in a particular R&D programme is a very crucial deciding factor in national R&D policies and public funding. It is generally true about R&D programmes and the organizations undertaking them that they cannot appropriate the integral returns of their investment unless the advances in knowledge spin-off to other disciplines and

their consumers are properly accounted for. Accordingly, the total social payoffs of any R&D activity are usually higher than the direct returns, especially true in the case of basic research. For example, the pressurized light water based nuclear reactor concept was originally developed for nuclear submarine propulsion at the Oak Ridge National Laboratory in the USA, but also resulted in great additional spin-offs in the areas of satellite communication, radiotherapy, etc., leading to substantial social and economic benefits and returns. Similar spin-offs have resulted in all other major science and technology R&D areas such as space research and high energy physics.

There are several types of spin-offs associated with fusion research. The foremost ones are the technology areas directly supporting fusion, for example superconducting magnets, neutral beam systems, cryogenics and vacuum technologies. A second category involves non-fusion plasma technologies and associated diagnostics that arise primarily in association with fusion plasma research, for example plasma processing of materials and a host of other industrial plasma applications. Yet another type of spin-off, which is uniquely dependent on fusion plasmas, are those that utilize the fusion neutrons and protons, like waste and material treatments, production of rare but useful isotopes of different elements and fusion based space propulsion systems.

Above all, there has been a great amount of knowledge spin-off. The ongoing activities in basic science and technology R&D in the areas of plasma and fusion technology have resulted in and continue to generate a great amount of knowledge spin-off through the vast number of publications, patents, codes and standards, highly trained workforces and social networks. This great wealth of knowledge base forms the basis for future advancement of applied R&D activities and is expected to increase over time with the construction of large scale experimental facilities like the ITER, IFMIF and DEMO reactors. The predominantly open and public nature of fusion R&D funding, unprecedented international collaborations among major R&D labs across all continents, the technological complexities and significant number of researchers and institutions involved in fusion R&D programmes emphasize the knowledge spin-off effects in fusion science and technology.

Probably the greatest beneficiaries of technology spin-off of fusion research are the technology areas that directly contribute to fusion science and technology. These include developments in superconducting magnets, high heat flux materials, remote handling technologies, neutral beam systems and various diagnostic systems, which have wide ranging applications in the fields of material and waste processing, medical sciences, space research and so on. For example, tremendous developments in the field of superconducting (SC) magnet technologies, especially NbTi magnet strands, driven primarily by large volume high field magnet requirements in magnetic confinement fusion devices, have contributed to SC magnets used in magnetic resonance imaging (MRI) devices to

scan body tissues in hospitals, as also to other R&D areas like the development of the SC magnets in the Large Hadron Collider (LHC) in CERN.

The development of high heat flux components like carbon fibre composite (CFC) to metal (e.g. CuCrZr) bondings developed for limiter, divertor and first wall components in magnetic confinement devices has contributed to applications in heavy duty electrical switchgears and high heat flux components in space shuttles. Optical laser diagnostics, developed for measuring plasma parameters such as velocity fields in fusion devices, has also led to the development of laser anemometers for detecting wind velocities in front of wind turbine blades. Developments in the field of high power radiofrequency generators such as gyrotrons, used widely for heating and current drive in magnetic confinement fusion devices like tokamaks, have led to their application in the field of material processing in the form of intense instantaneous, volumetric and homogeneous heating sources. They are now being used for industrial processing of materials with low thermal conductivity, such as powders, powder compacts, polymers, glass or composites. Heating with microwaves leads to a considerable reduction in processing time and energy consumption compared to conventional resistive heating or gas firing. Very comprehensive, robust and computationally exhaustive numerical codes and tools developed for modelling plasma and material properties have found wide applications in various other fields. For example, detailed computer codes have been developed to analyse the effects of fast plasma ions impinging on the material walls surrounding the hot plasma in a fusion device, aimed at simulating the trajectories of ions penetrating the wall with different energies and angles of incidence, getting implanted and causing material defects and damages. These codes are now being widely applied to study semiconductor properties where ion implantation changes the electrical conductivity of the materials.

One of the most remarkable examples of fusion spin-off is the development of a host of technologies developed for producing and manipulating low temperature plasmas in various industrial applications. As discussed in a recent report of the International Fusion Research Council (IFRC) [1.77], the all pervasive influence of plasma technology can be seen in practically all walks of life, starting from high efficiency fluorescent lamps and plasma displays to advanced plasma based systems for manufacturing computer chips, sterilization in medicine and the food industry, surface and exhaust gas cleaning, etc. The IFRC Report further goes on to state: "In the time period in which advances in fusion research have taken place, fusion science has established its own identity. Initially indebted to all other fields of physics, plasma physics, the basis of fusion, has made contributions back to astrophysics, space physics, applied mathematics, materials science and others. The design, construction and operation of fusion machines have contributed to progress in most engineering disciplines, and, more

generally, a whole family of practical applications of plasma technologies has emerged.”

The ongoing R&D on fusion technologies has a significant potential spin-off application to a host of crucial areas [1.24, 1.77, 1.78] involving high energy neutrons, thermal neutrons, high energy protons, electromagnetic radiation (microwaves to X rays to gamma rays), high energy electrons coupled with photons providing ultrahigh heat fluxes, etc.

One of the fundamental roles of fusion reactors would be production of tritium both for its own use as fuel as well as for industrial, medical and military applications. Calculations show that fusion reactors, specially designed to generate high neutron flux, for example a 300 MW spherical tokamak based volume neutron source (VNS), would be capable of producing an excess of tritium of 2 kg annually.

TABLE 1.4. USEFUL APPLICATIONS OF FUSION BY-PRODUCTS

Applications	Highenergy neutrons	Lowenergy neutrons	Highenergy protons	EM radiation	Ultrahigh heat fluxes
Production of radioisotopes for medical applications and research	✓	✓	✓		
Detection of specific elements or isotopes in complex environment	✓	✓	✓		
Radiotherapy	✓				
Alteration of the electrical, optical or mechanical properties of materials	✓				
Destruction of long-lived radioactive waste from fission reactors or fissile materials of nuclear warheads	✓	✓	✓		
Tritium breeding	✓	✓			
Production of fissile material	✓	✓			
Production of radioisotopes for portable gamma ray sources		✓			
Food and equipment sterilization				✓	
Pulsed X-ray sources				✓	
Ionization of waste materials and separation of municipal and medical wastes, spent reactor fuel elements, chemical weapons etc.					✓

Fusion reactor blankets can also be used for the production of critical radioisotopes in high demand in medical applications, for example <sup>32</sup>P, <sup>56</sup>Mn, <sup>60</sup>Co and <sup>99</sup>Mo. Especially <sup>60</sup>Co is an intensely radioactive material with primary use in sterilizing medical products and secondary applications in irradiating cancer

cells and food items. Present worldwide demand for replenishing  $^{60}\text{Co}$  is about 11 megacuries (MCi) per year, most of which is produced at the CANDU reactors in Canada. However, in future high demand scenarios, commercial fusion power reactors could produce hundreds of MCi of  $^{60}\text{Co}$  per year with a blanket optimized for  $^{60}\text{Co}$  production.

Another very important application of fusion neutrons is in processing of long lived toxic radioactive hazardous wastes produced in fission reactors. At present, fission reactor wastes have to be buried deep underground or underneath the ocean beds, but decay heat accumulated over a long time duration can potentially trigger the release of these radioactive materials to the environment long after they are buried. The neutrons from a fusion reactor could be used to change radioactive fission wastes into shorter lived materials that would decay more quickly and hence need to be buried over shorter periods. Table 1.4 shows the various useful applications of fusion by-products.

Another very significant spin-off of fusion research is the potential for application of fusion based highly efficient rocket propulsion systems in interplanetary voyages, which can make the entire solar system or even the space beyond accessible for future human explorations. Present day rocket engines based on chemical propulsion work for near-Earth space explorations like moon voyages, but are totally inadequate for interplanetary voyages because they lack the required thrust. The performance of various propulsion systems is measured in terms of their *specific impulse* (exhaust velocity divided by acceleration due to Earth's gravity at sea level); thus high fuel efficiency is equivalent to high specific impulse. Propulsive thrust for a particular fuel type is directly proportional to specific impulse, whereas the power required to generate thrust is proportional to the *square* of specific impulse. Today, only fusion based propulsion systems (or perhaps more exotic propulsion systems based on matter-antimatter annihilation) could provide the required thrust for interplanetary spaceships. Thus, manned spaceships to Mars and beyond would require a fusion reactor that produces about 10–100 GW of power. Table 1.5 provides a comparison of specific impulse comparison and thrust-to-weight ratio of various propulsion systems.

### 1.6. CONCLUSION

Nuclear fusion energy is an energy source which has the potential to satisfy humanity's hunger for a sustainable pollution-free and universally accessible option for tens of thousands of years. The research programme in magnetically confined and inertial confinement approaches is at a critical juncture today and is likely to lead to successful fusion ignition experiments within a decade or so and commercially viable fusion reactors generating electricity by the decade 2040–2050.

TABLE 1.5. SPECIFIC IMPULSE AND THRUST-TO-WEIGHT RATIOS OF DIFFERENT PROPULSION SYSTEMS

<b>Chemical fuels</b>	<b>200-400</b>	<b>0.1-10</b>
<b>Electromagnetic</b>	<b>1200-5000</b>	<b><math>10^{-4}</math> - <math>10^{-3}</math></b>
<b>Fission based propellants</b>	<b>500-3000</b>	<b>0.01-10</b>
<b>Fusion based propellants</b>	<b><math>10^4</math>-<math>10^5</math></b>	<b><math>10^{-5}</math> - <math>10^{-2}</math></b>
<b>Matter-antimatter annihilation</b>	<b><math>10^3</math>-<math>10^6</math></b>	<b><math>10^{-3}</math> - 1</b>

In this chapter it has been shown that fusion has many inherent merits to be the workhorse for sustainable human development. Fusion power is based on a virtually inexhaustible and universally accessible fuel. Fusion power plants would have inherent operational safety because of the low inventory of fuels in the reactor, low radioactivity related problems through proper choice of materials and negligible proliferation and terrorism concerns. Very high energy density makes fusion an appropriate energy source for economically profitable urban industrial complexes. Fusion power would have acceptable costs, greater socio-economic acceptability and significant spin-off applications. Fusion research has made tremendous strides over the last fifty years, which has culminated in the unprecedented international collaboration to start construction of the experimental thermonuclear reactor called ITER. A successful ITER experiment will lead to development of DEMO reactors which will supply electricity to the grid. Beyond successful DEMOs we can see commercial exploitation of fusion power. For reasons mentioned above, fusion power is likely to get greater public acceptability than competing energy sources of sustainable development.

Thus the potential merits of fusion as an energy source are so compelling that the stakes in this development are very large. It is also very heartening to note that in magnetic confinement fusion research, there is a very broad international cooperation among diverse nations of the world and the beneficiaries of this technology will involve countries such as China and India which, because of their population size and development needs, are likely to be among the most energy hungry nations of the globe. The biggest problem for this enterprise is its ability to attract and retain appropriate human resources for great lengths of time which are essential for the complete development of this challenging technology. It is hoped that a wide dissemination of the promise and potential of this energy resource worldwide will go a long way in attracting appropriate scientific and technical leadership for this effort.

## REFERENCES

- [1.1] PASTERNAK, A., Global Energy Futures and Human Development: A Framework for Analysis, US Department of Energy Report UCRL-ID-140773, Lawrence Livermore National Laboratory, Livermore, CA (2000) 38.
- [1.2] GOLDEMBERG, J., Energy and Human Well-being”, United Nations Development Programme Report, New York (2001).
- [1.3] NASERI, H., “The relationship between energy and human development”, IAOS Conf. on Statistics, Development and Human Rights, Session C-Pa 6e, Montreux, 2000.
- [1.4] SMIL, V., Energy at the Crossroads, MIT Press, Cambridge, MA (2003).
- [1.5] DIAS, R.A., MATTOS, C.A., BALESTIERI, J.A.P., The limits of human development and the use of energy and natural resources, Energy Policy **34** (9) (2006) 1026–1031.
- [1.6] UNITED NATIONS DEVELOPMENT PROGRAMME,  
*<http://hdr.undp.org/>*
- [1.7] UNDP Report on Energy Scenarios:  
*<http://stone.undp.org/undpweb/seed/wea/pdfs/chapter9.pdf>*
- [1.8] FELLS, I., The need of energy, Europhys. News **29** (1998) 193.
- [1.9] BARABASHI, S., et al, Fusion Programme Evaluation 1996. UR 17521, Office for Official Publications of the EU, Luxembourg.
- [1.10] ITER:  
*<http://www.iter.org/>*
- [1.11] NATIONAL IGNITION FACILITY, NIF:  
*<https://lasers.llnl.gov/programs/nif/>*
- [1.12] LASER MEGAJOULE:  
*<http://www-lmj.cea.fr/html/cea.htm>*
- [1.13] WORLD ENERGY COUNCIL (WEC):  
*<http://www.worldenergy.org/>*
- [1.14] INTERNATIONAL ENERGY AGENCY:  
*<http://www.iea.org/>*

- [1.15] SUBCOMMITTEE OF THE FUSION COUNCIL FOR FUSION DEVELOPMENT STRATEGY, Report on the Technical Feasibility of Fusion Energy and Extension of the Fusion Program and Basic Supporting Researches, May 17, 2000 (in Japanese; English translation is available at <http://www.naka.jaeri.go.jp/SCI/>).
- [1.16] UNITED NATIONS FRAMEWORK CONVENTION ON CLIMATE CHANGE: The Kyoto Protocol, [http://unfccc.int/kyoto\\_protocol/items/2830.php](http://unfccc.int/kyoto_protocol/items/2830.php)
- [1.17] MOOMAW, W., “Renewable Energy and Climate Change An Overview”, Proc. IPCC Scoping Meeting on Renewable Energy Sources, <http://www.ipcc.ch/pdf/special-reports/srren.pdf>
- [1.18] NATIONAL GEOGRAPHIC: [http://news.nationalgeographic.com/news/2005/01/0114\\_050114\\_solarplastic.html](http://news.nationalgeographic.com/news/2005/01/0114_050114_solarplastic.html)
- [1.19] KING, R.R., et al., Appl. Phys. Letters **90** (2007) 183516.
- [1.20] Large Scale Photovoltaic Power Plants: <http://www.pvresources.com/download/AnnualReport2007.pdf>
- [1.21] YAMAGUCHI, M., et al., Sol. Energy **80** (2006) 104.
- [1.22] US photovoltaic roadmap: [http://photovoltaics.sandia.gov/docs/PDF/PV\\_Road\\_Map.pdf](http://photovoltaics.sandia.gov/docs/PDF/PV_Road_Map.pdf)
- [1.23] OILGAE website: <http://www.oilgae.com>
- [1.24] GNANSOUNOU, E., BEDNYAGIN, D., Multi-regional long-term electricity supply scenarios with fusion, Fusion Sci. Technol. **52**(3) (2007) 388.
- [1.25] NAKICENOVIC, N., et al., UNDP report on Energy Scenarios (Chapter 9).
- [1.26] EHERER, C., BAUMANN, M., DÜWEKE, J., HAMACHER, T., Nuclear fusion as new energy option in a global single-regional energy system model”, Proc. 20th IAEA Fusion Energy Conf., 2004, Vilamoura, Portugal, paper SE/P3-39;. [http://www-naweb.iaea.org/napc/physics/fec/fec2004/papers/se\\_p3-39.pdf](http://www-naweb.iaea.org/napc/physics/fec/fec2004/papers/se_p3-39.pdf)

## THE CASE FOR FUSION

- [1.27] EHERER, C., BAUMANN, M., Long-Term Technology Based Modelling with TIMES, Interim Report, EFDA/SERF sub task TW3-TWE-FESA/A, Garching, June 2004.
- [1.28] LECHON, Y., et al, A global energy model with fusion, Fusion Eng. Des. **75-79** (2005) 1141.
- [1.29] BAUMANN, M., EHERER, Ch., “Recent long-term energy scenario results with the TUGIPP global single-regional energy model: ETL in the TUG-IPP model”, IEA Workshop on Socio-Economics of Fusion, Culham 2005.  
*<http://fusion.org.uk/socioecon/Eherer.pdf>*
- [1.30] INTERNATIONAL INSTITUTE FOR APPLIED SYSTEMS ANALYSIS:  
*<http://www.iiasa.ac.at>*
- [1.31] INTERGOVERNMENTAL PANEL ON CLIMATE CHANGE (IPCC):  
*<http://www.ipcc.ch>*
- [1.32] IIASA-WEC, “Global Energy Perspectives”, (NAKICENOVIC, N., GRUBLER, A., McDONALD, A., Eds), Cambridge University Press, ISBN 0-521-64569-7. Online version of the report also available at  
*[http://www.iiasa.ac.at/cgi-bin/ecs/book\\_dyn/bookcnt.py](http://www.iiasa.ac.at/cgi-bin/ecs/book_dyn/bookcnt.py)*
- [1.33] Global Warming page on Wikipedia:  
*[http://en.wikipedia.org/wiki/Global\\_warming](http://en.wikipedia.org/wiki/Global_warming)*
- [1.34] COOK, I., MILLER, R.L., WARD, D.J., “Prospects for Economic Fusion Electricity” Fusion Eng. Des. **63-64** (2002) 25.
- [1.35] Department of Atomic Energy (DAE), Government of India report:  
*<http://www.dae.gov.in/publ/doc10/>*
- [1.36] HAMACHER, T., SHUKLA, P.R., SEEBREGTS, T., The possible role of fusion in the Indian energy system of the future, Fusion Eng. Des. **69** (2003) 733.
- [1.37] KIKUCHI, M., INNOUE, N., “Role of fusion energy for the 21 century energy market and development strategy with international thermonuclear experimental reactor”, Proc. 18th World Energy Conf., Buenos Aires, 2001, DS-6, No 01-06-09  
*([http://fire.pppl.gov/energy\\_ja\\_wec01.pdf](http://fire.pppl.gov/energy_ja_wec01.pdf))*.
- [1.38] MAISONNIER, D., et al., “DEMO and fusion power plant conceptual studies in Europe”, Fusion Eng. Des. **81** (2006) 1123–1130.

- [1.39] MAISONNIER, D., et al., The European power plant conceptual study, *Fusion Eng. Des.* **75–79** (2005), 1173-1179.
- [1.40] TOBITA, K. et al., Design study of fusion DEMO plant at JAERI, *Fusion Eng. Des.* **81** (2006) 1151–1158.
- [1.41] NAJMABADI, F., et al., The ARIES-AT advanced tokamak advanced technology fusion power plant, *Fusion Eng. Des.* **80** (2006) 3–23.
- [1.42] SRINIVASAN, R., et al., Strategy for the Indian DEMO design, *Fusion Eng. Des.* **83** (2008) 889.
- [1.43] IFMIF website:  
*<http://www.frascati.enea.it/ifmif/>*
- [1.44] ABDOU, M.A., *Fusion Technol.* **9** (1986) 250; *ibid* **28** (1995) 5.
- [1.45] KUAN, W., ABDOU, M.A., A new approach for assessing the required tritium breeding ratio and startup inventory in future fusion reactors, *Fusion Technol.* **35** (1999) 309.
- [1.46] SWAN, M., ABDOU, M.A., Physics and technology conditions for attaining tritium self-sufficiency for the DT fuel cycle, *Fusion Eng. Des.* **81** (8–14) (2006) 1131.
- [1.47] LAWSON, J.D., “Some Criteria for a Useful Thermonuclear Reactor”, Atomic Energy Research Establishment, 1955 Culham Report No: A.E.R.E. GP/R – 1807.
- [1.48] HARMS, A.A., KINGDON, D.R., SCHOEPF, K.F., MILEY, G.H., *Principles of Fusion Energy*, World Scientific Publications, ISBN 978-981-238-033-3.
- [1.49] NRL Plasma Formulary Edn 2007, page 45.
- [1.50] ENDF database at the IAEA:  
*<http://www-nds.iaea.org/exfor/e4explorer.htm>*
- [1.51] NEVINS, W.M., SWAIN, R., The thermonuclear fusion rate coefficient for p-<sup>11</sup>B reactions, *Nucl. Fusion* **40** (2000) 865.
- [1.52] DAWSON, J.M., KAW, P.K., Current maintenance in tokamaks by used of synchrotron radiation, *Phys. Rev. Letters* **48** (1982) 1730.
- [1.53] ROMANELLI, F., GIRUZZI, G., A D-<sup>3</sup>He fusion reactor with an edge radiation barrier, *Nucl. Fusion* **38** (1998) 103.
- [1.54] ROSENBLUTH, M.N., HINTON, F., Generic issues for direct conversation of fusion energy from alternative fuels, *Plasma Phys. Control. Fusion* **36** (1994) 1255.

## THE CASE FOR FUSION

- [1.55] WESSON, J., Tokamaks, Oxford University Press, New York (1987) ISBN 0-19-856328-0.
- [1.56] ARTISIMOVICH, L.A., Controlled Thermonuclear Reactions, ISBN 067720020X (1964).
- [1.57] MYAMOTO, K., Plasma Physics for Nuclear Fusion, MIT Press, Cambridge, MA (1976).
- [1.58] DOLAN, T.J., Fusion Research, Pergamon Press, New York (1982).
- [1.59] WATAKANI, M., Stellarator and Heliotron Devices, Oxford University Press, New York, (1998), ISBN-0-19-507831-4.
- [1.60] LHD website:  
*<http://www.lhd.nifs.ac.jp/en/>*
- [1.61] Wendelstein-7X:  
*<http://www.ipp.mpg.de/ippcms/eng/pr/forschung/w7x/index.html>*
- [1.62] IPP:  
*<http://www.ipp.mpg.de/>*
- [1.63] EFDA-JET:  
*<http://www.jet.efda.org/>*
- [1.64] HOANG, G.T., JACQUINOT, J., Controlled fusion: the next step, Physics World (10.1.2004) 21.
- [1.65] LINDL, J.D., Inertial Confinement Fusion: The Quest for Ignition and Energy Gain Using Indirect Drive”, Springer-Verlag, New York (1998), ISBN: 1-56396-662-X.
- [1.66] ATZENI, S., MEYER-TER-VEHN, J., The Physics of Inertial Fusion, Beam Plasma Interaction, Hydrodynamics, Hot Dense Matter”, Oxford University Press, Oxford (2004), ISBN 0 19 856264 0.
- [1.67] RAEDER, J., et al., “Safety and Environmental Assessment of Fusion Power (SEAFP)”, Report of the SEAFP Project, European Commission DGXII, Fusion Programme, EURFUBRU XII-217/95, Brussels (June 1995).
- [1.68] ICRP Publication 60, Recommendations of the International Commission on Radiological Protection, 1990, Pergamon Press.
- [1.69] COOK, I., et al., Results, conclusions and implications of the SEAFP-2 programme, Fusion Eng Des. **51–52** (2000) 409.
- [1.70] COOK, I., et al., Safety and Environmental Impact of Fusion, EFDA report, 2001, EUR (01) CCE-FU / FTC 8/5.

- [1.71] HAMACHER, T., BRADSHAW, A.M., “Fusion as a future power source-recent achievements and prospects”, Proc. 18th Congress of World Energy Council, Buenos Aires, October 2001 ([http://fire.pppl.gov/energy\\_eu\\_wec01.pdf](http://fire.pppl.gov/energy_eu_wec01.pdf)).
- [1.72] BORELLI, G., et al., Socio-economic Research on Fusion – Summary of EU Research 1997-2000: [http://www.efda.org/eu\\_fusion\\_programme/downloads/scientific\\_and\\_technical\\_publications/SERF\\_final.pdf](http://www.efda.org/eu_fusion_programme/downloads/scientific_and_technical_publications/SERF_final.pdf)
- [1.73] ARGOTE, L., EPPLÉ, D., Learning curves in manufacturing, *Science* **247** (1990) 920.
- [1.74] ExternE homepage: <http://externe.jrc.es/>, <http://www.externe.info/>
- [1.75] SAEZ, R., et al., Socio-economic Research in Fusion SERF 1997-98: Externalities of the Fusion Fuel Cycle. Final Report. Coleccion Documentos CIEMAT (1999).
- [1.76] TOBITA, K., et al., Fusion reactor design towards radwaste minimum with advanced shield material, *J. Plasma Fusion Res.* **77** (2001) 1035.
- [1.77] International Fusion Research Council (IFRC), Status Report on Fusion Research, *Nucl. Fusion* **52** (2005) A1–A28.
- [1.78] McCARTHY, K., et al., Non-electric applications of fusion, *J. Fusion Energy* **21** (2002) 121.

# CHAPTER 2

## PHYSICS OF CONFINEMENT

**R.J. Goldston, R.B. White, T.S. Hahm, S. Kaye**  
Princeton Plasma Physics Laboratory,  
Princeton, United States of America

### 2.1. INTRODUCTION AND OVERVIEW

The measured radial fluxes of particles, ion and electron heat, and toroidal angular momentum in tokamaks are usually greater than given by neoclassical transport theory, described in Section 2.2. In this collisional theory, appropriate for a quiescent plasma, the random-walk step size is generally set by the width of closed banana trajectories in the steady state magnetic fields, and the step period is set by the collisional decorrelation time. At low collisionalities relevant to fusing plasmas, detailed calculations give radial transport coefficients of the form  $G_c \rho^2 \nu$ , where  $G_c$  is a dimensionless geometrical factor,  $\rho$  is the gyroradius of the species under consideration and  $\nu$  is the collision frequency.

The observation of enhanced, or anomalous, cross-field transport greater than the predicted neoclassical level is qualitatively consistent with theoretical considerations and large computer simulations, discussed in Section 2.3, which indicate that tokamak plasmas should be subject to strong dominantly electrostatic gyroBohm turbulence. In such turbulence the correlation length,  $\rho_c$ , is a modest multiple of the ion sound gyroradius,  $\rho_s$ , and the turbulence amplitude is of the order of the mixing length estimate ( $\delta n / n \sim (k_\perp L_n)^{-1}$ ) in which the gradient of the perturbed density approximately equals the gradient of the ambient density.  $L_n$  is the density scale length  $L_n \equiv n(dn/dr)^{-1}$  and  $k_\perp$  is the wavenumber perpendicular to the magnetic field. In electrostatic turbulence, one estimates  $e\delta\Phi/T \sim \delta n/n$ , where  $\Phi$  is the electrostatic potential. Note that temperature  $T$  is expressed everywhere in energy units eV suppressing Boltzmann's constant. Using the mixing length estimate for  $\delta n/n$ , the turbulent velocity can be estimated at  $\delta v \sim k_\perp \delta\Phi/B$ , and so a random-walk transport coefficient,  $\rho_c \delta v$ , takes the form  $G_T T / (eB)(\rho_s / L_n)$ , where  $G_T$  is a dimensionless factor that requires detailed calculation and can depend on such parameters as collisionality,  $\beta$  and  $q$ , but not further factors of  $\rho$  normalized by the system size.

In typical existing fusion plasma confinement systems, and especially in ITER, gyroBohm transport is a great deal weaker than the worst-case estimate of turbulent transport, the Bohm level, which obtains for extremely strong turbulence with  $\delta n/n \sim 1$  and  $k_\perp \rho_c \sim 1$ , and so scales as  $T/eB$  by the arguments above. However, consistent with experiment, gyroBohm transport dominates

neoclassical except in some cases where ion neoclassical thermal transport can be large (e.g. at high collisionality), or where turbulence is suppressed.

A quantitative, predictive understanding of gyroBohm turbulence, and full understanding of the roles of other potential sources of turbulent transport, such as turbulence driven on the electron gyroradius scale or electromagnetic turbulence, remain outstanding challenges. It is clear that full understanding will require:

- (1) Detailed measurements of transport;
- (2) Detailed measurements of turbulence;
- (3) Detailed comparisons of both with non-linear turbulence simulations.

All of these need to be undertaken over a sufficiently wide range of conditions and operating modes to establish that the basic understanding evolved from these studies, coupled in some cases with transport due to large scale instabilities discussed in Chapter 3, explains the observed scalings of global confinement with overall plasma parameters such as plasma current, major radius and heating power, described in Section 2.4. The scaling studies discussed there, particularly for energy confinement, have been very successful in correlating data from many experiments, with RMS errors typically in the range of 10–15%. They call out for full explication based on detailed measurements and simulation. Also described in Section 2.4 are global confinement studies to estimate at a global level the scaling of  $G_T$  with dimensionless parameters, and to examine any non-gyroBohm scaling with  $\rho$ .

As discussed in Section 2.5, local transport of particles, heat and momentum have been measured in many conditions, and comparisons have been made with theory over a more limited range of conditions, but most often only with linear stability calculations or quasi-linear estimates, not with fully non-linear simulations. Studies of the variation of local transport with dimensionless parameters have been made as well, providing further data on the variation of  $G_T$ , but not enough has been done to provide a satisfactory link to the observed global scalings.

The powerful technique of studying transport response to perturbations has been exploited. This and careful studies of temperature gradients versus power flows have confirmed a basic feature of the theoretical gyroBohm turbulence model for tokamaks discussed in Section 2.3, that turbulent transport, as measured against gyroBohm scaling, is low below a certain threshold, typically set by a critical logarithmic derivative ( $T^{-1}dT/dr$ ) of the ion or electron temperature, and when the temperature gradient exceeds this threshold, transport rises very quickly. This gives rise to the long-observed stiffness, particularly in the radial profile shape of the electron temperature, since the logarithmic temperature gradient tends to be stuck close to its critical value, independent of the level or profile of heating power.

GyroBohm transport theory has a further distinctive feature that has also been observed in experiments. The turbulent decorrelation rate,  $(\rho_c / \delta v)^{-1}$ , is calculated to be of the order of the linear growth rate, having a scaling of the form,  $c_s / L_n$ . If natural turbulent structures are torn apart by some mechanism at a rate much faster than the linear growth rate, or equivalently, faster than the non-linear decorrelation rate, one should expect strong suppression of the turbulence and its associated transport. A possible mechanism for destruction of turbulent structures is their breakup due to shear in ambient flows. The *velocity* at which the components of a structure move apart in a sheared flow is given by its scale size multiplied by  $dv/dr$ . The *time* to shear apart the structure is given by its scale size divided by this velocity — with the consequence that the shearing decorrelation rate is just  $dv/dr$ , independent of structure size. Thus theory predicts, in rough terms, that if  $d/dr(E/B)$  exceeds the linear growth rate of an instability one should see turbulence suppression. This effect is indeed observed both close to the plasma edge (in H-mode) and also in the plasma core, with strong shear flow and especially with reversed magnetic shear ( $dq/dr < 0$ ) such that the linear instability growth rates for both ion and electron turbulence are reduced, as described in Sections 2.3 and 2.6.

As described in Section 2.6, powerful techniques have been developed to measure turbulence within tokamak plasmas, but they are limited to date in their application and in their comparison with simulation. They are also limited in the turbulence properties they can detect. Full comparison between theory and experiment demands excellent spatial resolution as well as resolution in frequency and wavenumber, and reliable absolute calibration. Furthermore it is very valuable to measure more than one fluctuating quantity, and even to measure the phases between these quantities to determine turbulent transport rates, for example  $\Gamma = \langle \delta n \delta v_r \rangle$ . In any given case, it is possible to obtain only some aspects of the desired data. Nonetheless, results to date generally support the gyroBohm model. The wavelengths, and correlation times and distances, of the measured turbulence are consistent with the gyroBohm model, as is its rough magnitude. Confinement tends to decrease with increasing turbulence; for example, turbulence is generally seen to increase with increasing input power, which leads to decreased energy confinement. While almost all measurements have been of density fluctuations, ion and electron temperature fluctuations have been measured in some cases, and are found to be roughly as predicted.

Interestingly, analytic theory and computer models predict that localized sheared flows in the plasma, generated by the turbulence itself, provide for self-regulation of the turbulence level, and indeed break up meso-scale structures that could give rise to Bohm-like scaling. These flows have been observed in some experimental conditions. Furthermore, under conditions where theory predicts turbulence suppression due to sheared flows and/or reduced linear growth rates, turbulence has also been measured to be suppressed dramatically.

Overall, however, it should be recognized that the gyroBohm model of turbulence dominated by fluctuations at the ion scale, while highly successful, is not fully established; indeed a range of anomalies should be appreciated. In the L-mode, global scalings and local transport variations are more consistent with an overall Bohm-like scaling than with the gyroBohm variation as  $\rho_s / L_n$ . However, the turbulence driven self-regulating flows that should give rise to gyroBohm scaling have been detected in the L-mode, but fade below detectability in the H-mode. Furthermore, at the H-mode transition rapid changes have been observed in core transport and turbulence, at least suggesting a non-local effect. (Non-local effects, called turbulence spreading, are discussed in Section 2.3.) Turbulence and transport grow rapidly towards the plasma edge, and initial studies of this are inconsistent with simulations. Significant transport is also observed even when the electron temperature profile is very flat near the plasma centre, for example within a transport barrier established by magnetic shear reversal, but gyroBohm turbulence is calculated to be stable in this region. These two effects could also be due to non-local phenomena, in the one case perhaps edge turbulence leaking into the confinement region, and in the other confinement region turbulence leaking into the central region. It has been observed, as well, that some small scale instabilities can be driven by energetic beam ions, and these could be responsible for enhanced transport in the plasma core. In some circumstance electromagnetic instabilities are calculated to be unstable and potentially important. Finally, high resolution measurements have recently been made of turbulence at high wavenumber  $k$ , corresponding to instabilities driven by the electron temperature gradient. This turbulence grows and is even suppressed by reversed shear as predicted by theory, and may play a role in electron thermal transport.

Returning to the triad of requirements for measurements of transport and of turbulence, and for comparison of large scale simulations with experiment over a broad range of conditions, it is clear that with the advent of massively parallel computing, non-linear turbulence simulations have become much more detailed and complete, but they remain sufficiently costly and difficult that they have not been broadly compared with experiment. Experimental run time is also at a premium and as a consequence three-way correlations of measured transport, measured turbulence and non-linear simulation, across a broad enough range of conditions to make comparisons with global scalings, do not exist. Thus this most basic test of whether the gyroBohm model explains the observed phenomenology of tokamak confinement remains as a challenge.

While the overall picture that gyroBohm turbulence plays a key role in tokamak transport is reasonably secure, and together with global scaling results gives an acceptable basis for projection to future devices such as ITER, it is clear that a great deal of exciting research remains to be done in the area of plasma turbulence and transport.

## 2.2. NEOCLASSICAL TRANSPORT

### 2.2.1. Introduction

A plasma is completely described by a distribution function  $f(\vec{x}, \vec{v}, t)$  giving the time dependent histories of all the particles of which it is comprised. Particle positions evolve in time under the Lorentz force  $(e/m)(\vec{E} + \vec{v} \times \vec{B})$ , with  $\vec{E}$  and  $\vec{B}$  the local electric and magnetic fields. The Hamiltonian nature of the particle trajectories implies phase space conservation, or

$$\frac{\partial f}{\partial t} + \vec{v} \cdot \nabla f + (e/m)(\vec{E} + \vec{v} \times \vec{B}) \cdot \nabla_v f = 0 \quad (2.1)$$

with  $\nabla_v$  the velocity space gradient operator. Solution of this Vlasov equation in general is equivalent to solving the classical electromagnetic many-body problem, an impossible task. However, the distribution function contains vastly more information than is needed or can be possibly measured, so it is essential to simplify the description of the plasma. To smooth the discreteness of the distribution function  $f$ , an ensemble average is carried out, resulting in an additional term from the correlations due to close encounters, the collision term. The long range effect of particles on each other is accounted for by the self-consistent electric and magnetic fields of the plasma. Only very close interactions of particles, at distances smaller than a Debye length, are not treated by the Vlasov equation.

Approximations are made in two directions. First the equations of motion are simplified by expanding, in the available small parameters describing the system, the ratio of the cyclotron radius to the scale length of the fields, the ratio of the collision frequency to typical timescales of plasma response, and the ratio of electron to ion mass. Neglecting collisions and to lowest order in the expansion of the equations of motion in cyclotron radius the particles simply follow the field lines. The guiding centre approximation [2.1–2.4] includes the particle drifts, one order higher in this expansion. Gyrokinetic equations are obtained by carrying out the analysis to still one higher order in the gyroradius expansion [2.5–2.7]. Provided that the resulting approximate equations are Hamiltonian in nature, if collisions are neglected phase space conservation results in a Vlasov equation at each level.

Secondly, the magnetic fields are simplified by making use of the fact that they describe, at least very closely, a toroidal magnetohydrodynamic (MHD) equilibrium, allowing long time plasma confinement. Perturbations of the equilibrium are assumed to consist of small amplitude waves with scale lengths much larger than the cyclotron radius and frequencies small compared to the cyclotron frequency.

Finally, using the distribution function for each species,  $f(\vec{x}, \vec{v})$ , one can construct fluid theory functions depending only on position and time by taking velocity moments, such as density,  $n(\vec{x}) = \int d^3v f$ , particle flux density  $n\vec{u}(\vec{x}) = \int d^3v f\vec{v}$  (where  $\vec{u}$  is a fluid velocity and  $\vec{v}$  is particle velocity), stress tensor  $P_{\alpha,\beta}(\vec{x}) = \int d^3v f m v_\alpha v_\beta$  (where  $\alpha, \beta$  label components), and energy flux density,  $\vec{Q}(\vec{x}) = \int d^3v f m v^2 \vec{v} / 2$ . Taking moments of the ensemble averaged kinetic equation then results in fluid equations relating these quantities, but each quantity is coupled to higher order moments and one must make approximations to give closure to these equations [2.8–2.10]. The first few moments give, for a single species, and evaluated in the rest frame, the Braginskii equations for density, momentum and pressure

$$\frac{dn}{dt} + n\nabla \cdot \vec{u} = 0 \quad (2.2)$$

$$mn \frac{d\vec{u}}{dt} + \nabla p + \nabla \cdot \vec{\pi} - en(\vec{E} + \vec{u} \times \vec{B}) = \vec{F} \quad (2.3)$$

$$\frac{3}{2} \frac{dp}{dt} + \frac{5}{2} p \nabla \cdot \vec{u} + \vec{\pi}_{\alpha,\beta} \partial_\alpha u_\beta + \nabla \cdot \vec{Q} = W \quad (2.4)$$

where  $\partial_\alpha = \partial / \partial x_\alpha$ ,  $P_{\alpha,\beta} = p\delta_{\alpha,\beta} + \pi_{\alpha\beta}$ , with  $p$  the pressure and  $\pi$  the viscosity tensor,  $\delta_{\alpha,\beta}$  is the Kronecker delta function and  $\vec{F}$  and  $W$  are source terms. The coefficients of the terms describing cross-field particle and energy flux, momentum diffusion, bootstrap current and resistivity are dependent on the nature of the particle orbits in the system considered. For toroidal confinement systems these are called neoclassical transport coefficients [2.11, 2.12]. Normally their values are calculated using the guiding centre approximation for the particle trajectories. Other moments will be discussed in Section 2.5.5. If there exist fluctuating magnetic or electric fields, due to MHD or kinetic instabilities, this will produce additional anomalous transport.

In the following we first consider the simplification of the fields resulting from toroidal equilibrium, Section 2.2.2, then guiding centre motion in such an equilibrium, Section 2.2.3, and the resulting drift kinetic equation resulting from these two approximations in Section 2.2.4, used to calculate some neoclassical transport coefficients. Section 2.2.5 treats bootstrap current, and Section 2.2.6 the modification of transport due to field ripple. Section 2.2.7 discusses transport in a stochastic field.

### 2.2.2. Toroidal magnetic configuration

Because of the very high particle velocity along magnetic field lines, the field must, at least approximately, possess toroidal magnetic surfaces, to prevent rapid particle transport from the inside of the torus to the exterior, and thus allow the existence of pressure and temperature gradients. We introduce general coordinates  $\psi$ , labelling the flux surfaces,  $\theta$ , a poloidal angle, and  $\zeta$ , a toroidal angle. Since  $\vec{B}$  is orthogonal to  $\nabla\psi_p$ , use the Clebsch representation

$$\vec{B} = \nabla\psi_p \times \nabla G \quad (2.5)$$

and choose the function  $G = q(\psi_p)\theta - \zeta + \lambda(\psi_p, \theta, \zeta)$  where  $\theta$  and  $\zeta$  are arbitrary poloidal and toroidal angles, respectively. We choose  $2\pi\psi_p$  to be the poloidal flux inside the magnetic surface. We then find that  $\lambda$  is periodic in  $\zeta$ . We then have the contravariant representation for  $\vec{B}$ ,  $\vec{B} = (q + \lambda'_\theta)\nabla\psi_p \times \nabla\theta + (1 - \lambda'_\zeta)\nabla\zeta \times \nabla\psi_p$ , with primes indicating derivatives with respect to the subscripted variable. Now choose  $2\pi\psi = 2\pi \int_0^{\psi_p} q(\psi_p) d\psi_p$  to be the toroidal flux inside the surface. We then find that  $\lambda$  is periodic in  $\theta$  and  $d\psi / d\psi_p = q(\psi_p)$ , the flux surfaces can be labelled by either  $\psi$  or  $\psi_p$ .

Straight field line coordinates are often used for equilibrium and stability studies. Replace  $\zeta - \lambda$  with  $\zeta$  in Eq. (2.5), equivalent to setting  $\lambda$  equal to zero, possible because of the periodicity of  $\lambda$ . The **contravariant** representation for  $\vec{B}$  then becomes

$$\vec{B} = q(\psi_p)\nabla\psi_p \times \nabla\theta + \nabla\zeta \times \nabla\psi_p \quad (2.6)$$

and  $q(\psi_p)$  is the local helicity of the field line,  $d\theta / d\zeta$  following the field. It is referred to as the safety factor in tokamak research since if  $q < 1$  the equilibrium is unstable. The derivative of  $q$  gives the local shear of the equilibrium field. It is also useful to note the vector potential associated with  $\vec{B}$ , with  $\vec{B} = \nabla \times \vec{A}$ ,

$$\vec{A} = \psi\nabla\theta - \psi_p\nabla\zeta \quad (2.7)$$

Now we make use of the MHD equilibrium property of  $\vec{B}$ . We assume a scalar pressure equilibrium,  $p = p(\psi)$ . From the equilibrium condition  $\vec{j} \times \vec{B} = \nabla p$  with  $p = p(\psi)$  and  $\vec{j}$  the plasma current density, it follows that  $\vec{j} \cdot \nabla\psi = 0$ . Write  $\vec{j} = \nabla\psi \times \nabla W$ , and choose  $W = \bar{I}'(\psi)\theta + \bar{g}'(\psi)\zeta + \alpha(\psi, \theta)$ , where  $I' = dI / d\psi$  and  $g' = dg / d\psi$ . Then  $\vec{j} = (\bar{I}'(\psi) + \alpha'_\theta)\nabla\psi \times \nabla\theta + \bar{g}'(\psi)\nabla\psi \times \nabla\zeta$ , where  $\alpha'_\theta = \partial\alpha / \partial\theta$ . Choose  $2\pi\bar{I}$  to be the toroidal current inside  $\psi$ , and  $2\pi\bar{g}$  to be the poloidal current outside  $\psi$ . Then, as in the case with  $\lambda$ ,  $\alpha$  is periodic in  $\theta, \zeta$ . Then  $\nabla \times \vec{B} = \vec{j}$  gives the **covariant** representation for  $\vec{B}$

$$\vec{B} = g\nabla\zeta + I\nabla\theta + \delta\nabla\psi \quad (2.8)$$

with  $\langle g \rangle = \bar{g}$ ,  $\langle I \rangle = \bar{I}$  and the brackets indicate averaging over  $\theta$  and  $\zeta$ . In the case of axisymmetry  $g = g(\psi)$ , and also the poloidal coordinate can be chosen so that  $I = I(\psi)$ . In a stellarator equilibrium  $g$ ,  $I$ ,  $\delta$  are all functions of all three variables. With the coordinate system chosen as in Fig. 2.1,  $g$ ,  $q$  and  $I$  are all positive, the plasma current flows clockwise as seen from above, and the field helicity is positive.

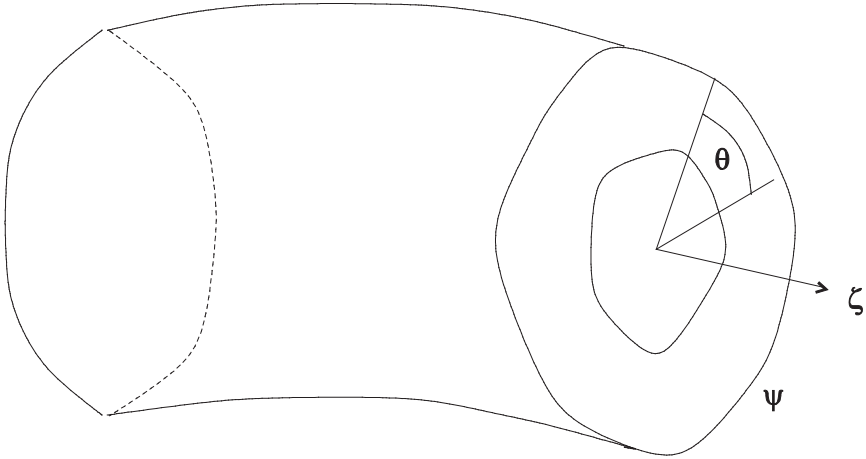


FIG. 2.1. General coordinates.

The ratio of the large toroidal axis  $R$  to the small toroidal axis  $a$  is called the aspect ratio. If  $R/a \gg 1$ , the toroidal plasma cross-section circular, and the plasma pressure small compared to the magnetic field pressure, plasma beta  $\beta = 2p/B^2 \ll 1$ , then the equilibrium is very simple, given by  $g = B_0 R$ ,  $\psi = B_0 r^2 / 2$ ,  $I = B_0 r^2 / (R^2 q(r))$ ,  $\delta = 0$ , and the field strength is  $B \simeq B_0 (1 - r \cos \theta / R)$  with  $B_0$  being the magnetic field on the axis, and  $\theta$  and  $\zeta$  are normal poloidal and toroidal coordinates and the flux surfaces coincide with the minor radius  $r$ . The helicity function  $q(r)$  is determined by the plasma current, hence the relation between  $q$  and  $I$ . Although most tokamaks are non-circular, and  $\beta$  can be a few per cent, the large aspect ratio quantities give good intuitive approximations to many properties. For high  $\beta$  and strongly shaped equilibria one must find the equilibrium field by solving the Grad-Shafranov equation [2.13, 2.14], but expansion in the inverse aspect ratio is also useful [2.15].

### 2.2.3. Guiding centre motion

The Larmor radius of charged particles in a reactor scale plasma is small compared to the plasma dimensions and the radius of curvature of the

magnetic field. Thus charged particle motion is well described using the drift approximation. The guiding centre motion is determined by the cyclotron radius and the field strength and configuration. It is very convenient to use units that make the equations of the problem being considered simple. Introducing units of time given by  $\omega_0^{-1}$ , where  $\omega_0 = eB / (mc)$  is the (signed) on-axis cyclotron frequency, and units of distance given by the major radius  $R$ , the basic unit of energy becomes  $m\omega_0^2 R^2$ , which can also be written as  $(mv^2 / 2)(2R^2 / \rho^2)$ , the gyroradius is  $\rho = v / B \ll 1$ , and the magnetic moment  $\mu = v_{\perp}^2 / (2B)$  is of order  $\rho^2$ . Particle motion both along and across the field lines is of order  $\rho$  but to leading order the cross-field motion is the periodic cyclotron motion, and cross-field drift is of order  $\rho^2$ . It is trivial to restore conventional MKS units to final results, and this will be illustrated in the following. See for example the next to last paragraph of this section.

Begin with the non-relativistic Lagrangian for the motion of a charged particle in an electromagnetic field [2.16],

$$L = \left[ \vec{A}(\vec{x}, t) + \vec{v} \right] \cdot \dot{\vec{x}} - H(\vec{v}, \vec{x}) \quad (2.9)$$

with  $\vec{B} = \nabla \times \vec{A}$ , and the Hamiltonian  $H = \vec{v}^2 / 2 + \Phi(\vec{x}, t)$ , where  $\Phi(\vec{x}, t)$  is the electric potential. Putting the Lagrangian in the form  $\sum p_i \dot{q}_i - H$  we recognize the canonical momentum for a charged particle in an electromagnetic field to be  $\vec{p} = \vec{v} + \vec{A}$ . Now explicitly separate the motion along the field from the cross-field motion through  $\vec{v} = v_{\parallel} \hat{b} + w \hat{c}$  with  $v_{\parallel}$  being velocity parallel to the magnetic field,  $\hat{b} = \vec{B} / B$ , and  $\hat{c} = -\sin \xi \hat{e}_1 - \cos \xi \hat{e}_2$  with  $\hat{e}_1$  and  $\hat{e}_2$  unit vectors orthogonal to  $\vec{B}$  and to each other chosen so that  $\hat{e}_1 \times \hat{e}_2 = \hat{b}$ , and  $\xi$  the gyrophase, and  $w$  the magnitude of the perpendicular velocity  $\vec{v}_{\perp}$ . Define the particle gyrocentre through  $\vec{x} = \vec{X} + w \hat{a} / B$  with  $\hat{a} = \cos \xi \hat{e}_1 - \sin \xi \hat{e}_2$ , so that  $\vec{c} \times \vec{a} = \hat{b}$ , and all quantities on the right are evaluated at the guiding centre  $\vec{X}$ . The Lagrangian then becomes

$$L = \left[ \vec{A}(\vec{x}, t) + v_{\parallel} \hat{b} + w \hat{c} \right] \cdot \left[ \dot{\vec{X}} + \frac{d}{dt} \left( \frac{w \hat{a}}{B} \right) \right] - H \quad (2.10)$$

Now make an expansion in the small parameter  $w$ . Assume that all spatial scales are large enough compared to  $w$  so that the time variations of the field viewed by the particle, as well as all explicit time variations of the field, are slow compared to the gyration frequency  $d\xi / dt$ . Add perfect derivatives to  $L$  and average over the fast time scale, giving

$$L = (\vec{A} + \rho_{\parallel} \vec{B}) \cdot \vec{v} + \mu \dot{\xi} - H \quad (2.11)$$

with  $H = \rho_{\parallel}^2 B^2 / 2 + \mu B + \Phi$  the Hamiltonian and  $\Phi$  the electric potential, and  $\rho_{\parallel} = v_{\parallel} / B$ .

We now use the contravariant and covariant representations for  $\vec{B}$ . Substitute Eq. (2.7) for  $\vec{A}$  and Eq. (2.8) for  $\vec{B}$  into the Lagrangian, giving  $L = (\psi + \rho_{\parallel} I)\dot{\theta} + (\rho_{\parallel} g - \psi_p)\dot{\zeta} + \mu\dot{\zeta} + \delta\rho_{\parallel}\dot{\psi}_p - H$ . Lagrange's equations give [2.1–2.3]

$$\begin{aligned} \dot{\rho}_{\parallel} = & -\frac{(1 - \rho_{\parallel} g')}{D} \left[ (\mu + \rho_{\parallel}^2 B) \frac{\partial B}{\partial \theta} + \frac{\partial \Phi}{\partial \theta} \right] - \\ & -\frac{(q + \rho_{\parallel} I')}{D} \left[ (\mu + \rho_{\parallel}^2 B) \frac{\partial B}{\partial \zeta} + \frac{\partial \Phi}{\partial \zeta} \right] \end{aligned} \quad (2.12)$$

$$\dot{\psi}_p = -\frac{g}{D} \left[ (\mu + \rho_{\parallel}^2 B) \frac{\partial B}{\partial \theta} + \frac{\partial \Phi}{\partial \theta} \right] + \frac{I}{D} \left[ (\mu + \rho_{\parallel}^2 B) \frac{\partial B}{\partial \zeta} + \frac{\partial \Phi}{\partial \zeta} \right] \quad (2.13)$$

$$\dot{\theta} = \frac{\rho_{\parallel} B^2}{D} (1 - \rho_{\parallel} g') + \frac{g}{D} \left[ (\mu + \rho_{\parallel}^2 B) \frac{\partial B}{\partial \psi_p} + \frac{\partial \Phi}{\partial \psi_p} \right] \quad (2.14)$$

$$\begin{aligned} \dot{\zeta} = & \frac{\rho_{\parallel} B^2}{D} (q + \rho_{\parallel} [I'_{\psi_p} - \delta'_{\theta}]) - \frac{I}{D} \left[ (\mu + \rho_{\parallel}^2 B) \frac{\partial B}{\partial \psi_p} + \frac{\partial \Phi}{\partial \psi_p} \right] + \\ & + \frac{\delta}{D} \left[ (\mu + \rho_{\parallel}^2 B) \frac{\partial B}{\partial \theta} + \frac{\partial \Phi}{\partial \theta} \right] \end{aligned} \quad (2.15)$$

with  $D = gq + I + \rho_{\parallel} (gI'_{\psi_p} - Ig'_{\psi_p} - g\delta'_{\theta} + I\delta'_{\zeta})$ .

Note that the function  $\delta$  modifies  $\psi_p$ ,  $\theta$  and  $\rho_{\parallel}$  only through a renormalization of the time interval, through the denominator  $D$ . Thus the projection of the orbit onto the poloidal plane is independent of this function.

The second order drift of a trapped particle over one transit of the orbit in  $\theta$  is

$$\Delta\zeta = \int \dot{\zeta} dt = \oint_{\theta} \frac{\dot{\zeta}}{\dot{\theta}} d\theta \quad (2.16)$$

Then from Eqs (2.14, 2.15), to first order in  $\rho_{\parallel}$  and with no potential,  $\Phi = 0$ ,

$$\begin{aligned} \Delta\zeta = & \oint d\theta (q + \rho_{\parallel} [I'_{\psi_p} - \delta'_{\theta} + g'q]) - \\ & - \oint d\theta \frac{(\mu + \rho_{\parallel}^2 B)}{\rho_{\parallel} B^2} \left[ (I + gq) \frac{\partial B}{\partial \psi_p} - \delta \frac{\delta B}{\delta \theta} \right] \end{aligned} \quad (2.17)$$

Using energy conservation with  $E = \rho_{\parallel}^2 B^2 / 2 + \mu B$  to find  $(\mu + \rho_{\parallel}^2 B) \partial_{\theta} B = -\rho_{\parallel} B^2 \partial_{\theta} B = -\rho_{\parallel} B^2 \partial_{\theta} \rho_{\parallel}$  the terms in  $\delta$  can be written as  $-\oint d\theta \partial_{\theta} [\delta \rho_{\parallel}] = 0$ . Thus neglecting  $\delta$  produces only a non-secular change in the guiding centre motion. Dropping the term in  $\delta$  by a redefinition of the guiding centre, the Lagrangian takes the form

$$L = (\psi + \rho_{\parallel} I) \dot{\theta} + (\rho_{\parallel} g - \psi_p) \dot{\zeta} + \mu \dot{\zeta} - H \quad (2.18)$$

and the canonical coordinates and momenta are immediately identified to be  $\theta$ ,  $\zeta$  and  $P_{\theta}$ ,  $P_{\zeta}$ , with  $P_{\zeta} = \rho_{\parallel} g - \psi_p$ ,  $P_{\theta} = \psi + \rho_{\parallel} I$ . These expressions are immediately recognizable as the covariant components of the sum of particle momentum and vector potential, just as in classical electrodynamics, Eq. (2.9) [2.17].

From the guiding centre equations we have the important fact that the particle trajectories depend only on the magnitude of  $B$ , not on its vector components. Thus it is not geometrical symmetry that determines an associated integral of the motion, but only symmetry of the field magnitude, referred to as quasi-symmetry. This property is exploited in the design of stellarators, which do not possess geometric symmetry, but nevertheless can approximate quasi-symmetry. With no electric field the particle energy takes the form

$$W = \frac{[P_{\zeta} + \psi_p(P_{\zeta}, P_{\theta})]^2 B^2}{2g^2} + \mu B \quad (2.19)$$

In an axisymmetric system  $\zeta = \phi + v(\psi, \theta)$ , with  $\phi$  the cylindrical toroidal coordinate and  $v$  the difference between general and cylindrical toroidal coordinate. Thus  $\partial / \partial \zeta = \partial / \partial \phi$  with  $\psi$  and  $\theta$  fixed and thus  $\zeta$  is also an ignorable coordinate. From the equations of motion we see that  $P_{\zeta}$  is constant if in the system  $\zeta$  is an ignorable coordinate, i.e. if  $B$  is independent of  $\zeta$ . This integral of the motion considerably simplifies the particle orbits. In this case,  $W$  is a function of  $P_{\theta} = \psi + \rho_{\parallel} I$  and  $\theta$ . But  $\rho_{\parallel} = (2W - 2\mu B)^{1/2} / B$  is also a function of  $\psi$ ,  $\theta$ , so  $W = \text{constant}$  defines closed curves in the  $\psi$ ,  $\theta$  plane. Thus the particle motion is restricted to a two dimensional drift surface characterized by the values of  $W$ ,  $\mu$ , regardless of the shape of the flux surface cross-section.

To first order in  $\rho$  a particle follows the field lines and to next order it drifts across the flux surfaces. The drift motion in the  $\psi_p$ ,  $\theta$  plane is given by the terms of second order in  $\rho$

$$\dot{\psi}_p = -\frac{g}{D} (\mu + \rho_{\parallel}^2 B) \frac{\partial B}{\partial \theta}, \quad \dot{\theta} = \frac{g}{D} (\mu + \rho_{\parallel}^2 B) \frac{\partial B}{\partial \psi_p} \quad (2.20)$$

where we neglect the (normally small)  $g'\rho_{\parallel}^2$  term and consider the case of zero potential. The motion across the flux surfaces is usually odd in  $\theta$  since  $B$  increases in the direction of decreasing major radius, the distance from the axis of symmetry, so  $\dot{\psi}_p < 0$  for  $0 < \theta < \pi$  and  $\dot{\psi}_p > 0$  for  $-\pi < \theta < 0$ , i.e. inward drift in the upper half of the torus and outward drift in the lower half. As it moves around  $\theta$  towards decreasing major radius it will normally encounter increasing field magnitude, and may encounter a mirror point, where  $\rho_{\parallel} = 0$  because  $B(\psi_p, \theta_b) = E / \mu$ ,  $\theta_b$  being the bounce angle. If such a point exists the particle is called trapped, otherwise it is called passing. Since drifts across  $\psi$  are proportional to  $\rho^2$  the orbit of a trapped particle has the form of a banana with width  $\sim \rho$ , as shown in Fig. 2.2. To calculate the drift from the flux surface  $\psi_p$  use conservation of  $P_{\zeta}$  and neglect variation of  $g$  along the orbit, which gives a higher order correction in  $\rho$ , to find  $\Delta\psi_p = g\Delta\rho_{\parallel}$ . For a trapped particle  $\rho_{\parallel}$  is zero near the banana tip so  $\rho_{\parallel} = (2E - 2\mu B)^{1/2} / B$ . Using large aspect ratio expressions we find the width to be  $\Delta r = 2q\rho(R/r)^{1/2}$  with  $r$  the minor radius, and from Eq. (2.20) the drift is vertically downward for ions, vertically upward for electrons. Here “down” is defined by the current direction: in the configuration shown the toroidal field and plasma current are clockwise from above; if one looks at the device from below they appear counterclockwise. Clearly for confinement the minor radius must be large compared to the banana width. This gives a condition on the poloidal field. For confinement of 3.5 MeV alpha particles we find a minimum plasma current of  $2 \times 10^6 \sqrt{r/R}$  [A].

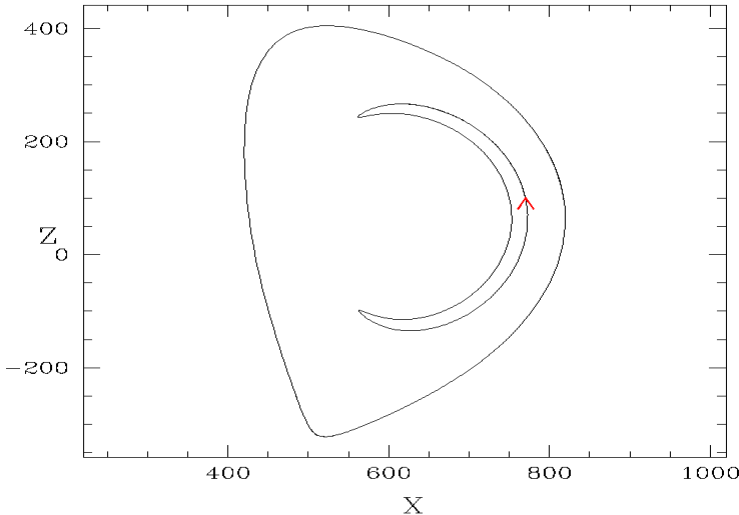


FIG. 2.2. A trapped particle drift orbit in ITER. On the outward part of the orbit an ion moves in the direction of the plasma current. Electrons do the opposite.

The toroidal drift for a trapped particle becomes  $\omega_d = \Delta\zeta / T$ , where  $T = \oint d\theta / \dot{\theta}$  is the time for one bounce period, giving

$$\omega_d \simeq -\frac{1}{T} \oint d\theta \frac{(\mu + \rho_{\parallel}^2 B)}{\rho_{\parallel} B^2} (I + gq) \frac{\partial B}{\partial \psi_p} \quad (2.21)$$

and  $T = \oint d\theta D / (\rho_{\parallel} B^2)$ . This precession is proportional to the particle energy. Deeply trapped particles spend their time near the outer midplane where for a low beta equilibrium  $\partial B / \partial \psi_p$  is negative, so the precession is in the direction of the toroidal current. For a deeply trapped particle we have  $\omega_d \simeq Eq / r$ , which upon restoring the units for energy ( $m\omega_0^2 R^2$ ), distance ( $R$ ) and time ( $\omega_0^{-1}$ ) becomes  $\omega_d \simeq Eq / (mRr\omega_0)$ . A convenient way to express this is  $\omega_d = (E / mc^2) qc^2 / (rR\omega_0)$ , recalling that  $mc^2 = 931$  MeV per proton and that  $\omega_0 = 9.58 \times 10^3 ZB / m$  with  $Z$  the charge in proton units,  $B$  in Gauss and  $m$  in proton masses. In this expression, if  $\omega_0$  is regarded as a signed quantity, the correct direction of precession is obtained also for electrons.

Toroidal precession of high energy particles is particularly important because of the possibility of a resonant interaction of deeply trapped high energy particles with otherwise stable MHD modes. The fishbone mode [2.18, 2.19] is a prime example of this.

#### 2.2.4. The drift kinetic equation

The collisional Vlasov or Boltzmann equation for guiding centre motion is

$$\frac{\partial f}{\partial t} + \vec{v} \cdot \nabla f = C(f) \quad (2.22)$$

where  $f$ , the distribution function, is a function of  $\psi_p$ ,  $\theta$ ,  $\zeta$ ,  $E$ ,  $\mu$  and  $\sigma = \text{sign}(v_{\parallel} / v)$ ,  $C(f)$  is the modification of  $f$  due to collisions, and  $\vec{v}$  is the guiding centre drift velocity. For an axisymmetric equilibrium any function of  $E$ ,  $\mu$ ,  $P_{\zeta}$  is a solution of Eq. (2.22) with  $C(f) = 0$ . The collisions can be approximated as being local and instantaneous, producing a flow of particles in velocity space only. Further, for a Maxwellian distribution,  $f_M$ ,  $C(f_M) = 0$ , since the Maxwellian is the state of highest entropy. For ions and electrons the collision term for the ion distribution  $f$  has the form  $C_{ii}(f_i) + C_{ie}(f_i, f_e)$ .

Analogous to the Braginskii equations, velocity space and flux surface averages of this equation multiplied by powers of the velocity give rise to equations coupling scalar quantities. Even if the system is in magnetohydrodynamic equilibrium, if one passes from a fluid to a kinetic description it is not in thermodynamic equilibrium, so the interest is in the rate at which it approaches the equilibrium state of zero density. The quantities of particular interest are the

fluxes of ions and electrons across the equilibrium surfaces, as well as the rate of momentum and energy flow, describing the quality of the confinement, and the induced currents, important because they modify the equilibrium. Many of these fluxes are due to toroidal geometry, and were first found by considering the special nature of particle orbits in a toroidal system, given by Eqs (2.12–2.15). There is an inward motion of trapped particles called the Ware pinch, induced toroidal current called the bootstrap current, and different regimes of cross-field transport depending on the magnitude of the collision frequency, known as banana, plateau and Pfirsch–Schlüter domains. Resistivity is modified by toroidal geometry, as well as the transport of momentum.

Many of these effects were calculated in detail by Rosenbluth et al. [2.20] in 1972. A 1995 review by Kikuchi and Azumi [2.21] gives expressions for velocity moments of the drift kinetic equation of first and third order showing the parallel friction force, viscous and electric forces, and momentum and heat sources. The equations take the form

$$LU_{\parallel} = M[U_{\parallel} - V] - S - E \quad (2.23)$$

where  $L$  and  $M$  are friction and viscosity matrices and  $U_{\parallel}$ ,  $V$ ,  $S$  and  $E$  are vectors of parallel heat flow, thermodynamic forces, momentum and heat sources, and the electric field, respectively. Matrix inversion of this equation gives a generalized Ohm's Law.

Some of these neoclassical expressions can be estimated by simple heuristic arguments, and we will do this in the following. The derivations assume a static axisymmetric equilibrium, so while some of the derived expressions are observed experimentally, there are also significant deviations from them due to fluctuation spectra of unstable plasma modes as well as deviations from axisymmetry caused by the discrete toroidal field coils. In particular, small scale fluctuations produce electron heat transport an order of magnitude larger than the neoclassical estimates, and also ion loss is typically a few times the neoclassical value. Toroidal magnetic field ripple due to discrete field coils above a low stochastic threshold value causes a very rapid loss of high energy trapped particles, and if fusion alpha particles are to be confined this places a severe restriction on machine design.

The collisions conserve the number of particles of each species; in a quasi-symmetric system the sum over all particles of the canonical toroidal momentum  $P_{\zeta}$  is conserved. These conditions are local, i.e. they hold on each flux surface. The canonical momentum is  $P_{\zeta} = \rho_{\parallel} g - \psi_p$ . The time derivative of the total canonical momentum is

$$\frac{d}{dt} \langle P_{\zeta} \rangle = \sum_s \int d^3v P_{\zeta} \frac{df}{dt} = \sum_s \int d^3v P_{\zeta} C(f) \quad (2.24)$$

where  $\sum_s$  indicates a sum over species. The  $\psi_p$  terms in  $P_\zeta$  do not contribute to this expression, because for each species  $\int d^3v C(f) = 0$ . This is simply the statement that collisions conserve the total number of particles of each species. Thus the conservation of total canonical momentum, following from symmetry, gives  $0 = \sum_s \int d^3v \rho_{\parallel} C(f)$ .

In a uniform magnetic field, classical cross-field particle diffusion occurs because of a particle's gyroradius. Collisions causing a  $90^\circ$  deflection in particle velocity result in a displacement of the particle gyrocentre by one gyroradius. A random walk approximation then gives for the classical diffusion coefficient  $D = \nu \rho^2 / 2$ , where  $\nu = \nu_{ei}$  is the electron-ion collision frequency for a  $90^\circ$  collision and  $\rho$  the electron gyroradius, and similarly for ions.

In toroidal geometry the class of trapped particles (in large aspect ratio having  $v_{\parallel} < (r/R)^{1/2} v_{\perp}$ ) have a bounce frequency less than  $\omega_b = (r/R)^{1/2} (v_{th} / Rq)$ , with  $v_{th}$  the thermal velocity. For collision frequencies larger than  $\omega_b$  so that banana orbits do not exist, there still exist passing particle orbits with excursions from the flux surface of  $\Delta r = q\rho$ . Collisions produce a random walk with a step of this magnitude, and we obtain  $D_{PS} = \nu_{ei} q^2 \rho^2 / 2$  for the Pfirsch-Schlüter diffusion coefficient.

If the collision time is long enough so that banana orbits can be completed, i.e.  $\nu_{ei} < \omega_b$ , the drift kinetic formalism is applicable. This collisionality domain is called the banana regime. Assuming toroidal symmetry with nested magnetic surfaces, the particle flux across a surface  $\psi_p$  is given by

$$\Gamma = \int d^3v \frac{f \vec{v} \cdot \nabla \psi_p}{|\nabla \psi_p|} \quad (2.25)$$

Substituting the expression for  $\vec{v}$  from Section 2.2.3 we find  $\vec{v} \cdot \nabla \psi_p = (\rho_{\parallel} / q) \partial \rho_{\parallel} / \partial \theta$  where we have used the large aspect ratio expression  $\nabla \psi_p = (r/q) \hat{r}$ . This drift term has the opposite sign for electrons. Substituting, we find for the average flux over a magnetic surface:

$$\bar{\Gamma} = \pm \int d^3v \frac{d\theta}{2\pi} f \frac{\partial}{\partial \theta} \left( \frac{\rho_{\parallel}^2}{2} \right) \quad (2.26)$$

with the  $\pm$  corresponding to the sign of the charge. Integrating by parts and using  $\int d^3v C(f) = 0$ , and  $\sum_s \int d^3v \rho_{\parallel} C(f) = 0$ , we find for the average flux through surface  $r$  for a single species:

$$\bar{\Gamma} = \pm \int \frac{q(r)}{4\pi} \int d\theta d^3v \rho_{\parallel} C(f_v) \quad (2.27)$$

Thus the flux due to collisions among particles of a single species is zero. In a two-component plasma, the ion and electron particle fluxes are equal, i.e. collisional diffusion is ambipolar. Changing integration variables through  $d^3v = \sum_{\sigma} 2\pi dE d\mu / |\rho_{\parallel}|$  (with  $\sigma$  referring to the sign of the pitch) where the summation is over the two signs of  $\rho_{\parallel}$  and substituting a Lorentz collision term  $C(f) = \nu \rho_{\parallel} \partial_u (\rho_{\parallel} \partial_u f)$  the modification of the distribution function can be found explicitly [2.22]. Substitution then gives for the average particle flux:

$$\bar{\Gamma} = -1.46 \left( \frac{r}{R} \right)^{1/2} \frac{\nu}{B_{\theta}^{1/2}} \frac{dp}{dr} \quad (2.28)$$

as originally found by Galeev and Sagdeev [2.23, 2.24], where  $B_{\theta}$  is the poloidal component of magnetic field. The diffusion rate in the banana regime can be obtained heuristically using large aspect ratio expressions. The diffusion is dominated by the trapped particles, and during a collision the step size becomes the banana width,  $\Delta r = 2q\rho(R/r)^{1/2}$ . In addition, since trapped particles must have  $v_{\parallel} / v_{\perp} < (r/R)^{1/2}$ , a corresponding smaller collisional modification of the velocity direction is necessary to change the orbit. For multiple small collisions  $(\Delta\theta)^2 = \nu t$ , so the effective collision frequency for a trapped particle is  $\nu_{eff} = (R/r)\nu_{ei}$ . In addition, only a fraction  $(r/R)^{1/2}$  of the particle population is trapped, giving for the diffusion coefficient in the banana regime  $D = 4\nu_{ei}q^2\rho^2(R/r)^{3/2}$ , in agreement with Eq. (2.28) except for the numerical constant. Plotted versus the effective collision frequency normalized to bounce frequency,  $\nu^* = \nu_{eff} / \omega_b$ , the neoclassical diffusion coefficient then has the approximate form [2.24] shown in Fig. 2.3. The transition region between banana and Pfirsch–Schlüter domains is called the plateau domain. However, a clear distinction between these domains is a result of the large aspect ratio approximation. In a real tokamak the domains smoothly merge, and with an aspect ratio of 4 the plateau domain is barely discernible.

Note that the diffusion scales as  $\rho^2\nu$ , with  $\nu$  the effective collision frequency for  $90^\circ$  scattering. This quantity thus scales with mass as  $m^{1/2}$  since for fixed energy  $\rho \sim \sqrt{m}$  and  $\nu \sim 1/\sqrt{m}$ . In an axisymmetric configuration the ion and electron rates must be equal, as required by Eq. (2.27). A more careful analysis shows that they should approximately equal the slower electron value [2.22]. In fact they are experimentally found to be a few times the ion neoclassical value, indicating that the electron diffusion is not neoclassical.

By operating in a regime of reversed shear, stable to confinement destroying fluctuations, several tokamaks achieved the theoretical minimum neoclassical level of transport [2.25]. The stabilizing influence of very small or even negative shear has led to the exploration of configurations with large  $q$  on-axis, referred to as an advanced tokamak configuration. However, there are associated restrictions due to the strong  $q$  dependence of stochastic ripple

loss (Section 2.2.6), and difficulty of thermal equilibrium associated with these configurations. The momentum equation involves the collision dependent viscosity term. The contributing effects are termed parallel-, perpendicular- and gyroviscosity, arising from collision induced random walks along and across the field, and gyroviscosity is similar to bootstrap current (Section 2.2.5) insofar that it is induced by collisions but its value is independent of collision frequency. Experiments performed on TFTR [2.26] and Alcator C-Mod [2.27] show however that momentum transport is not neoclassical, but much larger [2.25, 2.28]. Ion momentum and thermal diffusivities are found to be comparable in magnitude and vary similarly with plasma current and minor radius. This correlation is consistent with the anomalous transport driven by collisionless electrostatic instabilities including ion temperature gradient driven modes and collisionless trapped electron modes.

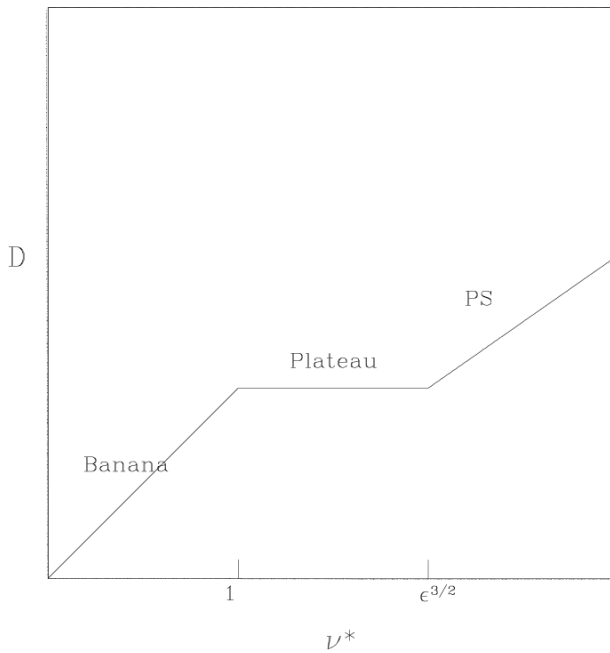


FIG. 2.3. Neoclassical diffusion.

### 2.2.5. Bootstrap current

The collisional trapping and detrapping of particles in the banana regime gives rise to a net toroidal current which is called the bootstrap current [2.29, 2.30]. It results from a small perturbation of the particle distribution from that of uniform particle pitch ( $\lambda = v_{\parallel} / v$ ), and is due to toroidal curvature and the

existence of banana orbits. It can be calculated by using the perturbed distribution function of Section 2.2.4, but it can also be arrived at directly.

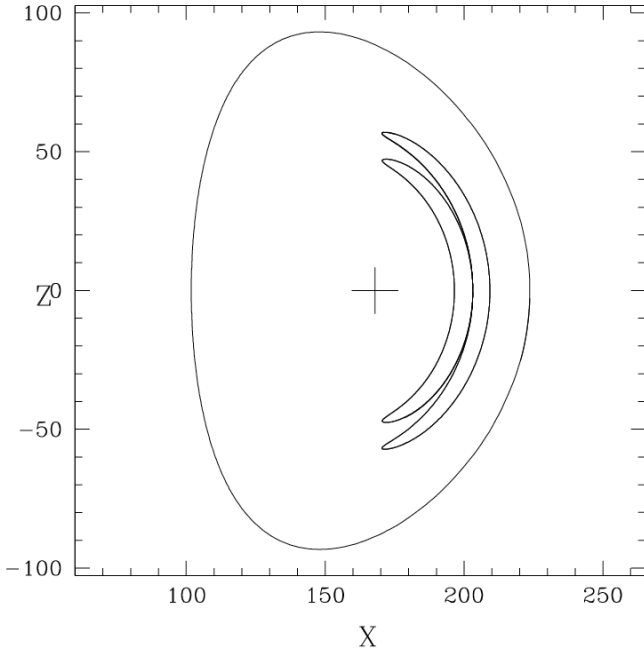


FIG. 2.4. Banana orbits originating at  $\theta = 0$  on the same flux surface with opposite pitches.

Consider a flux surface  $\psi$ , and the two associated ion banana orbits with opposite velocities at  $\theta = 0$  on the flux surface of their common origin, as shown in Fig. 2.4. To be trapped they must have pitch  $-\sqrt{r/R} < \lambda < \sqrt{r/R}$  at the midplane. The inside banana is co-moving at its initial point, and the outside banana is counter-moving. Because of the density gradient, on this flux surface the density of co-moving trapped particles will be larger than the counter-moving by a factor  $\delta n = (dn/dr)W_b/2$ , with  $W_b$  the banana width, as shown in Fig. 2.5. The bootstrap current is due to the associated asymmetry in the co- and counter-moving passing particles necessary to maintain steady state through small pitch angle scattering. Pitch angle scattering causes a diffusion in  $\lambda$ , and the constant source of trapped particles leads to a uniform pitch distribution of passing particles, with a density of  $1 + \delta n$  for co-moving, and  $1 - \delta n$  for counter-moving, as shown in Fig. 2.5. Substituting  $W_b = (R/r)^{1/2}q\rho$ , multiplying by the average velocity of the passing particles,  $\rho/2$ , and using the expression for the pressure,  $p = n\rho^2/2$ , we find for the bootstrap current density ( $r/R \ll 1$ )

$$j_{BS} = -\left(\frac{r}{R}\right)^{1/2} \frac{1}{B_\theta} \frac{\partial p}{\partial r} \quad (2.29)$$

This expression is for a given pressure, independent of mass. Electrons produce a flow in the opposite direction, and thus a current also given by Eq. (2.29). For an evaluation of the exact numerical coefficient for this expression see Ref. [2.20]. Note that this current, although dependent on the collisions for the equilibration of trapped and passing populations, is independent of the collision frequency. Bootstrap current is not free, it is driven by the diffusion of particles down the density gradient associated with the pitch angle scattering.

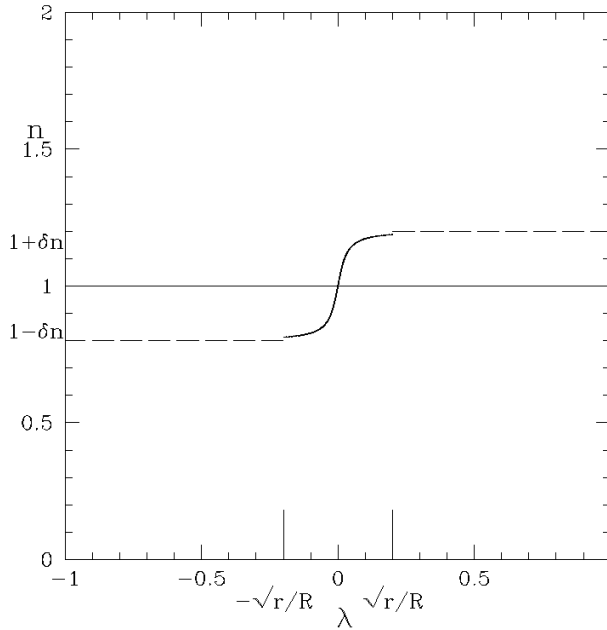


FIG. 2.5. Particle density versus pitch at the midplane. Particles with pitch  $-\sqrt{r/R} < \lambda < \sqrt{r/R}$  are trapped. There is a greater density of co-moving trapped particles than counter-moving. Pitch angle scattering then produces a uniform passing distribution in  $\lambda$ , as shown by the dashed lines.

In a stellarator the bootstrap current is more complex because of the possibility of resonances, and important because it may be the only source of current in the equilibrium. Particle motion in any equilibrium depends only on the magnitude of the magnetic field, which can be expanded in Fourier harmonics with respect to the poloidal and toroidal variables  $\theta$  and  $\zeta$ ,  $B = \sum_{m,n} B_{m,n} \cos(m\theta - n\zeta)$ , where  $m, n$  are poloidal and toroidal mode numbers respectively. The  $B_{m,n}$  are perturbations of the magnitude of  $\vec{B}$  only, and do not produce magnetic islands in the equilibrium. The analytic expression for the bootstrap current for a monoenergetic distribution is  $j_{BS} = -G_{BS} f_t E dn / d\psi$ , with  $G_{BS}$  a geometric factor and  $f_t$  the trapped distribution [2.31, 2.32] which may contain resonant denominators.

Trapped particles on orbits which take longer to complete than the time for them to collisionally scatter into passing orbits do not contribute to the bootstrap current. In the axisymmetric case (a tokamak) the correction has been analytically calculated [2.33] by finding the collisionally modified distribution function in the boundary layer between the trapped and untrapped particle regions of phase space. The result is that in the banana regime the bootstrap current is decreased by a function of the dimensionless collision frequency  $\nu^*$ . Clearly, if the collision frequency is so large that banana orbits do not exist, there is no bootstrap current.

Bootstrap current is especially important because of the possibility of producing almost all of the current profile for a tokamak. This is critical because the ohmic current is produced by pulsing the toroidal field coils, and thus it cannot be maintained in steady state. The bootstrap current makes it possible to extend the pulse length significantly. It was first observed in an octopole device [2.34], where both the bootstrap current and the Pfirsch–Schlüter current, which maintains charge neutrality in the presence of the diamagnetic current, were measured. First observation of the bootstrap current in a tokamak was performed on TFTR [2.35, 2.36] by comparing the measured surface voltage with simulations with and without bootstrap current. It was also observed in a high density discharge in the JET tokamak [2.37, 2.38], and later a large bootstrap fraction of 80% of the current was observed in the JT-60 tokamak [2.39, 2.40]. Knowledge of the bootstrap current is necessary in order to confirm the generalized Ohm's Law for current in a tokamak, given by  $E_{\parallel} = \eta_{\parallel}(j - j_{BS})$ , with  $E_{\parallel}$  the parallel electric field and  $\eta_{\parallel}$  the neoclassical resistivity. The validity of neoclassical resistivity was confirmed on JET [2.38], JT-60 [2.39] and TFTR [2.41]. The 1995 review by Kikuchi and Azumi [2.21] gives experimental evidence for bootstrap current and generalized Ohm's Law.

### 2.2.6. Magnetic field ripple

The toroidal field in a tokamak is not exactly axisymmetric due to the finite number of toroidal field coils. A simple model for the field magnitude including this ripple in a large aspect ratio circular device is given by  $B = B_0(1 - r \cos \theta + \delta \cos N\phi)$ , with  $r$  in units of the major radius  $R$  and  $\phi$  the toroidal angle,  $N$  the number of coils and  $\delta$  the ripple magnitude. The magnitude of the field along a field line is shown in Fig. 2.6. If the perturbation is strong enough, magnetic wells are formed. Along a field line  $\phi = q\theta$ ,  $r = \text{constant}$  so ripple wells exist if  $r|\sin \theta| < Nq\delta$ . To be trapped in one of these wells (a superbanana), a particle must have  $v_{\parallel} / v < \sqrt{\delta}$ . If trapped, the loss is very rapid, since the particle simply drifts down directly to the wall, shown also in Fig. 2.7: the particle executed a number of bounces in a poloidally trapped orbit before encountering a ripple well with a phase allowing it to be trapped in the well, after which it rapidly drifts to the wall.

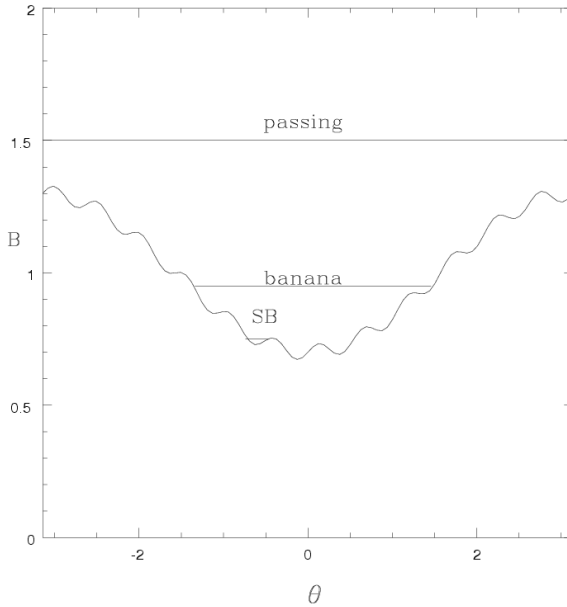


FIG. 2.6. Magnetic ripple along a particle trajectory.

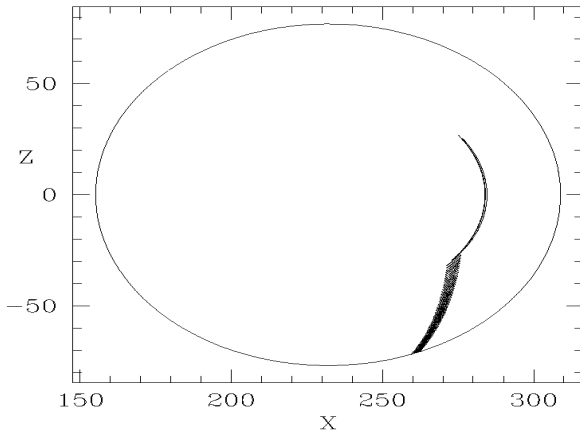


FIG. 2.7. Loss orbit for a particle trapped in a ripple well.

Even if ripple wells do not exist, the phase space of banana tip trajectories can become stochastic due to ripple. Because of particle drift, when the ripple causes a banana orbit to bounce either early or late it produces a small change in the radial position of the banana tip. Shown in Fig. 2.8 is the trajectory of a trapped particle in resonance with the field coils, shown at the left with an  $\times$ . Here  $\phi_b = 2q\theta_b$  is the toroidal motion along the field and  $\phi_p$  is the precessional drift motion in one bounce. For small ripple the plot of radial banana tip position

versus toroidal angle is periodic, but there are resonances producing islands at radii where the precessional motion of the tip moves one coil spacing in one bounce, as shown in Fig. 2.9. Typically there can be one hundred such resonances across the minor radius. If the ripple is sufficiently large the islands due to these resonances overlap and the banana tip motion becomes stochastic. Because of conservation of  $\mu$  and energy, the tip is confined to a surface of constant  $B$ , but this means it can move vertically until the particle is lost, as shown in Fig. 2.10.

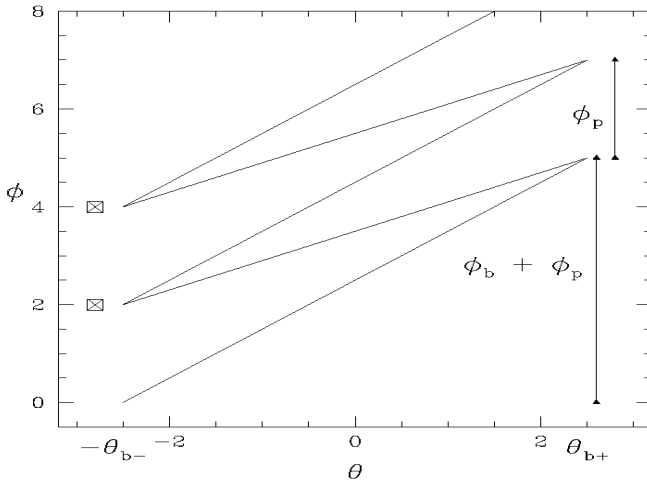


FIG. 2.8. Trapped particle orbit showing resonance with field coils.  $\theta_{b-}$  and  $\theta_{b+}$  are the positive and negative bounce points, respectively.

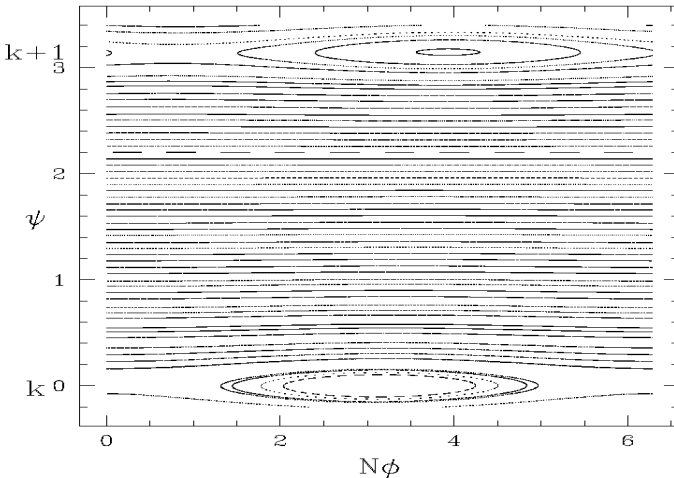


FIG. 2.9. Poincaré plot of banana tip motion showing ripple resonances.

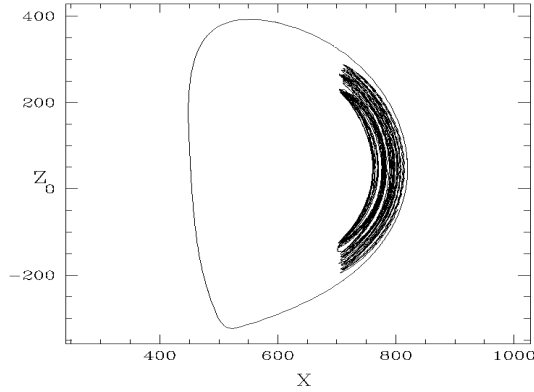


FIG. 2.10. Trajectory of stochastic ripple loss banana orbit.

The change of the bounce point due to the radial drift can be calculated using  $\phi_b = 2q\theta_b$  and  $B$  at the bounce points,  $B(\psi_b, \theta_b) = E / \mu$  giving  $d\phi_b / d\psi_b = 2\theta_b dq / d\psi_p - 2q \partial_{\psi_p} B / \partial_{\theta_b} B$ . The motion becomes stochastic approximately [2.42, 2.43] when the modification of the toroidal bounce point  $\Delta$  is as large as a ripple phase  $N\Delta d\phi_b / dr > 1$ . This loss produces an important restriction on ripple in a reactor

$$\delta \leq [r / (\pi RNq)]^{3/2} / (\rho q') \quad (2.30)$$

important only for high energies, particularly relevant for fusion product alpha particles.

The first experiments to give a confirmation of stochastic ripple loss were carried out on TFTR [2.44] measuring the loss of D-D fusion products. Two clearly separated loss peaks in toroidal pitch angle were observed, the first agreeing with the distribution of prompt loss particles and the second with those due to stochastic ripple loss. Experiments were carried out on JET [2.45], where the ripple magnitude can be adjusted by changing current in alternate coils. The plasma response to increased ripple is quite obvious and dramatic. The most obvious effect of increasing ripple is the large plasma density reduction in the H-mode phase. Both the plasma average density and the edge density show a pronounced “pump-out”. At the same time, the plasma electron temperature remains, on average, approximately constant as the ripple is increased. Increasing the ripple also results in a marked change of the plasma toroidal rotation. Since banana orbits exit the plasma while moving in the co-current direction, there is a transfer of momentum to the wall, and substantial plasma braking is observed, with the reduction of the positive (co-current) plasma rotation measured across the whole profile, the rotation becoming counter-current for ripple of 1%. Increased values of the toroidal field ripple also affect the edge localized mode

(ELM) behaviour. When the ripple is increased from 0.08% to 0.5%, the type I ELM frequency almost doubles, going from  $\sim 12$  Hz to  $\sim 20$  Hz. When the ripple is increased further to 0.7% and finally to 1%, ELMs become irregular, with Type I, Type III and long ELM-free phases, in spite of the fact that power across the separatrix remains approximately constant.

### 2.2.7. Transport in a stochastic field

Magnetic perturbations with a field component across the equilibrium flux surfaces can lead to a change in topology, with magnetic islands forming at surfaces where the perturbation is resonant with the local  $q$  value. These islands essentially short-circuit transport. Furthermore, if nearby islands overlap, field lines can wander between them [2.46], producing a broad region in which the field is stochastic, and in which a density gradient cannot be supported. Assuming that the perturbation amplitudes are well above the threshold for stochasticity, a random phase approximation may be used and the resulting diffusive motion of particles was calculated by Rechester and Rosenbluth [2.47].

For times long compared to the collision time, the particles move along the field line diffusively, i.e.  $(\Delta\phi)^2 = D_{\parallel}t$ , with  $D_{\parallel}$  the parallel collisional diffusion. If the field lines diffuse across the equilibrium surfaces with diffusion  $D_m$ , the particles will then move radially with  $D_s \sim t^{-1/2}$  giving zero for large time; there is no cross-field diffusion due to diffusive motion along the field line. However, another effect enters, namely the shift of the particle to a different field line during a collision, due to the gyroradius. If the field is stochastic, nearby field lines on the average diverge exponentially, with the distance between lines given by  $d = d_0 e^{hz}$ ,  $z$  being the distance along the line and  $h$  the Kolmogorov entropy. Then in a time  $\tau_h = L_h^2 / D_{\parallel}$  the particle will be carried a distance  $\delta_{\perp}$  from the initial line, with  $L_h = (1/h) \ln(\delta_{\perp})$  and  $\delta_{\perp}$  the wavelength across the unperturbed field, defining the decorrelation distance of the initial field.

The particle diffusion is then

$$D = D_m v \left( \frac{\lambda_v}{L_h} \right) = \frac{D_m D_{\parallel}}{L_h} \quad (2.31)$$

with  $\lambda_v$  the mean free path at velocity  $v$ .

A perfect testbed for the understanding of transport in stochastic magnetic fields is provided by the reversed field pinch, which has a well known steady state spectrum of saturated tearing modes. These modes produce a field which is well above stochastic threshold, but nevertheless still possesses a great deal of structure, including streamers formed by the partially destroyed island remnants. The field is sufficiently close to stochastic threshold that a random phase approximation for the particle motion is not valid, and thus Rechester–Rosenbluth transport is

not operative. Transport in this system has been shown [2.48] to be subdiffusive and non-local. Passing particles explore the stochastic field, participating in Levy flights [2.49] with flight time and radial displacement distributions with long tails that do not possess either a mean time or a mean distance. It is very possible that electron transport in tokamaks is also non-local and non-diffusive, increasing the complexity of understanding electron confinement.

## 2.3. TURBULENT TRANSPORT

### 2.3.1. Introduction

Confining hot and dense plasmas in the interior of fusion devices while keeping boundaries from being damaged by excessive heat necessarily creates an inhomogeneous state. Such magnetically confined high temperature plasmas are not only unstable to various linear instabilities with different wavelengths and complex frequencies, but often non-linearly self-organize themselves into more energetically favourable states.

A large scale MHD instability, when it is violently unstable, can terminate a tokamak plasma by throwing it into the wall, and this is called a disruption. Even in the absence of large scale MHD instabilities, tokamak transport is usually anomalous, which means that the transport rate is much higher than predictions from theories based on Coulomb collisions. This anomalous transport is caused by small scale collective instabilities which are typically driven by gradients in temperature, density and so on. These microinstabilities saturate at low amplitude due to non-linear mechanisms. As a consequence, particles  $\vec{E} \times \vec{B}$  drift radially in a random manner, due to fluctuating electric fields. This is how plasmas escape from the interior of a tokamak.

The amplitude of tokamak microturbulence is very low. The relative fluctuation amplitude,  $\delta n / n_0$ , is typically less than 1% in the core. Towards the edge, it can be greater than 10%. These general trends were confirmed in different machines, using different diagnostics as described in detail in Section 2.6. In summary, the properties of tokamak core microturbulence are as follows:  $\delta n / n_0 \sim 1\%$ ,  $k_r \rho_i \sim k_\theta \rho_i \sim 0.1 \sim 0.2$ ,  $k_\parallel \lesssim 1 / qR \ll k_\perp$ , and  $\omega - \vec{k} \cdot \vec{u}_E \sim \Delta\omega \sim \omega_*$ , where  $\vec{u}_E$  is the mean  $\vec{E} \times \vec{B}$  velocity. Here,  $\delta n$  and  $n_0$  are the fluctuating and mean parts of density respectively.  $\rho_i \equiv v_{T_i} (M_i c / eB)$  is the thermal ion gyroradius, where  $v_{T_i}$  and  $c$  are ion thermal speed and speed of light respectively, and  $k_r$ ,  $k_\theta$ ,  $k_\parallel$  and  $k_\perp$  are the radial, poloidal, parallel and perpendicular (to equilibrium magnetic field) components of the  $\vec{k}$  vector of the fluctuations respectively.  $q$  is the safety factor (see Section 2.3.5) and  $R$  is the major radius. In addition,  $\omega$  is the mode frequency, and  $\Delta\omega$  is the measured broadening thereof.  $\omega_*$  is the diamagnetic drift frequency. The broadband frequency ( $\Delta\omega \sim \omega$ ) indicates strong turbulence. Sometimes the Doppler shift

dominates in rotating plasmas, and this should be taken into account for the mode identification.

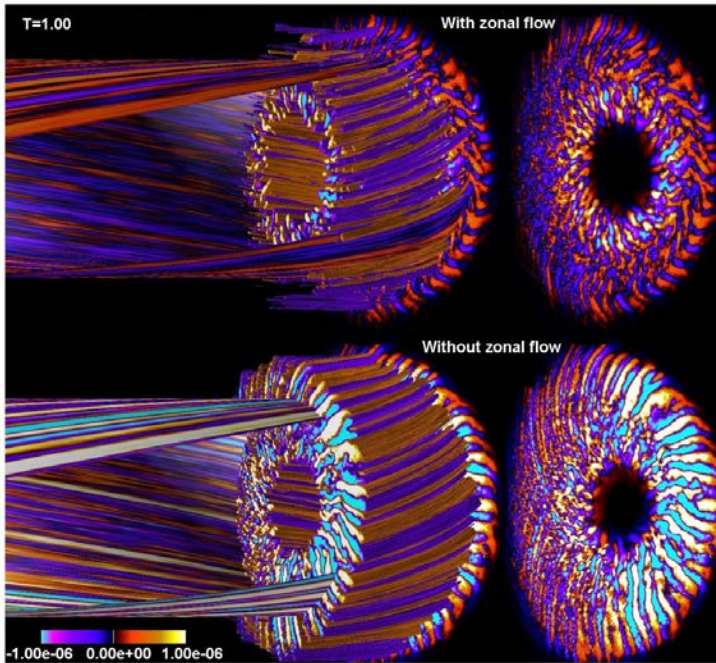


FIG. 2.11. Massively parallel gyrokinetic simulation of ITG turbulence using the GTS code [2.50] exhibits fluctuation spatial structures in 3-D and the effect of self-generated zonal flows on them. From “Powerful Beyond Imagination”, SC06 International Conference for High Performance Computing, Networking, Storage and Analysis, 11–17 November 2006, Tampa, Florida (<http://sc06.supercomputing.org/video.php>) [2.54]. Courtesy of W. Wang, Princeton Plasma Physics Laboratory, and S. Klasky, Oak Ridge National Laboratory.

These properties of tokamak microturbulence are now being reproduced from large scale gyrokinetic simulations. For instance, Fig. 2.11 is from an ion temperature gradient (ITG) driven turbulence simulation using the Gyrokinetic Tokamak Simulation (GTS) code [2.50] with shaping capability. Density fluctuation contours in the presence of self-generated zonal flows [2.51] indeed show that the average turbulence eddy size is around several ion gyroradii across the magnetic field, and the fluctuation is aligned almost parallel to the magnetic field, with parallel wavelength of the order of the connection length. Microturbulence in a tokamak plasma consists of many modes or eddies non-linearly interacting with each other. The small scale linear instabilities (often called microinstabilities) are driven by the expansion of the free energy source stored in  $\nabla n$ ,  $\nabla T_i$  or  $\nabla T_e$ . To make collective waves unstable, these free energies should be accessible for waves to tap. This is provided by dissipation

including wave–particle resonant interaction or reactive mechanisms including bad magnetic curvature and negative compressibility. Microinstabilities can be classified into various modes according to the variety of the free energy source, accessibility mechanism and magnetic geometry of a system. In this section, we first illustrate a few basic examples, and discuss candidates which are currently believed to be of experimental relevance in present day and future fusion devices. Due to severe space limitation, we limit our discussion to electrostatic fluctuations. A more detailed zoology of these microinstabilities can be found in review articles [2.52, 2.53]. A partial list is given in Table 2.1.

A much more detailed description of physical kinetics of turbulent plasmas, in particular on the subjects of spectral transfer, weak turbulence and strong turbulence theories which cannot be covered here, can be found in Ref. [2.55].

TABLE 2.1. LIST OF ELECTROSTATIC MICROINSTABILITIES

( $\omega_{*e} = k_{\theta} \rho_s c_s / L_n$  is the electron diamagnetic drift frequency defined with the density gradient scale length  $L_n$ ,  $\omega_{*pe} = k_{\theta} \rho_s c_s / L_p$  is the electron diamagnetic drift frequency defined with the pressure gradient scale length  $L_p$ ; subscripts  $e$  and  $i$  stand for electrons and ions respectively)

Classification: Free energy	Spatio-temporal scales (wavelength, frequency direction, rough magnitude)	Accessability mechanism for instability
Trapped ion mode $n, T_e$ or $T_i$	$\sim \rho_{\theta}$ $\sim \omega_{*e}$	Trapped ion precession resonance (collisionless) Collisions between trapped and passing ions (dissipative)
Ion temperature gradient mode $T_i$	$> \rho_i$ $< \omega_{*pi}$	Bad curvature or negative compressibility
Trapped electron mode $n$ or $T_e$	$\sim \rho_i$ $< \omega_{*e}$	Trapped electron precession resonance (collisionless) Collisions between trapped and passing electrons (dissipative)
Electron temperature gradient mode $T_e$	$> \rho_e$ $< \omega_{*pe}$	Bad curvature or negative compressibility

### 2.3.2. Examples of basic microinstabilities

In this section, we consider a slab geometry with a uniform magnetic field  $\vec{B} = B\vec{e}_z$  (where  $\vec{e}_z$  stands for the unit vector in the  $z$  direction) and  $n$ ,  $T_i$  and  $T_e$  varying only in the radial ( $x$ ) direction. Fourier decomposition of a fluctuating quantity in the  $y$  and  $z$  directions is understood, i.e.  $\delta\Phi = \sum_{\vec{k}, \omega} \delta\Phi_{\vec{k}, \omega} e^{i(\vec{k}\cdot\vec{x} - \omega t)}$ .

#### 2.3.2.1. Electron drift instabilities

Historically, electron drift waves (which propagate in the electron diamagnetic drift direction, driven by  $\nabla n$ ) were theoretically investigated first. For these electron drift waves, the ion dynamics in a uniform magnetic field, in its simplest non-trivial context ( $(\omega / k_{\parallel}) \gg v_{T_i}$ ,  $k_{\perp} \rho_i \ll 1$ , and  $T_i \ll T_e$ ) can be described by the fluid equations:

$$m_i \frac{d}{dt} \delta u_{\parallel i} = -e \nabla_{\parallel} \delta\Phi \quad (2.32)$$

$$\delta \vec{u}_{\perp} = \delta \vec{u}_E + \delta \vec{u}_{pol} = c \frac{\hat{b} \times \nabla \delta\Phi}{B} + \frac{M_i c^2}{e B^2} \frac{\partial}{\partial t} \nabla_{\perp} \delta\Phi \quad (2.33)$$

Here,  $c$  and  $v_{T_i}$  are the ion sound and ion thermal speed respectively,  $\rho_s \equiv \sqrt{T_e / T_i} \rho_i$ ,  $L_n$  is the density gradient scale length,  $\delta\Phi$  is the fluctuating electrostatic potential,  $\delta u_{\parallel i}$  is the fluctuating ion fluid velocity along  $\vec{B}$ ,  $\delta \vec{u}_{\perp}$  is the perpendicular fluid velocity and  $\delta \vec{u}_{pol}$  is the polarization drift velocity. By using the linearized ion density continuity equation,  $\partial_t \delta n_i + \nabla \cdot (n_0 \delta \vec{u}) = 0$ , we obtain the ion density response:

$$\frac{\delta n_i}{n_0} = \left( \frac{\omega_{*e}}{\omega} - k_{\perp}^2 \rho_s^2 + \frac{k_{\parallel}^2 c_s^2}{\omega^2} \right) \frac{|e| \delta\Phi}{T_e} \quad (2.34)$$

Electrons, on the other hand, can adjust quickly to potential variations, and equilibrate along the magnetic field owing to their high velocity ( $v_{T_e} \gg \omega / k_{\parallel}$  with  $v_{T_e}$  being the electron thermal velocity), i.e.  $|e| n_0 \nabla_{\parallel} \delta\Phi - T_e \nabla_{\parallel} \delta n_e = 0$  leads to the Boltzmann response for the electron density:

$$\frac{\delta n_e}{n_0} = \frac{|e| \delta\Phi}{T_e} \quad (2.35)$$

This is often called an adiabatic response, referring to the relatively slow timescale of the wave compared to the electron transit motion ( $\omega \ll k_{\parallel} v_{T_e}$ ). Since the Debye length  $\lambda_{De}$  is much shorter than the microinstability's spatial

scales, the Poisson equation can be approximated by a quasi-neutrality condition:  $\delta n_e = \delta n_i$ . Then, by using Eqs (2.34) and (2.35), we obtain the linear dispersion relation for the electron drift wave:

$$1 + k_{\perp}^2 \rho_s^2 - \frac{\omega_{*e}}{\omega} - \frac{k_{\parallel}^2 c_s^2}{\omega^2} = 0 \quad (2.36)$$

Note that Eq. (2.36) describes a wave which oscillates in time, not an instability which grows in time.

The radial flux of electron density carried by the electron drift wave is given by  $\Gamma_e \equiv \langle \delta n_e \delta v_r \rangle$ . Here,  $\langle \dots \rangle$  denotes an ensemble average which is replaced by an average over an ignorable coordinate (e.g. the toroidal direction in an axisymmetric tokamak, or the poloidal direction in simple slab geometry) or a time average. Since  $\delta \vec{v}_r \equiv (c/B) \vec{b} \times \vec{\nabla} \delta \Phi \cdot \hat{e}_x$  (where  $\hat{e}_x$  is the unit vector in the radial direction  $x$ ) and  $\delta n_e \propto \delta \Phi$ , we can easily observe that the “transporter”  $\delta v_r$  and the “transportee”  $\delta n_e$  are 90° degrees out of phase and  $\Gamma_e = 0$ . Therefore, for non-vanishing particle flux carried by an electron drift wave, a phase shift between  $\delta n_e$  and  $\delta \Phi$  is required. This can be provided by electron dissipation and the electron drift wave can be driven unstable by it. To be more precise, this is dissipation on electron particles such that waves gain energy from electrons. So unstable electron drift waves can drive a net outward flux of electron density. We emphasize “net” here, since the total flux consists of a diffusive part (always outward for normal, centrally peaked density profiles) and a (convective) pinch part which could be either inward or outward. This will be discussed in Section 2.3.6 in detail.

Depending on the electron dissipation mechanism, electron drift waves can be classified into the collisionless drift wave which is excited by the inverse Landau damping on electrons, and the collisional drift wave which becomes unstable due to Coulomb collisions of electrons on either electrons or ions. The collisionless electron drift instability has been sometimes called the “universal instability”, since it can occur with a density gradient which must exist in magnetically confined plasmas, even in the absence of collisions.

Since the ion Landau damping (when kinetic effects are included in the ion response in Eq. (2.34)) has a stabilizing effect, the linear stability of this universal instability in a sheared magnetic field was a subject of the highest theoretical interest until the late 1970s [2.56]. While the final word was “stability” in a sheared slab geometry [2.57], now it is believed that collisionless drift waves can become unstable in toroidal geometry with trapped electron precession-wave resonance as a more effective destabilizing mechanism, replacing the inverse Landau damping of passing electrons.

From the linearized drift kinetic equation which will be discussed in Section 2.3.3, the perturbed electron distribution function  $\delta f_e$  satisfies

$$\left( \frac{\partial}{\partial t} + v_{\parallel} \nabla_{\parallel} \right) \delta f_e = -\delta \vec{u}_{\vec{E}} \cdot \nabla F_0 - \frac{|e|}{m_e} \nabla_{\parallel} \delta \Phi \frac{\partial}{\partial v_{\parallel}} F_0 \quad (2.37)$$

where  $F_0$  is the equilibrium distribution function. Note that the left hand side (LHS) contains the wave-particle resonance (i.e. the Landau damping) and the right hand side (RHS) describes the competition between the destabilizing influence of density gradient relaxation and the stabilizing influence of electron heating. After subtracting the adiabatic electron response by defining  $\delta h_e \equiv \delta f_e - (|e| \delta \Phi / T_e) F_0$ , and taking the velocity moments for  $\omega / k_{\parallel} \ll v_{T_e}$ , we get

$$\frac{\delta n_e}{n_0} = \frac{|e| \delta \Phi}{T_e} + \int d^3 \vec{v} \delta h_e = \left\{ 1 + i \sqrt{\frac{\pi}{2}} \frac{\omega - \omega_{*e}}{k_{\parallel} v_{T_e}} \right\} \frac{|e| \delta \Phi}{T_e} \quad (2.38)$$

where only the dominant resonant part of  $\delta h_e$  (a contribution from a pole at  $v_{\parallel} = \omega / k_{\parallel}$ ) has been kept. From Eqs (2.36) and (2.38), we conclude that the aforementioned phaseshift between  $\delta n_e$  and  $\delta \Phi$  indeed destabilizes the electron drift wave if  $\omega < \omega_{*e}$ . This downshift of the eigenfrequency required for excitation of the electron drift wave is easily provided by the polarization drift effect contained in Eqs (2.33, 2.34) and Eq. (2.36). In the simple limit of  $k_{\parallel}^2 c_s^2 \ll \omega^2$ ,  $\omega \equiv \omega_{*e} / (1 + k_{\perp}^2 \rho_s^2)$ , where  $k_{\perp}^2 \rho_s^2$  comes from the polarization drift. It is also straightforward to include the effect of an electron temperature gradient in the first term on the RHS of Eq. (2.37). Then, one can show that  $\nabla T_e$  (for normal centrally peaked  $T_e$  profiles) is stabilizing. At this juncture, we warn the reader that, in a different system (e.g. in toroidal geometry with trapped electrons),  $\nabla T_e$  can be destabilizing. Furthermore,  $T_e$  is the main free energy source for the hyperfine ( $\sim \rho_e$ ) scale electron temperature gradient (ETG) mode, as the name suggests.

Another subset of electron drift waves is the collisional drift wave. Since ‘‘collisional’’ here implies that the electrons, rather than the ions (recall  $v_{ee} \simeq v_{ei} \sim \sqrt{(m_i / m_e)} v_{ii}$  with  $m_i, m_e$  the ion and electron mass respectively) are in a high collisionality regime, we can still use Eq. (2.34) for the ion density response. For electrons, we assume  $v_{ei} \gg k_{\parallel} v_{T_e} \simeq v_{T_e} / qR$ , such that typical electrons suffer a collision before circulating around the torus over a connection length,  $qR$ . We still look for a drift wave (such as in the case of a collisionless drift wave) satisfying  $\omega / k_{\parallel} \ll v_{T_e}$ . Then, we can use Braginskii fluid equations [2.8]:

$$\frac{\partial}{\partial t} \delta n_e + \delta \vec{u}_E \cdot \vec{\nabla} n_0 + n_0 \nabla_{\parallel} \delta u_{\parallel e} = 0 \quad (2.39)$$

$$-|e|n_0\nabla_{\parallel}\delta\Phi + T_e\nabla_{\parallel}\delta n_e + (1 + \alpha_t)n_0\nabla_{\parallel}\delta T_e = 0 \quad (2.40)$$

and

$$\frac{3}{2}n_0\left(\frac{\partial}{\partial t}\delta T_e + \delta\vec{u}_E \cdot \vec{\nabla}T_e\right) + n_0T_e\nabla_{\parallel}\delta u_{\parallel e} = \hat{\chi}_en_0\frac{v_{Te}^2}{v_e}\nabla_{\parallel}^2\delta T_e \quad (2.41)$$

where  $u_{\parallel e}$  is an electron fluid velocity along the magnetic field, and  $\alpha_t = 0.71$  and  $\hat{\chi}_e = 3.16$  are the coefficients defined in Ref. [2.8]. For  $k_{\parallel}^2v_{Te}^2 \gg \omega v_{ei}$ , electrons diffuse and thermalize along the equilibrium magnetic field on a timescale faster than one wave period. In this so-called semi-collisional regime, the electron density response is given by

$$\frac{\delta n_e}{n_0} = \left(1 - i\frac{0.51}{\hat{\chi}_e}\frac{\omega v_e}{k_{\parallel}^2v_{Te}^2}(1 + \alpha_t)\right)\left\{\left(\frac{\omega_{*e}}{\omega} - 1\right) - \frac{3}{2}\eta_e\frac{\omega_{*e}}{\omega}\right\}\frac{|e|\delta\Phi}{T_e} \quad (2.42)$$

where  $\eta_e \equiv d\ln T_e / d\ln n_0$  is the ratio between density gradient scale length and electron temperature gradient scale length. As in the collisionless case (Eq. (2.38)), instability occurs when  $\omega$  is downshifted below  $\omega_{*e}$  (by  $k_{\perp}^2\rho_s^2$ ), when  $\eta_e = 0$ . Then, by using the quasi-neutrality condition, we can obtain a dispersion relation from Eq. (2.34) and Eqs (2.39–2.41). If we further assume that  $\omega \simeq \omega_{*e} / (1 + k_{\perp}^2\rho_s^2)$ , with  $k_{\parallel}^2c_s^2 \ll \omega^2$ ,  $\eta_e = 0$ ,

$$\frac{\gamma}{\omega_{*e}} \propto \frac{\omega_{*e}v_e}{k_{\parallel}^2v_{Te}^2}(k_{\perp}^2\rho_s^2) \quad (2.43)$$

where  $\gamma$  is the linear growth rate. This is similar to the results in Refs [2.58, 2.59]. Positive  $\eta_e$  (or  $\nabla T_e$ ) has a stabilizing influence [2.59]. While this collisional drift instability is no longer relevant in the core (interior) of high temperature plasmas in present day large tokamaks, it is applicable to the relatively cold plasma edge, in particular for high collisionality plasmas as in C-Mod [2.60], and previously in TEXT [2.61].

### 2.3.2.2. Ion temperature gradient instabilities

Since a high central ion temperature is required for magnetic fusion, the ion temperature gradient (ITG) driven instabilities are of primary interest in magnetic confinement, and are now believed to be the major contributor to anomalous ion thermal transport. In this subsection, simple illustrations are given for both acoustic [2.62] and magnetic curvature driven [2.63] versions of ITG modes, using a fluid description. Unlike electron drift waves, ITG modes can be driven unstable even with electrons satisfying the Boltzmann response. In this limiting case, no particle flux is produced by ITG modes.

First, we consider the acoustic version of ITG modes in a straight magnetic field with a radial gradient in ion temperature. Once again, we consider a simple slab geometry with  $\vec{B} = B\hat{e}_z$ , and gradients in the  $x$  direction. Ion dynamics is described by the following set of linearized hydrodynamic (fluid) equations:

$$\frac{\partial}{\partial t} \delta n + \delta \vec{u}_E \cdot \nabla n_0 + n_0 \nabla_{\parallel} \delta u_{\parallel} = 0 \quad (2.44)$$

$$m_i \frac{\partial}{\partial t} \delta u_{\parallel} = -e \nabla_{\parallel} \delta \Phi - \frac{1}{n_0} \nabla_{\parallel} \delta p_i \quad (2.45)$$

$$\frac{\partial}{\partial t} \delta p_i + \delta \vec{u}_E \cdot \nabla p_0 + \Gamma p_0 \nabla_{\parallel} \delta u_{\parallel} = 0 \quad (2.46)$$

where  $\delta p_i$  is the perturbed ion pressure and  $p_0$  is the equilibrium ion pressure. Note that the  $\vec{E} \times \vec{B}$  flow  $\delta \vec{u}_E$  is incompressible in a straight system. Equations (2.44) and (2.45) contain the ion sound (acoustic) wave dynamics. Assuming a flat density profile (i.e.  $\nabla n_0 = 0$ ) for simplicity, we can obtain a dispersion relation from Eqs (2.44–2.46) and the quasi-neutrality condition with Boltzmann electron response (Eq. (2.35)). This procedure yields a cubic equation in  $\omega$ ,

$$1 - \frac{k_{\parallel}^2 c_s^2}{\omega} \left\{ \left( 1 + \frac{\Gamma}{\tau} \right) - \frac{\omega_{*T_i}}{\omega} \right\} = 0 \quad (2.47)$$

Here  $\omega_{*T_i} \equiv -(k_{\theta} \rho_i / L_{T_i}) v_{T_i}$  is the ion temperature gradient diamagnetic frequency,  $L_{T_i}$  is the ion temperature gradient length, and  $\tau \equiv T_e / T_i$ . Equation (2.47) describes the acoustic oscillation modified by the ion temperature gradient. Since the expression in  $\{\dots\}$  involves the adiabatic exponent  $\Gamma$  which quantifies the compressibility, we can regard that expression to be the effective compressibility. Equation (2.47) yields three roots in the limit  $|\omega_{*T_i}| \gg \omega \gg k_{\parallel} c_s$ :

$$\omega \equiv \left| \omega_{*T_i} \right|^{1/3} (k_{\parallel} c_s)^{2/3} e^{\frac{2\pi N}{3} i} \quad (2.48)$$

with  $N = 0, 1, 2$ . For  $N = 1$ , we obtain an instability ( $\text{Im}(\omega) > 0$ ) which propagates in the ion diamagnetic drift direction with an acoustic character. For this root, the effective compressibility (its real part) is negative! This negative compressibility is a key physical mechanism of ITG instability in a straight system. Note that while the instability gets stronger as  $k_{\parallel}$  is increased, this trend will be limited by the ion Landau damping as  $k_{\parallel} v_{T_i}$  gets closer to  $\omega$ . This important kinetic effect will be discussed in Section 2.3.4.1.

Another important limiting case of the ITG mode is now discussed in a toroidal geometry with a curved magnetic field. Once again, we only consider the radial gradient of the ion temperature (with a flat density profile). Neglecting

dynamics along  $\vec{B}_0$ , the essence of ion dynamics in a curved magnetic field in the long wavelength limit can be approximated by the following equations:

$$\frac{\partial}{\partial t} \frac{\delta n}{n_0} + \bar{\omega}_{di} \frac{\delta T_i}{T_i} \cong 0 \quad (2.49)$$

$$\frac{\partial}{\partial t} \delta T_i + \delta \vec{u}_E \cdot \nabla T_0 \cong 0 \quad (2.50)$$

Equation (2.49) describes a coupling between density fluctuations and temperature fluctuations which comes from the particle velocity dependence of the  $\nabla B$  and curvature drifts in toroidal geometry. Here,  $\bar{\omega}_{di} \equiv -\{(cT_i)/(eBR)\}k_y$  is the ion drift frequency evaluated at the low field side midplane. Equation (2.50) simply describes the relaxation of the temperature gradient via perturbed  $\vec{E} \times \vec{B}$  motion leading to a temperature fluctuation. With a quasineutrality condition for Boltzmann electron response, we obtain a linear dispersion relation

$$\omega^2 = -\frac{T_e}{T_i} \bar{\omega}_{di} \omega_{*T_i} = -\frac{T_e}{T_i} \left| \bar{\omega}_{di} \omega_{*T_i} \right| \quad (2.51)$$

Since  $\omega_{di} < 0$  at the bad curvature low field side, and  $\omega_{*T_i} < 0$  for normal temperature profiles, Eq. (2.51) clearly predicts the existence of a purely growing reactive instability in this simple limit. A pictorial description of the feedback loop leading to this instability can be found in Fig. 1.1 of Ref. [2.64]. In reality, ITG modes in tokamaks contain both toroidal and acoustic characteristics. While their amplitudes peak at the bad curvature low field side, such mode structures are only possible by having non-vanishing  $k_{\parallel}$ , not kept in Eqs (2.49, 2.50). Further discussion of the mode structure can be found in Section 2.3.5.2.

### 2.3.3. Non-linear gyrokinetic equations for tokamak turbulence

For more detailed discussions of microinstabilities and turbulence driven transport in the coming sections, we present the basics of the non-linear gyrokinetic equation. Despite the tremendous increase of computational power in recent years, the direct simulation of actual size fusion plasmas in realistic geometry using the primitive non-linear plasma equations (such as the Klimontovich [2.65] or Vlasov equations) is still far beyond the computational capability of even the foreseeable future. Thus, reduced equations have been employed to simplify the basic dynamical equations. In this section, we discuss basic procedures involved in derivations from the most fundamental, Vlasov equation, to the non-linear gyrokinetic equations which are now widely used in various turbulence research in magnetically confined plasmas. We focus our discussion on collisionless plasmas.

Evolution of a collisionless plasma can be described by the Vlasov equation for the particle distribution function for each particle species in a six-dimensional phase space,

$$\frac{\partial f}{\partial t} + \vec{v} \cdot \frac{\partial f}{\partial \vec{x}} + \frac{q}{m} \left( \vec{E} + \frac{1}{c} \vec{v} \times \vec{B} \right) \cdot \frac{\partial f}{\partial \vec{v}} = 0 \quad (2.52)$$

where  $\vec{E}$  and  $\vec{B}$  are the electric and magnetic fields produced by the particle motion which satisfy Maxwell's equations. This system of equations can describe various phenomena over a wide range of spatio-temporal scales. For instance, accurate descriptions of particle dynamics in the presence of high frequency electromagnetic waves are needed for studying plasma heating by waves [2.66].

For turbulence and transport problems in magnetically confined plasmas, the timescales of collective electromagnetic fluctuations of interest are much longer than the period of a charged particle's cyclotron motion (gyromotion), while the wavelengths and correlation lengths of such fluctuations are much smaller than the device size or the scale length of the magnetic field inhomogeneity. In these circumstances, details of the charged particle's gyration motion are not of physical interest, and it is desirable to develop a reduced set of dynamical equations which still captures the essential features of the low frequency phenomena of practical relevance. By decoupling the gyromotion, one can derive the gyrokinetic equation which describes the spatio-temporal evolution of the gyrocentre distribution function, which is independent of the gyrophase,  $\xi$ , defined over a five-dimensional phase space  $(\vec{R}, v_{\parallel}, \mu)$ . In simulating strongly magnetized plasmas, one can, thus, save enormous amounts of computing time by having a time step greater than the gyroperiod, and by reducing the number of dynamical variables. We note that in the gyrokinetic approach, the gyrophase is an ignorable coordinate and the magnitude of the perpendicular velocity enters as a parameter in terms of an adiabatic invariant ( $\mu = v_{\perp}^2 / 2B$ ). This is the leading term of an adiabatic invariant which does not change for each particle.

Due to the broad scope of this book and space limitations, it is not appropriate to describe here the rigorous derivations of the non-linear gyrokinetic equations in toroidal geometry. Details can be found in the literature, which includes:

- (i) a conventional perturbative derivation with introduction of a standard non-linear gyrokinetic ordering [2.67],
- (ii) a derivation mainly for the purpose of particle-in-cell simulation [2.68],
- (iii) the Hamiltonian derivations of non-linear gyrokinetic equations for electrostatic fluctuations [2.69], and electromagnetic fluctuations [2.70] in a uniform magnetic field, and finally,
- (iv) generalizations to arbitrary geometry using phase-space Lagrangian derivations (which are the most transparent and efficient to date

in the author's opinion) for electrostatic fluctuations [2.71], and electromagnetic fluctuations [2.72]. There is a theoretically oriented review of the subject in Ref. [2.5].

Both formulations and simulations traditionally focused on tokamak core turbulence in which the fluctuation amplitude is relatively small, i.e. the relative density fluctuation amplitude is less than 1% and the gradients in macroscopic parameters such as pressure are relatively mild with characteristic lengths of the order of a fraction of the minor radius. In the non-linear gyrokinetic theory, there exist three expansion parameters:  $\varepsilon_\omega \equiv \omega / \Omega_{ci}$  with  $\Omega_{ci}$  the ion cyclotron frequency,  $\delta_B \equiv \rho_i / L_B$  with  $L_B$  the scale length of the equilibrium magnetic field, and  $\varepsilon_\Phi \equiv \delta f / F_0 \simeq e\delta\Phi / T_e$ , where  $\varepsilon_\omega$ ,  $\delta_B$  and  $\varepsilon_\Phi$  characterize the slow timescale associated with turbulence, weak inhomogeneity of the equilibrium magnetic field and low relative amplitude of fluctuations respectively. The conventional gyrokinetic theory [2.67] assumes that all three parameters are comparable in formal ordering, although this choice needs to be modified in some cases including plasmas with transport barriers [2.73]. In addition, in the non-linear gyrokinetic ordering, the perpendicular wavelength can be comparable to the gyroradius, while the parallel wavelength of the fluctuation is comparable to the connection length of the system  $\sim qR$ . Thus, the ordering is consistent with the spatial structure of the fluctuation which aligns with the equilibrium magnetic field (see Fig. 2.11).

Here, we simply sketch a heuristic derivation procedure in a uniform magnetic field to illustrate some key features in the non-linear gyrokinetic equations. This is similar to one employed in Ref. [2.68]. For more details, readers should consult the aforementioned literature.

Transforming from the particle variables  $(\vec{x}, \vec{v})$  to the guiding centre variables  $(\vec{R}, \mu, v_\parallel, \xi)$  [2.74],  $\vec{R} = \vec{x} - \vec{\rho}$ ,  $\mu = v_\perp^2 / 2B$ ,  $\vec{v} = v_\parallel \vec{b} + v_\perp (\vec{e}_1 \cos \xi + \vec{e}_2 \sin \xi)$ , we can write Eq. (2.52) as

$$\begin{aligned} \frac{\partial}{\partial t} f + v_\parallel \hat{b} \cdot \frac{\partial}{\partial \vec{R}} f + \frac{c}{B} \vec{E} \times \hat{b} \cdot \frac{\partial}{\partial \vec{R}} f + \frac{q}{m} E_\parallel \frac{\partial}{\partial v_\parallel} f - \\ - \Omega_{ci} \frac{\partial}{\partial \xi} f + \frac{q\Omega_{ci}}{mB} \frac{\partial \Phi}{\partial \xi} \frac{\partial f}{\partial \mu} + \Omega_{ci} \frac{\vec{v}_E \cdot \vec{v}_\perp}{v_\perp^2} \frac{\partial f}{\partial \xi} = 0 \end{aligned} \quad (2.53)$$

where  $\vec{v}_E = (c/B)\vec{E} \times \hat{b}$  is the  $\vec{E} \times \vec{B}$  velocity. For  $\omega \ll \Omega_{ci}$ , the lowest order part of Eq. (2.53) is  $\Omega_{ci} \partial f / \partial \xi = 0$ . Writing  $f = \langle f \rangle + f_a$  with  $\langle f \rangle \gg f_a$  in which  $\langle \dots \rangle$  indicates a gyrophase average, and  $f_a$  is the gyrophase dependent part, the next order equations:

$$\begin{aligned} \frac{\partial}{\partial t}\langle f \rangle + v_{\parallel} \hat{b} \cdot \frac{\partial}{\partial \vec{R}} \langle f \rangle + \frac{c}{B} \vec{E} \times \hat{b} \cdot \frac{\partial}{\partial \vec{R}} \langle f \rangle + \frac{q}{m} E_{\parallel} \frac{\partial}{\partial v_{\parallel}} \langle f \rangle - \\ - \Omega_{ci} \frac{\partial}{\partial \xi} \left( f_a - \frac{q}{mB} \Phi \frac{\partial}{\partial \mu} \langle f \rangle \right) = 0 \end{aligned} \quad (2.54)$$

Here, we have ignored the last term in Eq. (2.55) which corresponds to a small local correction to the gyrofrequency  $\Omega_{ci}$  due to the perturbed  $\vec{E}$  field which is not of our primary interest. Gyrophase-averaging Eq. (2.54), we obtain the desired gyrokinetic Vlasov equation in a uniform magnetic field,

$$\frac{\partial}{\partial t}\langle f \rangle + v_{\parallel} \hat{b} \cdot \frac{\partial}{\partial \vec{R}} \langle f \rangle + \frac{c}{B} \langle \vec{E} \rangle \times \hat{b} \cdot \frac{\partial}{\partial \vec{R}} \langle f \rangle + \frac{q}{m} \langle E_{\parallel} \rangle \frac{\partial}{\partial v_{\parallel}} \langle f \rangle = 0 \quad (2.55)$$

We emphasize that Eq. (2.55) is in the reduced gyrocentre coordinates  $(\vec{R}, \mu, v_{\parallel})$ , i.e. without  $\xi$ , rather than in the particle coordinates  $(\vec{x}, \vec{v})$ .

To complete the gyrokinetic description of the influence of the particle motion on the electromagnetic field, one needs to express the charge density and the current density in Maxwell's equations in terms of the gyrocentre distribution function  $\langle f \rangle(\vec{R}, \mu, v_{\parallel}, t)$ . This requires the so-called ‘‘pull-back transformation’’ to the particle coordinates [2.75]. Subtracting Eq. (2.55) from Eq. (2.54), and keeping the lowest order term only, we obtain

$$f_a \simeq \frac{q}{mB} (\Phi - \langle \Phi \rangle) \frac{\partial \langle f \rangle}{\partial \mu} \quad (2.56)$$

Despite a widespread misconception that the gyrokinetic equation keeps only the gyrophase independent part (and throwing away the gyrophase dependent information), the gyrophase dependent part of the distribution function  $f_a$  in Eq. (2.56) has been kept in the gyrokinetic theories [2.68–2.70], and has been shown to play a crucial role. It can be shown that by performing a phase-space integral (equivalently a pull-back transformation), the ion polarization density  $n_{pol}(\vec{x})$ , which accounts for the difference between the actual ion particle density and the gyroaveraged gyrocentre density, is

$$\begin{aligned} n_{\theta}(\vec{x}) &\equiv \int d^3 \vec{R} d\mu dv_{\parallel} d\xi B \delta(\vec{R} + \vec{\rho} - \vec{x}) f_a = \\ &= -\frac{en_0}{T_i} \sum_{\vec{k}} (1 - \Gamma_0(b_i)) \delta \Phi_{\vec{k}} e^{i\vec{k} \cdot \vec{x}} \end{aligned} \quad (2.57)$$

for Maxwellian  $\langle f \rangle$ , and  $\Phi = \sum_{\vec{k}} \delta \Phi_{\vec{k}} e^{i\vec{k} \cdot \vec{x}}$  with  $\delta \Phi_{\vec{k}}$  being the  $k$  component of  $\Phi$ . Here,  $b_i = k_{\perp}^2 \rho_i^2$ ,  $\Gamma_0(b_i) = I_0(b_i) e^{-b_i}$ , and  $I_0$  is the modified Bessel function. This is the ion polarization density. In the gyrokinetic quasi-neutrality condition, it is the sum of the gyrocentre density at the particle position and this

polarization density, which should be equal to the electron density. We reiterate that the effect of the polarization drift appears in the gyrokinetic Poisson equation as the polarization density, rather than in the guiding centre drift in the Vlasov equation. That representation of the polarization drift as a shielding term has been found to be very useful computationally [2.68].

By taking the small Larmor radius limit ( $k_{\perp}\rho_i \rightarrow 0$ ) of the gyrokinetic equation, we can recover the drift kinetic equation. However, the drift kinetic equation can be derived without assuming a small relative fluctuation amplitude [2.76]. Therefore, the drift kinetic equation is not a subset of the gyrokinetic equation in a strict sense.

Another example of the reduced non-linear kinetic equations is the bounce-averaged kinetic equation. When one is interested in low frequency fluctuations such that the characteristic mode frequency  $\omega$  is lower than the bounce frequency of charged particles of species  $j$ ,  $\omega \ll \omega_{bj}$ , the bounce action (or the second adiabatic invariant)  $J = \oint dl v_{\parallel}$  is conserved where  $\oint dl$  is taken along the bouncing particle orbit. Then one can decouple the bounce motion from lower frequency dynamics related to the wave and the slower charged particle precession motion in the toroidal direction (see Section 2.2.3). Consequently the bounce angle becomes an ignorable coordinate, and a non-linear kinetic equation can be written for a distribution function  $F(\alpha, \beta, J, \psi)$ , where  $\alpha$  and  $\beta$  designate the equilibrium magnetic field, and  $d\psi = dl / v_{\parallel}$  is an angle variable for the motion along the field. There exists a conventional derivation for application to trapped-particle-driven microturbulence [2.77], as well as a modern derivation based on the phase-space Lagrangian method [2.78].

The bounce-averaged kinetic equation is useful for applications to the trapped electron mode (TEM) and the trapped ion mode (TIM), as will be discussed in Section 2.3.4.3. It is possible to calculate the real trapped particle density via the pull-back transformation from the bounce-averaged banana centre distribution function  $F(\alpha, \beta, J, \psi)$  in the reduced phase space. From this, one can identify the neoclassical polarization density [2.78], which is closely related to the neoclassical polarization shielding [2.79].

### 2.3.4. Kinetic description of microinstabilities

In Section 2.3.2.2, basic microinstabilities in a strong magnetic field have been discussed in the context of a fluid picture. While the fluid treatment offers a simpler physical picture and can be a good approximation when instability is very strong, a kinetic approach leads to more accurate results in most cases. In this section, we discuss kinetic effects, in particular the wave-particle resonant interaction (Landau damping). This section is organized in the order of the linear stability criterion for ITG modes, properties of ETG modes and finally trapped particle instabilities.

### 2.3.4.1. Linear onset condition for ion temperature gradient mode

In Section 3.2.2.2, we discussed the fluid treatment of ITG instabilities. For the acoustic version,  $\omega \gg k_{\parallel} v_{T_i}$  was assumed ignoring the ion Landau damping which occurs for  $v_{\parallel} \sim \omega / k_{\parallel}$ . As a consequence, the resulting dispersion relation,  $\omega \simeq e^{(2\pi/3)i} |\omega_{*T_i}|^{1/3} (k_{\parallel} c_s)^{2/3}$  indicates an instability even for an arbitrarily weak ion temperature gradient. This is not intuitively plausible. Indeed, as  $\nabla T_i$  becomes weaker,  $\omega_{*T_i}$  will decrease, making  $|\omega|$  smaller. At some point, the fluid approximation  $|\omega| \gg k_{\parallel} v_{T_i}$  cannot be satisfied anymore, and one should pursue a kinetic theory which captures a proper behaviour for  $|\omega| \sim k_{\parallel} v_{T_i}$ . Furthermore, one needs to relax the assumption of a flat density profile which was employed in Section 2.3.2.2 for a simple illustration.

Starting from the electrostatic gyrokinetic equation in a straight magnetic field, Eq. (2.55), we can make a linear approximation ignoring non-linear terms involving  $\delta\Phi$  and  $\delta f$ , after expanding  $F = F_0 + \delta f$ , and assuming that  $\delta\Phi$  and  $\delta f$  are infinitesimally small. Then, the non-adiabatic part of the perturbed gyrocentre distribution function  $\delta g$  satisfies:

$$\left( \partial_t + v_{\parallel} \nabla_{\parallel} \right) \delta g + \left( \frac{\partial}{\partial t} \langle \delta\Phi \rangle + \frac{c}{B} \hat{b} \times \nabla \langle \delta\Phi \rangle \cdot \nabla \right) F_0 = 0 \quad (2.58)$$

Here,  $\delta g = \delta f + (|e| \delta\Phi / T_i) F_0$ , and  $\langle \delta\Phi \rangle = J_0(k_{\perp} \rho_i) \delta\Phi$  is the gyrophase-averaged perturbed potential, where  $J_0$  is the Bessel function. With an adiabatic electron density response, the quasi-neutrality condition yields:

$$\frac{|e| \delta\Phi}{T_e} = -\frac{|e| \delta\Phi}{T_i} + \int d^3\vec{v} (J_0 \delta g) \quad (2.59)$$

After evaluating  $\vec{\nabla} F_0$  for a local Maxwellian  $F_0$  with non-uniform density and temperature profiles,  $\delta g$  is given by

$$\delta g = \frac{\omega_{*i} \left\{ 1 + \eta_i \left( \frac{v^2}{2v_{T_i}^2} - \frac{3}{2} \right) \right\} + \omega}{\omega - k_{\parallel} v_{\parallel}} \left( \frac{|e| \delta\Phi}{T_i} \right) J_0 F_0 \quad (2.60)$$

where  $\eta_i \equiv d \ln T_i / d \ln n_0$  is the density gradient length scale divided by the ion temperature length scale and  $\omega_{*i} \equiv -(T_i / T_e) \omega_{*e} = -k_{\theta} \rho_i v_{T_i} / L_n$ . Then, Eq. (2.59) becomes

$$\frac{2\pi}{(2\pi)^{3/2} v_{T_i}^3} \int_0^\infty dv_\perp v_\perp \int_{-\infty}^\infty dv_\parallel \frac{\omega + \frac{T_i}{T_e} \omega_{*e} \left\{ 1 + \eta_i \left( \frac{v_\perp^2 + v_\parallel^2}{2v_{T_i}^2} - \frac{3}{2} \right) \right\} J_0^2(k_\perp \rho_i) e^{-v^2/2v_{T_i}^2}}{\omega - k_\parallel v_\parallel} + 1 = \frac{T_i}{T_e} \quad (2.61)$$

By taking a long perpendicular wavelength limit ( $k_\perp \rho_i \rightarrow 0$ ), and the fluid approximation ( $\omega \gg k_\parallel v_\parallel$ ) in the denominator, we can recover the acoustic version of the fluid ITG dispersion relation (Eq. (2.47) from Eq. (2.59) for  $\Gamma = 0$  and  $\nabla n = 0$ ).

In the kinetic regime with strong ion Landau damping,  $\omega / k_\parallel \lesssim v_{T_i}$ , we can determine the linear threshold condition for ITG modes by noting that stability is determined by the imaginary part of Eq. (2.59). Note that  $\{\text{L.H.S.}\} = O\left[\omega_{*e} / (k_\parallel v_{T_i})\right] \gg 1$  meanwhile,  $\text{Re}\{\text{L.H.S.}\} \ll \text{Im}\{\text{R.H.S.}\}$  and  $\text{R.H.S.} = O(1)$ . Formally the imaginary part dominates. Since ion heating (due to the usual ion Landau damping in a homogeneous plasma) is negligible ( $\omega \ll \omega_{*e}$ ), the linear onset condition corresponds to near “zero” relaxation of the velocity dependent free energy. It is determined by

$$\lim_{\omega \rightarrow 0} \text{Im} \int_{-\infty}^\infty dv_\parallel \int_0^\infty dv_\perp v_\perp \frac{\frac{T_i}{T_e} \omega_{*e} \left\{ 1 + \eta_i \left( \frac{v_\perp^2 + v_\parallel^2}{2v_{T_i}^2} - \frac{3}{2} \right) \right\} J_0^2(k_\perp \rho_i)}{\omega - k_\parallel v_\parallel} e^{-v^2/2v_{T_i}^2} = 0 \quad (2.62)$$

Tracing back the physics origin of the numerator (the radial relaxation of free energy), it is

$$\frac{T_i \omega_{*e}}{T_e} \left\{ 1 + \eta_i \left( \frac{v_\perp^2 + v_\parallel^2}{2v_{T_i}^2} - \frac{3}{2} \right) \right\} = v_{T_i} \rho_i k_\theta \frac{\partial}{\partial r} \ln F_0 \quad (2.63)$$

By interchanging the order of  $\int_0^\infty dv_\perp$  and  $\partial / \partial r$ , we obtain

$$\lim_{\omega \rightarrow 0} \text{Im} \int_{-\infty}^\infty dv_\parallel \frac{1}{\omega - k_\parallel v_\parallel} \frac{\partial}{\partial r} \left[ \left( \frac{n_0}{T_i^{3/2}} \right) \int_0^\infty dv_\perp v_\perp e^{-v^2/2v_{T_i}^2} J_0^2(k_\perp \rho_i) \right] = -\frac{\pi}{|k_\parallel|} \lim_{\omega \rightarrow 0} \frac{\partial}{\partial r} \left[ e^{-(\omega/k_\parallel)^2/2v_{T_i}^2} \frac{n_0(r)}{T_i(r)^{1/2}} \Gamma_0(b_i) \right] = 0 \quad (2.64)$$

where  $b_i \equiv k_\perp^2 \rho_i^2$ . Therefore, for  $\omega / k_\parallel \ll v_{T_i}$ ,

$$\frac{\partial}{\partial r} \left[ \frac{n_0(r)}{T_i^{1/2}(r)} \Gamma_0(b_i) \right] = 0 \quad (2.65)$$

defines the linear threshold of ITG instability. Note that given a wavelength  $k_\perp$  and density profile  $n_0$ , “ $(n_0(r)/T_i^{1/2})\Gamma_0(b_i)$ ” gives a critical temperature profile  $T_i(r)$ . The onset condition for ITG instability can be written as

$$\eta_i \geq \frac{2}{1 + 2b_i \left( 1 - \frac{I_1(b_i)}{I_0(b_i)} \right)} \quad (2.66)$$

where  $I_0$  and  $I_1$  are modified Bessel functions. Equation (2.66) is the well known result by Kadomtsev and Pogutse [2.80]. This shows that an instability occurs if  $\eta_i$  exceeds a certain value of the order of unity, roughly 1~2. Due to this reason, ITG modes are sometimes called the  $\eta_i$  modes. Since the threshold is lowest for  $k_\perp \rho_i \sim 1$ , short wavelength modes with  $k_\perp \rho_i \sim 1$  are more easily excited by the ion temperature gradient. However, ITG mode is a better name since there exists a threshold in terms of  $\nabla T_i$ , even for a flat density profile such that  $\eta_i = \infty$ . An illuminating analytic formula for the instability condition in a sheared magnetic field (see Section 2.3.5.1) is given in Ref. [2.81]

$$\frac{L_s}{L_{T_i}} \geq 1.9 \left( \frac{T_i}{T_e} + 1 \right) \quad (2.67)$$

where  $L_s \equiv qR/\hat{s}$  is the magnetic shear length discussed in Section 2.3.5.1 and  $\hat{s} = d \ln q / d \ln r$  is the magnetic shear. This indicates the favourable roles of high  $T_i/T_e$  and high magnetic shear for ITG stability.

In toroidal geometry, one should consider the  $\nabla B$  and curvature drift ( $\omega_{di}$ ) in the gyrokinetic equation, and perform a similar but much more complicated kinetic calculation including a resonance given by  $\omega - \omega_{di}(\mathbf{v}_\perp, \mathbf{v}_\parallel) - k_\parallel v_\parallel = 0$ . The  $k_\parallel = 0$  limit has been considered (while  $k_\parallel = 0$  and ballooning mode structure strongly peaked at the low  $\vec{B}$  field and bad curvature side are not totally compatible) for which some analytic progress has been made [2.82]. Furthermore, a powerful Nyquist diagram technique has been applied to this problem and appeared in a textbook [2.83]. However, keeping both  $k_\parallel$  and  $\omega_{di}$  requires a numerical calculation [2.84]. For flat density, the linear instability condition given by Ref. [2.82] is

$$\frac{R}{L_{T_i}} \geq \frac{4}{3} \left( \frac{T_i}{T_e} + 1 \right) \quad (2.68)$$

### 2.3.4.2. Electron temperature gradient instability

The electron temperature gradient instability [2.85, 2.86] is a very short wavelength fluctuation with  $k_{\perp}\rho_i \gg 1$ . Since the ions with Larmor radius greater than the perpendicular wavelength of fluctuations feel the gyroaveraged electric field which is much smaller than the local electric field at one position, the ion dynamics becomes almost unmagnetized. Formally speaking, as  $k_{\perp}\rho_i \gg 1$ , the gyroaveraged reduction of potential ( $\langle\delta\Phi\rangle = J_0(k_{\perp}\rho_i)\delta\Phi \rightarrow 0$ ) leads the ion response to be adiabatic (since  $\delta g \rightarrow 0$ ), i.e.  $\delta n_i / n_0 = -|e|\delta\Phi\phi / T_i$ . On the other hand, with a general ordering  $k_{\perp}\rho_e \sim 1$  with  $\rho_e$  being the electron gyroradius, now the electron dynamics is described by the gyrokinetic equation. In this sense, the roles of ions and electrons are reversed for the ETG mode, compared to those for the ITG mode where the electron response was assumed to be adiabatic for a different reason. Therefore, in the simplest context, there exists an isomorphism between ITG and ETG. For instance, simplified onset conditions in Eqs (2.67, 2.68) apply to the ETG modes as well, with subscripts  $i$  and  $e$  exchanged. Now, high  $T_e / T_i$  is favourable for ETG stability.

Because the ion response is near adiabatic, the ETG mode produces negligible particle flux, ion heat flux and momentum flux. Since the radial width of ETG modes is related to the electron gyroradius,  $\rho_e$ , it cannot produce significant electron thermal transport unless there is a mechanism to enhance its radial width. Some gyrokinetic simulations report the existence of radially elongated fluctuations, so-called streamers [2.87, 2.88]. We discuss this further in Section 2.3.5.2. The relation between ITG and ETG is summarized in Table 2.2.

### 2.3.4.3. Trapped particle instabilities

Electron drift waves destabilized by magnetically trapped electrons are called trapped electron modes (TEM). In present day tokamak plasmas with low collisionality,  $v_{*e} \equiv v_{ei} / \varepsilon\omega_{be} < 1$  (where  $\varepsilon = r / R_0$  is the inverse aspect ratio and  $\omega_{be}$  the bounce frequency of trapped electrons) the trapped electron drive is typically stronger than that from the passing electrons which were discussed in Section 2.3.2.1. The destabilizing influence of passing electrons scales with  $\omega_{*e} / (k_{\parallel}v_{T_e})$  for collisionless electron drift waves, and with  $\omega_{*e}v_{ei} / (k_{\parallel}v_{T_e})^2$  for collisional drift waves.

As can be seen from the bounce averaged drift kinetic equation for trapped electrons, after a decoupling of the relatively fast bounce motion along the  $\vec{B}$  field, the trapped electron dynamics across the  $\vec{B}$  field has a hydrodynamic character describing  $\vec{E} \times \vec{B}$  motion and toroidal precession. The expansion-free energy in  $\nabla n$  or  $\nabla T_e$  is released by the radial component of  $\vec{E} \times \vec{B}$  motion. When the energy is transferred from trapped electrons to waves via wave-precession-drift resonance, the mode is called the collisionless trapped

TABLE 2.2. ITG–ETG ISOMORPHISM [2.51]

( $\chi_\phi$ ,  $\chi_i$ ,  $\chi_e$  and  $\chi_J$  are diffusivity for toroidal momentum, ion heat, electron heat and toroidal current respectively;  $\tilde{n}_e$  and  $\tilde{n}_i$  are perturbed density for electrons and ions respectively)

Key issue	ITG	ETG
Linear response in the electrostatic limit		
$\tilde{n}_i$	From gyrokinetic equation	$-e\Phi / T_i$ ; pure adiabatic
$\tilde{n}_e$	$e(\Phi - \langle \Phi \rangle) / T_e$ ; adiabatic with zonal flow	From gyrokinetic equation
Disparity in transport channels caused by particular turbulence	$\chi_i \sim \chi_\phi > \chi_e, D$	$\chi_e \sim \chi_J > D, \chi_i, \chi_\phi$
Zonal flow strength in non-linear regime	Typically strong	Typically weaker
Radial correlation length of ambient turbulence at non-linear saturation	Several $\rho_i$	Uncertain – current research
Isomorphism breaker	Zonal flow	Residual magnetization of ion response Electromagnetic effect Debye shielding

electron mode (CTEM), while if the energy transfer occurs via trapped electron collisions, it is called the dissipative trapped electron mode (DTEM). Both trapped electron instabilities require that most trapped electrons be in the banana collisionality regime  $v_{*e} < 1$ , such that they can execute a bounce motion before getting detrapped by collisions on average. Furthermore, both instabilities also require  $\omega \ll \omega_{be}$ , such that the second adiabatic invariant  $J \equiv \oint dl v_{\parallel}$  is conserved. There also exist trapped ion modes with extremely low frequency  $\omega / \omega_{bi}$  (where  $\omega_{bi}$  is the bounce frequency of trapped ions) and long wavelength. We discuss those in Section 2.3.4.3.3.

### 2.3.4.3.1. Collisionless trapped electron mode

The collisionless trapped electron mode (CTEM) can occur if collisions are rare enough that a trapped electron can also precession drift around the torus more than once in the toroidal direction before it gets detrapped by collisions. For the CTEM, the collisionless bounce-averaged drift kinetic equation [2.77] provides a very good description of trapped electron dynamics:

$$\left( \frac{\partial}{\partial t} + \vec{v}_{de} \cdot \nabla \right) \delta h_e^T - \left( \frac{\partial}{\partial t} \overline{\delta\Phi} + \frac{c}{B} \hat{b} \times \nabla \overline{\delta\Phi} \cdot \nabla \right) F_0 = 0 \quad (2.69)$$

where  $h_e^T$  is the non-adiabatic part of the perturbed trapped electron distribution function,  $\overline{\delta\Phi}$  is the bounce-averaged  $\delta\Phi$ , and  $\vec{v}_{de}$  is the precession velocity. In Fourier space, Eq. (2.69) becomes

$$-i(\omega - \overline{\omega}_{de}) \delta h_e^T = i(\omega_{*T_e}(E) - \omega) \frac{|e| \overline{\delta\Phi}}{T_e F_0} \quad (2.70)$$

where  $\omega_{*T_e}(E) \equiv \omega_{*e} \{1 + \eta_e(E/T_e - 3/2)\}$ . As described in Section 2.3.2.1, the imaginary part of the non-adiabatic electron density response determines the stability of the electron drift wave. Therefore, for the CTEM [2.89],

$$\begin{aligned} \text{Im}(\delta n^{NA} / n_0) &= \frac{1}{n_0} \text{Im} \int d^3v \delta f_e^T \\ &= 2\sqrt{\pi\epsilon} \left( \frac{\omega}{\overline{\omega}_{de} G} \right)^{3/2} e^{-\omega/\overline{\omega}_{de} G} \left[ 1 - \frac{\omega_{*e}}{\omega} \left\{ 1 + \eta_e \left( \frac{\omega}{\overline{\omega}_{de} G} - \frac{3}{2} \right) \right\} \right] \frac{|e| \overline{\delta\Phi}}{T_e} \end{aligned} \quad (2.71)$$

where  $n^{NA}$  is the non-adiabatic density response, and T in  $h_e^T$  stands for trapped. Note that an instability can occur (with  $\delta n^{NA} < 0$ ) for  $\omega < \omega_{*e}$  in the absence of the electron temperature gradient. For the CTEM,  $\nabla T_e$  (or positive  $\eta_e$ ) is destabilizing, in contrast to electron drift instabilities driven by passing electrons. Of course, this contribution comes from the  $\omega - \omega_{de}$  resonance. Since  $\omega_{de} \equiv G \overline{\omega}_{de}(E/T_e)$  with  $\overline{\omega}_{de} \simeq cT_e / (eBR)$ , mostly high energy electrons with  $E/T_e \simeq \omega_{*e} / G \overline{\omega}_{de} \simeq R / GL_n$  resonate with electron drift waves. Here, a dimensionless parameter  $G(\kappa, \hat{s})$  captures the pitch angle  $\kappa$  and the magnetic shear  $\hat{s}$  dependence of the trapped particle precession motion [2.89].

Furthermore,  $\overline{\omega}_{de}$  can change its sign  $G < 0$  for barely trapped electrons. These precession-reversed electrons cannot resonate with the electron drift wave and have a stabilizing influence on it. For reversed magnetic shear plasmas, a significant fraction of trapped electrons can precess in the favourable direction [2.90] (opposite to  $\omega_{*e}$ ) and the CTEM can be stabilized.

### 2.3.4.3.2. Dissipative trapped electron mode

This instability is relevant for an intermediate collisionality regime satisfying  $\omega_{be} > \nu_{ei} / \epsilon > \omega_{*e}$ . So on average, typical trapped electrons get detrapped by collisions during one wave period, but not during a shorter bounce motion period. Then the bounce-averaged kinetic equation can still be used, but with collisions included. While the conservation properties of the collisional operator are important for a quantitatively accurate derivation, here we simply

illustrate the basic trends of parametric dependences. If the effective collisional frequency is higher than  $\omega$  and  $\omega_{*e}$ , the simplest form of non-adiabatic trapped electron response is given by

$$\delta n_e^{NA} / n_0 = \int_{Tr} d^3v \delta f_e^T \simeq i\sqrt{\varepsilon} \frac{\omega - \omega_{*e} \left(1 + \frac{3}{2}\eta_e\right) |e| \delta\Phi}{\nu_{ei} / \varepsilon T_e} \quad (2.72)$$

For  $\eta_e = 0$ , instability occurs when  $\omega < \omega_{*e}$ .  $\eta_e > 0$  is destabilizing as in the case of CTEM. From this, the linear growth rate of the DTEM scales like  $\gamma \propto \eta_e \left(\varepsilon^{3/2} / \nu_{ei}\right) \omega_{*e}$  [2.91].

In reality, for given plasma parameters, one should solve a very complicated linear dispersion relation including all the effects discussed in Sections 2.3.4 and 2.3.5. Each ‘‘mode’’ we have discussed in each subsection is a very idealized limiting case. For instance, the adiabatic electron response for ITG was used just to show that the electron dissipation is not required for ITG excitation. Even with ITG dominated turbulence, significant electron thermal and particle transport can occur. However, this simplified classification is still useful since it gives an understanding of the global picture of the multidimensional parameter space ( $R/L_{Ti}$ ,  $R/L_n$ , collisionality, ...). On the other hand, even the most comprehensive, realistic and large scale simulation can be only done for one set of parameters at a time.

### 2.3.4.3.3. Trapped ion mode

While most of the drift waves discussed in this chapter are characterized by perpendicular wavelengths which scale with the ion gyroradius, there can be much longer wavelength electrostatic instabilities. Since the frequency of drift waves scales linearly with  $k_\phi$ , for  $k_\perp \rho_i \ll 1$ , long wavelength modes have low frequencies. If the mode frequency is smaller than the bounce frequency of trapped thermal ions, i.e.  $\omega < \omega_{bi} \simeq \sqrt{\varepsilon} \nu_{Ti} / (qR)$ , most passing ions can make a transit motion around the torus at least a few times during one wave period. Therefore the passing ion dynamics can be approximated by an adiabatic response, while the trapped ion dynamics should be described by the bounce-averaged kinetic equation. This is almost identical to the treatment of the electron dynamics for TEMs.

The trapped ion modes (TIMs) can occur for  $\omega < \omega_{bi}$ , corresponding to toroidal mode number  $n < 10$  in major tokamak core plasmas, and for ions in the banana collisionality regime  $\nu_{*i} < 1$ . As TEMs, the trapped ion instabilities can fall into two distinct classes depending upon whether they propagate in the electron or the ion diamagnetic direction. The dissipative version ( $\nu_{i,eff} \equiv \nu_{ii} / \varepsilon > \omega, \omega_{*e}$ ) of the first category is usually called the dissipative trapped ion mode [2.80, 2.92], while the dissipative ion temperature gradient

driven trapped ion mode [2.93] which occurs for  $\eta_i > 2/3$ , falls into the second. There also exists a collisionless trapped ion mode (with  $\bar{\omega}_{di} > v_{i,eff}$ ) [2.90]. The trapped ion instabilities were considered to be potentially very dangerous to confinement due to their large radial scales. Indeed, rather persistent trends of confinement scalings closer to Bohm rather than gyroBohm reported from major tokamak experiments justify attention to this class of large scale instabilities which were also observed in a comprehensive two-dimensional kinetic calculation [2.94].

### 2.3.5. Spatial structure of microturbulence

From the spatio-temporal scales of tokamak microturbulence, one can make a very rough estimate of the transport coefficient  $D_{turb}$  using dimensional analysis based on a random walk argument,

$$D_{turb} \sim \frac{(\Delta r)^2}{\Delta t} \sim \frac{\gamma}{k_r^2} \propto \frac{\omega_*}{k_r^2} \sim \left( \frac{k_\theta}{k_r^2 \rho_i} \right) \frac{\rho_i}{L} \frac{cT_i}{eB} \quad (2.73)$$

where  $\Delta r$  is the radial step size of the random walk and  $L$  is a macroscopic scale length of the order of the minor radius. While this elementary estimate reveals neither dynamical insight on the detailed transport process by random  $\vec{E} \times \vec{B}$  motion nor the significant role played by fluctuation amplitude in determining transport scalings, it illustrates the basic relation between the spatio-temporal scales of fluctuations and transport scaling. More detailed heuristic discussions have been given in Refs [2.53] and [2.95]. If it is assumed that  $k_\theta \sim k_r \sim \rho_i^{-1}$  as observed in gyrokinetic simulations with self-generated zonal flows and in some experiments [2.96, 2.97], then

$$D_{turb} \sim \frac{\rho_i}{L} \frac{cT_i}{eB} \quad (2.74)$$

This is called gyroBohm scaling because the Bohm scaling ( $\sim cT_i / eB$ ) is reduced by a factor  $\rho_i / L \ll 1$ , the ratio of gyroradius to a macroscopic length scale. This scaling is expected when local physics dominates the transport mechanism. It can be modified due to a variety of mesoscale phenomena such as avalanches [2.98] and turbulence spreading [2.99–2.101]. Some early turbulence simulations for small system size without self-consistently including zonal flow exhibited Bohm-like transport scaling in the presence of radially elongated eddies which can span a fraction of the minor radius. This can be understood by considering the worst strong turbulence case described in Section 2.1 of this chapter, i.e. by taking  $\Delta r \propto L \propto k_\theta^{-1}$  in Eq. (2.73). If we allow for a spectral anisotropy in the plane perpendicular to the equilibrium magnetic field,

somewhat weaker turbulence with mesoscale eddies also leads to Bohm scaling ( $D_{turb} \sim cT_i / eB$ ) from Eq. (2.73). In the latter case,  $\Delta r \propto \sqrt{L\rho_i}$  determines the fluctuation amplitude, while  $k_\theta \propto \rho_i^{-1}$ , alongside the potential fluctuation amplitude, determines the turbulent radial  $\vec{E} \times \vec{B}$  velocity. While the distinction between Bohm scaling and gyroBohm scaling may seem obvious, it can be complicated by many subtle issues.

Since the radial scale of microinstabilities plays a crucial role in determining the transport scaling, we discuss the important elements which affect those. In small size devices, quantization inside a device determines the radial wavelength of instabilities. For relatively large scale experiments in which  $\rho_i \ll a(\rho^* \ll 1)$ , the magnetic shear, toroidicity, and  $\vec{E} \times \vec{B}$  flow shear are believed to be important effects among others. The equilibrium magnetic field  $\vec{B}$  in toroidal geometry is given by  $\vec{B} = B_\phi \hat{e}_\phi + B_\theta \hat{e}_\theta$ , where the subscripts  $\phi$  and  $\theta$  denote toroidal and poloidal angles, respectively. For circular cross-section, high aspect ratio ( $R/a \gg 1$ ) plasmas,  $B \equiv |\vec{B}| = B_0(1 + (r/R)\cos\theta)^{-1}$ .

### 2.3.5.1. Role of magnetic shear: Sheared slab geometry

When one considers a perturbation with a given single set of mode numbers (i.e. a single helicity perturbation), it is convenient to introduce a sheared slab geometry to study the effect of magnetic shear on its stability and mode localization. Here, we deal with an electrostatic potential perturbation:

$$\delta\Phi(r, \theta, \phi) = \delta\Phi(r)e^{i(m\theta - n\phi)} \quad (2.75)$$

with toroidal mode number  $n$  and poloidal mode number  $m$ . The magnetic safety factor  $q(r)$  is approximately given by  $(B_\phi / B_\theta)(r/R)$ . We are interested in a set of  $(n, m)$  such that  $q(r_s) = m/n$  is satisfied somewhere inside the plasma. At  $r = r_s$ , the pitch of the magnetic field described by  $q(r)$  and the pitch of the perturbation (or helicity) are identical. We call this the mode rational surface. Since we have learned that the stability of various modes depends on the value of  $k_\parallel$ , we are motivated to find a model geometry and a coordinate system which simplifies the expression for  $k_\parallel$ . Noting that  $k_\phi = -n/R$ , and  $k_\theta = m/r$ ,

$$k_\parallel \equiv \frac{\vec{k} \cdot \vec{B}}{|\vec{B}|} = \frac{m}{r} \frac{B_\theta}{B} - \frac{n}{R} \frac{B_\phi}{B} = \frac{B_\theta}{rB} (m - nq(r)) \quad (2.76)$$

Therefore,  $k_\parallel = 0$  at the mode rational surface  $q(r_s) = m/n$ . For non-zero  $dq/dr$ , the pitch of the perturbation deviates from that of the magnetic field as one moves away from the mode rational surface radially. This trend is most easily captured in the helical coordinate system corresponding to  $(n, m)$ .

$$\hat{e}_y \equiv \hat{e}_\theta - \frac{n}{m} \frac{r}{R} \hat{e}_\phi \quad (2.77)$$

$$\hat{e}_z \equiv \hat{e}_\phi + \frac{n}{m} \frac{r}{R} \hat{e}_\theta \quad (2.78)$$

Then,

$$k_{\parallel} = \frac{m}{rB} \left( B_\theta - \frac{n}{m} q(r) B_\theta \right) \quad (2.79)$$

$$= \frac{m}{rB} \left( B_\theta - \frac{n}{m} \frac{r}{R} B_\phi \right) = \frac{m}{rB} \hat{e}_y \cdot \vec{B} \quad (2.80)$$

Expanding  $q(r) = q(r_s) + (r - r_s) \partial q / \partial r$ , ignoring  $\partial^2 q / \partial r^2$ ,

$$\begin{aligned} B_y &= \hat{e}_y \cdot \vec{B} = B_\theta \left( 1 - \frac{nq(r)}{m} \right) = B_\phi \frac{r}{q(r)R} \left( 1 - \frac{q(r)}{q(r_s)} \right) = -B_\phi \frac{r}{q(r_s)R} \frac{1}{q} \frac{\partial q}{\partial r} (r - r_s) \\ &= -\frac{B_\phi}{qR} \hat{s} (r - r_s) \end{aligned} \quad (2.81)$$

Therefore, one can model the magnetic field near the rational surface as

$$\vec{B} = B_0 \left( \hat{e}_z + \frac{x}{L_s} \hat{e}_y \right) \quad (2.82)$$

with magnetic shear  $\hat{s} \equiv (r/q)(dq/dr)$ , and magnetic shear length  $L_s \equiv qR/\hat{s}$ .

Now, we can discuss the effects of magnetic shear on the radial mode width and damping of drift waves in a sheared slab geometry. We closely follow a discussion in Ref. [2.102]. In a sheared slab,  $\delta\Phi(\vec{x}, t) = \delta\Phi(x) e^{i(k_y y - \omega t)}$ ,  $k_{\parallel} = (k_y / L_s) x$  (since  $k_z = 0$ , from Eq. (2.78)), and  $\nabla_{\perp}^2 = -k_y^2 + \partial^2 / \partial x^2$ . Therefore, the electron drift wave linear dispersion relation in the cold ion limit (Eq. (2.36)) becomes an eigenmode equation, which is similar to the Schrödinger equation,

$$\left( \rho_s^2 \frac{\partial^2}{\partial x^2} + \frac{\omega_{*e}}{\omega} - 1 - k_y^2 \rho_s^2 + \left( \frac{k_y c_s}{L_s \omega} x \right)^2 \right) \delta\Phi(x) = 0 \quad (2.83)$$

where  $c_s$  is the ion sound speed. Since the effective potential  $V(x) = -\left\{ (k_y / L_s) (c_s / \omega) x \right\}^2$  has an anti-well or potential hill structure for

$\text{Re}(\omega) \gg \text{Im}(\omega)$ , we should ensure that an appropriate boundary condition satisfies the causality requirement; i.e.

$$\lim_{|x| \rightarrow \infty} |\delta\Phi(x)| \rightarrow 0 \text{ for } \text{Im}(\omega) > 0 \quad (2.84)$$

which describes the fluctuation amplitude growing in time at the centre  $x \equiv 0$  first and localized in  $x$ , such that it should decay in space as  $|x| \rightarrow \infty$  at a given time.

It is straightforward to show from the large  $x$  asymptotic behaviour of the WKB solution,  $\Phi(x) \sim \exp[-i(k_y c_s x^2) / (2\omega L_s \rho_s)]$ , that it is equivalent to requiring that the radial group velocity  $v_{gx}$  satisfies the following:

$$\lim_{|x| \rightarrow \infty} v_{gx} = \lim_{|x| \rightarrow \infty} \frac{\partial \omega}{\partial k_x} > 0 \text{ for } x > 0 \quad (2.85)$$

and

$$\lim_{|x| \rightarrow \infty} v_{gx} = \lim_{|x| \rightarrow \infty} \frac{\partial \omega}{\partial k_x} < 0 \text{ for } x < 0 \quad (2.86)$$

i.e. the outgoing wave boundary condition. Physically, it describes the convective wave energy leakage from the centre to the  $|x| \rightarrow \infty$  region, and is called the magnetic shear damping of drift waves [2.56].

Indeed, the eigenvalue  $\omega$  now contains a sheared-induced damping term:

$$\frac{\omega}{\omega_{*e}} = \frac{1}{1 + k_y^2 \rho_s^2} - \frac{i(2n+1) L_n}{1 + k_y^2 \rho_s^2} \frac{L_n}{L_s} \quad (2.87)$$

where  $n = 0, 1, \dots$  is the radial mode (quantum) number.

Also, from the WKB solution  $\sim \exp(-i(k_y c_s) / (2\omega L_s \rho_s) x^2)$ , the radial width of an eigenmode scales like:

$$\Delta x \sim \sqrt{\frac{L_s \omega_{*e} \rho_s}{k_y c_s}} \sim \sqrt{\frac{L_s}{L_n}} \rho_s \quad (2.88)$$

Therefore, the stronger the magnetic shear, the shorter the radial width of the drift wave. Also, using a very simple random walk argument, one can speculate that the drift wave in a sheared slab geometry will result in a diffusion coefficient with gyroBohm scaling, since  $\Delta x \propto \rho_s$ . A similar scaling argument can be applied to the acoustic version of the ITG mode in a sheared slab [2.62].

### 2.3.5.2. Role of toroidal geometry: Ballooning representation

The magnetic curvature is unfavourable on the low field side of the tokamak, so that most instabilities can be more easily excited at

that location, resulting in a ballooning (at the outside) structure of the fluctuations. Obviously the usual Fourier representation of perturbations, i.e.  $\delta\Phi(r, \theta, \phi) = \sum_{n,m} \delta\Phi_{n,m}(r) e^{i(m\theta - n\phi)}$  is not an efficient representation of the ballooning-like fluctuations in toroidal geometry. In particular, since the poloidal mode number  $m$  is not a good quantum number in the torus, any eigenmode in the torus consists of many different poloidal harmonics which couple to each other. Fortunately if  $nq(r_s)$  is high enough for the fluctuations under consideration, there exists a more efficient way of representing perturbations in toroidal geometry. This takes advantage of the fact that for these high  $n$  fluctuations the radial characteristic length of the equilibrium (say  $L_p$ ) is much longer than that of the distance between two adjacent mode rational surfaces where each poloidal harmonic is located. Then, we can treat each poloidal harmonic as almost equivalent. Mathematically, we can express this as

$$\delta\Phi(r, \theta, \phi) = \sum_{j=0, \pm 1, \dots} \delta\hat{\Phi}_j \left( \frac{r - r_0}{\Delta r_s} \right) e^{i\{(m_0 + j)\theta - n\phi\}} \quad (2.89)$$

where  $m_0 \gg 1$ ,  $nq(r_0) = m_0$ , and  $\Delta r_s \equiv 1/(nq\hat{s})r_0$  is the distance between two adjacent rational surfaces for a given  $n$  [2.103]. Defining the dimensionless radial variable  $s \equiv (r - r_0)/r_s$ , we assume that each  $\delta\hat{\Phi}_j(s)$  has the same radial structure. Then, we can write  $\delta\hat{\Phi}_j(s) = \delta\hat{\Phi}(s - j)$  and this is called quasi-translational invariance (valid for  $|j| \ll m_0$ ). Then, we can check that the expression in Eq. (2.89) satisfies both periodicity ( $\delta\hat{\Phi}(r, \theta, \phi) = \delta\hat{\Phi}(r, \theta + 2\pi m, \phi + 2\pi n)$ ) for non-zero magnetic shear  $\hat{s}$  (and finite  $\Delta r_s$ ). The  $\delta\hat{\Phi}(s, j)$  are called quasi-modes, and for each quasi-mode  $k_{\parallel} = (s - j)/(qR)$ . A real toroidal eigenmode is a radial envelope consisting of a superposition of many poloidal harmonics as shown in Fig. 2.12.

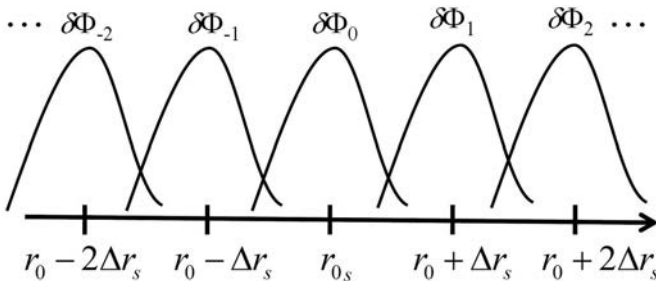


FIG. 2.12. Quasi-translational invariance of poloidal harmonics.

In theory [2.104, 2.105], its radial extent can be as large as a fraction of system size (determined by the shape of the equilibrium profiles), and at that scale, the quasi-translational invariance is broken. For instance, if  $\Delta r$  (the radial

extent of a toroidal eigenmode)  $\sim (a\rho_i)^{1/2}$ , from the random walk argument, one can obtain a Bohm-like scaling,

$$D_{turb} \sim \Delta r^2 / \Delta t \sim (a\rho_i)\omega^* \sim \frac{cT}{eB} \quad (2.90)$$

for  $k_\theta \rho_i \sim 1$ . In reality, the radial extent of the non-linearly saturated, finite amplitude fluctuations is the relevant quantity. The radially elongated non-linear structures are called “streamers”. Some theories suggest that the non-linear generation mechanism, rather than the linear toroidal coupling of different poloidal harmonics, plays a more essential role in the formation of streamers, while others emphasize the visual resemblance of streamers and the toroidal linear eigenmode. Implications of the existence of streamers include not only a consequent Bohm scaling of confinement due to the ion gyroradius scale fluctuations which has been just discussed, but also a possible relevance of ETG turbulence as a dominant electron thermal transport mechanism in some confinement regimes in spherical tori and tokamaks. As discussed in Section 2.3.4.2, the radial scale of the ETG mode is very short, and scales with the electron gyroradius. Unless the radially elongated streamers are dominant characteristics of ETG turbulence, the electron thermal transport driven by ETG turbulence is too small ( $\chi_e^{ETG} \sim \sqrt{m_e / M_i} \chi_i^{ITG}$ , roughly, due to the mass dependence of gyroradii) to be relevant to experimental results.

Now, the mode structure along the field line can be represented by a coordinate which is a Fourier conjugate to the radial variable  $z \equiv s - j$ ;

$$\hat{\xi}(\eta) \equiv \int_{-\infty}^{\infty} dz e^{i\eta z} \hat{\xi}(z) \quad (2.91)$$

The extended poloidal (or ballooning) angle “ $\eta$ ” is defined for  $-\infty < \eta < \infty$  [2.106, 2.107]. Various eigenmode equations for microinstabilities in a tokamak (including the effect of magnetic curvature and  $\nabla B$  drift:  $\omega_{di} = -(cT_i k_\theta) / (eBR)(\cos\eta + \hat{s}\eta \sin\eta)$ ) can be written in a relatively simple form in this ballooning coordinate. One useful example of this is a clear demonstration that the magnetic shear induced damping of drift waves discussed in the previous section becomes ineffective due to formation of a toroidicity induced electron drift wave [2.108].

### 2.3.5.3. Role of zonal flow shear

While the physics of the mean  $\vec{E} \times \vec{B}$  flow is relatively well established [2.109], study of turbulence driven zonal flows is still an active area of current research in both the theory and experimental communities even after publication

of an extensive review [2.51]. Zonal flows are  $\vec{E} \times \vec{B}$  flows associated with azimuthally ( $n = 0$ ) and poloidally ( $m = 0$ ) symmetric, but radially varying electric potential fluctuations. Therefore, zonal flows are not directly responsible for radial transport and, unlike various instabilities in confined plasmas, cannot grow at the expense of the expansion-free energy associated with the radial gradient of either temperature or density. Thus, zonal flows are linearly stable, and can only grow at the expense of fluctuation energy through a non-linear interaction. Zonal flows coexist with, and are excited by, ambient turbulence developed from a variety of collective instabilities, and regulate transport by shearing the ambient turbulence. As seen in Fig. 2.11, the spatial structure of turbulence eddies is modified by the presence of zonal flows. The main effect of  $\vec{E} \times \vec{B}$  shear associated with zonal flows is to reduce the radial size of eddies (shearing) [2.110–2.112] and turbulence amplitude and transport. Unlike the mean  $\vec{E} \times \vec{B}$  flow which can be driven externally (for instance, by neutral beam injection) and can exist in the absence of turbulence, zonal flows are spontaneously generated by turbulence [2.113–2.116].

Zonal flows are of practical importance since they reduce transport, and shift the effective threshold condition for the onset of significant transport. In the magnetic fusion community, the possible importance of self-generated zonal flows in regulating turbulence and transport was first recognized from fluid simulations of drift wave turbulence [2.117]. Following the observation from an early non-linear gyrofluid simulation [2.118], there were ensuing non-linear gyrokinetic simulations [2.119] with more realistic kinetic dynamics and a proper treatment of the undamped zonal flow component in collisionless toroidal geometry [2.79]. It is now widely recognized that understanding zonal flow dynamics is essential in predicting confinement in future devices [2.120].

Advances in theory and simulation of zonal flows have influenced the experimental community as described in a recent review [2.51]. In particular, characterization of the experimentally measurable features of zonal flow properties from non-linear gyrokinetic simulations [2.121] has motivated experimental measurements. In toroidal plasmas, GAMs (geodesic acoustic modes) consisting of the ( $n = 0, m = 1$ ) up–down asymmetric sideband pressure perturbation linearly coupled to the ( $n = 0, m = 0$ ) electric field potential perturbation via geodesic curvature [2.122] can also be non-linearly excited, in addition to the low frequency (near zero) zonal flow (see Fig. 2.13). The low frequency component of zonal flows has been shown to be more important in regulating core turbulence [2.123].

Remaining outstanding issues in zonal flow physics which need to be addressed in the near future include the following [2.124]. More direct links between the zonal flow amplitude and enhancement of confinement needs to be demonstrated. While there have been some systematic, but limited, scans

on the collisional damping of zonal flows [2.125], the  $q$  dependence of zonal flow properties [2.126, 2.127] and their effect on confinement, in most cases the effects of zonal flows have been exhibited in case by case simulations [2.64, 2.119, 2.120, 2.128] or in the context of simple non-linear models [2.115, 2.116]. A rigorous theory based quantitative prediction of zonal flow induced confinement improvement with enough physics realism is still non-existent. Without theoretical understanding of saturation of zonal flows in collisionless plasmas, such a predictive capability remains elusive.

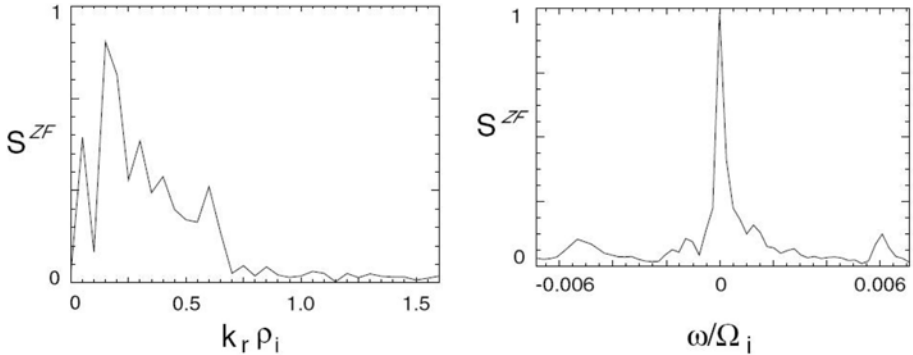


FIG. 2.13. ITG core turbulence simulation using GTC code exhibits  $k_r$  and frequency spectra of self-generated zonal flows, consisting of zero-frequency zonal flow and GAM sideband [2.121].

### 2.3.6. Different channels of turbulence transport

One of the major goals in tokamak fusion research is to achieve high ion temperature. Experimentalists usually plot the central ion temperature as a function of the heating power (Fig. 2.14). On the other hand, theoreticians prefer to think about the plasma confinement problem in terms of the flux-gradient relation which is familiar from Fick's law in thermodynamics. For instance, the ion heat flux can be plotted as a function of temperature gradient (see Fig. 2.14).

In confined plasmas, there exist many sources of free energy for instabilities and transport. These include the radial gradients of ion temperature, electron temperature, density and toroidal rotation. One can formally write a generalized flux-gradient-relation in matrix form. We note that the radial flux of each quantity can not only be driven by the radial gradient of that quantity itself, but also by the gradients of other quantities. The contribution of the diagonal term in the transport matrix is called the diffusive term. The contributions from the off-diagonal terms are called the non-diffusive flux. Some of them are casually called the pinch term or the convective flux.

The ion thermal transport is discussed in Section 2.3.6.1; Sections 2.3.6.2 and 2.3.6.3 cover ion and electron thermal transport and particle transport respectively. Finally, momentum transport is discussed in Section 2.3.6.4.

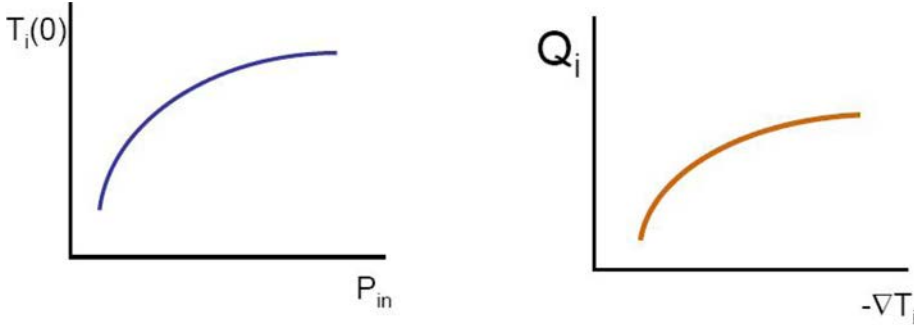


FIG. 2.14. Ion temperature  $T_i$  as a function of heating power  $P_{in}$ , and heat flux  $Q_i$  as a function of ion temperature gradient  $-\nabla T_i$ . These diagrams illustrate that the central temperature of a tokamak can be increased by applying more heating power, and that radial heat flux can increase as the temperature gradient steepens.

### 2.3.6.1. Ion thermal transport

Ion thermal transport is currently better understood compared to other channels of transport. In auxiliary heated plasmas, an anomalous level of ion thermal transport has been observed which is much greater than the prediction from neoclassical collisional transport theory. Ion temperature gradient driven turbulence is the leading candidate for the anomalous ion thermal transport. The linear threshold of ITG instability is also of high practical interest in tokamak experiments. This is because strongly unstable ITG modes can drive large amounts of radial ion heat flux, resulting in a reduction of the local ion temperature gradient. In combination with a competing effect due to ion heat deposition (via neutral beam injection (NBI) or ion cyclotron resonance heating (ICRH), for instance), this results in ion temperature profiles which do not deviate significantly from the onset condition. This onset condition can be calculated accurately using various gyrokinetic codes. A parametrization of various dependences can be found in Ref. [2.129], for instance. There is theoretical evidence that “the onset condition” is further modified by the bursty nature of a driven system near marginality [2.98] and the  $\vec{E} \times \vec{B}$  zonal flows [2.120]. Theoretical predictions from different gyrokinetic codes begin to converge for simple cases, not only in numbers, but also in underlying non-linear physics mechanisms. An outstanding example is the zonal flow induced upshift of the ITG onset condition [2.120].

In the last decade, the recognition of the importance of zonal flows has brought a paradigm shift in the tokamak turbulence theory community, from the drift wave turbulence problem to the drift wave–zonal flow system problem [2.51]. Zonal flows exist in nature, for instance on Jupiter and the Sun, and have been observed in many gyrokinetic simulations. Many theoreticians believe they should exist in ITER plasmas as well. Zonal flow is a toroidally symmetric, poloidally symmetric and radially varying  $\vec{E} \times \vec{B}$  flow. The interaction of zonal flows with drift wave turbulence is schematically illustrated in Fig. 33 of Ref. [2.51]. Zonal flows can be damped by the collisional friction between trapped and passing ions [2.130]. Also, zonal flows regulate turbulence via  $\vec{E} \times \vec{B}$  shearing [2.110–2.112].

Next, some examples are presented in which the zonal flows play crucial roles in determining the transport scalings with respect to key dimensionless parameters. Transport scaling with respect to the machine size, or  $\rho^* = \rho_i / a$ , is very important, since we want to know by how much the future larger machines will perform better than the present ones. As our understanding of ITG turbulence got deeper, our predictions were modified. Theoretical predictions of toroidal ITG instabilities in the early 1980s [2.63] and of their global radial structures in the early 1990s [2.104, 2.105] seemed to indicate the possibility of Bohm scaling. Since the mid-1990s, extensive studies of zonal flows indicated that the radially elongated global ITG eigenmodes get broken up by zonal flows into smaller eddies [2.118, 2.119, 2.128]. Naturally, most people expected gyroBohm scaling from the eddy size scaling. More recently, it has been indicated that, from global gyrokinetic simulations, for a moderate system size, non-negligible deviations from gyroBohm scaling can exist [2.131]. This can occur due to turbulence spreading into the linearly stable zone [2.100]. While the studies on turbulence spreading go back at least to the mid-1990s [2.99], it was the importance of its relation to the  $\rho^*$  scaling which revived wide interest in the theory community [2.100, 2.101, 2.132–2.137].

Plasma current scaling of confinement, as described in Section 2.4, is one of the remaining puzzles of ion thermal transport. It is possible to obtain the  $q$  dependence of the transport from zonal flow characteristics which depend on the  $q$  value. Due to their Landau damping, geodesic acoustic modes (GAMs) can exist only in a high- $q$  region. Therefore, in a low- $q$  region, only stationary zonal flows will persist. Since GAMs oscillate with a relatively high frequency, they are not very effective in reducing turbulence [2.123]. So we expect a lower level of turbulence in the low- $q$  region where static zonal flow dominates. As shown from a recent non-linear gyrofluid simulation [2.126], the ion heat flux from ITG turbulence is lower for the case with lower  $q$ , since the stationary zonal flows dominate. This is confirmed by an independent gyrokinetic simulation [2.127]. However, the relevance of this mechanism to experiment still remains to be demonstrated.

The collisionality dependence of ion heat transport observed in tokamak experiments is a puzzle too, since the transport level was much higher than the predictions from collisional transport theory, while ITG turbulence in the core of a tokamak is essentially collisionless. Recognizing that the zonal flows regulate the turbulence level, near ITG marginality, collisional damping of zonal flows controls the transport, and the transport level can increase with an increasing ion collisionality as shown from gyrokinetic simulations [2.125] and confirmed by an independent gyrofluid simulation [2.138]. From a theoretical point of view, it is important to note that this trend can be reversed if one includes the trapped electron response, which decreases with electron collisionality [2.139]. While some experiments report transport increases with collisionality, further parameter scans are required to identify the underlying physics mechanisms.

### 2.3.6.2. *Electron thermal transport*

It has been well known for many years that all operational modes of tokamaks and spherical tori have exhibited anomalous electron thermal transport. There is evidence that electron temperature profiles are stiff in tokamaks. Perturbative transport experiments, including heat pulse propagation, and the need for an inward heat pinch term in transport analysis of auxiliary heated plasmas, all indicate this possibility. Possible theoretical candidates for electron thermal transport include the trapped electron mode (TEM) and the ITG mode with trapped electrons, the electron temperature gradient (ETG) mode, and magnetic flutter driven transport.

Starting with the TEM, it can produce an electron thermal diffusivity of experimental relevance when strongly turbulent. It is interesting to note that DTEM based non-linear theory [2.140] can produce a scaling of electron thermal diffusivity  $\chi_e$  close to the Neo-Alcator scaling which has been widely observed in many ohmically heated tokamak plasmas. One supporting result for TEM comes from the ASDEX-Upgrade ECH experiment. The transport shows a threshold behaviour in agreement with the TEM theory prediction. Furthermore, the experimentally measured heat flux and the calculated TEM linear growth rate show a similar trend as functions of the electron temperature gradient [2.141]. On the other hand, evidence for TEM-like fluctuations from measurements is relatively rare, as discussed in Section 2.6.2.

Another candidate is ETG turbulence. In some spherical torus plasmas such as NSTX, electron transport is highly anomalous even when low- $\vec{k}$  fluctuations are believed to be linearly stable. In NSTX neutral beam heated plasmas [2.142], most of the heating power from the energetic particles goes to electrons, and this is similar to a situation expected for ITER. The linear stability analysis shows that the low- $\vec{k}$  fluctuations are expected to be stable due to the high  $\vec{E} \times \vec{B}$  shearing rate, leaving only high- $\vec{k}$  ETG modes unstable. Note that the ion thermal diffusivity is

down to a neoclassical level, qualitatively consistent with the stabilization of low- $\vec{k}$  ITG/TEM modes. Due to its low magnetic field and consequent large electron gyroradius, NSTX is an ideal place to look for ETG-like fluctuations with good spatial resolution. Recent progress in experimental measurements using high- $\vec{k}$  tangential scattering indeed supports the existence of density fluctuations in the ETG spectral range [2.143]. More details can be found in Section 2.6.2.

To produce electron heat transport at a level of experimental relevance in tokamaks, the radial correlation length of ETG turbulence has to be significantly enhanced over the electron gyroradius. Radially elongated streamers have been observed in many non-linear gyrokinetic simulations [2.87, 2.88]. However, from a different simulation, the correlation between the electron heat flux and the radial size of streamers has been reported to be weak [2.144]. As of now, there is no consensus in the theory community regarding whether the ETG-driven electron heat transport is high enough to explain experimental observations.

### 2.3.6.3. Particle transport

Particle transport is also anomalous in most cases, while its associated diffusion coefficient is typically smaller than that associated with ion thermal or electron thermal transport. In many experiments, electron density profiles are observed to be centrally peaked, even when the particle source exists only at the edge. This has motivated theoretical research on an inward convective flux (pinch) of particles. The particle flux can be written as

$$\Gamma = -D \frac{\partial n}{\partial r} + n v_{pinch} \quad (2.92)$$

i.e. as a sum of diffusion (the first term) and a convective flux proportional to a pinch velocity  $v_{pinch}$ . As described in Section 2.2, an inward pinch of particles can occur through a collisional process involving magnetically trapped particles. This Ware pinch can account for density peaking in some tokamak cores [2.145], but there seems to be no shortage of counter examples to this, including cases without an inductive electric field [2.146, 2.147] which is required for the Ware pinch. From the form of Eq. (2.92), it is clear that an electron particle pinch can be driven by either  $\nabla T_e$  or  $\vec{\nabla} B$ , i.e. magnetic field inhomogeneity. The first class of pinch is called the thermoelectric pinch, for the obvious reason, while the second class is called the turbulent equipartition (TEP) pinch [2.148], for a reason that we explain shortly.

For the ITG dominated case (but with non-adiabatic electron response, contributing to turbulent particle flux), it has been known for a few decades that inward particle flux can occur when the collisionality of the plasma is either very high or very low. The first possibility is called the ion mixing mode [2.58], which occurs for high collisionality satisfying  $\nu_{*e} > 1$ , and  $\nu_e > k_{\parallel} v_{T_e} > \omega, \omega_{*e}$ . The ion

mixing mode can be of very high pedagogical value since the instability is driven by  $\nabla T_i$ , while  $\nabla n$  and  $\nabla T_e$  drive diffusive and convective particle fluxes associated with it, respectively. Electron drift wave stability in this regime has been discussed in Section 2.3.2.1. The second possibility, which is more relevant to present day and future tokamak core plasmas, occurs when  $v_{*e} \ll 1$ , such that the trapped electron response becomes collisionless enough that  $\omega_{*e} > \bar{\omega}_{de} \lesssim v_{eff} = v_e / \varepsilon$ . Since its first discovery [2.149], there has been gradual theoretical progress in refining the calculations, including more realistic effects [2.150–2.152]. Comparisons to experiments are also under way, as discussed in Ref. [2.153], for instance.

Another class of particle pinch can occur due to the inhomogeneity of the equilibrium magnetic field. The fundamental concept behind the turbulent equipartition (TEP) pinch can be elucidated by considering a 2-D system with straight but inhomogeneous magnetic field  $\vec{B} = B(x, y)\hat{z}$ , in which density is mixed by  $\vec{E} \times \vec{B}$  flow [2.154]. In 2-D, the density continuity equation is

$$\frac{\partial}{\partial t} n + \vec{\nabla} \cdot (n\vec{u}_E) = 0 \quad (2.93)$$

with  $\vec{u}_E = -(c/B)\vec{\nabla}\Phi \times \hat{z}$ . Now,  $\vec{u}_E$  is no longer incompressible due to the inhomogeneity in  $\vec{B}$ . However, we can write Eq. (2.93) as

$$\frac{\partial}{\partial t} \left( \frac{n}{B} \right) + \vec{u}_E \cdot \vec{\nabla} \left( \frac{n}{B} \right) = 0 \quad (2.94)$$

using the fact that  $\vec{\nabla} \cdot \vec{\nabla}\Phi \times \hat{z} = 0$ . Then a magnetically weighted density “ $n/B$ ” is advected by the  $\vec{E} \times \vec{B}$  flow. Thus,  $n/B$  is locally conserved and eventually mixed or homogenized by the turbulent  $\vec{E} \times \vec{B}$  flow. Then, the spatial profile of the mean  $n/B$  would relax according to  $\Gamma_{n/B} = -D_{n/B} \partial \langle n/B \rangle / \partial x$  so that  $\partial \langle n \rangle / \partial t + \partial \Gamma_{n/B} / \partial x = 0$ .

According to the conventional classification given in Eq. (2.92),

$$\Gamma_{n/B} \equiv -D_{n/B} \left( \frac{1}{B} \frac{\partial}{\partial x} \langle n \rangle - \frac{\langle n \rangle}{B^2} \frac{\partial}{\partial x} \bar{B} \right) = -D_n \frac{\partial}{\partial x} \langle n \rangle + v_{pinch} \langle n \rangle \quad (2.95)$$

where  $D_n = (D_{n/B}) / \bar{B}$ ,  $v_{pinch} = -(D_{n/B} / \bar{B}^2) \partial \bar{B} / \partial x$ , and  $\bar{B} \equiv \langle n \rangle / \langle n/B \rangle \simeq \langle B \rangle$ . Relaxation of gradients of the locally advected, magnetically weighted quantity “ $n/B$ ” led to a pinch  $v_{pinch} \equiv -(D_{n/B} / \bar{B}^2) \partial \bar{B} / \partial x$  of an observed physical quantity  $\langle n \rangle$ . This is the simplest example of the TEP pinch. It is called the TEP pinch since time-asymptotically it will lead to a complete relaxation, mixing, or “equipartition” of  $\langle n/B \rangle$ . Note that unlike  $\nabla T_e$ ,  $\vec{\nabla} B$  is not a thermodynamic force, and TEP is of a different sort from a thermoelectric pinch.

In toroidal geometry, most of the TEP particle pinch comes from magnetically trapped electrons [2.155, 2.156]. This leads to a simple formula from

$$v_{pinch}^{TEP} / D = -\frac{2}{R_0} \left( \frac{1}{4} + \frac{2\hat{s}}{3} \right) \quad (2.96)$$

with  $R_0$  being the major radius at the axis. Some degree of agreement with experiments exist for L-mode plasmas, in particular in its relation to  $q$  profiles (through the  $\hat{s}$  dependence) [2.146, 2.157].

#### 2.3.6.4. Momentum transport

Now, it is well appreciated that plasma rotation plays a central role in magnetic confinement.  $\vec{E} \times \vec{B}$  shear can reduce turbulence and transport, and in turn rotation can be generated by microturbulence via Reynolds stress [2.158]. It can stabilize MHD instabilities, such as resistive wall modes, but can be damped via non-axisymmetric magnetic fields produced by MHD instabilities. In addition, the radial electric field interacts with energetic particles. Therefore, understanding momentum transport is important. In particular, for successful operation of ITER, we want to know whether ITER will have enough wave and neutral beam power to generate sufficient rotation for turbulence and transport reduction as well as stabilization of resistive wall modes.

Historically, momentum diffusivity has been predicted [2.159], and observed [2.26] to be very close to ion thermal diffusivity. But, more recently, many tokamak experiments indicated that the ratio between these two quantities can deviate from unity significantly. This may suggest the existence of an off-diagonal contribution to the momentum flux as demonstrated in detailed experimental studies [2.160]. Indeed, a momentum pinch has been indicated by modulation experiments [2.161, 2.162]. It is also important to note that fluctuation measurements indicate that plasma rotation is related to the Reynolds stress [2.163].

Intrinsic toroidal rotation has been observed in the absence of an external torque input from neutral beams in nearly all tokamaks [2.164, 2.165]. The behaviour of L-mode plasmas remains complex, and is closely tied to scrape-off layer flows [2.166]. On the other hand, Hmode plasmas demonstrate simple and clear empirical trends, summarized as the Rice scaling [2.167]. Toroidal rotation in H-mode plasmas is in the co-current direction, increases with incremental stored energy and decreases with plasma current. These observations appear to be consistent with rotation originating at the edge with the transition and building inward from there. There are also experimental observations that cannot be explained by diffusion and a pinch only [2.168].

The radial flux of momentum can be semi-theoretically written as a sum of the diffusive flux, the convective flux proportional to the momentum pinch velocity  $v_{mom,pinch}$  and the residual stress,

$$\Gamma_\phi = -\chi_\phi \frac{\partial}{\partial r} \langle u_\phi \rangle + v_{mom, pinch} \langle u_\phi \rangle + \Pi_{RS} \quad (2.97)$$

This can be viewed as a quasi-local expression resulting from a Taylor expansion of a general expression for  $\Gamma_\phi$  in  $\partial \langle u_\phi \rangle / \partial r$  and  $\langle u_\phi \rangle$ . There is no a priori reason to rule out the residual stress  $\Pi_{RS}$  which is independent of toroidal flow and toroidal flow shear. It can be proportional to the gradient of pressure or density. In the presence of residual stress, the resulting flow evolution equation governed by the divergence of  $\Gamma_\phi$  should satisfy the basic coordinate transformation properties, such as Galilean invariance in a simple geometry. Now, we discuss diffusive flux, the momentum pinch and finally the residual stress.

Fluid theory [2.159] predicted that the intrinsic Prandtl number (the ratio of momentum diffusion to ion heat diffusion), defined with only the diffusive momentum flux, should be near unity. From the gyrokinetic theory point of view, momentum and ion thermal transport involve different velocity moments respectively. Therefore, if a certain particular set of particles (for instance, those resonant with waves) contribute dominantly to transport, the intrinsic Prandtl number should deviate from unity [2.169].

A pinch can come from various physical mechanisms [2.170] including wave-particle resonance. In this section, we discuss the curvature driven toroidal momentum pinch, which has two parts. The first part is the turbulent equipartition (TEP) pinch which is mode independent, originating from the fact that the  $\vec{E} \times \vec{B}$  flow is no longer incompressible in a torus [2.171]. This is the simple and robust part. The second part is the thermoelectric pinch which is mode dependent, and sensitive to turbulence characteristics. The physics of the TEP pinch is well illustrated by the particle pinch in a slab with an inhomogeneous  $B$  field in the previous section. Mixing of the magnetically weighted, locally conserved quantity  $n/B$  leads to an effective pinch in the observed physical quantity  $n$ . Then, how about for momentum? Starting from angular momentum density conservation, and using the  $\vec{E} \times \vec{B}$  flow compressibility, one can show that the magnetically weighted angular momentum  $nu_\phi R/B^2$  is convected by the turbulent  $\vec{E} \times \vec{B}$  flow [2.171]. As a consequence of mixing and diffusion of the magnetically weighted quantity  $nu_\phi R/B^2$ , we can obtain an inward pinch in the observed quantity  $nu_\phi$  by performing a quasi-linear calculation [2.172, 2.173]. By separating the radial gradients of this expression into two parts, we can identify the TEP pinch term. The resulting pinch velocity, normalized to the momentum diffusivity, is  $-4/R$ , if we define the momentum diffusivity with respect to the angular rotation frequency. These results can also be derived from the conservative gyrokinetic equation [2.171]. For this toroidal pinch, the symmetry breaking comes from ballooning fluctuations which have more intensity on the unfavourable curvature, low field side.

The thermoelectric pinch is a thermodynamic part of the Reynolds stress related to the ion temperature fluctuations. It is dependent on mode characteristics, in particular, the phase angle between  $\delta T_i$  and  $\delta \Phi$ . It is also sensitive to the proximity to marginality, the gyrofluid approximation, and the dispersion relation used in the derivation [2.174]. An independent formulation in the rotating frame attributes the aforementioned curvature driven momentum pinch to Coriolis pinch force related terms [2.175].

In contrast to the particle transport problem where particle number is conserved, and the pinch is the only off-diagonal flux, momentum can be transferred between particle and waves. This can lead to the residual stress, the last term in Eq. (2.97) [2.174]. Since the residual stress can make a net contribution after a radial integration from the plasma boundary, it can accelerate the resting plasma. Therefore, the residual stress acting with an appropriate boundary condition can generate an intrinsic rotation [2.176]. To get a finite residual stress, we need a broken symmetry in the turbulence. The key point about the residual stress is that  $\vec{E} \times \vec{B}$  shear converts poloidal rotation shear into toroidal rotation shear via asymmetry in the wave to particle momentum deposition. This asymmetry can be provided by having a finite  $\vec{E} \times \vec{B}$  shear and generic drift-acoustic coupling, which will shift the eigenmode in the radial direction, resulting in a preferred sign of  $k_{\parallel}$ , as noted by many authors [2.177, 2.178]. The underlying physics mechanism behind the residual stress is a directional imbalance in the acoustic wave populations and in the profile of momentum deposition by ion Landau damping [2.169].

### 2.3.7. Physics of transport barriers

Over recent years, the performance in tokamak plasmas has been improved considerably by exploiting enhanced confinement regimes. While there are differences between the operational techniques as well as the initial locations for a wide variety of transport barriers, a considerable amount of similarity in the transition dynamics appears to exist.

In this section, we discuss the common physics elements which constitute the conceptual building blocks of many transport barrier theories and simulations [2.179]. A more quantitative, theoretically oriented review also exists [2.180]. Significant insight into turbulence suppression by the sheared mean  $\vec{E} \times \vec{B}$  flow has been gained via extensive experimental investigation in the 1990s of the physics of transport barrier formation [2.181, 2.182]. On the theory side, development of the  $\vec{E} \times \vec{B}$  shear driven non-linear decorrelation theory in a simple geometry [2.110], and its extension to general toroidal geometry [2.112, 2.183], as well as non-linear gyrofluid simulations [2.128], have led to an approximate criterion for ion thermal transport barrier formation: namely the  $\vec{E} \times \vec{B}$  shearing rate [2.112] versus the maximum linear growth rate of microinstabilities in the

absence of flow. While this is an oversimplified “rule of thumb”, rather than a final statement of the  $\vec{E} \times \vec{B}$  shear suppression, it has been widely used in the experimental community as a rough measure for the assessment of the role of  $\vec{E} \times \vec{B}$  shear in transport barrier formation. Now, there is a significant effort towards self-consistent, non-linear dynamic simulations of transport barrier formation.

The strength of the  $\vec{E} \times \vec{B}$  shear effect is characterized by the shearing rate  $\omega_E$  in general toroidal geometry [2.112]:

$$\omega_E = \frac{\Delta\psi_0}{\Delta\phi} \frac{\partial}{\partial\psi} \left( \frac{E_r}{RB_\theta} \right) = \frac{\Delta r_0}{\Delta l_\perp} \frac{(RB_\theta)^2}{B} \frac{\partial}{\partial\psi} \left( \frac{E_r}{RB_\theta} \right) \quad (2.98)$$

Here,  $\psi$  is the poloidal flux representing the radial coordinate via  $d\psi = RB_\theta dr$ ,  $\Delta r_0 = \Delta\psi_0 / RB_\theta$  is the radial correlation length and  $R\Delta\phi$  is the toroidal correlation length, and  $\Delta l_\perp = RB_\theta \Delta\phi / B$  is the correlation length of the ambient turbulence in the direction perpendicular to the field line, but in the flux surface. Other notations are standard.  $(\partial / \partial\psi)(E_r / RB_\theta)$  is a flux function in most cases.

The radial force balance relation for a plasma ion species  $i$  reads

$$E_r = \nabla p_i / Z_i e n_i + u_{i\phi} B_\theta - u_{i\theta} B_\phi \quad (2.99)$$

where  $E_r$  is the mean radial electric field, and  $p_i$ ,  $u_{i\phi}$  and  $u_{i\theta}$  are ion pressure, ion toroidal velocity and ion poloidal velocity respectively. Therefore,  $E_r / RB_\theta$  can come from the poloidal flow, the toroidal flow and the pressure gradient. This is one of the reasons that this paradigm has been widely applicable to various cases including:

- (i) ITB formation in TFTR [2.184] and JET [2.185] plasmas, and ETB formation [2.182, 2.186, 2.187] in high (H)-mode plasmas [2.188], where the poloidal flow plays a crucial role in the transition, while the pressure gradient is significant after the transition [2.186, 2.189];
- (ii) plasmas with strong toroidal rotation such as negative central shear (NCS) [2.190] and very high (VH)-mode [2.191] plasmas in DIII-D, optimized shear (OS) plasmas in JET [2.192], and in many other tokamaks [2.193–2.195] and in spherical torii [2.142]; here  $E_r$  is typically positive for co-rotating plasmas and negative for counter-rotating plasmas.

Now, we discuss the role of  $q$  profiles and magnetic shear in forming transport barriers. From a theoretical point of view, the  $q$  profile can affect turbulence in many ways:

- (i) Each poloidal harmonic of a toroidal eigenmode is centred on a rational  $q$  surface, as illustrated in Fig. 2.12.
- (ii) Its radial extent is often limited by linear Landau damping and resistive dissipation, which increase away from the rational surface at a rate which depends on the magnetic shear  $s = d(\ln q) / d(\ln r)$ .
- (iii) The radial overlap of these poloidal harmonics strongly depends on the density of the rational surfaces, which in turn depends on the  $q$  profile shape. Radial overlap gets easier as higher mode numbers are considered. Low mode number fluctuations can exhibit discontinuities for low  $s$  values, especially near the radial location where  $q$  becomes a minimum in reversed shear (RS) plasmas, due to a rarefaction of rational  $q$  surfaces [2.105].
- (iv) Reversed shear has a stabilizing influence on curvature driven instabilities.

The discovery of the H-mode in a diverted tokamak [2.188] motivated an early theory of the H-mode [2.196], which relied on mechanism (ii), which becomes pronounced when  $s$  becomes very high at the edge, either just inside the last closed flux surface of the diverted tokamak plasma or due to current rampdown [2.197]. There have been numerous linear stability analyses (for instance Refs [2.90, 2.198–2.204]) on various microinstabilities addressing effect (iv). Non-linear simulations in flux tube geometry [2.87, 2.128, 2.201, 2.205] take into account effects (i), (ii) and (iv). However, the “ballooning representation” is closely related to the quasi-translational lattice symmetry as discussed in Section 2.3.5.1, which is not applicable to low mode number fluctuations or near  $q_{\min}$  of reversed shear plasmas. Consequently, these simulations find that reversed magnetic shear (via mechanism (iv)) is more favourable for transport reduction compared to low magnetic shear (via mechanism (iii)) which should be more pronounced for low mode number fluctuations.

Global gyrokinetic simulations keeping relatively low toroidal mode number fluctuations observe transport reduction near  $q_{\min}$  due to a lack of radial overlap (discontinuity) of poloidal harmonics [2.206]. However, this effect gets weaker and transport tunnels through the  $q_{\min}$  surface as more modes are added in an independent global gyrokinetic simulation [2.207]. A study based on global fluid simulations of ITG turbulence [2.208] addressed all the aforementioned effects associated with  $q$  profiles, although sub-ion-gyroradius-scale high mode number fluctuations are not kept. The overall conclusion is that an ITB is most easily formed near  $q_{\min}$  of RS plasmas, especially when  $q_{\min}$  is near a low order rational value due to a rarefaction of rational  $q$  surfaces. However, ITB formation near  $q_{\min}$  when its value is near a low order rational number does not necessarily imply that mechanism (iii) is responsible for it. More recent gyrokinetic simulations exhibited turbulence driven zonal flows being preferentially generated

near gaps in the density of rational surfaces localized in the vicinity of  $q_{\min}$  [2.209]. It has also been pointed out from analytic theory [2.210] that low mode number electrostatic convective cells may play a key role in the mean profile flattening localized to the low- $q$  surface as a transition precursor as observed in experiment [2.211]. These effects could play a role in the type II ERS transitions in TFTR [2.212] which occur near  $q_{\min}$  when its value reaches near 2, and in internal transport barriers in RS plasmas in DIII-D [2.211]. Other theoretical possibilities supporting the important role of low order rational  $q$  surfaces include the generation of localized velocity via MHD instability as proposed by the JET team [2.213] and via a loss of fast ions as proposed by the ASDEX-Upgrade team [2.214].

On the other hand, recent findings from NSTX experiments [2.215] seem to support the hypothesis that while ion thermal transport barriers are formed in the region where the  $\vec{E} \times \vec{B}$  shearing rate is a maximum, the electron thermal transport barrier location correlates well with the (negative) magnetic shear minimum location, i.e. where the negative magnetic shear is strongest. The appearance of an electron barrier for negative magnetic shear has previously been reported in many tokamaks including JET [2.216]. Finally, an analysis of the Tore-Supra plasmas has yielded a puzzling result that the time of internal barrier formation shows little correlation with either the value of  $q_{\min}$  or the value of (the negative) magnetic shear [2.217]. It correlates with the central  $q$  value,  $q(0)$ , crossing a low order rational value in time. In summary, there exist a variety of both experimental and theoretical findings regarding the role of the  $q$  profile in transport barrier formation. Further study on this subject is required.

It is useful to discuss the basic physics mechanism associated with transport barrier formation and evolution in the context of the transport flux landscape [2.218] which describes transport flux in the radial position-density gradient (or temperature gradient, or pressure gradient) space. Usually, the density gradient is considered for simplicity. At each radius within the barrier zone, the flux  $\Gamma$  is typically an inverted  $S$ -shaped non-monotonic single valued function [2.219] of a local gradient of density. We focus our discussion on this case, which is called a (soft) “first order transition”. Discussions of the “hard” transition when the flux is a multivalued function of a local gradient or of a “second order transition” when the flux is a monotonic function with a change of slope, can be found in Refs [2.180, 2.220]. Most theoretical studies based on the  $\vec{E} \times \vec{B}$  shear and the reversed magnetic shear mechanisms use a transport coefficient  $D$  in the form:

$$D = D_{turb} f\left(\frac{\omega_E}{\gamma_{lin}}\right) + D_{neo} \quad (2.100)$$

where  $f(\omega_E / \gamma_{lin}) = 1 / (1 + c_1(\omega_E / \gamma_{lin})^{c_2})$ , with  $\gamma_{lin}$  the characteristic linear growth rate of instability and  $c_1, c_2$  constants of the order of unity, for instance

Refs [2.219, 2.221], characterize the  $\vec{E} \times \vec{B}$  shear induced reduction of the anomalous diffusivity  $D_A$ . While various authors have tried different functional forms of the monotonic  $f(x)$  with  $f(0) = 1$  and  $f(x) = 0$  for  $x \gg 1$ , we confine our discussions to the generic features of this class of models [2.222]. We also note that the favourable role of reversed magnetic shear can be contained in the radial variations of  $D_A$  and  $\gamma_{lin}$ . Since  $\omega_{E0}$  is related to the density gradient through radial force balance, Eq. (2.100) will produce a non-monotonic single valued  $S$ -shaped curve for the particle flux  $\Gamma = -D(\partial n / \partial r)$  as a function of local density gradient  $-(\partial n / \partial r)$  (Fig. 2.15), and a different  $S$ -shaped curve will apply at each minor radius. Correspondingly, for a given density gradient, the flux landscape depicts the familiar  $\Gamma$  curve which increases with minor radius. Until recently, it had been thought [2.219] that for each  $S$ -shaped curve, the local maximum and the local minimum (at a higher density gradient) define the threshold particle flux for the forward (RS to ERS, or L to H) transition and the backward (ERS to RS, or H to L) transition respectively. Therefore, the situation exhibits hysteresis. However, there is a new theoretical development which indicates that the aforementioned simple picture overpredicts the hysteresis [2.223]. Indeed, some tokamaks report a lack of strong hysteresis in L–H and H–L transitions, unlike DIII-D. It is encouraging to note that data from C-Mod Hmode plasmas [2.224] can be characterized by the aforementioned  $S$ -curve based theoretical picture. Finally, identification of practical ways to generate sheared flows [2.225, 2.226] in reactor relevant future devices will be, of course, highly desirable.

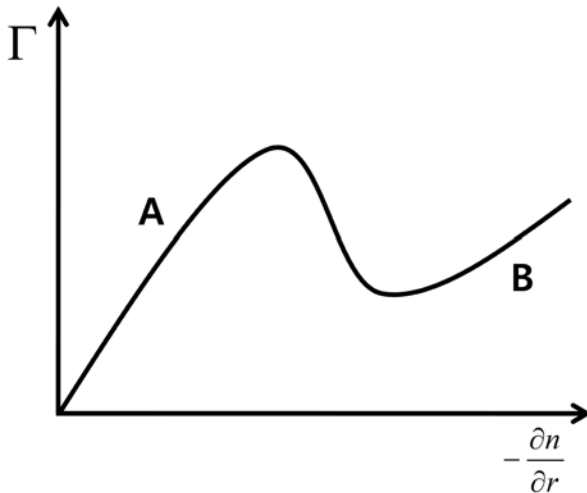


FIG. 2.15. Particle flux as a function of density gradient. “A” corresponds to the L-mode root with a high slope given by  $D_{turb} (\gg D_{neo})$ , while “B” corresponds to the H-mode root with a low slope given by  $D_{neo}$ , with  $D_{turb}$  significantly reduced by the  $\vec{E} \times \vec{B}$  shear associated with a strong density gradient.

## Acknowledgments

T.S. Hahm gratefully acknowledges E.S. Yoon for help in preparing the manuscript. This work was supported by the US Department of Energy Contract No. DE-AC02-09CH11466 (PPPL).

## 2.4. GLOBAL ENERGY CONFINEMENT SCALING STUDIES

### 2.4.1. Introduction

Global confinement scaling studies serve to provide a high level perspective on the behaviour of the plasma energy confinement as discharge parameters are independently varied. Scalings have been developed that describe quantitatively how the energy confinement time  $\tau_E$  and L-mode to H-mode threshold power varies as other parameters vary across a wide range of plasma conditions and energy states (L-mode, H-mode, etc.), and thus they can provide insights into and tests on the validity of theories believed to drive local energy transport. The parameters to which most attention is paid are the so-called engineering parameters such as plasma current, toroidal magnetic field, density, heating power, that can be controlled externally. Other, more physics based parameters, such as the plasma beta  $\beta$ , collisionality  $\nu_*$  and normalized gyroradius  $\rho_*$ , depend on the plasma response to external control, and are not as easily imposed.

One of the usual misnomers is to refer to global scalings as “laws”. They cannot, in any sense, be viewed as on a par with the fundamental laws of physics. They are derived descriptions of the behaviour of data, and as such, and as will be seen, each scaling expression has considerable uncertainty associated with its quantitative formulation. Their usefulness is to serve as guides for theory; ultimately any validated transport theory, or combination of theories that profess to explain transport in tokamaks, must end up giving rise to the global trends observed in experiment.

There are simple approaches to deriving the global scaling expressions (GSEs), such as ordinary least squares regression, to more sophisticated approaches such as error-in-variables or maximum-likelihood and Bayesian. As will be seen, the different approaches lead to expressions that have quantitative differences. Because the GSEs are descriptive and are not based on fundamental physics, there is danger in using these expressions for extrapolations, especially if the extrapolations extend well beyond the range of independent parameters being studied, without understanding the systematic and random uncertainties inherent in the expressions and their predictions.

At the heart of any global or local study is the determination of the confinement and transport properties of the plasma, and to do this, good measurements of the plasma characteristics are necessary. At the most basic

level, equilibrium reconstructions based on magnetics measurements can, in certain circumstances [2.227], give reasonable estimates of the total stored energy of the thermal plasma and any fast ion energy component created by auxiliary heating methods such as neutral beams, radiofrequency waves, etc. More detailed determinations and separation of these components can be obtained through measurements of the thermal ion and electron energy content directly. This can be done by measuring the electron and ion temperature and density. The electron temperature and density can be measured directly. The main plasma species ion temperature and density is presently covered through measurements of these profiles for the main plasma impurity (e.g. carbon) and then corrections due to collisions between the impurity and main ion species. The capability to measure the main ion species temperature and density directly is presently being developed. Since both low- $Z$  and high- $Z$  impurities typically are observed in plasmas, the thermal ion density is less than that of the electrons. Determination of the fast ion or electron component of the plasma is coupled to the use of modelling codes, and these will be described in Section 2.5.

Plasma profiles are generally peaked in the centre of the plasma, and decrease with increasing radial distance towards the plasma edge. In low-confinement, or L-mode, plasmas, the density and temperatures are usually near zero at the plasma separatrix. Highconfinement, or Hmode, plasmas are typified by temperature pedestals of up to several hundred eV and density pedestals of up to several  $10^{19} \text{ m}^{-3}$  within (inside) a few cm of the plasma separatrix. These pedestals lead to strong pressure gradients in the plasma edge, which can lead to intermittent destabilization of edge localized modes, instabilities driven near the plasma edge, resulting in a temporary decrease in the edge pressure gradient and thus confinement. Other, more core localized instabilities such as sawteeth and tearing modes, can cause degradation of confinement in that region.

In this section, we will describe the background leading to the development of GSEs, the approaches towards their development and the results of these efforts. Reviews and overviews of the results can be found in Refs [2.228–2.231].

## 2.4.2. Energy confinement scalings: Dimensional parameters

### 2.4.2.1. Ohmic and L-mode plasma confinement trends

Ohmic plasmas from a number of experiments [2.232] provided the first basis for developing energy confinement time scalings. At lower densities, the confinement time in ohmic plasmas was found to depend on plasma density, size and  $q$ , leading to the Alcator (or INTOR) scaling  $\tau_E \sim n_e a^2 q^{1/2}$  where  $n_e$  is the line averaged plasma density,  $a$  the plasma minor radius and  $q$  the inverse cylindrical rotational transform. A modification to this scaling was made by Pfeiffer and Waltz [2.233], with  $\tau_E \sim n_e a R^2$ , and, with an additional  $q^{1/2}$

factor, was subsequently called “neo-Alcator” scaling. The confinement time in this linear (with density) ohmic confinement (LOC) regime depended neither on the plasma current nor the toroidal field. At higher densities, however, the confinement time showed no further increase with density (saturated ohmic confinement, or SOC regime), but did show a dependence on plasma current.

It was quickly realized, however, that in order for significant fusion power to be produced, temperatures in excess of those produced by ohmic heating alone were necessary. Consequently, the mid to late 1970s and early 1980s saw an increasing number of experiments incorporating neutral beam injection to heat the plasmas. The earliest neutral injection results came from small tokamaks, such as CLEO [2.234], ATC [2.235], ORMAK [2.236] and TFR [2.237], but while the neutral beam powers were effective in increasing the ion temperature to values  $\sim 1.8$  keV, well in excess of the ohmic value, this auxiliary power level was still small compared to the ohmic heating power, and thus showed only limited heating of the electrons. A more than doubling of the central electron temperature was measured, however, when the auxiliary heating power level was increased to twice the ohmic level [2.235]. With 2.4 MW of neutral beam power injected into the PLT tokamak [2.238], ion and electron temperatures increased up to 7 and 4 keV respectively.

The neutral beam heated discharges from a number of tokamaks exhibited energy confinement trends that were quite different from those observed in ohmic plasmas in the IOC regime. Approximately 16 tokamaks, with minor radii,  $a$ , ranging from 0.13 to 0.44 m, major radii  $R = 0.70$  to 1.47 m, plasma current  $I_p = 0.08$  to 1 MA, toroidal magnetic field  $B_\phi = 1.2$  to 3.5 T, line averaged density  $n_e = 2.5$  to  $13 \times 10^{19} \text{ m}^{-3}$  and neutral beam injection powers  $P_{inj} = 0.05$  to 8 MW comprised the basis for establishing the fundamental trends that, to this day, describe confinement in low confinement, or L-mode discharges. These experiments were carried out primarily in tokamaks whose plasmas were limited by either poloidal rail or toroidal bumper limiters, or through the use of magnetic divertors that allowed unimpeded transport of neutral particles from the divertor region to the plasma main chamber. A summary of these experiments and their results is detailed in Ref. [2.228].

One of the key observations, which was observed in all devices, was that for injected powers greater than approximately twice the ohmic power, the energy confinement time decreased at the onset of neutral beam injection (NBI) by a factor of 1.4 to 4 from that observed during the ohmic phase (see Ref. [2.228] and references therein). A typical L-mode discharge evolution from PDX is shown in Fig. 2.16; note the drop in confinement time when the neutral beams are injected at 0.4 s. Increasing neutral beam power resulted in decreasing confinement time, although the degradation of  $\tau_E$  was less than linear, with  $\tau_E$  going as  $P_{heat}^{-1/3}$  to  $-2/3$ , where  $P_{heat}$  is the total heating power. Furthermore, the energy confinement time, unlike in ohmic discharges, did not increase with increasing  $q$ ,

but rather showed a nearly linear increase with plasma current,  $I_p$ , similar to that observed in the SOC regime. The global confinement time in L-mode discharges showed little if any dependence on  $B_\phi$  or  $n_e$ , but experiments on D-III [2.239] did indicate an increase in  $\tau_E$  with increasing plasma elongation,  $\kappa$ . Increased plasma shaping allowed more current to be carried by the plasma, but when the current was fixed, it was found that shaping still played an important role, with  $\tau_E \sim \kappa^{1/2}$ . NBI experiments in ASDEX [2.240], DIII-D [2.241] and JFT-2M [2.242] indicated that plasma isotope, or mass, was an important consideration, with  $\tau_E \sim (m_i / m_p)^{1/2}$ , where  $m_i$  is the ionic mass and  $m_p$  is the proton mass. The ASDEX results were obtained from experiments comparing performance in H<sup>0</sup> NBI injection into H<sup>+</sup> and H<sup>0</sup> injection into D<sup>+</sup> plasmas (see Ref. [2.228] and references therein). The direction of injection, either co- or counter- to the plasma current, was also found to influence confinement. Beam orbit losses with counter-injection on PDX and ISX-B led to a loss of approximately 40% of the input power, as compared to only ~10% with co-injection. Despite this, little difference in stored energy was observed between co- and counter- on the respective devices, leading to an increase in energy confinement time of between 30 and 50%.

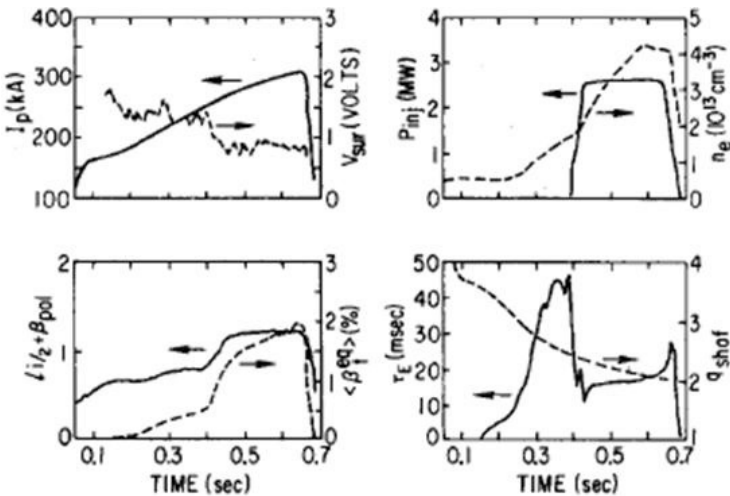


FIG. 2.16. Output from a 0-D, between discharge analysis programme for a typical PDX L-mode discharge. The energy confinement time (lower right) is calculated from measured magnetics information, an assumed current profile shape, and the total (NBI + ohmic) heating power. Reprinted from Ref. [2.228], Copyright (2010), American Institute of Physics.

What was lacking from the results of these individual experiments was just how the confinement time scaled from device to device, i.e. with plasma and machine size. Because the majority of these L-mode experiments exhibited

similar parametric trends, it was possible to pull together these data and, from the differences in average confinement time from device to device, determine how the confinement time varied with plasma minor and major radius if all other parameters are fixed. This approach was adopted by Goldston [2.243], who started the analysis by noting that the density and current scaling of high density ohmic plasmas was similar to that in NBI L-mode plasmas, thus enabling a coupling between the two regimes (ohmic and auxiliary heated L-mode plasmas). He proposed an energy confinement scaling of the form:

$$\tau_E = \left[ \frac{1}{\tau_{E,OH}^2} + \frac{1}{\tau_{E,AUX}^2} \right]^{1/2} \quad (2.101)$$

where the ohmic scaling,  $\tau_{E,OH}$ , was obtained from surveys of low density ohmic scaling experiments, and the non-size portion for the auxiliary heating scaling portion  $\tau_{E,AUX}$  was obtained from averaging the parametric dependences of confinement on  $I_p$ ,  $\kappa$  and  $P_{heat}$  ( $= P_{heat,NBI} + P_{OH}$ ), where  $P_{heat,NBI}$  is the absorbed beam heating power and  $P_{OH}$  is the ohmic heating power, from ISX-B, ASDEX, D-III and PDX L-mode discharges. The size scaling portion of  $\tau_{E,AUX}$  was obtained from a regression of the device-to-device confinement variation about some reference  $I_p$ ,  $\kappa$  and  $P_{heat}$ . The expressions that resulted from this technique are:

$$\tau_{E,OH} [s] = 7.1 \times 10^{-22} n_e^{1.00} [\text{cm}^{-3}] a^{1.04} [\text{cm}] R^{2.04} [\text{cm}] q^{0.50} \quad (2.102)$$

and

$$\tau_{E,AUX} [s] = 6.4 \times 10^{-8} \kappa^{0.50} I_p^{1.00} [\text{A}] P_{heat}^{-0.50} [\text{W}] a^{-0.37} [\text{cm}] R^{1.75} [\text{cm}] \quad (2.103)$$

Although this scaling expression was developed on the basis of data from small to medium-sized devices, it did a remarkably good job “predicting” the L-mode confinement trends and actual energy confinement times in the generation of large machines (TFTR and JET) that would soon, at that time, be operational [2.244, 2.245].

To extend this study, Kaye [2.246] embarked on assembling a much broader spectrum of data from a larger number of devices in order to better parameterize, in a statistical manner, the scaling of L-mode confinement. Neutral beam heated data were used to assemble the first global confinement database, which consisted of 677 representative L-mode discharges from ISX-B, DITE, TFR, D-III, PDX, PLT and ASDEX. The dataset consisted of mixed  $D^+$  and  $H^+$  plasmas, so no isotope scaling could be derived. The analysis that was performed assumed that the energy confinement time depended on the independent engineering variables in a power law fashion, and using a two-step weighted regression procedure, first to develop the non-size variable scaling and then the size variable scaling, found that the energy confinement time scaled as:

$$\tau_E [\text{s}] = 2.77 \cdot 10^{-8} \kappa^{0.28} I_p^{1.24} [\text{kA}] B_\phi^{-0.09} [\text{T}] n_e^{0.26} [10^{13} \text{cm}^{-3}] \cdot P_{heat}^{-0.58} [\text{MW}] a^{-0.49} [\text{cm}] R^{1.65} [\text{cm}] \quad (2.104)$$

The fit of the scaling to the full dataset was good, with a coefficient of determination  $R^2 = 0.94$ .

Yushmanov et al. [2.247] used an expanded database, which included data from the devices used in Kaye-Goldston as well as from JT-60, TFTR, JET, JFT-2M, DIII-D and T-10 to produce an updated scaling known as *ITER89P*, which included a dependence on isotopic mass,  $M (= m_i / m_p)$ , given by

$$\tau_E [\text{s}] = 0.048 M^{0.5} \kappa^{0.5} I_p^{0.85} [\text{MA}] B_\phi^{0.2} [\text{T}] n_e^{0.1} [10^{20} \text{m}^{-3}] \cdot P_{heat}^{-0.5} [\text{MW}] a^{0.3} [\text{m}] R^{1.2} [\text{m}] \quad (2.105)$$

Finally, Kaye [2.248] updated the L-mode database, for the final time to date, by including additional data from the devices already in the database as well as data from Alcator C-MOD, TEXTOR and TORE-SUPRA. This database consisted of 1881 L-mode time slices that included radiofrequency as well as NBI heated discharges. A number of variations of the power law scaling expressions can be found in Ref. [2.229].

Global scalings for L-mode plasmas were also cast in the form of an offset-linear expression, which attempted to separate the confinement behaviour in the core from that farther out, near the edge. The offset-linear expression by Rebut–Lallia [2.249] did not fit the data as well as the power law scalings. The Rebut–Lallia expression, however, was meant to describe electron confinement only, with the total plasma energy assumed to be twice that of the electrons. As such, the model does well in describing the confinement scaling in many electron dominated plasmas.

#### 2.4.2.2. H-mode confinement trends and scalings

The L-mode represents only just one confinement state in plasmas, and, in the absence of severe MHD activity, appears to give the minimum energy for a set of given engineering parameters. Other confinement states exist, ones in which transport barriers (i.e. regions of reduced transport resulting in large pressure gradients) occur both within or near the plasma core (ITBs or internal transport barriers) or near the plasma edge (ETBs or edge transport barriers). The H-mode is an example of an ETB plasma. The H-mode was initially seen in experiments with closed divertor operation (impeded neutral transport from the divertor to the main chamber regions), and it was first reported on ASDEX [2.188], shortly followed by reports from PDX [2.250] and later on from D-III

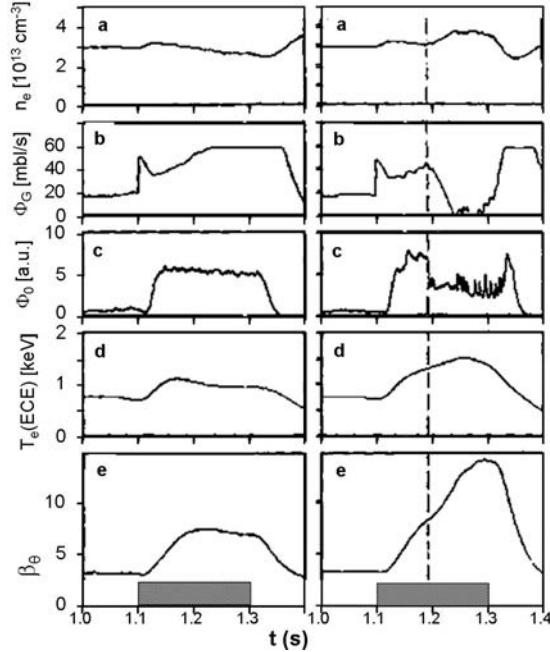


FIG. 2.17. Time dependence of various plasma parameters of the L-mode (left column) and H-mode (right column): (a) line-averaged density, (b) external gas flux in millibar-litre per second, (c) atom flux reflected from divertor plate, (d) central electron temperature, (e) beta poloidal  $\beta_\theta$ . Reprinted from [2.188], Copyright (2010), the American Physical Society<sup>1</sup>.

[2.251]. The H-mode was due to a spontaneous transition of the plasma from the L-mode confinement state to a new state in which the energy confinement could be a factor of approximately 2 higher for similar engineering parameters. The transition to the H-mode was seen as a sudden drop in the  $D_\alpha$  emissivity, an indicator of recycling at the plasma edge, an increase in the time rate of increase of the plasma density, indicating possibly a higher particle confinement, and the development of pedestals in the edge electron temperature and density profiles, reflecting the development of an edge transport barrier. A comparison of the time evolution of an L-mode (left column) and H-mode (right column) early ASDEX discharge (from Ref. [2.188]) is shown in Fig. 2.17. While the earliest H-modes were seen only in NBI heated discharges, this confinement regime was later on seen in plasmas with RF heating, in those with open divertors or even in limiter

<sup>1</sup> For material reproduced with permission from the American Physical Society, readers may view, browse, and/or download material for temporary copying purposes only, provided these uses are for non-commercial personal purposes. Except as provided by law, this material may not be further reproduced, distributed, transmitted, modified, adapted, performed, displayed, published or sold, in whole or part, without prior written permission from the American Physical Society.

configurations, and on stellarators [2.252]. The H-mode has proved itself to be a robust feature throughout the range of magnetic confinement configurations. Because of the large gradients near the plasma edge, a class of instabilities, called edge localized modes or ELMs was found to be a distinctive and unique feature of the H-mode. The ELMs, seen in the right panel (c) in Fig. 2.17, are driven unstable by the edge pressure and/or current gradients [2.253, 2.254], periodically lower the edge confinement in the H-mode. The size and frequency of these ELMs vary, but can cause significant instantaneous deposition of power on the divertor plates.

The H-mode confinement time showed trends qualitatively similar to those in L-mode plasmas. The trends are a degradation of confinement with heating power, and an increase of confinement nearly linearly with  $I_p$  and approximately as  $\kappa^{1/2}$ . As in the L-mode, virtually no dependence on toroidal field or plasma density was seen for the *total*, including beam particles, confinement.

In order to determine the confinement trends more quantitatively and comprehensively, an effort was undertaken starting in 1988–1989 to assemble an H-mode confinement database similar to that for the L-mode database. Representatives from ASDEX, D-III, JET, JFT-2M, PBX-M and PDX met regularly for approximately two years to define the elements of the database and to ensure that the data submitted by each experiment were defined similarly by all. This database went farther than the L-mode database in that the *thermal* plasma confinement time was defined and input as well as the *total* confinement time (plasma plus fast ion content). A total of 3466 observations were assembled in the first H-mode confinement database [2.255]. The group went a step farther, and that was to define a set of selection criteria that could focus analysis on a subset of discharges. The selection criteria eliminated those discharges from the analysis that had high radiated power or fast ion fractions, that were too transient, and that had too much MHD activity either through beta being too high or  $q$  being too low. After applying these criteria, a total of 1239 observations formed the subset to be analysed. The first multiple linear regression result for this “standard” H-mode data set yielded a scaling, for total energy confinement time, given by

$$\tau_E [\text{s}] = 0.025 M^{0.5} \kappa^{0.68} I_p^{0.75} [\text{MA}] B_\phi^{0.60} [\text{T}] n_e^{0.16} [10^{19} \text{m}^{-3}] \cdot P_L^{-0.55} [\text{MW}] a^{-0.05} [\text{m}] R^{2.04} [\text{m}] \quad (2.106)$$

with a root mean square error (RMSE) of 13.8%. The RMSE is a metric of the deviation of the fit to the experimental points, and it will be defined later in this chapter. In the above expression,  $P_L$  is defined as the total heating power less the time rate of change of the stored energy ( $P_{heat} - dW/dt$ ). It was important to determine whether this, or any other scaling, was representative of each device, or whether it represented an average of all. This could be done by computing the uncertainties in each scaling parameter coefficient, and it was found that the

above expression did indeed represent the trends across all machines, except for the  $B_\phi$  scaling, which is artificially strong in the above expression due to interdependences among some of the scaling parameters. How to handle these interdependences is discussed in the next section. Various other scalings were derived from this dataset, further constrained on whether the discharges were ELM-ing or ELM-free.

Updates to the H-mode confinement database, selection criteria for standard subsets, and, thus, confinement scaling have continually taken place since the first results were reported. These were reported in Refs [2.230, 2.256, 2.257]. The updates to the database involved adding data from existing machines as well as data from additional devices (ultimately with data included from Alcator C-MOD, ASDEX-Upgrade, COMPASS-D, DIII-D, JT-60U, MAST, NSTX, START, T-10, TCV, TdeV, TEXTOR, TFTR and TUMAN-3M in addition to the data from the original six devices). Various additional constraints were applied on the full dataset to develop a number of “standard” subsets; the additional constraints (not all applied simultaneously) included (but were not limited to) those on ion to electron temperature ratio, an upper limit to the internal inductance, isotopic mass, ELM activity and type, density evolution and ITER-specific criteria narrowing the range of  $\kappa$ ,  $q_{cyl}$  and isotopic mass, where  $q_{cyl}$  is the cylindrical equivalent  $q$ . The full, and present, H-mode database consists of a total of 10 382 data entries from twenty devices. Only 3093 of these discharges qualify for the most basic standard dataset.

The most widely used power law scaling, called *ITER98y,2* [2.230] is based on the parametric trends of the *thermal* confinement time, and given by the expression

$$\tau_E[s] = 0.0562M^{0.19}\kappa_a^{0.78}I_p^{0.93}[\text{MA}]B_\phi^{0.15}[\text{T}]n_e^{0.41}[10^{19}\text{m}^{-3}] \cdot P_L^{-0.69}[\text{MW}]a^{0.58}[\text{m}]R^{1.39}[\text{m}] \quad (2.107)$$

In this expression, the elongation  $\kappa_a$  is defined as ( $Area / \pi a^2$ ) instead of the usual ratio of vertical/horizontal extent.

The power law scaling expression determined from the most up-to-date standard dataset is given by

$$\tau_E[s] = 0.0593M^{0.08}\kappa_a^{0.84}I_p^{0.86}[\text{MA}]B_\phi^{0.21}[\text{T}]n_e^{0.39}[10^{19}\text{m}^{-3}] \cdot P_L^{-0.65}[\text{MW}]a^{0.68}[\text{m}]R^{1.31}[\text{m}] \quad (2.108)$$

and the resulting fit to the data used to determine the scaling, taken from Ref. [2.257], is shown in Fig. 2.18.

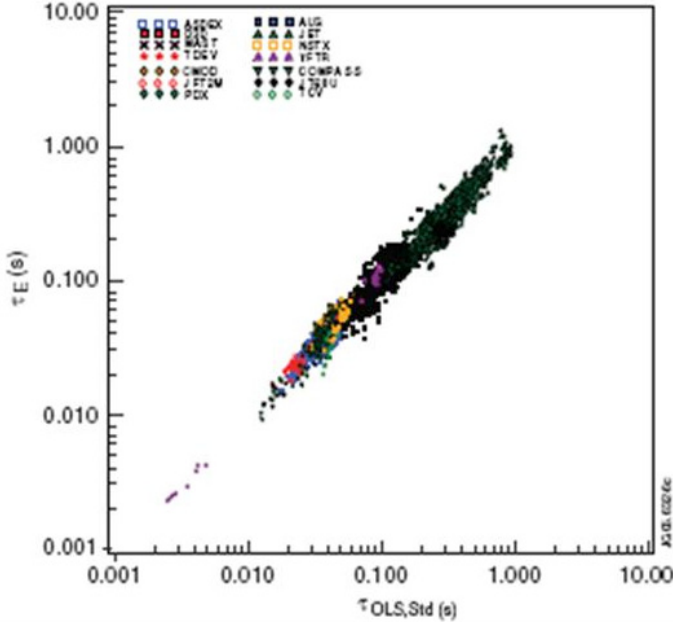


FIG. 2.18. Comparison of the experimentally observed energy confinement time with a scaling expression derived from an ordinary least squares fit to the standard dataset. Taken from Fig. 6 in Ref. [2.257].

In Ref. [2.258], Kaye et al. specifically took into account the confinement trends introduced by the low aspect ratio tokamaks, NSTX and MAST. These tokamaks, whose aspect ratio  $R/a \sim 1.3$ , as compared to conventional aspect ratio tokamaks, where Ref.  $R/a \sim 2.5-3$ , exhibit confinement trends that are different. Specifically, as reported in Refs [2.142, 2.259, 2.260], the confinement time varies almost linearly with toroidal magnetic field and only as the square root of the plasma current. These trends were confirmed in recent experiments on MAST, another low aspect ratio tokamak [2.261]. The magnitude of the power degradation of confinement depends on whether the plasma is ELM-ing or not. It can be near zero (no ELMs) or quite high (large ELMs at high power). Previous scaling expressions tended to overpredict the confinement time at low aspect ratio. Including these specific aspect ratio effects did change the scalings to some extent, increasing the dependence on  $B_\phi$ , reducing the dependence on  $I_p$ , and changing the aspect ratio dependence to compensate for the overprediction. A scaling resulting from this analysis, and obtained by ordinary least squares regression, is

$$\tau_E [\text{s}] = 6.25 \cdot 10^{-10} I_p^{0.80} [\text{MA}] B_\phi^{0.32} [\text{T}] n_e^{0.39} [\text{m}^{-3}] \cdot P_L^{-0.66} [\text{MW}] a^{0.95} [\text{m}] R^{1.17} [\text{m}] \quad (2.109)$$

for deuterium only discharges ( $M = 1.6$  to  $2.4$ ), and with  $\kappa$  in the range from 1.6 to 2.4.

Two term H-mode scalings, separating the core and the pedestal confinement, have also been developed [2.257, 2.262], where the core and pedestal stored energies are given by

$$W_{core}[\text{MJ}] = 0.103M^{0.23}\kappa_a^{0.24}I_p^{0.88}[\text{MA}]B_\phi^{0.11}[\text{T}]n_e^{0.49}[10^{19}\text{m}^{-3}] \cdot P_L^{0.25}[\text{MW}]a^{1.22}[\text{m}]R^{0.80}[\text{m}] \quad (2.110)$$

and

$$W_{ped}[\text{MJ}] = 6.43 \cdot 10^{-4}M^{0.20}\kappa_a^{1.81}I_p^{1.58}[\text{MA}]B_\phi^{0.06}[\text{T}]n_e^{-0.08}[10^{19}\text{m}^{-3}] \cdot P_L^{0.42}[\text{MW}]a^{-2.13}[\text{m}]R^{3.21}[\text{m}]F_q^{2.09} \quad (2.111)$$

where  $F_q = (q_{95} / q_{cyl})$  and  $\tau_E = (W_{core} + W_{ped}) / P_L$ . Here,  $q_{95}$  is the  $q$ -value at the 95% flux surface. The fit to the two-term model is not as tight as that to the better power law expressions, with about a 60% increase in the RMSE.

#### 2.4.2.3. Advanced statistical methods and error analysis

The GSEs discussed to this point were all determined using ordinary least squares multiple linear regression (OLSR). This technique [2.263] is a direct method of calculating fit coefficients from a linear equation. The assumption that the confinement time can be cast in the form of a power law,  $\tau_E = c \prod_{j=1}^{NVAR} (X_j^{\alpha_j})$ , where the  $X_j$  are the independent variables and  $NVAR$  is the number of independent variables, lends itself to linearization by taking the logs of the independent (predictor) and dependent (response) variables, so that

$$\log \tau_E = \alpha_0 + \sum_{j=1}^{NVAR} \alpha_j \log X_j \quad (2.112)$$

where  $\alpha_0, \alpha_1$  are the scaling coefficients.

For a set of  $N$  observations and  $NVAR$  independent variables, the least squares solution can be set up as a minimization problem, where

$$S = \sum_{i=1}^N \left( \log \tau_E - \alpha_0 - \sum_{j=1}^{NVAR} \alpha_j \log X_j \right)^2 \quad (2.113)$$

and the  $\alpha_j$  scaling coefficients are determined by solving the matrix given by  $\partial S / \partial \alpha_j = 0$ . In the applications described in the previous sections a weighted OLSR technique was used in which the observations from each device were

weighted by a value  $w_j$  inversely proportional to the number of observations from that device, using either  $w_j = 1 / N_j^{1/2}$  or  $w_j = 1 / (2 + N_j^{1/2} / 4)$ .

The precision of the fit given by OLSR can be defined by a number of metrics, one of which is the root mean square error, defined as

$$\text{RMSE} = \left[ \sum_{i=1}^N \frac{(y_{\text{exp}} - y_{\text{fit}})^2}{N - 2} \right]^{1/2} \quad (2.114)$$

where  $y_{\text{exp}}$  is the log of the experimental value,  $y_{\text{fit}}$  is the log of the corresponding value from the scaling and  $N$  is the number of observations. Another metric is the coefficient of determination, defined as  $R^2 = \sum_i (y_{i,\text{fit}} - y_{\text{avg}})^2 / \sum_i (y_{i,\text{exp}} - y_{\text{avg}})^2$ , where  $y_{\text{avg}}$  is the average value of the dependent variable. In addition, variances, or uncertainties, in each scaling coefficient can be readily calculated [2.263].

The simple OLSR technique by its nature does not consider errors in either the independent or dependent variables. There are several methods that have been used [2.230, 2.248, 2.255, 2.257, 2.258, 2.264–2.266] that can take into account the measurement errors, which can be significant. The first such method is to perform a regression not on the variables themselves, but the principal components (PCs) of the variables. The PCs are a set of orthogonal eigenvectors whose variance is related to the eigenvalue. A PC with a small eigenvalue is one in which the variation of data in that direction is small. The regression is performed only on the “most important” PCs, which are taken to be those whose variance,  $\lambda_{pc}$ , is significantly greater than the measurement errors,  $\lambda_e$ , in the variables that make up that PC. Typically, the measurement error has been considered to be negligible relative to the variance in the PC if  $\lambda_{pc} > 4\lambda_e$ .

An offshoot of this technique is the principal component error-in-variable (PCEIV) technique, also called EIV or EVOR (error-in-variables orthogonal regression). In this approach the PCs of the logs of the predictor and response variables, normalized by their individual errors, are computed. A PC with a zero eigenvalue gives an exact linear relation among the variables (i.e.  $w_j = \sum_i \alpha_{ij} z_i = 0$ , where the summation is over the number of predictor variables  $z_i$ ). In practice, the minimum eigenvalue is not zero, but it is small and it is related to the scatter of the data about the PC. For this PC, the eigenvalue is assumed to be zero, and the normalized variables are expressed in their non-normalized form to give an expression for the  $\tau_E$ . Differences between the OLSR and PCEIV solutions can be readily seen in Refs [2.257, 2.258].

The PCEIV method is particularly powerful for being able to quantify the uncertainties in the scaling coefficients. This can be done by varying the experimental uncertainties of the dependent and independent variables. Figure 2.19 is taken from Ref. [2.265], and it shows the scaling coefficients for

power  $P$  and density  $n$  as a function of the relative uncertainty in  $P$  for three different uncertainties in thermal plasma stored energy  $W_{th}$ . For the dataset used in this analysis, the average relative uncertainties in these variables are  $\delta W_{th} = 12\%$ ,  $\delta P = 12\%$  and  $\delta n = 5.9\%$ . These variables have the largest uncertainties of all the variables used in the analysis. As can be seen in Fig. 2.19, large variations in both exponents can result as the uncertainties are varied, leading to large uncertainties in extrapolations of the resulting scaling expressions.

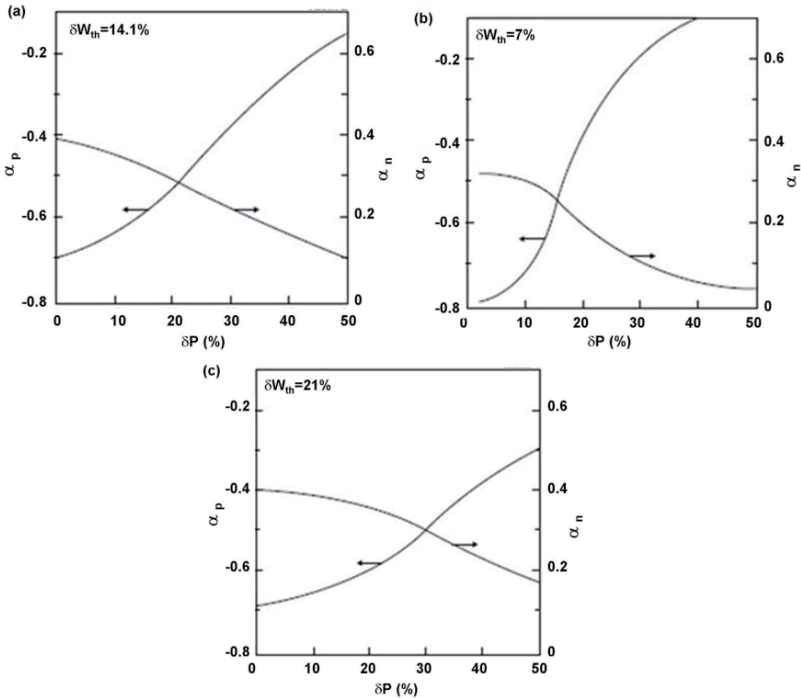


FIG. 2.19. Scaling coefficients with power  $\alpha_P$  and density  $\alpha_n$  versus the error in power in per cent for three different errors in  $W_{th}$  [2.231].

Other statistical methods that have been used include two closely related ones, maximum-likelihood and a Bayesian approach. These methods have differing philosophies regarding the approach to probabilistic determinations, but both use expressions describing the probability density for the measured data that incorporates both the data and the errors. In applications of both methods for the confinement studies, the value of the independent variables is assumed to come from a normal distribution with a known standard deviation. In maximum-likelihood, the best fit to the probability distributions gives rise to the parametric scaling (see Ref. [2.266] and references therein).

The Bayesian approach, while similar, assumes also a distribution for the dependent variable that is based on prior knowledge of its value. In the application in Ref. [2.258], the value of the dependent variable was also modelled as coming from a normal distribution, but one with a prior known value but unknown error (large variance). In this application, the Bayesian approach actually gave rise to the scaling with the lowest RMSE (best fit), although the data in this, and the maximum-likelihood, analysis in Refs [2.257, 2.258] were not weighted, and thus the result was biased towards the devices with the largest number of datapoints.

### 2.4.3. Dimensionless analysis

#### 2.4.3.1. Basics

The use of engineering variables to describe energy confinement trends is convenient in that it allows experimenters to “control” confinement by defining the set of operational parameters for which the experiment is to be run. Engineering parameters, however, do not reflect the basic plasma physics processes that truly control confinement. To take into account constraints imposed by plasma theory, a different set of parameters that describe confinement must be chosen. These parameters are dimensionless and represent fundamental internal plasma characteristics. The set of these include  $\beta \propto nT / B^2$ ,  $\rho_* \propto T^{0.5} / aB$  and  $v_* \propto anq\varepsilon^{-2.5} / T^2$ , and these, coupled with other dimensionless variables ( $\varepsilon = a / R$ ,  $\kappa$ ,  $q$  ...) form a set that can describe plasma confinement:

$$B\tau_E = F(\beta, \rho_*, v_*, \varepsilon, M, \kappa, q, \dots) \approx \beta^{\alpha_1} \rho_*^{\alpha_2} v_*^{\alpha_3} \dots \quad (2.115)$$

where  $\alpha_1, \alpha_2, \dots$  are the scaling coefficients.

Note that because these dimensionless (or physics) variables can be expressed in terms of the dimensional (engineering) ones (e.g.  $B\tau_E \sim T^{x_1} B^{x_2} n^{x_3} a^{x_4}$ , with  $T$  being related to  $P$ ,  $n$ ,  $\tau_E$  and geometry and  $x_1, x_2, x_3, \dots$  being the scaling coefficients), the scalings derived for one set can be expressed in terms of the other set by the above transformations using a simple matrix inversion technique. As will be seen, this is important for assessing which physics models most closely match the global scaling expressions.

In 1977, Connor and Taylor used the principle of scale invariance to constrain the number of permissible scaling expressions [2.267–2.269]. Starting with the Vlasov equation, the equation for charge neutrality in the electrostatic limit, and including Maxwell’s equations (Faraday’s and Ampere’s Laws) in the electromagnetic limit, scale invariance implies that there is a constraint imposed on the scaling coefficients,  $x_i$ , so that the scaling of  $B\tau_E$  is invariant under a linear transformation of the parameters that define the above equations. Applying physics constraints imposed by various theoretical plasma models (e.g. ideal and

resistive MHD, collisional and collisionless drift waves), Connor and Taylor [2.267] and Connor [2.268] developed generalized scaling expressions based on the functional forms with  $\beta$ ,  $\rho_*$  and  $\nu_*$  among the fundamental scaling parameters. The relations among the scaling coefficients of these parameters determined how well the confinement trends could be described by the various physics models.

Because of the importance of the physics variable scalings in reflecting underlying physics models controlling confinement, a large number of carefully planned experiments studied the confinement variation with these parameters. In these experiments, one dimensionless parameter was varied while the others were held as constant as possible across their entire profile. An excellent recent review of these experiments and their results is given in Ref. [2.269]. We will follow closely the format of Ref. [2.269] in describing the highlights of the dimensionless single parameter scaling experiments and we will focus on the results of the H-mode experiments.

All devices found that the normalized confinement time increased with increasing collisionality, with  $B\tau_E \sim \nu_*^{\alpha_\nu}$ , where the scaling coefficient for  $\nu$ ,  $\alpha_\nu$ , varied from 0.2 to  $\sim 0.8$ . The values of  $\alpha_\nu$ , however, were found to depend on  $\nu$  itself, with  $\alpha_\nu$  increasing with increasing  $\nu$  (Fig. 2.20), indicating that the  $\nu$  dependence was not a simple one. The overall scaling is consistent with physics models indicating increased damping of zonal flows that suppress turbulence, or decreased resistive ballooning modes, with decreasing collisionality.

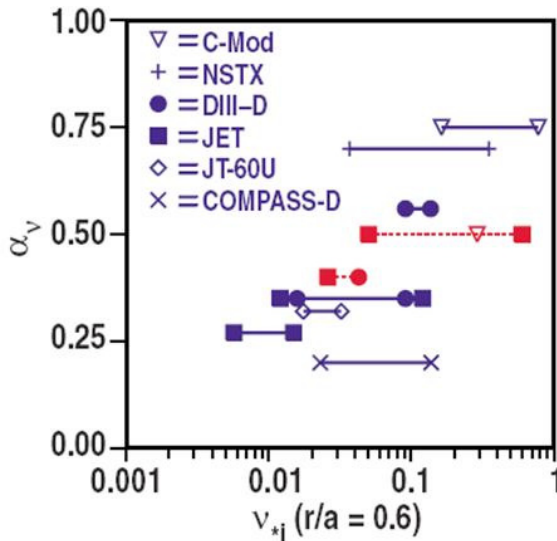


FIG. 2.20. Collisionality scaling exponent of thermal energy confinement for H-mode plasmas as a function of the ion collision frequency normalized to the bounce frequency. Taken from Fig. 2 in Ref. [2.269].

Single parameter scans with well controlled ELM activity in DIII-D [2.270], JET [2.271] and NSTX [2.142] showed that there was little scaling of normalized confinement with  $\beta$ . In particular, a large range of toroidal beta  $\beta_\phi$  was accessible in the low aspect ratio, low  $B_\phi$  NSTX device. Such results could imply that electromagnetic effects are not important. Results from ASDEX-U [2.272] and JT60-U [2.273], however, indicate a strong degradation of confinement on  $\beta$ . The difference between these two sets of results is that the strong degradation of confinement on  $\beta$  was observed in plasmas that were more weakly shaped ( $\kappa, \delta$ , where  $\delta$  is triangularity). Future experiments will attempt to identify if plasma shape is controlling, and why. Similar to Fig. 2.20, Fig. 2.21 shows the range of scaling coefficients,  $\alpha_\beta$ , for the  $B\tau_E \sim \beta^{\alpha_\beta}$  results.

The situation for the scaling of confinement with normalized gyroradius is not so clear. This scaling is particularly important in that it determines whether the diffusion step-size is of the order of the ion gyroradius ( $B\tau_E \sim \rho_*^{-3}$ ) or the device size ( $B\tau_E \sim \rho_*^{-2}$ ). The former is called ‘‘gyroBohm’’ scaling, while the latter is referred to as ‘‘Bohm’’ scaling. GyroBohm scaling gives a much more optimistic picture of confinement in future, lower  $\rho_*$  devices. While H-mode plasmas overall were found to scale in the gyroBohm regime, the transport was found to have a local dependence, with the core transport scaling as gyroBohm, but the transport in the outer region scaling as Bohm. Reference [2.269] goes on to examine scaling trends with other dimensionless parameters, and the reader is encouraged to read that article.

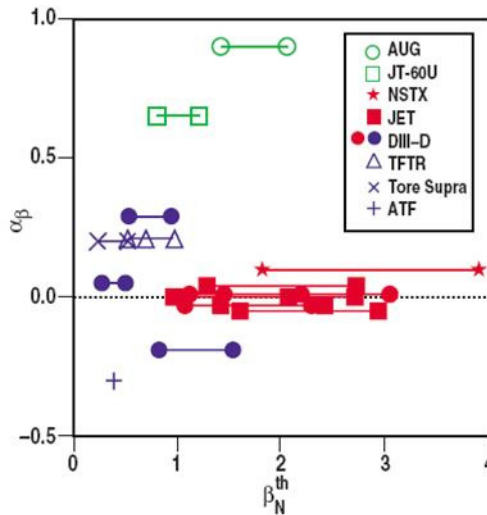


FIG. 2.21.  $\beta$ -scaling exponents of the thermal energy confinement time of L-mode plasmas (blue) and H-mode plasmas (red and green). Reprinted from Fig. 7 in Ref. [2.269]. Copyright (2010), American Institute of Physics.

2.4.3.2. *Scalings*

Full dimensional scaling expressions can be determined in two ways. One way is to use the dimensionless variables as predictor (independent) variables and perform direct statistical analysis as was done for the engineering variables. The second is to cast the engineering variable scalings in terms of the physics variables through the transformation between the two. Use of the first approach is complicated by the fact that the physics variables can have high correlations among themselves, due to the fact that they are, in part, defined by the same parameters (e.g.  $T$  appears in  $\beta$ ,  $v_*$  and  $\rho_*$ ,  $n$  appears in  $\beta$  and  $v_*$ ). Correlations were found even in a “reduced” set of physics variables, with common factors normalized out [2.258]. Also, correlations are found among some of the variables that are not even this direct. For instance, a strong correlation was found between  $\varepsilon$  and  $\beta$  or  $\rho_*$  since the low aspect ratio devices NSTX and MAST, with high  $\varepsilon = a/R$ , operate at low  $B_\phi$  and thus at high  $\beta$  and  $\rho_*$ . Consequently, due to the correlations among the variables and their errors, the fits based on these physics parameters tend to be poor (in terms of the fit metrics) and uncertain.

It has, then, been more common to develop scalings based on the engineering variables and then transform to physics variables. For instance, the *ITER98y,2* scaling transforms to, in physics variables,

$$B\tau_E \sim \rho_*^{-2.70} \beta^{-0.90} v_*^{-0.01} q^{-3.00} \kappa_a^{3.30} \varepsilon^{0.73} M^{0.96} \quad (2.116)$$

The expression from Ref. [2.258], discussed previously, which takes into account data from low aspect ratio devices but which was constrained to a narrow range of elongation  $\kappa$  and isotopic mass  $M$ , transforms to

$$B\tau_E \sim \rho_*^{-2.86} \beta^{-0.70} v_*^{-0.09} q^{-2.26} \varepsilon^{0.62} \quad (2.117)$$

Both expressions show a near gyroBohm scaling, but both show a strong degradation of the normalized confinement on  $\beta$ , in contradiction to the single parameter scans. Cordey et al. [2.265] showed that the uncertainties inherent in the engineering parameters, which translate into uncertainties in the dimensionless physics variables, as well as the relatively small range in these parameters that is accessible experimentally [2.274], can lead to a large uncertainty in the  $\beta$ -scaling coefficient, with  $\alpha_\beta$  ranging from 0 to  $-0.6$ . The later work by Kaye et al. [2.258] also showed a large range in the  $\beta$ -scaling coefficient ( $\alpha_\beta \sim 0$  to  $-0.8$ ), and further showed how this range related to the range of  $\varepsilon$ -scaling coefficients due to the correlation between these two variables. The latter result is shown in Fig. 2.22 [2.258]. These results indicate the issues with a statistical approach to determining the physics variable scaling in light of the magnitude of the uncertainties, their interdependences and the limited accessible experimental

range in these parameters. Future experiments must be carefully thought out to avoid these pitfalls.

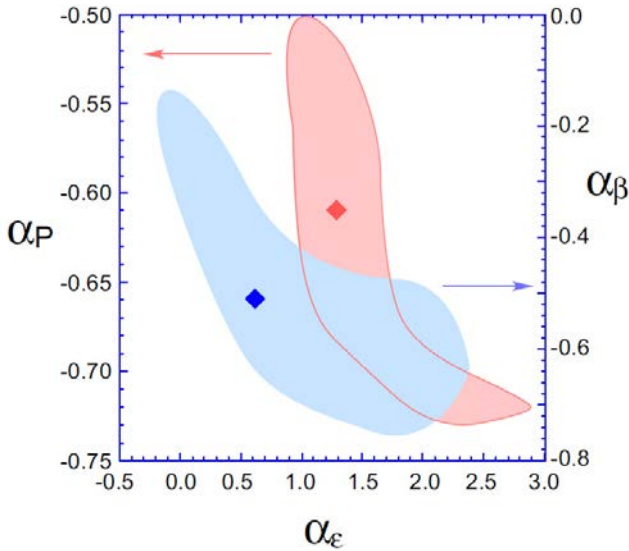


FIG. 2.22. Range of exponents for power (red) and  $\beta$  (blue) as a function of the exponent of  $\epsilon$  from error analysis based on the PCEIV method. Taken from Fig. 4 in Ref. [2.258].

#### 2.4.4. L-H threshold scalings

Operation in H-mode is critical to achieving high performance, and thus the performance goals, in present and future devices. The design and operating scenarios of these devices have to be developed based on confidence that such a regime can be obtained. In an approach similar to that for the global confinement scalings, controlled experiments have been conducted to study regimes in which the H-mode is accessible, and these device-specific studies have been coupled to a statistical approach in order to understand what variables are key to obtaining the H-mode. These studies have been mostly empirical ones, and an understanding of all the underlying physics that causes the L-H transition has been elusive.

The H-mode is achieved when a certain threshold power is surpassed. This threshold power, like the energy confinement, depends on plasma parameters in both gross as well as subtle ways. It is the case that the transition occurs at the plasma edge, setting up temperature and density pedestals (i.e. transport barriers) that can be confined to just inside the separatrix to extending farther into the plasma on timescales of less than 100  $\mu\text{s}$ . The L-H transition is most easily

obtained on devices using magnetic divertors, although transitions have been observed both in limiter plasmas [2.275] and on stellarators [2.252].

The most important dependences of the L-H threshold are summarized in Refs [2.230, 2.231, 2.276]. Early attempts to connect the L-H phenomenology to theory are discussed in Refs [2.277, 2.278]. Studies to understand the L-H transition in the framework of turbulence reduction due to a buildup of  $E \times B$  shear at the plasma edge, and the relation to zonal flow generation, can be found in Refs [2.277, 2.279]. While some attempts to connect experimental results to the theories have been successful [2.280, 2.281], others have not [2.282, 2.283], underscoring the present lack of complete understanding of the transition dynamics.

The key characteristics of the threshold dependences from early studies are as follows. The threshold power is lower for single null plasmas with the ion  $\nabla B$  drift towards the dominant X-point than for single null configurations where the drift is in the opposite direction or in a double null configuration that is not perfectly balanced. Good wall conditioning and a divertor configuration leading to good retention of neutrals in the divertor region, and a reduced neutral density in the main plasma chamber, also lead to lower power thresholds. The threshold power, based on single parameter scans across a range of devices, is found to depend in almost a linear fashion on plasma density (above some critical density) and toroidal field. Finally, the power threshold was found to be approximately a factor of two greater for hydrogen than for deuterium plasmas.

Based on these results, a global database was assembled with the aim of establishing empirical scalings of the L-H threshold. The database focused on parameters that included global variables ( $B_\phi$ ,  $I_p$ ,  $n_e$ , plasma size and shape, etc.) as well as other information found to influence the threshold power (plasma-wall gaps, ion  $\nabla B$  drift direction, divertor configuration and some limited edge plasma information). The edge information, however, is not complete owing to difficulties in measuring some of these parameters accurately. A full description of the L-H threshold database can be found in Ref. [2.276].

Analysis of this combined dataset at first attempted to determine the dependence of the threshold power,  $P_{LH}$ , on the variables such as  $B_\phi$  and  $n_e$ , which were the most important dependences found in individual device scans.  $P_{LH}$  was defined to be the total power through the separatrix without core radiation subtracted. This is a good assumption for present day devices, where core radiation is small, but the assumption can be violated in future burning plasma devices where core radiation from bremsstrahlung can be large. Statistical analysis found dependences consistent with those found in the individual scans. Dependence on device size could be found only through analysis of the combined database, with the initial results revealing a strong dependence on device size, with  $P_{LH} \sim n_e B_\phi R^{2.5}$  or  $n_e^{0.75} B_\phi S$ , where  $S$  is the surface area of the plasma. These scalings are consistent with  $P_{LH}$  being expressed in a dimensionally correct

form  $P \sim nTvS$ , with  $T$  is temperature and  $v$  is velocity, taken to be the thermal velocity  $\propto (T/M)^{1/2}$  ([2.284, 2.285] and references therein).

As more data were added to the database, the analyses evolved but still remained focused on the few global variables and reached similar conclusions. The  $P_{LH}$  scalings, however, had larger uncertainties in the scaling coefficients than did the  $\tau_E$  scalings, and the  $P_{LH}$  scalings led to wider ranges in values due to these uncertainties when extrapolated to future devices [2.286]. This was found also even when different statistical techniques were applied to analyse the threshold database [2.287]. Factors of almost two were found in predictions to ITER, depending on which scaling expression was used.

These results suggested strongly that sufficient information was not contained in the parametric descriptions, and that more advanced statistical techniques could not overcome the lack of information. The consideration of several other important factors was reported in Refs [2.286, 2.288]. In Ref. [2.286], the role of aspect ratio was considered by including a parameter  $R_{mm} = (R + a) / (R - a)$  in the analysis, and this inclusion led to a small, but statistically significant improvement in the fit (see Eq. 7 in Ref. [2.287]). The consideration of aspect ratio was necessary owing to data from MAST and NSTX, two low aspect ratio tokamaks, being included in the updated database. In Ref. [2.288], aspect ratio was taken into account in two fashions. The first was by using  $|B| = \{B_\phi^2 + B_\theta^2\}^{1/2}$  instead of just  $B_\phi$ . Here,  $B_\theta$  is the poloidal magnetic field. This recognizes that  $B_\phi \sim B_\theta$  in the outer midplane for low aspect ratio devices ( $|B| \sim B_\phi$  at higher aspect ratio). The second was based on an assumption that the details of the particle distribution, namely the trapped to untrapped fraction, play a role in the transition dynamics. Thus, a parameter  $F(A) = A/f(A)$ , where  $A = R/a$  and  $f(A)$  is the fraction of trapped particles  $\approx 1 - \{2 / (1 + A)\}^{1/2}$ , was included in the scaling. This work further considered the effect of  $Z_{eff}$  which was clearly seen in the JT60-U data, as well as on other devices where this information was available (although with greater scatter). The scaling emerging from this analysis was

$$P_{LH} \propto |B|^{0.7} \bar{n}_e^{0.7} S^{0.9} Z_{eff}^{0.7} F(A)^\gamma \quad (2.118)$$

where  $\gamma = 0.5 \pm 0.5$  (highly uncertain possibly due to non-linear dependences). This scaling resulted in a better fit than for scalings using only the standard global parameters. Not included in this scaling was an  $I_p$  dependence of  $P_{LH}$  that was observed on the low aspect ratio NSTX device [2.289], but not at higher aspect ratio.

Recent work has confirmed the roles, or has shown the importance, of other variables in determining the threshold power. The  $P_{LH}$  was found to be the same for pure D<sup>+</sup> and pure He<sup>++</sup> plasmas heated by ECRH in ASDEX-U (Fig. 2.23, taken from Ref. [2.290]), although most other experiments indicate that  $P_{LH}$  (He)

is about 20 to 40% higher than  $P_{LH}(D)$ . The threshold for  $H^+$  plasmas was found to be two times greater than that for  $D^+$  with NBI heating [2.291]. Further, it was shown also in Ref. [2.291] that the minimum threshold power for otherwise fixed conditions occurred at low rotation, where the neutral beam torque was actually less than zero (Fig. 2.24, taken from Ref. [2.291]). Other studies [2.286] have shown that there exists a minimum in threshold power that is controlled by plasma density. This “minimum threshold density” is a common feature in a large number of tokamaks, and it occurs in the  $2$  to  $4 \times 10^{19} \text{ m}^{-3}$  range with larger machines generally having smaller minimum threshold densities. This can be seen in the ASDEX-U data in Fig. 2.23. Figure 2.25 shows this parameter plotted as a function of toroidal field. For ASDEX-U, C-Mod and JFT-2M, the value is seen to increase strongly with  $B_\phi$  while for JET and JT-60U, the two larger devices, the dependence is weaker (left panel). When normalized to the Greenwald density value,  $I_p / \pi a^2$  [2.292], a slight decrease with  $B_\phi$  for all devices is seen (right panel).

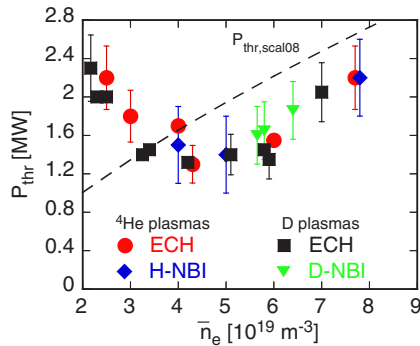


FIG. 2.23. Threshold power versus line-averaged density from ASDEX-U. Taken from Fig. 4 in Ref. [2.290].

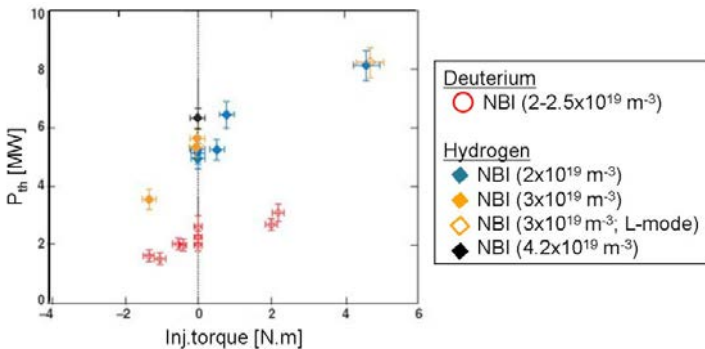


FIG. 2.24. Power threshold for  $D^+$  and  $H^+$  plasmas on DIII-D as a function of injected neutral beam (NB) torque. Adapted from Fig. 3 in Ref. [2.291].

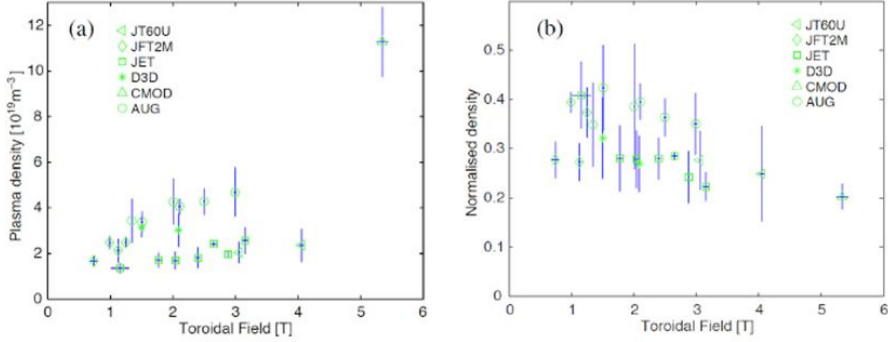


FIG. 2.25. (a) Minimum threshold density plotted as a function of  $B_\phi$ ; (b) density normalized to the Greenwald parameter versus  $B_\phi$  [2.286].

An important physics issue having to do with these threshold scaling studies is the confinement quality for heating powers very close to the threshold power. Related to this is whether there is a hysteresis effect; that is, will a discharge remain in H-mode as it evolves post-transition to a state where  $P_{\text{heat}} < P_{\text{LH}}$  (i.e. at fixed heating power but higher density)? Studies [2.286] have shown that the H-mode confinement enhancement is generally in the range of  $H_{98y,2} = 0.6$  to 1.4, and it does not depend on the power ratio  $P_{\text{heat}}/P_{\text{LH}}$ .

#### 2.4.5. Implications relative to theoretical models

Trying to relate the results of global scaling analyses to detailed physics theories can be quite difficult. For one thing, theoretical underpinnings are most often expressed in terms of local parameters that are not readily transferable to global variables. Further, validation of these theories often takes place at a lower level (e.g. local turbulence and transport properties), not at the global level. Comparisons to specific theories, then, are best made at the local level, and this will be covered in another subsection.

The global scalings can nevertheless be related to general classes of theories, and this has been discussed to some extent in the section on dimensionless scalings. For instance, when the scalings based on engineering parameters are converted to those based on physics variables, it was generally found that L-mode plasmas were more Bohm-like ( $\Delta \sim a$ ) rather than gyroBohm-like ( $\Delta \sim \rho_i$ ) [2.269]. This result is not that straightforward, however, in that while the ions appeared to be Bohm-like or worse, the electrons were in the gyroBohm regime. H-mode scalings typically appeared to be more in the gyroBohm regime, but even here there were subtleties, with the core being in the gyroBohm regime but the edge behaving more Bohm-like in some cases. There were, however, variations from device to device that depended on the level of heating power relative to

$P_{LH}$  and  $\vec{E} \times \vec{B}$  shearing rate ([2.269] and references therein). Other dependences that directly relate to theory include, among others, plasma isotope,  $T_e/T_i$  and ion charge state, and studies to establish and relate these observed dependences to theory are ongoing.

In terms of the dimensionally constrained physics models [2.268], the global L-mode scaling [2.248] is most consistent both with Models D (Quasi-neutral high- $\beta$  Fokker–Planck) and G (High- $\beta$  Vlasov), while the H-mode scaling as embodied in the *ITER98y,2* scaling is most consistent with Models C (Quasi-neutral high- $\beta$  Vlasov) and G (High- $\beta$  Vlasov).

Work to establish a theoretical understanding of the L-H threshold is continuing, and it is focusing on macro- and micro-instability properties of the plasma edge, as determined through profile and turbulence measurements and connection to theory.

## 2.5. LOCAL TRANSPORT

### 2.5.1. Basics

The basic equations governing the steady state transport of particles, momentum and heat for tokamak plasmas in transport codes such as TRANSP [2.293, 2.294] and ONETWO [2.295] are, in simple form for each species:

$$\text{Particles: } \frac{\partial n}{\partial t} = S_{in} - \frac{1}{r} \frac{\partial}{\partial r} [rnv_r] \quad (2.119)$$

$$\begin{aligned} \text{Momentum: } \frac{\partial}{\partial t} [mRnv_\phi] &= T_{in} - \frac{1}{r} \frac{\partial}{\partial r} [mrRnv_r v_\phi] + \\ &\frac{1}{r} \frac{\partial}{\partial r} \left[ rRmn\chi_\phi \frac{\partial v_\phi}{\partial r} \right] - \frac{mRv_\phi}{\tau_{cx}} \end{aligned} \quad (2.120)$$

$$\begin{aligned} \text{Heat: } \frac{\partial W}{\partial t} &= P_{in} - \frac{1}{r} \frac{\partial}{\partial r} [\alpha r R n T v_r] - v_r \frac{\partial}{\partial r} [nT] + \\ &\frac{1}{r} \frac{\partial}{\partial r} \left[ rn\chi \frac{\partial T}{\partial r} \right] - P_{out} \end{aligned} \quad (2.121)$$

where  $n$  is the density,  $r, R$  are the minor and major radial coordinate respectively,  $v_r$  is the radial convective velocity,  $m$  is species mass,  $v_\phi$  is toroidal velocity,  $\chi_\phi$  is momentum diffusivity,  $\tau_{cx}$  is the charge-exchange loss time (another momentum loss term is from the drag due to magnetic field ripple),  $T$  is temperature, and  $\alpha$  is a constant typically chosen to be 3/2 or 5/2 [2.293]. Also contained in these equations are terms representing the input of particles ( $S_{in}$ ), momentum or

torque ( $T_{in}$ ), and heat ( $P_{in}$ ), as well as a combination of energy loss terms ( $P_{out}$ ). These equations represent a balance between source and loss terms; the terms proportional to  $\partial[\dots n v_r]/\partial r$  represent losses due to radial convection (particle, momentum and heat), while those containing the diffusivity term,  $\chi$ , represent losses due to conduction. The heat transport term  $v_r \partial[nT]/\partial r$  modifies the losses due to convection, but is small. The source of particles can come from gas, pellet or NB fuelling, the torque input from direct collisions between the NB and plasma particles due to  $\vec{j} \times \vec{B}$  forces resulting from non-ambipolar loss of neutral beam ions from radiofrequency (RF) wave-drive or from residual stress [2.176]. The heat input can come from neutral beams, RF, ohmic heating (electrons only) or through the ionization of thermal neutrals by collisions with the thermal ions (ions only). The heat sinks,  $P_{out}$ , are specific to the species. For instance, energy is lost from the electron channel through radiation or ionization of neutrals through collisions. The ion channel can lose energy through charge exchange. An additional term to consider is the collisional coupling between the electrons and ions, a term which is proportional to  $(T_i - T_e)/T_e^{3/2}$ . If  $T_i > T_e$ , there is a net power flow out of the ion channel (heat loss) into the electrons (heat source). The energy flow is reversed when  $T_e > T_i$ .

These equations, which are composed essentially of the diagonal terms of the transport matrix, represent the most straightforward solution for the steady state transport. Other terms, such as those proportional to pinches, are not given in this set, although they can be determined through perturbation techniques (see Section 2.3). In solving the equations given above, however, most of the terms in these transport relations can be measured or calculated. The density, temperature, rotation profiles and their time evolution are measured. The radiated power is also measured. The convective radial velocity,  $v_r$ , can be calculated from the particle balance equation once the source of particles is determined, and this term is carried through to the momentum and heat transport equations. Source and loss terms due to convection, ionization and charge exchange are calculated, as are the source terms, although this calculation relies heavily on models (see following sections). In typical transport analysis calculations, the only term not calculated or measured is the term due to conduction. Thus, the standard approach to this transport analysis, which assumes diffusive-convective processes, is to determine the diffusivities for comparison to theory, whether it be neoclassical [2.11, 2.296, 2.297] or turbulence-driven (see Refs [2.52, 2.53, 2.87, 2.231, 2.298] and references therein). As mentioned, critical to the determination of these transport coefficients, however, is knowledge of the source terms, and this knowledge is highly model, and assumption, dependent.

## 2.5.2. Models

### 2.5.2.1. Neutral beam models

Neutral beam heating has been the most effective and widely understood auxiliary heating method for magnetically confined plasmas. It has been used across a wide range of devices, from small to large tokamaks to stellarators, and it has been successful in heating plasmas to temperatures necessary for fusion energy production [2.299, 2.300].

In this heating method, high energy neutral particles, with energies typically  $\gg T_e$ , are injected into the plasma, and if the plasma is dense enough to minimize “shine-through” losses, the fast neutrals are ionized through collisions with, primarily, the electrons. The fast ions are trapped by the magnetic field, but they can be lost from the system through charge exchange, bad orbits (fast ions hitting material surfaces due to large gyro- and/or banana orbits) or through static or time-varying inhomogeneities in the magnetic field (e.g. ripple, MHD modes respectively). Those fast ions that are not lost slow down (lose energy) via collisions with electrons and ions [2.301], thus acting as a heating, torque and particle source for the thermal plasma.

The classical description of the fast ion behaviour, that in steady and axisymmetric magnetic fields, is well understood theoretically, and it has been modelled successfully. The simplest approach to describing the fast ion distribution,  $f$ , is through the Boltzmann equation, which relates  $df/dt$  to the change in  $f$  due to collisions [2.302]. The Fokker–Planck expression for  $df/dt|_{col}$  is used, which represents long-distance binary collisions. A further development in neutral beam modelling was to treat the beam particles not as an ensemble (i.e. represented by a distribution function), but by tracking individual guiding centre orbits, with finite Larmor radius effects, of a large collection of particles [2.294]. While this Monte Carlo method increased computational time significantly, a large number of effects, not taken into account in the Fokker–Planck treatment, could now be considered. These included detailed beam and device geometry, re-ionization of escaping fast neutrals (fast ions that had been neutralized through charge exchange), finite Larmor radius/banana orbit corrections, collisions between beam particles themselves in addition to beam–plasma collisions, and the transport of neutrals created by charge exchange with beam ions (for both fast and thermal neutrals). The most up-to-date version of this treatment, called NUBEAM [2.303], is publically accessible on the Web in the National Transport Code Collaboration (NTCC) module library (<http://w3.pppl.gov/NTCC>).

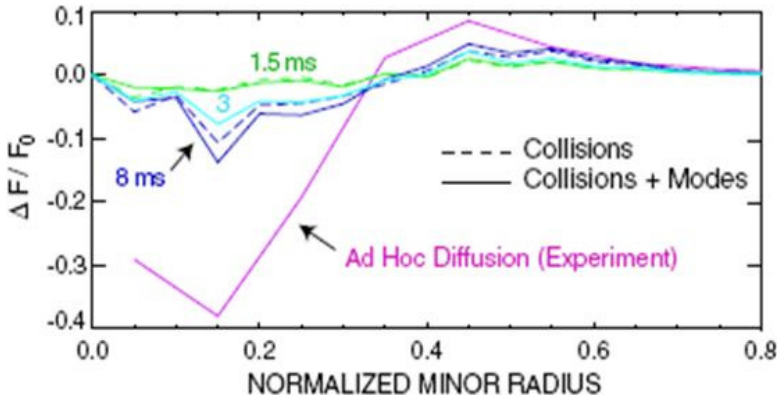


FIG. 2.26. Relative change in fast ion distribution function due to collisions alone (dashed) and collisions plus the effect of the AE modes, with the mode amplitudes enhanced by a factor of five (solid). The red curve is from an assumed ad-hoc fast ion diffusivity with a magnitude of  $5 \text{ m}^2\text{s}^{-1}$  inside of  $r = 0.55$  and zero outside, which is required for agreement with experimental measurement. Reprinted from Fig. 5 in Ref. [2.304], Copyright (2010), American Physical Society.

For MHD quiescent plasmas, this Monte Carlo method gives excellent agreement with measurements on both a global level (e.g. calculated versus measured neutron flux) and for indirect or direct measurements of the fast ion profiles from neutral particle analysers or from the fast ion diagnostic (FIDA) [2.304] respectively. Given the uncertainties in the local plasma/impurity composition and the neutral density, both of which can affect fast ion confinement, agreement to within 15% should be considered satisfactory. The presence of MHD activity, most notably Alfvén eigenmodes (AEs), which are driven unstable by free energy in the fast ion distribution, and which non-linearly couple to and modify the fast ion distribution, can lead to significant disagreements between classical calculations and measurement. Agreement can be restored in most cases by applying a spatially constant, ad hoc fast ion diffusivity whose magnitude is  $\sim 0.5 \text{ m}^2/\text{s}$  [2.260, 2.305]. However, in some cases, a much more elaborate anomalous diffusivity must be used, one that is spatially and/or time varying and energy dependent [2.304, 2.306]. One such example is taken from Ref. [2.304], in which an anomalous diffusivity with a very large core value ( $\sim 5 \text{ m}^2\text{s}^{-1}$ ) is needed to resolve the discrepancy with neutrons and FIDA on DIII-D. This level of fast ion transport far exceeds that deduced from measured AE mode amplitudes, even when these amplitudes are enhanced by a factor of five (Fig. 2.26, taken from Ref. [2.304]). While these cases tend to be in the minority, it is nevertheless important to understand the physics behind the ad hoc corrections, and to consider indirect effects due to the fast ions. One example of the latter is the proposed stochastic heating of thermal ions due to compressional AEs driven unstable by the perpendicular component of the beam ion distribution [2.307].

### 2.5.2.2. *Neutral transport*

A key component of determining the particle, momentum and energy balance in a tokamak is an accurate description of the neutral particle transport, as the neutral population serves as a source of plasma particles. Low energy neutrals (several eV) enter the plasma through gas injection, pellet injection or reflection (recycling) off the wall, and then undergo ionization or charge exchange collisions to give rise to plasma ions and electrons. These sources of neutrals are restricted primarily to the outer region of the plasma. Multiple processes, however, can take part in the transport of these neutrals, and an accurate accounting must consider all of them. For instance, as mentioned, a very low energy (cold) primary neutral from the wall can undergo charge exchange with a thermal (up to several hundred eV) ion, creating a much hotter neutral. This secondary, or halo, neutral can penetrate farther into the core, where it can also be a source of ions and electrons through charge exchange or ionization. Low or high energy neutrals can escape from the plasma, especially at high energies where the mean free path is greater than the plasma dimensions, and they can hit the wall. This bombardment causes reflections, or recycling of neutrals with energies from zero up to the incident energy, back into the plasma. In these scenarios, simple diffusion theory is not adequate to describe these multiple processes, long mean free paths and wall recycling. Furthermore, the processes can be highly non-isotropic spatially.

Another source of plasma is the fast neutral population from high energy beam heating systems. Similar to the cold neutrals, these hot neutrals can undergo multiple ionization/charge exchange and recombinations, and the processes are also non-isotropic and highly spatially localized at least for the first generation. The plasma source from the beam neutrals, which is determined in beam Monte Carlo calculations such as NUBEAM [2.303], tends to dominate in the plasma core.

Several approaches have been employed to determine the neutral transport in tokamak plasmas. The most accurate solution is a full Monte Carlo calculation such as that in DEGAS or DEGAS-II [2.308, 2.309], although this calculation, with virtually no simplifying assumptions, is very time consuming. Consequently, various simplifying assumptions have been made to make the calculation more tractable. The code developed by Burrell [2.310] assumes the collision cross-sections to be independent of the energy of the incident neutral, and that the charge exchange collision source is Maxwellian at the local ion temperature. The SPUDNUT [2.311] code takes into account the velocity dependence of the collision cross-sections, but it assumes an isotropic monoenergetic energy distribution of newly born neutrals, and is valid in a slab geometry. ANTIC [2.312] extends SPUDNUT to cylindrical geometry and is presently being used in such transport codes as TRANSP.

The NUT [2.313] code extends the calculation potentially to three dimensions using a technique where small-scale variations are isolated and treated analytically, thus leaving the longer-scale variations to determine the grid spacing for the numerical solution. This approach is valid when the scale lengths of the plasma do not vary much. The larger grid size allows for a “fast and compact” numerical solution. An energy dependent reflection coefficient is also used in NUT. The most recently developed neutrals code is the two dimensional GTNEUT [2.314], which avoids the Monte Carlo method’s issues of numerical noise and computational time requirements by what is called the “transmission and escape probabilities” method [2.315]. The approach is numerically efficient and allows for an accurate treatment of neutral transport even in systems with complex geometries, near walls, and with either short or long mean free paths. GTNEUT has been benchmarked successfully against Monte Carlo calculations from DEGAS. Benchmarking against experimental data for any of these codes has been challenging due to the relative lack of direct neutral density measurements. Any of the multi-D neutral transport codes requires a multi-D source of particles in order to be used effectively.

### 2.5.2.3. RF heating and current drive models

Because radiofrequency (RF) heating and current drive techniques are employed over a range of frequencies, depending on the particular heating and current drive schemes, codes specific to those schemes have been developed. In the ion cyclotron (ICRF) range of frequencies, bounce averaged, zero ion orbit-width Fokker–Planck codes such as CQL3D [2.316] have been coupled to full-wave solvers that employ a plasma response developed in either the ion finite ion Larmor radius (FLR) limit (TORIC [2.317]) or for arbitrary perpendicular wavelength relative to the ion gyroradius (AORSA [2.318]). These coupled models [2.319] perform an iteration whereby the full-wave solver employs the plasma response due to the full non-thermal ion and electron distribution functions and the Fokker–Planck code advances the non-thermal particle distribution based on the most recent computation of the RF quasilinear diffusion coefficient from the full-wave solver. These calculations have been recently extended to include the full toroidal mode spectrum coupled by the ICRF launcher [2.320]. Synthetic diagnostic codes for phase contrast imaging of mode converted ICRF waves [2.321] and for neutral particle analyser measurements of fast ion distributions [2.322] have been successfully implemented in conjunction with these simulation models. Linear antenna coupling models have been developed that consist of full-wave field solvers (TORIC) and 3-D electromagnetic antenna codes (TOPICA [2.323]), but only for a single mode excited by the RF launcher.

Boundary conditions for RF sheath formation and dissipation have been derived for the near — and far — field sheath problems, in both 1-D and 2-D

[2.324], but have not yet been incorporated self-consistently into full-wave electromagnetic field solvers. In the ICRF regime, self-consistent coupling of Monte Carlo orbit codes (ORBIT RF [2.325]) to ICRF full-wave solvers must still be carried out to account for finite ion drift-orbit effects. Then it will be possible to properly assess the importance of these effects for ICRF fast waves interacting with fast minority ions generated by the ICRF itself as well as with energetic ions due to NBI and fast fusion alpha particles. In the area of ICRF antenna – edge plasma interactions, the linear coupling analysis using a full-wave solver and antenna code still must be carried out using the full toroidal antenna spectrum of the RF launcher. Also, non-linear formation of near and far field RF sheaths must be addressed self-consistently by implementing metal wall boundary conditions for the sheaths in ICRF full-wave solvers.

In the lower hybrid (LHRF) range of frequencies, zero electron orbit-width Fokker–Planck solvers (CQL3D) have been combined with toroidal ray tracing codes (GENRAY [2.326]) to compute LH current drive and heating. The Fokker–Planck solvers include spatial diffusion operators that incorporate phenomenological diffusion coefficients for the fast electrons. Linear coupling codes have been used successfully to predict the coupled power spectrum from phased waveguide arrays in this regime. Synthetic diagnostic codes for hard X ray emission, motional Stark effect measurement of the toroidal current density, and for non-thermal electron cyclotron emission (ECE) have been successfully implemented in conjunction with these simulation codes [2.327]. In the LHRF regime it will be very important to assess the validity of the geometrical optics approach in computing wave propagation since this treatment does not account for potentially important full-wave effects due to focusing and diffraction. Thus application of electromagnetic (EM) full-wave solvers to the LHRF regime is critical for answering these questions and the field solutions from the full-wave solvers will ultimately have to be combined with electron Fokker–Planck analyses for a complete description of LHCD in present day devices and in ITER.

Currently, the computation of electron cyclotron current drive (ECCD) and EC heating sources is performed using bounce-averaged Fokker–Planck codes coupled to toroidal ray tracing descriptions of the EC wave propagation (CQL3D and GENRAY) [2.328]. These simulation models have been found to be an adequate description of ECCD experiments to date, but have not been coupled to extended MHD simulations of the plasma. In the ECRF regime an important outstanding problem will be to assess the feasibility of sawteeth stabilization via ECCD. This requires a non-trivial coupling of the ECCD simulation to a resistive MHD code.

#### 2.5.2.4. Current drive models

The non-inductive current in tokamaks can be generated both internally and externally, and both have to be modelled correctly to determine the total plasma current profile. Internally, or self-generated, current results from a momentum exchange between trapped and untrapped particles in the presence of a density gradient. This collisional exchange, which leads to what is called “bootstrap” current, is modelled within the framework of neoclassical theory [2.297, 2.329, 2.330].

The current drive models for neutral beams and RF are integrated into the suite of codes used to model the respective methods of heating. For NB current drive, the NUBEAM Monte Carlo module performs a comprehensive calculation assuming classical slowing down and loss processes, as described above. In MHD-quiescent plasmas, this is a good assumption and gives current profiles that agree quite well with measurement, as shown in Fig. 2.27(b), taken from NSTX experiments described in Ref. [2.306]. In the figure, the “reconstructed” (grey) current profile is obtained from equilibrium reconstructions constrained by motional Stark effect (MSE) measurements of the magnetic field pitch, and it is within 5–10% of the profile calculated from inductive, bootstrap and beam driven sources, the latter computed by NUBEAM. As was discussed earlier in this section, MHD activity can have a large effect on the fast ions, and thus the NB current driven profiles; this is seen in Fig. 2.27(c), which is taken later on in the discharge shown in Fig. 2.27(a), during a period of saturated  $n = 1$  mode activity. The discrepancy between the calculated and reconstructed current density in this case reached 40%. Agreement during this period could be restored by applying an energy dependent and temporally and spatially varying anomalous fast ion diffusivity to simulate the MHD-induced redistribution of the fast ions (Fig. 2.27(d)). For this time period, an anomalous fast ion diffusivity of 20–50  $\text{m}^2 \cdot \text{s}^{-1}$  confined to the inner 20% of the plasma was needed for consistency.

Negative neutral beam injection, where the fast ion energies can reach several hundred keV, and thus are suited for use in high temperature burning plasma devices, has been demonstrated in JT60-U [2.331]. Current drive estimates for this injection scenario were performed using the ACCOME [2.332] code, and agreement with measured driven currents over a range of plasma currents from 0.1 to 1 MA was found.

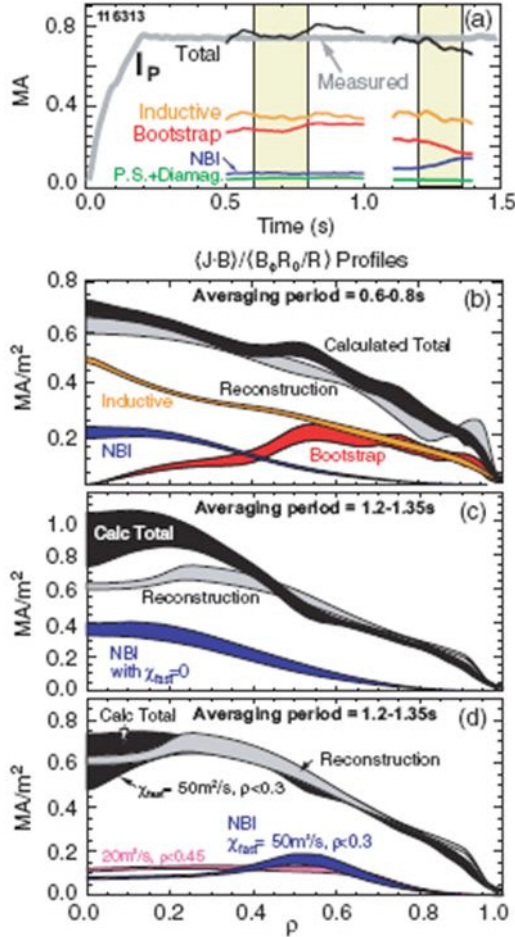


FIG. 2.27. (a) Comparison of measured (grey) and calculated (black) total plasma current with calculated inductive and NB contributions also shown. (b) Comparison of profiles during MHD-quiescent period. (c) Comparison during period of saturated  $n = 1$  activity assuming no anomalous fast ion diffusion. (d) Comparison during period in (c) assuming anomalous fast ion diffusion [2.306].

Electron cyclotron wave absorption is highly localized near the wave resonances, and this method therefore offers the potential to drive current in a localized and controllable manner. The current drive from this source has been used to sustain total current as well as to drive current near rational surfaces in order to suppress virulent MHD modes such as sawteeth [2.333] and neoclassical tearing modes [2.334, 2.335], as well as to maintain internal transport barriers (ITBs) [2.336]. The EC driven current is usually calculated using ray tracing codes coupled to a Fokker–Planck treatment of the affected electron distribution, and excellent agreement between experimental and theoretical estimates of EC

driven current has been found. Codes used for this calculation include CQL3D [2.316], BANDIT [2.337] and a code by Giruzzi [2.338]. An example of the good agreement between measured ECCD and that calculated by CQL3D from DIII-D is shown in Fig. 2.28 (taken from Ref. [2.339]). The current drive efficiency of ECCD, however, is lower than that from NBI. Benchmarking has also shown the importance of including a full relativistic treatment of the electrons for plasma parameters that might be found in ITER [2.340].

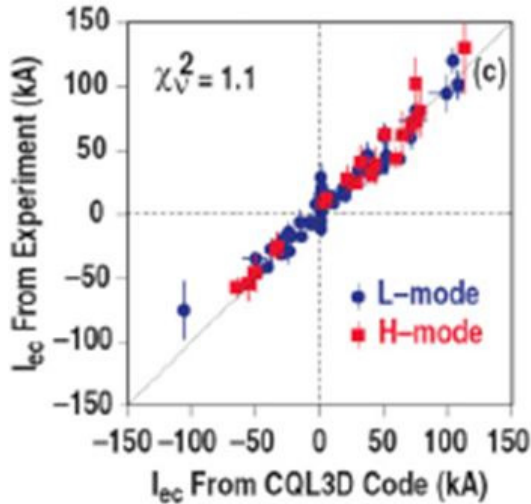


FIG. 2.28. Comparison of experimental and calculated EC driven currents [2.339].

Lower hybrid waves, which damp at high parallel phase velocities, have higher current drive efficiencies than EC waves, and they can drive current effectively outside the plasma core. LHCD is used primarily to drive current in advanced scenarios and as a means to trigger and control ITBs. Numerical models of LHCD couple ray tracing to a Fokker–Planck treatment, similar to that for ECCD. Codes used for LHCD calculations include CQL3D, BANDIT, ACCOME and DELPHINE [2.341]. The codes have been successful in reproducing measured current profiles; an example from JT-60U [2.342] is shown in Fig. 2.29. The experimental LHCD profile (left panel) is taken to be the difference between the total current, as inferred by MSE measurements, and the sum of the numerically calculated bootstrap and NBI driven current plus the inductive current as evaluated from the temporal evolution of the poloidal flux. The calculated profile (right panel) shows excellent agreement with the experimental one.

ICRH heating and current drive can be effected directly through the bulk ions, minority ions or electrons. Typically, the current drive is performed through fast waves (FW), whose energy is absorbed directly by the electrons. FWCD is,

however, more difficult than either ECCD or LHCD due to issues with wave absorption on fast ions as well as coupling issues [2.343–2.346]. Benchmarking between experiment and theory for FWCD has not been as extensive as that for ECCD or LHCD, although agreement has been found in FWCD experiments on DIII-D [2.346] and recently using high harmonic fast waves on NSTX [2.347].

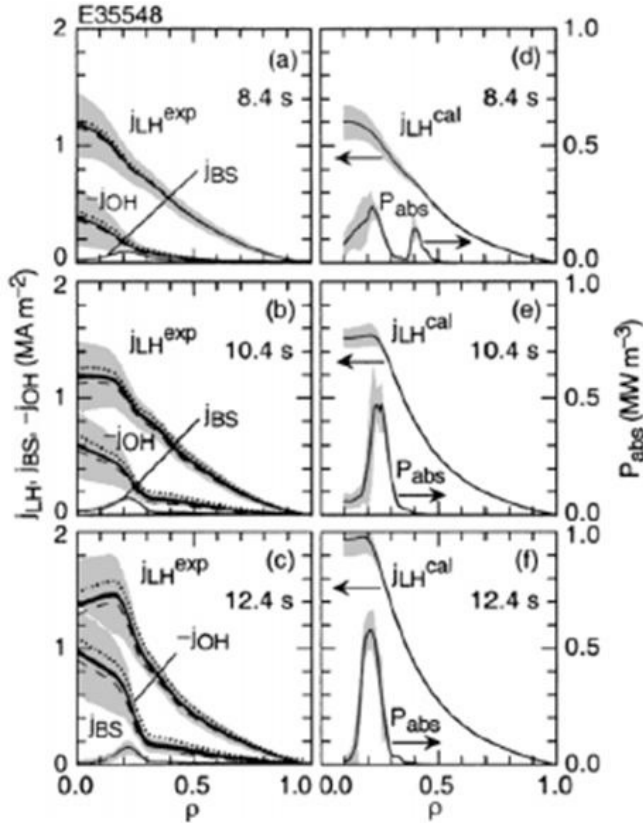


FIG. 2.29. Comparison between measured LH current profiles in JT-60U (Reprinted from Ref. [2.342]. Copyright (2010), American Physical Society) and those from the combined ray tracing and Fokker-Planck calculation in ACCOME.

### 2.5.3. Perturbative transport

The solution of the particle, momentum and energy balance equations described earlier in this section offers the simplest and most straightforward means of determining the transport coefficients in toroidal devices. In general, the transport fluxes are related to the gradients through the generalized transport matrix.

$$\begin{bmatrix} \Gamma \\ Q_e \\ Q_i \\ M \end{bmatrix} = \begin{bmatrix} D & a_{12} & a_{13} & a_{14} \\ a_{21} & \chi_e & a_{23} & \dots \\ \dots & \dots & \dots & \dots \\ \dots & \dots & \dots & \dots \\ \dots & \dots & \dots & \chi_\Omega \end{bmatrix} \begin{bmatrix} \frac{\partial n}{\partial \rho} \\ \frac{\partial T_e}{\partial \rho} \\ \frac{\partial T_i}{\partial \rho} \\ \frac{\partial \Omega}{\partial \rho} \end{bmatrix} \quad (2.122)$$

where  $\Gamma$  is the particle flux,  $Q_{e,i}$  is the electron and ion heat fluxes,  $M$  is the momentum flux,  $\rho$  is the radial coordinate and  $\Omega$  is rotation velocity. Here, only four fluxes are shown, but others, such as that related to the toroidal current, can be included as well. The diffusivities are given by the diagonal terms in the matrix. In the “steady-state” solution of these flux balance equations, it is the diagonal terms that are taken to be dominant, despite the possible importance of the off-diagonal terms. This is done for ease of solution, as the off-diagonal terms are more difficult to determine, for readily comparing to theory, and so as not to compound data uncertainties. A description of the most general form of the transport equations can be found in Ref. [2.348].

Results of these analyses have led to some general conclusions. The ion thermal diffusivity can be as low as that given by neoclassical theory, but it can also be at anomalously high levels (up to a factor of ten greater than neoclassical), especially in NB-heated discharges in conventional or low aspect ratio devices. The electron thermal transport, however, is always anomalous (see Refs [2.349, 2.260] and references therein). Momentum diffusivity  $\chi_\Omega$  is well above neoclassical levels, which for momentum transport is near zero, and it has been determined to be a factor of 0.1–1 times the ion thermal diffusivity [2.26, 2.162, 2.350, 2.351].  $\chi_\Omega = \chi_i$  suggests that similar underlying transport is controlling both fluxes. Early attempts were made to parameterize the anomalous  $\chi_e$ , and dependences on  $n_e$ ,  $T_e$  and  $B_\theta$  were found (see Ref. [2.228] and references therein). Similar to the case for energy confinement, different parametric scalings of  $\chi_e$  were found between low and high aspect ratio devices, with  $\chi_e(r/a \sim 0.65) \sim 1/B_\theta$  for low aspect ratio [2.260]. It was later found that there is a dependence of  $\chi_{e,i}$  on rotation, but it can be complicated, depending on whether the profiles are near an instability threshold (i.e. at marginal stability) [2.352], and depending on the magnitude of the local rotation shear [2.353]. While these parameterizations were done to facilitate direct comparisons to theory, no link between the experimentally inferred  $\chi_e$  and that from theory has been unambiguously established.

It is not at all clear, however, that there should be such a simple linear relation between a particular flux and a single gradient (e.g.  $q_e \propto n\nabla T_e$ ). Off-diagonal terms, which reflect dependences on other gradients, may be important as can be anomalous convective pinches and non-local transport (instabilities in one portion of the plasma affecting portions where these instabilities are predicted to be stable). These more complex relations can be uncovered through “perturbative” transport studies, an excellent review of which is given in Ref. [2.354]. These studies are performed by applying small perturbations to a steady state plasma, varying only one plasma characteristic if possible, and then measuring the response of the plasma to this perturbation. An example of this is to change temperature gradients locally through localized heating, and then measuring the change in temperature, or “heat pulse” propagating away from that position. The time it takes for the heat pulse to arrive at various radii can yield a determination of the thermal diffusivity under various simplifying assumptions. This will be discussed later on. The perturbative technique allows for isolating the effect of different gradients, thus allowing for a determination of the off-diagonal elements, and to separate diffusive from convective components of the transport.

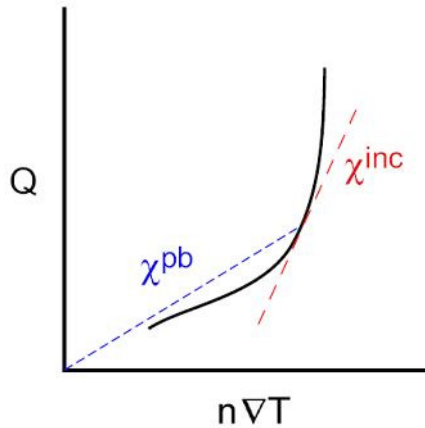


FIG. 2.30. Graphical representation of the difference between  $\chi^{inc}$  and  $\chi^{pb}$ . Heat flux is plotted versus  $n\nabla T$ .

The difference between the steady state (power balance) and perturbative analysis is illustrated qualitatively in Fig. 2.30, where the heat flux is plotted against  $n\nabla T$  for a case in which the relation between the two is not linear. The power balance diffusivity,  $\chi^{pb}$  is defined as  $Q/n\nabla T$ , but this does not take into account this non-linear relation between  $Q$  and  $n\nabla T$  at the  $n\nabla T$  (i.e. location) of interest. The so-called incremental diffusivity, or diffusivity that is determined by a change in the local gradient, at this point is defined as  $\chi^{inc} \propto dQ/d(n\nabla T)$ . The  $\chi^{inc}$  is the diffusivity that, for instance, is determined

by the heat pulse propagation in perturbative experiments, and is often denoted  $\chi^{hp}$ ; this notation will be adopted from here on. It is seen, for the relation between  $Q$  and  $n\nabla T$  shown in Fig. 2.30, that  $\chi^{hp} > \chi^{pb}$ ; power balance analysis underestimates the diffusivity in this case, and this is a general result from perturbative analysis. In addition, the power balance diffusivity can exhibit stronger dependences than  $\chi^{hp}$ , which is to be expected if off-diagonal terms which are implicitly contained in  $\chi^{pb}$  are important.

Various techniques can be used to deduce the incremental diffusivity. These include natural perturbations in the plasma such as sawteeth and ELMs (ELMs actually induce propagating cold pulses), and methods that require externally applied perturbations such as ECH and other RF, and pellet, impurity and main plasma gas injection. The various perturbations require different analysis techniques. For instance, time-to-peak analysis is used for sawtooth or ELM perturbations, which can be considered to be isolated events. The time-to-peak method is based on measuring the time it takes for the maximum temperature perturbation due to a heat or cold pulse to occur at a given radius. For sawteeth, the heat source is modelled as a dipole (two opposing delta functions on either side of the mixing radius), and the density and diffusivity is assumed to be constant. The thermal diffusivity from the sawtooth heat pulse is  $1/8(r^2 - r_s^2)/t_p$ , where  $t_p$  is the time of maximum temperature perturbation at radius  $r$ , and  $r_s$  is the mixing radius [2.355]. An extension to this model, accounting for large temperature perturbations, is given in Ref. [2.356].

A more general approach, and one which has been used with externally controlled parameters such as modulated ECH, is the Fourier transform technique. In this technique, the perturbation is applied periodically (i.e. modulated), and the periodic plasma response is measured. The Fourier transforms of the response signals yield the amplitude decay and phase as functions of radius. If the simplifying assumption is made that the system is purely diffusive, then the resulting diffusion equation,  $\partial u / \partial t = D\nabla^2 u$ , where  $u$  is the measured response of the temperature, for instance, and in that case  $D = 2/3\chi$ . If slab geometry is assumed, then the solution to the diffusion equation is  $u(x,t) = u_0 e^{-x/\lambda} e^{i(\omega t - \xi)}$ , where  $\lambda$  is the decay length and  $\xi$  is the phase. The solution yields a relation between  $D$  and both the decay length and the phase, given by  $\lambda = \sqrt{2D/\omega}$  and  $\xi = x\sqrt{\omega/2D}$ . The geometric mean of the two estimates of  $D$  (from amplitude and from phase) is typically taken. Finally, forward modelling based on transport coefficient assumptions has also been used as a tool to test the plasma response to perturbations. In general, the heat and cold pulse propagation studies have focused on the electron response, and thus  $\chi_e$ , for the simple reason that the diagnostics measuring the electron response (electron cyclotron emission) have a much higher time resolution, and an adequate time resolution for these experiments, than those for measuring the ion response.

The results of these perturbation experiments have, for the most part, indicated that processes other than pure diffusion are operating. As mentioned  $\chi^{hp} > \chi^{pb}$  by a factor of two to ten, indicating the importance of non-local transport, convective or pinch terms, or off-diagonal transport matrix elements. The difference between the two diffusivities can also point to modelling assumptions that are not valid, such as assuming constant  $n$  and  $\chi$  in space and/or in time. An example of this would be a case where  $\chi$  depends on  $T$  or  $\nabla T$ , which change due to the heat pulse itself. In effect, the  $\chi$  is perturbed through modifications in underlying instability thresholds and saturation levels caused by local changes by the pulse. Finally, instrumental sensitivities and data reduction methods (e.g. inversion of line-integral signals) can introduce uncertainties in the determination of  $\chi$ .

There are a number of perturbative analysis results using these studies, and it is not possible to cover them all. Some highlights will be discussed here, but good references that cover much of this work are [2.347, 2.348, 2.354, 2.357, 2.358] and references therein. Heat pulse propagation studies have been performed in most tokamaks with the result that  $\chi^{hp} > \chi^{pb}$ . Aside from the possibilities leading to this relation that were discussed in the previous paragraphs, Fredrickson [2.359] reported a “ballistic”, or non-local response, where heat was deposited outside the mixing radius on timescales of 200  $\mu\text{s}$ , much shorter than the typical assumed diffusive timescale, bringing into question the assumptions and modelling of  $\chi^{hp}$  in this case. Coupling of heat and density pulses was observed in JET [2.360] and TEXT [2.361] ohmic plasmas, with JET finding that  $\chi_e / D_e \sim 7$  from sawtooth pulses as well as pellet-induced cold pulses. On TEXT, at higher collisionality, the density and temperature perturbations were highly correlated, with similar amplitudes, timescales and parametric dependences, suggesting a much stronger coupling between the two than on JET. Ion heat pulses, with  $\chi_i^{hp} \sim \chi_e^{hp}$  were found following sawteeth on JFT-2M [2.362], and an ion response to a sawtooth crash was also found on JET [2.360]. The simple sawtooth transport model was applied to cold pulse propagation due to ELMs in NSTX [2.363].

Modulated ECH provides a localized and controllable source of electron heating which can be used to determine  $\chi_e$  with the Fourier method. Detailed experiments on ASDEX-U [2.358] revealed diffusive-like behaviour of an inward propagating heat pulse from a modulated ECH source at  $\rho = 0.85$  into a radius of  $\rho = 0.4$ . Inside that radius, however, the plasma response changed character to one with near constant amplitude and phase, reflecting a non-propagating, or non-local, behaviour that depends more on the arrival of the pulse at  $\rho = 0.4$  than on the initial perturbation. Here,  $\rho$  is the normalized radial coordinate which equals 0 in the centre and 1 at the edge. Non-local response to ECH has been observed even with steady ECH heating, as reported on DIII-D [2.364], where the  $T_e$  profiles remained peaked even with off-axis ECH.

Evidence for non-local transport has also been found from the results of cold pulse propagation experiments, where impurities have been introduced into the plasma using laser blowoff, or pellet or gas injection to induce the cold pulse. In ASDEX-U [2.11], the rapidly propagating cold pulse outside of the sawtooth mixing radius was accompanied by heating of the plasma inside the mixing radius. Similar observations were made in TFTR [2.365]. The inversion was seen to disappear as the plasma density increased; in ASDEX-U, the temperature drop due to the cold pulse was seen across the entire radius when the line-averaged density was  $> 2.2 \times 10^{19} \text{ m}^{-3}$ . However, the plasma response was not consistent with a purely diffusive process at any density. At lower densities, for instance, the amplitude clearly increased as the cold pulse propagated towards the centre. Two differences between cold and heat pulses that could account for differences in results are that, firstly, in addition to the change in temperature, the impurity injection also generates a particle source. Secondly, the cold pulse affects both the ions and electrons.

Similar differences in non-local effects have been observed in cold pulse experiments in stellarators as well [2.366]. Further, early stellarator studies using modulated ECH have shown, unlike tokamaks, that  $\chi^{hp} \sim \chi^{pb}$  [2.367], which can be reconciled only by using a model for  $\chi$  that depends on the non-local, total input heating power [2.368]. The difference in the relation between  $\chi^{hp}$  and  $\chi^{pb}$  between tokamaks and stellarators also suggests the possible importance of an off-diagonal term in the transport matrix that depends on toroidal current density, which is present in tokamaks but not stellarators. Later work on LHD [2.369] has shown also that  $\chi^{hp} \sim \chi^{pb}$ , but with a strong dependence of  $\chi^{hp}$  on  $\nabla T_e$  in ITB plasmas, suggesting non-local transport.

#### 2.5.4. Profile stiffness

The heat pulse  $\chi_e$  introduced in the previous section can be expressed as an expansion to first order in the temperature gradient,  $\chi_e^{hp} = \chi_e + [\partial \chi_e / \partial (n \nabla T_e)] \nabla T_e$ , with the quantities on the right hand side being determined from power balance (i.e.  $\chi_e = \chi_e^{pb} q_e / (n \nabla T_e)$ ) in the purely diffusive case. Separating the  $\chi^{hp}$  from  $\chi^{pb}$  in this fashion allows the investigation of the concept of ‘‘profile stiffness’’. The stiffness of the temperature profile reflects how close the profile or profile gradients are to those set by an instability threshold that is governed by the local gradient or gradient scale lengths. A profile that remains similar to the marginal profile (i.e. the profile at the instability threshold) is considered stiff, while a profile with gradients that can vary considerable away from that marginal or critical value, either higher or lower, is considered to be not stiff. The stiffness can be quantified by the value of  $\chi^{hp} / \chi^{pb}$  [2.370], although other metrics have been defined both for the tokamak [2.371] and stellarator [2.372]. If this parameter is near 1, then the

profiles are not stiff (the local gradients do not affect the value of  $\chi$ ), while if the value is  $>1$ , the profiles are stiff (the term explicitly containing the dependence on  $\nabla T_e$  is important).

This concept can be put into a framework for a functional form for the diffusivity which contains a term representing the underlying minimum transport level and a term that represents an enhanced transport when the local gradient exceeds that of the instability threshold, with the level of enhanced transport governed by how far the local gradient exceeds the critical value. Using this approach, an expression for  $\chi_e$  can be written:

$$\chi_e = \chi_0 + cT_e^\alpha \left[ \frac{|\nabla T_e|}{T_e} - \kappa \right]^\beta H \left[ \frac{|\nabla T_e|}{T_e} - \kappa \right] \quad (2.123)$$

where H is the Heaviside function,  $\chi_0$  represents the background diffusivity when  $\nabla T_e / T_e$  is less than the critical value given by  $\kappa$  with no explicit dependence on  $\nabla T_e$ .  $\chi_0$  is typically taken to be  $\chi_e^{pb}$ . The choices for coefficients  $\alpha$  and  $\beta$  are  $3/2$ , which represents electrostatic gyroBohm transport, and 1 respectively, from best fits to data [2.373]. A consequence of this form is that  $\chi^{hp} \sim \chi^{pb}$  for gradients below the threshold while  $\chi^{hp} > \chi^{pb}$  for gradients above the threshold, the latter leading to adjustments of the gradients in order to maintain the critical values, leading to the concept of profile stiffness. Below the threshold, where the profiles are not stiff, the gradients can be varied by varying heating power, etc. Above the threshold, when the profiles are stiff, additional heating power leads to no change in the gradients. A graphical representation of this is shown in Fig. 2.31, taken from Ref. [2.373]. The departure of  $\chi^{hp}$  from  $\chi^{pb}$  occurs at gradients greater than the threshold value.

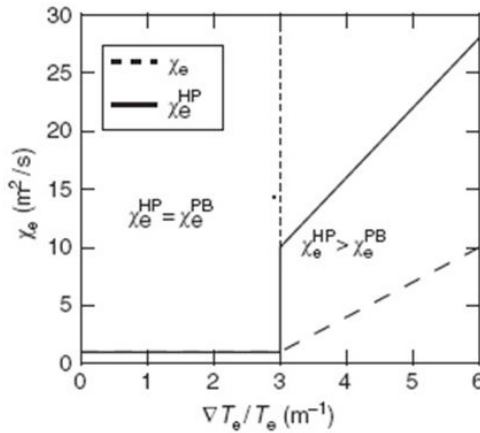


FIG. 2.31. Graphical representation of  $\chi^{hp}$  and  $\chi^{pb}$  given by the relation above. The critical gradient is shown by the vertical dashed line [2.373].

A direct measurement of  $\kappa$  can be made using modulated ECH to vary the local gradients and to determine  $\chi^{hp}$  using the Fourier method. This has been carried out most notably on ASDEX-U [2.141, 2.373, 2.374] and Tore-Supra [2.375]. In particular, experiments at low current on ASDEX-U [2.141] were able to explore regimes of very low gradients. In these experiments, the ECH power was modulated at  $\pm 10\%$  of the total power in order to determine  $\chi^{hp}$  from the amplitude and phase. The  $\chi^{pb}$  was calculated as well. The result of this experiment is shown in Fig. 2.32, which is taken from Ref. [2.141]. The critical gradient, as determined from both the power balance and heat pulse techniques, is seen to be at  $R/L_{Te} \sim 2.5$ , where  $L_{Te}$  is the electron temperature gradient scale length. When results from other devices are considered, the threshold is seen to range from 2.5 to  $\sim 8$  [2.374]. In Fig. 2.32 it is clearly seen that the transport level above the critical gradient is much greater than that below it. The slope of the line through the points above the threshold also reflects the stiffness. While the terms “critical gradient” and “critical gradient scale length” have been used somewhat interchangeably here, it should be noted that the measured  $\chi_{eS}$  are best fit by a parameterization expressed in terms of  $\nabla T_e / T_e$  (inverse scale length), rather than  $\nabla T_e$  alone [2.260]. It also has been shown that the  $T_e$  profiles are not stiff near the edge of the plasma where  $T_e < 500$  eV, or in the core of the plasma at low  $\nabla T_e$  [2.370, 2.371], which leads to a separation of transport zones in the plasma.

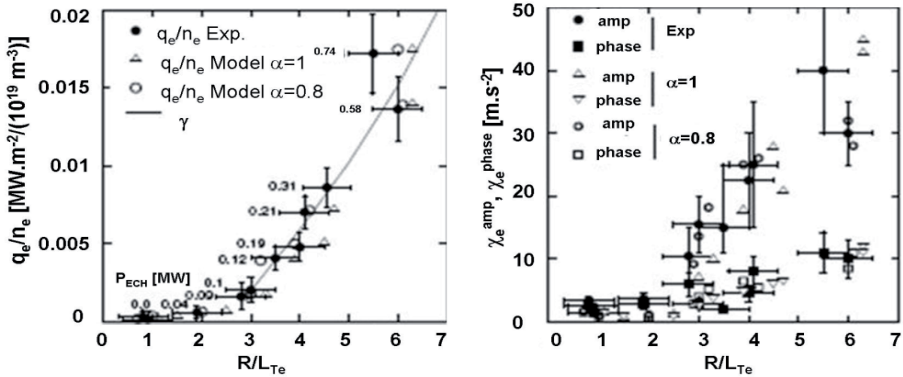


FIG. 2.32. (left) Electron heat flux versus  $R/L_{Te}$ , (right)  $c_e s$  determined from amplitude and phase versus  $R/L_{Te}$  (Reprinted from Ref. [2.141]. Copyright (2010), American Physical Society.) The perturbative technique used to derive  $\chi_e^{\text{amp}}$  and  $\chi_e^{\text{phase}}$  is described in Ref. [2.141] and in Section 2.5.5.1 in this chapter.

## 2.5.5. Transport barriers

### 2.5.5.1. Core

A phenomenon that appears to violate profile stiffness in the core of the plasma is the formation of so-called “internal transport barriers” (ITBs). The ITB is characterized by steep, localized gradients in some or all of the electron temperature, ion temperature, plasma density and plasma velocity, which lead to peaked profiles in these parameters and improvements in energy, particle and/or momentum confinement. ITB gradients generally exceed the normalized value,  $\rho_{*T} = \rho_s / L_{Te} \sim 1.4 \times 10^{-2}$  (for electron temperature in this example), where  $\rho_s$  is the ion Larmor radius calculated with  $T_e$ , and  $L_{Te}$  is the electron temperature gradient scale length. ITBs are seen in both tokamaks and helical (non-axisymmetric) configurations. The ITB is a particularly attractive regime in that the peaked profiles enhance fusion power production, which is proportional to the square of the central pressure. Peaked profiles, however, tend to be more transient than quiescent H-mode plasmas, for instance. Considerable work has been undertaken to develop steady state ITB scenarios, and this will be discussed later in this section. An excellent review of the theory of ITBs and efforts to develop steady state ITB scenarios can be found in Ref. [2.376].

The first ITBs were seen in JET plasmas that were pellet fuelled [2.377]. This pellet-enhanced-performance regime was characterized by high central  $q$ ,  $q_0 (>1)$  and reversed magnetic shear,  $s = (r/q)\partial q/\partial r < 0$  near the magnetic axis following the pellet injection. This PEP mode was also observed in TFTR discharges that were fuelled by pellets [2.378] and these plasmas also exhibited  $q_0 > 1$ , but with weak positive, not negative, magnetic shear. Ion Bernstein wave heating of PBX-M plasmas resulted in the development of an ITB in H-mode plasmas [2.379]. ITBs in neutral beam heated plasmas were observed in both JT-60U [2.380] and TFTR [2.381]. In JT-60U, the ITB was observed in the ion temperature profile, while in TFTR D-D and D-T plasmas, it was observed in the density profile when the power exceeded a certain threshold that was dependent on plasma current and power deposition profile (these plasmas were dubbed enhanced reversed shear, or ERS, plasmas), or in the electron temperature profile when the NB power was below the threshold (Type II). The transition to ERS plasmas from normal reversed shear (RS) plasmas was sudden, while the Type II ITB developed more slowly at rational values of  $q_{min}$  (e.g. 3 or 5/2), similar to what was observed in DIII-D negative central shear (NCS) and JET optimized shear plasmas [2.190, 2.382]. Shear reversal was a necessary condition for the development of ITBs in both TFTR scenarios. Transient precursors to the ERS plasmas were seen in both the poloidal velocity and radial electric field, with reversals in both parameters localized near the  $q_{min}$  surface.

As will be seen, underlying the creation of ITBs in all the studies have been changes to either the magnetic or  $\vec{E}_r \times \vec{B}$  shear (as well as  $E_r$  itself in helical configurations), and thus attempts to understand the fundamental processes causing the ITBs have focused on these parameters. The role of  $\vec{E}_r \times \vec{B}$  here was carefully studied in TFTR plasmas, where the ERS regime was most easily accessed with balanced beam injection, as compared to co- or counter-injection. This was understood in terms of the radial force balance,  $E_r = \nabla p / eZn + v_\phi B_\theta + v_\theta B_\phi$ . With co-injection, the positive  $v_\phi$  driven by the beams was of opposite sign to the pressure gradient term, thus reducing  $E_r$ . With balanced injection,  $v_\phi$  was reduced, and the  $\nabla p$  term dominated, leading to greater values of  $E_r$  and  $\vec{E}_r \times \vec{B}$  shear.

Studies following these initial ones employed localized heating or current drive to facilitate the formation of ITBs. Among other devices, localized heating and current drive studies of ITB formation and maintenance were carried out on Tore-Supra [2.383], JET [2.384] and TCV [2.385]. In Tore-Supra and JET, LHCD was used early in the discharge to both heat the electrons and delay the relaxation of the hollow current density formed during the ramp-up phase (see Fig. 2.33 taken from Ref. [2.384]). In these discharges in Tore-Supra,  $q_0 \sim 3.5$  and  $q_{min} \sim 2.5$  at  $r/a = 0.45$ . A spontaneous increase in  $T_{e0}$  from 2.5 to 4.5 keV was observed with as little as 1.6 MW of LH heating power, with the increase being confined to the reversed magnetic shear region. ITBs also developed in fully non-inductive Tore-Supra plasmas with 3 MW of LH power. With use of LHCD during the ramp-up phase of JET discharges, ion ITBs were observed using both NB and ICRH heating during the flattop phase in D-D and D-T plasmas [2.384]. The highest fusion yield in JET was obtained using this scenario [2.192].

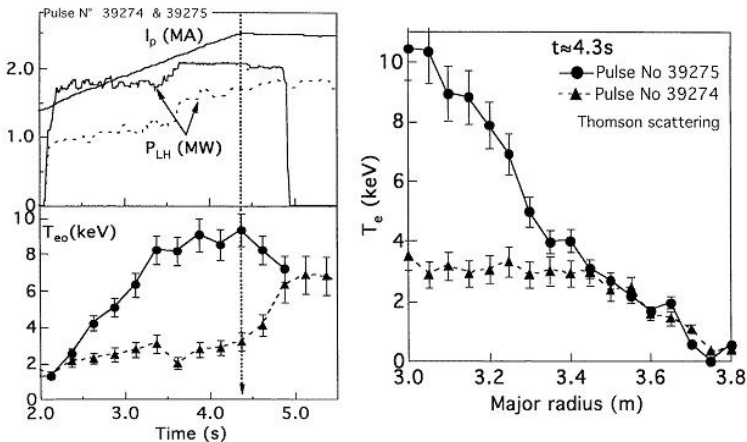


FIG. 2.33. (left) Time evolution of plasma current, LH power and central electron temperature in two JET discharges, one with and one without an electron ITB. (right) Electron temperature profiles for these two discharges. Taken from Ref. [2.384].

Off-axis ECCD was used in TCV to drive a hollow current profile [2.385]. A rapid rise in electron temperature (Fig. 2.34 taken from Ref. [2.385]) was seen to occur on timescales faster than the electron energy confinement time, and this ITB formation, according to modelling the  $q$ -profile evolution, was triggered by the appearance of a zero shear ( $s = 0$ ) surface. The transition was observed to occur at earlier times the more off-axis was the current drive, and improvements in energy, particle and/or momentum confinement. ITB gradients and the strength of the barrier, as given by  $\rho_{*T}$ , were found to correlate with the depth of the shear reversal region ( $\sim |(q_0 - q_{\min}) / q_{\min}|$ ). Experiments using NBI-heating in NSTX showed that while the electron ITB was most closely associated with the region of maximum negative magnetic shear, the ion ITB was displaced from that location, and was more closely associated with the region of maximum  $\vec{E}_r \times \vec{B}$  shear (Fig. 2.35 taken from Ref. [2.386]). Experiments on DIII-D have shown the formation of ITBs in the presence of Alfvén eigenmodes [2.387]. Redistribution of fast ions due to these modes serves to reduce or reverse the central magnetic shear. In addition to that, the  $E_r$  generated by this redistribution can induce a sheared  $\vec{E}_r \times \vec{B}$ , aiding the formation of the ITB.

It was also found that transient improvements in local confinement could be triggered by the appearance of integer or low order rational  $q$ -surfaces in the plasma [2.211]. These incipient ITBs could develop further and be maintained only in the presence of other effects, such as  $\vec{E} \times \vec{B}$  or negative magnetic shear.

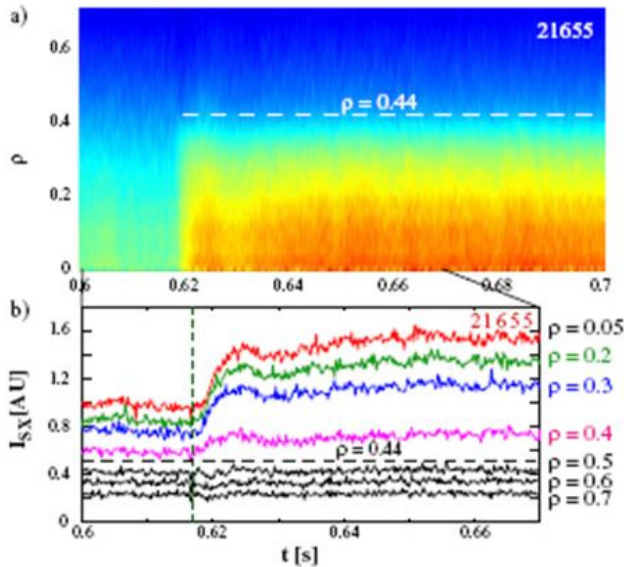


FIG. 2.34. (a) Temporal evolution of the line integrated soft X ray emission across the plasma cross-section. (b) Close-up at selected values of  $r$  during the ITB transition. The barrier foot is at  $\rho = 0.44$ . Taken from Ref. [2.385].

Analysis of a large collection of data from a 0-D ITB database confirmed the existence of a threshold power for ion ITB formation that scales as [2.376]

$$P_{th} \approx n_e^{0.9} a^{2.13} \kappa_{95}^{1.34} (0.2 + \delta_{95})^{-0.15} B_\phi^{0.23} \quad (2.124)$$

(where  $\kappa_{95}$  and  $\delta_{95}$  are the elongation and triangularity at the 95% flux surface) with the power threshold decreasing with more centrally peaked power deposition. Data from JT-60U, JET, DIII-D and ASDEX-U fit this scaling quite well. In contrast, the power threshold for electron ITBs shows a weak dependence on  $n_e$  but a strong dependence on  $1/q_{95}$ , and it is not as well defined as that for ion ITBs. The power threshold can be reduced by the presence of low order rational  $q$ -surfaces.

While the width of the ITB can vary, and an ITB is typically defined as such when  $\rho_{*T} > 1.4 \times 10^{-2}$  for conventional aspect ratio tokamaks, there is some evidence from JT-60U and TFTR that it can be comparable or proportional to the ion poloidal Larmor radius.

Improvements to the core confinement, as evidenced not only by profile peaking, but by large decreases in the transport coefficients, are associated with ITBs. This is shown in Fig. 2.36, taken from Ref. [2.376], which indicates a sharp drop in  $\chi_i$  and  $\chi_e$  in the region of strong  $\nabla T_e$  and  $\nabla T_i$ . In this case,  $\chi_i$  was comparable to the neoclassical value of ion heat diffusivity; in TFTR,  $\chi_i < \chi_{i,neoclassical}$ . Furthermore, in some cases,  $\chi_e < \chi_{gyro-Bohm}$  [2.384]. As can also be seen in the figure, the region of strong temperature gradients occurs in the localized region where  $s \leq 0$  and where the  $\vec{E}_r \times \vec{B}$  shear is the greatest.

Theoretical approaches to understanding ITB formation have focused on common characteristics across the different devices. These are that ITBs are associated with certain classes of  $q$ -profiles, namely ones with reversed or weak magnetic shear, and profiles with low order rational- $q$ -surfaces present. ITBs are also associated with  $\vec{E}_r \times \vec{B}$  flow shear. The favourable magnetic shear profiles can be produced by driving current externally or by redistribution of the current driven by fast particles that are interacting with Alfvén eigenmodes. This latter mechanism also produces sheared  $\vec{E}_r \times \vec{B}$ . These relationships suggest strongly that ITBs are produced through suppression of microturbulence, and this hypothesis has been supported by numerical and analytical theory calculations (see Ref. [2.376] and references therein, and Ref. [2.388]). These have shown ITB formation through stabilization of ion temperature gradient (ITG) modes via  $\vec{E}_r \times \vec{B}$  shear, leading to  $\chi_i \sim \chi_{i,neoclassical}$  [2.389]. ETG turbulence that can induce electron transport is strongly stabilized by negative magnetic shear. The role of TEMs is less clear; it has actually been suggested that TEMs driven unstable by peaked density profiles (large  $\eta_e = \partial \ln T_e / \partial \ln n_e$ ) can lead to the collapse of ITB [2.388].

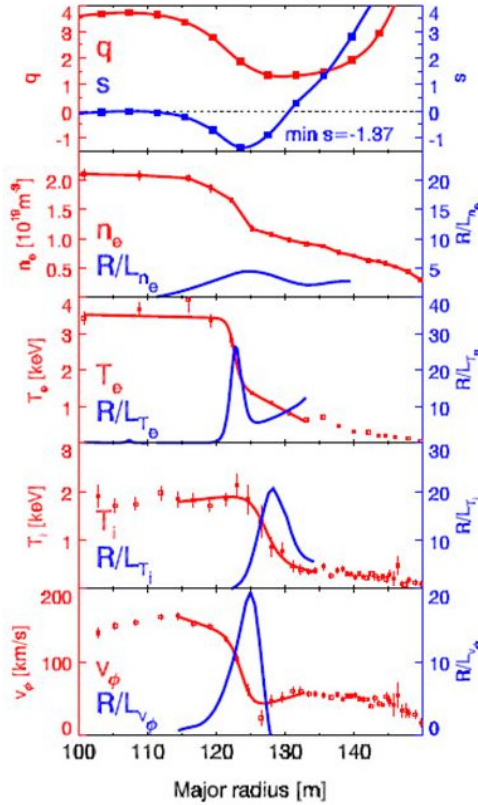


FIG. 2.35. The  $q$ ,  $n_e$ ,  $T_e$ ,  $T_i$  and  $v_\phi$  profiles and their normalized gradients from NSTX. Reprinted from Ref. [2.386].

ITBs have been observed also in non-axisymmetric (helical) devices (see Refs [2.390, 2.391] and references therein). A transition to a strongly peaked electron temperature profile regime was found in LHD when ECH power, above a threshold, was injected into a low density, counter-NB sustained discharge [2.390]. The  $T_e$  peaking was accompanied by a large positive radial electric field in the core, which is interpreted as a transition to the “electron root” regime. In this regime, the positive  $E_r$  is needed to preserve ambipolarity; in the absence of this field, the electron flux would exceed the ion flux ( $\Gamma_e > \Gamma_i$ ). This regime has therefore been dubbed the core electron root confinement (CERC) regime.  $T_e$  is peaked in the centre of these discharges, even in the absence of significant  $\vec{E}_r \times \vec{B}$  shear. In tokamaks, the  $T_e$  profile is flat in the very core where the  $\vec{E}_r \times \vec{B}$  shear is small. It is suggested that the strong  $E_r$  in the very core maintains the  $T_e$  peaking in the helical systems through a reduction of the collisional damping of large scale zonal flows, which are more important in this region in helical, than in tokamak, systems. Non-local transport was also recently observed in helical plasmas, with

core  $T_e$  increases associated with rapid edge cooling. This observation suggests, in contradiction to what was suggested earlier, that it is not the current that is necessarily a dominant off-axis term for energy transfer, but possibly large scale (low  $k_r$ ) fluctuations.

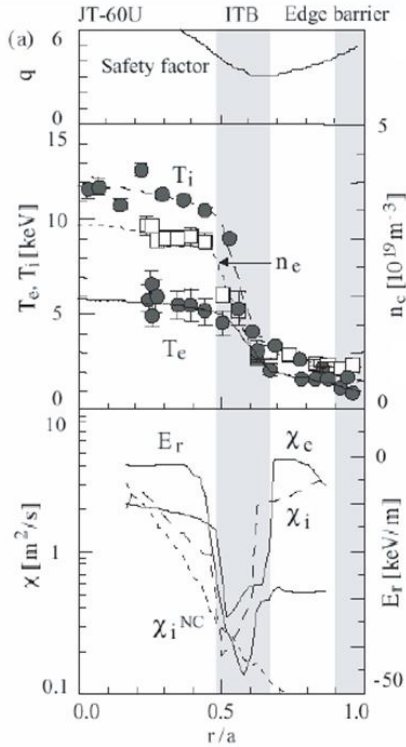


FIG. 2.36. Safety factor,  $T_e$ ,  $T_i$ ,  $n_e$  and thermal diffusivity profiles from JT-60U ITB discharge. The barriers are formed just inside the  $q_{min}$  radius. Taken from Ref. [2.376].

As previously discussed, ITBs can benefit fusion power production if their inherent transient nature and lower global stability limitations can be overcome. Development of steady state ITBs is necessary in order to make this regime relevant to long pulse burning plasma scenarios. The keys to doing this are to: (1) overcome the lower global  $\beta$ -limit in these plasmas; and (2) employ careful real-time tailoring of the current profile (which can aid the global stability limits as well), which means external control of at least one current drive scheme.

To avoid low global  $\beta$ -limits and increase the ITB plasma pulse length,  $\beta$  can be controlled directly using feedback on the neutron rate or diamagnetic flux, which has been accomplished in TFTR, JET and JT-60U. Another method to accomplish this is to form an ITB in steady H-mode plasmas, resulting in plasmas with two barriers, one in the core and one at the edge. This has been accomplished

in TFTR, JET, JT-60U, DIII-D and ASDEX-U. In particular, double barrier discharges have been produced in both D-D and D-T plasmas in JET, with the D-T double barrier plasmas being the basis for sustaining high fusion yield for several energy confinement times [2.392]. Use of LHCD during current rampup and flattop has yielded fully non-inductive double barrier plasmas [2.393]. Fully non-inductive double barrier plasmas with an 80% bootstrap fraction have been achieved in JT-60U, with the barriers being maintained for up to six energy confinement times [2.394]. With more externally driven current (e.g. LHCD, NBI) and less bootstrap drive, double barrier plasma durations in JT-60U for up to 9 s (50 energy confinement times) were achieved. Other steady ITB scenarios include the quiescent double barrier (QDB) regime in DIII-D [2.395], the LHEP regime in Tore-Supra using LHCD alone [2.396], and a steady regime for 300 energy confinement times with 80% bootstrap current in TCV [2.397]. Processes limiting these long-pulse double barrier modes include neoclassical tearing mode (NTM) and resistive wall mode (RWM) MHD instabilities. The former can be controlled through localized current drive in an island,  $\beta$ -control or plasma rotation, while control of the latter has been accomplished through use of feedback control systems utilizing external mode sensors and field application coils. Impurity accumulation is also a potential limiting factor in any long-pulse discharge. A detailed discussion of these issues can be found in Ref. [2.376].

#### 2.5.5.2. Edge

As discussed in the previous section, the temperature gradient in the mid-region of the plasma is often determined by the condition of marginality to transport inducing microinstabilities, leading to profile stiffness. Just how high the temperature reaches in a stiff regime is then dependent on the boundary temperature; the higher the boundary temperature, the higher the central temperature for fixed gradient. A characteristic of H-mode plasmas is the edge pedestal in either or both the density and temperature. Just outside the top of these pedestals are steep gradients in the profiles, reflecting a sharp reduction in transport in this region, and these form what has been termed edge transport barriers (ETBs). The temperatures at the top of the ETB (or pedestal) serve as boundary conditions for the temperature profile inside under the condition of profile stiffness. Consequently, it is important to understand the characteristics of the pedestal (e.g. height and width), if not its underlying physics, in order to predict performance with confidence in future devices. Good recent reviews of ETBs can be found in Refs [2.398, 2.399], and the discussion here is based on the details presented in these articles. ETBs have also been observed in stellarators [2.252, 2.400], most notably at very high density ( $> 1 \times 10^{20} \text{ m}^{-3}$ ).

The ETB occurs just inside the last closed flux surface (LCFS), and it is believed to be formed by the reduction of plasma turbulence due to enhanced

$\vec{E}_r \times \vec{B}$  shearing in that location. Various specific theories have been tested against experimental data to explain the L-H transition as well as the formation of the ETB, which occurs simultaneously, to within measurement uncertainties, with the drop in the  $D_\alpha$  emissivity that reflects the transition. Such theories include drift-resistive MHD ballooning modes [2.401], peeling modes [2.402], drift-Alfvén turbulence [2.403] and finite  $\beta$ -drift waves [2.280].

The studies have specifically tested whether the plasma conditions just prior to the L-H transition could lead to stabilization of the respective instabilities. While agreement was found with some theories on some devices, several counter-examples were found for each of these theories [2.399]. In addition, it was found that while the testable parameters in these theories could distinguish between L- and H-mode plasmas, there was no consistent predictive capability [2.282].

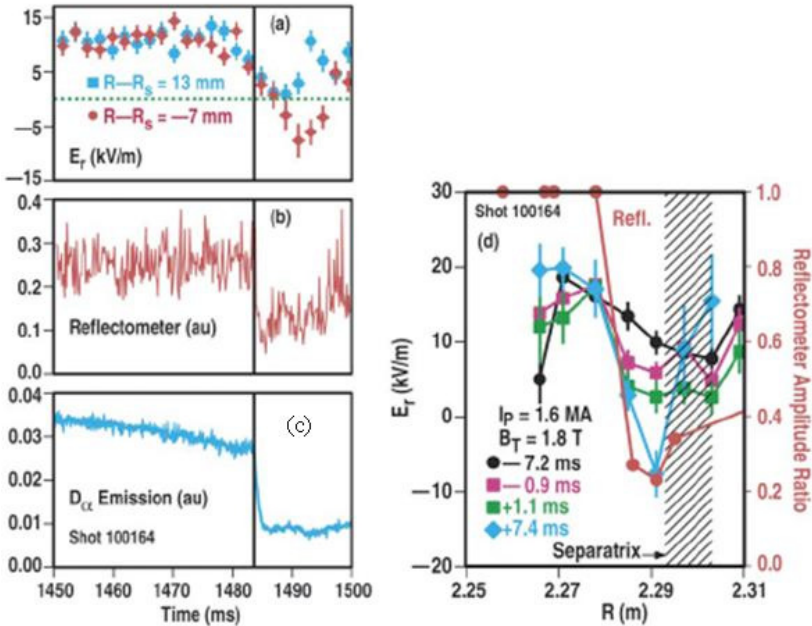


FIG. 2.37. Temporal and spatial changes in several edge quantities at the formation of an ETB in DIII-D. (a) radial electric field  $E_r$ , (b) density fluctuation, (c)  $D_\alpha$  emission, (d)  $E_r$  and density fluctuation profiles at the plasma edge. Reprinted from Ref. [2.404], copyright (2010), American Institute of Physics.

Since the “static” plasma parameters themselves could not account for the turbulence stabilization, attention turned to studying the radial electric field and  $\vec{E}_r \times \vec{B}$  shear characteristics in the edge region. Detailed measurements of the edge in DIII-D have provided a wealth of information on the role of  $E_r$ , as is seen in Fig. 2.37, which is reprinted from Ref. [2.404]. The  $E_r$  just inside and

just outside the LCFS starts to decrease just prior to the L-H transition, which is shown by the vertical line in Figs 2.37(a)–(c). The decrease prior to the transition is not universally observed. At the transition, the density fluctuations reflecting the microturbulence at the edge decrease as the large shear in the radial electric field develops (Fig. 2.37(d)). The  $\vec{E}_r \times \vec{B}$  shearing rate is generally determined to be greater than the turbulence decorrelation rate, which is considered to be a necessary condition for turbulence suppression. Causality between the change in  $E_r$ , the turbulence suppression and the L-H transition was established through experiments in which an electric field was externally applied in the plasma edge through electrodes (see references in [2.398]). The origin of the sheared flows, however, is still not known, but it is believed to be related to large scale zonal flows ( $n = 0, m = 0, \omega \sim 0$ ) or geodesic acoustic modes ( $\omega > 0$ ), which exist in L-mode plasmas.

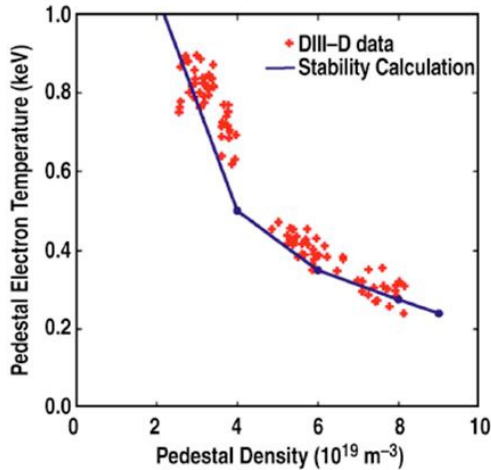


FIG. 2.38. Comparison of pedestal stability limit calculated with ELITE from DIII-D data as a function of pedestal density [2.254].

The temperature and density gradients of the ETB itself have been found to be consistent with limits set by the intermediate wavenumber ( $n = 6-8$ ) peeling-ballooning mode [2.254]. An example of this is shown in Fig. 2.38, where it is seen that the temperature and density at the top of the pedestal agree with predictions from the peeling-ballooning stability analysis. Because the gradient is fixed by this instability, the pedestal values of temperature and density, and the pedestal width, are inexorably tied. In practice, due to measurement limitations, it can be difficult to resolve pedestal widths, as they can be narrow, ranging from 0.5 cm to several cm. The peeling-ballooning mode also sets the threshold for edge localized modes (ELMs); once beyond the critical gradient, an ELM will occur, which will relax the gradient as a result of a sudden loss of particles and

energy. The gradient will then build back up to the critical value before the next ELM occurs.

As it appears the gradient in the ETB is set by the peeling-ballooning limit, although some work has suggested that the limit is set by low- $n$  kink modes [2.253], understanding the processes controlling either the pedestal height or width allows a determination of the other. Neither the parameterization of these variables nor an understanding of the underlying physics has yet been resolved, however. Of particular importance is how the ETB scales with ion poloidal gyroradius,  $\rho_i$ , which will allow a direct test of several theories, and is the parameter for which there is the largest extrapolation from present day operating regimes to those in future burning plasma experiments. Single parameter scans and cross machine comparisons [2.398, 2.405] were not able to identify any consistent change of the transport barrier width or height with  $\rho_i$ . Additional work to determine a dependence on this important parameter is under way. Similar inconclusive results have been found with the dependence with respect to neutral density and penetration. On the other hand, it was found that the pedestal height could be increased by operating at higher  $\beta_\theta$  through operation at higher power; this is due to an increase in Shafranov shift at higher  $\beta_\theta$ , which increases the pedestal stability limit [2.398]. The pedestal width has also been found to increase with increasing  $\beta_\theta$ , reflecting an increase in ion temperature. Plasma shape has significant effects on the ETB height; for instance, higher triangularity is more stabilizing, allowing for higher pedestal pressure. Subtle changes in plasma squareness, a higher order shape parameter, can have a large (>30%) effect on pedestal height, as is seen in Fig. 2.39, taken from Ref. [2.406]. Furthermore, higher pedestal pressures were obtained in configurations with favourable ion  $\nabla B$  drift direction (towards the dominant X-point) due to higher density. Finally, toroidal field ripple also has a significant impact on pedestal pressure; increased ripple,

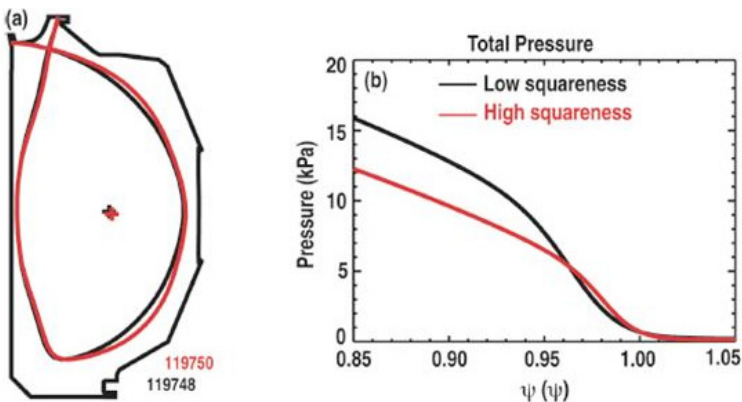


FIG. 2.39. Modest change in discharge shape squareness (a) produces a significant change in the pedestal pressure profile in DIII-D [2.406].

which is associated with increased counter-rotation and ion orbit loss, resulted in lower density due to higher frequency ELMs, and thus led to a reduction in pedestal pressure. A truly quantitative understanding of the pedestal height and width scaling is yet to be established, but it is being worked on actively.

### 2.5.6. Comparison with theoretical models

The focus of most of the comparisons between experiment and theory has been with respect to electrostatic models, although more recently finite- $\beta$  effects, and directly relating experimentally inferred transport to electromagnetic models in some situations, have been studied. The electrostatic models include long wavelength ( $k_\theta \rho_s \sim 0.1-1$ ) turbulence driven by ion temperature gradients (ITG modes), trapped electron modes in the presence of strong density gradients (TEM) and short wavelength ( $k_\theta \rho_e \sim 0.1-1$ ) modes driven by electron temperature gradients (ETG modes). A simple assessment of the stability of these modes had been made by examining the parameter  $\eta = \partial \ln n / \partial \ln T = L_n / L_T$ , where  $L_{n,T}$  are the scale lengths for the density and temperature profiles respectively. For  $\eta > \eta_{crit}$ , the mode was expected to be unstable. Typically,  $\eta_{crit} \sim o(1)$ . In the case of flat temperature profiles,  $\eta \rightarrow \infty$  and a more relevant parameter to assess the linear stability of various electrostatic modes is the normalized gradient,  $R/L_T$ . An early example of using this metric to assess stability characteristics is from Alcator-C. Pellet injection in Alcator-C resulted in improvements in OH confinement accompanied by a reduction of ion thermal diffusivity to neoclassical levels. A result of the pellet injection was a peaking of the density profile, and thus a reduction in  $\eta_i$ . It was suggested that  $\eta_i$  decreased to values below the critical value for ITG modes, leading to their suppression [2.407].

Comparisons between experiment and theory have been made on several levels. The first is by examining the parametric dependence of the thermal diffusivity and relating this to a particular instability or to a class of instabilities. The second is by direct modelling of the experiment using numerical or analytical procedures. Early attempts at the former have been described earlier in this chapter, and they have been inconclusive. Some insight into the physics controlling the transport was achieved, however, through examination of the dependence of  $\chi_i$  and  $\chi_e$  on dimensionless variables. One prime example of this is from experiments on DIII-D, where the scaling of transport coefficients on the normalized gyroradius,  $\rho_*$ , was studied in pairs of discharges in which the other dimensionless parameters such as  $\nu_*$  and  $\beta$ , and their profiles, were held fixed [2.408]. In dimensionless form, the thermal diffusivity can be described as

$$\chi = \chi_B \rho_*^x F(\nu_*, \beta, q, T_e/T_i, \alpha_n, \alpha_T \dots) \quad (2.125)$$

where  $\chi_B = cT_e / (eB)$  and  $\alpha_{n,T}$  represent the density and temperature profile peaking factors. For the exponent  $x = 1$ , the turbulence scale length is proportional to  $\rho_*$ , and transport under this condition is described as gyroBohm. For  $x = 0$ , the turbulence scale length is device size dependent,  $\propto a$  (the device minor radius), and the transport is described as Bohm. The DIII-D L-mode discharges used for this study found that while  $\chi_e$  scaled as gyroBohm,  $\chi_i$  scaled as Bohm or worse. This was also found for H-mode discharges [2.409].

Understanding these results and tying them into first principles physics models was accomplished by using either flux-tube or global gyrokinetic simulations [2.131, 2.410, 2.411]. It was shown in this work that Bohm-like transport driven by ITG modes was expected for the ions in both L- and H-modes in present day devices. The calculations were carried out using both GTC [2.131] and GYRO [2.410, 2.411]. Common to these calculations was the importance of self-consistent zonal flows, whose turbulent eddy shearing action was the dominant turbulence saturation mechanism. The work in Refs [2.410, 2.411] also pointed out the importance of including kinetic electrons, collisions and finite- $\beta$  effects. In order to match the experimentally inferred ion and electron thermal diffusivities quantitatively for these cases, it was necessary to reduce the input  $\nabla T_i$  by about 12%, which was well within measurement uncertainty.

ITG modes were also the basis for a quantitative understanding of ion transport in L-modes and supershots in TFTR [2.412, 2.413]. In Ref. [2.412] it was shown that ITG-based,  $\chi_i$  parameterizations, interpolated from non-linear gyrofluid simulations, led to excellent agreement between measured and predicted ion temperature profiles for both modes. The higher ion temperatures in supershots, where the central ion temperatures reached nearly 30 keV as compared to  $<5$  keV for L-modes, were attained due to higher boundary temperatures in supershots than in L-modes. Profile stiffness allowed the  $T_i$  to increase and pull away from  $T_e$ . Higher values of  $T_i / T_e$  then exerted a stabilizing influence on ITGs, allowing the ion temperature to increase even further. Also discussed in this work was the stabilizing influence of magnetic shear, high values of which were achieved in discharges with peaked current profiles. The work of Ref. [2.413] showed the importance of sheared flows in being able to reproduce measured  $T_i$  and  $T_e$  profiles in supershots within the ITG framework. The role of ITG modes in pre-ITB and ITB plasma on C-Mod was studied using GYRO, and these results also suggested the dominance of these modes in reproducing the experimentally inferred transport levels and measured fluctuation spectra to within experimental uncertainty [2.414]. A review of these and other results can be found in Ref. [2.415] and references therein.

Closely related to the level of ion energy transport in conventional aspect ratio tokamaks is the level of momentum transport. The understanding of the source of momentum transport is important since plasma rotation plays a critical

role for optimizing performance in magnetic confinement devices through shear stabilization of both the microturbulence that is associated with energy transport and macroscopic magnetohydrodynamic (MHD) instabilities. Similar to the ion thermal diffusivity in these devices, the momentum diffusivity, as determined from steady state momentum balance assumptions, is anomalous (higher than neoclassical), but its magnitude is roughly comparable to that of the ion thermal diffusivity to within a factor of two to three. This agreement is expected from theoretical predictions that are based on electrostatic drift wave turbulence, namely ITG and TEM modes [2.159, 2.416]. Further observations of rotation in plasmas with no identifiable torque [2.165], such as that from neutral beams, has challenged momentum transport theory to explain the source of this so-called “intrinsic rotation” and the transport of momentum associated with it (i.e. an inward momentum pinch). Gurcan et al. [2.176] have identified a possible edge source for the intrinsic rotation, the “residual stress”, which has to do with pressure gradients at the plasma edge leading to  $\vec{E} \times \vec{B}$  rotation. The edge rotation is then transported inward radially by a non-diffusive mechanism that could arise from either ITG or TEM modes, or both [2.171, 2.175]. This inward momentum pinch can achieve radial speeds of up to several tens of  $\text{m}\cdot\text{s}^{-1}$ , which can have approximately a factor of two influence on the value of momentum diffusivity determined from steady state power balance considerations. Evidence of this inward pinch has been seen in devices with and without external torque.

The paradigm in which ITG modes, whose turbulent transport level exceeds that of neoclassical transport in conventional aspect ratio L- and H-modes, is violated at low aspect ratio. In low aspect ratio, or spherical tokamak (ST) devices such as NSTX and MAST, operation with NBI at the low operating toroidal fields (as little as 10% of that at higher aspect ratio) leads to large  $\vec{E}_r \times \vec{B}$  shearing rates and inferred ion transport levels that are comparable to those predicted by neoclassical theory [2.260, 2.305]. Linear and non-linear gyrokinetic analyses indicate that these shearing rates are large enough to suppress ITG-driven transport to levels less than those given by neoclassical transport, consistent with the experimental inferences. There are indications from momentum transport studies that residual low- $k$  turbulence driven momentum transport still exists, but it is subdominant to neoclassical for thermal transport [2.292].

The modulated ECH experiments performed in ASDEX-U, DIII-D and Tore-Supra, described earlier in this chapter, provide a localized source of electron heating and thus serve as a basis to study the source of electron transport in electron heated regimes. These experiments indicate that there is enhanced transport when the electron temperature gradient exceeds a critical value. In ASDEX-U, the scaling of the threshold and transport point to the TEM mode being the underlying cause [2.141]. Above the critical value of  $R / L_{Te} \sim 1.5$  (see Fig. 2.32), the linear growth rate of the TEM, which is given by the solid line in the top portion of the figure, increases in concert with the electron heat flux.

Furthermore, the transport decreases with increasing collisionality, consistent with a reduction in TEM drive due to collisional detrapping of electrons. Modelling of the electron response to modulated ECH in DIII-D shows better agreement between experiment and models that contain TEM physics than with those that do not [2.417].

In Tore-Supra [2.375], the critical gradient for enhanced electron transport was found to be independent of density, but it was strongly dependent on the quantity  $s/q$ , consistent with expectations from electromagnetic ETG theory. However, linear theory suggested that above the critical gradient the TEM instability dominated. The importance of ETG in driving electron transport was further shown in Ref. [2.386] for NSTX ITB plasmas. In this low aspect ratio regime, where ITG modes are believed to be suppressed by strong  $\vec{E}_r \times \vec{B}$  shear, strong linkages among high- $k$  turbulence measurements, profile stiffness, inferred transport levels and linear gyrokinetic calculations, and their dependence on magnetic shear, are consistent with ETG-driven transport with finite- $\beta$  effects.

At low aspect ratio, other sources of electron transport, with electromagnetic components, are also possible. One is microtearing modes, which are believed to be important only at the edge at conventional aspect ratio but can be important in the core of an ST within a range of collisionality and electron temperature gradient. Agreement was found between theoretical expectations and inferred transport levels in NSTX hybrid discharges [2.418]. In addition, it has been suggested that high frequency global Alfvén eigenmodes, driven by super-Alfvénic fast ions, can cause electron transport in the core region of NSTX, where the electron temperature profile can be flat and where  $\nabla T_e$ -driven modes are stable [2.419]. Supporting calculations show that the inferred levels of electron transport in this region are consistent with levels of transport predicted by theory using estimates of mode amplitudes based on interferometric measurements. Clearly, much work remains to be done to identify the source(s) of electron transport and under what conditions various modes dominate.

## 2.6. TURBULENCE MEASUREMENTS

Arguably the weakest link in the full understanding of turbulent transport, and the most important, is the area of detailed turbulence measurements. Turbulence is extremely difficult to measure in the unforgiving environment of the interior of tokamak plasmas, but it is just this turbulence that is believed to be the underlying cause of anomalous transport, so detailed measurements provide the most direct tests of theory. In this section we overview the techniques that have been applied to turbulence measurement in the core of tokamak plasmas and the results that have been obtained. For more depth a recent review [2.420] as well as prior reviews [2.421] are recommended.

### 2.6.1. Measurement techniques

It is possible to insert material probes into the scrape-off-layer (SOL) and the edge of the confinement zone of tokamaks, which can then be used to measure density, temperature, potential, perturbed magnetic fields, and even flows [2.422]. In high power plasmas, these probes need to be plunged and extracted quickly, to prevent overheating. Nonetheless it is possible to measure the properties of edge and SOL plasma turbulence in remarkable detail, including such interesting features as correlations between fluctuating quantities and the poloidal variation of fluctuation amplitudes.

Fluctuations in the core of hot plasmas require more indirect measurement techniques. Beams of microwaves or of far infrared light are injected into plasmas and either scattered or reflected off of the ambient turbulence. Indeed new techniques have been developed, called Doppler backscattering, that combine some features of each of these. In all cases the emerging light is shifted in frequency by the turbulence, and either spatial or wavenumber information about the turbulence, or in some case both, can be deduced.

In addition to probing plasmas with electromagnetic waves, particle beams have been used effectively to measure turbulence. Singly charged heavy ion beams can be accelerated to the MeV range, and cross the magnetic fields of moderate-size tokamaks. As they traverse the plasma they can become doubly ionized, and then leave on tighter orbits, carrying with them information on the local density and electric potential. More commonly, as the  $\sim 100$  keV neutral deuterium beams often used for plasma heating traverse a plasma they are collisionally excited and emit  $D_\alpha$  radiation proportional to the fluctuating local plasma density.

Some established temperature measurement techniques can be enhanced to measure fluctuating ion and electron temperatures. Charge exchange recombination spectroscopy is based on charge transfer from  $\sim 100$  keV neutral deuterium atoms to, for example, fully stripped carbon ions. It is possible to determine the fluctuation in the temperature of the carbon ions from very high throughput measurements of the light spectrum emitted as captured electrons fall to lower excitation states. High throughput optics cannot be used in an analogous manner to enhance the time resolution of electron temperature measurements of electron cyclotron emission, due to photon statistics at long wavelengths, and correlation techniques, looking at slightly different frequencies, are used for this purpose.

#### 2.6.1.1. Probe techniques

Electrostatic probes can be inserted into the SOL and edge of tokamak plasmas, and used to measure a number of plasma parameters [2.421]. If the

probe tips are held at relatively high steady negative potential, they will gather the ion saturation current, which depends most sensitively on the fluctuating plasma density. If a triple probe is utilized, information can be gathered on the fluctuating electron temperature and floating potential as well. Closely spaced probes can be used to measure fluctuating electric fields. More widely spaced probe arrays can be used to measure the poloidal and toroidal structure of turbulence, something which is particularly difficult to achieve with other techniques.

### 2.6.1.2. Electromagnetic wave scattering

In some ways the most powerful technique for measuring turbulence is scattering of electromagnetic waves [2.423]. A collimated beam (yellow in Fig. 2.40) is injected into the plasma, and encounters turbulent density fluctuations (orange region). The beam is scattered coherently off of the turbulence, and radiation is emitted from the plasma (pink) with wave angular frequency  $\omega_s = \omega_i + \omega$  and wavenumber vector  $\vec{k}_s = \vec{k}_i + \vec{k}$ , where the subscripts  $i$  and  $s$  stand for incident and scattered waves respectively.

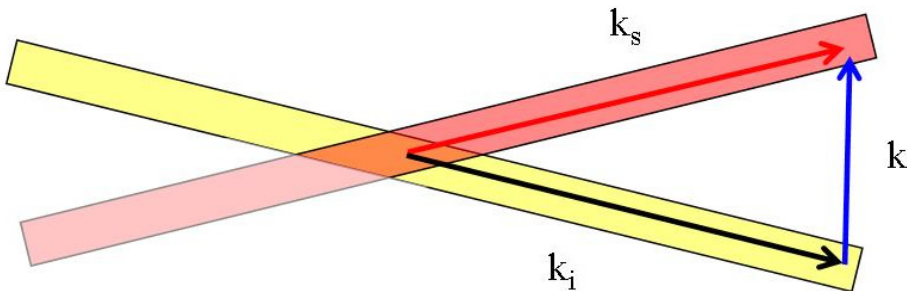


FIG. 2.40. In wave scattering measurements, incident radiation (yellow) scatters off of turbulence in orange region, giving rise to scattered radiation (pink).

The incident radiation, either microwave or far infrared, is generally chosen to be at least in the range of hundreds of GHz ( $k_i = 62 \text{ cm}^{-1}$  at frequency  $f = 300 \text{ GHz}$  and wavelength  $\lambda = 1 \text{ mm}$ ) to assure propagation in the plasma without too much refraction. Since tokamak plasma turbulence is generally found in the range of 1 MHz and below, the scattered and incident radiation are nearly at the same frequency, and thus at nearly the same wavenumber. As a result, the incident wavenumber vector,  $\vec{k}_i$ , and scattered wavenumber vector,  $\vec{k}_s$ , form nearly an isosceles triangle with the turbulent wavenumber vector,  $\vec{k}$ . If the detected signal is mixed with a frequency shifted from the incident wave frequency (heterodyne detection) the sign of  $\omega$  can be determined, so the direction of turbulent wave propagation can be measured.

A problem with this technique is that with 1 mm or smaller wavelength incident beam, and typical  $k \sim 1 \text{ cm}^{-1}$  for ion-scale turbulence, the scattering angle between  $\vec{k}_i$  and  $\vec{k}_s$  is very small. This results in a highly extended region of overlap between the incident beam and the region of sensitivity of the detector, the orange parallelogram in Fig. 2.40. If the incident and scattered beams are in the same poloidal plane, then this parallelogram can include most of the plasma radius. A means to ameliorate this problem, developed recently [2.424], is to inject the incident beam in the toroidal direction, and arrange for the scattering region to be located where the beam is tangent to the toroidal magnetic field, putting its extended direction along the ignorable coordinate. Further advantage is accrued from the fact that the turbulence is known to have very low  $\vec{k}_{\parallel}$ , with the result that the matching condition is necessarily violated at the ends of the parallelogram.

### 2.6.1.3. Electromagnetic wave reflectometry

Instead of scattering electromagnetic waves off of turbulent structures in a plasma, one can also reflect such waves off of a surface where the wave is cut off [2.425]. Ordinary waves are reflected at the location in the plasma where the electron plasma frequency rises to equal the wave frequency,  $\omega_{pe} = \omega$ , and extraordinary waves are reflected where the right-hand cut-off rises to the wave frequency,  $\omega_{ce} + (\omega_{ce}^2 + 4\omega_{pe}^2)^{1/2} / 2 = \omega$ , where  $\omega_{ce}$  is the electron cyclotron frequency. With extraordinary waves it is possible to probe the high-field side of the plasma, while launching from the low-field side. The usual arrangement is to propagate waves directly to the cut-off layer, and measure the directly reflected radiation. In a simple, non-turbulent situation, it can be shown that the phase difference between the incoming and outgoing waves is given by the usual WKB integral,  $\Delta\varphi = \int k dl$ , with an additional factor of  $\pi$ . This factor arises where the WKB approximation breaks down near the cut-off, as  $k \rightarrow \infty$ . Thus by tracking the variation in the phase difference  $\Delta\varphi$  one can, in an idealized case of a perpendicular surface moving back and forth in front of the beam, track the turbulent velocity of the cut-off layer. Most of the variation in  $k(l)$  arises near the cut-off layer itself, so this measurement should in principle be well localized.

While the technique of reflectometry is relatively straightforward, its interpretation is in general problematic. Indeed in the turbulence regime of tokamaks, where  $\delta n / n \sim (k_{\perp} L_n)^{-1}$ , the turbulent cut-off surface forms angles of order one radian with respect to the equilibrium cut-off surface, and the situation becomes akin to shining a flashlight on moving, crumpled tin foil, far from the idealized case of a flat surface moving back and forth in front of the beam (see Fig. 2.41). The deeply non-linear inversion problem has not yet proved to be tractable, except in the case of very low turbulence levels.

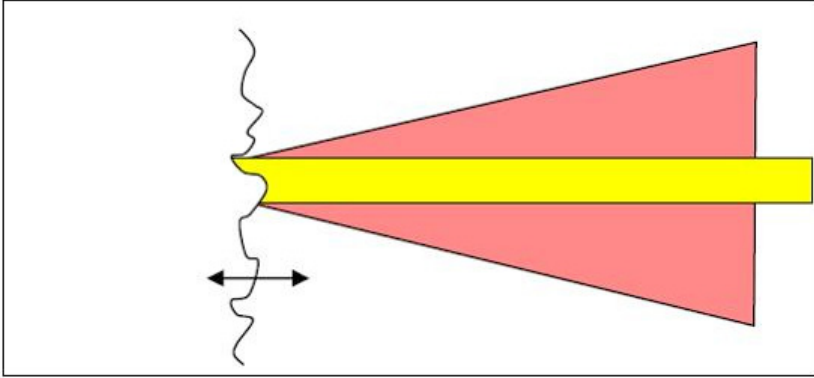


FIG. 2.41. In reflectometry measurements incident (yellow) radiation is reflected from a cut-off in the plasma. With  $\delta n/n \sim (k_{\perp} L_w)^{-1}$ , however, the reflected radiation (pink) is broad, complex and difficult to interpret due to strong variation of the turbulent surface's angle with respect to the incoming radiation.

One technique that avoids some of the complexity of interpretation is to measure the correlation between the reflected signals at two different radii, with the idea that this will provide at least a measure of the radial correlation length of the plasma turbulence.

#### 2.6.1.4. Electromagnetic wave Doppler backscattering (DBS)

A technique has been developed recently [2.426] which in effect takes advantage of some aspects of both reflectometry and scattering. As shown in Fig. 2.42, a beam of microwaves in the O- or X-mode enters the plasma at an oblique angle  $\theta$ , with the idea that it will turn parallel to its cut-off layer as it approaches, and then travel in the plasma close to the layer, maximizing the scattering signal from this localized region. In plane geometry the incident radiation wavenumber in the plasma near the cut-off layer is reduced by  $\sin \theta$  compared to its launch value,  $k_0$  (see Fig. 2.42). Since this technique depends on  $180^\circ$  backscattering towards the source of the incident radiation, the probed wavelength is then  $k_{\perp} = 2k_0 \sin \theta$ . In the non-planar geometry encountered in actual experiments, ray tracing is used to determine  $k_{\perp}$  at the cut-off layer. The amplitude of the scattered power depends on the fluctuation level at  $k_{\perp}$ , and the frequency shift provides a direct Doppler measurement of the propagation velocity of the measured turbulence.

The use of different frequencies of incident radiation allows radial profiles of turbulence and flow, including turbulence-driven flows, to be measured, and correlation lengths to be determined. The use of different wave injection angles allows different  $k_{\perp}$ 's to be probed, and to check whether the apparent propagation velocity is independent of  $k_{\perp}$ .

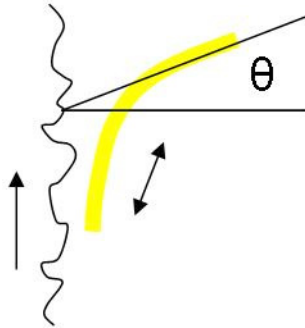


FIG. 2.42. In Doppler backscattering measurements, incident radiation is directed at a plasma cut-off layer where it turns parallel to the layer.  $180^\circ$  backscattering provides a localized measurement of turbulence intensity and phase velocity for  $k_\perp = 2k_0 \sin \theta$ .

A somewhat more complex backscattering technique [2.427] has been developed using the upper hybrid resonance. At resonances  $k \rightarrow \infty$ , and rays turn towards the resonance layer where they are amplified in intensity, so this technique provides enhanced access to short wavelength instabilities, albeit requiring complex interpretation.

#### 2.6.1.5. Phase contrast imaging (PCI)

In phase contrast imaging [2.428], a laser beam of finite width is passed through the plasma. Each part of the beam undergoes phase shift proportional to the line integral of the density it traverses. By arranging to shift the phase of the light from the centre of the beam after it exits from the plasma by  $\pi/2$  and then mix this light with the rest of the exiting beam, the small phase variation across the beam is transformed to an intensity variation. With a sufficiently large number of closely spaced detectors, it is possible to measure quite short wavelength instabilities. A weakness of this technique is that it is a line-integrated measurement. Some spatial resolution can be obtained, however, by recognizing that phase variations due to instabilities in the plasma are expected to be field-aligned. Thus the rotation of the poloidal magnetic field along a vertical chord can be used to provide a degree of spatial localization [2.429].

#### 2.6.1.6. Heavy ion beam probe (HIBP)

The heavy ion beam probe [2.430] depends on accelerating a tightly collimated beam of singly charged heavy ions, such as thallium, to high energy, typically in the range up to several MeV. For moderate-size tokamaks the gyroorbits of these ions are greater than the plasma cross-section, so the ions can travel directly into the plasma from the accelerator. As these singly charged

ions travel through the plasma, however, some undergo a second ionization, and then exit the plasma on a tighter orbit. An electrostatic energy analyser and ion detector designed to accept doubly charged ions from a short segment of the initial orbit can measure the intensity and energy of the exiting ions, giving measurements of the plasma density and potential, and their fluctuations, at the second ionization location. With proper design the beam and detector properties can be swept to cover a significant fraction of the plasma cross-section. This technique suffers from providing only a single-point measurement without very fine spatial resolution, but its interpretation is relatively direct [2.431]. With detectors capable of measuring two points along the incident trajectory, it provides a very powerful method for detecting the radial electric fields associated with flows, including those driven by the plasma turbulence.

#### 2.6.1.7. Beam emission spectroscopy (BES)

Beam emission spectroscopy [2.432] depends on the use of high current neutral deuterium atomic beams in the energy range of  $\sim 100$  keV. This would not be a practical method to use, except for the fact that many tokamaks are equipped with very powerful beams of this type for the purpose of plasma heating. Quite conveniently, the energy of these beams is of necessity chosen such that a significant fraction reaches the plasma core to provide heating, and so is available for plasma diagnosis.

As the neutral atoms cross the plasma they can be excited by neutral ion collisions. The lifetime of these excited states is in the range of a few nanoseconds, so the radiative decay of these states, including emission of  $D_\alpha$  light ( $3 \rightarrow 2$  transition, 656.1 nm) gives a reasonably well localized measurement of the fluctuating plasma density. Detectors are arranged to view tangentially to the magnetic field where the energetic beam neutrals cross the plasma, in order to maximize spatial resolution perpendicular to  $\vec{B}$ . Filters are used to accept only  $D_\alpha$  light Doppler shifted appropriately for having been emitted by the energetic beam neutrals. The most powerful approach used to date employs an array of  $\sim 30$  detectors, providing imaging capability over an area of  $\sim 30$  cm<sup>2</sup>, with MHz sampling rates. The imaging array is scanned across the plasma on a shot-by-shot basis. It is possible with this technique to measure fluctuation amplitudes,  $k$  spectra over a modest range, and flow rates of fluctuations, as markers for plasma flows, including flows self-generated by the turbulence.

A problem with this technique is that fluctuations in the beam ion density arising from fluctuations in the ion source are imprinted on the beam within the plasma, as is beam depletion by the larger scale fluctuations in the outer region of the plasma. Careful use of common-mode rejection techniques can minimize such effects. Often the radial profile of plasma rotation raises the lab-frame frequency

of core rotating instabilities out of the frequency range of the ion source and large amplitude plasma edge instabilities.

#### *2.6.1.8. High frequency charge exchange spectroscopy (HF CHERS)*

Beams of energetic neutrals used for plasma heating support another technique [2.432] for measuring plasma turbulence, in this case fluctuations in the ion temperature. Neutral deuterium atoms at  $\sim 100$  keV have a significant cross-section for charge transfer to fully stripped carbon, leaving the carbon in a highly exciting state, with  $N \sim 8$ . As this excited state radiatively decays, visible light is emitted which carries with it Doppler broadening and shift due to the temperature and flow velocity of the carbon ions. This signal is strong enough that with high throughput optics, and relatively few, wide wavelength detection channels, it is possible to measure fluctuations in the local ion temperature, flow velocity and density. These can even be locally correlated. While this technique has not been widely applied, it is an example of the sort of breadth in fundamental measurement that may be required to fully understand the physics of plasma turbulence.

#### *2.6.1.9. Correlated electron cyclotron emission (CECE)*

Electron cyclotron emission (ECE) at the second harmonic is generally quite optically thick in tokamaks, except at the very edge, and so should provide an accurate measurement of local electron temperature. Indeed the optical depth is generally high enough that the beam spot size against the plasma sets the spatial resolution of an ECE fluctuation diagnostic more than the depth from which the emission originates. Electron cyclotron emission can also be cut off in high beta, high density plasmas, but a wide operating window is often available. One might be tempted to think that high sensitivity detectors for ECE emission would be well suited to providing accurate measurements of fluctuating electron temperature. Interestingly, however, the statistics of long-wavelength photons are such that the intrinsic noise level prevents this.

Recently it has been recognized that this problem can be overcome [2.433] by correlating the signals from two ECE measurements at slightly different frequencies. They need to be separated by more than the detection bandwidth of each channel, to avoid the intrinsic statistical problem, but be closely enough spaced to assure high correlation of any fluctuations within the plasma. This technique has also not been applied broadly, but again provides an important fundamental test of the understanding of plasma turbulence.

## 2.6.1.10. Analysis techniques

A wide range of mathematical techniques have been applied to the fluctuation data accumulated using the measurement techniques discussed above, and a full review [2.420] is beyond the scope of this text. Many of them can be reduced, however, to the fairly simple form of testing the correlation of two time series,  $A$  and  $B$ , and using the resulting correlation to deduce an important physical property. Typically  $A$  and  $B$  have been Fourier analysed over some time window, and one asks for their correlation over some window in frequency. Often an average over this window is formed to provide a normalized cross power spectrum of the type:

$$\frac{\langle AB^* \rangle}{\sqrt{\langle AA^* \rangle \langle BB^* \rangle}} \quad (2.126)$$

where  $A^*$  and  $B^*$  are the complex conjugates of  $A$  and  $B$  in the frequency domain.

The absolute magnitude of this cross-correlation between  $A$  and  $B$  can be used to measure, for example, radial correlation lengths by varying the radial separation of the  $A$  and  $B$  measurements, and determining the scale length over which their correlation falls. The complex phase angle provides information about the phase delay between location  $A$  and location  $B$  in the chosen frequency window.

Alternatively, if two measurements are spatially separated along the direction of propagation of the turbulence, for example in the poloidal direction, one can insert a time lag into  $B$ , and then determine the lag of  $B$  relative to  $A$  that gives the highest cross-correlation, and so determine the speed at which the non-linear turbulent structures propagate. This can of course be done in the time domain, using imaging techniques, which permit more localized measurements [2.434].

A range of sophisticated spectral analysis techniques has been applied to turbulence, such as using three-wave correlations to look for the possibility that zonal flows or geodesic acoustic modes are associated with coupling of components of the measured turbulence. One can construct a self bi-coherence between angular frequencies  $\omega_1$  and  $\omega_2$  of the type:

$$\hat{b}(\omega_1, \omega_2) = \frac{\langle A(\omega_1)A(\omega_2)A^*(\omega_1 + \omega_2) \rangle}{\sqrt{\langle |A(\omega_1)A(\omega_2)|^2 \rangle \langle |A(\omega_1 + \omega_2)|^2 \rangle}} \quad (2.127)$$

If the phases between the different frequency components of  $A$  are uncorrelated, the magnitude of this quantity will converge to zero like  $1/\sqrt{N}$

as more data sets (of number  $N$ ) are averaged together. However if, for example, a wave at frequency  $\omega_1$  is driven in a coherent manner by two other waves in the system, then the magnitude of the self bi-coherence will peak at  $\omega_1$ . The complex phase angle of the self bi-coherence provides information on the physics of coupling, but does not necessarily clarify the direction of energy flow, which requires more sophisticated techniques.

A very important modern advance has been the realization that no experimental measurement of turbulence has a simply describable relationship to the non-linear turbulence theory or simulations. It is necessary, therefore, to include in the turbulence simulations *synthetic diagnostics* which take into account the properties of the measurement techniques applied in the experimental case of interest. Ideally it is only these synthetic signals that should be compared directly with measurements.

It will likely be revealing to apply the numerical analysis techniques used on experimental data to these synthetic signals as well.

## 2.6.2. Experimental results

It is not possible here to discuss or even summarize fully the many results that have been obtained from turbulence measurements on tokamaks. The reader is referred to review articles on this subject [2.420, 2.421]. Here we provide a general overview of the experimental results, and present some recent and particularly clear examples of data that support or challenge current understanding based on the gyroBohm transport model.

### 2.6.2.1. Wavenumber spectra

From the earliest measurements of turbulence in tokamaks [2.435] significant activity has been observed in the range of the expected frequency and wavelength for ITG and TEM modes, broadly  $k_{\perp} \rho_s \sim 0.1-1$ . Estimates of transport based on absolute measured fluctuation amplitudes have been found to be in qualitative agreement with measured transport rates [2.96, 2.436]. In many experiments these fluctuations are observed to increase when confinement falls, for example with increasing input power, or decrease when confinement improves, for example with the transition to H-mode. Thus it is well established that turbulence of the type predicted by the gyroBohm model is present in tokamaks, and may play an important role in transport.

A particularly interesting scaling experiment was undertaken on Tore-Supra [2.437], using far infrared ( $\text{CO}_2$  laser light with  $\lambda = 10.6 \mu\text{m}$ ) scattering to examine the variation of both the turbulent spectra versus wavenumber and their correlation times as the toroidal magnetic field was varied, shown in Fig. 2.43.

Far forward scattering gives poor spatial resolution, so this measurement was sensitive essentially to the full radial profile. Since fluctuations are strongest towards the edge of the plasma, these measurements are assumed to originate from  $r/a = 0.7-1.0$ .

More recent studies on Tore-Supra [2.438], using Doppler backscattering at  $r/a = 0.65$ , with ICRH heating, found a very similar scaling variation with  $k_{\perp}$  as shown in the left-hand panel of Fig. 2.43. Interestingly, it was found that the new data, as well as the previous scattering data, could be well fit with a single scaling,  $\sim \exp(-4k\rho_i)$ , giving a good straight line within the scatter of the data on a semi-logarithmic plot. This may suggest that the picture of a self-similar power-law cascade in  $k$  is incorrect.

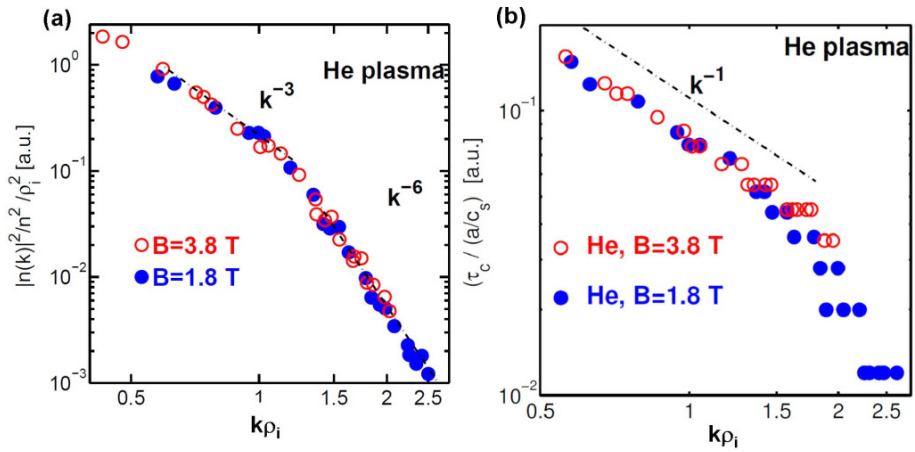


FIG. 2.43. (a)  $k$  spectra and (b) correlation times from far infrared scattering measurements from ohmically heated plasmas in Tore-Supra, at two different magnetic fields, showing gyroBohm-like ( $k\rho_i$ ) scaling in both cases [2.437].

Measurements of radial correlation lengths [2.439] in L-mode plasmas at 1 T and 2 T on DIII-D using beam emission spectroscopy, and so lower values of  $k\rho_i$ , gave gyroBohm scaling: radial correlation length  $L_{c,r} \sim 5\rho_i$ . The correlation time was also found to scale as  $a/c_s$ , and the fluctuation amplitude scaled approximately with the gyroradius.

Recent PCI measurements of turbulence [2.414] in a C-Mod H-mode plasma have provided reasonable agreement in absolute magnitude and  $k$ -spectrum with non-linear ITG simulations using the GYRO code and a synthetic diagnostic, taking into account the relatively broad vertical and radial acceptance of the PCI technique.

These data support the gyroBohm picture of long wavelength turbulence. However it should be noted that scaling studies have not been undertaken broadly, and particularly not in H-mode; furthermore some anomalies have been

observed. One is that confinement in tokamaks scales favourably with ion mass, while the gyroBohm picture suggests the opposite. Turbulence measurements have been ambiguous on this point [2.421].

### 2.6.2.2. Frequency spectra

Turbulent frequency spectra have been measured by many techniques, and it is clear that there is very considerable non-linear broadening beyond the calculated region of linear instability (as for wavenumber spectra). Thus spectral comparisons should be made against simulation codes, using synthetic diagnostics to mimic the limitations of the applied diagnostic techniques. Initial results from DIII-D [2.440] are shown in Fig. 2.44.

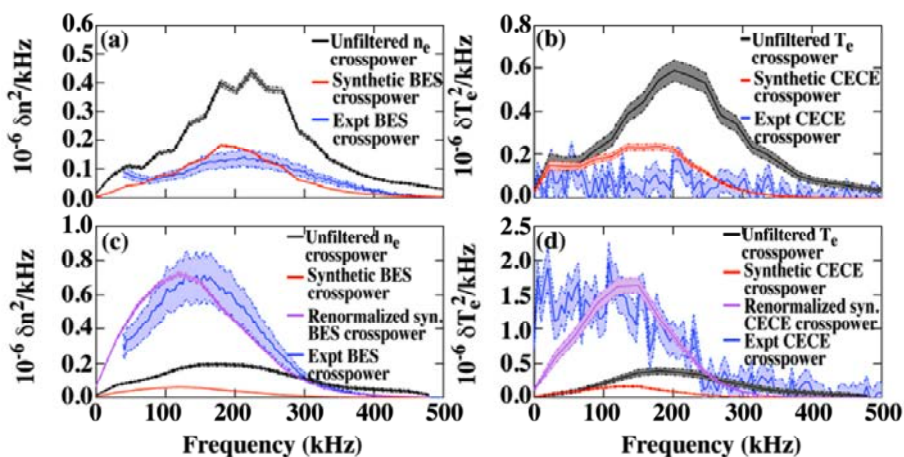


FIG. 2.44. Lab-frame cross-spectra of  $\delta n_e$  (a), (c) and  $\delta T_e$  (b), (d) from local GYRO simulations of  $r/a = 0.5$  (a), (b) and  $r/a = 0.75$  (c), (d). Spectra calculated from the unfiltered GYRO calculation are shown in black, from the synthetic BES data in red, and from the experimental data in blue. Reprinted from Ref. [2.440]. Copyright (2010), American Institute of Physics.

Figure 2.44 includes a great deal of data, and we will return to it in the next two sections. For now we note that in frame (a) at  $r/a = 0.5$  the absolute fluctuation level and frequency spectrum from long wavelength BES measurements (blue region) are in remarkably good agreement with the synthetic diagnostic (red curve) applied to non-linear turbulence calculations. In frame (c), at  $r/a = 0.75$ , the spectral shape remains in good agreement (blue region versus purple curve), but the absolute agreement between the blue region and the red curve is in poor agreement. Indeed while the experiment showed the peak fluctuation level rising by a factor of  $\sim 5$ , the simulation has it falling by a factor of  $\sim 2.5$ . One should be cautious, however, that close to marginal stability turbulence and transport levels are very sensitive.

Confirmation of the existence of trapped electron mode turbulence with  $k_r \rho_s \sim 1$  has been somewhat elusive. Figure 2.43 includes signals at these wavenumbers from Tore-Supra, but it is not clear whether this activity is driven by lower- $k$  turbulence. Phase contrast imaging has been used to study trapped electron mode turbulence in Alcator C-Mod [2.441]. Central ICRF heating was employed to raise the central temperature and arrest the density rise in an internal transport barrier plasma (see Section 2.6.2.5). The steep density gradient in the core region, coupled with the increase in  $T_e$ , were calculated to increase the region of TEM instability based on linear GS2 flux-tube calculations, and also to increase turbulence at  $r/a \sim 0.4$ , based on non-linear GS2 flux-tube calculations. When the non-linear calculations were used to generate a synthetic simulation of the line-integrated PCI measurements, reasonable agreement was achieved for the measured spectral shape (the absolute magnitude was not compared). However, there is not an unambiguous technique to determine how a local flux-tube calculation should be used for this purpose. Finally, the measured and synthesized spectra had the majority of their power in the range of  $k \rho_s \sim 0.25$ , not significantly upshifted relative to the measurements on C-Mod when ITG turbulence was calculated to be dominant, although consistent with calculations for the density gradient driven TEM mode of this case.

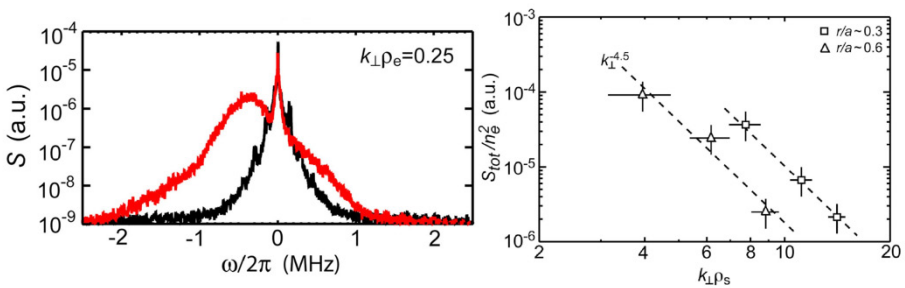


FIG. 2.45. Electron scale turbulence measured in NSTX.  $S$  (a.u.) indicates scattered power in arbitrary units.  $S_{\text{tot}}/n_e^2$  (a.u.) indicates scattered power integrated over frequency, also in arbitrary units. Red spectrum on left ( $R = 1.2 \pm 0.025$  m) taken during period calculated to be unstable to ETG modes, black during stable period. Squares in right-hand spectrum are for  $R = 1.2$  m, triangles for  $R = 1.35$  m.  $R_0 = 0.85$  m,  $a = 0.65$  m,  $B = 0.55$  T,  $T_e$  at  $1.2$  m =  $1$  keV [2.442].

Recently it has become possible to measure ETG-scale turbulence and to determine the frequency and wavenumber spectra for highly localized regions. Figure 2.45 shows spectra measured in the core region of NSTX [2.442]. The black frequency spectrum, dominated by stray light near the incident radiation frequency, is from a time with low  $\nabla T_e$ , when ETG modes are theoretically predicted to be stable (see Section 2.6.2.5), while during the period of the red spectrum, ETG modes are predicted to be unstable. The frequency shift

corresponding to electron diamagnetic rotation in this low-rotation RF heated plasma is consistent with ETG predictions.

Experiments on DIII-D using mm wave backscattering have provided measurements of high- $k$  fluctuations,  $\sim 35 \text{ cm}^{-1}$ , with spatial resolution of  $\pm 6.5 \text{ cm}$  at  $r/a = 0.35$  and  $0.6$  ( $35 \text{ cm}^{-1}$  corresponds to  $k\rho_e \sim 0.14$  and  $0.1$  at these values of  $r/a$ ), during ECH heating at  $r/a = 0.6$  [2.443]. At the inner location the fluctuation level actually dropped by 14% with the onset of ECH, while it rose by 43% at the outer location. These results are generally consistent with the lowered transport observed in the core region with off-axis heating, and the increased transport in the region beyond  $0.6a$ , but detailed comparisons with linear stability analysis showed significant discrepancies, indicating full stabilization at  $r/a = 0.35$  and a reduction in growth rate at  $r/a = 0.6$ , due to a reduction in  $|\nabla \ln(T_e)|$  at both locations.

On the FT-2 tokamak, ETG scale instabilities were studied using DBS techniques, enhanced through use of the upper hybrid resonance to shorten the wavelength and increase the amplitude of the incident radiation [2.429]. Furthermore two different but closely spaced frequencies of incident radiation were employed to allow correlation studies. During LH plasma heating fluctuations were observed with frequency  $\sim 2 \text{ MHz}$  and  $k_r \rho_s \sim 8$ , close to the peak of the growth rate predicted using the GS2 code. After LH heating, when the ETG was predicted to be stable, this mode was absent.

The evidence appears conclusive that ETG modes are present in tokamak plasmas approximately as predicted. More evidence needs to be developed, however, to determine their level of contribution to transport.

### 2.6.2.3. Radial profiles

Tokamak thermal transport coefficients generally rise rapidly from the core of the plasma to the edge, resulting in a characteristic Gaussian radial profile shape, especially for  $T_e$ , which typically broadens as  $q$  is lowered. Since gyroBohm scaling varies as  $T^{3/2} / L_n$ , naïve interpretation predicts high transport in the core, and less at the edge. Experimentally, from the earliest measurements, it has been observed that turbulence rises rapidly from the core to the edge, especially in L-mode, consistent with rising transport and inconsistent with naïve interpretation. Recent results from DIII-D using beam emission spectroscopy [2.444] provide a particularly clear modern example of a radial profile measurement of relatively long wavelength fluctuations ( $k_\perp \rho_s < 0.2$ ) as expected for ITG modes, shown in Fig. 2.46. Estimating  $L_n \sim a \sim 0.6 \text{ m}$  and  $k_\perp \sim 0.5 \text{ cm}^{-1}$  gives an expected turbulence level from the mixing-length estimate of  $\sim 1\%$ .

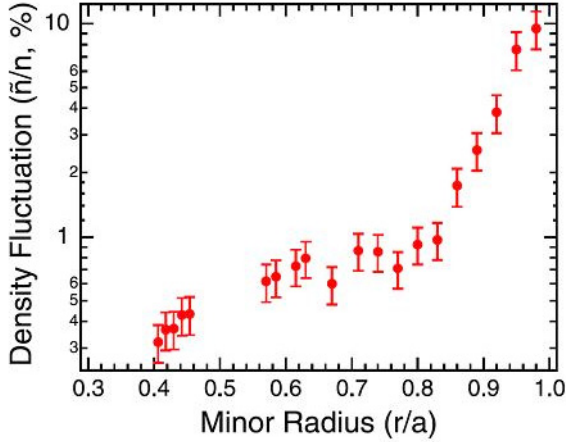


FIG. 2.46. Radial profile of frequency-integrated density fluctuations  $\tilde{n}/n$  (where  $\tilde{n}$  is perturbed density) in low density (central electron density  $n_{e0} = 2.9 \times 10^{19}/m^3$ ) DIII-D L-mode plasma, from BES. Detector spot size on the plasma  $\sim 1$  cm. Half the central electron temperature is  $T_{e0}/2 \sim 1.1$  keV, giving  $\rho_s \sim 0.2$  cm [2.444].

The gyroBohm interpretation of radial profiles of transport and turbulence peaked to the outside is that the effect of the edge boundary condition is to drive the outer region of the plasma more strongly against the critical logarithmic temperature gradients, and so increase transport. While this appears to be qualitatively reasonable, in that models that constrain temperature profiles to be close to marginal stability [2.412] successfully reproduce experimental radial profiles, the detailed attempt to simulate the radial profile of turbulence shown in Fig. 2.44 was not successful. In frame (a), the absolute density turbulence level at half-radius is found to be consistent with simulation, as is the overall transport level, a considerable accomplishment, but this agreement does not hold further out in minor radius, frame (c). In general it appears that global simulations do not tend to show the strongly rising turbulence towards the plasma edge that is seen experimentally, particularly in the L-mode. Both the predicted turbulence and the predicted transport are low. Additional experimental work is required in this area, but this suggests, perhaps, a role for non-local effects from edge or even SOL turbulence affecting the outer part of the confinement region. H-mode plasmas show very strong suppression of turbulence in the outer regions, and studies of this nature in H-mode conditions would be most revealing.

It is worth noting that low aspect ratio, low field and high beta spherical torus/tokamak plasmas do not show the strong variation of transport with minor radius typical of tokamaks, and surprisingly show broadening of the electron temperature profile with rising  $q$ . Furthermore, confinement scales more favourably with  $B_\phi$  than with  $I_p$  in STs, unlike tokamaks. These differences may be due to suppression of ion scale gyroBohm turbulence by geometrical factors

and rotational shear, but more detailed turbulence data are required to determine if these exceptions to the general rule of tokamak profile variation are actually proof of the more sophisticated rules of gyroBohm turbulence, or instead hints that additional phenomena are at play.

Finally, it is important to note that radial profiles tracking along the outer midplane of plasmas do not tell the whole story. Rather extensive studies were made of the poloidal variation of fluctuations on TEXT using far infrared scattering [2.421]. Reflectometry has been used on T-10 [2.445] to determine that the fluctuation level is higher on the low field side than on the high field side, and that this asymmetry rises with heating power.

### 2.6.3.3. Ion and electron temperature fluctuations

In TFTR a high frequency charge exchange recombination spectroscopy system was used to measure fluctuating ion temperature. By the use of high throughput optics and four wavelength passbands, it was possible to measure  $\delta T_i / T_i$  at a sampling rate of up to 300 kHz and compare it with both the fluctuating carbon density and the fluctuating electron density (from BES). The relative fluctuation level of the carbon density  $\delta n_c / n_c$  was found to be close to the relative fluctuation level of electron density,  $\delta n_e / n_e$  from BES.  $(\delta T_i / T_i) / (\delta n / n)$  was found to be  $2 \pm 0.5$ , from  $r/a = 0.6-0.9$ , close to the measured value of  $\eta_i = d \ln(T_i) / d \ln(n_e)$ . This is what had been predicted by quasilinear theory for ITG modes.

Correlation electron cyclotron emission has been used to study electron temperature fluctuations on DIII-D [2.444], as shown in Fig. 2.44. The CECE vertical  $1/e^2$  diameter against the plasma was measured at the distance of  $r/a = 0.5$  to be 3.8 cm, while the radial  $1/e^2$  width was taken from the natural line width in the plasma to be 1 cm. (The two channels used for detection were spread by 0.4 cm.) By averaging over 400 ms it was possible to reduce the noise level to 0.2%. The electron temperature fluctuation profile was found to be similar to the density fluctuation profile from BES (see Fig. 2.46). Full non-linear gyrokinetic simulations, with synthetic diagnostics, were used to model  $(\delta T_e / T_e)_{CECE} / (\delta n_e / n_e)_{BES}$ . At  $r/a = 0.5$ , the measured value is 0.72, while the simulation gives 1.4. At  $r/a = 0.75$  the experimental value is  $1.0 \pm 0.23$  while the simulation gives 1.65. As visible in Fig. 2.44, the simulation underpredicts both the electron temperature and density fluctuation levels.

It is quite challenging to measure multiple fluctuating quantities in tokamak plasmas, but these may help to provide important clues as to the driving mechanisms of transport. For example the electron temperature fluctuation measurements may suggest more rapid electron thermal equilibration along field lines than modelled in the numerical simulation.

#### 2.6.3.4. Zonal flows and geodesic acoustic modes

Recently there have been a large number of measurements of zonal flows (ZFs) and geodesic acoustic modes (GAMs), using BES, material probes, DBS, HIBP and reflectometry. A very complete review [2.446] is available. Here we focus on the most recent results.

In the case of BES and DBS, the plasma flow associated with the ZF or GAM is deduced from the propagation speed of turbulence. In the case of material probes and HIBP, radial electric fields, and thus  $\vec{E} \times \vec{B}$  flows, are measured directly. The results from DBS measurements of GAMs on ASDEX-Upgrade (AUG) [2.447] shown in Fig. 2.47 are particularly extensive.

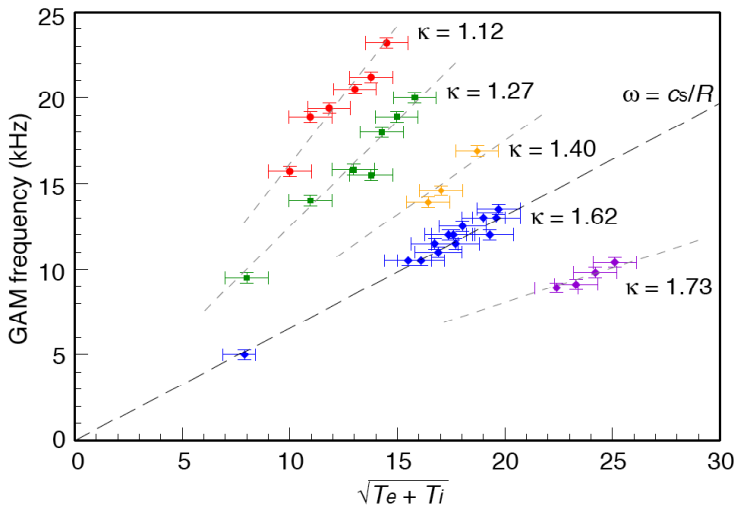


FIG. 2.47. Scaling of GAM frequency in the edge region of ASDEX Upgrade [2.447].

GAM oscillations are only observed in the steep density gradient region near the edge of AUG; none are observed in the SOL region, nor deep inside of the edge pedestal. GAMs have been observed in ohmic and L-mode plasmas, but not in H-modes, nor at high collisionality. The variation of the GAM frequency with the ion sound speed is in good agreement with theoretical prediction. The correct scaling is also observed with ion mass between H, D and He plasmas, but the complex variation with elongation, local  $q$  value, and position within the plasma is not well explained.

Density fluctuations are seen to be counter-modulated with the peak GAM intensity, consistent with the idea that GAMs limit turbulence. Furthermore, in ohmic and L-mode plasmas, GAMs grow in amplitude with  $\nabla T_e$ , consistent with the idea that more strongly driven turbulence causes growth in GAM amplitude. The absence of the observation of GAMs in H-mode plasmas may be consistent

with this understanding, but then brings up the question as to what breaks up the meso-scale turbulence structures in H-modes. The AUG authors (as others, see below) indicate that the absence of GAM observations in H-mode may be due to the lack of strong fluctuation levels to allow accurate flow measurements. It is to be noted, however, that GAMs in ASDEX L-modes are observed using DBS with amplitude 2–3 orders of magnitude above background.

On DIII-D BES has been used to measure both ZFs and GAMs [2.448]. Long wavelength eddy structures are tracked across poloidally separated channels, using time-lag cross-correlation. Velocities in the range of 10–15 km·s<sup>-1</sup> are observed, with radial correlation length  $\sim 10\rho_p$ , comparable to that of the turbulent density fluctuation spectrum. Zero mean frequency oscillations are observed, peaking near zero frequency and extending up to 20–30 kHz, qualitatively consistent with simulation results. These are identified as ZFs.

The poloidal velocity spectrum in DIII-D is dominated by finite-frequency GAMs in the edge region ( $0.9 < r/a < 0.95$ ) while the zero-mean-velocity flow dominates inwards, and has been measured at least in to  $r/a = 0.65$ . As on AUG, the GAM has not been detected in the SOL region. The GAM is observed to be strongly damped as  $q_{95}$  falls from 6.5 to 4.5, in qualitative agreement with theory. As with DBS on AUG, GAMs and ZFs have not been observed in H-mode plasmas with BES on DIII-D, perhaps due the low amplitude of the marker fluctuations.

Energy cascade analysis techniques indicate the transfer of energy from density fluctuations with frequency  $f_0 - f_{GAM}$  to density fluctuations with frequency  $f_0$ , qualitatively consistent with the understanding that GAMs break up the turbulent eddies, and with numerical simulations.

On JFT-2M, a heavy ion beam probe was used to measure fluctuating flows [2.449] directly via fluctuating potential measurements in L-mode plasmas. The amplitude of the potential was found to be  $\sim 15$  V,  $\sim 3$  cm inside the separatrix with FWHM of  $\sim 4$  cm and frequency  $\sim 15$  kHz. Fluctuation levels with  $f \gtrsim 3$  kHz drop by an order of magnitude with transition to the H-mode, and the GAM at  $\sim 15$  kHz, which was observable one order of magnitude above the L-mode background turbulence, disappears in  $\sim 10$  ms.

An HIBP was used on the T-10 tokamak to investigate GAMs [2.450]. Since the HIBP can simultaneously in one location measure both density and potential fluctuations, the demonstration that the potential fluctuation level is much greater than that of the density, as expected theoretically for such a mode, is particularly convincing. The phase angle between density and potential was found to be  $\pi/2$ , also consistent with what is expected in such a sound wave. With ECH heating in L-mode, GAMs become more pronounced and can be seen over the outer one third of the minor radius. Using reflectometry in conjunction with the HIBP, it was shown that GAMs have a significant correlation and no phase shift at least 1/4 of the way around the torus, consistent with  $n = 0$ . Using reflectometry [2.451] it

was shown that as predicted theoretically, the GAM density fluctuation amplitude is greater at the top of the torus than at the outer midplane, and negligibly small on the inner midplane. Zonal flows were not observed on T-10.

Both zonal flows and GAMs were observed using electrostatic probes in the outer region ( $r/a > 0.9$ ) of ohmically heated deuterium plasmas in the HL-2a tokamak [2.452] ( $R = 1.65$  m,  $a = 0.4$  m,  $I_p = 160$ – $180$  kA). High coherence was found for both ZFs, with frequency  $\lesssim 3$  kHz, and GAMs, with frequency  $\sim 8.5$  kHz, between probes in the outer midplane separated by 1.3 m. Similarly high coherence was found for probes separated by 0.05 m poloidally. The phase shift between the three sets of probes was found to be consistent with zero, as expected theoretically. For zonal flows the  $\langle k_r \rho_i \rangle$  was found in the range of 0.033 and  $\Delta k_r \rho_i \sim 0.19$ . These results are consistent with predictions. It is found that the envelope of the higher frequency ambient turbulence is significantly modulated by the GAMs, and more weakly modulated by the lower amplitude ZFs. Similarly, bi-coherence analysis shows a strong non-linear coupling of the wave triads  $(f_1, f_{GAM}, f_1 + f_{GAM})$ , and a weaker coupling of  $(f_1, f_{ZF}, f_1 + f_{ZF})$ , where  $f_1$  is an arbitrary frequency in the spectrum,  $f_{GAM}$  is in the GAM range and  $f_{ZF}$  is in the zonal flow range.

In sum, ZFs and GAMs appear to have been identified in the outer region of ohmically heated and L-mode plasmas, with the properties expected theoretically, including a kind of predator–prey relationship with ambient turbulence. It is, however, troubling that they have not been observed in the core region of H-mode plasmas. This could be due to the lower amplitude of the turbulence, making them harder to detect. If, alternatively, they are absent because of the weakness of the drive in lowered turbulence plasmas, this raises the question of what sets the turbulent eddy size to the gyroBohm value in such plasmas.

### 2.6.3.5. Core turbulence suppression

A signature of the enhanced confinement H-mode is improved particle and energy confinement, corresponding to an edge localized transport barrier, associated with a flow shear layer near the plasma boundary. This topic is discussed in Sections 2.3.7 and 2.5.5. Internal transport boundaries, in the core of the plasma, are also observed, although these generally require adjustments to the magnetic shear profile that reduce instability growth rates, as well as flow shear. There is evidence that in some cases low shear in the region of low order rational  $q$  surfaces plays a role in triggering these effects. These are remarkable and distinctive results, in at least qualitative agreement with the gyroBohm picture of transport, and indeed supporting the picture that transport is driven by drift instabilities subject to magnetic shear and shear-flow stabilization. The feature that the increasing pressure gradients that result from turbulence suppression are self-reinforcing makes them in some cases quite dramatic. The simplest form

of self-reinforcement is the increased local flux-surface shift, which results in a reduction in the trapped particle instability drive. Unfortunately, these same very steep pressure gradients, particularly in low magnetic shear regions, tend to cause instability to low order MHD modes at modest values of  $\beta$ , so the application of these turbulence suppressed regimes to ITER and fusion reactors is not straightforward. A possible approach might be to control carefully the flow shearing rate to avoid the steepest pressure gradients [2.453].

Here we examine the experimental evidence on core turbulence suppression in these conditions. Important measurements have been made on TFTR, DIII-D, JT-60U and NSTX. On TFTR with reversed core magnetic shear and high power heating, an “enhanced reversed shear” regime was found with greatly reduced particle transport, and greatly reduced ion thermal transport [2.454]. The improved confinement in this regime required not only magnetic shear reversal, but also a flow shearing rate comparable to the fastest instability growth rate [2.455]. This was demonstrated by adjusting the torque input from tangential neutral beams, aimed co- and counter- to the plasma current. DIII-D did experiments with reversed (or negative) magnetic shear in the core of the plasma, simultaneous with an edge H-mode transport barrier [2.190]. This resulted in a strong reduction in measured long wavelength turbulence and transport across the full plasma, as measured by the spatially integrated microwave scattering technique. The Doppler shift due to toroidal rotation provided a measure of localization, and the strong reduction across the full spectrum was dramatic. Results in JT-60U [2.195] are somewhat different. Absolute fluctuation levels, measured by reflectometry, were not reduced with the production of an internal transport barrier, but their radial correlation length was dramatically lessened. NSTX provided a localized measurement of electron-scale turbulence, which was dramatically suppressed with an internal transport barrier associated with reversed shear operation [2.442].

### 2.6.3.6. Evidence for non-local effects

The basic gyroBohm picture of transport largely supported by the data discussed here is challenged by at least two classes of turbulence measurement. First, both in JET [2.456] and in DIII-D [2.444] fluctuations have been observed to drop very rapidly in the core of the plasma at the time of the H-mode transition, which originates at the plasma boundary. Extensive analysis in JET resulted in the conclusion that this rapid change, and the associated rapid change in local transport, could not be explained by rapid changes in the local temperature gradient. The results from DIII-D, while apparently very rapid, have not been fully compared with changes in local gradients. It is possible that changes in shear-flow could also occur rapidly, and should be analysed. In general, however, these data and the fact that fluctuations in the outer region of L-mode plasmas

fall off so rapidly towards the core (see Fig. 2.46) suggest that there may be a direct influence of the edge turbulence, perhaps via the theoretically predicted turbulence spreading mechanism, or turbulence further within the plasma.

Another result that seems to lie outside the realm of gyroBohm turbulence is that most analyses of drift turbulence show complete stability at the plasma centre. However it is clear on the one hand that heat does diffuse away from the centre of the plasma, and on the other that turbulence is present on the axis. All of this is evidenced for example by the measurements in the core of JT-60U reversed shear plasmas, discussed above. Recent short-wavelength scattering results from NSTX [2.457], also, are highly localized, and show clear signals of short-wavelength turbulence very close to the magnetic axis. This may be another example of turbulence spreading. We may not have identified the mechanisms of transport right in the centre of the plasma. Measurements have identified Alfvén instabilities in this region [2.458], which may play a role.

## REFERENCES

- [2.1] WHITE, R.B., *The Theory of Toroidally Confined Plasmas*, Imperial College Press, London (2006).
- [2.2] WHITE, R.B., CHANCE, M.S., Hamiltonian guiding center drift orbit calculation for toroidal plasmas of arbitrary cross section, *Phys. Fluids* **27** (1984) 2455.
- [2.3] LITTLEJOHN, R.G., Hamiltonian formulation of guiding center motion, *Phys. Fluids* **24** (1981) 1730.
- [2.4] CARY, J.R., BRIZARD, A.J., Hamiltonian theory of guiding center motion, *Rev. Mod. Phys.* **81** (2009) 693.
- [2.5] BRIZARD, A.J., HAHM, T.S., Foundations of nonlinear gyrokinetic theory, *Rev. Mod. Phys.* **79** (2007) 421.
- [2.6] HAZELTINE, R.D., Recursive derivation of drift kinetic equation, *Plasma Phys.* **15** (1973) 77.
- [2.7] SIMAKOV, A.N., CATTO, P.J., Drift kinetic equation exact through second order in gyroradius expansion, *Phys. Plasmas* **12** (2005) 012105.
- [2.8] BRAGINSKII, S.I., Transport processes in a plasma, *Reviews of Plasma Physics* (LEONTOVICH, M.A., Ed.), Consultants Bureau, New York (1974) 205.
- [2.9] FITZPATRICK, R., *The Physics of Plasmas* (2008); available online at: [www.lulu.com/content/3802836](http://www.lulu.com/content/3802836)
- [2.10] HAMMETT, G.W., DORLAND, W., PERKINS, F.W., Fluid models of phase mixing, Landau damping, and nonlinear gyrokinetic dynamics, *Phys. Fluids B* **4** (1992) 7.
- [2.11] HINTON, F.L., HAZELTINE, R.D., Theory of plasma transport in toroidal confinement systems, *Rev. Mod. Phys.* **48** (1976) 239.
- [2.12] HAZELTINE, R.D., HINTON, F.L., Collision-dominated plasma transport in toroidal confinement systems, *Phys. Fluids* **16** (1973) 1883.
- [2.13] GRAD, H., Toroidal containment of a plasma, *Phys. Fluids* **10** (1967) 137.
- [2.14] SHAFRANOV, V.D., Plasma equilibrium in a magnetic field, *Reviews of Plasma Physics*, Vol. 2, Consultants Bureau, New York (1966) 103.

- [2.15] GREENE, J.M., JOHNSON, J.L., WEIMER, K.E., Tomakak equilibrium, *Phys. Fluids* **14** (1971) 671.
- [2.16] LANDAU, L., LIFSHITZ, E., *The Classical Theory of Fields*, Vol. 2, Addison Wesley, Cambridge, MA (1951).
- [2.17] CARY, J.R., BRIZARD, A.J., *Rev. Mod. Phys.* **81** (2009) 693.
- [2.18] McGUIRE, K., et al., Study of high beta magnetohydrodynamic modes and fast ion losses in PDX, *Phys. Rev. Lett.* **50** (1983) 891.
- [2.19] CHEN, L., WHITE, R.B., ROSENBLUTH, M.N., Excitation of internal kink modes by trapped energetic beam ions, *Phys. Rev. Lett.* **52** (1984) 1122.
- [2.20] ROSENBLUTH, M.N., HAZELTINE, R.D., HINTON, F.L., Plasma transport in toroidal confinement systems, *Phys. Fluids* **15** (1972) 116.
- [2.21] KIKUCHI, M., AZUMI, M., Experimental evidence for the bootstrap current in a tokamak, *Plasma Phys. Control. Fusion* **37** (1995) 1215.
- [2.22] RUTHERFORD, P.H., Collisional diffusion in an axisymmetric torus, *Phys. Fluids* **13** (1970) 482.
- [2.23] GALEEV, A., SAGDEEV, R., Neoclassical diffusion in toroidal geometry - banana regime, *J. Exp. Theor. Phys.* **26** (1968) 223.
- [2.24] GALEEV, A., SAGDEEV, R.A., *Rev. Plasma Phys.* **7** (1979) 1 (LEONTOVICH, M.A., Ed.).
- [2.25] SHIRAI, H., et al., Reduced transport and  $E_r$  shearing in improved confinement regimes in JT-60U, *Nucl. Fusion* **39** (1999) 1713.
- [2.26] SCOTT, S.D., et al., Local measurement of correlated momentum and heat transport in the TFTR tokamak, *Phys. Rev. Lett.* **64** (1990) 531.
- [2.27] LEE, W.D., Observation of anomalous momentum transport in tokamak plasmas with no momentum input, *Phys. Rev. Lett.* **91** (2003) 205003.
- [2.28] NAGASHIMA, K., KOIDE, Y., SHIRAI, H., Experimental determination of non-diffusive toroidal momentum, *Nucl. Fusion* **34** (1994) 449.
- [2.29] GALEEV, A.A., Diffusion-electrical phenomena in a plasma confined in a tokamak machine, *Sov. Phys. J. - JETP (Engl. Trans.)* **32** (1971) 752.
- [2.30] BICKERTON, R.J., CONNER, J.W., TAYLOR, J.B., Diffusion driven plasma currents and bootstrap tokamak, *Nature* **229** (1971) 110.

- [2.31] SHAINING, K.C., CARRERAS, B.A., DOMINGUEZ, N., LYNCH, V.E., TOLLIVER, J.S., Bootstrap current in stellarators, *Phys. Fluids B* **1** (1989) 1663.
- [2.32] WATANABE, K., NAKAJIMA, N., OKAMOTO M., NAKAMURA, Y., WAKATANI, M., Three dimensional MHD equilibrium in the presence of bootstrap current for the large helical device, *Nucl. Fusion* **32** (1992) 1499.
- [2.33] HINTON, F.L., ROSENBLUTH, M.N., Transport properties of a toroidal plasma at low-to-intermediate collision frequency, *Phys. Fluids* **16** (1973) 836.
- [2.34] ZARNSTORFF, M., PRAGER, S.C., Experimental study of neoclassical currents, *Phys. Fluids* **29** (1986) 298.
- [2.35] ZARNSTORFF, M., et al., Bootstrap current in TFTR, *Phys. Rev. Lett.* **60** (1988) 1306.
- [2.36] ZARNSTORFF, M., et al., Transport in TFTR supershots, *Proc. 12th Conf. on Plasma Physics and Controlled Fusion Research, Vol. 1, IAEA, Vienna (1988)* 183.
- [2.37] JET TEAM, Latest JET results and future prospects, *Proc. 12th Conf. on Plasma Physics and Controlled Nuclear Fusion Research, IAEA, Vienna, Vol. 1 (1989)* 95.
- [2.38] CHALLIS, C.D., et al., Non-inductively driven currents in JET, *Nucl. Fusion* **29** (1989) 563.
- [2.39] KIKUCHI, M., AZUMI, M., TSUJI, S., TANI, K., KUBO, H., Bootstrap current during perpendicular neutral injection in JT-60, *Nucl. Fusion* **30** (1990) 343.
- [2.40] ISHIDA, S., et al., Observation of a fast beta collapse during high poloidal beta discharges in JT-60, *Phys. Rev. Lett.* **68** (1992) 1531.
- [2.41] ZARNSTORFF, M., et al., *Phys. Fluids B* **2** (1990) 1306.
- [2.42] GOLDSTON, R.J., WHITE, R.B., BOOZER, A.H., Confinement of high energy trapped particles in tokamaks, *Phys. Rev. Lett.* **47** (1981) 647.
- [2.43] WHITE, R.B., Chaos in trapped particle orbits, *Phys. Rev. E* **58** (1998) 1774.
- [2.44] BOIVIN, R.L., ZWEBEN, S.J., WHITE, R.B., Study of stochastic toroidal field ripple losses of charged fusion products at the midplane of TFTR, *Nucl. Fusion* **33** (1993) 449.

- [2.45] SAIBENE, G., et. al., Toroidal field ripple effects on H-modes in JET and implications for ITER, Proc. 34th EPS Conf. on Plasma Phys., Warsaw, Poland, Vol. 31F (2007).
- [2.46] CHIRIKOV, B.V., A universal instability of many-dimensional oscillator systems, Phys. Rep. **52** (1979) 263.
- [2.47] RECHESTER, A., ROSENBLUTH, M.N., Electron heat transport in a tokamak with destroyed magnetic surfaces, Phys. Rev. Lett. **40** (1978) 38.
- [2.48] SPIZZO, G., WHITE, R.B., CAPPELLO, S., Chaos generated pinch effect in toroidal confinement devices, Phys. Plasmas **14** (2007) 102310.
- [2.49] VAN MILLIGEN, B.Ph., CARRERAS, B.A., SANCHEZ, R., The foundations of diffusion revisited, Plasma Phys. Control. Fusion **47** (2005) B743.
- [2.50] WANG, W.X., et al., Nonlocal properties of gyrokinetic turbulence and the role of  $E \times B$  flow shear, Phys. Plasmas **14** (2007) 072306.
- [2.51] DIAMOND, P.H., ITOH, S.I., ITOH, K., HAHM, T.S., Zonal flows in plasma – a review, Plasma Phys. Control. Fusion **47** (2005) R35.
- [2.52] TANG, W.M., Microinstability theory in tokamaks, Nucl. Fusion **18** (1978) 1089.
- [2.53] HORTON, C.W., Drift waves and transport, Rev. Mod. Phys. **71** (1999) 735.
- [2.54] Personal communication from ETHIER, S., Princeton Physics Laboratory, USA.
- [2.55] DIAMOND, P.H., ITOH, S.I., ITOH, K., “Physical kinetics of turbulent plasmas”, Modern Plasma Physics, Vol. 1, Cambridge University Press (2010).
- [2.56] PEARLSTEIN, L.D., BERK, H.L., Universal eigenmode in a strongly sheared magnetic field, Phys. Rev. Lett. **23** (1969) 220.
- [2.57] ANTONSEN, T., Stability of bound eigenmode solutions for the collisionless universal instability, Phys. Rev. Lett. **41** (1978) 33.
- [2.58] COPPI, B., SPIGHT, C., Ion-mixing mode and model for density rise in confined plasmas, Phys. Rev. Lett. **41** (1978) 551.

- [2.59] HORTON, C.W., VARMA, R.K., Electrostatic stability theory of tokamaks from two-component fluid equations, *Phys. Fluids* **15** (1972) 620.
- [2.60] MARMAR, E.S., ALCATOR C-MOD GROUP, The Alcator C-Mod Program, *Fusion Sci. Technol.* **51** (2007) 261.
- [2.61] RITZ, Ch.P., et al., Fluctuation-induced energy flux in the tokamak edge, *Phys. Rev. Lett.* **62** (1989) 1844.
- [2.62] COPPI, B., ROSENBLUTH, M.N., SAGDEEV, R.Z., Instabilities due to temperature gradients in complex magnetic field configurations, *Phys. Fluids* **10** (1967) 582.
- [2.63] HORTON, C.W., CHOI, D.I., TANG, W.M., Toroidal drift modes driven by ion pressure gradients, *Phys. Fluids* **24** (1981) 1077.
- [2.64] BEER, M.A., Gyrofluid Models of Turbulent Transport in Tokamaks, PhD Thesis, Princeton University (1995).
- [2.65] KLIMONTOVICH, Y.L., The Statistical Theory of Non-equilibrium Processes in a Plasma (TER HAAR, D., Ed.), Pergamon Press, Oxford and New York (1967).
- [2.66] STIX, T.H., *Waves in Plasmas*, American Institute of Physics, Springer-Verlag, New York (1992) 247.
- [2.67] FRIEMAN, E.A., CHEN, L., Nonlinear gyrokinetic equations for low-frequency electromagnetic waves in general plasma equilibria, *Phys. Fluids* **25** (1982) 502.
- [2.68] LEE, W.W., Gyrokinetic approach in particle simulation, *Phys. Fluids* **26** (1983) 556.
- [2.69] DUBIN, D.H.E., KROMMES, J.A., OBERMAN, C., LEE, W.W., Nonlinear gyrokinetic equations, *Phys. Fluids* **26** (1983) 3524.
- [2.70] HAHM, T.S., LEE, W.W., BRIZARD, A.J., Nonlinear gyrokinetic theory for finite-beta plasmas, *Phys. Fluids* **31** (1988) 1940.
- [2.71] HAHM, T.S., Nonlinear gyrokinetic equations for tokamak microturbulence, *Phys. Fluids* **31** (1988) 2670.
- [2.72] BRIZARD, A.J., Nonlinear gyrokinetic Maxwell-Vlasov equations using magnetic co-ordinates, *J. Plasma Phys.* **41** (1989) 541.
- [2.73] HAHM, T.S., Nonlinear gyrokinetic equations for turbulence in core transport barriers, *Phys. Plasmas* **3** (1996) 4658.
- [2.74] CATTO, P.J., Linearized gyrokinetics, *Plasma Phys.* **20** (1978) 719.

- [2.75] LITTLEJOHN, R.G., Hamiltonian perturbation theory in noncanonical coordinates, *J. Math. Phys.* **23** (1982) 742.
- [2.76] KULSRUD, R.M., *Handbook of Plasma Physics*, Vol. 1. (ROSENBLUTH, M.N., SAGDEEV, R.Z., Eds), North-Holland Publishing Company, Amsterdam, New York and Oxford (1983) 115.
- [2.77] GANG, F.Y., DIAMOND, P.H., A nonlinear bounce-kinetic equation for trapped electrons, *Phys. Fluids B* **2** (1990) 2976.
- [2.78] FONG, B.H., HAHM, T.S., Bounce-averaged kinetic equations and neoclassical polarization density, *Phys. Plasmas* **6** (1999) 188.
- [2.79] ROSENBLUTH, M.N., HINTON, F.L., Poloidal flow driven by ion-temperature-gradient turbulence in tokamaks, *Phys. Rev. Lett.* **80** (1998) 724.
- [2.80] KADOMTSEV, B.B., POGUTSE, O.P., *Reviews of Plasma Physics*, Vol. 5 (LEONTOVICH, M.A., Ed.), Consultants Bureau, New York (1970) 249.
- [2.81] HAHM, T.S., TANG, W.M., Properties of ion temperature gradient drift instabilities in H-mode plasmas, *Phys. Fluids B* **1** (1989) 1185.
- [2.82] ROMANELLI, F., Ion temperature-gradient-driven modes and anomalous ion transport in tokamaks, *Phys. Fluids B* **1** (1989) 1018.
- [2.83] GOLDSTON, R.J., RUTHERFORD, P.H., *Introduction to Plasma Physics*, Institute of Physics, Bristol (1995).
- [2.84] BIGLARI, H., DIAMOND, P.H., ROSENBLUTH, M.M., Toroidal ion-pressure-gradient-driven drift instabilities and transport revisited, *Phys. Fluids B* **1** (1989) 109.
- [2.85] LEE, Y.C., DONG, J.Q., GUZDAR, P.N., LIU, C.S., Collisionless electron temperature gradient instability, *Phys. Fluids* **30** (1987) 1331.
- [2.86] HORTON, C.W., HONG, B.G., TANG, W., Toroidal electron temperature gradient driven drift modes, *Phys. Fluids* **31** (1988) 2971.
- [2.87] JENKO, F., DORLAND, W., KOTSCHENREUTHER, M., ROGERS, B.N., Electron temperature gradient driven turbulence, *Phys. Plasmas* **7** (2000) 1904.
- [2.88] DORLAND, W., JENKO, F., KOTSCHENREUTHER, M., ROGERS, B.N., Electron temperature gradient turbulence, *Phys. Rev. Lett.* **85** (2000) 5579.

- [2.89] ADAM, J.C., TANG, W.M., RUTHERFORD, P.H., Destabilization of the trapped-electron mode by magnetic curvature drift resonances, *Phys. Fluids* **19** (1976) 561.
- [2.90] KADOMTSEV, B.B., POGUTSE, O.P., Plasma instability due to particle trapping in a toroidal geometry, *Sov. Phys. – JETP (Engl Trans.)* **24** (1967) 1172.
- [2.91] KADOMTSEV, B.B., POGUTSE, O.P., Dissipative, trapped-particle instability in a dense plasma, *Sov. Phys. - Dokl. (English Translation)* **14** (1969) 470.
- [2.92] ROSENBLUTH, M.N., ROSS, D.W., KOSTOMAROV, D.P., Stability regions of dissipative trapped-ion instability, *Nucl. Fusion* **12** (1972) 3.
- [2.93] TANG, W.M., ADAM, J.C., ROSS, D.W., Residual trapped-ion instabilities in tokamaks, *Phys. Fluids* **20** (1977) 430.
- [2.94] TANG, W.M., REWOLDT, G., Long-wavelength microinstabilities in toroidal plasmas, *Phys Fluids B* **5** (1993) 2451.
- [2.95] KROMMES, J.A., Lecture notes on turbulence and coherent structures, in *Fluids, Plasmas and Nonlinear Media*, (STARTS, M., PUNZMANN, H., Eds), World Scientific, Singapore (2006) 115.
- [2.96] FONCK, R.J., et al., Long-wavelength density turbulence in the TFTR tokamak, *Phys. Rev. Lett.* **70** (1993) 3736.
- [2.97] MCKEE, G.R., et al., Experimental characterization of coherent, radially-sheared zonal flows in the DIII-D tokamak, *Phys. Plasmas* **10** (2003) 1712.
- [2.98] DIAMOND, P.H., HAHM, T.S., On the dynamics of turbulent transport near marginal stability, *Phys. Plasmas* **2** (1995) 3640.
- [2.99] GARBET, X., LAURENT, L., SAMAIN, A., CHINARDET, J., Radial propagation of turbulence in tokamaks, *Nucl. Fusion* **34** (1994) 963.
- [2.100] HAHM, T.S., DIAMOND, P.H., LIN, Z., ITOH, K., ITOH, S.I., Turbulence spreading into the linearly stable zone and transport scaling, *Plasma Phys. Control. Fusion* **46** (2004) A323.
- [2.101] LIN, Z., HAHM, T.S., Turbulence spreading and transport scaling in global gyrokinetic particle simulations, *Phys. Plasmas* **11** (2004) 1099.
- [2.102] CHEN, L., *Waves and Instabilities in Plasmas*, World Scientific Lecture Notes in Physics, Vol. 12, World Scientific Publishing, Singapore (1987).

- [2.103] LEE, Y.C., VAN DAM, J.W., Proc. Finite Beta Theory Workshop, Varenna, 1977 (COPPI, B., SADOWSKI, W., Eds), US Department of Energy (1977) 55.
- [2.104] COWLEY, S.C., KULSRUD, R.M., SUDAN, R.N., Considerations of ion-temperature-gradient-driven turbulence, Phys. Fluids B **3** (1991) 2767.
- [2.105] ROMANELLI, F., ZONZA, F., The radial structure of the ion-temperature-gradient-driven mode, Phys. Fluids B **5** (1993) 4081.
- [2.106] CONNOR, J.W., HASTIE, R.J., TAYLOR, J.B., Proc. R. Soc. **365** (1979) 1.
- [2.107] GLASSER, A.H., Proc. Finite Beta Theory Workshop, Varenna, 1977 (COPPI, B., SADOWSKI, W., Eds), US Department of Energy (1977) 55.
- [2.108] CHEN, L., CHENG, C.Z., Drift-wave eigenmodes in toroidal plasmas, Phys. Fluids **23** (1980) 2242.
- [2.109] TERRY, P.W., Suppression of turbulence and transport by sheared flow, Rev. Mod. Phys. **72** (2000) 109.
- [2.110] BIGLARI, H., DIAMOND, P.H., TERRY, P.W., Influence of sheared poloidal rotation on edge turbulence, Phys. Fluids B **2** (1990) 1.
- [2.111] ITOH, S.I., ITOH, K., Change of transport at L- and H-mode transition, J. Phys. Soc. Jpn. **59** (1990) 3815.
- [2.112] HAHM, T.S., BURRELL, K.H., Flow shear induced fluctuation suppression in finite aspect ratio shaped tokamak plasma, Phys. Plasmas **2** (1995) 1648.
- [2.113] HASEGAWA, A., MACLENNAN, C.G., KODAMA, Y., Nonlinear behavior and turbulence spectra of drift waves and Rossby waves, Phys. Fluids **22** (1979) 2122.
- [2.114] SAGDEEV, R.Z., SHAPIRO, V.D., SHEVCHENKO, V.I., Convective cells and anomalous plasma diffusion, Sov. J. Plasma Phys. (English Translation.) **4** (1978) 306.
- [2.115] DIAMOND, P.H., et al., Proc. Conf. on Plasma Physics and Controlled Nuclear Fusion Research, Vienna, 1998, IAEA-CN-69/TH3/1.
- [2.116] CHEN, L., LIN, Z., WHITE, R., Excitation of zonal flow by drift waves in toroidal plasmas, Phys. Plasmas **7** (2000) 3129.

- [2.117] HASEGAWA, A., WAKATANI, M., Self-organization of electrostatic turbulence in a cylindrical plasma, *Phys. Rev. Lett.* **59** (1987) 1581.
- [2.118] HAMMETT, G.W., BEER, M.A., DORLAND, W., COWLEY, S.C., SMITH, S.A., Developments in the gyrofluid approach to tokamak turbulence simulations, *Plasma Phys. Control. Fusion* **35** (1993) 973.
- [2.119] LIN, Z., HAHM, T.S., LEE, W.W., TANG, W.M., WHITE, R.B., Turbulent transport reduction by zonal flows: Massively parallel simulations, *Science* **281** (1998) 1835.
- [2.120] DIMITS, A., et al., Comparisons and physics basis of tokamak transport models and turbulence simulations, *Phys. Plasmas* **7** (2000) 969.
- [2.121] HAHM, T.S., BURRELL, K.H., LIN, Z., NAZIKIAN, R., SYNAKOWSKI, E.J., Zonal flow measurements concept I, *Plasma Phys. Control. Fusion* **42** (2000) A205.
- [2.122] WINDSOR, N., JOHNSON, J.L., DAWSON, J.M., Geodesic acoustic waves in hydromagnetic systems, *Phys. Fluids* **11** (1968) 2448.
- [2.123] HAHM, T.S., et al., Shearing rate of time-dependent  $E \times B$  flow, *Phys. Plasmas* **6** (1999) 922.
- [2.124] ITOH, K., ITOH, S.I., DIAMOND, P.H., HAHM, T.S., Physics of zonal flows, *Phys. Plasmas* **13** (2006) 055502.
- [2.125] LIN, Z., HAHM, T.S., LEE, W.W., TANG, W.M., DIAMOND, P.H., Effects of collisional zonal flow damping on turbulent transport, *Phys. Rev. Lett.* **83** (1999) 3645.
- [2.126] MIYATO, N., KISHIMOTO, Y., Global structure of zonal flow and electromagnetic ion temperature gradient driven turbulence in tokamak plasmas, *Phys. Plasmas* **11** (2004) 5557.
- [2.127] ANGELINO, P., et al., Effects of plasma current on nonlinear interactions of ITG turbulence, zonal flows and geodesic acoustic modes, *Plasma Phys. Control. Fusion* **48** (2006) 557.
- [2.128] WALTZ, R.E., KERBEL, G.D., MILOVICH, J., Toroidal gyro-Landau fluid model turbulence simulations in a nonlinear ballooning mode representation with radial modes, *Phys. Plasmas* **1** (1994) 2229.
- [2.129] KOTSCHENREUTHER, M., DORLAND, W., BEER, M., HAMMETT, G.W., Quantitative predictions of tokamak energy confinement from first-principles simulations with kinetic effects, *Phys. Plasmas* **2** (1998) 2381.

- [2.130] HINTON, F.L., ROSENBLUTH, M.N., Dynamics of axisymmetric and poloidal flows in tokamaks, *Plasma Phys. Control. Fusion* **41** (1999) A653.
- [2.131] LIN, Z., ETHIER, S., HAHM, T.S., TANG, W.M., Size scaling of turbulent transport in magnetically confined plasmas, *Phys. Rev. Lett.* **88** (2002) 195004.
- [2.132] VILLARD, L., et al., Full radius linear and nonlinear gyrokinetic simulations for tokamaks and stellarators: zonal flows, applied  $E \times B$  flows, trapped electrons and finite beta, *Nucl. Fusion* **44** (2004) 172.
- [2.133] WALTZ, R.E., CANDY, J.M., Heuristic theory of nonlocally broken gyro-Bohm scaling, *Phys Plasmas* **12** (2005) 072303.
- [2.134] NAULIN, V., NEILSEN, A.H., JUUL RASMUSSEN, J., Turbulence spreading, anomalous transport, and pinch effect, *Phys. Plasmas* **12** (2005) 122306.
- [2.135] GURCAN, O.D., DIAMOND, P.H., HAHM, T.S., Nonlinear triad interactions and the mechanism of spreading in drift-wave turbulence, *Phys. Rev. Lett.* **97** (2006) 024502.
- [2.136] YAGI, M., et al., Turbulence spreading in reversed shear plasmas, *Plasma Phys. Control. Fusion* **48** (2006) A409.
- [2.137] ZONCA, F., et al., Physics of burning plasmas in toroidal magnetic confinement devices, *Plasma Phys. Control. Fusion* **48** (2006) B15.
- [2.138] FALCHETTO, G.L., OTTAVIANI, M., Effect of collisional zonal-flow damping on flux-driven turbulent transport, *Phys. Rev. Lett.* **92** (2004) 25002.
- [2.139] MIKKELSEN, D.R., DORLAND, W., Dimits shift in realistic gyrokinetic plasma-turbulence simulations, *Phys. Rev. Lett.* **101** (2008) 135003.
- [2.140] SIMILON, P., DIAMOND, P.H., Nonlinear interaction of toroidicity-induced drift modes, *Phys. Fluids* **27** (1984) 916.
- [2.141] RYTER, F., et al., Experimental study of trapped-electron-mode properties in tokamaks: Threshold and stabilization by collisions, *Phys. Rev. Lett.* **95** (2005) 085001.
- [2.142] KAYE, S., et al., Confinement and local transport in the National Spherical Torus Experiment (NSTX), *Nucl. Fusion* **47** (2007) 499.

- [2.143] MAZZUCATO, E., et al., Study of turbulent fluctuations driven by the electron temperature gradient in the National Spherical Torus Experiment, *Nucl. Fusion* **49** (2009) 055001.
- [2.144] LIN, Z., et al., Wave-particle decorrelation and transport of anisotropic turbulence in collisionless plasmas, *Phys. Rev. Lett.* **99** (2007) 265003.
- [2.145] STORTH, U., WAGNER, F., Transport in toroidal devices — the experimentalist’s view, *Plasma Phys. Control. Fusion* **35** (1993) 1321.
- [2.146] HOANG, G.T., et al., Parametric dependence of turbulent particle transport in Tore-Supra plasmas, *Phys. Rev. Lett.* **93** (1993) 135003.
- [2.147] WEISEN, H., et al., Shear and collisionality dependences of particle pinch in JET L-mode plasmas, *Plasma Phys. Control. Fusion* **46** (2003) 751.
- [2.148] YANKOV, V.V., The pinch effect explains turbulent transport in tokamaks, *JETP Lett. (English Translation)* **60** (1994) 171.
- [2.149] TANG, W.M., REWOLDT, G., CHEN, L., Microinstabilities in weak density gradient tokamak systems, *Phys. Fluids* **29** (1986) 3715.
- [2.150] TERRY, P.W., Anomalous particle pinch for collisionless plasma, *Phys. Fluids* **B1** (1989) 1932.
- [2.151] WEILAND, J., JARMEN, A.B., NORDMAN, H., Diffusive particle and heat pinch effects in toroidal plasmas, *Nucl. Fusion* **29** (1989) 1810.
- [2.152] WALTZ, R.E., DOMINGUEZ, R.R., Note on detailed models for trapped electron transport in tokamaks, *Phys. Fluids* **B1** (1989) 1935.
- [2.153] ANGIONI, C., PEETERS, A.G., PEREVERZEV, G.V., RYTER, F., TARDINI, G. (ASDEX Upgrade Team), Density peaking, anomalous pinch, and collisionality in tokamak plasmas, *Phys. Rev. Lett.* **90** (2003) 205003.
- [2.154] NAULIN, V., NYCANDER, J., JUUL RASMUSSEN, J., Equipartition and Transport in Two-Dimensional Electrostatic Turbulence, *Phys. Rev. Lett.* **81** (1998) 4148.
- [2.155] ISICHENKO, M.B., GRUZINOV, A.V., DIAMOND, P.H., Invariant measure and turbulent pinch in tokamaks, *Phys. Rev. Lett.* **74** (1995) 4436.
- [2.156] GARBET, X., et al., Turbulent fluxes and entropy production rate, *Phys. Plasmas* **12** (2005) 082511.

- [2.157] BAKER, D., ROSENBLUTH, M.N., Density profile consistency and its relation to the transport of trapped versus passing electrons in tokamaks, *Phys. Plasmas* **5** (1998) 2936.
- [2.158] DIAMOND, P.H., KIM, Y.B., Theory of mean poloidal flow generation by turbulence, *Phys. Fluids B* **3** (1991) 1626.
- [2.159] MATTOR, N., DIAMOND, P.H., Momentum and thermal transport in neutral-beam-heated tokamaks, *Phys. Fluids* **31** (1988) 1180.
- [2.160] IDA, K., et al., Evidence for a toroidal-momentum-transport nondiffusive term from the JFT-2M tokamak, *Phys. Rev. Lett.* **74** (1995) 1990.
- [2.161] YOSHIDA, M., et al., Effects of ripple loss of fast ions on toroidal rotation in JT-60U, *Plasma Phys. Control. Fusion* **48** (2006) 1673.
- [2.162] SOLOMON, W., et al., Momentum-transport studies in high EB shear plasmas in the National Spherical Torus Experiment, *Phys. Rev. Lett.* **101** (2008) 065004.
- [2.163] HIDALGO, C., et al., Physics of sheared flow development in the boundary of fusion plasmas, *Plasma Phys. Control. Fusion* **48** (2006) S169.
- [2.164] ERIKSSON, L.G., RIGHI, E., ZASTROW, K.D., Toroidal rotation in ICRF-heated H-modes on JET, *Plasma Phys. Control. Fusion* **39** (1997) 27.
- [2.165] RICE, J.E., MARMAR, E.S., BOMBARDA, F., QU, L., X-ray observations of central toroidal rotation in ohmic Alcator C-Mod plasmas, *Nucl. Fusion* **37** (1997) 421.
- [2.166] LABOMBARD, B., et al., Transport-driven scrape-off-layer flows and the boundary conditions imposed at the magnetic separatrix in a tokamak plasma, *Nucl. Fusion* **44** (2004) 1047.
- [2.167] RICE, J.E., et al., Inter-machine comparison of intrinsic toroidal rotation in tokamaks, *Nucl. Fusion* **47** (2007) 1618.
- [2.168] YOSHIDA, M., et al., Role of pressure gradient on intrinsic toroidal rotation in tokamak plasmas, *Phys. Rev. Lett.* **100** (2008) 105002.
- [2.169] DIAMOND, P.H., MCDEVITT, C.J., GURCAN, O.D., HAHM, T.S., NAULIN, V., Transport of parallel momentum by collisionless drift wave turbulence, *Phys. Plasmas* **15** (2008) 012303.
- [2.170] COPPI, B., Accretion theory of 'spontaneous' rotation in toroidal plasmas, *Nucl. Fusion* **42** (2002) 1.

- [2.171] HAHM, T.S., DIAMOND, P.H., GURCAN, O.D., REWOLDT, G., Nonlinear gyrokinetic theory of toroidal momentum pinch, *Phys. Plasmas* **14** (2007) 072302.
- [2.172] HAHM, T.S., DIAMOND, P.H., GURCAN, O.D., REWOLDT, G., Turbulent equipartition theory of toroidal momentum pinch, *Phys. Plasmas* **15** (2008) 055902.
- [2.173] GURCAN, O.D., DIAMOND, P.H., HAHM, T.S., Turbulent equipartition and homogenization of plasma angular momentum, *Phys. Rev. Lett.* **100** (2008) 135001.
- [2.174] DIAMOND, P.H., et al., Physics of non-diffusive turbulent transport of momentum and the origins of spontaneous rotation in tokamaks, *Nucl. Fusion* **49** (2009) 045002.
- [2.175] PEETERS, A.G., ANGIONI, C., STRINTZI, D., Toroidal momentum pinch velocity due to the Coriolis drift effect on small scale instabilities in a toroidal plasma, *Phys. Rev. Lett.* **98** (2007) 265003.
- [2.176] GURCAN, O.D., DIAMOND, P.H., HAHM, T.S., SINGH, R., Intrinsic rotation and electric field shear, *Phys. Plasmas* **14** (2007) 042306.
- [2.177] WANG, X.H., DIAMOND, P.H., ROSENBLUTH, M.N., Stability of ion-temperature-gradient-driven modes in the presence of sheared poloidal flows, *Phys. Fluids B* **4** (1992) 2402.
- [2.178] DOMINGUEZ, R.R., STAEBLER, G.M., Anomalous momentum transport from drift wave turbulence, *Phys. Fluids B* **5** (1993) 3876.
- [2.179] HAHM, T.S., Physics behind transport barrier theory and simulations, *Plasma Phys. Control. Fusion* **44** (2002) A87.
- [2.180] CONNOR, J.W., WILSON, H.R., A review of theories of the L-H transition, *Plasma Phys. Control. Fusion*, **42** (2000) R1.
- [2.181] BURRELL, K.H., Effects of  $E \times B$  velocity shear and magnetic shear on turbulence and transport in magnetic confinement devices, *Phys. Plasmas* **4** (1997) 1499.
- [2.182] SYNAKOWSKI, E.J., et al., Local transport barrier formation and relaxation in reverse-shear plasmas on the Tokamak Fusion Test Reactor, *Phys. Plasmas* **4** (1997) 1736.
- [2.183] HAHM, T.S., Rotation shear induced fluctuation decorrelation in a toroidal plasma, *Phys. Plasmas* **1** (1994) 2940.
- [2.184] LEVI NTON, F.M., et al., Improved confinement with reversed magnetic shear in TFTR, *Phys. Rev. Lett.* **75** (1995) 4417.

- [2.185] CROMBE, K. et al., Poloidal rotation dynamics, radial electric field, and neoclassical theory in the JET internal-transport-barrier region, *Phys. Rev. Lett.* **95** (2005) 155003.
- [2.186] MOYER, R.A., et al., Beyond paradigm: Turbulence, transport, and the origin of the radial electric field in low to high confinement mode transitions in the DIII-D tokamak, *Phys. Plasmas* **2** (1995) 2397.
- [2.187] MAZZUCATO, E., et al., Turbulent fluctuations in TFTR configurations with reversed magnetic shear, *Phys. Rev. Lett.* **77** (1996) 3145.
- [2.188] WAGNER, F., et al., Regime of improved confinement and high beta in neutral-beam-heated divertor discharges of the ASDEX tokamak, *Phys. Rev. Lett.* **49** (1982) 1408.
- [2.189] MCDERMOTT, R.M., et al., Edge radial electric field structure and its connection to H-mode confinement in Alcator C-Mod plasmas, *Phys. Plasmas* **16** (2009) 056103.
- [2.190] STRAIT, E.J., et al., Enhanced confinement and stability in DIII-D discharges with reversed magnetic shear, *Phys. Rev. Lett.* **75** (1995) 4421.
- [2.191] BURRELL, K.H., et al., *Plasma Physics and Controlled Nuclear Fusion Research*, Vol. 1, IAEA, Vienna (1995) 221.
- [2.192] SOLDNER, F.X., JET TEAM, Shear optimization experiments with current profile control on JET, *Plasma Phys. Control. Fusion* **39** (1997) B353.
- [2.193] RICE, J.E., et al., Impurity toroidal rotation and transport in Alcator C-Mod ohmic high confinement mode plasmas, *Phys. Plasmas* **7** (2000) 1825.
- [2.194] WOLF, R.C., et al., Performance, heating and current drive scenarios of ASDEX Upgrade advanced tokamak discharges, *Nucl. Fusion* **41** (2001) 1259.
- [2.195] NAZIKIAN, R., et al., Measurement of turbulence decorrelation during transport barrier evolution in a high-temperature fusion plasma, *Phys. Rev. Lett.* **94** (2005) 135002.
- [2.196] HAHM, T.S., DIAMOND, P.H., Resistive fluid turbulence in diverted tokamaks and the edge transport barrier in H-mode plasmas, *Phys. Fluids* **30** (1987) 133.

- [2.197] TOI, K., et al., Role of edge magnetic shear on the limiter H-mode transition of the JIPP T-IIU tokamak, *Phys. Rev. Lett.* **64** (1990) 1895.
- [2.198] TANG, W.M., Theory of Fusion Plasmas (SIDONI, E., TROYON, F., VACLAVIK, J., Eds) Editrice Compositori Bologna (1990) 31.
- [2.199] KESSEL, C., MANICKAM, J., REWOLDT, G., TANG, W.M., Improved plasma performance in tokamaks with negative magnetic shear, *Phys. Rev. Lett.* **72** (1994) 1212.
- [2.200] ROACH, C.M., CONNOR, J.W., JANJUA, S., Trapped particle precession in advanced tokamaks, *Plasma Phys. Control. Fusion* **37** (1995) 679.
- [2.201] BEER, M.A., et al., Gyrofluid simulations of turbulence suppression in reversed-shear experiments on the Tokamak Fusion Test Reactor, *Phys. Plasmas* **4** (1997) 1792.
- [2.202] REWOLDT, G., LAO, L.L., TANG, W.M., Microinstability properties of negative magnetic shear discharges in the Tokamak Fusion Test Reactor and DIII-D, *Phys. Plasmas* **4** (1997) 2393.
- [2.203] MAGET, P., GARBET, X., GERAUD, A., JOFFRIN, E., Drift wave stability of PEP discharges in Tore-Supra, *Nucl. Fusion* **39** (1999) 949.
- [2.204] KIM, J.Y., WAKATANI, M., Negative shear effect on toroidal ion temperature gradient mode, *Phys. Plasmas* **2** (1995) 1012.
- [2.205] DIMITS, A.M., WILLIAMS, T.J., BYERS, J.A., COHEN, B.I., Scalings of ion-temperature-gradient-driven anomalous transport in tokamaks, *Phys. Rev. Lett.* **77** (1996) 71.
- [2.206] KISHIMOTO, Y., et al., Toroidal mode structure in weak and reversed magnetic shear plasmas and its role in the internal transport barrier, *Plasma Phys. Control. Fusion* **41** (1999) A663.
- [2.207] IDOMURA, Y., WAKATANI, M., TOKUDA, S., Stability of  $E \times B$  zonal flow in electron temperature gradient driven turbulence, *Phys. Plasmas* **7** (2000) 3551.
- [2.208] GARBET, X., et al., Global simulations of ion turbulence with magnetic shear reversal, *Phys. Plasmas* **8** (2001) 2793.
- [2.209] WALTZ, R.E., AUSTIN, M.E., BURRELL, K.H., CANDY, J., Gyrokinetic simulations of off-axis minimum-q profile corrugations, *Phys. Plasmas* **13** (2006) 052301.

- [2.210] MCDEVITT, C.J., DIAMOND, P.H., Low-q resonances, transport barriers, and secondary electrostatic convective cells, *Phys. Plasmas* **14** (2007) 112306.
- [2.211] AUSTIN, M.E., et al., Core barrier formation near integer q surfaces in DIII-D, *Phys. Plasmas* **13** (2006) 082502.
- [2.212] BELL, R.E., et al., Proc. 23rd European Physical Society Conf. on Controlled Fusion and Plasma Physics, Kiev, **20 C**, Part I (1996) 59.
- [2.213] JOFFRIN, E., et al., Triggering of internal transport barrier in JET, *Plasma Phys. Control. Fusion* **44** (2002) 1739.
- [2.214] GÜNTER, S., et al., MHD phenomena in advanced scenarios on ASDEX Upgrade and the influence of localized electron heating and current drive, *Nucl. Fusion* **41** (2001) 1283.
- [2.215] YUH, H.Y., et al., Internal transport barriers in the National Spherical Torus Experiment, *Phys. Plasmas* **16** (2009) 056120.
- [2.216] BARANOV, Y., et al., On the link between the q-profile and internal transport barriers, *Plasma Phys. Control. Fusion* **46** (2004) 1181.
- [2.217] TURCO, F., GIRUZZI, G., ARTAUD, J.F., MAZON, D., Internal transport barrier formation in the Tore-Supra tokamak, *Plasma Phys. Control. Fusion* **51** (2009) 065021.
- [2.218] DIAMOND, P.H., et al., Dynamics of transition to enhanced confinement in reversed magnetic shear discharges, *Phys. Rev. Lett.* **78** (1997) 1472.
- [2.219] HINTON, F.L., Thermal confinement bifurcation and the L- to H-mode transition in tokamaks, *Phys. Fluids B* **3** (1991) 696.
- [2.220] ITOH, K., Theoretical progress on H-mode physics, *Plasma Phys. Control. Fusion* **36** (1994) A307.
- [2.221] ZHANG, Y.Z., MAHAHAN, S.M., Edge turbulence scaling with shear flow, *Phys. Fluids B* **4** (1992) 1385.
- [2.222] LEBEDEV, V.B., DIAMOND, P.H., Theory of the spatiotemporal dynamics of transport bifurcations, *Phys. Plasmas* **4** (1997) 1087.
- [2.223] MALKOV, M., DIAMOND, P.H., Analytic theory of L→H transition, barrier structure, and hysteresis for a simple model of coupled particle and heat fluxes, *Phys. Plasmas* **15** (2008) 122301.

- [2.224] HUBBARD, A., et al., Variation of edge gradients with heat flux across L-H and H-L transitions in Alcator C-Mod, *Plasma Phys. Control. Fusion* **44** (2002) A359.
- [2.225] CRADDOCK, G.G., DIAMOND, P.H., Theory of shear suppression of edge turbulence by externally driven radio-frequency waves, *Phys. Rev. Lett.* **67** (1991) 1535.
- [2.226] LIN, Y., et al., Observation of ion cyclotron range of frequencies mode conversion plasma flow drive on Alcator C-Mod, *Phys. Plasmas* **16** (2009) 056102.
- [2.227] SWAIN, D.W., NEILSON, G.H., *Nucl. Fusion* **22** (1982) 1015.
- [2.228] KAYE, S.M., *Phys. Fluids* **28** (1985) 2327.
- [2.229] KAYE, S.M., BARNES, C.W., BELL, M.G., et al., *Phys. Fluids B* **2** (1990) 2926.
- [2.230] ITER Physics Basis, *Nucl. Fusion* **39** (1999) 2175.
- [2.231] DOYLE, E.J., HOULBERG, W.A., KAMADA, Y., et al., *Nucl. Fusion* **47** (2007) S18.
- [2.232] JASSBY, D., COHN, D., PARKER, R., *Nucl. Fusion* **16** (1976) 1045.
- [2.233] PFEIFFER, W., WALTZ, R., *Nucl. Fusion* **19** (1979) 51.
- [2.234] CORDEY, J.G., GORBUNOV, E., HUGILL, J., et al., *Nucl. Fusion* **15** (1975) 441.
- [2.235] BOL, K., CECCHI, J., DAUGHNEY, C., et al., *Phys. Rev. Lett.* **32** (1973) 661.
- [2.236] MURAKAMI, M., ISERL, R., LYON, J., et al., *Phys. Rev. Lett.* **39** (1977) 615.
- [2.237] EQUIPE TFR, *Nucl. Fusion* **18** (1978) 1271.
- [2.238] GOLDSTON, R.J., DAVIS, S., EUBANK, H., et al., in *Heating in Toroidal Plasmas*, Proc. 2nd Joint Grenoble-Varenna Int. Symp., Vol. 2, Como 1980, CEC, Brussels (1980) 711.
- [2.239] BURRELL, K.H., STAMBAUGH, R.D., ANGEL, T.R., et al., *Nucl. Fusion* **23** (1983), 536.
- [2.240] MURMANN, H., WAGNER, F., ASDEX NI, ICRH TEAMS, in *Controlled Fusion and Plasma Heating*, Proc. 15th Eur. Conf. on Controlled Fusion and Plasma Physics (EPS), Dubrovnik, Vol. 1 (1988) 3.

- [2.241] DEBOO, J., BURRELL, K.H., EJIMA, S., et al., Nucl. Fusion **26** (1986) 211.
- [2.242] SUZUKI, N., et al., in Controlled Fusion and Plasma Heating, Proc. 14th Eur. Conf. on Controlled Fusion and Plasma Physics, Madrid, Vol. 2 (1987) 217.
- [2.243] GOLDSTON, R., Plasma Phys. Control. Fusion **26** (1984) 87.
- [2.244] BELL, M.G., ARUNASALEM, W., BITTER, M., et al., Plasma Phys. Control. Fusion **28** (1986) 1329.
- [2.245] BICKERTON, R.J., AINSORTH, A., ATTMAN, H., et al., Plasma Phys. Control. Fusion **28** (1986) 1943.
- [2.246] KAYE, S.M., GOLDSTON, R.J., Nucl. Fusion **25** (1985) 65.
- [2.247] YUSHMANOV, P.N., TAKIZUKA, T., RIEDEL, K.S., et al., Nucl. Fusion **30** (1990) 1999.
- [2.248] KAYE, S.M., ITER CONFINEMENT DATABASE WORKING GROUP, Nucl. Fusion **37** (1997) 1303.
- [2.249] REBUT, P., LALLIA, P., WATKINS, M., Proc. 12th Int. Conf. on Plasma Physics and Controlled Nuclear Fusion Research, Nice, Vol. 2 (1988) 191.
- [2.250] KAYE, S.M., BELL, M.G., BOL, K., et al., J. Nucl. Mater. **121** (1984) 115.
- [2.251] NAGAMI, M., KASAI, M., KITZUNEZAKI, A., et al., Nucl. Fusion **24** (1985) 65.
- [2.252] ERCKMANN, V., WAGNER, F., BALDZUHN, J., et al., Phys. Rev. Lett. **70** (1993) 2086.
- [2.253] KAYE, S.M., MANICKAM, J., ASAKURA, N., et al., Nucl. Fusion **30** (1990) 262.
- [2.254] SNYDER, P.B., WILSON, H.R., OSBORNE, T.H., LEONARD, A.W., Plasma Phys. Control. Fusion **46** (2004) A131.
- [2.255] CHRISTIANSEN, J.P., CORDEY, J.G., THOMSEN, K., et al., Nucl. Fusion **32** (1992) 291.
- [2.256] ITER H-MODE DATABASE WORKING GROUP, Nucl. Fusion **34** (1994) 131; Plasma Phys. Control. Fusion **2** (1995) 525.
- [2.257] MCDONALD, D.C., CORDEY, J.G., THOMSEN, K., et al., Nucl. Fusion **47** (2007) 147.

- [2.258] KAYE, S.M., VALOVIC, M., CHUDNOVSKIY, A., et al., Plasma Phys. Control. Fusion **48** (2006) A429.
- [2.259] KAYE, S.M., BELL, M.G., BELL, R.E., et al., Nucl. Fusion **46** (2006) 848.
- [2.260] KAYE, S.M., BELL, R.E., GATES, D., et al., Phys. Rev. Lett. **98** (2007) 175002-1.
- [2.261] VALOVIC, M., et al., Nucl. Fusion **49** (2009) 075016.
- [2.262] CORDEY, J.G. for the ITAP H-mode Database Working Group, Nucl. Fusion **43** (2003) 670.
- [2.263] DRAPER, N.R., SMITH, H., Applied Regression Analysis, 2nd edn, John Wiley and Sons, New York (1981).
- [2.264] THOMSEN, K., CORDEY, J.G., KARDAUNN, O.J., et al., “Analysis of bias in H-mode confinement scaling expressions related to measurement errors in variables”, Proc. 31st EPS Conf. on Plasma Physics, London, 2004, ECA, Vol. 28G (2004) 145.
- [2.265] CORDEY, J.G., THOMSEN, K., CHUDNOVSKIY, A., et al., Nucl. Fusion **45** (2005) 1078.
- [2.266] MCDONALD, D.C., MEAKINS, A.J., SVENSSON, J., et al., Plasma Phys. Control. Fusion **48** (2006) A439.
- [2.267] CONNOR, J.W., TAYLOR, J.B., Nucl. Fusion **17** (1977) 1047.
- [2.268] CONNOR, J.W., Plasma Phys. Control. Fusion **30** (1988) 61.
- [2.269] PETTY, C.C., Phys. Plasmas **15** (2008) 080501.
- [2.270] PETTY, C.C., LUCE, T.C., MCDONALD, D.C., et al., Phys. Plasmas **11** (2004) 2514.
- [2.271] MCDONALD, D.C., CORDEY, J.G., PETTY, C.C., et al., Plasma Phys. Control. Fusion **46** (2004) A415.
- [2.272] VERMARE, L., RYTER, F., ANGIONI, C., et al., Nucl. Fusion **47** (2007) 490.
- [2.273] URANO, H., TAKIZUKA, T., TAKENAGA, H., et al., Nucl. Fusion **46** (2006) 781.
- [2.274] CORDEY, J.G., UKAEA, Culham Laboratory, Abingdon, Oxfordshire, UK, personal communication, 2008.
- [2.275] BUSH, C.E., GOLDSTON, R.J., SCOTT, S.D., et al., Phys. Rev. Lett. **65** (1990) 424.

- [2.276] RYTER, F., H-MODE POWER THRESHOLD DATABASE WORKING GROUP FOR ITER, Nucl. Fusion **36** (1996) 1217.
- [2.277] BURRELL, K.H., CARLSTROM, T.M., DOYLE, E.J., et al., Plasma Phys. Control. Fusion **34** (1992) 1859.
- [2.278] GROEBNER, R.J., Phys. Fluids B **5** (1993) 2343.
- [2.279] GUZDAR, P.N, KLEVA, R.G., DAS, A., KAW, P.K., Phys. Rev. Lett. **87** (2001) 015001.
- [2.280] GUZDAR, P.N, KLEVA, R.G., GROEBNER, R.J., GOHIL, P., Phys. Rev. Lett. **89** (2002) 265004.
- [2.281] HUBBARD, A.E., CARRERAS, B.A., BASSE, N.P., et al., Plasma Phys. Control. Fusion **46** (2004) A95.
- [2.282] KAYE, S.M., BUSH, C.E., FREDRICKSON, E., et al., Phys. Plasmas **10** (2003) 3953.
- [2.283] ZWEBEN, S.J., MAQUEDA, R.J., TERRY, J.L.. et al., Phys. Plasmas **13** (2006) 056114.
- [2.284] ITER CONFINEMENT DATABASE AND MODELING GROUP, “Projection of ITER performance using the multimachine L- and H-mode databases”, Proc. 15th Int. Conf. on Plasma Physics, Seville, 1994, Vol. 2 (1995) 525.
- [2.285] ITER CONFINEMENT DATABASE AND MODELING GROUP, Threshold Power and Energy Confinement for ITER, Proc. 16th Int. Conf. on Plasma Physics, Montreal, 1996, Vol. 2 (1997) 795.
- [2.286] MARTIN, Y.R., TAKIZUKA, T., ITPA CDBM H-MODE THRESHOLD WORKING GROUP, J. Phys. Conf. Series **123** (2008) 012033.
- [2.287] ITPA H-MODE THRESHOLD DATABASE WORKING GROUP, H-mode threshold power dependences in ITPA threshold database, Proc. 21st Fusion Energy Conf., Chengdu, 2006, Paper IT/P3-35.
- [2.288] ITER H-MODE POWER THRESHOLD DATABASE WORKING GROUP, “Roles of aspect ratio, absolute B and effective Z for the H-mode power threshold in tokamaks of the ITPA database”, Proc. 9th IAEA Tech. MTg on H-mode Physics and Transport Barriers, San Diego, 2003, Plasma Phys. Control. Fusion **46** (2004) A227.
- [2.289] BUSH, C.E., BELL, M.G., BELL, R.E., et al., Phys. Plasmas **10** (2003) 1755.

- [2.290] RYTER, F., PUTTERICH, T., REICH, M., et al., Proc. 22nd Fusion Energy Conf., Geneva, 2008, Paper PD/1-1; Nucl. Fusion **49** (2009) 062003.
- [2.291] GOHIL, P., et al., Proc. 22nd Fusion Energy Conf., Geneva, 2008, Paper PD/P1-1; Nucl. Fusion **49** (2009) 115004.
- [2.292] GREENWALD, M., TERRY, J.L., WOLFE, S.M., et al., Nucl. Fusion **28** (1988) 2199.
- [2.293] HAWRYLUK, R., “Physics of plasmas close to thermonuclear conditions” Proc. Course Varenna 1979, Vol. 1, Commission of the European Communities, Brussels (1979) 19.
- [2.294] GOLDSTON, R.J., et al., J. Comput. Phys. **43** (1981) 61.
- [2.295] ST.JOHN, H.E., et al., Proc. 15th Int. Conf. on Plasma Physics and Controlled Nuclear Fusion Research, Seville, 1994, Vol. 3, IAEA, Vienna (1995) 603.
- [2.296] CHANG, C.S., HINTON, F.L., Phys. Fluids **25** (1982) 1493.
- [2.297] HOULBERG, W.A., et al., Phys. Plasmas **4** (1997) 3230.
- [2.298] JENKO, F., et al., Plasma Phys. Control. Fusion **47** (2007) S18.
- [2.299] HAWRYLUK, R.J., et al., Phys. Plasmas **5** (1998) 1577.
- [2.300] GIBSON, A., THE JET TEAM, Phys. Plasmas **5** (1998) 1839.
- [2.301] STIX, T.H., Plasma Phys. **14** (1972) 367.
- [2.302] DOLAN, T.J., Fusion Research, Vol 1, Pergamon Press, New York (1982).
- [2.303] PANKIN, A., et al., Comput. Phys. Commun. **159** (2004) 157.
- [2.304] HEIDBRINK, W.W., et al., Phys. Rev. Lett. **99** (2007) 2450021.
- [2.305] TOURNIANKSKI, M.R., et al., Plasma Phys. Control. Fusion **47** (2005) 671.
- [2.306] MENARD, J.E., et al., Nucl. Fusion **47** (2007) S645.
- [2.307] GATES, D.A., et al., Phys. Rev. Lett. **87** (2001) 205003.
- [2.308] HEIFETZ, D.B., et al., J. Comput. Phys. **46** (1982) 309.
- [2.309] STOTLER, D.P., et al., Contrib. Plasma Phys. **34** (1994) 392.
- [2.310] BURRELL, K., Phys. Fluids **21** (1978) 2202.
- [2.311] AUDENARDE, K., et al., J. Comput. Phys. **34** (1980) 268.

- [2.312] TAMOR, S., J. Comput. Phys. **40** (1981) 104.
- [2.313] VALANJU, P.M., J. Comput. Phys. **88** (1990) 114.
- [2.314] MANDREKAS, J., Comput. Phys. Comm. **161** (2004) 36.
- [2.315] STACEY, W.M., MANDREKAS, Nucl. Fusion **34** (1994) 1385.
- [2.316] HARVEY, R.W., MCCOY, M.G., "The CQL3D Fokker-Planck Code", Proc. IAEA Tech, Comm. Mtg on Simulation and Modeling of Thermonuclear Plasmas, Montreal, Canada, 1992, USDOC NTIS Document No. DE93002962.
- [2.317] BRAMBILLA, M., Plasma Phys. Control. Fusion **41** (1999) 1; WRIGHT, J.C., et al., Phys. Plasmas **11** (2004) 2473.
- [2.318] JAEGER, E.F., et al., Phys. Plasmas **9** (2002) 1873.
- [2.319] JAEGER, E.F., et al., Nucl. Fusion **46** (2006) S397.
- [2.320] JAEGER, E.F., et al., Phys. Plasmas **15** (2008) 072513.
- [2.321] NELSON-MELBY, E., et al., Phys. Rev. Lett. **90** (2003) 155004.
- [2.322] LIN, Y., et al., Plasma Phys. Control. Fusion **47** (2005) 1207.
- [2.323] LANCELLOTTI, V., et al., Nucl. Fusion **46** (2006) S476.
- [2.324] D'IPPOLITO, D.A., MYRA, J.R., Phys. Plasmas **13** (2006) 102508.
- [2.325] CHOI, M., et al., Nucl. Fusion **46** (2006) 409.
- [2.326] SMIRNOV, A.P., HARVEY, R.W., Calculations of the current drive in DIII-D with the GENRAY Ray Tracing Code, Bull. Am. Phys. Soc. **40** (1995) 1837; Abstract 8P35; also SMIRNOV, A.P., HARVEY, R.W., The GENRAY Ray Tracing Code, CompX Report CompX-2000-01 (2001).
- [2.327] BONOLI, P.T., et al., Phys. Plasmas **15** (2008) 056117 .
- [2.328] PRATER, R., FARINA, D., GRIBOV, Y., HARVEY, R.W., et al, Nucl. Fusion **48** (2008) 035006.
- [2.329] HIRSHMAN, S., Phys Fluids **31** (1988) 3150.
- [2.330] SAUTER, O., et al., Phys. Plasmas **6** (1999) 2834.
- [2.331] OIKAWA, T., et al., Nucl. Fusion **41** (2001) 1575.
- [2.332] TANI, K., et al., J. Comput. Phys. **98** (1992) 332.
- [2.333] PIETRZYK, Z.A. et al., Phys. Rev. Lett. **86** (2001) 1530.
- [2.334] PRATER, R., et al., Nuc. Fusion **43** (2003) 1128.

- [2.335] ZOHM, H., et al., Nucl. Fusion **43** (2003) 1570.
- [2.336] IKEDA, Y., et al., Nucl. Fusion **42** (2002) 375.
- [2.337] O'BRIEN, M.R., et al., Proc. IAEA Tech. Comm. Mtg on Advances in Simulation and Modeling of Thermonuclear Plasmas, Montreal (1992) 527.
- [2.338] GIRUZZI, G., et al., Nucl. Fusion **32** (1992) 1011.
- [2.339] PETTY, C.C., et al., Nucl. Fusion **42** (2002) 1366.
- [2.340] GORMENZANO, C., et al., Nucl. Fusion **47** (2007) S285.
- [2.341] IMBEAUX, F., PEYSSON, Y., Plasma Phys. Control. Fusion **47** (2005) 2041.
- [2.342] NAITO, O., et al., Phys. Rev. Lett. **89** (2002) 065001.
- [2.343] PETTY, C.C. et al., Nucl. Fusion **43** (2001) 1747.
- [2.344] HELLSTEN, T., et al., Proc. Conf. on RF Power in Plasmas, Moran (2003) 197.
- [2.345] ROSENBERG, A.L., et al., Phys. Plasmas **11** (2004) 2441.
- [2.346] PETTY, C.C., et al., Nucl. Fusion **773** (1995) 773.
- [2.347] HOSEA, J., et al., Phys. Plasmas **15** (2008) 056104.
- [2.348] GENTLE, K.W., Phys. Fluids **31** (1988) 1105.
- [2.349] BURRELL, K.B., et al., Phys. Fluids B **2** (1990) 2904.
- [2.350] DEVRIES, P.D., et al., Plasma Phys. Control. Fusion **48** (2006) 1693.
- [2.351] YOSHIDA, M., et al., Nucl. Fusion **47** (2007) 856.
- [2.352] URANO, H., et al., Nucl. Fusion **48** (2008) 1.
- [2.353] KAYE, S.M., et al., Nucl. Fusion **49** (2009) 045010.
- [2.354] LOPES CARDOZO, N., Plasma Phys. Control. Fusion **37** (1995) 799.
- [2.355] SOLER, M., CALLEN, J.D., Nucl. Fusion **19** (1979) 703.
- [2.356] FREDRICKSON, E.D., et al., Nucl. Fusion **26** (1986) 849.
- [2.357] CALLEN, J.D., KISSICK, M.W., Plasma Phys. Control. Fusion **39** (1997) B173.
- [2.358] RYTER, F., et al., Nucl. Fusion **40** (2000) 1917.
- [2.359] FREDRICKSON, E.D., et al., Phys. Rev. Lett. **65** (1990) 2869.

- [2.360] GONDHALEKAR, A., et al., Plasma Phys. Control. Fusion **31** (1989) 805.
- [2.361] BROWER, D.L., et al., Phys. Rev. Lett. **65** (1990) 337.
- [2.362] MIURA, Y., et al., Ion Heat Pulse After Sawtooth Crash in the JFT-2M Tokamak, NIFS Report 240, Aug. 1993.
- [2.363] TRITZ, K., et al., Phys. Plasmas **15** (2008) 056119.
- [2.364] LUCE, T.C., et al., Phys. Rev. Lett. **68** (1991) 52.
- [2.365] KISSICK, M.W., et al., Nucl. Fusion **34** (1994) 349.
- [2.366] VAN MILLIGAN, B. PH., et al., "Cold pulse propagation in the stellarator TJ-II", Proc. 13th International Stellarator Workshop, Canberra, 2002, Paper OIII:2.
- [2.367] HARTFUSS, J.J., et al., Plasma Phys. Control. Fusion **36** (1994) 17.
- [2.368] STROTH, U., et al., "Non-local model analysis of heat pulse propagation and simulation of experiments in W7-AS", Proc. Workshop on Local Transport Studies in Fusion Plasmas, Varenna (1993) 161.
- [2.369] INAGAKI, S., et al., Nucl. Fusion **46** (2006) 133.
- [2.370] RYTER, F., et al., Phys. Rev. Lett. **86** (2001) 2325.
- [2.371] GARBET, X., et al., Plasma Phys. Control. Fusion **46** (2004) 1351.
- [2.372] VAN MILLIGAN, B. PH., et al., Plasma Fusion Res. **3** (2008) S1070.
- [2.373] IMBEAUX, F., et al., Plasma Phys. Control. Fusion **43** (2001) 15.
- [2.374] RYTER, F., et al., Nucl. Fusion **43** (2003) 1396.
- [2.375] HOANG, G.T., et al., Phys. Rev. Lett. **87** (2001) 125001.
- [2.376] CONNOR, J.W., et al., Nucl. Fusion **44** (2004) R1.
- [2.377] SCHMIDT, G.L., et al., Plasma Phys. and Control. Fusion (Proc. 12th Int. Conf. on Fusion Energy, Nice, 1988) **1** (1989) 215.
- [2.378] MILORA, S.L., et al., Plasma Phys. Control. Fusion **28** (1986) 1435.
- [2.379] LEBLANC, B., et al., Phys. Plasmas **2** (1995) 741.
- [2.380] KOIDE, Y., et al., Phys. Rev. Lett. **72** (1994) 3662.
- [2.381] BELL, M.G et al., Plasma Phys. Control. Fusion **41** (1999) A719.
- [2.382] GORMENZANO, C., et al., Plasma Phys. Control. Fusion (Proc. 16th Int. Conf. on Fusion Energy, Montreal, 1996) Vol. 1 (1997) 487.

- [2.383] EQUIPE TORE-SUPRA, Plasma Phys. Control. Fusion **38** (1996) A251.
- [2.384] LITAUDON, X., et al., Plasma Phys. Control. Fusion **41** (1999) A733.
- [2.385] HENDERSON, M.A., et al., Nucl. Fusion **45** (2005) 1642.
- [2.386] YUH, H., et al., Phys. Plasmas **16** (2009) 056120.
- [2.387] WONG, K.L., et al., Nucl. Fusion **45** (2005) 30.
- [2.388] ERNST, D.R., et al., Phys. Plasmas **11** (2004) 2637.
- [2.389] TOKUNAGA, S., et al., J. Phys. Conf. Series (Proc. 11th IAEA Tech. Comm. Mtg on H-mode Physics and Transport Barriers, Tsukuba, 2007) **123** (2008) 012030.
- [2.390] SHIMOZUMA, T., et al., J. Phys. Conf. Series (Proc. 11th IAEA Tech. Comm. Mtg on H-mode Physics and Transport Barriers, Tsukuba, 2007) **123** (2008) 012022.
- [2.391] IDA, K., J. Phys. Conf. Series (Proc. 11th IAEA Tech. Comm. Mtg on H-mode Physics and Transport Barriers, Tsukuba, 2007) **123** (2008) 012004.
- [2.392] GORMENZANO, C., et al., Plasma Phys. Control. Fusion **41** (1999) B367; Nucl. Fusion **39** (1999) 1875.
- [2.393] CRISANTI, F., et al., Phys. Rev. Lett. **88** (2002) 145001.
- [2.394] KAMADA, Y., et al., Nucl. Fusion (Proc. 17th Int. Conf. on Fusion Energy, Yokohama, 1998) **39** (1999) 1845.
- [2.395] BURRELL, K., et al., Phys. Plasmas **8** (2001) 2153.
- [2.396] MOREAU, D., et al., in Proc. 14th Int. Conf. on Fusion Energy, Wurtzburg, **1** (1992) 649.
- [2.397] SAUTER, O., et al., in Proc. 29th EPS Conf. on Controlled Fusion and Plasma Physics, Montreaux, 2002, Vol. 26b, paper P-2.087.
- [2.398] GOHIL, P., C.R. Physique **7** (2006) 606.
- [2.399] LEONARD, A.W., J. Phys. Conf. Series (Proc. 11th IAEA Tech. Comm. Mtg on H-mode Physics and Transport Barriers, Tsukuba, 2007) **123** (2008) 012001.
- [2.400] MCCORMICK, K., et al., Phys. Rev. Lett. **89** (2002) 015001.
- [2.401] ROGERS, B.P., et al., Phys. Rev. Lett. **81** (1998) 4396.
- [2.402] WILSON, H.R., et al., Phys. Plasmas **6** (1999) 1925.

- [2.403] POGUTSE, O., et al., Control. Fusion Plasma Phys. (Proc. 24<sup>th</sup> EPS Conf. Berchtesgaden, 1997) **21A** (1997), 1545.
- [2.404] BURRELL, K.H., Rev. Sci. Inst. **72** (2001), 906.
- [2.405] FENSTERMACHER, M.E. et al., Nucl. Fusion **45** (2005) 1493.
- [2.406] LEONARD, A.W. et al., **47** (2007) 552.
- [2.407] WOLFE, S.M., et al., Effect of Pellet Fueling on Energy Transport in Ohmically Heated Alcator-C Plasmas, Report PFC/JA-85-31, Sept. 1985.
- [2.408] PETTY, C.C., et al., Phys. Rev. Lett. **74** (1995) 1763.
- [2.409] PETTY, C.C., et al., Phys. Plasmas **2** (1995) 2342.
- [2.410] CANDY, J., WALTZ, R.E., Phys. Rev. Lett. **91** (2003) 045001.
- [2.411] WALTZ, R.E., et al., Phys. Plasmas **13** (2006) 072304.
- [2.412] KOTSCHENREUTHER, M., et al., Phys. Plasmas **2** (1995) 2381.
- [2.413] ERNST, D.R., et al., Phys. Rev. Lett. **81** (1998) 2454.
- [2.414] LIN, L. et al., Phys. Plasmas **16** (2009) 012502.
- [2.415] GARBET, X., et al., Plasma Phys. Control. Fusion **46** (2004) B557.
- [2.416] HAHM, T.S., TANG, W.M., Proc. U.S. Japan Joint Institute for Fusion Theory Program on Structures in Confined Plasmas, Nagoya, Japan, 1989 (National Inst. for Fusion Science, Nagoya, Japan, 1990) 55.
- [2.417] DEBOO, J.C., et al., Nucl. Fusion **39** (1999) 1935.
- [2.418] WONG, K.L., et al., Phys. Rev. Lett. **99** (2007) 135003.
- [2.419] STUTMAN, D., et al., Phys. Rev. Lett. **102** (2009) 115002.
- [2.420] TYNAN, G.R., FUJISAWA A., MCKEE, G., Plasma Phys. Control. Fusion **51** (2009) 113001.
- [2.421] WOOTTON, A.J., et al., Plasma Phys. Control. Fusion **30** (1988) 1479; LIEWER, P.C., Nucl. Fusion **25** (1985) 543.
- [2.422] ZWEBEN, S.J., et al., Plasma Phys. Control. Fusion **49** (2007) S1.
- [2.423] SHEFFIELD, J., Plasma Scattering of Electromagnetic Radiation, Academic Press, New York (1975).
- [2.424] MAZZUCATO, E., Phys. Plasmas **10** (2003) 753.
- [2.425] NAZIKIAN, R., et al., Phys. Plasmas **8** (2001) 1840.
- [2.426] HIRSCH, M., et al., Plasma Phys. Control. Fusion **43** (2001) 1641.

- [2.427] GUZAKOV, E.Z., et al., IAEA FEC, EX/10-2Rb.
- [2.428] PORKOLAB, M., et al., IEEE Trans. Plasma Sci. **34** (2006) 229.
- [2.429] LIN, L., et al., Rev. Sci. Instrum. **77** (2006) 10E918.
- [2.430] CROWLEY, T.P., et al., Rev. Sci. Instrum. **61** (1990) 2989.
- [2.431] HEARD, J.W., et al., Rev. Sci. Instrum. **64** (1993) 1001.
- [2.432] FONCK, R.J., DUPPEREX, P.A., PAUL, S.F., Rev. Sci. Instrum. **61** (1990) 3487.
- [2.433] CIMA, G., et al., Phys. Plasmas **2** (1995) 720.
- [2.434] MCKEE, G. et al., Rev. Sci. Instrum. **75** (2004) 3490.
- [2.435] MAZZUCATO, E., Phys. Rev. Lett. **36** (1976) 792.
- [2.436] BRAVENEC, R.V., et al., Nucl. Fusion **31** (1991) 687.
- [2.437] HENNEQUIN, P., et al., Plasma Phys. Control. Fusion **46** (2004) B121.
- [2.438] HENNEQUIN, P., et al., IAEA FEC 2006, EX/P4-36.
- [2.439] MCKEE, G.R., et al., Nucl. Fusion **41** (2001) 1235.
- [2.440] HOLLAND, C., et al., IAEA FEC 2008, TH/8-1; WHITE, A.E., et al., Phys. Plasmas **15** (2008) 056116.
- [2.441] ERNST, D.R., et al, IAEA FEC, 2006 TH/1-3.
- [2.442] MAZZUCATO, E., et al., Nucl. Fusion **49** (2009) 055001.
- [2.443] RHODES, T.L., et al., Plasma Phys. Control. Fusion **49** (2007) B183–193.
- [2.444] MCKEE, G.R., et al., Plasma and Fusion Research: JSME **2** (2007) S1025.
- [2.445] SHELUKIN, D.A., et al. IAEA FEC 2008, EX/P5-37.
- [2.446] FUJISAWA, A., Nucl. Fusion **49** (2009) 013001.
- [2.447] CONWAY, G.D., et al., IAEA FEC 2006, EX/2-1; CONWAY, G.D., et al., Plasma Phys. Control. Fusion **50** (2008) 055009.
- [2.448] MCKEE, G.R., et al., IAEA FEC 2006, EX/2-3.
- [2.449] HOSHINO, K., et al., IAEA FEC 2006, EX/2-2.
- [2.450] MELNIKOV, A.V., et al., IAEA FEC 2008, EX/P5-36.
- [2.451] SHELUKHIN, D.A., et al., IAEA FEC 2008, EX/P5-37.
- [2.452] LIU, A.D., et al., IAEA FEC 2008, EX/P5-32.

- [2.453] SYNAKOWSKI, E.J., et al., Nucl. Fusion **39** (1999) 1733.
- [2.454] MAZZUTO, E., et al., Phys. Rev. Lett. **77** (1996) 3145.
- [2.455] SYNAKOWSKI, E.J., et al., Phys. Rev. Lett **78** (1997) 2972.
- [2.456] CORDEY, J.G., et al., Nucl. Fusion **35** (1995) 505.
- [2.457] SMITH, D.R., PhD. Thesis, Princeton University (2009).
- [2.458] NAZIKIAN, R., et al., Phys. Rev. Lett. **96** (2006) 105006; STUTMAN, D., et al., Phys. Rev. Lett. **102** (2009) 115002.

# CHAPTER 3

## EQUILIBRIUM AND MACROSCOPIC STABILITY OF TOKAMAKS

**K. Lackner, S. Günter, P. Lauber, G. Pautasso, B.D. Scott**  
Max-Planck-Institut für Plasmaphysik IPP,  
Garching bei München,  
Germany

### 3.1. INTRODUCTION

A homogenous magnetic field forces particles onto circular orbits perpendicular to it, but does not limit motion along the field lines. Inhomogeneities in the magnetic field  $\vec{B}$  introduce the drifts and give rise to the mirror force discussed in the previous chapter. To reduce contact between a thermonuclear grade plasma, with temperatures in the  $10^7$  K range, with the walls, we can follow two possible strategies: either to limit field lines to closed surfaces, or to increase  $|\vec{B}|$  along field lines before wall contact, so as to reflect a sufficient fraction of the energetic particles. In both cases, the magnetic fields will be inhomogeneous, and we will have to worry also about losses due to the drift of particles.

During the more than fifty years of fusion motivated plasma research a large variety of possible magnetic confinement configurations [3.1] have been considered (see Chapters 8 and 9). By far the most successful in the approach to fusion reactor values of pressure, temperature and energy confinement time has been the tokamak line [3.2], to be continued also by the ITER experiment. The description of fusion physics and technology in this book therefore largely focuses on this configuration. The tokamak stands, however, paradigmatically also for all confinement systems with closed magnetic surfaces forming topological tori.

In simplest terms, the role of the magnetic field in a confinement device is twofold: to balance the pressure gradients of the plasma and to reduce the diffusive losses of particles and energy out of the core of the device towards the walls, and Chapter 2 and Chapter 3 essentially deal with the associated physics. This distinction would be neat also in a methodological sense, if we were to deal only with the equilibrium and with collision induced (“laminar”) losses. Instabilities and turbulence, however, cut across this boundary, and a better justified classification is into “macro-scale” phenomena whose basic scale varies with the global dimensions of the plasma — treated here — and those which orient themselves on a “micro-scale”  $v/\omega$ , which can be either the drift scale ( $v = \sqrt{kT_e/m}$ ,  $\omega = \omega_{ci} = eB/m_i$ ), the ion or electron gyroradius ( $v = \sqrt{kT_{i,e}/m_{i,e}}$ ,  $\omega = \omega_{ci,e} = eB/m_{i,e}$ ) or the inertial skin depth

( $v = v_A = B / \sqrt{\mu_0 n_i m_i}$ ,  $\omega = \omega_{ci}$ ). (Here, as in the rest of the book, dimensional units are in S.I., and  $e$ ,  $m_{i,e}$ ,  $T_{i,e}$ ,  $n_{i,e}$ ,  $B$  have their usual meaning of elementary charge, ion/electron mass, temperature and density and magnetic induction;  $v_A$  denotes the Alfvén speed.) Again this separation is not completely clean, as we will see examples in this chapter where “macroscopic” phenomena critically depend on “microscopic” sublayers. On the other hand, also microturbulence can produce perturbations on a device-scale (e.g. the so-called zonal flows).

A hierarchy of plasma models have been employed to describe equilibrium and dynamics of magnetically confined plasmas. Ideal MHD is generally sufficient to describe macroscopic equilibrium and the fastest possible large scale instabilities. This model, however, places a very severe constraint on possible plasma motion and magnetic field changes, and finite electrical resistivity, important only in thin (“resonant”) layers, can significantly restrict the range of stable plasma equilibria, albeit giving rise to perturbations growing only at a slower rate. Taking into account realistic values of the plasma resistivity, these models tend, however, to predict extremely small characteristic dimensions of these resonant layers, so that two-fluid (drift-) effects and finite Larmor radii can affect the actual local dynamics. Finally, fast particles, associated with the heating of the plasma, can influence plasma stability in a variety of ways. Their motion is typically decoupled from that of the background plasma (described by a fluid), which can result in an averaging effect on the perturbation, but can allow also a resonant exchange as parallel velocity or drift speeds can equal the propagation speed of intrinsic plasma modes.

In this chapter, after a description of the basic tokamak configuration and its equilibrium properties, we describe in three largely self-contained sections the basic theory of macroscopic perturbations to it, following the hierarchy of plasma models outlined above. The fastest growing modes can be captured by an ideal MHD model, which — still within the realm of a single-fluid description — can be extended to capture also dissipative effects in either limited plasma regions, or in outside structures which define the boundary conditions to the possible plasma modes. A quantitatively consistent description of plasma motion in the singular layers near resonant surfaces (on which unperturbed field lines close after a finite number of toroidal and poloidal transits) requires, however, two-fluid models of different sophistication, which are introduced in Section 3.1.1. Finally, qualitatively new effects — among them whole new classes of macroscopic instabilities — can arise from the presence of fast particles in the plasma, which require the addition of a kinetic model for them to the usual (fluid-like) response of the bulk plasma.

The final two sections give an overview of the most significant experimental observations. We have chosen to separate disruptions from other macroscopic

perturbations: whereas the latter can generally be ascribed to identifiable instabilities and classified in a reproducible form, disruptions are not a well defined instability (as death is no well defined illness) and can have a variety of causes resulting also in quite different dynamics during the initial phases. In fact, any of the instabilities described in Section 3.4 can result in a disruption if it does not saturate at a sufficiently small amplitude. The section on disruptions therefore emphasizes the very practical need of controlling them as a menace to the integrity of the device: experimental characterization and theoretical understanding serve primarily to estimate and extrapolate the resulting loads and to devise strategies to avoid or mitigate these events.

### 3.1.1. Basic tokamak configuration

Figure 3.1 gives a schematic view of a tokamak plasma and the magnetic field coil set in their simplest configuration. In the confinement region, the superposition of a strong toroidal field  $\vec{B}_{tor}$ , due to the toroidal field (TF) coils, and a poloidal field, due to a toroidal plasma current  $I_p$ , produces helically twisted field lines forming nested toroidal surfaces. The plasma torus constitutes the secondary coil of a transformer — formed mainly by the central solenoid — which induces the plasma current and maintains it against resistive dissipation. The pinching force of this current also balances in part the plasma pressure in the torus. The current ring alone would, however, not be in force equilibrium in the major radius direction — remember that oppositely directed currents, like those on opposite sides of the vertical axis, repel. In addition an outward force arises also when we fill the torus with plasma. It is similar to that tending to expand the diameter of a rubber tube when increasing its filling pressure and is due to the difference in area over which the pressure drop acts on the smaller and larger major radius sides of the torus. These expanding “hoop” forces can be balanced by the Lorentz force between the toroidal plasma current and an applied field in the vertical direction. The poloidal field (PF) coil set produces this field, and additionally shapes the cross-section of the plasma in the poloidal plane.

The toroidal field in a tokamak is required for stability reasons, and could in principle just be a vacuum field also over the plasma region. In this case, Ampere’s Law would relate its magnitude to the sum of the currents passing through the inner legs of the TF-coils  $I_{TF}$  via  $\oint \vec{B}_{tor} \cdot \vec{e}_\phi R d\phi = 2\pi R B_\phi = -\mu_o I_{TF}$ , and hence result in a field depending only on major radius, decaying outward like  $\sim 1/R$ . Plasma pressure and toroidal plasma currents are determined, however, at least in part by independent processes: energy and particle sources and sinks in one, and applied loop voltage and plasma resistance (or other current drive methods) in the other case. A stationary force balance therefore requires, in the general case, the additional degree of freedom provided by the flow of poloidal plasma currents, associated with a Lorentz force  $\vec{j}_{pol} \times \vec{B}_{tor}$ , and a depression or an enhancement

of the toroidal field strength in the plasma compared to the vacuum value. These currents also make a contribution to the force on the plasma torus in the major radius direction, which is directed inwards or outwards, depending on whether the toroidal field in the plasma is larger or smaller than the vacuum value.

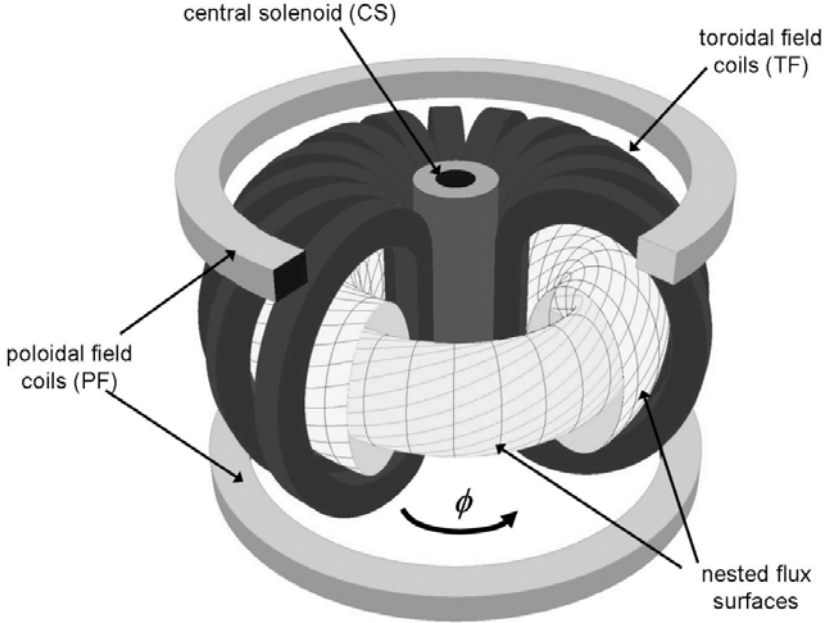


FIG. 3.1. Schematic representation of the magnetic field system of a tokamak. The TF coil set produces a magnetic field in the toroidal ( $\vec{e}_\phi$ ) direction, the PF coils and the toroidal plasma currents one in the poloidal plane, perpendicular to  $\vec{e}_\phi$ .

### 3.1.2. Timescales of tokamak dynamics

The most basic plasma model is that of ideal MHD, described by the set of equations

$$\frac{d\rho}{dt} = -\rho \nabla \cdot \vec{v} \quad (3.1)$$

$$\rho \left( \frac{d\vec{v}}{dt} \right) = \vec{j} \times \vec{B} - \nabla p \quad (3.2)$$

$$\frac{dp}{dt} = -\gamma p \nabla \cdot \vec{v} \quad (3.3)$$

$$\vec{E} + \vec{v} \times \vec{B} = 0 \quad (3.4)$$

$$\nabla \times \vec{E} = -\frac{\partial \vec{B}}{\partial t} \quad (3.5)$$

$$\nabla \times \vec{B} = \mu \mu_o \vec{j} \quad (3.6)$$

$$\nabla \cdot \vec{B} = 0 \quad (3.7)$$

where  $d/dt = \partial/\partial t + \vec{v} \cdot \nabla$  and  $\gamma$ ,  $\rho$ ,  $p$ ,  $\vec{v}$  are the adiabatic index, fluid mass density, pressure and velocity and  $\vec{j}$ ,  $\vec{E}$  and  $\vec{B}$  the electric current density and field and the magnetic flux density (induction), respectively. As, in plasma physics, it is usual to describe all magnetization effects explicitly in terms of the associated currents,  $\mu$  will be assumed in the following always to be 1 and we will refer to  $\vec{B}$  also as the magnetic field strength.

Linearizing the above system of equations around a homogenous, static equilibrium one finds that it contains two characteristic wave speeds:  $v_A = \sqrt{B^2/(\mu_o \rho)}$  and  $c_s = \sqrt{\gamma p/\rho}$ . If our experiment is of a characteristic dimension  $L_o$  — which we can identify, for example with either the circumference of the plasma torus in the toroidal  $2\pi R_o$  or poloidal direction  $2\pi a$  — they define characteristic MHD timescales  $\tau_A = L_o/v_A$  and  $\tau_s = L_o/c_s$ , and any state persisting significantly longer than those has to satisfy the stationary equilibrium condition

$$\rho \vec{v} \cdot \nabla \vec{v} = \vec{j} \times \vec{B} - \nabla p \quad (3.8)$$

Typically the steady state flow velocities in tokamaks are of gasdynamic Mach number  $|\vec{v}|/c_s \ll 1$ , so that inertial forces (Coriolis and centrifugal forces) can be neglected compared to pressure ones. Equilibria then are static on the MHD timescales, and satisfy

$$\vec{j} \times \vec{B} = \nabla p \quad (3.9)$$

During a discharge, plasma parameters change in time, for example due to changes in the externally applied heating power or loop voltage. The plasma profiles adjust to these imposed variations on diffusive timescales, defined by the transport of energy or the diffusion of magnetic fields across the plasma column. These timescales — the “energy confinement” and the “current diffusion” timescale — are much longer than the MHD scales  $\tau_s$  and  $\tau_A$ , so that — during these slow variations — the plasma passes through sequences of static MHD equilibrium states.

Stationary states, corresponding to solutions of Eq. (3.8), may nevertheless not be stable to (infinitely) small perturbations. If these perturbations grow, satisfying everywhere the equations of ideal MHD and stationary boundary conditions (not involving time derivatives), they will do so on an MHD timescale. Situations can, however, also exist, where perturbations grow only because the ideal MHD equations do not hold in some region of the plasma, or if boundary conditions introduce an additional timescale. Typically in these cases, the growth of the perturbation will be much slower than given by  $\tau_s$  or  $\tau_A$ , and — in the regions of validity of Eqs (3.1)–(3.7) — the plasma will actually pass through a sequence of solutions to Eq. (3.8) even during these instabilities. Table 3.1 lists relevant space and timescales for representative operating conditions of tokamaks that are presently considered mid-size (ASDEX-Upgrade, DIII-D), or large (JET, JT60-U), and for the conditions expected to prevail during  $Q = 10$  operation of ITER.

TABLE 3.1. PLASMA LENGTH AND TIMESCALES IN TOKAMAKS  
(Indicative values for present mid-size and large tokamaks and for ITER, where  $a$  is the mid-plane minor radius,  $\rho_i$  the ion gyroradius,  $1/\omega_{ci}$  the inverse ion gyrofrequency,  $2\pi R_0/v_A$  an Alfvén transit time,  $2\pi R_0/v_{th,i}$  the thermal ion transit time,  $\tau_{ii}$  an ion–ion collision time,  $\tau_E$  an energy confinement time,  $\tau_s$  the plasma current redistribution time (skin time) and  $\tau_{pulse}$  the pulse length)

	$a$	$\rho_i$	$1/\omega_{ci}$	$2\pi R_0/v_A$	$2\pi R_0/v_{th,i}$	$\tau_{ii}$	$\tau_E$	$\tau_s$	$\tau_{pulse}$
Units	[m]		[ $\mu$ s]				[s]		
Mid-size	0.5	0.003	0.008	3	40	800	0.1	1	10
Large	1.0	0.003	0.007	4	50	3000	0.5	10	30
ITER	2.0	0.003	0.004	5	60	15000	4	200	500

### 3.2. TOKAMAK EQUILIBRIUM

We will introduce the tokamak equilibrium in three steps: first considering an infinitely long straight, cylindrically symmetric plasma column, then bending it into a torus and ultimately applying additional external fields to shape its poloidal cross-section.

### 3.2.1. The straight cylinder

In cylinder coordinates  $r, \theta, z$  and under cylindrical symmetry, the static force balance (Eq. (3.9)) and Ampere's Law (Eq. (3.6)) become

$$j_\theta B_z - j_z B_\theta = \frac{dp}{dr} \quad (3.10)$$

and

$$-\frac{dB_z}{dr} = \mu_o j_\theta \quad (3.11)$$

$$\frac{1}{r} \frac{d(rB_\theta)}{dr} = \mu_o j_z \quad (3.12)$$

respectively, which can be combined to give

$$\frac{dp}{dr} = -\frac{1}{\mu_o} \left( \frac{d}{dr} \left( \frac{B_\theta^2 + B_z^2}{2} \right) + \frac{B_\theta^2}{r} \right) \quad (3.13)$$

Equation (3.13) shows that a radial plasma pressure gradient can be balanced by either gradients in the total magnetic pressure  $(B_\theta^2 + B_z^2)/(2\mu_o)$  or the tension along the curved azimuthal field lines giving rise to an inward directed force  $-B_\theta^2/(\mu_o r)\vec{e}_r$ . Linear, cylindrical confinement geometries were extensively studied in early pinch experiments. They took their name from the direction of the plasma currents, which were either induced in the  $\theta$ -direction by rapidly varying, externally applied  $B_z$ -fields ("theta-pinch"), or driven between electrodes in the  $z$ -direction "z-pinch". A combination of both configurations, with magnetic field components in both the  $\theta$ - and  $z$ -directions, was called "screw-pinch". Particularly for the discussion of plasma stability we will use the latter geometry also as the simplest tokamak model. The axial direction in the screw pinch will be taken as equivalent to the toroidal direction of the tokamak, and the topological nature of the torus is accounted for by imposing periodicity in the  $z$ -direction with  $L_z = 2\pi R$  for all perturbed quantities.

Integration of Eq. (3.13), weighted by  $r^2$ , from the axis to the plasma boundary yields the relation

$$\langle p \rangle = \frac{2}{a^2} \int_0^a p(r) r dr = \frac{\mu_o}{8\pi^2 a^2} I_z^2 + \frac{1}{2\mu_o} (\langle B_z^2 \rangle - B_{z,r=a}^2) \quad (3.14)$$

where  $I_z (= I_p)$  is the total longitudinal plasma current, and the plasma is assumed to be surrounded by vacuum for  $r \geq a$ . Equation (3.14) quantifies the

two contributions which can balance the average plasma pressure: the pinch force associated with the longitudinal plasma current and the reduction of the average  $B_z$ -field magnetic pressure compared to its vacuum value. They are quantified by  $\beta_{pol} = 8\pi^2 \langle p \rangle / (\mu_o I_z^2)$  and  $1 - \beta_{pol}$ , respectively, where the subscript *pol* indicates that the magnetic field component  $B_\theta$  associated with the plasma current.  $I_z$  will correspond to the field in the poloidal plane in the tokamak geometry of Fig. 3.1. For  $\beta_{pol} > 1$ , the  $B_z$ -field makes a positive contribution to the containment of the plasma pressure, whereas for  $\beta_{pol} < 1$ , the pinch force of  $I_z$  not only balances the plasma pressure, but also compresses the longitudinal magnetic field.

### 3.2.2. Toroidal plasma equilibrium

To eliminate end losses, the plasma column has to be bent into a torus. The ideal tokamak equilibrium is described by axisymmetric solutions to the set of Eqs (3.6), (3.7) and (3.9). It is convenient to split the vector fields of current density and magnetic field into poloidal and toroidal parts:  $\vec{j} = \vec{j}_{pol} + \vec{j}_{tor}$ ,  $\vec{B} = \vec{B}_{pol} + \vec{B}_{tor}$ , and to express the poloidal components in terms of stream functions  $F(R, z), \psi(R, z)$ :

$$\vec{j}_{pol} = \frac{1}{R} \vec{e}_\phi \times \nabla F \quad (3.15)$$

$$\vec{B}_{pol} = -\frac{1}{R} \vec{e}_\phi \times \nabla \psi \quad (3.16)$$

in cylindrical  $R, \phi, Z$ -coordinates (see Fig. 3.2). We use different symbols for the dependent variables to highlight the different orientation of the cylindrical coordinates used in straight, cylindrical and general, toroidal equilibria: bending a cylindrical plasma column into a torus corresponds to a transformation  $dz \rightarrow R d\phi$ . This ansatz, together with the  $\phi$ -independence of  $\vec{j}_{tor}, \vec{B}_{tor}$  satisfies the divergence-freeness of currents and magnetic fields. Equation (3.15) implies, through Ampere's Law, that

$$\vec{B}_{tor} = -\mu_o (F / R) \cdot \vec{e}_\phi \quad (3.17)$$

Ansatz Eq. (3.16) ensures that field lines will stay on surfaces  $\psi(R, z) = \text{constant}$ , and taking the inner product of Eq. (3.9) with  $\vec{B}$  shows that plasma pressure has to be constant along field lines. We can hence write the pressure as a function  $p(\psi)$ . From axisymmetry, and by taking the inner product of Eq. (3.9) with  $\vec{e}_\phi$ , it follows that  $\vec{j}_{pol} \times \vec{B}_{pol} = 0 = \nabla F \times \nabla \psi$ , so that also the flux function of the poloidal current  $F$  can be generally written as  $F(\psi)$ . The latter condition implies that poloidal currents will not cross flux surfaces.

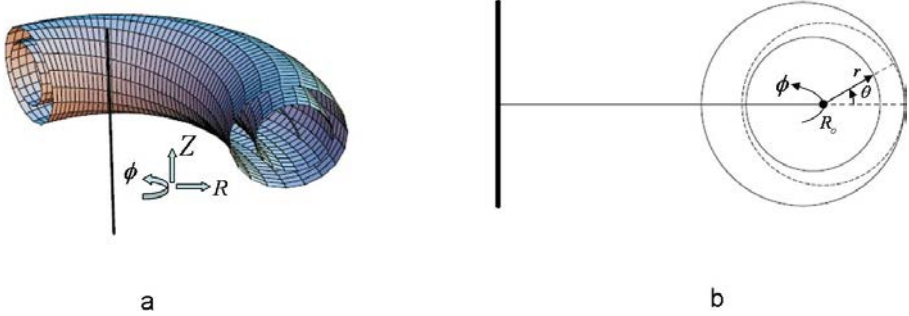


FIG. 3.2. Coordinate systems used in tokamaks: cylindrical  $(R, \phi, Z)$ -coordinates for general 2-D equilibria (a) and toroidal coordinates  $r, \phi, \theta$  used in the large aspect ratio circular cross-section tokamak approximation (b).

The third projection of Eq. (3.9), as inner product with  $\nabla\psi$ , yields the non-trivial part of the force balance, through

$$\nabla\psi \cdot \nabla p = (\nabla\psi)^2 p' = \nabla\psi \cdot (\vec{j}_{pol} \times \vec{B}_{tor}) + \nabla\psi \cdot (\vec{j}_{tor} \times \vec{B}_{pol}) = (\nabla\psi)^2 \left( -\frac{\mu_0}{R^2} FF' + j_\phi \frac{1}{R} \right) \quad (3.18)$$

which constitutes an equation for the toroidal current density  $j_\phi$ . Inserting it into the toroidal component of Ampere's Law this finally gives rise to a second-order, elliptic, semi-linear partial differential equation for the poloidal flux function  $\psi$

$$\frac{\partial^2 \psi}{\partial R^2} - \frac{1}{R} \frac{\partial \psi}{\partial R} + \frac{\partial^2 \psi}{\partial Z^2} = -\mu_0 R j_\phi = -\mu_0 R^2 p'(\psi) - \frac{\mu_0^2}{2} (F(\psi)^2)' \quad (3.19)$$

which has been independently derived in the 1960s by several authors and is usually called the Grad-Shafranov equation. The non-linearity is contained in the two functions  $p'(\psi)$  and  $(F(\psi)^2)'$ , which, in the framework of ideal MHD can be arbitrarily prescribed. A vacuum region surrounding the plasma is described by  $p'(\psi), F'(\psi) = 0$ , for  $\psi \leq \psi_c$ , where the value  $\psi_c$  defines the plasma boundary.

The validity of Eq. (3.19) is based (apart from the symmetry assumption, and the neglect of displacement currents in Eq. (3.6)) only on the assumptions inherent in the force balance of Eq. (3.9). Plasma rotation and anisotropic plasma pressure can lead to measurable corrections, in particular violating the constancy of pressure on magnetic flux surfaces: in the case of toroidal rotation  $v_\phi$  (the poloidal rotation is strongly damped by the neoclassical effects described in Chapter 2) the associated variation  $\delta p/p$  is approximately  $2\varepsilon\gamma M^2$ , with  $M = v_\phi/c_s$  the gasdynamic Mach number, and  $\varepsilon = r/R$  the inverse aspect ratio of the toroidal flux surface considered. Chapter 2 describes macroscopic flows within and across flux surfaces induced by collisions and small scale turbulent fluctuations: averaged over times much longer than the Alfvén and sound wave

propagation time these will, however, not change the form of Eq. (3.17). The slow dynamic evolution of an axisymmetric tokamak discharge will hence pass through sequences of solutions of Eq. (3.19), depending parametrically on time through the two functions  $p(\psi, t)$ ,  $F(\psi, t)$  and the boundary conditions  $\psi_c(t)$ .

### 3.2.2.1. The large aspect ratio approximation

To understand the effect of toroidicity onto the straight pinch equilibria of Section 3.2.1, we apply Eq. (3.19) to a large aspect ratio  $R_o/a=1/\varepsilon$  case with a circular plasma boundary. We use the coordinate system described in Fig. 3.2, in which, for  $\varepsilon \ll 1$  the Grad–Shafranov equation reads:

$$\frac{1}{r} \frac{\partial}{\partial r} r \frac{\partial}{\partial r} \psi - \frac{r}{R_o} \cos \theta \frac{1}{r} \frac{\partial}{\partial r} \psi + \frac{1}{r^2} \frac{\partial^2}{\partial \theta^2} \psi = -\mu_o \left( R_o^2 \left( 1 + 2 \frac{r}{R_o} \cos \theta \right) p'(\psi) + \frac{\mu_o}{2} \left( F(\psi)^2 \right)' \right) \quad (3.20)$$

For  $r/R_o \rightarrow 0$ , we recover the screw pinch momentum balance equation if we multiply Eq. (3.20) by  $B_\theta/(\mu_o R_o)$  and take into account Eqs (3.16, 3.17). Toroidicity will produce corrections to the straight cylinder solution  $\psi_o(r)$  with even parity in  $\theta$ , so we make the ansatz

$$\psi(r, \theta) = \psi_o(r) + \psi_1(r) \cdot \cos \theta \quad (3.21)$$

with  $\psi_o(r)$  the solution of the screw pinch case. Flux surfaces in the toroidal case will be shifted circles  $\psi_o(r - \Delta(r) \cdot \cos \theta) = \text{constant}$  and the displacement of the magnetic axis with respect to the plasma boundary circle, usually termed ‘‘Shafranov shift’’  $\Delta_S$ , depends on the average normalized plasma pressure  $\beta_{pol}$  and on both current and pressure profiles. For a class of plasma profiles

$$j_\phi(r) = j_{\phi o} \left( 1 - (r/a)^2 \right)^{v_j} \quad (3.22)$$

$$p(r) = p_o \left( 1 - (r/a)^2 \right)^{v_p} \quad (3.23)$$

the Shafranov shift can be expressed as  $\Delta_S/(\varepsilon a) = 0.125 + 0.036 v_j + \beta_{pol} \Delta^*(v_j, v_p)$ , with  $\Delta^*(v_j, v_p)$  shown in Fig. 3.3. At low  $\beta_{pol}$ , current density peaking contributes to the outward axis shift, but usually the  $\beta_{pol}$  contribution dominates, which is maximum for peaked pressure and flat current density profiles.

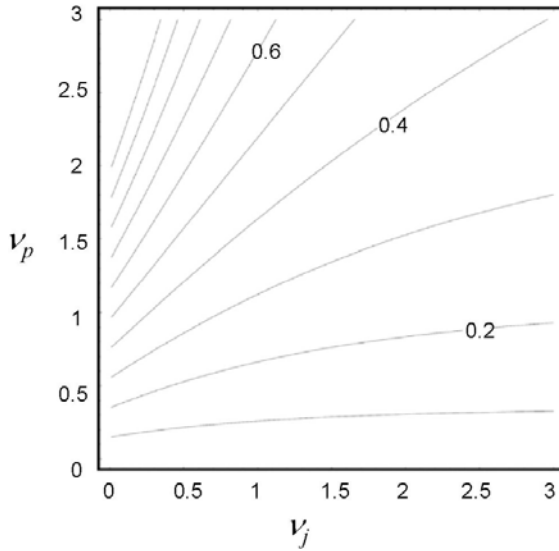


FIG. 3.3. Shafranov shift: the coefficient of  $\beta_{pol}$  in its dependence on current density exponent  $\nu_j$  and pressure exponent  $\nu_p$  for the profile class of Eqs (3.22, 3.23).

In the above discussions we have considered the Grad–Shafranov equation as a boundary value problem, prescribing  $\psi(r, \theta) = \psi_c$  at a given (here circular) plasma surface. We can express the poloidal fields and  $\psi(R, Z)$ , however, through their sources  $j_\phi(R, Z)$  by integrating Ampere’s Law (corresponding to a Green’s function approach over an infinite domain). The resulting field  $\psi_p(R, Z)$  produced exclusively by the plasma currents would not satisfy the boundary condition  $\psi(r, \theta) = \psi_c$ , and has to be complemented by an externally applied flux contribution  $\psi_{ext}(R, Z)$  [3.3]. In the circular cross-section, large aspect ratio approximation, the latter corresponds to a vertical field

$$B_{Z,ext} = -\frac{\mu_o I_p}{4\pi R_o} \left( \ln \left( \frac{8R_o}{a} \right) + \Lambda - \frac{1}{2} \right) \quad (3.24)$$

where the  $\Lambda$  depends only on  $\beta_p$ , and the normalized poloidal field energy inside the plasma, as

$$\Lambda = \beta_{pol} + \frac{\ell_i}{2} - 1 \quad (3.25)$$

with

$$\ell_i = \frac{8\pi^2 \int_0^a B_\theta^2 r dr}{\mu_o^2 I_p^2} \quad (3.26)$$

where, for the current distributions of Eq. (3.23) the so-called internal inductance  $\ell_i$  is given approximately by  $\ell_i = \ln(1.65 + 0.89 \nu_j)$  [3.4].

In terms of a global force balance, the inward directed force  $I_p B_{Z,ext}$  has to balance three self-force contributions from the plasma column, making additive contributions to the required value of  $4\pi R_o B_{Z,ext} / (\mu_o I_p)$ : the hoop force of the toroidal plasma current  $(\ln(8R_o/a) + \ell_i/2 - 1)$ , the tube force from the action of the plasma pressure and the inside-outside area difference  $(\beta_{pol}/2)$ , and the force exerted by a toroidal field on the plasma ring  $((\beta_{pol} - 1)/2)$ . The latter arises from the diamagnetic depression of the toroidal field associated with  $\beta_{pol} > 1$  and the  $B_\phi \propto 1/R$  variation on a flux surface. It can be easily understood from the fact that poloidal currents have to close within a flux surface, and will cross a higher magnetic field on the torus inside. Evidently this last force contribution changes sign if  $\beta_{pol} < 1$  and the plasma becomes “paramagnetic” with respect to the toroidal field.

In present day tokamaks, the external field is provided by actively controlled poloidal field (PF) coils. Early, short pulse tokamaks could rely, however, on induced currents in a copper shell surrounding the plasma, which transiently ensured  $\psi$  to be *spatially* constant on its surface. The plasma column was then displaced outward with respect to the centre of the copper shell, and this effect could be compensated by applying (prior to the start of the discharge) an additional vertical magnetic field  $B_{Z,ext}$ . In this more general situation the shift of the centre of a circular cross-section plasma column (radius  $a$ ) with respect to that of the circular cross-section copper shell (radius  $b$ ) is given approximately by [3.3]

$$\Delta = \frac{b^2}{2R} \left( \ln \frac{b}{a} + \left( 1 - \frac{a^2}{b^2} \right) \left( \Lambda + \frac{1}{2} \right) \right) + \frac{\mu_o b^2 B_{Z,ext}}{4\pi I_p} \quad (3.27)$$

### 3.2.2.2. Formulations of the Grad–Shafranov equation

As the static Grad–Shafranov equation remains valid even under dynamically slowly evolving situations — it can even be viewed as a constitutive relation between plasma profiles and the poloidal field — the need for its solution appears in differing mathematical formulations. In the following we will list them, together with the corresponding physics situations in which they arise, without going into details of the actual algorithms developed for their solution.

The most elementary formulation corresponds to the prescription of the plasma boundary (e.g. parametrically in terms of the normalized arc-length  $s^*$  varying between  $0 \leq s^* \leq 1$ ) as  $\psi(R_c(s^*), Z_c(s^*)) = \psi_c$ , the two profiles  $p'(\psi), (F(\psi)^2)$  appearing on the RHS of Eq. (3.19). As the function  $(F(\psi)^2)$

is experimentally not directly controllable, frequently the profile of the averaged toroidal current density defined by

$$\langle j_\phi \rangle(\psi) = \frac{\partial}{\partial S} \int_S j_\phi dS = \oint j_\phi \frac{ds^*}{RB_{pol}} \bigg/ \oint \frac{ds^*}{RB_{pol}} \quad (3.28)$$

or an average over the parallel current density, defined as

$$\langle j_\parallel \rangle(\psi) = \frac{\partial}{B_o \partial V} \int_V (\vec{j} \cdot \vec{B}) dV = \frac{1}{B_o} \oint (\vec{j} \cdot \vec{B}) \frac{ds^*}{B_{pol}} \bigg/ \oint \frac{ds^*}{B_{pol}} \quad (3.29)$$

are specified instead, where  $S(\psi)$  and  $V(\psi)$  are, respectively, the poloidal cross-section area and the enclosed volume of the flux surface  $\psi$ ,  $B_{pol} = |\vec{B}_{pol}|$ ,  $B_o$  is the vacuum toroidal field at a reference radius  $R_o$  and  $s^*$  the normalized arc-length along the poloidal circumference of the flux surfaces. This “fixed-boundary” formulation is sufficient input for all ideal MHD stability analyses, which will be shown to require equilibrium information only inside the plasma boundary. In this region, flux surface coordinates, as introduced in Chapter 2 (Fig. 2.1) can be convenient, and  $B_{pol}$  is equal to the physical component  $B_\theta$  used there.

For most other applications — in the design of devices, for the planning of discharge scenarios, and for the correlation and interpretation of experimental measurements — the plasma boundary is not a priori known. Typically it is assumed that the current density and the plasma pressure are ignorable on flux surfaces in contact with material walls. In the case of a limiter tokamak, where closed flux surfaces are in direct wall contact, this implies that  $\psi_c$  is defined as the innermost flux surface touching a prescribed (limiter) contour (see Chapter 7). In the case of a divertor, the nominal plasma boundary is given by the separatrix, defined by the innermost flux surface passing through a saddle point of  $\psi$ . The problem is therefore in both cases a free boundary problem for  $\psi$ , with  $\langle j_\phi \rangle$ ,  $p'$  or some order derivatives discontinuous at  $\psi = \psi_c$  and boundary conditions on  $\psi$  defined at infinity. The external fields necessary to ensure equilibrium are defined through additional sources in Ampere’s Law (first part of Eq. (3.19)), which of course do not have to satisfy the plasma equilibrium constraint (second part of Eq. (3.19)), but correspond to the conductor currents of the PF system. If they are explicitly specified, this is a well posed problem.

For the planning of discharges, however, the desired plasma shape, rather than the coil currents in the PF system, is the prescribed input. During the early design stage of a device, even the positions of the conductors are not fixed. In all these cases, one wants to impose, at least approximately, a given plasma surface contour  $R_c(s^*)$ ,  $Z_c(s^*)$ , leaving open the currents (or even the position) of PF coils. This formulation does not correspond a priori to a well posed problem in

the sense of Hadamard, and requires imposition of constraints on the PF currents and the relaxation of the requirement of an exact fit of

$$\psi(R_c(s^*), Z_c(s^*)) = \psi_c \quad (3.30)$$

usually in the form of the minimization of a weighted sum of mean square deviations from the surface and poloidal field energy of the PF-system.

Knowledge of constant- $\psi$  surfaces in the plasma interior is universally required for the interpretation of experimental data. In this case, the two functions  $\langle j_\phi \rangle, p'$  are not directly known, but have to be inferred from magnetic measurements. In the large aspect ratio, circular flux surfaces limit, the poloidal field distribution outside the plasma column depends on plasma profiles only through the parameter  $\Lambda$ , and this is hence the only information that can be gained in this limit from magnetic measurements outside the plasma. More information on profiles can be gained from such measurements in the case of non-circular plasma cross-sections, but the essential improvement has come with the availability of diagnostics giving direct information on  $B_{pol}$  in the plasma interior (see Chapter 4), mostly based on the motional Stark effect (MSE). Mathematically codes for this application specify profiles of  $\langle j_\phi \rangle, p'$  as functions of  $\psi$  with a limited number of free parameters, which are iteratively determined to give a judicious best fit to all relevant diagnostic information.

If we want to predict the dynamic performance of a tokamak discharge, we have to formulate and solve transport equations as described in Chapter 2. On closed flux surfaces, scalar quantities (pressures, densities, temperatures) vary little over a flux surface, so that it is a good approximation to solve equations for their flux-surface averages. It is convenient to introduce a radius-like coordinate  $\rho(\psi)$ , where we define

$$\rho = \sqrt{\frac{\Phi_B}{\pi B_o}} \quad (3.31)$$

$$\Phi_B = \int B_\phi dS = \int \frac{F}{R} dS \quad (3.32)$$

in terms of the toroidal magnetic flux  $\Phi_B$  enclosed by the flux surface  $\psi$ . The resulting transport equations — determining, among others, the function  $p(\psi)$  appearing in Eq. (3.19) — contain, however, geometrical quantities requiring a knowledge of  $\psi(R, Z)$ . A transport equation describing the resistive diffusion of the magnetic field is obtained by taking the flux surface averages over the parallel component of Ampere's, Ohm's and Faraday's Laws, which for  $B_o$  constant in time yields a diffusion equation for the poloidal flux across the toroidal flux

$$\sigma_{\parallel} \frac{\partial \psi}{\partial t} = \frac{F^2}{\rho B_o} \frac{\partial}{\partial \rho} \frac{G}{F} \frac{\partial \psi}{\partial \rho} \quad (3.33)$$

with  $\sigma_{\parallel}$  the parallel electrical conductivity and  $G(\rho)$  a dimensionless geometry function. To describe the time development of a discharge we have to solve a set of 1-D, time dependent, diffusion/convection type equations for  $\psi(\rho, t)$ ,  $p(\rho, t)$  and possibly other variables. At each time step we have then to solve the Grad–Shafranov equation, with the two functions of  $\psi$  on the RHS of Eq. (3.19) iteratively adjusted to fit  $\psi(\rho, t)$  and  $p(\rho, t)$ . This procedure, combining 1-D transport equations with the 2-D equilibrium solutions, is usually termed 1.5-D transport models. It can involve either fixed or free boundary solutions to the Grad–Shafranov equation, depending on whether only the development of plasma profiles, or also the changes in shape and position of the plasma column are of interest.

So far, we have assumed the stream function of poloidal currents  $F(\psi)$  to be constant on open flux surfaces, implying no currents to flow in and out of material structures into the plasma. In this case, in particular, no net vertical force is exerted by the toroidal field onto the plasma, as, for any value of  $R$ , the integral  $\int_{Z_1}^{Z_2} j_R B_{\phi} R dZ = -(\mu_o / 2R)(F(Z_2)^2 - F(Z_1)^2)$  vanishes between the intersection points  $Z_1, Z_2$  of every flux surface with  $R = \text{constant}$ . If, on the other hand, poloidal currents flow on open surfaces, they will have to close through material structures, giving rise to a net vertical force onto the plasma given by  $-\pi\mu_o \oint F^2 / R (\partial R / \partial s) ds$ , where the integration is to be taken along the poloidal circumference of the material walls. Also an additional radial force can arise. Such poloidal currents along open flux surfaces are termed halo-currents, and can arise either due to thermoelectric effects in the scrape-off layer (SOL) — see Section 7.6.1. of Chapter 7 — or can be induced by rapid plasma motion. In the latter form we will encounter them in the discussion of disruptions. They may play also a part during the startup phase of plasma discharges. Their effect on plasma equilibrium can be taken into account also in the solution of the Grad–Shafranov equation by including a finite value of  $FF'$  also on open flux surfaces, albeit only in the presumably plasma filled region up to the contact with the divertor or the limiter target plates.

### 3.2.2.3. Dimensionless parameters characterizing the plasma equilibrium

Dimensionless parameters allow a physics-based comparison of results between different devices and produce a universal map for the approach to intrinsic performance limits. Axisymmetric equilibria of isotropic pressure, non-rotating plasmas depend on two ratios between characteristic parameter values that can be varied independently — within limits — in every given device: the ratio between a reference plasma pressure and a magnetic field energy density and the ratio of poloidal to toroidal field strengths. In addition, one can define an arbitrary number of dimensionless numbers characterizing the plasma geometry

and plasma profiles, and can, of course produce further ones as combinations of them. For most of them there exist more than one definition, coinciding in the large aspect ratio, circular cross-section approximation, but leading to potentially large differences in highly shaped, low aspect ratio plasmas at high normalized pressures. We follow the usage of Ref. [3.4] as the most widely used source book.

Generalizing the expression used in the straight cylinder and low aspect ratio cases, we define a poloidal  $\beta$  in terms of a cross-section area-averaged plasma pressure and the toroidal plasma current  $I_p$ , as

$$\beta_{pol} = \frac{\int p df \, 2 \left( \oint ds \right)^2}{\mu_o I_p^2 \int df} \quad (3.34)$$

where the contour integral measures the poloidal circumference of the plasma. In the Shafranov shift  $\beta_{pol}$  enters in combination with the inverse aspect ratio as  $\epsilon \beta_{pol}$ . Occasionally a local value of  $\beta_{pol}(\psi)$  is used, in which integrals (including the plasma current  $I_p(\psi)$ ) are taken only over the interior of a flux surface  $\psi$ , and the pressure in Eq. (3.34) is substituted by  $p - p(\psi)$ . For a circular plasma cross-section, near the axis, this definition becomes  $\beta_{pol}(r_o) = \left( 2\mu_o / B_{pol}^2(r_o) \right) \int_0^{r_o} (r/r_o)^2 (-dp/dr) dr$ , which generally has a finite value  $\beta_{pol,o}$  also at the axis.

Tokamak equilibria as described by solutions of the Grad–Shafranov equation depend on the toroidal field only through  $(F(\psi)^2)'$  and can hence be transformed to any vacuum field  $B_{\phi,o}$  (taken at a reference location  $R_o$ ), by substituting  $F(\psi) \rightarrow (F^2(\psi) - F^2(\psi_c) + (\mu_o B_{\phi,o} R_o)^2)^{1/2}$ .

The ratio of toroidal to poloidal field strengths is governed by considerations of MHD stability, determining the number of toroidal transits of a helical field line between passages through identical poloidal positions:

$$q(\psi) = \oint \hat{q}(\psi, s) ds / \oint ds = \frac{1}{2\pi} \oint \frac{B_\phi}{RB_{pol}} ds = \frac{1}{2\pi} \frac{d\Phi_B}{d\psi} \quad (3.35)$$

where we have used the definition of the toroidal flux and introduced also a *local* value of the relative rate of progress of a field line along the toroidal to the poloidal circumference:  $\hat{q}(\psi, s) = B_\phi(\oint ds) / (2\pi RB_{pol})$  important in stability and transport theory. In *divertor* tokamaks (see Chapter 7) the plasma is bound by a separatrix at  $\psi = \psi_s$ , and the existence of an X-point implies locally  $B_{pol} \rightarrow 0$  and a logarithmic singularity of  $q(\psi)$  for  $\psi \rightarrow \psi_s$ . As a convention, for such configurations the value  $q_{95}$ , defined at 95% of the poloidal flux between magnetic axis and separatrix, is usually quoted. We will later see that for stability reasons,  $q(\psi)$  can nowhere go significantly below 1, and has to be larger than 2 at the plasma boundary.

In the circular, large aspect ratio limit, expression Eq. (3.35) becomes

$$q(r) = \frac{B_{\phi,o}}{\mu_o R_o} \cdot \frac{r^2}{r \int_0^r j_\phi r dr} \quad (3.36)$$

corresponding to

$$q_o = q(0) = \frac{2B_{\phi,o}}{\mu_o R_o j_\phi(0)} \quad (3.37)$$

and

$$q_a = q(a) = \frac{aB_{\phi,o}}{R_o B_{pol}(a)} = \frac{2\pi a^2 B_{\phi,o}}{\mu_o R_o I_p} \quad (3.38)$$

at the magnetic axis and at the plasma boundary, respectively.  $q(r)$  is proportional to the inverse of the average current density within the given radius. In the vacuum region it increases therefore outwards  $\sim r^2$ .

The proper normalization of the plasma pressure — relevant, for example, for reactor economics — is in terms of the average total magnetic energy density  $(B_\phi^2 + B_{pol}^2)/(2\mu_o)$ , which for “conventional” tokamak aspect ratios is close to  $B_{\phi,o}^2/(2\mu_o)$ . This definition of  $\beta$ ,

$$\langle \beta_{tor} \rangle = \frac{\int p dV / V}{B_{\phi,o}^2 / 2\mu_o} \quad (3.39)$$

in the small- $\varepsilon$ , circular cross-section limit is related to  $\beta_{pol}$  and  $q_a$ , by

$$\langle \beta_{tor} \rangle = \frac{\varepsilon^2}{q_a^2} \beta_{pol} \quad (3.40)$$

As fusion power production — a prime economics driver — is, over a significant temperature range,  $\propto p^2$ , a correspondingly weighted  $\beta_{tor}$  definition

$$\beta^* = \frac{\sqrt{\int p^2 dV / V}}{B_{\phi,o}^2 / 2\mu_o} \quad (3.41)$$

is also sometimes used.

Both theoretical and experimental observations have established that the dependence of macroscopic plasma stability on pressure is best characterized by the ratio  $\langle p \rangle / (B_{\phi,o} \cdot I_p / a)$ , where  $a$ , for general (non-circular) plasma cross-sections is taken as the plasma half-width in the horizontal plane of the magnetic axis. It has become custom to use for this *normalized*  $\beta$  the practical definition:

$$\beta_N = \frac{10^8 \langle \beta_{tor} \rangle}{(I_p / a B_{\phi,o})} = \frac{\langle \beta_{tor} [\%] \rangle}{(I_p [MA] / a B_{\phi,o})} \quad (3.42)$$

giving a number of  $O(1)$  with a maximum value around 3.

Plasma equilibrium and stability (but also energy confinement) depend on aspect ratio, plasma shape and profiles. In basic theoretical studies, the most important shape parameters — aspect ratio ( $R_o/a$ ), elongation ( $\kappa$ ) and triangularity ( $\delta$ ) — are defined through a parametric representation of the plasma surface, by:  $R = R_o + a \cos(\theta + \delta \sin(\theta))$ ,  $z = \kappa a \sin(\theta)$ , with  $0 \leq \theta \leq 2\pi$ .

The plasma current profile determines the poloidal field energy stored in the plasma and the  $q(\psi)$ -profile. In normalized form, the former is measured by  $\ell_i$  introduced in the discussion of the Shafranov shift, which in analogy to  $\beta_{pol}$  is generalized to

$$\ell_i = \frac{\int \vec{B}_{pol}^2 df \left( \oint ds \right)^2}{\mu_o^2 I_p^2 \int df} \quad (3.43)$$

The  $q(\psi)$ -profile depends strongly not only on current profile, but also on plasma shape. In particular, close to the separatrix, the region close to the X-point makes a divergent contribution. For instance for a plasma with square cross-section and a very peaked current distribution, it leads to a behaviour  $q \sim (B_{\phi,o} a^2 / R_o I_p) \log(\sqrt{2} a/d)$ , with  $a$  the half-width of the square, and  $d$  the closest distance of a given flux surface to the X-point. Even though the divergence is only logarithmic, it implies that  $q(\psi)$  will pass through all rational values  $m/n \geq q_{min}$  with integer  $m, n$  inside the plasma.

For a circular cross-section, large aspect ratio tokamak, stability constraints on the plasma current limit  $q_a > 2$  and the pressure contribution to the Shafranov shift  $\Delta_s$  gets large ( $-a/4$ , for  $\nu_j, \nu_p = 1$ ) for  $\varepsilon \beta_{pol} = 1$ . Combining these constraints suggests  $\langle \beta_{tor} \rangle \leq \varepsilon/4$  as upper bound to the total beta. Expression Eq. (3.42), based on exact equilibria and extensive numerical stability calculations, suggests, however, a much more stringent limit of  $\langle \beta_{tor} \rangle \leq (3/20) \varepsilon/q_a$  for a circular plasma. Fortunately, however, non-circular plasma cross-sections and small aspect ratio make it possible to raise the plasma current substantially above the value compatible with a given  $a, q_a$  according to Eq. (3.38), as we shall see in Section 3.3.1.4.

#### 3.2.2.4. Shaping of plasma cross-section and the tokamak poloidal field system

In the large aspect ratio limit a homogenous applied vertical field (satisfying Eq. (3.24)), together with the plasma currents would produce circular equilibrium flux surfaces. Finite aspect ratio effects lead, however, to a vertical elongation and a D-shape deformation of them, which depends significantly also on the current distribution ( $\ell_i$ ) and  $\beta_{pol}$ . This “natural” shape of the plasma cross-section is of practical importance, as on one hand, the MHD stability

arguments given in Section 3.3.1.1.4 will favour elongated (and D-shaped) plasma cross-sections, but on the other an inhomogeneous applied external field can give rise to an axisymmetric positional instability of the plasma column. Configurations corresponding to  $B_{Z,ext} = \text{constant}$  are clearly indifferent to any vertical displacement and therefore correspond to marginal stability against such a mode. Figure 3.4 shows this limiting plasma boundary shape (corresponding to the flux surface  $\psi = \psi_c$ ) for different aspect ratio cases,  $\beta_{pol} = 0$ , and two current distributions inside the plasma:  $p'(\psi)$ ,  $(F^2(\psi))' = \text{constant}$  and  $p'(\psi)$ ,  $(F^2(\psi))' \sim (\psi - \psi_c)$ , respectively.

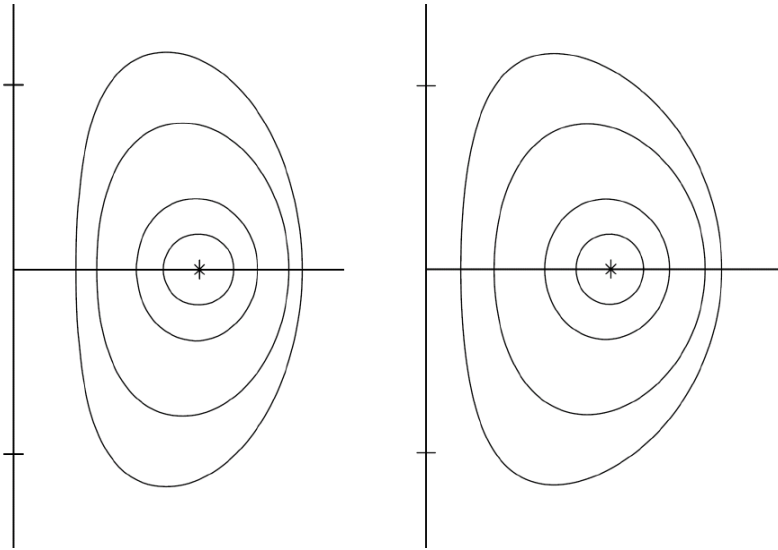


FIG. 3.4. Natural elongation of plasmas in a homogeneous magnetic field, as function of aspect ratio, for flat (left) and moderately peaked (right) current distribution and  $\beta_{pol} = 0$ .

The plasma shape is controlled by position and currents in the poloidal field (PF) coils. Figure 3.5 shows the PF coil system of ITER, together with a reference plasma equilibrium. The elongation of a plasma is mainly produced by PF coils above and below the plasma column, carrying a current parallel to the plasma current. This gives also rise to X-points in the poloidal cross-section of  $\psi$ , with the innermost one (on the separatrix) separating the region of closed field lines from those intersecting somewhere a material wall. This feature is nowadays generally used to displace the location of the main plasma-wall contact into a region remote from the plasma: the divertor.

We can think of the external shaping fields also in terms of a multipole expansion. In the infinite aspect ratio case, these fields would decay radially inwards  $\sim r^{m-1}$ , so that only low order deformations of the plasma column (mainly  $m = 2$  by quadrupole coils;  $m = 3$  by hexapole coils) can be effectively

produced by PF coils at a distance practically feasible in a fusion reactor. Fortunately this covers the elongated D-shaped plasmas suggested by stability theory, which are also convenient for arranging a divertor. Toroidal effects furthermore facilitate the production of such shapes (see Fig. 3.4). Figure 3.5 also shows the currents required in the PF coils to maintain this ITER equilibrium for a plasma current of 15 MA. Note that the current in the main divertor PF-coil is even larger than the plasma current. The main function of the central solenoid (CS) coils is to constitute the primary windings of the ohmic transformer: their flux changes make the major contribution to the loop voltage driving the plasma current.

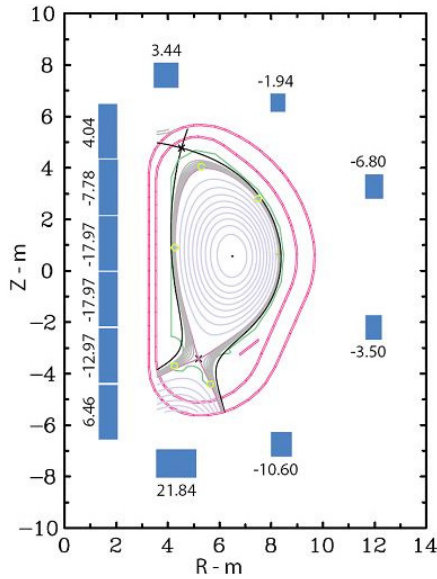


FIG. 3.5. ITER poloidal field (PF) coil set and currents for the reference equilibrium conditions, corresponding to  $I_p = 15$  MA, and expected to attain  $Q = 10$  (see Ref. [3.2]).

### 3.2.2.5. Axisymmetric stability of tokamak equilibria

In an inhomogeneous magnetic field, the plasma column can be positionally unstable. This instability can be rigorously treated with the methods described in Section 3.3.1. In the large aspect ratio limit it can be simply related to the radial decay index  $n_{ext}$  of the externally applied magnetic field

$$n_{ext} = -\frac{R}{B_{Z,ext}} \frac{\partial B_{Z,ext}}{\partial R} \quad (3.44)$$

linked to the curvature of  $\vec{B}_{ext}$  and the vertical variation of its radial component. A negative decay index corresponds to a variation of the vertical force

$I_p (\partial B_{R,ext} / \partial z) > 0$  and gives therefore rise to an unstable vertical displacement. For radial motion, the forces resulting from compression of the plasma, and the conservation of poloidal flux inside the plasma ring during any fast displacement have to be taken into account [3.3] giving rise to a stable, finite range for the decay index:  $0 \leq n_{ext} \leq 3/2$ . This is the same criterion as known in particle accelerator design as the “weak focusing” principle. (The analogy to the strong focusing — or alternating gradient — principle is the net-current carrying  $\ell = 2$  stellarator.)

Of practical importance, however, is the regime of  $n_{ext} < 0$ , as external fields with this characteristic are required to produce D-shaped plasmas with an elongation larger than the natural one illustrated by Fig. 3.4. In this regime, a simple engineering model can be applied to the vertical displacement instability, which illustrates also the methods available to stabilize it, and serves as paradigm for some aspect of resistive wall modes. We consider a circular, vertically movable wire, with radius  $R_o$ , total mass  $M_p$ , carrying a current  $I_p$ , placed in an external field  $\vec{B}_{ext}$ , and a system of passive conductors with a self-inductance  $L_{cc}$ , coupled to the wire with a mutual inductance  $L_{pc} = L_{cp}$ . A vertical motion of the wire, originally in equilibrium, with  $B_{R,ext}(Z=0) = 0$ , will induce a current  $I_c$  in the conductor. The system can then be described by the induction equation for the passive conductor system, and the equation of motion for the wire:

$$\frac{dL_{pc}}{dZ} I_p \dot{Z} + L_{cc} \dot{I}_c = -\mathfrak{R}_c I_c \quad (3.45)$$

$$M_p \ddot{Z} = \frac{dL_{pc}}{dZ} I_p I_c + 2\pi R_o I_p \frac{dB_{R,ext}}{dZ} Z \quad (3.46)$$

where  $\mathfrak{R}_c$  is the resistance of the passive conductors, which we set to zero for the present *ideal* case. In the plasma analogue, the equilibrium field  $B_{Z,ext}$  (see Eq. (3.24)) would be of the order  $\mu_o I_p / (2\pi R_o)$ , suggesting use of the normalized quantities

$$s^* = \frac{2\pi R_o^2}{\mu_o I_p} \left( \frac{dB_{R,ext}}{dZ} \right) \quad (3.47)$$

$$c_L = \frac{R_o (dL_{pc}/dZ)^2}{\mu_o L_{cc}} \quad (3.48)$$

where  $s^*$  measures the unstable drive and  $c_L$  the stabilizing coupling to the passive conductors.

The ansatz  $Z, I_c \sim \exp(\gamma t)$  shows that the position of the wire will be unstable if  $s^* > c_L$  and that the displacement will accelerate in this case at an inertia limited rate

$$\gamma = \sqrt{c_L} \sqrt{\mu_o I_p^2 / (R_o M_p)} \sqrt{s^*/c_L - 1} \quad (3.49)$$

The passive conductors can either be the surrounding vessel walls, or dedicated structures allowing for proper closing of the induced, stabilizing (according to Lenz's rule) currents. A tight coupling to the plasma — implying closeness — and a low self-inductance of the passive structures are therefore necessary for positional stability.

### 3.3. THEORY OF MACROSCOPIC INSTABILITIES IN TOKAMAKS

#### 3.3.1. One-fluid MHD stability theory

##### 3.3.1.1. Ideal MHD stability

In this section we study the reaction of a plasma in stationary ideal MHD equilibrium — as described in Section 3.2 — to small amplitude perturbations with a spatial scale comparable to the plasma dimensions. These are to be distinguished from the micro-instabilities dealt with in Chapter 2, which give rise to the turbulent fluctuations causing the “anomalous” transport of energy, particles and momentum. This distinction is justified by the different consequences for the plasma, but is not completely rigorous, and there exist cases of overlap, most evidently the so-called ballooning modes.

The fastest and most violent global instabilities grow on a shear Alfvén timescale  $\pi R_o / v_A$  (but typically, as we observe them close to threshold, still one or two orders of magnitude slower) and can be described by an ideal MHD model. Two simple model situations illustrate the basically different sources of their drive: the current density parallel to the magnetic field (the so-called *kink* drive) and the pressure gradient (*interchange* mode). To illustrate the first, we assume a cylindrical, pressure-less plasma, in which a surface current layer at  $r = a$  separates an inner region with a purely axial from an outer region with a purely poloidal magnetic field (Fig. 3.6 left: the unperturbed state):

$$\vec{B} = (0, 0, B_{z1}) \text{ for } r < a \text{ and } \vec{B} = (0, B_{\theta 2} \cdot (r/a), 0) \text{ for } r > a \quad (3.50)$$

with  $B_{\theta 2}, B_{z1} = \text{constant}$  and  $B_{\theta 2}^2 = B_{z1}^2$  to satisfy force balance at the interface. Perturbing the equilibrium by a kinking perturbation, as in Fig. 3.6 right, leads to an increase/decrease of  $B_\theta$  on the inside/outside of the knee tending to further enhance the perturbation, but also a stretching of the longitudinal field

lines, counteracting it. The destabilizing force wins — as we will show for a more general case in Section 3.3.1.1.4 — if  $|B_{\theta 2}/B_{z1}| = 1 > k_z a$ , where  $k_z$  is the longitudinal wavenumber of the perturbation. As the equilibrium considered is pressure-less, the plasma currents have to be “force-free”, satisfying  $\vec{j} \times \vec{B} = 0$ , flowing everywhere parallel to  $\vec{B}$ . The kink instability, in the form described here, is therefore only driven by the current density  $j_{\parallel} = (\vec{j} \cdot \vec{b})$  parallel to the magnetic field direction  $\vec{b} = \vec{B}/|B|$ .

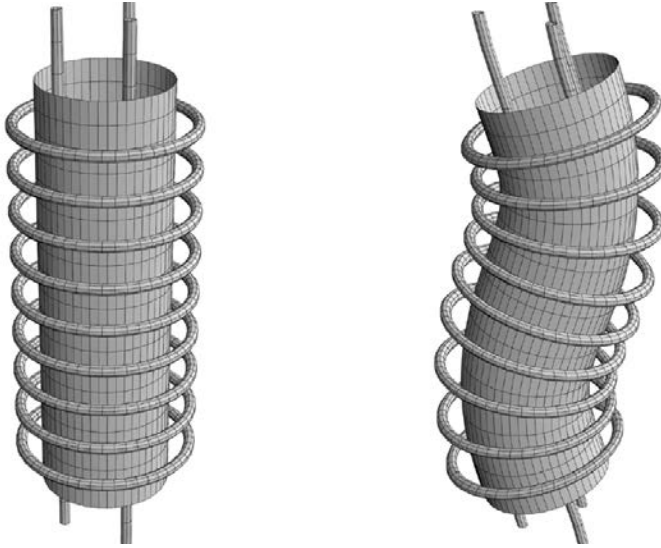


FIG. 3.6. Kink instability of a plasma column in a surface current model; left: unperturbed; right: perturbed plasma surface and axial and solenoidal field lines.

To illustrate a purely pressure driven interchange mode we consider again a surface current, straight cylinder equilibrium, albeit with only a poloidal magnetic field produced by an axial current  $I_z$  at the plasma–vacuum interface and — in the so-called “anti-pinch” case — by an equal, but oppositely directed current  $-I_z$  in a central (solid material) rod. The plasma, with a pressure  $p$ , fills either the region  $r < a$  in the pinch, or  $r > a$  in the anti-pinch situation, and is balanced by a poloidal magnetic field which jumps at  $r = a$  from 0 to  $\sqrt{2\mu_o p}$  in the pinch, or from  $\sqrt{2\mu_o p}$  to 0 in the anti-pinch case. A “sausage-like” perturbation of the surface (Fig. 3.7 showing the pinch case) maintains axisymmetry, so that the  $z$ -component of Ampere’s Law continues to give  $B_{\theta}(r, z) = \int_0^r j_z r dr$ . For a slow enough perturbation (compared to the sound transit time  $(k_z c_s)^{-1}$ ) the plasma pressure will equilibrate, but  $B_{\theta}$  at the plasma surface will vary along  $z$ . In both the pinch and the anti-pinch case it will increase in the waist and decrease in the bulge region, but with diametrically different consequences for the force balance: the imbalance between  $B_{\theta}^2/(2\mu_o)$

and  $p$  at the displaced plasma surface further increases the distortion in the pinch, but decreases it in the anti-pinch situation. The discriminating element is the orientation of the field-line curvature vector  $\vec{\kappa} = (\vec{b} \cdot \nabla) \vec{b}$  with respect to the direction of increase of plasma pressure:  $\vec{\kappa} \cdot \nabla p > 0$  is destabilizing and  $\vec{\kappa} \cdot \nabla p < 0$  is stabilizing. We therefore talk about “bad” and “good” curvature of the confining magnetic field, depending on whether field lines are bent towards or away from the plasma.

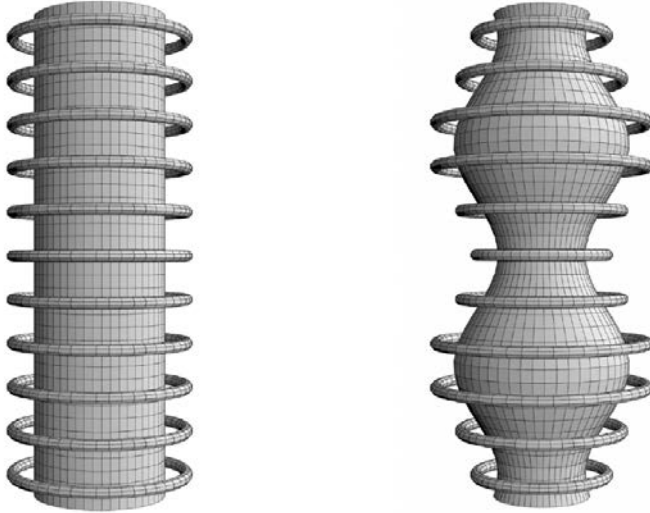


FIG. 3.7. Sausage instability of a plasma column in a surface current model: perturbed plasma surface and solenoidal field lines for the pinch case.

The evolution of today’s surviving confinement configurations has been largely driven by the effort to adjust to stability constraints, but “ideal MHD” stability limits constitute still major bounds to their operational parameter range. Their theoretical determination requires sophisticated calculations, as — for these highly optimized systems — potentially stabilizing and destabilizing forces are orders of magnitude larger than the resulting differences: this is equivalent to stating that we want to determine growth rates that are much smaller than  $v_A / a$ , the inverse of the intrinsic timescale of ideal MHD.

### 3.3.1.1.1. The MHD energy principle

The theoretical foundations, detailed derivations and proofs regarding ideal MHD stability are described in detail in Refs [3.5, 3.6] and only sketched in the following. The starting point of stability investigations within an ideal MHD model are Eqs (3.1)–(3.7), linearized around a *static* equilibrium state satisfying

$$\vec{j}_o \times \vec{B}_o = \nabla p_o \quad (3.51)$$

$$\mu_o \vec{j}_o = \nabla \times B_o \quad (3.52)$$

We introduce the displacement vector

$$\frac{\partial \vec{\xi}}{\partial t} = \vec{v}_1 \quad (3.53)$$

combine Eq. (3.5) and the curl of Eq. (3.4) to

$$\frac{\partial \vec{B}}{\partial t} = \nabla \times (\vec{v} \times \vec{B}) \quad (3.54)$$

and choose the perturbations (index 1) to satisfy, at  $t = 0$ :  $\vec{\xi} = \vec{B}_1 = p_1 = \rho_1 = 0$ , but allow for an initial velocity perturbation  $\vec{v}_1$ . Equations (3.1, 3.3, 3.53), in their linearized form, can then be integrated over time, and we can express all perturbed quantities in terms of  $\vec{\xi}$  and equilibrium quantities as:

$$\rho_1 = -\vec{\xi} \cdot \nabla \rho_o - \rho_o \left( \nabla \cdot \vec{\xi} \right) \quad (3.55)$$

$$p_1 = -\vec{\xi} \cdot \nabla p_o - \gamma p_o \left( \nabla \cdot \vec{\xi} \right) \quad (3.56)$$

$$\vec{B}_1 = \nabla \times \left( \vec{\xi} \times \vec{B}_o \right) \quad (3.57)$$

The time-integrated electric field  $E_1$  — which does not appear as an independent variable in the ideal MHD equations, but in boundary conditions and in the expression of the electromagnetic energy flux — is given by:

$$\int dt \vec{E}_1 = -\vec{\xi} \times \vec{B}_o \quad (3.58)$$

Inserting the above expressions into the linearized equation of motion (Eq. (3.2)) reduces the ideal MHD response to small initial velocity perturbations to a system of partial differential equations which are second order in time, and can be written in vector form as

$$\rho_o \frac{\partial^2 \vec{\xi}}{\partial t^2} = \frac{1}{\mu_o} \left( (\nabla \times \vec{B}_o) \times \vec{Q} + (\nabla \times \vec{Q}) \times \vec{B}_o \right) + \nabla \left( \vec{\xi} \cdot \nabla p_o + \gamma p_o \left( \nabla \cdot \vec{\xi} \right) \right) \quad (3.59)$$

where

$$\vec{Q} = \vec{B}_1 = \nabla \times \left( \vec{\xi} \times \vec{B}_o \right) \quad (3.60)$$

An evident approach to solution is the ansatz

$$\vec{\xi}(\vec{r}, t) = \vec{\xi}(\vec{r}) \exp(-i\omega t) \quad (3.61)$$

which, together with a suitable set of boundary conditions, converts Eq. (3.59) into an eigenvalue problem

$$-\omega^2 \rho_o \vec{\xi} = \frac{1}{\mu_o} \left( (\nabla \times \vec{B}_o) \times \vec{Q} + (\nabla \times \vec{Q}) \times \vec{B}_o \right) + \nabla \left( \vec{\xi} \cdot \nabla p_o + \gamma p_o (\nabla \cdot \vec{\xi}) \right) = \vec{F}(\vec{\xi}) \quad (3.62)$$

with  $\vec{Q} = \nabla \times (\vec{\xi} \times \vec{B}_o)$ .

The operator  $\vec{F}(\vec{\xi})$  can be proven to be self-adjoint [3.5], i.e. to satisfy, for two arbitrary vectors  $\vec{\eta}$ ,  $\vec{\xi}$ ,

$$\int \vec{\eta} \cdot \vec{F}(\vec{\xi}) d\vec{r} = \int \vec{\xi} \cdot \vec{F}(\vec{\eta}) d\vec{r} \quad (3.63)$$

from which it follows that all eigenvalues  $\omega^2$  are real. In most practically relevant cases (with the notable exception of the Alfvén modes discussed in Section 2.4) these eigenvalues are discrete.

The eigenvalues of Eq. (3.62) can also be found as stationary points of the variational principle

$$\omega^2 = \frac{\delta W(\vec{\xi}^*, \vec{\xi})}{K(\vec{\xi}^*, \vec{\xi})} \quad (3.64)$$

with

$$\delta W(\vec{\xi}^*, \vec{\xi}) = -\frac{1}{2} \int (\vec{\xi}^* \cdot \vec{F}(\vec{\xi})) d\vec{r} = -\frac{1}{2} \int (\vec{\xi}^* \cdot \vec{F}(\vec{\xi})) d\vec{r} \quad (3.65)$$

as the work done by a virtual displacement  $\vec{\xi}$  against the reaction force of the plasma, and

$$|\omega^2| K(\vec{\xi}^*, \vec{\xi}) = \frac{1}{2} |\omega^2| \int \rho \vec{\xi}^* \cdot \vec{\xi} d\vec{r} \quad (3.66)$$

its associated kinetic energy. Negative values of  $\omega^2$  correspond to unstable growing solutions and imply the possibility of displacements which set free magnetic energy or plasma enthalpy; positive  $\omega^2$  perturbations require an initial supply of energy, which then is periodically redistributed between kinetic and potential.

Stationary points of Eq. (3.64) give quantitatively the actual growth rates of instabilities and the oscillation frequencies of stable modes, and this variational

principle is the basis of all modern ideal MHD stability codes (see Ref. [3.7] for numerical techniques). For qualitative information on stability or instability it is, however, sufficient to show whether any admissible displacement compatible with boundary conditions can be found which makes  $\delta W$  negative. One can thus derive necessary criteria for stability, choosing suitable “trial” displacements  $\vec{\xi}$ , and this technique has proved immensely successful in developing our general physics insight. This use of  $\delta W$  to decide only qualitatively on stability or instability is generally referred to as the “energy principle” [3.5].

Admissible displacements have to satisfy compatible boundary conditions. For a plasma in contact with an impenetrable, infinitely conducting surface at  $\vec{r} = \vec{r}_W$  with the wall-normal vector  $\vec{n}_W$ , the displacement *normal* to and the electric field (and hence its time integral) parallel to the bounding surface have to vanish:

$$\vec{n}_W \cdot \vec{\xi} \Big|_{\vec{r}_W} = 0 \quad (3.67)$$

$$\vec{n}_W \times \int \vec{E} dt \Big|_{\vec{r}_W} = -\vec{n}_W \times (\vec{\xi} \times B_o) \Big|_{\vec{r}_W} = -(\vec{n}_W \cdot \vec{B}_o) \vec{\xi} \Big|_{\vec{r}_W} + (\vec{n}_W \cdot \vec{\xi}) \vec{B}_o \Big|_{\vec{r}_W} = 0 \quad (3.68)$$

In realistic situations it is difficult to imagine an ideally conducting plasma to be in contact *along* field lines with a wall, so that  $(\vec{n}_W \cdot \vec{B}_o)$  is generally assumed zero, and the two boundary conditions become equivalent.

A more realistic model assumes the ideal plasma to be separated from the walls by a vacuum region, in which no currents can flow, and where the perturbed magnetic field  $\vec{B}_1$  has to satisfy  $\nabla \times \vec{B}_1 = 0$  and  $\nabla \cdot \vec{B}_1 = 0$ . From the vanishing of the magnetic field perpendicular to the perturbed plasma–vacuum interface  $\vec{r}_p$ , and continuity of the sum of magnetic and plasma pressure, follow

$$\vec{n}_p \cdot \vec{B}_1 \Big|_{\vec{r}_p} = \vec{n}_p \cdot \vec{Q} \Big|_{\vec{r}_p} = \vec{n}_p \cdot \nabla \times (\vec{\xi} \times \vec{B}_o) \Big|_{\vec{r}_p} \quad (3.69)$$

and

$$\left( p_1 + \frac{(\vec{B}_o \cdot \vec{Q})}{\mu_o} + \vec{\xi} \cdot \nabla \left( p_o + \frac{B_o^2}{2\mu_o} \right) \right) \Big|_{\vec{r}_p} = \left( \frac{(\vec{B}_o \cdot \vec{B}_1)}{\mu_o} + \vec{\xi} \cdot \nabla \left( \frac{B_o^2}{2\mu_o} \right) \right) \Big|_{\vec{r}_p} \quad (3.70)$$

respectively.

In an ideal (dissipation-free) model, the vacuum region is again assumed to be limited by an infinitely conducting wall, which can, however, be placed also at infinity. Along it, the electric field has to vanish, which implies

$$\vec{n} \cdot \vec{B}_1 \Big|_{\vec{r}_W} = 0 \quad (3.71)$$

Note that an ideal MHD stability analysis does not require  $\vec{n} \cdot \vec{B}_o = 0$  at the vacuum–conductor interface  $\vec{r} = \vec{r}_W$ , and it is in fact realistic to regard walls as penetrable for the magnetic field during the slow development of the equilibrium, but flux conserving on the timescale of ideal MHD instabilities.

For a finite vacuum region surrounding the plasma, it is difficult to impose the boundary conditions onto the admissible functions  $\vec{\xi}$  in Eq. (3.65). It is convenient to modify the energy principle so as to make them appear as natural boundary conditions in the variation. This is equivalent [3.5] to considering variation of the sum of the plasma (“fluid”) part  $\delta W_F$  and a vacuum part  $\delta W_V$  of a potential energy. The latter makes a positive contribution to the  $\delta W$ :

$$\delta W_V = \frac{1}{2\mu_o} \int \vec{B}_1 \cdot \vec{B}_1 d\vec{r} \quad (3.72)$$

which is minimized by  $\vec{B}_1$  satisfying  $\nabla \times \vec{B}_1 = 0$  and  $\nabla \cdot \vec{B}_1 = 0$  subject to the boundary conditions described above. Any virtual plasma displacement around an equilibrium with  $\vec{n} \cdot \vec{\xi}|_{\vec{r}_p} \neq 0$  implies a transfer of energy across the original plasma–vacuum interface, which we can express through the Poynting vector:

$$\delta W_V = -\frac{1}{2\mu_o} \int \vec{n} \cdot \left( \int \vec{E}^* dt \times \vec{B}_1 \right) dS = -\frac{1}{2\mu_o} \int \vec{n} \cdot \left( \left( \vec{\xi}^* \times \vec{B}_o \right) \times \vec{B}_1 \right) dS = \frac{1}{2\mu_o} \int \left( \vec{n} \cdot \vec{\xi}^* \right) \left( \vec{B}_o \cdot \vec{B}_1 \right) dS \quad (3.73)$$

As ideal conducting boundary conditions at the walls imply also vanishing Poynting flux through them, the two expressions for the change in vacuum energy Eq. (3.72) and Eq. (3.73) are equivalent. Although the formulation Eq. (3.73) involves only the perturbed quantities at the plasma–vacuum interface, we need — to obtain  $\vec{B}_1(\vec{r}_p)$  — still a solution to Maxwell’s equations over the whole vacuum domain.

For plasma equilibrium models with surface currents an additional term  $\delta W_S$  arises (see, e.g., Ref. [3.5]), and a distinction between the equilibrium fields on the two sides of the plasma–vacuum interface has to be made: we do not discuss this case here, as such models are primarily of (albeit significant) historical interest.

Using integration by parts one can derive alternative forms of  $\delta W_F$ , which are either more convenient for numerical analyses, or allow for improved physical insight. We give here three forms (the mutual equivalence of which is shown, for example, in Ref. [3.5]):

$$\delta W_F = -\frac{1}{2} \int \vec{\xi}^* \cdot \left( \frac{1}{\mu_o} (\nabla \times \vec{B}_o) \times \vec{Q} + \frac{1}{\mu_o} (\nabla \times \vec{Q}) \times \vec{B}_o + \nabla \left( \vec{\xi} \cdot \nabla p + \gamma p \nabla \cdot \vec{\xi} \right) \right) d\vec{r} \quad (3.74)$$

$$\delta W_F = \frac{1}{2} \int \left( \frac{|\vec{Q}|^2}{\mu_o} + \gamma p |\nabla \cdot \vec{\xi}|^2 - \vec{\xi}_\perp^* \cdot (\vec{j}_o \times \vec{Q}) + (\vec{\xi}_\perp \cdot \nabla p) (\nabla \cdot \vec{\xi}_\perp^*) \right) d\vec{r} \quad (3.75)$$

$$\begin{aligned} \delta W_F = & \\ = \frac{1}{2} \int & \left( \frac{|\vec{Q}_\perp|^2}{\mu_o} + \frac{|\vec{B}_o|^2}{\mu_o} |\nabla \cdot \vec{\xi}_\perp + 2\vec{\kappa} \cdot \vec{\xi}_\perp|^2 + \gamma p |\nabla \cdot \vec{\xi}|^2 - j_{o\parallel} (\vec{\xi}_\perp \times \vec{b}_o) \cdot \vec{Q}_\perp - 2(\vec{\xi}_\perp \cdot \nabla p) (\vec{\kappa} \cdot \vec{\xi}_\perp^*) \right) d\vec{r} \end{aligned} \quad (3.76)$$

where we have partly split  $\vec{\xi}, \vec{Q}, \vec{j}_o$  into components parallel and perpendicular to  $\vec{b}_o = \vec{B}_o / |\vec{B}_o|$  and introduced the curvature vector of the unperturbed field line  $\vec{\kappa} = \left( \vec{B}_o \cdot \nabla \right) \vec{B}_o / |\vec{B}_o|^2$ .

The formulation in Eq. (3.76), separates, in particular, positive definite terms from potentially destabilizing ones. For a homogenous plasma, immersed in a homogenous magnetic field,  $\vec{\kappa}$  and  $j_{o\parallel}$  vanish, and the three terms  $|\vec{Q}_\perp|^2 / \mu_o, |\vec{B}_o|^2 |\nabla \cdot \vec{\xi}_\perp|^2 / \mu_o, \gamma p |\nabla \cdot \vec{\xi}|^2$  give rise to shear Alfvén, compressional Alfvén and sound waves, respectively. The last two terms in Eq. (3.76) describe the two potentially destabilizing effects of parallel plasma currents and of pressure gradients in the direction of the curvature vector of the magnetic field lines, which we illustrated in the sample configurations given in Section 3.3.1.1.

In the formulation Eq. (3.76), the parallel displacement component  $\xi_\parallel \vec{b}_o$  appears only in the positive definite compression term  $\gamma p |\nabla \cdot \vec{\xi}|^2$ . The search for unstable situations can therefore be limited to incompressible displacements if we can choose

$$\vec{B}_o \cdot \nabla \left( \xi_\parallel / |\vec{B}_o| \right) = -\nabla \cdot \vec{\xi}_\perp \quad (3.77)$$

as these will then not constrain  $\vec{\xi}_\perp$ . The latter is, however, not possible for field aligned perturbations in some highly symmetrical configurations (an example will be given immediately below) for which compressible displacements have to be included in the minimization.

### 3.3.1.1.2. Stability of one-dimensional (cylindrical) equilibria

In Section 3.2.1 we have described  $z$ -,  $\theta$ - and screw-pinches as basic cylindrical equilibrium configurations. Their ideal MHD-stability properties offer also instructive sample applications of the above energy principle, illustrating how sufficient criteria for instability can be derived by successive steps of minimization. As  $p_o, \vec{B}_o$  in this case are independent of  $\theta, z$  we can make the ansatz

$$\vec{\xi}(\vec{r}) = (\xi_r(r) \vec{e}_r + \xi_\theta(r) \vec{e}_\theta + \xi_z(r) \vec{e}_z) e^{i(m\theta + k_z z)} \quad (3.78)$$

for the virtual displacement and treat individual  $m, k$  modes separately.

Configurations with pure axial currents ( $z$ -pinches) could be readily bent into toroidal equilibria, but have unfavourable stability properties. In the straight geometry the quantities and terms appearing in Eq. (3.76) can be written as

$$\vec{Q}_\perp = \frac{imB_\theta}{r} (\xi_r \vec{e}_r + \xi_z \vec{e}_z) \quad (3.79)$$

$$\vec{\kappa} = -\frac{\vec{e}_r}{r}, \nabla \cdot \vec{\xi}_\perp + 2\vec{\kappa} \cdot \vec{\xi}_\perp = r \left( \frac{\xi_r}{r} \right)' + ik_z \xi_z \quad (3.80)$$

with  $(\ )$  denoting  $d(\ )/dr$ . The condition Eq. (3.77) reads  $irm\xi_\theta = -(r\xi_r) - ik_z r\xi_z$  and can be used — for  $m \neq 0$  — to eliminate the compression term. In this case, we can write Eq. (3.76) as

$$\frac{\delta W_F}{2\pi R_o \mu_o} = \int r dr \left( \frac{m^2 B_\theta^2}{r^2} (|\xi_r|^2 + |\xi_z|^2) + B_\theta^2 \left| r \left( \frac{\xi_r}{r} \right)' + ik_z \xi_z \right|^2 + 2 \frac{p' \mu_o}{r} |\xi_r|^2 \right) \quad (3.81)$$

where (to connect these results to toroidal cases of plasmas with a major radius  $R_o$ ) we have extended the integrals over an axial length  $2\pi R_o$ , and have dropped the index  $o$  from the equilibrium quantities.

Varying  $\xi_z$ , the integrand is algebraically minimized for

$$\xi_z = -\frac{ik_z r^2}{m^2 + k_z^2 r^2} \left( \frac{\xi_r}{r} \right)' \quad (3.82)$$

which inserted, results in the expression

$$\frac{\delta W_F}{2\pi R_o \mu_o} = \int r dr \left( m^2 B_\theta^2 + 2\mu_o r p' \right) \left( \frac{|\xi_r|^2}{r^2} \right) + r^2 B_\theta^2 \left( \frac{m^2}{m^2 + k_z^2 r^2} \right) \left| \left( \frac{\xi_r}{r} \right)' \right|^2 \quad (3.83)$$

For a short enough wavelength in the axial direction the last, positive definitive term can be made arbitrarily small, so that a displacement  $\xi_r$ , localized to a region with

$$-rp' > m^2 B_\theta^2 / (2\mu_o) \quad (3.84)$$

would make  $\delta W_F$  negative. The relation Eq. (3.84) gives thus a limit to the pressure gradient, which is most severe for the  $m = 1$  mode. Using the equilibrium relation Eq. (3.13) we can convert it into a condition for the current density profile, which for stability would have to satisfy everywhere

$$j_z(r) / \langle j_z \rangle_r < m^2 / 4 \quad (3.85)$$

with  $\langle j_z \rangle_r \Big| = 2 \int_0^r r dr j_z(r) / r^2$  which, at least for  $m=1$ , is not the case for realistic  $z$ -pinch profiles except in the outermost plasma regions. The resulting  $m=1$  mode has the geometrical form of a *kink*-instability, but differs from the one described in the introductory paragraph as it is pressure gradient driven (the parallel equilibrium current density vanishes for the pure  $z$ - and  $\theta$ -pinches).

The  $m=0$  mode in the  $z$ -pinch is *field-aligned* and we cannot choose  $\xi_\theta$  so as to make the displacement incompressible. We can rewrite the energy principle, however, in terms of  $\nabla \cdot \vec{\xi}_\perp$  and  $\xi_r$ :

$$\frac{\delta W_F}{2\pi R_o} = \frac{\pi}{\mu_o} \int r dr \left( B_\theta^2 \left( \left| \nabla \cdot \vec{\xi}_\perp - 2 \frac{\xi_r}{r} \right|^2 \right) + \gamma p \left| \nabla \cdot \vec{\xi} \right|^2 + 2 \frac{p' \mu_o}{r} |\xi_r|^2 \right) \quad (3.86)$$

and partially minimize it by choosing  $\nabla \cdot \vec{\xi} = \left\{ (2B_\theta^2 / \mu_o) / (\gamma p + B_\theta^2 / \mu_o) \right\} \xi_r / r$ . The argument of the integral becomes then locally negative, if

$$-rp' > \frac{2\gamma B_\theta^2 / \mu_o}{\gamma p + B_\theta^2 / \mu_o} \quad (3.87)$$

This condition is violated even by rather flat pressure profiles in the case of  $\gamma = 5/3$ . It corresponds to the sausage-type mode, which we described as the archetype of a pressure driven instability in the introduction.

The  $\theta$ -pinch, with  $B_\theta = 0$ , is qualitatively different as its equilibrium field lines have no curvature. Using successive partial minimizations in a similar fashion as above, one can readily show that perturbations of the form Eq. (3.78) with  $k_z \neq 0$  are positively stable; and field aligned perturbations ( $k_z = 0$ ) marginal. Unfortunately, a pure  $\theta$ -pinch cannot be turned into a toroidal equilibrium configuration, so that we have to consider the cylindrical screw-pinch, with both  $B_\theta, B_z \neq 0$ , as starting point for possible stable toroidal equilibrium configurations. It is convenient, in this case, to decompose the displacement vector as

$$\vec{\xi}(\vec{r}) = \left( \xi(r) \vec{e}_r + \eta(r) \vec{e}_\eta + \xi_\parallel(r) \vec{b} \right) e^{i(\vec{k} \cdot \vec{r})} \quad (3.88)$$

with  $\vec{e}_\eta = \vec{e}_r \times \vec{b}$ , but to continue expressing the wave vector  $\vec{k}$  in its  $\vec{e}_\theta, \vec{e}_z$  components. Except for the special case of field aligned perturbations  $\vec{k} \cdot \vec{B} = 0$  in configurations with  $q = rB_z / (R_o B_\theta)$  equal to a rational value  $m/n$  over a finite radial region, incompressible  $\vec{\xi}(\vec{r})$  will again be the most unstable displacements, making it possible to eliminate  $\xi_\parallel$ . As  $\eta$  appears only algebraically in  $\delta W_F$  its contribution can be minimized by proper choice in terms of  $\xi_r, \xi_r'$ , allowing us to cast the plasma contribution into the form

$$\frac{\delta W_F}{2\pi R_o} = \frac{\pi}{\mu_o} \left\{ \int_0^a (f \xi_r'^2 + g \xi_r^2) dr + \left( \frac{k_z^2 r^2 B_z^2 - m^2 B_\theta^2}{k_o^2 r^2} \right)_{r=a} \cdot \xi_a^2 \right\} \quad (3.89)$$

(see Ref. [3.8]) using the abbreviations:

$$f = \frac{r F^2}{k_o^2} \quad (3.90)$$

$$g = 2\mu_o \frac{k_z^2}{k_o^2} p' + \frac{k_o^2 r^2 - 1}{k_o^2 r^2} r F^2 + 2 \frac{k_z^2}{r k_o^4} \left( k_z B_z - \frac{m B_\theta}{r} \right) F \quad (3.91)$$

$$F = \vec{k} \cdot \vec{B}_o = (m/r) B_\theta + k_z B_z \quad (3.92)$$

$$k_o^2 = k_z^2 + (m/r)^2 \quad (3.93)$$

The displacement at the plasma boundary  $\xi_a = \xi_r(a)$  appears as use has been made of partial integration. Together with the location of a possible conducting wall at  $r=b$ ,  $\xi_a$  fixes also the perturbed vacuum field, which can be obtained explicitly using the magnetic potential [3.5]  $\vec{B}_1 = \nabla \Phi_1$ , by solving  $\nabla^2 \Phi_1 = 0$  subject to the boundary conditions  $\Phi_1'(a) = iF(a)\xi_r(a)$ ,  $\Phi_1'(b) = 0$ . For  $k_z b \ll 1$  the vacuum energy  $\delta W_V$  is given by

$$\frac{\delta W_V}{2\pi R_o} = \frac{\pi}{\mu_o} \left( \frac{r^2 F^2 \Lambda_W}{|m|} \right)_a \xi_a^2 \quad (3.94)$$

with  $\Lambda_W \approx \left( 1 + (a/b)^{2|m|} \right) / \left( 1 - (a/b)^{2|m|} \right)$  showing that for higher  $m$ -modes, this stabilizing contribution of the vacuum energy decays very rapidly with growing distance of the wall.

The determination of plasma stability requires therefore the minimization of

$$\frac{\delta W}{2\pi R_o} = \frac{\pi}{\mu_o} \left\{ \int_0^a (f \xi_r'^2 + g \xi_r^2) dr + \left( \frac{k_z^2 r^2 B_z^2 - m^2 B_\theta^2}{k_o^2 r^2} + \frac{r^2 F^2 \Lambda}{|m|} \right)_{r=a} \cdot \xi_a^2 \right\} \quad (3.95)$$

which in general requires numerical calculations. Two simpler to evaluate, general criteria can, however, be derived from it, which are important for the physical insight they give into more complex and realistic situations.

*Suydam's criterion* (for the derivation see, for example, Ref. [3.5]) is a test against a localized perturbation around a rational surface  $q(r_s) = m/n$ , resonant and field-aligned on it:  $F(r_s) = \vec{k} \cdot \vec{B}_o = 0$ ;  $k_z = -n/R_o$ . Expanding  $p, F, q$  in the proximity of  $r=r_s$ , an unstable trial function can be constructed, if

$$1 - 4D_s < 0 \quad (3.96)$$

with

$$D_s = - \left. \frac{2\mu_o p'}{rB_z^2} \cdot \frac{q^2}{q'^2} \right|_{r_s} \quad (3.97)$$

The necessary condition for stability resulting from this,

$$\frac{8\mu_o r p'}{B_z^2} + \left( \frac{r q'}{q} \right)^2 > 0 \quad (3.98)$$

is known as *Suydam's criterion* and expresses the balance between the destabilizing effect of an unfavourable pressure gradient/field-line curvature combination and the stabilizing effect of shear in the magnetic field. In a straight cylinder, only the  $B_\theta$ -field contributes to the field-line curvature, which is unfavourable in combination with the (generally) inward directed pressure gradient. Shear in the pitch of the field lines, on the other hand, associates perturbations which are field aligned at the resonant surface with a bending of field lines in its proximity, and can hence stabilize them. Note that this effect depends only on the magnitude of the shear, but not its sign. These basic effects will appear also in practically more relevant confinement configurations, but toroidal curvature will give rise to a qualitative modification of this criterion.

*Newcomb's analysis* for general internal modes (i.e. with  $\xi_a = 0$ ) is not an analytical criterion like Eq. (3.99), but requires a (generally numerical) solution of a differential equation. We present here an ad hoc derivation (a formal one is given in Ref. [3.5]) which stresses the relation to the energetics of ideal MHD modes and will later help to understand the effects of resistive dissipation (in tearing and resistive wall modes). We start from the Euler–Lagrange equation for the variational principle Eq. (3.89)

$$\left( f \xi_r' \right)' - g \xi_r = 0 \quad (3.99)$$

where admissible perturbations should satisfy  $\xi_r(a) = 0$  and a regularity condition at the origin. We note the similarity to the classical eigenvalue equation, which would, however, have an additional term  $\lambda \xi_r$  on the left-hand side, and which would have a non-trivial regular solution satisfying the specified homogeneous boundary conditions only for  $\lambda$  corresponding to an eigenvalue. Equation (3.99), with the physically motivated boundary conditions, will therefore have a regular solution only in the marginal stability case, where the minimizing perturbation needs no external energy input, but also produces no surplus to feed into kinetic energy of the displacement: it is therefore also termed *marginal ideal MHD equation*.

In the general case, a solution regular in  $r=0$  will therefore not have a zero right at  $r=a$ : Newcomb's criterion (in the more straightforward case of  $F(r) \neq 0$  in  $0 \leq r \leq a$  for a given  $m, n$  considered) states that if this solution has no zero in  $0 \leq r \leq a$  the plasma is ideal-MHD *stable* against the mode  $m, n$  considered, but unstable otherwise. One can construct a solution to Eq. (3.99) by combining an inner solution  $\xi_1$  (for  $r \leq r_o$ ) satisfying the regularity condition at the origin with an outer solution (for  $r \geq r_o$ ) satisfying  $\xi_2(a) = 0$ . Both solutions can be normalized to the same value  $\xi_1(r_o) = \xi_2(r_o) = \xi_o$ , but will differ in  $\xi_1'(r_o) \neq \xi_2'(r_o)$ . We note that the time-integrated radial energy flux through a surface, associated with the perturbation, is given by

$$\int dt \left( \frac{\gamma}{\gamma-1} p_1 (\vec{n} \cdot \vec{v}_1) + (\vec{E}_1 \times \vec{Q}) \cdot \vec{n} \right) = -\frac{\gamma}{\gamma-1} p_o' \frac{\xi_r^* \xi_r'}{2} - \frac{1}{2\mu_o} \vec{n} \cdot \left( (\vec{\xi}^* \times \vec{B}_o) \times \nabla \times (\vec{\xi} \times \vec{B}_o) \right) \quad (3.100)$$

and contains, besides terms  $\sim \xi_r^* \xi_r'$ , and hence continuous, also a contribution  $-(F^2 / (2\mu_o k_o^2)) \xi_r^* \xi_r'$  which will have a jump for the "patched" solution composed above. It corresponds to a net energy in- or out-flow into the (infinitely thin) discontinuity zone, depending on the sign of  $\xi_o (\xi_2' - \xi_1')$ . An energy surplus (corresponding to  $\xi_o (\xi_2' - \xi_1') > 0$ , and an associated energy inflow) of this solution implies that the computed displacement would have reserves to invest in kinetic energy, and hence for an unstable growth with a finite growth rate. The opposite case would need external energy input to grow, and hence corresponds to a stable situation. The correspondence of this statement to Newcomb's criterion is easy to visualize for simple examples; the rigorous proof and the generalization to equilibria where  $F(r) = 0$  at a radius  $0 \leq r \leq a$  is given in Ref. [3.5]. We will encounter a related situation in the case of tearing modes, where the location of the discontinuity will, however, be fixed at a resonant surface with  $F(r) = 0$ , and the energy input implied by the discontinuity will have a real physical meaning driving resistive dissipation and flows in a singular layer.

### 3.3.1.1.3. The "straight" tokamak model

The tokamak can be viewed as a sub-class of screw-pinches, distinguished by the basic ordering of the field components and of the pressure outlined in Section 3.2.2.3. Due to  $B_{tor} / B_{pol} \approx qR_o / a$  (with  $B_{tor} = |\vec{B}_{tor}|$ ), however, the toroidal field curvature — decisive for the effect of the pressure gradient (see Eq. (3.76)) — cannot be neglected, and a straight cylinder model gives a reasonable first approximation only for "current" driven modes. The torus topology is taken account of in this model only through a constraint on the permitted mode numbers:  $k_z = -n/R_o$ , with integer  $n$ . In terms of the inverse aspect ratio  $\varepsilon = a/R_o$ , used in the following as expansion parameter, we order the characteristic dimensionless quantities as:  $q \approx 1$ ,  $B_\theta / B_z (= B_{pol} / B_{tor}) \approx \varepsilon$ ,

$\beta_{pol} \approx 1$ ,  $\beta_{tor} \approx \varepsilon^2$ . We first consider internal modes, for which  $\xi_a = 0$ . (Physically we can imagine this condition to be imposed by a tight-fitting, infinitely conducting shell.) Expanding Eq. (3.95) in powers of  $\varepsilon^2$  as

$$\delta W = \varepsilon^0 \delta W_0 + \varepsilon^2 \delta W_2 + \varepsilon^4 \delta W_4 + \dots \quad (3.101)$$

we obtain as lowest order non-vanishing contribution

$$\frac{\varepsilon^2 \delta W_2}{W_0} = \frac{1}{a^2} \int_0^a \left( \frac{1}{q} - \frac{n}{m} \right)^2 \left( r^2 \xi_r'^2 + (m^2 - 1) \xi^2 \right) r dr \quad (3.102)$$

$$W_0 = 2\pi^2 a^2 R_0 \frac{B_o^2}{\mu_o} \quad (3.103)$$

which is positive definite for all modes with  $m > 1$  and also for  $m = 1$ , if  $q(0) > 1$  and monotonically increasing. (In deriving Eqs (3.102, 3.103) we have been using  $k_o^2 = (m/r)^2 (1 + \varepsilon^2 (n/m)^2) \approx (m/r)^2$ , excluding thereby  $m = 0$  modes — which can be easily shown to be strongly stable — from the range of its validity.) To allow possibly destabilizing higher order contributions to become effective,  $\delta W_2$  has nearly to vanish, which can be the case for modes localized around the rational surfaces (see Suydam's criterion), and for global  $m = 1$  perturbations of the form shown in Fig. 3.8. Higher order corrections or non-ideal MHD effects will ultimately decide the stability of this mode but with only small changes to this lowest-order shape.

Removing the constraint on  $\xi_a$  increases the range of admissible trial functions and raises the possibility of instabilities already in second order. In the absence of any stabilizing wall ( $b/a \rightarrow \infty$ ) the second-order contribution to  $\delta W_p + \delta W_v$  is given by

$$\frac{\varepsilon^2 \delta W_2}{W_0} = \frac{1}{a^2} \int_0^a \left( \frac{1}{q} - \frac{n}{m} \right)^2 \left( r^2 \xi_r'^2 + (m^2 - 1) \xi^2 \right) r dr + \left( \frac{n}{m} - \frac{1}{q_a} \right) \left( \left| m \left( \frac{n}{m} - \frac{1}{q_a} \right) + \left( \frac{n}{m} + \frac{1}{q_a} \right) \right| \right) \xi_a^2 \quad (3.104)$$

which adds to Eqs (3.102, 3.103) a term which is destabilizing for  $1 < m/(nq_a) < (m+1)/(m-1)$ , i.e. if the rational surface  $q(r_s) = m/n$  is in the vacuum, but (as in a straight cylinder,  $q \sim r^2$  in the vacuum region) at a close distance from the plasma:  $1 < r_s/a < \sqrt{(m+1)/(m-1)}$ . In particular, for the case of  $m = 1$ , we can construct a simple trial function  $\xi(r) = \text{constant} = \xi_a$ , which shows  $q_a > 1$  to be a *necessary* condition for stability (also called the *Kruskal–Shafranov* limit and the origin of the label *safety factor* sometimes applied to  $q_a$ ).

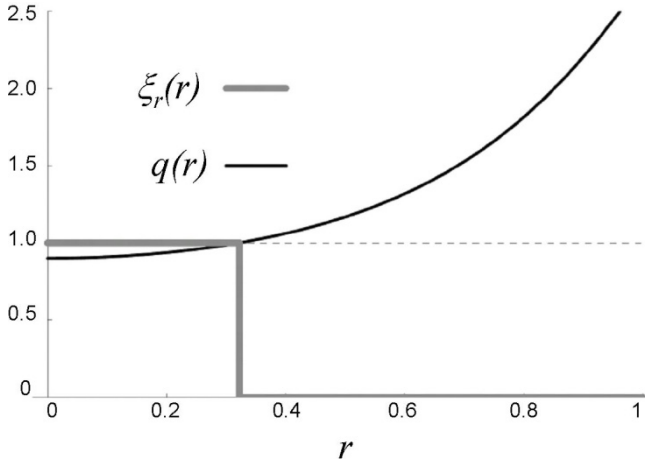


FIG. 3.8. Lowest order radial displacement for  $m = 1$  internal kink mode, for  $q$ -profile shown.

In general the identification of the perturbation minimizing Eq. (3.104) requires numerical methods. For the class of model current profiles given by Eq. (3.22) the resulting unstable regions in the plane spanned by  $q_a/q_o = \nu_j + 1$  and  $q_a$  are shown in Fig. 3.9 (see Ref. [3.9]). The internal  $m = 1, n = 1$  mode is unstable if  $q_o = q(0) < 1$ , i.e. in the region to the right of the diagonal. Each external mode  $(m, n)$  is unstable in the range

$$m/n > q_a > m/n - (\delta q)_{m,n} \quad (3.105)$$

where the interval  $(\delta q)_{m,n}$  decreases with stronger peaking of the current distribution (i.e. increasing  $\nu_j$ ). For profiles flatter than corresponding to  $\nu_j \leq 1$ , the unstable ranges given by the different  $(m, n)$  combinations overlap. For  $q_a > 2$  stable intervals appear with increasing  $q_a/q_o$  and/or (not shown here) in the presence of a sufficiently close conducting wall, in particular for  $q_a$ -values slightly above low-order rational values  $(m, n)$ .

These results suggest that the current density or its gradient near  $r = a$  have a strong destabilizing effect on free-boundary modes, and this can be confirmed analytically for the case of  $m \gg 1$  [3.5]. The most unstable perturbations in this case are localized close to the plasma boundary (and hence termed *peeling* modes) and are unstable for finite current density at the boundary  $j_z(a)$ , over an interval  $(\delta q)_{m,n} = j_z(a) / (n \langle j_z \rangle|_a)$ . A peeling instability can persist even for vanishing  $j_z(a)$ , but over a narrow region  $(\delta q)_{m,n} = \exp\left(-\left(2m \langle j_z \rangle|_a\right) / \left(a \left| j_z' \right|_a\right)\right)$ .

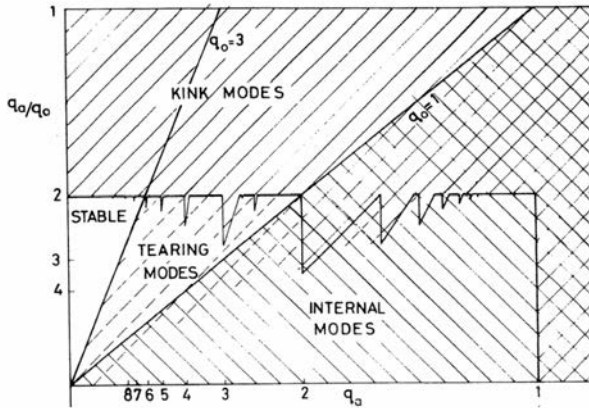


FIG. 3.9. Stable and unstable regions for current driven modes (internal and external kinks and tearing modes) in the parameter space of  $q_a$  and  $q_a/q_0$  for a circular cross-section infinite aspect ratio tokamak and current profiles of the class of Eq. (3.22) [3.9].

Despite the highly simplified model, the  $\delta W_2$ -analysis in the straight cylinder approximation to a tokamak yields some robust results clearly borne out by experiments:

- Internal  $m = 1$  modes observed generally conform to a plasma displacement as shown in Fig. 3.8.
- Without a close fitting shell it is impossible to obtain discharges with  $q_a$  (properly defined to take into account toroidicity and non-circular plasma cross-sections)  $\leq 2$ .
- High edge current densities have a strongly destabilizing effect, as can be most clearly noted during the current ramp-up phase in circular tokamaks, where the passage through rational  $q_a$ -values is usually accompanied by strong MHD activity.
- *Peeling* modes are now considered a prime suspect as drive for a class of edge localized modes observed in *H-mode* discharges in divertor tokamaks.

#### 3.3.1.1.4. Stability of realistic tokamak configurations

Due to the tokamak ordering introduced above, pressure gradient effects on stability cannot be described — even qualitatively — correctly in the straight cylinder approximation. The normal curvature  $\kappa_n = (\vec{n} \cdot \vec{\kappa})$  responsible for the pressure gradient destabilization in straight geometry acquires a contribution from the toroidal field, which is of lower order in  $\varepsilon$  than that of the poloidal field, as can easily be seen for an equilibrium with circular, concentric flux surfaces (using the coordinate system of Fig. 3.2).

$$\vec{\kappa} \cdot \vec{n} = - \left( \frac{B_\phi^2}{B^2} \frac{\cos \theta}{R} + \frac{1}{r} \frac{B_\theta^2}{B^2} \right) \approx - \frac{1}{r} \left( \frac{r}{R_0} \cos \theta (1 - (r/R_0) \cos \theta) + \left( \frac{r}{R_0 q} \right)^2 \right) \quad (3.106)$$

It changes, however, sign with  $\theta$ , being destabilizing on the low- and stabilizing on the high-field side, and necessitates therefore an accurate calculation to determine its net effect.

Modern tokamaks typically have an aspect ratio  $2.5 \leq R_o/a \leq 4$  (and lower, for the so-called *spherical* tokamaks), and a strongly non-circular plasma cross-section in the poloidal plane. The assessment of their linear stability against *global* modes requires numerical analysis with elaborate code packages (see, for example, Refs [3.10–3.13]). In the axisymmetric tokamak case (assuming also no or ideally-axisymmetric conducting walls) these codes can exploit the independence of equilibrium parameters from the toroidal angle  $\phi$ , making use of an ansatz for the perturbations  $\vec{\xi}(R, \phi, z) = \sum_n \vec{\xi}_n(R, z) \exp(in\phi)$ , with separating  $n$ -modes.

Modes localized around a rational surface  $q(\psi) = m/n$  can be assessed in a simpler way. In a straight cylinder they have an *interchange* mode structure, with perturbations constant along the resonant field direction and consisting of an interchange of flux bundles. They are destabilized by unfavourable field line curvature, and stabilized by finite shear, which — in the neighbourhood of the rational surface — associates these displacements with a bending and compression of field lines. The equivalent to the *Suydam* criterion is the *Mercier* criterion describing *interchange* modes (with a displacement constant along the rational field lines) in general toroidal geometry. Analytic evaluation of it is possible in some cases by expansion, and for a circular cross-section, large aspect ratio tokamak the necessary condition for stability becomes

$$\frac{8\mu_o r p'}{B_z^2} (1 - q^2) + \left( \frac{r q'}{q} \right)^2 > 0 \quad (3.107)$$

It differs hence from the *Suydam* result Eq. (3.98), actually changing the sign of the pressure gradient term for  $q > 1$ . Around the minimum of  $q$  — for peaked current distributions at the axis — shear stabilization is ineffective, so that Eq. (3.107) requires in this standard case  $q(0) = q_o \geq 1$ .

A near-axis expansion can be carried through also for non-circular plasmas. Using the parameterization of flux surface shape in terms of local inverse aspect ratio  $r/R_o$ , elongation  $\kappa$  and triangularity  $\delta$  introduced in Section 3.2.2.4 (noting that from an expansion of Eq. (3.19) it follows that  $\delta(r) \sim r$  has to hold near the magnetic axis), this generalization yields as necessary stability condition

$$q_o \geq 1 / \sqrt{1 - \frac{4}{1 + 3\kappa^2} \left( \frac{3\kappa^2 - 1}{4\kappa^2 + 1} \left( \kappa^2 - \frac{2\delta}{r/R_o} \right) + \frac{(\kappa - 1)^2 \beta_{pol}(0)}{\kappa(\kappa + 1)} \right)} \quad (3.108)$$

Finite plasma pressure  $\beta_p(0)$  and plasma elongation alone are hence destabilizing, but a sufficient triangularity  $r\delta/R_o \geq \kappa^2/2$  can turn the effect of elongation into a stabilizing one. Together with the fact that elongation allows a higher plasma current at given aspect ratio,  $q(\psi_c)$ , and  $B_\phi(R_o)$ , this motivates from the physics side the D-shaped cross-section of all modern tokamak designs. (Happily it also leads to a separatrix near — or at — the boundary, and hence to a natural divertor, and can be well matched to a technically advantageous pure tension design of the outer legs of the toroidal field coils.)

If the interchange modes described by *Mercier's* criterion are stable, pressure driven modes exploiting more effectively the bad curvature, the outer torus region can still be unstable: the *ballooning* modes. The method universally used now for testing for their stability [3.14] is a prime example that elegance and relevance can rime nicely, and has had spin-offs in other fields of plasma theory. The modes to be tested in Eq. (3.76) should vary slowly along, but rapidly across, field lines, which suggests their description by an eikonal-ansatz

$$\vec{\xi}_\perp = \vec{\eta}_\perp \exp(iS) \quad (3.109)$$

with  $\vec{\eta}_\perp$  varying only on the spatial scale of the equilibrium, and  $S$  constant along field lines

$$\vec{B}_o \cdot \nabla S = 0 \quad (3.110)$$

but varying rapidly perpendicular to them:  $\vec{k}_\perp = \nabla S \rightarrow \infty$ . The impossibility of finding a physically acceptable function  $S$  in the case of finite shear can be seen even in the cylindrical limit, where we write  $z = 2\pi\phi$  to take account of the periodicity requirement. In this case, the ansatz

$$S \approx n(-\phi + q(r_o)(\theta - \theta_o) + (r - r_o)q'(r_o)(\theta - \theta_o)) \quad (3.111)$$

satisfies Eq. (3.110) in the vicinity of a surface  $r_o$ , but this solution will satisfy the periodicity constraint

$$\vec{\xi}_\perp(r, \theta, \phi) = \vec{\xi}_\perp(r, \theta + 2\pi, \phi) = \vec{\xi}_\perp(r, \theta, \phi + 2\pi) \quad (3.112)$$

only on a rational surface  $q(r) = m/n$ , but (in the general, finite shear case) not in its proximity. A function  $\xi(r, \theta)$ , periodic in  $0 \leq \theta \leq 2\theta$ , can, however, be constructed from a function  $\xi_Q(r, \theta)$ , defined in  $-\infty < \theta < \infty$  (with  $\xi_Q(r, \theta) \rightarrow 0$  for  $\theta \rightarrow \pm\infty$ ), by

$$\xi(r, \theta) = \sum_p \xi_Q(r, \theta + 2p\pi) \quad (3.113)$$

and will satisfy the same eigenvalue equation  $L(r, \theta)\xi(r, \theta) + \lambda\xi(r, \theta) = 0$  for an operator  $L(r, \theta)$  periodic in  $\theta$ , with the same eigenvalue  $\lambda$  (and hence marginal stability point) as  $\xi_Q$ , since

$$\begin{aligned} & \sum_p L(r, \theta)\xi_Q(r, \theta + 2p\pi) + \lambda \sum_p \xi(r, \theta + 2p\pi) = \\ & = \sum_p L(r, \theta + 2p\pi)\xi_Q(r, \theta + 2p\pi) + \lambda \sum_p \xi(r, \theta + 2p\pi) \end{aligned} \quad (3.114)$$

We can therefore use trial functions for Eq. (3.76) satisfying boundary conditions only at  $\pm\infty$ , making the ansatz Eqs (3.109, 3.110).

The ballooning mode ansatz for pressure driven, localized modes in a tokamak leads to a 1-D variational principle or a corresponding Euler–Lagrange equation which have to be solved numerically on each flux surface. Some qualitative physics understanding can again be gained from a small  $r/R_o$  expansion of the circular cross-section case, where stability is determined by shear  $s = (r/q)q'$  and normalized pressure gradient

$$\alpha = -\left(2R_o q^2 / B_\phi^2\right) p' \quad (3.115)$$

resulting in the  $s - \alpha$  stability diagram shown as Fig. 3.10. As expected, at low  $\alpha$  (in the *first* stable region) the permissible pressure gradient increases with shear, approaching a linear dependence

$$\alpha \leq 0.6s \quad (3.116)$$

for shear values of  $O(1)$ . Surprisingly a *second* stable regime appears for higher pressure gradients which can be traced back to the pressure-gradient driven modulation of  $\hat{q}(\psi, s)$  (see Eq. (3.35) along a flux surface and its local shear). Ballooning modes are driven by the pressure gradient on the unfavourable curvature region of a flux surface. The extent of this region for a circular-boundary plasma (but rigorously computed plasma equilibrium) is shown in Fig. 3.11 taken from Ref. [3.15]. Typical plasma current profiles such as described by Eq. (3.22) produce a positive average shear  $s$ , but the pressure gradient effect will weaken it on the torus outside, adding to the destabilization of the ballooning mode. For large enough pressure gradients, however, the local shear will become negative over the whole region of unfavourable curvature (see Fig. 3.11 right), stabilizing now by itself against ballooning deformations.

A low or even negative average shear is therefore advantageous for accessing this *second* stability regime in agreement with Fig. 3.10. In fact, *second* regime stability plays primarily a part in regions with weak or reversed shear, where a favourable symbiosis can exist between *second* stability, the *bootstrap*

current and the suppression of *micro-turbulence*. The bootstrap current (described in Chapter 2) is a thermoelectric current driven by the pressure gradient which can make a substantial contribution to the total plasma current. As also described there, micro-turbulence is the main drive of anomalous energy transport, but can be suppressed over a range of flux surfaces — either in the plasma interior (*internal transport barriers – ITBs*) or close to the separatrix of a divertor tokamak (*the H-mode pedestal*) — in a reproducible, but as yet not completely understood, way. Second stability and turbulence suppression allow for steep pressure gradients, which give rise to a high bootstrap current density. The latter in turn can reduce or reverse the average shear if it becomes comparable on a magnetic surface to the average current density inside of it (see Section 3.2.2.3). Fortuitously, reduced or reversed magnetic shear in turn also appears to facilitate the suppression of micro-turbulence by sheared flow rotation.

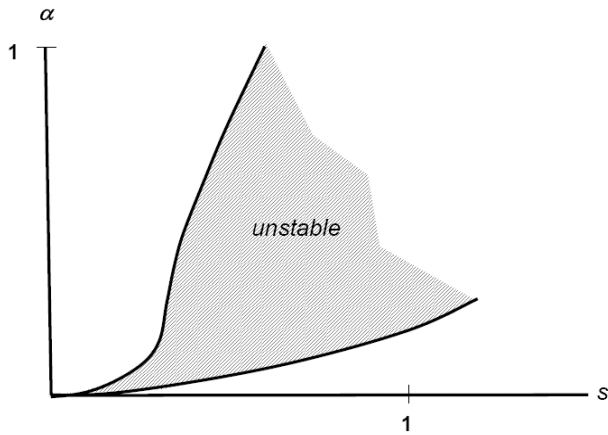


FIG. 3.10.  $s - \alpha$  stability diagram of ballooning modes, based on a large aspect ratio, circular flux surface expansion. Reprinted from Ref. [3.16]. Copyright (2010), with permission from Elsevier.

Within the *first* stability regime, ballooning modes would give a limit to the pressure gradient on each flux surface, and hence also a global limit depending on pressure and safety factor profiles. For a fixed profile of shear, Eq. (3.116) would predict a maximum  $\beta_{tor}$  (as defined in Eq. (3.39))  $\sim 1/q^2$ , but this scaling — at low enough  $q_a$  — would violate the requirement for the stability of the  $(m,n)=(1,1)$  mode. The latter limit reduces therefore the allowable shear for increasing  $q_a$  and leads, over a large parameter range, to  $\beta_{tor,max} \sim 1/q_a$ .

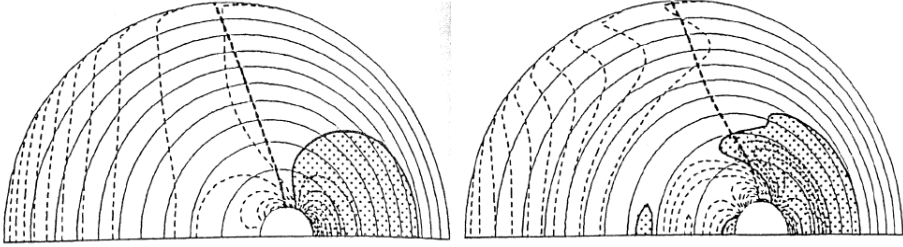


FIG. 3.11. Region of favourable and unfavourable curvature (separated by bold broken line) and of reversed local shear (shaded region) for a circular cross-section equilibrium with  $\langle \beta_{tor} \rangle = 0.025$  (left) and  $\langle \beta_{tor} \rangle = 0.048$  (right). The high  $\langle \beta_{tor} \rangle$  case enters the second stable regime on flux surfaces where the negative local shear extends into the favourable curvature region [3.15].

Numerically one can readily carry out a systematic optimization of current and pressure profiles to determine the maximum  $\beta$  compatible with all localized necessary stability conditions for arbitrary plasma cross-section shapes. For profiles everywhere in the first stable regime, this leads to a surprisingly universal expression, called the Sykes limit [3.17]

$$\langle \beta_{tor} \rangle \leq 0.035 \frac{\mu_o I_p}{B_{\phi,o} a} \quad (3.117)$$

This expression contains implicitly a strong, favourable dependence on elongation  $\kappa$  and inverse aspect ratio  $A^{-1} = a/R_o$  of the plasma cross-section, as the plasma current — at given  $q_\psi$  (required for global free boundary modes) and  $B_{\phi,o} a$  — increases with these parameters (see below). At the same time, a significant triangularity  $\delta$  is required to satisfy the Mercier criterion near the axis and to maintain the scaling implied by Eq. (3.117) at high normalized plasma currents.

*Global internal*, ideal MHD modes in tokamaks are strongly stabilized by the order  $\varepsilon^2$  terms in Eqs (3.102, 3.103). An exception to this is the  $(m, n) = (1, 1)$  *internal kink* mode, where  $\delta W_2$  can be made to vanish by the trial function shown in Fig. 3.8. Stability for this mode is therefore decided by the  $\varepsilon^4 \delta W_4$  terms. For a toroidal circular cross-section equilibrium and a model current distribution  $j_\phi \sim 1 - (r/a)^{\nu_B}$  these can be analytically computed by an expansion procedure [3.18], which has to include also the toroidal coupling to the stable  $(m, n) = (2, 1)$  mode. The straight cylinder contributions to  $\delta W_4$  vanish for the relevant  $n = 1$  mode, and toroidicity gives rise to

$$\frac{\varepsilon^4 \delta W_4}{W_o} \approx 3 \left( \frac{r_{1,1}}{a} \right)^4 (1 - q(0)) \left( \frac{13}{48} \frac{4 - \nu_B}{4 + \nu_B} - \beta_{pol}^2(r_{1,1}) \right) \xi_o^2 \quad (3.118)$$

valid for  $v_B < 4$  and  $1 - q(0) \ll 1$ . In this expression  $r_{1,1}$  is the radius of the  $q = 1$  surface, and  $\xi_o$  the magnitude of the lowest order trial function inside this surface. For  $q(0) < 1$ , Eq. (3.118) gives a limit to the pressure gradient near the axis.

As stability of the  $(m, n) = (1, 1)$  is only determined by higher order ( $\varepsilon^4$ ) terms, non-MHD effects can become decisive under realistic conditions. The lowest order ( $\varepsilon^2$ ) structure of the mode — determined by the requirement to avoid field-line bending — will remain, however, universally true, except for very low shear around  $q \approx 1$ . The stability constraint on  $q(0)$  will also vary only little between different regimes, but the manifestations of the instability (growth rate, non-linear consequences) can vary significantly. We will return to discuss the ideal *internal kink* in a general context of  $(m, n) = (1, 1)$  modes, including *resistive MHD stability*, and it will also appear in Section 3.3.3 in the context of kinetic *effects* on macroscopic electromagnetic modes.

In tokamak ordering, the lowest-order terms in  $\delta W$  are positive definite for fixed boundary modes with  $m > 1$ , and stabilize therefore any other global *internal* mode. If, however, a low shear region exists with  $q$  close to a low order rational value  $m/n$ ,  $\varepsilon^2 \delta W_2$  as given by Eqs (3.102, 3.103) will become small over a finite region, and the clear separation of  $\varepsilon^2$  and  $\varepsilon^4$  terms will lose validity. In this region the pressure gradient term in Eq. (3.89) may overcome the stabilizing effect of field line bending and a non-localized, finite- $n$  pressure-driven instability (which may not be captured by a ballooning mode analysis) can arise: the so-called *infernal* mode [3.19]. For the existence of this mode it is not even necessary that  $q(\psi)$  reaches  $m/n$ : it just has to have a minimum close to this value. Sufficiently low shear, and the violation of the  $\varepsilon$ -expansion of Eqs (3.95, 3.102, 3.103) can affect also the  $(m, n) = (1, 1)$  mode, which will change in this case its structure from the rigid displacement for  $q(r) \leq 1$  to a quasi-interchange one [3.4].

Allowing for a displacement also of the plasma boundary adds a potentially destabilizing contribution to  $\delta W_2$ , and global *external* modes — together with *ballooning* modes — usually pose the most restrictive ideal MHD stability constraints. Their analysis requires numerical codes [3.10–3.13], but extensive scans of pressure and  $q$ -profiles and plasma cross-section shapes have identified some quantitative universal relations. Usually, in the absence of close conducting walls, the  $n = 1$  mode is the most restrictive *global* mode. Maximum  $\langle \beta_{tor} \rangle$  values and optimized profiles were therefore usually searched for by examining *ballooning* and  $n = 1$  free-boundary instabilities, but were tested afterwards also against  $n = 2, 3, \dots$  modes.

As in the scans considering only *ballooning* modes, the parameter  $\mu_o I_p / B_{\phi, o} a$  turns out to be the most important one, and  $\beta_N^* = \langle \beta_{tor} \rangle B_{\phi, o} a / \mu_o I_p$  to be the quantity showing the most universal limitation. In the paper

highlighting first this limit as covering both ballooning and free boundary modes, the maximum value of  $\beta_N^*$  was found to be 0.022 [3.20]. For practical convenience, a (*not dimensionless*) definition of this so-called *Troyon* limit has been universally adopted (see Eq. (3.42))

$$\beta_N = \frac{\langle \beta_{tor} \rangle [\%] \cdot a [m] \cdot B_\phi [T]}{I_p [MA]} \leq g_{Troyon} \quad (3.119)$$

with  $g_{Troyon} = 2.8$  (according to Ref. [3.20]). This expression holds, however, only up to plasma currents corresponding to an edge safety factor  $q_a$  slightly above 2 (in [3.20], the highest  $\langle \beta_{tor} \rangle$  values were obtained for  $q_a \approx 2.2$ ). The benefit of plasma shaping arises from the relation of the normalized plasma current  $\mu_o I_p / B_{\phi,o} a$  to  $q_a$ , which follows from the solution of the Grad–Shafranov equation (for separatrix-bound plasmas,  $q_a$  is usually substituted by  $q_{95}$  — see Section 3.2.2.3). This ratio is generally expressed as a *shape-factor*:

$$S_q = \frac{q_a I_p [MA]}{a [m] B_\phi [T]} \quad (3.120)$$

which can be approximated by

$$S_q \approx 5\varepsilon \left( 1 + \kappa^2 (1 + 2\delta^2 - 1.2\delta^3) \right) \frac{1.17 - 0.65\varepsilon}{(1 - \varepsilon^2)^2} \quad (3.121)$$

From Eq. (3.119) and Eq. (3.121) follows a significant increase in the maximum attainable  $\langle \beta_{tor} \rangle$  with strong shaping and low aspect ratio:  $S_q$  according to this expression would be 1.1 for a circular, large aspect ratio device  $(\varepsilon^{-1}, \kappa, \delta) = (5, 1, 0)$ , but 7.3 for a strongly shaped DIII-D discharge with  $(2.6, 1.8, 0.7)$  [3.21]. Values of  $S_q$  up to 41 have been obtained in very low aspect ratio *spherical* tokamaks [3.22], which benefit, in addition to the explicit  $\varepsilon$ -dependence of expression Eq. (3.121), also from the improved vertical stability, which makes it possible to control higher  $\kappa$  discharges at low  $\varepsilon$  (see Section 3.2.2.5).

The achievement of  $\beta_N$  values in the range of  $\geq 3$  requires, however, optimized current and plasma pressure profiles. In particular, peaked current profiles are favourable, and both theoretical and experimental studies find good agreement with an expression [3.23], relating it to the internal inductance (see Eq. (3.43)):

$$\beta_N \leq 4\ell_i \quad (3.122)$$

as long as low  $q_a$  and high  $\ell_i$  do not lead to  $q_o \approx 1$  and a violation of the *Mercier* criterion near the axis.

The criterion Eq. (3.122) would be strongly unfavourable for plasmas with an extended region of negative shear in the core, which could benefit from *second* regime ballooning stability, but would be limited in overall  $\langle \beta_{tor} \rangle$  by global modes due to the low  $\ell_i$  associated with the hollow current profile. This picture changes, however, if credit can be taken for conducting walls sufficiently close to the plasma surface. Figure 3.12 shows, for two sets of plasma equilibria with positive (high- $\ell_i$ ; see Fig. 3.12 left) and partially negative shear (low- $\ell_i$ ; see Fig. 3.12 right) the stability limited  $\beta_N$  values for toroidal mode numbers  $1 \leq n \leq 6$ , including or not the effect of a conducting wall [3.24]. The presence of the wall has generally a strong stabilizing effect on the  $n=1$  mode, but a progressively weaker one for higher- $n$  modes. The beneficial effect on the low- $n$  modes is, however, much more significant for the low- $\ell_i$  plasmas, as the plasma currents flow more in the periphery and are more closely coupled to the conducting shell. At the same time, the higher- $n$  modes, for which the wall has no significant effect, are less important in the negative-shear case, whereas they limit severely the benefit from the conducting wall for a positive shear plasma.

Positive shear plasmas can therefore attain  $\beta_N$  values in the range  $\approx 3.5$  even without conducting walls and the potential benefits of the latter are limited also by the appearance of higher  $n$ -modes. Negative shear plasmas, on the other hand, have a lower stability limit in the absence of conducting walls, but can achieve even higher  $\beta_N$  values than positive shear ones in their presence.

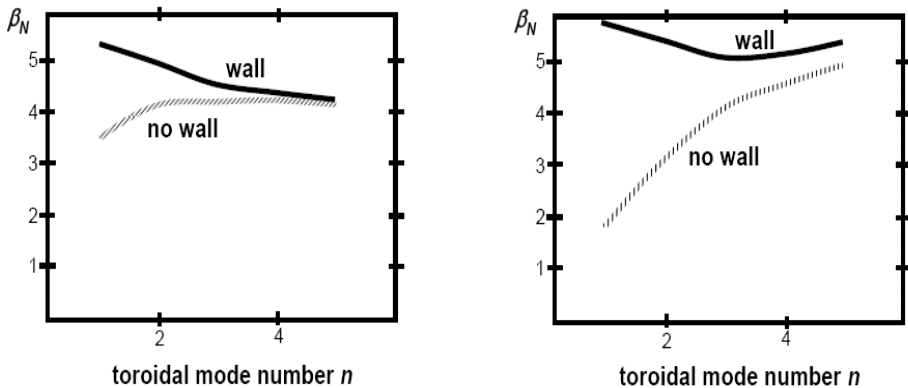


FIG. 3.12. Effect of conducting walls on the ideal MHD stability limit for different  $n$  modes at high- $\ell_i$  (left) and low- $\ell_i$  (right) [3.24].

### 3.3.1.2. Effects of dissipation on linear stability of global modes

In the preceding section we have seen that the variational formulation of the linearized plasma response gives criteria for the stability against infinitely

small perturbations, or even growth rates. For large scale modes the boundary conditions imposed on the perturbations are important, and the straightforward application of the ideal MHD energy principle requires them to conserve magnetic flux and particles: a corollary of this is the vanishing of the Poynting flux through the assumed boundary of the system (which can, of course, also lie at infinity). The growth rate of a mode is determined by the conversion of magnetic energy and plasma enthalpy into kinetic energy, as an eigenvalue.

Non-ideal MHD effects can give more stringent limits, allowing for an unstable growth of perturbations even in *ideally stable* plasmas. The conceptually simplest non-ideal effect is finite electrical resistivity, either in the plasma, or in wall structures. For global modes, non-ideal effects usually concern only a limited space region, and perturbations grow on a timescale  $\gg \pi R_o / v_A$ . Inertia then plays no role in the *ideal plasma region*, which passes adiabatically through a sequence of equilibrium states. The boundary conditions at the interface to the non-ideal zone, however, have now to allow for a finite energy flux into the latter, and the growth rate of the mode is determined mainly by equating the energy set free by the plasma displacements in the ideal plasma region to the dissipation and/or plasma acceleration in the non-ideal one. Ideal MHD, and the tools developed for treating, it remain at least partly useful also in this case, although they have to be interfaced to a more complete plasma model or to equations for magnetic field diffusion or circuit equations in the resistive regions.

### 3.3.1.2.1. Resistive wall modes

In the simplest case, resistive effects do not regard the plasma, but the conducting walls, which were so far assumed to be infinitely conducting. Modes becoming unstable in this case are termed *resistive wall modes*. The classical example (although the name is typically not used for them) are the *axisymmetric* modes described in Section 3.2.2.2.5. The simple rigid-conductor model introduced there is also instructive to show the transition from resistivity- to inertia-limited mode growth.

We consider now  $\Re_c$  finite and introduce, in addition to  $s^*$  and  $c_L$ , a normalized rate of field penetration through the walls as  $\gamma_W^* = (\Re_c / L_{cc})(1 / \sqrt{c_L})(R_o M_p / (\mu_o I_p^2))^{1/2}$  keeping the same normalization also for the growth rate  $\gamma^* = \gamma(1 / \sqrt{c_L})(R_o M_p / (\mu_o I_p^2))^{1/2}$ . The dispersion relation for the full system of Eqs (3.45, 3.46) now becomes a cubic

$$\gamma^{*2} + \frac{\gamma^*}{\gamma^* + \gamma_W^*} - \frac{s^*}{c_L} = 0 \quad (3.123)$$

with an unstable branch, if  $s^* > 0$  (rather than if  $s^* > c_L$  as in the ideal conducting wall case). Figure 3.13 shows  $\text{Re}(\gamma^*)$  of the most unstable root, as a function of  $s^*/c_L$ , for different  $\gamma_W^*$ , illustrating that, for any finite  $\gamma_W^*$ , passive elements

cannot suppress the displacement instability: they can, however, reduce the growth rate from an inertia-limited to a wall-resistance timescale. In the ideal case, the drive ( $\sim s^*$ ) — the curvature of the external field — is counteracted by the forces resulting from the induced currents  $\sim c_L$ , and in the ideal case both forces depend only on the displacement. In the resistive case, however, for a given displacement the induced currents will decay with time, and the instability can always grow, being affected by the induced currents only in the magnitude of the growth rate. The conclusion — if a plasma is unstable in the absence of walls, resistive walls can only reduce the growth rate of the instability but not suppress it completely — can be shown to hold quite general for ideal MHD modes — *in the absence of rotation of the plasma or of the walls* [3.25].

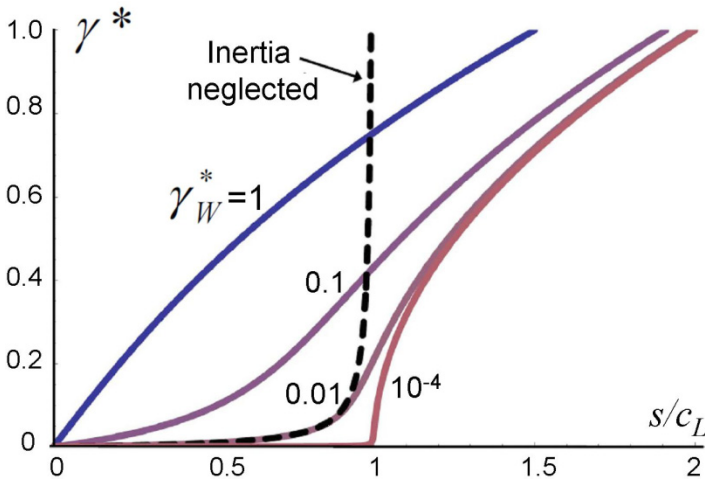


FIG. 3.13. Toy problem illustrating the transition from resistivity to inertia limited unstable behaviour: a current carrying wire in a curved magnetic field between resistive passive conductors. Growth rate  $\gamma^*$  as a function of normalized destabilizing ( $s$ ) and stabilizing ( $c_L$ ) forces and resistivity ( $\gamma_w^*$ ) of the passive conductors.

The transition from resistive to inertia limited growth in the vicinity of  $s^*/c_L = 1$  is rather abrupt in the case of  $\gamma_w^* \ll 1$ . For  $\gamma_w^* \ll (1 - s^*/c_L)/\sqrt{s^*/c_L}$ , the unstable root of Eq. (3.123) is approximately given by

$$\gamma^*/\gamma_w^* \approx \frac{s^*/c_L}{1 - s^*/c_L} \quad (3.124)$$

and could be also obtained neglecting the inertia of the wire (or plasma). Prototypically for all resistive wall modes, the unstable motion in the latter case passes through a sequence of equilibria, determined by the changing currents in the passive conductors.

The great practical relevance of resistive wall modes is that they proceed on a timescale amenable to active feedback stabilization. For their theoretical analysis (away from the ideal-wall stability limit) we can neglect inertia, and proceed (in analogy to the *Newcomb* analysis in Section 2.3.1.3) in the general case to a solution of the marginal stability problem (corresponding to  $\lambda = 0$ ) in the plasma:

$$\delta W_F + \delta W_V = 0 \quad (3.125)$$

with  $\delta W_F, \delta W_V$  given by Eq. (3.76) and Eq. (3.72), but with boundary conditions allowing for a finite energy flux into the resistive walls. Equating the latter to the ohmic dissipation in them determines then the actual growth rate for the mode [3.26]. Codes based on this principle can treat quite realistic walls, even including non-axisymmetric structures (leading to a coupling of different toroidal modes  $n$ ) and feedback circuits. They show that — in particular for low or reversed shear configurations — substantial benefits in achievable  $\beta$  could be derived from a combination of sufficiently close passive elements and a feedback system. The role of the instability driving parameter is taken by  $\beta_N$ , and the results of scans of plasma pressure and vessel resistivity can generally be well fitted to an expression like Eq. (3.124), if the substitutions are made:  $s^* \rightarrow \beta_N - \beta_N^{no\ wall}$  and  $c_L \rightarrow \beta_N^{wall} - \beta_N^{no\ wall}$ , with  $\beta_N^{wall}, \beta_N^{no\ wall}$  the  $\beta_N$  limits with and without ideally conducting walls.

For complete stabilization of resistive wall modes in non-rotating plasmas, an active feedback system is therefore always required. For axisymmetric modes this is now a common engineering procedure in tokamaks. Regarding more general ( $n \neq 0$ ) modes, the most conclusive results have been obtained in reverse field pinches, where several unstable modes can co-exist, but have a simpler geometrical structure of the eigenmodes. In present tokamak experiments, non-axisymmetric resistive wall modes are closely linked to the question of plasma rotation, which requires a more sophisticated plasma model, and will be further addressed in this section below.

### 3.3.1.2.2. Tearing modes

Also in tearing modes, resistivity effects are important only in a restricted region, albeit in this case inside the plasma. Resistivity adds a term to Eq. (3.4),

$$\vec{E} + \vec{v} \times \vec{B} = \eta \vec{j} \quad (3.126)$$

describing the ohmic resistance and removing the frozen-in constraint on magnetic fields and plasma motion. We will use in the following the “straight” tokamak model and the ordering of Section 3.3.1.1, with  $\vec{B}_o(r) = B_{\theta,o}(r)\vec{e}_\theta + B_{z,o}(r)\vec{e}_z$ . This implies that variations in equilibrium quantities and perturbations will satisfy

$\delta p \sim \varepsilon^2 B_z^2 / (2\mu_o) \sim \delta B_z^2 / (2\mu_o)$ . We will therefore assume  $B_z$  to be constant, and perturbations to be incompressible and with a much shorter characteristic length in the  $r, \theta$  plane than in the  $z$ -direction ( $k_z = n/R_o \approx (\varepsilon/q)m/r$ ; already used in Section 2.3.1.4). As inertia will turn out to play a part only in a thin layer (over which we can neglect variations of density) we can also take  $\rho$  as constant.

For the flow velocity and the magnetic field in the  $r, \theta$  plane we make an ansatz in terms of stream-functions  $\Phi, \psi$ :  $\vec{v}_\perp = (1/B_z) \cdot \vec{e}_z \times \nabla \Phi$ ,  $\vec{B} = B_z \vec{e}_z + \vec{e}_z \times \nabla \psi$ . Inserting for  $\vec{B}$  in Eq. (3.5) and Eq. (3.6) shows that this corresponds to  $\vec{E} = -\nabla \Phi + (\partial \psi / \partial t) \vec{e}_z$ , with the electrostatic description of the  $E$ -field in the  $r, \theta$ -plane reflecting the constancy of  $B_z$ . From the  $z$ -component of Ohm's Law Eq. (3.126) and the above ansatz we get

$$\frac{\partial \psi}{\partial t} - \vec{B} / B_z \cdot \nabla \Phi = \frac{\eta}{\mu_o} \nabla^2 \psi \quad (3.127)$$

Taking the curl of Eq. (3.2) eliminates the pressure term, and taking again the  $z$ -component gives

$$\frac{\partial \omega}{\partial t} + \vec{v}_\perp \cdot \nabla_\perp \omega_\perp - (\vec{B} / \rho) \cdot \nabla (\vec{j} \cdot \vec{e}_z) = 0 \quad (3.128)$$

with  $\omega = \vec{e}_z \cdot \nabla \times \vec{v}_\perp = \nabla_\perp^2 \Phi / B_z$ .

Together, Eqs (3.127, 3.128) form a *two-field* model of resistive MHD, in terms of  $\psi, \phi$ . Dimensionless units based on the toroidal field  $B_z$ , the Alfvén speed  $v_A = B_z / \sqrt{\mu_o \rho}$ , the minor plasma radius  $a$ , and the resistivity  $\eta$  introduce the *Lundquist* number  $S = \mu_o a v_A / \eta$  into Eq. (3.127) as a characteristic dimensionless quantity, which is very large (for an ITER-range plasma, with  $T_e = 10$  keV,  $Z_{\text{eff}} = 2$ ,  $a = 2$  m,  $B_{z,o} = 5.2$  T,  $n_e = 10^{20} \text{ m}^{-3}$ ,  $S \approx 10^{10}$ ). Considering linearized perturbations  $\sim \exp(\gamma t + i(m\theta - nz/R_o))$ , ohmic resistance can compete with convection only around resonant surfaces (where  $\vec{B}_\perp / B_z \cdot \nabla_\perp \sim (mB_{\theta,o}/r - nB_z/R_o) \rightarrow 0$ ) in a thin layer, over which we can neglect curvature and treat the plasma as a slab.

Outside this layer, resistivity plays no part, and — as long as we remain distant from ideal MHD limits — plasma motion will be on a timescale much slower than  $a / v_A$ , so that we can also neglect inertia. Equation (3.128) in this region reduces to the equilibrium constraint:  $\vec{B} \cdot \nabla (\vec{j} \cdot \vec{e}_z) = 0$ , or

$$\frac{1}{\hat{r}} \frac{d}{d\hat{r}} \hat{r} \frac{d}{d\hat{r}} \hat{\psi} - \frac{m^2}{r^2} \hat{\psi} - \frac{R_o}{a} \frac{d\hat{j}/d\hat{r}}{(1/q - n/m)} \hat{\psi} = 0 \quad (3.129)$$

in our dimensionless units  $\hat{r} = r/a$ ,  $\hat{\psi} = \psi / (aB_z)$ ,  $\hat{j} = j_z / (B_{z,o} / (\mu_o a))$ . Equation (3.127), in this ideal region, serves only to compute the plasma flow

field, once the solution to the perturbed flux function is determined. In fact, setting

$$\xi_r = -\frac{R_o}{a} \frac{\hat{\psi}}{\hat{r}(1/q - n/m)} \quad (3.130)$$

shows Eq. (3.129) to be equivalent (under the above tokamak ordering assumptions) to the Euler–Lagrange equation (3.99) used for *Newcomb's* criterion. Evidently, however, the formulation in  $\hat{\psi}$  is better suited to deal with the singularity at  $q(r_{m,n}) = m/n$ . (In the following we will drop the circumflex mark from dimensionless units.) As in the discussion of *Newcomb's* criterion, Eq. (3.129) will, in general, not have a non-trivial continuous solution which satisfies the physical boundary conditions: regularity at the axis and homogeneous boundary conditions (either  $\psi = 0$  or the condition following from Eq. (3.94) in the case of a surrounding vacuum at  $r = 1$ ). For tearing modes, however, we are now interested in modes with a resonant surface in the plasma and we seek separate solutions  $\psi_1$  for  $0 \leq r \leq r_{m,n}$  and  $\psi_2$  for  $r_{m,n} \leq r \leq 1$  satisfying, respectively, boundary conditions at  $r = 0$  and  $r = 1$ , and continuity of  $\psi$  across the resonant layer. At  $r = r_{m,n}$  they will in general have, however, a discontinuity in the derivative

$$\psi_2'(r_{m,n}) - \psi_1'(r_{m,n}) = \Delta' \cdot \psi(r_{m,n}) \quad (3.131)$$

corresponding to a surface current of density  $\Delta' \cdot \psi(r_{m,n})$  and to a discontinuity in the Poynting energy flux across the surface given by  $\gamma \cdot \Delta' \cdot |\psi(r_{m,n})|^2$ . The latter, if positive, corresponds to power available for driving dissipation and acceleration of flow in the singular layer. Negative  $\Delta'$ , on the other hand, requires a net input of magnetic energy from this region into the rest of the plasma. From the point of linear, purely resistive MHD this latter case is unphysical and implies stability, but we will see in Section 3.3.1.3 that it can acquire practical relevance in the context of a modified Ohm's Law and non-linear perturbations.

Within a region  $r_{m,n} \pm \delta_t$  (with  $\delta_t$  being the tearing layer width) we have to solve the linearized versions of Eqs (3.127, 3.128). Using the slab approximation, with  $x = r - r_{m,n}$  and linearizing  $q \approx (m/n) \left(1 + (s/r_{m,n})x\right)$ , they become (for the time dependence written as  $\sim \exp(\gamma t)$  and using a prime for  $d/dx$ )

$$\gamma \psi = i \frac{n s / r_{m,n}}{(R_o/a)} x \Phi + \psi'' / S \quad (3.132)$$

$$\gamma \Phi'' = i \frac{n s / r_{m,n}}{(R_o/a)} x \psi'' \quad (3.133)$$

which involves only real coefficients, if we introduce  $\Phi_i = -i\Phi$ , and allow for  $\psi(x)$  to have even and  $\Phi_i(x)$  odd parity. Using this as boundary conditions at

$x = 0$ , and seeking for solutions on a stretched scale  $x/\delta_t$  which asymptotically match to the frozen-in condition  $\gamma\psi = \left\{ (n s/r_{m,n}) / (R_o/a) \right\} x\Phi_i$  for  $|x/\delta| \rightarrow \infty$ , one obtains from this inner solution a relation between  $\gamma$  and  $\Delta'$  (see Ref. [3.4]):

$$\gamma \approx 0.55 (\Delta')^{4/5} \left( \frac{n s/r_{m,n}}{(R_o/a)} \right)^{2/5} / S^{3/5} \quad (3.134)$$

The general scaling of this expression can also be derived from a qualitative balance of the terms, using  $\psi'' \approx (\Delta' \cdot \psi) / \delta_t$  and the following estimates of the leading terms,

$$\text{at } x = 0 : \gamma\psi \approx (\Delta' \cdot \psi) / (\delta_t \cdot S) \quad (3.135)$$

and

$$\text{at } x \approx \delta_t : \gamma\psi \approx \frac{n s/r_{m,n}}{(R_o/a)} \Phi \delta_t \text{ and } \gamma\Phi / \delta_t^2 \approx \frac{n s/r_{m,n}}{(R_o/a)} (\Delta' \cdot \psi) \quad (3.136)$$

relating the quantities  $\psi/\Phi(\delta)$ ,  $\gamma$ ,  $\delta_t$  to the equilibrium properties and  $\Delta'$ . In particular, they also can be used for estimating the tearing layer width, as

$$\delta_t \approx (\Delta')^{1/5} / \left( \frac{n s/r_{m,n}}{(R_o/a)} S \right)^{2/5} \quad (3.137)$$

For the above reference ITER parameters these estimates predict characteristic growth times and layer widths in the range of  $\approx 100$  ms and  $\approx 0.1$  mm, respectively.

The determination of the tearing mode parameter  $\Delta'$  requires the solution of Eq. (3.129) in the regions  $0 \leq r \leq r_{m,n}$  and  $r_{m,n} \leq r \leq 1$ , respectively, where we can apply the boundary condition  $\psi_2(r) = 0$  either at the plasma boundary  $r = 1$  (*fixed boundary*), at a wall positioned at  $r = b/a$ , or at  $\infty$  (*the free boundary case*). The result depends on the current profile and on  $q$  at some reference point, and can, in general, be obtained only numerically. For the class of current profiles Eq. (3.22) the unstable regions are shown in Fig. 3.9 together with those for the external kink- and the internal (1,1)-mode already discussed in Section 3.3.1.1.4. Including the tearing modes removes the discontinuous behaviour when a resonant surface — as result of a decrease in the total current — passes from the vacuum into the plasma: resistive reconnection now may allow displacements lowering the magnetic energy also when the resonant surface is in the plasma.

Tearing stability depends on the current density gradient, in particular close to the resonant surface, with steep gradients in the region  $r \leq r_{m,n}$  destabilizing. For higher  $m$ -numbers the term  $-(m/r)^2 \psi$  (associated with the stabilizing influence of field-line bending) strongly localizes the perturbation around the resonant surface, and allows the formulation of a local stability criterion in terms

of the current density  $j$ , its derivative  $j'$  and its average value  $\langle j \rangle$  inside  $r_{m,n}$ . High- $m$  tearing modes are unstable according to it (see Ref. [3.9]) only if, at  $r_{m,n}$ ,  $|rj'/j| > m(\langle j \rangle / j - 1)$  holds, which is difficult to satisfy for  $m > 3$ .

Toroidicity modifies tearing mode stability in two ways. Pressure gradient effects, neglected in the reduced MHD equations used above, become important in the vicinity of the rational surface, and need — as they are linked to the average curvature of the field-lines — a toroidal description. These effects modify the inner-layer solution and can result in stability below a finite positive value of  $\Delta'$  [3.27]. Toroidicity, however, also modifies the outer solution and  $\Delta'$ , as it couples poloidal mode numbers, and several resonant surfaces have to be considered for a given toroidal mode number  $n$ . Nevertheless, the basic paradigm of tearing mode analysis — the possibility to solve the outer (ideal, marginal MHD) and the inner layer problem separately — remains valid, although now a set of independent solutions ( $M + N$ , with  $M$  the number of modes and  $N$  the number of rational surfaces considered) of the ideal problem is required and the matching to the inner solutions involves a non-linear eigenvalue problem of the form  $(E - \text{diagonal}(\{\Delta_m(\gamma)\})) = 0$ , with the  $E$ -matrix containing the results of the outer solutions and  $\Delta_m(\gamma)$  the relation between the discontinuity in the logarithmic derivative of the resonant component  $m$  at the respective rational surface and the growth rate [3.28].

### 3.3.1.2.3. Resistive $m = 1$ modes

The wire model and Fig. 3.13 illustrate that resistive instabilities change their growth rate scaling significantly when approaching the limit to ideal instability  $s^*/c_L = 1$ . In contrast to  $m > 1$  modes, the internal  $m = 1$  can become ideally unstable, and we expect therefore at least in some parameter range a qualitative difference to the tearing mode behaviour described above. For the ideal (1,1)-mode the positive definite order  $\varepsilon^2$  terms are minimized by choosing a lowest-order displacement  $\xi_r$ , as in Fig. 3.8, and pressure gradient and toroidal terms decide upon stability to order  $\varepsilon^4$ . Resistive stability depends on the minimized potential energy  $\delta W_{\min}$  of this ideal mode (given, for a model current distribution, by Eq. (118)) and the Lundquist number  $S$ , where the former is usually quantified in terms of the parameter  $\lambda_H = -\pi \delta W_{\min} / (\xi_{o,r} B_{\theta,o} q')^2_{r_{1,1}}$ . In the ideal MHD-limit (for  $\lambda_H \gg S^{-1/3}$ ), the mode grows at the rate

$$\gamma_{id} = \lambda_H (v_{A,\theta} / r_{1,1}) \quad (3.138)$$

where the Alfvén velocity  $v_{A,\theta} \sqrt{2}$  is based on the poloidal field strength  $B_{\theta,0}(r_{1,1})$ . The Heaviside-function shape of  $\xi_r$  is smoothed by the higher order corrections

$$\xi_r = \frac{1}{2} \xi_o \left( 1 - (2/\pi) \arctan \left( (r - r_{1,1}) / (\lambda_H r_{1,1}) \right) \right) \quad (3.139)$$

As the internal solution is based on a slab approximation, it should not depend sensitively on geometry, which will enter into the growth rate through  $\delta W_{\min}$ , respectively  $\lambda_H$ . A dispersion relation, covering both ideally and only resistive unstable cases has been derived by the authors of Ref. [3.29]:

$$\hat{\gamma} = \hat{\lambda}_H \left( \frac{\hat{\gamma}^{9/4} \Gamma((\hat{\gamma}^{3/2} - 1)/4)}{8 \Gamma((\hat{\gamma}^{3/2} + 5)/4)} \right) \quad (3.140)$$

in which the explicit dependence on the Lundquist number is eliminated through the normalizations  $\hat{\gamma} = S^{1/3} \gamma / (v_{A,\theta} / r_{1,1})$ , and  $\hat{\lambda}_H = \lambda_H S^{1/3}$ . The validity of this expression is primarily limited by two-fluid and kinetic effects, which can become easily important due to the steep gradients of the lowest-order solution.

This dispersion relation is shown in Fig. 3.14, and shows a strong qualitative similarity to that of the wire model for the resistive wall mode, with  $\lambda_H$  taking the role of  $s^*/c_L - 1$ . For large  $\hat{\lambda}_H$  it reduces to the ideal growth rate (Eq. (3.129)), but for lower values of  $\hat{\lambda}_H$  resistivity becomes important, changing the mode into a *resistive kink* mode, with a growth rate

$$\hat{\gamma}_{rk} \approx 1 + (2/3\sqrt{\pi}) \hat{\lambda}_H \quad (3.141)$$

valid for  $0 < \hat{\lambda}_H < 1$ . In the ideal-MHD marginally stable case this becomes

$$\gamma_{rk} = (v_{A,\theta} / r_{1,1}) / S^{1/3} \quad (3.142)$$

and the unstable radial displacement takes the form  $\xi_r = 0.5 \xi_o \left( 1 - \operatorname{erf} \left( (r - r_{1,1}) / (\sqrt{2} \delta \cdot r_{1,1}) \right) \right)$ , with a characteristic scale  $\delta \sim S^{-1/3}$ . As in the resistive wall mode case, the instability persists also into the ideally stable region of negative  $\lambda_H$ , and assumes there the characteristic of a *tearing mode*. In this regime  $\lambda_H$  is related to the tearing-mode parameter  $\Delta' = -\pi/\lambda_H$ , the growth rate  $\gamma_{tear}$  is given by Eq. (3.134), and the characteristic layer width  $\delta$  scales as  $\sim (\Delta')^{1/5} / S^{2/5}$ .

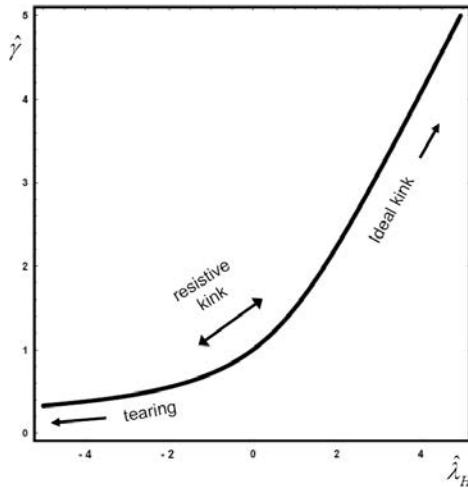


FIG. 3.14. Normalized growth rate  $\hat{\gamma}$  of  $m = 1$  instability in different regimes characterized by the ideal kink drive  $\hat{\lambda}_H$ .

Figure 3.15 shows the structure of the unstable perturbation for the three forms of (1,1) instability: *ideal kink*, *resistive kink* and *tearing mode* in the proximity of  $r_{1,1}$  in the form of the radial profiles of the displacement and the perturbation flux function and of a 2-D plot in  $(r, r \cdot \theta)$  projection of the total helical flux  $\psi + \int_{r_{1,1}}^r (B_\theta(r) - (r/R_o)B_z) dr$ .

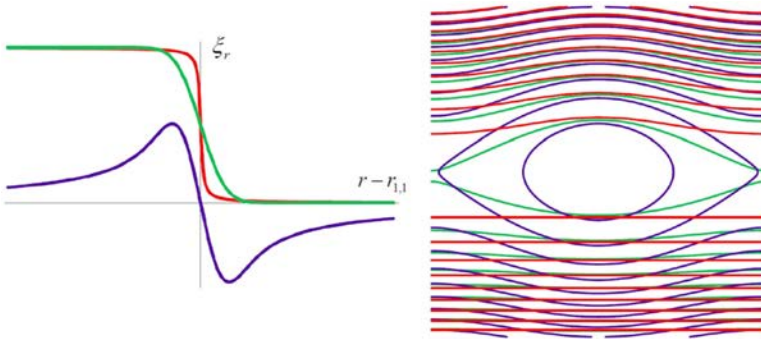


FIG. 3.15. Structure of unstable  $m = 1$  mode near the resonant layer in the ideal kink (red), resistive kink (green) and tearing mode (blue) regime. Radial displacement (left); helical flux surfaces (right).

### 3.3.1.2.4. Resistive wall modes in rotating plasmas

For modes with  $n \neq 0$  plasma rotation can modify drastically the influence of resistive walls. Quantitatively their effect depends strongly on the plasma

model used, as the latter determines the coupling of the rotating mode to the plasma motion. A one-fluid model used here [3.30] involving viscosity for the latter purpose, captures, however, paradigmatically much of the essential physics. It is based on a *straight tokamak* model (Section 3.3.1.1) of a plasma column of radius  $a$ , surrounded by a resistive wall at  $r = r_w$ . Both the regions  $a \leq r \leq r_w$  and  $r_w \leq r < \infty$  are treated as vacuum and the mode  $(m, n)$  considered has a resonant surface just beyond the plasma boundary. As the modes considered grow slowly compared to Alfvénic times, rapid plasma motion will be confined to a thin layer close to the resonant surface, just adjacent to the boundary. One can hence neglect inertia and viscosity effects in the bulk of the plasma and describe its dynamic by the *marginal ideal MHD equation* used in the Newcomb and the tearing mode analyses (Eq. (3.129)). Solved as an initial value problem starting at the axis, the solution obtained will (in general) have finite values  $\psi$ , and  $\psi'$  at  $r = a$ . The quantity  $-\Delta = -\psi'/\psi$  corresponds to the normalized energy flux across the plasma–vacuum boundary (the time-integrated Poynting vector is given by  $\int \wp dt = -\Delta \cdot \psi^2 / 2$ ; we choose here the sign of  $\Delta$  to remain consistent with the usage of  $\Delta'$  in the tearing-mode theory). If we match it continuously to a vacuum solution to Maxwell's equations:  $\psi_v = c_1 r^m + c_2 r^{-m}$ , the latter will give, for negative  $\Delta$ ,  $\psi_v(r_c) = 0$  at a radius

$$r_c = a \left( \frac{a \cdot \Delta - m}{a \cdot \Delta + m} \right)^{1/(2m)} \quad (3.143)$$

For a wall indeed placed at  $r_w = r_c$ , we would thus have found the marginally stable solution. This wall position approaches  $r_c \rightarrow a$  for increasing energy made available by the marginal ideal MHD perturbation. Conversely, for  $-\Delta < m/a$  even the vacuum energy for an infinitely distant wall exceeds this available energy and the plasma is *no-wall stable*. To measure the effect of an actually existing wall it is convenient to define a  $(-\Delta_{wo})$  given by the normalized free plasma energy that could be just stabilized by it, if it were ideally conducting, as

$$\Delta_{wo} = -\frac{m (r_w/a)^{2m} + 1}{a (r_w/a)^{2m} - 1} \quad (3.144)$$

(corresponding to  $\frac{r_w}{a} = \left( \frac{a \cdot \Delta_{wo} - m}{a \cdot \Delta_{wo} + m} \right)^{1/(2m)}$ ), and introduce the ratio

$$\kappa = \frac{\Delta + m/a}{\Delta_{wo} + m/a} \quad (3.145)$$

With these definitions,  $\kappa < 0$  for no-wall stable (ideal and *non-rotating*) plasmas,  $0 \leq \kappa \leq 1$  corresponds to plasmas that would be stabilized by an ideal wall at the position  $r_w$ , and  $\kappa > 1$  corresponds to instability even if the wall were indeed ideal.

Surplus free energy  $-(\Delta + m/a)(\psi(a))^2/2$  not required to build up the no-wall vacuum energy is available to drive acceleration and viscous and resistive dissipation in the two thin layers considered: in the plasma, near  $r = a$ , and in the resistive wall. This energy balance is ensured by asymptotically matching the inner solutions in these two layers to the global ones in the ideal plasma and the vacuum regions. It yields a dispersion relation [3.31] in normalized quantities:

$$\left( (\hat{\gamma} - i\hat{\Omega}_\phi)^2 + \hat{\nu}(\hat{\gamma} - i\hat{\Omega}_\phi) + (1 - \kappa)(1 + m/(a\Delta_{wo})) \right) (\hat{\gamma}/\hat{\gamma}_w + 1 - m/(a\Delta_{wo})) = 1 - (m/(a\Delta_{wo}))^2 \quad (3.146)$$

for growth rate  $\hat{\gamma}$  in terms of the parameters  $\Delta_{wo}$  and  $\kappa$ , the angular plasma rotation velocity  $\hat{\Omega}_\phi$  and the viscosity  $\hat{\nu}$  in the edge layer, and the resistive wall penetration rate  $\hat{\gamma}_w$ .

Figure 3.16 shows the unstable region predicted by Eq. (3.146), in the plane of  $\kappa$  drive and the angular plasma velocity  $\hat{\Omega}_\phi$  at the edge. In the absence of rotation, the stability limit of the resistive wall mode coincides with the no-wall limit  $\kappa = 0$ . As in the cases considered before (e.g. Eq. (3.123)), the growth rate changes, however, from a wall-resistivity dominated to an ideal MHD one, when we approach the ideal wall limit ( $\kappa = 1$ ).

For finite rotation velocity, a minimum in growth rate appears at finite surplus drive energy  $-(\Delta + m/a)(\psi(a))^2/2$ , which gives rise to a *second stable regime* for  $\hat{\Omega} > 2\sqrt{(1 + m/(a\Delta_{wo}))}/(S^* \nu^*)$ . Two conditions have to be met, at a given  $\kappa$  in the interval  $(0, 1)$ , for stability: the plasma has to have a sufficient grip on the mode to force it to (nearly) co-rotate, and the mode rotation with respect to the wall has to be fast enough to prevent penetration of the perturbation fields, making them act again like a perfect conductor. At  $\kappa$  approaching 1 (i.e. at given  $\Delta$ , for a distant wall) the stabilizing effect of the wall is weak, and even so the unstable mode rotates nearly with the plasma velocity; its penetration is sufficient to allow growth. For a very close wall ( $\kappa \rightarrow 0$ ), the mode-wall coupling is strong and overcomes that to the plasma: the mode moves slowly in the wall frame, can penetrate it, and hence grows.

The unstable branch at lower  $\kappa$  feeds partly also on the rotation energy of the plasma. In fact, as seen in Fig. 3.16, raising the rotation frequency extends the unstable region also to negative values of  $\kappa$ . The marginal stability curve on the low  $\kappa$  side corresponds to error field amplification, when an externally applied perturbation with wavenumber  $(m, n)$  gets amplified by the rotating plasma by a factor limited by dissipation in the plasma.

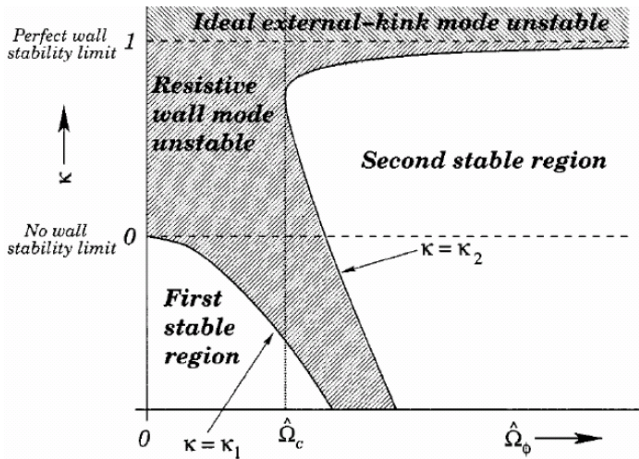


FIG. 3.16. Resistive wall mode stability for a rotating plasma, according to the model of Ref. [3.31]. Reprinted from Ref. [3.31]. Copyright (2010), American Institute of Physics.

As expected from the above, the stability of resistive wall modes in rotating plasmas depends strongly on the plasma model, and the resulting coupling of wave propagation to plasma motion. Several candidate mechanisms have been advanced — neoclassically enhanced viscosity or kinetic damping of the waves, toroidal coupling of external modes to resistively reconnecting modes in the plasma — and this is a field of very active, ongoing research. Some features of these models are, however, common and robust — like the prediction of error field amplification for plasmas in the proximity of the no-wall stability threshold — and are experimentally confirmed. As the non-linear consequence of error field amplification is the breaking of plasma rotation and hence a loss of the stabilizing influence of the walls, this has resulted in significant efforts to reduce the low- $n$  components of static externally applied magnetic fields.

### 3.3.1.3. Finite amplitude perturbations

Experimentally, macroscopic instabilities in tokamaks — described in Sections 3.4 and 3.5 — show three classes of behaviour. The *sawtooth* is typical for a limit-cycle behaviour, where the profile of current density and pressure profiles steepen, till an unstable (1,1)-mode arises which ultimately leads to their flattening. A similar behaviour is shown by *ELMs*, the edge-localized modes limiting the pressure gradient and/or the bootstrap driven currents in the separatrix vicinity of *H-mode* discharges.

In some cases — notably the *neoclassical tearing modes* described below — the instability saturates at a finite amplitude, resulting in a stable, helical

equilibrium state. As plasmas generally rotate, these modes are seen as periodic oscillations with constant amplitude.

Instabilities that do not saturate result in a disruption of the plasma discharge. Disruptions, described in detail in Section 3.5, are not a well defined instability and can have a variety of causes resulting in a variety of initial dynamic behaviour. At a given instance, however, they universally involve a large scale reconnection of magnetic flux and a rearrangement of the current distribution. If the region concerned by the reconnection process extends up (or sufficiently close) to the walls, this results in a strong cooling and impurity contamination of the plasma, making it impossible to recover a stationary discharge.

In general the non-linear development of macroscopic instabilities is a complex and multi-faceted problem, and the subject of major code developments and intensive experimental investigations. Some observable non-linear effects can, however, be understood in terms of simple, analytical models.

### 3.3.1.3.1. Tearing modes at finite amplitude

The tearing mode is a particular and highly relevant case of non-linear unstable behaviour [3.32]. On the one hand, non-linear effects start to dominate early, invalidating the growth rate expression Eq. (3.134), while on the other hand additional driving terms can appear at finite island size. The latter give rise to the *neoclassical tearing mode* (NTM), an important  $\beta$ -limiting instability.

Quasilinear coupling of the resonant  $(m, n)$ -perturbations gives rise to a modification of the axisymmetric fields  $\delta\psi_o$  and associated currents. Taking the perturbations as  $\tilde{\psi} = \psi_1(x, t) \cos(ky)$ ,  $\Phi = \Phi_1(x, t) \sin(ky)$  and averaging the reduced resistive MHD Eqs (3.132, 3.133) in the slab approximation over  $y$ , we get

$$\frac{\partial(\delta\psi_o)}{\partial t} - \eta(\delta j_o) = \frac{k\psi_1}{2} \frac{\partial}{\partial x} \Phi_1 \quad (3.147)$$

$$\rho \frac{\partial}{\partial t} \frac{\partial^2}{\partial x^2} \Phi_1 - k\psi_1 \frac{\partial}{\partial x} (\delta j_o) = kj'_o \psi_1 - xkB'_{\theta, o} j_1 \quad (3.148)$$

As the skin depth, based on the linear tearing growth rate  $\gamma$  is larger than the tearing layer width  $\delta_t$ , the current density  $\delta j_o$  over most of this layer will be determined by balance of advection and ohmic dissipation, and the first term in Eq. (3.147) can be neglected. Inserting for  $\delta j_o$  into Eq. (3.148) shows that among the terms proportional to  $(\partial^2 \Phi_1 / (\partial x^2))$ , the one expressing inertia can be neglected, if  $|\rho \partial / \partial t| \ll k^2 \psi_1^2 / (2\eta)$ . This is the case when the diameter of the magnetic island at the resonant surface

$$w = 4 \sqrt{\frac{r\psi_1}{sB_{\theta,o}}} = 4 \sqrt{\frac{\psi_1}{\psi''_o}} \quad (3.149)$$

exceeds the tearing layer width  $\delta_t$ . After this stage, the tearing mode, even in the reconnection zone, passes through a sequence of helical equilibrium states, satisfying  $B \cdot \nabla j = 0$ , so that  $j$  must be a function of the total (unperturbed + perturbed) flux  $\psi$ . An equation for the variation in time of  $j(\psi)$  is then obtained by averaging Eq. (3.127) over a *perturbed* flux surface, to give

$$\left\langle \frac{\partial \psi}{\partial t} \right\rangle_{\psi} = \eta j(\psi) - E_{z,o} \quad (3.150)$$

with the average defined by  $\langle f \rangle_{\psi} = \oint f(d\ell / |\nabla \psi|) / \oint (d\ell / |\nabla \psi|)$  and  $E_{z,o}$  the externally applied toroidal electric field. To asymptotically match the solution of Eq. (3.150) for the *inner* to the *external* (ideal MHD) region, we multiply by  $\cos(ky)$  and integrate Eq. (3.150) across the tearing mode layer, to give

$$\frac{4}{\pi} A \sqrt{\frac{\psi_1}{2\psi''_o}} \dot{\psi}_1 = \eta \Delta' \cdot \psi_1 \quad (3.151)$$

or, using Eq. (3.149) and the numerical value of  $A \cong 1.827$  [3.32], the so-called *Rutherford* [3.33] equation for the growth of the magnetic island

$$\dot{w} = 1.22 \eta \Delta' \quad (3.152)$$

This describes a phase of algebraic growth following the stage of exponential behaviour described in Section 3.3.1.2.2, after the island width has exceeded the linear tearing layer width  $\delta_t$ . During this phase of growth the *Poynting* flow of energy into the layer around the singular surface is balanced only by ohmic dissipation.

Additional terms in the Rutherford equation would arise if the resistivity  $\eta$  or any mechanism driving additional currents were to have a  $\cos(ky)$  dependence. This can happen, as the helical island forms a separate region of confinement, being bypassed by the radial heat flow which passes preferentially through the X-point proximity. The resistivity in the O-point region can then be significantly enhanced if radiation losses are large and dominate over local heat deposition, or if impurities or a cold plasma have accumulated there. The latter effects can give rise to the formation of the so-called *snakes*: persistent high resistivity helical structures, sometimes observed following the injection of pellets, or of high-Z impurities.

An example of much larger practical importance are, however, the *neoclassical tearing modes* arising from the reaction of the bootstrap current

density (discussed in Chapter 2 and referred to also in Section 3.3.1.1.5) to the changes in the pressure profile inside the island. The latter will be reduced inside the island by the efficient transport parallel to the field lines, resulting in a local current density reduction. The degree of pressure flattening is determined by the competition of parallel and perpendicular heat conductivity and the former will become dominant only if the island size approaches a value  $w_d = 5(\kappa_{\perp}/\kappa_{\parallel})^{1/4}/\sqrt{\varepsilon sn}$ . To account for the bootstrap drive we have to subtract its contribution (like that of any other non-inductive current drive) in Ohm's Law from the total current density  $j(\psi) = \nabla^2\psi$  in Eq. (3.150). As a result, also Rutherford's equation has to be modified, to read [3.34]

$$\dot{w} = 1.22\eta \left( \Delta' + 4.63\sqrt{\varepsilon} \frac{\beta_{pol}}{s} \frac{w}{w_d^2} \frac{2}{1 + (w/w_d)^2} \right) \quad (3.153)$$

where all quantities including the local

$$\beta_{pol} = -\frac{q^2}{(\varepsilon)^2} \frac{\mu_o r p'}{B_{\phi}^2} \quad (3.154)$$

are to be taken at the resonant surface.

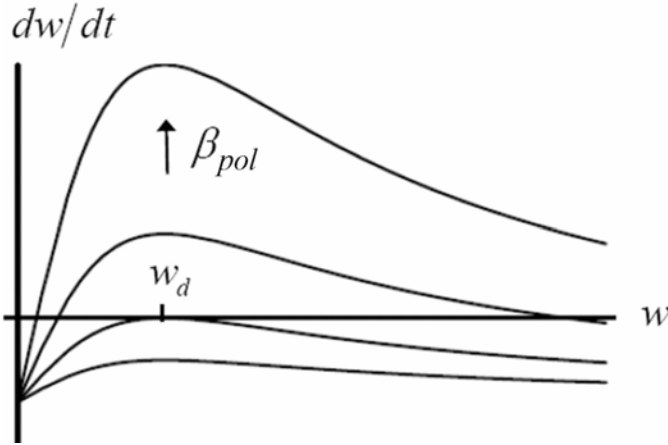


FIG. 3.17. Growth rate of neoclassical tearing mode (NTM) as a function of island size  $w$ , for different  $\beta_{pol}$ , increasing in the direction of the arrow.

For the standard tearing mode stable case ( $\Delta' < 0$ ) Eq. (3.153) describes a non-linear instability, as illustrated in Fig. 3.17, with island growth setting in only above a certain minimum island size. The growth rate will reach a maximum for  $w = w_d$  and the island will saturate at a finite size given by the second zero of the RHS. Growing of the perturbation at negative values of  $\Delta'$  implies an *outflow* of magnetic energy from the island region into the rest of the plasma, with the

energy provided by the decay of the pressure gradient. The *neoclassical tearing mode* requires for growth a certain minimum value of  $\beta_{pol}$ , but also the presence of a seed island. These and other features arising from its nature as a non-linear instability (e.g. hysteresis between onset and disappearance of the perturbation in  $\beta_{pol}$  scans) have been verified experimentally, although additional kinetic effects associated with plasma and mode rotation and the bootstrap current behaviour when the island size is small or comparable to the banana orbit width make the exact form of the neoclassical terms uncertain. The derivation of the modified Rutherford equation outlined above also suggests a strategy for the external control of this instability: applying localized external current drive in a form that it makes a dominating contribution  $\sim \cos(ky)$  of opposite sign to that of the missing bootstrap current.

### 3.3.1.3.2. Ergodization and reconnection

In a straight-cylinder model, even non-linear perturbations of a single helicity (representable as  $f(m\theta + nz/(2\pi R_o))$  with integer  $m, n$  conserve closed flux surfaces, and produce islands around unperturbed resonant ones. The addition of a perturbation of a different helicity  $m_1, n_1$  with  $m_1/n_1 \neq m/n$  of sufficient amplitude, however, leads to an ergodization of field lines over a certain spatial region, which, due to the very high parallel heat conductivity, tends to increase strongly the effective radial transport. Figure 3.18 shows a Poincaré map — the intersection points of selected field lines with a plane  $z(= \phi R_o) = \text{constant}$  during subsequent toroidal transits — for a case with two imposed helical perturbations  $(m, n) = (3/2), (4, 3)$  with equal amplitudes  $\tilde{\psi}_{m,n} / (aB_{z0}) = 10^{-4}$  (see Fig. 3.18 left) and  $\tilde{\psi}_{m,n} / (aB_{z0}) = 9 \cdot 10^{-4}$  (see Fig. 3.18 right), respectively.

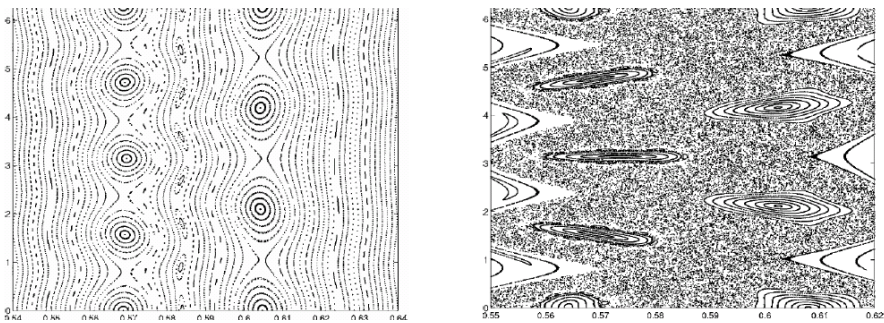


FIG. 3.18. Poincaré maps showing the effect of ergodization due to the superposition of two helical perturbations onto a cylinder-symmetric equilibrium field, for low and high amplitude of the perturbation fields [3.36].

Ergodization sets in when neighbouring islands — with their size given by Eq. (3.152) — start to overlap (*Chirikov criterion* [3.35]). Multiple helicities arise

through linear, geometric coupling in the poloidal plane via toroidicity ( $m$  to  $m+1$ ) or ellipticity ( $m$  to  $m+2$ ) and higher-order deformations of the cross-section, or through non-linear effects. Ergodization is one of the effects through which helical instabilities can produce a flattening in the axisymmetric plasma profiles and eliminate thereby their unstable drive. Ergodization is believed to play a major part in many phenomena observed in tokamaks, in particular during disruptions. It can also be produced in a stationary fashion by externally applied non-axisymmetric perturbation fields, sometimes intentionally used to enhance transport and limit temperature and pressure gradients over a determined region of the plasma. The clearest manifestations of ergodization as a dynamic phenomenon are observed in reverse field pinches (RFPs) where co-existing tearing modes of different helicity are considered responsible for maintaining a quasi-stationary current profile, and the associated transport in ergodic fields dominates the energy confinement in the so-called *standard* regime.

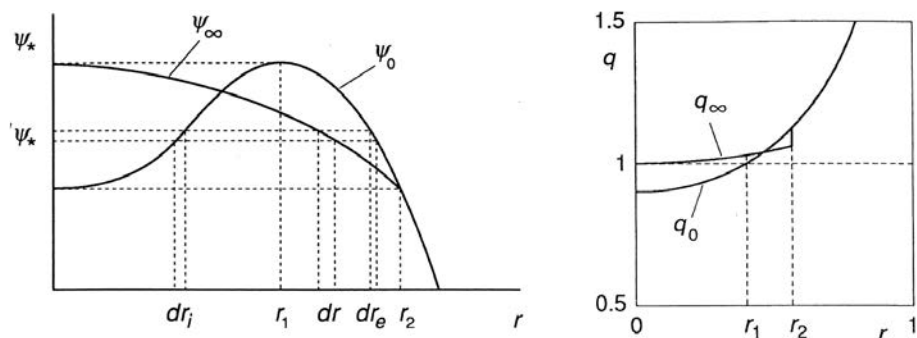


FIG. 3.19. Kadomtsev model for sawtooth reconnection: profiles of the helical flux function  $\Psi_{1,1}(r)$  and the safety factor  $q(r)$  before and after the event. As  $B_\phi$  is assumed constant, reconnection conserves the area between two flux surfaces  $\Psi_{1,1} + d\Psi_{1,1}$  before and after the crash.

In the case of the  $(m,n)=(1/1)$  resistive kink mode, a single helicity reconnection model gives a qualitatively self-consistent picture of the non-linear dynamics [3.32] of the sawtooth phenomenon and explains a range of experimental observations. The consequences of this so-called *Kadomtsev* [3.37] model are schematically illustrated in Fig. 3.19 (from Ref. [3.32]) by the radial profiles of the helical flux function  $\Psi_{1,1}$  and of  $q$  before the onset of the  $(1,1)$  instability and after re-establishment of an axisymmetric state. In a straight tokamak model it assumes a transition between two cylinder-symmetric stages conserving the area (and hence the toroidal magnetic flux) between the helical flux surfaces, but resulting in a final state where the resonant surface  $q=1$  is at the axis. The reconnection proceeds through the growth of a helical island starting at the initial  $q=1$  surface (at  $r_{1,1}$ ), which ultimately becomes the core

of a new cylinder-symmetric state. Although this reconnection process proceeds much faster than resistive dissipation of flux, it can, however, still not explain the short timescales of the so-called *sawtooth* crashes in large, high temperature tokamak plasmas. It is now generally accepted that fast reconnection events in toroidal confinement devices — as in space and astrophysics — require a more advanced plasma model than single fluid MHD to describe the dynamics in the reconnection zone.

### 3.3.2. Extensions to the MHD model

#### 3.3.2.1. Introduction

Ideal MHD represents a model in which the basics of equilibrium and global stability against large scale disturbances are well understood. The model is both elegant and deeply consistent, as no part of field/plasma energy or momentum conservation is approximate. However, as soon as further considerations such as saturation of small scale instabilities or even dissipative effects on large scale disturbances still in the linear growth phase enter consideration, the relevant dynamics is often outside of the MHD picture entirely. Relatives to the MHD model which are often used are reduced MHD and resistive MHD, referring to the low frequency regime and dissipation by collisional friction between electrons and ions, respectively. Reduced MHD treats the plasma velocity perpendicular to the magnetic field as an  $\vec{E} \times \vec{B}$  drift with the electrostatic potential acting as a stream function. The velocity can be adiabatically compressible due to the spatial variation of the magnetic field. In a torus the dominant part of this is the inverse variation with respect to the major radius. Treatment of the velocity as a drift excludes the fast magnetosonic (compressible Alfvén) wave from the dynamics, due to the scale separation in frequency. Resistive MHD adds resistivity (momentum transfer from electrons to ions as a frictional drag) to Ohm's Law. This addition can be applied in either full- or resistive-MHD, and its role is usually to resolve singular layers as was explained previously. A good reference for the concepts raised here and in the rest of this section is Ref. [3.38].

Within these models, the basic physical picture remains the one which underlies MHD: Alfvén dynamics involves the current and the  $\vec{E} \times \vec{B}$  velocity, and any instabilities are driven by the current gradient. Sound wave dynamics (including the spread of plasma along magnetic field lines) involves the parallel flow and parallel pressure gradients, and any instabilities are driven by the parallel flow velocity gradient. Interchange dynamics involves the  $\vec{E} \times \vec{B}$  velocity and the pressure, and any instabilities are driven by the pressure gradient. Within MHD these classes of motion are conceptually separate, even when the parallel dynamics can constrain the action of instabilities driven by the perpendicular dynamics (in MHD, always involving the  $\vec{E} \times \vec{B}$  velocity). For

example, in the ballooning instability the basic interchange motion is constrained by the Alfvén dynamics because the  $\vec{E} \times \vec{B}$  velocity represented by the turnover motion of a vortex bends the field lines. The instability exists when the free energy release in the interchange motion overcomes the cost of bending the field lines. But the Alfvén motion involves only the current and the electric field, tied to the magnetic and  $\vec{E} \times \vec{B}$  flow disturbances via Ampere's Law and Lorentz force balance, respectively. Within MHD there is no coupling of Alfvén motion to the pressure gradient in Ohm's Law and hence no direct energetic coupling of parallel currents to pressure gradients. Similar considerations exist for the kink instability, in which as a current driven instability the pressure gradient has no role, and for dissipative dependent dynamics such as field line reconnection and the tearing instability, in which resistivity is not only the only available dissipative mechanism but also the only effect not present within pure ideal MHD.

The conditions under which these restrictions hold are basically the same as the conditions under which one can derive MHD from within a more general model in which the one-fluid assumptions are not made. Within the strictly fluid physical picture the more general model is usually the Braginskii equations. These comprise a set of dissipative conservation laws for particles, momentum and thermal energy for each species whose velocities and pressures are now treated separately. Dissipation is treated generally, resulting from the action of collisions both within and across species. Modifications are sometimes needed to treat the parallel heat flux as a dynamical variable, so that the temperature/heat-flux pair has similar properties to the density/velocity pair. This enters particularly when special effects due to drive by temperature gradients are treated and the collisional dissipation effects are not completely dominant in determining the relation between heat flux and temperature gradient. However, the idea of a set of separate fluids, one for each particle species, coupled by Maxwell's equations, under sufficiently non-relativistic conditions to allow the neglect of the displacement current (hence directly non-neutral plasma effects), is clear enough to be used as a starting point. The MHD model is found from within this system by making a minimal set of assumptions necessary to obtain the MHD equations. Ultimately, this consists of neglecting any corrections to the statement that the components of the single-fluid Lorentz force are large compared to any corrections. This yields the  $\vec{E} \times \vec{B}$  velocity as the perpendicular flow,

$$\vec{E} + \vec{v} \times \vec{B} = 0 \Rightarrow \vec{v} = \frac{1}{B^2} \vec{E} \times \vec{B} + \frac{v_{\parallel}}{B} \vec{B} \quad (3.155)$$

For electrons and ions separately, the pressure force and inertia are assumed to be small. Then, the MHD force equation is derived by summing the momentum equations for all the fluid species. Here, the single-fluid Lorentz force cancels out because it is common to all the species and the plasma is assumed to be neutral.

There remains the inertia, the total pressure force and the summed Lorentz force. The last is the familiar  $\vec{j} \times \vec{B}$  effect which distinguishes a highly conductive plasma from a neutral fluid. Currents and pressure gradients are respectively retained only when the main velocity or the electric field are eliminated by subtraction, which then becomes the procedure for deriving the MHD model from within the two-fluid equations. The procedure is shown in detail below using a simplified, isothermal two-fluid model as a starting point.

Within the two-fluid model, the separation between Alfvén dynamics and pressure or fluid dynamics is no longer part of the set of the assumptions. It is still possible to obtain this separation in the results, however, depending on parameters and the scale of the instability considered (i.e. small amplitude instabilities in a tokamak may be chosen according to the toroidal mode number, due to axisymmetry; the perpendicular wavenumber has a component within the flux surface arising from the finiteness of the poloidal component of the magnetic field; in general this leads to a drift of the eigenmode within the flux surface which has both poloidal and toroidal components). This type of investigation then yields the best understanding of the validity and restrictions of the MHD model, which is useful background even for work done primarily within MHD. It is very often the case that a small amplitude instability itself is well described by MHD but then some of the two-fluid effects enter qualitatively as soon as the dynamics becomes non-linear and the aftermath is no longer described by the MHD model. Indeed, the two-fluid effects enter not only due to ideal-MHD singular layers but also due to non-linear coupling processes among the degrees of freedom, most prominently, turbulence. Most vulnerable to this are pressure driven instabilities which become turbulent in the aftermath. The usual reason is coupling to degrees of freedom which are either damped or subdominant in the linear phase, and the direct coupling between pressure gradients and currents determines this other component (usually a form of dissipative Alfvén response).

MHD instabilities in a tokamak are usually slowly growing modes for which the magnetosonic frequency for the same wavenumber is arbitrarily fast. These fall into the reduced MHD physical picture. Originally conceived as an expansion in the inverse aspect ratio, it is equivalently well cast in terms of a low frequency expansion, as for small scales the underlying frequency ordering remains satisfied even for arbitrary magnetic geometry. A derivation of this is given as a primary example in Section 3.3.2.2. The limitation on the dynamical frequencies is that they be small compared to the singly-charged ion gyrofrequency,  $\Omega_i = eB / m_i$ , which allows the inertia to be considered as a small correction to the flow, and small compared to the magnetosonic frequency,  $k_{\perp} v_A$ , which allows the perpendicular flow to be treated as a drift (here,  $k_{\perp}$  is the perpendicular wavenumber and  $v_A$  is the Alfvén velocity). Perpendicular compression in this model is adiabatic (quasistatic) in the sense that it does not involve reactive dynamics but still conserves energy and entropy. The parallel

dynamics remains compressible, with sound wave effects unaltered. The shear Alfvén dynamics is retained by allowing time dependent variation in the parallel current and (from Ampere’s Law) hence the parallel component of the magnetic potential. Rather than vector velocity and magnetic disturbances  $\vec{v}$  and  $\vec{B}$ , one calculates in terms of electric and magnetic potentials  $\Phi$  and  $A_{\parallel}$  whose perpendicular Laplacians are proportional to the  $\vec{E} \times \vec{B}$  vorticity and parallel current, respectively. The perpendicular flow is now more properly an  $\vec{E} \times \vec{B}$  drift, found by substituting  $\vec{E} = -\nabla\Phi$  into Eq. (3.155),

$$\vec{v} = \frac{1}{B^2} \vec{B} \times \nabla\Phi + \frac{v_{\parallel}}{B} \vec{B} \quad (3.156)$$

by which  $\vec{v}_{\perp}$  is determined by  $\Phi$  and the equation for  $v_{\perp}^2\Phi$  is given by charge continuity (here, quasineutrality represented by  $\nabla \cdot \vec{j} = 0$ , which implicitly underlies the MHD model, becomes explicit). The  $\vec{E} \times \vec{B}$  velocity can still be compressible due to an inhomogeneous magnetic field, but the substitution  $\vec{E}_{\perp} = v_{\perp}^2\Phi$  eliminates the compressional perpendicular Alfvén motion (also called “fast Alfvén”). With the parallel dynamics remaining electromagnetic, the parallel Alfvén responses (also called “shear Alfvén”) are retained. The derivation of this is simple and will be given below. Subsequently, all of the discussion will be within the low frequency limits of  $\omega \ll \Omega_i$  and  $\omega \ll k_{\perp} v_A$ .

Many instabilities and their non-linear aftermath are affected by the finite ion gyroradius (labelled FLR — finite Larmor radius). This is always outside of the MHD physical picture. However, it is not necessarily outside of a fluid picture. The role played in the ion inertia by the finite ion pressure gradient is the manifestation of FLR effects within a fluid model which is fundamentally based on a small-gyroradius expansion, in which pressure gradients add to the drift velocity, producing what are called the “diamagnetic drifts” of the various species (dependent on the partial pressure and the charge state of the species).

The traditional fluid description and its MHD subset are based on an underlying kinetic model. The equations may be derived by taking velocity space moments of a kinetic equation for a distribution function  $f$  and applying hierarchy closure rules for moments higher than the temperature. For a dissipative closure, the heat flux and viscosity components are thereby given as constitutive formulas in terms of the gradients of the lower moments. This kinetic equation includes the entire Lorentz force and the fluid derivation leads to  $\vec{v} \times \vec{B}$  terms. Then, the commonly used reduced MHD and two-fluid models are found by assuming the perpendicular inertia terms to be corrections and solving for the  $\vec{v}$  in the Lorentz force to find the drift formula. Alternatively, the low frequency limit is taken at the kinetic level first. This gives the gyrokinetic model, covered in Chapter 2. Moments taken over the gyrokinetic equation produce the gyrofluid model. This turns out to be a better description for non-linear computations which approach the ion gyroradius scale, as it is described purely in terms of scalar

quantities, and difficulties with the dissipation-free part of the viscosity tensor in non-linear situations within a fluid model are replaced by additional non-linear advection terms which are well behaved at all scales.

### 3.3.2.2. Derivation example: reduced (low frequency) MHD

We start with the steps required to obtain the reduced MHD model, valid in the aforementioned low frequency limit where both  $\omega \ll \Omega_i$  and  $\omega \ll k_{\perp} v_A$  are satisfied. To simplify matters these examples will be given in terms of their isothermal versions. For each species  $z$  the pressure  $p_z$  is given by  $T_z n_z$  with  $T_z$  constant. We also restrict to a fully ionized, neutral, single component plasma with singly charged ions, so that the electron and ion species are labelled with  $e$  and  $i$  subscripts and  $n_e = n_i = n$ . The total pressure is given by  $p = (T_e + T_i)n$ . The mass density is given by  $\rho_M = (m_e + m_i)n$  or simply  $nm_i$  with  $m_e \ll m_i$ . Within this isothermal MHD the list of dependent variables is  $n$ ,  $\vec{v}$  and  $\vec{B}$ , with  $\vec{E}$  and  $\vec{j}$  given by auxiliary relations.

We justify the dynamical  $\vec{E} \times \vec{B}$  incompressibility by forming equations for  $\nabla \cdot \vec{v}$  and  $B^2$ :

$$\frac{\partial}{\partial t} \nabla \cdot \vec{v} + \nabla \cdot (\vec{v} \cdot \nabla \vec{v}) + \nabla \cdot \frac{1}{nM_i} \nabla \left( \frac{B^2}{2\mu_0} \right) = \nabla \cdot \frac{1}{\mu_0 n M_i} (\vec{B} \cdot \nabla \vec{B}) \quad (3.157)$$

$$\frac{\partial}{\partial t} \frac{B^2}{2} + \vec{v} \cdot \nabla \frac{B^2}{2} + B^2 \nabla \cdot \vec{v} = \nabla \cdot (\vec{B} \cdot \nabla \vec{v}) \quad (3.158)$$

If we can assume that  $\vec{v} \cdot \nabla$  is the same size as  $\partial/\partial t$  and that  $\vec{B} \cdot \nabla \ll \vec{B} \times \nabla$ , in essence that motions are advective and that the scale of parallel motion is larger than that of perpendicular motion (in terms of wavenumber components we write  $k_{\parallel} \ll k_{\perp}$ ), and further assume a small plasma beta,  $\beta = 2\mu_0 p / B^2 \ll 1$ , holding under gradients or otherwise, then these equations suggest that  $\partial/\partial t$  should scale as  $v_A \nabla_{\perp}$ , where  $v_A$  given by  $v_A = B^2 / \mu_0 n m_i$  is the Alfvén velocity. On the other hand, if the dynamics is determined in the other equations (through density, rotational velocity and shear Alfvén magnetic disturbances), and  $\partial/\partial t \ll v_A \nabla_{\perp}$ , then the partial time derivative terms for  $\nabla \cdot \vec{v}$  and  $B^2$  may be neglected. Formally, this is the step by which the “fast Alfvén” waves are filtered out of the dynamical system.

Under the resulting low frequency conditions, the quantities  $B^2/2$  and  $\nabla \cdot \vec{v}$  are then given by constitutive formulas. Specifically, the equation for  $B^2/2$  gives  $\nabla \cdot \vec{v}$  in terms of motion across the inhomogeneous magnetic field. With the partial time derivative neglected but magnetic disturbances kept, this means that the latter should be perpendicular to  $\vec{B}$  and hence given by  $\vec{B}_{\perp} = \nabla \times (A_{\parallel} \vec{B} / B)$ . Therefore the electric field expressed by Faraday’s Law (integrate one operation of  $\nabla \times$  out of the induction equation for  $\vec{B}$  in the MHD equations),

$$\vec{E} = -\frac{\partial \vec{A}}{\partial t} - \nabla \Phi \quad (3.159)$$

becomes

$$\vec{E} = -\frac{\partial \vec{A}_{\parallel}}{\partial t} \frac{\vec{B}}{B} - \nabla \Phi \quad (3.160)$$

In terms of perpendicular and parallel components this is

$$\vec{E}_{\perp} = -\nabla_{\perp} \Phi \quad (3.161)$$

$$\vec{E}_{\parallel} = -\frac{\partial A_{\parallel}}{\partial t} - \nabla_{\parallel} \phi \quad (3.162)$$

The  $\vec{E} \times \vec{B}$  velocity is no longer a dependent variable but a drift due to a spatially dependent potential,

$$\vec{v}_{\perp} = \vec{v}_E \equiv \frac{1}{B^2} \vec{B} \times \nabla \Phi \quad (3.163)$$

The MHD auxiliary equation for  $\vec{E}$  is now equivalent to the statement that  $\vec{E}_{\parallel} = 0$ , or

$$\frac{\partial \vec{A}_{\parallel}}{\partial t} \frac{\vec{B}}{B} = -\nabla \Phi \quad (3.164)$$

This is Ohm's Law within the dissipation-free version of reduced MHD.

With the  $\vec{E} \times \vec{B}$  velocity determined by the electrostatic potential  $\Phi$  we seek an equation to determine  $\Phi$ . The MHD force equation may be solved for the current,

$$\vec{j} = j_{\parallel} \frac{\vec{B}}{B} + \frac{1}{B^2} \vec{B} \times \nabla p + \frac{nm_i}{B^2} \vec{B} \times \left( \frac{\partial \vec{v}}{\partial t} + \vec{v} \cdot \nabla \vec{v} \right) \quad (3.165)$$

These three pieces are called the parallel, diamagnetic and polarization currents, respectively. The MHD form of Ampere's Law ( $\nabla \times \vec{B} = \mu_0 \vec{j}$ ) already implies  $\nabla \times \vec{j} = 0$ , so that

$$\nabla \cdot \frac{nm_i}{B^2} \vec{B} \times \left( \frac{\partial \vec{v}}{\partial t} + \vec{v} \cdot \nabla \vec{v} \right) + \nabla \cdot \frac{1}{B^2} \vec{B} \times \nabla p + \vec{B} \cdot \nabla \frac{j_{\parallel}}{B} = 0 \quad (3.166)$$

It remains to substitute the form of the velocity given by the  $\vec{E} \times \vec{B}$  drift and parallel velocity in Eq. (3.156) to obtain an equation for  $\Phi$ . In doing this,

however, the ordering scheme concerning relative scales of motion is applied. It is explained differently for global motion under large aspect ratio assumptions or for micro-instabilities or turbulence, but the math is the same. The scale of  $\vec{B}$  is assumed to be large compared to that of  $\Phi$ , the density is assumed to be either slowly varying or given by small amplitude disturbances on a fixed background, and the parallel advection is assumed to be subdominant so that  $v_{\parallel} \nabla_{\parallel} \ll v_{\perp} \nabla_{\perp}$ , and the resulting manipulation of the inertia term yields an equation for the  $\vec{E} \times \vec{B}$  vorticity,

$$\frac{\partial \Omega_E}{\partial t} + \vec{v} \cdot \nabla \Omega_E = \vec{B} \cdot \nabla \frac{j_{\parallel}}{B} + \nabla \cdot \frac{1}{B^2} \vec{B} \times \nabla p \quad (3.167)$$

where the vorticity is given by

$$\Omega_E = \nabla \cdot \frac{nm_i}{B^2} \nabla_{\perp} \Phi \quad (3.168)$$

This equation determines the evolution of  $\Phi$  which has been promoted in favour of  $\vec{v}$  as a dependent variable.

The remaining quantities are  $n$  and  $v_{\parallel}$ . The former is simply given by its original equation

$$\frac{\partial n}{\partial t} + \vec{v} \cdot \nabla n + n \nabla \cdot \vec{v} = 0 \quad (3.169)$$

and the latter is given by the parallel component of the original equation for  $\vec{v}$ , or

$$nm_i \left( \frac{\partial \vec{v}_{\parallel}}{\partial t} + \vec{v} \cdot \nabla v_{\parallel} \right) = -\nabla_{\parallel} p \quad (3.170)$$

The above equations for  $A_{\parallel}$ ,  $\Phi$ ,  $n$  and  $v_{\parallel}$  form a closed set and represent the formulation of reduced MHD.

There is a further consideration made clear by the cumbersome nature of the inertia expression in the vorticity equation in the case that the scale-separation orderings are not made. If the time and space dependence of  $n$  and  $\vec{B}$  are arbitrary then this procedure to find the vorticity equation does not bring computational tractability. Reduced MHD is therefore used merely as a model: internally consistent, qualitatively but not precisely correct. To understand the physical nature of MHD instabilities, however, one may simply declare the following model: non-linearities are kept only in advection by the  $\vec{E} \times \vec{B}$  velocity and in the part of the parallel gradient due to magnetic disturbances, the perpendicular scale of motion  $\Delta_{\perp}$  is arbitrarily small compared to that of  $\vec{B}$ , which in turn is comparable to the parallel scale of motion  $\Delta_{\parallel}$ , and the relative amplitude of fluctuations  $\delta$  remains small even if the dynamics is non-linear. Retention of the non-linearities implies use of mixing level ordering, described by  $\Delta_{\perp} / \Delta_{\parallel} \sim \delta$ .

If  $\Delta_{\perp}$  is assumed to order with  $\rho_i$ , conventional gyrokinetic ordering (also called drift ordering) is the result. If, as for large scale MHD instabilities,  $\Delta_{\perp}$  is ordered with the tokamak minor radius, then the ordering is a form of large aspect ratio ordering. This is admissible only within conventional MHD scenarios, as the replacement of the mass density  $\rho_M$  in the inertia term by a normalizing constant implies that gradients are perturbations. On the other hand, in a linear analysis  $\rho_M$  may retain spatial dependence (time dependence of  $\rho_M$  in this term implies non-linearity). It is important to note that although such considerations always enter development of the next state-of-art computational models, they do not affect basic understanding of the qualitative nature (including such things as energetic processes) of the basic instabilities treatable by this class of models.

Under the simplified ordering, reduced MHD becomes

$$\frac{\partial \Omega_E}{\partial t} + \vec{v}_E \cdot \nabla \Omega_E = B \nabla_{\parallel} \frac{j_{\parallel}}{B} + \nabla \cdot \frac{1}{B^2} \vec{B} \times \nabla p \quad (3.171)$$

$$\frac{\partial n}{\partial t} + \vec{v}_E \cdot \nabla n + n_0 B \nabla_{\parallel} \frac{v_{\parallel}}{B} + n_0 \nabla \cdot \frac{1}{B^2} \vec{B} \times \nabla \Phi = 0 \quad (3.172)$$

$$\frac{\partial A_{\parallel}}{\partial t} + \nabla_{\parallel} \Phi = 0 \quad (3.173)$$

$$n_0 m_i \left( \frac{\partial v_{\parallel}}{\partial t} + \vec{v}_E \cdot \nabla v_{\parallel} \right) + \nabla_{\parallel} p = 0 \quad (3.174)$$

where  $n_0$  is a constant parameter representing the density, and  $n$  and  $p$  include gradients in the density profile as well as the disturbances (these are often written separately). Terms involving the  $\nabla \cdot (1/B^2) \vec{B} \times \nabla$  combination are referred to as (magnetic) curvature terms since they vanish in a homogeneous magnetic field. The list of dependent variables is  $\Phi$ ,  $n$ ,  $A_{\parallel}$  and  $v_{\parallel}$  with

$$\Omega_E = \nabla \cdot \frac{n_0 m_i}{B^2} \nabla_{\perp} \Phi \quad (3.175)$$

$$j_{\parallel} = -\frac{1}{\mu_0} \nabla_{\perp}^2 A_{\parallel} \quad (3.176)$$

as auxiliary relations assuming  $\nabla_{\perp} \gg \nabla_{\parallel}$ . The latter is the reduced-MHD form of Ampere's Law.

A further simplification often used is to neglect compressibility in the dynamics, so that only  $\Phi$  and  $A_{\parallel}$  (therefore  $\Omega_E$  and  $j_{\parallel}$ ) are involved. This is sufficient to treat tearing and kink modes, but not ballooning or interchange modes.

Under these equations the standard MHD instabilities are described as follows. Current driven dynamics arises from the gradient term  $B\nabla_{\parallel}(j_{\parallel}/B)$ , in which a radial disturbance in  $\vec{B}_{\perp}$  multiplies the radial derivative of the background current profile (see Section 3.3.1.2). The resulting disturbance in  $\Phi$  re-excites  $A_{\parallel}$ , hence  $\vec{B}_{\perp}$  and then  $j_{\parallel}$  through Ampere's Law. The linear field line bending term in the vorticity equation constrains the dynamics. Non-linear phases of the  $m=1$  internal kink are traditionally studied computationally using these equations (in which dynamics in  $n$  and  $v_{\parallel}$  may be neglected). Study of pure-MHD tearing instabilities, both linear and non-linear, are also done with these equations, with the addition of the resistivity to form the resistive reduced MHD Ohm's Law:

$$\frac{\partial A_{\parallel}}{\partial t} + \nabla_{\parallel}\Phi = -\eta_{\parallel}j_{\parallel} \quad (3.177)$$

where  $\eta_{\parallel} = 0.51m_e v_e / ne^2$  is the Braginskii parallel resistivity with  $v_e$  the Braginskii electron collision frequency. Using Ampere's Law, the resistivity term represents a diffusive decay in  $A_{\parallel}$  with diffusion coefficient  $\eta_{\parallel} / \mu_0$ . This is necessary for the existence of magnetic field line reconnection, for which the tearing mode is a special case. Lastly, the pressure driven modes are excited by the advection term  $\vec{v}_E \cdot \nabla n$ , in which the radial component of an  $\vec{E} \times \vec{B}$  eddy velocity multiplies the radial derivative of the background pressure profile. The resulting disturbance in  $p$  re-excites  $\Omega_E$  due to the curvature term in the vorticity equation. This by itself describes the interchange dynamics, which is destabilized if the pressure and magnetic field strength gradients have a positive contraction. This occurs on the outer half of a given magnetic flux surface. However, since  $\nabla_{\parallel}$  cannot vanish over finite-sized regions for eddy disturbances in tokamak geometry (closed magnetic flux surfaces with shear in the pitch parameter  $q$ ), the current is also excited by the  $\nabla_{\parallel}$  term in Ohm's Law. The resulting field line bending constrains the dynamics, providing the ideal MHD threshold in  $\beta$ . If still unstable, the result is the ideal ballooning mode. With resistivity present, there is a finite growth rate for all  $\beta$  although the spectrum peak is at short wavelength not far above the  $\rho_i$  scale. Hence, although the equations are derived assuming long wavelengths, the result occurs at short wavelength and then we have to consider the validity of the MHD model in the first place. It is also true that while the tearing mode is a long wavelength instability, the effects of resistivity are confined to a narrow layer of width  $\Delta_{\perp}$  in which the frequency combination  $\omega(\eta_{\parallel} / \mu_0)\Delta_{\perp}^2$  can compete with  $v_A^2 / (q^2 R^2)$ . Ultimately, the  $m=1$  instability is also controlled by the dynamics of a narrow layer. This entrance of small scale dynamics is what forces consideration of more general physical models.

### 3.3.2.3. Derivation example: two-fluid equations

A two fluid model for a single-ion neutral plasma in the isothermal simplification results from a continuity equation and a momentum equation for each species

$$\frac{\partial n_z}{\partial t} + \nabla \cdot n_z \vec{u}_z = 0 \quad (3.178)$$

$$n_z m_z \left( \frac{\partial \vec{u}_z}{\partial t} + \vec{u}_z \cdot \nabla \vec{u}_z \right) + \nabla \cdot \vec{\Pi}_z + \nabla p_z = n_z Ze (\vec{E} + \vec{u}_z \times \vec{B}) = 0 \quad (3.179)$$

where  $Z$  is the charge state and  $\vec{\Pi}_z$  is the viscosity tensor (which we will not discuss in detail here). Subtracting the continuity equations and multiplying by  $e$  obtains the charge continuity equation. Adding the momentum equations and assuming the electron inertia is small results in the MHD force equation. Multiplying the ion continuity equation by  $m_i$  gives the MHD mass continuity equation. The electron momentum equation assuming all effects save the Lorentz force are small gives the ideal MHD Ohm's Law: in Eq. (3.179), the terms on the left hand side should be small for all species, and then the single-fluid Lorentz force is set to zero, determining  $\vec{u}_z \rightarrow \vec{v}$  as in Eq. (3.155). If  $\vec{u}_z$  can be replaced by  $\vec{v}$  then the MHD model is recovered. The validity of the MHD model depends on the validity of these assumptions. On the other hand, if  $\nabla p_z$  or the ion inertia is sufficient to break this approximation, we must solve for each  $\vec{u}_z$  independently.

Solving Eq. (3.179) for  $\vec{u}_z$  by isolating the  $\vec{u}_z \times \vec{B}$  term and then applying  $B^{-2} \vec{B} \times$ , we find

$$\vec{u}_z = u_{z\parallel} \vec{b} + \frac{1}{B^2} \vec{B} \times \nabla \Phi + \frac{1}{n_z Ze} \frac{1}{B^2} \vec{B} \times \nabla p_z + \frac{1}{n_z Ze} \frac{1}{B^2} \vec{B} \times (\text{inertia}) \quad (3.180)$$

where the terms involving  $n_z m_z$  and  $\vec{\Pi}_z$  are collected as the inertia effects. To lowest order in the ratio  $\omega / \Omega_z$  the perpendicular velocity is

$$\vec{u}_{z\perp}^{(0)} = \frac{1}{B^2} \vec{B} \times \nabla \Phi + \frac{1}{n_z Ze} \frac{1}{B^2} \vec{B} \times \nabla p_z \quad (3.181)$$

The two terms represent the  $\vec{E} \times \vec{B}$  and diamagnetic velocities, respectively, and we no longer assume that  $\nabla \Phi$  is large compared to  $(T_z / Ze) \nabla \log p_z$  as would be required to derive the reduced MHD equations.

This form is then substituted into the inertia term to obtain what is known as the polarization drift, formally representing an  $O(\omega / \Omega_z)$  correction ( $\Omega_z = ZeB / m_z$ ). However, not only is the polarization drift the quantity which represents the time derivative of the electrostatic potential  $\Phi$ , it is also true that in many instabilities and turbulence types the divergence of the ion polarization

drift is the main mechanism which provides for charge separation and ultimately the release of free energy. So the polarization drift is kept in the derivation. We can only provide the details herein by assuming the ions are cold and the electron inertia is small. This leaves

$$\vec{u}_e = u_{e\parallel} \vec{b} + \frac{1}{B^2} \vec{B} \times \nabla \Phi - \frac{T_e}{n_e e} \frac{1}{B^2} \vec{B} \times \nabla n_e \quad (3.182)$$

$$\vec{u}_i = u_{i\parallel} \vec{b} + \frac{1}{B^2} \vec{B} \times \nabla \Phi - \frac{m_i}{e B^2} \left( \frac{\partial}{\partial t} + \vec{v}_E \cdot \nabla \right) \nabla_{\perp} \Phi \quad (3.183)$$

for the electrons and ions, respectively. The  $\vec{E} \times \vec{B}$  velocity is of course the same as in the reduced MHD model. The electron diamagnetic and ion polarization velocities provide for charge separation, as does the difference among the parallel velocities. Substituting these into the subtraction of the continuity equations confirms that the charge density term is small compared to the ion polarization divergence if  $c^2 \gg v_A^2$ , which is the condition for quasineutrality ( $\nabla \cdot \vec{j} = 0$  despite the existence of  $\vec{E} \times \vec{B}$  vorticity, noting that the Poisson equation is  $\epsilon_0 \nabla^2 \Phi = n_e e - n_i Z e$  and  $\epsilon_0 \mu_0 = c^{-2}$ ). Hence we can take  $n_e = Z n_i = n$  and the  $\vec{E} \times \vec{B}$  velocity does not cause charge separation. This is also equivalent to neglecting the electric field energy  $\epsilon_0 E^2 / 2$  in favour of the kinetic energy  $n_i m_i E^2 / 2 B^2$  of  $\vec{E} \times \vec{B}$  motion of the ions.

In all the derivation steps, multiplying factors of  $ne$  and  $nm_z$  are replaced by the normalizing constants  $n_0 e$  and  $n_0 m_z$  (ultimately, this step is necessary for energy conservation in the model). The equation  $\nabla \cdot \vec{j} = 0$  becomes another way to derive the reduced MHD vorticity equation (which retains its form in a cold-ion two-fluid model).

The form of Ohm's Law changes importantly, as even with neglect of electron inertia we have

$$\frac{\partial A_{\parallel}}{\partial t} + \nabla_{\parallel} \Phi = \frac{T_e}{n_0 e} \nabla_{\parallel} n - \eta_{\parallel} j_{\parallel} \quad (3.184)$$

where  $T_e \nabla_{\parallel} n = \nabla_{\parallel} p_e$  and we keep the resistive friction between electrons and ions as in the resistive form of reduced MHD. This equation shows how Alfvén dynamics can be launched by pressure inhomogeneity, an effect which is missing in the MHD model. The physical picture is one of the parallel current responding to the difference in the two static forces represented by the parallel gradients of  $p_e$  and  $\Phi$ .

Corresponding to this is the change in the continuity equation. We can use the electron or ion one equivalently, as the vorticity equation gives the difference. The electron one makes the symmetry involving  $\nabla_{\parallel} p_e$  and  $j_{\parallel}$  obvious:

$$\frac{\partial n}{\partial t} + \vec{v}_E \cdot \nabla n + n_0 B \nabla_{\parallel} \frac{v_{\parallel}}{B} = \frac{1}{e} B \nabla_{\parallel} \frac{j_{\parallel}}{B} + n_0 \nabla \cdot \frac{1}{B^2} \vec{B} \times \nabla \left( \frac{T_e}{n_0 e} n - \Phi \right) \quad (3.185)$$

where we have redefined the velocities in terms of

$$v_{\parallel} = u_{i\parallel} \quad (3.186)$$

$$j_{\parallel} = n_0 e (u_{i\parallel} - u_{e\parallel}) \quad (3.187)$$

The extra terms (the ones not present in the reduced MHD continuity equation) are the ones involving the parallel current and the compression of the diamagnetic velocity. The fact that the dynamics is compressible is important: conservative energy transfer between this equation and Ohm's Law proceeds through  $\nabla_{\parallel}(j_{\parallel}/B)$  here and  $\nabla_{\parallel} p_e$  there. This is the energy transfer process which changes the dynamics, especially in the non-linear aftermath of any of the MHD instabilities.

The rest of the dynamics is the same as in reduced MHD, and in the same ordering limits as above the cold-ion two-fluid model system is given by

$$\frac{\partial \Omega_E}{\partial t} + \vec{v}_E \cdot \nabla \Omega_E = B \nabla_{\parallel} \frac{j_{\parallel}}{B} + T_e \nabla \cdot \frac{1}{B^2} \vec{B} \times \nabla n \quad (3.188)$$

$$\frac{\partial n}{\partial t} + \vec{v}_E \cdot \nabla n + n_0 B \nabla_{\parallel} \frac{v_{\parallel}}{B} = \frac{1}{e} B \nabla_{\parallel} \frac{j_{\parallel}}{B} + n_0 \nabla \cdot \frac{1}{B^2} \vec{B} \times \nabla \left( \frac{T_e}{n_0 e} n - \Phi \right) \quad (3.189)$$

$$\frac{\partial A_{\parallel}}{\partial t} + \frac{m_e}{n_0 e^2} \left( \frac{\partial j_{\parallel}}{\partial t} + \vec{v}_E \cdot \nabla j_{\parallel} \right) = \nabla_{\parallel} \left( \frac{T_e}{n_0 e} n - \Phi \right) - \eta_{\parallel} j_{\parallel} \quad (3.190)$$

$$n_0 m_i \left( \frac{\partial v_{\parallel}}{\partial t} + \vec{v}_E \cdot \nabla v_{\parallel} \right) + T_e \nabla_{\parallel} n = 0 \quad (3.191)$$

where all the pressure derivatives are written explicitly in terms of  $n$  and the electron inertia and resistivity effects on  $j_{\parallel}$  are kept in Ohm's Law. The only differences between this model and reduced, resistive MHD are the existence of  $\nabla_{\parallel} n$  and the electron inertia in Ohm's Law,  $\nabla_{\parallel}(j_{\parallel}/B)$  in continuity, and diamagnetic compression, also in continuity. The first two describe the energetic coupling between pressure disturbances and Alfvén dynamics, which constitutes the most important generalization to the MHD model at the qualitative level. The energy functional conserved by both models is the same but these terms provide an additional energy transfer effect. The consequences this has are summarized in the next section. The electron inertia is usually small for MHD instabilities, but it is the mechanism which allows for collisionless reconnection, so we have formally kept it here.

## 3.3.2.4. Relation to kinetic models

One further comment involves the correspondence between low frequency fluid models such as this to gyrokinetic and gyrofluid models. The gyrokinetic model, described in Chapter 2, is a method of taking the low frequency approximations at the kinetic level. A distribution function for gyrocentres rather than particles results. The physical picture treats particles as charged rings of finite gyroradius and the motion of the centres of these rings is followed (it is important to note however that the formal validity of the gyrokinetic model does not depend on the existence of closed orbits, rather, a local coordinate transformation). The part of the dynamics dependent on the gyroangle (position along the ring) appears as a contribution to the space charge density, the sum of which over species is assumed to vanish (the manifestation of quasineutrality). The gyrofluid model results from treating the density and parallel velocity (and temperature, etc.) moments of gyrocentres rather than particles. The simplest version assumes a perturbed distribution function given by

$$\delta f = F^M \left( \frac{\delta n}{n_0} + \frac{\delta u_{\parallel}}{T_0} p_{\parallel} \right) \quad (3.192)$$

for each species, where  $F^M(n_0, T_0)$  is a Maxwellian depending on background density and temperature parameters,  $p_{\parallel}$  is the gyrocentre parallel momentum, and  $\delta n$  and  $\delta u_{\parallel}$  are the gyrofluid density and parallel velocity dependent variables (if temperature dynamics is considered, then there are more moments). Integrating the gyrokinetic equation to find equations for these moments produces the isothermal gyrofluid model, and if this is done for electrons and ions in a plasma as described above the resulting equations are very similar to the two-fluid model above. Sparing the expense of displaying this and defining all the expressions, we merely note that the correspondence of the gyrofluid and two-fluid models has been proved in the limits under which the fluid models are derived (expansion in small gyroradii, dominance by collisions in the expressions for parallel viscosity and heat flux, and implicit assumptions in the derivation of the Braginskii fluid equations that specific conductive heat fluxes are small compared to corresponding velocities). However, the gyrofluid model is well behaved at all values of finite gyroradii and can be used to treat phenomena at scales between the electron and ion gyroradii, including the overlap between dynamics above and below the  $\rho_i$  scale. This turns out to be necessary in computational edge turbulence. The main limitation of a gyrofluid model is that formulations designed to treat trapped electron or ion effects are very problematic and none has been proved to be functional in that respect in direct comparison to kinetic results, especially non-linear results.

### 3.3.2.5. Qualitative two-fluid effects on MHD instabilities

The classical tearing mode is described by the resistive form of reduced MHD, with the details given in Section 2.1. Under the two fluid equations it is generalized as follows. Both the  $\vec{E} \times \vec{B}$  vorticity (hence the electrostatic potential) and the density react to the field line bending effects represented by  $\nabla_{\parallel} (j_{\parallel} / B)$ . If the tearing layer width is less than the ion sound gyroradius  $\rho_s = c_s / \Omega_i$  then the coefficients of  $\partial\Phi / \partial t$  are larger than those of  $(T_e / n_0 e) \partial n / \partial t$ , and the relative density disturbance reacting to the current dynamics is therefore larger. The “relative units” are set by the static force terms  $\nabla_{\parallel} \Phi$  and  $(T_e / n_0 e) \nabla_{\parallel} n$  in Ohm’s Law. If these disturbances are comparable, then it makes sense to scale  $\Phi$  versus  $T_e / e$  and then the coefficients of  $\nabla_{\perp}^2 \Phi$  give rise to the scale definition

$$\rho_s^2 = \frac{m_i T_e}{e^2 B^2} \quad (3.193)$$

and hence  $\rho_s = c_s / \Omega_i$ . With  $\rho_s^2 \nabla_{\perp}^2 > 1$ ,  $n$  takes over the role of  $\Phi$ , and the diamagnetic velocity replaces the  $\vec{E} \times \vec{B}$  velocity in the dynamics. This regime is referred to as “semi-collisional” for historical reasons. Additionally, any density gradient gives a real part to the frequency: in the ideal MHD system  $\omega^2$  takes real values because the linear equations are Hermitian, and linear disturbances are either purely growing/damped ( $\omega^2 < 0$ ) or purely oscillating. With a finite density gradient in the presence of a near-balance between  $\nabla_{\parallel} \Phi$  and  $(T_e / n_0 e) \nabla_{\parallel} n$ , the  $\vec{E} \times \vec{B}$  advection of the background gradient produces a rough balance between  $\partial n / \partial t$  and  $\vec{v}_E \cdot \nabla x$  times  $\partial n_0 / \partial x$ . Evaluating these coefficients, one obtains the tendency to produce a real frequency close to the diamagnetic frequency given by

$$\omega_* = \frac{T_e k_y}{e B L_n} = k_y \rho_s \frac{c_s}{L_n} \quad (3.194)$$

where  $L_n = |\nabla \log n_0|^{-1}$  is the density gradient scale length of the background, and  $y$  is a distance coordinate in the electron drift direction given by  $\vec{B} \times \nabla p_0$  of the background. The tearing mode can still be an instability, but the action of density disturbances in the dynamics and the partial cancellation of the static forces in Ohm’s Law changes the scaling of the growth rate. Growth rates are almost always much slower than  $c_s / L_p$  in a tokamak ( $L_p$  is the pressure profile scale length, which should be considered if the density profile is flat, in which case we would have  $L_n \gg a$ ). Ultimately, if temperature gradient and disturbance effects are considered, the instability can be stabilized, especially at  $\beta$  values of several per cent or in toroidal geometry. It re-emerges as a neoclassical tearing mode if trapped ion and bootstrap current effects are considered, but these processes are well outside the domain of the fluid models.

Kink instabilities have a similar origin to tearing except that the access to the free energy results from geometrical deformation rather than direct dissipation. Kink instabilities exist in ideal MHD and in a tokamak they can be described by reduced MHD (their consideration in the low frequency limit is what motivated the development of reduced MHD in the first place). The prototypical example in a tokamak is the  $m=1$  instability described in Section 2.3. The existence of a singular surface introduces similar narrow-layer effects as in the tearing mode. The diamagnetic effects referred to above also enter in a similar way, but with quantitative effects depending on each particular situation. At small  $\beta$  the Alfvén and sound wave dynamics separate perfectly in the two-fluid model. The reason a finite  $\beta$  matters is that it enters the ratio between  $\omega_*$  and the growth rate of any instability dependent on Alfvén dynamics (hence, any current driven instability).

A finite gyroradius (ratio of  $\rho_i$  to the layer width) can affect the existence of either of these instabilities. In a fluid analysis, the reason is the way the ion polarization current is modified. Recall that ion polarization results from an expansion in  $\omega/\Omega_i$ , whereby the lowest-order perpendicular velocity is placed into the inertia term. In a cold-ion model or an MHD model, this is the  $\vec{E} \times \vec{B}$  velocity  $\vec{v}_E$ . However, with finite ion temperature the ion diamagnetic velocity  $\vec{u}_{i*}$  adds to this, such that the derivative combination involves the ion force potential  $\Phi + (T_i / Ze) \log p_i$  (in an isothermal model  $T_i$  is constant and  $\log p_i$  is replaced by  $\log n$ ). Moreover, extra non-linearities result from the presence of  $\nabla \cdot \vec{\Pi}_i$  as the finite  $\rho_i \nabla \vec{u}_i$  tensor terms enter as dissipation free corrections. This is referred to as “gyroviscosity” for historical reasons and actually represents diamagnetic momentum flux. In the gyrofluid model these effects are equivalently treated though finite gyroradius non-linearities entering as additional advection terms. Recall that  $\rho_s$  enters through the tendency of  $\nabla_{\parallel} \Phi$  and  $(T_e / e) \nabla_{\parallel} \log p_e$  to balance in Ohm’s Law and the presence of  $\nabla_{\perp}^2 \Phi$  in the ion polarization. In an isothermal model both  $\log p_e$  and  $\log p_i$  are equivalent to  $\log n$  in the disturbances, so a coefficient of  $T_i$  rather than  $T_e$  represents  $\rho_i$  rather than  $\rho_s$ . Stabilization of the instabilities can result from the way  $\vec{v}_{\perp}^2 \log p_i$  responds to the advection of the background gradient by the  $\vec{E} \times \vec{B}$  velocity (so-called “ion diamagnetic stabilization” which is what “FLR stabilization” properly is). The non-linear phases are also affected by qualitative changes in the properties of the non-linearities (basically,  $\nabla \vec{v}_E : \nabla \nabla \Phi$  vanishes but  $\nabla \vec{v}_E : \nabla \nabla \log p_i$  does not).

Where these modifications have the greatest effect is with pressure driven instabilities. Indeed, for small scale turbulence the prototypical model assumes an “adiabatic response” in the electrons, which in a fluid model refers to the static force balance in Ohm’s Law. In a kinetic model this is derived by assuming the distribution function to vary directly with the disturbed Hamiltonian including  $e\Phi$  along the magnetic field lines. This “Boltzmann response” means the same thing as parallel force balance. But an adiabatic response is impossible within

MHD or reduced MHD due to the neglect of  $\vec{j} \times \vec{B}$  in the MHD version or  $\nabla_{\parallel} p_e$  in the low frequency version of Ohm's Law. Hence, if the tendency to develop an adiabatic electron response defines the properties of any mode or instability, then no form of single-fluid MHD can describe it. This is obviously true of ion temperature gradient microinstabilities (the so-called "ITG modes") as their prototypical form assumes strictly adiabatic electrons (and "ITG mode structure" is defined by near-adiabaticity in the electrons in the presence of ion temperature gradient and disturbance effects controlling the energetics). The most critical effects are on resistive ballooning modes. Due to the relatively short wavelength, the growth rate  $\gamma_L$  is usually smaller than  $\omega_*$ . Under these conditions either pure or semi-collisional MHD describes the instability well. The curvature terms due to  $\nabla p$  in the vorticity equation and  $\nabla \Phi$  in continuity describe a conservative transfer between thermal and  $\vec{E} \times \vec{B}$  free energy due to toroidal compression. When pressure gradient driven instabilities with  $\gamma_L < \omega_*$  become non-linear, the non-linear polarization current can become larger than the diamagnetic current in the divergences. In the non-linear stage the polarization and parallel currents can control the vorticity balance. This is subtle and can be demonstrated only by measuring the details of the mode structure and energetics. However, this consideration only affects small scale instabilities turning into turbulence. In a pressure driven disruption, the MHD instability is powerful enough to significantly relax the profile and the scales of motion are larger. With the smaller  $k_y \rho_s$  the dynamics is faster than  $\omega_*$  and at long wavelength the qualitative nature of the dynamics remains as described by MHD even when the quantitative results are changed by the coupling of the pressure disturbances to Alfvén dynamics.

### 3.3.3. Energetic particle physics and kinetic MHD

#### 3.3.3.1. Introduction

A considerable fraction of super-thermal particles generated by external heating or by fusion reactions changes substantially the linear and the non-linear behaviour of large-scale MHD instabilities and even introduces a completely new class of modes, the so-called energetic particle modes (EPMs). The crucial physical mechanism responsible for this is the resonant interaction of plasma waves with the periodic, tokamak-specific motion of the fast ions. This wave-particle resonance makes possible effective transfer of the energy that is "stored" in the spatial gradients and the gradients in velocity space of the energetic particle (EP) distribution function  $F_{hot}$  to the waves and vice versa. As a consequence, modes can be destabilized (or also stabilized, depending on the details of the mode and the fast particle distribution function), and hot particles are transported

radially outwards, leading to a loss of confinement and to a possible damage of the first wall.

In order to predict the stability boundaries for fast-particle-driven modes, not only do the details of the fast particle distribution has to be considered, but also the damping due to background kinetic effects has to be determined. This damping is due to electron and ion Landau damping, due to mode conversion to other, non-MHD waves and due to collisional damping. Whereas the latter damping mechanism is usually very small (collisionless regime), the conversion to secondary waves, for example to kinetic Alfvén waves (discussed later in detail) in form of continuum damping or radiative damping, is very sensitive to the equilibrium background profiles and can cause large damping, as discussed later. Therefore, already the prediction of linear growth rates can be challenging due to the delicate balance between damping and drive.

For determining the fast ion transport due to collective modes beyond the stability limits the non-linear saturation level of all excited modes has to be known. In principle, saturation is caused by the local flattening of the driving gradient due to the distribution of the fast ion population. However, the non-linear behaviour, especially for strongly driven cases, can also be oscillatory or bursty due to the formation of phase space structures, non-linear mode–mode coupling or the stochastization of the fast particle orbits.

Shear-Alfvén (SAW) and shear-Alfvén-acoustic (SAAW) waves are considered as the most important candidates for causing fluctuation induced transport of fast ions. In general, two types of modes exist: discrete or so-called ‘gap’ modes or Alfvén eigenmodes (AE) and energetic particle continuum modes (EPM). Whereas the properties of the AEs are essentially determined by the background plasma, i.e. mainly by the details of the SAAW continuum, the EPMs are dominated by the driving fast particle characteristics.

As pointed out above, the key difference to thermal plasmas is the importance of the resonant wave–particle interaction. Clearly, a fluid description for this problem is not sufficient. In fact, the correct description of these macro-scale modes requires meso-scale physics for the drive (drift-orbit-width of the energetic particles) as well as micro-scale physics for the damping (Larmor radius of the thermal ions). Due to the complexity of this multi-scale problem, up to date a fully-consistent non-linear numerical implementation is not yet available. For recent reviews and references on this subject refer to Refs [3.39–3.42].

### 3.3.3.2. Models

The number density of energetic particles in typical fusion plasmas is relatively small compared to the background plasma. However, due to their large kinetic energy the related pressure (moment proportional  $\sim v^2$ ) is comparable to the pressure of the background species. For that reason, the fast particle

dynamics is often introduced via a fast particle pressure tensor derived from drift or gyrokinetic models that account for the intrinsic wave–particle resonances in the Alfvénic frequency range far below the ion cyclotron frequency  $\Omega_{ci}$ . The fluid  $\nabla p$  pressure term in ideal MHD is replaced by an anisotropic  $\nabla p + \nabla \vec{P}_{hot}$ , leading to an extension of the energy principle of ideal MHD:

$$\omega^2 W_{kin} = \delta W_{MHD} + \delta W_{hot} \quad (3.195)$$

with  $\delta W_{MHD}$  being the energy functional described in Section 3.3.1.1.1 and  $\delta W_{hot}$  the potential energy contribution of the hot particles, with

$$\delta W_{hot} \sim \int dE d\mu dP_\phi d\theta d\phi \sum_{k=-\infty}^{\infty} \frac{\partial F_{hot}}{\partial E} \frac{(\omega - \omega_{*k}) |L_k|^2}{\omega - \omega_D - (nq - k)\omega_t} \quad (3.196)$$

$$\omega_{*k} = \frac{\partial F_{hot}}{\partial P_\phi} \bigg/ \frac{\partial F_{hot}}{\partial E} \quad (3.197)$$

This expression constitutes a phase space integral over all possible fast particle trajectories and all possible resonances of a mode of frequency  $\omega$  with the transit frequency  $\omega_t$  (and its harmonics, counted by the index  $k$ ) and with the precession drift frequency  $\omega_D$ .  $n$  is the toroidal mode number and  $q$  the safety factor. The real space integration variables are the poloidal angle  $\theta$ , the toroidal angle  $\phi$  and the generalized toroidal momentum  $P_\phi = Ze\psi + ZeR / \Omega_{ci} v_{\parallel} B_\phi$ . This expression for  $P_\phi$  is valid for axisymmetric systems and due to its dependence on the flux function  $\psi$  it can be used here as radial variable. The velocity phase space is represented by the single particle energy  $E$  and the adiabatically invariant magnetic momentum  $\mu$ .  $L_k$  are the Fourier coefficients of the linearized perturbed Lagrangian

$$\tilde{L} = Ze\vec{A} \cdot \vec{R} - Ze\tilde{\Phi} - \mu\tilde{B} \quad (3.198)$$

for the unperturbed particle motion in the potential of the wave characterized by  $\vec{A}$  (electromagnetic) and  $\tilde{\Phi}$  (electrostatic).

The complex or ‘resonant’ part of  $\delta W_{hot}$  describes the irreversible energy transfer from particles to waves or vice versa depending on the gradients of  $\partial F_{hot} / \partial E$  and  $\partial F_{hot} / \partial P_\phi$ . Mathematically, the complex contributions arise due to the velocity phase space integration over the resonances (Landau pole integration). The real or ‘non-resonant’ part leads to a small frequency shift and is usually neglected for perturbative problems such as Alfvén eigenmodes. However, in other cases such as energetic particle modes and sawtooth stabilization it plays an important role.

The presence of  $\delta W_{hot}$  destroys the self-adjoint structure of the ideal MHD operator. As a consequence, the system now has complex eigenvalues, i.e. purely

oscillating waves become damped or unstable. If it can be assumed that  $\delta W_{hot}$  is small compared to  $\delta W_{MHD}$ , Eq. (3.195) can be iterated: the zeroth order eigenfrequency and the mode structure are obtained by the solution of the ideal MHD equations, and the first order correction for the eigenvalue is determined via:

$$(\omega_r + i\gamma)^2 W_{kin} = \delta W_{MHD} + \delta W_{hot} \Rightarrow \frac{\gamma}{\omega_r} = \frac{\text{Im}(\delta W_{hot})}{2\omega_r^2 W_{kin}} \quad (3.199)$$

This expression gives an upper limit of the instabilities' growth rate since it does not include background damping and the energetic particles' influence on the eigenfunction.

For a more accurate and complete description, especially for mode conversion and mode damping, a number of additional physics elements beyond ideal MHD have to be introduced: the parallel electric field due to background damping and mode conversion, finite ion-Larmor-radius effects and finite orbit-width effects. The following two kinetic models can be employed.

The kinetic wave equations are derived from the linearized version of Vlasov's equation and therefore describe the stability of waves with harmonic time dependence. This ansatz allows formal integration over time and velocity space and leads together with Maxwell's equations to a 'constitutive relation' (or a dielectric tensor) that describes the relation between current and electromagnetic fields. Usually, this model is applied to high frequency (i.e. cyclotron frequency) phenomena, but in the last decade it has also been extended to low frequency regions, including the compressional and SAW regime. For global modes with small  $k_{\perp} \rho_i$ , the gyroaveraging operators can be expanded, transforming the system of integral equations into a sixth order differential equation.

In the framework of gyrokinetic theory several systems of kinetic equations can be derived: gyrokinetic MHD equations, where the compressional wave is usually filtered out by neglecting the perpendicular component of the vector potential  $A_{\perp}$  (fourth order differential equation), 'gyrogauge' equations that make full contact to the kinetic dielectric tensor model, and the gyrokinetic equations in the ballooning formulation. Within this framework, all species are treated on the same footing leading to a system of equations consisting of a quasi-neutrality equation, a vorticity equation and an equation for the evolution of the perturbed distribution function.

Deriving the shear Alfvén Law from this set of equations changes the ideal MHD result due to the presence of background finite Larmor radius effects from

$$\omega^2 = k_{\parallel}^2 v_A^2 \quad (3.200)$$

to

$$\omega^2 = k_{\parallel}^2 v_A^2 \left[ 1 + \rho_i^2 k_{\perp}^2 \left( T_e / T_i + \frac{3}{4} \right) \right] \quad (3.201)$$

This is the dispersion relation of the kinetic Alfvén wave (KAW). Clearly, the KAW is dispersive since  $\partial\omega/\partial k_{\perp} \neq 0$  and its damping rate can be determined straightforwardly via the imaginary part of the background plasma dispersion functions. Mathematically, the presence of a fourth order Larmor-radius term removes the shear Alfvén singularity of the ideal MHD operator and thus the  $\delta$ -function-like structure of the shear Alfvén continuum modes changes into a localized wave-like mode as can be seen in Fig. 3.20.

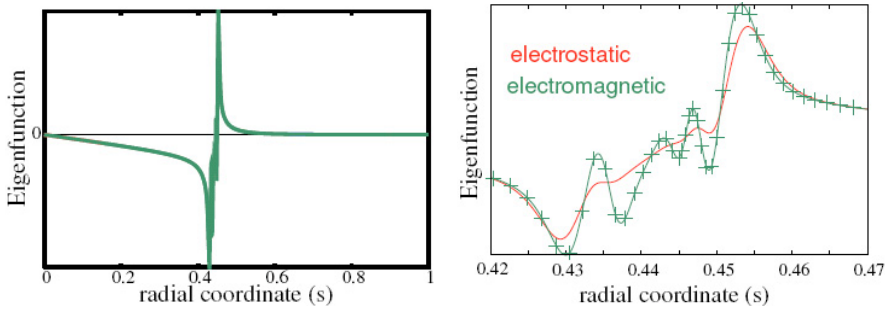


FIG. 3.20. Eigenfunction of a kinetic Alfvén wave (left), detailed view of the resonance layer (right): the singular structure of a MHD eigenfunction is replaced by an oscillating short wavelength feature. The red and the green line (the crosses indicating the radial resolution of the simulation) are the electrostatic potential  $\Phi$  and electromagnetic variable  $\psi$  with  $A_{\parallel} = (\nabla\psi)_{\parallel}$ , respectively.

The KAW is an important example for a coupling mechanism between a global shear Alfvén wave and a small scale kinetic wave that is beyond the hybrid MHD model. In the next section the importance of this ‘mode conversion’ will become obvious when the modifications of the eigenfunctions and the damping rates of global MHD modes will be discussed in detail.

### 3.3.3.3. Global modes in toroidal geometry

For typical equilibrium profiles of the magnetic field, the safety factor  $q$  and the density, the SAW resonance condition in a straight cylinder varies with the radial coordinate according to:

$$\omega^2 = k_{\parallel}^2 v_A^2 = \left(\frac{n-m/q(r)}{R}\right)^2 \frac{B(r)^2}{\mu_0 m_i n(r)} \quad (3.202)$$

leading to an SAW-continuum as plotted on the left of Fig. 3.21. Here,  $m$  and  $n$  are the poloidal and toroidal mode numbers. For any SAW propagating at a certain frequency there is at least one intersection with the continuum, leading to the excitation of a KAW at the resonant layer with strong damping as a consequence. Toroidal geometry removes the crossing points of two

neighbouring ( $m_1, m_2 = m_1 + 1$ ) continuum branches, generates ‘gaps’ (Fig. 3.21) in the SAW continuum and permits global modes within these gaps. The gap frequency  $\omega_{TAE}$  of the toroidal Alfvén eigenmode corresponding to two poloidal mode numbers  $m_1$  and  $m_2$  and toroidal mode number  $n$  can be obtained from the condition for the two corresponding parallel components of the wave vectors  $k_{m_{1,2}}(r) = nq(r) - m_{1,2} / Rq(r)$ :

$$k_{m_1}(r_m) = -k_{m_2}(r_m) \quad (2.203)$$

leading to

$$q_{m_1} = q(r_{m_1}) = \frac{m_1 + 1/2}{n} \quad (3.204)$$

and

$$\frac{\omega_{TAE}}{\omega_A} = \frac{n}{2m_1 + 1} \quad (3.205)$$

with  $\omega_A = v_A / R$ . This relation defines  $r_m$ , the radial position of the gap. The gap width is of the same order as the coupling terms, i.e. the inverse aspect ratio  $\varepsilon = r / R$ . Within the gap an even and an odd solution can be found: the even TAE is usually located at the low frequency boundary of the gap, however its exact frequency depends on the magnetic shear  $s = rq'(r_m) / q(r_m)$ . The odd mode is located at the high frequency boundary of the gap (see Fig 3.22).

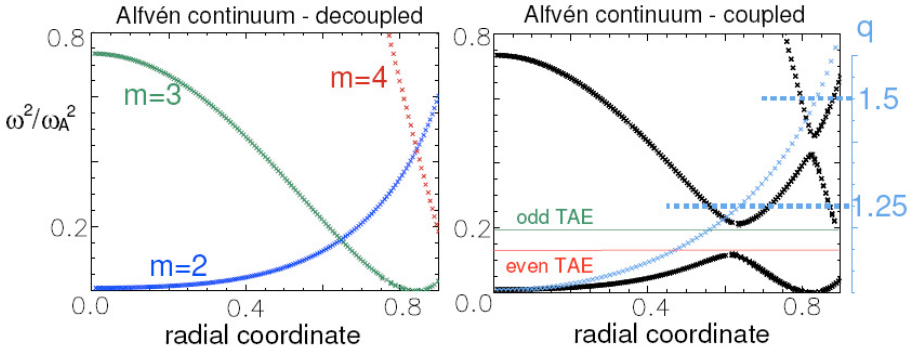


FIG. 3.21. In toroidal geometry the shear Alfvén continuum branches (here  $m = 2$  and  $m = 3$  and  $m = 3$  and  $m = 4$ ) couple and create gaps in frequency space ( $n = 2$ ).

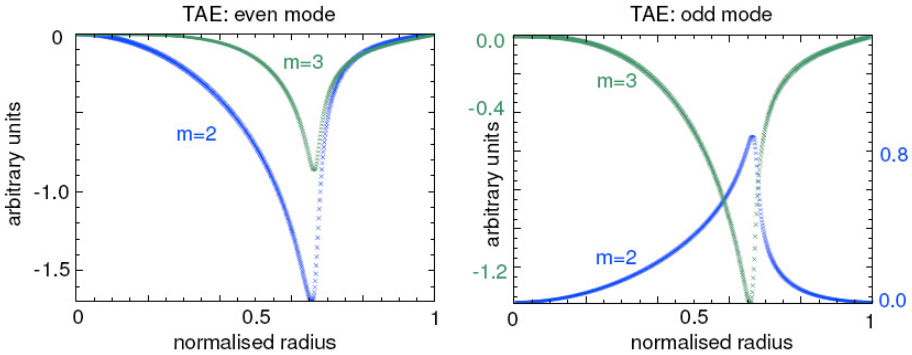


FIG. 3.22. Poloidal components of the TAE eigenfunction: even (left) and odd (right) mode.

Analogous to the TAE gap also further gaps of higher order, caused by the coupling of the  $m, m+2$  and  $m, m+3$  branches, arise. The corresponding gap modes are named by the equilibrium shape properties responsible for the higher order coupling: Figure 3.23 shows for example the ellipticity induced AE (EAE) gap and the non-up-down-symmetric AE (NAE) gap.

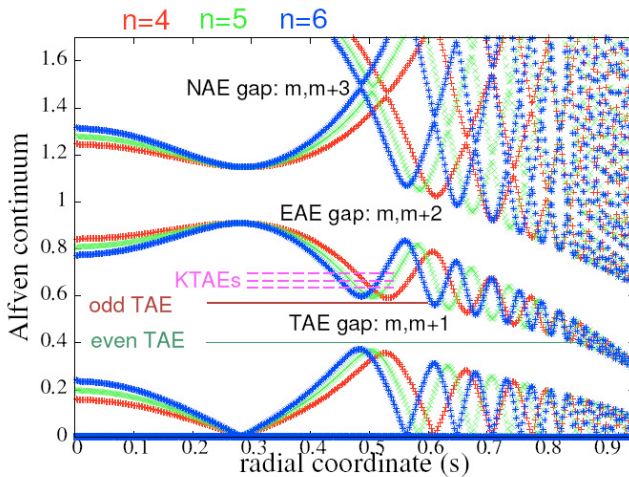


FIG. 3.23. The shear Alfvén continuum of the ASDEX-Upgrade shot # 21067 at 2.99 s shows not only the toroidicity induced gap (that is closed at the plasma edge) but also the ellipticity-induced gap and a small gap due to non-up-down symmetry.

Within the gaps there is no interaction (except radiative damping, see below) with the SAW continuum and therefore TAE modes are only weakly damped (typically  $\gamma / \omega \approx 0.01\% \dots 0.1\%$ ) by Landau damping (for higher densities/lower temperatures also trapped electron collisional damping plays a role). For typical profiles, however, the gap is often closed at the plasma edge

(see Fig. 3.23), resulting in an increased damping rate ( $\gamma / \omega \approx 0.5\% \dots 5\%$ ) due to mode conversion to a KAW (non-local continuum damping).

For a sufficiently large non-ideal parameter  $\lambda$

$$\lambda = \frac{4ms\rho_i}{r_m\hat{\epsilon}^{3/2}} \sqrt{\frac{3}{4} + \frac{T_e}{T_i}} \tag{3.206}$$

with  $\hat{\epsilon}^{3/2} = 5r_m / 2R$  that describes finite electric field effects (e.g. due to finite Larmor radii), radiative damping within the gap can become significant. This kind of damping is also called “tunnelling”: although there is no direct intersection with the shear Alfvén continuum, the kinetic Alfvén wave structure is present in the TAE mode. Figure 3.24 shows this tunnelling and the dependence of the damping on the background ion Larmor radius.

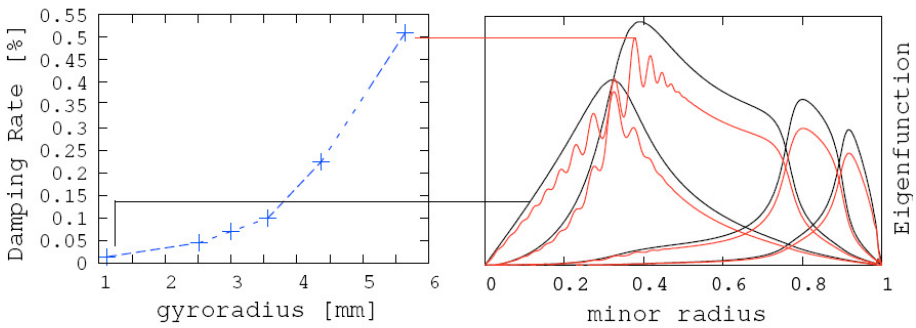


FIG. 3.24. The damping rate in dependence of the Larmor radius for a circular equilibrium based on JET shot #38573 at 5.0 s (left). On the right: eigenfunctions calculated for  $\rho_i = 1$  mm (black) and for  $\rho = 5$  mm (red).

Another type of TAE, called ‘kinetic TAE’ (KTAE) is found on top of the gap: KTAEs are generated by two KAWs that propagate towards each other and form a standing wave between the two continuum intersections at a given frequency. With increasing frequency the two intersections layers move away from each other, allowing for more and more maxima in between as shown in Fig. 3.25. The first four KTAEs with “quantum numbers”  $p = 0, 1, 2, 3$  are shown in this plot.

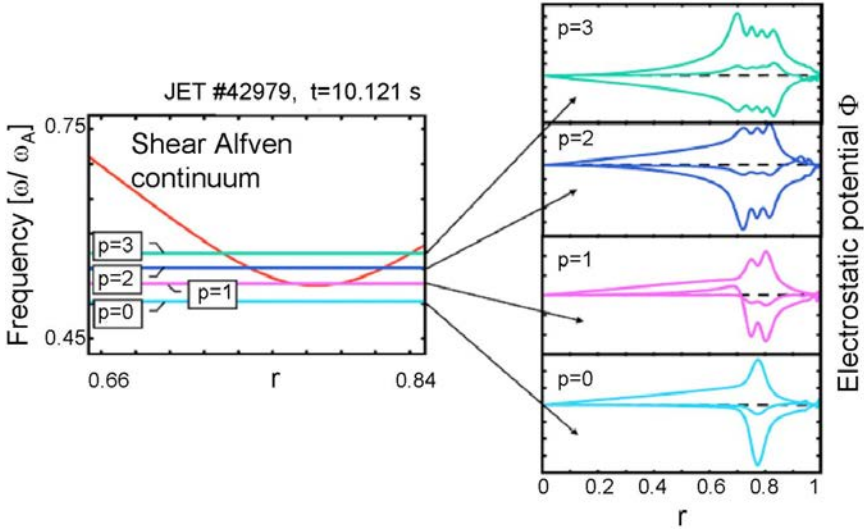


FIG. 3.25. The first four kinetic TAEs (KTAEs) at the upper boundary of the TAE gap.

Non-monotonic  $q$ -profiles can give rise to a further type of AE: a local minimum in the safety factor causes a local maximum in the SAW (see Fig. 3.26). On top of this maximum, no continuum damping is present and therefore a global AE called Alfvén cascade mode (AC) with one dominant poloidal mode number can exist (depending also on pressure, density and their profile lengths). Its frequency follows the dispersion relation

$$\omega_{AC}(t) \approx \left| \frac{m}{q_{\min}(t)} - n \right| \frac{v_A}{R} \quad (3.207)$$

tracing the evolution of the  $q$ -profile. Therefore, from the experimental signal of ACs the time evolution of the  $q$ -profile can be inferred. As  $q_{\min}$  approaches  $q_{TAE}$  the AC starts to develop two dominant poloidal harmonics and finally transforms into a TAE.

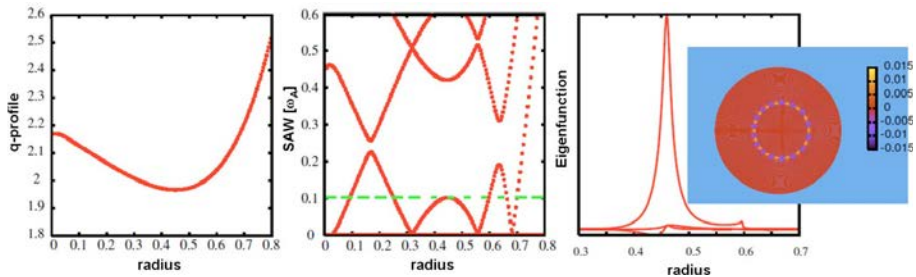


FIG. 3.26. Non-monotonic  $q$ -profile, the corresponding shear Alfvén continuum and mode structure of an Alfvén cascade.

The coupling of the shear Alfvén branch and the ion acoustic branch due to finite compressibility and toroidicity gives rise to more gaps and gap modes. The most prominent gap mode in this lower frequency regime  $\omega_A > \omega > \omega_*, \omega_{ti}$  (with  $\omega_{ti}$  the ion thermal transit frequency) is the  $\beta$ -induced Alfvén eigenmode (BAE) (whose kinetic dispersion relation is degenerate with the geodesic acoustic mode ( $k_{\parallel} = 0$ ) in the long wavelength limit and if diamagnetic effects are neglected):

$$\frac{\omega^2}{v_A^2} - k_{\parallel}^2 - \frac{2c_s^2}{v_A^2 R_0^2} = 0 \quad (3.208)$$

$$c_s^2 = (7/4 + T_e / T_i) T_i / m_i \quad (3.209)$$

Due to sideband coupling ( $m \pm 1$ ) another gap below the BAE gap arises, the so-called  $\beta$ -induced Alfvén-acoustic gap (BAAE).

Including consistently diamagnetic drift terms modifies further the shear Alfvén-acoustic continuum structure, especially if density and temperature gradients are large. In the simplest limit, the substitution  $\omega^2 \rightarrow \omega(\omega - \omega_{*p})$  with  $\omega_{*p} = \omega_{*n} + \omega_{*T} = m_i / (eB) k_{\theta} (\nabla n / n + \nabla T / T)$  accounts for this modification. This extension allows us to describe the transition from the BAE branch to the purely pressure driven and small scale kinetic ballooning branch. Furthermore, finite  $\nabla T_i$ -effects give rise to another potentially unstable branch, the Alfvénic ion temperature gradient (AITG) modes that become unstable, if  $\omega \omega_{*T_i} > \omega_{ti}$  (with  $\omega_{*T_i} = m_i / (eB) k_{\theta} (\nabla T_i / T_i)$ ) is fulfilled (no energetic particle drive needed for destabilization).

For low  $n$ -numbers however, these low frequency modes are usually more heavily damped than the TAEs or ACs, predominantly by ion-Landau damping. Nevertheless, BAEs and BAAEs are seen regularly during strongly heated discharges in present day experiments.

### 3.3.3.3.1. Mode drive and energetic particle modes (EPMs)

So far, a short survey over the most important potentially unstable MHD and kinetic MHD modes has been given. For determining their stability in the presence of a fast particle population, a third species has to be added to the system of equations. Note that due to their small number density compared to the plasma background, the energetic particles can be neglected in the quasi-neutrality equation. A close inspection of the term responsible for the fast particle drive (Eqs (3.196, 3.197)) shows that the magnetic curvature drifts (hidden in the integrals over the unperturbed particle motion) play a crucial role. Due to this fact, the energy exchange between mode and particles becomes efficient if the characteristic energetic ion drift orbit width and the perpendicular wavelength of

the mode  $k_{\perp}$  are comparable. Whereas for present day tokamaks this condition favours typically modes with  $n = 2 \dots 7$  (depending on the heating scheme), it is expected that for ITER ( $\alpha$ -particle drive, higher magnetic field) modes with  $n = 7 \dots 15$  will dominate.

Inserting, for example, the TAE-frequency and the corresponding  $q_{TAE}$  (Eqs (3.204, 3.205)) in the resonance condition (denominator of Eq. (3.196)), leads to a condition for the parallel velocity of the fast particles

$$v_{\parallel} = \frac{v_A}{|2p-1|} = v_A, v_A/3, \dots \text{ for } p = 0, 1, \dots \quad (3.210)$$

illustrating that not only particles fulfilling the primary resonance  $v_{\parallel} = v_A$  contribute to the mode drive but also particles with lower energies  $v_{\parallel} = v_A/3$  via higher order resonances.

As indicated in the introduction, the second ingredient for mode drive is a sufficiently large gradient of the energetic particle distribution function. For the  $\alpha$ -particle drive of low- $n$  TAE modes the formula [3.43]

$$\frac{\gamma}{\omega} = \frac{9}{4} \beta_{EP} \left( \frac{\omega_{* \alpha}}{\omega} - \frac{1}{2} \right) F \left( \frac{v_A}{v_{\alpha}} \right) \quad (3.211)$$

with  $F(x) = x(1 + 2x^2 + 2x^4)e^{-x^2}$  demonstrates that the drive due to the spatial gradient ( $\omega_{* \alpha} = -(k_{\theta} T_{\alpha}) / (e_{\alpha} B_0) (\nabla \beta_{EP} / \beta_{EP})$ ) has to overcome (in addition to the background damping, as discussed in the last section) the damping due to the energetic particles themselves via the  $\partial F / \partial E$ -term that is always negative for a slowing down  $\alpha$ -particle population (represented by the  $-1/2$  term). (In Eq. (3.211) the slowing-down distribution of the thermonuclear  $\alpha$ -particle is described by the normalized energy density  $\beta_{EP}$ , an effective average particle energy  $T_{\alpha}$  and a corresponding velocity  $v_{\alpha}$ .)

A completely new branch of unstable modes are the energetic particle modes (EPMs). These modes are no eigenmodes of the background plasma but rather “forced oscillations” with a frequency determined alone by the fast particle characteristic frequency (usually the transit frequency  $\omega_t$ ). Clearly, the drive has to be strong enough to overcome the continuum damping. For demonstrating the difference between gap eigenmodes and EP-continuum modes, a generalized fishbone dispersion relation can be derived:

$$-i\Omega + \delta W_{core} + \delta W_{hot} = 0 \quad (3.212)$$

where  $\Omega$  is a generalized inertia term and  $\delta W_{core}$  and  $\delta W_{hot}$  are the potential energy contribution due to the plasma background and the hot particles, respectively. For TAEs, for example,  $\Omega^2 = (\omega_l^2 - \omega^2) / (\omega_u^2 - \omega^2)$  with  $\omega_l$  and  $\omega_u$  being the lower and the upper shear Alfvén continuum gap frequency. For  $\Re(\Omega) < 0$  one obtains the usual gap mode, and for  $\Re(\Omega) > 0$  the energetic

particle continuum modes. It should be noted that all terms of Eq. (3.212) can be of the same order and therefore Eq. (3.212) is non-perturbative.

### 3.3.3.3.2. Non-ideal and fast particle effects on the $m = 1, n = 1$ mode

As discussed in Section 3.3.1.1, the ideal MHD stability of the  $m = 1, n = 1$  internal kink mode in a tokamak is determined by higher order terms ( $\varepsilon^4$ ). Therefore, non-ideal effects such as energetic particles compete with the small MHD contributions to  $\delta W_{MHD}$ . Both situations, stabilizing and destabilizing, are possible in the presence of fast particles.

The fast particle stabilization of the low frequency (1,1) MHD mode is a consequence of the conservation of the third adiabatic invariant of the particle motion that in a tokamak corresponds to a conservation of the poloidal magnetic flux through the area described by the trajectory of the precessional drift motion in the toroidal direction. The adiabatic invariance of this quantity is ensured if the time the particles need to complete a full orbit  $\tau_D = 2\pi / \omega_D$  is short compared to the mode's characteristic time  $2\pi / \omega$ . In a tokamak  $\omega_D$  is given by the following expression:

$$\omega_D = [\vec{v}_D \cdot \nabla(\phi - q\theta)]^{(0)} = \frac{v_{D0}}{r} [(\cos\theta)^{(0)} + \hat{s}(\theta \sin\theta)^{(0)}] \quad (3.213)$$

where  $v_{D0} = \mu / (m\Omega R)$  is the vertical magnetic drift,  $\Omega = ZeB / m$ ;  $\mu B = mv_{\perp}^2 / 2$ ;  $\hat{s} = r / q(dq / dr)$  the magnetic shear and  $\phi$  and  $\theta$  the toroidal and poloidal angle, respectively. The superscript  $(0)$  denotes the bounce average operator. If a low frequency perturbation is trying to adiabatically change the flux through these orbits, the orbits will tilt or shift in space in order to preserve this flux. Depending on the details of the fast particle distribution function (especially the anisotropy plays an important role here) and on the  $q$ -profile, this can result in a positive sign for  $\delta W_{hot}$ , i.e. the mode has to do positive work to the fast particles, i.e. they can have a stabilizing influence on the mode according to the generalized energy principle given in Eq. (3.195). As a consequence the internal kink growth rate is reduced and since the internal kink is considered as triggering mechanism for so-called sawtooth crashes the sawtooth-free period in a tokamak discharge can be greatly extended by the presence of energetic particles.

If the third adiabatic invariant breaks down, for example if the fast particles are not energetic enough, or the fast particle density exceeds a critical threshold, the (1,1) mode can be destabilized. In this case, the gradients of the resonant trapped ion distribution function and background diamagnetic effects provide the energy reservoir that drives the mode. The corresponding unstable branches are called precessional and diamagnetic fishbones. In the first case an energy transfer

occurs due to the resonance between the toroidal precession frequency  $\omega_{Dh}$  of fast trapped ions (i.e. the frequency with which the banana tips of a trapped particle orbit drift in the toroidal direction) and the kink mode. The energy is tapped from the spatial and/or velocity space gradients of the fast ion distribution function, similar to the TAE case describe above. Writing down the energy principle (Eq. (3.195)) for this case leads to

$$-\frac{i(\omega(\omega - \omega_{*i}))^{1/2}}{\omega_A} + \delta W_{MHD} + \delta W_{hot} = 0 \quad (3.214)$$

with

$$\delta W_{hot} \sim \int d^3v dr \frac{\partial F_{hot}}{\partial r} \frac{\omega}{\omega - \omega_{Dh}} \phi(\omega, \vec{v}, r) \quad (3.215)$$

showing that the resonance condition in this case is indeed  $\omega = \omega_{Dh}$  and that the drive depends again on the radial gradient of the distribution function. Whereas the first two terms describe the MHD part of internal kink mode, the third term accounts for its destabilization below the ideal-MHD threshold. The associated instability is called fishbone mode because of its bursty pattern: the missing drive after the resonant particles have been expelled by the mode leads to a “cyclic” behaviour that is observed in several diagnostics.

The branch related to  $\omega_{*i}$  in Eq. (3.214) is called diamagnetic fishbone, where  $\omega_{*i} = k_\theta / (eBn_i) (\partial p_i / \partial r)$  and  $k_\theta = -m / r = -1 / r$  have to be evaluated at the  $q = 1$  surface. It can be excited in situations where the fast particle density is not high enough to trigger the precessional fishbones. The driving force in this case is the gradient of the background thermal ions. Furthermore, for the instability to develop, a “viscous” dissipative force is required, for example produced by a mode–particle resonance that scatters energetic ions. It can be shown that the drive becomes optimal when  $\omega_{Dh} \sim \omega_{*i}$ .

Figure 3.27 shows the relationship between the two fishbone types for a given normalized growth rate  $\hat{\gamma}_{MHD} = (\omega_A / \bar{\omega}_{Dh}) \gamma_{MHD} = 0.1$ , where  $\bar{\omega}_{Dh}$  is the energy averaged precession frequency of the hot particles and  $\bar{\omega}_{Di}$  that of the thermal particles. Experimentally, both branches can be observed but also intermediate situations where both excitation mechanisms are present simultaneously can be realized.

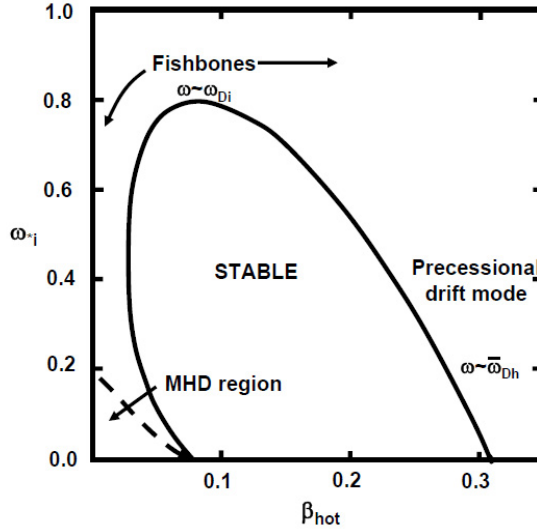


FIG. 3.27. Stability diagram of the fishbone mode in the  $\beta_{hot} - \omega_i$  plane [3.44, 3.45].

### 3.3.3.3. Non-linear fast particle dynamics

For ITER it is expected that the energetic particle (EP) drive will be strong enough to destabilize AEs and/or EPs. Therefore, their non-linear behaviour, possible saturation mechanisms and the related EP-transport will be one of the main research topics at ITER.

For weakly unstable AEs with  $|\gamma/\omega| \sim 10^{-2}$  it was found that the simple bump-on-tail model explains successfully many of the complex non-linear features observed experimentally. According to this model, near marginal stability the mode evolution is determined by four characteristic quantities: the linear growth rate,  $\gamma_l$ , the damping rate  $\gamma_d$ , the resonant frequency  $\omega_b$  of EPs that are trapped in the potential well of the wave and the effective collision frequency  $\nu_{eff}$  for the EPs to be scattered out of this resonance by collisions or other stochastic processes. Due to the formation and the evolution of holes and clumps in phase space mode, chirping with  $\delta\omega \sim \sqrt{\delta t}$  can occur. Furthermore, repetitive bursts and frequency splitting of a single-frequency mode can be explained with this model.

Another saturation mechanism for weakly unstable AEs is due to mode-mode coupling via the  $(n=0, m=0)$  zonal fields that are generated by the beating of several unstable modes with similar  $n$ . The transport associated with single AEs is expected to scale linearly with the perturbed mode amplitude  $\sim \delta B / B$  if the perturbation stays below a stochastic threshold (for a single AE typically  $\sim \delta B / B \sim 10^{-3}$ ). The loss mechanism (or radial transport) in this case

is related to the “scattering” of an energetic particle due to the wave across a topological boundary (e.g. passing-trapped boundary). Above the stochastic threshold (that might be reduced significantly for multiple modes to typically  $\sim \delta B / B \sim 10^{-4}$ ) the transport scales with  $\sim (\delta B / B)^2$ . Since the EP-orbit widths in ITER will be quite small compared to the system size, the latter transport mechanism is expected to dominate.

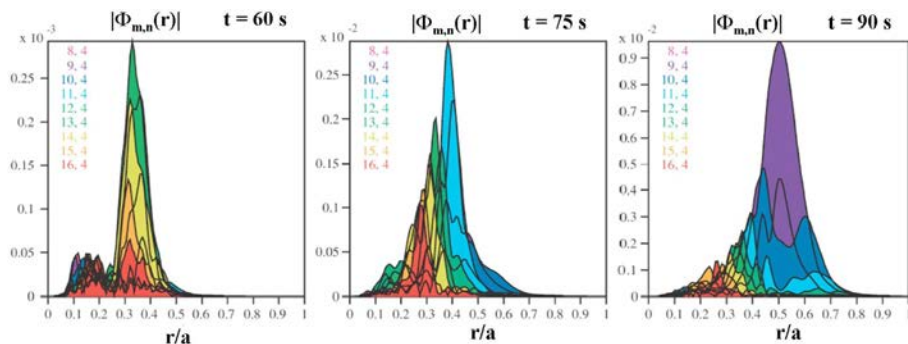


FIG. 3.28. Radial structure of a typical EPM scalar potential fluctuation, with  $n = 4$  and decomposed in (toroidally coupled) poloidal Fourier harmonics  $m = 8\text{--}16$ . The radial envelope of the EPM wave-packet propagates radially as time progresses from left to right. Here, time is in units of  $\tau_A = R_0 / v_{A0}$ . (Numerical results obtained with the HMGC code [3.46].) Reproduced from Ref. [3.46]. Copyright (2010), American Institute of Physics.

If the system is far above the stability threshold, there may be enough energy available (usually due to a steep enough radial EP-gradient) to destabilize the strongly damped EPs. In this case, the transport occurs in avalanche-like events, where an unstable front is convectively amplified as it moves radially outwards (see Fig. 3.28). Both the radial gradient and the mode structure change on a very fast timescale (typically 100–200 Alfvén times,  $\tau_A = R_0 / v_{A0}$ ) and therefore no stochasticization of particle orbits in phase space can take place. Clearly, this regime needs a non-perturbative treatment.

Numerical simulations in this field are mostly based on global hybrid-MHD codes. In these models the core plasma is described by non-linear MHD equations and the EP-dynamics is taken into account by the fast ion pressure tensor (as described above). However, more sophisticated kinetic models have to be implemented for shorter wavelength modes (Alfvénic turbulence).

### 3.4. EXPERIMENTAL OBSERVATIONS OF MHD MODES

As has become evident already from the theoretical sections, macroscopic plasma perturbations are a multifaceted and still expanding field of research. In particular the application of new diagnostics, or the extension of the frequency

range of existing ones has repeatedly led to the observation of qualitatively new phenomena. By and large this constitutes a highly gratifying field of research, characterized by a fruitful interplay of theory and experiment. Most often this has produced a satisfactory understanding of observations and in several cases has suggested strategies for active control or suppression of instabilities. Some, rather complex – partly non-linear – phenomena have even first been postulated by theory, before being identified in experiments (notably the neoclassical tearing modes).

Only a fraction of them — albeit the most important one — lead to unlimited growth of the perturbations and ultimately to a disruption as described in Section 3.5. Many, instead, give rise to a limit-cycle behaviour, and are instrumental in keeping time-average gradients of plasma parameters constant. In this function they are beneficial by avoiding larger gradients and possibly fatal instabilities, but may become in larger devices also by themselves a menace to the integrity of in-vessel components (e.g. ELMs). When limited to tolerable amplitude and theoretically well understood they can constitute sensitive tools of plasma diagnostics, giving, for example, the precise location of resonant surfaces.

### 3.4.1. Internal kink modes

The  $(m,n) = (1,1)$  mode is observed in tokamak discharges as soon as the minimum  $q$  value is close to or below 1. Although sometimes continuous  $(1,1)$  mode activity is found, the most prominent feature are sawtooth oscillations: quasi-periodic magnetic reconnection events, often accompanied by  $(1,1)$  precursor oscillations. Sawteeth have been first observed at the ST tokamak. Their name results from corresponding time traces of central soft X ray measurements (essentially equivalent to the central electron temperature): the quasiperiodic oscillations start with a slow rise followed by a sudden fall (see Fig. 3.29).

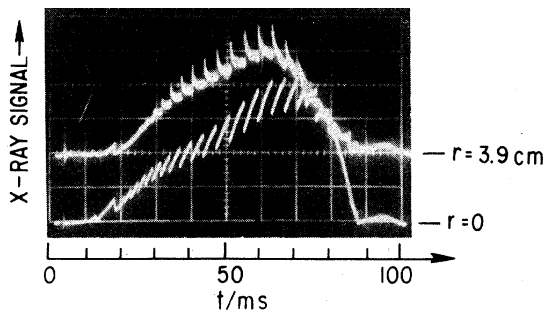


FIG. 3.29. Oscillograms of soft X ray (SXR) emissions demonstrating the typical sawtooth oscillations in the plasma centre (ST tokamak). The sawtooth is “inverted”, showing a fast rise and a slow exponential drop if one considers a region away from the plasma centre. Reprinted from Ref. [3.47]. Copyright (2010), American Physical Society.

As seen in Fig. 3.29, the sudden decrease in the central electron temperature is accompanied by a corresponding temperature rise at a larger minor radius, indicating a rapid transport of energy from the region inside the  $q=1$  surface outwards. Right after the sawtooth crash, the electron temperature profile inside the so-called “mixing radius” is completely flat, the temperature gradient re-establishes afterwards on a much longer timescale, consistent with the local energy confinement time. As the  $q=1$  radius is typically about 20–40% of the minor plasma radius, the effect of sawteeth on energy confinement is usually benign. Actually sawteeth can be very beneficial for stationary plasma conditions, in particular due to their effect on the distribution of high- $Z$  impurities: they counteract their tendency to accumulate in the plasma centre.

The actual sawtooth crash is usually preceded by a (1,1) precursor oscillation. Sawteeth without any detectable precursor activity have been observed, however, in high temperature discharges as well. Although it is not yet clear if the sawtooth precursors are of ideal or resistive character, the sawtooth crash certainly involves reconnection. The timescale on which the crashes occur ( $\sim 100 \mu\text{s}$ ) is however not consistent with a simple resistive MHD description. By inclusion of two-fluid effects, in particular the parallel electron pressure gradient and electron inertia, the theoretically predicted timescales are much closer to the experimentally observed crash times.

According to the Kadomtsev model described in Section 3.3.1.3 (and any non-linear resistive MHD theory) the whole region inside the  $q=1$  radius should be involved in the reconnection event, resulting in a  $q$  value above 1 everywhere in the plasma. This “full reconnection” model, however, contradicts many experimental observations in which only partial reconnection was found. Measurements of the minimum  $q$  value by Faraday rotation or motional Stark effect (MSE) measurements often show a much weaker variation of the  $q$  profile as demonstrated in Fig. 3.30 for a TFTR discharge, where the central  $q$  value varies between 0.7 and 0.8 only. Even for such partial reconnection events, sawteeth prevent extreme peaking of the current profile by both direct influence on the current profile as well as by limiting the peaking of the temperature (and thus the resistivity) profile.

Although in present day experiments the direct influence of sawteeth on plasma confinement is small, there are worries that much larger sawteeth associated with a large  $q=1$  radius might occur in a tokamak reactor. The reason is the experimental observation of so-called “monster sawteeth”, which have been found in discharges with intense ion cyclotron heating (Fig. 3.31). These discharges are characterized by a much larger sawtooth period that can well exceed the energy confinement time. This effect is believed to be caused by a stabilizing influence of the very energetic minority ions (reaching energies in the MeV range) on the internal kink mode.

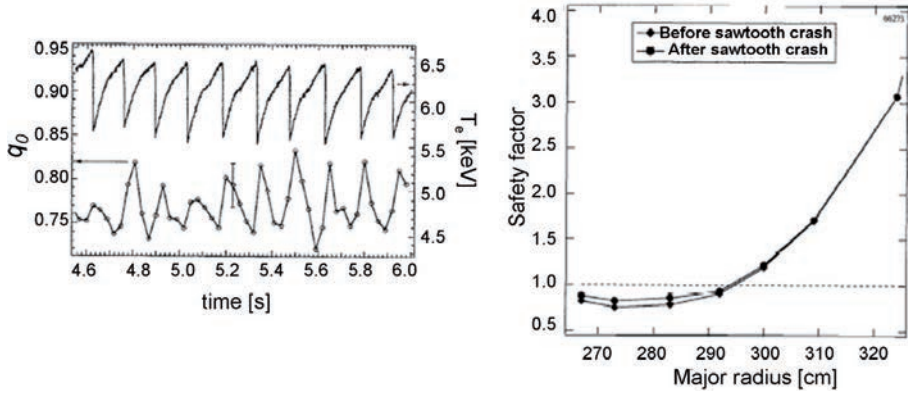


FIG. 3.30. Time evolution of the central safety factor  $q_0$  (left) and  $q$  profiles derived from motional Stark effect (MSE) before and after a sawtooth on TFTR. Reprinted from Ref. [3.48]. Copyright (2010), American Institute of Physics.

In such discharges, sawteeth do not efficiently limit the central temperature, which might even saturate well before a sawtooth appears. The resulting peaking of the current profile leads to an increase of the  $q=1$  radius (up to 50% of the minor plasma radius). The eventually appearing sawtooth has much larger amplitude and might have significant consequences.

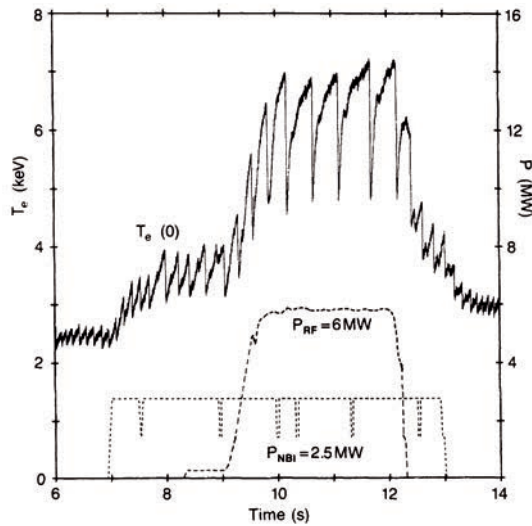


FIG. 3.31. Time trace of the central electron temperature during sawtooth activity showing increasing amplitude and period during additional heating in a JET discharge. Particularly large amplitude (“monster”) sawteeth are observed during the RF heating period. Reprinted from Ref. [3.49]. Copyright (2010), American Physical Society.

According to the theory, the stability of the internal kink mode (for resistive MHD as well as in two-fluid theory) should be strongly dependent on the magnetic shear close to the  $q=1$  surface. Such dependence has indeed been found: sawteeth appear only above a certain critical magnetic shear. This behaviour offers a possibility for sawtooth control that might be required in reactor relevant conditions when the fast  $\alpha$  particles stabilize sawteeth as it was found for the energetic ICRF heated minority ions. The most efficient way for localized modifications of the current profile is electron cyclotron current drive. It has been demonstrated that localized co-current drive just outside the  $q=1$  surface (lowering the magnetic shear there) stabilizes sawteeth, whereas steepening the current gradient at  $q=1$  destabilizes sawteeth.

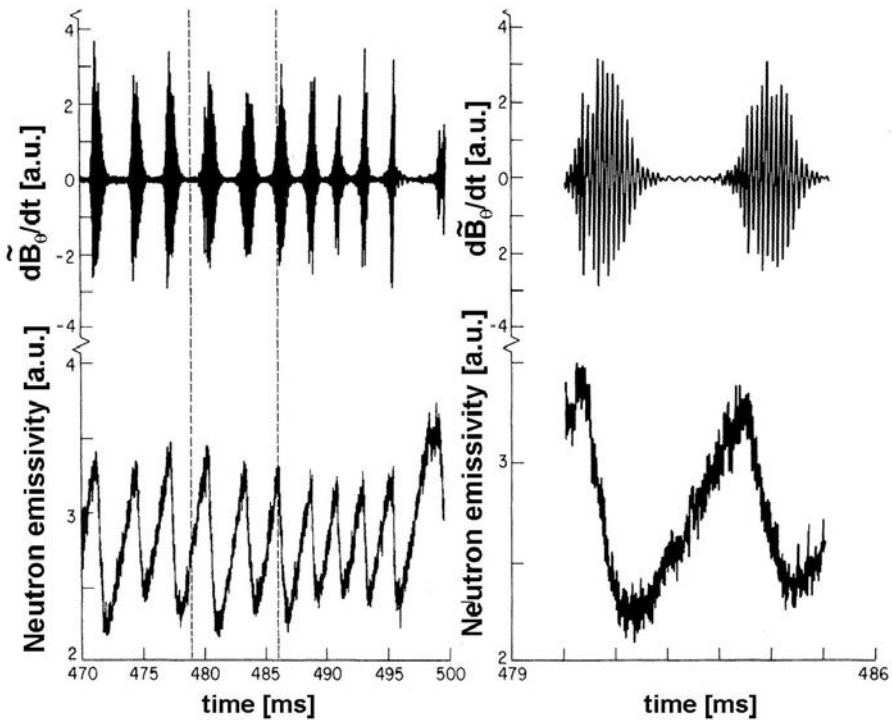


FIG. 3.32. Time evolution of the  $dB_{\theta}/dt$  signal and the neutron flux during fishbone activity on PDX (left), zoom into the data (right). Reproduced from Ref. [3.50]. Copyright (2010), American Physical Society.

The example of monster sawteeth discussed above has already demonstrated that non-thermal particles may have a significant influence on the stability properties of internal kink modes. Besides the stabilizing effect discussed there, energetic ions may as well destabilize the mode. A prominent example for such an effect is the occurrence of fishbone oscillations, named according to the

shape of the magnetic oscillations  $dB/dt$  associated with this mode (Fig. 3.32). Fishbones are bursts of (1,1) mode activity that are accompanied by a radial redistribution or even a loss of fast ions. This effect is demonstrated in Fig. 3.31 by the reduction in the neutron rate (the huge majority of D-D fusion reactions in present day deuterium plasma experiments is caused by collision of fast ions with the background plasma).

As discussed earlier, in the case of fishbones, the ideal internal kink mode is destabilized due to a resonance of the mode frequency with a characteristic frequency of the fast particle motion, usually the precessional drift frequency of the energetic ions. The actual source of free energy to drive the mode is the radial gradient in the fast ion distribution function. The energy transfer from the fast ions to the kink mode results in an outward motion of the fast ions and thus in a reduction of the radial gradient of the fast ion density. This fact explains why the mode frequency is chirping down during a burst as seen in Fig. 3.33: the mode activity starts with the highest frequency, with the mode being in resonance with the precessional drift of the most energetic ions. As the mode grows, the redistribution of the resonant fast ions reduces the mode drive. An ideal mode, however, is free to choose any rotation frequency with respect to the plasma. At a somewhat lower frequency it can gain energy via a resonant interaction with less energetic ions.

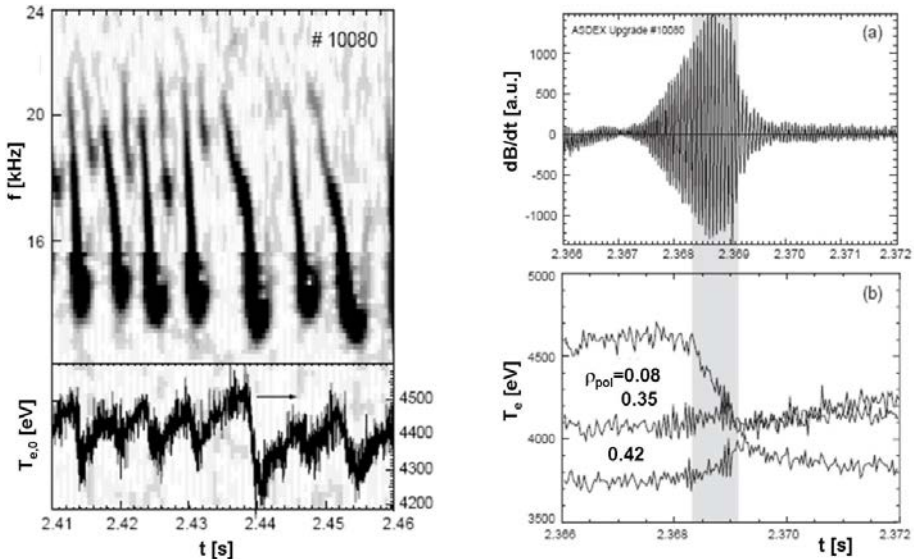


FIG. 3.33. Left: Wavelet plot of fishbone activity from a central SXR channel together with the central electron temperature as measured by electron cyclotron emission (ECE). Right: Mirnov signal ( $dB/dt$ ) together with the temperatures at several plasma radii for one fishbone [3.51].

As expected for an ideal mode, small fishbones do not influence the parameters of the background plasma. As shown in Fig. 3.33, however, fishbones with large amplitudes have a very similar influence for example on the electron temperature and the impurity density profile as discussed above for sawteeth, although the magnitude of the resulting modifications by a single fishbone is much smaller.

### 3.4.2. Classical tearing modes

As discussed above, tearing modes are driven by the negative current gradient just inside the corresponding rational surface (classical tearing mode). As the pressure gradient at the rational surface is, however, stabilizing in a tokamak, tearing modes are usually linearly stable. Exceptions are, for example, special current profiles as they occur during the current buildup in a tokamak, just prior to a disruption or in advanced tokamak scenarios, where two low order rational surfaces may appear radially close to each other. Nevertheless, tearing modes play an essential role in the MHD stability of a tokamak as they are often non-linearly unstable in high beta plasmas due to the flattening of the pressure gradient inside “seed” magnetic islands and the associated drive due to the loss of bootstrap current in the island (neoclassical tearing modes).

During the current ramp up, the  $q$  value at the plasma edge (actually well defined in limiter tokamaks only) decreases and passes low order rational surfaces. This situation is destabilizing both for the external kink mode as well as for tearing modes at the plasma edge. Corresponding mode activity is indeed being observed, in particular in limiter tokamaks: one finds a subsequent onset of  $n=1$  mode activity, starting with high  $m$  numbers (corresponding to high  $q$  values), decreasing in time (Fig. 3.34). These modes are called “Mirnov oscillations”. The modes observed are found to rotate in the electron diamagnetic drift direction which is characteristic for resistive modes. A distinction between a resistive external kink or a tearing mode is quite artificial as the region “outside the plasma” anyway corresponds to a highly resistive, low density plasma. Therefore an external kink mode (associated with the resonant surface located in the vacuum region) actually is equivalent to a tearing mode: the magnetic perturbation creates a fast growing magnetic island with the growth rate determined by the large plasma resistivity and finite mass density in that region.

Tearing modes often act as precursors to disruptions: If the plasma resistivity increases by, for example, too strong gas puffing or impurity influx due to contact with the wall, the current profile becomes steepened. If the steep region extends to the  $q = 2$  surface, a classical (2,1) island starts growing. The rotating magnetic perturbation induces eddy currents in the wall, resulting in a torque and thus a decelerating force onto the mode. This force, being proportional to the square of the perturbation field, leads to mode locking, as

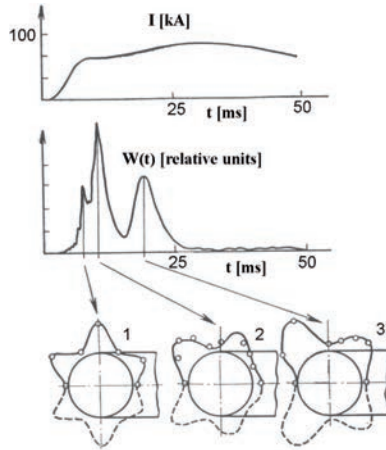


FIG. 3.34. Plasma current and magnetic field perturbations as measured by magnetic coils early in a T-3 discharge together with the poloidal structure of the perturbations in polar coordinates. Decreasing  $q$ -values at the plasma edge result in subsequent  $m = 6, 5$  and  $4$  mode activity. Adapted from Ref. [3.52].

soon as a certain critical mode amplitude is reached. Whereas for a rotating tearing mode the wall has a stabilizing effect as the perturbation field can hardly penetrate the wall, as discussed above, the modified boundary condition for a locked mode further destabilizes the tearing mode. This effect is often observed in experiments. The upper time trace in Fig. 3.35 shows the time derivative of the magnetic perturbation; the time integral of the perturbation is shown below. This signal strongly increases after mode locking, the mode reaches a large amplitude ( $> 2$  mT) which is accompanied by a strong impact on the plasma stored energy.

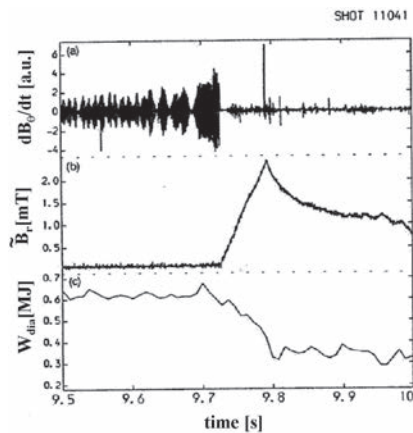


FIG. 3.35. Mirnov signal ( $dB_{\theta}/dt$ ), strength of the radial magnetic field perturbation and plasma energy during mode locking in JET [3.53].

If a tearing mode locks to the wall, it often stops the plasma rotation over a large radial extent. This reduction in the differential plasma rotation between the rational surfaces in combination with the steep current profile (further enhanced by the modification of the current profile by the island) may cause the growth of further islands at neighbouring rational surfaces. The interaction of this mode with other islands can finally lead to a global current rearrangement and expulsion of hot plasma.

Error fields play an important role for mode locking as they lead to a breaking force on the plasma, depending linearly on mode amplitude. They hence dominate at low amplitudes the quadratic interaction associated with the induced vessel currents. Slowly rotating modes often become completely locked by perturbation fields associated with field errors. Therefore, one often finds a well defined toroidal phase for locked modes, in particular in machines with larger error fields. Resonant error fields can even create magnetic islands even in MHD stable plasmas: the error fields generate currents at the corresponding rational surface. The force associated with these error fields slow down the plasma rotation, allowing even stronger field penetration creating in that way magnetic islands.

The non-monotonic current profiles typical for steady state tokamak operational scenarios often correspond to  $q$ -profiles with two (or even more) low order rational surfaces located close to each other. This situation is often unstable against tearing modes at one or both rational surfaces involved. However, even if single tearing modes at their respective rational surfaces would be stable, double tearing modes can become unstable if the differential plasma rotation between the two rational surfaces is sufficiently small to allow for mode coupling. The two coupled island chains arrange such that the perturbation currents generating the magnetic field structure attract each other. As the magnetic shear necessarily has different sign at the two rational surfaces, this corresponds to a coupling of the X- to the O-points at the two island chains (Fig. 3.36).

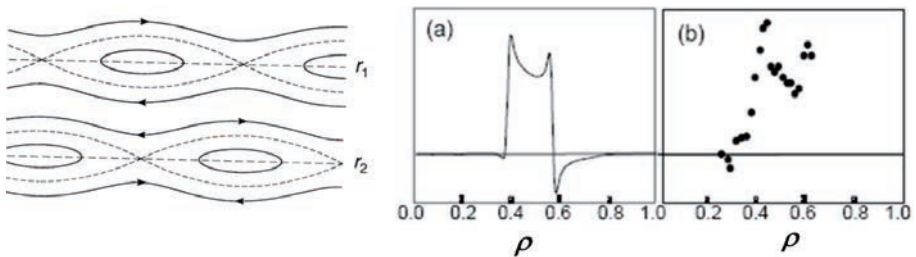


FIG. 3.36. Left: Perturbation of the magnetic field structure  $B-B_{(q=m-n)}$  as characteristic for double tearing modes [3.32]. Right: Displacement vector  $\xi$  according to CASTOR simulations (a) together with a corresponding measurement of the temperature perturbation  $\xi = \tilde{T}_e / \nabla T_e$  caused by double tearing modes in ASDEX Upgrade (b) [3.54]. The radial coordinate  $\rho$  is as defined in Eq. (3.31).

### 3.4.3. Neoclassical tearing modes (NTMs)

In conventional tokamak operation the onset of neoclassical tearing modes (see Section 3.3.1.3) can be considered the practical limit to the maximum achievable  $\beta_{pol}$  values, although the ideal  $\beta$  limit is usually much higher (see below). The ideal  $\beta$  limit can often be achieved only for a very short time period during a discharge, before a magnetic perturbation creates a sufficiently large “seed island” allowing the pressure to flatten across the island which drives the island to a large amplitude. The trigger event for NTMs is usually provided by sawteeth. In addition, fishbones and edge localized modes can provide seed islands.

Neoclassical tearing modes have first been recognized at TFTR. A time evolution of the magnetic island size is shown in Fig. 3.37 together with the theoretically expected time trace according to the generalized Rutherford equation. The agreement between the predicted and measured time traces is usually very good as the drive and saturation mechanisms are well understood. The onset conditions of NTMs — trigger mechanisms and required seed island sizes — however, are still quite uncertain as many different physics phenomena are involved. An empirical scaling law based on present day experiments predicts the critical  $\beta$  value for NTM onset to be proportional to the ratio of ion gyroradius to plasma dimensions:  $\rho^* = \rho_i / a$ . According to that scaling law the  $\beta$  values for mode onset would be much smaller for ITER and a tokamak reactor than in present day experiments. The impact of NTMs on confinement, however, would be similar as the saturated island width just depends on the local value of  $\beta_{pol}$ .

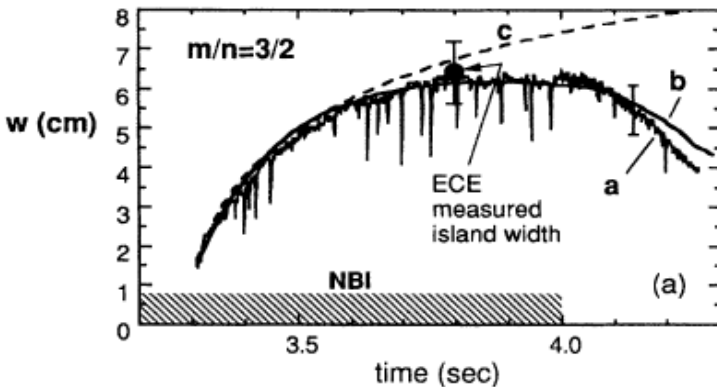


FIG. 3.37. Comparison of measured island width for a neoclassical tearing mode on TFTR (curve a) with theory (b and c). Curve b takes into account the non-linear modification of the plasma parameters by the island. Reprinted from Ref. [3.55]. Copyright (2010), American Physical Society.

In present day tokamaks usually (2,1), (3,2) and (4,3) NTMs are observed, with the (2,1) mode being the most dangerous one. This is particularly true for low values of  $q_{95}$  with the  $q = 2$  surface located close to the plasma edge. In such discharges the island often locks to the walls which leads, as discussed above, to enhanced mode growth and eventually often to disruptions. Typical values for energy confinement degradation caused by (3,2) NTMs are 20–25%, depending on the island size and  $q$ -profile.

Usually a large hysteresis is observed in the  $\beta$  values for NTM onset and offset. This is particularly pronounced in the case of (2,1) NTMs showing the largest  $\beta$  value for mode onset, but the lowest  $\beta$  value for mode disappearance. In fact these modes usually cannot be stabilized by reduction in heating power before the back transition to L-mode occurs, i.e. (2,1) NTMs are metastable over the whole parameter regime of H-mode operation.

In order to avoid confinement degradation or even disruptions caused by NTMs, means for their avoidance or stabilization have been developed. One obvious method is to prevent the creation of seed islands by background MHD, in particular by sawteeth which might have large amplitude in a reactor due to the stabilizing effect of the fast  $\alpha$  particles. As discussed above, this can be done by controlling sawteeth via the magnetic shear at the  $q = 1$  surface. As, however, NTMs are expected to be metastable already at low  $\beta$  values, any accidental MHD event can trigger mode onset. Therefore, one needs to be able to remove an already existent mode as well. This can be done by replacing the helical perturbation of the bootstrap current caused by the island with externally driven current. Particularly suited for this method is electron cyclotron current drive which allows for localized current drive in the island region. This method has been proved to be successful (Fig. 3.38), and is foreseen as a tool for NTM control in ITER.

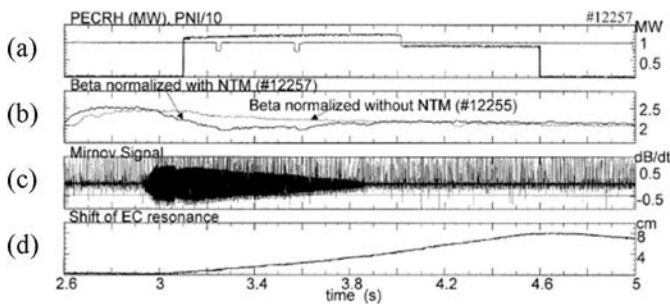


FIG. 3.38. Time traces of a typical plasma discharge for NTM stabilization on ASDEX Upgrade: (a) NBI heating power and ECRH power (multiplied by 10). (b)  $\beta_N$  values compared to a very similar discharge but without NTM activity. (c) (3,2) NTM induced Mirnov signal showing complete NTM stabilization at about 3.85 s. The frequently occurring spikes are caused by ELMs. (d) Shift of the location of the ECRH resonance by a magnetic field ramp. Reprinted from Ref. [3.56]. Copyright (2010), American Physical Society.

### 3.4.4. Edge localized modes (ELMs)

ELMs are MHD related, spontaneous periodic relaxations of the plasma edge which lead to a fast loss of particles and energy from the plasma edge (Fig. 3.39). They are characteristic for the high confinement regime (H-mode) only. Similar to sawteeth, ELMs are beneficial for achieving stationary plasma conditions as they lead to impurity and helium ash expulsion, allowing for cleaner plasmas. Their effect on global energy confinement is not too large but the associated high heat loads onto the divertor plates are a major concern for the plasma-wall interaction. Figure 3.39 shows an example of a typical ELM cycle: a sudden crash reduces edge density and temperature. The most obvious diagnostic for an ELM event is the increase in the  $D_\alpha$  line radiation in the divertor plasma, resulting from the expulsion of particles and energy from the plasma. The profiles recover until the following ELM starts the cycle again.

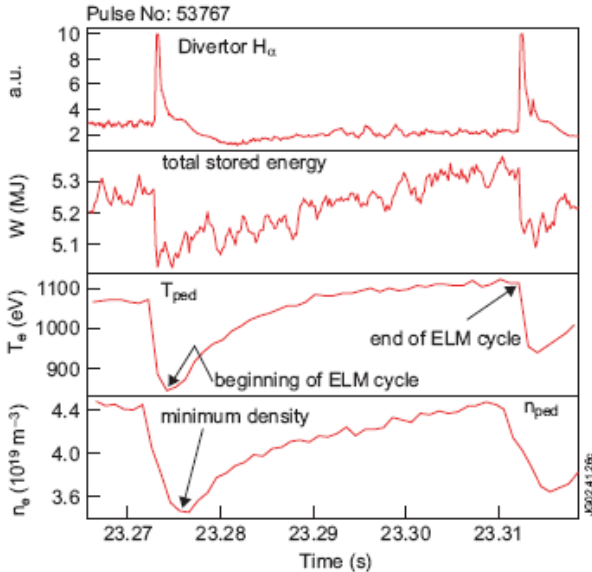


FIG. 3.39. Example of a typical ELM cycle for type I ELMs on JET. Time traces for the  $D_\alpha$  emission from the divertor, the total stored energy as well as pedestal temperature and density are given [3.57].

ELMs have been first observed in connection with the discovery of the H-mode in ASDEX, and have subsequently been observed on all divertor tokamaks. Various types of ELMs have been found in various experiments. A classification according to three types has been developed by DIII-D:

*Type I* ELMs occur if the heating power is sufficiently (a factor 1.5–2) above the L-H transition threshold. H-modes with Type I ELMs are the reference

operating scenario for ITER. Type I ELMs are characterized by an increase of the ELM frequency with heating power, and they occur above a critical temperature only (see Fig. 3.40). Type I ELMs are associated with the largest effect on energy confinement (10–20% of the stored energy in the pedestal) and therefore cause the largest heat loads onto the divertor plates. The instability usually starts at the low field side of the tokamak, which is consistent with the onset of an ideal ballooning instability (see below).

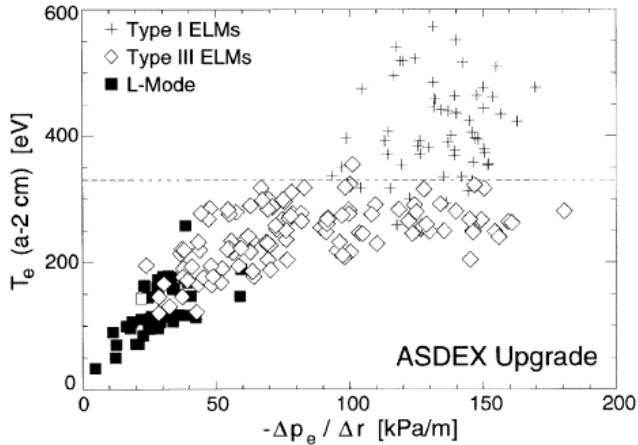


FIG. 3.40. Electron temperature versus average electron pressure gradient. Type III ELMs occur below a certain edge temperature limit [3.58].

Type II ELMs have a higher repetition rate than Type I ELMs, they only cause small perturbation of the plasma edge perturbations and are therefore no concern for plasma–wall interaction. Beneficial for the occurrence of Type II ELMs are: strong plasma shaping, large values of  $q_{95}$ , high density (collisionality) and high  $\beta_{pol}$ . It is not clear yet if Type II ELMs are consistent with the low collisionality plasmas in ITER and a tokamak reactor.

Type III ELMs are found if the heating power is just above L-H threshold power or at high density. H-modes with Type III ELMs have a higher ELM frequency and a significantly smaller energy loss per ELM, but a reduced energy confinement compared to Type I ELMy H-modes (by 10–30%). In contrast to Type I ELMs the ELM frequency decreases with heating power. As seen in Fig. 3.40 they exist below the critical temperature, which is proportional to  $1/n$  at low density and constant otherwise.

Actually, there are some regimes in which impurity control is achieved without any periodic ELMs. These regimes, like the enhanced  $D_\alpha$  (EDA) H-mode or the quiescent H-mode, are, however, characterized by continuous edge localized fluctuations that are obviously sufficient to ensure the required enhanced particle transport.

As ELMs are considered MHD events, it is instructive to discuss the MHD stability properties at the plasma edge in some detail. Although the exact mechanism of the L-H mode transition is not yet clear, it is generally believed that the edge pressure gradient is limited by the onset of MHD modes. In fact, the pressure gradient achieved in Type I ELMy H-mode is close to the predicted ideal MHD ballooning limit. This is also in line with the shape dependence of the edge pressure gradient: triangularity is very beneficial for achieving large edge pressure gradients (it allows access to the second stable ballooning regime). While this is of course very beneficial for the confinement properties, the absolute size of Type I and III ELMs increases with triangularity as well. The relative size of the energy loss per ELM, normalized to the pedestal energy content, however, depends only weakly on the plasma shape.

The stability properties of Types I and II ELMs are usually described within ideal MHD stability as well, in terms of coupled ballooning-peeling modes. Peeling modes are driven by the current density at the plasma edge, and are essentially very edge localized (high  $m$ ) external kink modes. The large edge pressure gradient drives ballooning modes unstable. It is associated, however, as well with a large (bootstrap) current density albeit with a time delay due to inductive effects. The latter, on one hand, is stabilizing for ballooning modes as it lowers the magnetic shear and thus allows access to the second stable ballooning regime; on the other hand it destabilized the current driven peeling modes. Increasing edge pressure gradient finally destabilizes modes driven by both, the pressure gradient and the current density, with intermediate toroidal mode numbers  $n \sim 6-12$ . As an example, a stability diagram for the plasma edge is shown in Fig. 3.41 for a JET discharge. Dedicated ideal stability investigations on DIII-D have demonstrated that the spontaneous onset of Type I ELMs is associated with the ideal stability boundary if stabilizing diamagnetic effects are taken into account. As Type III ELMs usually occur already at pressure gradients well below the ideal stability limit, their onset cannot be described within an ideal MHD model, and there is no clear physics model for Type III ELMs yet.

Despite the success of a simple linear ideal MHD description for the ELM onset, to model their non-linear evolution certainly requires a more sophisticated physics model. The lack of a physics model that would correctly describe the L-H transition hampers as well the development of a rigorous model for a whole ELM cycle. A sketch of a time evolution of the marginal stability curve during an ELM cycle is given in Fig. 3.42, together with a possible explanation of the different size of the various ELM types.

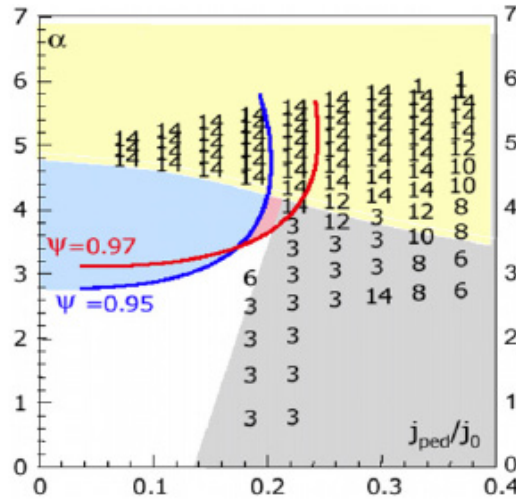


FIG. 3.41. Linear MHD stability calculations for a JET discharge: normalized pressure gradient  $\alpha$  versus edge current density  $j_{ped}$  normalized to the total current density  $j_0$ . Shaded areas are unstable, the numbers indicate the toroidal mode numbers for the most unstable modes, and the curves correspond to the  $n \rightarrow \infty$  ballooning stability boundaries at the two flux surfaces [3.58].

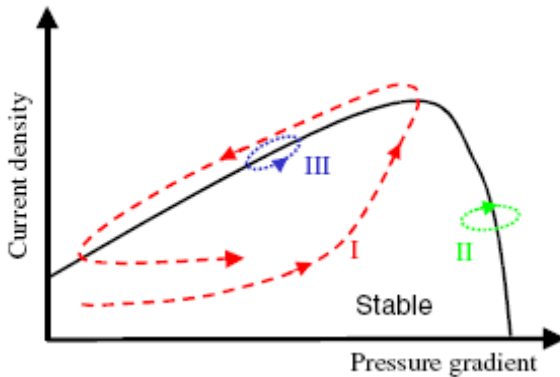


FIG. 3.42. Sketch of the marginal stability boundaries of the edge current density and the pressure gradient (solid black line). In addition possible time traces for the various ELM types are given [3.58].

The large heat loads to the divertor plates caused by Type I ELMs are a major concern for a fusion reactor. This problem has stimulated the search for small ELM regimes and appropriate mitigation methods which reduce the divertor peak heat loads, but do not strongly affect the energy. The observation that the energy loss per ELM is inversely proportional to the ELM repetition

frequency suggests triggering ELMs more frequently. This is indeed possible, for example by injecting small pellets into the plasma. In discharges that are prone to ELMs, one can find that each pellet immediately triggers an ELM event. Interestingly this does not happen in ELM free (ohmic, L-mode or QH-mode) discharges. Obviously, in usual H-mode discharges, ELMs are always non-linear unstable (similar to the neoclassical tearing modes discussed above), but need a trigger to grow. For spontaneously appearing ELMs this trigger is given by the growth of linearly unstable MHD modes. Another possibility for ELM mitigation is ergodization of the plasma edge by resonant magnetic perturbations, generated by external magnetic field coils. That way, in particular the particle confinement is reduced, which is actually in contrast to simple diffusive transport models that would predict a much larger decrease in the electron temperature by ergodization of the magnetic field lines at the plasma edge. The resulting reduction in the edge pressure gradient prevents the plasma edge from reaching the ideal MHD stability limits and thus the occurrence of ELMs.

### 3.4.5. Ideal pressure limiting modes

The ideal  $\beta$  limit in conventional (monotonic  $q$ -profile) tokamak discharges is usually discussed in terms of the  $n = 1$  external kink modes or  $n \rightarrow \infty$  ballooning modes. However, in regions with low magnetic shear, one can find as well intermediate  $n$  pressure driven modes, the so-called “infernial modes”. These modes are a particular concern for discharges with non-monotonic  $q$  profiles in the low shear region around the minimum  $q$  value  $q_{min}$ . Discharges with internal transport barriers are often characterized by a large pressure gradient in the low magnetic shear region around  $q_{min}$ , and therefore particularly unstable against infernal modes. The latter extend at least over the low shear region, and often cause disruptions that are extremely dangerous due to the short timescales involved. Figure 3.43 shows the radial displacement of an ideal  $n = 1$  precursor to a disruption in TFTR compared to that resulting from a linear stability analysis (adjusted in amplitude).

Large current gradients close to the plasma edge, in particular as characteristic for the broad current profiles associated with non-monotonic  $q$  profiles, are prone to low  $n$  external kink modes. These modes are quite localized at the plasma edge for peaked pressure profiles and large values of  $q_{95}$ . On the other hand, broad pressure profiles and low values of  $q_{95}$  facilitate, however, a coupling to low order rational surfaces in the core plasma and thus the growth of more global modes which might be able to cause disruptions as well.

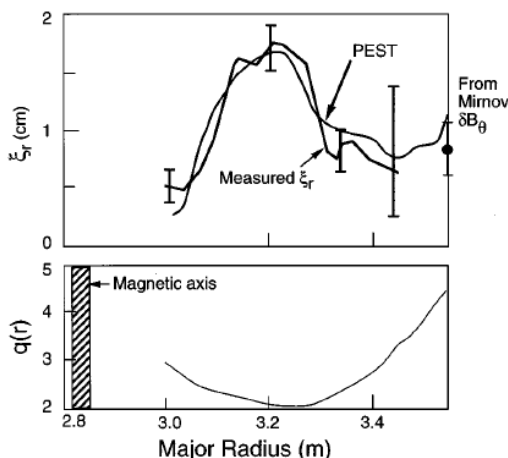


FIG. 3.43. Comparison of measured (ECE) and theoretical (PEST) radial displacement  $\xi_r$  of a disruption precursor (infernal mode) together with the  $q$  profile of a TFTR discharge. Reprinted from Ref. [3.59]. Copyright (2010), American Institute of Physics.

The experimentally observed  $\beta$  limit in conventional tokamak discharges is roughly given by  $\beta_N = 4 l_i$  (Fig. 3.44). The “Troyon-limit”  $\beta_N, \max \approx 3.5$ , resulting from theoretical ideal MHD considerations, is essentially equivalent to this, as for the conventional monotonic  $q$  profiles  $q(0) \sim 1$  and  $q_{95} \sim 3 \dots 4$  one finds  $l_i \sim 0.8 \dots 1$ .

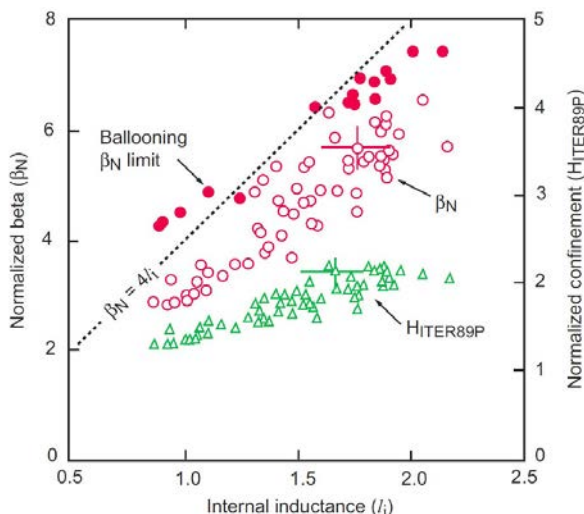


FIG. 3.44. Energy confinement (relative to ITER89P scaling) and peak  $\beta_N$  values in DIII-D current ramp down L-mode plasmas versus internal inductance  $l_i$ . The limit  $\beta_N = 4 l_i$  is also shown together with explicitly calculated ideal ballooning limits for various  $l_i$  values [3.60].

According to the relation  $\beta_N = 4l_i$ , the maximum  $\beta$  values should be achieved for discharges with peaked current profiles. In order to test the maximum achievable  $\beta_N$  values, the internal inductance can be increased transiently by, for example, fast ramp down of the plasma current, a rapid increase in plasma elongation or by expanding the plasma minor radius. That way, in conventional tokamaks record values of  $\beta_N$  up to 6.3 (DIII-D) have been transiently achieved. In spherical tokamaks the ideal  $\beta$  limit is rather given by  $\beta_N = 6l_i$ ; however, record values up to  $\beta_N = 11l_i$  ( $\beta_N = 7.2$ ) have been achieved (NSTX) in cases where wall stabilization played an important role. The quoted limits of  $\beta_N = 4l_i$  and  $6l_i$ , respectively, are valid without the stabilizing effect of external conducting wall structures. For sufficient plasma rotation such wall structures act like ideally conducting walls that have a stabilizing influence as discussed below. Although the  $\beta_N$  values achieved in conventional and spherical tokamaks are quite similar, the limit to the plasma pressure normalized to the pressure of the magnetic field  $\beta_{tor} = 2\mu_0 \langle p \rangle / B_\phi^2$  is much larger in spherical tokamaks as the reduced aspect ratio increases the plasma current at given plasma minor radius, magnetic field strength and  $q_{95}$ . Values of  $\beta_{tor} = 39\%$  (NSTX) have been achieved transiently (at the end of a ramp down phase of  $B_\phi$ ).

The ideal  $\beta$  limit for tokamak discharges with monotonic current profiles discussed above can be achieved for a short time in a discharge only. On a longer timescale, usually sawteeth or other MHD events trigger neoclassical tearing modes that limit the normalized plasma pressure to much lower values. As mentioned above, the stationary  $\beta$  limit is therefore given by the onset conditions for neoclassical tearing modes.

Plasmas with hollow current profiles are very attractive as they offer the opportunity for non-inductive tokamak operation due to the possible alignment of the bootstrap current density with the total current density profile. As the ultimate aim is to replace 80–90% of the total plasma current by the bootstrap current, very large normalized plasma pressures ( $\beta_{pol}$ ) are required in such scenarios. This is very challenging for MHD stability and requires a careful tailoring of current and pressure profiles. The negative or low magnetic shear in the plasma centre allows for large pressure gradients as  $n \rightarrow \infty$  ballooning modes are stable. Optimization of pressure and current profiles corresponds to avoiding core localized or global instabilities, for example an optimal  $q$  profile should not have any low order rational surfaces in regions with positive magnetic shear and large pressure gradients that could drive NTMs unstable. Large pressure gradients in low shear regions should not occur either as they destabilize infernal modes.

An example for profile optimization aiming at steady state tokamak operation, developed in the frame of the ARIES-AT study, is given in Fig. 3.45. The large radius of the  $q_{min}$  surface allows for a broad pressure profile, being essential for achieving large  $\beta$  values. In the vicinity of  $q_{min}$  the magnetic shear

is quite large, which is achieved by the strongly shaped plasma cross-section. The ultimate limit to the normalized plasma pressure for such optimized profiles is usually given by the onset of low- $n$  external kink modes. As discussed below, these modes can effectively be stabilized by conducting wall structures close to the plasma.

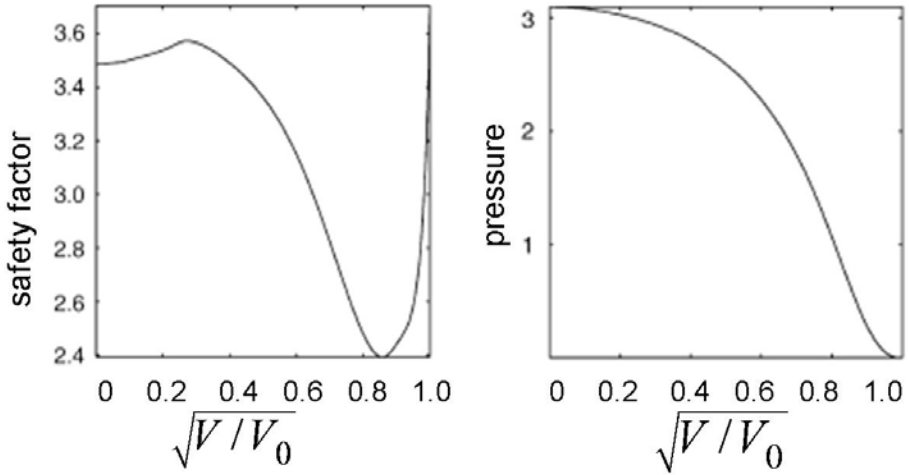


FIG. 3.45. Equilibrium profiles for ARIES-AT, showing the safety factor and plasma pressure as functions of a radial coordinate defined through the ratio of the volume enclosed by a given flux surface ( $V$ ) to that of the total plasma ( $V_0$ ). Reprinted from Ref. [3.61]. Copyright (2010), with permission from Elsevier.

### 3.4.6. Wall effects on MHD modes

Ideally conducting walls have a stabilizing effect on MHD modes as the magnetic flux associated with the perturbation cannot penetrate the walls. This situation is stabilizing for all plasma modes with finite amplitude at the plasma boundary. Wall stabilization is particularly effective for the above mentioned external kink modes which would not occur in case of ideally conducting walls at the plasma boundary.

The equilibrium shown in Fig. 3.45 is unstable against low- $n$  external kink modes if wall stabilization is not taken into account (see Section 3.3.1.2). A conforming (ideally) conducting wall sufficiently close to the plasma can stabilize the kink mode up to high  $\beta_N$  values. As the magnetic perturbations decay much faster with the distance from the plasma boundary for larger poloidal mode numbers, usually modes with intermediate mode numbers determine the maximum allowed wall distance (see Fig. 3.12). Figure 3.46 demonstrates that plasma shaping and pressure profile have a strong influence on the effect of wall

stabilization. The optimal stabilizing effect of a wall at a reasonable distance to the plasma boundary can be found for strong plasma shaping in combination with a broad pressure profile (small peaking factor, defined by the ratio of axis to volume average pressure:  $p_o/\langle p \rangle$ ).

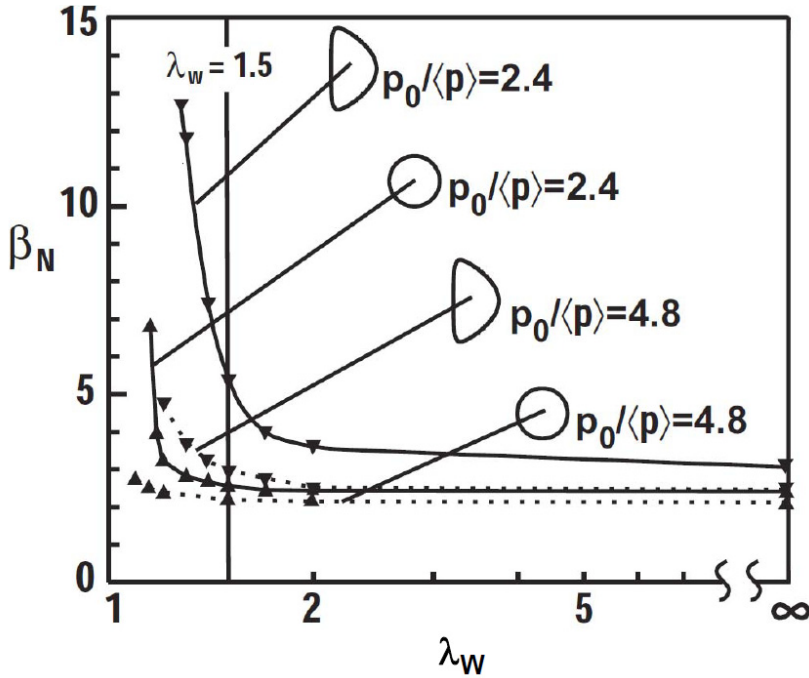


FIG. 3.46. Dependence of the  $\beta_N$  limit on conformal wall position (measured by the ratio of wall to plasma radius  $\lambda_w$ ) for broad and peaked pressure profiles and two plasma cross-sections: circular and D-shaped [3.21].

So far we have discussed the effect of ideally conducting walls only. A realistic wall with finite resistivity can be considered ideally conducting only if the mode growth and/or rotation are much faster than the inverse skin time of the wall. Otherwise, the currents induced in the wall decay on its resistive timescale. While the wall would be stabilizing on a typical short ideal MHD growth time, the mode can still grow on the resistive wall timescale if the mode is locked to the wall. This mode is called resistive wall mode (RWM). For non-rotating plasmas, the mode is unstable for normalized plasma pressures above the  $\beta$  limit without wall stabilization effects (no-wall limit). Figure 3.47 shows an example for the growth of an  $(m, n) = (3, 1)$  resistive wall mode. The mode's growth time is 5 ms, consistent with the resistive time of the wall. It is interesting to note that the RWM does not appear immediately after the no-wall  $\beta$  limit is exceeded. Instead it only grows after the plasma rotation at the  $q = 3$  surface vanishes.

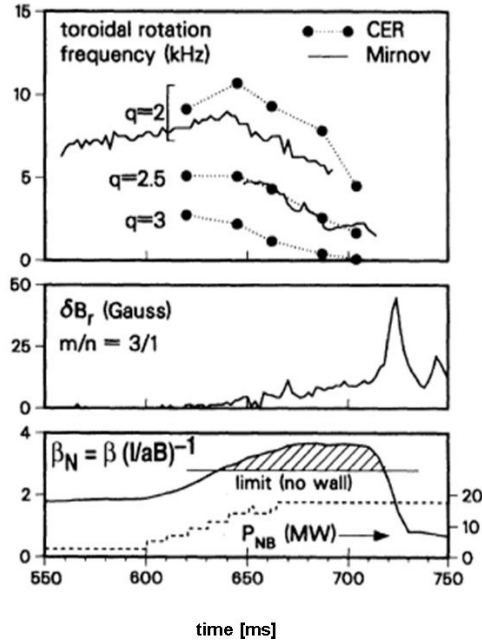


FIG. 3.47. Development of a resistive wall mode on DIII-D illustrated by time traces of the magnetic perturbation (Mirnov) and the plasma rotation frequency (determined by charge exchange recombination spectroscopy — CER) at several rational surfaces, the radial magnetic perturbation field ( $\delta B_r$ ) of a non-rotating  $m/n=3/1$  mode, and the normalized plasma pressure  $\beta_N$  and neutral beam power  $P_{NB}$ . Reprinted from Ref. [3.62]. Copyright (2010), American Physical Society.

Plasma rotation is obviously stabilizing for RWMs. This is actually surprising for an ideal plasma mode which should actually be free to rotate with respect to the plasma. Nevertheless, a strong stabilizing effect of plasma rotation is usually observed, pointing at non-ideal effects causing a finite friction for the mode rotation with respect to the plasma (see Section 3.3.1.2). Possible explanations are the occurrence of resonances between the mode frequency and characteristic frequencies of the particle motion such as the toroidal precession frequency, or resonant excitation of plasma waves. The stabilizing effect of plasma rotation makes it possible to achieve  $\beta$  values well above the no-wall limit in present day experiments which are often characterized by strong beam heating and thus strong plasma rotation. In dedicated experiments, it has been found, however, that already a low plasma rotation of the order of 0.3% of the Alfvén velocity can stabilize resistive wall modes (see, for example, Ref. [3.63]). The physics effects that determine the threshold value for a stabilizing effect of plasma rotation are not yet well understood. It is therefore uncertain if the plasma rotation in ITER or a tokamak reactor is sufficient for RWM stabilization. For that reason, specific feedback mechanisms are being developed which mimic an

ideally conducting wall by cancelling the magnetic field perturbation close to the wall.

### 3.4.7. Alfvén and energetic particle modes (EPMs)

In discharges with sufficient fast particle pressure, Alfvén waves are often observed. In present day tokamaks usually toroidicity induced Alfvén eigenmodes (TAEs) are detected with intermediate toroidal mode numbers ( $n = 3-5$ ). Except for specially designed discharges with low magnetic field strength, the resonance condition  $v_{\parallel} = v_A$  is usually not fulfilled. Instead NBI ions drive TAE modes via the sideband resonance  $v_{\parallel} = v_A / 3$ , or fast trapped particles, generated by ICRH, fulfil the corresponding resonance condition  $\omega_{AE} = \omega_D + p\omega_b$  with  $\omega_{AE}$  being the mode frequency,  $\omega_D$  the precession frequency,  $\omega_b$  the bounce frequency and  $p$  the bounce harmonic. Besides TAE modes located in the lowest gap of the shear Alfvén continuum, sometimes also modes located in higher order gaps that require coupling of poloidal harmonics  $m$  and  $m+2$  (ellipticity-induced eigenmodes (EAEs), or  $m$  and  $m+3$  (non-circular triangularity-induced eigenmodes (NAEs)) are found (Fig. 3.48).

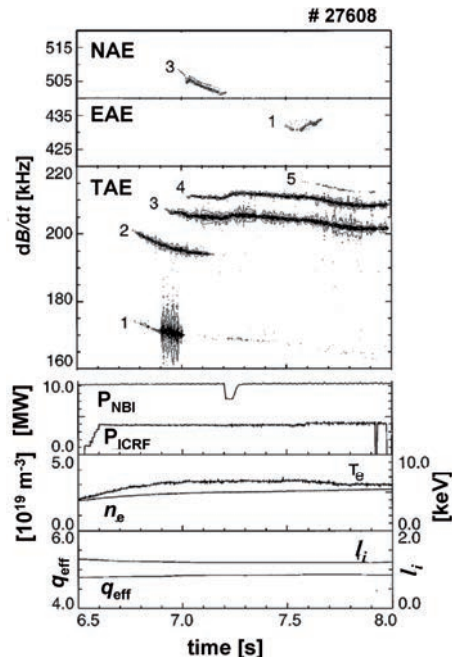


FIG. 3.48. Magnetic signals for NAE, EAE and TAE mode activity for a discharge with time traces of heating power and plasma parameters shown in the lower figure: neutral beam power ( $P_{NBI}$ ) and ICRF power ( $P_{ICRF}$ ), electron temperature ( $T_e$ ) and line averaged density ( $n_e$ ), safety factor at the edge ( $q_{eff}$ ) and internal inductance ( $I_i$ ) [3.64].

The frequency of the observed Alfvén waves agrees within the experimental error bars with the predicted values from theory (Fig. 3.49). The experimental uncertainties are mainly due to inaccuracies in the determination of the  $q$ -profile and the plasma rotation frequency, the latter determining the Doppler shift of the measured mode frequencies. The good knowledge of the correct mode frequencies is sometimes used to eliminate the uncertainties in the  $q$ -profile measurements for equilibrium reconstructions.

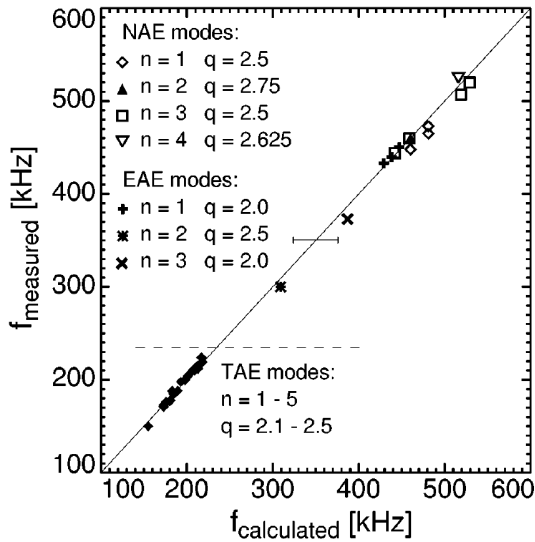


FIG. 3.49. Comparison of the observed mode frequencies and the calculated frequencies  $\omega = v_A \Delta m / (2qR)$  with  $\Delta m = 1, 2, 3$  for the TAE, EAE and NAE modes, respectively.  $v_A$  is the Alfvén velocity and  $R$  the major radius. The Doppler shift ( $n$  times the toroidal plasma rotation) is included in the calculated frequency. At 350 kHz a typical error bar for the calculated frequency is shown (due to uncertainties in the measured density,  $q$  and plasma rotation profiles). Reproduced from Ref. [3.64]. Copyright (2010), American Physical Society.

Valuable tools in this respect are in particular the so-called reversed shear Alfvén eigenmodes (RSAE). These modes are located in the vicinity of the minimum  $q$  value, where a gap opens if  $q_{min}$  is slightly below a low order rational value. The occurrence of these modes and their frequency is very sensitive to the value of  $q_{min}$ . As most of the reversed shear discharges rely on slow current diffusion, and are thus characterized by an evolving  $q$ -profile in time, RSAEs appear once  $q_{min}$  falls below a low order rational value, with their frequency chirping up in time until it reaches the TAE frequency where the mode becomes mode global and usually disappears. This kind of mode activity is usually called Alfvén cascades. As  $q_{min}$  is usually located in the plasma core, the modes are hard to detect by Mirnov coils, but well seen, for example in the interferometry signals (Fig. 3.50).

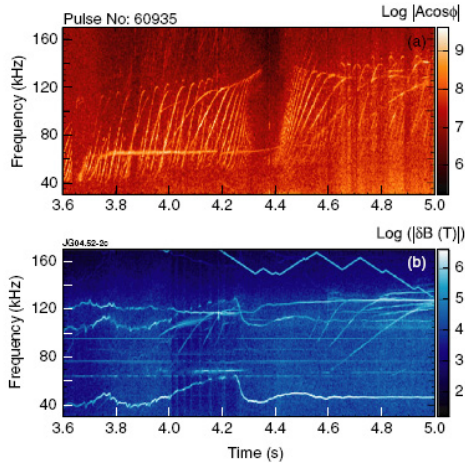


FIG. 3.50. Reversed shear Alfvén eigenmodes (RSAEs) in a JET discharge detected with O-mode interferometry (top) and Mirnov coils (bottom). The interferometer signal shown ( $|A\cos\phi|$ ) is a measure of the line integral of the perturbed density, and monitors hence also changes in the plasma interior [3.65].

Recent improvements in the diagnostics have also enabled detailed measurements of the mode structure of Alfvén waves. As for the mode frequency, the mode structure as derived from linear MHD calculations agrees very well with the measurements; an example is given in Fig. 3.51 for both a TAE and a RSAE.

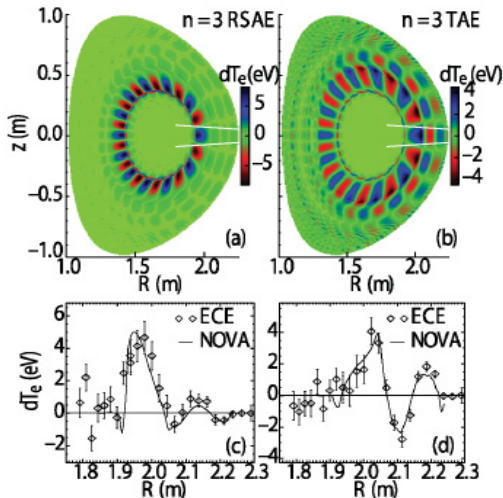


FIG. 3.51. Calculated temperature perturbation for  $n = 3$  RSAE and  $n = 3$  TAE together with corresponding low field side ECE measurements on DIII/D. Reprinted from Ref. [3.66]. Copyright (2010), American Physical Society.

As far as linear physics is concerned, the only remaining open question is the physics of mode damping. Direct measurements of the damping rate are possible via measurements of the plasma response to external perturbation fields generated by magnetic field coils. A simultaneous measurement of the mode structure and the damping rate, required for a detailed comparison with theory, is, however, still missing.

The occurrence of Alfvén waves is usually accompanied by fast ion losses. Fast measurements of fast ion losses have shown these losses to be in phase with the magnetic perturbation (Fig. 3.52). Fast ion losses associated with TAE modes are usually quite small in conventional H-mode discharges of present day tokamaks. For specially designed discharges, however, large losses, up to 70% of NBI power, can be observed. In such experiments, for example, a reduced magnetic field strength is used to decrease the Alfvén velocity and thus achieve the resonance condition  $v_{\parallel} = v_A$  for NBI ions, which strongly increases the observed losses (Fig. 3.53). Limiter discharges avoid H-mode access and thus allow operation at low densities and therefore high fast ion pressure. In such discharges, at DIII-D fast ion losses up to 70% have been observed.

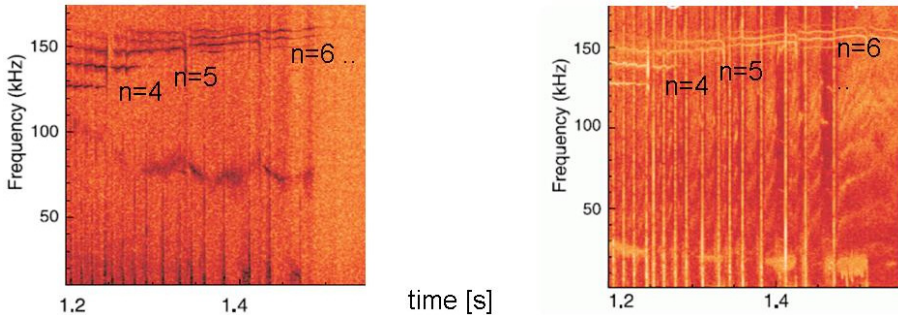


FIG. 3.52. TAE induced fast ion losses measured by a fast ion loss detector on ASDEX Upgrade (left), corresponding magnetic perturbation signal (right) [3.67].

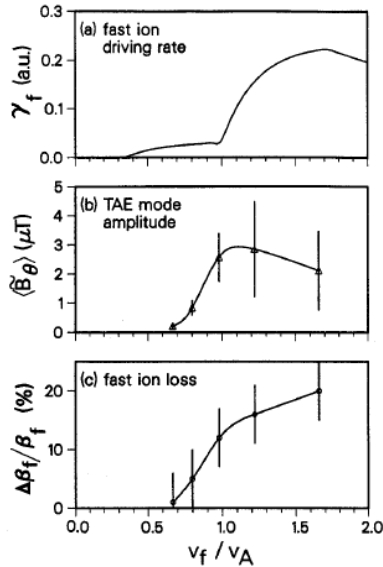


FIG. 3.53. Comparison of predicted and measured threshold in the ratio of injected fast ion velocity to the Alfvén velocity  $v_f / v_A$  for a DIII-D discharge: (a) predicted TAE growth rate  $\gamma_f$ , (b) measured (Mirnov) time averaged TAE amplitude  $\langle \tilde{B}_\theta \rangle$ , (c) proportion of fast ions lost due to MHD activity  $\Delta\beta_f / \beta_f$ , as estimated from neutron emission [3.68].

In addition to the Alfvén waves discussed above, energetic particle modes (EPMs) may lead to fast ion losses. Characteristic of EPMs is that they can adjust their frequency to maximize fast ion drive. Their signature is thus a characteristic frequency chirping as seen above for fishbones already. Besides fishbones, however, also higher  $n$  modes are observed, in particular in discharges with  $q(0) > 1$  (see Fig. 3.54).

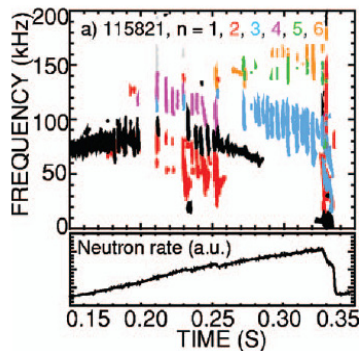


FIG. 3.54. Spectrogram of magnetic fluctuations for three shots showing “low” frequency fast ion driven instabilities, including toroidal Alfvén eigenmodes and various forms of energetic particle (chirping) modes. Reprinted from Ref. [3.69]. Copyright (2010), American Institute of Physics.

### 3.5. DISRUPTIVE INSTABILITIES

#### 3.5.1. Introduction

A plasma discharge in the existing tokamaks is generated and controlled during its whole duration by a complex feedback system. It can last from a few seconds, as illustrated in Fig. 3.55 (left), up to hours and its duration is limited by the capacity of the energy supply system driving the plasma toroidal current. Moreover, a tokamak discharge can only exist within a large but bounded region of the multidimensional operational space. Any attempt of crossing these boundaries results in a major plasma instability, known as disruption, which terminates the discharge. Decades of tokamak operation have allowed the investigation of these boundaries and some of them are now known with a certain level of accuracy. It is for example well known that the ranges of attainable plasma density, current and pressure are limited by MHD instabilities and any attempt to raise these parameters above the stable value ends in a disruption. Unstable current and pressure profiles can also occur away from the density, current and pressure limits; in fact the stability boundaries are complex functions of the plasma parameter profiles.

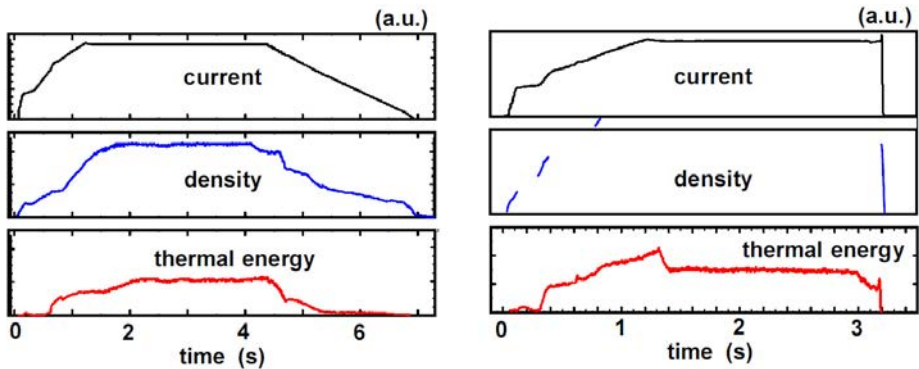


FIG. 3.55. In the discharge on the left, the plasma current is raised following a pre-programmed trajectory, reaches a constant value and at 4.4 s is ramped down. Thermal energy and electron density follow a similar time behaviour. The plasma discharge on the right is terminated abruptly by a disruption at 3.2 s.

The phenomenon is experimentally well defined, since it coincides with the fast (on the millisecond timescale) termination of the plasma discharge, as illustrated in Fig. 3.55 (right). The disruption is usually preceded by the development of helical perturbations of the magnetic equilibrium, clearly detected by poloidal field coils, as shown in Fig. 3.56. These so-called MHD modes grow and essentially destroy the magnetic flux surfaces, creating magnetic field

lines, which fill the whole plasma in a stochastic manner. The plasma energy confinement is lost as a consequence of the ergodicity of the magnetic field. This phase, called thermal quench, is followed by the increase of the plasma resistivity and by the ohmic dissipation of the plasma current. The plasma is a reservoir of two kinds of energy: thermal, since the ionized particles are very hot, and magnetic, since the plasma carries a large toroidal current. A disruption causes the loss of energy confinement, which translates into significant thermal loads and mechanical forces for the machine components. Therefore disruptions do not only interrupt the discharge and limit the operational space but are a hazard to the integrity of the tokamak. Methods of predicting their occurrence, of avoiding them and mitigating their consequences are being developed on all major tokamaks.

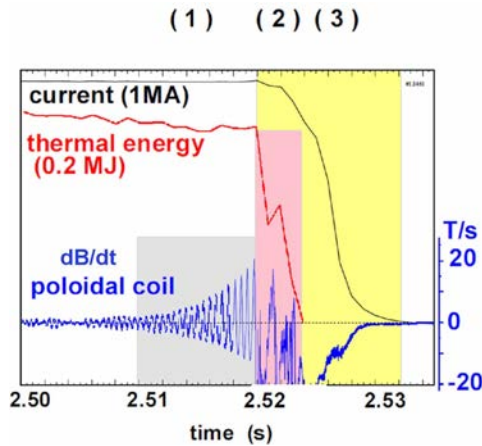


FIG. 3.56. Phases of a disruption: (1) development of MHD modes, detected by the poloidal field coils, followed by (2) the loss of thermal energy and (3) the decay of the plasma current.

### 3.5.2. Classification by causes

#### 3.5.2.1. Density limit disruptions

The plasma density achievable in a tokamak is roughly proportional to the current density. The attempt of increasing the density further with gas puffing gives rise to radiated power losses from the edge, where the temperature is low and impurities are present. Often the cooling of the edge leads to a poloidally localized region of cold high density plasma on the high field side, called MARFE (multifaceted asymmetric radiation from the edge), which radiates and cools down the plasma. The electrical resistivity in the plasma edge increases and the toroidal current diffuses inward, steepening the profile. The peaked current profile may

develop helical perturbations on rational flux surfaces, especially on the  $q = 2$ . These are tearing modes, which form magnetic islands as shown in Fig. 3.57 (right), grow and trigger the disruption. A high impurity density and the growth of neoclassical and classical tearing modes have a similar effect of cooling the edge.

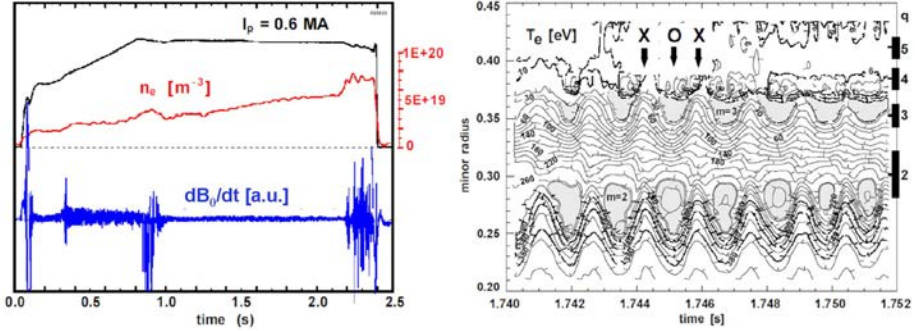


FIG. 3.57. The electron density is increased by gas puffing until MHD modes develop and trigger the disruption (left). Islands formed by tearing modes with  $m = 2$  and  $m = 3$  poloidal mode number (right) [3.70].

### 3.5.2.2. Beta limit

Also hot plasmas disrupt. The plasma energy, or in its dimensionless form the normalized beta, has upper boundaries. For peaked current profiles, this is usually set by the appearance of neoclassical tearing modes, which limit the plasma thermal energy by increasing the confinement degradation but do not necessarily lead to disruption. For reversed shear profiles, instead, the reachable normalized beta is higher but unstable. The disruption in this case is caused by the kinking of the magnetic surfaces and plasma boundary driven by the pressure gradient.

### 3.5.2.3. Limit on $q$

A fast kink instability also terminates plasmas with  $q \propto B_\phi / I_p < 2$  limiting the plasma current achievable with a given toroidal magnetic field. The common feature of these phenomena is that they lead to the development of helical perturbations of the magnetic equilibrium of the form

$$\xi(r, t) = \xi(r) \exp i(\omega t + m\theta - n\phi) \quad (3.216)$$

( $\theta$  and  $\phi$  are the poloidal and toroidal angles, and  $m$  and  $n$  integer mode numbers) which are described in the framework of the MHD theory. They are categorized by the physics in the generalized Ohm's Law required for the instability to be

described (e.g. ideal, resistive, neoclassical) and grow on different timescales (the ideal mode growing faster than the other modes). Linear MHD code analysis succeeds in predicting both spatial structure (location and mode number) of the modes and the timescale of their growth, once current and pressure profiles are known. Non-linear MHD codes can follow the evolution of the different modes as they grow, interact and ergodize — that is, they do not close on themselves but fill the whole space — the magnetic field region between them. They go as far as simulating the thermal quench reproducing the  $m=1$  erosion of the electron temperature, described in the following. Figure 3.58 shows the magnetic equilibrium evolution of a plasma whose pressure profile is unstable.

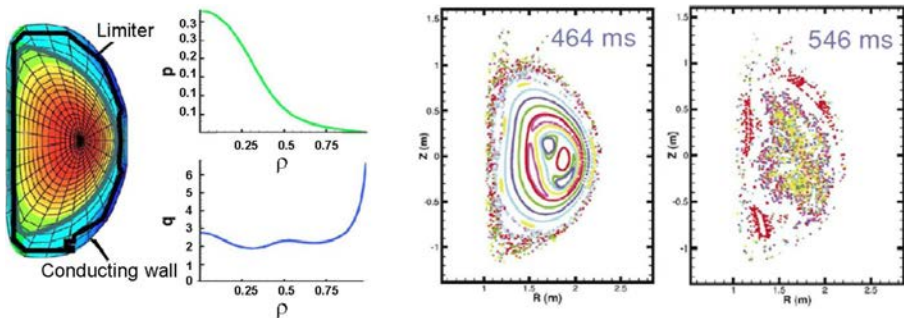


FIG. 3.58. Magnetic equilibrium (a) pertaining to unstable pressure and current profiles (b). Development of the magnetic islands and ergodic magnetic field clearly seen in the equilibrium reconstructed after  $464 \mu\text{s}$  (c) and  $546 \mu\text{s}$  (d). Reproduced from Ref. [3.71]. Copyright (2010), American Institute of Physics.

Magnetic islands develop on the rational flux surfaces, ergodize the magnetic field first at the edge (because they are closer together) and then in the plasma centre, providing a conductive transport mechanism for the thermal quench.

### 3.5.3. Phases of disruptions

#### 3.5.3.1. Thermal quench

The ergodization of the magnetic field may lead firstly to a gradual deterioration of the confinement and then to the sudden loss of the remaining thermal energy. This fast phase is called thermal quench. The plasma thermal energy is deposited, mostly by conduction, on the limiter and divertor surfaces and its duration depends strongly on the machine size. It is of the order of tens of microseconds in small tokamaks and reaches a few milliseconds in JET.

The thermal quench can happen in one (Fig. 3.59) or more phases (Fig. 3.60). In the case shown in Fig. 3.59, the central temperature drops within

100  $\mu\text{s}$  and the thermal energy is found again deposited on the divertor plates. To allow such a fast loss of confinement, the perpendicular electron thermal conductivity must increase by three orders of magnitude in this short time interval. In the case shown in Fig. 3.60 instead, the cooling of the plasma centre happens first without much loss of plasma energy. In a second phase, the energy barrier within the closed flux surface region breaks, the whole electron temperature profile collapses and the energy is lost to the divertor plates. The electron temperature and SXR measurements show an  $m = 1$  erosion of the profile, which is similar to the prediction of the cold bubble model. According to this model, sketched in the upper corner of Fig. 3.60, a cold bubble forms at the plasma edge and penetrates into the centre of the plasma, displacing the hot core towards the edge and triggering the thermal quench.

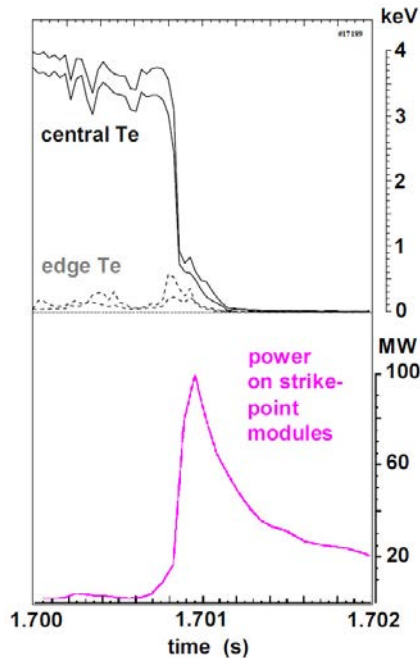


FIG. 3.59. Sudden and fast decay of the electron temperature,  $T_e$ , at the thermal quench and thermal energy deposited on the divertor plates [3.72].

Another signature of the thermal quench is a positive spike in the toroidal plasma current, as shown in Fig. 3.61 (left). This corresponds to the flattening of the toroidal current (which is reflected in the decrease of the plasma inductance  $L$ ) under conservation of the magnetic energy

$$\frac{d}{dt} \frac{LI_p^2}{2} \cong 0 \quad (3.217)$$

$$\frac{-\Delta I_p}{2} \equiv L \Delta I_p \quad (3.218)$$

The redistribution of the current is very fast and cannot be explained by its resistive diffusion.

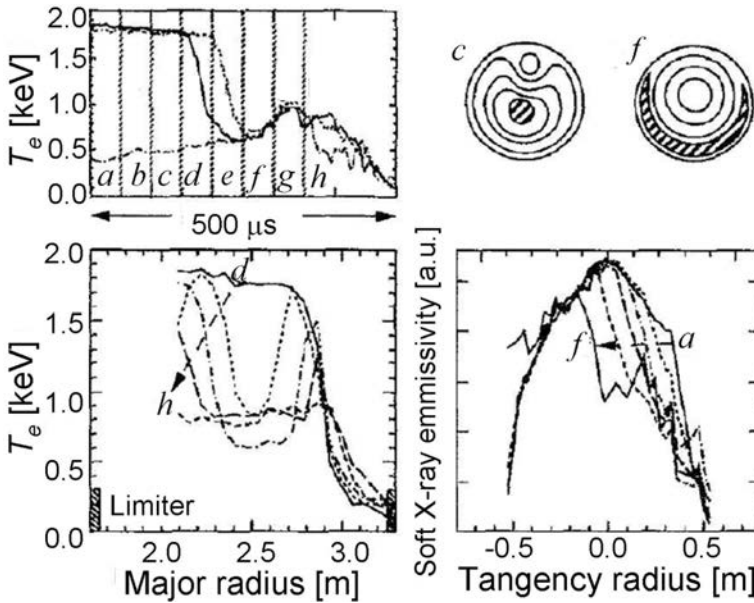


FIG. 3.60. Decay of the electron temperature in two phases (top left). Erosion of pressure profile seen in the temperature (left bottom) and SXR profiles (right bottom), similar to the prediction of the cold bubble model (top right). Letters (a)–(h) refer to the time instances for which plasma profiles are shown. Reprinted from Ref. [3.73]. Copyright (2010), American Institute of Physics.

For the plasma this represents a strong perturbation of the magnetic equilibrium, which can cause the loss of vertical stability after a disruption.

### 3.5.3.2. Current quench

One consequence of the loss of plasma thermal energy and cooling of the plasma during the thermal quench is the increase of the plasma electrical resistivity. The resistivity is a strong function of the electron temperature and scales as  $\eta \propto T_e^{3/2}$ . Following a drop of the temperature from 10 keV to 10 eV, the resistivity changes by a factor of  $3 \times 10^4$ . The OH system of the tokamak is not designed to provide a voltage increase of this order of magnitude within milliseconds and cannot maintain constant toroidal plasma current.

Therefore the current decays. This decay can be described by a simple circuit equation:

$$\frac{d(LI)}{dt} + RI = V \quad (3.219)$$

where the plasma is assumed to be a conductor of self-inductance  $L$ , resistance  $R$ , with an applied voltage  $V$ .

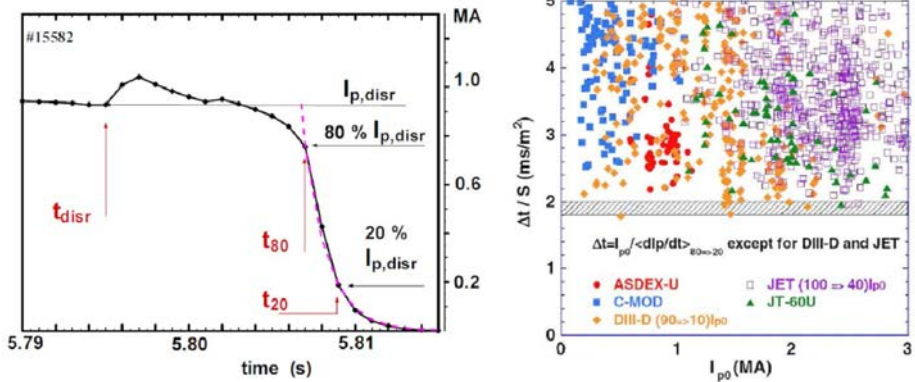


FIG. 3.61. Time history of the current decay. The times at which the current has decayed to 80 and 20% of the pre-disruption value are shown (left). Database of conductivity from several tokamaks (right) [3.72].

The currents in the OH and PF coils cannot significantly change during a fast current quench (some milliseconds) and have little influence on the current decay. Also the voltage due to the mutual inductance between plasma and vessel structures is smaller than the self-inductance. Therefore the plasma current decays according to

$$-L \frac{dI}{dt} \cong RI \quad (3.220)$$

For  $L/R$  constant in time, the decay time constant  $\tau$  is given by:

$$-\frac{dI}{dt} \frac{1}{I} = \frac{R}{L} = \tau^{-1} \quad (3.221)$$

$$\tau \propto S / \eta \quad (3.222)$$

with  $S$  being the plasma cross-section and  $\eta$  the plasma resistivity.

The expected rate of current decay is an important design parameter for future large tokamaks because it determines, among other parameters, the magnitude of the electromagnetic forces on the tokamak and the rate of generation

of runaway electrons. Nevertheless, it is difficult to predict, since it depends on the plasma temperature, which results from a complex balance between resistive dissipation of the magnetic energy and heat losses by radiation of impurities.

Nevertheless the mechanism controlling the plasma temperature during the current quench is believed to be similar in every tokamak. Figure 3.61 (right) shows that the value of  $\Delta t / S$  (proportional to  $\tau / S$  in Eq. (3.222) and to the electrical conductivity) from several tokamaks has a lower boundary of  $1.8 \text{ ms} \cdot \text{m}^{-2}$ .  $\Delta t$  is defined as  $(t_{20} - t_{80}) / 0.6$  where  $t_{80}$  and  $t_{20}$  are the times at which the plasma current has decayed to 80 and 20% of the pre-disruption value, as illustrated in Fig. 3.61 (left).

### 3.5.4. Damage potential

#### 3.5.4.1. Heat pulse

Most of the thermal energy lost by the plasma during the thermal quench is conducted through the SOL to the limiter and divertor plates. A significant fraction of it can also be radiated during this phase, if the heat pulse on the plasma facing components causes the ablation of surface material or if impurities are already present in the plasma. During the current quench, the whole plasma recombines and radiates most of the magnetic energy; localized deposition of energy is expected by conduction and convection there where the plasma contacts the wall. Thermographic measurements like the one shown in Fig. 3.62 allow us to infer the surface temperature of the wall and to calculate the deposited power flux. In addition they show that there is a clear expansion of the SOL during the thermal quench which distributes the thermal load on a large surface around the footprint of the pre-disruptive strike points.

The amount of deposited energy ( $E_{th}$ ), extension of the surface on which the heat is deposited ( $S$ ) and the duration of the heat pulse ( $\tau_{hp}$ ) determine, together with the thermal properties of the wall material, the increase of the surface temperature  $T_w$ , since  $T_w \propto E_{th} (S \sqrt{\tau_{hp}})^{-1}$ . The temperature reached on the surface determines then if the material facing the plasma evaporates or melts during a disruption. The physics determining the broadening of the SOL and the timescale of the heat pulse duration is partly known and described by conduction parallel and perpendicular to the open magnetic surface of the SOL, affected by turbulence and stochasticity, and flux limit through the sheath at the plasma-wall interface. Nevertheless there is not yet a solid physics model for the quantitative evaluation of the main mechanisms determining the broadening of the SOL and the prediction of the thermal effect of disruptions in future larger machines is uncertain. Nevertheless local melting and erosion of the surfaces intersecting the expanded SOL are expected in a larger machine, since the thermal energy density will be larger.

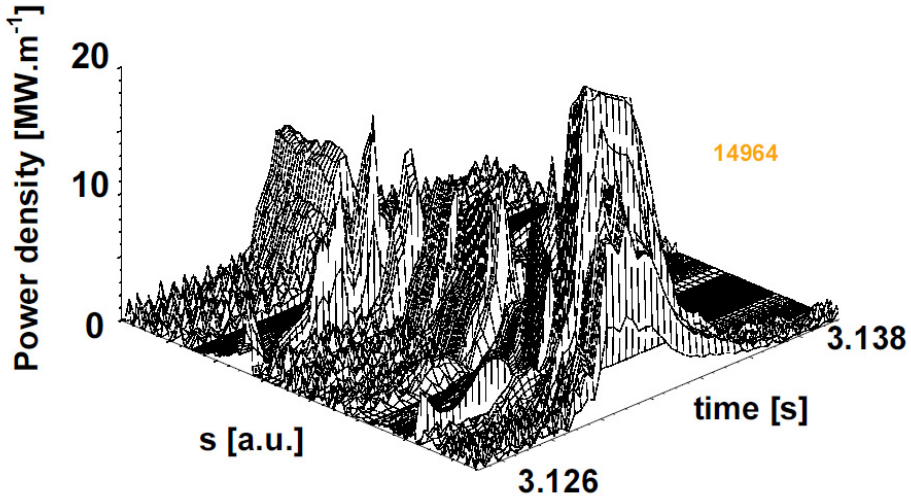


FIG. 3.62. Distribution of the heat flux on the divertor of ASDEX Upgrade during a disruption; parameter  $s$  describes the position along a poloidal cut of the divertor surface. Reprinted from Ref. [3.74]. Copyright (2010), American Nuclear Society.

#### 3.5.4.2. Electromagnetic forces

Large electromagnetic forces act on the vessel components during the current quench for two reasons. Firstly, the decay of the toroidal plasma current induces currents in the surrounding conductors according to the circuit equations

$$\frac{d(L_p I_p)}{dt} + \sum_i \frac{d(L_{ip} I_i)}{dt} + R_p I_p = 0 \quad (3.223)$$

$$\frac{d(L_i I_i)}{dt} + \sum_i \frac{d(L_{pi} I_p)}{dt} + R_i I_i = U_i \quad (3.224)$$

where the indices  $p$  and  $i$  pertain to the plasma and to the  $i$ -th coil or passive conductor, and  $L, I, R$  and  $U$  are inductance, current, resistance and applied voltage respectively. The conductors are immersed in a magnetic field and therefore subject to a force  $\vec{F} = \int (\vec{j} \times \vec{B}) dV$ . A compressive force is acting on the vessel during the current quench, for example. Secondly, all reactor relevant plasmas have a vertically elongated cross-section and they are unstable to vertical motion. The shaped cross-section is achieved by means of coils located above and below the plasma, in which a current flows in the same direction of the plasma current and *stretches* it. The resulting magnetic field created by external coils is shown in Fig. 3.63. An elongated plasma is in a vertically unstable equilibrium in

the sense that, in the absence of surrounding conductors and of feedback control, every small displacement would be followed by the vertical displacement of the plasma against the vessel. Surrounding conductors slow down the vertical movement and a feedback control system keeps the plasma in a reference position within the vessel. Large perturbations of the plasma equilibrium, such as the current redistribution and the increase of plasma elongation, can initiate a vertical displacement which cannot be stabilized by the feedback coils. In this case the plasma carrying the toroidal current moves vertically on a timescale dictated by the  $L/R$  timescale of the conductors around the plasma. In this case the movement of the plasma induces in the vessel components a toroidal current which gives rise to a net total vertical force on the vessel, which is of the order of magnitude of the vessel weight.

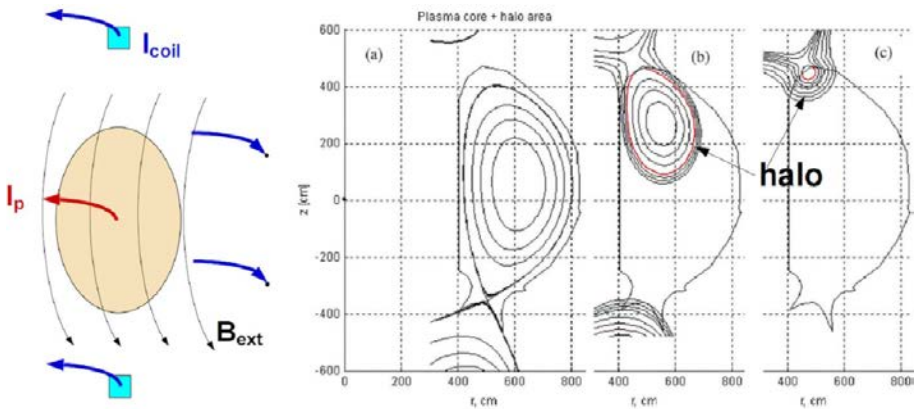


FIG. 3.63. Schematic representation of an elongated plasma, the associated external field  $B_{ext}$  and the conductor currents producing it. The pair of coils carrying  $I_{coil}$  gives rise to a destabilizing force, as discussed for the wire model in Section 3.2.2.5 (left). Simulation of an ITER plasma undergoing vertical instability (right) [3.75].

Frequently such events are triggered by the rapid change in plasma current during a disruption, which induces currents in the vessel attracting the plasma to the magnetically more tightly coupled passive elements. For a positionally stable plasma with approximately circular cross-section this effect can be recognized and well observed, but will result only in a shift of the equilibrium position. In an elongated plasma, however, it can be the trigger of an unstable displacement event. Evidently, a significant benefit for the controllability of the plasma can be derived from positioning the plasma at the neutral point [3.76] of the vessel structures, defined by the requirement that the inductive response of the vessel to plasma current changes does not give rise to an average radial field.

The plasma moves vertically until one of the two divertors starts acting as a limiter. This limited plasma consists of a region of closed flux surfaces, which

keeps shrinking and shifting vertically, until it disappears, and leaves behind a region of open magnetic flux surfaces intersecting the vessel structures. This plasma region is called the halo and is shown in Fig. 3.63 (right). The term “halo current” is commonly used to designate the poloidal component of the current flowing from this region onto the vessel structures and back during the current quench phase of a plasma disruption.

The halo current is driven both by the time variation of the toroidal magnetic flux across the shrinking plasma poloidal cross-section and by the decay of the plasma current in the core. It contributes significantly to the vertical force acting on the plasma and slows it down during the vertical displacement. The maximum halo current can amount to 50% of the pre-disruption plasma current and is monitored in all tokamaks because its magnitude is so large as to potentially cause damage to the in-vessel components in which it flows.

### 3.5.4.3. Runaway generation

A toroidal electric field is commonly present in a tokamak and driven by external coils, to maintain the toroidal current required for the plasma stability. The electrons are accelerated by the electric field and decelerated by collisions with the background electrons and ions. The increased friction exerted by the air as a bicycle speeds up is well known. The drag force on the test electrons, instead, decreases at large velocities with the kinetic energy of the test electron and increases with the electron density of the background plasma as

$$F_{e,e} = \frac{e^4 n_e \ln \Lambda}{4\pi\epsilon_0^2 m_e v_e^2} \quad (3.225)$$

During the disruption the force on the electrons due to the electric field can overcome the drag force and the electrons are accelerated to relativistic velocities, i.e. they run away. The threshold field is found from the force balance  $F_{e,e} = eE$ . Given a certain electron density, the electron field strength at which the electrons runaway is called the Dreicer field,

$$E_D = \frac{e^3 n_e \ln \Lambda}{4\pi\epsilon_0^2 T_e} \quad (3.226)$$

The density necessary to suppress the runaway electrons by collisions can be derived from the condition  $F_{e,e} > eE$ .

Three main mechanisms can give rise to runaway electrons in a tokamak. Firstly, when the acceleration due to the electric field overcomes the drag force, electrons diffuse through the velocity space towards relativistic velocities. This is called primary generation. Secondly, a runaway electron can collide with a thermal electron and transfer so much energy at once to knock it into the runaway

region of the velocity space. This mechanism is called secondary generation (or avalanche) because it requires the presence of existing fast electrons to be active. Thirdly, in a fusion reactor energetic particles ( $\alpha$ ,  $\beta$ ) and gamma rays are present. They can also transfer part of their energy to thermal electrons and generate a small population of fast electrons that a strong electric field amplifies through the avalanche mechanism. An example of a disruption which generated runaway electrons is shown in Fig. 3.64. Runaway electrons can form a plateau during the current quench because they are better confined than the colder electrons, which suffer more frequent collisions. When they are lost by the plasma at the end of the current quench, they interact with the surrounding structures, depositing their kinetic energy and causing localized melting of the structure surface.

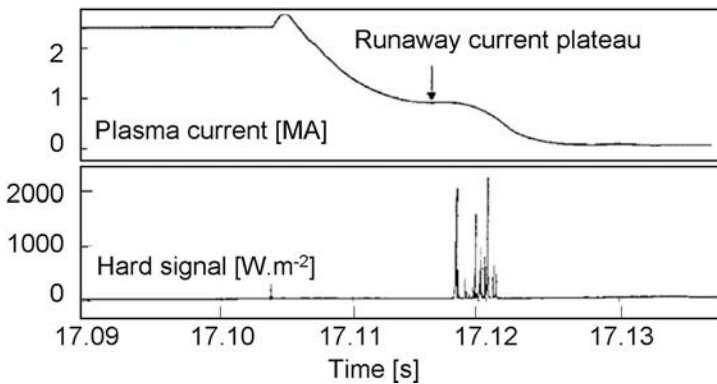


FIG. 3.64. The plateau during the current quench of a JET disruption is due to the presence of runaway electrons. The hard X rays are a signature of their presence: they are generated when the fast electrons are lost by the plasma and slow down in surrounding structures [3.77].

### 3.5.5. Mitigation methods

Disruptions can often be avoided because they happen in known regions of the parameter space. In addition they are often preceded by degradation of the confinement and the development of MHD modes, which can be detected and used for their prediction and mitigation.

The disruption effects described in the previous chapter can all be reduced by injecting impurity atoms in the plasma. The injection of cryogenic or solid pellets was originally used to initiate a plasma shutdown with impurity injection. But this method showed a series of disadvantages, such as insufficient ablation of the solid pellets and the tendency to provide a seed for runaway electrons, and was abandoned in favour of massive gas injection.

The massive injection of an impurity gas into a disruptive plasma influences the disruption effects described above since it increases the plasma

density and cools the plasma by dilution and radiation before the thermal quench occurs. The optimal disruption mitigation requires that all three deleterious effects of disruptions be reduced below acceptable engineering margins.

In order to reduce the localized heat deposition during the thermal quench of the disruption, the injected impurity gas must radiate most of the thermal energy of the plasma before magnetic instabilities can cause the thermal quench.

The reduction of the forces follows the reduction of the induced toroidal, poloidal and eddy currents in the structure of the plasma. Depending on the vertical stability characteristics of the plasma, the methods of impurity injection can follow two different strategies.

In tokamaks with vertically stable plasmas, the largest mechanical forces are eddy currents caused by the plasma current quench. In this case the current quench should develop slowly. This contributes to the avoidance of the runaway electrons. Low-Z impurities are suitable for injection in this case, because they radiate less and cool down the plasma more slowly. In vertically unstable plasmas, on the other hand, the toroidal and poloidal (halo) currents induced in the mechanical structures of the machine must be reduced. This can be done by anticipating the current quench before the vertical displacement starts. The consequence of increasing the amount of injected impurities is illustrated in Fig. 3.65. The currents in the passive stabilizing vessel structures and the halo current diminish gradually, reducing the overall vertical force on the vessel.

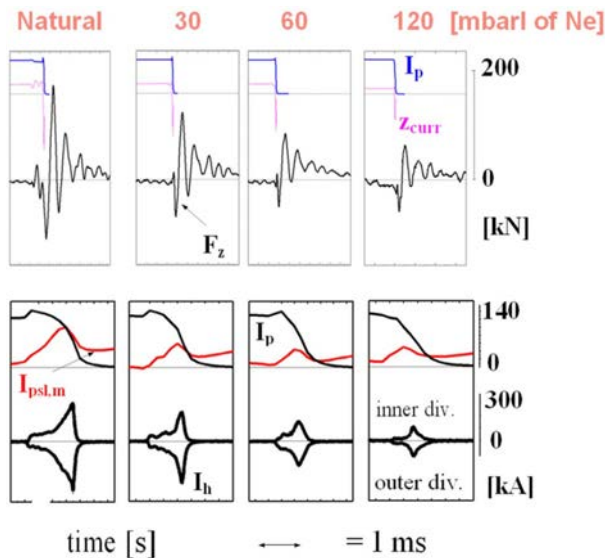


FIG. 3.65. Decrease of the total vertical force on the vessel ( $F_z$ ) of ASDEX Upgrade, of the current in the passive stabilizing loop ( $I_{psl,m}$ ) and of the halo current ( $I_h$ ) as functions of the increase of injected neon in the plasma ( $z_{curr}$  is the vertical position of the centre of the plasma current). Reprinted from Ref. [3.74]. Copyright (2010), American Nuclear Society.

The suppression of the runaway electron generation requires that the electric field  $E = \eta j \propto T_e^{-3/2}$  generated during the current quench remains below the critical electric field,  $E_c \propto n_e$ . This condition implies that the total (free and bound to partially ionized ions) electron density should be increased above a critical value. This density is very large, of the order of  $10^{22}$ – $10^{23} \text{ m}^{-3}$  for ITER, 2–3 orders of magnitude larger than the plasma density during standard operation. Present experiments have reached the lower boundary of this density range. An alternative method to avoid the formation of a large runaway current is the excitation of oscillatory magnetic perturbations with external coils. These increase the perpendicular diffusion of the electrons during their acceleration and enhance their losses from the plasma.

## REFERENCES

- [3.1] BRAAMS, C.E., STOTT, P.E., Nuclear Fusion: Half a Century of Magnetic Confinement Fusion Research, IOP Publishing, Bristol and Philadelphia (2002).
- [3.2] IKEDA, K., et al., Progress in the ITER Physics Basis, Nucl. Fusion **47** 6 (2007) S1.
- [3.3] MUKHOVATOV, V.S., SHAFRANOV, V.D., Plasma equilibrium in a tokamak, Nucl. Fusion **11** (1971) 605.
- [3.4] WESSON, J.A., Tokamaks, Clarendon Press, Oxford (1997).
- [3.5] FREIDBERG, J.P., Ideal Magnetohydrodynamics, Plenum Press, New York and London (1987).
- [3.6] GOEDBLOED, J.P.H., POEDTS, S., Principles of Magnetohydrodynamics: With Applications to Laboratory and Astrophysical Plasmas, Cambridge University Press, Cambridge (2004).
- [3.7] GRUBER, R., RAPPAZ, J., Finite element Methods in Linear Ideal Magnetohydrodynamics, Springer Verlag (1985).
- [3.8] NEWCOMB, W.A., Ann. Phys. (NY) **10** (1960) 232.
- [3.9] WESSON, J.A., Nucl. Fusion **18** (1978) 87.
- [3.10] GRUBER, R., et al., Comput. Phys. Commun. **21** (1981) 323.
- [3.11] GRIMM, R.C., DEWAR, R.L., MANICKAM, J., J. Comput. Phys. **49** (1983) 94.
- [3.12] BERNARD, L.C., HELTON, F.J., MOORE, R.W., GATO: An MHD stability code for axisymmetric plasmas with internal separatrices, Comp. Phys. Commun. **24** (1981) 377.
- [3.13] KERNER, W., et al., "CASTOR: Normal mode analysis of resistive MHD plasmas, J. Comput. Phys. **142** (1998) 271.
- [3.14] CONNOR, J.W., HASTIE, R.J., TAYLOR, J.B., Shear, periodicity and plasma ballooning modes, Phys. Rev. Letters **40** (1978) 396.
- [3.15] SEKI, S., et al., Nucl. Fusion **27** (1987), 330.
- [3.16] LORTZ, D., NÜHRENBERG, J., J. Phys. Lett. **68A** (1978) 49.
- [3.17] SYKES, A., et al., in Proc. 11th European Conf. on Controlled Fusion and Plasma Physics, Aachen, II 363, 1983.

- [3.18] BUSSAC, M.N., et al., Internal kink modes in toroidal plasmas with circular cross sections, *Phys. Rev. Lett.* **35** (1975) 1638.
- [3.19] CHARLTON, L.A., CARRERAS, B.A., LYNCH, V.E., Linear and nonlinear properties of infernal modes, *Phys Fluids B* **2** (1990) 1574.
- [3.20] TROYON, F., et al., MHD-limits to plasma confinement, *Plasma Phys. Control. Fusion* **26** (1984) 209.
- [3.21] TURNBULL, A.B., *Nucl. Fusion* **38** (1998) 1467.
- [3.22] GATES, D.A., *Nucl. Fusion* **47** (2007), 1376.
- [3.23] TAYLOR, T.S., et al., in Proc. 13th IAEA Fusion Energy Conf. Washington, 1990, IAEA, Vienna (1991) paper CN-53/A-III-1.
- [3.24] MANICKAM, J., et al., *Phys. Plasmas* **1** (1994) 1601.
- [3.25] PFIRSCH, D., TASSO, H., *Nucl. Fusion* **11** (1971) 259.
- [3.26] MERKEL, P., SEMPF, M., “Feedback stabilisation of resistive wall modes in the presence of multiply connected wall structures”, Proc. 21st IAEA Fusion Energy Conf, Chengdu, China, 2006, IAEA Vienna (2006) paper TH/P3-8.
- [3.27] GLASSER, A.H., GREENE, J.M., JOHNSON, J.L., *Phys. Fluids* **18** (1975) 875.
- [3.28] CONNOR, J.W., HASTIE, R.J., TAYLOR, J.B., *Phys. Fluids* **B3** (1991) 1532.
- [3.29] ARA, G., et al., *Ann. Phys.* **112** (1978) 443.
- [3.30] FITZPATRICK, R., AYDEMIR, A.Y., *Nucl. Fusion* **36** (1996) 11.
- [3.31] FITZPATRICK, R., *Phys. Plasmas* **9** (2002) 3459.
- [3.32] BISKAMP, D., *Nonlinear Magnetohydrodynamics*, Cambridge University Press, Cambridge (1993).
- [3.33] RUTHERFORD, P.H., Nonlinear growth of the tearing mode, *Phys. Fluids* **16** (1973) 1903.
- [3.34] FITZPATRICK, R., Helical temperature perturbations associated with tearing modes in tokamak plasmas, *Phys. Plasmas* **2** (1995) 825.
- [3.35] CHIRIKOV, B.V., Resonance processes in magnetic traps, *J. Nucl. Energy Part C: Plasma Phys.* **1** (1960) 253.
- [3.36] YU, Q., Numerical modelling of diffusive heat transport across magnetic islands and local stochastic field, *Phys. Plasmas* **13** (2006) 062310.

- [3.37] KADOMTSEV, B.B., Disruptive instability in tokamaks, *Sov. J. Plasma Phys* **1** (1975) 389.
- [3.38] HAZELTINE, R.D., MEISS, J.D., *Plasma Confinement*, Dover Publications, Mineola NY (2003).
- [3.39] ZONCA, F., *Int. J. Mod. Phys. A* **23** (2008) 1165.
- [3.40] ZONCA, F., et al., *Plasma Phys. Control. Fusion* **48** (2006) B15.
- [3.41] HEIDBRINK, B.W., *Phys. Plasmas* **15** (2008) 055501.
- [3.42] CHEN, L., ZONCA, F., *Nucl. Fusion* **47** (2007) 727.
- [3.43] FU, G.Y., VanDAM, J.W., *Phys. Fluids B* **1** (1989) 1949.
- [3.44] PORCELLI, F., *Plasma Phys. Control. Fusion* **33** (1991) 1601.
- [3.45] COPPI, B., et al., *Phys. Rev. Lett.* **63** (1989), 2733.
- [3.46] BRIGUGLIO, S., et al., *Phys. Plasmas* **2** (1995), 3711.
- [3.47] Von GOELER, S., et al., *Phys. Rev. Lett.* **33** (1974), 1201.
- [3.48] YAMAHA, M., et al., *Phys. Plasmas* **1** (1994), 3269.
- [3.49] CAMPBELL, D., et al., *Phys. Rev. Lett.* **60** (1988) 2148.
- [3.50] McGUIRE, K., et al., *Phys. Rev. Lett.* **50** (1983) 891.
- [3.51] GÜNTER, S., et al., *Nucl. Fusion* **39** (1999) 1535.
- [3.52] MIRNOV, S.V., SEMENOV, B., *Atomnaya Energiya* **30** (1971) 20.
- [3.53] SNIPES, J.A., et al., *Nucl. Fusion* **28** (1988) 1085.
- [3.54] GÜNTER, S., et al., *Nucl. Fusion* **41** (2001) 1287.
- [3.55] CHANG, Z. et al., *Phys. Rev. Lett.* **74** (1995) 4663.
- [3.56] GANTENBEIN, G., et al., *Phys. Rev. Lett.* **85** (2000) 1242.
- [3.57] DOYLE, E.J., et al., *Nucl. Fusion* **47** (2007) S18.
- [3.58] SUTTROP, W., et al., *Plasma Phys. Control. Fusion* **39** (1997) 2051.
- [3.59] FREDRICKSON, E.D., et al., *Phys. Plasmas* **4** (1997) 1589.
- [3.60] ITER Physics Basis Editors et al., *Nucl. Fusion* **39** (1999), 2137.
- [3.61] KESSEL, C.E., *Fusion Eng. Des.* **80** (2006) 63.
- [3.62] STRAIT, E.J., et al., *Phys. Rev. Lett.* **74** (1995) 2483.
- [3.63] TAKECHI, M., et al., *Phys. Rev. Lett.* **98** (2007) 055002.
- [3.64] KRAMER, G.J., et al., *Phys. Rev. Lett.* **80** (1998) 2594.

- [3.65] SHARAPOV, S.E., et al., Nucl. Fusion **46** (2006) S868.
- [3.66] Van ZEELAND, M.A., et al., Phys. Rev. Lett. **97** (2006) 135001.
- [3.67] GARCIA/MUNOZ, M., Fast Response Scintillator Based Detector for MHD Induced Energetic Ion Losses in ASDEX Upgrade, PhD thesis, LMU Munich (2006).
- [3.68] STRAIT, E.J., et al., Nucl. Fusion **33** (1993) 1849.
- [3.69] FREDRICKSON, E.D., et al., Phys. Plasmas **13** (2006) 056109.
- [3.70] SUTTROP, W., et al., Nucl. Fusion **37** (1997) 119.
- [3.71] KRUGER, S.E., et al., Phys. Plasma **12** (2005) 056113.
- [3.72] HENDER, T.C., et al., Nucl. Fusion **47** (2005) 128.
- [3.73] FREDRICKSON, E.D., et al., Phys. Plasma **2** (1995) 4216.
- [3.74] PAUTASSO, G., et al., Fusion Sci. Technol. **44** (2003) 716.
- [3.75] LUKASH, V.E., et al., Nucl. Fusion **47** (2007) 1476.
- [3.76] YOSHINO, R., NAKAMURA, Y., NEYATANI, Y., Nucl. Fusion **36** (1996) 295.
- [3.77] GILL, R.D., et al., Nucl. Fusion **40** (2000) 163.

# CHAPTER 4

## PLASMA DIAGNOSTICS

### 4.1. INTRODUCTION

**V. Zaveryaev**

Kurchatov Institute, Moscow,  
Russian Federation

The success in achieving peaceful fusion power depends on the ability to control a high temperature plasma, which is an object with unique properties, possibly the most complicated object created by humans. Over years of fusion research a new branch of science has been created, namely plasma diagnostics, which involves knowledge of almost all fields of physics, from electromagnetism to nuclear physics, and up-to-date progress in engineering and technology (materials, electronics, mathematical methods of data treatment).

Historically, work on controlled fusion started with pulsed systems and accordingly the methods of plasma parameter measurement were first developed for short lived and dense plasmas. Magnetically confined hot plasmas require the creation of special experimental techniques for diagnostics.

The diagnostic set is the most scientifically intensive part of a plasma device. During many years of research operation some scientific tasks have been solved while new ones arose. New tasks often require significant changes in the diagnostic system, which is thus a very flexible part of plasma machines.

Diagnostic systems are designed to solve several tasks. As an example here are the diagnostic tasks for the International Thermonuclear Experimental Reactor — ITER [4.1]:

- (1) Measurements for machine protection and basic control;
- (2) Measurements for advanced control;
- (3) Additional measurements for performance evaluation and physics.

Every new plasma machine is a further step along the path to the main goal — controlled fusion — and nobody knows in advance what new phenomena will be met on the way. So in the planning of diagnostic construction we should keep in mind further system upgrading to meet possible new scientific and technical challenges.

The procedure of creating the diagnostic set is a complicated one and includes several stages:

- (a) Definition of the plasma parameters to be measured and elaboration of the measurement requirements (spatial and temporal resolution, dynamic range, accuracy, etc.);
- (b) Selection of the most suitable diagnostic methods;
- (c) Allocation of diagnostic equipment inside and around the machine (so called *integration*);
- (d) Development of the diagnostics themselves — design and construction;
- (e) Testing and calibration of the apparatus in the laboratory or on existing machines;
- (f) Installation on the machine and commissioning;
- (g) Further development and upgrading.

These stages must be performed by the joint efforts of scientists and technicians because sometimes there is a contradiction between scientific requirements and technical capabilities.

The first step in diagnostic development is mathematical modelling of the expected plasma parameters to forecast the shape and position of the plasma, temperature and density profile, etc. The necessary startup diagnostic set which is required for the very first shot must be defined. The content of the startup diagnostic set depends weakly on the peculiarities of the machine.

Sometimes it is not possible to apply a single method to satisfy the measurement requirements. Moreover, for reliability of the key parameter measurements, a duplication of methods is needed. Sometimes special techniques have to be applied for core, edge and divertor plasmas.

More than fifty diagnostic methods have been developed during the past few decades. All of them have their own peculiar properties. Not many methods can directly measure the plasma parameters and it is important to distinguish what is measured and what is the result of interpretation. As a rule, the simplest method technically is the most difficult for interpretation. Local measurements are always preferable to averaged ones owing to the simpler interpretation.

Diagnostic methods can be divided into two groups: *passive* and *active*. The passive methods measure the plasma radiation, while the active methods measure the plasma reaction to external impact. The passive methods, as a rule, give averaged information, whereas the active methods often provide local measurements. The influence of the probing on plasma parameters must be minimal (“contact-free problem”).

There are many good reviews of plasma diagnostics, the most complete description of various diagnostic methods developed up to 1965 is presented in Ref. [4.2]. A very useful review has been published by Equipe TFR [4.3],

while the most recent progress in hot plasma diagnostics can be found in Ref. [4.4]. The continuous progress in the development of plasma diagnostic methods and techniques is presented in a series of workshops (see, for example, Refs [4.5–4.8]).

This chapter just briefly describes the diagnostic techniques and it is intended to show the progress achieved in this field of science during several decades. The chapter is rather intended for post-graduate students beginning experimental research in the field of high temperature plasma diagnostics. The list of references directs the readers to the original papers where more detailed descriptions of diagnostic techniques, methods and results are presented.

## 4.2. PASSIVE DIAGNOSTIC METHODS

### 4.2.1. Magnetic measurements

**M. Dremin**

Kurchatov Institute, Moscow,  
Russian Federation

Magnetic diagnostics is the measurement of magnetic field and flux around a plasma column, as a rule, with inductive sensors — magnetic probes and loops. This is one of the oldest and most widely used diagnostic because it is contactless and relatively simple. It makes it possible to obtain so called macroscopic plasma characteristics, and, under favourable conditions, to assess the plasma parameters in detail, as well as to gain knowledge about plasma MHD activity. Magnetic diagnostics were always considered in plasma diagnostic review papers [4.3, 4.9, 4.10] and have been presented in special papers [4.11–4.15].

The interpretation of magnetic measurements follows from the equilibrium equations of plasma current in a magnetic field [4.16–4.18], although the first measurements of this kind were based on simpler assumptions [4.19]. These measurements allow one to get the following parameters of the plasma and discharge: loop voltage  $U_{loop}$ , plasma current  $I_p$ , its position in the vacuum vessel (shift of magnetic axis or outer magnetic surface relative to the vessel axis horizontally  $\Delta_h$  and vertically  $\Delta_v$ ), the shape of the outer magnetic surface (sometimes the current distribution as well), plasma energy  $W$  or the ratio of plasma pressure to pressure of poloidal magnetic field  $\beta_p$ , the characteristics of the MHD activity, the magnitude of the most dangerous modes with small  $m$  and  $n$  numbers, and the amplitude and velocity of magnetic perturbations in the poloidal and toroidal directions and their temporal evolution.

(I) Plasma current  $I_p$  is one of the most important parameters which defines plasma equilibrium. Usually it is measured by means of multi-coil

distributed solenoids called Rogowski belts [4.9], which surround the plasma column (Fig. 4.1). As the plasma current changes, a voltage is induced in this solenoid, the magnitude of which is proportional to the rate of current change:  $V \sim (nS/r)dI_p/dt$ , where  $n$  is the number of solenoid turns,  $S$  is the cross-section of the turn and  $r$  is the solenoid radius. After signal integration, it is possible to obtain the total plasma current. The full current flowing along the solenoid axis is registered regardless of the current distribution and mutual orientation of the current and solenoid. Furthermore, if the solenoid winding is uniform it is not sensitive to other magnetic fields. But the Rogowski belt winding itself in its simplest design constitutes a loop which is sensitive to the toroidal magnetic field. To avoid this, special precautions are usually taken — dividing the solenoid into two halves, adding a counter-turn (this role can be played by the central conductor of the coaxial cable on which Rogowski belt or its conductive core is wound), making the solenoid winding in two layers with opposite pitches and so on. Some peculiarities of the Rogowski belt design are described in Refs [4.10, 4.14, 4.20].

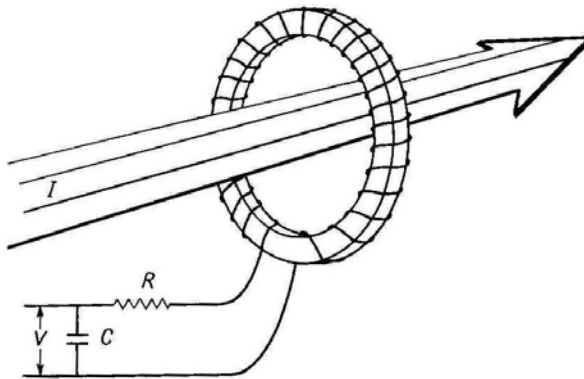


FIG. 4.1. Scheme of plasma current measurements by Rogowski belt [4.9].

(II) The loop voltage characterizes the level of plasma contamination with impurities and it must be known in order to calculate the ohmic power. Knowing the plasma current, loop voltage and plasma cross-section, it is possible to define the plasma average resistivity; we can use the Spitzer formula

$$\rho_H = 1 / \sigma_H = 1.65 \times 10^{-9} \ln \Lambda / T_e^{3/2} \Omega m \quad (4.1)$$

$$1 / \sigma_Z = N(Z)Z / \sigma_H \quad (4.2)$$

here  $\rho_H$  is the resistivity of a pure hydrogen plasma,  $T_e$  is in keV,  $\ln \Lambda$  is the so-called Coulomb logarithm, which is weakly dependent on plasma density and can be taken as 17, the parameter  $N$  is weakly dependent on the effective charge

of the plasma ions ( $N = 0.5$  for  $Z = 2$  and  $N = 0.74$  for  $Z = 4$ ) to estimate the effective plasma charge  $Z_{eff}$ , if the electron temperature  $T_e$  is independently measured. More exact equations and values for  $\ln \Lambda$  and  $N(Z)$  are given in Ref. [4.21]. Or, vice versa, it is possible to estimate  $T_e$  if  $Z_{eff}$  is known. The loop voltage is measured by means of single-turn loops placed along the torus. For a circular plasma it is sufficient to install two ring loops in the equatorial plane on the inner and outer sides. For a non-circular plasma it is necessary to know the voltage distribution in the poloidal direction along the contour embracing the plasma column for accurate assessment of the ohmic power [4.22]. Moreover, a large number of loops are needed also for correct reconstruction of the edge magnetic surface shape. Of course, all of these considerations correspond to a stationary or quasistationary state of the plasma discharge. In practice this ideal situation rarely prevails and interpretation of flux measurements for resistivity requires a lot of corrections. In the case of time varying parameters it is necessary to take into account the inductive terms in the loop voltage like  $L(dI_p / dt)$  and  $I_p(dL / dt)$ , where  $L$  is the plasma inductance. Additional corrections are necessary for discharges with beam or wave current generation and for discharges where runaway electrons play a significant role.

(III) To avoid contact between the plasma and plasma facing components (PFC) it is necessary to maintain a proper position along the major radius. The first measurements of plasma shift relative to the vessel centre were made with a couple of magnetic probes detecting the poloidal magnetic field in the horizontal plane [4.19] (see Fig. 4.2).

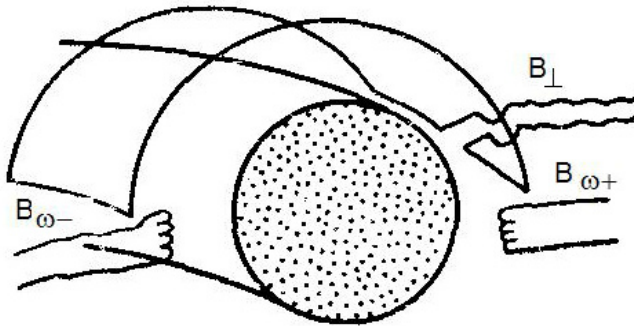


FIG. 4.2. Scheme of plasma position measurements in a circular tokamak [4.18].

Later for this purpose Rogowski belts with a variable winding density of  $n(\theta) = n \cos \theta$  were used [4.23, 4.24], where  $\theta$  is the poloidal angle. As was shown in Ref. [4.18], to know the position of the edge magnetic surface for a circular plasma it is necessary to measure the azimuthal field at the inner and outer sides of the plasma and the average perpendicular magnetic field as well:

$$\begin{aligned} \frac{\Delta}{b} = & \frac{b}{2R} \left[ \frac{a^2}{b^2} \ln \frac{b}{a} + \frac{1}{2} \left( 1 - \frac{a^2}{b^2} \right) \right] + \\ & + \frac{cb}{4I_p} \left[ \frac{B_{\omega+} - B_{\omega-}}{2} \left( 1 - \frac{a^2}{b^2} \right) - B_{\perp} \left( 1 + \frac{a^2}{b^2} \right) \right] \end{aligned} \quad (4.3)$$

where  $\Delta$  is the horizontal shift of the plasma current,  $a$  is the plasma radius,  $b$  is the radius of the probe location,  $c$  is the speed of light,  $B_{\omega+}$  and  $B_{\omega-}$  represent an azimuthal magnetic field at the outer and inner sides of the torus, and  $B_{\perp}$  is the average perpendicular magnetic field.

To define the vertical plasma position (which can be not optimal due to stray fields), it is sufficient to measure the magnetic field by a couple of probes installed on top of and below the plasma or by means of a Rogowski belt with winding density  $n(\theta) = n \sin \theta$ .

From the equilibrium equation it follows that magnetic measurements can give such an important parameter as  $\beta_{pol} + l_i / 2$ , where  $\beta_{pol}$  is the ratio of the plasma pressure to the poloidal magnetic field pressure, and  $l_i$  is the internal plasma inductance depending on the plasma current distribution:

$$\frac{2I_p}{cR} \left( \ln \frac{b}{a} + \beta_{pol} + \frac{l_i}{2} - 1 \right) = \frac{B_{\omega+} - B_{\omega-}}{2} + B_{\perp} \quad (4.4)$$

For non-circular plasmas the task of finding the position of the outer magnetic surface becomes more complicated and can be solved simultaneously with defining its shape (see below).

(IV) The equilibrium equation gives the basis for defining the plasma energy content [4.18]. For this purpose it is necessary to measure the toroidal magnetic flux variation due to hot plasma diamagnetism in a magnetic field:

$$\Delta\Phi = \frac{2\pi}{B_{\phi}} \left[ \left( 0.1I_p \right)^2 - 2W_{\perp} \right] = \frac{2\pi \left( 0.1I_p \right)^2}{B_{\phi}} \left( 1 - \beta_{pol} \right) \quad (4.5)$$

The main difficulty in these measurements is a low value of diamagnetic flux ( $\sim 10^{-4}$ – $10^{-3}$ ) relative to the toroidal magnetic flux. That is why with these measurements the main efforts were directed to toroidal field signal compensation and elimination of inductive coupling with other fields.

Two measurement schemes have been used. In the first one, the toroidal flux variation was measured as a current variation in toroidal coils [4.25–4.27] (the total flux in a toroidal coil is constant if the impedance of the power supply system is low). The second scheme of flux variation measurement by a special

diamagnetic loop requires the application of a compensative winding and accurate adjustment of loops to avoid the inductive coupling with other fields coils [4.28–4.32].

It is necessary to note that diamagnetic measurements characterize only the transverse component of plasma energy whereas plasma equilibrium is determined by the full plasma energy content and, in particular by the contribution of fast particles and not only the thermal ones.

(V) One of the aims of magnetic measurements is to define the shape of an outer magnetic surface, its position and, if possible, the plasma current distribution. This is especially essential for non-circular plasmas [4.11]. At first, the problem to reconstruct the magnetic configuration was solved as a direct task of finding a model current distribution which gives the best fit to the experimentally measured poloidal field distribution [4.33]. Later, the magnetic field and flux distributions along some contour enclosing the plasma measured by magnetic probes and loops were considered as the boundary conditions in solving the inverse MHD equilibrium problem. An exact solution of this problem requires a lot of computing time. So a few methods of faster solution were suggested and used. In one of them the plasma current was represented as a set of discrete filament currents with values chosen to describe in the best way the measured fields and fluxes [4.34–4.36]. An analysis was made of how the values and locations of these currents affect the shape reconstruction accuracy [4.37, 4.38]. Also used was a version where the plasma current was assumed to be distributed over a limited number of inner surfaces or contours [4.39]. The other version confined itself to a few lowest moments in describing the magnetic field around the plasma [4.40–4.42]. One further approach has recently been developed: first, within a wide range of equilibrium plasma conditions one determines the magnetic field and flux distributions along the contours corresponding to the magnetic sensor locations. Then, using the determined distributions, one interpolates or chooses the equilibrium parameter sets to fit the best [4.43]. It is more difficult to get the plasma current density distributions and equilibrium plasma configuration structure from external magnetic measurements; however, in some conditions this is possible [4.44–4.46].

(VI) A large part of magnetic measurements is determining the plasma MHD perturbation parameters (the amplitude, frequency, mode structure, correlation coupling) by measuring the magnetic field fluctuation characteristics. At first, the signals from discrete magnetic probes were used [4.47], then that of distributed detectors, namely separate Rogowski belts with winding density corresponding to the registered poloidal mode of perturbation [4.48]. The first method is more universal and flexible (using one set of probes one can extract a few poloidal modes while with a toroidal probe location one can get

the corresponding characteristics), but it requires a lot of time for analysis. The second method requires separate detectors to be installed for each mode; it is less universal (since the law of detector winding for each mode depends on the discharge parameters while in practice only one law can be realized), but it gives an analogue signal corresponding to the mode amplitude in real time. Poloidal magnetic field perturbations have been measured in all tokamaks. A description of detector design, signal handling algorithms and the results obtained may be found elsewhere [4.49–4.55].

(VII) Though magnetic measurements and their interpretation seem easy, in fact these involve some difficulties especially in modern large machines. For example, when the discharge duration is long, measurement of magnetic fields and fluxes by inductive sensors reacting to the field variation rate becomes a problem because this requires sensor signal integration. Analogue integrators for long times ( $\sim 10^3$ – $10^4$  s) give very low signals while application of active integrators requires accounting for, minimizing or compensating the amplifier drifts or applying special measuring schemes. This problem is solved by applying non-inductive sensors, for example Hall detectors [4.56]; however, here an availability problem arises when the sensors of this kind are used in the fusion reactor environment (high temperature, neutron irradiation, etc.). Research in this direction is under way [4.57]. Also under development are alternative sensor designs to measure stationary magnetic fields [4.58, 4.59] and measuring techniques [4.60]. It is worth mentioning separately that at this time magnetic measurement systems are considered as an important part of plasma/discharge parameter control systems. To maintain proper parameters (plasma cross-section and location) suitable fast algorithms should be developed and applied to allow real-time control. At the same time it should be noted that with increasing computer system power and performance this problem is becoming less important.

(VIII) In conclusion, we note that magnetic measurement data could be supplemented and their accuracy raised with methods of magnetic field measuring which are not based on using inductive sensors. At present, there are many such techniques which include the use of atomic, molecular and charged particle beams, X ray and electron cyclotron emission measurements, charge exchange and laser scattering data, Zeeman and Stark effects, Faraday effect in radiation beams, and also harmonic generation, wave excitation and discrete spectrum peculiarities. All these techniques are rather difficult and time-consuming in themselves and we will not describe them in detail, but note once more that they may give additional information, improving the validity of traditional magnetic measurements [4.61, 4.62].

## 4.2.2. Electrical probes (Langmuir probes)

**S. Grashin**

Kurchatov Institute, Moscow,  
Russian Federation

### 4.2.2.1. Introduction to electrical probes

In modern magnetic fusion experiments, it has become increasingly clear that edge plasmas play an important role and often even dominate central plasma processes. This understanding is reflected in the increasing efforts devoted to the experimental study of the edge and scrape-off layer plasma. Of particular concern are aspects of the plasma–surface interaction leading to impurity production and the subsequent impurity transport and contamination of the core plasma.

The understanding of the plasma edge and the control of the edge conditions critically depend on measurements of the local plasma parameters. Reviews of techniques used for edge plasma diagnosis can be found in Refs [4.63, 4.64]. Electrical probe measurements are one of the earliest approaches in plasma diagnostics. In plasmas in which probes can survive, this diagnostic remains the easiest and most accurate way to measure the local plasma parameters. Frequently, only the edge plasma is accessible, but its importance makes the prospects bright for further use of electrical probes. Furthermore, electrostatic turbulence driven transport, as well as local particle fluxes can only be fully evaluated with electrical probes [4.65, 4.66].

Electrical probes in general include the variety of diagnostics with one or several electrodes contacting with a plasma and using an electrical measurement technique: the application of some additional voltage to the electrodes and measurement of some current or voltage response from these electrodes depending on the plasma parameters.

Other information such as ion temperature, ion and electron energy distribution and impurity ions content can be obtained with more complicated and sophisticated kinds of electrical probes. Among them are retarding field analysers, mass spectrometers, ion energy analysers,  $\vec{E} \times \vec{B}$  probes, Larmor radius probes, Katsumata probes, and so on. Information about these diagnostics can be found in excellent reviews by Matthews [4.67] and Van Oost [4.68] and also in a number of other works [4.69–4.72]. This section is concerned only with the application of Langmuir probes for edge tokamak plasma measurements.

### 4.2.2.2. Langmuir probes

The use of Langmuir probes still represents one of the most widely reported edge diagnostics in tokamaks as a relatively simple and inexpensive method to

measure the time averaged and fluctuating values of the electron temperature and concentration, particle fluxes, floating potential, electric field and Mach number. Langmuir probes consist of small electrodes of various forms which are inserted into the plasma and externally biased with respect to the plasma and to some reference electrodes (counter electrode, wall, limiter, etc.). Reviews of the theoretical and experimental basis for the interpretation of Langmuir probes have been made by Manos and McCracken [4.73] and by Stangeby [4.70]. Unfortunately, the relative ease with which one can apply a voltage to a probe and measure a current is offset by serious issues of interpretation. There is still no entirely satisfactory theory for Langmuir probes in strongly magnetized plasmas. Fortunately, however, there is a significant body of experimental evidence that a simple interpretation yields results consistent with other diagnostics in many circumstances. So, Langmuir probe diagnostics has been used in almost all tokamaks from the oldest and smallest up to the largest modern machines.

#### 4.2.2.2.1. Single Langmuir probes

The theory of probes in general discussed in Refs [4.74–4.76]. In accordance with this theory, the usual method to determinate the values of electron temperature and density with a probe is to register the current–voltage characteristics. Figure 4.3 shows typical current–voltage characteristics of different kinds of electrical probes in a plasma consisting of electron and singly charged ions, where both particle species have a Maxwellian energy distribution. A conventional analysis of such characteristics involves fitting the data up to the voltage at which electron current saturates with the standard Langmuir formula:

$$I = I_{is} (1 - e^{(V-V_f)/T_e}) \quad (4.6)$$

where  $I$  is the current drawn by the probe at applied voltage  $V$ ,  $I_{is}$  is the ion saturation current,  $T_e$  is the electron temperature and  $V_f$  is the floating potential of the probe.

The characteristics are asymmetric, since the ion saturation current is much smaller than the electron saturation current. The floating potential  $V_f$  of such a probe is more negative than the plasma potential  $V_p$ . The reason for the strong discrepancy between the currents lies in the fact that the electrons have a much smaller mass than the ions and therefore a much higher mean velocity and average flux than those of the ions. In the absence of a magnetic field, the ratio between the ion and electron saturation currents should be around 50 but in a tokamaks it is found to be much lower [4.77].

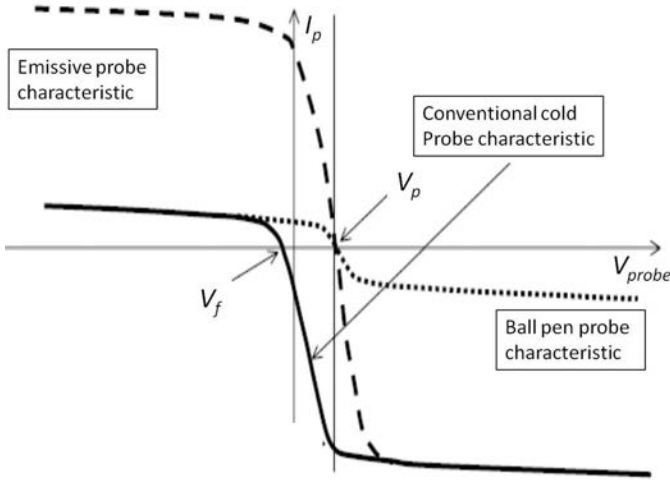


FIG. 4.3. Typical current–voltage characteristics of a cold probe (solid line) and of an emissive probe (dashed line), in a plasma with Maxwellian velocity distributions for the electrons and ions. Here  $V_{probe}$  is the variable potential of the probe.

If the electron temperature  $T_e$  is known, it is possible to measure the floating potential of a Langmuir probe, and to calculate the plasma potential using the well known relation between the floating potential of a cold probe and the plasma potential in the case of a conventional Maxwellian plasma:

$$V_p = V_f + kT_e \quad (4.7)$$

where  $k = 1.9\text{--}2.8$  under different plasma conditions [4.78]. However, it is not so easy to measure  $T_e$  with sufficient accuracy. Also  $T_e$  can fluctuate during the measurement and there can be temperature gradients in the region of investigation. The electron emissive probe is a kind of a Langmuir probe heated sufficiently to have a high electron emission current [4.79]. When the emission current just compensates the electron saturation current, the floating potential of such a probe equals the plasma potential (the dashed line in Fig. 4.3). This equilibrium is largely self-establishing, and the established floating potential is little sensitive to the probe temperature. So, it can be obtained directly without  $T_e$  measurements.

When the electron temperature  $T_e$  is known it is also possible to calculate the electron density  $n_e$  from the standard probe formula:

$$I_{is} = n_e S_{pr} e c_s \quad (4.8)$$

where  $c_s = (k(T_e + T_i) / m_i)^{1/2}$  is the ion sound speed. Assuming  $T_i \approx T_e$  which is valid in many cases, we have a relation for electron density ( $S_{pr}$  is the probe surface):

$$n_e [10^{19} \text{ m}^{-3}] = 1.12 I_{is} [\text{mA}] / S_{pr} [\text{mm}^2] (T_e [\text{eV}] / m_i [\text{at.u.}])^{1/2} \quad (4.9)$$

A disadvantage of the determination of the plasma parameters from the current/voltage characteristics of a single Langmuir probe is its low temporal resolution, which naturally is limited by the frequency with which the characteristic can be scanned. Also  $T_e$  can fluctuate during the measurement. The advantages of the measurements with a single Langmuir probe are high locality of the measurements (one of the best amongst tokamak diagnostics) due to the small size of the probes and high signal to noise value due to the usual high level of the probe signal.

#### 4.2.2.2.2. Double and triple Langmuir probes

The double probe scheme uses a small counter electrode as the reference for the return current and the entire system floats at a potential dictated by  $V_p$  and  $T_e$ . This scheme makes it possible to avoid recording the large electron saturation current during the voltage scan and to increase the safety of the measurements. The principal disadvantage of a double probe is that the floating potential is not measured since both electrodes are floating. However, this is easily overcome by using the *triple probe* scheme.

A further modification of Langmuir probes involves adding a third electrode in close proximity to a double probe. This electrode is used for independent measurement of the floating potential and the entire configuration is called a triple probe [4.80]. The principle of the probe scheme is illustrated in Fig. 4.4.

Three points on the probe characteristics are measured simultaneously using three separate probe tips: the ion saturation current  $I_{is}$ , the floating potential  $V_f$  and the potential of the “positive” probe  $V_e$ . A measurement of the voltage between the “positive” probe and the floating probe yields  $T_e$  directly. Analysis based on the assumption of plasma uniformity across three probes gives:

$$T_e = (V_e - V_f) \ln 2 \quad (4.10)$$

The obvious advantage of this scheme is that one does not need to know the current–voltage characteristic to determine electron temperature. So it is possible to have  $T_e$  measurements with a good time resolution in parallel with  $n_e$  and  $V_f$  measurements.

The disadvantage is connected with the assumption that the plasma is uniform across the three probes. This scheme works poorly in a plasma with high  $T_e$  fluctuations or strong  $T_e$  gradients. Also, using three probes reduces the spatial resolution of the diagnostic.

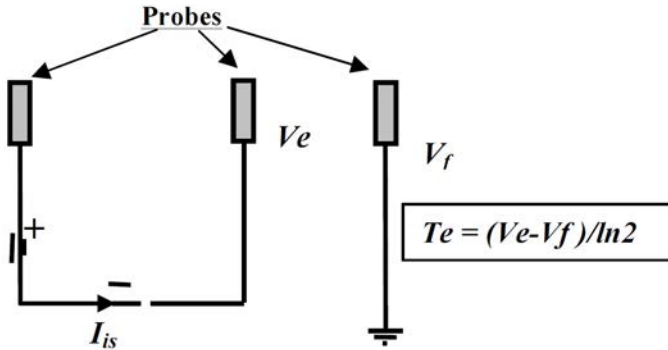


FIG. 4.4. Scheme of the triple Langmuir probe.

#### 4.2.2.2.3. Mach probes

The Mach (directional) probe is another kind of Langmuir probe for determination of the plasma flow velocity along the magnetic field lines. Such measurements are of particular interest for tokamaks with divertors since divertor impurity retention depends on the balance between the flow of ions towards the divertor and impurity diffusion which drives the impurities out [4.81]. Mach probes provide diagnostics with sufficient sensitivity and spatial resolution to study these flow characteristics. The basic principle of the Mach probe is illustrated in Fig. 4.5. Two probe elements are placed back to back with a larger separating barrier between them. In this configuration they can only receive an ion flux from one direction. The Mach number ( $M$ ) of the plasma is defined as the ratio of the plasma flow velocity to the sound speed  $c_s$ .

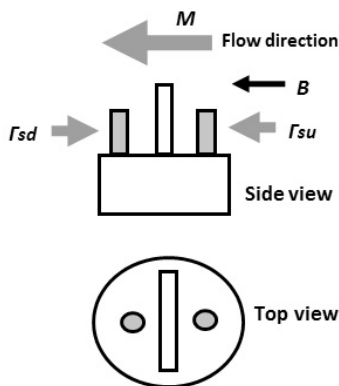


FIG. 4.5. Schematic view of the Mach probe. The ion saturation current is measured on upstream and downstream facing pins.  $\Gamma_{su}$  and  $\Gamma_{sd}$  are the upstream and downstream ion flows.

Mach probes are a common diagnostic to measure particles flows and the electric field profile in the edge of fusion machines. The Mach numbers of the parallel and perpendicular flows are derived from the ratio of the up- and down-stream ion saturation currents ( $R$ ). To derive  $M$ , Stangeby [4.82] and then Hutchinson [4.83] developed a 1-D fluid probe model. These models essentially relate the ion saturation currents measured at the probe surfaces to the Mach numbers of the flow of the plasma not perturbed by the probe. In a more complicated analysis, the cross-field viscosity should be included. When the viscosity is zero we have the formula for Mach probe measurements:

$$M = 2(1 - R) / (1 + R) \quad (4.11)$$

Note that the interpretation of Mach probe measurements becomes difficult at higher  $M$  values ( $M$  close to 1 or exceeding it).

#### 4.2.2.2.4. Present application of Langmuir probes

There are now three distinct types of Langmuir probe systems used on tokamaks.

- (1) A system of multi-pin probes fixed inside the SOL space which measures the plasma parameter distribution at these fixed points through the whole discharge.
- (2) Probes (usually also multi-pin) on fast (reciprocating) drives which are intended to make non-perturbing measurements of the plasma parameter distribution.
- (3) Langmuir probes flush mounted into limiters and divertor targets whose purpose is to deduce plasma parameters at the plasma–surface interface.

The first type of probe was widely used previously as it is suitable for small and medium size tokamaks. For modern large tokamaks, the problem of the probes surviving under the large heat load (during long pulses or as a result of disruptions) is the most severe in the application of Langmuir probe diagnostics. Different construction schemes from the second and third types of probe system are used to cope with the thermal load: fast moving probes, heat sink probes in good thermal contact with a large (cooled) heat sink and flush mounted probes (which are exposed to the plasma at grazing incidence).

The fast reciprocating probes systems reduce the energy deposited and obtain full profiles using movements with duration of order 10–100 ms [4.66, 4.84, 4.85]. Usually such systems are driven electrically or pneumatically.

The development of limiter and divertor flush mounted probe arrays and fast moving probe systems has made Langmuir probes relevant for even the largest

tokamaks in operation today (see Ref. [4.86] for JT-60U) and even for future machines. A system of divertor target Langmuir probes is under construction for ITER [4.87].

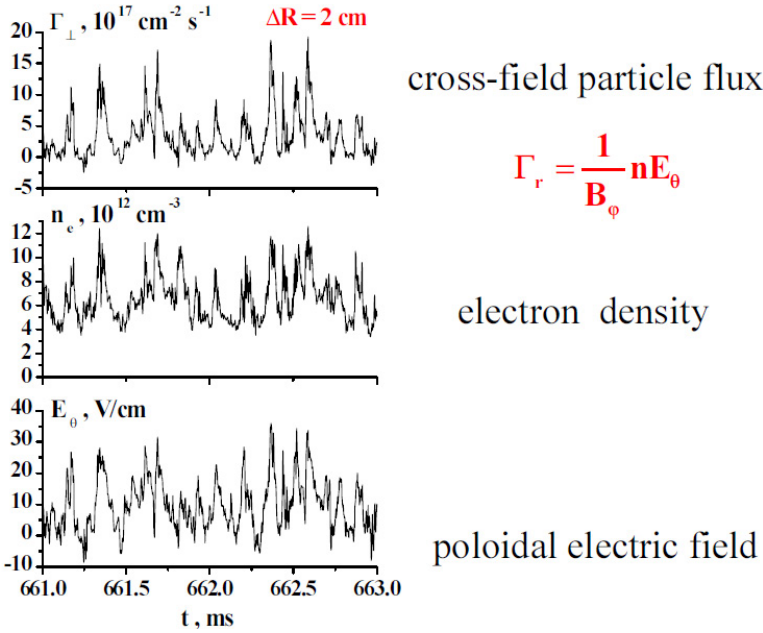


FIG. 4.6. Fluctuations of SOL plasma parameters in the T-10 tokamak [4.88].  $\Gamma_\perp = n_e E_\theta / B_\phi$  is the cross-field (radial) particle flux,  $n_e$  is the local electron density,  $E_\theta$  is the poloidal electric field, and  $\Delta R$  is the distance from the last closed magnetic surface.

Concerning modern applications of the Langmuir probes it is necessary to note that they are widely used not only for determination of slow variable plasma parameters but also for investigation of fast plasma fluctuations. Owing to the high space and time resolution, Langmuir probes are the unique instrument providing detailed data of local plasma parameters. Furthermore, electrostatic turbulence driven transport, which is generally believed to be the origin of anomalous edge particle transport in tokamaks, can only be fully evaluated with these probes [4.65, 4.66].

An example of such measurements can be seen in Fig. 4.6. Fluctuations of the cross-field turbulent flux  $\Gamma_\perp$

$$\Gamma_\perp = \frac{1}{B_\phi} n E_\theta \quad (4.12)$$

are evaluated from the measurement of the plasma density  $n_e$  (ion saturation current) and poloidal electrical field  $E_\theta$  fluctuations measured with high (up to 2  $\mu$ s) time resolution by three separate single Langmuir probes.

#### 4.2.3. Visible and UV spectroscopy

##### D. Shcheglov

Kurchatov Institute, Moscow,  
Russian Federation

Progress in nuclear fusion programmes requires application of “no contact” techniques for measurements of high temperature plasma parameters and for basic control of discharge performance. Monitoring of plasma discharge performance by measurement of hydrogen Balmer lines or by lines of intrinsic light impurities proved to be very useful at various stages of controlled fusion studies. Then, investigation of the spatial distribution of emitters, absolute measurements of atom (or ion) line emission, development of interpretative (collisional-radiative (CR)) models provided an opportunity to obtain a number of plasma parameters of importance for plasma studies. The measurement of Balmer alpha line emission has been performed in a TM-3 tokamak experiment [4.89] with the aim of estimating particle confinement time via the theoretical value of the number of ionizations per emitted photon. Oxygen and carbon were the most abundant low- $Z$  impurities in the early stage of magnetic confinement programmes and line emission of the ions in the visible and UV spectral region was used for particle transport studies [4.90, 4.91] and for example for investigation of such phenomena as enhanced influx of carbon during neutral beam injection [4.92]. The controlled injection of trace elements is another approach to obtaining impurity confinement time estimates and to studying impurity transport effects. For example, a puff of argon is released from a pulsed gas valve during the transport study experiment in the PLT tokamak. The time and space evolution of ArVIII, ArXV (spectroscopic symbols related to the spectral lines of the argon ion with charge equal to 7 and 14 respectively — while ArI denotes the argon neutral atom) spectral lines gives an estimate of transport rate [4.93]. Another injection technique — laser blow off — was used to inject cobalt into the JET machine [4.94]. The decay time of the line intensity of the cobalt ions has been used to study impurity transport. Atomic level population models have been developed for interpretation of spectroscopic data in impurity transport studies. Detailed calculations have been performed for atoms and low ionization stage ions [4.95, 4.96]. Nowadays, the development of interpretative CR-models is an integral part of practically any programme of quantitative spectroscopy applications. Doppler broadening of a spectral line profile gives information on ion temperature. Measurements in the visible and UV spectrum

region have been used. The broadening of OV and CV ion lines was measured to estimate  $T_i$  [4.91], but measurements in the VUV and soft X ray regions are more popular now. Doppler measurements enable us also to obtain plasma macroscopic velocity data. Toroidal plasma rotation in the PLT tokamak has been measured by the Doppler shift of FeXX and CV spectral lines [4.97]. In modern experiments the detailed analysis of D- $\alpha$  line signals is applied to study ELM (edge localized mode) phenomena. The studies are necessary for example for development of operating scenarios for burning plasma experiments [4.98, 4.99]. The measurement of intrinsic impurities in the 200–1000 nm spectral range, and identification of impurity elements and of local sources of plasma contamination also continue to be of importance. The interest in spectroscopic measurements of rare gases is due to the investigation of “radiating mantle” discharges designed to diminish the transient power load to the divertor target plates and other critical elements of the vacuum vessel by transformation of particle energy into impurity radiation. Mainly argon and neon injection was used, but sometimes nitrogen was injected also [4.100–4.103]. Lines in the VUV were measured: the NeVII 77.4 nm line [4.100], the ArXV 22.1 nm line at the JT-60 [4.102] and so on. It is essential also to measure intrinsic impurities in such experiments, as it was done in Ref. [4.103]; the carbon lines CIII, CIV and CV at wavelengths of 229.6, 580.5 and 227.1 nm respectively have been used. Intensity measurement of continuum radiation in the visible spectral region is one of the most popular methods to estimate the effective charge of plasma ions  $Z_{eff}$ . The continuum intensity is proportional to  $Z_{eff} n_e^2 T_e^{-1/2}$  and when independent data on  $n_e$  and  $T_e$  are provided, it is possible to calculate  $Z_{eff}$ , but the continuum radiation is integrated along the line of sight and it is necessary to apply multi-chord measurements in order to obtain the spatial distribution of  $Z_{eff}$ . Moreover, a problem can arise with reflection from the vacuum vessel walls [4.104]. At present, the development of mathematical models is being carried out in order to derive the corrections. Most of the studies described above were performed in the spectral region  $\lambda > 200$  nm. However, multi-charged ions in high temperature plasmas radiate in the VUV region and spectroscopic measurements in this wavelength interval are of importance. The difficulty with VUV spectrometers consists in the absence of any possibility to use optical windows. Therefore, it is necessary to have a common vacuum with the vessel and to use differential pumping. During the last few decades, significant progress was achieved in the field of detector and diffraction grating development [4.105]. A VUV system consisting of four spectrometers is described in [4.105, 4.106]. Overlapping of spectral characteristics makes it possible to work in the spectral interval from 2.5 nm to 160 nm. Application to burning plasma experiments meets rather serious problems: firstly the presence of tritium in the volume and secondly the necessity to protect the hardware of the diagnostics from neutron and gamma radiation. Nevertheless, experience obtained during D-T campaigns on JET [4.107], where devices were

placed inside a specially protected housing, is encouraging. Taking into account this experience and the technique described in Refs [4.105, 4.106] it is proposed to use a six-channel VUV system for the spectroscopic studies of the ITER bulk plasma [4.108].

Nowadays there is considerable activity on the ITER diagnostic system. This very ambitious project [4.108] includes a number of spectroscopic techniques also. The greater part of diagnostics under development has been briefly discussed above: measurement of impurity and D,T influxes,  $Z_{eff}$  and ELMs. D- $\alpha$  line radiation will be used as an L-H transition indicator. An important problem is the evaluation of the hydrogen isotope ratio. The diagnostic system “impurity influx monitor” — a spectroscopic system for the investigation of impurities and isotopes of hydrogen in ITER divertor plasmas [4.109, 4.110] — provides a good example of the work necessary for the development of spectroscopic diagnostics of future machines. A spectral range of 200–1000 nm is used. The diagnostic set includes the following spectrometers:

- (a) General spectrometer with spectral resolution  $\Delta\lambda_s \sim 0.1$  nm;
- (b) Spectrometer on the basis of optical filters ( $\Delta\lambda_s \sim 1$  nm);
- (c) High resolution spectrometer ( $\Delta\lambda_s \sim 0.01$  nm) designed for measurement of ion temperature and isotope density ratio.

The system is characterized by a large number of lines of sight (see Fig. 4.7).

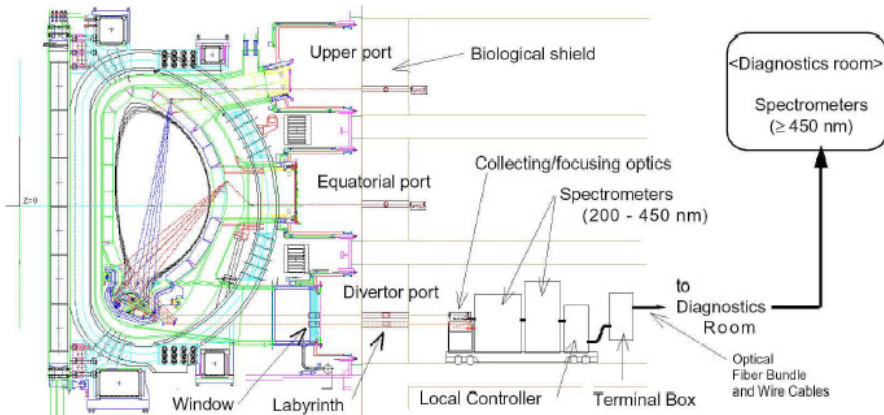


FIG. 4.7. Arrangement and lines of sight of optical measurements in ITER divertor plasmas [4.109].

At present, the development of support for the calibration of the system sensitivity, adjustment and focusing of optical elements (a considerable part of which is in the vacuum chamber) is in progress. The expected impurities are

Be, C, W, Cu (the materials of the vacuum vessel and diverter target plates), He – “ash” from the thermonuclear reactions and extrinsic impurities such as the rare gases (Ne, Ar, Kr) and nitrogen that may be injected.

In conclusion, one may note that methods of emission spectroscopy have been successfully used throughout the whole history of high temperature plasma studies and they will be applied to solve different diagnostic problems in the future.

#### 4.2.4. Bolometry

##### D. Sarychev

Kurchatov Institute, Moscow,  
Russian Federation

From the very first experiments the bolometric measurements of the energy losses with electromagnetic radiation and neutral particles became an important diagnostic tool for hot plasmas. Over the years, both the design of bolometric systems and parameters of detectors such as the signal-to-noise ratio, temporal resolution, radiation hardness, working temperature range have been steadily improving. In the 1960s and early 1970s, single review bolometers flush mounted on discharge chamber and limiters were used [4.111–4.113]. They gave important information on the total radiated power in tokamaks, its role in energy balance as well as its dependence on discharge parameters and chamber conditioning. Later, scanning and multichannel collimated systems appeared [4.114–4.116] giving the time evolution of radiation loss profiles necessary for studying the plasma and impurity transport. More references to the early bolometer experiments may be found in Ref. [4.117].

On today’s machines, where the plasma generally has a complex shape, the measurement of the spatial distribution of radiation losses needs several multichannel bolometric arrays with different directions of sight to be installed in a poloidal cross-section. Moreover, additional channels are used for obtaining the radiation loss distribution in the region of the divertor and X-point that is important for radiative divertor experiments. Generally, *tomography* is used for reconstruction of the local emissivity (in  $\text{W}\cdot\text{m}^{-3}$ ) profiles from the set of line-of-sight integrated measurements of brightness (in  $\text{W}\cdot\text{m}^{-2}$ ).

##### 4.2.4.1. Thermal devices

Obviously, the essential feature required of any bolometric detector is flatness of the spectral response curve over a wide wavelength range (practically, from the visible to soft X rays in experimental tokamaks). Up to now, the only types of detector satisfying this requirement are *thermal devices*. Their operating

principle consists of heating of the detector absorber by incident radiation and measurement of the corresponding rise in its temperature. Depending on the principle of the temperature measurement, thermocouple, resistive (metal or semiconductor), IR and pyroelectric bolometric detectors can be distinguished. But thermocouple detectors have generally shown insufficient signal-to-noise ratio for spatially resolved radiation loss measurements. Because of this they are not used in today's experiments. The other three types of thermal detectors, as applied to the plasma radiation loss measurements, will be considered in detail below.

It is apparent that the spectral sensitivity of any kind of thermal device is determined only by the spectral dependence of the radiation absorption coefficient of their surface. For UV and soft X ray radiation at normal incidence, this coefficient is usually very close to unity. Some deviations may take place only for visible and soft UV radiation because of reflection and, if a thin film absorber is used, for hard X ray radiation because of through penetration. As an example, the absorption of the 4  $\mu\text{m}$  gold film used as absorber in the older JET resistive bolometers [4.118] is shown in Fig. 4.8 (8  $\mu\text{m}$  gold is used in the newer ones). It should be noted that the drop in the absorption at lower photon energies can be further remedied by some kind of surface blackening, which may be important if an absolute calibration with visible light is employed. On the other hand, for the reactor operation a thicker absorber able to stop higher energy photons may be needed.

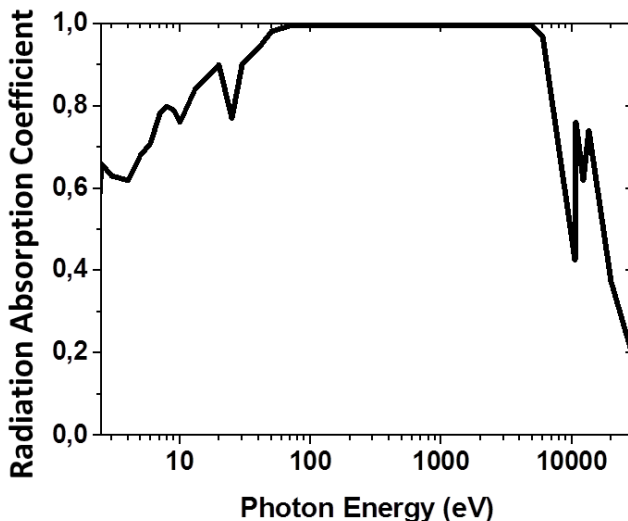


FIG. 4.8. Absorption coefficient of 4  $\mu\text{m}$  gold film in the photon energy range from 2.5 eV to 20 keV [4.118].

#### 4.2.4.1.1. Bolometer equation

The thermal balance of the detector for a time  $dt$  can be written as  $k.dE_{rad} = C.d\Delta T + \Lambda.\Delta T.dt$ , where  $k$  is the absorption coefficient of the detector surface (which can usually be set equal to unity for UV and soft X ray radiation),  $E_{rad}$  is the incident radiation energy,  $C$  is the detector thermal capacitance,  $\Delta T$  is the temperature increase, and  $\Lambda$  is the value of the detector heat loss through the support at  $\Delta T = 1$  for unit time. Dividing this relation by  $dt$  gives *the bolometer equation*

$$P_{rad} = C\left(\frac{d\Delta T}{dt} + \frac{1}{\tau_{\tilde{N}}}\Delta T\right) \quad (4.13)$$

where  $P_{rad}$  is the detector incident power and  $\tau_{\tilde{N}} = C / \Lambda$  is the cooling constant of the bolometer. The heat loss term is essential if the time of discharge is of the order of or greater than  $\tau_{\tilde{N}}$ .

#### 4.2.4.1.2. Resistive bolometers

*Semiconductor bolometers (thermistors)* owing to their high sensitivity and low noise equivalent power density (NEPD) have been successfully used for spatially resolved measurements of radiation losses on smaller devices [4.119, 4.120]. But on the large machines *metal resistor bolometers* are preferred. Their capability to withstand high radiation doses and high temperatures outweighs the disadvantage of higher NEPD than that of semiconductor bolometers. Several types of metal resistor bolometers were developed [4.116, 4.121–4.124], but from the 1990s on so-called “ASDEX-type” miniaturized improved metal foil bolometers [4.125] have become generally accepted. They are now used on JET [4.118], JT-60U, ASDEX-Upgrade, LHD [4.126], Alcator C-mod, Tore-Supra [4.125], RFX [4.127], etc. These bolometers are considered as the basis of the ITER bolometer design [4.128].

Each detector element of these bolometers [4.118] consists of 20  $\mu\text{m}$  mica substrate with a 4  $\mu\text{m}$  gold absorber layer facing the plasma. On the other side of the substrate, two interwoven gold meanders are positioned. In order to compensate for temperature drifts as well as electromagnetic disturbances, a second reference bolometer is employed which is optically shielded from plasma view. The two reference meanders and two measurement meanders are coupled in a Wheatstone bridge circuit such that the output voltage  $V_{br}$  is proportional to the instantaneous temperature excursion of the measuring absorber. Hence, the bolometer Eq. (4.13) gives

$$P_{rad} = \frac{\tau_C}{S} \left( \frac{dV_{br}}{dt} + \frac{V_{br}}{\tau_C} \right) \quad (4.14)$$

where the sensitivity  $S$  and  $\tau_{\tilde{N}}$  are determined by calibration.

The essential feature of this improved bolometer design is the use of an AC-excited bridge circuit with a carrier frequency of 50 kHz and synchronous demodulation (the refinement of the bolometer equation for the case of AC-operation is given in Ref. [4.125]). This feature together with improved shielding allowed a decrease in the NEPD to  $1 \mu\text{W}\cdot\text{cm}^{-2}$  (for a time resolution of about 2 ms), which surpasses all other thermal detectors including semiconductor bolometers. Another advantage of the metal foil bolometers is the simplicity of their in situ absolute calibration, which is achieved just by ohmic heating of the bolometer with a known current [4.129].

#### 4.2.4.1.3. Pyroelectrics

Pyroelectric detectors are used for measurements of the total radiated power on many machines [4.115, 4.130–4.132]. The principle of operation is based on the fact that pyroelectric materials exhibit a spontaneous (in the absence of an external electric field) polarization  $P_s$ , the value of which depends on temperature. For the commonly used lithium niobate or tantalate, the pyroelectric coefficient  $\gamma = dP_s/dT$  remains constant at temperatures up to about 400°C. The detector is a capacitor formed by depositing metal electrodes on pyroelectric material. A change of the detector temperature leads to the generation of charges on the electrodes and the occurrence of a current  $I = dQ/dt = A\gamma dT/dt$ , where  $A$  is the area of the electrodes. This current is measured as a voltage drop  $V$  on an external resistor  $R$ . Hence, the bolometer Eq. (4.13) for pyroelectrics takes the form:

$$P_{rad}(t) = \frac{1}{RS}(V(t) + \frac{1}{\tau_C} \int_0^t V(t)dt) \quad (4.15)$$

where the sensitivity  $S$  (in  $\text{A}\cdot\text{W}^{-1}$ ) and  $\tau_C$  are determined from calibration. The advantages of pyroelectric detectors are the high temporal resolution, low price, wide region of operating temperatures and the possibility to obtain the radiation power without differentiation of experimental quantities. Among their disadvantages are low radiation hardness, the stray piezoelectric effect which drastically reduces the signal-to-noise ratio in a tokamak environment, and the very low operational currents of  $\sim 1$  pA. Nevertheless, if the proper shielding and vibration protection are implemented, the NEPD value of  $\sim 10 \mu\text{W}\cdot\text{cm}^{-2}$  is reached for a time resolution of  $\sim 10$  ms.

#### 4.2.4.1.4. IR bolometers

The idea of these bolometers is to measure the temperature of the radiation absorbing foil by its infrared thermal radiation. In the first experiments [4.133–4.135] a single-channel IR detector was used to monitor the foil temperature in order to provide better electrical noise immunity than that of the resistive method. Sometimes the foil was preheated to  $\sim 1000^\circ\text{C}$ , which increases the temperature derivative of the thermal radiation intensity as well as gives a better coincidence of its spectrum with the spectral sensitivity of the IR detector. In Ref. [4.136], a negative thermal feedback was implemented to improve the parameters of an IR bolometer such as time resolution, linearity and dynamic range.

Recently, an *IR imaging bolometer* using a gold foil behind a pinhole and IR camera has been developed [4.137, 4.138]. This bolometer, which gives a 2-D image of the plasma, may have hundreds of “channels” (pixels). This is very useful for today’s fusion plasmas that have a complex shape and need position control. Moreover, the radiation hardness of the IR imaging bolometer can be very high since no wires are needed while the IR camera itself could be placed behind the neutron shield by using IR mirrors.

The bolometers have been tested on LHD and JT-60U. An NEPD of the order of  $500 \mu\text{W}\cdot\text{cm}^{-2}$  (at a time resolution of  $\sim 50$  ms) was obtained on LHD [4.126] and JT-60U [4.138], but this value can be greatly reduced by using a better IR camera. IR imaging bolometers are still under development and a considerable improvement in their parameters as well as refinement of the calibration technique is expected (with upgraded design and a new camera, NEPD values up to  $25 \mu\text{W}\cdot\text{cm}^{-2}$  have been recently reported [4.139] on JT-60U for 192 channels and a time resolution of 10 ms). Bolometers are planned to be used on ITER, so the question of the foil radiation hardness is to be addressed. Possibly for both the imaging bolometer and the resistive bolometers platinum would be a suitable replacement for gold, avoiding the transmutation of gold to mercury.

#### 4.2.4.2. AXUV detectors

The inherent drawbacks of thermal devices are low temporal resolution and rather low signal-to-noise ratio. Moreover, their signals are influenced by any stray heat sources such as unabsorbed heating microwaves, IR radiation of hot spots on PFCs and even cooling by gas puff.

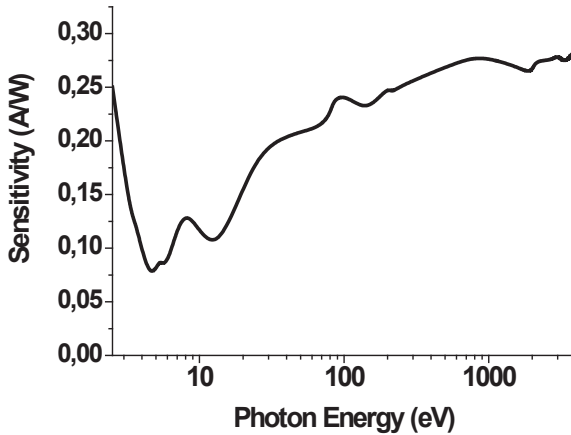


FIG. 4.9. AXUV spectral sensitivity curve [4.140]. Reprinted from Ref. [4.140]. Copyright (2011), American Institute of Physics.

In recent years, progress in silicon deposition technology has allowed the fabrication of photodiodes with a very thin surface dead layer. These photodiodes (also known as AXUV — Absolute eXtreme UltraViolet detectors) exhibit a near flat spectral response down to VUV, which justifies their use as bolometers for high temperature plasmas [4.140, 4.141]. The spectral response curve of the AXUV detector is shown in Fig. 4.9 [4.140]. It can be seen that the theoretical value of  $0.27 \text{ A}\cdot\text{W}^{-1}$  (corresponding to 3.6 eV/pair for silicon) is reached for photon energies higher than about 50 eV.

Unlike thermal devices, AXUV detectors have a very high time resolution up to a fraction of a microsecond. They possess a high sensitivity (about a million times higher than that of pyroelectrics), which allows an NEPD of  $60 \text{ nW}\cdot\text{cm}^{-2}$  [4.126], ensuring the possibility of very high spatial resolution. AXUV detectors are not sensitive to IR and microwave radiation [4.126, 4.141]. One interesting feature is their insensitivity to neutral particles (with energies below 1 keV) in contrast to thermal devices, which measure them as well as photons.

Using AXUV detectors on Alcator C-Mod [4.140], TCV [4.141], T-11 [4.142], T-10, DIII-D, etc., has shown that they can give new unique information on fast and small scale radiative phenomena such as MHD events and ELMs. At the same time the ratio of radiation loss powers obtained from thermal bolometers and AXUV (with assumed flat spectral response of  $0.27 \text{ A}\cdot\text{W}^{-1}$ ) appears to be in the range of 1–2.5 on different machines. The spatial and temporal behaviour of AXUV signals sometimes differs from that of bolometers too. In some cases these differences can be explained by the losses with neutral particles [4.140], but in other cases [4.126, 4.143] they are believed to be because of the variation in the AXUV spectral response for lower photon energies (Fig. 4.9). Moreover, some indications of gradual and scarcely controllable growth of this variation under

tokamak conditions have been reported (CHS, T-10, T-11); this may be caused by the deposition of thin films on the detector surface effectively adding their thickness to the dead layer. Hence, the non-linear spectral response at low photon energies really limits the applicability of AXUV detectors as a calibrated measure of total radiated power. An approach to resolve this problem was proposed on DIII-D [4.144] by introducing a spectral averaged sensitivity  $S_{eff}$  found from optically filtered AXUV measurements for particular discharge conditions.

Recently, detectors called SPD diodes, which are generally similar to the AXUV but have a “zero-edge” design allowing stacking into larger matrices and arrays, have been developed (see Ref. [4.145] for details and the SPD spectral sensitivity curve).

#### 4.2.5. Methods based on electron cyclotron emission measurements

##### V. Poznyak

Kurchatov Institute, Moscow,  
Russian Federation

Electron cyclotron emission (ECE) from a plasma has been used for a long time for measurements of the spatial distribution of electron temperature,  $T_e(r)$ , and for analysis of various kinetic phenomena in fusion plasmas. At present, this method is applied, for example, in all tokamaks and stellarators. The application of ECE diagnostics to plasma control is an important issue and looks promising for ITER.

The theoretical background of ECE was developed during the 1960s and 1970s [4.146–4.150]. The review in Ref. [4.151] contains a detailed list of references. The regular international Joint Workshops on Electron Cyclotron Emission (ECE) and Electron Cyclotron Heating (ECH) play an important role in the development of ECE theory and applications [4.152, 4.153].

The main principles of the method are given below. Electrons in plasma rotate around magnetic force lines with the angular (cyclotron) frequency:

$$\omega_{ce} = \frac{eB}{m_e c} \quad (4.16)$$

where  $e$  and  $m_e$  are the electron charge and mass at rest,  $B$  is magnetic field and  $c$  is the speed of light. Electrons move with an acceleration along the spiral trajectories and correspondingly emit electromagnetic energy on harmonics of the cyclotron frequency. The radiation is elliptically polarized. Two polarization modes are intrinsic for a plasma. In the general case, the ellipsoid parameters are expressed by a complicated function but polarization of the emission is linear after passage through the plasma boundary [4.154]. The electric field in the ordinary wave (O-mode) is parallel to the main magnetic field ( $\vec{E} \parallel \vec{B}$ ) while

in the extraordinary wave (X-mode) it is perpendicular ( $\vec{E} \perp \vec{B}$ ). The received frequency can be expressed as follows when account is taken of the Doppler effect and the relativistic dependence of mass on velocity:

$$\omega = \omega_{ce} \sqrt{1 - \beta^2} + k_{\parallel} v_{\parallel} \quad (4.17)$$

where the wave vector component  $k_{\parallel}$  is parallel to the magnetic field,  $\beta = v / c$ ,  $v$  is the full electron velocity and  $v_{\parallel}$  is the longitudinal velocity. For transverse wave propagation ( $k_{\parallel} = 0$ ), only the relativistic effect of shifting down the emission frequency is important. The full power received from a space point by an observer can be determined after integration of the local emissivity over the electron distribution function and the receiving angles, with the absorption along the trajectory taken into account. The X-mode at the second harmonic resonance and the O-mode at the first harmonic resonance are equivalent for  $T_e$  measurements for spherically symmetrical electron velocity distributions. Regular ECE measurements in the O-mode are carried out only on JET and T-10. This is due to the various limitations on plasma density under wave propagation with different polarizations (Fig. 4.10).

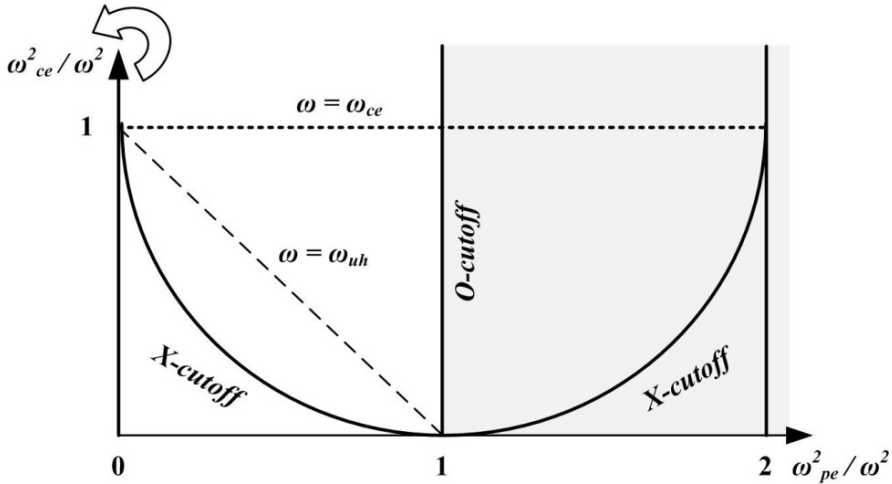


FIG. 4.10. The transparency conditions versus plasma parameters. Cut-off for the ordinary wave (O) is realized when  $\omega = \omega_{pe}$ , where  $\omega_{pe}$  is the electron plasma frequency and  $\omega_{uh} = \sqrt{\omega_{ce}^2 + \omega_{pe}^2}$  is the upper hybrid frequency. The solid line shows cut-off and the dotted line shows resonance.

The inaccessible area for the O-mode is marked in grey. Such a cut-off appears as usual in the central plasma where the density is maximal. Cut-off for the X-mode  $\omega = \omega_{ce} / 2 + ((\omega_{ce} / 2)^2 + \omega_{pe}^2)^{1/2}$  depends essentially also on the value of the magnetic field. Therefore measurements on the first X-resonance

is possible only from the high magnetic field side (HFS) that is shown with the arrow. Measurements on the second X-resonance is possible from both the HFS and the low field side (LFS). Limitation on the density for the second X-mode harmonic under typical conditions is four times higher than for the first O-mode harmonic.

Under local thermodynamic equilibrium, the emission power from a space point is *black body* emission and depends directly on the electron temperature:

$$P_{bb} = \frac{\omega^2 T_e}{8\pi^3 c^2} \quad (4.18)$$

An observer receives the power:

$$P(\omega) = \frac{\omega^2 T_e}{8\pi^3 c^2} (1 - e^{-\tau}) \quad (4.19)$$

where the exponential term allows for the absorption of radiation along the trajectory  $l$ ;  $\tau \equiv \int \alpha(\omega) dl$  is the optical plasma depth and  $\alpha(\omega)$  is an absorption coefficient (i.e. absorption per unit length). The depth  $\tau$  depends on the electron temperature and density, the magnetic field, the wave mode and the frequency. If the optical density is significantly high ( $\tau \gg 1$ ), the emission power is proportional only to the electron temperature. This property is used for measurement of the temperature distribution in plasmas.

The one-to-one correspondence between the space coordinate and temperature takes place for  $\beta \ll 1$  and a known magnetic field distribution. In particular, the magnetic field distribution in a tokamak can be expressed as:

$$B = B_0 \frac{R_0}{R_0 + r \cos \theta} \quad (4.20)$$

where  $R_0$  is major radius of the torus,  $r$  is the radius of the magnetic surface,  $\theta$  is the poloidal angle and  $B_0$  is the value of field at the plasma centre. Since the properties of emission, absorption and refraction are complicated functions of many parameters, numerical codes are used (see, for example, Refs [4.155–4.157]). The confining magnetic field in modern fusion experiments is in the range  $B = 2\text{--}8$  T, and registration of cyclotron emission occurs in the frequency range 60–600 GHz.

The first regular measurements of a wide ECE spectrum in CLEO were carried out by A.E. Costley et al. [4.158]. Radiation from the plasma was detected in a two-beam polarization-type scanning interferometer with a Putley indium antimonide detector. Three ECE harmonics were observed. Many-pass emission (“optically thin plasma”) and reflection from the wall complicated the interpretation of the data because of emission by high energy electrons.

Different techniques are now applied for measurements: Michelson spectrometer, Fabry-Perrot interferometer, grating polychromator (GPC) and

others. Superheterodyne receivers are the most widely used [4.159]. In particular, the radiometer in JET uses the range 73–139 GHz. Six mixers with fixed heterodyne frequencies are applied. The radiometer registers both extraordinary and ordinary modes. Signals in a wide band of intermediate frequencies after the mixers are separated into 12 narrow frequency channels where amplification takes place [4.160].

Two 20-channel grating polychromators were used for ECE X-mode measurements on TFTR [4.161]. They were arranged in two toroidal sections of the tokamak through  $126^\circ$ . Figure 4.11 shows the evolution of the temperature profile obtained by one GPC in a regime with locked mode disruption [4.162].

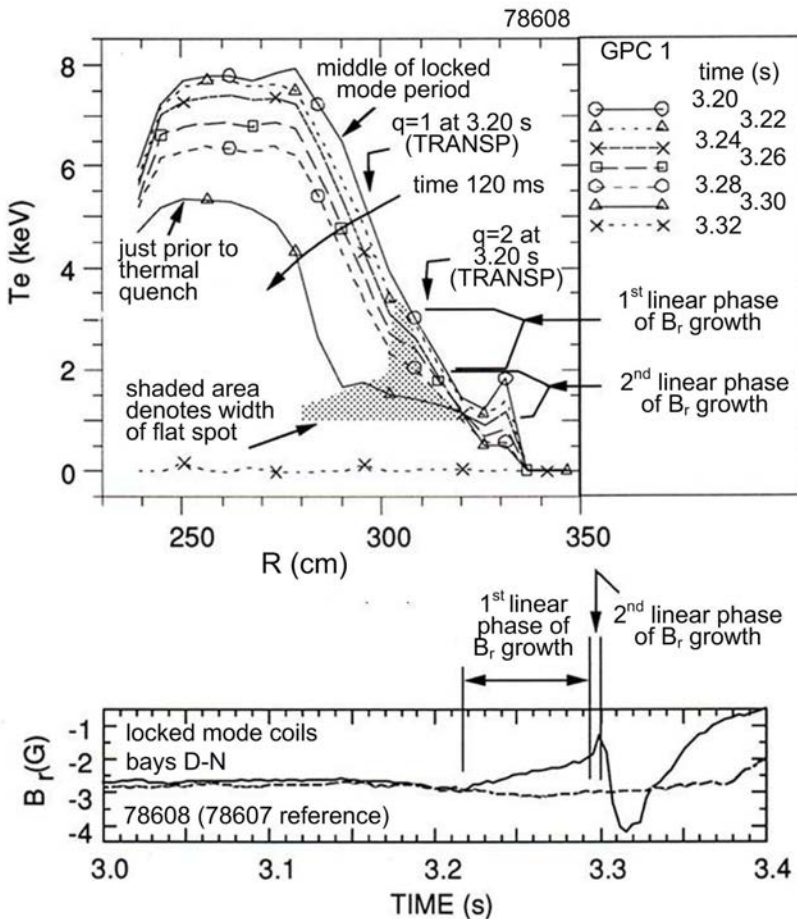


FIG. 4.11. Evolution of the  $T_e$  profile (top) observed at one GPC during the growth of  $m/n = 2/1$  locked mode [4.162]. The growth of the flat spot due to the island is correlated with the growth of the radial magnetic field  $B_r$  signal measured by the locked mode coils (bottom). Reprinted from Ref. [4.162]. Copyright (2011) by the World Scientific Publishing Company.

Tomographic pictures of the different global perturbations were obtained by comparison of two temperature profiles which were measured along two lines in the equatorial plane, using a theoretical model [4.163]. Figure 4.12 shows the ECE electron temperature profile evolution during internal disruption.

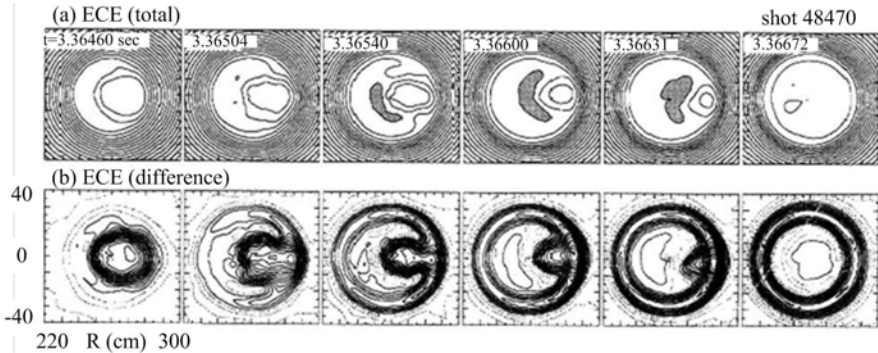


FIG. 4.12. (a) Series of contour plots of the ECE electron temperature profile during a full sawtooth crash. The contour step size is 250 eV. The hatched area indicates the temperature region. (b) Reconstruction of the temperature difference. The contour step size is 50 eV and the dotted lines indicate less than 250 eV. The numbers on the left shoulder of the figures indicate the reconstruction time in seconds. Radial and vertical scales are the same for all plots.  $R$  is the distance from the major torus axis. Reprinted from Ref. [4.163]. Copyright (2011) by the World Scientific Publishing Company.

Data were obtained at discharges with a mixture of deuterium and tritium (D-T). The neutron thermonuclear power achieved was 10.7 MW. In this case, the SXR measurements are accompanied by a high noise level and the SXR detectors suffer from fast degradation. The GPC system operated over a distance of  $\sim 40$  m. The neutron flux did not influence its efficiency, and the weakening of ECE power in the waveguide path was less than 6 dB. Thus the high reliability of the ECE method under thermonuclear operation conditions was confirmed.

There is a diagnostic method which opens up opportunities to obtain the ECE distribution directly over a certain area of the poloidal plane — the electron cyclotron emission imaging system (ECEI). Such systems have been applied in RTP and TEXT and are planned for KSTAR. The already operating ECEI system on TEXTOR possesses the best characteristics [4.164]. Figure 4.13 illustrates the principles of the device. Mirror and lens optics carry the image data from the focal plane in plasma to the detector array. Here, eight antenna components are disposed along a vertical line. A local oscillator (LO) on the backward wave oscillator (BWO) supports frequency biasing. The primary wide intermediate frequency (IF) band in each antenna pass is divided into sixteen narrow bands that create the radial coordinate of a matrix. The vertical resolution is determined by the antenna pattern of  $\sim 2$  cm (full width at half maximum) for each pixel and

## PLASMA DIAGNOSTICS

the radial resolution is  $\sim 1$  cm across the core of the tokamak plasma (total of 128 channels). The time resolution is primarily limited by the digitizer and the fastest timescale can be up to  $5 \mu\text{s}$ . The ECE frame location is determined by the choice of the LO carrier frequency and can be shifted from the outer to the inner side of the torus.

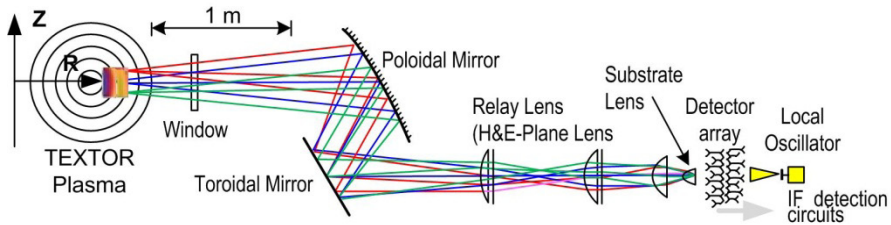


FIG. 4.13. Schematic arrangement of the ECEI system on TEXTOR [4.164]. Reprinted from Ref. [4.164]. Copyright (2011), American Institute of Physics.

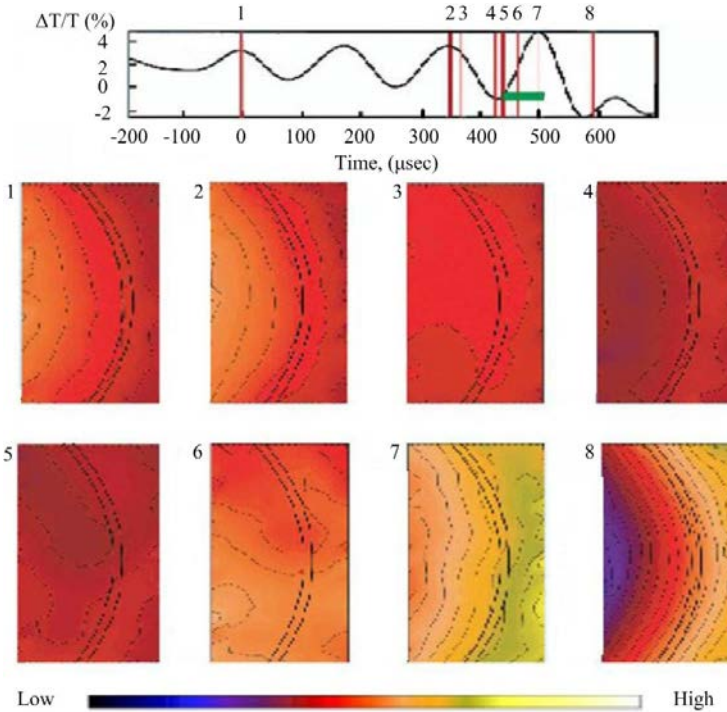


FIG. 4.14. TEXTOR 2-D images of the sawtooth crash at the LFS corresponding to the times indicated in the electron temperature time trace at  $z = 0$  cm,  $R = 191$  cm. Width of every frame — from 158.5 to 163.5 cm, height — from  $-4.5$  to 8.5 cm. The inversion radius drawn here (the double dotted line) is estimated based only on the ECEI measurements [4.165]. Reprinted from Ref. [4.165]. Copyright (2011), American Institute of Physics.

The ECEI method makes it possible to analyse the plasma dynamics during internal disruption (so called reconnection process) [4.165]. Figure 4.14 illustrates the heat fluxes during a sawtooth crash at the LFS while Fig. 4.15 shows the transport processes when a sawtooth crash takes place at HFS.

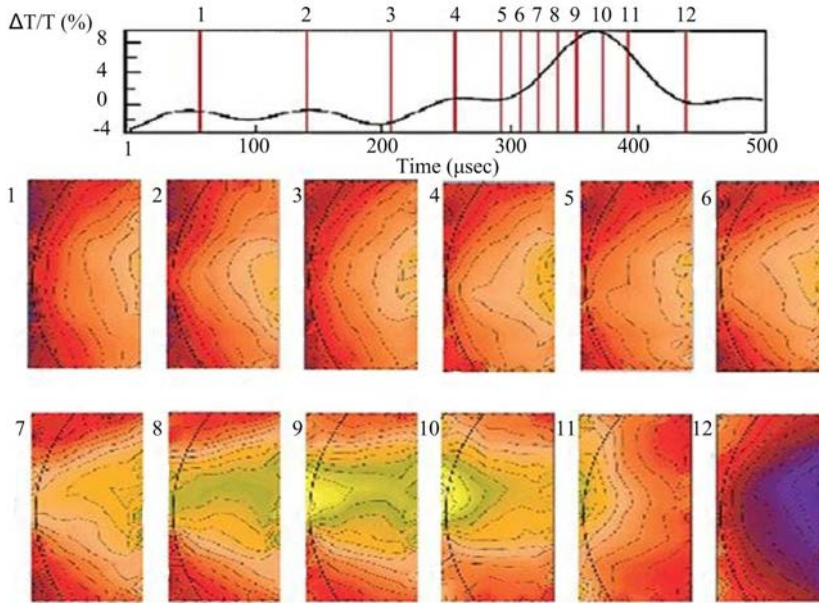


FIG. 4.15. TEXTOR 2-D images from the sawtooth crash at the HFS are shown with the time history of the electron temperature fluctuations at  $z = 0$ ,  $R = 191$  cm. Width of every frame is from 191 to 197 cm, height — from  $-4.5$  to  $8.5$  cm. The inversion radius drawn here (the dotted line) is estimated based only on the ECEI measurements [4.165]. Reprinted from Ref. [4.165]. Copyright (2011), American Institute of Physics.

Usually, as in the above mentioned examples, the ECE measurements are carried out along the ray in the equatorial plane from the LFS perpendicular to the magnetic field lines. In such cases, the emission power in the laboratory system is proportional to the average energy of the bulk plasma, which is equivalent to temperature. The emission by small numbers of suprathermal electrons on the down shifted frequencies is dumped (due to the relativistic effect) into the main body of the plasma in the region with lower magnetic field. Radiation emitted by the main electron part in the HFS direction is partly absorbed by the high energy electron tail. The radiation by suprathermal electrons leaves the plasma practically free. The spectra on the LFS and HFS can be essentially different. In this way, information about the behaviour of the high energy electrons can be obtained [4.166, 4.167].

We assumed in discussing measurements of the electron temperature that the plasma is in a state of thermodynamic equilibrium. But this approximation

can be far from reality. The plasma is created by electromagnetic fields; currents flow through the plasma; and generation of so-called runaway electrons happens. Thus the electron distribution function is not Maxwellian.

The ECE method makes it possible to analyse the anisotropy of the electron distribution at least under certain conditions. Actually the electron emissivity in the X-mode across the magnetic field is determined only by the electron perpendicular velocity  $v_{\perp}$ . The emissivity for the second resonance is  $\eta_{\omega}^{(x)}(\pi/2) \sim v_{\perp}^4$ , where ‘x’ stands for X-mode resonance. Generation of O-mode ECE occurs only for larger values of the longitudinal velocity  $v_{\parallel}$  [4.168]. The emissivity for the first resonance is  $\eta_{\omega}^{(o)}(\pi/2) \sim v_{\perp}^2 v_{\parallel}^2$ , where ‘o’ stands for O-mode resonance [4.146]. Similar properties are inherent also to the absorption coefficients. Simultaneous measurements in the X- and O-mode in the range of down shifted frequencies permits detection of radiation emitted by high energy electrons (Fig. 4.16) and an estimation of their total perpendicular and longitudinal energy with account for the different dependence of ECE modes on the velocity components [4.169]. Such conditions (“optically thin plasma”) are realized throughout the plasma volume in the first stage of discharge and almost always on the plasma periphery.

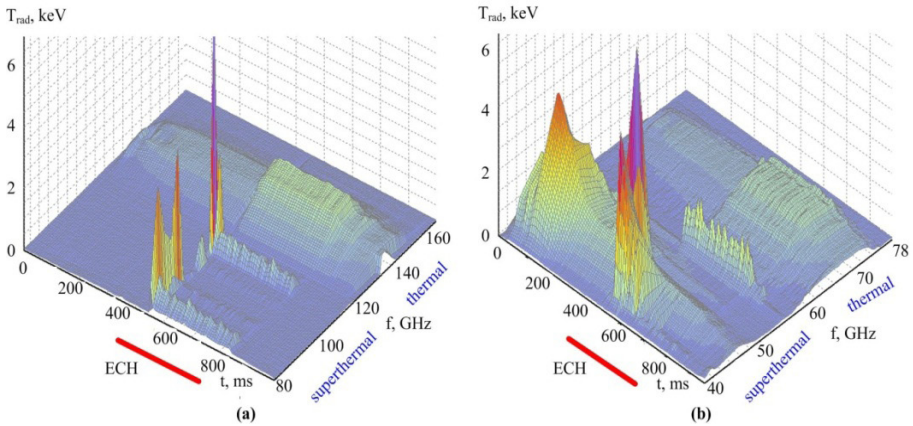


FIG. 4.16. (a) Spectrum evolution of 2nd X-mode ECE. Spectrum allocation lower than 120 GHz corresponds only to suprathermal emission. (b) Spectrum evolution of 1st O-mode ECE. Frequencies lower than 60 GHz correspond only to emission by electrons with longitudinal energy up to 250 keV and average transverse energy less than several keV [4.169]. Reprinted from Ref. [4.169]. Copyright (2011) by the World Scientific Publishing Company.

There is a possibility to analyse the behaviour of perturbations in the main body plasma when the optical depth is high (“optically thick plasma”). Figure 4.17 shows X- and O-mode signals from the same point in space, registered by common analog-to-digital converter (ADC) in a regime with strong plasma oscillations  $m/n = 1/1$  and periodical internal disruptions under on-axis

electron cyclotron heating (ECH) [4.170]. When the level of ECH is low, the signals are similar, including the absolute values, as must hold for a thermodynamically equilibrium plasma (Fig. 4.17(a)). However, oscillations of ECE intensity in different modes have a phase shift  $\sim 45 \mu\text{s}$  for a period of  $\sim 270 \mu\text{s}$ . The signal dynamics are very different under the high level of ECH (Fig. 4.17(b)). This phenomenon indicates strong periodic oscillations in the main part of the electron distribution function. A rough estimate shows variation of the velocity components up to 50% during each period. The longitudinal velocity is changed more strongly instead of the permanent ECH pumping of energy into transverse degree of freedom.

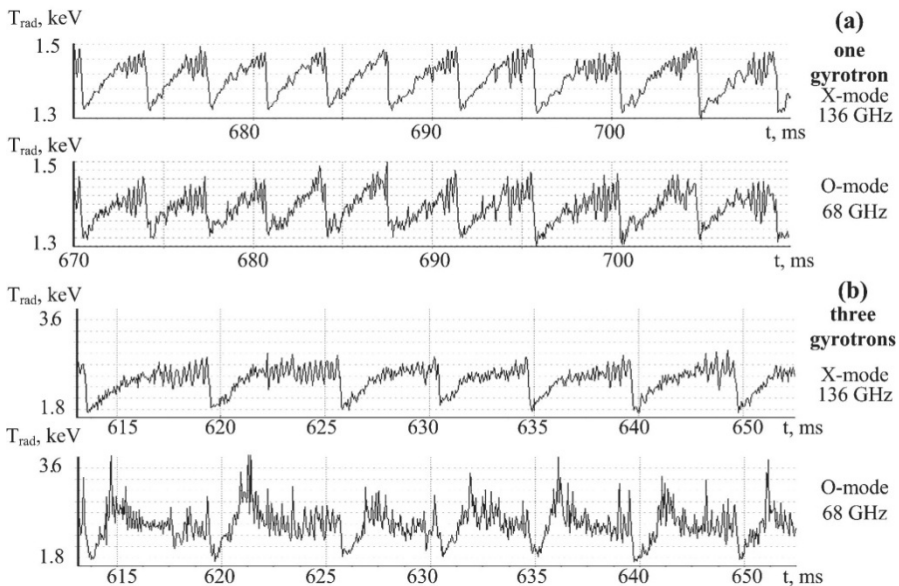


FIG. 4.17. Different dynamics of 2nd X-mode and 1st O-mode from plasma with high optical depth for both polarizations [4.170]. Reprinted from Ref. [4.170]. Copyright (2011) by the World Scientific Publishing Company.

Experiments using electron Bernstein wave (EBW) heating and current drive (CD) have recently become popular. This method is usually applied under very high plasma density when propagation of external EC waves is not possible. Those conditions are typical for “spherical” tokamaks [4.171]. Experiments with EBW heating are also conducted in helical installations [4.172]. The principle is based on the transformation, under certain conditions, of the incident oblique electromagnetic wave to a plasma wave, for example EBW. This wave is absorbed in the region of electron cyclotron resonance that may provide local electron heating and current drive. Thermal EBW emission (EBE) measurements, for example via oblique EBE-X-O double mode conversion, have been used to

determine the EBW transmission efficiency and the electron temperature value for a wide range of plasma conditions [4.173]. The wavelengths of EBE are in the millimetre and centimetre range and the receiving technique is similar to that for ECE.

Modern theory and a wide experience of work on large toroidal installations make it possible to formulate the requirements for future ECE diagnostics on ITER. Some problems that can arise under thermonuclear reactor conditions are discussed in Refs [4.108, 4.174, 4.175]. In particular, there is an essential widening of the local spectral function for the expected temperature of  $\sim 40$  keV and respective deterioration of the spatial resolution of the measurements. Powerful ECE at the high harmonics can influence the energy balance in the plasma column and render harmonic overlapping phenomena essential [4.176]. Since the overlapping between the third and second harmonic is enhanced by the relativistic effect, the observation of fundamental O-mode ECE along the major radius from the LFS seems to be best for electron temperature measurements in a reactor grade high temperature plasma [4.177].

We might mention some aspects which will be essential for the hot ITER plasma such as real time mode control with real time identification of the mode location and ECH mirror steering [4.178], oblique ECE measurement for analysis of high energy electrons under low hybrid heating (LHH) [4.179] and so on. A wide range of new information on theory and experimental methods including applications for the ITER programme is presented in special issues on ECE and ECH problems [4.180–4.182].

Further development of ECE methods in both theoretical and practical fields will presumably be connected with the investigation of plasma kinetics on electron distribution function analysis.

#### **4.2.6. Passive neutral particle analysis**

**M. Petrov**

Ioffe Institute, Saint Petersburg,  
Russian Federation

Even a high temperature hydrogen plasma in fusion devices emits neutral hydrogen atoms generated by the processes of recombination and charge exchange. Passive neutral particle diagnostics are based on the detection and analysis of hydrogen isotope neutral atoms emitted by a plasma. Those atoms pass freely through magnetic fields and yield important information about the behaviour of hydrogen ions in hot magnetized plasmas. The energy spectra of neutral atomic fluxes emitted by the plasma provide not only the ion temperature but also the ion energy distribution function. The latter is important both for understanding the particle and energy confinement mechanisms of the ion

component and for studying the behaviour of ions produced by neutral beam heating and by the application of radio frequency (RF) heating. In these studies, the importance of CX diagnostics should not be underestimated [4.183, 4.184]. In addition, CX diagnostics provide a direct measure of the plasma fuel isotope composition which can be defined from the H/D/T ratio of corresponding atom fluxes detected outside the plasma. The measurement of H/D/T isotope composition of the plasma is now one of the main goals of fusion plasma diagnostics. There are at least two objectives of these measurements. One is the control of the D/T fuel composition of burning plasmas to get the optimal regime of ignition and fusion burning because deuterium and tritium are the main fuel components in burning plasmas. It is necessary to have the optimal D/T density ratio for achieving the most effective burning regime. As far as a fusion reactor is concerned the absence of D/T ratio optimization leads to a decrease in fusion reactor efficiency and this in turn makes electricity production in the reactor more expensive. From this point of view the D/T ratio inside the plasma is one of the most important parameters to be measured and controlled in any fusion reactor.

Another objective is the study of energy confinement scaling in plasmas having different hydrogen isotope compositions (H/D/T). Transport analysis performed on tokamaks has shown that the plasma energy confinement time  $\tau_E$  depends on the isotope composition. This effect was first studied in detail on ASDEX [4.185]. It has been shown that plasma energy confinement is much better in a deuterium plasma than in hydrogen and the authors predicted further improvement of confinement for a deuterium–tritium plasma. Transport analysis performed on large plasma machines like TFTR [4.186, 4.187] and JET [4.188, 4.189] in D-T experiments shows that plasma conditions also depend on the isotope composition. In TFTR, it has been found that plasma confinement improves with increasing tritium density. In the case of JET, this effect was not observed but it has been found that an increase in tritium content leads to a decrease in the transition threshold to H-mode. It should be noted that basic limitations and intrinsic difficulties of interpretation of passive neutral particle analysis arise from the line integrated nature of the signal, limited plasma transparency for analysed atoms and the steep inwards decrease in source strength. Results obtained by CX diagnostics are chord integrated, emissivity weighted measurements that enable radial profiles to be obtained by using multi-chord measurements or by scanning the plasma on a shot-by-shot basis (or by a combination of the two techniques). These limitations can be mitigated by the use of modelling of the atomic fluxes emitted by the plasma, which is very well developed now on the basis of the solution of the kinetic equations and Monte Carlo simulations [4.190].

Since the end of the 1950s, neutral particle diagnostics with the use of neutral particle analysers (NPA) has been intensively developed at the Ioffe Institute (St. Petersburg, Russian Federation). The world's first NPA developed at the Institute

is described in Ref. [4.191]. More recently, this technique has been intensively developed in other fusion laboratories all over the world [4.192, 4.193].

The NPA is an energy and mass spectrometer. Its operating principle is based on the ionization of neutral particles emitted by a plasma with subsequent analysis of resulting secondary ions in the electric and magnetic fields. The ionization occurs due to stripping in a gas cell or due to passage through a thin carbon foil. The electric and magnetic fields provide mass resolved energy spectra of the particles. The traditional scheme of NPA uses parallel electric and magnetic fields ( $\vec{E} \parallel \vec{B}$ ), which leads to mass and energy separation of particles in the detector plane. The following types of detectors are employed in analysers: channel electron multipliers ('channeltron'), micro-channel plates (MCP), and scintillator counters (photomultiplier tubes (PMT) with scintillators).

The ISEP (ion separator) NPA used to measure hydrogenic isotope ratios and ion energy distribution functions [4.194] can be presented as an example of the most advanced contemporary instrument of this kind. It was developed at the A.F.Ioffe Institute and deployed on JET. Figure 4.18 shows the instrument layout. The instrument consists of three main parts: accelerator chamber, magnet chamber and detector chamber. The elements of the acceleration chamber are: input diaphragm (1), collimator slit mechanism (2), auxiliary movable calibration detector (3), stripping foil (4) and output diaphragm (5). The acceleration chamber provides acceleration of the secondary ions after stripping (up to 100 kV). It is important for plasma installations with a D-T plasma where the neutron background is high. The elements of the magnet and detector chambers are: light emission diode (6), laser for alignment (7), Hall probe (8), analysing magnet (9), analysing electrostatic condenser (10) and detector array (11). In Fig. 4.18,  $A^0$  is the atomic flux emitted by the plasma and  $A^+$  is the flux of secondary ions. The ISEP NPA has excellent H/D/T mass separation (with rejection of neighbouring masses  $<10^{-3}$ ) and high detection efficiency (up to 100% for higher energies) in the energy range 5–740 keV for H<sup>0</sup>, 5–370 keV for D<sup>0</sup> and 5–250 keV for T<sup>0</sup>. Therefore the ISEP has the following specific features:

- (a) Stripping of neutral atoms using a thin diamond-like carbon foil.
- (b) Acceleration of the secondary ions to compensate for scattering after stripping and to get sufficient signal-to-background ratio in D-T experiments.
- (c)  $\vec{E} \parallel \vec{B}$  analysis of ions in specially designed non-uniform electric and magnetic fields providing two dimensional focusing in the dispersion system and therefore high detection efficiency for ions.
- (d) ISEP detectors having a high sensitivity for hydrogenic ions ( $\sim 1$ ) and simultaneously very low sensitivity for neutron and gamma radiation ( $<10^{-7}$  pulses per electron).

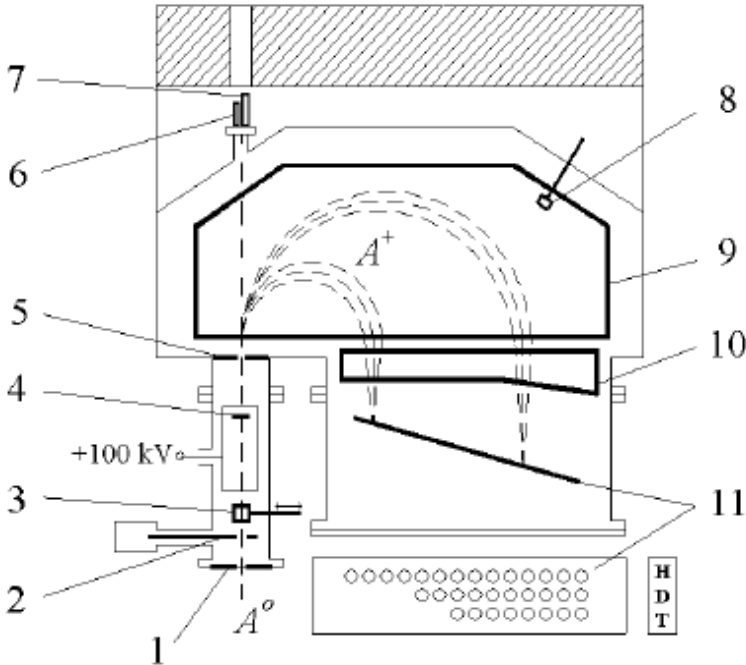


FIG. 4.18. ISEP NPA layout [4.194]. The instrument consists of three main parts: accelerator chamber, magnet chamber and detector chamber. The elements of the acceleration chamber are: 1 – input diaphragm, 2 – collimator slit mechanism, 3 – auxiliary movable calibration detector, 4 – stripping foil and 5 – output diaphragm. The elements of the magnet and detector chambers are: 6 – light emission diode, 7 – laser for alignment, 8 – Hall probe, 9 – analysing magnet, 10 – analysing electrostatic condenser and 11 – detector array. The box shows the front view of three rows of detectors for H, D and T ions.  $A^0$  is the atomic flux emitted by plasma and  $A^+$  the flux of secondary ions. Reprinted from Ref. [4.194]. Copyright (2011), American Institute of Physics.

Figure 4.19 shows deuterium and hydrogen atom spectra for the case of the JET beam heated high density plasma [4.194]. Black and open symbols correspond to deuterium and hydrogen. The central ion temperature taken from a comparison of calculated and experimental atom spectra equals  $T_i(0) = 15$  keV. In the modelling (lines) it was supposed that deuterium and hydrogen temperatures are equal. The deviation of deuterium points from the calculated spectrum (dotted line) at energies of 30.9 keV and 41.3 keV is the result of the influence of slowing down heating beam particles. The measurements presented in Fig. 4.19 and corresponding modelling give values of isotope composition for a JET plasma  $n_H / n_D = \text{constant}$  and  $(r/a) = 0.1$ .

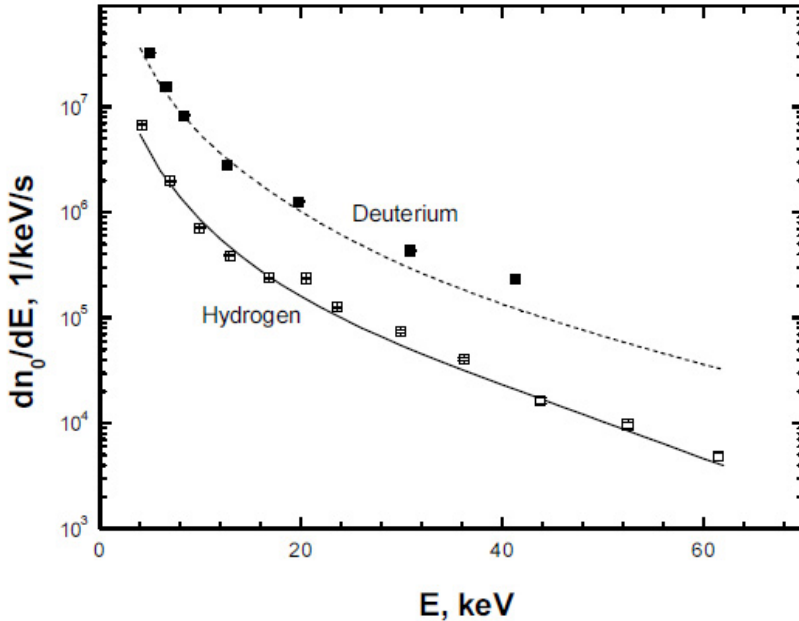


FIG. 4.19. Deuterium and hydrogen atom spectra on JET [4.194]. Black and open symbols correspond to deuterium and hydrogen. Lines correspond to modelling, dotted line for D, solid line for H.  $E$  is the energy of the particles. Reprinted from Ref. [4.194]. Copyright (2011), American Institute of Physics.

In the experiments with neutral beam heating, it is very interesting to measure the energy spectra of slowing down heating beam particles. Figure 4.20 presents this for the spherical tokamak Globus-M [4.195]. In this case, the energy of the heating beam was  $E_{NBI} = 24$  keV, and the power of the hydrogen beam was 0.47 MW and of the deuterium beam 0.42 MW. On the left hand side, one can see the Maxwellian-like spectrum of the bulk plasma corresponds to an ion temperature of 430 eV. The horizontal part of the curve corresponds to the spectrum of slowing down heating beam particles. It is seen that this spectrum corresponds well to the classical slowing down conditions. The information presented above is related to the NPA measurements in the thermal (keV) range. Another very interesting topic is the NPA measurements of MeV ions generated, for example, by ICRF minority ion heating or by products of D-D and D-T fusion reactions. These measurements require not only suitable instrumentation but also an appropriate mechanism for charge exchange neutralization of such ions. For passive NPA measurements in the MeV range, the neutral flux is produced mainly by  $H^+$ ,  $D^+$ ,  $T^+$  ions undergoing electron capture from hydrogen-like low- $Z$  impurity ions [4.196]. In the case of  $He^{2+}$  ions, neutralization in the MeV range occurs by double electron capture from helium-like low- $Z$  impurity ions [4.197]. The most probable donors for electron capture in large plasma machines like

JET or ITER (in future) are carbon and beryllium ions because they are the main low-Z impurities in these machines and their densities in the plasma core are higher than the density of  $H^0$ . Good examples of MeV ion measurements are the experiments performed on JET [4.198], TFTR [4.199] and JT-60U [4.200] using the high energy NPA Gemma-2 [4.201] developed in the Ioffe Institute. Some examples of experimental results on NPA measurements in the MeV range are presented in Section 2.2.4.

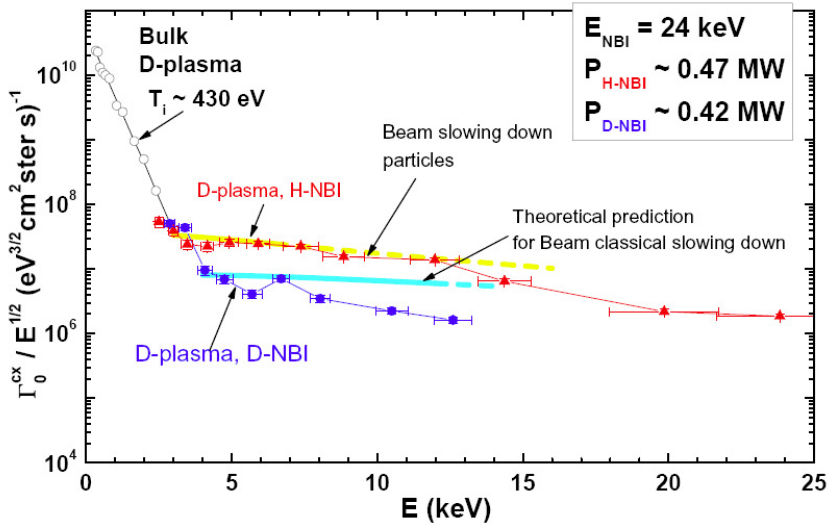


FIG. 4.20. Energy spectra of slowing down heating beam particles for spherical tokamak Globus-M [4.195]. Spectra of bulk ions and slowing down ions in the case of H- and D-beam injection. Here  $E_{NBI}$  is the energy of the beam,  $P_{H-NBI}$  and  $P_{D-NBI}$  are the powers of the hydrogen and deuterium beams. The vertical axis shows the atomic flux normalized in terms of a Maxwellian distribution. The horizontal axis shows energy of the detected atoms  $E$ .  $\Gamma_{cx}^0$  is the energy distribution of the charge exchange atomic flux detected by the NPA.

We turn briefly to the prospects for NPA measurements on ITER. There are two important tasks for charge exchange neutral particle diagnostics on the ITER tokamak. The first is the measurement of the hydrogen isotope composition of the plasma on the basis of measurements of neutralized fluxes of corresponding hydrogen ions, namely protons, deuterons and tritons in the 10–200 keV energy range. One of the main tasks of the ITER control system is to provide an optimal D/T ratio in the plasma.

The second task of neutral particle diagnostics is the measurement of the distribution functions of MeV ions generated by auxiliary heating and fusion reactions. This includes measurement of the confined D-T alpha particle distribution function by detection of He atom energy spectra in the MeV range [4.202].

Figure 4.21 presents a tandem arrangement of two neutral particle analysers developed in the Ioffe Institute and proposed to be used on ITER [4.203]. The NPA system consists of two devices: a low energy neutral particle analyser (LENPA) for the 10–200 keV energy range to provide measurement control of the isotope ratio and a high energy neutral particle analyser (HENPA) for the energy range 0.1–4 MeV to measure the fast ion and confined alpha particle distribution functions by detection of the energy spectra of the neutralized fast ions and alpha particles. Prototypes of both NPAs are the ISEP NPA presented above and the NPA Gemma-2. These instruments have been already successfully used on JET, TFTR and JT-60.

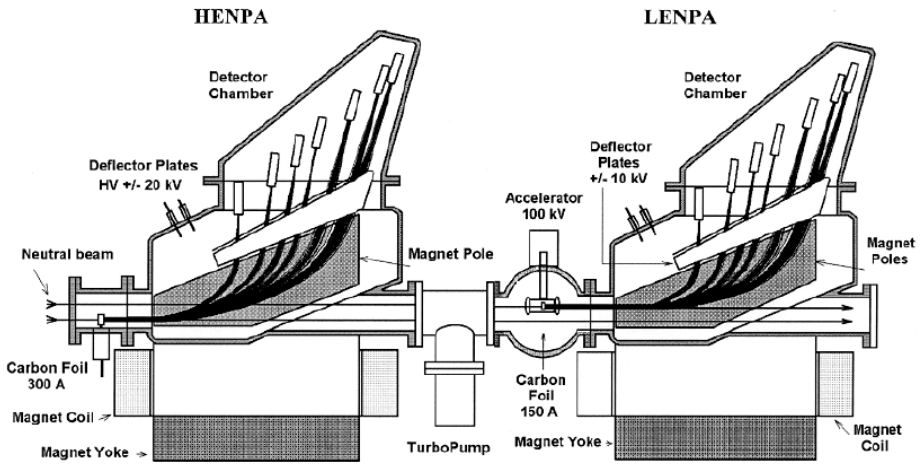


FIG. 4.21. A tandem arrangement of two neutral particle analysers proposed to be used on ITER [4.203].

Both HENPA and LENPA view along a major radius close to the equatorial plane of the torus and through the same straight vacuum opening of 20 cm diameter at the blanket face in the ITER horizontal port. Both analysers can operate simultaneously because the LENPA is shifted horizontally to ensure an independent line of sight.

#### 4.2.7. Methods based on X ray radiation

**Yu. Gott, E. Baronova**  
Kurchatov Institute, Moscow,  
Russian Federation

##### 4.2.7.1. Soft X ray radiation

Investigation of X ray plasma radiation is a very important addition to spectral measurements in the visible and ultraviolet ranges. Traditionally, the name “X ray radiation” is connected with a photon spectral wavelength which is shorter than 50 Å, which corresponds to a photon energy greater than, approximately, 250 eV. The photon energy of soft X rays is less than 100 keV. It is believed that the first soft X ray radiation investigations in plasma physics were carried out in the year 1949, when the solar corona X ray radiation was visualized. The plasma radiation spectrum usually consists of two components — one is continuous and another is a line spectrum. The continuous radiation consists of bremsstrahlung and recombination radiation. Up to the time when laboratory plasma temperatures were not greater than 100 eV the possibility of experimental investigations of plasma X ray radiations was very limited. At present, when on many installations the plasma electron temperature exceeds several keV, the value of such research has risen considerably.

If the plasma electron temperature is greater than 200 eV and amount of impurities is low the influence of recombination radiation may be ignored. In this situation, the continuous spectrum is determined generally by bremsstrahlung, which arises due to scattering of free electrons by plasma ions. If the electron energy distribution function is Maxwellian the photon energy spectrum is described by

$$\frac{dn_{hv}}{dE} = 2.41 \cdot 10^{-16} \frac{Z_{eff}}{\sqrt{T_e}} n_e^2 \frac{e^{-E/T_e}}{E} \quad [\text{quanta} \cdot \text{cm}^{-3} \cdot \text{s}^{-1} \cdot \text{ster}^{-1} \cdot \text{keV}^{-1}] \quad (4.21)$$

Here,  $dn_{hv} / dE$  is the number of photons radiated from unit volume (1 cm<sup>3</sup>) per steradian per second in a 1 keV range,  $Z_{eff}$ ,  $T_e$  and  $n_e$  are the plasma effective charge, temperature (in keV) and density (electrons per cm<sup>3</sup>) respectively, and  $E$  is the quanta energy in keV. From Eq. (4.21) one can see that from the X ray spectrum it is possible to find the plasma electron temperature and from the absolute value of flux one can find the plasma electron density. The time evolution of the X ray flux provides information about MHD activity. The energy losses from the plasma due to X ray radiation can be found from the absolute value of the total flux.

4.2.7.1.1. Bremsstrahlung investigations

For MHD plasma activities and energy losses, integral detectors which can measure plasma radiation over a wide energy range are used. These detectors are ionization chambers including multi-wire chambers [4.204, 4.205], semiconductor detectors [4.206], vacuum photoelectric detectors [4.207, 4.208], AXUV type semiconductor photodiodes, etc. [4.209, 4.210].

As an example, Fig. 4.22 shows the signal obtained on T-10 with the help of a multi-wire chamber (curve 1). The high frequency electron cyclotron power is also shown (curve 2). It can be seen that variation of plasma electron temperature changes the X ray flux. On the lower plot in Fig. 4.22 one can see zoomed sawtooth oscillations showing the specific MHD activity.

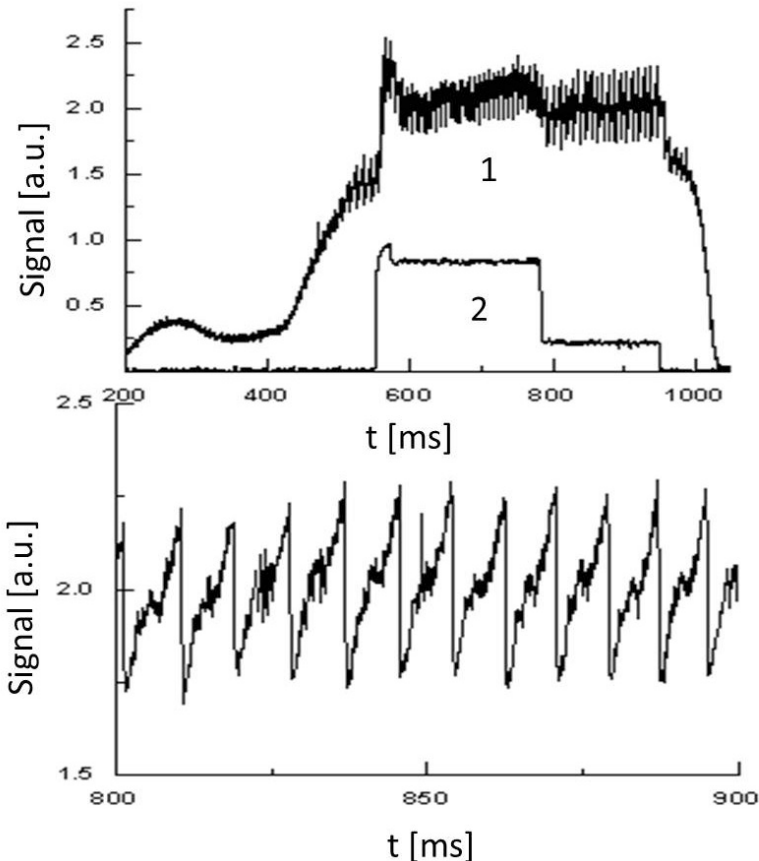


FIG. 4.22. Soft X ray flux from T-10, measured with the help of a multi-wire chamber. a) Curve 1 corresponds to the flux during the tokamak shot and curve 2 the ECRH power; b) Zoomed sawtooth oscillations. From T-10 database. The figure is a compilation from [4.211] and [4.212].

The computerized tomography technique, which permits the reconstruction of the emissivity plasma cross-section from its line integral measurements, has been applied in fusion plasma science since the early 1980s. Soft X ray tomography gives the possibility to measure plasma position and shape, and plasma MHD activity, and to use this information in feedback control system. Some 100–200 detectors are usually employed for these measurements. In Fig. 4.23, one can see the line-of-sights of such detectors in TCV. Recently, soft X ray measurements have been used to study fast-ion losses induced by high frequency MHD perturbations in the ASDEX Upgrade Tokamak [4.213]. For exploring both detailed structures of the magnetic surfaces and helical islands induced due to either magnetic field errors or MHD instabilities, a tangentially viewing soft X ray camera system was installed on the Large Helical Device (LHD) [4.214]. Preliminary systems were successfully used on TEXTOR-94 [4.215]. On DIII-D the shape of the safety factor  $q$  profile was determined from information inferred from surfaces of constant SXR emissivity obtained with the help of X ray tomography [4.216].

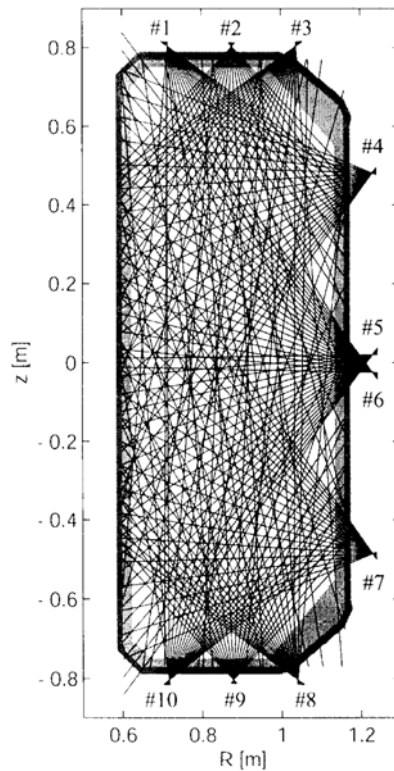


FIG. 4.23. Diagnostic setup for soft X ray tomography in TCV [4.217].

4.2.7.1.2. Plasma electron temperature measurements

One of the first approaches to plasma electron temperature measurements was the filter method. In this method the photon flux penetrates through filters of different materials with different thicknesses. The absorption of X ray radiation in these filters give us the possibility to calculate the plasma temperature. Figure 4.24 shows an example of such measurements [4.218]. One can see that the electron temperature in this case is 250–270 eV. If we know the electron temperature and the absolute value of the X ray flux we can calculate the plasma density by means of expression Eq. (4.21).

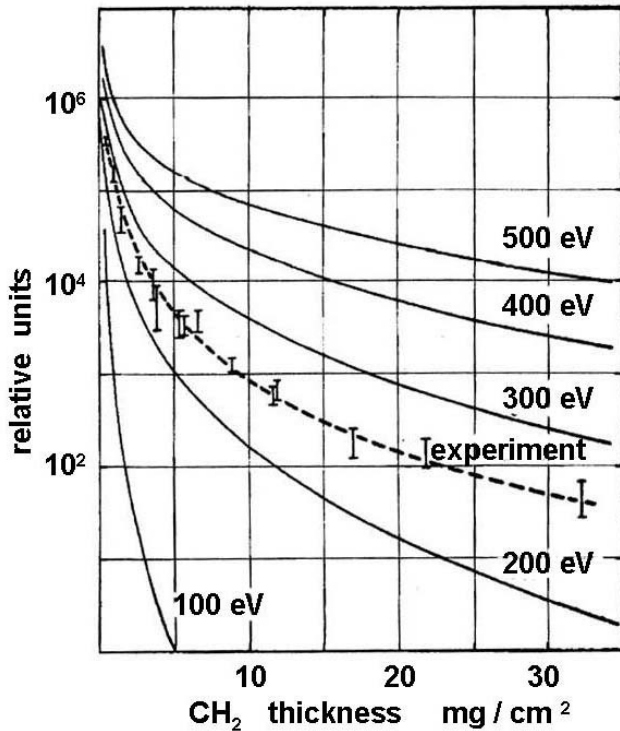


FIG. 4.24. Experimental polyethylene ( $CH_2$ ) absorption curve compared with calculated transmissions. The solid lines are calculated for different plasma electron temperatures. The dotted line fits the experimental data. The experimental curve is located between curves corresponding to temperatures of 200 eV and 300 eV and it can be concluded that the measured temperature is about 250 eV. Taken from Ref. [4.219].

Several important plasma parameters such as electron temperature and the content of metallic impurities can be obtained from a soft X ray pulse height analyser (PHA) [4.220, 4.221]. Semiconductor detectors are generally used for these measurements. Figure 4.25 shows the spectral distribution of photon flux

measured on the ST installation. In addition to bremsstrahlung, it is possible to see the accelerated electrons radiation and spectral lines of wall materials (Fe, Cr, Ni) and limiter (Mo). From expression Eq. (4.21) one can see that the slope of the curve  $E(dn_{hv}/dE)$  presented in semi-logarithmic scale as a function of  $E$  gives an estimate of the electron temperature of the bulk plasma of about 1450 eV and of the “temperature” of the accelerated electron group of about 5900 eV.

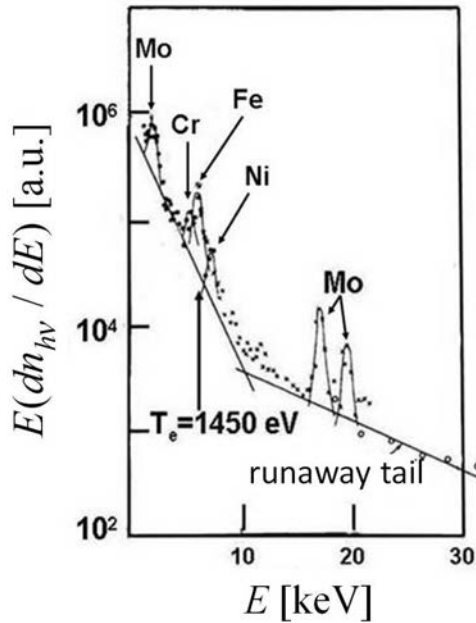


FIG. 4.25. Typical X ray spectrum measured in ST, exhibiting thermal continuum ( $T_e = 1450$  eV), impurity lines of limiter and wall material (molybdenum, iron, chromium, nickel), and high energy tails produced by runaway electrons. (●), (x) and (o) are data obtained with the help of different detectors. Reproduced from Ref. [4.222].

#### 4.2.7.2. High resolution X ray spectroscopy

One of the most important applications of high resolution X ray spectroscopy is the measurement of ion directional velocity and temperature in the central and peripheral plasma. These measurements are performed by the analysis of Doppler width and shift of X ray lines emitted by highly charged ions of middle and high  $Z$  elements, which are unavoidably present in a plasma (as impurities) or added for diagnostics purposes. On the other hand, the strong radiation of impurities substantially contributes to the power losses of the plasma in present magnetically confined plasma devices. Thus investigation of impurity behaviour is an important task on the way towards a fusion reactor. Spectroscopic

studies of the radiation emitted by impurities is one of the most informative approaches in determining the effects of impurities on plasma behaviour and in measurements of plasma parameters such as electron temperatures and densities, particle transport, ionization equilibrium and particle influx rates.

The primary interest in X ray spectroscopy is the spectra of helium-like ions, since those ions exist in wide range of electron temperatures and their emission can be observed over a wide range of electron temperatures. The choice of elements depends on the central electron temperature  $T_e$  in present devices, which is from 1 to 6 keV, so that line radiation is predominately emitted in the soft X ray region between 0.1 and 0.5 nm, where the elements from argon to nickel (Ar XVII, FeXXV, Kr XXXV are mostly used) are in helium-like charge states. However for future tokamaks, such as ITER, the expected electron temperature will be 25 keV and krypton is considered to be the best choice [4.223].

Over the past three decades, high resolution X ray crystal spectroscopy became a conventional tool to measure ion temperature and plasma rotation velocity from the Doppler width and Doppler shift of lines emitted by middle  $Z$  elements ( $18 < Z < 36$ ).

Today's requirements for X ray spectrometry and X ray spectrometers are as follows: in the first stage, the choice is made of the best impurity candidates for spectroscopy with confirmation that required concentrations are acceptable; in the second stage, a spectrometer is designed with high spectral resolution  $\lambda / \delta\lambda = 5000-10000$  in the wavelength range 0.1–0.5 nm, with low signal-to-noise ratio, with high spatial and time resolution, equipped by 2-D detectors, with integration into ITER port plugs, and gamma and neutron shields; in the third stage the model for data analysis, including Abel inversion procedure and construction of synthetic spectra, is developed.

The key element of X ray spectrometers which is used to detect X ray lines is a crystal which reflects X radiation according to Bragg's Law  $2d \sin \Omega = k\lambda$ , where  $k$  is the reflection order,  $\lambda$  is the wavelength,  $d$  is the internal crystal distance and  $\Omega$  is Bragg's angle. The first X ray spectrometer equipped with a flat crystal was developed to diagnose line radiation from impurities on ST [4.224]. The K- $\alpha$  spectra of iron were compared with synthetic spectra, constructed from theoretical data by A.L. Mertz and R.D. Cowan, which included predictions about the contribution from dielectronic recombination to the spectra from different charge states. Experimental data were taken from several discharges with varying electron temperatures, but even this qualitative comparison showed that the contribution from dielectronic recombination was significant, as was also predicted theoretically in Ref. [4.225].

Iron line radiation was then more thoroughly investigated on the PLT tokamak with a much improved X ray focusing spectrometer. The goal of this spectroscopic study was to experimentally verify the validity and accuracy of theoretical predictions based on coronal equilibrium and test their applicability

to tokamak plasmas [4.226]. The spectrometer consisted of a cylindrically bent ( $6 \times 1.5$ ) inch 220-germanium crystal with curvature radius 2.42 m and a position sensitive multi-wire proportional counter; this made it possible to obtain time resolved spectra in the Johann scheme [4.227] (Fig. 4.26). The spectrometer covered a large spectral range and observed the features of all the ion charge states simultaneously, in contrast to the spectrometer on ST, where the position of the crystal and detector had to be adjusted between plasma discharges to access a different wavelength range. Spectra from several hundred PLT discharges with a central electron temperature from 800 to 1500 eV were analysed by comparing the data with theoretical predictions by Mertz and Cowan. It was concluded that coronal equilibrium was satisfied in the central region of the plasma with an uncertainty factor of 2 associated with the ionization cross-sections used in the computations.

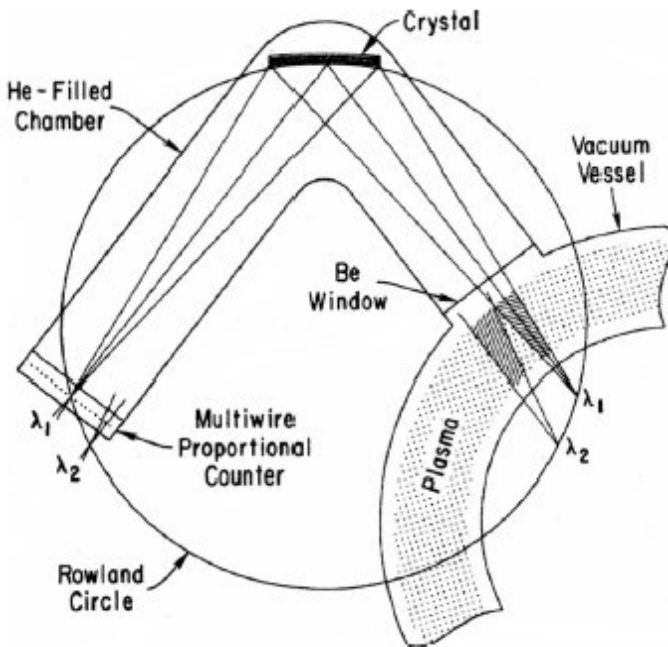


FIG. 4.26. Johann spectrometer on PLT.  $\lambda_1$  corresponds to the wavelength detected in the central part of the detector;  $\lambda_2$  is the maximum detected wavelength [4.221].

A further aim of the PLT experiments was the measurement of  $T_i$  in the hot core of the plasma. Since the plasma diameter as well as the electron temperature  $T_e$  on PLT were much larger than on ST, the standard techniques, charge exchange diagnostics and Doppler broadening measurements of the extreme ultraviolet (EUV) line radiation were problematic because the mean free path for neutral charge exchange is smaller than the plasma diameter and the EUV

line radiation was primarily emitted from the edge of the plasma. Determination of  $T_i$  from a measurement of the neutron yield cannot be applied in the absence of Maxwellian ion velocity distribution (during the neutral beam injection, for example). On the other hand, it was logical to expect a larger fraction of X rays emitted from the core plasma with a higher electron temperature. That is why Doppler broadening measurements of X ray lines were started and experiments by Hill et al. [4.226] have shown that the 1s-2p resonance line of helium-like iron (FeXXV),  $\lambda = 1.85 \text{ \AA}$ , appeared to be well separated from other spectral lines and suitable for measuring a central electron temperature  $T_e \approx 1.2 \text{ keV}$ . The spectral resolution of the X ray spectrometer on PLT was improved to  $\lambda / \delta\lambda = 15\,000$  by using a new quartz crystal 22(-4)3 with radius of curvature 3.33 m. The spectrometer became an important diagnostic tool for the core  $T_i$  on PLT starting from the first neutral beam heating experiments, which produced a plasma with core  $T_i = 4 \text{ keV}$  [4.228].

The parameters of TFTR and JET plasmas (plasma current  $>2 \text{ MA}$ ), with electron and ion temperatures in the ranges 1–3 keV, 3–6 keV in the regime of ohmic heating and with  $T_e = 30 \text{ keV}$ ,  $T_i = 10 \text{ keV}$  respectively in regimes with auxiliary heating, give a foretaste of what is to be expected from ITER. TFTR and JET were designed for D-T experiments and a demonstration of fusion breakeven, so plasma diagnostics had to operate in an environment of intense gamma and neutron radiation. A massively shielded Johann type X ray crystal spectrometer is situated in the horizontal mid-plane [4.229] of TFTR and an array of up to five Johann spectrometers with near vertical sightlines are mounted for profile measurements of  $T_i$  [4.230, 4.231]. The latter instruments were located in the TFTR basement, shielded by 1.83 m thick concrete. The detectors were surrounded by an additional 20 cm lead and borated polyethylene wall. The dimensions of those spectrometers were large, according to the curvature radius of cylindrical crystals 10 m and 12 m. Figure 4.27 shows the 1s<sup>2</sup>-1s2p resonance line of helium-like Fe, recorded during the period 2.5–3.0 s. The time history of the central ion temperature of the TFTR plasma with auxiliary heating testifies that  $(T_i)_{\text{max}} = 30 \text{ keV}$ , maintaining a high value  $>15 \text{ keV}$  during 1 s.

A Johann spectrometer of even large dimensions (25 m radius of curvature of the crystal, Bragg angle  $50.75^\circ$ ) was built for JET by ENEA Laboratories in Frascati [4.232]. Because of the large dimensions the dispersion and spectral resolution ( $\lambda / \delta\lambda = 20\,000$ ) were very high so that only a small wavelength range was detected, which included the resonance line of helium-like nickel at  $1.59 \text{ \AA}$  and associated dielectronic satellites in its close vicinity.

The experiments on JET and TFTR, where plasmas produced by an intense auxiliary neutral beam and RF heating have ion temperatures  $>20 \text{ keV}$  have shown that Doppler broadening is so large that spectral lines were blended with each other and correct measurements of  $T_e$  and  $T_i$  could only be made by least-squares fit comparisons with synthetic spectra, constructed from accurate

theoretical predictions. So very important for the interpretation of results is a collaboration with atomic physicists providing the theoretical data on wavelengths and various atomic processes responsible for the formation of line emission and with physicists who performed additional experimental studies on electron beam ion traps, for example [4.233, 4.234]. And vice versa, various theoretical predictions might be verified using the results obtained with high resolution X ray spectrometers on tokamak plasmas which are well diagnosed and reproducible. X ray crystal spectrometers are now conventional diagnostic equipment on tokamaks, likewise helping to obtain atomic data on hydrogen-, helium-like ions, etc. The extensive work done in this area is beyond the scope of this review and can be found in Refs [4.235–4.240]. The numerous X ray spectrometers designed for tokamaks are described in Refs [4.241–4.261].

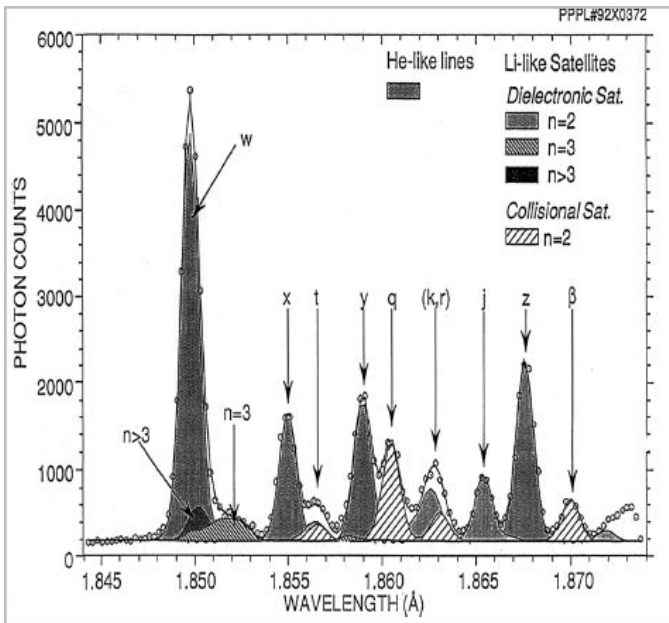


FIG. 4.27. Spectra of FeXXV, emitted by TFTR plasma, recorded from 2.5 s to 3 s. *W* is a resonance line, *y* an inter-combination line; *t*, *q*, *k*, *r*, *j* are satellites and *z* is a forbidden line [4.221].

Relating to the helium-like spectra on tokamak experiments, theoretical predictions of dielectronic satellites, inner shell lithium- and beryllium-like satellites, lying in the vicinity of resonance lines, are in excellent agreement with experimental data [4.236–4.240]. A comparison between experimental data and theoretical predictions has demonstrated that the line ratios of the dielectronic and inner shell satellites with respect to the helium-like resonance lines (see Fig. 4.27) might be used for diagnosis of the central electron temperature and

measurements of ionization equilibrium [4.242]. However, the ratios of inter-combination and forbidden line to resonance line of helium-like ions were found to be larger than predicted values in most tokamak experiments. The reason for this discrepancy is not yet understood; probably it might be caused by profile effects, which were not properly taken into account in the analysis of the chord integrated spectral data.

In this sense, the development of new instrumentation, recording spectra with a spatial resolution of one to a few centimetres would help to find a solution to the discrepancy problem mentioned above. One of the approaches is to use a doubly curved (spherical, toroidal, etc.) crystal which provides spatial resolution in the direction perpendicular to the dispersion direction. Another way is to use several spectrometers to measure spectra from many chords. The former task was solved in the imaging spectrometer recently installed on NSTX [4.235]. The imaging spectrometer mounted on Alcator C-Mod consists of a spherically bent crystal and a 2-D position sensitive detector [4.243], or new pixellated semiconductor detectors of a very high photon count rate capability of 1 MHz per pixel. The spectrometer records spectra from the entire height (72 cm) of the elongated plasma cross-section with a spatial resolution of about 1 cm. Figure 4.28 shows a surface plot of spatially resolved helium-like argon spectra obtained from the Alcator C-Mod discharge. The spectra that are emitted from the central plasma region consist of resonance lines of helium-like argon and lithium-like satellites, whereas the spectra emitted by the colder region consist only of helium-like lines  $w$ ,  $x$ ,  $y$ ,  $z$ , with  $z$  the strongest. The lines in the outer plasma region are produced by recombination of hydrogen-like argon ions; since the electron density on Alcator C-Mod is 10 times higher than in other tokamak experiments, one would expect the ion distribution to be close to corona equilibrium. However, hydrogen-like ions appeared to be far out; the reason is presently under consideration. Ion temperature and toroidal rotation velocity profiles versus time are extracted from time resolved spectroscopic data as well.

In the last decade, plasma polarization spectroscopy has started to be a powerful tool to study the anisotropy of laboratory and solar plasmas [4.262, 4.263]. It was shown theoretically that resonance and inter-combination lines in helium-like spectra, as well as some of the satellites, might be polarized. Polarization of EUV spectra, emitted by a tokamak plasma was also detected experimentally [4.262]. However, to measure the polarization of X ray spectra is not a trivial task: two identical X ray spectrometers with dispersion directions oriented mutually perpendicular should be installed on the machine. That is why X ray polarization measurements on tokamaks are not numerous and to our knowledge were only performed on TEXTOR. Interpretation of the results appeared to be problematic because of the lack of information on the field of view of the two spectrometers. The future development of X ray spectro-polarimetry on tokamaks, free from field of view problems, is to use the single crystal

X ray spectro-polarimeter recently developed and patented in the Kurchatov Institute [4.264–4.266]. We note that experimental evidence of the polarization of helium-like spectra would be evidence that the conventional approaches to the determination of plasma parameters from X ray spectra should be critically reconsidered.

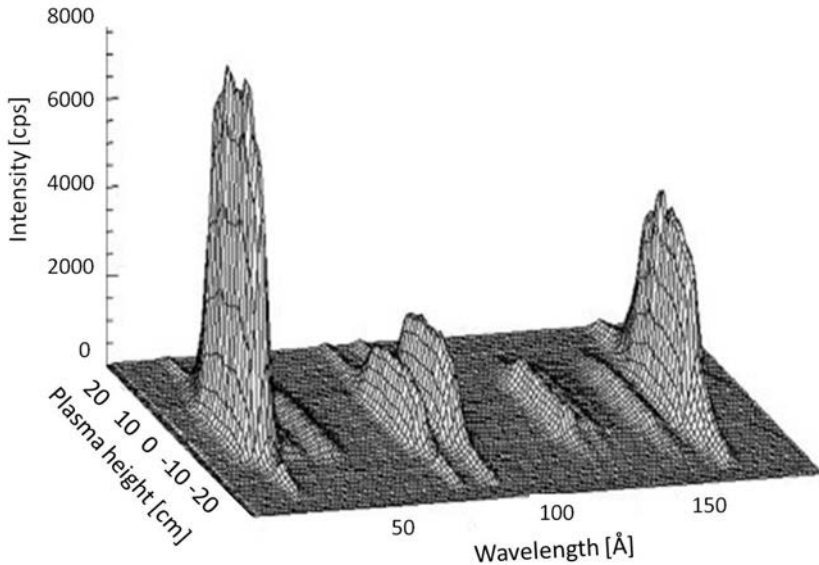


FIG. 4.28. Spatially resolved ArXVII line recorded on Alcator C-Mod [4.221].

The spectral resolution of existing instruments depends on the resolution of the detector (0.3 mm for widely used proportional counters), the rocking curve of bent crystals, and the optical aberrations. Special attention has been given to the development and characterization of bent crystals used in X ray spectrometers with the aim of optimizing the characteristics of the devices. A study of the rocking curve was made for a variety of chemically polished/unpolished bent crystals [4.267], for the displacement of the rocking curve of heated crystals, and for the optical quality of the crystal surface. It was shown that crystals connected to the substrate by optical contact provide the best resolution and withstand a higher neutron flux compared to glued crystals. An analysis of the advantages of the Johansson geometry versus the Johann one was carried out, and the manufacturing technology was developed and a spherical Johansson crystal manufactured.

Nowadays, minimization of geometrical sizes is an important direction in designing X ray spectrometers. A super-compact imaging Johann type X ray spectrometer operating in asymmetric schemes at large Bragg angles (around  $70^\circ$ , see Fig. 4.29) was recently built in the Kurchatov Institute and mounted on tokamak ASDEX Upgrade. Its typical size is 0.5 m, weight 10 kg, energy range

3.2–27 keV; the spectrometer is equipped with two large spherical crystals and X ray sensitive CCD with  $26 \mu$  pixel and quantum efficiency  $QE \approx 90\%$  at 3 keV. In spite of its extremely compact size the spectrometer has two channels to measure the ion temperature of the core and periphery plasma from the Doppler width of resonance lines of helium-like Ar, Fe, Kr with a lower  $T_i$  limit of 0.32 keV and  $d\lambda / \lambda = 5000$ .

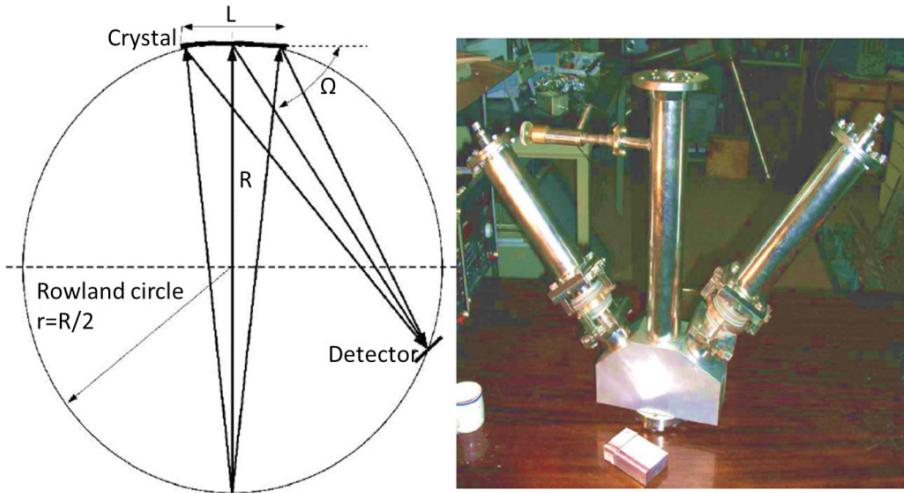


FIG. 4.29. Scheme and photo of super-compact X ray spectrometer with non-symmetrical regime of operation. Here,  $\Omega$  is the Bragg angle and  $L$  is the crystal length.

The spectrometer is supplied with a processing integrated diagnostic package in which the line profile is represented as the integral of elementary Gaussian profiles along a line of sight. So the spectral data obtained with such spectrometers are Abel inverted and the line width, line shifts and line ratios are determined locally at each point along the plasma radius to eliminate the profile effect. This method is good for multi-chord measurements and assumes the availability of information on electron temperature and density. The instrument is the result of an EFDA project on the development of an ITER relevant X ray crystal spectrometer (EFDA reference: TW5-TPDSDIARFA). The latest version of this imaging X ray spectrometer has even smaller sizes, being a suitable prototype for measurements on ITER. A comprehensive analysis has been made of the apparatus function of focusing spectrometers and the reconsidered analytical formulation for spectral resolution is given in Ref. [4.268].

## 4.2.8. Experimental nuclear physics methods

**V. Zaveryaev**

Kurchatov Institute, Moscow,  
Russian Federation

**I. Chugunov, A. Shevelev**

Ioffe Institute, Saint Petersburg,  
Russian Federation

**V. Kiptily**

JET, United Kingdom

The experimental techniques which have been initially developed in nuclear physics are applied to measure high energy fusion products (neutrons and charged particles) and hard X rays and gamma rays as well.

Neutrons and charged high energy particles are the result of thermonuclear reactions in D-D and D-T plasmas (Table 4.1).

TABLE 4.1. Thermonuclear reactions in D-D and D-T plasmas	
$D + D$	$\rightarrow t (1.01 \text{ MeV}) + p (3.02 \text{ MeV})$
$D + D$	$\rightarrow {}^3\text{He} (0.82 \text{ MeV}) + n (2.5 \text{ MeV})$
$D + {}^3\text{He}$	$\rightarrow {}^4\text{He} (3.7 \text{ MeV}) + p (14.7 \text{ MeV})$
$D + T$	$\rightarrow {}^4\text{He} (3.5 \text{ MeV}) + n (14.1 \text{ MeV})$
$T + T$	$\rightarrow {}^4\text{He} + n + n + 11.3 \text{ MeV}$

Moreover, various gamma rays arise under the interaction of charged fusion products (CFP) themselves and with low- $Z$  nuclei of impurities. Hard X rays are the result of the slowing down of high energy electrons by plasma ions and nuclei of the first wall and limiter material.

### 4.2.8.1. Neutrons, charged fusion products, hard X rays

#### 4.2.8.1.1. Neutrons

Neutrons easily leave the machine and can be detected by detectors located outside the vacuum vessel. From neutron measurements it is possible to receive information about the fusion yield and its temporal evolution, about the value and profile of ion temperature, and the energy distribution of plasma ions.

Thermonuclear neutrons were first detected at Tokamak-3 and reported in 1969 [4.269], and then have been studied in more detail [4.270]. The ion temperature was several hundreds of eV and fusion reaction yield was very low. The main goal of these measurements was just the demonstration of fusion neutron existence. For this purpose, the most sensitive neutron detectors have been used — long gas counters filled with  $\text{BF}_3$ . Neutron detection is based on the nuclear reaction  $^{10}\text{B} + n \rightarrow ^4\text{He} + ^7\text{Li}$ , which has a high reaction energy (2.9 MeV) and high cross-section for thermal neutrons. Neutron counters were inserted into the paraffin moderator to slow down D-D neutrons to thermal energies. During one shot, only a few events of neutron detection have been observed.

This was the outstanding success on the way to controlled fusion but the neutron intensity was too low to use these measurements for plasma diagnostics. Neutron measurement was becoming the standard diagnostic on larger machines with increased shot duration, plasma density and ion temperature. A good review of the neutron measurement techniques and results obtained before 1993 is presented in Ref. [4.271]. More recent review is Ref. [4.272]. Here, we concern ourselves only with the basic principles of diagnostics. The cross-sections of fusion reactions strongly depend on the interacting particle energies so the neutron intensity for a Maxwellian plasma is a strong function of the fuel temperature if the latter does not exceed several keV. Accordingly, an absolute measurement of neutron intensity performed even with relatively low accuracy gives an estimate of the ion temperature. Later, when the detector efficiency problem became unimportant in large machines, fission chambers, which have a low sensitivity to hard X rays and gamma rays, were used.

The absolute calibration of neutron detectors is a very important task because the neutron intensity is directly linked with the fusion power released. A plasma as a neutron source is an extended object with unknown spatial source strength distribution. Usually, to simulate this object experimentally radioactive neutron sources (Po-Be, Pu-Be,  $^{252}\text{Cf}$ ) are moved toroidally along the torus and the detector signal  $S_d$  counts per second is recorded for many source positions. Integrating the curve measured along the source position gives the calibration factor as:

$$k[\text{neutrons per count}] \approx 2\pi R I_s / \left[ \int S_d dl \right] \quad (4.22)$$

where  $R$  [cm] is the major torus radius,  $I_s$  [neutrons per second] is the neutron source intensity and  $l$  is a coordinate of the calibrating neutron source position on the line along which it is moved. It is assumed that this line is a circle with major radius  $R$  (see Fig. 4.30).

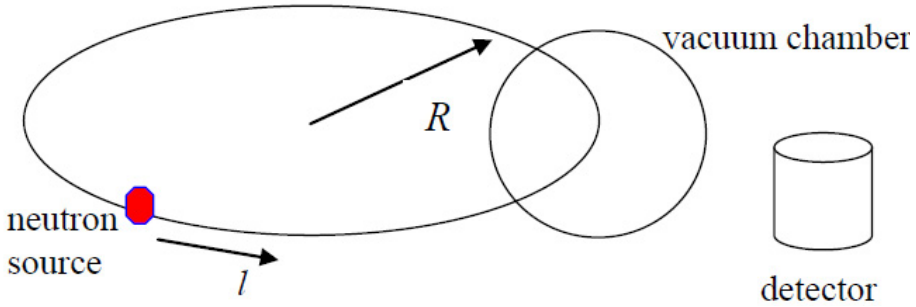


FIG. 4.30. Scheme of neutron detector calibration by means of moving neutron radiation source.

In modern machines the neutron intensity varies in a very large range (up to  $10^7$  in ITER expected) in time and from regime to regime and neutron monitoring systems should cover the full range. There are no detectors which can operate in this dynamic range, so several monitors having different efficiencies are applied. As a rule, only the most efficient detectors can be calibrated in situ using radioactive sources while other detectors are calibrated in real experiment by comparing their signals with signals of already calibrated monitors (so called “cross-calibration”).

It should be noted that the radioactive neutron source energy spectrum differs from the D-D (2.5 MeV) and D-T (14.1 MeV) neutron energies. To minimize this factor, the neutron monitor should have flat sensitivity dependence on neutron energy. For D-T plasmas the calibrations are performed using compact D-T neutron generators. The calibration procedure must be repeated periodically and certainly after installation or removal of large structure components near the detectors.

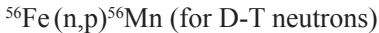
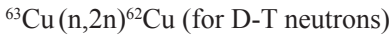
Integration of neutron intensity in time gives the total neutron yield:

$$Y_n = \int I_s dt \quad (4.23)$$

However, to measure  $Y_n$  directly the activation technique is used; this is based on activation of material samples under neutron radiation. As a result of nuclear reactions new unstable isotopes are born and their decays are measured.

In early tokamak studies, when the neutron yield was rather low, activation reactions caused by slow neutrons were used, for example,  $^{109}\text{Ag} + n = ^{110}\text{Ag}$ , which has a high cross-section for thermal neutrons. The Ag foil and detector were inserted in a paraffin moderator and located as close to the machine as possible. After the plasma discharge the  $\beta$ -decay of  $^{110}\text{Ag}$  ( $\tau_{1/2} = 24.5$  s) was measured. The anomalous neutron yield ( $>10^{14}$  neutrons/shot) caused by the photonuclear reaction was measured in regimes with runaway electrons [4.273].

Later, when fusion power increased, it became possible to apply the threshold activation reactions caused by fast neutrons (see, for example, Ref. [4.274]). Some of these reactions are as follows:



Before a plasma shot these samples are located close to the vacuum vessel and just after the shot they are transferred to measurement equipment by means of gas flow. Low values of activation cross-sections do not allow calibration of these detectors in situ with neutron sources, so to measure absolute neutron yield, numerical calculations of neutron transport in tokamak structure materials are needed.

In Ref. [4.275] an original method to apply fluid liquid activation for neutron flux monitoring was suggested. It is possible that this technique will be used in future commercial fusion reactors. In tokamaks, the origin of neutrons can be not only thermal fusion reactions but other phenomena as well: disintegration of deuterons by relativistic electrons, photonuclear ( $\gamma,n$ ) reactions, interaction of a deuterium heating beam with bulk plasma ions. To reveal the nature of neutron origin, measurement of the neutron energy spectrum was used. Direct measurements of neutron energy spectra were first performed in the PLT device using a liquid scintillator based detector [4.276]. In different plasma regimes, neutron groups of different origins have been observed (Fig. 4.31). However, in present day tokamaks the role of photonuclear reactions and disintegration of deuterons by an electron beam is negligible.

Later, neutron spectrometry was applied at many large machines with magnetic confinement. For these measurements, the spectrometric detectors (organic scintillators, diamond detectors) and specially developed neutron spectrometers were used. The shape of the neutron spectrum for Maxwellian ions is a Gaussian with FWHM depending on the ion temperature as  $\Delta E \sim (T_i)^{1/2}$ . This gives the opportunity in principle to measure the ion temperature. These measurements have been performed at some machines (see, for example, Ref. [4.277]).

The behaviour of charged fusion products in a plasma is very important because these particles have to be confined and provide thermonuclear plasma heating. The first experiments in this field were made in the PLT machine [4.278] when a heating deuterium atomic beam was injected into a D-plasma and neutrons were measured as a result of the beam-plasma interaction. From an analysis of the results it was possible to make an important conclusion about the classical nature of high energy particle movement and slowing down processes.

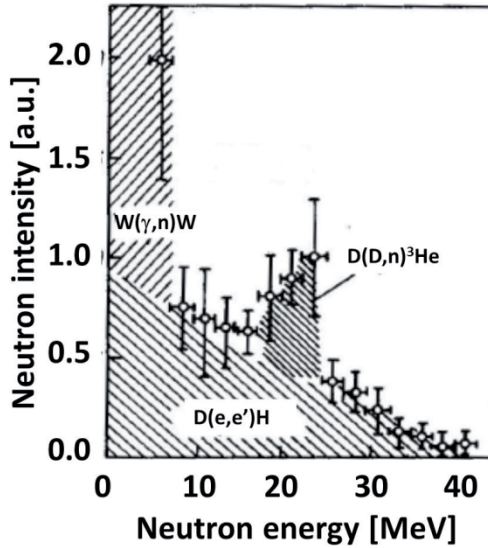


FIG. 4.31. Neutron spectrum measured at PLT [4.276]. Three groups of neutrons are observed: upper left — result of photoneuclear reaction on tungsten  $W(\gamma,n)W$ , below — result of disintegration of deuterons by relativistic electrons  $D(e,e'n)H$ , upper right — thermonuclear neutron D-D peak and scattered D-D neutrons.

Under high fusion yield conditions, it became possible to measure the neutron source profile by means of detectors and spectrometers situated in the channels of a multichannel collimator. It should be noted that there is an opportunity in principle to assess the relative concentration of deuterium and tritium by measurements of the D-D and D-T neutron flux ratio. However, the application of this method is not easy owing to the high background of initially scattered D-T neutrons ( $E = 14$  MeV) slowed down to energies 2–3 MeV.

The alpha particles produced in the D-T reaction and confined in the plasma in close collisions with bulk ions (deuterons and tritons) transfer some energy to them and these fast ions produce a special neutron group under the D-T reaction with plasma ions (tritons and deuterons correspondingly) — so called knock-on neutrons with energies up to 17 MeV. The energy spectrum of these neutrons reflects the energy distribution function of the confined alphas. The fraction of knock-on neutron tails is only  $10^{-4}$  of the conventional D-T neutrons and their detection is a difficult task. Nevertheless they have been observed at JET with a magnetic proton recoil neutron spectrometer [4.279].

#### 4.2.8.1.2. Charged fusion products

Charged products of thermonuclear reactions (alphas,  $^3\text{He}$ , protons and tritons) can almost immediately escape the plasma (first orbit loss) or be

confined, slow down and transfer their energy to bulk plasma. The destiny of a particle depends on its momentum vector and magnetic configuration. If the particle velocity is perpendicular to the magnetic field vector (pitch angle close to  $\pi/2$ ), the particle can be trapped in a magnetic field ripple, drift in a vertical direction and leave the vacuum vessel. If the particle falls within a “banana” orbit it leaves the plasma close to the equatorial plane. Due to their high energy, the particles practically do not interact with the bulk plasma and their trajectories depend only on the magnetic configuration.

Measurements of the escaping CFP make it possible to obtain the ion temperature value (from Doppler widening of the energy spectrum) but also information on the poloidal magnetic field. For the first task, the energy spectrum must be measured, while for the second the pitch angle distribution is required at the point where particles leave the plasma.

In principle, CFP spectrometry is much simpler than neutron spectrometry; however, its application on fusion machines becomes complicated due to technical aspects. To actually measure escaping particles the detectors should be placed very close to the plasma and, accordingly, must operate under a harsh environment (high temperature, particle and photon flux, magnetic field). The first measurements of CFP were made on PLT [4.280] using spectrometric silicon diodes. Later, these measurements were performed on several tokamaks. To measure simultaneously the energy and pitch angle distribution of the escaping alphas from the reaction  $D(^3\text{He},p)^4\text{He}$  on PLT an original scheme was used (Fig. 4.32) [4.281]. Later, this scheme was applied in TFTR [4.282], in particular, to study CFP diffusion in the plasma [4.283].

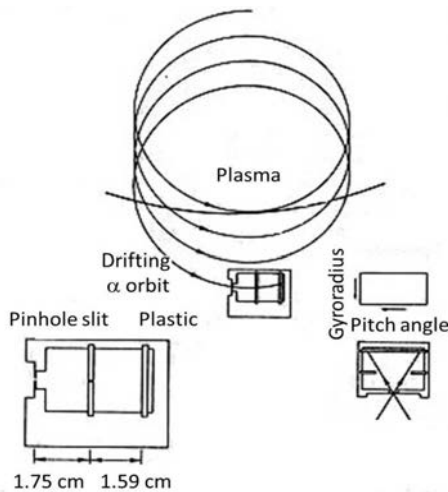


FIG. 4.32. Schematic of the nuclear track detector, showing the relative placement of the pinhole, slit and CR-39 plastic, and how the parameters of the particle orbit affect the placement of the track [4.281].

Recently, a scintillator probe [4.284], was used in JET to measure escaping fast ions [4.285]. To measure escaping CFP on the T-10 machine, several spectrometric silicon diodes have been used which were placed in a joint housing [4.286]. To protect the detectors from hard X ray radiation, the housing was made of metal alloy containing 80% of tungsten. Typical fusion product energy spectra are shown in Fig. 4.33. The detectors were supplied with collimators oriented at different angles, which made it possible to obtain the pitch angle distribution of the fusion product flux. Later, each detector was partially shaded by foils of different thicknesses with individual collimators in front of the foils. Protons with initial energy 3 MeV lost a certain energy in the foil and, therefore, the proton flux detected at a specific angle was characterized by its energy. This scheme, together with the plasma radial shift, was used to assess the ion temperature profile in the plasma core [4.287].

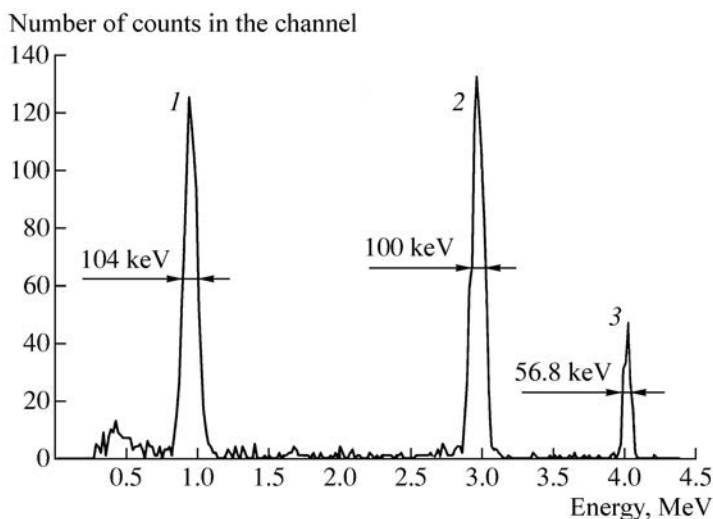


FIG. 4.33. CFP energy spectrum measured during 0.1 s in T-10 shot: (1) tritons, (2) protons, (3) pulser [4.287].

To analyse the results of charged product measurements, special numerical codes are used (see, for example, Ref. [4.288]) in which the trajectory of particle is calculated on the assumption that it moves from the detection point to the plasma, i.e. on an inverse time scale.

When the fusion rate is very high the escaping CFP coming to the first wall can cause undesirable events such as local overheating of the wall and even its burn-through. To prevent such phenomena, their development was observed by means of Faraday cups located at the vacuum vessel wall [4.289].

To probe the magnetic structure of a tokamak, the use of alpha particles produced in the fission reaction was suggested [4.290, 4.291]. For this purpose,

the radiation alpha particle source must be installed close to first wall and the alphas are detected after their passage through the plasma. For a typical tokamak, magnetic field alphas with energy 5.5 MeV have a Larmor radius of about 10 m and they can reach the central plasma area in a moderate size machine. The spatial and pitch angle distribution of the alphas at the point of detection are defined by the influence of the magnetic field because they practically do not interact with the plasma. With a known point of detection and point of alpha source location as well as toroidal magnetic field, the calculated orbits depend on the distribution of the poloidal magnetic field only. These measurements have been carried out on the T-10 tokamak (not published); however, the low statistics and uncertainty of the magnetic coils positioning do not permit explanation of the results obtained.

#### 4.2.8.1.3. Hard X rays

Hard X ray (HXR with energy greater than hundreds of keV) radiation arises when fast relativistic electrons strike the limiter or the first wall. In present day tokamaks, runaway electrons constitute a serious concern. The final runaway energy can become sufficiently large as to cause serious damage to the machine structures. This issue is of special practical importance in the case of disruption generated runaway electrons.

The large electric fields induced during the current quench phase may produce a large number of runaway electrons with energies as high as tens of MeV and the runaway current is more than 1 MA. Moreover, it has been predicted that, in future tokamak reactors, the production of runaway electrons during disruptions will be noticeably increased because of the so-called avalanche mechanism, consisting of the production of runaway electrons by close Coulomb collisions of already existing runaway electrons with bulk electrons. All tokamaks without any exception are provided with a HXR monitoring system. It begins to operate just at the very first plasma discharge. The actual implementation of this system is determined by the objectives of measurements at each particular machine.

The first and the most common goal of HXR measurement is simple evidence of the presence of runaway electrons in tokamak plasmas. For this purpose one or a few collimated or not collimated HXR intensity monitors (i.e. without energy resolution) are installed around a machine. The most widely used detectors are inorganic scintillators (NaI(Tl) and others) coupled with photomultipliers. As a rule, they work in current mode. The detectors are in the torus hall at a distance of several metres from the tokamak axis. In small and medium machines, there is no need to take special measures to protect the detectors from background radiation (gamma rays, neutrons) because of their low level. In large tokamaks, the influence of these factors has to be taken into

account. The HXR monitor signal can be used in a feedback control system to terminate the discharge in order to avoid the danger related to runaway electrons. Several methods have been suggested to control the runaway electron production in tokamaks, such as a “killer pellet” injection [4.292], active impurity injection [4.293], and the use of magnetic coils to disturb the magnetic structure [4.294].

Direct measurements of the X ray energy distribution can be obtained by pulse height analysis. The main goal of these measurements is an assessment of the maximum energy of runaway electrons and the temporal evolution of this parameter. The time resolution is defined by statistics. Such measurements are necessary to study the runaway electron physics in detail. Usually, the spectrometers are installed at some distance from the tokamak as intensity monitors and also do not require any interface with the machine itself. Collimated heavy inorganic scintillator detectors are used in spectrometric studies [4.295, 4.296]. The application of several collimated spectrometers directed to different limiters in the equatorial plane of the tokamak chamber can provide information on the influence of MHD activity on the behaviour of a runaway electron beam. The use of two HXR spectrometers with high time resolution in experiments carried out on the Globus-M spherical tokamak made it possible to detect HXR bursts correlating with different MHD modes (see Fig. 4.34).

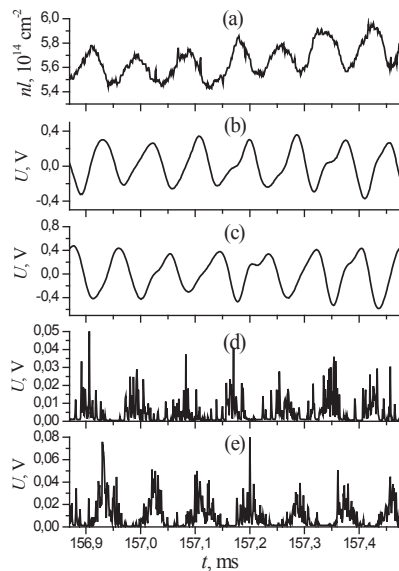


FIG.4.34. (a) Waveform of the plasma density averaged over the vertical chord  $R = 42$  cm in the Globus-M tokamak shot no. 5660 and signals from (b) Mirnov coil M1, (c) Mirnov coil M2, (d) HXR detector D1 and (e) HXR detector D2. The period of HXR bursts is  $85 \mu\text{s}$ . Periodicity of HXR bursts recorded by two NaI(Tl) detectors and their phase shift are related to the modulation of the runaway flux onto the limiters by rotating magnetic islands ( $m/n=2/1$  mode). Taken from Ref. [4.296].

The further development of HXR measurements lies in the application of fast electron bremsstrahlung (FEB) cameras [4.297, 4.298]. This system is intended for time, spatial and energy resolved measurements of bremsstrahlung originated in interaction of fast electrons with bulk plasma, gas puff or injected pellet. The essential advantage of this technique is a possibility to observe the runaway electrons “in flight” before their interaction with the plasma facing components. An FEB camera (or two cameras for 2-D measurements) is installed directly on the diagnostic port and requires very strong shielding of detectors against the much stronger bremsstrahlung coming from the limiter and against the background gamma radiation from the surrounding structure. Neutron shielding has to be used as well. As a rule the detectors used are rather compact and, therefore, are not very efficient for high energy photons.

In general, the experimental results are in reasonable agreement with the theories developed [4.299–4.302]. It has been shown that the runaway electrons are generated in a small region of plasma core at the early phase of the discharge — during plasma breakdown and current ramp-up when the loop voltage is high and plasma density is low. Then, if there are no runaway electron fast loss mechanisms (e.g. strong MHD activities), the electron beam becomes steady, moves outwards and reaches its maximum energy (mainly limited by synchrotron radiation losses) at a level of about several tens of MeV. The electron beam has a shell structure and hits the limiter. Sometimes it hits the inner wall as well. In the steady state, the runaway electron confinement time, which has been assessed for some machines, is determined by radial diffusion. The nature of the diffusion is not very clear and may be caused by static magnetic field perturbations, low frequency MHD instabilities, electrostatic and magnetic turbulences, and so on.

Many runaway electrons are produced during a major disruption. The time evolution of the electron beam during this event was examined in detail in Ref. [4.303]. It was shown that the avalanche process plays a dominant role and secondary electrons are generated. Avalanching leads to runaway current increase and decrease of the average energy of the electrons. The total current of the runaway may reach 50% of the plasma current before disruption.

#### *4.2.8.2. Gamma ray spectrometry*

Gamma spectrometry is used to diagnose high energy (MeV range) ions by means of the detection of high energy gamma rays arising as a result of nuclear reactions in a plasma [4.304]. This method has a history over a number of decades. First measurements on the tokamaks Doublet-III [4.305], JET [4.306, 4.307], TFTR [4.308] and JT-60U [4.309] showed that intense gamma ray emission is produced when fast ions (fusion products, ICRF driven ions and NBI-injected ions) react either with plasma fuel ions or with plasma impurities such as beryllium, boron, carbon and oxygen. Today, nuclear reaction gamma ray

diagnosis is one of the important techniques used on the JET tokamak, today's largest machine, for studying confined fast ions (ICRF driven ions, fusion products, NBI injected ions) [4.304].

There are three sources of fast particles in plasmas that can induce gamma ray emission. Firstly, fusion reactions between the plasma fuel ions produce fusion products such as fast tritons, protons,  $^3\text{He}$  and  $^4\text{He}$  ions with energies in the MeV range. Secondly, ICRF heating of H and  $^3\text{He}$ -minority ions accelerates these ions to energies in the MeV range. There are also ICRF schemes to accelerate D, T and  $^4\text{He}$  ions. And, thirdly, NBI heating introduces D, T, H,  $^4\text{He}$  and/or  $^3\text{He}$  ions (with energies below 160 keV in JET and 1 MeV in ITER).

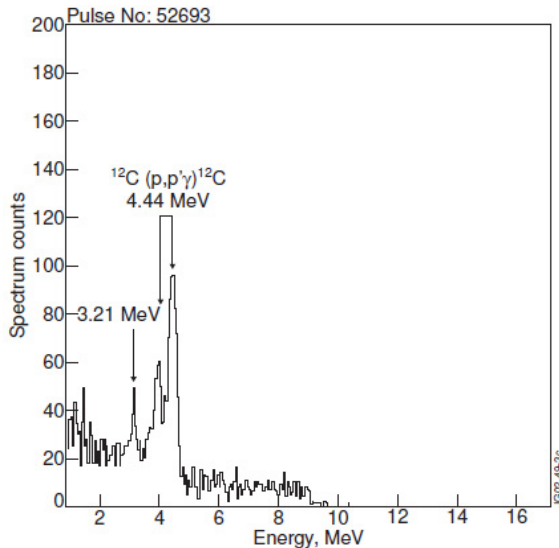


FIG. 4.35. Gamma ray spectrum measured in discharge with H-minority ICRF heating in deuterium JET plasma [4.304]. Reprinted from Ref. [4.304]. Copyright (2011), IOP Publishing Ltd.

About twenty essential diagnostic reactions have been identified in the gamma ray spectra recorded at JET [4.304]. The most important reactions are the threshold and the resonant capture reactions. The inelastic scattering of protons on carbon,  $^{12}\text{C}(p,p')^{12}\text{C}$ , is a typical threshold reaction which takes place in JET plasma with ICRF heating tuned to hydrogen. Excitation of the first level of the nucleus  $^{12}\text{C}$  is energetically allowed for protons with energies of 4.44 MeV. However, due to the Coulomb interaction, the cross-section of the reaction only becomes noticeable for protons with energies above 5 MeV. In order to excite the second level of the nucleus  $^{12}\text{C}$  at 7.65 MeV, the hydrogen ions have to be accelerated up to roughly 8 MeV. The reaction produces 3.21 MeV gamma rays

by virtue of the sequential decay through the 4.44 MeV level and is indicated in the gamma ray spectrum (Fig. 4.35).

Another type of nuclear reaction, although exothermic, exhibits a threshold feature because its Q value lies below the energy of the first excited state, for example  $^{12}\text{C}(\text{d},\gamma)^{13}\text{C}$ . Observation of gamma rays de-exciting these states is evidence of the threshold crossing.

Of the gamma diagnostic nuclear reactions with protons which can take place in a plasma, the capture reaction  $\text{D}(\text{p},\gamma)^3\text{He}$  is very useful for the analysis of the proton tail distribution function. The first observation of 5.5 MeV gammas produced in this reaction was made in the experiment performed with the 70 keV hydrogen beam on Doublet-III [4.305]. Measurements of the Doppler broadening of the 5.5 MeV peak, which depends on the distribution functions for both the ICRF accelerated protons and the bulk deuterium, have been made in JET [4.304].

The relatively high gamma ray yield from the reactions  $\text{D}(^3\text{He},\gamma)^5\text{Li}$  and  $\text{D}(\text{T},\gamma)^5\text{He}$ , which are the weak branches ( $\sim 10^{-5}$ ) of the reactions  $\text{D}(^3\text{He},\text{p})^4\text{He}$  and  $\text{D}(\text{T},\text{n})^4\text{He}$  correspondingly, is used for an assessment of the fast ion population during ICRF heating and could be utilized for fusion reaction rate measurements in burning plasma experiments. The 17 MeV gammas are rather practical for diagnosis because a low background level is produced in this gamma ray energy range. Unfortunately, a natural broadening of these gamma lines does not allow measurement of the distribution function of fast ions. The  $\text{D}(^3\text{He},\gamma)^5\text{Li}$  reaction has been used in  $^3\text{He}$ -minority heating experiments in JET and TFTR [4.304, 4.307, 4.308] for fusion power assessments. However, for the H-minority heating experiments in tritium plasmas the reaction  $\text{T}(\text{p}, \gamma)^4\text{He}$  could be useful for fast ion studies. The 20 MeV gamma line is very narrow and could be exploited for Doppler broadening analysis.

Finally, there is the reaction  $^9\text{Be}(\alpha,\text{n}\gamma)^{12}\text{C}$ , the significance of which was investigated in detail in Ref. [4.304] for fusion born alpha particle measurements. This is another type of resonant reaction, which also has thresholds. The excitation functions of the first two levels in the final nucleus  $^{12}\text{C}$  have resonance patterns. The presence of the 4.44 MeV peak in the gamma ray spectra is evidence for the existence of alphas with energies that exceed 2 MeV. Moreover, the 3.21 MeV gamma rays indicate that alphas with energies in excess of 4 MeV exist in the plasma. This nuclear reaction was used on JET for  $^4\text{He}$  ion and fusion alpha particle diagnosis [4.304, 4.310]. It has been proposed for alpha particle diagnostics in ITER [4.311].

The environment in which gamma ray diagnostics is to be carried out is a very severe one. Diagnostic nuclear reactions must be measured against a background of high neutron flux and the associated neutron induced gamma rays. In this case, the gamma ray detector must have reasonable energy resolution and be capable of maintaining the resolution while operating at high count rates. In addition, the detector should have a high enough detection efficiency to allow

a statistically significant number of counts to be measured in the relatively short time of a plasma discharge. Furthermore, the detector should be able to withstand the moderate flux of neutrons that are associated with a broad class of fusion plasmas.

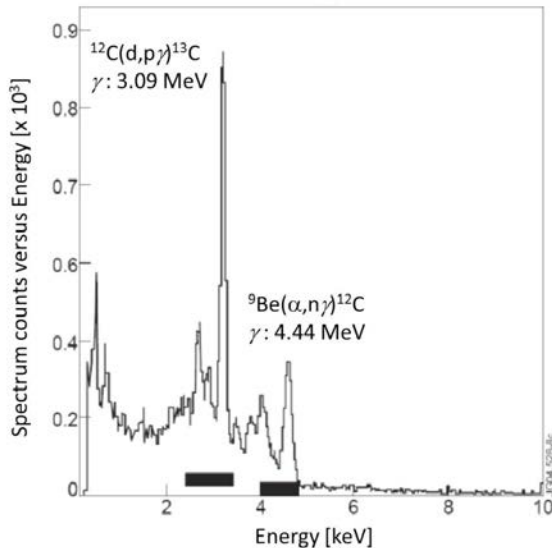


FIG. 4.36. A typical gamma ray spectrum recorded by an NaI(Tl) detector in the  $^4\text{He}$ -beam ion acceleration experiments in JET [4.304]. Reprinted from Ref. [4.304]. Copyright (2011), IOP Publishing Ltd.

For example, at JET, to measure the gamma ray emission profile in the energy range  $E_\gamma > 1$  MeV, the fast electron bremsstrahlung diagnostic system that is incorporated into the neutron profile monitor is used. The detector array is comprised of 19 CsI(Tl) photodiodes [4.304]. This makes it possible to allocate specific gamma ray peaks in the windows to be counted separately. In particular, the energy windows containing the 3.09 MeV and 4.44 MeV peaks (Fig. 4.36) were set up to measure the spatial profiles of the gamma ray emission from D and  $^4\text{He}$  ions accelerated with 3rd harmonic ICRH of  $^4\text{He}$  beam injected ions. These JET experiments were dedicated to the investigation of burning plasmas with 3.5 MeV fusion alpha particles [4.304]. Figure 4.37 shows tomographic reconstructions of 4.44 MeV gamma ray emission from the reaction  $^9\text{Be}(^4\text{He},n\gamma)^{12}\text{C}$  (right) and the 3.09 MeV gamma ray emission from the reaction  $^{12}\text{C}(d,p\gamma)^{13}\text{C}$  (left) deduced from simultaneously measured profiles.

An active background suppressed multi-crystal spectrometer GAMMACELL has been proposed [4.304]. It consists of nine, optically independent, scintillation  $\text{BaF}_2$  detectors assembled in a single housing. The GAMMACELL was optimized for measuring high energy gamma rays (in the

range up to 30 MeV) for ITER-like reactors in the presence of high levels of low energy background radiation and neutron fluxes. To minimize the neutron induced background, a dedicated neutron absorber for fusion gamma ray spectrometers, a hermetically sealed cylinder containing  ${}^6\text{LiH}$ , was designed and fabricated [4.304]. The gamma ray measurements at the JT-60U tokamak during experiments with deuterium NBI heated plasmas [4.24] showed substantial reduction of the neutron induced background. First results using  ${}^6\text{LiH}$  for gamma ray background reduction were obtained during JET experiments with deuterium plasmas [4.312].

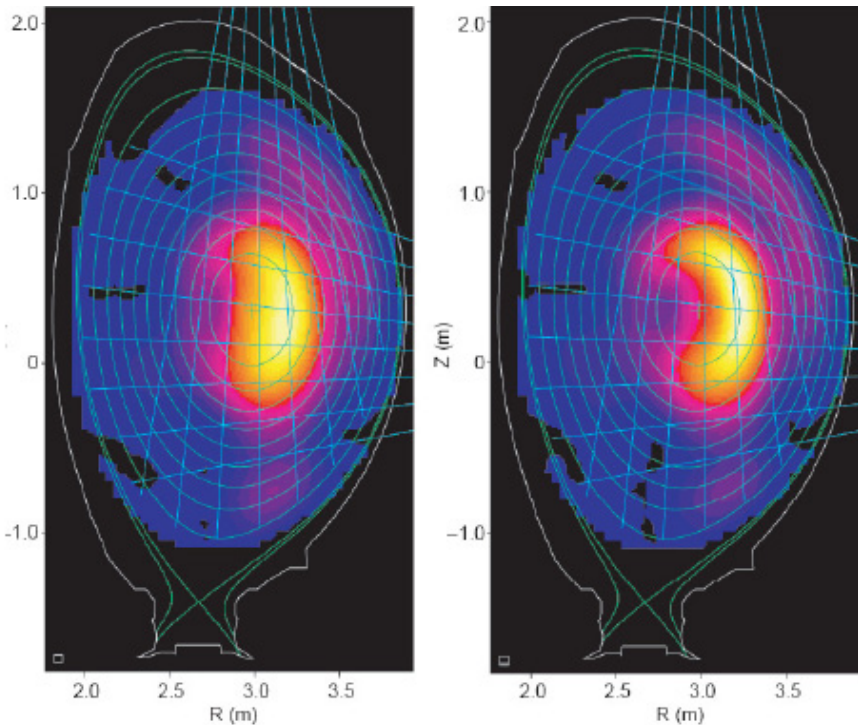


FIG. 4.37. Tomographic reconstructions of 4.44 MeV (right) and 3.09 MeV (left) gamma ray emissions deduced from simultaneously measured profiles [4.304]. Reprinted from Ref. [4.304]. Copyright (2011), IOP Publishing Ltd.

The data acquisition system (DAQ) is a key issue for gamma ray pulse height analysis (PHA) measurements in high performance plasma discharges and in future burning plasma experiments. Conventional ADC systems limit the total counting rate to about 100–200 kHz. However, on the TFTR [4.313] count rate capabilities in excess of 10 MHz were achieved using the fast scintillator (2 ns) and 15 single-channel analysers with a linear fan-out of the PMT signal. A modern DAQ system for gamma ray diagnostics based on a 2-channel transient recorder

was installed in JET [4.304]. It is used for digitizing signals from NaI(Tl) and bismuth germanate (BGO) scintillator detectors at a maximum average pulse rate of 1 MHz. Dedicated software allows avoidance of the pile-up effect and gain instability that leads to a distortion of gamma ray spectra at high count rates with fast rate variations. The main limitation for further improving the counting rate capabilities with NaI(Tl) and BGO detectors is the rather long scintillation decay times, of 250 ns and 300 ns, respectively. Modern fast high  $Z$  heavy scintillators  $\text{LaBr}_3(\text{Ce})$ , known as “BriLanCe” and  $\text{Lu}_{1.8}\text{Y}_{0.2}\text{SiO}_5(\text{Ce})$  “LYSO” have short decay times, of 16 ns and 40 ns, and high photons yields. Their striking properties open the possibility to extend the counting rate limit beyond 5 MHz [4.304].

### 4.3. ACTIVE DIAGNOSTIC METHODS

#### 4.3.1. Probing by laser beams

**V. Sannikov, D. Shcheglov**  
Kurchatov Institute, Moscow,  
Russian Federation

##### *4.3.1.1. Thomson scattering*

Thomson scattering (TS) has been a widely applied technique to investigate the electron component of a thermonuclear plasma since the first TS diagnostics was carried out in early 1963 [4.314]. The first demonstration of TS as a suitable diagnostic tool for hot plasmas was made in 1969 on the Russian tokamak T-3A [4.315]. Detailed descriptions of TS diagnostics can be found in books and review papers [4.316–4.319].

TS refers to the scattering of electromagnetic waves by free electrons. It is based on Doppler broadening of the scattering spectrum, reflecting the velocity distribution of the electrons. The theory of this process has been described in literature by many authors [4.320–4.322].

The main characteristics that dominate the accuracy in most Thomson scattering (TS) diagnostics are the power of the probing source, the quantum efficiency of the detectors and the transparency of the collection optics with spectral devices. Lasers have a high spectral brightness and their beams can be focused in the plasma to produce a good spatial resolution. Also, lasers do not perturb the plasma owing to the relatively small interaction cross-sections. Multi-pulsed or frequency operated lasers can provide reliable measurements of the evolution of plasma parameters with a high temporal resolution. Moreover, with relay optics and mirrors the Thomson scattering diagnostic can be located far from the machine. This diagnostic can measure such important plasma

parameters as electron temperature and density as well as their distributions in the plasma. In other special tasks, it can measure the poloidal magnetic field, the current density profile, the ion temperature, the fast ion population and electron density fluctuations.

Light scattering by electrons depends on the interaction between them and the ions. The correlation interaction scale length is the Debye radius  $\lambda_D = v_e / \omega_{pe} \approx 7.4 \times 10^3 T_e^{1/2} / n_e$  (in m); where  $v_e$  is the thermal velocity of the electrons,  $\omega_{pe} = (4\pi n_e e^2 / m_e)^{1/2}$  is the electron plasma frequency,  $T_e$  is in eV, and  $n_e$  is in  $m^{-3}$ . Another scale in the scattering process is the Salpeter (or scattering) parameter  $\alpha_S$  — the ratio between  $\lambda_D$  and  $\lambda_0$  (wavelength of incident electromagnetic wave):

$$\alpha_S = (k\lambda_D)^{-1} = \lambda_0 / 4\pi\lambda_D \sin \theta / 2 \tag{4.24}$$

where  $k$  is the differential scattering vector, and  $\xi$  is the angle between the incident wave ( $k_0$ ) and scattered wave directions ( $k_s$ ) (Fig. 4.38).

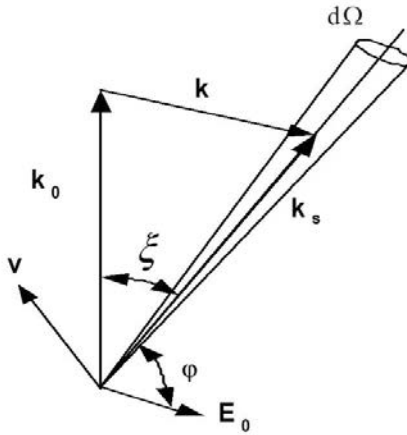


FIG. 4.38. Wave vector diagram.  $k = k_s - k_0$  is the differential scattering vector,  $\xi$  is the angle between the incident wave ( $k_0$ ) and scattered wave directions ( $k_s$ ),  $d\Omega$  is solid angle,  $v$  is the electron velocity,  $\phi$  is the angle between the scattered wave directions ( $k_s$ ) and  $E_0$  the electric field vector of the incident wave.

The value of the scattering parameter is important because  $\alpha_S$  depends on the correlation between the length of the “probing wave” ( $\lambda_0 / 4\pi \sin \xi / 2$ ) and the size of the Debye sphere. Depending on the value of the parameter  $\alpha_S$  ( $\alpha_S \ll 1$ ,  $\alpha_S \gg 1$  and  $\alpha_S \sim 1$ ), three different types of laser light scattering processes exist with strong differences in the shapes of the scattering spectrum.

When  $\alpha_S \ll 1$ , the probing radiation is scattered by individual electrons without influence from shielding charges inside the Debye sphere. This type of scattering is called “incoherent TS” and is used to measure the local electron

temperature and density of the plasma and, in a special scattering geometry, the local current density.

If the electrons have a Maxwellian velocity distribution the scattering spectrum has a Gaussian shape. From the width and total intensity of this spectrum experts can calculate the electron temperature and density of the plasma. The theory of TS in a hot plasma is presented in [4.321], where an analytical description is given of relativistic effects, which lead to a blue shift and deformation of the classical Gaussian shape (Fig. 4.39 left).

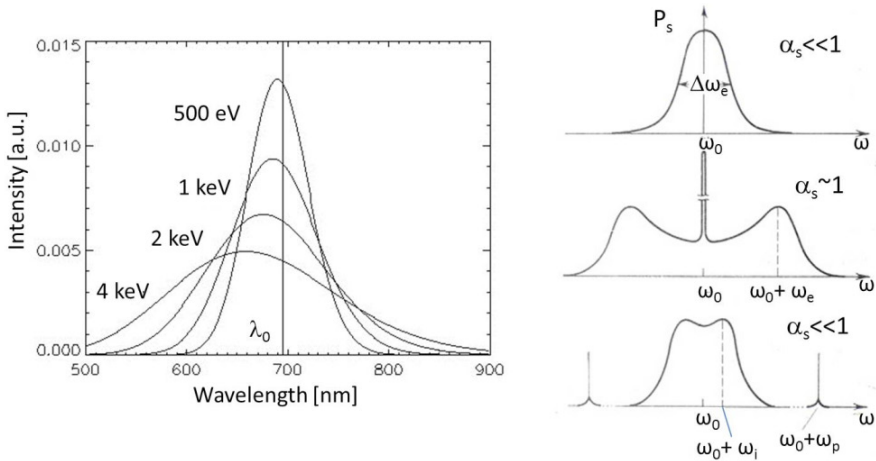


FIG. 4.39. Left: Theoretical relativistic scattering spectra. Taken from Ref. [4.318]. Right: Spectra of scattering radiation for different Salpeter parameter values ( $\alpha_s \ll 1$ ,  $\alpha_s \approx 1$ ,  $\alpha_s \gg 1$ ).  $P_s$  is the scattered power;  $\omega_0$  is the angular frequency of the laser radiation,  $\omega_e$  and  $\omega_i$  are the electron and ion cyclotron frequencies, and  $\Delta\omega_e$  is the width of the scattering spectrum. Reproduced from Ref. [4.323].

When  $\alpha_s \gg 1$  the scattering contribution from an electron and its surrounding shielding cloud will add up coherently since there is negligible phase difference between them. In this case, the scattering from an electron will be connected with the scattering from its shielding zone. It is the scattering by the electrons in the shielding cloud of the ions which can be observed experimentally. This type of scattering is called “coherent TS” (or ion Thomson scattering).

When  $\alpha_s \sim 1$ , a third experimental possibility exists. When the electrons exhibit collective behaviour, as in the case of density fluctuations, the scattering contribution from an electron and its shielding cloud do not exactly cancel. Therefore, considerable amounts of scattered vectors of the electron density wave, the incident wave and the scattered wave are present in the scattering act. This kind of scattering is also called “coherent scattering” and is used to measure the electron density fluctuation spectrum in a plasma [4.324]. All three cases are illustrated in Fig. 4.39 right.

The total scattering energy towards the detector during the laser pulse can be calculated as:

$$P_s = P_0 \frac{d\sigma}{d\Omega} \sin^2 \varphi n_e \Delta L d\Omega \tau S(k, \omega) \quad (4.25)$$

where  $P_0$  is the power of the probing laser,  $d\sigma/d\Omega$  is the differential Thomson scattering cross-section,  $n_e$  is the density of the electrons,  $\Delta L$  is the length of the scattering volume,  $\varphi$  is the angle between the electric field of the probing wave and the scattering plane,  $d\Omega$  is solid angle, and  $\tau$  is the transmission of the optical system. Usually in experiments the angle  $\varphi = 90^\circ$ .  $S(k, \omega)$  is the dynamic form factor, which describes the frequency shifts due to the electron motions, with  $k$  and  $\omega$  being the differential scattering vector and the frequency of the propagating wave respectively. The value of the scattering cross-section is very small  $d\sigma/d\Omega = 7.94 \times 10^{-30} \text{ m}^{-2}$ . Thus the quantity of scattered photons to be detected by the collecting optics will be also poor. Because the plasma emits bremsstrahlung and spectral line radiation, the spectrometer must be designed with a good optical arrangement and with special appliances to decrease this radiation. The additional equipment can reject the strong stray light from the reflection of the laser radiation on the diagnostic windows or the walls inside vacuum chamber. Moreover, in the tokamak the input and output ports for the laser beam must have Brewster angle windows, a series of light baffles, and, if it is possible, viewing and laser beam dumps.

#### 4.3.1.1.1. Incoherent Thomson scattering

During the progress of TS diagnostics, many complicated types of equipment were built to increase the accuracy and reliability of the experimental data. The most recent lasers can generate a high output power; moreover, in mode-locked operation, lasers can generate radiation with high repetition rates. These lasers solve the difficult problem of high temporal resolution during fast plasma evolutions. At the present time for periodic TS measurements the equipment is based on different types of Nd:YAG lasers ( $E_o = 1-8 \text{ J}$ ,  $\Delta t = 15 \text{ ns}$ , repetition rate from 10 up to 60 Hz). The high power multi-pulse Nd:glass laser (8 impulses in the laser burst, 20–30 J/pulse on original mode ( $\lambda_o = 1 \text{ }\mu\text{m}$ ) and 5–6 J after frequency doubling ( $\lambda_{o,2} = 0.53 \text{ }\mu\text{m}$ )) is used on T-10 (Russian Federation) [4.325]. For TS experiments on TEXTOR to investigate the fast dynamic evolution of the plasma structures and transport barrier events in the plasma column, a repetitive high resolution TV Thomson scattering system was built. In this system the intra-cavity ruby laser can produce a burst of high energy pulses ( $\sim 15 \text{ J/pulse}$ ,  $\Delta t \sim 1 \text{ }\mu\text{s}$ ) with a repetition rate of 10 kHz [4.326] (see Fig. 4.40).

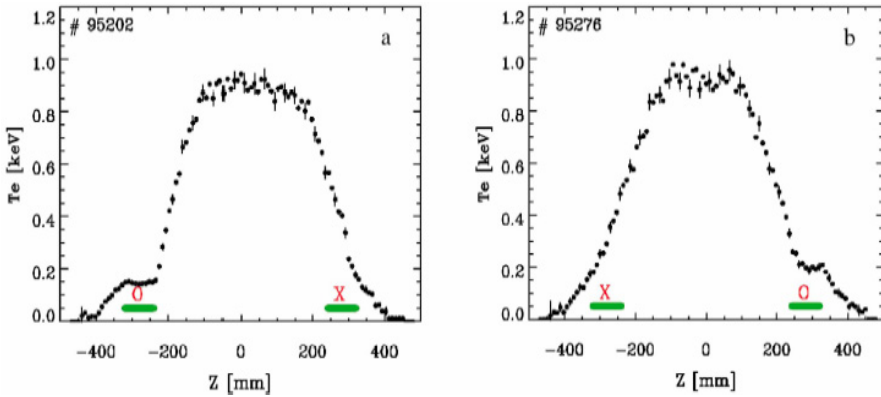


FIG. 4.40. The results of the TS measurements on TEXTOR are shown: electron temperature profiles with static magnetic island for two positions of the island [4.326]. 0 on the x-axis is the centre of the vacuum chamber; Z is the inner (left) and outer (right) distance from 0; X and O are the locations of the magnetic islands. The symbols a) and b) are for different discharges.

The collection and relay optics are designed to achieve a transmission of the optical system as high as possible. Usually, lenses, mirrors and fiberglass guides are employed. The fiber array allows construction of an optical subsystem which can reproduce the maximum part of the scattered volume of the plasma with high spatial resolution. The first employment of fiber guides was described in Ref. [4.327]. If the optical part from the tokamak is long, the fiber guides are manufactured from fused quartz because this has very good transmission. In early TS experiments, the detection system consisted of mechanically ruled grating spectrometers for dispersing the scattered light and photomultipliers. In modern TS systems, holographic gratings or a few channel interference filter polychromators are used. The dispersed light is detected by silicon avalanche photodiodes (APD) [4.328, 4.329], and TV or charge coupled device (CCD) cameras. APD detectors are successfully being used on DIII-D and ASDEX-Upgrade [4.330]. In current YAG laser TS systems APD detectors are widely used.

On PLT the detector consists of a microchannel-plate (MCP) image intensifier fiber optically coupled to a silicon-intensified-target (SIT) TV tube. The image of the laser beam is focused by a wide angle lens onto an array of light pipes which reform the image as the entrance slit of a spectrometer. The device resolves 76 spatial channels [4.331]. The intensified CCD (ICCD) camera can display, with many pixels, a very large number of wavelength channels and spatial points along the laser beam in the plasma [4.332].

## 4.3.1.1.2. Coherent Thomson scattering (CTS)

Diagnostics CTS in a plasma is sensitive to a wide range of plasma parameters, including the spatially localized velocity distributions of fast ions such as alpha particles generated in fusion reactions. In the event of anomalous loss of fast ions in ITER, such measurements may be essential in finding methods of maintaining a high confinement. CTS is at present the most promising diagnostic for this task [4.333].

CTS has been successfully applied as the diagnostic to investigate ion temperature using a D<sub>2</sub>O laser ( $\lambda_o = 385 \mu\text{m}$ ) [4.334], and using millimetre waves generated by gyrotrons [4.335]. The CTS, based on a 2.14 mm (140 GHz) gyrotron source with 400 kW power, has been used for the preliminary measurement of fast ion populations and temperature at JET and W7-AS [4.336, 4.337]. The same type of source was installed on FTU to measure the plasma ion temperature and test the theory of CTS. The scattered radiation was collected at 90° scattered angle by a symmetric in-vessel optical system and a low power quasi-optical transmission line which collected the scattered radiation on a superheterodyne receiver which was based on 32 channels, 1.2 GHz global bandwidth, with a measured noise temperature  $T_{rec} = 1 \text{ eV}$  and minimum integration time of 1 ms [4.337].

## 4.3.1.1.3. LIDAR system

The LIDAR (light detection and ranging) method is based on the time-of-flight technique for measurement of a short light pulse and is an incoherent Thomson scattering method. The required spatial resolution is achieved by recording the backscattered light from a sub-nanosecond laser pulse with a high speed detection system. The time resolution of a single measurement is given by the transit time of the laser pulse through the plasma. The use of a laser system with a high repetition rate provides the required time resolution of periodic measurements. Usually, the line of sight is in the poloidal cross-section and passes through the plasma centre. The LIDAR diagnostic on JET consist of a Q-switched ruby laser ( $E_o = 3\text{--}5 \text{ J}$  per pulse depending on repetition rate,  $\Delta t = 300 \text{ ps}$ ) and detection subsystem located outside the biological shield, the optical transmission lines for the laser and the collected light, a common window for input and output at the flange of the standard equatorial port, and the collection optics located within the port [4.338]. To reduce the escaping neutron flux through the blanket penetration a 3-fold labyrinth with minimized cross-section is used. The large relative movements between vacuum vessel and cryostat are taken up by a self-aligning connection.

Thus the laser beam passes through the same optics inside the vacuum vessel as the scattered light to reduce alignment problems. Backscattered light is

collected by a spherical mirror and led to a six-channel filter spectrometer. The spectrally resolved light is detected by fast MCP photomultipliers. The position of the laser pulse within the plasma is well known at any instance as a function of the space coordinate along the line of sight, since the light from different positions arrives at different times at the detector. The electron temperature and density are determined along the line of sight at 47 points with a spatial resolution of about 10 cm. The accuracy of the measurements is 6% at  $n_e = 3 \times 10^{19} \text{ m}^{-3}$ . The LIDAR TS is a very promising diagnostic for ITER [4.339].

#### 4.3.1.2. Laser induced fluorescence technique

The diagnosis of hydrogen atoms was a typical aim of the laser induced fluorescence (LIF) technique at the initial stage of its applications to plasma experiments. The measurement of hydrogen atom density on FT-1 [4.340] can be used as an example.

The optical pumping and detection of fluorescence light have been carried out at the wavelength of the  $H_\alpha$  line. The detection limit of the measured atomic hydrogen densities was equal to  $\sim 10^{14} \text{ m}^{-3}$ . Similar experiments have been performed on stellarators, reversed field pinches and mirror machines; the resonance fluorescence at the spectral lines of the Balmer series has been also used. The next step was the measurement of atomic hydrogen densities by  $L_\alpha$  fluorescence ( $\lambda = 121.6 \text{ nm}$ ). Tunable probing radiation has been produced by third harmonic generation in an argon–krypton gas mixture; the spectral width of the radiation at the  $L_\alpha$  line was very small ( $\Delta\lambda \sim 1 \text{ pm}$ ). As a result, an opportunity to measure narrow spectral profiles at  $L_\alpha$  has been provided [4.341]. The experiments on ASDEX [4.342] and TEXTOR-94 [4.343] can be used as examples.

Making use of the LIF-technique has brought considerable progress into the investigation of the plasma–surface interaction. Measurements of metal atom fluxes, the density of sputtered particles near plasma facing components, and the velocity distribution of sputtered atoms have been successfully investigated; for most metal atoms in the plasma boundary the LIF-technique can be applied if the density is higher than  $\sim 10^{12} \text{ m}^{-3}$  [4.341]. The basic set of metals under investigation has included iron (FeI, FeII), nickel, molybdenum, titanium and beryllium (BeI, BeII). Besides hydrogen and metals, the velocity distribution has been obtained by scanning the profile of the spectral line for the helium atom also. This was the main aim of LIF-measurements on T-10 [4.344]. Scanning of the 587.6 nm line and detection of fluorescence radiation at  $\lambda = 388.9 \text{ nm}$  has been used (Fig. 4.41).

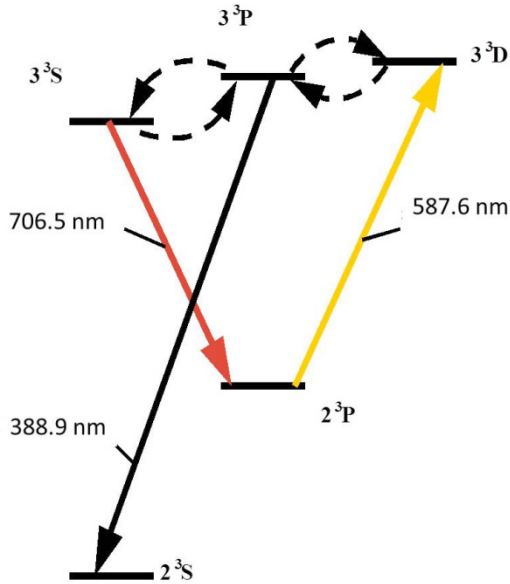


FIG. 4.41. Spectroscopic scheme of helium atom probing by LIF-technique [4.344]. The scanning of the 587.6 nm absorption line by tunable laser radiation and detection of the fluorescence light at the 388.9 nm line has been applied; the detection of fluorescence radiation at the 706.5 nm line also can be used [4.346].

Besides the parameters of the helium atom, the LIF-technique has been applied for estimates of electron density. The ratio of fluorescence signals at two helium spectral lines depends on  $n_e$  and  $T_e$ . Detection of fluorescence signals at two singlet lines with the aim of estimating local values of electron density has been used in Ref. [4.345]. Optical pumping has been performed by 501.6 nm laser radiation, and the fluorescence light has been detected at the 501.6 nm and 667.8 nm spectral lines. Fluorescence of triplet lines at  $\lambda = 388.9$  nm and  $\lambda = 706.5$  nm was excited by 587.6 nm laser light in experiments on the multi-cusp trap PNX-U [4.346]. The results of LIF-measurements were in a good agreement with data on  $n_e$  measurements by Langmuir probes. It is worthwhile mentioning that the accuracy of the electron density also depends on the relevant collisional-radiative model calculation. Development of CRMs is an inalienable part of work on LIF-techniques and experimental testing of CRM calculation results are of importance for practical applications of the diagnostic. The experiments on TEXTOR [4.347] can be used as an example of such activity. CRM calculations are required also in the case of helium density measurements. Investigation of helium — the “ash” of thermonuclear reactions — becomes a problem of importance for burning plasma experiments. The measurement of ion temperature in divertor plasmas is another difficult problem, including the necessity to have a species for LIF applications. Because it is planned to inject “extrinsic” impurities

(Ne, Ar, Kr) into ITER — in order to improve confinement with edge radiative cooling — there is an opportunity to use these rare gases as tracing elements for the local Doppler measurements of ion (atom) temperatures by the laser spectroscopy method. Modelling measurements of  $T_i$  by LIF techniques have been performed on PNX-U on the argon ion  $\text{Ar}^{1+}$  [4.348]; a number of ITER measurement requirements [4.108] have been taken into account: accuracy  $\Delta T_i/T_i$ , spatial resolution along a laser beam and in transverse direction, etc. The wavelengths for optical pumping and fluorescence light are shown in Fig. 4.42.

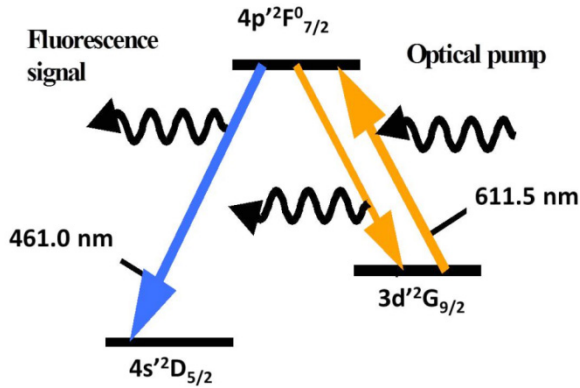


FIG. 4.42. Spectroscopic scheme of  $\text{Ar}^{1+}$  ion temperature measurements by the laser spectroscopy method [4.348].

### 4.3.2. Probing by particles

**A. Ivanov, V. Davydenko**  
Budker Institute, Novosibirsk

**S. Tugarinov**  
TRINITI, Moscow Region

**M. Petrov**  
Ioffe Institute, Saint Petersburg

**V. Strelkov, V. Krupin, A. Melnikov**  
Kurchatov Institute, Moscow

Russian Federation

#### 4.3.2.1. Diagnostic neutral beams for plasma studies in magnetic fusion devices

In recent years, neutral beams dedicated for plasma diagnostics have become widely used in magnetic fusion experiments [4.349–4.351]. Even though the number of diagnostics based on neutral beam injection is already quite large, nevertheless new promising ideas continue to emerge.

The required beam parameters are determined by the diagnostic and the parameters of the plasma under study. Generally, the beam intensity should be high enough to provide a desirable signal-to-noise ratio, especially for fluctuation studies where a good time resolution is required. The beam size must be small enough to provide a good spatial resolution. The beam species and the energy of the particles are also determined by the diagnostic in which the beam is used. In particular, in the spectroscopy of neutral beam induced radiation for impurity studies [4.349–4.351], hydrogen beams with energies of 50–60 keV, about at the maximum of the charge exchange cross-section for excitation of the 7-8 transition of  $C^{5+}$  ions, are of particular interest. This energy also provides reasonable beam penetration into the plasma interior in modern plasma physics experiments with a minor plasma radius of 0.5–1 m and average density of  $\sim 10^{20} \text{ m}^{-3}$ . Estimates suggest that an equivalent beam current incident on a plasma of about 1 A or higher provides reasonable signals in the spectroscopic detection system [4.349, 4.352]. At the same time, the beam power density should be small enough to prevent significant local heating of the plasma. This requirement is generally consistent with the requirement of having sufficient signal in the detection system if the beam current is limited to several equivalent amperes. A number of dedicated diagnostic neutral beams have been developed for application in plasma physics experiments [4.353].

Diagnostic neutral beams with energies up to 100 keV are produced by the charge exchange method. In the ion source of a diagnostic injector, an ion beam with current of several amperes is formed by a multi-aperture ion optical system from the surface of the plasma emitter. The ion beam obtained is charge exchanged into atoms in a neutralizer gas target. Such a formation scheme is also used in powerful neutral beam injectors for plasma heating. However, in diagnostic injectors for the achievement of a high neutral atom flux density in the plasma observation zone, an extremely small angular divergence and focusing of the initial ion beam is required. In experiments, modulation of the diagnostic beam and a high energy stability are rather often required.

Diagnostic probe beams of fast lithium atoms with energies in the range 30–70 keV and a neutral equivalent current greater than 1 mA have been effectively used for spectroscopic measurements of edge plasma density profiles in tokamak and stellarator experiments [4.353]. These beams are also produced by the charge exchange method. The initial ion beam is formed by a single aperture ion optical system from the surface of a thermoionic emitter. The ion beam formed is accurately focused by cylindrical electrostatic lenses and neutralized into atoms in lithium or sodium vapour targets.

The development of neutral beam injectors for plasma physics experiments was started in the Budker Institute of Nuclear Physics, Novosibirsk, more than three decades ago. Initially, the developed beams had a pulse duration of 0.1–0.2 ms and a beam energy of 10–25 keV, which was consistent with the characteristic plasma parameters achieved at that time in toroidal systems and magnetic mirrors. These short pulse beams were provided by extracting ions from a plasma jet expanding from the anode orifice of a high current arc discharge. The specific mechanism of plasma cooling during jet expansion makes it feasible to form ion beams with transverse temperatures as low as  $\sim 0.2$  eV [4.354] and angular divergence  $\sim 5$  mrad.

Later on, a series of diagnostic hydrogen (or helium) beams, which are based on unified basic elements, i.e. plasma box and ion optical system, were developed for experiments on modern plasma devices. The required beam current can be provided by changing the size of the plasma box and the grids. The distinguishing feature of the beams developed is that the grids of the ion optical system are inertially cooled, i.e. have no channels for water cooling inside, as is always necessary for high power long pulse ion sources. Due to the limited pulse duration (2–10 s) and long enough intervals between the pulses in present day magnetic fusion facilities, the average thermal power loads on the grids appear to be rather moderate. Therefore, the heat capacity of the grids can be made high enough to limit the temperature rise during the pulse. Subsequently, the heat can be removed from the grids by water cooling from the periphery because of the very moderate time averaged heat loads. At the same time, such arrangement of the grids makes it possible to form them as spherical segments, thus providing

geometrical focusing of the extracted and accelerated ion beam. Note that this approach is not really applicable when the grids have internal cooling channels.

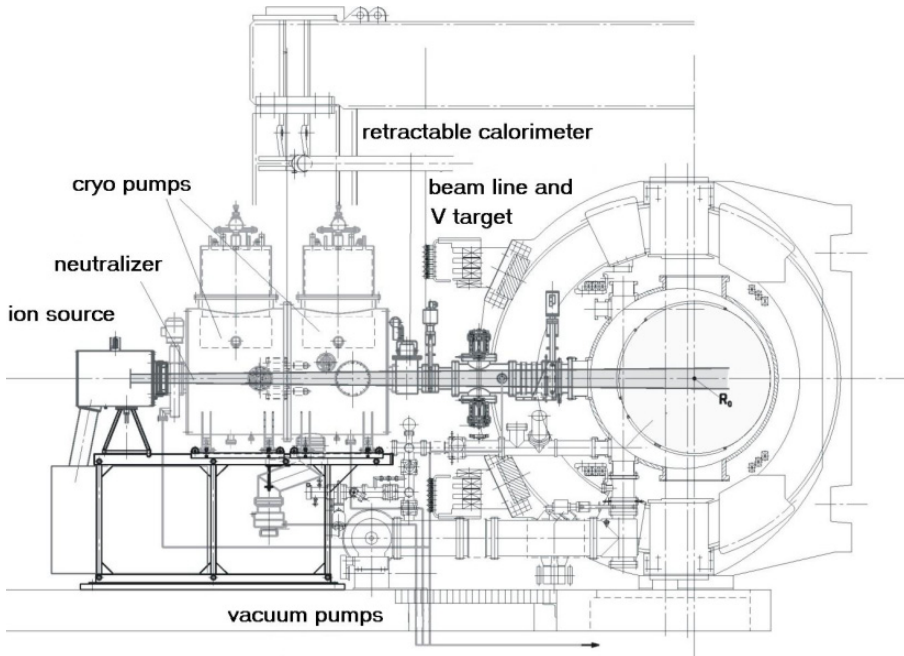


FIG. 4.43. Diagnostic neutral beam injector set-up at TEXTOR [4.531]. Reprinted from Ref. [4.351]. Copyright (2011), American Institute of Physics.

The developed ion sources are based on an RF discharge plasma box [4.352], or, alternatively, on an arc discharge plasma box [4.355, 4.356]. As a matter of fact, the RF version appears to be more appropriate for generating beams with a pulse duration exceeding 1 s. The arc discharge version is used for relatively shorter beams. Its advantage, in comparison to the RF version, is a higher proton fraction in the extracted beam.

A typical arrangement of the diagnostic neutral beam injector, which incorporates all systems required for the beam control and measurements, is shown in Fig. 4.43. This particular version has been developed for the TEXTOR-94. For shorter pulses, the diagnostic beam injector actually may comprise only an ion source and a neutralizer.

To provide a beam for active beam emission spectroscopy measurements in the W-7X large stellarator the diagnostic neutral beam injector RUDI-X is being developed in the Budker Institute. The RUDI-X beam will have an energy of 60 keV, an equivalent beam current (for hydrogen) up to 5 A, and pulse duration of up to 10 s. A multi-slit, water cooled ion optical system with geometrical beam focusing will be applied in the injector.

Active beam emission spectroscopy will be applied in ITER. In order to provide beam penetration into the plasma, the energy of the hydrogen atoms should be about 100 keV. The equivalent current of the neutral beam injected into the plasma should be  $\sim 10$  A. To provide this beam by the charge exchange method, an initial proton beam with  $\sim 50$  A current is required. The diagnostic neutral beam can be also obtained by stripping the negative hydrogen ion beam with a 15–18 A current in a gas target.

#### 4.3.2.2. Active charge exchange recombination spectroscopy diagnostic

The ideology of charge exchange recombination spectroscopy (CXRS) measurements and a technique for carrying it out were developed for the diagnostics of a high temperature plasma at the end of the 1970s. The first measurements on a tokamak installation were performed practically simultaneously in the USA and the USSR at the beginning of the 1980s [4.357, 4.358]. Now, CXRS diagnostics with the use of diagnostic or heating beams of atoms is widely used in practically all modern tokamaks. This technique is utilized for a wide variety of measurements in the plasma edge and core, including ion temperature (via Doppler broadening of intrinsic impurity lines, which are efficiently populated by charge exchange from beam atoms), plasma rotation (via Doppler shift of the same impurity lines), and impurity density profile information (via quantitative spectroscopy of the impurity line intensities) [4.359].

In the presence of neutral beam injection, an intense charge exchange recombination reaction appears in the plasma volume intersected by the beam. The equation that describes this process is:



where  $\text{A}^{z+}$  is a fully stripped ion,  $\text{A}^{*(z-1)+}$  is a hydrogen-like ion in an excited state that subsequently decays by prompt emission.

The visible radiation is produced by the most intense cascade decay transitions with  $\Delta n = 1$  between high  $n$ -levels. The most attractive visible transitions for CXRS are the following:

- (1) HI ( $n = 3-2$ );  $\lambda = 656.3$  nm
- (2) HeII ( $n = 4-3$ );  $\lambda = 468.6$  nm
- (3) BeIV ( $n = 6-5$ );  $\lambda = 465.8$  nm
- (4) CVI ( $n = 8-7$ );  $\lambda = 529.1$  nm
- (5) OVIII ( $n = 10-9$ );  $\lambda = 606.8$  nm

The ion temperature and plasma rotation velocity are measured by the use of Doppler broadening and the shift of the spectral line profiles, and the light impurity concentration is measured from the absolute intensity of the spectral line radiation.

The formula connecting the intensity of a spectral line radiation and the concentration of impurity ions is:

$$I_{\lambda} = 1 / 4\pi * \sum_{j=1}^m \langle \delta v \rangle^{\lambda j * } \int n_z n_j dl \tag{4.27}$$

where  $\langle \delta v \rangle^{\lambda j}$  is the excitation rate coefficient for a given wavelength transition due to interaction with the  $j$  component of the atomic beam;  $n_z$  is the concentration of nuclei of the given impurity;  $n_j$  is the concentration of atoms of the  $j$  component of the atomic beam. The integral is taken along the length of the viewing chord and injected beam intersection.

One of the major advantages of CXRS diagnostics is the ability to carry out local measurements of the plasma parameters due to the fact that the detected active signal is coming from the local area of the viewing chord and injected atomic beam intersection. In this case, it is possible to achieve a spatial resolution of about several centimetres, even in the case when the plasma column has the size of a few metres. From Eq. (4.27), it is necessary to have independent data about the local concentration of the injected atomic beam [4.360].

The general scheme of an active CXRS diagnostic is shown by the example of the active spectroscopy system which is used on JET (Fig. 4.44).

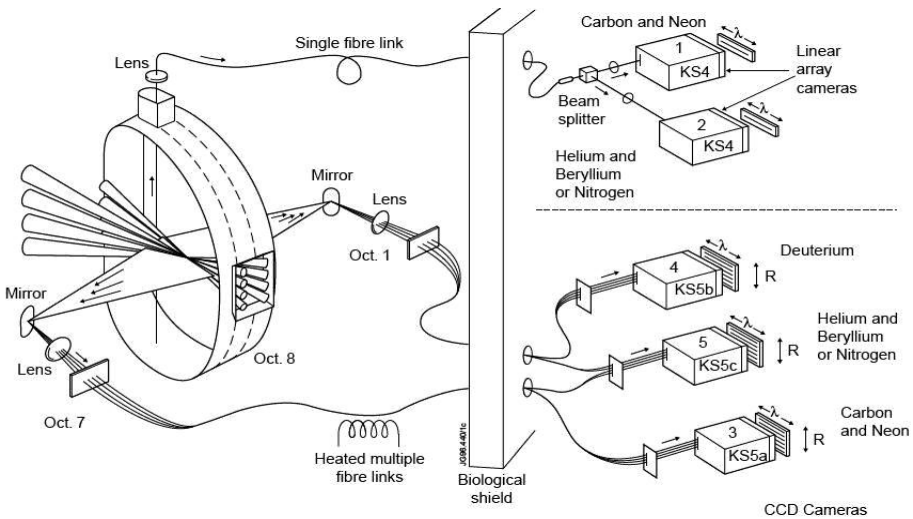


FIG. 4.44. General scheme of the active CXRS diagnostic used on JET [4.365]. Reprinted from Ref. [4.365]. Copyright (2011), IOP Publishing Ltd.

A heating atomic beam which is injected from an equatorial port tangentially relative to the tokamak magnetic lines is used for CXRS diagnostics. Three viewing systems are used to carry out the measurements. One viewing system

is installed at the upper tokamak port. Two other viewing systems are installed in neighbouring equatorial ports relative to the observation plasma volume, in one horizontal plane. Several observation systems are necessary to measure separately the toroidal and poloidal plasma rotation velocities. Quartz optical fibers are used for transportation of the light from the experimental hall to the spectroscopic equipment installed behind the biological shield. The spectrometers which are used for active CXRS measurements possess high spectral resolution to carry out spectral lines profile width and shift measurements. Active CXRS diagnostics is planned to be used at ITER for delivering information about ion plasma components including the helium ash [4.361–4.364].

The optical system collects the entire amount of light along the viewing chord length. It means that in addition to an active charge exchange signal, all passive plasma radiation is detected too. As a result, the measured spectral profile has a complex shape which is a superposition of the active and passive radiation coming from various plasma regions [4.365]. Partial or full overlapping of the spectral line profiles relating to various element ions could take place. Therefore, the experimentally measured spectral profiles need precise mathematical processing to allocate the spectral structure corresponding to an active charge exchange signal. Multi-Gaussian fitting of experimental data by the least squares method is usually used for this purpose (Fig. 4.45).

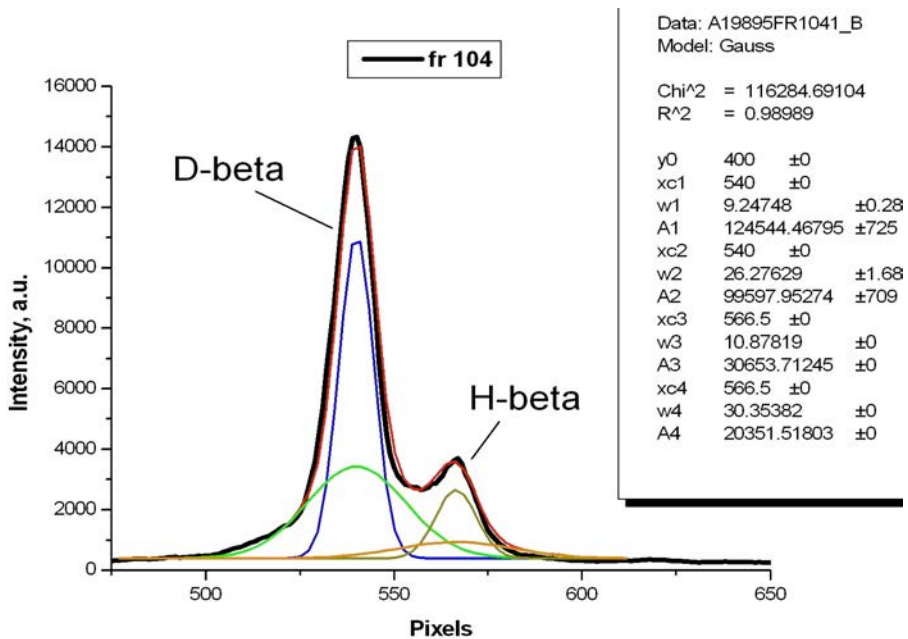


FIG. 4.45.  $D_{\beta}$  and  $H_{\beta}$  lines profile multi-Gaussian fitting of experimental spectrum obtained on T-11M [4.362].

An experimental profile of the plasma radiation of T-11M in the  $D_{\beta}$ ,  $H_{\beta}$  spectral lines region is shown in Fig. 4.45. An experimentally measured spectrum of T-11M plasma radiation is shown in black. One can see that the  $D_{\beta}$  and  $H_{\beta}$  lines profiles are partially overlapped. The red curve shows the simulated summary spectral profile. The  $D_{\beta}$  line profile consists of the profile of passive  $D_{\beta}$  line radiation from the peripheral plasma, caused by electronic impact (this profile is shown in blue), and also the profile of  $D_{\beta}$  line passive radiation caused by charge exchange on neutral atoms in the peripheral plasma (this profile is shown in green). The  $H_{\beta}$  line profile also consists of two similar components, which are shown in Fig. 4.45 in orange and khaki. In the table in the right hand top corner of Fig. 4.45, the parameters of the modelling Gaussian curves are presented. From Fig. 4.45 it can be seen that the resulting modelling profile very well coincides with the experimental data. This example shows that precise mathematical modelling of CXRS experimental data is important.

As was mentioned above, the plasma poloidal and toroidal rotation velocities could be measured via the Doppler shift of the impurity lines. It gives the possibility to measure the radial electric field that contributes to the force balance and transport inside the plasma column. For a magnetically confined plasma, the radial electric field is related to the plasma's flow velocity by the lowest-order force balance equation for a single ion species [4.366]:

$$E_r = (1/n_i \vec{Z}_i e) \nabla P_i - (\mathbf{v}_i \times \vec{B})_r \quad (4.28)$$

where  $n_i$  is the ion density,  $Z_i$  is the ion charge,  $e$  is the electron charge,  $P_i$  is the ion pressure,  $\mathbf{v}_i$  is the ion fluid flow velocity,  $B$  is the total magnetic field, and  $i$  labels the ion species. Examples of experimental data on the poloidal velocity and radial electric field behaviour measured during the L-H transition in DIII-D [4.366] are shown in Fig. 4.46. Experimental data on the ion temperature, and toroidal and poloidal velocity profiles measured during the L-H transition in DIII-D [4.366] are shown in Fig. 4.47.

CXRS gives the possibility for local measurements of various very important plasma parameters such as ion temperature and density, poloidal and toroidal rotation velocities and so on that permit direct measurements of transport research inside the plasma column [4.367, 4.368].

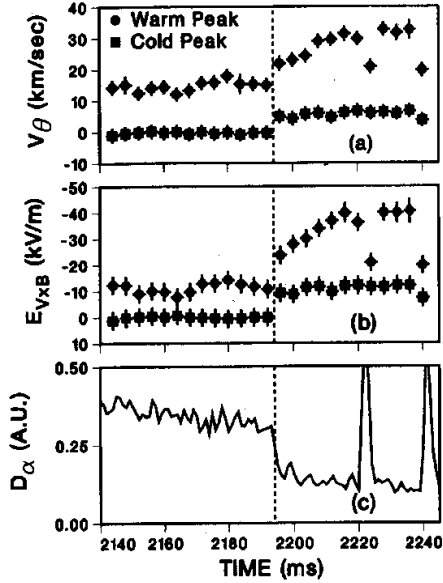


FIG. 4.46. Poloidal velocity (a) and radial electric field (b) time behaviour measured during L-H transition in the DIII-D tokamak [4.366]. Reprinted from Ref. [4.366]. Copyright (2011), American Institute of Physics.

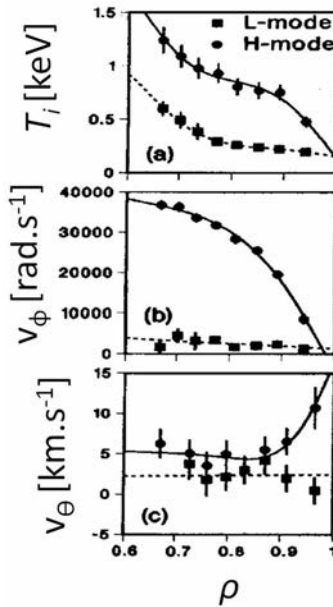


FIG. 4.47. (a) Ion temperature, (b) toroidal velocity and (c) poloidal velocity profiles measured during L-H transition in the DIII-D tokamak (plotted against  $\rho$  ( $\rho = 1$  at separatrix) [4.366]. Reprinted from Ref. [4.366]. Copyright (2011), American Institute of Physics.

#### 4.3.2.3. Motional Stark effect

The magnetic field configuration is defined by the superposition of the toroidal magnetic field  $\vec{B}_\theta$ , the magnetic field of the plasma current and the magnetic field from the inductor and controlling coils. Every magnetic vector can be calculated except  $\vec{B}_\theta(r)$ , which is defined by the spatial distribution of the plasma current.

The ratio  $\vec{B}_\theta(r) / \vec{B}_\phi$  can be expressed through the rotary transformation (pitch angle)  $\gamma_{pitch}$  defined as

$$\gamma_{pitch}(r) = \arctg(\vec{B}_\theta(r) / \vec{B}_\phi) \approx \vec{B}_\theta(r) / \vec{B}_\phi \quad (4.29)$$

The  $q(r)$  value at every point is defined by the plasma column geometry and the pitch angle  $q(r) = (r/R)/\gamma(r)$ , where  $R$  is the major torus radius. The derivative of the  $q$  value on the radius,  $s = (r/q)(dq/dr)$ , characterizes the shear of the magnetic lines in the plasma which has an influence on the stabilization of plasma instabilities. So measurements of the rotary transformation angle is an important task for studying and controlling the tokamak magnetic configuration. One of the main methods to learn the pitch angle value is to measure the angle of inclination of the polarization vector of the spectral lines radiated by injected hydrogen atoms (motional Stark effect or MSE).

The basic idea is as follows. The direction of the injected hydrogen beam atoms as a rule is not collinear with the magnetic field vector. In the coordinates of the moving atom, an electric field (Lorentz field) is induced:

$$\vec{E}_{Lor} = \frac{1}{c}(\vec{v} \times \vec{B}) \quad (4.30)$$

where  $\vec{v}$  is the velocity of fast atoms, and  $\vec{B} = \vec{B}_\theta + \vec{B}_\phi$  is the total magnetic field. The estimated  $\vec{E}_{Lor}$  value is from tens to hundreds of  $\text{keV} \cdot \text{cm}^{-1}$ . Under this field, the radiation of the atom is polarized and atomic quantum levels split into a set of sub-levels (Stark effect). The level with the main quantum number  $n$  is splits into  $2n - 1$  sub-levels. The levels splitting of the hydrogen atom is characterized by the linear Stark effect; i.e. the energy interval between sub-levels is proportional to the electric field. In the atomic radiation spectrum so-called Stark components arise. For  $\vec{E}_{Lor} = 70 \text{ keV} \cdot \text{cm}^{-1}$ , the interval between the components for the  $H_\alpha$  line equals  $\Delta\lambda \sim 2\text{\AA}$ . A peculiarity of the Stark spectrum is the presence of two types of transitions with different polarization vector directions: the  $\pi$  component (polarization vector parallel to the electric field vector  $\vec{E}$ ) and the  $\sigma$  component (polarization vector perpendicular to  $\vec{E}$ ).

For observation along the vector  $\vec{E}$  the  $\pi$  component disappears, while the  $\sigma$  component is depolarized, so in experiments the observation is usually performed in the direction perpendicular to  $\vec{E}$  (i.e. across  $\vec{E}_{Lor}$ ). In this case,

the  $H_\alpha$  spectrum is fully polarized and both components ( $\pi$  and  $\sigma$ ) are linearly polarized. This makes it possible to define the direction of the vector  $\vec{E}_{Lor}$  by measurements of the polarization direction of any component. If the direction of injection ( $\vec{v}$ ) is known, the angle of inclination of  $\vec{E}_{Lor}$  gives the pitch angle value at the point of intersection of the atom beam and the observation chord.

Experimentally, measurements of the Stark component polarization are performed in the presence of bulk plasma  $H_\alpha$  radiation collected along the line of sight. However, the beam  $H_\alpha$  lines are shifted due to the Doppler effect because the beam atoms have some velocity component along the line of sight. This is a favourable factor for performing the measurements. The MSE diagnostic was developed near the end of the 1980s by F.M. Levinton in PBX-M [4.369]. Later, this technique was applied at almost all tokamaks where heating beams were used (TFTR, DIII-D, JT-60U, JET, etc.). A typical experiment layout is shown in Fig. 4.48.

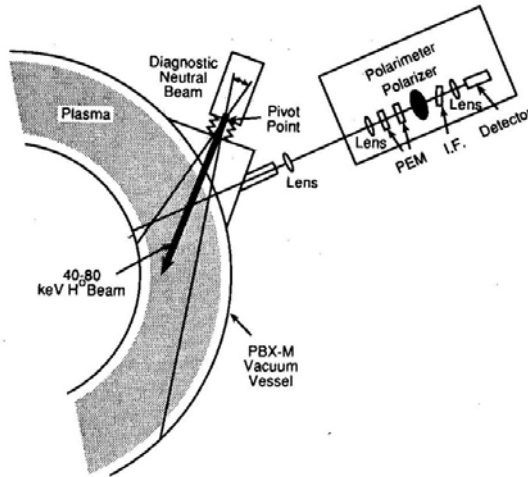


FIG. 4.48. Schematic layout of the motional Stark effect measurement [4.370]. Reprinted from Ref. [4.370]. Copyright (2011), American Institute of Physics.

The hydrogen beam is injected in the equatorial plane at a sharp angle to the toroidal magnetic field. If there is no plasma current the resultant Lorentz field vector  $\vec{E}_{Lor}$  is located at a right angle to the equatorial plane of the torus. In the presence of a plasma current its deviation from normal is determined by the deviation of the total magnetic field vector  $\vec{B}$  from the toroidal magnetic field  $\vec{B}_\phi$ , due to the poloidal magnetic field presence. A measurement of the angle of inclination of the polarization plane of one of the Stark components to the equatorial plane permits us to get the directions of the  $\vec{E}_{Lor}$  and  $\vec{B}$  vectors. These measurements, if made at different points of the beam, give the inclination value of the total magnetic field as a function of the small plasma

radius. Thus one can obtain such parameters as the poloidal field, the plasma current distributions and the  $q(r)$  value distributions if the plasma is circular. For a non-circular cross-section plasma, additional information is needed, namely the plasma pressure profile, the plasma current value, the currents in the controlling coils and magnetic flux measurements. The piezoelectric modulator used in the experiment and data recording system makes it possible to measure the angle of inclination with an accuracy of  $0.1^\circ$ . The typical range of the angle is  $0-6^\circ$  and is determined by the  $q(r)$  value and the geometry of the facility.

The authors estimated the accuracy of  $q(r)$  measurements at the plasma axis as 5%. The results of the measurements are shown in Fig. 4.49.

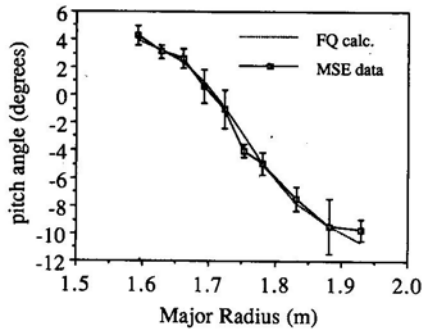


FIG. 4.49. Comparison of MSE polarimeter pitch angle measurements and corresponding equilibrium profile (PBX-M machine) [4.371]. Reprinted from Ref. [4.371]. Copyright (2011), American Institute of Physics.

#### 4.3.2.4. Active charge exchange and Rutherford scattering

##### 4.3.2.4.1. Active charge exchange

Active CX diagnostics is the power tool of local plasma parameters. A good option to measure the ion temperature radial profile  $T_i(r)$  in tokamaks is to use an active version of the CX diagnostic by scanning the plasma cross-section with a diagnostic neutral beam (DNB) along the line of sight of the NPA, or the other way around. The atoms of DNB (mainly hydrogen) serve as an artificial target for charge exchange of plasma ions [4.372]. The energy of the DNB should be high enough to reach the plasma centre without strong attenuation because of the ionization by plasma ions and electrons and charge exchange with plasma ions. For medium tokamaks it is equal to some tens of keV. The density of beam atoms, i.e. the intensity of the DNB, has to be high enough to provide sufficient active signal detected by the NPA. The first application of active CX was made in 1973 [4.373], where instead of a neutral beam a hydrogen atomic stream from

a plasma gun was used. It should be noted that attenuation of charge exchanged neutrals is very large in large tokamaks. That is a significant limitation of this method.

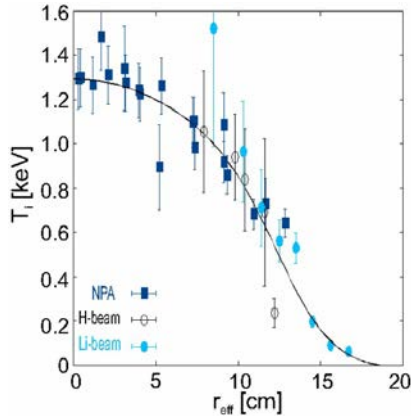


FIG. 4.50. Actively measured  $T_i$  profiles by a multi-chord NPA diagnostic array on the W7-AS stellarator in combination with active spectroscopy measurements on H and Li beams. Here  $r_{\text{eff}}$  is the averaged radius of magnetic surfaces in the stellarator. The solid line is the fit of experimental data. Taken from Ref. [4.374].

A very demonstrative example of the actively measured  $T_i$  profiles by a multi-chord NPA diagnostic array on the W7-AS stellarator in combination with active spectroscopy measurements on H and Li beams is shown in Fig. 4.50 [4.374].

Another option to measure the active flux atoms is to use the pellet charge exchange (PCX) technique. PCX measurements obtained with the use of lithium (or boron) pellets injected into the plasma were used in TFTR for measuring the distributions of ICRF driven  $H^+$  ions and fusion alpha particles in the MeV energy range [4.375, 4.376]. For lithium pellets,  $H^+$  and  $He^{2+}$  ions interacted with the pellet ablation cloud of  $Li^+$  to form an equilibrium neutral fraction as a result of the reactions  $H^+ + Li^+ \rightarrow H^0 + Li^{2+}$  and  ${}^4He^{2+} + Li^+ \rightarrow {}^4He^0 + Li^{3+}$ . After that,  $H^0$  and  ${}^4He^0$  are detected by the NPA. Note that PCX provides information on fast ions only for the very short time of pellet ablation (a few hundred microseconds).

Active NPA measurements of ICRF driven  $H^+$  minority ions were also made on TFTR deuterium plasmas with the NPA for the MeV energy range in the passive and active (PCX) modes [4.199]. Figure 4.51 shows the active (PCX) energy spectrum of ICRF driven  $H^+$  ions and the passive spectrum averaged over 100 ms during an ICRF power pulse in two reproducible discharges with the same parameters on TFTR. In deriving the passive  $H^+$  spectrum, it is important to use the proper donor for neutralization of the  $H^+$  ions. The most probable donors for electron capture in TFTR plasmas were  $C^{5+}$  ions because the main low  $Z$

impurity was carbon. It can be seen that the active and passive spectra have the same exponential shapes and very similar effective temperatures of ICRF driven  $H^+$  ions. That is because both methods in this case provide information on the effective temperature in the plasma core where ICRF power had been absorbed.

High energy NPA was used on TFTR mainly for PCX measurements in which active charge exchange measurements of the energy and radial distributions of D-T alpha particles and D-D tritons were obtained in conjunction with impurity pellet injection. With the use of PCX measurements it was possible to measure the D-T alpha and D-D triton energy spectra and to compare the experimental data with predictions of numerical simulation, in which a classical slowing down of alphas and tritons was assumed. Good agreement between the PCX measurements and modelling indicated that the alpha and triton energy distributions and their density ratio are very close to the code predictions.

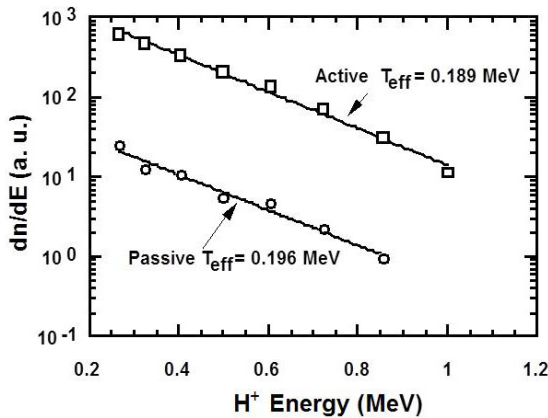


FIG. 4.51. The active (PCX) energy spectrum of ICRF driven  $H^+$  ions and the passive spectrum averaged over 100 ms during an ICRF power pulse in two reproducible discharges with the same parameters on TFTR [4.199]. Reprinted from Ref. [4.199]. Copyright (2011), American Institute of Physics.

#### 4.3.2.4.2. Rutherford scattering

Rutherford scattering diagnostics (RSD), also called active-beam scattering diagnostics, is based on the scattering of neutral atoms from a mono-energetic diagnostic beam by the plasma ions [4.377]. A collision between a neutral beam particle and a plasma ion is considered to be Rutherford scattering if the impact parameter of the collision is much smaller than the Bohr radius and hence electron screening can be omitted. Due to momentum and energy conservation, the energy of the scattered beam atoms will depend on the energy and momentum of the plasma ions. Theoretical studies show [4.377, 4.378] that if the scattering

angle  $\vartheta$  is small and  $W_b \gg T_i$ , where  $W_b$  is the energy of the beam atoms and  $T_i$  is the plasma ion temperature,  $W$  is the energy of scattered atoms,  $\gamma = m_p/m_b$ , the mass ratio of plasma ions and beam atoms, the energy distribution function of scattered atoms is a Gaussian distribution function with full width at half maximum  $\Delta W_{\text{FWHM}}$ , given by

$$\Delta W_{\text{FWHM}} \cong 4\vartheta \sqrt{\gamma W_b T_i \ln 2} \quad (4.31)$$

To arrange a Rutherford scattering experiment in practice, one needs to use a beam energy much larger than the typical energies of the plasma ions. For application to present day magnetic confinement devices, this implies beam energies in the range of several tens to several hundreds of keV. Given the large difference in beam energy and plasma ion energy, the scattering angles are in general fairly small (depending on the experiment typically less than  $10^\circ$ ). To obtain still a rather localized measurement, both the diameter of the probing beam and the width of the viewing cone need to be as small as possible. RSD yields the local ion temperature in the scattering volume. In the case where the plasma ions have a collective motion it is possible to measure the velocity of this motion with RSD. The first experimental realization of a RSD on the T-4 tokamak was reported in Refs [4.379] and [4.380]. In Fig. 4.52, a schematic illustration of the RSD is given [4.378]. Shifting the ion source from left to right moves the scattering volume from bottom to top. Larger scattering angles correspond to a lower scattering yield but have a better spatial resolution.

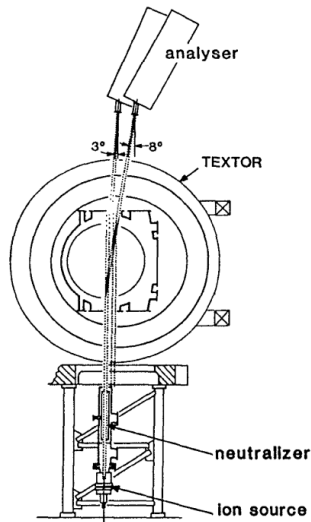


FIG. 4.52. A schematic layout of the Rutherford scattering diagnostic [4.378]. Reprinted from Ref. [4.378]. Copyright (2011), American Institute of Physics.

In this experiment, an 8 keV neutral helium beam was employed, with an equivalent current density (i.e. the current density if the beam particles were not neutral but charged) of  $\sim 10\text{--}30 \text{ mA}\cdot\text{cm}^{-2}$  and a pulse length of 200  $\mu\text{s}$ . At the used scattering angle of  $9^\circ$ , the spatial resolution was 1 cm across the beam and about 10 cm along the beam. The experimental set up at T-4 had the special features that the scattering angle could be adapted from 0 to  $16^\circ$ , and that the scattering volume could be positioned at various places along the equatorial plane of the tokamak from centre to edge. In this way, it was possible to measure the ion temperature profile with 10–15% accuracy on a shot-to-shot basis.

Figure 4.53 presents the energy distribution of the scattered particles (left) and ion temperature profile (right) measured in T-4. The minor plasma radius is 15 cm. The squares in the left panel represent the energy spectrum of the probing beam, full circles the spectrum of atoms scattered in a gas and empty circles the spectrum of atoms scattered by the plasma. After these first experiments, Rutherford scattering was successfully applied on JFT-2 [4.381], the large tokamak JT-60 [4.382], the Madison symmetric torus reversed-field pinch [4.383], the TEXTOR tokamak [4.384] and other smaller plasmas.

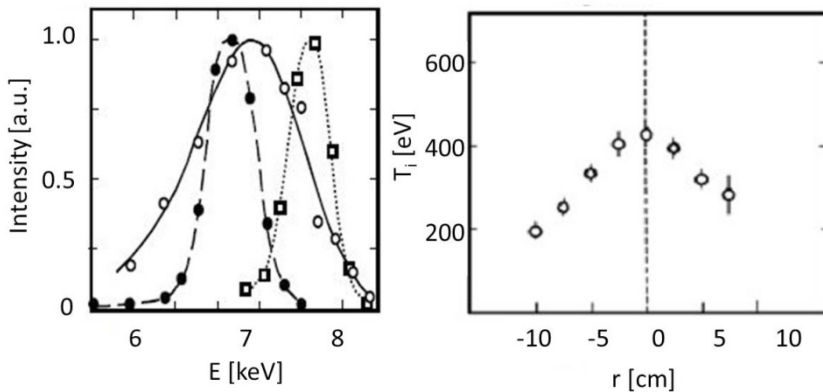


FIG. 4.53. Energy distribution of scattered particles (left) and ion temperature profile (right) measured in T-4 [4.379, 4.380]. Left: squares — energy spectrum of the probing beam, full circles — spectrum of atoms scattered in a gas, empty circles — spectrum of atoms scattered by the plasma. Reprinted from Ref. [4.379]. Copyright (2011), JETP.

#### 4.3.2.5. Heavy ion beam probe diagnostics

The principle of heavy ion beam probing (HIBP) diagnostics was proposed at the end of the 1960s [4.385] and was tested and used in many magnetic confinement experiments in the 1970s, 1980s and later [4.386]. The

HIBP diagnostic is the most effective and unique direct technique to measure local electric potentials in a plasma. This parameter has become very important for studies of magnetized plasma confinement. In addition, it can provide information about the local electron density and temperature and also the plasma current density profile. The HIBP diagnostic is based on the injection of a beam of heavy ions (usually singly charged) into the magnetically confined plasma. On passing through the plasma, some of the probing ions experience ionizing collisions with the plasma particles (mainly with electrons). This results in a fan of secondary ions with higher charges (see Fig. 4.54).

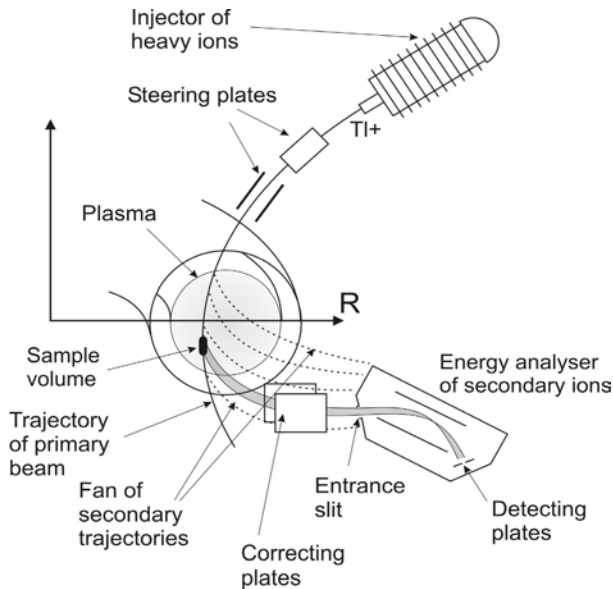


FIG. 4.54. The layout of heavy ion beam probing diagnostics ( $Tl^+$  is a singly charged ion of thallium).

If the Larmor radius of the secondary ions  $\rho_L$  is large enough compared to the plasma radius  $a$ , ( $\rho_L \geq a$ ), they can be analysed and detected outside the plasma. The small volume emitting secondary ions can be moved through the plasma cross-section by varying either the probing beam energy  $W_b$  or the poloidal entrance angle  $\alpha$ . By changing both parameters, a two-dimensional grid of sample volume positions (called a detection grid) can be obtained. The basic principle behind the electric potential measurement is as follows. The probing beam enters the plasma with an initial energy  $W_b$ . As the particles move through the plasma their kinetic energy varies according to the spatial potential. At a point of ionization having potential  $\Phi_{pl}$  the energy of the ions becomes equal to  $W_b - q_p \Phi_{pl}$  and they leave the plasma with energy  $W_d = W_b - q_p \Phi_{pl} + q_s \Phi_{pl}$ , where  $q_p$  and  $q_s$  are the charges of the primary and

secondary particles, respectively. Therefore, the plasma potential at the point of ionization can be obtained from the energy difference between the secondary and primary particles by

$$\Phi_{pl} = \frac{(W_d - W_b)}{(q_s - q_p)} \quad (4.32)$$

In principle, the HIBP diagnostic can measure simultaneously a number of plasma parameters as well as their fluctuations with high temporal (up to 1  $\mu$ s) and spatial resolution (range of 1  $\text{cm}^3$ ). These are: the electric potential  $\Phi_{pl}$ , the electron density  $n_e$ , the electron temperature  $T_e$  and the poloidal magnetic field  $B_\theta$  (or equivalently the plasma current density).

A good example of the capabilities of HIBP is provided by the experiments on T-10. The phenomenon of geodesic acoustic modes (GAMs), suggested theoretically about 40 years ago, was quite difficult to identify experimentally with other diagnostics since the clearest manifestation of GAM is plasma electric potential quasi-coherent oscillations. T-10 HIBP presents an effective instrument for studying both mean potential and its oscillatory component, including GAMs, and density oscillations as well. The power spectral densities for the plasma potential and electron density obtained for a plasma discharge with strong auxiliary ECR heating is presented in Fig. 4.55 [4.387].

Active diagnostics based on particle beam probing and neutral particle analysis has up to now played a very important role in measurements of local plasma parameters in a magnetized plasma. A good overview of this subject is presented in Ref. [4.388].

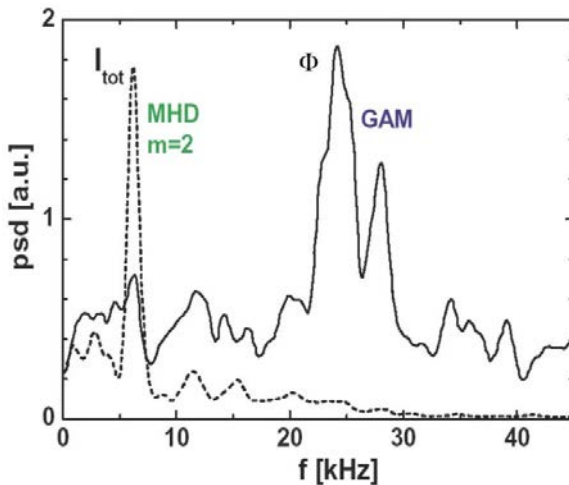


FIG. 4.55. Comparison of power spectral density (psd) for the plasma potential (solid line) and the total beam current proportional to plasma density (dash) during ECRH [4.387].

### 4.3.3. Probing by microwaves and laser beam: interferometry, polarimetry, reflectometry

**A. Petrov, V. Petrov**

TRINITI, Moscow Region

**P. Bagryanski**

Nuclear Physics Institute, Novosibirsk

**V. Vershkov**

Kurchatov Institute, Moscow

Russian Federation

#### 4.3.3.1. Introduction

Recently, in magnetic confinement devices active diagnostics methods of plasma interferometry, polarimetry and reflectometry have been widely adopted. These methods are based on measuring the parameters of a probing wave (total phase shift, or group time delay) spreading in a plasma.

If probing on several spatial chords is used, interferometry makes it possible to define the mean density of the plasma and its spatial distribution. Major advantages of this diagnostic method are: no absolute calibration of the instrument is required; no additional information is needed from other diagnostics; and there is high time resolution (in contrast to Thomson scattering). Thus, currently interferometry is a standard technique for measuring the line-integrated electron density in magnetically confined plasmas. The disadvantage of the interferometry is that inversion procedures are required to transform the line-integrated measurements to local quantities.

Plasma polarimetry makes it possible to determine an important plasma parameter, namely the distribution of a poloidal magnetic field in tokamak plasma and, accordingly, the spatial profile of the safety factor  $q(r)$ . This is important for better understanding of magnetohydrodynamic (MHD) instabilities such as sawteeth and tearing modes, as well as plasma transport and  $\beta$  limits. For these purposes, the measurements of the Faraday effect, i.e. measurements of the angle of rotation of the polarization plane of a linear polarized wave induced by plasma birefringence, are performed. This angle is proportional to the product of plasma density and the component of the magnetic field parallel to the probing. Experiments on measurements of the poloidal magnetic field in tokamaks were initiated by papers of F. de Marco and S. Segre, who proposed using the Faraday effect for measuring the poloidal magnetic field in tokamaks [4.389]. Multi-chord probing is used for determining the spatial distribution of the poloidal magnetic

field. The Faraday rotation effect was first demonstrated on TFR [4.390], but the first full-scale profile measurements were performed on TEXTOR by Soltwisch [4.391].

Plasma reflectometry is based on the effect on the total reflection of probing radiation with carrier frequency  $f$  from a plasma layer where the refractive index vanishes (cutoff). In principle, both the ordinary mode (with its electric field parallel to the external magnetic field) and the extraordinary mode (with its electric field perpendicular to the external magnetic field) may be employed in reflectometry [4.392]. The position of the reflecting layer  $r_c(f)$  is determined by measuring the change of phase  $\Phi(f)$  that the wave undergoes in the plasma or by measuring the time delay  $\tau(f)$  of the wave in the plasma.

By changing the probing frequency, it is possible to explore plasma layers from the peripheral plasma with a small concentration up to the central areas with a large density. In reflectometry, the parameters of the reflected wave (phase, amplitude, group delay time) are most sensitive to local values of electron concentration and magnetic field in the reflecting layer; this makes it possible separately to carry out local studies of plasma oscillations. A separate paragraph will describe the problem in detail. A review covering practically all aspects of the application of reflectometry to plasma studies can be found in [4.393].

Unfortunately, the accuracy of plasma density measurements by a reflectometer is reduced in the central part of the plasma column because of the diminution of the density gradient and because of signal damping. Furthermore, at the plasma edge one may face problems connected with the interpretation of the reflectometry data due to violations of the ray approximation (in the case of low frequency probing waves) [4.394]. Therefore, reflectometry and interferometry of plasma are, as a matter of fact, complementary to one another. As a rule, in most modern tokamaks both methods are applied.

These methods have a rather long history of development; in particular this is true for plasma interferometry. As a matter of fact, already in the first tokamak plasma confinement experiments there was a need to measure one of the major parameters describing the plasma — the mean density. And this problem was successfully solved exactly with the help of a microwave interferometry [4.395–4.397]. The first interferometers had only one probing chord so they give information on chord averaged plasma density. More references to the early interferometer experiments may be found in Refs [4.397–4.400]. Later, the plasma polarimetry was added to interferometry, and, as a rule, measurements of the phase difference and Faraday effect were combined in one instrument. As an example here it is possible to mention the classic work of Soltwisch [4.391]. Also scanning [4.401–4.403] and multichannel systems appeared [4.404, 4.405], giving the time evolution of plasma density profiles necessary for studying plasma transport and other plasma phenomena. The phase image method makes

it possible to restore the plasma density profile without any prior assumptions about the symmetry of the plasma [4.406].

An increase in time resolution is reached by raising the intermediate frequency in the heterodyne schemes up to MHz values and above [4.407]. Apart from measuring the time evolution of the electron density profile as well as that of the current density profile, interferometry/polarimetry can be successfully integrated into the control systems for the plasma position, plasma density and additional heating [4.408, 4.409].

#### 4.3.3.2. Interferometry and polarimetry

In interferometry, comparison of the phase of a wave which has passed through the plasma (signal branch of the interferometer) with the phase of a reference wave (reference branch of the interferometer) is carried out. As a rule, in the interferometry of a plasma a linearly polarized probing wave with its polarization plane parallel to the toroidal magnetic field in the tokamak (ordinary wave) is used and the probing wave is directed across the toroidal magnetic field. Thus the measured difference in phase is defined directly by the integral of density along the probing chord [4.397]:

$$\Delta\varphi = \frac{2\pi \cdot f}{c} \int_0^l (1 - \sqrt{1 - n_e(z)/n_c}) dz \approx \frac{\pi \cdot f}{c \cdot n_c} \int_0^l n_e(z) dz \quad (4.33)$$

where  $c$  is the light velocity,  $n_e(z)$  is the plasma electron density,  $n_c = 4\pi^2 \cdot \varepsilon_0 m_e \cdot f^2 / e^2$  is the critical density for frequency  $f$ , and the integral is evaluated along a beam trajectory  $l$  in plasma. The formula Eq. (4.33) takes into account that the probing of the plasma is carried out by waves with high frequency (when refraction effects are negligible)  $f \gg f_{pe}$  (where  $f_{pe}$  is the electron plasma frequency), and the index of refraction of the plasma is close to 1 and  $n_e(z) \ll n_c$ . Different interferometer schemes have been developed to measure the phase shift of a probing wave in a plasma. One of the simplest schemes for the experimental arrangement (Mach-Zehnder homodyne interferometer) is shown in Fig. 4.56.

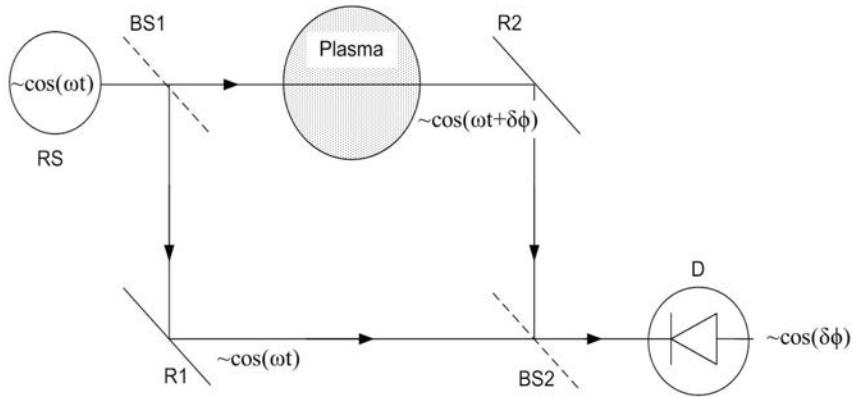


FIG. 4.56. Scheme of a single-channel homodyne Mach-Zehnder interferometer.

The signal from the radiation source (microwave oscillator or laser) is split into two beams. One beam (the reference beam) is sent to the detector D by means of beam splitters BS1, BS2 and reflector R1 and the other (the probe beam) is transmitted through the plasma before being brought to the detector. So the signal from the detector contains a component which is proportional to the cosine of the phase shift  $\delta\phi$  between these beams:  $U_{\text{det}} = A \cos(\delta\phi)$ , where  $A$  is the amplitude of the signal. So, the output signal is a function of both the phase shift and the power of the radiation source. Thus, there is ambiguity between the amplitude and phase changes. Moreover, because of the cosine dependence of the detector signal it is not possible to determine unambiguously whether  $\delta\phi$  is increasing or decreasing. This can be a problem, for example, in plasmas that initially increase in density, and drop before reaching a steady state. This ambiguity can be resolved by sweeping the frequency of the microwave source many times during the tokamak pulse. This technique gives a display on an oscilloscope known as zebra striping [4.397]. Another modification of the Mach-Zehnder interferometer which eliminates the ambiguity is shown in Fig. 4.57.

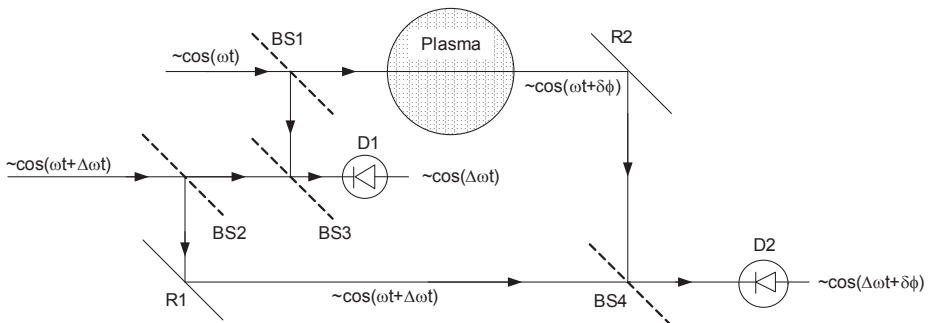


FIG. 4.57. Scheme of a single-channel heterodyne Mach-Zehnder interferometer.

The basic idea is to introduce a frequency shift  $\delta\omega$  between the probe and reference beams. This can be done either by using two separate frequency-locked sources with frequency shift  $\delta\omega$  or by shifting the frequency of the beam reflected from the beam splitter BS1 (using, for instance, a cylindrical rotating grating in the case of a laser interferometer [4.398]). In both cases, the scheme contains two detectors, reference D1 and probe D2, and the total phase shift is measured by applying signals from these detectors to the input of a phase-to-voltage converter.

Apart from the Mach-Zehnder geometry, the Michelson type of interferometer is also often used for plasma density measurements. In this setup the probing beam is reflected back after passage through the plasma, so it passes along the same probe chord twice and is recombined with the reference beam. This type of interferometer needs only one diagnostic port for access to the plasma, which can be preferable in conditions of limited free space near the tokamak. Generally, the Michelson interferometer is more sensitive to refraction effects due to the double pass through the plasma. In other respects, the basics of the Michelson setup are similar to those of the Mach-Zehnder interferometer. The heterodyne interferometer type now is the most commonly used.

On today's machines, plasma interferometry is a well developed, routine method permitting determination of the line integrated plasma density and density profile. But it measures the average value of plasma density along a chord. So there is a problem to deduce local values from available chord measurements (the inverse problem) [4.398, 4.410]. An exact reconstruction requires measurements along a number of chords under different viewing angles. In practice, however, access to the plasma and the number of sightlines which can be realized are restricted and this limits the spatial information that can be achieved. A finite number of  $N$  sightlines delivers a maximum of  $N$  independent pieces of information on the profile shape. The missing information has to be obtained to some degree by making use of the inherent symmetry of the problem. A necessary condition for magnetic confinement is that the magnetic field lines form nested flux surfaces characterized by their effective radius coordinate  $r_{\text{eff}}$ . On a flux surface, the equilibrium plasma parameters such as the electron density are practically constant so that their distribution can be described by a radial profile  $n(r_{\text{eff}})$  with  $r_{\text{eff}}$  as the only coordinate. The information content of a single interferometer channel  $i$  is mostly determined by its penetration depth characterized by the minimum effective radius  $x_i = X = \min\{r_{\text{eff}}\}$  which is just touched by the beam (see Fig. 4.58). The channel collects information on densities  $n(r_{\text{eff}} > X)$  whereas densities inside this radius are omitted. With  $N$  sightlines available, the profile can be intersected in shells each with an inner boundary given by  $r_{\text{eff}} = x_1 \cdots x_N$ . A straightforward profile inversion then can be conducted serially proceeding from the outermost shell towards the centre. For each shell the corresponding channel with  $x_i$  measures a phase shift  $\Delta\varphi_i$  exceeding those of the next outer sightline  $\Delta\varphi_{i-1}$  due to its additional

contribution by the probing shell  $i$ . Information about the central density is carried by the innermost sightline passing the plasma centre. For the first step of the serial reconstruction of  $n(r_{\text{eff}})$ , the phase shift of a (hypothetical) interferometer sightline tangential to the plasma boundary  $r_{\text{eff}} = a$  is needed. This requires an assumption on the edge density  $n(a)$  and the behaviour of  $n(r_{\text{eff}})$  for  $r_{\text{eff}} > a$ . For the integration along the sightline in Eq. (4.33), the relation between the sightline coordinate and the effective radius  $r_{\text{eff}}(z)$ , (the topology of the magnetic flux surfaces) has to be sufficiently well known. For the particular case of a circular plasma cross-section where the density is constant on concentric circles,  $r_{\text{eff}}(z) = r(z)$  is an analytical function such that the line integration and its inversion can be performed analytically by the so-called Abel inversion (see, for example, Ref. [4.398]). In this case, we can rewrite Eq. (4.33) in the form:

$$\Delta\varphi(r) = \frac{\pi \cdot f}{c \cdot n_c} \cdot \int_X^a \frac{n_e(r)}{\sqrt{r^2 - X^2}} r dr \quad (4.34)$$

and then find the density distribution:

$$n_e(r) = -\frac{n_c \cdot c}{\pi^2 \cdot f} \cdot \int_r^a \frac{d(\Delta\varphi(X))}{dX} \cdot \frac{dX}{\sqrt{X^2 - r^2}} \quad (4.35)$$

In practice, tokamak and stellarator plasmas are not cylindrically symmetric and a numerical integration along the beam path becomes necessary. As a rule, for plasma density profile recovery from interferometry data different abelization procedures are used (see for instance Refs [4.411, 4.412]).

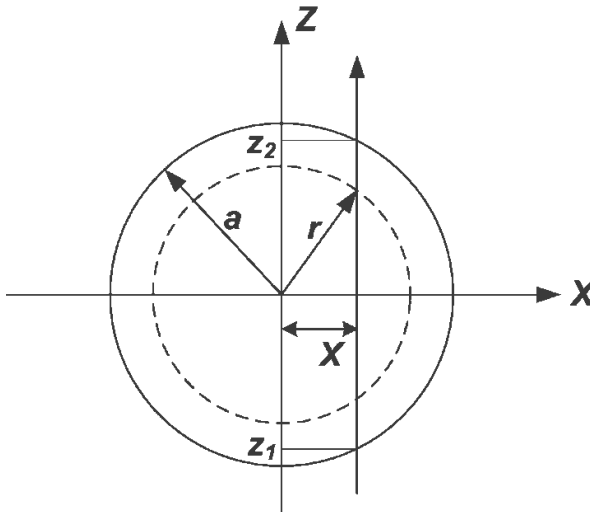


FIG. 4.58. Coordinate system for the calculation of the phase shift along a chord.

One of the important parameters of any interferometer is the density range, which is capable of being measured. This density range is determined mainly by the sensitivity on the one hand (the lowest measurable density) and by refraction on the other (with increasing density the refraction angle increases). The sensitivity is defined mainly by the probing frequency (see Eq. (4.33), which shows that the phase shift is proportional to the value of  $1/f$ ). So if we assume that our apparatus can measure some minimal fixed phase shift  $\Delta\varphi_{\min}$ , we should use probing frequencies  $f < f_{\max}$ , which results in a phase shift  $\Delta\varphi \geq \Delta\varphi_{\min}$ .

For an axisymmetric parabolic density profile with a central density  $n_0$ , the maximum value of the refraction angle  $\alpha_m$  is given to a good approximation by [4.413]:

$$\alpha_m \cong \frac{n_0}{n_c} = \frac{e^2 \cdot n_0}{4\pi^2 c^2 \cdot \epsilon_0 \cdot m_e \cdot f^2} \quad (4.36)$$

So the refraction angle is inversely proportional to the probing wave frequency. Therefore, we cannot use too low frequencies in the interferometer (in order to increase the sensitivity of the instrument). For low frequencies, the refraction of the probe wave in the plasma is increased, so part of the radiation will miss the detector, and the signal from the detector will fall. For some frequency  $f_{\min}$ , this results in a detector signal which will be less than the intrinsic noise of the detector and the possibility for measurements will be lost (signal-to-noise ratio will be too low). For this reason, the optimal choice of the probing frequency for each interferometer should be made for each plasma device depending on a number of factors such as the density range, the geometrical sizes, the schematic of the interferometer and so on. This problem is discussed in Refs [4.398, 4.399] in detail.

As mentioned above, a combination of interferometer and polarimeter is often used in one instrument. Many of the interferometers/polarimeters applied nowadays are based on the scheme originally proposed and used by Veron [4.398]. To avoid reflection and refraction distortion of beam trajectories, interferometric (polarimetric) measurements are usually carried out with waves whose frequency  $f$  is much greater than the plasma frequency  $f_p$  ( $f \geq 3f_p$ ) at the centre of the plasma column ( $n_e(0) \ll n_c$ ), when the dielectric constant of the plasma is close to unity. The plasma in modern tokamaks has densities of the order of  $10^{19}$ – $10^{21}$   $m^{-3}$ , which correspond to plasma frequencies in the range of 30–300 GHz. Therefore, in modern tokamaks, interferometry in a range from microwave ( $\lambda \leq 3$  mm,  $f \geq 100$  GHz) up to the infrared ( $\lambda \geq 10.6$   $\mu m$ ,  $f \leq 30\,000$  GHz) is used.

Because of the influence of refraction in current tokamaks with higher densities and large sizes, laser interferometers/polarimeters with probing wavelengths from the submillimetre to the infrared range are used more often than microwave systems. Though the schematics of microwave and laser systems

are similar (Mach-Zehnder or Michelson type interferometer), the technique used is different. For this reason it is advisable to consider these systems separately.

#### 4.3.3.2.1. Microwave interferometry and polarimetry

As an example, let us consider a simple, single-channel 1 mm microwave interferometer which was developed to measure the line-integrated electron density on the horizontal mid-plane of TFTR [4.414]. This orientation allows the density to be measured during major radial compression of the plasma. A wavelength of 1 mm was chosen for several reasons. Reliable 2 mW solid-state sources are readily available at this wavelength. The cut-off density of the probing wave frequency,  $10^{15} \text{ cm}^{-3}$ , is more than three times higher than the highest density to be measured. Also, a low loss oversized waveguide allows remote location of the interferometer to minimize environmental problems and the interferometer can be made relatively insensitive to vibrations. The interferometer is required to measure up to 500 fringes with possible power variations of up to 50 dB during a TFTR plasma pulse. Homodyne systems can only provide a maximum dynamic range of 30 dB. A heterodyne system was therefore designed which allows continuous wave operation of the transmitting source, avoids amplitude modulation problems of swept systems and a high (3.7–4.2 GHz) IF reduces noise sidebands (Fig. 4.59). A second harmonic mixer was adopted to avoid the use of a more expensive 1 mm wavelength local oscillator source.

One of the most serious problems in large tokamaks for interferometers is losses of the signal during its propagation through long transmission lines. In order to keep losses to a minimum over the 25 m, a WR-187 (C-band) transmission path guide was used. The two-pass design (Michelson type) consists of two open-ended WR-187 waveguides aimed at a stainless steel, spherical surfaced, rectangular mirror with a focal length of 200 cm mounted on the inner vacuum vessel wall. The antenna was mounted on a vacuum flange, with the microwave electric field parallel to the tokamak magnetic field (ordinary wave). A fused silica vacuum window was used at the vacuum interface. The measured round trip propagation loss inside the vacuum vessel was 6 dB in the absence of plasma after proper alignment. The bends and the waveguides of the transmission line were also aligned with a laser and after alignment the total transmission loss was better than 21 dB.

The return transmission guide from TFTR tapers into a harmonic mixer mounted in a cross-guide configuration. The mixer has a conversion efficiency of 15 dB. The local oscillator klystron can be tuned from 136 to 144 GHz with a 40 mW minimum output power. In heterodyne receiver systems the local oscillator is usually locked to the transmitter frequency. However, experience with tokamak operation has shown that electromagnetic interference can make conventional frequency locking techniques unreliable. To overcome this difficulty, a broadband

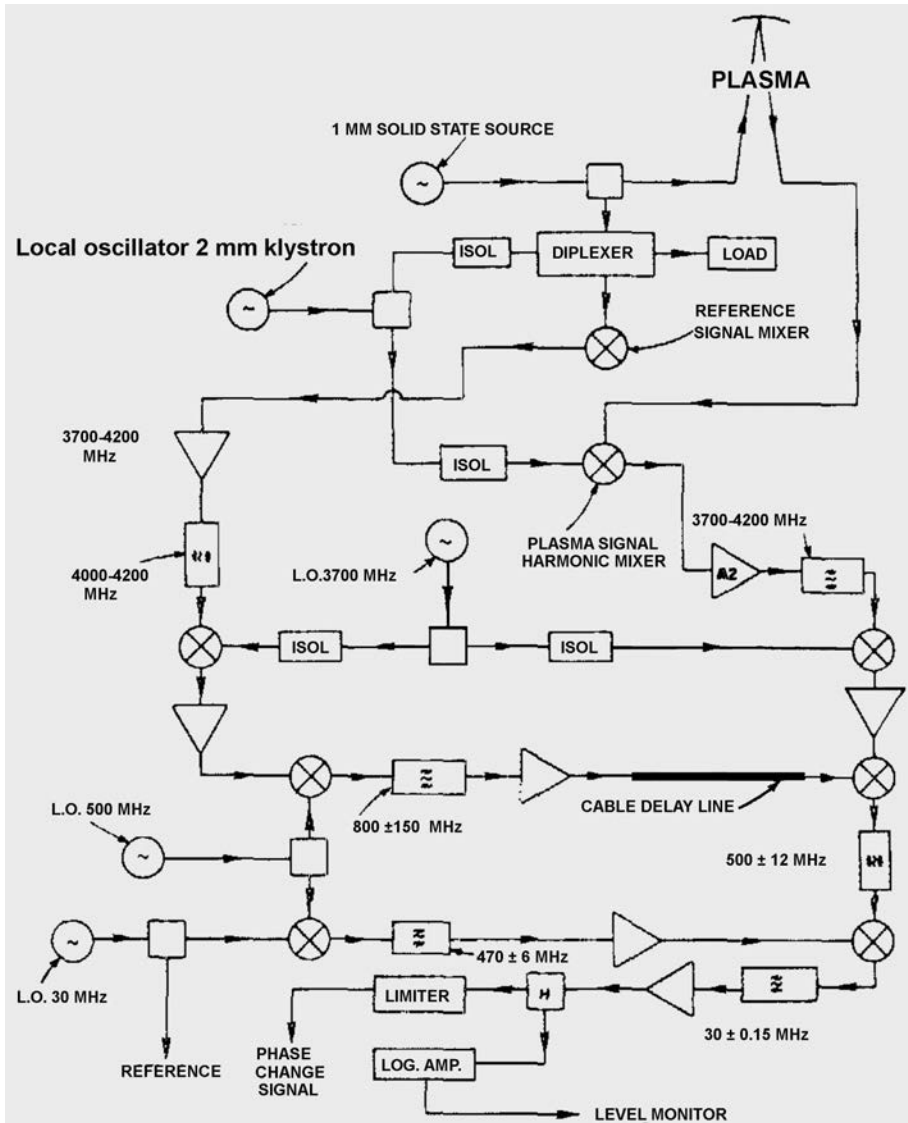


FIG. 4.59. Block diagram of the microwave and IF sections in the interferometer on TFTR (scanned from Ref. [4.414]). A superheterodyne feed forward tracking system provides immunity against frequency drift in the 1 mm transmitter and 2 mm local oscillator.

superheterodyne tracking circuit was adopted. An IF tracking network is used to offset frequency drifts in the transmitter and the local oscillator (LO). A second LO operating at 3.7 GHz is used to down convert the plasma and reference IF signals to a second IF nominally at 300 MHz. The reference signal still includes any frequency offsets in the transmitter or the 2 mm LO and this is up converted

by mixing with a 500 MHz LO. The up converted signal is passed through a band pass filter ( $800 \pm 150$  MHz) and a wide band amplifier to function as a LO for another mixer used to down convert the plasma signal. A coaxial delay line in the circuit compensates for the differences of signal delay due to the unequal lengths of the transmitter and reference paths. In this mixing stage, the offsets in the 2 mm LO and the 1 mm transmitter frequency are cancelled, leaving only the 500 MHz signal modulated by the density phase shift.

There was an additional down conversion at a third IF operating at 30 MHz. Both reference and phase change signals are processed through phase-lock-loop circuits and a fringe counter.

The signal from the interferometer is used to control the gas flow rate into TFTR to automatically maintain the pre-programmed waveform. The interferometer also provides a threshold density to prevent the neutral beams from firing when the plasma density is too low. The interferometer has been operated daily on TFTR and has provided data for confinement studies.

Multichannel [4.415, 4.416] and two dimensional phase imaging [4.417] microwave interferometers and microwave polarimeters [4.418] have also recently been developed and used successfully for plasma diagnostics in different plasma machines. The phase image method allows restoration of the plasma density profile without any prior assumptions about the symmetry of the plasma [4.417, 4.419].

#### 4.3.3.2.2. Laser interferometry and polarimetry

The application of multichannel interferometers that utilize far-IR (FIR) laser radiation became a standard diagnostic mean for measuring line-integrated electron densities along various chords through the plasma in current fusion experiments. The design of many existing laser instruments follows the principles outlined by Veron [4.398]. The simultaneous measurement of the Faraday rotation that the probing beams undergo can be achieved by an extension of the instrument and offers the possibility to determine the poloidal magnetic field in a tokamak [4.1]. Knowledge of the poloidal field and, hence, the profiles of the current and safety factor is important for studies of the transport, magneto-hydrodynamic stability and confinement properties of the plasma. Among the different methods, Faraday rotation measurements have proven their reliability and become a routinely operated diagnostic tool for many tokamak experiments (see, for example, the review articles [4.420, 4.421]).

A brief description of the multichannel FIR interferometer/polarimeter [4.422] installed on the TEXTOR tokamak will be presented below as an example to explain the basic features of interferometers of this type, including the typical phase detection principle and method of Faraday rotation measurement. This interferometer is a phase modulated Mach-Zehnder arrangement. The applied

light source is a continuous HCN laser with a wavelength of  $336.6 \mu\text{m}$  and a maximum output power of 150 mW. The wavelength is chosen to fulfil different conditions. It should be sufficiently large to give measurable effects, but has to be short enough to minimize beam deflection and elliptization.

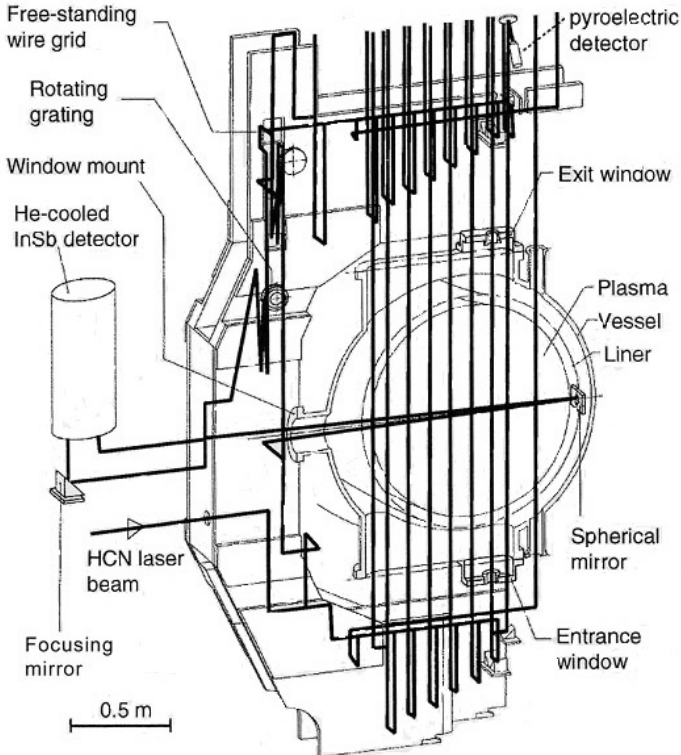


FIG. 4.60. Schematic view of the HCN interferometer/polarimeter. The line-integrated electron density and the Faraday rotation angles are measured along nine vertical and one horizontal lines of sight [4.422]. Reprinted from Ref. [4.422]. Copyright (2011), with permission from Elsevier.

Figure 4.60 shows a schematic diagram of the interferometer setup and the positions of the probing beams. The HCN laser beam is divided by crystal quartz beam splitters into the reference beam, nine vertical probing beams that cover nearly the whole poloidal cross-section of the plasma, and one horizontal beam (which passes through the plasma twice, because of reflection from a spherical mirror mounted on the liner). All of the optical components are mounted on a rigid, free standing C-shaped frame that embraces the vacuum vessel. The frame rests on one of the lower transformer yokes but is vibrationally isolated from the tokamak components. The reference beam that serves as a local oscillator for heterodyne detection is frequency shifted by 10 kHz utilizing the reflection

on a rotating grating. The probing waves are mixed with the local oscillator waves on the applied square-law detectors (pyroelectric crystals are used for the vertical channels). The signals from the horizontal channel are detected with an He-cooled InSb detector with improved time response to allow fast measurement of the polarimeter signal.

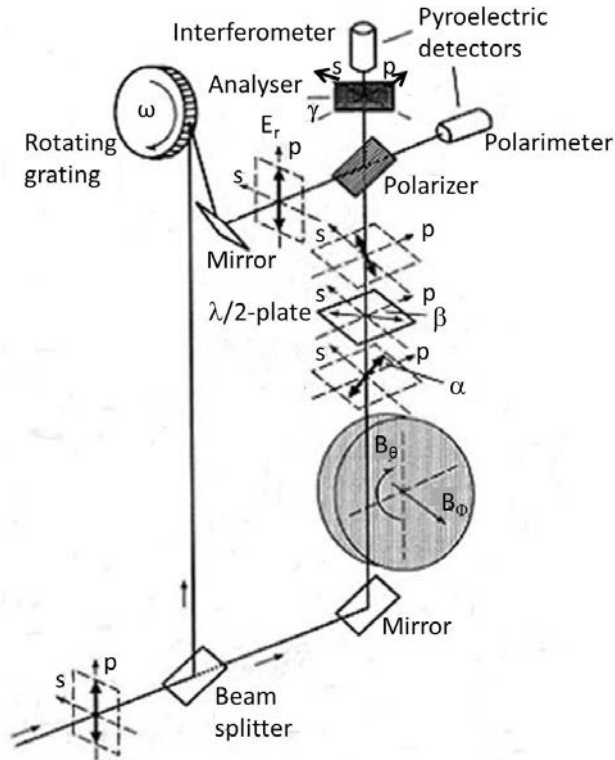


FIG. 4.61. Optical arrangement for one probing beam. The bold arrow indicates the polarization. After passage through the plasma, the components parallel and perpendicular to the original polarization of the probing beam are analysed [4.422]. Reprinted from Ref. [4.422]. Copyright (2011), with permission from Elsevier.

The optical arrangement for one probing beam is shown in Fig. 4.61. The polarization of the wave is indicated by the bold double headed arrows. On entrance into the plasma, the polarization is aligned perpendicularly to the toroidal magnetic field; on exiting it is slightly rotated by the Faraday effect, so it is no more perpendicular to the toroidal magnetic field. The polarizer combines the probing beam with the local oscillator beam, and simultaneously reflects the part of the signal which is polarized perpendicular to the beam onto the polarimeter detector. The  $\lambda/2$  plate in front of the polarizer serves to align the polarization so that the signal disappears in the absence of a plasma. The main

component of the probing beam is transmitted through the polarizer and mixed with the reflected part of the reference beam. Because both polarizations are oriented perpendicular to each other, and interference between these components is not possible, an analyser in a diagonal position is required to mix them and to make these waves interfere.

The interferometer signal is determined from a phase comparison of the beam signal from the detector with the output signal from a reference interferometer outside the vessel. The phase difference  $\Delta\varphi$  is measured either in real time, with an appropriate multi-fringe phase detector, or it is digitized and stored in memory. A phase resolution of  $0.01 \times 2\pi$  is achieved. The measurement of the polarimeter signal requires a more refined technique to determine the amplitude of this signal. Here, the application of a lock-in amplifier that uses the interferometer signal to detect the correct frequency component from the rather noisy signal, and a monitoring of the beam intensity allow a resolution of  $0.1^\circ$  for the Faraday rotation angle. Calibration of the signal is achieved by rotating the  $\lambda/2$  plate through well known angles.

#### 4.3.3.2.3. Two-colour interferometers

The choice of laser wavelength for future burning plasma experiments (ITER for example) must be made to avoid the refraction effect by a dense large plasma, and the Faraday rotation effect due to a large magnetic field, especially in the case of a tangential chord. A  $\text{CO}_2$  laser wavelength of  $10.6 \mu\text{m}$  is not as long as the FIR region where laser beams suffer much from the above effects, and is not as short as the visible region where laser beams are less sensitive to density change. Therefore, the  $\text{CO}_2$  laser is a suitable light source for the interferometry of burning plasma experiments. On the other hand, to complete a density measurement on large tokamaks by a two-colour system requires simultaneous measurements along the same optical path by a different wavelength interferometer in order to compensate for optical path length changes due to mirror vibration and displacement [4.423, 4.424]. For this purpose, a combination with an IR HeNe laser ( $3.39 \mu\text{m}$ ) has been proposed [4.425–4.427] as being preferable to a visible HeNe laser ( $0.633 \mu\text{m}$ ) from the point of view of avoiding a reduction of optical transmission through darkened mirrors and windows in a shorter wavelength region. Dual  $\text{CO}_2$  laser interferometer systems developed for JT-60U [4.426] and ITER [4.427] will be described below as examples of a two-colour scheme.

For the interferometer on JT-60U, the  $10.6 \mu\text{m}$  and  $3.39 \mu\text{m}$  combination system for a toroidally tangent line of sight [4.426] is used. This system has been successfully used for the central density measurement. However, there were several problems in the operation of this combination, including the following:

- (1) A darkening of windows and mirrors substantially decreased the return probing IR HeNe intensity. The signal-to-noise ratio of the IR HeNe interferometer was so greatly reduced that stable phase measurement became difficult.
- (2) The zero level of a calculated density trace often drifted on a time scale of several minutes. This indicates that there was a slight frequency difference between both beat signals and/or an unbalanced changing of the path length in two interferometers.

In order to resolve these problems, the system was modified to be a dual CO<sub>2</sub> system which uses close wavelengths of 10.6 μm and 9.27 μm. Though this close-wavelength combination causes a reduction of density resolution compared to the combination of 10.6 μm and 3.39 μm wavelengths, this system provides many advantages, including a better robustness to the darkening of vacuum windows and mirrors, a better capability for large mechanical vibration and the displacement of reflection mirrors, and ease of laser beam monitoring. Furthermore, the layout of optical components is simplified by using the close wavelengths of the CO<sub>2</sub> oscillators. Additionally, a new technique using a single frequency shifter, the acousto-optic modulator, in common for different wavelength lasers has been developed. This technique contributes to suppressing the zero-level drift by completely matching both beat frequencies.

It is important to note that two-colour interferometer made it possible in principle to avoid using vibration insulation structures encompassing the torus. The basic optical components of the interferometer on JT-60U for example are placed on a vibration isolated bench. Only the relay mirrors, windows and cube-corner-reflectors are installed on the parts of vacuum vessel and transformer yoke. This important circumstance and the performance achieved show the feasibility of the dual CO<sub>2</sub> laser interferometer for future burning plasma devices such as ITER.

In order to measure the line integrated electron density on ITER, a vibration-compensated five-channel CO<sub>2</sub> laser interferometer/polarimeter system has been developed [4.39]. The design of the interferometer/polarimeter has been improved on the basis of experience gained with the dual system on JT-60U. The line density resolution of the interferometry is  $\sim 0.5 \times 10^{19} \text{ m}^{-2}$  for a time resolution of 1 ms. The Faraday rotation is measured with a good angle resolution of  $\sim 0.01^\circ$  with a temporal resolution of 1 ms.

#### 4.3.3.2.4. Recent progress in interferometry and polarimetry

Lately, the method of an interferometry has gone through much development, progressing basically in the following directions:

- Improvement of the spatial resolution;
- Increase of time resolution;
- Improvement of insensitivity to vibrations.

The first interferometers were single-channel instruments [4.395–4.397]. In more recent works improvement of the spatial resolution was reached by increase in the number of discrete channels [4.404, 4.405], by spatial scanning of a probing beam [4.401–4.403], or by shaping of an extended section of the probing beam and the application of matrices (lines) of detectors (building-up of the phase image of the plasma) [4.406, 4.419]. Modern and future fusion devices present ever increasing requirements to diagnostic systems. These are: higher stability of diagnostic system operation under conditions of strong radiation loadings, capability to operate in conditions of rather restricted access to the plasma (because of a blanket and biological protection) and capability to function under conditions of an incremental level of vibrations.

In order to reduce the influence of vibrations, several solutions are commonly applied:

- (1) Mounting of optical elements on massive vibration isolation structures (e.g. C-shaped rigid frames encompassing the torus);
- (2) Use of far infrared probe radiation (118  $\mu\text{m}$ , 337  $\mu\text{m}$ , see for example Ref. [4.422]);
- (3) Application of two-colour interferometers that are a combination of two traditional interferometers operating on different probe radiation wavelengths (see for example Refs [4.428, 4.429]).

The first solution has a serious disadvantage. It will be almost impossible to realize an interferometer system based on a rigid frame on large future devices for burning plasma experiments. This conclusion came from the basic design requirements: the necessity to use labyrinths in neutron shielding blocks mounted in diagnostic ports and the impossibility of using pairs of opposite ports for light guiding. The second and third solutions allow us in principle to develop a frameless interferometer. The use of longer wavelengths is constrained by the influence of refraction, since a steep plasma density gradient is a known feature of modern plasma devices. A two-colour diagnostic is deemed to be quite complicated and the task of finding simpler and more cost effective alternatives is still important.

The problem of reliability of density measurements is critical for ITER and other large facilities due to the necessity of operation with lengthy (more than 500 s) impulses, especially in applications regarding density data for fuel control or for plasma column position control. Use for this purpose of classic methods measuring the time history of probing wave phase in major facilities

meets particular difficulties, because the reliability of methods operating with conventional phase measurements (classic interferometers and phase reflectometers) in an “on-line” mode of operation is quite often insufficient due to the fact that these measurements are unique only in the  $0-2\pi$  range. This is especially true for facilities with high plasma density, when the phase changes are large, and also under conditions of lengthy discharges, when recently developed algorithms for the elimination of phase jumps [4.430, 4.431] will be insufficient. In order to have authentic measurements, the rate of density variation has to be less than its maximal value defined by the condition:

$$\frac{d(\Delta\varphi)}{dt} \leq 2\pi\Delta f \quad (4.37)$$

where  $d(\Delta\varphi)/dt$  is the rate of phase variation caused by the density variation, and  $\Delta f$  is the frequency bandwidth of the interferometer under consideration, given basically by the intermediate frequency of the interferometer. For instance, on JET during pellet experiments, the rate of density variation is too high (more than one fringe ( $\sim 10^{19} \text{ m}^{-3}$ ) of phase in  $10 \mu\text{s}$  in the DCN interferometer ( $\lambda = 195 \mu\text{m}$ )), the intermediate frequency of the DCN interferometer being equal to 100 kHz, and band-pass filters with  $\Delta f = 80 \text{ kHz}$  (60–140 kHz) being used [4.430, 4.432].

So particular difficulties arise with fast plasma density variations, connected, for example, with pellet injection of fuel, the development of MHD oscillations, etc. It is necessary also to note that the need in classical phase interferometers of vast access to the plasma, and of build-up of the bulky bypass reference channel that essentially complicates the system, results in the necessity to use a rigid mechanical frame for diminution of the vibration level and this increments the cost of the diagnostics system. Therefore, a remaining outstanding problem is to develop reliable methods of measuring the mean plasma density and spatial distribution of density with better stability against vibrations and radiation loadings while maintaining a simple optical scheme and not requiring vast access to plasma.

Within the framework of the solution of this problem, procedures are available permitting basic improvement to insensitivity to vibrations. This is especially important as the density and the sizes of plasmas in tokamaks are increasing. For reducing refraction it is necessary to use probing in the sub-millimetre and infrared range, which increases the sensitivity of the method to vibrations. With this aim, double-frequency interferometers are now widely applied. They consist of two probing beams (having essentially distinct wavelengths) which transit along the same path. This makes it possible (after corresponding treatment of the signals obtained) to greatly diminish the influence of vibrations on plasma density measurements [4.423].

A so-called dispersion interferometer using simultaneous probing of a plasma by basic and second harmonics of laser radiation in the optical or IR ranges was recently proposed [4.433, 4.434] and tested in tokamaks [4.435–4.438]. This method makes it possible to reduce the sensitivity of an interferometry to vibrations.

#### 4.3.3.2.5. Dispersion interferometers

The probing and reference channels of a dispersion interferometer (DI) [4.433, 4.434] have the same geometrical path, but they are separated in frequency. This feature determines the key advantage of the DI: the measured phase difference is determined in principle only by the dispersion of the medium and independently of the interferometer path length. Dispersion interferometers based on a Nd:YAG laser ( $\lambda = 1.06 \mu\text{m}$ ) were developed and successfully used for nuclear fusion experiments [4.435, 4.436, 4.438]. However, it is advantageous to use a longer wavelength in the  $\text{CO}_2$  emission region ( $\gg 10 \mu\text{m}$ ) to gain a higher sensitivity to plasma dispersion and a lower sensitivity to the coatings of windows and mirrors placed inside the vacuum vessel of the device.

A single-channel prototype of the DI based on a continuous-wave  $\text{CO}_2$  laser was developed for measurements of the line-integrated electron density in the TEXTOR tokamak (Forschungszentrum Jülich, Germany) and the GDT mirror device (Budker Institute, Russian Federation) [4.438]. The DI was successfully tested in various experiments. A sensitivity of  $\langle n_e l \rangle_{\text{min}} = 2 \times 10^{17} \text{m}^{-2}$  and a temporal resolution of 1 ms have been achieved. The main advantages of the dispersion interferometer, high sensitivity to plasma dispersion and low sensitivity to vibrations, allowed an the optical layout with double plasma passage utilizing a corner cube retro-reflector. The optical elements of the DI are installed on a compact optical bench placed outside the plasma torus.

A schematic drawing of the optical system of the DI mounted on TEXTOR is shown in Fig. 4.62. Two mirrors (3a and 4a) focus radiation from the  $\text{CO}_2$  laser (2a) on to the non-linear crystal (5a) which converts the radiation at the fundamental frequency partially to the second harmonic. The dimensions of the  $\text{ZnGeP}_2$  non-linear crystal are  $5 \times 5 \times 5 \text{mm}$ . The beam containing radiation at both wavelengths is then directed to the spherical mirror (7a) which adjusts the beam waist to allows it to travel a long distance without any significant change of diameter. The laser beam then passes through two optical wedges (11a). Their function is to tune the interferometer to the maximum sensitivity. Mirror (3) is used to reflect the beam into the TEXTOR vacuum vessel through a plane-parallel  $\text{BaF}_2$  window (2) which has a wedge of  $< 20''$ . After passing once through the plasma, it is reflected by a hollow corner cube reflector (1). The incident beam is displaced relative to the centre of this reflector. Consequently, the reflected beam does not coincide spatially with the incident beam but propagates in parallel through

the optical system in the reverse direction. After the second passage through the plasma, the beam enters again the non-linear crystal where the remaining fundamental harmonic radiation is partially converted to the second harmonic. As a result, the beam contains three components of radiation: the first harmonic, the second harmonic produced before the first passage through the plasma, and the second harmonic produced after the second passage through the plasma. A mutual lateral displacement of the forward and backward beams allows the backward beam to be separated from the forward beam on the focusing mirror (4a) which was cut into two equal parts and one half removed. The forward beam is focused onto the crystal by the half mirror, whereas the backward travelling beam passes through the space corresponding to the removed half of the mirror and is focused by lens (9a) onto the photo detector (10a). An entrance window made of sapphire ( $\text{Al}_2\text{O}_3$ ) is used to absorb the radiation at the fundamental frequency. Almost all optical elements are arranged on the optical table (1a), except the retro-reflector, which is attached to the upper diagnostic port outside the vacuum chamber (see Fig. 4.62), and the mirror (3), which is attached to the transformer yoke.

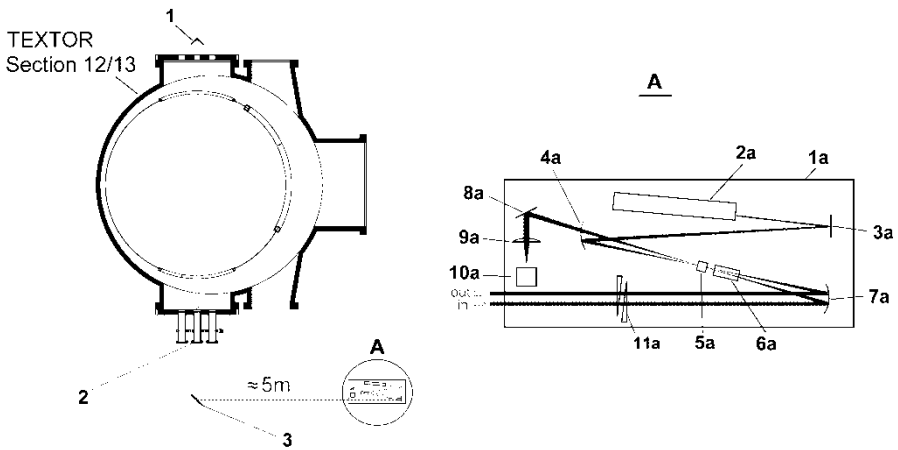


FIG. 4.62. Left: Dispersion interferometer on TEXTOR: 1 – hollow retro-reflector, 2 –  $\text{BaF}_2$  window with diameter  $d = 1.5$  inches ( $d = 3.8$  cm), 3 – additional turning mirror. A (zoomed on the right): optical bench with DI elements. 1a – optical table, 2a –  $\text{CO}_2$  laser, 3a – plane mirror, 4a – half mirror ( $r = 0.5$  m), 5a – frequency doubler crystal, 6a – electro-optic cell, 7a – mirror ( $r = 1$  m), 8a – plane mirror, 9a – focusing lens, 10a – photo detector, 11a – optical wedge [4.438]. Reprinted from Ref. [4.422]. Copyright (2011), with permission from Elsevier.

A photo detector (10a) measures the intensity of the SH radiation. This detector has its maximum spectral sensitivity close to the second harmonic wavelength ( $\sim 5 \mu\text{m}$ ). The photo detector records a signal proportional to the sine of the phase shift in the plasma. Since the sine is not a monotonic function, the phase change can be reconstructed unambiguously only within the limited

region of the linear plasma density where the sine of the phase change remains monotonic. This would restrict the range of applicability of the interferometer to measurements of line-integrated electron densities smaller than  $10^{19} \text{ m}^{-2}$ .

In order to overcome this limitation, several improvements of the interferometer scheme and signal processing were introduced. The method of initial radiation phase sweep, which is similar to the well known *zebra stripes* method [4.395–4.397], was applied. An electro-optical cell (EOC, 6a in Fig. 4.62) which changes the phase incursion for one of the passing waves with a frequency  $\omega = 250 \text{ kHz}$  was placed in the beam path. The detector signal is digitized and stored in the local buffer memory. The phase reconstruction algorithm is programmed in the field programmable gate array (FPGA). Usage of a FPGA for signal processing enables a guaranteed real-time rate of output  $\langle n_l \rangle$  values calculation. This approach also gives flexibility to change programmed calculation algorithms. The real time data processing module delivers the output signal via the serial fiber line to the remote signal conditioning rack connected to TEXTOR engineering systems controlling gas-puff valves and correction magnetic coils. The maximal temporal resolution of the measurements is  $4 \mu\text{s}$ . The possibility to control plasma density using the reference signal from DI was successfully demonstrated in experiment. The modification of the basic layout of a DI for multi-chord measurements is quite obvious and it does not require any additional complicated technologies for its realization.

For plasma density determination, it is also proposed to use a plasma polarimetry — measuring the Faraday effect and the Cotton–Mouton effect in the plasma. The polarimetry, basically, is insensitive to vibrations (longitudinal), as both interfering waves transit along the same optical trajectories. As is well known, the angle of rotation of the plane of polarization of probing radiation in a plasma (Faraday effect) is proportional to the product of the plasma density and the magnetic field component parallel to the probing direction. In the case of sounding along the toroidal magnetic field, the Faraday effect will be determined basically by the product of the plasma density and the toroidal field, which is well known in tokamaks [4.439]. Successful measurements of density by a Faraday polarimeter with sounding in the IR range have been conducted [4.440]. A Faraday polarimeter for density measurements is projected to be used on ITER [4.108].

#### 4.3.3.2.6. Cotton–Mouton polarimetry

Measurements of the Cotton–Mouton effect for determining plasma density have been suggested and tested on the T-11M tokamak. For this purpose, the method of a multi-chord Cotton–Mouton polarimetry [4.441, 4.442] was developed, based on measuring the “linear” birefringence of a plasma — the difference in phase between two linearly polarized components of probing

radiation — one parallel to the magnetic field in the tokamak, and the other perpendicular to it. This difference in phase  $\Delta\varphi_{o,e}$  (the subscripts “o” and “e” relate to the ordinary and extraordinary waves, respectively) is defined by the formula [4.398]:

$$\Delta\varphi_{o,e}(\omega, x) = \frac{\omega}{c} \cdot \int_l \Delta\eta_{o,e}(\omega, x, z) dz \approx 2.45 \cdot 10^{-11} \cdot \lambda^3 \cdot B_\phi^2(x) \cdot \int_l n(x, z) dz \quad (4.38)$$

where  $\Delta\eta_{o,e}$  is the difference between the refractive indices for the ordinary and extraordinary waves and  $\lambda$  is the wavelength of the probing wave. Here, we take into account that, for a tokamak, the poloidal field is  $B_\theta \leq 0.1B_\phi$ , and the total magnetic field  $B$  is replaced with the toroidal magnetic field  $B_\phi$ . By proper choice of the wavelength  $\lambda$ , the phase shift in the plasma can be made less than  $2\pi$  [4.441]. The typical scheme of a Cotton–Mouton polarimeter in T-11M is given in a Fig. 4.63. The modulating voltage was applied from a sawtooth voltage oscillator stabilized by a quartz resonator to the control input of a 15 mW tunable impact ionization avalanche transit time (IMPATT) oscillator operating at a frequency of nearly 140 GHz. To obtain two mutually perpendicular and frequency-shifted components of probing radiation, a microwave delay line (DL) consisting of a grid polarization beam splitter (PBS), two corner reflectors

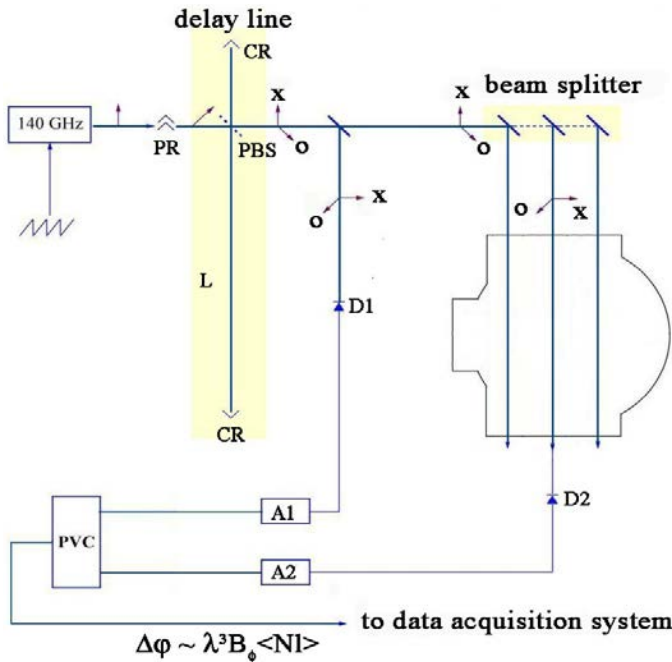


FIG. 4.63. The Cotton–Mouton polarimeter arrangement on T-11M. PR is polarization rotator; D1 and D2 are detectors of the reference and signal channels; A1 and A2 are the amplifiers; PVC is the phase-to-voltage converter [4.442].

(CR) and a segment of the transmission line (L) have been used. The frequency-shifted components have been used to transform the phase difference to an intermediate frequency. To obtain a signal at the intermediate frequency, it is sufficient to orient the polarization planes of the antennas of detectors D1 and D2 at an angle of about  $45^\circ$  to the toroidal magnetic field. In this case, the phases of the beat signals in the quadratic detectors will be equal to the phase difference between the ordinary and extraordinary waves. The signal from detector D1 is a reference signal, whereas the signal from detector D2 is a measured signal. In this way, we avoid the influence of oscillator frequency instability on the results of the measurements. In this scheme, the propagation path of the two probing waves outside the plasma is the same after the delay line DL. Consequently, the influence of vibrations of the vacuum chamber and antenna feeder on the results of measurements is also avoided. Probing was performed along vertical chords. Schottky barrier diodes were used as mixers.

This method is largely free from the above mentioned deficiencies of classic phase methods. The stability to phase jumps is ensured by selection of the carrier frequency of the probing wave so that the resulting phase shift in the plasma does not exceed  $2\pi$ ; that is easily enough reached owing to the strong (cubic) dependence of the measured phase difference on the carrier frequency of the probing wave.

Recently, the Cotton–Mouton polarimetry method was tested also on other facilities, namely the W7-AS stellarator in Germany [4.443, 4.444] and CHS in Japan [4.445]. It is being intensively developed on JET [4.432, 4.446] and it is also proposed to be used in ITER [4.108]. The distinctive feature of the method is a simple optical scheme, due to the absence of a bulky bypass tract for the reference channel, and rather simple access to the plasma. At T-11M, the refractometry method using an ordinary wave for plasma density measurements was proposed and tested [4.447, 4.448]. This method is based on measuring an acyclic quantity — the time of propagation of a wave through the plasma — uniquely interlinked to the line density. It should be noted that successful measurements of the mean plasma density with the help of a pulse time-of-flight refractometer have been produced also by extraordinary wave probing in the FTU tokamak [4.449]. During these experiments in FTU, densities of about  $10^{20} \text{ m}^{-3}$  (up to a cut-off) have been measured when the probing frequency was 60 GHz. So the upper limit of measured density is expanded approximately by one order of magnitude compared to ordinary wave probing (under the conditions of FTU, with a toroidal magnetic field  $B_\phi = 6 \text{ T}$ ).

Plasma refractometry has the following attractive properties. Firstly, the measured absolute time delay of a signal which has passed through the plasma is free from phase jumps, which allows unique treatment of the data obtained. Secondly, the influence of parasitic reflections in the transmitting tracts and in the tokamak chamber is eliminated by filtration such as with a “time window”.

Thirdly, the use of relatively low probing frequencies (operation near the cut-offs) makes it possible to avoid the “first mirror problem”, which gives an opportunity to increase the precision of measurements allowing for the influence of the density profile on the results obtained. The distinctive feature of the method is a simple optical scheme, due to the absence of a bulky by-pass tract for the reference channel, and rather simple access to the plasma. X-mode refractometry permits the use of lower frequencies for plasma probing, allowing rather easy solution of the problems of radiation stability of the vacuum windows and other elements.

In summary, we may note that on ITER it is proposed to conduct polarimetric measurements of both the Faraday and Cotton–Mouton effects. Together with interferometry this will make it possible to derive complete information about both the electron density profile and the profile of the poloidal magnetic field in the plasma [4.108, 4.450].

#### 4.3.3.3. Plasma reflectometry for electron concentration profile measurements

Reflectometry is one of the rapidly upcoming methods of fusion plasma diagnostics [4.451, 4.452]. One of the main achievements of recent reflectometry is its transition from a diagnostic under test status to a routine density profile diagnostic. As mentioned above, the method is based on the effect of the total reflection of probing radiation with carrier frequency  $f$  from a plasma layer where the refractive index is equal to zero (cut-off condition). In principle, both the ordinary mode (O-mode) (with its electric field parallel to the external magnetic field) and the extraordinary mode (X-mode) (with its electric field perpendicular to the external magnetic field) may be employed in reflectometry [4.392]. Cut-off of the ordinary mode occurs when the following condition is satisfied:

$$f = f_{pe} = \frac{1}{2\pi} \cdot \sqrt{\frac{n_e(r) \cdot e^2}{\epsilon_0 m_e}} \quad (4.39)$$

where  $f_{pe}$  is the electron plasma frequency,  $n_e(r)$  is local plasma electron density,  $\epsilon_0$  is permittivity of free space,  $m_e$  is the electron mass, and  $e$  is the charge of the electron. Cut-off of the extraordinary mode occurs when either of the following conditions is satisfied:

$$f^2 = f_{pe}^2(r) - \omega_{ce}^2(r) \quad (\text{low cut-off}) \quad (4.40)$$

$$f^2 = f_{pe}^2(r) + \omega_{ce}^2(r) \quad (\text{high cut-off}) \quad (4.41)$$

where  $f_{ce}(r) = (1/2\pi)(eB(r)/m_e)$  is the electron cyclotron frequency, and  $B(r)$  is the magnetic field. After reflection, the wave at the output of the plasma will have phase shift  $\varphi$  with respect to the incident wave:

$$\varphi_{O,X} = \frac{2\omega}{c} \int_0^{r_{\varepsilon=0}} \eta_{O,X}(\omega, r) dr - \frac{\pi}{2} \quad (4.42)$$

where  $O$  and  $X$  note ordinary and extraordinary modes, respectively,  $\eta$  is the refractive coefficient and  $\omega = 2\pi f$  is the angular carrier frequency. Thus, it is possible to obtain information about the plasma density profile and reflective layer dynamics by measuring the phase shift at several different frequencies.

The foregoing considerations refer to monochromatic probing waves. Reflectometry measurements have been conducted since the beginning of magnetic confinement studies [4.397]. The techniques used were very similar to conventional microwave interferometers [4.396]. Now this approach could be called “narrow-band sweep reflectometry with phase measurements”.

A main feature of phase measurements is the cyclic nature of the phase function. The measurements have a unique meaning within the range of values from 0 to  $2\pi$  only. This fact could lead to considerable uncertainties in determining the distance to the reflecting layer in a real plasma experiment. To overcome this, it is convenient to use the group time delay of the wave propagating through the plasma. In this case, the distance up to the reflection layer can be determined by measuring the propagation time of microwave radiation up to the point of reflection and return. This group time delay  $\tau$  can be measured directly (pulsed radar-reflectometer), or through the relationship:

$$\tau = \frac{d\varphi}{d\omega} \quad (4.43)$$

where  $\varphi$  is the phase and  $\omega$  is the angular frequency of the probing wave (phase reflectometer with continuous microwave radiation, either sweep or fixed frequency).

Reflectometry, as a rule, provides better localization of the measurements, in contrast to plasma interferometry. With probing by an ordinary wave:

$$n = (0.0111f)^2 \quad (4.44)$$

where  $n$  is the electronic density of the plasma in units of  $10^{14} \text{ cm}^{-3}$  and  $f$  is the probing frequency in GHz.

To make an assessment of plasma reflectometry, let us look at Fig. 4.64, where cut-off frequencies are shown as a function of plasma radius assuming a parabolic plasma density profile. For this figure the parameters of T-11M (traditional tokamak with limiter configuration in TRINITY, Troitsk, Russian

Federation) have been used:  $a = 25$  cm,  $R_0 = 70$  cm,  $I_p = 100$  kA, toroidal field distribution  $B(r) = B_0 R_0 / (R_0 + r)$ , electron density distribution  $n(r) = n_0 [1 - (r/a)^2]$ .  $\theta$  indicates local values of parameters at the centre of the plasma column:  $B_0 = 1.2$  T,  $n_0 = 4.5 \times 10^{13}$  cm<sup>-3</sup>.

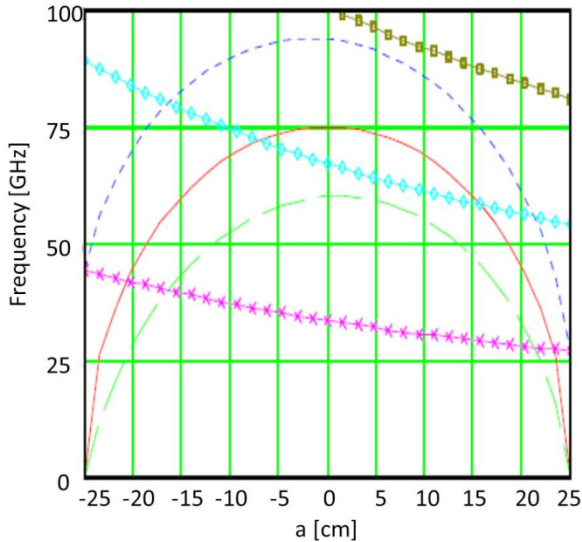


FIG. 4.64. Resonances and cut-offs for typical T-11M tokamak regime. Plasma frequency – solid red line; X-mode lower cut-off – dashed green line; X-mode upper cut-off – dark blue dotted line; electron cyclotron frequency – magenta (x) line; 2nd harmonic of the electron cyclotron frequency – light blue ( $\diamond$ ) line; 3rd harmonic of the electron cyclotron frequency – khaki ( $\square$ ) line. Imported from Ref. [4.459].

It can be seen that the plasma in T-11M is transparent for frequencies higher than 75 GHz (O-mode) and also 90 GHz (X-mode). Below these frequencies it is possible to use reflectometry on both O- and X-modes from the low field side (LFS) and high field side (HFS). A relative complication in X-mode use is that the position of the reflecting layer depends not only on the electron density, but also on the local value of the total magnetic field. Nevertheless, it might be convenient to use X-mode probing in case of necessity to distinguish the plasma central region or improve the spatial resolution by use of shorter wavelengths in upper cut-offs.

In the transparency area of the plasma, there are absorption lines in the vicinity of the electron cyclotron frequency and its harmonics. The value of the absorption coefficient depends on the local plasma electron temperature and local electron concentration. The non-Maxwellian behaviour by the **electron velocity distribution function** could also have an influence on the absorption (runaway electrons). The absorption could be expressed in terms of the optical thickness

in the cyclotron resonances field [4.394]. It should be noted that for higher harmonics the optical thickness is diminished.

In the case of high electron temperatures (ITER), this absorption could seriously affect the access to plasma due to significant relativistic widening of resonance regions. Moreover, relativistic effects will seriously modify the cut-offs and transparency areas of the plasma [4.108, 4.453] (see Fig. 4.65).

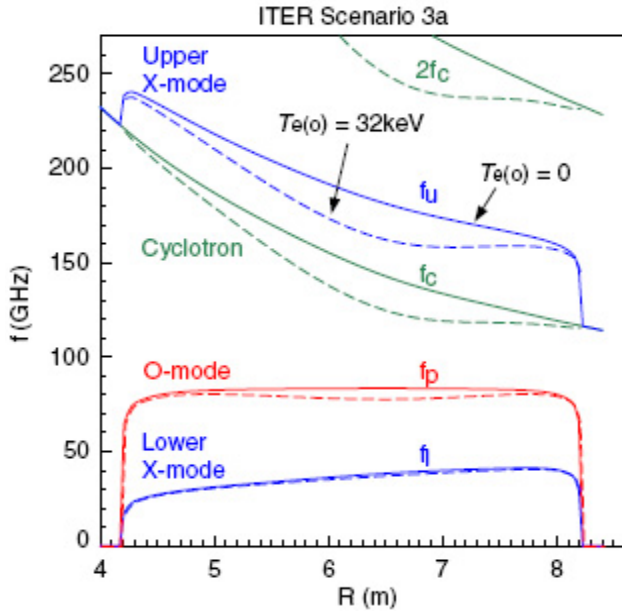


FIG. 4.65. Cut-offs and resonances for the ITER standard 3a scenario ( $I_p = 13.8$  MA,  $n_e = 0.93 \times 10^{19} \text{ m}^{-3}$  and  $T_e = 32$  keV) with non-relativistic ( $T_e = 0$ ) and relativistic correction ( $T_e = 32$  keV) [4.108].

Other obstacles to the assessment are caused by the shape (practically flat) of the density profile in the ITER H-regime. Under these conditions, only the lower X-mode cut-off observed from the HFS will offer the possibility to reach the plasma central area by using frequencies in the range 30–60 GHz for different regimes. This is another example of the necessity to use X-mode rather than O-mode probing.

Nevertheless, in ITER reflectometry will be used to measure density profiles, density fluctuations and plasma position (understood as the position for a given density layer) [4.108]. The reasons why great attention is being given to the reflectometry application in ITER are the high spatial and time resolution of the method and also its relative insensitivity to the so-called “first mirror problem” (degradation of in-vessel optical component under a high neutron flux). In this case, all the possible ways of probing will be involved: HFS and

LFS, both O-and X-modes and also probing in some additional (non-horizontal) directions and in different tokamak cross-sections. Besides that, there is a rather wide spectrum of tools and methods based on the principles of reflectometry for tokamak plasma diagnostics. Most of them use measurements of the phase of a continuous probing wave. Thus, as was already mentioned, the measurements have an unambiguous meaning only within the range of values from 0 to  $2\pi$ . This often gives considerable difficulties in the interpretation of data when such effects, as “loss of coherence” [4.453, 4.454] and “phase runaway” [4.455] occur. On the other hand, the use of short microwave pulses for plasma probing with follow-on measurement of group time delay of reflected pulses [4.456] reveal opportunities to overcome these problems.

Direct measurements of time delay are implemented in a relatively new method of pulsed radar-reflectometry. Pulsed radar has a series of remarkable features compared to continuous wave reflectometers:

- (1) Undesirable retro-reflections of the probing signal in the antenna-waveguide channel and also inside the vacuum chamber of a tokamak can be easily filtered by a pulse technique and thus do not introduce essential errors into the measurements.
- (2) It is possible to consider plasma fluctuations and the plasma itself as “frozen” during the time period of a single measurement ( $\sim 2a/c$ ), which means that pulsed reflectometry can also be used for a non-stationary plasma.
- (3) Measurements of time delay have an absolute nature (compare with the phase method).
- (4) Incidental losses (fading) of the probing signal do not entail a complete loss of information, as such events can be eliminated from consideration, since each reflected pulse carries complete information on a reflecting layer of the plasma.

The first measurements by single-frequency pulsed radar-reflectometer were conducted on the T-11M tokamak [4.457]. The first density profile measurements with the help of four-frequency pulsed system were conducted on START [4.458]. The basic scheme of a single-frequency pulsed radar-reflectometer is shown in Fig. 4.66.

In this relatively simple tool, a stable continuous microwave oscillator MO provides microwave power at a single frequency of 32.1 GHz. MO is connected with the pulse microwave amplifier MPA through the isolator I. After MPA, a powerful microwave pulse ( $\sim 50$  ns duration) passes to the amplitude modulator M in order to get the desired parameters of a short ( $\sim 5$  ns) microwave pulse with a rise time less the 2 ns. This pulse goes to the antenna and then to the plasma (where it is reflected). After the receiving antenna, the pulse passes on

to the detector D, where a video signal proportional to the microwave power is produced. Thus, the signal STOP is obtained. The signal START is obtained from the control signal oscillator (CSO), which controls and synchronizes the whole system. The START and STOP signals are elaborated by the time-to-voltage converter TVC, where a voltage  $U$  proportional to the round trip time of the microwave pulse in the plasma is developed. This voltage is then recorded by the data acquisition system.

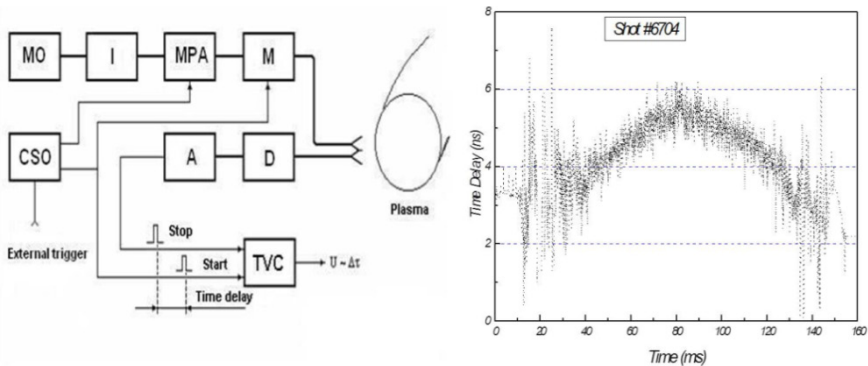


FIG. 4.66. Left: Scheme of pulsed radar-reflectometer on T-11M. MO is a stable continuous microwave oscillator with frequency of 32.1 GHz, I is an isolator, MPA a microwave pulse amplifier; M an amplitude modulator; D a signal detector, A a pulsed amplifier; CSO a control signal oscillator and TVC a time-to-voltage converter. Right: Raw data from T-11M pulsed radar. (Imported from Ref. [4.459].)

However, the density profile of a plasma was first obtained by reflectometry by evaluation of the time delay from the measured dependences of phase shifts for different frequencies, not from direct measurements of the time delays of signals of corresponding frequencies.

As an example, let us consider the swept reflectometer which was used on TFR [4.392] (Fig. 4.67). In this tool, X-mode probing in the vertical direction was used for density profile measurements.

A BWO was swept over the frequency range 75–110 GHz in 5 ms to explore densities between  $7 \times 10^{13} \text{ cm}^{-3}$  and  $1.5 \times 10^{14} \text{ cm}^{-3}$  (this corresponds to a scan across approximately one-half of the plasma radius of TFR). The microwave power wave was divided into two parts by a directional coupler: a reference beam and a beam directed along a vertical chord in the plasma by the emitting horn. The reference beam propagates through a delay line whose length is chosen to compensate for the change of phase that the transmitted wave undergoes through the microwave components on the other arm of the reflectometer (waveguide, horns, vacuum windows, etc.) The reflected wave is received by a separate horn and mixed with the reference beam in a wide band Schottky diode where the beat

frequency  $f_b(t) = (1/2\pi) \cdot (d\phi/dt)$  of the order of 30 kHz has been recorded with an accuracy  $\sim 5\%$ .

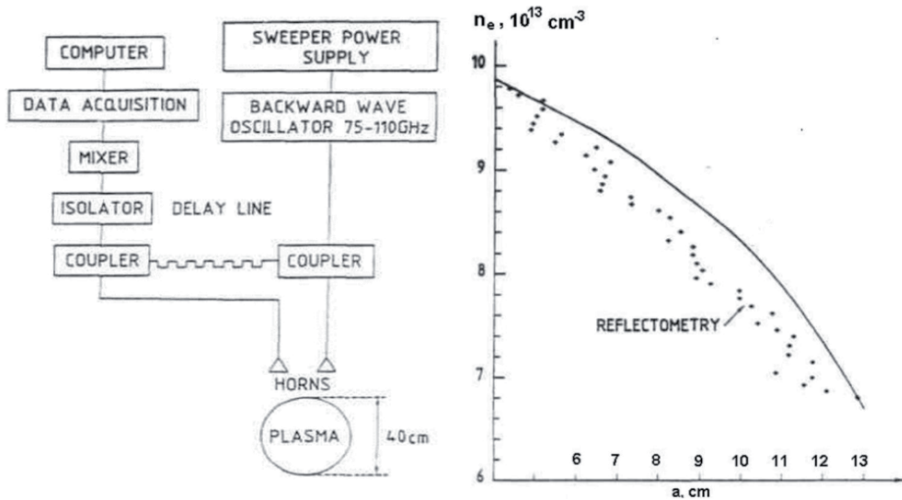


FIG. 4.67. Left: Schematics of the reflectometer on TFR. Right: Density profiles obtained by the microwave reflectometer (dots) and by the interferometer (solid line) at  $t = 250$  ms with a horizontal displacement of  $+1$  cm. Taken from Ref. [4.392]. Reprinted from Ref. [4.392]. Copyright (2011), American Institute of Physics.

The profile obtained is shown on the right side of Fig. 4.67. The results are compared with those given by the multichannel interferometer. Each point given by the reflectometer corresponds to one oscillation in the beat signal. The great number of fringes in a sweep permits accurate determination of the density profile behaviour by the reflectometry technique.

Broadband sweep reflectometry is now a routine diagnostic tool on many tokamaks [4.460–4.463] due to its very attractive spatial and temporal resolution. At the same time, there are a number of problems mainly concerning plasma fluctuations, which frequently restrict the opportunities for density profile reconstruction from the data obtained. First, density fluctuations can bring strong modulation of the amplitude and phase of the reflected wave that recalls such effects as “phase runaway”, “loss of coherence” and simply signal loss because of the declination of a reflecting layer or interference effects [4.464]. In the case of the phase method of data recording, it is highly probable that there will be unavoidable uncertainties in phase with values of multiples of  $2\pi$ , which, generally speaking, are not always possible to remove or to restore correctly. Examples of successful application of FM reflectometers for density profile measurements on modern tokamaks are given in Refs [4.465, 4.466] (broad-band sweeping) and [4.457] with narrow-band frequency modulation.

It should be noted that both broad band FM and pulsed radar methods are under consideration for the ITER HFS reflectometer application, which is designed to measure the density profile. A proposed schematic of the HFS reflectometer system in ITER is shown in Fig. 4.68.

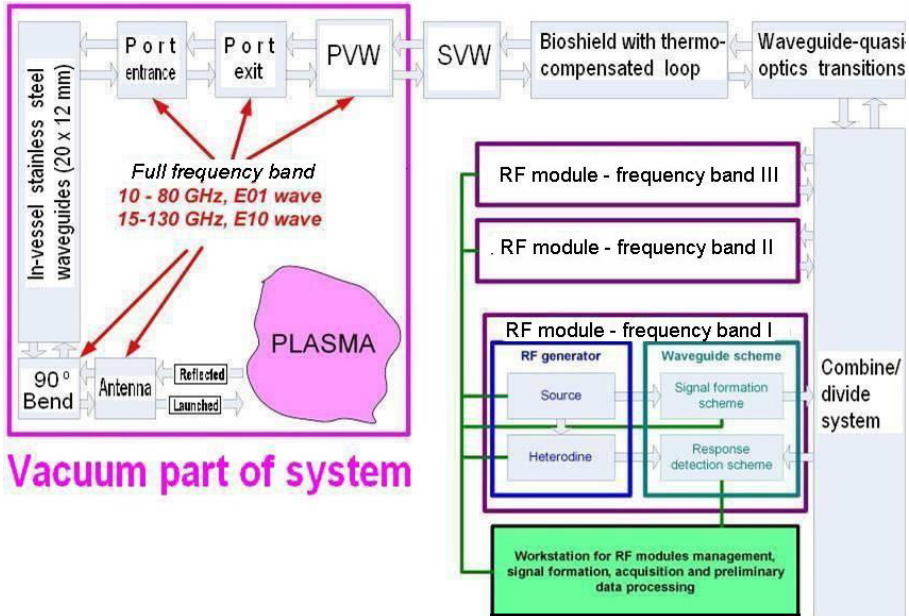


FIG. 4.68. Proposed schematic of HFS reflectometer in ITER: PVW – primary vacuum window; SVW – secondary vacuum window, port exit – 40° bend, port entrance – 40° waveguide bend. The system is designed to work on both O- and X- modes [4.467].

It is well known that an HFS reflectometer for ITER is a rather complicated instrument in order to meet all the requirements needed. Use of O- and X- mode probing at several waveguide frequency bands is proposed. A significant effort has been devoted to the design and testing of waveguides able to carry the signal to the HFS through the narrow spaces available on ITER.

The other way to measure group time delay is realized in reflectometry with amplitude modulation of the carrier frequency [4.468] by means of measuring a phase delay on a modulation frequency. The modulation frequency is chosen rather high to provide good sensitivity, but not higher than  $f \approx c/4a$  to maintain unambiguity in the phase measurements. Conceptually, both pulsed and AM reflectometry methods are very close to each other; however, in the latter filtration of the modulating frequency is always used. Therefore, the time for the single measurement here is noticeably larger. Density profile measurements by AM reflectometry are being carried out on the TJ-II stellarator, the FTU and T-10 tokamaks, etc. [4.468, 4.469].

The “pulse compression” reflectometry method uses the idea of probing a plasma by a short video pulse [4.470]. Thus, the reflected signal is recorded by its synthesis from the measured amplitude and phase characteristics of the Fourier components of the reflected pulse. The amplitude-phase measurements of the Fourier harmonics are conducted with the help of a precise fast tunable (hyper-abrupt) frequency synthesizer, switched step by step from one frequency of a Fourier-image of a video pulse to another. The phase and amplitude of the wave reflected from the plasma are measured at the same time for each frequency. It should be noted that in this method extremely fast retuning of the probing frequency is required (the initial title of the method is “chirp-radar”). The number of Fourier components to be measured for one video pulse is usually about 100; thus the measurements on all components are carried out during  $\sim 10 \mu\text{s}$ .

The first experiments on a plasma with the single-frequency variant of a reflectometer with pulse compression were conducted on JET [4.471]. Using reflectometry, the density profile of the plasma can be measured with high spatial and time resolution. It is especially important for studies of regimes with improved confinement, when some important features of the spatial distribution of density are observed, for sharpening of the density profile in the central part of the plasma column, and also high density gradients in the plasma peripheral, for fast ELM measurements, etc. [4.472, 4.473].

Another interesting method of measuring the plasma density profile is probing of the plasma by a powerful super-short electric pulse exciting the antenna system [4.474]. As the result of this excitation, the antenna radiates a video pulse of electromagnetic waves with a very wide spectrum (the shorter stimulating impulse, the wider the transmitted spectrum). The recording of reflected signals is conducted by band-pass detectors. By measuring the signal delays in different frequency bands, it is possible to reconstruct the density profile of the plasma.

Methods of measuring the local value of total magnetic field by reflectometry are proposed too, as a simultaneous probing on ordinary and extraordinary modes [4.475]. Also, a direct method of measurements of magnetic fluctuations [4.476] with the help of reflectometry has been proposed. Recently, reflectometry has been successfully applied to define the boundary and shape of the plasma column on ASDEX-U [4.477].

Many interesting applications of reflectometry (for example, imaging reflectometry [4.478]) are devoted mainly to density fluctuation measurements and could be considered in a separate section. Thus, this brief review of conventional and rather new methods of plasma reflectometry and their application in modern fusion facilities displays a wide variety of methodical approaches and diagnostic problems solved by these methods. As mentioned above, reflectometry has been one of the most rapidly upcoming diagnostic methods in the last decade. It extends from minor, auxiliary diagnostics to a set of basic diagnostics which provides relevant information about the dynamics of

the electron concentration distribution and other parameters of a plasma during a discharge. Therefore, it is reasonable that in ITER a whole complex of reflectometers will be used, namely for measuring the density profile both in the basic and divertor plasmas, for measuring the position and shape of the plasma column, and also for measuring fluctuations in electron density [4.108, 4.393].

#### 4.3.3.4. *Application of reflectometry to density fluctuation measurements*

The main technical limitation on investigations of the turbulence characteristics in the core are the capabilities of presently available diagnostics. Each diagnostic is characterized by the measured plasma parameter, the range of turbulence wavelengths, the spatial localization of the measurements and the frequency response. One of the most powerful type of turbulence diagnostic at the present time is reflectometry. It is based on the reflection of a launched electromagnetic wave from the critical plasma layer where the permittivity  $\epsilon$  is zero. Since a tokamak plasma is confined in a strong magnetic field, it is possible to use two waves: the ordinary (O-wave) with the electric field of the wave along the magnetic field line and the low and high frequency extraordinary waves ( $X_l$  and  $X_u$ -modes, where the subscripts  $l$  and  $u$  stand for “low” and “up” respectively) with the electric field of the wave perpendicular to the magnetic field lines. The reflected wave is received with a second antenna and the characteristics of the density fluctuations are derived from an analysis of the phase and amplitude fluctuations of the reflected millimetre waves. Like all techniques for the measurement of the parameters of a hot thermonuclear plasma, reflectometry had a long record of improvements since the 1960s, which finally converted it into a powerful and widely used diagnostic. Although the first application of reflectometry for turbulence measurements was by E. Mazzucato in the ATC tokamak in 1975 [4.479], it was used only occasionally in later experiments. The reason was the discussion about the spatial localization of the measured data. In a 1-D geometrical approach, the phase of the reflected wave is the integral over the whole path from the launcher to the receiver. Moreover, the finite probing beam width results in additional averaging in the perpendicular direction. So, in general, reflectometry should have severe restrictions as a diagnostic of local plasma density perturbations. This is true for the case of long poloidal perturbations like low  $m/n$  MHD modes. In this case, the 1-D approach works well and the local density perturbations could be found only after solving an integral equation [4.480–4.482].

The problem of spatial localization of reflectometry has been extensively discussed for more than a decade [4.454, 4.483–4.487]. It was found that the localization increases in the case of cylindrical reflection layers [4.486]. At the present time, the capabilities of reflectometry have become much clearer as a result of the great progress in analytical approaches [4.485–4.487] and the

appearance of computer simulations with powerful 2-D full-wave numerical codes [4.485–4.490], solving the electromagnetic wave reflection from a plasma. Significant efforts were devoted to the characterization of reflectometry capabilities in the real plasma and antenna geometry of T-10 [4.491]. First, it includes extensive simulations of the electromagnetic wave reflection from a turbulent plasma with a 2-D full-wave code and comparison of the simulation results with analytical theory [4.484]. Second, conclusions about the local properties of reflectometry were obtained from a special set of experiments, where reflectometry and Langmuir probes were observed simultaneously at the same plasma radii in the plasma edge [4.491]. The data from the two diagnostics were found to be in good qualitative and quantitative agreement.

The most interesting reflectometry technique is correlation reflectometry (CR). It was developed at JET in the 1980s [4.475], but its full potential was realized later in T-10 [4.492–4.494]. The area of investigations was significantly extended by means of the development of similar CR in the TEXTOR [4.495, 4.496] and FTU [4.493] tokamaks. A joint experiment with the same experimental setup at all three machines strongly increases the range of toroidal magnetic fields from 1.5 to 8 T and densities from  $0.08 \times 10^{20} \text{ m}^{-3}$  to  $3 \times 10^{20} \text{ m}^{-3}$ . In CR, the reflected wave is received with an antenna array, enabling observation of poloidal turbulence structures at a fixed launched wave frequency. Simultaneous work at two or more probing frequencies makes it possible to reveal the radial turbulence structure. The main common feature was the presence of two or three antenna arrays, enabling long and short distance poloidal and radial correlations. The presence of several antenna arrays also makes it possible to make long distance toroidal correlation measurements along a magnetic field line. The O- and XI-modes were used in T-10 and FTU, while only the O-mode was used in TEXTOR.

The T-10 heterodyne CR [4.492] measures the properties of small scale plasma density fluctuations by means of the poloidal and radial turbulence correlation characteristics. The CR has three antenna arrays, probing the plasma from the top at the LFS and HFS and from the equatorial plane at the HFS. All antennas were aligned to the centre of the plasma column. It was possible to probe the plasma simultaneously from both the HFS and the LFS in order to measure the poloidal asymmetry of the turbulence and the long distance poloidal and toroidal [4.492] correlations. The use of a heterodyne system ensures high sensitivity. The amplitude  $A$  and phase  $\varphi$  of the reflected electric field vector were decomposed by a quadrature detector at the level of the intermediate frequency into imaginary ( $U_1 = A \times \sin(\varphi)$ ) and real ( $U_2 = A \times \cos(\varphi)$ ) parts. All signal processing was made in complex form. For each time interval of interest, the signals were divided into sub-intervals and in each sub-interval a complex FFT was applied. The sub-spectra were then averaged to obtain two global complex spectra with Fourier amplitudes  $F_{1,2}(f)$ , where the subscript index is the channel

number and  $f$  is the frequency of the Fourier harmonic in the signal. At the same time, the normalized cross-spectrum between the two channels was determined as follows:  $C(f) = (F_1(f) \times F_2(f)) / (|F_1(f)| \times |F_2(f)|)$ . The argument of the cross-spectrum  $\text{Arg } C(f)$  gives the cross-phase between the signals in the two channels and the absolute value  $|C(f)|$  of the cross-spectrum gives the coherency of the signals. Auto and cross-correlation functions were also calculated for the data sequences.

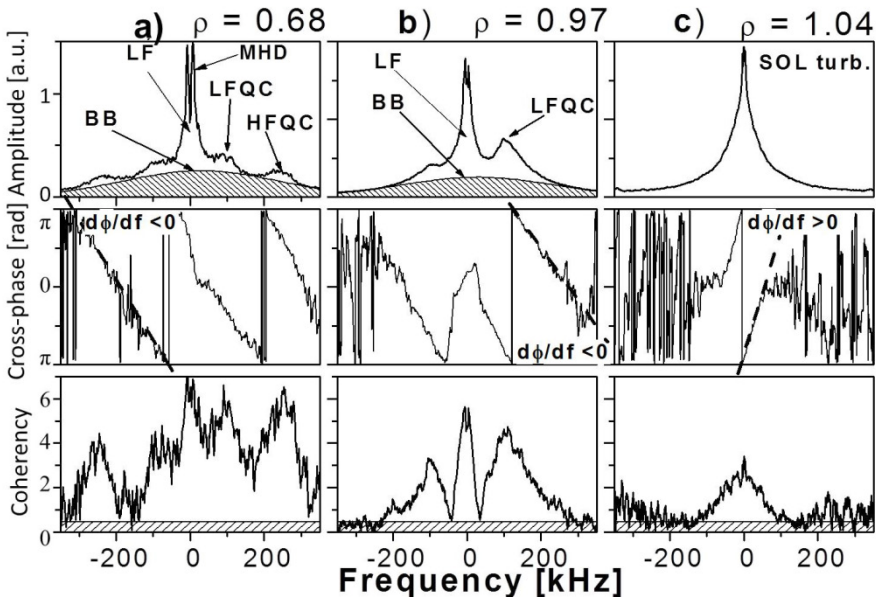


FIG. 4.69. Typical Fourier spectra of CR signals from poloidally separated antennas. Case (a) corresponds to reflection from the plasma central region; case (b) is the reflection from the core edge plasma; and case (c) is the reflection from the SOL. The top panels represent the Fourier amplitude spectra, the middle panels the poloidal cross-phase and the bottom panels the poloidal coherency. The shaded regions correspond to the “confidence levels”. Produced according to Ref. [4.492].

Figure 4.69 presents the results of complex poloidal correlation analysis of the fluctuations of the two signals reflected from two poloidally separated spots. The typical amplitude Fourier spectrum of the first signal (top traces) and cross-spectra between the two signals, including the poloidal cross-phase (middle) and coherency (bottom) spectra, are shown for the central (a), core edge (b) and SOL (c) regions of the plasma. A pronounced difference is clearly seen. The central turbulence has a complex structure and rotates in the electron diamagnetic drift direction, which follows from the negative cross-phase slope. It is possible to distinguish five components in the central spectrum. The first is the background spectrum with a wide frequency band, which was referred to in

Ref. [4.495] as broad band (BB). The second and third components are the maxima at the frequencies 100 and 220 kHz, which were referred to in Ref. [4.495] as low frequency quasi-coherent (LF QC) and high frequency quasi-coherent (HF QC) modes. The fourth component is the maximum at the zero frequencies, which was referred to in Ref. [4.495] as stochastic low frequency (SLF) turbulence. The fifth component (not shown in Fig. 4.6a) is the monochromatic peaks of the global magnetohydrodynamic modes (MHD) and geodesic acoustic modes (GAM), which are typical for experimental reflectometry spectra. The “core edge” turbulence retains only the LF QC spectral maxima, while the HF QC spectral maxima vanish (Fig. 4.69b). In contrast to the core, the SOL fluctuations have a single spectral maximum at zero frequency and the turbulence rotation changes sign from the electron to the ion diamagnetic drift direction (Fig. 4.69c). Thus, a shear layer of turbulence velocity occurs at the plasma periphery.

As the reflectometry integrates the phase along the wave propagation, it gives rise to a great deal of discussion about the radial localization and the range of the resolved poloidal wavelengths of turbulence using CR. It has been shown analytically [4.487] and experimentally [4.492] that the radial correlation function has two components: the first narrow one corresponds to the reflection from the critical layer and brings information about the local turbulence properties, while the second (wide in radii) integrates the scattering of the wave over the whole region and is not very informative. The wavelength resolution depends on the geometry of the antennas and experimental conditions and should be estimated for each configuration separately. Estimates of T-10 geometry showed that CR is sensitive to wavelengths of turbulence longer than 2 cm.

A special modification of the reflectometry scheme, called “Doppler reflectometry” [4.497] also permits direct measurements of the phase velocity of the turbulence. Contrary to the CR technique, measurements of the velocity in this case become possible due to the Doppler effect. In this case, the wave is launched at some angle to the magnetic field line so that the wave at the reflection layer has non-zero  $k$  vector along the magnetic surface. Thus a back scattered wave arises, the frequency of which is shifted due to reflection from the moving turbulence. This frequency shift is translated into the turbulence velocity, taking into account the geometry of the experiment.

#### 4.4. ENGINEERING PROBLEMS

**Yu. Gott**

Kurchatov Institute, Moscow,  
Russian Federation

The new generation of thermonuclear machines with magnetic plasma confinement makes it necessary to solve complex engineering problems caused

mainly by the increased fusion power and shot duration. These problems will be more critical in future machines, for example in ITER. In this section we briefly list the influence of radiation on materials.

Incident neutrons and fast particles knock atoms from lattice sites, producing radiation defects. These defects can drastically change the mechanical, electrical and optical characteristics of solids.

#### 4.4.1. Changing of mechanical properties

##### *Radiative swelling*

The irradiation usually causes the sample to expand.

##### *Irradiation hardening and embrittlement*

The material becomes stronger and more brittle after irradiation.

##### *Relaxation and creep*

Radiation relaxation and creep can cause bolted connections to loosen and the elasticity of springs to decline.

##### *Amorphization*

Irradiation of crystalline materials with fast neutrons can lead to their amorphization.

##### *Transmutation*

The constituent elements of structural materials can be modified as a result of neutron induced nuclear reactions. For example, due to the reaction  $^{197}\text{Au}(n,\gamma)\rightarrow^{198}\text{Au}(\beta)\rightarrow^{198}\text{Hg}$ , the resistance of the gold bolometer meander increases considerably; difficulties also appear with gold contacts.

##### *Radiation-induced diffusion*

Radiation-induced diffusion can result in the diffusion welding of contacting parts.

##### *Sputtering*

The material which is sputtered from the vacuum walls can be deposited on the mirrors and change its characteristics. The sputtering produces a lot of dust (several hundred kilograms per year for ITER). This dust absorbs a large amount of tritium and so is very dangerous.

#### 4.4.2. Changing in electrical properties

##### *Radiation induced electromagnetic force (RIEMF)*

This effect is most prominent during the irradiation of electric cables. In certain cases, the EMF induced is comparable to the amplitude of the useful signal.

##### *Radiation induced electrical degradation (RIED)*

As a rule, the specific resistance of pure conductors increases under irradiation.

*Radiation induced conductivity (RIC)*

The conductivity of insulators increases upon irradiation, sometimes by several orders of magnitude.

**4.4.3. Changes in optical properties***Radioluminescence*

Irradiation causes transparent materials to luminesce over different ranges of wavelengths.

*Radiation induced absorption*

Transparent materials acquire colour under irradiation, and should the dose be sufficiently high, become opaque (at least to visible light).

Radioluminescence and radiation induced absorption create big problems for optical cables and standard optical elements to be used in a reactor.

*Radiation effects on polymers*

Upon irradiation, the conductivity of polymeric materials increases by 3–4 orders of magnitude, and polymers can be broken up through radiolysis. Therefore, it will be impossible to use cables with polymer insulators.

Thus, the radiation environment in both the reactor and the space around it will exert a significant and sometimes governing effect on diagnostic instruments. All these must be taken into account during diagnostic design for future fusion plasma facilities.

Other engineering problems are as follows. Magnetic fields in a future fusion reactor will be created by coils with superconducting windings which must be kept at ultra-low temperatures. Thus, it is necessary to minimize their heating caused by neutron radiation by means of special shielding — blanket modules. The presence of a blanket makes it difficult to access the diagnostic sensors located near the plasma. To exclude direct radiation to superconductors, labyrinths will be used for signal transfer.

The detectors, cables and optical components placed inside the blanket should be radiation resistant or have radiation shielding, which makes diagnostic integration rather difficult. Although machine sizes have increased, the problem of locating diagnostic equipment has become more conspicuous. As an example, Fig. 4.70 shows the proposed location of some out-of-vessel diagnostics in ITER. The diagnostic system to be installed in ITER is presented in Ref. [4.108] in detail.

Some diagnostic components, such as first optical elements and soft X ray detectors, must be placed in such a way that these detectors will be directly illuminated by the plasma radiation. Under the effect of radiation, they will be heated and this will require active cooling. To prevent tritium escape from the vacuum vessel, two independent vacuum barriers are needed.

A new problem is the measurement of the quantity, content and allocation of dust inside vacuum vessel. This dust can be radiotoxic and highly explosive. Although this task has no direct relation to plasma diagnostics, the methods developed for plasma measurements will be applied for dust measurement.

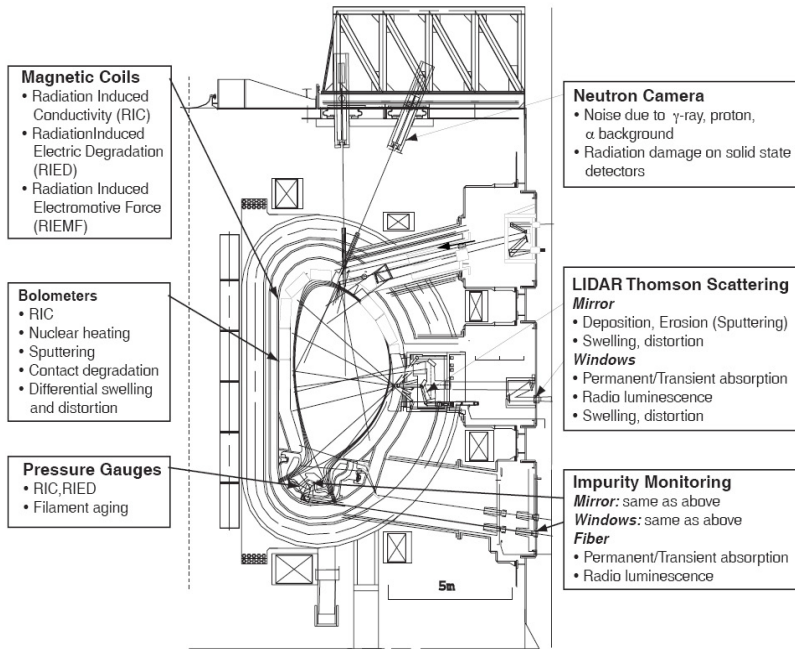


FIG. 4.70. Location of some representative diagnostic components and the principal radiation induced physical effects of interest [4.498].

Difficulties with access to diagnostics components cause increased requirements on their reliability, especially because of the impossibility of manual replacement due to personal radiation safety under condition of induced radioactivity in materials. Replacement, adjustment, alignment and in situ calibration of diagnostic components must be made remotely by special manipulators.

The application of some conventional detectors (e.g. semiconductors) is restricted or totally excluded. This leads to the development and study of new kinds of radiation resistant detectors. The first element of optical diagnostics, instead of the widely used lens, will be the metal mirror. The problem of their reflectance stability is extremely important as well as the problem of optical component stability. Investigations in this field have continued over many years [4.499, 4.500].

Differences in the temperature of reactor structural components will lead to their mutual displacement by about a few centimetres and this must be also taken

into account during diagnostic design. Plasma currents create high magnetic fields in the area of diagnostic allocation and in the case of charged particle detection the effect of the magnetic field should be considered. Magnetic shielding must be used in some cases.

### 4.5. CONCLUSION

**V. Zaveryaev**

Kurchatov Institute, Moscow,  
Russian Federation

During the last few decades, the development of plasma diagnostic methods went on concurrently with progress in thermonuclear plasma studies. These two processes cannot be separated. As a matter of fact, due to improved diagnostic techniques new phenomena and plasma regimes have been found which, in turn, have required further diagnostics development. The new generation of plasma devices, which differs from the previous generation in terms of size, plasma duration, increased current and magnetic field, plasma fuel (D-T), high fusion power, presence of divertor, etc. brought new challenges to diagnostics development. The duration of plasmas in older machines with magnetic confinement was about several milliseconds while in modern machines it reaches several tens of seconds. In earlier plasma studies, it was sufficient to measure plasma parameters from shot to shot, but in present research work it is necessary to receive spatial and/or spectral distributions during a single shot. The wide use of feedback control systems for plasma position, shape and density has increased the requirements on the temporal resolution of the measurements.

The larger size of plasma installations and higher plasma energies have raised the requirements on diagnostics reliability because undesirable events such as plasma disruption can be very dangerous for the machine itself and the diagnostics should inform the experimentalists in advance about possible transition to an uncontrolled stage. At present, it is difficult to foresee which diagnostic methods will be used in future fusion reactors but obviously some of the existing techniques will be applied.

An important stage on the road to controlled fusion is the creation of the International Thermonuclear Experimental Reactor (ITER). Already on this device it will be necessary to solve a number of new problems (e.g. dust measurements, tritium migration).

Experience shows that all new problems have been sooner or later successfully solved. There is no doubt that plasma diagnostics, being a fast developing field of science, will meet the challenges of creating a commercial fusion reactor.

## REFERENCES

- [4.1] *www.iter.org*
- [4.2] Plasma Diagnostic Techniques (HUDDLESTONE, R.H., LEONARD, S.L., Eds), Academic Press, New York and London (1965).
- [4.3] EQUIPE TFR, Tokamak plasma diagnostics, Nucl. Fusion **18** (1978) 647–731.
- [4.4] Special issue on plasma diagnostics for magnetic fusion research (COSTLEY, A.E., JOHNSON, D.W., Eds), Fusion Sci. Technol. **53** (2008) 2.
- [4.5] Diagnostics for Experimental Thermonuclear Fusion Reactor (STOTT, P.E., GORINI, G., SINDONI, E., Eds), Plenum Press, New York (1996).
- [4.6] Diagnostics for Experimental Thermonuclear Fusion Reactor 2 (STOTT, P.E., GORINI, G., PRANDONI, G.P., SINDONI, E., Eds), Plenum Press, New York (1998).
- [4.7] Advanced Diagnostics for Magnetic and Inertial Fusion (STOTT, P.E., WOOTTON, A., GORINI, G., SINDONI, E., BATANI, D., Eds), Kluwer Academic/Plenum Press, New York (2002).
- [4.8] Burning Plasma Diagnostics (ORSITTO, F., GORINI, G., SINDONI, E., TARBOCCHI, M., Eds), Melville, New York, American Institute of Physics (2008).
- [4.9] LEONARD, S.L., “Basic macroscopic measurements”, Plasma Diagnostic Techniques, (HUDDLESTONE, R.H., LEONARD, S.L., Eds), Academic Press (1965).
- [4.10] STOTT, P.E., “Macroscopic measurements”, Course on Plasma Diagnostic and Data Acquisition Systems, Summer School, Varenna, Italy (1975).
- [4.11] BRUSATI, M., CHRISTIANSEN, J., CORDEY, G., JARRETT, K., LAZZARO, E., et al., Analysis of magnetic measurements in tokamaks, Computer Phys. Rep. **1** (1984) 345.
- [4.12] KUZNETSOV, Yu., “Magnetic measurements in ITER”, in ITER-IL-PH-7-9-S-06 (1989).
- [4.13] PUSTOVITOV, V.D., Magnetic diagnostics: General principles and the problem of reconstruction of plasma current and pressure profiles in toroidal systems, Nucl. Fusion **41** (2001) 721–730.

- [4.14] STRAIT, E.J., Magnetic diagnostic system of the DIII-D tokamak, *Rev. Sci. Instrum.* **77** (2006) 023502.
- [4.15] STRAIT, E.J., FREDRICKSON, E.D., MORET, J.-M., TAKECHI, M., Magnetic diagnostics, *Fusion Sci. Technol.* **53** (2008) 304–334.
- [4.16] SHAFRANOV, V.D., Magnetohydrodynamical equilibrium configurations, *Sov. Phys. JETP* **33** (1957) 710; English translation in *Soviet Physics - JETP* **6** (1958) 545.
- [4.17] MUKHOVATOV, V.S., SHAFRANOV, V.D., Plasma equilibrium in a tokamak, *Nucl. Fusion* **11** (1971) 605–633.
- [4.18] ZAKHAROV, L.E., SHAFRANOV, V.D., Equilibrium of current-carrying plasmas in toroidal configurations, *Rev. Plasma Phys.* **11** (1968) 153–302.
- [4.19] MIRNOV, S.V., Probe method of measurement of current column displacement in the cylindrical and toroidal chambers, *Atomnaya Energiya* **17** (1964), 209 (in Russian); English translation in *Sov. At. Energy* **17** (1964), 209.
- [4.20] McCORMACK, B., THOMAS, J.P., Design, fabrication and testing of the TFTR Rogowski and diamagnetic loop, *Proc. 9th Symp. on Engineering Problems of Fusion Research, Chicago* (1981) 1130.
- [4.21] SPITZER, L., Jr., *Physics of Fully Ionized Gases*, Interscience Publishers, New York and London (1962).
- [4.22] SHAFRANOV, V.D., Determination of the parameters  $\beta_i$  and  $l_i$  in a tokamak for arbitrary shape of plasma pinch cross-section, *Plasma Phys.* **13** (1971) 757–762.
- [4.23] VAN HEJNINGEN, R.J.J., et al., *Jutphaas Report IR 70/057* (1970).
- [4.24] KING, R.E., ROBINSON, D.C., VERHAGE, A.J.L., The application of Fourier analysis of the azimuthal field distribution to a study of equilibria and instabilities in a toroidal pinch discharge, *J. Phys. D: Appl. Phys.* **5** (1972) 2015–2025.
- [4.25] RAZUMOVA, K.A., Measurement of the plasma energy in a tokamak machine by the change in longitudinal magnetic flux, *Atomic. Energy* **20** (1966), 459; English translation in *Sov. At. Energ.* **20** (1966) 531.
- [4.26] MIRNOV, S.V., Measurement of plasma energy in T-3 device, *Atomnaya Energiya* **26** (1969), 458 (in Russian); English translation in *Sov. At. Energ.* **26** (1969), 525.

- [4.27] THOMAS, P., Diamagnetic Flux measurement Using the PDX TF Coils, PPPL-1979 (1983).
- [4.28] HAEGI, M., SAND, F., Compensated coil system for measuring the plasma diamagnetism in toroidal devices, *Plasma Phys.* **17** (1975) 997–999.
- [4.29] NEILSON, G.H., Diamagnetic Measurements on ISX-B: Method and Results, ORNL/TM-8767 (1983).
- [4.30] COSLER, A., FUCHS, G., WAIDMAN, G., “Construction, fabrication and performance of a compensated magnetic coil system in TEXTOR”, *Proc. 13th Symp. Fus. Technol., Varese, Italy*, **2** (1984) 1107.
- [4.31] SHEPARD, T.D., Diamagnetic measurements on the Alcator C tokamak, PVC/PR-85-13 (1985).
- [4.32] TONETTI, G., CHRISTIANSEN, J.P., DE KOCK, L., Measurement of the energy content of the JET tokamak plasma with a diamagnetic loop, *Rev. Sci. Instrum.* **57** (1986) 2087.
- [4.33] BORTNIKOV, A., BREVNOV, N., GERASIMOV, S., ZHUKOVSKIY, V., MAKSIMOV, Yu., et al., The shape of the transverse cross-section of a plasma column in the finger-ring tokamak, *Plasma Phys. Control. Nucl. Fusion Res.* **1** (1974) 147–159 (in Russian).
- [4.34] BRAAMS, B.J., Magnetic diagnostics: general principles and the problem of reconstruction of plasma current and pressure profiles in toroidal systems, *Plasma Phys. Control. Fusion* **33** (1996) 715.
- [4.35] DE KOCK, L., KUZNETSOV, Yu.K., Magnetic diagnostics for fusion plasmas, *Nucl. Fusion* **36** (1996) 387–400.
- [4.36] BETTINI, P., BELLINA, F., FORMISANO, A., MARTONE, R., STELLA, A., et al., Identification of the plasma magnetic contour from external magnetic measurements by means of equivalent currents, *Eur. Phys. J. AP* **13** (2001) 51–57.
- [4.37] SWAIN, D.W., NEILSON, G.H., An efficient technique for magnetic analysis of non-circular, high-beta tokamak equilibria, *Nucl. Fusion* **22** (1982) 1015–1030.
- [4.38] KUZNETSOV, Yu.K., NASCIMENTO, I.C., GALVAO, R.M.O., YASIN, I.V., Plasma boundary determination in ITER by the optimized current filament method, *Nucl. Fusion* **38** (1998) 1829–1838.
- [4.39] LUXON, J.L., BROWN, B.B., Magnetic analysis of non-circular cross-section tokamaks, *Nucl. Fusion* **22** (1982) 813–821.

- [4.40] IDA, K., TOYAMA, H., A method to determine shape of plasma cross-section in a non-circular tokamak, *Jpn. J. Appl. Phys.* **22** (1983) 1587–1591.
- [4.41] ALLADIO, F., CRISANTI, F., Analyses of MHD equilibria by toroidal multipolar expansions, Preprint RT/FUS/85/7 (1985).
- [4.42] KESSEL, C.E., Determination of cross plasma equilibrium from magnetic multipoles, Preprint UCLA/PPG-941 (1986).
- [4.43] LEE, D.K., PENG, Y.-K.M., An approach to rapid plasma shape diagnostics in tokamaks, *J. Plasma Phys.* **25** (1981) 161–173.
- [4.44] KUZNETSOV, Yu.K., PYATOV, V.N., YASIN, I.V., Determination of equilibrium current profiles and plasma shapes in a tokamak, *Sov. J. Plasma Phys.* **13** No.8 (1987) 139–148 (in Russian).
- [4.45] LAO, L.L., JOHN, H.S., STAMBAUGH, R.D., PFEIFFER, W., Separation of  $\beta_p$  and  $I_i$  in tokamaks of non-circular cross-section, *Nucl. Fusion* **25** (1985) 1421–1436.
- [4.46] LAO, L.L., JOHN, H.S., STAMBAUGH, R.D., KELLMAN, A.G., PFEIFFER, W., Reconstruction of current profile parameters and plasma shapes in tokamaks, *Nucl. Fusion* **25** (1985) 1611–1622.
- [4.47] MIRNOV, S.V., SEMENOV, I.B., Investigation of the instabilities of the plasma string in the Tokamak-3 system by means of a correlation method, *Sov. Atomnaya Energiya* **30** (1971) 22 (in Russian).
- [4.48] MEREZHKIN, V.G., Structure of the magnetic field perturbations in the disruptive instability in the T-6 tokamak, *Sov. J. Plasma Phys.* **4** (1978) 152.
- [4.49] DE KOCK, L., MEDDENS, B.J.H., ORNSTEIN, L.T.M., SCHRAM, D.C., VAN HEIJNINGEN, R.J.J., Measurements of Poloidal Magnetic Field Perturbations in Alcator, Rijnhuizen Report 74–86 (1974).
- [4.50] GERNHARDT, J., ALLGEYER, R., GROENING, D.E., HOHENÖCKER, H., KARGER, F., et al., Design of magnetic probes for MHD measurements in ASDEX tokamak, Preprint IPP III/59 (1980).
- [4.51] GRANETZ, R.S., The m-spectrum analyzer on ALCATOR-C, Preprint PFC/RR-81-25 (1981).
- [4.52] ROBINSON, D.C., HAYNES, P., MORRIS, A.W., MHD Activity on JET, Preprint JET-P (1985) 11.

- [4.53] FREDRICKSON, T., COLCHIN, E.R., McGUIRE, K., MORRIS, W., SAUTHOFF, N., TFTR Mirnov loop system, *Rev. Sci. Instrum.* **57** (1986) 2084.
- [4.54] HARLEY, T.R., BUCHENAUER, D.A., COONROD, J.W., McGUIRE, K.M., TFTR Mirnov coil analysis with toroidal effects at plasma startup, *Nucl. Fusion* **29** (1989) 771.
- [4.55] ZOHM, H., GREENE, J.M., LAO, L.L., STRAIT, E.J., Mirnov coil analysis in the DIII-D tokamak using the singular value decomposition method, Preprint GA-A20886 (1992).
- [4.56] DURAN, I., STÖCKEL, J., MANK, G., FINKEN, K.H., FUCHS, G., VAN OOST, G., Measurements of magnetic field fluctuations using an array of hall detectors on TEXTOR tokamak, *Rev. Sci. Instrum.* **73** (2002) 3482.
- [4.57] BOLSHAKOVA, I., BRUDNYI, V., HOLYAKA, R., KOLIN, N., KUMADA, M., LEROY, C., Stable semiconductor magnetic field sensors under doses of high radiation, *Proc. 30th Conf. on Control. Fusion and Plasma Phys.* **27A** (2003), P-4 68–71.
- [4.58] HARA, S., KASAI, S., NISHITANI, T., NAGASHIMA, A., NAKAYAMA, T, Development of steady-state magnetic sensor, *Rev. Sci. Instrum.* **70** (1999) 435.
- [4.59] YAMAMOTO, S., Magnetic measurements for ITER. magnetic sensors, ITER-IL-PH-07-0-82 (1990) 1–19.
- [4.60] CHANDLER, G.I., JAHODA, F.C., Current measurements by Faraday rotation in single-mode optical fibers, *Rev. Sci. Instrum.* **56** (1985) 852.
- [4.61] BLUM, J., STEPHAN, Y., “Determination of the plasma current density profile in a tokamak from magnetic and polarimetric measurements”, *Proc. 17th EPS Conf. on Control. Fusion and Plasma Phys.*, Amsterdam, Netherlands, **14B**, Pt.II (1990) 872.
- [4.62] ZAKHAROV, L.E., FOLEY, E.L., LEVINTON, F.M., YUH, H.Y., Reconstruction of the  $q$  and  $p$  profiles in ITER from external and internal measurements, *Plasma Phys. Rep.* **34** (2008) 173.
- [4.63] STANGEBY, P.C., McCracken, G.M., Plasma boundary phenomena in tokamaks, *Nucl. Fusion.* **30** (1990) 1225–1379.
- [4.64] HUTCHINSON, I.H., *Principles of Plasma Diagnostics*, Cambridge University Press, New York (1987).

- [4.65] DONNE, A.J.H., Diagnostics for fluctuation measurements, *Trans. Fusion Sci. Technol.* **49** (2006) 367–375.
- [4.66] BOEDO J., GRAY D., CHOUSAL L., CONN R., HILLER B., et al., Fast scanning probe for tokamak plasmas, *Rev. Sci. Instrum.* **69** (1998) 2663–2670.
- [4.67] MATTHEWS, G.F., Tokamak plasma diagnosis by electrical probes, *Plasma Phys. Control. Fusion* **36** (1994) 1595–1628.
- [4.68] VAN OOST, G., Probe diagnostics for fusion devices, *Trans. Fusion Sci. Technol.* **49** (2006) 357–366.
- [4.69] SAMM, U., Plasma-wall interaction, *Trans. Fusion Sci. Technol.* **33** (1998) 338–348.
- [4.70] STANGEBY, P., Edge probes, *J. Nucl. Mater.* **145–147** (1987) 105–116.
- [4.71] ADAMEK, J., STOCKEL, J., DURAN, I., HRON, M., PANEK, R., et al., Comparative measurements of the plasma potential with the ball-pen and emissive probes on the CASTOR tokamak, *Czech. J. Phys.* **55** (2005) 235–242.
- [4.72] GUNN, J.P., SCHRITTWIESER, R., BALAN P., ADAMEK, J., STOCKEL J., et al., Tunnel probes for measurements of the electron and ion temperature in fusion plasmas, *Rev. Sci. Instrum.* **75** (2004) 4328–4330.
- [4.73] MANOE, D.M., McCracken, G.M., “Probes for plasma edge diagnostics in magnetic confinement fusion devices”, *Physics of Plasma Wall Interactions in Controlled Fusion* (POST, D.E., BEHRISCH, R., Eds), Plenum Press, New York (1986) 135–209.
- [4.74] SCHOTT, L., BOYD, R.L.F., “Electrical probes”, *Plasma Diagnostics* (LOCKTE-HOLTGREVEN, W., Ed.), North Holland, Amsterdam (1968) 459–479.
- [4.75] CHEN, F.F., “Electrical probes”, *Plasma Diagnostic Techniques* (HUDDLESTONE, R.H., LEONARD, S.L., Eds), Academic, New York (1965) 94–164.
- [4.76] SWIFT, J.D., SCHWAR, M J., *Electric Probes for Plasma Diagnostic*, American Elsevier, New York (1971).
- [4.77] GUNTER, K., HERRMANN, A., LAUX M., PECH P. REINER H.-D., Characteristics of electric probes in the tokamak SOL: influences of the magnetic field, *J. Nucl. Mater.* **176–177** (1990) 236–239.

- [4.78] MATTHEWS, G.F., McCRACKEN, G.M., SEWELL, P., WOODS, M., HOPKINS B.J., The determination of sheath potential from retarding field analyser measurements in tokamak edge plasma, *J. Nucl. Mater.* **145–147** (1987) 225–230.
- [4.79] SCHRITTWIESER, R., ADAMEK, J., BALAN, P., HRON, M., IONITA, C., et al., Measurements with an emissive probe in the CASTOR tokamak, *Plasma Phys. Control. Fusion* **44** (2002) 567–578.
- [4.80] CHEN, S.L., SEKIGUCHI, T., Instantaneous direct-display system of plasma parameters by means of triple probe, *J. Appl. Phys.* **36** (1965) 2363–2375.
- [4.81] KEILHACKER, M., DEKSNIS, E., HARBOUR, P., REBUT, P.H., et al., *Plasma Phys. and Contr. Fusion Research*, IAEA-CN-53/A-V-1 (1990) 345–364.
- [4.82] STANGEBY, P.C., Measuring plasma drift velocities in tokamak edge plasmas using probes, *Phys. Fluids* **27** (1984) 2699–2704.
- [4.83] HUTCHINSON, I.H., A fluid theory of ion collection by probes in strong magnetic field with plasma flow, *Phys. Fluids* **30** (1987) 3777–81.
- [4.84] DAVIES, S.J., ERENTS, S.K., MATTHEWS, G.F., McCORMIK, K., MONK, R.D., et al., Overview of probe measurements at JET, *JET Report JET-P(97)39* (1997) 1–12.
- [4.85] ERENTS, S., TAGLE, J., McCRACKEN, G., IRAEL, G., DE KOCK, L., et al., The behaviour of the scrape-off layer in JET with toroidal belt limiters, *J. Nucl. Mater.* **162–164** (1989) 226–230.
- [4.86] ASAKURA, N., TSUJI-LIO, S., IKEDA, Y., NEYATANI, Y., SEKI, M., Fast reciprocating probe system for local scrape-off layer measurements in front of the lower hybrid launcher on JT-60U, *Rev. Sci. Instrum.* **66** (1995) 5428–5432.
- [4.87] DE KOCK, L., “Langmuir probes and optical diagnostic for the ITER divertor”, *Diagnostics for Experimental Fusion Reactors* (STOTT, P.E., GORINI, G., SINDONI, E., Eds), Plenum Press (1996) 591–594.
- [4.88] KIRNEV, G.S., GRASHIN, S.A., BUDAEV, V.P., GERASIMOV E.V., KHIMCHENKO, L.N., Plasma structures and transport in the SOL of the T-10 tokamak, *J. Nucl. Mater.* **337–339** (2005) 352–356.

- [4.89] ABRAMOV, V.A., VINOGRADOVA, N.D., KOGAN, V.I., KUZNETSOV, E.I., ŠČEGLOV, D.A., Measurements of fluxes of neutral H-atoms and impurities by spectroscopic methods in Tokamak TM-3, *Plasma Phys.* **10** (1968) 428–429.
- [4.90] HINNOV, E., SUCKEWER, S., BOL, K., HAWRYLUK, R.J., HOSEA, J., et al., Low-Z impurities in the PLT Tokamak, *Plasma Phys.* **20** (1978) 72-734.
- [4.91] BUGARYA, V.A., VASIN, N.L., GEGECHKORI, N.M., ZHIDKOV, A.G., “Spectroscopy research of light impurities in T-10 device”, Proc. 10th Europ. Conf. on Control. Fusion and Plasma Phys., Moscow, Russian Federation, Vol. **1** (September 1981) Pt. 1, A-11.
- [4.92] RAMSEY, A.T., BUSH, C.E., DYLLA, H.F., OWENS, D.K., PITCHER, C.S., et al., Enhanced carbon influx into TFTR supershot, *Nucl. Fusion* **31** (1991) 1811–1825.
- [4.93] STODIEK, W., GOLDSTON, R., SAUTHHOF, N., ARUNASALAM, V., BARNES, C., et al., Transport studies in the Princeton Large Torus, *Nucl. Fusion Suppl.* **1** (1981) 9–22.
- [4.94] HAWKES, N., WANG, Z., BARNSLEY, R., BEHRINGER, K., COHEN, S., et al., “Transport studies during sawteeth and H-modes on JET using laser ablation”, Proc. 16th Conf. on Control. Fusion and Plasma Phys., Venice, 13–17 March 1989, Vol. **13B** (1989) Pt.1 79 –82.
- [4.95] BEHRINGER, K., SUMMERS, H.R., DENNE, B., FORRE STAND, M., STAMP, M., Spectroscopic determination of impurity influx from localized surfaces, *Plasma Phys. Control. Fusion* **31** (1989) 2059–2099.
- [4.96] SUMMERS, H.P., DICKSON, W.J., BOILEAU, A., BURKE, P.G., DENNE–HINNOV, B., et al., Spectral emission from berillium in plasmas, *Plasma Phys. Control. Fusion* **34** (1992) 325–352.
- [4.97] SUCKEWER, R.S., EUBANK, H.P., GOLDSTON, R.J., HINNOV, E., SAUTHHOF, N., Toroidal plasma rotation in the Princeton Large Torus, *Phys. Rev. Lett.* **43** (1979) 207–210.
- [4.98] BÉCOULET, M., HUYSMANS, G., SARAZIN, Y., GARBET, X., GHENDRICH, Ph., et al., Edge localized mode physics and operational aspects in tokamaks, *Plasma Phys. Control. Fusion* **45** (2003) A98–A113.
- [4.99] MONIER-GARBET, P., ANDREW, Ph., BELO, P., BONHEURE, G., CORRE, Y., et al., Impurity-seeded ELMy H-mode in JET, with high density and reduced heat load, *Nucl. Fusion* **45** (2005) 1404–1410.

- [4.100] ONGENA, J., MESSIAEN, A.M., UNTERBERG, B., BUDNY, R.V., BUSH, C.E., et al., Overview of experiments with radiation cooling at high confinement and high density in limited and diverted discharges, *Plasma Phys. Control. Fusion* **41** (1999) A379–A399.
- [4.101] MADDISON, G.P., BRIX, M., BUDNY, R., CHARLET, M., COFFEY, I., et al., Impurity-seeded plasma experiment in JET, *Nucl. Fusion* **43** (2003) 49–62.
- [4.102] KUBO, H., SAKURAI, S., ASAKURA, N., KONOSHIMA, S., TAMAI, H., et al., High radiation and high density experiment in JT-60U, *Nucl. Fusion* **41** (2001) 227–233.
- [4.103] TELESKA, G., UNTERBERG, B., JASPERS, R., MESSIAEN, A.M., ONGENA, J., et al., Neon radiation efficiency for different confinement regimes in TEXTOR-94, *Nucl. Fusion* **40** (2000) 1845–1858.
- [4.104] SCHUNKE, B., HUYSMANS, G., THOMAS, P., “Evidence of the influence of reflections on the  $Z_{\text{eff}}$  profile measurements and their mitigation”, Proc. 30th EPS Conference on Control. Fusion and Plasma Phys., London, UK, 28 June–2 July 2004, ECA Vol. **28G** (2004) P-4.111
- [4.105] BIEL, W., BERTSCHINGER, G., BURHENN, R., KÖNIG, R., JOURDAIN, E., Design of high-efficiency extreme ultraviolet overview spectrometer system for plasma impurity studies on the stellarator experiment Wendelstein 7-X, *Rev. Sci. Instrum.* **75** (2004) 3268–3275.
- [4.106] GREICHE, A., BIEL, W., MARCHUK, O., BURHENN, R., Absolute intensity calibration of Wendelstein 7-X high-efficiency extreme ultraviolet overview spectrometer system, *Rev. Sci. Instrum.* **79** (2008) 093504.
- [4.107] BARNESLEY, R., COFFEY, I., LUCOCK, R., STAMP, M.F., JET beamline with integrated X-rays, VUV and visible spectrometer for burning plasma experiments, *Rev. Sci. Instrum.* **74** (2003) 1969–1973.
- [4.108] DONNÉ, A.J.H., COSTLEY, A.E., BARNESLEY, R., BINDSLEV, H., BOIVIN, R., et al., “Diagnostics”, Chapter 7, *Nucl. Fusion* **47** (2007) 337–384.
- [4.109] SUGIE, T., COSTLEY, A., MALAQUIAS, A., MEDVEDEV, A., WALKER, C., “Spectroscopic measurement system for ITER divertor impurity monitor”, Proc. 30th EPS Conference on Contr. Fusion and Plasma Phys., St. Petersburg, Russian Federation, 7–11 July 2003, ECA Vol. **27A** (2003) P-4.63.

- [4.110] OGAWA, H., SUGIE, T., KATSUNUMA, A., KASAI, S., Design of Impurity Influx Monitor (Divertor) for ITER, JAEA Report, JAEA-Technology 2006-015 (2006).
- [4.111] GORELIK, L.L., RAZUMOVA, K.A., SINITSYN, V.V., “Plasma energy losses in the toroidal chamber of the TM-2 tokamak”, Proc. 2nd Int. Conf. Culham, 1965, PPCNFR, IAEA, Vienna, **2** (1966) 647–658.
- [4.112] GORELIK, L.L., MIRNOV, S.V., NIKOLAEVSKY, V.G., SINITSYN, V.V., Radiation power of a plasma as a function of the discharge parameters in the Tokamak-3 device, Nucl. Fusion **12** (1972) 185–189.
- [4.113] HSUAN, H., BOL, K., ELLIS, R.A., Measurement of the energy balance in ATC tokamak, Nucl. Fusion **15** (1975) 657–661.
- [4.114] ODAJIMA, K., MAEDA, H., SHIHO, M., KIMURA, H., YAMAMOTO, S., et al., Radiation loss and power balance in DIVA, Nucl. Fusion **18** (1978) 1337–1345.
- [4.115] LUKJANOV, S.Yu., MAKSIMOV, Yu.S., VERTIPOROKH, A.N., Radiative losses in the T-10 tokamak, Sov. J. Plasma Phys. **6** (1980) 7–11.
- [4.116] MÜLLER, E.R., MAST, F., A new metal resistor bolometer for measuring vacuum ultraviolet and soft X-radiation, J. Appl. Phys. **55** (1984) 2635–2641.
- [4.117] ORLINSKIJ, D.V., MAGYAR, G., Review paper: Plasma diagnostics on large tokamaks, Section 9 “Measurements of radiation losses”, Nucl. Fusion **28** (1988) 664–667.
- [4.118] HUBER, A., McCORMICK, K., INGESSON, L., ANDREW, C.P., BEAMOUNT, P., et al., Upgraded bolometer system on JET for improved radiation measurements, Fusion Eng. Des. **82** (2007) 1327–1334.
- [4.119] PAUL, S.F., FONCK, R.J., MacAULAY, A.K., Using a free-standing thermistor array to measure VUV emission from a tokamak plasma, Rev. Sci. Instrum. **64** (1993) 2423–2427.
- [4.120] JOYE, B., MARMILLOD, Ph., NOWAK, S., Multichannel bolometer for radiation measurements on the TCA tokamak, Rev. Sci. Instrum. **57** (1986) 2449–2454.
- [4.121] LEONARD, A.W., MEYER, W.H., GEER, B., BEHNE, D.M., HILL, D.N., 2D tomography with bolometry in DIII-D, Rev. Sci. Instrum. **66** (1995) 1201–1204.

- [4.122] SCHIVELL, J., Performance of the tokamak fusion test reactor bolometers, *Rev. Sci. Instrum.* **56** (1985) 972–974.
- [4.123] MAST, K.F., KRAUSE, H., BEHRINGER, K., BULLIARD, A., MAGYAR, G., Bolometric diagnostics in JET, *Rev. Sci. Instrum.* **56** (1985) 969–971.
- [4.124] NISHITANI, T., NAGASHIMA, K., SUGIYAMA, T., HARA, M., TAKEUCHI, H., et al., Bolometric measurements in JT-60, *Rev. Sci. Instrum.* **59** (1988) 1866–1868.
- [4.125] MAST, K.F., VALLET, J.C., ANDELFINGER, C., BETZLER, P., KRAUS, H., et al., A low noise highly integrated bolometer array for absolute measurement of VUV and soft X-radiation, *Rev. Sci. Instrum.* **62** (1991) 744–750.
- [4.126] PETERSON, B.J., KOSTRIOUKOV, A.Yu., ASHIKAWA, N., LIU, Y., OSAKABE, M., et al., Bolometer diagnostics for one- and two-dimensional measurements of radiated power on the Large Helical Device, *Plasma Phys. Control. Fusion* **45** (2003) 1167–1182.
- [4.127] MURARI, A., MAST, K.F., D’AMBRA, L., LANG, P.T., MARRELLI, L., et al., Multichord calibrated bolometer array for the RFX experiment, *Rev. Sci. Instrum.* **66** (1995) 665–667.
- [4.128] GIANNONE, L., QUEEN, D., HELLMAN, F., FUCHS, J.C., Prototype of a radiation hard resistive bolometer for ITER, *Plasma Phys. Control. Fusion* **47** (2005) 2123–2143.
- [4.129] MURARI, A., CECCONELLO, M., MARRELLI, L., MAST, K.F., Analysis of the calibration methods and error propagation for the sensitivity  $S$  and the cooling time constant  $\tau_c$  of the gold metal foil bolometers, *Rev. Sci. Instrum.* **75** (2004) 2692–2699.
- [4.130] CÔTÉ, C., DE SILVA, A.W., Fast pyroelectric detector for broadband radiated power measurements, *Rev. Sci. Instrum.* **67** (1996) 4146–4149.
- [4.131] FENG, B., GABDULLIN, P.G., KAPRALOV, V.G., KUTEEV, B.V., GUSEV, V.K., et al., Measuring radiative losses in the Globus-M spherical tokamak, *Tech. Phys. Lett.* **29** (2003) 441–443.
- [4.132] OCHANDO, M.A., MIRONES, E., RUEDA, C., RODRÍGUEZ, P., Bolometry systems for the TJ-II flexible heliac, *Rev. Sci. Instrum.* **70** (1999) 384–386.
- [4.133] KAGANSKII, M.G., LASHKUL, S.I., SHAKHOVETS, K.G., Bolometer with high time resolution for studying the energy loss in tokamaks, *Sov. J. Plasma Phys.* **3** (1977) 386–388.

- [4.134] TFR GROUP, Bolometric technics on TFR 600, *J. Nucl. Mater.* **93–94** (1980) 377–382.
- [4.135] APRUZZESE, G., TONINI, G., Proposal of infrared bolometry on Frascati tokamak upgraded, *Rev. Sci. Instrum.* **61** (1990) 2976–2977.
- [4.136] ALEKSEYEV, A.G., “Thermal feedback bolometer with infrared thermal sensing”, *Proc. 30th EPS Conf. Contr. Fusion and Plasma Phys., St. Petersburg, Russian Federation, 7–11 July 2003, ECA 27A* (2003) P-1.70.
- [4.137] WURDEN, G.A., PETERSON, B.J., SUDO, S., Design of an imaging bolometer system for the large helical device, *Rev. Sci. Instrum.* **68** (1997) 766–769.
- [4.138] PETERSON, B.J., KONOSHIMA, S., PARCHAMY, H., KANEKO, M., OMORI, T., et al., Observation of divertor and core radiation in JT-60U by means of bolometric imaging, *J. Nucl. Mater.* **363–365** (2007) 412–415.
- [4.139] PETERSON, B.J., PARCHAMY, H., ASHIKAWA, N., KAWASHIMA, H., KONOSHIMA, S., et al., Development of imaging bolometers for magnetic fusion reactors, *Rev. Sci. Instrum.* **79** (2008) 10E301.
- [4.140] BOIVIN, R.L., GOETZ, J.A., MARMAR, E.S., RICE, J.E., TERRY, J.L., High resolution bolometry on the Alcator C-Mod tokamak, *Rev. Sci. Instrum.* **70** (1999) 260–264.
- [4.141] FURNO, I., WEISEN, H., MLYNAR, J., PITTS, R.A., LLOBET, X., et al., Fast bolometric measurements on the TCV tokamak, *Rev. Sci. Instrum.* **70** (1999) 4552–4556.
- [4.142] ALEKSEYEV, A., PEROV, G., KURNOSOV, A., CHERNOBY, A., KORDE, R.A., et al., Fast multichannel plasma radiation losses measuring system, *Plasma Devices and Operations* **7** (1999) 139–147.
- [4.143] SUZUKI, C., AKIYAMA, T., FUJISAWA, A., IDA, K., ISOBE, M., et al., Determination of the major impurity radiators in the reheat mode discharges in the compact helical system, *Plasma and Fusion Research* **2** (2007) S1062-1-4.
- [4.144] GRAY, D.S., LUCKHARDT, S.C., CHOUSAL, L., GUNNER, G., KELLMAN, A.G., et al., Time resolved radiated power during tokamak disruptions and spectral averaging of AXUV photodiode response in DIII-D, *Rev. Sci. Instrum.* **75** (2004) 376–381.

- [4.145] ALEKSEYEV, A.G., BELOV, A.M., ZABRODSKY, V.V., SUKHANOV, V.L., PETERSON, B.J., et al., Fast XUV 16x16 array hybrid module for plasma imaging applications, *Plasma Fusion Res.* **2** (2007) S1061-1-3.
- [4.146] BEKEFI, G., *Radiation Processes in Plasmas*, John Wiley and Sons, New York (1966).
- [4.147] GINZBURG, V.L., *Propagation of Electromagnetic Waves in Plasmas*, Pergamon, New York (1964).
- [4.148] RYTOV, S.M., *Theory of Electric Fluctuations and Thermal Radiation*, Electronics Research Directorate, Air Force Cambridge Research (1959).
- [4.149] HEALD, M.A., WARTON, C.B., *Plasma Diagnostics with Microwaves*, Wiley, New York (1965).
- [4.150] ENGELMANN, F., CURATOLO, M., Cyclotron radiation from a rarefied inhomogeneous magnetoplasma, *Nucl. Fusion* **13** (1973) 497–507.
- [4.151] BORNATICH, M., CANO, R., DE BARBIERI, O., ENGELMANN, F., Electron cyclotron emission and absorption in fusion plasmas, *Nucl. Fusion* **23** (1983) 1153–1257.
- [4.152] CLASSEN, I.G.J., WESTERHOF, E., DOMIER, C.W., “2D ECE measurements inside tearing modes, revealing the suppression mechanism by ECRH at TEXTOR”, *Proc. 14th Joint Workshop on ECE and ECH, Santorini Island, Greece* (2006) 134–144.
- [4.153] ALBAJAR, F., BORNATICH, M., ENGELMANN, F., “Recent progress in electron cyclotron radiative transport modelling of fusion plasmas in view of ITER and DEMO applications”, *Proc. 15th Joint Workshop on ECE and ECH, Yosemite National Park, California, USA* (2008) 345–354.
- [4.154] SHAFRANOV, V.D., “Electromagnetic waves in plasmas”, in *Problems of Plasma Theory*, (LEONTOVICH, M.A., Ed.), Pergamon Press, New York, Vol. 3 (1965) 3.
- [4.155] HARVEY, R.W., SAUTER, O., PRATER, R., NIKKOLA, P., Radial transport and electron-cyclotron-current drive in the TCV and DIII-D Tokamaks, *Phys. Rev. Lett.* **88** (2002) 205001, 1–4.

- [4.156] WESTREHOF, E., “Fokker-Planck quasi-linear codes for the study of electron cyclotron resonance heating and electron cyclotron current drive”, Proc. 9th Joint Workshop on ECE and ECH, Borrego Springs, California, USA (1995) 3–30.
- [4.157] ALBAJAR, F., BORNATICI, M., ENGELMANN, F., EC radiative transfer in fusion plasmas, Nucl. Fusion **42** (2002) 670–678.
- [4.158] COSTLEY, A.E., HASTLIE, R.J., PAUL, J.W.M., CHAMBERLAIN, J., Electron cyclotron emission from a tokamak plasma: experiment and theory, Phys. Rev. Let. **33** (1974) 758–761.
- [4.159] HARTFUSS, H.J., GEIST, T., HIRSCH, M., Heterodyne methods in millimeter wave plasma diagnostics, Plasma Phys. Control. Fusion **39** (1997) 1693–1769.
- [4.160] PORTE, L., BARTLETT, D.V., CONWAY, G., SMEULDERS, P., “Application of high spatial and temporal resolution ECE measurements on JET”, Proc. 10th Joint Workshop on ECE and ECH, Ameland Island, Netherlands (1997) 217–224.
- [4.161] CAVALLO, A., CUTLER, R.C., MCCARTHY, M.P., Twenty-channel grating polychromator for millimeter wave plasma emission measurement, Rev. Sci. Instrum. **59** (1988) 889–894.
- [4.162] JANOS, A., FREDRICKSON, E., MCGUIRE, K., TAYLOR, G., PARK, W., “Thermal and non-thermal electron cyclotron emission during high beta, high density, and locked mode disruptions during D-D and D-T operation of TFTR”, Proc. 9th Joint Workshop on ECE and ECH, Borrego Springs, California, USA (1995) 167–197.
- [4.163] NAGAYAMA, Y., EJIRI, A., KAWAHATA, K., FREDRICKSON, E., JANOS, A., et al., “ECE image reconstruction of MHD mode structure on fusion plasmas”, Proc. 9th Joint Workshop on ECE and ECH, Borrego Springs, California, USA (1995), World Scientific, New Jersey, 455–458.
- [4.164] PARK, H., CHANG, C.C., DENG, B.H., DOMIER, C.W., DONNÉ, A.J.H., Recent advancements in microwave imaging plasma diagnostics, Rev. Sci. Instrum. **74** (2003) 4239–4263.
- [4.165] PARK, H.K., MAZZUCATO, E., LUHMANN, N.C., DOMIER, C.W., XIAET, Z., et al., Self-organized  $T_e$  redistribution during driven reconnection processes in high-temperature plasmas, Phys. Plasmas **13** (2006) 055907 1–12.

- [4.166] BLANCHARD, P., ALBERTI, S., WEISEN, H., NIKKOLA, P., KLIMANOV, I., High field side measurements of non-thermal electron cyclotron emission on TCV plasmas with ECH and ECCD, *Plasma Phys. Control. Fusion* **44** (2002) 2231–2249.
- [4.167] LONTANO, M., POZZOLI, R., SUVOROV, E.V., Cyclotron emission from a toroidal plasma with an isotropic two-temperature electron distribution, *Nuovo Cimento* **63** (1981) 529–540.
- [4.168] LITVAK, A.G., PERMITIN, G.V., SUVOROV, E.V., FRAIMAN, A.A., Electron-cyclotron heating of plasma in toroidal systems, *Nucl. Fusion* **17** (1977) 659–665.
- [4.169] POZNYAK, V.I., PITERSKY, V.V., PLOSKIREV, G.N., PLOSKIREV, E.G., “Application of X- and O-ECE for electron distribution analysis under OH and ECH in T-10 tokamak plasma”, *Proc. 15th Joint Workshop on ECE and ECH, Yosemite National Park, California, USA* (2008) 256–262.
- [4.170] POZNYAK, V.I., PITERSKY, V.V., PLOSKIREV, G.N., PLOSKIREV, E.G., VALENSIA, O., “Space structure analysis of the large scale plasma oscillations  $m/n=1/1$  by means of X- and O-ECE at T-10 tokamak”, *Proc. 15th Joint Workshop on ECE and ECH, Yosemite National Park, California, USA* (2008), *World Scientific, New Jersey*, 136–142.
- [4.171] SHEVCHENKO, V., CUNNINGHAM, G., GURCHENKO, A., GUSAKOV, E., SAVELIEV, A., et al., “EBW heating experiments on MAST”, *Proc. 14th Joint Workshop on ECE and ECH, Santorini Island, Greece*, (2006) 54–58.
- [4.172] LAQUA, H.P., ANDRUCZYK, D., MARSEN, S., OTTE, M., PODOVA, Y.Y., et al., “Experiments with electron Bernstein waves at the WEGA stellarator, *Proc. 15th Joint Workshop on ECE and ECH*”, *Yosemite National Park, California, USA* (2008) 149–154.
- [4.173] DIEM, S.J., TAYLOR, G., EFTIMION, P.C., KUGEL, H.W., LEBLANC, B.P., PHOLLIPS, C.K., “Investigation of EBW thermal emission and mode conversion physics in H-mode plasmas on NSTX”, *Proc. 15th Joint Workshop on ECE and ECH, Experiments with Electron Bernstein Waves at the WEGA stellarator, Yosemite National Park, California, USA, 2008, World Scientific, New Jersey*, 226–231.
- [4.174] BARTLETT, D.V., “Physics aspect of the ITER ECE system design”, *Proc. 10th Joint Workshop on ECE and ECH, Ameland Island, Netherlands* (1997) 217–224.

- [4.175] BARTLETT, D.V., “Physics issues of ECE and ECA for ITER”, Diagnostics for Experimental Thermonuclear Fusion Reactor (STOTT, P.E., GORINI, G., SINDONI, E., Eds), Plenum Press, New York (1996) 183–196.
- [4.176] CHEREPANOV, K.V., KUKUSHKIN, A.B., “Influence of superthermal electrons kinetics on cyclotron radiation transport in hot toroidal plasmas”, Proc. 20th IAEA Fusion Energy Conference, Vilamoura, Portugal (2004) TH/P6-56.
- [4.177] SATO, M., ISIDA, S., ISEI, N., Relativistic broadening effect on application of electron cyclotron emission measurements to high temperature tenuous tokamak plasma, *J. Phys. Soc. Jpn.* **62** (1993) 3106–3113.
- [4.178] LA HAYE, R.J., “Stabilization of neoclassical tearing modes in tokamaks by electron cyclotron current drive”, Proc. 15th Joint Workshop on ECE and ECH, Yosemite National Park, California, USA (2008) 87–95.
- [4.179] SOZZI, C., FARINA, D., FIGINI, L., GAVARAVAGLIA, S., GROSSETTI, G., et al., “Results and prospects of oblique ECE measurements”, Proc. 15th Joint Workshop on ECE and ECH, Yosemite National Park, California, USA (2008) 190–199.
- [4.180] IMAI, T., SAKAMOTO, K., Eds, *Fusion Eng. Des.*, **53**, issues 1–4 (2001).
- [4.181] UCKAN, N., Ed., *Fusion Sci. Technol.* **52**, 2 (2007).
- [4.182] UCKAN, N., Ed., *Fusion Sci. Technol.*, **53**, 1 (2008).
- [4.183] PETROV, M.P., Particle diagnostics of quasistationary thermonuclear plasma, *Sov. J. Plasma Phys.* **2** (1976) 371–387.
- [4.184] HEIDBRINK, W.W., SADLER, G.J., The behaviour of fast ions in tokamak experiment, *Nucl. Fusion* **34** (1994) 535–616.
- [4.185] KISLYAKOV, A.I., KICK, M., W7-AS Team, Measurements of  $n_p/n_d$  Ratio in the W7-AS Stellarator, *Plasma Phys. Rep.* **24** (1998) 165–168.
- [4.186] ZARNSTORFF, M.C., SCOTT, S.D., BARNES, C.W., BELL, R., BUSH, C.E., et al., “Heating and transport in TFTR D-T plasmas”, Proc. 15th IAEA Conference, Seville, Spain (1994), Report IAEA CN-60/A2-2 Vol. **1**, IAEA, Vienna (1995) 183–197.

- [4.187] HAWRYLUK, R.J., ADLER, H., ALLING, P., ANCHER, C., ANDERSON, H., et al., Confinement and heating of a deuterium-tritium plasma on the tokamak fusion test reactor, *Phys. Rev. Lett.* **72** (1994) 3530–3533.
- [4.188] START, D.F.H., JACQUINO, J., BERGAUUD, V., BHATNAGARV, P., COTTRELL, G.A., et al., D-T fusion with ion cyclotron resonance heating in the JET tokamak, *Phys. Rev. Lett.* **80** (1998) 4681–4684.
- [4.189] THOMAS, P.R., ANDREW, P., BALET, B., BARTLETT, D., BULL, J., et al., *Phys. Rev. Lett.* **80** (1998) 5548–5551.
- [4.190] KISLYAKOV, A.I., PETROV, M.P., SUVORKIN, E.V., *Plasma Phys. Control. Fusion* **43** (2001) 1775–1783.
- [4.191] AFROSIMOV, V.V., GLAKOVSKII, I.P., GORDEEV, Yu.S., KALIKEVICH, I.F., FEDORENKO, N.V., Method of investigation of the flux of atoms emitted by a plasma, *Sov. Phys. – Technical Physics* **5** (1961) 1378–1388.
- [4.192] MEDLEY, S.S., DONNÉ, A.J.H., KAITA, R., KISLYAKOV, A.I., PETROV, M.P., ROQUEMORE, A.L., Contemporary instrumentation and application of charge exchange neutral particle diagnostics in magnetic fusion energy experiments, *Rev. Sci. Instrum.* **79** (2008) 011101–011117.
- [4.193] KISLYAKOV, A.I., DONNÉ, A.J.H., KRUPNIK, L.I., MEDLEY, S.S., PETROV, M.P., “Particle diagnostics”, *Fusion Sci. Technol, Special Issue “MFE Diagnostics”* **53** (2008) 577–603.
- [4.194] AFANASYEV, V.I., GONDHALEKAR, A., BABENKO, P.Yu., BEAUMONT, P., DE ANTONIS, P., et al., A neutral particle analyzer/isotope separator for measurement of hydrogen isotope composition of JET plasmas, *Rev. Sci. Instrum.* **74** (2003) 2338–2352.
- [4.195] CHERNYSHEV, F.V., AYUSHIN, B.B., DYACHENKO, V.V., et al., “Recent results from CX diagnostics at Ioffe institute tokamaks”, *Proc. 34th EPS Conference on Plasma Physics, Warsaw, Poland*, **31F** (2007) P-5.107.
- [4.196] KOROTKOV, A.A., GONDHALEKAR, A., STUART, A.J., Impurity induced neutralization of megaelectronvolt energy protons in JET plasmas, *Nucl. Fusion* **37** (1997) 35–52.

- [4.197] KOROTKOV, A., ERMOLAEV, A.M., “Impurity induced neutralization of alpha-particles and application to ITER diagnostics”, Proc. 22nd EPS Conf. on Controlled Fusion and Plasma Physics, Bournemouth (1995), **19C**, Contributed Papers, Part III, European Physical Society, Geneva (1995) 389–392.
- [4.198] PETROV, M.P., AFANASYEV, V.I., CORTI, S., GONDHALEKAR, A., KHUDOLEEV, A.V., et al., “Neutral particle analysis in the MeV range in JET”, Proc. of International Conference on Plasma Physics, Innsbruck, Austria, (1992), **16C**, Part II, European Physical Society, Geneva (1992) 1031.
- [4.199] PETROV, M.P., BELL, R., BUDNY, R.V., GORELENKOV, N.N., et al., Effective temperatures, sawtooth mixing and stochastic diffusion ripple loss of fast  $H^+$  minority ions driven by ion cyclotron heating in the tokamak fusion test reactor, Phys. Plasmas **6** (1999) 2430–2436.
- [4.200] AFANASSIEV, V.I., KUSAMA, Y., NEMOTO, M., KONDOH, T., PETROV, S.Ya., et al., Neutral particle analysis in MeV energy range and relative role of  $He^+$  and  $C^{5+}$  ions in fast proton neutralization in ICRF and combined ICRF/NBI-heated JT-60U plasmas, Plasma Phys. Control. Fusion **39** (1997) 1509–1524.
- [4.201] KISLYAKOV, A.I., KHUDOLEEV, A.V., KOSLOVSKIY, S.S., PETROV, M.P., High energy neutral particle analyzer, Fusion Eng. Des. **34–35** (1997) 107–113.
- [4.202] PETROV, M.P., FISHER, R.K., “Charge-exchange diagnostics of fast confined alphas: Present situation and prospects for ITER”, Diagnostics for Experimental Thermonuclear Fusion Reactor, Plenum Press, New York (1996) 495–505.
- [4.203] AFANASYEV, V.I., KISLYAKOV, A.I., KOZLOVSKIY, S.S., LJUBLIN, B.V., PETROV, M.P., et al., Neutral particle analysis on ITER-FEAT, Proc. of 30th EPS conference on controlled fusion and plasma physics, St. Petersburg, Russia, ECA 27a (2003), O-4.4D.
- [4.204] VEKSLER, V., GROSHEV, L., ISAEV, D., Ionizing methods of radiation investigations, State Publishing House of Technical-theoretical Literature, Moscow–Leningrad (1949).
- [4.205] SUSHKOV, A., ANDREEV, V., CAMENEN, Y., POCHELON, A., KLIMANOV, I., et al., High-resolution multiwire proportional soft X-ray diagnostic, Rev. Sci. Instrum. **79** (2008) 023506-1 – 023506-5.
- [4.206] WOLDSETH, R., X-ray Energy Spectrometry, Kevex Corporation, Burlingame, California (1973).

- [4.207] GOTT, Yu.V., STEPANENKO, M.M., Vacuum photodiode detectors for soft X-ray ITER plasma tomography, *Rev. Sci. Instrum.* **76** (2005) 073506-1 – 073506-4.
- [4.208] GOTT, Yu.V., STEPANENKO, M.M., The radiation-tolerant X-ray monitor, *Rev. Sci. Instrum.* **79** (2008) 10E930-1 – 10E930-3.
- [4.209] MAQUEDA, R.J., WURDEN, G.A., GRAWFORD, E.A., Wideband “silicon bolometers” on the LSX field reversed configuration, *Rev. Sci. Instrum.* **63** (1992) 4717–4719.
- [4.210] GRAY, D.S., LUCKHARDT, S.C., CHOUSAL, L., GUNNER, G., KELLMAN, A.G., et al., Time resolved radiated power during tokamak disruptions and spectral averaging of AXUV photodiode response in DIII-D, *Rev. Sci. Instrum.* **75** (2004) 376–381.
- [4.211] SUSHKOV, A.V., ANDREEV, V.F., KRAVTSOV, D.E., *Rev. Sci. Instrum.* **79** (2008) 10E319-10E319-3.
- [4.212] KADOMTSEV, B.B., *Osnovi fiziki plazmi tokamaka (The foundation of tokamak plasma physics), Itogi nauki i tehniki (Results of the science and technik), Fizika Plazmi*, **10**, 1991 Moscow (in Russian).
- [4.213] GARCIA-MUNOZ, M., FAHRBACH, H.-U., GUNTER, S., IGOCHINE, V., MANTSINEN, M.J., et al., Fast-ion losses due to high-frequency MHD perturbations in the ASDEX upgrade tokamak, *Phys. Rev. Lett.* **100** (2008) 055005-1 – 055005-4.
- [4.214] ODACHI, S., TOI, K., FUCHS, G., VON GORLER, S., Tangential soft X-ray camera for Large Helical Device, *Rev. Sci. Instrum.* **72** (2001) 724–726.
- [4.215] FUCHS, G., PICALOV, V., TOI, K., et al., Tomographic inversion in toroidal geometry using flux coordinates, *Proc. 26th EPS Conf., Maastricht, 1999, ECA, in Control. Fusion Plasma Phys.* **23J** (1999) 757–760.
- [4.216] QIAN, J.P., LAO, L.L., REN, Q.L., RINDERKNECHT, H., VOLPE, F., et al., Equilibrium reconstruction of plasma profiles based on soft X-ray imaging in DIII-D, *Nucl. Fusion* **49** (2009) 025003-1 – 025003-8.
- [4.217] MLYNAR, J., DUVAL, B.P., HORACEK, J., LISTER, J.B., *Fusion Eng. Des.* **66–68** (2003) 905–909.
- [4.218] LUK’JANOV, S.Yu., *Hot Plasmas and Nuclear Fusion, Science, Moscow* (1975).

- [4.219] JAHODA, F.C., LITTLE, E.M., QUINN, W.E., SAWYER, G.A., STEATTON, T.F., Continuum Radiation in the X-Ray and Visible Regions from a Magnetically Compressed Plasma (Scylla), *Phys. Rev.* **119** (1960) 843–856.
- [4.220] SHI, Yu., CHEN, Z., WAN, B., LU, B., HU, L., et al., Soft X-ray pulse height analyzer in the HT-7 tokamak, *Rev. Sci. Instrum.* **75** (2004) 4930–4933.
- [4.221] BITTER, M., HILL, K.W., STRATTON, B., ROQUEMORE, A.L., MASTROVITO, D., et al., Spatially resolved spectra from a new X-ray imaging crystal spectrometer for measurement of ion and electron temperature profiles, *Rev. Sci. Instrum.* **75** (2004) 3660–3665.
- [4.222] VON GOELLER, S., STODIEK, W., EUBANK, H., FISHMAN, H., GREBENSCHIKOV, S., Thermal X-ray spectra and impurities in the ST tokamak, *Nucl. Fusion* **15** (1975) 301–311.
- [4.223] STRATTON, B.S., BITTER, M., HILL, K.W., Passive spectroscopic diagnostics for magnetically confined fusion plasmas, *Fusion Sci. Technol.* **53** (2008) 431.
- [4.224] VON GOELER, S., in *Proc. European Conf. on CF and Plasma Physics*, Lausanne, Switzerland, 1–5 September 1975, Vol. **II** (1975) 71.
- [4.225] SEATON, M.J., STOREY, P.J., *Atomic Processes and Applications* (BURKE, P.J., MOISEVITSCH, B.L., Eds), Springer, Amsterdam, New York, Oxford (1976) 113.
- [4.226] HILL, K.W., GOELER, S.V., BITTER, M., CAMPBELL, L., COWAN, R.D., et al., Determination of Fe charge-state distributions in the Princeton Large Torus by Bragg crystal X-ray spectroscopy, *Phys. Rev. A* **19** (1979) 1770–1779.
- [4.227] JOHANN, H., *Z. Phys.* **69** (1931) 185–192.
- [4.228] BITTER, M., VONGOELER, S., HORTON, R., GOLDMAN, M., HILL, K.W., et al., Doppler-broadening measurements of X-ray lines for determination of the ion temperature in tokamak plasmas, *Phys. Rev. Lett.* **42** (1979) 304–308.
- [4.229] HILL, K.W., BITTER, M., TAVERNIER, M., DIESSO, M., VONGOELER, S., et al., Tokamak fusion test reactor horizontal high-resolution Bragg X-ray spectrometer, *Rev. Sci. Instrum.* **56** (1985) 848–852.

- [4.230] BITTER, M., HILL, K.W., COHEN, S., VONGOELER, S., HSUAN, H., High-resolution Bragg X-ray spectrometer for the Tokamak Fusion Test Reactor, *Rev. Sci. Instrum.* **57** (1986) 2145–2148.
- [4.231] BITTER, M., HSUAN, H., RICE, J.E, HILL, K.W., DIESSO, M., et al., Measurements of radial profiles of the ion temperature and the plasma rotation velocity with the TFTR vertical X-ray crystal spectrometer, *Rev. Sci. Instrum.* **59** (1988) 213–218.
- [4.232] BARTIROMO, R., BOMBARDA, F., GIANELLA, R., et al., *Rev. Sci. Instrum.* **60** (1989) 237–241.
- [4.233] BEIERSDORFER, P., BITTER, M., VONGOELER, S., COHEN, S., HILL, K.W., et al., High-resolution  $n=3$  to  $n=2$  spectra of neon-like silver, *Phys. Rev. A* **34** (1986) 1297–1315.
- [4.234] BEIERSDORFER, P., BITTER, M., VONGOELER, S., HILL, K.W., Experimental-study of the X-ray transitions in the helium-like isoelectronic sequence, *Phys. Rev. A* **40** (1989) 150–156.
- [4.235] GABRIEL, A.H., Dielectronic satellite spectra for highly charged helium-like ion lines-I, *Mon. Not. R. Astr. Soc.* **160** (1972) 99–119.
- [4.236] BHALLA, C.P., GABRIEL, A.H., PRESNYAKOV, L.P., Dielectronic satellite spectra for highly charged helium-like ion lines-II, *Mon. Not. R. Astr. Soc.* **172** (1975) 359–365.
- [4.237] VAINSHTEIN, L.A., SAFRONOVA, U.I., *At. Data Nucl. Data Tab.* **21** (1978) 49–57.
- [4.238] BELY-DUBAU, F., GABRIEL, A.H., VOLONTE, S., Dielectronic satellite spectra for highly charged helium-like ion lines-III. Calculations of  $n=3$  solar flare iron lines, *Mon. Not. R. Astr. Soc.* **186** (1979) 405–419.
- [4.239] GABRIEL, A.H., PHILLIPS, K.J.H., Dielectronic satellite spectra for highly charged helium-like ion lines-IV. Iron satellite lines as a measure of non-thermal electron energy distributions, *Mon. Not. R. Astr. Soc.* **189** (1979) 319–327.
- [4.240] BELY-DUBAU, F., GABRIEL, A.H., VOLONTE, S., Dielectronic satellite spectra for highly charged helium-like ion lines-V. Effect of total satellite contribution on the solar flare iron spectra, *Mon. Not. R. Astr. Soc.* **189** (1979) 801–816.

- [4.241] BITTER, M., HILL, K.W., ROQUEMORE, A.L., BEIERSDORFER, P., KAHN, S.M., et al., Imaging X-ray crystal spectrometers for the National Spherical Torus Experiment, *Rev. Sci. Instrum.* **70** (1999) 292–296.
- [4.242] BITTER, M., HILL, K.W., SAUTHOFF, N.R., EFTHIMION, P.C., MESERVEY, E., et al., Dielectronic satellite spectrum of helium-like iron (Fe-XXV), *Phys. Rev. Lett.* **43** (1979) 129–134.
- [4.243] FRAENKEL, B.S., BITTER, M., New concepts for X-ray spectroscopy of tokamak plasmas, *Rev. Sci. Instrum.* **70** (1999) 296–299.
- [4.244] PLATZ, P., MARGERIT, Y., ARTAUD, J.-F., MATIOLLI, M., MOULIN, B., X-ray line diagnostics on the Tore-Supra tokamak, *Rev. Sci. Instrum.* **70** (1999) 308–312.
- [4.245] RICE, J., MARMAR, E.S., Five chord high-resolution X-ray spectrometer for Alcator C-Mod, *Rev. Sci. Instrum.* **61** (1990) 2753–2577.
- [4.246] RICE, J., BOMBARDA, F., GRAF, M.A., MARMAR, E.S., WANG, Y., Observations of Alcator C-Mod plasmas from five chord high energy resolution X-ray spectrometer array, *Rev. Sci. Instrum.* **66** (1995) 752–758.
- [4.247] BARTIROMO, R., GIANELLA, R., APICELLA, M.L., BOMBARDA, F., MANTOVAI, S., et al., Time resolving bent crystal spectrometer for tokamak plasma diagnostics, *Nucl. Instrum. Methods Phys. Res.* **225** (1984) 378–382.
- [4.248] KALLNE, E., KALLNE, J., MARMAR, E.S., RICE, J.E., Plasma atomic X-ray spectroscopy on tokamaks, *Nuclear Instrum. Methods Phys. Res. B* **9**, issue 4 (2007) 698–703.
- [4.249] HILL, K.W., BITTER, M., TAVERNIER, M., DIESSO, M., VONGOELER, S., et al., Tokamak Fusion Test Reactor horizontal high-resolution Bragg X-ray spectrometer, *Rev. Sci. Instrum.* **56** (1985) 1165–1171.
- [4.250] BITTER, M., HILL, K.W., COHEN, S., VONGOELER, S., HSUAN, H., et al., Vertical high-resolution Bragg X-ray spectrometer for the Tokamak Fusion Test Reactor, *Rev. Sci. Instrum.* **57** (1986) 2145–2147.
- [4.251] BARTIROMO, R., BOMBARDA, F., GIANELLA, R., MANTOVANI, S., PANACCIONE, L., et al., JET high resolution bent crystal spectrometer, *Rev. Sci. Instrum.* **60** (1989) 237–241.

- [4.252] MATTIOLI, M., RAMETTE, J., SAOUTIC, B., DENNE, B., KALLNE, E., Impurity ion temperature and toroidal rotation velocity in JET from high resolution X-ray and EUV spectroscopy, *J. Appl. Phys.* **64** (1988) 3345–3351.
- [4.253] WEINHEIMER, J., AHMAD, I., HERZOG, O., KUNZE, H.-J., High resolution X-ray crystal spectrometer/polarimeter at torus experiment for technology oriented research, *Rev. Sci. Instrum.* **72** (2001) 2566–2570.
- [4.254] BRETON, C., MICHELIS, C., MATTIOLI, M., MONIER, M., RAMETTER, D., et al., Spatially resolved soft X-ray spectroscopy of tokamak plasmas, *Meas. Sci. Technol.* **1** (1990) 50–52.
- [4.255] BARNSLEY, R., PEACOCK, N.J., DUNN, J., Versatile high resolution crystal spectrometer with X-ray charge coupled device detector, *Rev. Sci. Instrum.* **74** (2003) 2388–2392.
- [4.256] BARNSLEY, R., EVANS, K.D., PEACOCK, N.J., HAWKES, N.C., Bragg rotor spectrometer for tokamak diagnostics, *Rev. Sci. Instrum.* **57** (1986) 2159–2163.
- [4.257] BARTIROMO, R., BOMBARDA, F., GABELLIERI, L., PIZZICAROLI, G., TUKKILO, A.A., ZAGARELLA, G., High counting rate soft X-ray spectrometer for tokamak plasma diagnostics, *Nucl. Instrum. Methods Phys. Res.* **B95** (1995) 537–541.
- [4.258] BITTER, M., HILL, K.W., STRATTON, B., ROQU, C., MASTROVITO, D., et al., Spatially resolved spectra from a new X-ray imaging crystal spectrometer for measurements of ion and electron temperature profiles, *Rev. Sci. Instrum.* **75** (2004), 3660–3665.
- [4.259] BERTSCHINGER, G., BIEL, B., HAEGERS, H., MARCHUK, O., Compact imaging Bragg spectrometer for fusion devices, *Rev. Sci. Instrum.* **75** (2004) 3727–3731.
- [4.260] BERTSCHINGER, G., MARCHUK, O., High temperature plasma diagnostics by X-rays spectroscopy in the low density limit, *Nucl. Fusion Res. (CLARK, E., REITER, D.H., Eds), Springer* (2005).
- [4.261] LEE, S.G., BAK, J.G., BITTER, M., HILL, K., NAM, U.W., KIM, Y.J., MOON, M.K., Research and development of X-ray imaging crystal spectrometers for KSTAR, *Rev. Sci. Instrum.* **75** (2004) 3693–3697.
- [4.262] FUJIMOTO, T., IWAMAE, A., *Plasma Polarization Spectroscopy, Springer* (2007).
- 4.263] FUJIMOTO, T., *Plasma Spectroscopy, Clarendon Press, Oxford* (2004).

- [4.264] BARONOVA, E.O., STEPANENKO, M.M., STEPANENKO, A.M., X-ray spectropolarimeter, *Rev. Sci. Instrum.* **79** (2008) 083105.
- [4.265] BARONOVA, E.O., STEPANENKO, M.M., “Novel polarimeter-spectrometer for X-rays”, *Plasma Polarization Spectroscopy* (FUJIMOTO, T., IWAMAE, A., Ed.), Springer (2007) 334–345.
- [4.266] BARONOVA, E.O., STEPANENKO, M.M., X-ray Polarimeter, Patent RRC KIAE № 2322684, *Bul. №11, 20.4.* (2008).
- [4.267] LIDER, V.V., BARONOVA, E.O., STEPANENKO, M.M., Experimental characterization of bent focusing crystals, *Cryst. Rep.* **46** (2001) 341–349.
- [4.268] STEPANENKO, M.M., Spectral resolution of X-ray spectrometers with bent crystals, *Plasma Devices and Operations* **17**, No.3 (2009) 191–200.
- [4.269] ARTSIMOVICH, L.A., ANASHIN, A.M., GORBUNOV, E.P., IVANOV, D.P., PETROV, M.P., et al., Heating of ions in the Tokamak 3 installation, *Letters to Sov. ZhETF* **10** (1969) 130–133 (in Russian).
- [4.270] ARTSIMOVICH, L.A., ANASHIN, A.M., GORBUNOV, E.P., IVANOV, D.P., PETROV, P., et al., Investigation of plasma neutron radiation from the Tokamak 3A installation, *Sov. Phys. - ZhETF* **61** (1971), 575-581 (in Russian).
- [4.271] JARVIS, O.N., Neutron measurement techniques for tokamak plasmas, *Plasma Phys. Control. Fusion* **36** (1994) 209–244.
- [4.272] SASAO, M., NISHITANI, T., KRASILNILOV, A., POPOVICHEV, S., KIPTILY, V., et al., Fusion product diagnostics, *Fusion Sci. Technol.* **53** (2008) 604–639.
- [4.273] ZAVERYAEV, V.S., LUK’YANOV, S.Yu., Neutron emission in big tokamaks, *Sov. Phys. - ZhETF* **73** (1977) 1783–1793 (in Russian).
- [4.274] BARNES, C.W., LARSON, A.R., LeMUNYAN, G., LOUGHLIN, M.J., Measurements of DT and DD neutron yields by neutron activation on the Tokamak Fusion Test Reactor, *Rev. Sci. Instrum.* **66** (1995) 888.
- [4.275] NISHITANI, T., EBISAWA, K., KASAI, S., WALKER, C., Neutron activation system using water flow for ITER, *Rev. Sci. Instrum.* **74** (2003) 1735–1783.

- [4.276] STRACHAN, J.D., JASSBY, D.L., Observation of electrodisintegration neutron production in the Princeton Large Tokamak, *Trans. Amer. Nucl. Soc.* **26** (1977) 509–510.
- [4.277] FISHER, W.A., CHEN, S.H., GWINN, D., PARKER, R.R., Measurement of the D-D fusion neutron energy spectrum and variation of the peak width with plasma ion temperature, *Phys. Rev. A* **28** (1983) 3121–3124
- [4.278] STRACHAN, J.D., COLESTOCK, P.L., DAVIS, S.L., EAMES, D., EFTHIMION, P.C., et al., Fusion neutron production during deuterium neutral-beam injection into the PLT tokamak, *Nucl. Fusion* **21** (1981) 67–81.
- [4.279] KÄLLNE, J., BALLABIO, L., FRENJE, J., CONROY, S., ERICSSON, G., et al., Observation of the alpha particle “Knock-On” neutron emission from magnetically confined DT fusion plasmas, *Phys. Rev. Lett.* **85** (2000) 1246–1249.
- [4.280] CHRIEN, R.E., COLESTOCK, P.L., EUBANK, H.P., HOSEA, J.C., HWANG, D.Q., et al., Observation of  $d$ - $^3\text{He}$  fusion reactions in a tokamak plasma, *Phys. Rev. Lett.* **46** (1981) 535–538.
- [4.281] MURPHY, T.J., STRACHAN, J.D., Spatially resolved measurement of alpha particle emission from PLT plasmas heated by ICRH, *Nucl. Fusion* **25** (1985) 383.
- [4.282] ZWEBEN, S.J., Pitch angle resolved measurements of escaping charged fusion products in TFTR, *Nucl. Fusion* **29** (1989) 825–833.
- [4.283] BOIVIN, R.L., “Measurements of charged fusion products”. Diffusion in TFTR, Report PPPL-2797, Princeton Plasma. Phys. Lab., NJ (1991).
- [4.284] REICH, M., BÄUMEL, S., DARROW, D., FAHRBACH, H.-U., FULLARD, K., et al., Ion loss measurements with scintillator probes at JET and ASDEX Upgrade, *Rev. Sci. Instrum.* **75** (2004) 3563.
- [4.285] KIPTILY, V.G., PEREZ VON THUN, C.P., PINCHES, S.D., SHARAPOV, S.E., BORBA, D., et al., Recent progress in fast ion studies on JET, *Nucl. Fusion* **49** (2009) 065030.
- [4.286] ZAVERYAEV, V.S., MAJSUKOV, V.D., POPOVICHEV, S.V., SHEVCHENKO, A.P., “Charged fusion products behavior in T-10 tokamak plasma”, *Proc. 20th Eur. Conf., Lisboa, 1993*, **17C**, Part I, European Physical Society, Geneva (1993), 75; *Control. Fusion Plasma Phys.* **1** (1993) 75–78.

- [4.287] ZAVERYAEV, V.S., MAISJUKOV, V.D., POPOVICHEV, S.V., SHEVCHENKO, A.P., KHRAMENKOV, A.V., Evaluation of ion temperature profile at T-10 by measurements of DD fusion products, *Plasma Phys. Rep.* **26** (2000) 109–114.
- [4.288] FELT, J., BARNES, C.W., CHRIEN, R.E., COHEN, S.A., HEIDBRINK, W.W., et al., PPPL Lorentz orbit code, *Rev. Sci. Instrum.* **61** (1990) 3262.
- [4.289] CECIL, F.E., ROY, B., KERN, S., NOWAK, A., TAKIMOTO, Y., Development and operation of a thin foil Faraday collector as a lost ion diagnostic for high yield DT tokamak fusion plasmas, *Rev. Sci. Instrum.* **70** (1999) 1149–1153.
- [4.290] ZAVERYAEV, V.S., MAISYUKOV, V.D., KHRAMENKOV, A.V., POPOVICHEV, S.V., SHEVCHENKO, A.P., et al., Diagnostics proposal for T-15 fusion research by means of charged products and neutrons, *Nucl. Fusion* **35** (1995) 1631–1637.
- [4.291] ZWEBEN, S.J., DARROW, D.S., ROSS, P.W., LOWRANCE, J.L., RENDA, G., Measurement of the internal magnetic field of plasmas using an alpha particle source, *Rev. Sci. Instrum.* **75** (2004) 3610–3612.
- [4.292] YOSHINO, R., KONDOH, T., NEYATANI, Y., ITAMI, K., KAWANO, Y., et al., Fast plasma shutdown by killer pellet injection in JT-60U with reduced heat flux on the divertor plate and avoiding runaway electron generation, *Plasma Phys. Control. Fusion* **39** (1997) 313–332.
- [4.293] PANKRATOV, I.M., JASPERS, R., FINKEN, K.H., ENTROP, I., MANK, G., Control of runaway electron secondary generation by changing  $Z_e$ , *Nucl. Fusion* **38** (1998) 279–286.
- [4.294] KAWANO, Y., YOSHINO, R., NEYATANI, Y., KONDO□T., NOBUAKI, I., et al., “Suppression of runaway-electrons generation during disruptive discharge-terminations in JT-60U”, *Proc. 24th EPS Conf. on Control. Fusion and Plasma Physics, Berchtegaden, Germany, June 1997*, **21A**. P. II (1997) 501–504.
- [4.295] ESPOSITO, B., BERTALOT, L., KASCHUCK, Yu.A., PORTNOV, D.V., MARTIN-SOLIS, J.R., A gamma-ray spectrometer system for fusion applications, *Nucl. Instrum. Methods Phys. Res. A.* **476** (2002) 522–526.
- [4.296] SHEVELEV, A.E., CHUGUNOV, I.N., GUSEV, V.K., PETROV, Yu.V., ROZHDESTVENSKI, V.V., et al., Studies of runaway electrons in the Globus-M Tokamak, *Fiz. Plazmy* **30** (2004), 180-184; English translation in *Plasma Phys. Rep.* **30** (2004), 159-163.

- [4.297] ESPOSITO, B., MARTIN-SOLIS, R., VAN BELLE, P., JARVIS, O.N., MARCUS, F.B., et al., Runaway electron measurements in the JET tokamak, *Plasma Phys. Control. Fusion* **38** (1996) 2035–2049.
- [4.298] ESPOSITO, B., MARTIN-SOLIS, R., POLI, F.M., MIER, J.A., SANCHEZ, R., PANACCIONE, L., Dynamics of high energy runaway electrons in the Frascati Tokamak Upgrade, *Phys. Plasmas* **10** (2003) 2350–2360.
- [4.299] DREICER, H., Electron and ion runaway in a fully ionized gas, *Phys. Rev.* **115** (1959) 238–249.
- [4.300] KNOEPFEL, H., SPONG, D.A., Runaway electrons in toroidal discharges, *Nucl. Fusion* **19** (1979) 785–829.
- [4.301] PARAIL, V.V., POGUTSE, O.P., “Runaway electrons in a tokamak”, *Review of Plasma Physics*, Vol. **11** (LEONTOVICH, M.A., Ed.), Consultants Bureau, New York (1986).
- [4.302] MARTIN-SOLIS, J.R., ESPOSITO, B., SANCHEZ, R., ALVAREZ, J.D., Energy limits on runaway electrons in tokamak plasmas, *Phys. Plasmas* **6** (1999) 238–252.
- [4.303] HELANDER, P., ERIKSSON, L.-G., ANDERSSON, F., Runaway acceleration during magnetic reconnection in tokamaks, *Plasma Phys. Control. Fusion* **44** (2002) B247–B262.
- [4.304] KIPTILY, V.G., CECIL, F.E., MEDLEY, S.S., Gamma ray diagnostics of high temperature magnetically confined fusion plasmas, *Plasma Phys. Control. Fusion* **48** (2006) R59–R82.
- [4.305] NEWMAN, D.E., CECIL, F.E., Observation of gamma rays from fusion reactions in a tokamak plasma, *Nucl. Instrum. Methods* **227** (1984) 339–341.
- [4.306] SADLER, G.J., JARVIS, O.N., BELL, P.V., HAWKES, N., SYME, B., “Observation of fusion reaction gamma-rays in JET”, *Proc. 14<sup>th</sup> European Conf. on Controlled Fusion and Plasma Physics*, Madrid, Spain, *European Conference Abstracts*, Vol. III (1987) 1232.
- [4.307] BOYD, D.A., CAMPBELL, D.J., CORDET, J. CORE, G.W., CHRISTIANSEN, J.P., et al., He-D fusion reaction rate measurements during ICRH heating experiments in JET, *Nucl. Fusion* **29** (1989) 593–604.
- [4.308] CECIL, F.E., MEDLEY, S.S., Gamma ray measurements during deuterium and <sup>3</sup>He discharges on TFTR, *Nucl. Instrum. Methods* **271** (1989) 628–635.

- [4.309] KONDOH, T., KUSAMA, Y., KIMURA, H., SAIGUSA, M., FUJII, T., et al., Investigation of interaction between MeV-ions and first wall from neutron and  $\gamma$ -ray measurements in JT-60U, *J. Nucl. Mat.* **241–243** (1997) 564–568.
- [4.310] KIPTILY, V.G., BARANOV, Yu.F., BARNSLEY, R., BERTALOT, L., HAWKES N.C., et al., First gamma-ray measurements of fusion alpha particles in JET trace tritium experiments, *Phys. Rev. Lett.* **93** (2004) 115001–115004.
- [4.311] KIPTILY, V.G., KONDOH, T., NAIDENOV, V.O., POLUNOVSKI, L.A., TUBOLTSEV, Yu.V., et al., “Gamma ray spectrometry in ITER: conceptual design”, *Diagnostics for Experimental Thermonuclear Fusion Reactors 2* (STOTT, P.E., GORINI, G., SINDONI, E., Eds), Plenum Press, New York and London (1998) 511–519.
- [4.312] CHUGUNOV, I.N., SHEVELEV, A.E., GIN, D.B., NAIDENOV, V.O., KIPTILY, V., et al., Testing the neutron attenuator based on 6LiH for  $\gamma$ -ray diagnostics of plasmas in the JET tokamak, *Instrum. Exp. Tech.* **51** (2008) 166–170.
- [4.313] MEDLEY, S.S., SCOTT, S.D., ROQUEMORE, A.L., CECIL F.E., Performance of the fusion gamma diagnostic on TFTR, *Rev. Sci. Instrum.* **61** (1990) 3226–3228.
- [4.314] FIOCCO, G., THOMPSON, E., Thomson scattering of optical radiation from an electron beam, *Phys. Rev. Lett.* **10** (1963) 89–91.
- [4.315] PEACOCK, N.J., ROBINSON, D.C., FORREST, M.J., WILCOCK, P.D., SANNIKOV, V.V, Measurement of the electron temperature by Thomson scattering on tokamak T-3A, *Nature* **224** (1969) 488–490.
- [4.316] SHEFFILD, J., *Plasma Scattering of Electromagnetic Radiation*, Academic Press, New York, London, San Francisco (1975).
- [4.317] EVANS, D.E., KATZENSTEIN, J., *Rep. Prog. Phys.* **32** (1969) 207.
- [4.318] DONNE, A.J.H., BARTH, C.J., WIESEN, H., Laser-aided plasma diagnostics, *Fusion Sci. Technol.* **53** Chapter 4 (2008) 405–414.
- [4.319] BARTH, C.J., BEURSKENS, M.N.A., CHU, C.C., DONNE, A.J.H., LOPES CARDOZO, N.J., et al., A high resolution multiposition Thomson scattering system for the Rijnhuizen Tokamak Project, *Rev. Sci. Instr.* **68** (1997) 3380–3392.
- [4.320] SALPETER, E., Electron density fluctuations in a plasma, *Phys. Rev.* **120** (1960) 1528–1536.

- [4.321] MATTIOLI, M., Incoherent light scattering from high temperature plasmas, EUR-CEA-EC-752 (1974).
- [4.322] MATTIOLI, M., PAPOULAR, R., Analysis of light scattering data from relativistic plasmas, *Plasma Phys.* **17** (1975) 165–172.
- [4.323] LUKJANOV, S.Yu., Hot plasma and Controlled Nuclear Fusion, Science Publishing House, Moscow (1975) 203 (in Russian).
- [4.324] DONNÈ, A.J.H., “Incoherent Thomson scattering”, Course on 2nd Carolus Magnus Summer School on Plasma Physics, Aachen, Germany, 1995; *Int. J. Amer. Nucl. Soc.* **29**, 2T, 1–432 (1996) 324–331.
- [4.325] GORSHKOV, A.V., BARTH, C.J., BEL’BAS, I.S., DONNÈ, A.J.H., MASLOV, M.V., et al., “High resolution Thomson scattering diagnostic on T-10 tokamak”, Report 11th Int. Symp. on Laser-aided Plasma Diagnostics, Abstract P20 (2003) 57.
- [4.326] VAN DER MEIDEN, H.J., VARSHNEY, S.K., BARTH, C.J., OYEVAAR, T., JASPERS, R., DONNE, A.J.H., et al., 10 kHz repetitive high-resolution TV Thomson scattering on TEXTOR: design and performance, *Review of Scientific Instruments* **77**, 10E512 (2006).
- [4.327] JOHNSON, D., DIMOCK, D., GREK, B., LONG, D., NEILL, D., et al., Multichannel Thomson scattering system with high spatial resolution, *Rev. Sci. Instrum.* **57** (1986) 1856–1870.
- [4.328] CARLSTROM, T.N., CAMPBELL, G.L., DeBOO, J.C., EVANKA, R., EVANS, J., et al., Design and operation of the multipulse Thomson scattering diagnostic on DIII-D, *Rev. Sci. Instrum.* **63** (1992) 4901–4906.
- [4.329] MURMANN, H., GOTSCH, S., ROHR, H., SALZMANN, H., STEUER, K.H., The Thomson scattering systems of the ASDEX-Upgrade tokamak, *Rev. Sci. Instrum.* **63** (1992) 4941–4943.
- [4.330] BRETZ, N., DIMOCK, D., FOOTE, V., JOHNSON, D.J., LONG, D., et al., Multichannel Thomson scattering apparatus, *Appl. Opt.* **17** (1978) 192–202.
- [4.331] BARTH, C.J., VAN DER MEIDEN, H.J., OYEVAAR, T., LOPES CARDOZO, N.J., High-resolution multiposition Thomson scattering on TEXTOR, *Rev. Sci. Instr.* **72** (2001) 1138.
- [4.332] BINDSLEV, H., “Collective Thomson scattering for diagnosis of fast ions”, Proc. 8th Int. Symp. on Laser-Aided Plasma Diagnostic, Doorwerth, Netherlands (1997) 265–276.

- [4.333] BEHN, R., DICKEN, D., HACKMANN, J., SALITO, S.A., SIEGRIST, M.R., et al., Ion temperature measurement of tokamak plasmas by collective Thomson scattering of D<sub>2</sub>O laser radiation, *Phys. Rev. Lett.* **62** (1989) 2833–2836.
- [4.334] SUVOROV, E.V., ERCKMANN, V., HOLZHAUER, E., KASPAREK, W., DRYAGIN, Y.A., et al., Ion temperature and beam-driven plasma waves from collective scattering of gyrotron radiation in W7-AS, *Plasma Phys. Control. Fusion* **37** (1995) 1207–1213.
- [4.335] STOTT, P.E., Review of JET Diagnostics and Results: JET report JET-P(87)04 (1987).
- [4.336] SUVOROV, E.V., DRYAGIN, Y.A., FILCHENKO, S.E., FRAIMAN, A.A., KUKIN, L.M., et al., First results on ion temperature measurements on W7-AS by collective scattering of 140 GHz gyrotron radiation, Proc. 9<sup>th</sup> Joint workshop on ECE and ECH, Borrego Spring, California (1995) 501–508.
- [4.337] ORSITTO, F., BRUSADIN, A., BRODSKY, Yu., FILCHENKOV, S., GROSSO, G., et al., Characterization and preliminary results of the collective Thomson scattering (CTS) system on FTU tokamak, Proc. 8<sup>th</sup> Int. Symp. on Laser-Aided Plasma Diagnostic, Doorwerth, Netherlands (1997) 277–280.
- [4.338] GOWERS, C.W., BROWN, B.W., FAJEMIROKUN, H., NIELSEN P., NIZIENKO, Y., et al., Recent developments in LIDAR Thomson scattering measurements on JET, *Rev. Sci. Instr.* **66** (1995) 471–475.
- [4.339] WALSH, M., BEURSKENS, M., CAROLAN, P.G., GILBERT, M., MOUGHLIN, L., et al., Design challenges and analysis of the ITER core LIDAR Thomson scattering system, *Rev. Sci. Instr.* **77** (2006) 10E525(4).
- [4.340] RAZDOBARIN, G.T., SEMENOV, V.V., SOKOLOVA, L.V., FOLOMKIN, I.P., BURAKOV, V.S., Measurement of the neutral density profile in the tokamak plasma by an absolute resonance fluorescence on the H $\alpha$  line, *Nucl. Fusion* **19** (1979) 1439–1446.
- [4.341] BOGEN, P., HINTZ, E., “Plasma edge diagnostics using optical methods”, *Physics of Plasma-wall Interaction in Controlled Fusion* (POST, D.E., BERISCH, R., Eds), Plenum Publishing Corporation (1986) 229–249.
- [4.342] BOGEN, P., DREYFUS, R.W., LIE, Y.T., LANGER, H., Measurement of atomic hydrogen densities and velocities by laser-induced fluorescence at Lyman- $\alpha$ , *J. Nucl. Mater.* **111–112** (1982) 75–80.

- [4.343] MERTENS, Ph., POSPIESZCZYK, A., Radial and spectral profiles of atomic deuterium in front of a limiter in TEXTOR-94: results of laser-induced fluorescence at Lyman- $\alpha$ , *J. Nucl. Mater.* **266–269** (1999) 884–889.
- [4.344] GORYUSHKIN, G.V., LAZARENKO, Yu.V., MOSKALENKO, I.V., SHCHEGLOV, D.A., Application of laser-induced fluorescence for study of helium in plasma edge, *Sov. J. Plasma Phys.* **12** (1986) 807–810.
- [4.345] TSUCHIDA, K., MIYAKE, S., KADOTA, K., FUJITA, J., Plasma electron density measurements by the laser- and collision-induced fluorescence method, *Plasma Phys.* **25** (1983) 991–999.
- [4.346] SHCHEGLOV, D.A., VETROV, S.I., MOSKALENKO, I.V., SKOVORODA, A.A., SHUVAEV, D.A., Laser spectroscopy for measuring the parameters of a plasma containing helium and argon, *Plasma Phys. Rep.* **32** (2006) 119–122.
- [4.347] KRYCHOWIAK, M., MERTENS, Ph., KÖNIG, R., SCHWEER, B., BREZINSEK S., et al., LIF measurements on an atomic helium beam in the edge of a fusion plasma, *Plasma Phys. Control. Fusion* **50** (2008) 065015.
- [4.348] MOSKALENKO, I.V., MOLODTSOV, N.A., ZHILTSOV, V.A. SKOVORODA, A.A., SHCHEGLOV, D.A., Laser spectroscopy measurements of effective temperature of argon ions in the PNX-U plasma neutralizer, *Plasma Phys. Rep.* **30** (2004) 432–436.
- [4.349] HINTZ, E., SCHWEER, B., Plasma edge diagnostics by atomic beam supported emission spectroscopy – status and perspectives, *Plasma Phys. Control. Fusion* **37** (1995) A87–A101.
- [4.350] JAKUBOWSKI, M., Application of wavelet spectral analysis to plasma fluctuation measurements using beam emission spectroscopy, *Rev. Sci. Instrum.* **70** 1 (1999) 874.
- [4.351] CARRARO, L., Requirements for an active spectroscopy diagnostic with neutral beams on the RFX reversed field pinch, *Rev. Sci. Instrum.* **70**, No.1 (1999) 861.
- [4.352] IVANOV, A., Radio frequency ion source for plasma diagnostics in fusion experiments, *Rev. Sci. Instrum.* **71**, No.10 (2000) 3728.
- [4.353] SASAO, M., CONNOR, K.A., IDA, K., IGUCHI, H., IVANOV, A.A., et al., Ion sources for fusion plasma diagnostics, *IEEE Trans Plasma Sci.* **33** (2005) 1872–1900.

- [4.354] DAVYDENKO, V.I., IVANOV, A.A., Development of neutral beam injectors for plasma diagnostic in Budker Institute of Nuclear Physics, *Rev. Sci. Instrum.* **75** (2004) 1809–1812.
- [4.355] ABDRAHIMOV, G.F., DAVYDENKO, V.I., DEICHULI, P.P., DEN HARTOG, D.J., FIKSEL, G., et al., A diagnostic neutral beam system for the MST reversed-field pinch, *Rev. Sci. Instrum.* **72** (2001) 594–597.
- [4.356] IVANOV, A.A., DAVYDENKO, V.I., DEICHULI, P.P., SHULZHENKO, G.I., STUPISHIN, N.V., Ion sources with arc-discharge plasma box driven by directly heated LaB<sub>6</sub> electron emitter or cold cathode, *Rev. Sci. Instrum.* **79** (2008) 02C103.
- [4.357] FONCK, R.J., DARROW, D.S., JAEHNUG, K.P., Determination of plasma-ion velocity distribution via charge-exchange recombination spectroscopy, *Phys. Rev. A* **29** (1984) 3288–3309.
- [4.358] BUGARYA, V.I., GORSHKOV, A.V., GRASHIN, S.A., IVANOV, I.V., KRUPIN, V.A., et al., Measurements of plasma column rotation and potential in the TM-4 Tokamak, *Nucl. Fusion* **25**, No.12 (1985) 1707–1717.
- [4.359] ISLER, R.C., An overview of charge-exchange spectroscopy as a plasma diagnostic, *Plasma Phys. Control. Fusion* **36** (1994) 171–208.
- [4.360] JANEV, R.K., BOLEY, C.D., POST, D.E., Penetration of energetic neutral beams into fusion plasma, *Nucl. Fusion* **29** No.12 (1989) 2125–2140.
- [4.361] VON HELLERMANN, M.G., CORE, W.G.F., HOWMAN, A., JUPEN, C., KENIG, R.W.T., et al., “Feasibility of quantitative spectroscopy on ITER”, *Diagnostics for Experimental Thermonuclear Fusion Reactors*, Plenum Press, New York (1996) 321–330.
- [4.362] TUGARINOV, S., KRASILNIKOV, A., DOKOUKA, V., KHAYRUTDINOV, R., BEIGMAN, I., et al., Conceptual design of the charge exchange recombination spectroscopy diagnostic for ITER, *Rev. Sci. Instrum.* **74**, No.3 (2003) 2075–2079.
- [4.363] MARMAR, E.S., “Active spectroscopic diagnostics for ITER utilizing neutral beams”, *Diagnostics For Experimental Thermonuclear Fusion Reactor*, Plenum Press, New York (1996) 281–290.

- [4.364] THOMAS, D.M., BURRELL, K.H., WADE, M.R., SNIDER, R.T., “Prospects for core helium density and related measurements on ITER using active charge exchange”, *Diagnostics for Experimental Thermonuclear Fusion Reactors*, Plenum Press, New York (1998) 361–370.
- [4.365] VON HELLERMANN, M.G., CORE, W.G.F., FRIELING, J., HORTON, L.D., KENIG, R.W.T., et al., Observation of alpha particle slowing-down spectra in JET helium beam fuelling and heating experiments, *Plasma Phys. Control. Fusion* **35** (1993) 799–824.
- [4.366] GROEBNER, R.J., BURRELL, K.H., GOHIL, P., SERAYDARIAN, R.P., Spectroscopic study of edge poloidal rotation and radial electric fields in the DIII-D tokamak, *Rev. Sci. Instrum.* **61**, No.10 (1990) 2920–2925.
- [4.367] VON HELLERMANN, M.G., MANDL, W., SUMMERS, H.P., WEISEN, H., BOILEAU, A., et al., Visible charge exchange spectroscopy at JET, *Rev. Sci. Instrum.* **61**, No.11 (1990) 3479–3486.
- [4.368] KOIDE, Y., SAKASAI, A., SAKAMOTO, Y., KUBO, H., SUGIE, T., Multichordal charge exchange recombination spectroscopy on the JT-60U tokamak, *Rev. Sci. Instrum.* **72**, No.1 (2001) 119–127.
- [4.369] LEVINTON, F.M., FONCK, R.J., GAMMEL, G.M., KAITA, R., KUGEL, H.W., Magnetic field pitch-angle measurements in the PBX-M tokamak using the motional Stark effect, *Phys. Rev. Lett.* **63** (1989) 2060.
- [4.370] LEVINTON, F.M., GAMMEL G.M., KAITA, R., KUGEL, H.W., ROBERTS, D.W., Magnetic field pitch angle diagnostic using the motional Stark effect, *Rev. Sci. Instrum.* **61** (1990) 2914–2919.
- [4.371] ROBERTS, D.W., KAITA, R., LEVINTON, F.M., Equilibrium q-profile determination and stability analysis from magnetic field pitch angle measurements using motional Stark effect polarimetry, *Rev. Sci. Instrum.* **61** (1990) 2932–2934.
- [4.372] BAYFIELD, J.E., Measurement of the total cross-section for charge transfer into the metastable state H-2S for proton collisions with atomic hydrogen, *Phys. Rev.* **185** (1969) 105–120.
- [4.373] AFROSIMOV, V.V., PETROV, M.P., SADOVNIKOV, V.A., Measurement of the local values of the ion temperature in a tokamak using charge exchange of plasma ions with jet of hydrogen atoms, *Sov. JETF Phys. Letters* **18** (1973) 300–302.

- [4.374] KRETER, A., BALDZUHN, J., EHMLER, H., HIRSCH, M., KICK, M., et al., Optimized confinement discharges with high ion temperatures after installation of the island divertor in W7-AS, Proc. 29th EPS Conference on Plasma Physics and Controlled Fusion, Montreux, Switzerland (2002) report P-5.033 ([http://epsppd.epfl.ch/Montreux/pdf/P5\\_033.pdf](http://epsppd.epfl.ch/Montreux/pdf/P5_033.pdf)).
- [4.375] FISHER, R.K., McCHESNEY, J.M., PARKS, P.B., DUONG, H.H., MEDLEY, S.S., et al., Measurements of fast confined alphas on TFTR. Phys. Rev. Lett. **75** (1995) 846–849.
- [4.376] MEDLEY, S.S., MANSFIEL, D.K., ROQUEMORE, A.L., FISHER, R.K., DUONG, H.H., et al., Design and operation of the pellet charge exchange diagnostic for measurement of energetic confined alpha-particles and tritons on Tokamak Fusion Test Reactor, Rev. Sci. Instrum. **67** (1996) 3122–3135.
- [4.377] ABRAMOV, V.G., AFROSIMOV, V.V., GLADKOVSKII, I.P., KISLYAKOV, A.I., PEREL, V.I., et al., Temperature measurement in a low-density medium with an atomic beam, Sov. Phys. Tech. Phys. **16** (1972) 1520–1526.
- [4.378] VAN BLOKLAND, A.A.E., BARBIAN, E.P., DONNE, A.J.H., VAN DER GRIFT, A.F., GIMBERGEN, T.W.M., et al., Ion temperature measurements in tokamak plasmas by Rutherford scattering, Rev. Sci. Instrum. **63** (1992) 3359–3370.
- [4.379] ALEKSANDROV, E.V., AFROSIMOV, V.V., BEREZOVSKII, E.L., IZVOZCHIKOV, A.B., MARASEV, V.I., et al., Measurement of the local ion parameters in the Tokamak-4 plasma, JETP Lett. **29** (1979) 1–3.
- [4.380] BEREZOVSKII, E.L., KISLYAKOV, A.I., PETROV, S.Ya., ROSLYAKOV, G.V., Determination of the ion temperature in a hot plasma from the scattering of fast atoms, Sov. J. Plasma Phys. **6** (1980) 760–766.
- [4.381] TAKEUCHI, H., MATSUDA, T., NISHITANI, T., SHIHO, M., KONAGAI, C., et al., Active beam scattering method for measurement of ion temperature in JFT-2 tokamak plasma, Jpn. J. Appl. Phys. **22** (1983) 1717–1721.
- [4.382] TAKEUCHI, H., TOBITA, K., KUSAMA, Y., NEMOTO, M., ITOH, T., et al., Ion temperature measurements on JT-60 using He beam scattering, Rev. Sci. Instrum. **59** (1988) 1652–1661.

- [4.383] REARDON, J.C., FIKSEL, G., FOREST, C.B., ABDRASHITOV, A.F., et al., Rutherford scattering diagnostic for the Madison symmetric torus reversed-field pinch, *Rev. Sci. Instrum.* **72** (2001) 598–601.
- [4.384] VAN BLOKLAND, A.A.E., BARBIAN, E.P., DONNE, A.J.H., VAN DER GRIFT, A.F., GIMBERGEN, T.W.M., et al., Ion temperature measurements in tokamak plasmas by Rutherford scattering, *Rev. Sci. Instrum.* **63** (1992) 3359–3370.
- [4.385] JOBES, F.C., HICKOK, R.L., A direct measurement of plasma space potential, *Nucl. Fusion* **10** (1970) 195.
- [4.386] DONNÉ, A.J.H., MELNIKOV, A.V. and VAN OOST, G., Diagnostics for radial electric field measurements in hot magnetized plasmas, *Czech J. Phys.* **55** (2002) 1077–1093.
- [4.387] MELNIKOV, A., VERSHKOV, V.A., ELISEEV, L.G., GRASHIN, S.A., GUDOZHNIK, A.V., et al., Investigation of geodesic acoustic mode oscillations in the T-10 tokamak, *Plasma Phys. Control. Fusion* **48** (2006) S87–S110.
- [4.388] KISLYAKOV, A.I., DONNÉ, A.J.H., KRUPNIK, L.I., MEDLEY, S.S., PETROV, M.P., Particle diagnostics, *Fusion Sci. Technol.*, Special issue “MFE Diagnostics” **53** (2008) 577–603.
- [4.389] DE MARCO, F., SEGRE, S., The polarization of an electromagnetic wave propagating in a plasma with magnetic shear, *Plasma Phys.* **14** (1972) 245–252.
- [4.390] KUNZ, W, TFR GROUP, First measurement of poloidal-field induced Faraday rotation in a tokamak plasma, *Nucl. Fusion* **18** (1978) 1729–1732.
- [4.391] SOLTWISCH, H., Current distribution measurement in a tokamak by FIR polarimetry, *Rev. Sci. Instrum.* **57** (1986) 1939–1945.
- [4.392] SIMONET, F., Measurement of electron density profile by microwave reflectometry on tokamaks, *Rev. Sci. Instrum.* **56** (1985) 664–669.
- [4.393] CONWAY, G.D., Microwave reflectometry for fusion plasma diagnosis, *Nucl. Fusion* **46** (2006) S665–S669.
- [4.394] GOLANT, V.E., Basic Plasma Physics, (GALEEV, A., SUDAN, R., Eds), Vol. 2, North-Holland Publishing Company, Amsterdam (1989).
- [4.395] WHARTON, C.B., Microwave diagnostic for controlled fusion research, preprint UCRL-4836 Rev. (September 1957).
- [4.396] WHARTON, C.B., GARDNER, A.L., US Patent No. 2.971.153 (1959).

## PLASMA DIAGNOSTICS

- [4.397] HEALD, M.A., WHARTON, C.B., Plasma Diagnostics with Microwaves, John Wiley and Sons, New York (1965).
- [4.398] VERON, D., “Submillimeter interferometry of high-density plasmas”, Infrared and Millimeter Waves (BUTTON, K.J., Ed.), Vol. 2, Academic Press, New York (1979) 69–135.
- [4.399] HUTCHINSON, I.H., Principles of Plasma Diagnostics, Cambridge University Press (2005) 460.
- [4.400] LUHMANN, Jr., N.C., PEEBLES, W.A., Instrumentation for magnetically confined fusion plasma diagnostics, Rev. Sci. Instrum. **55** (1984) 279–332.
- [4.401] HOWARD, J., Novel scanning interferometer for two-dimensional plasma density measurements, Rev. Sci. Instrum. **61** (1990) 1086–1095.
- [4.402] INNOCENTE, P., MARTINI, S., CANTON, A., TASINATO, L., TUDISCO, O., Spatially scanned two-color mid-infrared interferometer for FTU, Rev. Sci. Instrum. **72** (2001) 1085–1089.
- [4.403] OLIVER, D., HOWARD, J., SANTHOSH, T., KUMAR, A., PRETTY, D.G., BLACKWELL, B.D., Three view electronically scanned interferometer for plasma electron density measurements on the H-1 heliac, Rev. Sci. Instrum. **77** (2006) 10E907-1-10E907-2.
- [4.404] WARR, G.B., BLACKWELL, B.D., WACH, J., HOWARD, J., First results from the three-view far-infrared interferometer for the H1 heliac, Fusion Eng. Des. **34–35** (1997) 387–391.
- [4.405] GIEST, T., WÜRSCHING, E., HARTFUSS, H.-J., Multichannel millimeter wave interferometer for W7-AS, Rev. Sci. Instrum. **68** (1997) 1162–1167.
- [4.406] OYAMA, N., MASE, A., TOKUZAWA, T., IMAMURA, K., ITAKURA, A., et al., Millimeter-wave two-dimensional imaging array for the GAMMA 10 tandem mirror, Rev. Sci. Instrum. **68** (1997) 500–503.
- [4.407] HUGENHOLTZ, C.A.J., MEDDENS, B.J.H., Heterodyne CO<sub>2</sub>-laser interferometer with direct phase read-out, Rev. Sci. Instrum. **50** (1979) 1123–1124.
- [4.408] SOLTWISCH, H., Plasma position detection and control in the Textor tokamak by means of a far-infrared interferometer/polarimeter, Nucl. Fusion, **23** (1983) 1681–1685.

- [4.409] BRUSSAU, W.D., SOLTWISCH, H., Real-time acquisition of electron and current density profile shapes in tokamak plasma, *J. Phys. E: Sci. Instrum.* **20** (1987) 1243–1246.
- [4.410] AIRILA, M.I., DUMBRAJS, O., HIRSCH, M., GEIGER, J., NEUNER, U., HARTFUSS, H.-J., Sightline optimization of the multichannel laser interferometer for W7-X, *Rev. Sci. Instrum.* **76** (2005) 023501-1- 023501-9.
- [4.411] GOTTARDI, N.J., Evaluation of electron density profiles in plasmas from integrated measurements, *Appl. Phys.* **50** (1979) 2647–2651.
- [4.412] PARK, H.K., A new asymmetric Abel-inversion method for plasma interferometry in tokamaks, *Plasma Phys. Contr. Fusion* **31** (1989) 2035–2046.
- [4.413] SHMOYS, J., Proposed diagnostic method for cylindrical plasmas, *J. Appl. Phys.* **32** (1961) 689–696.
- [4.414] EFTHIMION, P.C., TAYLOR, G., ERNST, W., GOLDMAN, M., McCARTHY, M., et al., 1-millimeter wave interferometer for the measurement of line integral electron density on TFTR, *Rev. Sci. Instrum.* **56** (1985) 908–910.
- [4.415] GEIST, T., WURSCHING, E., HARTFUSS, H.-J., Multichannel millimeter wave interferometer for W7-AS, *Rev. Sci. Instrum.* **68** (1997) 1162–1167.
- [4.416] FOREST, C.B., GREENE, G., ONO, M., CDX-U two dimensional scanning microwave system, *Rev. Sci. Instrum.* **61** (1990) 2888–2890.
- [4.417] OYAMA, N., MASE, A., NEGISHI, H., TOKUZAWA, T., ITAKURA, A., et al., Development of millimeter-wave 2D imaging array, *Rev. Sci. Instrum.* **70** (1999) 1003–1006.
- [4.418] HWANG, Y.S., FREDRIKSEN, A., QIN, H., FOREST, C.B., ONO, M., Microwave polarimetry system in the CDX-U tokamak, *Rev. Sci. Instrum.* **66** (1995) 379–381.
- [4.419] HOWARD, J., DOYLE, E.J., REIBEIZ, G., SAVAGE, Jr., R.L., PEBBLES, W.A., et al., Density profile reconstructions from 2D interferometric data on Microtor using novel tomographic analysis techniques, *Rev. Sci. Instrum.* **59** (1988) 2135–2138.
- [4.420] SOLTWISCH, H., Current density measurements in tokamak devices, *Plasma Phys. Control. Fusion* **34** (1992) 1669–1698.

- [4.421] DONNE, A.J.H, High spatial resolution interferometry and polarimetry in hot plasmas, *Rev. Sci. Instrum.* **66** (1995) 3407–3423.
- [4.422] KOSLOWSKI, H.R., SOLTWISCH, H., Electron density and  $q$  profile measurements with the far-IR interferometer-polarimeter on the TEXTOR tokamak, *Fusion Eng. Des.* **34–35** (1997) 143–150.
- [4.423] BAKER, D.R., LEE, S.T., Dual laser interferometer for plasma density measurements on large tokamaks, *Rev. Sci. Instrum.* **49** (1978) 919–922.
- [4.424] CARLSTROM, T.N., AHLGREN, D.R., CROSBIE, J., Real-time, vibration-compensated CO<sub>2</sub> interferometer operation on the DIII-D tokamak, *Rev. Sci. Instrum.* **59** (1988) 1063–1067.
- [4.425] MUKHOVATOV, V.S. for ITER team, ITER operation and diagnostics, *Rev. Sci. Instrum.* **61** (1990) 3241–3246
- [4.426] KAWANO, Y., NAGASHIMA, A., ISHIDA, S., FUKUDA, T., MATOBA, T., CO<sub>2</sub> laser interferometer for electron density measurement in JT-60U tokamak, *Rev. Sci. Instrum.* **63** (1992) 4971–4973.
- [4.427] SNIDER, R.T., CARLSTROM, T.N., Short wavelength interferometer for ITER, *Rev. Sci. Instrum.* **63** (1992) 4977–4980.
- [4.428] KONDOH, T., COSTLEY, A.E., SUGIE, T., KAWANO, Y., et. al., Toroidal interferometer/polarimeter density measurement system on ITER, *Rev. Sci. Instrum.* **75** (2004) 3420–3422.
- [4.429] TANAKA, K., SANIN, A.L., VYACHESLAVOV, L.N., Precise density profile measurements by using a two color YAG/CO<sub>2</sub> laser imaging interferometer on LHD, *Rev. Sci. Instrum.* **75** (2004) 3429–3432.
- [4.430] ZABEO, L., MURARI, A., INNOCENTE, P., JOFFRIN, E., MAZON, D., RIVA, M., JET EFDA contributors, Different approaches to Real Time Correction of Fringe Jumps in Interferometers for Nuclear Fusion, preprint EFDA-JET-PR (04) 11 (2004).
- [4.431] ELBEZE, D., GIL, C., GIANNELLA, R., DE PASQUAL, L., Spurious oscillations affecting FIR polarimetry measurements, *Rev. Sci. Instrum.* **75** (2004) 3405–3407.
- [4.432] BOBOC, A., ZABEO, L., MURARI, A., JET EFDA contributors, Simultaneous Cotton-Mouton and Faraday rotation angle measurements on JET, *Rev. Sci. Instrum.* **77** (2006) 10F324–10F327.
- [4.433] ALUM, K.P., KOVALCHUK, Yu.V., OSTROVSKAYA, G.V., Nonlinear dispersion interferometer, *Sov. Tech. Phys. Lett.* **7** (1981) 1359–1364.

- [4.434] HOPF, F.A., TOMITA, A., AL-JUMAILY, G., Second-harmonic interferometers, *Opt. Lett.* **5** (1980) 386–388.
- [4.435] DRACHEV, V.P., KRASNIKOV, Yu.I., BAGRYANSKY, P.A., Dispersion interferometer for controlled fusion devices, *Rev. Sci. Instrum.* **64** (1993) 1010–1013.
- [4.436] BRETZ, N., JOBES, F., The design of a second harmonic tangential array interferometer for C-Mod, *Rev. Sci. Instrum.* **68** (1997) 713–716.
- [4.437] IRBY, J., MURRAY, R., ACEDO, P., LAMELA, H., A two-color interferometer using a frequency doubled diode pumped laser for electron density measurements, *Rev. Sci. Instrum.* **70** (1999) 699–702.
- [4.438] BAGRYANSKY, P.A., KHILCHENKO, A.D., KVASHNIN, A.N., LIZUNOV, A.A., VOSKOBOYNIKOV, R.V., et. al., Dispersion interferometer based on a CO<sub>2</sub> laser for TEXTOR and burning plasma experiments, *Rev. Sci. Instrum.* **77** (2006) 053501-1-053501-7.
- [4.439] JOBES, F.C., MANSFIELD, D.K., Midplane Faraday rotation: A densitometer for large tokamaks, *Rev. Sci. Instrum.* **63** (1992) 5154–5156.
- [4.440] KAWANO, Y., NAGASHIMA, A., Two-color polarimeter for electron density measurement on large tokamaks, *Rev. Sci. Instrum.* **68** (1997) 4035–4037.
- [4.441] SHEVCHENKO, V.F., PETROV, A.A., PETROV, V.G., CHAPLYGIN, Yu.A., Polarization microwave interferometer with unambiguous phase reading, *Plasma Phys. Rep.* **22** (1996) 28–33.
- [4.442] PETROV, V.G., PETROV, A.A., MALYSHEV, A.Yu., MARKOV, V.K., BABARYKIN, A.V., Microwave measurements of the time evolution of electron density in the T-11M tokamak, *Plasma Phys. Rep.* **30** (2004) 111–120.
- [4.443] FUCHS, Ch., HARTFUSS, H.J., Cotton-Mouton effect measurement in a plasma at the W7-AS stellarator, *Phys. Rev. Lett.* **81** (1998) 1626–1629.
- [4.444] FUCHS, Ch., HARTFUSS, H.J., Line integrated density measurements based on Cotton–Mouton polarimetry, *Rev. Sci. Instrum.* **70** (1999) 722–725.
- [4.445] AKIYAMA, T., KAWAHATA, K., ITO, Y., OKAJIMA, S., NAKAYAMA, K., et al., Cotton-Mouton polarimeter with HCN laser on CHS, *Rev. Sci. Instrum.* **77** (2006) 10F118-1-10F118-4.

- [4.446] GUENTHER, K., JET-EFDA Contributors, Approximate method to extract the pure Faraday and Cotton–Mouton effects from polarimetry measurements in a tokamak, *Plasma Phys. Control. Fusion* **46** (2004) 1423–1442.
- [4.447] PETROV, A.A., PETROV, V.G., MALYSHEV, A.Yu., MARKOV, V.K., BABARYKIN, A.V., Pulsed time-of-flight refractometry measurements of the electron density in the T-11M tokamak, *Plasma Phys. Rep.* **28** (2002) 806–813.
- [4.448] PETROV, A.A., PETROV, V.G., Time-of-flight refractometry for robust line integral electron density measurements and control in ITER”, *Rev. Sci. Instrum.* **74** (2003) 1465–1469.
- [4.449] PETROV, V.G., PETROV, A.A., MALYSHEV, A.Yu., DE BENEDETTI, M., TUDISCO, O., Measurements of the plasma density in the FTU tokamak by a pulsed time-of-flight X-wave refractometer, *Plasma Phys. Reports* **34** (2008) 24–30.
- [4.450] DONNE, A.J.H., GRASWINCKEL, M.F., CAVINATO, GIUDICOTTI, M.L., ZILLI, E., et al., Poloidal polarimeter for current density measurements in ITER, *Rev. Sci. Instrum.* **75** (2004) 4694–4701.
- [4.451] DOMIER, C.W., CHUNG, E., DOYLE, E.J., LIU, H.-X.L., LAPIDUS, A., et al., Development of technology and techniques for reflectometry, *Rev. Sci. Instrum.* **63** (1992) 4666–4668.
- [4.452] MAZZUCATO, E., Microwave reflectometry for magnetically confined plasmas, *Rev. Sci. Instrum.* **69** (1998) 2201.
- [4.453] MAZZUCATO, E., Relativistic effects on microwave reflectometry, *Phys. Fluids B*, **4** (1992) 3460–3461.
- [4.454] MAZZUCATO, E., NAZIKIAN, R., Microwave reflectometry for the study of density fluctuations in tokamak plasmas, *Plasma Phys. Control. Fusion* **33** (1991) 261–274.
- [4.455] HOLZHAUER, E., HIRSCH, M., GROSSMANN, T., BRAÑAS, B., SERRA, F., Theoretical and experimental investigation of the phase-runaway in microwave reflectometry, *Plasma Phys. Control. Fusion* **40** (1998) 1869–1886.
- [4.456] SHEVCHENKO, V.F., PETROV, A.A., PETROV, V.G., Pulse radar reflectometry for fusion plasma diagnostics, *Int. J. Infrared Millim. Waves* **14** (1993) 1755.

- [4.457] SHEVCHENKO, V.F., PETROV, A.A., PETROV, V.G., CHAPLYGIN, Yu.A., Pulsed reflectometry experiments in T-11M tokamak: Preliminary results, *Plasma Phys. Rep* **20**, 1 (1994) 27–29.
- [4.458] SHEVCHENKO, V., WALSH, M.J., First results from the small tight aspect ratio tokamak multifrequency pulse radar reflectometer, *Rev. Sci. Instrum.* **68** (1997) 2040.
- [4.459] SHEVCHENKO, V.F., Development and Application of Method of Pulsed Radar-Reflectometry for Studies of Electron Component of Tokamak Plasmas, Doctoral thesis, MIPT (Moscow Institute of Physics and Technology – State University), Moscow (1997).
- [4.460] BRUSKIN, L., MASE, A., KUBOTA, S., TOKUZAWA, T., ITAKURA, N., TAMANO, T., et al., Application of Wavelet Analysis to Plasma Fluctuation Study on GAMMA 10, *J. Appl. Phys.* **37** (1998) L956–L958.
- [4.461] KUBOTA, W., PEEBLES, A., NGUYEN, X.V., CROCKER, N.A., ROCKUEMOR, A.L., Ultrafast millimeter-wave frequency-modulated continuous-wave reflectometry for NSTX, *Rev. Sci. Instrum.* **77** (2006) 10E926.
- [4.462] SILVA, A., MANSO, M., VARELA, P., CUPIDO, L., MENESES, L., Recent improvements of the broadband FMCW reflectometry system for density profile measurements on ASDEX Upgrade, *Rev. Sci. Instrum.* **77** (2006) 10E932.
- [4.463] HACQUIN, S., SHARAPOV, S.E., ALPER, B., CHALLIS, C.D., FONSECA, A., et al., Localized X-mode reflectometry measurements of Alfvén eigenmodes on the JET tokamak, *Plasma Phys. Control. Fusion* **49** (2007) 1371–1390.
- [4.464] VARELA, P., MANSO, M.E., SILVA, A., CFN Team and ASDEX Upgrade Team, Review of data processing techniques for density profile evaluation from broadband FM-CW reflectometry on ASDEX Upgrade, *Nucl. Fusion* **46** (2006) S693–S707.
- [4.465] LAVIRON, C., DONNÉ, A.J.H., MANSO, M.E., SANCHEZ, J., Reflectometry techniques for density profile measurements on fusion plasmas, *Plasma Phys. Control. Fusion* **38** (1996) 905–936.
- [4.466] SIPS, A.C.C., KRAMER, G.J., Analysis of reflectometry density profile measurements in JET, *Plasma Phys. Control. Fusion* **35** (1993) 743–755.

- [4.467] Personal communication with Dr. SHELOUKHIN, D., Kurchatov Institute, Moscow, Russian Federation, *sheoloukhin@nfi.kiae.ru*
- [4.468] ESTRADA, T., SÁNCHEZ, J., VAN MILLIGEN, B., CUPIDO, L., SILVA, A., MANSO, M.E., ZHURAVLEV, V., Density profile measurements by AM reflectometry in TJ-II, *Plasma Phys. Control. Fusion* **43** (2001) 1535–1545.
- [4.469] BURATTI, P., ZERBINI, M., BRODSKY, Y., KOVALEV, N., SHTANUK, A., Amplitude modulation reflectometry system for the FTU tokamak, *Rev. Sci. Instrum.* **66** (1995) 409.
- [4.470] KUBOTA, S., ONUMA, T., MASE, A., TOKUZAWA, T., OYAMA, N., et al., Development of an ultrashort-pulse reflectometer for density profile measurements on GAMMA 10, *Jpn J. Appl. Phys.* **37** (1998) L300–L302.
- [4.471] LAVIRON, C., MILLOT, P., PRENTICE, R., First experiments of pulse compression radar reflectometry for density measurements on JET plasma, *Plasma Phys. Control. Fusion* **37** (1995) 975–987.
- [4.472] FATTORINI, L., LANG, P.T, MANSO, M.E., SANTOS, J., HORTON, L.D., et al., High temporal and spatial resolution reflectometry investigations of Type I ELMs induced edge barrier collapse at ASDEX Upgrade, *Plasma Phys. Control. Fusion* **50** (2008) 125001.
- [4.473] OYAMA, N., ASAKURA, N., CHANKIN, A.V., OIKAWA, T., SUGIHARA, M., et al., Fast dynamics of Type I ELMs and transport of the ELM pulse in JT-60U, *Nucl. Fusion* **44** (2004) 582–592.
- [4.474] DOMIER, C.W., LUHMANN, N.C., CHOU, A.E., ZHANG, W.M., ROMANOWSKY, A.J., Ultrashot pulse reflectometry, *Rev. Sci. Instrum.* **66** (1995) 399.
- [4.475] COSTLEY, A.E., CRIPWELL, P., PRETINCE, R., SIPS, A.C.C., Recent developments in microwave reflectometry at JET, *Rev. Sci. Instrum.* **61** (1990) 2823–2828.
- [4.476] ZOU, X.L., LAURENT, L., RAX, J.M., Scattering of an electromagnetic wave in a plasma close to a cut-off layer. Application to fluctuation measurements, *Plasma Phys. Control. Fusion* **33** (1991) 903–918.
- [4.477] SANTOS, J., MANSO, M., VARELA, P., NEUHAUSER, J., the ASDEX Upgrade Team, Plasma position measurements from ordinary FM-CW reflectometry on ASDEX Upgrade, *Rev. Sci. Instrum.* **74** (2003) 1489–1492.

- [4.478] MUNSAT, T., MAZZUCATO, E., PARK, H., DENG, B.H., DOMIER, C.W., et al., Microwave imaging reflectometer for TEXTOR (invited), *Rev. Sci. Instrum.* **74** (2003) 1426.
- [4.479] MAZZUCATO, E., Density Fluctuations in the Adiabatic Toroidal Compressor, Princeton University PPL Report MATT-1151 (1975).
- [4.480] VERSHKOV, V.A., SOLDATOV, S.V., BAGDASAROV, A.A., CHISTIYAKOV, V.V., DNESTROVSKII, Yu.N., et al., “Investigation of plasma oscillations in regimes with  $m=2,3$  instabilities in T-10 tokamak”, *Proc. 24th EPS Conf. on Control. Fusion and Plasma Phys.*, Berchtesgarden, **21A** (1997), Part 2, 673–676.
- [4.481] VERSHKOV, V.A., SOLDATOV, S.V., SHELUKHIN, D.A., CHISTYAKOV, V.V., Experimental investigations of ITG-like turbulence characteristics in T-10 tokamak core plasma with toroidal and poloidal correlation reflectometry, *Nucl. Fusion* **39** (1999) N11Y, 1775–1787.
- [4.482] VERSHKOV, V.A., DREVAL, V.V., SOLDATOV, SV., A three-wave heterodyne correlation reflectometer developed in the T-10 tokamak, *Rev. Sci. Instrum.* **70** (1999) 1700–1712.
- [4.483] MAZZUCATO, E., NAZIKIAN, R., Radial scale length of turbulent fluctuations in the main core of TFTR plasmas, *Phys. Rev. Lett.* **71** (1993) 1840–1843.
- [4.4784] NAZIKIAN, R., MAZZUCATO, E., Reflectometer measurements of density fluctuations in tokamak plasmas, *Rev. Sci. Instrum.* **66** (1995) 392–397.
- [4.485] CONWAY, G., VAYAKIS, G., FESSLY, J.A., BARTLETT, D.V., A reflectometer for fluctuation and correlation studies on the Joint European Torus tokamak, *Rev. Sci. Instrum.* **70** (1999) 3921–3929.
- [4.486] LIN, Y., NAZIKIAN, R., IRBY, J.H., MARMAR, E.S., Plasma curvature effects on microwave reflectometry fluctuation measurements, *Plasma Phys. Control. Fusion* **43** (2001) L1–L8.
- [4.487] GUSAKOV, E.Z., YAKOVLEV, B.O., Two-dimensional linear theory of radial correlation reflectometry diagnostics, *Plasma Phys. Control. Fusion* **44** (2002) 2525–2537.
- [4.488] IRBY, J.H., HORNE, S., HATCHINSON, I.H., STEK, P.C., 2D full-wave simulation of ordinary mode reflectometry, *Plasma Phys. Control. Fusion* **35** (1993) 601–609.

- [4.489] GROSSMANN, M.T., HOLZHAUER, E., HIRSH, M., SERA, F., MANSO, M.E., et al., “A 2D code for analysis of microwave reflectometry measurements in fusion experiments”, Proc. 24th EPS Conf. on Control. Fusion and Plasma Phys., Berchtesgaden, Germany, **21A**, Part 4 (1997) 457–1500.
- [4.490] ESTRADA, T., SANCHEZ, J., ZHURAVLEV, V., DE LUNA, E., BRANAS, B., Turbulence and beam size effects on reflectometry measurements, Phys. Plasmas **8** (2001) 2657–2665.
- [4.491] VERSHKOV, V.A., SOLDATOV, S.V., SHELUKHIN, D.A., URAZBAEV, A.O., GRASHIN, S.A., et al., “Direct comparison of turbulence measurements with Langmuir probes and reflectometry at the same radial locations in T-10 and reflectometry simulations with 2D full-wave code”, Proc. 30th EPS Conf. on Control. Fusion and Plasma Phys., St. Petersburg, Russia, 2003, EC, **27A** (2003) 2.56–2.59.
- [4.492] VERSHKOV, V.A., SHELUKHIN, D.A., SOLDATOV, S.V., URAZBAEV, A.O., ELISEEV, L.G., et al., Summary of experimental core turbulence characteristics in ohmic and electron cyclotron resonance heated discharges in T-10 tokamak plasmas, Nucl. Fusion **45** (2005) S203–S226.
- [4.493] VERSHKOV, V.A., TUCCILLO, A.O., TUDISCO, O., DE BENEDETTI, M., BURATTI, P., et al., “First results of turbulence measurements in FTU tokamak with heterodyne correlation reflectometer”, Proc. 28th EPS Conf. on Control. Fusion and Plasma Phys., Madeira, Portugal, **25A** (2001) 65–68.
- [4.494] SHELUKHIN, D.A., SOLDATOV, S.V., VERSHKOV, V.A., URAZBAEV, A.O., Estimates of the local parameters of plasma density fluctuations by reflectometry measurements, Plasma Phys. Rep. **32** (2006) 707; Pleiades Publishing, Inc., (2006).
- [4.495] KRAEMER-FLECKEN, A., SOLDATOV, S.V., KOSLOVSKII, H.R., ZIMMERMANN, O., Properties of geodesic acoustic modes and the relation to density fluctuations, Phys. Rev. Lett. **97** (2006) 045006–045010.
- [4.496] KRAMER-FLECKEN, A., DREVAL, V., SOLDATOV, S., ROGISTER, A., VERSHKOV, V., the TEXTOR Team, Turbulence studies with means of reflectometry at TEXTOR, Nucl. Fusion **44** (2004) 1143–1157.
- [4.497] CONWAY, G., Turbulence measurements in fusion plasmas, Plasma Phys. Control. Fusion **50** (2008) 124026.

- [4.498] COSTLEY, A.E., DONNE, A.J.H., EBISAWA, K., JANESCHITZ, G., KASAI, S., MALAQUIAS, A., VAYAKIS, G., WALKER, C.I., YAMAMOTO, S., ZAVERYAEV, V., “The Challenge of ITER Diagnostics”, Proc. 28th EPS Conf. on Control. Fusion and Plasma Physics, Madeira, Portugal (2001) 1333–1336.
- [4.499] ORLINSKI, D.V., VOITSENYA, V.S., VUKOLOV, K.Yu., Simulation mirror tests under neutron and ion bombardment, Plasma Device Oper. **15** (2007) 33–75.
- [4.500] LITNOVSKY, A., VOITSENYA, V.S., COSTLEY, A., DONNE, A.J.H., First mirrors for diagnostic systems of ITER, Nucl. Fusion **47** (2007) 833–838.

## CHAPTER 5

# PLASMA HEATING AND CURRENT DRIVE BY NEUTRAL BEAM AND ALPHA PARTICLES

**M. Kikuchi, Y. Okumura**

Fusion Research and Development Directorate,  
Japan Atomic Energy Agency, Japan

### 5.1. HEATING AND CURRENT DRIVE PHYSICS BY NEUTRAL BEAM AND ALPHA PARTICLES

#### 5.1.1. Basic processes of neutral beam injection

The purpose of plasma heating is to raise the plasma temperature enough to produce a deuterium and tritium reaction ( $D + T \rightarrow {}^4\text{He} + n$ ). The required plasma temperature  $T$  is in the range of 10–30 keV. Since the high temperature plasma is confined by a strong magnetic field, injection of energetic ions from outside to heat the plasma is difficult due to the Lorentz force. The most efficient way to heat the plasma by energetic particles is to inject high energy “neutrals” which get ionized in the plasma. Neutral beam injection (NBI) with a beam energy much above the average kinetic energy of the plasma electrons or ions is used (beam energy typically ~40 keV – 1 MeV). This heating scheme is similar to warming up cold water by pouring in hot water.

There are two types of neutral beam, called P-NBI and N-NBI (P- and N- means “positive” and “negative”, respectively). P-NBI uses the acceleration of positively charged ions and their neutralization, while N-NBI uses the acceleration of negative ions (electrons attached to neutral atoms) and their neutralization. Details are given in NBI technology Section 5.2. The first demonstration of plasma heating by P-NBI was made in ORMAK [5.1] and ATC [5.2] in 1974, while that by N-NBI was made in JT-60U [5.3] for the first time in 1996. ITER has also adopted the N-NBI system as the heating and current drive system with a beam energy of 1 MeV. Figure 5.1 shows a typical bird’s eye view of a tokamak with N-NBI and N-NBI (JT-60U).

Since the magnetic confinement system is a torus and the tokamak has a toroidal plasma current, there are three injection geometries, namely co-tangential, counter-tangential and perpendicular injection, as shown schematically in Fig. 5.2. “Co-” means that beam is injected parallel to the toroidal plasma current, while “counter” means that beam is injected anti-parallel to the plasma current. “Perpendicular” means that beam is injected (nearly) perpendicular to

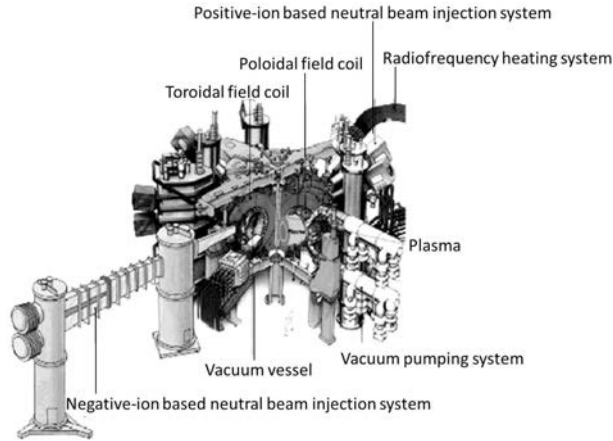


FIG. 5.1. Bird's eye view of tokamak with P-NBI and N-NBI (JT-60U) [5.4]. Reprinted from Ref. [5.4]. Copyright (2011), IOP Publishing Ltd.

the magnetic field. A plasma can be heated in all injection geometries. In addition to plasma heating, co-injection can also drive the plasma current (see Sections 5.1.7–5.1.9) and also drive co-toroidal rotation through its momentum input, while counter-injection can drive a counter-plasma current and counter-toroidal rotation.

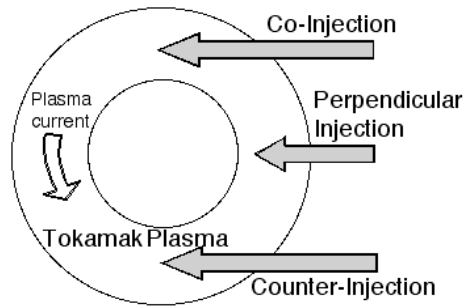


FIG. 5.2. Schematics of tokamak plasma geometry and NBI beam orientations.

After the injection, beam neutrals are ionized through various atomic processes such as charge exchange, ionization by ions and ionization by electrons, which will be described in detail in Sections 5.1.2 and 5.1.3. After the ionization, there is some possibility of re-neutralization and loss of fast ions due to charge exchange with residual neutrals in the plasma. The main sources of neutrals in a high temperature plasma are edge warm neutrals and halo neutrals. The source of edge neutrals is neutrals from the wall and divertor, while the source of halo neutrals is charge exchange processes between the neutral beam and bulk plasma ions.

Ionized ions are magnetically trapped in the plasma and their orbit follows the magnetic surface with only slight deviation. There are two types of particle orbits, namely, passing particles and trapped particles (see Section 5.1.5). The magnetic field should be strong enough to confine these energetic ions until they transfer their energy to plasma electrons and ions. The tokamak system is axisymmetric but real machines have small non-uniformities in the toroidal direction because of the finite number of toroidal field coils; this is called toroidal field ripple. This ripple causes loss of fast ions. The detailed physics of particle orbits in a tokamak will be described in Sections 5.1.5 and 5.1.10.

The energy transfer from ionized beam fast ions to thermal ions and electrons is basically through classical Coulomb collision processes. The basic processes of Coulomb collision between fast ions and a thermal plasma are slowing down and diffusion in the velocity space. If the beam energy  $W_b$  is sufficiently high ( $W_b > 15T_e$ ), fast ions transfer their energy mainly to electrons, while more energy is transferred to ions when  $W_b < 14.8$  for hydrogen and  $W_b < 19$  for deuterium. Details of classical beam–plasma Coulomb interactions will be given in Section 5.1.4.

### 5.1.2. Physics of ionization of injected neutral beam

Here we discuss the basic atomic processes which are important during the ionization of a neutral beam in a high temperature plasma. For simplicity we consider the case of injection of a deuterium neutral beam into an electron–deuterium impurity plasma. The processes are direct ionization of the ground state (1s) of the deuterium neutral beam through charge exchange (CX) with bulk ions, ionization by ion impact, ionization by impurity and ionization by electron impact.

Decay of the neutral beam intensity  $I_b(t)$  is governed by the processes given in Table 5.1.

TABLE 5.1. BASIC ATOMIC PROCESSES DURING IONIZATION OF A NEUTRAL BEAM IN A HIGH TEMPERATURE PLASMA	
<i>(The subscript 'b' stands for beam, and D and A for the deuterium and impurity species, respectively)</i>	
Charge exchange	$D_b^0(1s) + D^+ \rightarrow D_b^+ + D^0$
Ionization by ions	$D_b^0(1s) + D^+ \rightarrow D_b^+ + D^+ + e$
Ionization by impurities	$D_b^0(1s) + A^{z+} \rightarrow D_b^+ + A^{z+} + e$
Impurity CX	$D_b^0(1s) + A^{z+} \rightarrow D_b^+ + A^{(z-1)+}$
Ionization by electrons	$D_b^0(1s) + e \rightarrow D_b^+ + 2e$

$$\frac{dl_b}{dt} = -n_e \sigma_s v_b l_b \quad (5.1)$$

$$\sigma_s = (n_i \sigma_{cx} + n_i \sigma_i + n_z \sigma_z) / n_e + \langle \sigma_e v_e \rangle v_b \quad (5.2)$$

where  $n_e$ ,  $n_i$ ,  $n_z$ ,  $\sigma_s$ ,  $\sigma_{cx}$ ,  $\sigma_i$ ,  $\sigma_z$ ,  $\langle \sigma_e v_e \rangle$  and  $v_b$  are the electron density, the ion density, the impurity density, the stopping cross-section, the charge exchange cross-section, the ionization cross-section by ions, the ionization and CX by impurities, the electron ionization rate coefficient and the beam speed, respectively. Since the pioneering work of Riviere [5.5] on ionization of a neutral beam in a high temperature plasma, extensive efforts have been made to accumulate atomic data for fusion under the auspices of the IAEA.

The analytical equations for the ionization cross-sections  $\sigma_{cx}$  and  $\sigma_i$  of ground state hydrogen isotopic atoms by hydrogen isotopic ions under the condition of  $v_{th,i} \ll v_b$  are given by Janev and Smith [5.6] (Table 5.2). Since the beam speed is dominant in the relative speed ( $v_{r,i} = |v_b - v_{th,i}| \sim v_b$ ), the cross-sections  $\sigma_{cx}$  and  $\sigma_i$  are simply functions of energy/mass number ( $u = W_b/A_b$ ) and shown for the case of a deuterium beam in Fig. 5.3.

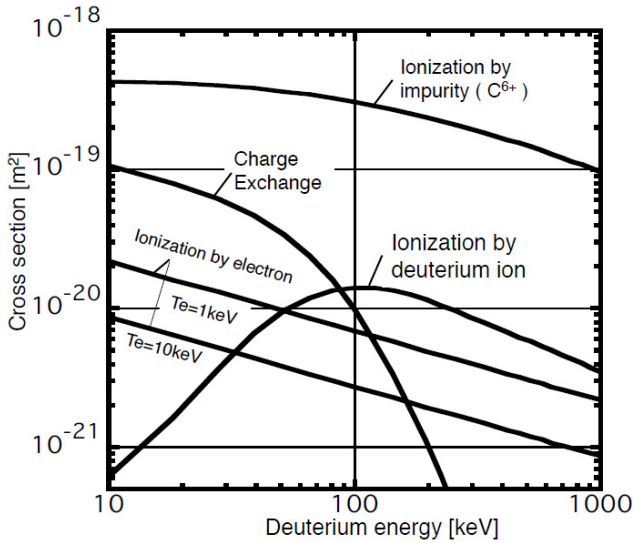


FIG. 5.3. Beam energy dependence of charge exchange, ion, impurity and electron ionization cross-sections (calculated from Table 5.2).

Charge exchange is the dominant process in the low energy regime ( $W_b/A_b < 45\text{keV}$ ) and ionization by hydrogen ions is dominant in the high energy regime ( $W_b/A_b > 45\text{keV}$ ). A fusion plasma is always accompanied by some impurities such as carbon and helium. The cross-section for ionization by impurities  $\sigma_z$

includes both charge exchange and ionization and scales as  $\sigma_z \sim Z_f (W_b / A_b / Z)$  (where  $Z_f$  is the  $Z$  of the fast ions) as found by Olson [5.7]. Janev [5.8] gave an analytical formula for  $\sigma_z$  (see Table 5.2), which is consistent with various charge state impurity measurements (He, C, O, Fe). In Fig. 5.3,  $\sigma_z$  for fully stripped carbon ( $Z = 6$ ) is shown. Although the cross-section  $\sigma_z$  is much larger than  $\sigma_{cx} + \sigma_i$ , its contribution to the stopping cross-section is comparable or smaller if the impurity content is small. The relative speed of ionization processes by electrons is dominated by the electron speed ( $v_{r,e} = |v_b - v_{th,e}| \sim v_{th,e}$ ). So the reaction has to be averaged over the Maxwellian electrons. Janev [5.9] gave an analytical formula for the electron ionization rate coefficient (see Table 5.2). This rate coefficient becomes a maximum just above 0.1 keV and decreases with  $T_e$ . The contribution to the stopping cross-section from this process is  $\langle \sigma_e v_e \rangle / v_b$  (where  $v_e$  stands for the electron velocity and  $\langle \rangle$  for the average over velocity) and is shown in Fig. 5.3 for  $T_e = 1$  keV and 10 keV.

TABLE 5.2. CROSS-SECTION AND RATE COEFFICIENT FORMULAS

Charge exchange [5.6]	$\sigma_{cx}[\text{m}^2]=[a_1 \ln(a_2/u+a_6)]/[1+a_3u+a_4u^{3.5}+a_5u^{5.4}]$ ; $[a_n]=[3.2345 \times 10^{-20}, 235.88, 0.038371, 3.8068 \times 10^{-6}, 1.1832 \times 10^{-10}, 2.3713]$
Ionization by ions [5.6]	$\sigma_i[\text{m}^2]=b_1[\exp(-b_2/u)\ln(1+b_3u)/u+$ $b_4 \exp(-b_5u)/(u^{b_6}+b_7u^{b_8})]$ ; $[b_n]=[12.899 \times 10^{-20}, 61.897, 9.2731 \times 10^3,$ $4.9749 \times 10^{-4}, 3.9890 \times 10^{-2}, -1.5900, 3.1834, -3.7154]$
Ionization by impurities [5.8]	$\sigma_z[\text{m}^2]=c_1Z[(1+c_2u/Z)^{-1}+c_3(c_4+u/Z)^{-1}\ln(1+c_5u/Z)]$ ; $[c_n]=[7.457 \times 10^{-20}, 0.08095, 2.754, 64.58, 1.27]$
Electron ionization rate coefficient ( $T_e$ [keV] > 0.002) [5.9]	$\langle \sigma_e v_e \rangle [\text{m}^3/\text{s}]=10^{-6} \exp[\sum_{n=1,9} d_n (\ln T_e)^{n-1}]$ ; $[d_n]=[-32.714, 13.537, -5.7393, 1.5632, -0.28771,$ $0.034826, -2.6320 \times 10^{-3}, 1.1195 \times 10^{-4},$ $-2.0392 \times 10^{-6}]$  $u=W_b/A_b[\text{keV}]$

The solution of Eq. (5.1) is given as  $I_b = I_0 \exp(-v_b t / \lambda)$ , where  $\lambda = 1 / n_e \sigma_s$  is called the e-folding length of the beam attenuation. The electron density will be around  $10^{20} \text{ m}^{-3}$  in ITER or the DEMO reactor. For a deuterium beam energy of 1 MeV, the stopping cross-section  $\sigma_s$  is  $\sim 4 \times 10^{-21} \text{ m}^2$  and the e-folding length  $\lambda = 2.5 \text{ m}$ , which is comparable with the plasma minor

radius of ITER and the DEMO reactor. But the above discussion is based on the ionization from the ground state and the inclusion of multi-step ionization through excited states changes the situation. This effect will be discussed in the next section.

### 5.1.3. Multi-step ionization and Lorenz ionization

In the previous section, we considered ionization only from the ground state. Ionization can also occur from excited states ( $n = 2-6, \dots$ ). In this case, we have to consider first excitation from the ground state (for example,  $D(1s) \rightarrow D^*(2s,2p)$ ), and then ionization from an excited state (for example,  $D^*(2s,2p) \rightarrow D^+$ ). So, the ionization process becomes “multi-step” ionization (MSI). This MSI is important for high energy beams, especially those for ITER (1 MeV) and beyond [5.8, 5.10]. Figure 5.4 shows a comparison of the measured neutral beam current profile and the calculated one (both with and without multi-step ionization process in the N-NBI experiment) [5.11]. Good agreement is obtained only for the calculation with multi-step ionization processes. So, it is important to understand these processes.

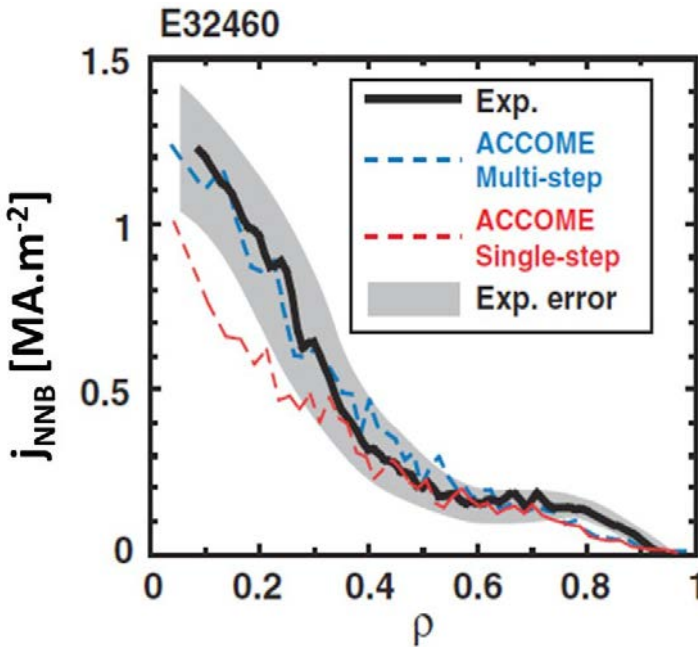


FIG. 5.4. Experimental NBCD current profile compared with calculation with and without multi-step ionization [5.11]. Here  $j_{\text{NNB}}$  is the non-inductively driven current density by the injection of negative ion based neutral beam injection.  $\rho$  (horizontal axis) is the plasma minor radius normalized to the plasma minor radius  $a$ .

Comprehensive atomic data including excitation from the ground state and ionization from excited states are compiled by the IAEA [5.6]. The excitation cross-section  $\sigma_{ex}$  from the ground state to the excited state with principal quantum number  $n$  is a decreasing function of  $n$ , while the ionization cross-section from an excited state increases with  $n$  as seen in Fig. 5.5.

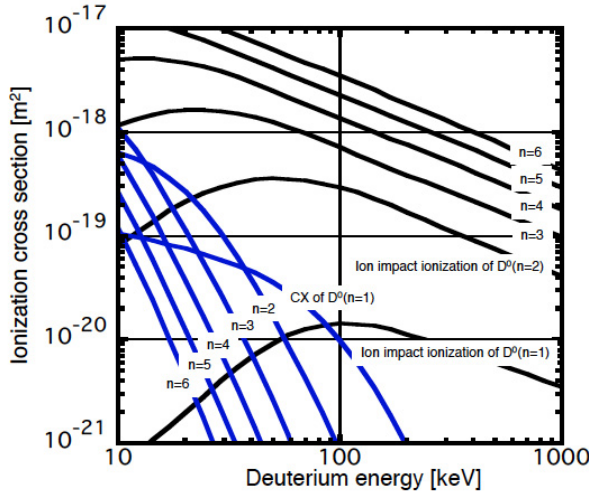


FIG. 5.5. Ionization and CX cross-sections from excited ( $n = 2\sim 6$ ) and ground ( $n = 1$ ) states (calculated from  $\sigma_{ion}$  and  $\sigma_{cx}$  formulas given in Sections 2.2 and 2.3 of Ref. [5.6] with obvious correction of  $W_n = (n/3)^2 W$  on page 74 of Ref. [5.6]).

Higher excited states are subject to ionization by the Lorenz field  $\vec{E}_L = \vec{v}_b \times \vec{B}$ . The critical electric field for Lorenz ionization is given by  $E_{L,c}(n) = \varepsilon_0 / (16n^4)$  and an excited state  $n$  is ionized if  $E_L > E_{LC}(n)$  where  $\varepsilon_0$  is the classical electric field at the first Bohr radius. The highest principal quantum number of an excited hydrogen atom determined by the Lorenz field ionization limit is given by  $N = (\varepsilon_0 / 16E_L)^{1/4}$ . For 1 MeV/amu and  $B = 5$  T,  $N$  is calculated to be 4. The neutral beam intensity  $I_b(x)$  at a distance  $x$  from the entry of the injection is the sum of the intensities at quantum number  $n$  as follows:

$$I_b(x) = \sum_{n=1}^N I_n(x) \quad (5.3)$$

The rate equations can be expressed by

$$v_b \frac{dI_n}{dx} = \sum_{n'} Q_{n'n} I_{n'} \quad (5.4)$$

$$\begin{aligned}
 v_b \frac{dI_n}{dx} = & -K_n I_n + \sum_{n' < n} \left[ K_{n'n}^e I_{n'} - (K_{nn'}^d + A_{nn'}) I_n \right] - \\
 & - \sum_{n' > n} \left[ K_{nn'}^e I_n - (K_{n'n}^d + A_{n'n}) I_{n'} \right]
 \end{aligned} \tag{5.5}$$

where  $K_n$  is the rate for electron loss from state  $n$  due to ionization including Lorentz ionization and charge exchange.  $K_{nn'}^d$  and  $K_{nn'}^e$  are the rates of de-excitation from  $n$  to  $n'$  due to collisions, and the rate of excitation from  $n$  to  $n'$ ,  $A_{nn'}$  is the radiative decay and  $v_b$  is the beam speed, respectively. The collisional transition rate is given as  $K_{n'n} = \sum_j n_j \langle \sigma_{n'n}^j v \rangle$ , where  $n_j$  is the density of particles  $j$ ,  $\sigma_{n'n}^j$  is the cross-section of hydrogen for transition from  $n'$  to  $n$  through collision with particle  $j$  ( $= e, i, I$ ) being electron, ion or impurity respectively. Equations (5.4) and (5.5) can be approximately rewritten by using the beam stopping cross-section  $\sigma_s$  as

$$\frac{dI_b}{dx} = -n_e \sigma_s I_b \tag{5.6}$$

where  $I_b = \sum I_n$ ,  $\sigma_s = -\xi / v_b n_e$ , where  $\xi$  is the minimum eigenvalue of the transition matrix  $\{Q_{n'n}\}$ . The contributions of multi-step processes and ionization by the Lorentz field are given by the following enhancement factor  $\delta$  defined by

$$\delta = \frac{\sigma_s - \sigma_s^{(0)}}{\sigma_s^{(0)}} \tag{5.7}$$

where  $\sigma_s^{(0)}$  is the stopping cross-section in which the multi-step processes and ionization by the Lorentz field are not taken into account. For a beam energy range of 0.5–1 MeV expected in ITER, the enhancement factor  $\delta$  can be of the order of 0.3–0.5 for an electron density  $n_e = 10^{20} \text{ m}^{-3}$  [5.8]. The stopping cross-section  $\sigma_s$  has a strong dependence on the beam energy  $W$ , the electron density  $n_e$ , the electron temperature  $T_e$  and the effective charge  $Z_{\text{eff}}$  and has almost no dependence on ion temperature  $T_i$  and the magnetic field  $B$ . An analytical fit of the stopping cross-section based on recent data is given in Ref. [5.12] and typical values of  $\delta$  are shown in Fig. 5.6.

An experimental measurement of the multi-step effect has been made in various tokamaks and was published in the ITER physics basis as shown in Fig. 5.6. The shine through rate ( $\eta = I_b(L)/I_b(0)$ , where  $I_b(x)$  is the beam intensity at  $x$ ) is compared with calculations with and without multi-step ionization in JT-60U showing better agreement with the multi-step process as shown in Fig. 5.6.

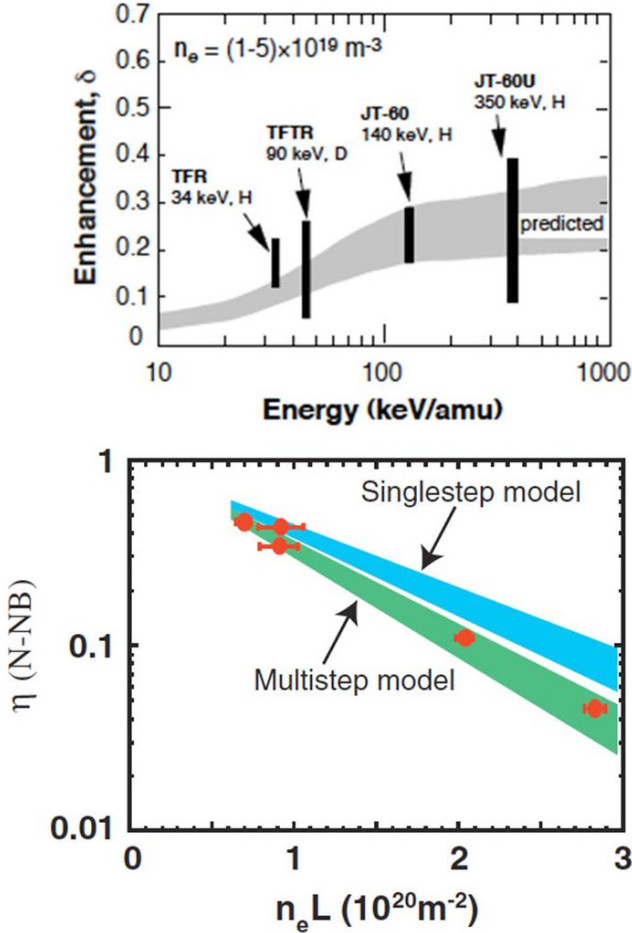


FIG. 5.6. Top: Comparison of measured and calculated enhancement  $\delta$  [5.13]. Below: Comparison of measured shine through rate  $\eta$  with calculation with and without multi-step ionization [5.14]. Here  $L$  is the plasma length along the beam path.

#### 5.1.4. Energy transfer to electrons and ions by neutral beam injection

A fundamental feature of heating by a neutral beam was clarified by Stix [5.15] and can be seen in introductory textbooks such as that by Wesson [5.16]. Here, we discuss the issue using the correct impurity contribution. Neutral beam “heating” occurs through energy transfer by the Coulomb collision of the energetic beams with bulk Maxwellian electrons and ions (deuterium, tritium and impurities) with the electron temperature  $T_e$  and ion temperature  $T_i$  respectively. The beam speed  $v_b$  is usually much larger than the ion thermal speed

$v_{th,i}$  due to the heating objective and much less than the electron thermal speed  $v_{th,e}$  due to the large mass ratio (for beam mass  $m_b$  ( $m_b/m_e$ )<sup>1/2</sup>  $\sim 42.8A_b^{1/2}$ ),  $v_{th,i} \ll v_b \ll v_{th,e}$ . Under this condition the energy loss of the beam is given by [5.15]

$$\frac{dW_b}{dt} = -\frac{2}{\tau_{se}} \left( 1 + \frac{W_c^{3/2}}{W_b^{3/2}} \right) W_b \quad (5.8)$$

where  $W_b$  is the beam energy, and  $W_c$  and  $\tau_{se}$  are called the critical energy and beam electron slowing down time, respectively. The formulas for  $W_c$  and  $\tau_{se}$  are as follows

$$W_c [\text{keV}] = \left( \frac{9\pi m_p}{16m_e} \right)^{1/3} \left[ \sum_j \frac{n_j Z_j^2}{n_e A_j} \right]^{2/3} A_b T_e = 14.8 \bar{Z}^{2/3} \bar{A}_b^{1/3} T_e [\text{keV}] \quad (5.9)$$

$$\tau_{se} [\text{s}] = \frac{3(2\pi)^{3/2} \epsilon_0^2 m_b T_e^{3/2}}{e^4 Z_b^2 n_e m_e^{1/2} \ln \Lambda} = \frac{0.2 A_b T_e [\text{keV}]^{3/2}}{Z_b^2 n_e [10^{20} \text{m}^{-3}] \ln \Lambda} \quad (5.10)$$

Here,  $\bar{Z} = \sum_j n_j Z_j^2 A_b / (n_e A_j)$ . The first term on the right hand side of Eq. (5.8) is the energy loss through beam–electron Coulomb collisions. Since the electron mass is much smaller than beam ion (see Fig. 5.7a),  $m_e/m_p \sim 1/3672$ , beam ions lose energy through the friction with bulk electrons  $\langle \Delta W \rangle = m_b v_b \langle \Delta v_{\parallel} \rangle$  (where  $v_{\parallel}$  is the velocity of ions in the parallel direction) with negligible diffusion in velocity space in both the parallel and perpendicular directions. The energy decay time by the electron channel does not depend on the beam energy and is half of the slowing down time,  $\tau_{se}/2$ , since the energy is proportional to the square of the speed. This power  $2W_b/\tau_{se}$  is transferred from the beam to the bulk Maxwellian electrons.

The second term is the energy loss through beamion/impurity Coulomb collisions (see Fig. 5.7a). Since the field particles have equal or larger mass than the beam ions, the beam ions lose energy through friction with bulk ions,  $\langle \Delta W \rangle = m_b v_b \langle \Delta v_{\parallel} \rangle$  and gain less energy by the pitch angle scattering with bulk ions,  $\langle \Delta W \rangle = m_b \langle (\Delta v_{\perp})^2 \rangle / 2$  (where  $v_{\perp}$  is the ion velocity in the direction perpendicular to the magnetic field), while there is negligible energy diffusion in the parallel direction. The energy decay time by the ion channel depends on the beam speed ( $\tau \sim v_b^3$ ). If the beam energy  $W_b$  is higher than  $W_c$ , the energy transfer to ions is smaller than that to electrons, while the energy transfer to ions becomes dominant when  $W_b$  becomes less than  $W_c$ . This is the reason why  $W_c$  is called the ‘‘critical energy’’. The instantaneous ion heating fraction is given by  $F_i(W_b/W_c) = 1/(1+(W_b/W_c)^3)$ . The fast ion distribution function  $f_b(W_b)$  is given by the flux conservation in energy space and is shown in Fig. 5.7b as follows:

$$f_b(W_b) = \frac{S}{-dW_b/dt} = \frac{\tau_{se}S}{2W_b(1+(W_c/W_b)^{3/2})} \quad (5.11)$$

Equation (5.8) can be solved to obtain the thermalization time  $\tau_{th}$  as the time required for the beam energy to reach the ion thermal energy  $W_{th,i}$

$$\begin{aligned} \tau_{th} &= \frac{\tau_{se}}{3} \int_{W_{th,i}}^{W_{b0}} \frac{dW_b^{3/2}}{W_b^{3/2} + W_c^{3/2}} = \frac{\tau_{se}}{3} \ln \frac{W_{b0}^{3/2} + W_c^{3/2}}{W_{th,i}^{3/2} + W_c^{3/2}} \\ &\sim \frac{\tau_{se}}{3} \ln((W_{b0}/W_c)^{3/2} + 1) \end{aligned} \quad (5.12)$$

and the integrated power fraction to ions as a function of  $x = W_{b0}/W_c$  (with  $W_{b0}$  being the initial beam energy),  $F_i(x)$ , is given as follows,

$$F_i(x) = \frac{1}{x} \left[ \frac{1}{3} \ln \frac{1-x^{1/2}+x}{(1+x^{1/2})^2} + \frac{2}{\sqrt{3}} \left( \tan^{-1} \frac{2x^{1/2}-1}{\sqrt{3}} + \frac{\pi}{6} \right) \right] \quad (5.13)$$

The integrated ion heating fraction  $F_i(W_{b0}/W_c)$  is shown in Fig. 5.7c. Consider the typical ITER case ( $T_e = 20$  keV,  $W_{b0} = 1$  MeV,  $n_e = 10^{20} \text{ m}^{-3}$ ,  $D^0 \rightarrow D^+$ ), beam electron slowing down time  $\tau_{se} = 0.5$  s, critical energy  $W_c = 18.6T_e = 372$  keV,  $W_{b0}/W_c = 2.7$  and the thermalization time  $\tau_{th} = 0.28$  s. In this case, the initial heating is dominated by the electron heating but the integrated heating is almost equal between ions and electrons.

The Coulomb interaction of the beam with bulk electrons and ions also includes pitch angle scattering, which becomes significant when the beam energy is less than the critical energy. The deflection time  $\tau_d$  (defined as  $\langle dW_{b\perp}/dt \rangle \equiv W_b/\tau_d$ , where  $W_{b\perp} = m_b v_{b\perp}^2/2$ ) is a good measure of pitch angle scattering. For  $v_b \gg v_{th,i}$ , the deflection time  $\tau_d$  is given by

$$\tau_d = \frac{2^{5/2} \pi \epsilon_0^2 m_b^{1/2} W_b^{3/2}}{e^4 Z_b^2 \sum_j n_j Z_j^2 \ln \Lambda} \quad (5.14)$$

Here we note that  $\tau_d \sim 1/Z_{eff}$ . The ratio of the energy increase rate in the perpendicular direction over the total energy loss is given by  $-\langle dW_{b\perp}/dt \rangle / dW_b/dt \sim Z_{eff}/\bar{Z} / (1+(W_b/W_c)^{3/2})$  from Eqs (5.8), (5.9), (5.10) and (5.14). When  $W_b \gg W_c$ ,  $\langle dW_{b\perp}/dt \rangle$  is small, but it becomes comparable with the total energy loss rate  $dW_b/dt$  when  $W_b < W_c$ . For a pure electron-ion plasma without impurities, we have  $-\langle dW_{b\perp}/dt \rangle / dW_b/dt \sim A_j/A_b [1+(W_b/W_c)^{3/2}]$ .

When impurities exist, pitch angle scattering is enhanced since  $1/\tau_d \sim Z_{eff}$ , while  $\bar{Z}$  has a weaker dependence on the impurity content.

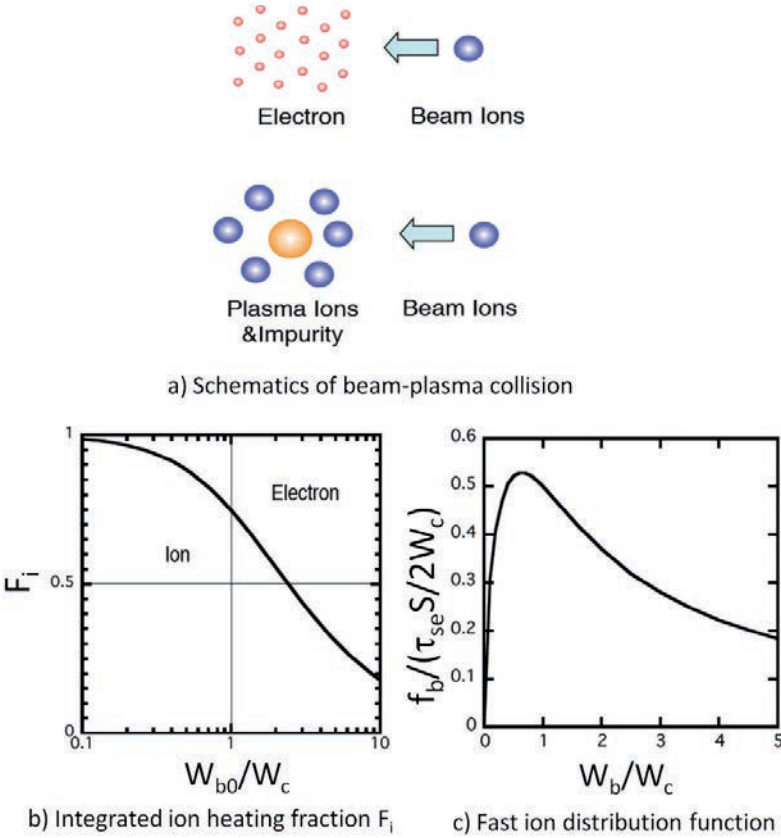


FIG. 5.7. a) Schematics of beam electron, beam ion/impurity collision; b) normalized fast ion distribution function as a function of  $W_{b0}/W_c$ ; c) integrated ion-heating fraction  $F_i$  (Eq. (5.11)) as a function of  $W_b/W_c$ .

### 5.1.5. Energetic particle orbits on the axisymmetric magnetic surfaces

Energetic particle orbits are well discussed in many textbooks such as Wesson [5.16] and Miyamoto [5.17] and also in Chapter 2, Section 2.2 of this book. Here, we discuss the beam ion motion on the axisymmetric magnetic surfaces without collisions by using the conservation of canonical momentum and introduce longitudinal adiabatic invariants (Fig. 5.8). In an axisymmetric system without collisions, the energy  $W = m_b v^2/2$  and the magnetic moment  $\mu = m_b v_\perp^2 / 2B$  are conserved and the parallel velocity is given by

$$v_{\parallel} = \pm \left[ \frac{2(W - \mu B)}{m_b} \right]^{1/2} = \pm v \left( 1 - \frac{\mu B}{W} \right)^{1/2} \quad (5.15)$$

If we define  $B_x = W / \mu$  for a particle, this particle will undergo reflection by the magnetic mirror at  $B = B_x$  (since  $v_{\parallel} = 0$  at  $B = B_x$ ), and it is called a trapped particle. The maximum of  $B$  ( $B_{\max}$ ) appears at the inboard side and the trapped particle with  $B_x \sim B_{\max}$  is called “a barely trapped particle”. There is another conserved quantity in an axisymmetric system such as a tokamak, namely the “canonical angular momentum”

$$p_{\phi} = m_b R v_{\phi} + e_b \psi = \text{constant} \quad (5.16)$$

where  $p_{\phi}$ ,  $v_{\phi}$ ,  $e_b$  are the canonical toroidal angular momentum, the beam toroidal velocity and beam electric charge, respectively. Since  $R v_{\phi}$  varies along the beam trajectory, the flux function  $\psi = R A_{\phi}$ , where  $A_{\phi}$  is the  $\phi$  component of the vector potential  $\vec{A}$ , is not a constant of motion. The radial excursion of the beam ions  $\Delta$  can be given by expanding Eq. (5.16) as follows:

$$\Delta = -\frac{m_b \delta(R v_{\phi})}{e_b |\nabla \psi|} = -\frac{m_b \delta(R v_{\phi})}{e_b R B_{\theta}} \quad (5.17)$$

For the passing beam ions, the change in  $v_{\phi}$  is small and  $\delta R \sim \pm r$ , giving  $\Delta \sim \pm (r / R_0) \rho_{B_{\theta}}$ , where  $q$ ,  $\rho_{B_{\theta}}$ ,  $\rho_{B_x}$  are the safety factor, gyroradius for the poloidal magnetic field (poloidal gyroradius) and gyroradius for the toroidal field, respectively. For the trapped ions, the change in  $v_{\phi}$  is dominant (see Eq. (5.15)) and  $\delta v_{\phi} \sim \pm v(1 - B_{\min} / B_x)^{1/2}$  giving  $\Delta \sim \pm (1 - B_{\min} / B_x)^{1/2} \rho_{B_{\theta}}$ . Since  $B_x$  varies between  $B_{\min}$  and  $B_{\max}$ ,  $\Delta$  is maximized for barely trapped particles,  $\Delta_{\max} \sim \pm (1 - B_{\min} / B_{\max})^{1/2} \rho_{B_{\theta}}$ .

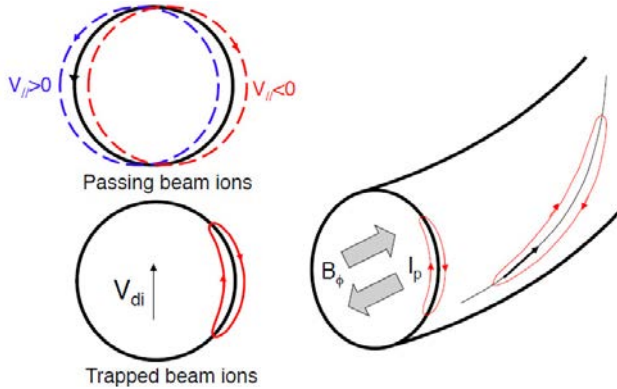


FIG. 5.8. Schematic view of passing and trapped beam ion orbits for a circular tokamak. The  $v_{di} (= m(v_{\parallel}^2 + v_{\perp}^2 / 2) e R B)$  is the toroidal drift due to  $\nabla B$  and the curvature drifts.

The guiding centre of the trapped particle has a large scale periodic bounce motion in the magnetic mirror along a so-called banana orbit. In this case, the

so-called second adiabatic invariant or longitudinal adiabatic invariant  $J$  is conserved. The bounce time of trapped particle  $\tau_{bounce}$  is given by

$$\tau_{bounce} = \oint \frac{dl_{\parallel}}{v_{\parallel}} = \frac{\partial J}{\partial H} \quad (5.18)$$

$$J = \oint \vec{p} \cdot d\vec{q} = m_a \oint v_{\parallel} dl_{\parallel} \quad (5.19)$$

$$H = \frac{1}{2} m_a v_{\parallel}^2 + \mu B(\vec{r}) + e_a \Phi(\vec{r}, t) \quad (5.20)$$

where  $H$ ,  $\mu$ ,  $\Phi$  are the Hamiltonian, magnetic moment and electrostatic potential, respectively, and  $p$ ,  $q$  and  $l_{\parallel}$  are the canonical momentum, canonical coordinate and length along the magnetic field, respectively. The subscript  $a$  stands for species  $a$ .

Banana orbits have a slow precession motion in the toroidal direction and the precession speed is given by

$$R \frac{d\phi}{dt} = \frac{R}{e_a} \frac{\partial J / \partial \psi}{dJ / dH} \quad (5.21)$$

where  $R$ ,  $\phi$ ,  $\psi$  are major radius, toroidal angle and poloidal flux, respectively [5.17].

For typical ITER parameters ( $W_b = 1$  MeV,  $I_p = 15$  MA,  $B_{\theta} = \mu_0 I_p / (2\pi a) = 1.5$  T,  $a/R = 2$  m/6.2 m),  $\Delta \sim 0.04$  m for passing beam ions and  $\Delta \sim 0.1$  m for barely trapped beam ions. For medium sized tokamaks this radial excursion becomes significant. Figure 5.9 shows banana orbit shapes for 1 MeV triton due to the D-D reaction produced at  $r/a = 0.2$  in elliptically shaped JT-60U plasma with normal shear (NS) and reversed shear (RS). The orbit excursion becomes larger for RS since  $B_{\theta}$  is smaller due to the hollow current profile.

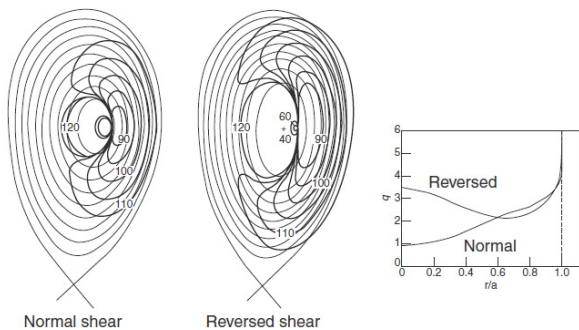


FIG. 5.9. Orbits of 1 MeV triton born at  $r/a = 0.2$  due to D-D reaction for NS (normal shear) and RS (reversed shear) plasmas with  $I_p = 2.4$  MA for various pitch angles of the triton in degrees [5.18].

### 5.1.6. Fast ion behaviour and high temperature production with NB injection

The first experiments of neutral beam heating were reported from ATC and ORMAK devices at the 7th IAEA International Conference on Plasma Physics and Controlled Nuclear Fusion Research in 1974. Significant efforts in neutral beam system development were made and 2.4 MW injection heating into PLT produced significant ion and electron heating ( $T_i = 1$  keV to 6.6 keV) in 1979. Based on this successful plasma heating, further implementation of the NBI system has been made worldwide, especially for three large tokamaks (TFTR, JT-60U and JET). NB injection of 40 MW was achieved in TFTR in 1994 and in JT-60U in 1996.

A comprehensive review of fast ion behaviour in tokamaks is given in Heidbrink [5.19]. The behaviour of fast ions agrees fairly well with the prediction of classical Coulomb collision theory for a quiescent plasma where no significant MHD modes are observed. The slowing down time of fast ions was measured in various tokamaks, showing good agreement with classical slowing down formula Eq. (5.8). Pitch angle scattering was also roughly consistent with the prediction of the Fokker–Planck equation. The radial transport of fast ions under the turbulent fluctuations was very small compared with that for thermal ions and electrons. Figure 5.10 shows TFTR experiments to measure the fast ion diffusion coefficient showing  $D_{fast} \sim 0 \text{ m}^2 \cdot \text{s}^{-1}$  [5.20].

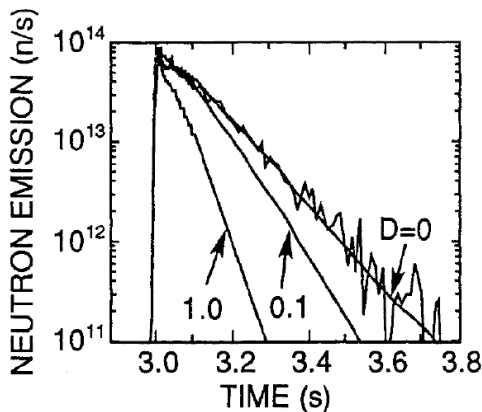


FIG. 5.10. Fast ion diffusion coefficient measured in TFTR [5.20]. The unit n/s means neutrons/second and the three curves are plotted for different values of fast ion diffusion coefficient  $D = 0 \text{ m}^2 \cdot \text{s}^{-1}$ ;  $D = 1.0 \text{ m}^2 \cdot \text{s}^{-1}$  and  $D = 0.1 \text{ m}^2 \cdot \text{s}^{-1}$ . Reprinted from Ref. [5.20]. Copyright (2011), American Institute of Physics.

The behaviour of fast ions following classical slowing down and virtually no fast ion diffusion in an MHD-free tokamak led to good agreement of measured

D-D and D-T neutron emission rates with simulation using measured plasma parameters and a classical slowing down fast ion model with no fast ion diffusion. TRANSP simulation of JET D-D and D-T experiments is shown in Fig. 5.11 [5.21]. Both D-D and D-T discharges are characterized by significant neutrons from beam-plasma reaction. So, the agreement of total neutron emission rate between measurement and simulation provides fair confidence of the absence of anomalous slowing down and fast ion diffusion in axisymmetric tokamaks.

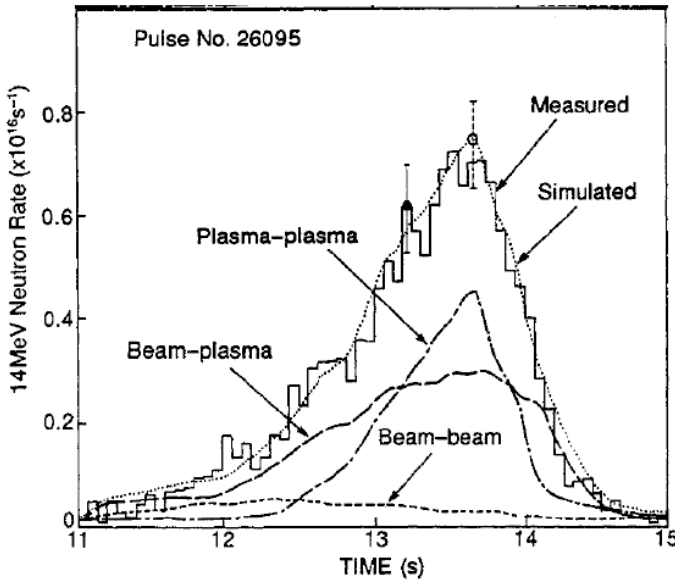


FIG. 5.11. Measured and simulated D-D and D-T neutrons with significant beam-plasma reactions in JET [5.21].

Excellent simple physics led to the adoption of NBI heating as the main auxiliary heating system in tokamaks. Figure 5.12 shows the results from JT-60U under intensive neutral beam heating  $P_{abs} = 27$  MW (absorbed part of the injected NB) with the beam energy of 92 keV into the discharge with plasma current  $I_p = 2.4$  MA and toroidal magnetic field  $B_\phi = 4.3$  T. The discharge went into the H-mode 0.6 s after the start of beam injection, and the plasma stored energy reached 8.6 MJ with a D-D neutron emission rate  $S_n = 5.2 \times 10^{16} \text{ s}^{-1}$ , and a global energy confinement time  $\tau_E = 0.75$  s. An H-factor above L-mode of 3.3 was achieved and a central ion temperature  $T_i(0)$  of 45 keV ( $5.2 \times 10^8$  centigrade) and a central electron temperature  $T_e(0)$  of 10.6 keV were achieved as measured by charge exchange recombination spectroscopy (CXRS) of fully stripped carbon impurities for the ion temperature and by an ECE Fourier spectrometer (ECE) for the electron temperature [5.22, 5.23]. In this case, the critical energy  $W_c = 198$  keV and  $W_b/W_c = 0.46$ . So, about 90% of the total heating power goes to ions and

10% goes to electrons. This preferential ion heating resulted in  $T_i(0) \sim 4T_e(0)$  and it is called a “hot ion regime”. Although the ion temperature is measured for impurities, it is confirmed that classical energy exchange between deuterium and carbon is enough to reach  $T_i(0) \sim T_i(0)$ , where the subscript  $I$  stands for impurity. This central ion temperature was the world’s highest plasma temperature in 1996 as certified by the Guinness Book of Records.

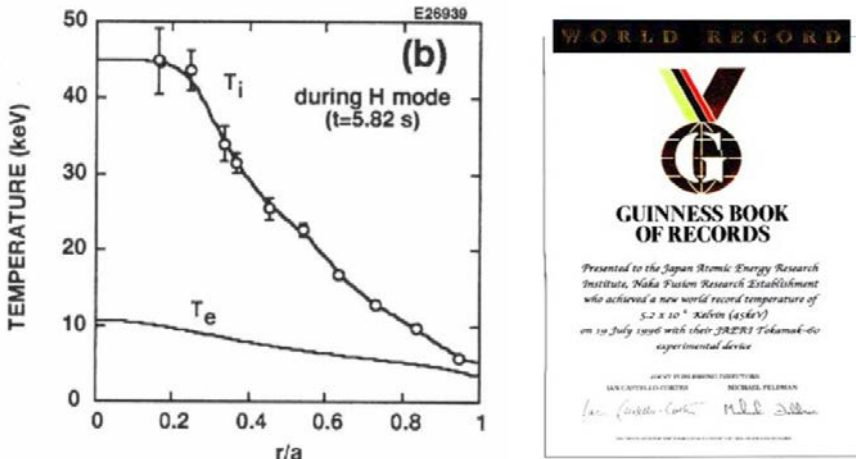


FIG. 5.12.  $T_i$  and  $T_e$  profiles for the world’s highest central ion temperature in JT-60U and Guinness Book of Records on achievement of 45 keV in 1996 [5.22].

### 5.1.7. Physics of neutral beam current drive: fast ion distribution function

Neutral beam injection produces fast ion current circulating around the torus. The current carried by a single beam is not large but multiple circulations around the torus give a large fast ion current. Collision of these directional fast ions with bulk electrons produces an electron drift in the same direction as the fast ions, whose current is in the opposite direction to the fast ion current. This electron current is called the “shielding current” and will be discussed in Section 5.1.8. It can cancel the fast ion current completely if there are no trapped electrons and impurities. In reality, the existence of trapped electrons and impurities in the toroidal plasma provides great opportunity for current drive by neutral beam injection. The fast ion trajectory is assumed to be on the magnetic surface ( $\psi$ ) in the following theory of neutral beam current drive but trapping in the magnetic mirror is taken into account for beam ions.

The velocity distribution function of fast ions  $f_b$  is determined as a solution of the Fokker–Planck equation valid for  $v_{th,i} \ll v_b \ll v_{th,e}$ . Since a tokamak has variation of the magnetic field  $B$  along the fast ion trajectory, part of the

fast ion population is trapped in the magnetic mirror as discussed in the previous section. The fast ion current is carried by the passing particles and the trapped particles do not contribute to the fast ion current since the return motion cancels the current under the assumption of a fast ion trajectory on the magnetic surface. The degree of trapping can be measured by the constant of motion of a single particle  $\eta = (1 - \mu B_{\min} / W)^{1/2}$ , where  $\mu = m_b v_{\perp}^2 / 2B$  is the magnetic moment,  $W = m_b v^2 / 2$  is the fast ion energy and  $B_{\min}$  is the minimum of the total magnetic field on the magnetic surface, usually at the outboard side of the torus. The value of  $\eta$  varies from 0 (at  $\mu = W / B_{\min}$ ) to 1 (at  $\mu = 0$ ) and the value at the trapped-passing boundary  $\eta_t$  is given by  $\eta_t = (1 - B_{\min} / B_{\max})^{1/2}$ , where  $B_{\max}$  is the maximum total magnetic field on the magnetic surface, usually at the inboard side of the torus. The physical meaning of  $\eta$  is  $v_{\parallel} / v$  at  $B = B_{\min}$ . The fast ion Fokker-Planck equation in a non-uniform magnetic field is given by Connor [5.24] as follows:

$$\begin{aligned} \tau_{se} \frac{\partial f_b}{\partial t} = v^{-2} \frac{\partial}{\partial v} \left[ (v_c^3 + v^3) f_b \right] + \\ + \frac{\beta v_c^3}{v^3 \eta \langle v / v_{\parallel} \rangle} \frac{\partial}{\partial \eta} \left[ \frac{(1 - \eta^2)}{\eta} \left\langle \frac{v_{\parallel}}{v} \right\rangle \frac{\partial f_b}{\partial \eta} \right] + \tau_{se} S(v, \eta) \end{aligned} \quad (5.22)$$

where  $\tau_{se}$  is the beam electron slowing down time given by Eq. (5.10),  $v_c$  is the critical velocity defined by  $v_c = (2W_c / m_b)^{1/2}$  where  $W_c$  is given by Eq. (5.9),  $v_b$  is the beam velocity ( $= (2W_b / m_b)^{1/2}$ ),  $\beta$  is defined by  $\beta = Z_{eff} n_e \ln \Lambda_e / (2m_b \Sigma (m_j^{-1} Z_j^2) \ln \Lambda_i)$ , where  $\ln \Lambda_e$  and  $\ln \Lambda_i$  are the Coulomb logarithms of the electron and ion species.  $S(v, \eta)$  is the bounce averaged fast ion source rate per unit volume,  $Z_{eff}$  is the effective charge defined by  $Z_{eff} = \Sigma_j n_j Z_j^2 / n_e$ ,  $\langle v / v_{\parallel} \rangle$  is given by  $\langle v / v_{\parallel} \rangle = (2 / \pi) K[(\eta_t / \eta)^2]$  and  $\langle v_{\parallel} / v \rangle$  is given by  $\langle v_{\parallel} / v \rangle = (2 / \pi) E[(\eta_t / \eta)^2]$  for passing ions, where  $K$  and  $E$  are complete elliptic integrals of the first and second kind, respectively. The solution of Eq. (5.22) is given in Ref. [5.25] as follows:

$$f_b(v, \eta) = S_0 \tau_{se} \sum_n a_n(v) c_n(\eta) \quad (5.23)$$

where  $S_0$ ,  $c_n$  are neutral beam source intensity and eigenfunction of  $\eta$ , respectively, and  $a_n(v)$  is the analytical solution for a uniform magnetic field given by Gaffey [5.26],

$$a_n(v) = \frac{k_n}{v^3 + v_c^3} \left[ \frac{v^3 (v_b^3 + v_c^3)}{v_b^3 (v^3 + v_c^3)} \right]^{\beta \lambda_n / 3} \quad \text{for } v < v_b \quad (5.24)$$

$$= \frac{k_n}{v_b^3 + v_c^3} \exp \left[ - \frac{2W_b (1 + (v_c / v_b)^3) v - v_b}{T_e + (v_c / v_b)^3 T_i} \frac{v - v_b}{v_b} \right] \quad \text{for } v > v_b \quad (5.25)$$

Here,  $S(v, \eta) = S_0 \delta(v - v_b) k(\eta) = S_0 \delta(v - v_b) \sum k_n c_n(\eta)$ , where  $\delta$  is the Dirac delta function,  $k_n$  the  $n$ 'th source coefficient in the  $c_n$  expansion of the source, and the fast ion distribution function above the beam energy ( $v > v_b$ ) comes from energy diffusion in velocity space. The following equation defines the eigenvalue  $\lambda_n$  and eigenfunction  $c_n(\eta)$ :

$$\frac{1}{\eta \langle v / v_{\parallel} \rangle} \frac{d}{d\eta} \left[ (1 - \eta^2) \left\langle \frac{v_{\parallel}}{v} \right\rangle \frac{dc_n}{d\eta} \right] + \lambda_n c_n = 0 \quad (5.26)$$

This equation can be solved numerically by the Rayleigh–Ritz method in the ACCOME code [5.27]. Using the above formulas, the flux surface averaged parallel fast ion current multiplied by  $B$ ,  $\langle \vec{j}_{fast} \cdot \vec{B} \rangle$ , can be calculated as

$$\langle \vec{j}_{fast} \cdot \vec{B} \rangle = e Z_b \int_0^{\infty} v^3 dv \int_{-1}^1 d\eta f_b(v, \eta, \psi) H(v, \eta, \psi) \quad (5.27)$$

$$H(v, \eta, \psi) = v^{-1} \int B dl_{\parallel} / \int v_{\parallel}^{-1} dl_{\parallel} \quad (5.28)$$

Here  $Z_b$  is the electric charge of a fast ion. Wesson [5.16] gave a lowest order expression of this fast ion current using the first Legendre polynomial component without trapping effect  $f_1$  as follows:

$$\begin{aligned} j_{fast} &= \frac{S \tau_{se} Z_b v_{b0}}{1 + W_c / W_{b0}} \int_0^1 f_1 u^3 du \\ &= \frac{S \tau_{se} Z_b v_{b0}}{1 + W_c / W_{b0}} \int_0^1 u^{2\beta} \left[ \frac{1 + (W_c / W_{b0})^{3/2}}{u^3 + (W_c / W_{b0})^{3/2}} \right]^{1+2\beta/3} u^3 du \end{aligned} \quad (5.29)$$

where  $u$  is the fast ion  $v_{\parallel}$  normalized to the beam injection velocity  $v_{b0}$ .

### 5.1.7.1. Rayleigh–Ritz method

The  $c_n$  is expanded in a series of  $\xi = \eta - \eta_t$ , which should satisfy the boundary conditions  $c_n(\xi = 0) = 0$  and  $c_n(\xi = 1) = 1$  as follows:

$$c_n = \sum_{m=1}^{\infty} a_{mn} \xi^{2m-1} \quad (5.30)$$

Here only odd components of  $c_n(\eta)$  are obtained for the fast ion current calculation. The eigenvalue  $\lambda_n$  is a solution of the following equation:

$$|\alpha_{mn} + \lambda_n \beta_{mn}| = 0 \quad (5.31)$$

$$\alpha_{mn} = \int_0^{1-\eta_t} \left\{ \left[ 1 - (\xi + \eta_t)^2 \right] E(k)(2m-2) + \left[ -2(\xi + \eta_t)E(k) - \left[ 1 - (\xi + \eta_t)^2 \right] \frac{dE(k)}{dk} \frac{2\eta_t}{(\xi + \eta_t)^3} \right] \xi \right\} (2m-1) \xi^{2m+2n-4} d\xi \quad (5.32)$$

$$\beta_{mn} = \int_0^{1-\eta_t} K(k)(\xi + \eta_t) \xi^{2m+2n-2} d\xi \quad (5.33)$$

where  $k = \eta_t^2 / (\xi + \eta_t)^2$  and  $E$  and  $K$  are complete elliptic integrals. The  $a_{mn}$  are obtained from the following simultaneous linear equations with a large number  $M$  sufficient for convergence:

$$\sum_{m=1}^M (\alpha_{mn} + \lambda_n \beta_{mn}) a_{mn} = 0 \quad (5.34)$$

$$\sum_{m=1}^M (1 - \eta_t)^{2m-1} a_{mn} = 1 \quad (5.35)$$

### 5.1.8. Physics of neutral beam current drive: shielding current and NBCD efficiency

In reality, the existence of trapped electrons and impurities in the toroidal plasma provides a great opportunity for current drive by neutral beam injection. The beam driven current  $\vec{j}_{bd}$  is a current in response to the external momentum source  $S_b$ , which is obtained by solving parallel momentum and heat momentum balance equations for electrons, ions, impurities and fast ions (only momentum balance for fast ions) [5.28], as follows:

$$\langle \vec{j}_{bd} \cdot \vec{B} \rangle = \sum_{a=e,i,I,b} e_a n_a \langle \vec{u}_a \cdot \vec{B} \rangle = \sum_{a=e,i,I,b} e_a n_a (\hat{M} - \hat{L})_{ab}^{-1} S_b \quad (5.36)$$

Here,  $e_a$ ,  $n_a$ ,  $\hat{M}$  and  $\hat{L}$  are the electrical charge, density, viscous and friction matrixes, respectively, and  $S_b$  is the momentum source from fast ions. Also  $u_a$  is the flow velocity of species  $a$  ( $a = e, i, I, b$ ). So, if we divide the beam driven current  $\vec{j}_{bd}$  into the fast ion current  $\vec{j}_{fast}$  and the shielding current  $\vec{j}_{shield}$   $\langle \vec{j}_{bd} \cdot \vec{B} \rangle = \langle \vec{j}_{fast} \cdot \vec{B} \rangle + \langle \vec{j}_{shield} \cdot \vec{B} \rangle$ , we obtain

$$\langle \vec{j}_{fast} \cdot \vec{B} \rangle = e_b n_b (\hat{M} - \hat{L})_{bb}^{-1} S_b \quad (5.37)$$

$$\langle \vec{j}_{shield} \cdot \vec{B} \rangle = \sum_{a=e,i,l} e_a n_a (\hat{M} - \hat{L})_{ab}^{-1} S_b \quad (5.38)$$

where  $e_b$ ,  $n_b$  and  $S_b$  are the electrical charge, density and momentum source density of the beam ions, respectively. Therefore, the shielding factor defined as  $F = \langle \vec{j}_{bd} \cdot \vec{B} \rangle / \langle \vec{j}_{fast} \cdot \vec{B} \rangle$  can be obtained as follows [5.28, 5.29]:

$$F = \frac{\sum_{a=e,i,l,b} e_a n_a (\hat{M} - \hat{L})_{ab}^{-1}}{e_b n_b (\hat{M} - \hat{L})_{bb}^{-1}} \quad (5.39)$$

Various physical processes have been included self-consistently in Eq. (5.39). the friction between the bulk electrons and fast ions produces shielding of the fast ion current, while the electron viscosity gives a neo-classical drag force to the passing electrons from the trapped electrons, as a result of which the shielding current carried by the passing electrons is partially cancelled. Friction between electrons and impurities also reduces the shielding current. This stacking factor  $F$  has  $Z_{eff}$  and  $\varepsilon = r/R$  dependences but no  $v_b/v_e$  dependence if  $v_b \ll v_e$ . The parametric dependences of  $F$  on  $Z_{eff}$  and  $\varepsilon$  for an arbitrary aspect ratio ( $0 \leq \varepsilon \leq 1$ ) can be calculated from Eq. (5.39) and are shown in Fig. 5.13.

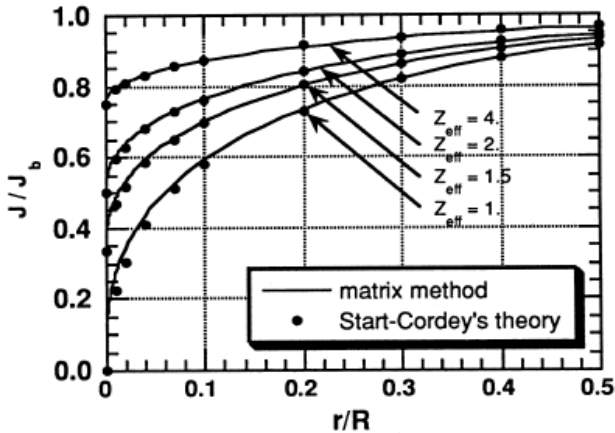


FIG. 5.13. Shielding factor  $F$  as a function of  $r/R$  and  $Z_{eff}$  [5.28] in comparison with Ref. [5.30]. Here,  $J/J_b$  stands for  $j_{bd}/j_{fast}$  in the text.

At  $r/R = 0$  (case with no trapped particles), the stacking factor  $F$  can be derived from a simple momentum balance equation for the electrons, namely,

$f_{eb} + f_{ei} = \nu_{eb} m_e n_e u_b - \nu_{ei} m_e n_e u_e = 0$ , where  $f_{eb}$  is the momentum transfer rate from beam ions to electrons and  $f_{ei}$  is the momentum loss rate from electrons to ions, and  $\nu_{eb}$ ,  $\nu_{ei}$ ,  $u_b$  and  $u_e$  are the electron beam collision frequency, electron ion collision frequency, fast ion drift velocity and electron drift velocity, respectively, giving the stacking factor  $F$  as

$$F = \frac{j_{bd}}{j_{fast}} = 1 - \frac{en_e v_d}{eZ_b n_b v_b} = 1 - \frac{Z_b}{Z_{eff}} \quad (5.40)$$

Enhanced collisions with impurities reduce the drift speed of electrons and hence reduce the shielding current. Since trapped electrons cannot drift in the toroidal direction, they effectively drag the passing electrons and further reduce the shielding current with increasing  $r/R$  as seen in Fig. 5.13.

Wesson [5.16] gave a rough estimate of the beam current drive efficiency by assuming  $j_{bd} \sim j_{fast}$  (see Eq. (5.29)) divided by the driving power per unit volume,  $P_d = SW_{b0}$ , as follows,

$$\frac{j_{bd}}{P_d} \sim \frac{2\tau_{se} e Z_b F}{m_b v_{b0} (1 + W_c / W_{b0})} \int_0^1 f_1 u^3 du \quad (5.41)$$

Here  $u = v / v_{b0}$  is the ratio of the normalized fast ion velocity to fast ion injection speed. The parametric dependence can be given by  $j_{bd} / P_d \propto (T_e / n_e) \eta(W_b / W_c)$ ,

$$\eta(W_{b0} / W_c) = \frac{1}{1 + W_c / W_{b0}} \int_0^1 \left[ \frac{1 + (W_c / W_{b0})^{3/2}}{u^3 + (W_c / W_{b0})^3} \right]^{1+2\beta/3} u^{2\beta+3} du \quad (5.42)$$

Although this equation neglects the trapped particle effect and the electron shielding current, it is useful in understanding the qualitative parametric dependence of the current drive efficiency on  $W_{b0}/W_c$  (0, which stands for ‘initial’, is omitted hereafter for  $W_b$ ) as given in Fig. 5.14. Integration over the power deposition profile gives the following formula for the current drive efficiency:

$$\eta_{CD} \equiv R n_e I_{CD} / P_{CD}$$

$$\eta_{CD} \equiv \frac{I_{CD} \bar{n}_e R}{P_{CD}} = \frac{\bar{n}_e R \int j_{bd} dS}{\int P_{CD} dV} \propto \langle T_e \rangle \eta(W_b / \langle W_c \rangle) \quad (5.43)$$

where  $I_{CD}$  and  $P_{CD}$ ,  $\bar{n}_e$  are the driven current and current drive power, and line averaged density, respectively. Also,  $dS$  and  $dV$  are surface and volume elements, respectively. This equation tells us that higher electron temperatures and higher beam energies to approach the optimum  $W_b/W_c \sim 5$  are key to achieving the highest current drive efficiency.

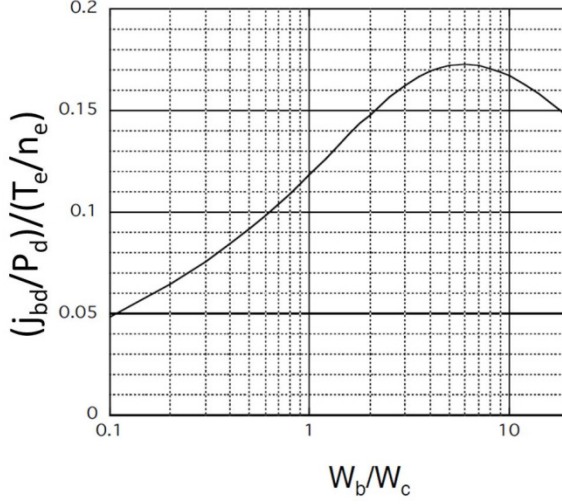


FIG. 5.14.  $W_b/W_c$  dependence of normalized NBCD efficiency  $\eta$ .

Viscosity and friction matrices valid for an arbitrary aspect ratio, all collisionality and multi-species (electron, ion, impurity and beam) at  $v_{th,i} \ll v_b \ll v_{th,e}$  are given in Ref. [5.28] as follows:

$$\hat{M} = \begin{vmatrix} \mu_1^e & 0 & 0 & 0 & \mu_2^e & 0 & 0 \\ 0 & \mu_1^i & 0 & 0 & 0 & \mu_2^i & 0 \\ 0 & 0 & \mu_1^l & 0 & 0 & 0 & \mu_2^l \\ 0 & 0 & 0 & \mu_1^b & 0 & 0 & 0 \\ \mu_2^e & 0 & 0 & 0 & \mu_3^e & 0 & 0 \\ 0 & \mu_2^i & 0 & 0 & 0 & \mu_3^i & 0 \\ 0 & 0 & \mu_2^l & 0 & 0 & 0 & \mu_3^l \end{vmatrix} \quad (5.44)$$

$$\hat{L} = \begin{vmatrix} l_{11}^{ee} & l_{11}^{ei} & l_{11}^{el} & l_{11}^{eb} & -l_{12}^{ee} & -l_{12}^{ei} & -l_{12}^{el} \\ l_{11}^{ie} & l_{11}^{ii} & l_{11}^{il} & l_{11}^{ib} & -l_{12}^{ie} & -l_{12}^{ii} & -l_{12}^{il} \\ l_{11}^{le} & l_{11}^{li} & l_{11}^{ll} & l_{11}^{lb} & -l_{12}^{le} & -l_{12}^{li} & -l_{12}^{ll} \\ l_{11}^{be} & l_{11}^{bi} & l_{11}^{bl} & l_{11}^{bb} & 0 & 0 & 0 \\ -l_{21}^{ee} & -l_{21}^{ei} & -l_{21}^{el} & -l_{21}^{eb} & l_{22}^{ee} & l_{22}^{ei} & l_{22}^{el} \\ -l_{21}^{ie} & -l_{21}^{ii} & -l_{21}^{il} & 0 & l_{22}^{ie} & l_{22}^{ii} & l_{22}^{il} \\ -l_{21}^{le} & -l_{21}^{li} & -l_{21}^{ll} & 0 & l_{22}^{le} & l_{22}^{li} & l_{22}^{ll} \end{vmatrix} \quad (5.45)$$

where  $l$  and  $\mu$  are friction and viscosity coefficients, respectively, and detailed expressions are given in Ref. [5.28].

### 5.1.9. Experimental observation of beam-driven current

First observations of a beam induced current in a tokamak were made in DITE [5.31], where 1 MW of H beam with  $W_b = 24$  keV was injected tangentially and  $T_e(0) = 0.9$  keV achieved, showing 33 kA driven non-inductively as shown in Fig. 5.15. Since then, a wide range of experimental data have been accumulated including those from DIII-D, JET, TFTR and JT-60U. In particular, the electron temperature was increased to 14 keV and the beam energy was increased to 360 keV in JT-60U experiments [5.32].

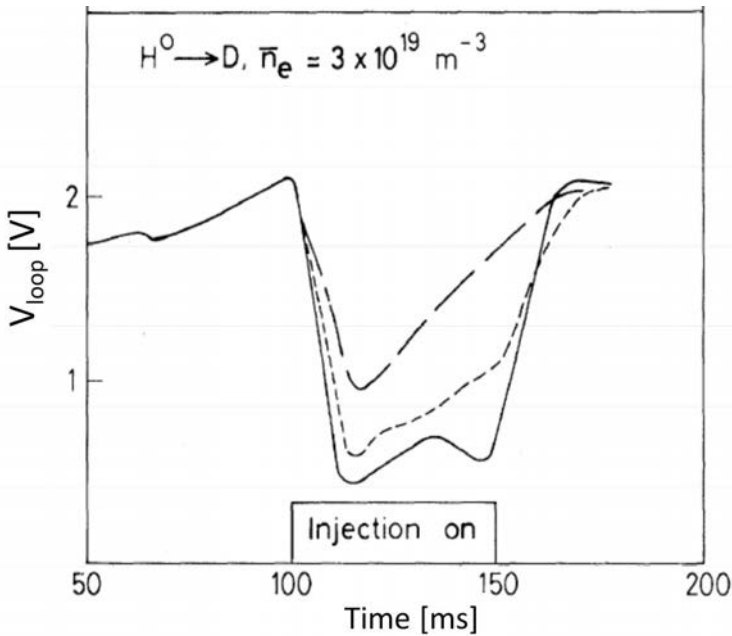


FIG. 5.15. DITE tokamak showing existence of beam driven current (— experimental loop voltage  $V_{loop}$ , - - - theory with beam driven current, — calculation with beam driven current) [5.31]. Reprinted from Ref. [5.31]. Copyright (2011) by the American Physical Society.

Methods to calculate plasma equilibrium with inductive and non-inductive (beam driven and bootstrap) current densities  $j_{NI}$  have been established in various numerical codes such as ACCOME [5.27] and ASTRA [5.33] incorporating the physical processes described in previous sections. A method for the experimental determination of non-inductively driven current was established by Forest [5.34]. Ohm's Law in general toroidal geometry is given by

$$\langle \vec{j} \cdot \vec{B} \rangle = \sigma \langle \vec{E} \cdot \vec{B} \rangle + \langle \vec{j}_{NI} \cdot \vec{B} \rangle \quad (5.46)$$

where

$$\langle \vec{E} \cdot \vec{B} \rangle = \frac{\langle B_\phi^2 \rangle}{F} \frac{\partial \psi}{\partial t} \Big|_\Psi \quad (5.47)$$

Here  $\psi$  and  $\Psi$  are the poloidal and toroidal flux, respectively. The time evolution of the poloidal flux  $\psi(\rho, t)$  with  $\rho$  being a radial coordinate and  $\langle \vec{j} \cdot \vec{B} \rangle$  can be measured by MSE diagnostics with an equilibrium magnetic fitting code such as EFIT [5.35]. By calculating the ohmic current using the measured  $\partial\psi/\partial t$ , density, temperature and  $Z_{eff}$  profiles, the non-inductively driven current  $\langle \vec{j}_{NI} \cdot \vec{B} \rangle$  can be “measured” as the difference  $\langle \vec{j}_{NI} \cdot \vec{B} \rangle_m = \langle \vec{j} \cdot \vec{B} \rangle - \sigma \langle \vec{E} \cdot \vec{B} \rangle$ . This current density profile can be compared with the numerical calculation of  $\langle \vec{j}_{NI} \cdot \vec{B} \rangle_c$  using the measured density, temperature and  $Z_{eff}$  profiles. A comparison is shown in Fig. 5.16. It is worth noting that “calculated” and “measured” non-inductively driven current profiles agree when multi-step ionization effects are taken into account in the calculation of  $\langle \vec{j}_{NI} \cdot \vec{B} \rangle$ .

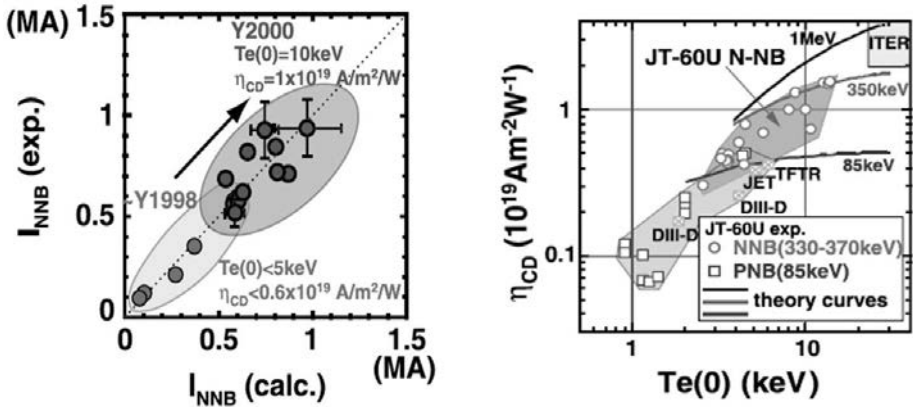


FIG. 5.16. Left: Comparison of calculated and measured beam driven current. Right: NBCD current drive efficiency as a function of central electron temperature  $T_e(0)$  [5.14, 5.32]. Here  $I_{NNB}$  stands for  $I_{CD}$  with a negative ion based neutral beam.

Agreement between measured and calculated total driven current is good in a range of 0.1–1 MA as shown in Fig. 5.16. The theoretical NB current drive efficiency increases with electron temperature  $T_e$  (see Eq. (5.43)). This dependence is also confirmed experimentally as shown in Fig. 5.16. Maximum NBCD efficiency  $\eta_{CD} = 1.55 \times 10^{19} \text{ A} \cdot \text{W}^{-1} \cdot \text{m}^{-2}$  is achieved at  $T_e(0) = 14 \text{ keV}$  with a beam energy of 360 keV. The projected NBCD efficiency for  $W_b = 1 \text{ MeV}$  in ITER is  $2 - 3 \times 10^{19} \text{ A} \cdot \text{W}^{-1} \cdot \text{m}^{-2}$  for  $T_e(0) = 10 - 20 \text{ keV}$ . For the DEMO, a higher

central temperature  $T_e(0) \sim 30$  keV and higher beam energy  $W_b \sim 2$  MeV might be necessary to have a high NBCD efficiency of  $5 \times 10^{19} \text{ A} \cdot \text{W}^{-1} \cdot \text{m}^{-2}$ . These experimental results are encouraging for steady state operation of ITER, DEMO and beyond.

Redistribution of beam driven current and/or reduced driven current have been observed in various tokamaks [5.14] if the discharge is associated with MHD activities, such as toroidicity-induced Alfvén eigenmodes (TAEs), sawteeth, fishbones and tearing modes, while the characteristics of these modes are introduced in Chapter 3 of this book. So, it is important to control MHD activity so that NBCD does not deteriorate. Recent experiments on ASDEX-U show the appearance of a discrepancy with theory in high power off-axis NBCD experiments without any MHD activity [5.36]. This subject is left for future investigation.

### 5.1.10. Physics of ripple loss of fast ions: banana drift and ripple trapped losses

Ideally, a tokamak is an axisymmetric system. But the finite number of toroidal field coils leads to the loss of perfect axisymmetry and produces ripple loss [5.37]. The toroidal variation of vacuum toroidal magnetic field  $B_\phi$  and ripple  $\delta$  are defined by

$$B_\phi = B_0(R)(1 - \delta(R, Z) \cos(N\phi)) \quad (5.48)$$

$$\delta(R, Z) = (B_{\max} - B_{\min}) / (B_{\max} + B_{\min}) \quad (5.49)$$

where  $N$  and  $\phi$  are the number of toroidal field coils and the toroidal angle. The ripple at the mid-plane  $Z = 0$  can be approximately given by

$$\delta = \beta \left[ \frac{1}{(R_{out}/R)^N - 1} + \frac{1}{(R/R_{in})^N - 1} \right] \quad (5.50)$$

where  $R_{in}$  and  $R_{out}$  are the major radius of the outer and inner legs of the toroidal field coils and the numerical constant  $\beta \sim 1.5$ . An analytical formula of the ripple for a circular TF coil is given by Yushmanov [5.38].

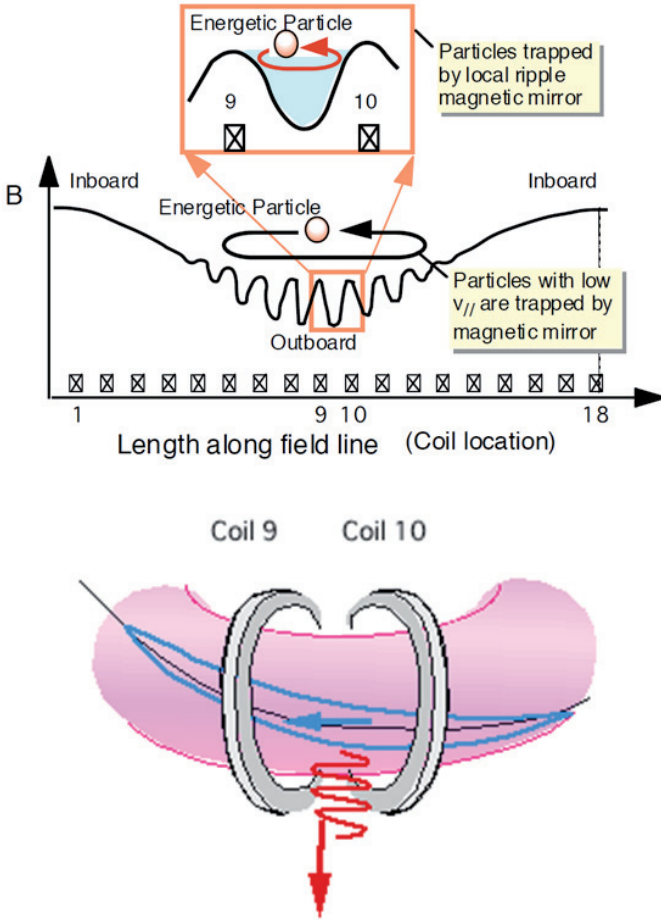


FIG. 5.17. Top: Variation of toroidal magnetic field with a ripple field and two types of trapped particle orbits. Bottom: Schematics of banana drift orbit (blue) and ripple trapped orbit (red).

In Fig. 5.17, the field strength along a magnetic field line is shown, which contains two variations, namely the large scale  $\cos \phi$  and the small scale  $\cos(N\phi)$  variations. The ripple well parameter  $\alpha$  is defined by

$$\alpha = \left| \frac{\partial \bar{B} / \partial l}{\left[ \frac{\partial \tilde{B}}{\partial l} \right]_{\max}} \right| \quad (5.51)$$

where  $\bar{B}(= B_0(R))$  and  $\tilde{B}(= B_0(R)\delta(R,Z)\cos(N\phi))$  are axisymmetric and non-axisymmetric fields, respectively. If  $\alpha$  is less than 1, there will be a local ripple well. Using  $\partial / \partial l = (\bar{B}_R / \bar{B})\partial / \partial R$  for an axisymmetric field (here,  $B_R$  is the  $R$  component of the magnetic field), and  $\partial / \partial l = R^{-1}\partial / \partial \phi$  for a non-axisymmetric field, the ripple well parameter  $\alpha$  can be simplified as follows:

$$\alpha = \left| \frac{\overline{B}_R}{\overline{BN}\delta} \right| \quad (5.52)$$

Since  $\alpha$  is proportional to  $I_p / B_\phi \sim 1/q$ , the ripple well region becomes wider for low current and high  $q$  operation.

There are two types of ripple loss mechanism in the presence of toroidal field ripple. One is ripple trapped loss in which fast ions are trapped in the local magnetic mirror due to the toroidal field ripple, which is shown as a red orbit in Fig. 5.17 and occurs in the ripple well region  $\alpha < 1$ . In this case trapped fast ions drift vertically due to the toroidal drift. Another mechanism is the banana drift loss in which axisymmetric banana orbit drifts horizontally due to the toroidal field ripple, which is shown as a blue orbit in Fig. 5.17.

Quantitative comparison of measured and calculated ripple loss was made in JT-60U [5.39]. The heat flux was estimated from the IR measurement of the temperature rise of the first wall and the magnitude and location of the hot spot agree with those from measurement and calculation for banana drift loss (Fig. 5.18), while the effect of the radial electric field should be included for ripple trapped loss [5.40].

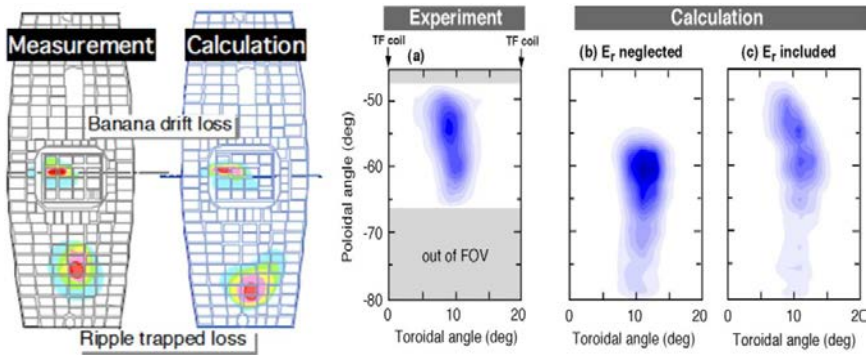


FIG. 5.18. Left: Comparison of contour plots of measured and calculated heat flux due to ripple loss. Calculation is done without including the radial electric field  $E_r$  effect. Right: Measured heat flux contour compared with calculations with and without  $E_r$  [5.40]. Reprinted from Ref. [5.40]. Copyright (2011), American Nuclear Society.

The effect of collisions can be simulated using the Monte Carlo technique [5.41]. The change in the parallel and perpendicular velocities of a test particle from  $(v_{\parallel}, v_{\perp})$  to  $(v'_{\parallel}, v'_{\perp})$  after Coulomb collision can be given by the following relations:

$$v'_{\parallel} = v_{\parallel} + \Delta v_L \frac{v_{\parallel}}{v} + \Delta v_T \frac{v_{\perp}}{v} \sin \Omega \quad (5.53)$$

$$v'_{\perp} = \left[ (v + \Delta v_L)^2 + \Delta v_T^2 - v_{\parallel}^2 \right]^{1/2} \quad (5.54)$$

where  $v$  is the total velocity,  $\Omega$  is the Larmor phase, and  $\Delta v_L$  and  $\Delta v_T$  are the longitudinal and transverse components of velocity change, respectively. The  $\Delta v_L$  and  $\Delta v_T$  can be computed by generating normal random numbers with mean values ( $\langle \Delta v_L \rangle$ ,  $\langle \Delta v_T \rangle$ ) and mean square deviations ( $\langle \Delta v_L^2 \rangle$ ,  $\langle \Delta v_T^2 \rangle$ ) to match theoretical values given by Turbunikov [5.42]. The Larmor phase  $\Omega$  in Eq. (5.53) can be simulated by a uniform random number between 0 and  $2\pi$ .

### 5.1.11. Physics of particle trajectories in non-axisymmetric fields

Fast ion trajectories in a non-axisymmetric magnetic field with toroidal ripple are much more complicated than those described in Section 5.1.5. In this case, the physics of a particle trajectory in a tokamak becomes very much similar to that of a helical system. Despite such complications, the magnetic moment  $\mu = mv_{\perp}^2 / 2B$  is conserved for most magnetic configurations of interest. The particle energy  $W = m_a v_{\parallel}^2 / 2 + \mu B + e_a \Phi$  is also conserved under a static confinement field.

In the case  $\Phi = 0$ , this equation means that the turning point of a banana orbit ( $v_{\parallel} = 0$ ) is always on a  $B = W / \mu = \text{constant}$  surface and drift of the banana turning point occurs along the  $B = \text{constant}$  surface. If we consider the case  $\Phi = \Phi(\psi)$ , the turning point of a banana particle drifts along a  $W = \text{constant}$  surface ( $\mu B(\psi, \theta) + e_a \Phi(\psi, \theta) = W$ ), where  $\theta$  is the poloidal angle. Usually, a  $B = \text{constant}$  surface does not match the flux surface  $\psi = \text{constant}$  and is typically a vertical line for the case of a tokamak, while it can be closed inside the closed magnetic surface if  $\Phi$  is strong enough so that the  $\vec{E} \times \vec{B}$  drift ( $v_E = E / B$ ) is much larger than the toroidal drift  $v_d$  ( $v_E \gg v_d$ ). The effect of electrostatic potential is particularly important for helical magnetic configurations for improving particle confinement, where Boozer coordinates are used to analyse particle dynamics [5.43].

It is also important to note that the longitudinal adiabatic invariant  $J = m_a \int v_{\parallel} dl$  (Eq. (5.19)) is conserved in most cases. The longitudinal adiabatic invariant  $J$  is an area of closed surface in  $(l, v_{\parallel})$  phase plane as shown in Fig. 5.19(a). Conservation of  $J$  implies that the precession motion of a banana is along the  $J = \text{constant}$  surface. When the toroidal field ripple exists, an equi-contour map of  $B$  has a local well as seen in Fig. 5.19(b). For such a case, the topological structure of a phase space  $(l, v_{\parallel})$  orbit changed from simple conformal ellipses to separated ellipses with separatrix and peanut-shape phase space orbit as seen in Fig. 5.19(b). We define  $J_s$  as the area of a local ripple well. It is obvious that  $J_s = 0$  means that there is no local ripple well close to the  $\alpha = 1$  boundary.

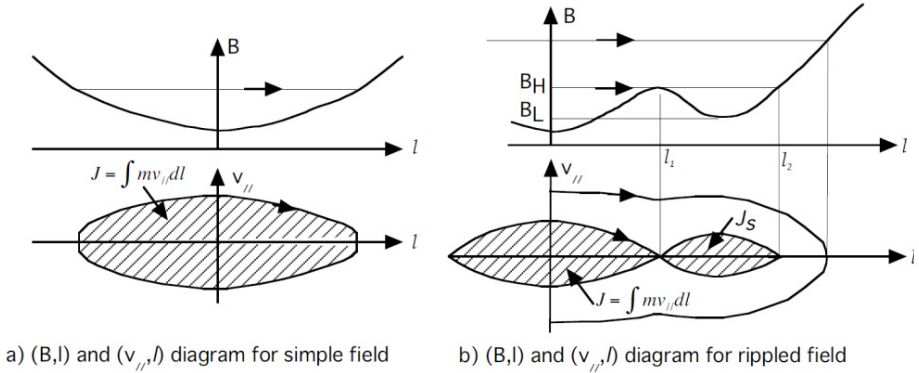


FIG. 5.19. Magnetic field strength  $B$  along particle orbit  $\vec{x}$  ( $l$ : orbit length along the magnetic field ( $dl = (\vec{B}/B) \cdot d\vec{x}$ ) and the geometrical meaning of longitudinal adiabatic invariant  $J$  in a tokamak without (a) and with (b) a rippled field. Here,  $J$  corresponds to the area inside the separatrix.  $B_H$  and  $B_L$  are the local maximum and minimum of the magnetic field, respectively. Also,  $l_1$  and  $l_2$  correspond to orbit length  $l$  where  $B = B_{tr}$

Spatial variation of ripple well depth produces interesting phenomena called “collisionless ripple-trapping” of banana particles as shown in Fig. 5.20a. Consider a banana particle and its motion near its turning point ( $v_{\parallel} \sim 0$ ). The remaining particle drift velocity is toroidal drift (and  $\vec{E} \times \vec{B}$  drift) velocity, which is in the  $Z$  direction in most cases. If the effective ripple well gets larger with  $z$ , a banana ion which barely passed the local ripple field is reflected at the turning point and undergoes toroidal drift in the  $z$  direction and feels a larger magnetic field ripple and may be reflected into the local magnetic mirror.

Figure 5.20b shows the poloidal cross-section of the tokamak and banana orbit. The thick blue line shows the  $\alpha = 1$  condition. When a banana ion is bouncing near the separatrix in Fig. 5.19b, it can be collisionlessly trapped into the local mirror if the effective well  $\delta_{eff} = B_H / B_L - 1$  is increasing in the direction of total drift  $(\vec{v}_d + \vec{v}_E) \cdot \nabla \delta_{eff} > 0$  where  $\delta_{eff}$  is given as a function of  $\alpha$  (Eqs (5.49), (5.51) and (5.52)) as follows [5.41, 5.44]:

$$\delta_{eff} = 2\delta \left[ \sqrt{1 - \alpha^2} - \alpha \left( \frac{\pi}{2} - \sin^{-1}(\alpha) \right) \right] \quad (5.55)$$

So collisionless ripple-trapping can occur in the shaded region 2 of Fig. 5.20b bounded by  $\alpha = 1$  and  $(\vec{v}_d + \vec{v}_E) \cdot \nabla \delta_{eff} = 0$ . As the particle moves along the banana orbit, it encounters a deeper magnetic well after turning from the banana tip and is trapped to the local magnetic well. These locally trapped particles drift vertically and are lost, which is called ripple trapped loss. Similar collisionless trapping occurs in the shaded area 1 but ripple trapped fast ions drift vertically to the top banana tip and can be detrapped to the banana orbit. Yushmanov gave a condition for this collisionless ripple-trapping by using the

longitudinal adiabatic invariant  $J_s$  as  $(\vec{v}_d + \vec{v}_E) \cdot \nabla J_s > 0$  [5.38]. The possible collisionless ripple-trapped region is bounded by  $J_s = 0$  and  $(\vec{v}_d + \vec{v}_E) \cdot \nabla J_s = 0$ .

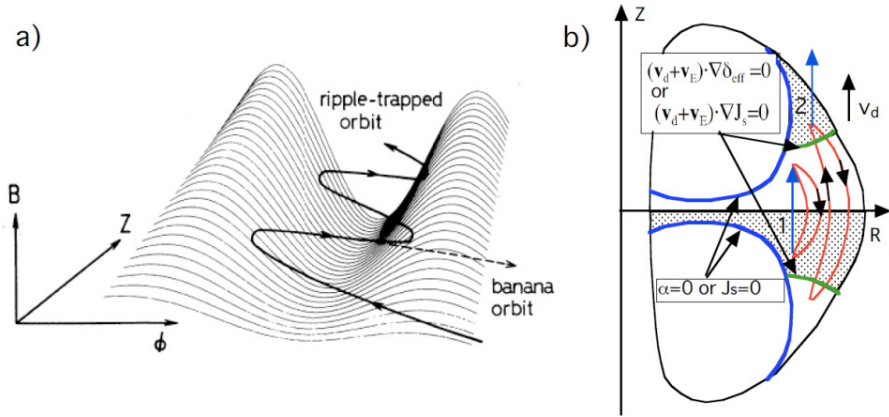


FIG. 5.20. a) Collisionless ripple trapping of banana particle in spatially varying ripple field [5.41]. b) Region of possible collisionless ripple trapping region and poloidal cross-section of typical banana orbits.

Even without trapping, a non-axisymmetric field can modify the banana orbit of fast ions through stochastic processes. The radial position of the banana tip is characterized by  $B = W / \mu$  and is always the same for the axisymmetric case. But the radial position of the banana tip changes with the ripple field. The radial displacement  $\delta_r$  is given by [5.38]

$$\begin{aligned} \delta_r &= \oint \frac{dr}{dt} dt = \oint v_d \sin \theta \frac{dl}{v_{\parallel}} = \\ &= v_d \sqrt{\frac{m}{2\mu}} \left[ \oint \frac{\sin \theta dl}{\sqrt{B(\theta_b) - \bar{B} - \tilde{B}}} - \oint \frac{\sin \theta dl}{\sqrt{B(\theta_b) - \bar{B}}} \right] \end{aligned} \quad (5.56)$$

where  $v_d$  is the toroidal drift velocity and  $\theta_b$  is the poloidal angle of the bounce point,  $\bar{B}$  and  $\tilde{B}$  are the axisymmetric and non-axisymmetric components of  $B$ , respectively. This displacement can be modelled as a radial kick at the banana tip, leading to a stochastic diffusion of fast banana ions [5.45]. This is the physical background of the banana drift loss described in the previous section.

### 5.1.12. Alpha heating

When the plasma reaches a high temperature by strong auxiliary heating, deuterium and tritium can fuse and energetic helium ( $Z = 2$ ,  $A = 4$ ) or an “alpha particle” with energy  $W_{\alpha 0} = 3.52$  MeV is produced. This “alpha” heating is called

“self-heating” since the plasma itself produces the “heating”. The power density of alpha heating  $P_\alpha$  is given by

$$P_\alpha = n_D n_T \langle \sigma v \rangle_{DT} W_\alpha \quad (5.57)$$

where  $\sigma$  is the fusion cross-section and  $\langle \sigma v \rangle$  is the fusion reaction rate averaged over the Maxwellian distribution. The D-T fusion reaction rate  $\langle \sigma v \rangle_{DT}$  is approximately given by [5.46]

$$\langle \sigma v \rangle_{DT} [\text{m}^3 \cdot \text{s}^{-1}] = \frac{3.7 \times 10^{-18}}{T_i^{2/3}} \exp\left(-\frac{20}{T_i^{1/3}}\right) \quad (5.58)$$

Here  $T_i$  is in keV. More accurate reaction rates within 1% for  $1 \text{ keV} < T_i < 100 \text{ keV}$  can be given as follows [5.47]:

$$\langle \sigma v \rangle_{DT} [\text{m}^3 \cdot \text{s}^{-1}] = \frac{3.7 \times 10^{-18}}{h(T_i) T_i^{2/3}} \exp\left(-\frac{20}{T_i^{1/3}}\right) \quad (5.59)$$

$$h(T_i) = \frac{T_i}{37} + \frac{5.45}{3 + T_i(1 + (T_i / 37.5)^{2.8})} \quad (5.60)$$

Combining Eq. (5.57) and Eq. (5.58),  $P_\alpha$  is given as follows:

$$P_\alpha [\text{MW} \cdot \text{m}^{-3}] = \frac{20383 n_D n_T}{h(T_i) T_i^{2/3}} \exp\left(-\frac{20}{T_i^{1/3}}\right) \quad (5.61)$$

where  $n_D$ ,  $n_T$  and  $T_i$  are in  $10^{20} \text{ m}^{-3}$  and in keV respectively.

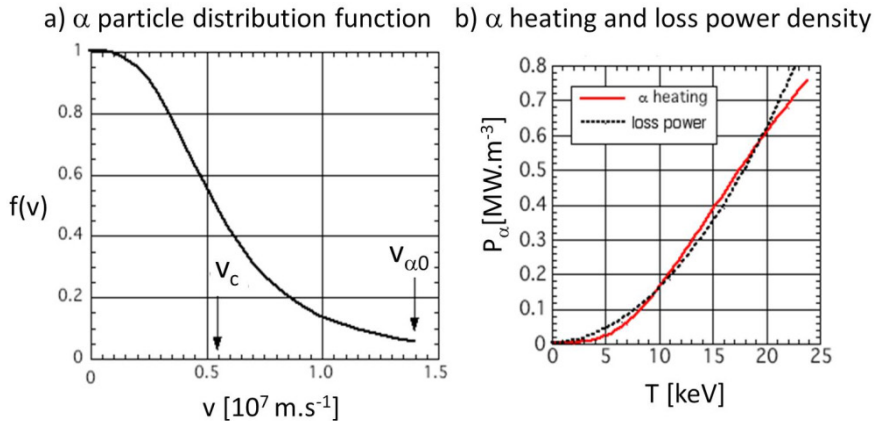


FIG. 5.21. a) Particle distribution function  $f(v)$  ( $T_e = 20 \text{ keV}$ ); b) Comparison of a heating power and loss power densities with  $T$  ( $\tau_E \sim 1/T$ ,  $P_\alpha = P_{\text{loss}}$  at  $10 \text{ keV}$ ). Here,  $v_c$  is the critical velocity defined for alpha particles and  $v_{\alpha 0}$  is the alpha birth velocity.

The steady state distribution functions of alpha particles  $f_\alpha(v) = f_\alpha(W)dW / 4\pi v^2 dv$  (with  $f_\alpha(W)$  defined by Eq. (5.11)) and density  $n_\alpha$  are

$$f_\alpha(v) = \frac{\tau_{se} S_\alpha}{4\pi(v^3 + v_c^3)} \quad (5.62)$$

$$n_\alpha = 4\pi \int_0^{v_\alpha} f_\alpha(v) v^2 dv = S_\alpha \tau_{th} \quad (5.63)$$

where  $S_\alpha = P_\alpha / W_{\alpha 0}$  is the alpha particle production rate,  $\tau_{se}$  is the alpha-electron slowing down time (Eq. (5.10)),  $\tau_{th}$  is the thermalization time and  $W_\alpha = m_\alpha v_\alpha^2 / 2$ ,  $W_c = m_\alpha v_c^2 / 2$  ( $W_c$  is given in Eq. (5.9)), respectively. Figure 5.21a shows the steady state velocity distribution  $f_\alpha(v)$  for a D-T plasma at  $T = 20$  keV. If the empirical energy confinement time  $\tau_E$  is proportional to  $1/T$ , the loss power  $P_{loss}$  is proportional to  $T^2$ . The alpha heating and loss powers are plotted as a function of plasma temperature for a D-T density of  $n_D = n_T = 0.5 \times 10^{20} \text{ m}^{-3}$  in Fig. 5.21b.

A rough parametric dependence of the alpha particle parameters can be given as particle production rate  $S_\alpha \sim n^2 T_i^2 S$ , particle thermalization time  $\tau_{th,\alpha} \sim T_e^{3/2} / n$ , local particle density  $n_\alpha = S_\alpha \tau_{th,\alpha} \sim n T_i^2 T_e^{3/2}$ , average particle during slowing down  $\langle W_\alpha \rangle \sim 1.3$  MeV (nearly independent of plasma parameters), and  $\beta_\alpha / \beta \sim T^{5/2}$ , where  $\beta_\alpha(0)$  is the central alpha pressure over the toroidal magnetic pressure  $B_\phi^2 / 2\mu_0$ . Typical values for ITER are  $P_\alpha \sim 0.3 \text{ MW} \cdot \text{m}^{-3}$ ,  $\tau_{th,\alpha} \sim 1 \text{ s}$ ,  $n_\alpha(0) / n_e(0) \sim 0.3\%$ ,  $\beta_\alpha(0) \sim 0.7\%$ , which were almost achieved in D-T experiments on TFTR and JET. Since the alpha particle velocity is much larger than the critical velocity, alpha particles interact mainly with electrons and the slowing down is dominant over pitch angle scattering. The particle distribution function was measured in TFTR as shown in Fig. 5.22 and was consistent with collisional transport theory [5.48, 5.49].

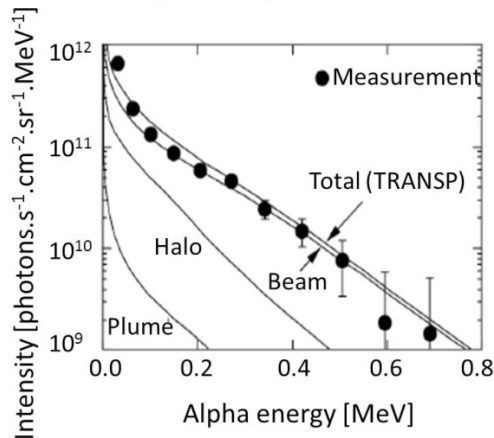
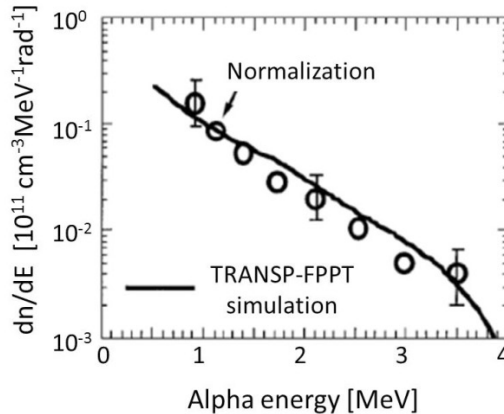
a)  $\alpha$ -CHERS diagnostics spectrum in DT dischargeb) Pellet CS  $\alpha$  measurement in DT discharge

FIG. 5.22. Measurements of alpha velocity distribution by  $\alpha$ -CHERS (top) and pellet CX (bottom) compared with calculations [5.48, 5.49]. Here three sources of alpha charge exchange are considered in alpha-CHERS. One is neutral beam-alpha particle charge exchange; the second is charge exchange with halo neutrals produced by beam-ion charge exchange; and the third is electron and ion impact excitation of  $\text{He}^+$  ions (called alpha plume). Partly reprinted from Ref. [5.48]. Copyright (2011) by the American Physical Society.

### 5.1.13. D-T experiments in large tokamaks (TFTR and JET)

Experimental demonstration of D-T fusion power production in a magnetically confined plasma was made in JET and TFTR. There are number of reviews on scientific achievements in D-T experiments [5.50–5.52]. The first experiments using T in a magnetically confined plasma were carried out in JET at a JET Joint Undertaking in 1991 as the Preliminary Tritium Experiment

(PTE), in which fusion power over 1.5 MW and fusion energy of 2 MJ were produced with a 10% tritium concentration [5.53]. TFTR at Princeton Plasma Physics Laboratory started D-T experiments in December 1993. Experimental observation of electron heating by fusion alpha particles was reported for the first time by TFTR [5.54] and systematically by JET [5.55] as shown in Fig. 5.23.

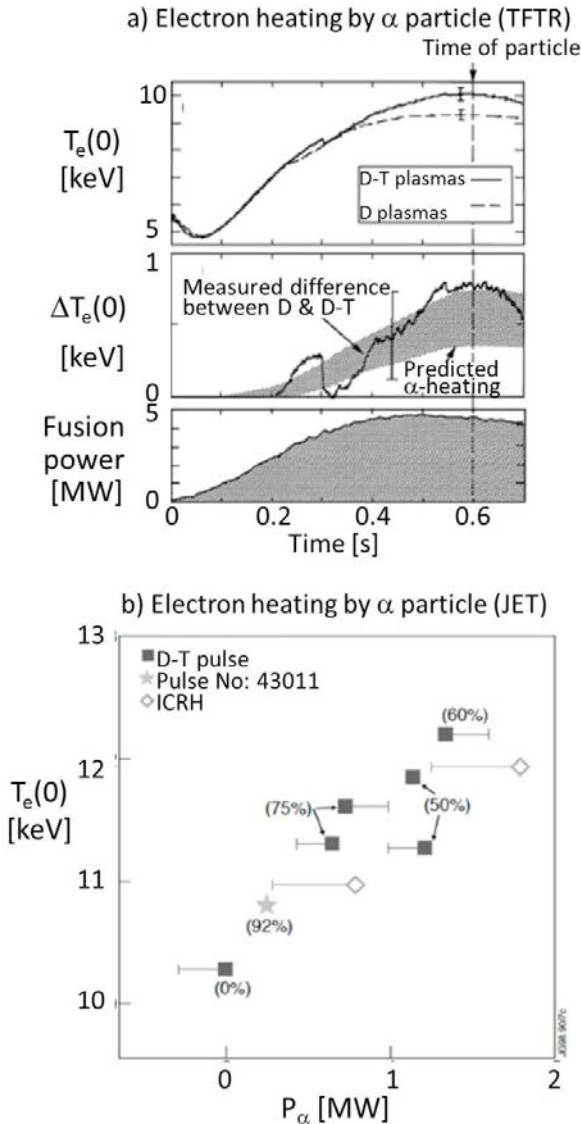


FIG. 5.23. Direct evidence of electron heating by alpha particles at TFTR (top) [5.54] (reprinted from Ref. [5.54]. Copyright (2011) by the American Physical Society) and JET (bottom) [5.55].

Significant fusion power production by the use of a D and T fuel mixture was demonstrated in TFTR ( $P_{fusion} = 10.7$  MW) in 1994 [5.56]. JET achieved the largest fusion power production of  $P_{fusion} = 16.1$  MW in 1997 [5.50] as shown in Fig. 5.24. This highest fusion power production was achieved with 25.4 MW of additional heating, and central ion and electron temperatures of 28 keV and 14 keV were recorded. The TFTR operation was completed in April 1997. There were a total of 300 D-T discharges. A total of  $\sim 5$  g of tritium was introduced into the TFTR vessel and a total energy of  $\sim 1.5$  GJ of fusion power was produced.

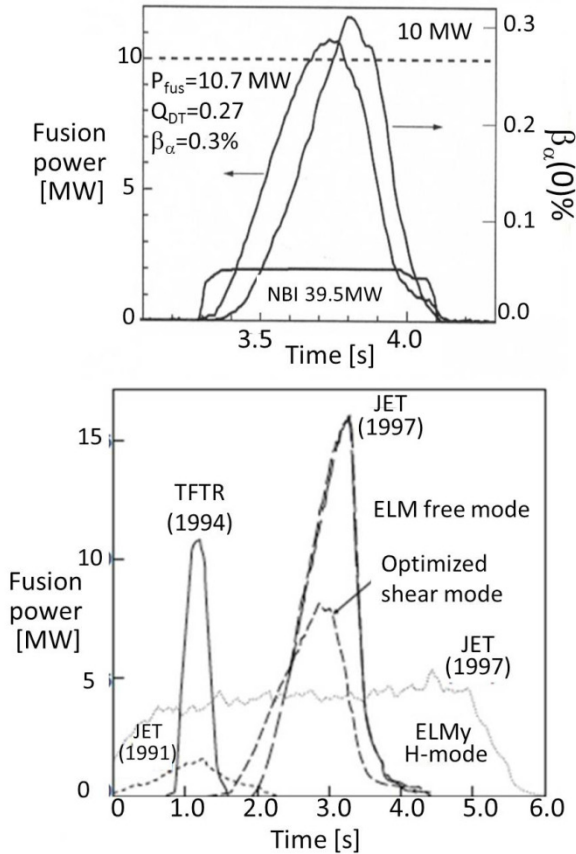


FIG. 5.24. Significant D-T fusion power production in TFTR [5.56] and JET [5.50].

## 5.2. NEUTRAL BEAM HEATING

**Y. Okumura**

Fusion Research and Development Directorate,  
Japan Atomic Energy Agency, Japan

### 5.2.1. Introduction

Neutral beam heating (NBH) is one of the most promising and best understood methods to heat a dense plasma and to drive plasma current in fusion machines. The concept of using energetic neutral beams for heating the plasma was proposed in the 1950s [5.57] and the first beam injection experiments were performed in mirror machines using PHOENIX [5.58], OGRA [5.59] and ALICE [5.60] in the 1960s. But the technology for producing neutral beams with enough power to significantly heat the plasma did not evolve until the 1970s [5.61, 5.62]. In the 1970s high current positive ion sources producing multi-ampere positive hydrogen ion beams were developed, which made it possible to carry out neutral beam heating experiments in a number of tokamak machines such as CLEO [5.63], ORMAK [5.64], ATC [5.65] and PLT [5.66]. High power neutral beam injection experiments have been also carried out in mirror machines such as 2X-IIB [5.67] and TMX [5.68], and in stellarators such as JIPP T-II [5.69] and Wendelstein VII-A [5.70]. In the 1980s multi-megawatt positive ion sources were developed for large tokamak machines such as TFTR [5.71], JET [5.72] and JT-60 [5.73] to inject several tens of MW neutral beams at beam energies of 80–120 keV.

In the 1990s a multi-ampere, multi-megawatt negative ion source was developed [5.74] and the construction of the first negative-ion-based neutral beam injector was carried out in JT-60 [5.75] followed by LHD [5.76, 5.77]. At present a negative ion source producing 40 A, 1 MeV deuterium negative ion beam is being developed to realize neutral beam injection in ITER [5.78, 5.79].

Figure 5.25 shows the schematics of the neutral beam injector (NBI). The heart of the NBI is the ion source, where hydrogen or deuterium ions are generated by a plasma generator and accelerated to a desired energy by an extractor/accelerator. The ion source is followed by a neutralizer cell in which a fraction of the accelerated ions is converted into energetic neutrals typically by a charge exchange process with collisions of the background gas. It is necessary to convert the ions into neutrals to inject the neutral beams into the magnetically confined plasma. The energetic neutral beam goes straight towards the plasma through a drift duct which connects the injection port of the plasma device. The un-neutralized ions are removed from the neutral beam and guided to ion beam dumps by a bending magnet. High speed vacuum pumps such as a cryosorption

pump with pumping speeds approaching  $1000 \text{ m}^3\cdot\text{s}^{-1}$  are generally employed to exhaust the residual neutral gas. A complex electrical system that repetitively switches high voltage electrical power is employed to accelerate the ions.

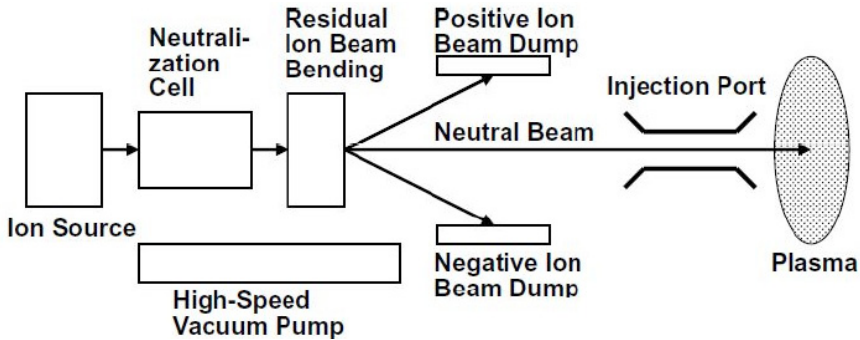


FIG. 5.25. Schematic of a neutral beam injector.

Figure 5.26 shows the NBI system for LHD [5.76, 5.77] as an example of the real NBI. The LHD-NBI has a negative ion source producing energetic negative hydrogen ion beams which are converted to neutral beams during passage through a gas neutralizer. The neutral beam power and its profile are measured by a movable calorimeter located downstream of the ion beam dumps. During the beam injection, the calorimeter is removed from the beam axis.

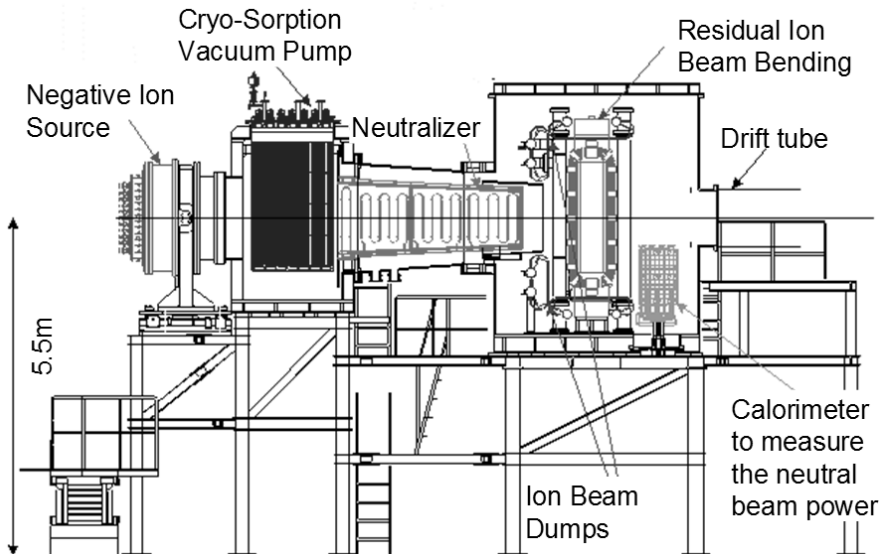


FIG. 5.26. Cross-sectional view of negative ion based NBI for LHD [5.76].

The overall power efficiency of NBI is mainly determined by the neutralization efficiency in the neutralizer. Figure 5.27 shows the neutralization efficiency as a function of the beam energy for the gas neutralizer (solid line), where the positive ions are neutralized by the charge exchange process in the gas neutralizer. The efficiency decreases rapidly as the beam energy increases. The efficiency is only 20% at a beam energy of 100 keV for hydrogen positive ion beams and decreases to almost zero at energies higher than 500 keV. Higher beam energies are preferable for denser and bigger plasmas, but positive ion based NBI cannot be used because of the low power efficiency above energies of 100 keV per nucleon. To overcome this difficulty, negative ion beams have to be used, whose neutralization efficiency is 60% even at energies higher than 100 keV per nucleon.

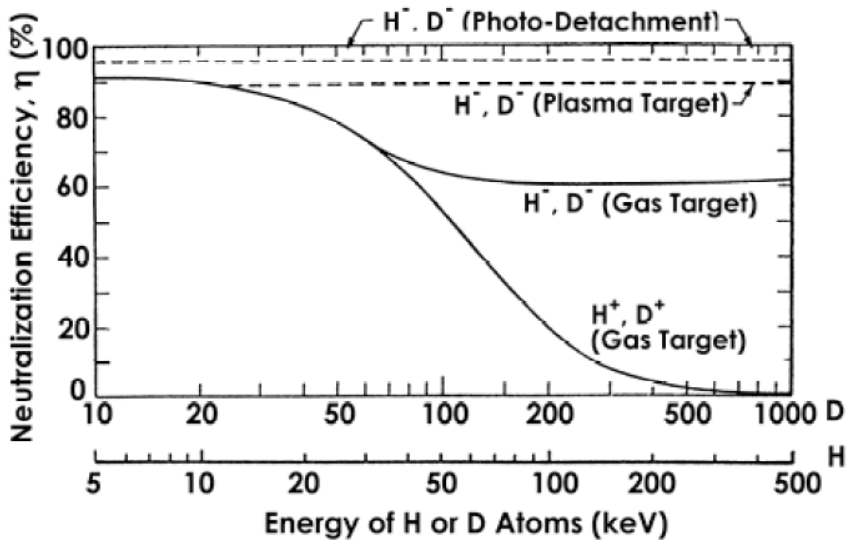


FIG. 5.27. Neutralization efficiency of positive and negative ions as a function of energy [5.80].

Table 5.3 summarizes typical NBI systems using positive ion sources (positive ion based NBI) and negative ion sources (negative ion based NBI). Positive ion based NBIs have been used for TFTR [5.71], JET [5.72] and JT-60 [5.73] at beam energies lower than 100 keV per nucleon. Above this energy negative ion based NBIs have been developed for JT-60U [5.75], LHD [5.76, 5.77] and ITER [5.78, 5.79].

	Positive-ion-based NBI			Negative-ion-based NBI		
	TFTR	JET	JT-60	JT-60U	LHD	ITER
Beam Energy [keV]	120	125	100	500	180	1000
Injection Power [MW]	27	24	20	10	15	33
Pulse Length [s]	0.5	10	10	10	10	3600
Number of Ion Sources	12	16	28	2	4	2
Ion Species	D <sup>+</sup>	D <sup>+</sup>	H <sup>+</sup>	D <sup>-</sup>	H <sup>-</sup>	D <sup>-</sup>
Ion Source Output	120kV/ 65A	125kV/ 60A	100kV/ 40A	500kV/ 22A	180kV/ 30A	1000kV/ 40A

Figure 5.28 shows the history of the development of high current positive and negative ion sources. High current positive ion sources were developed in the 1960s to 1980s; then high current negative ion sources were developed beginning in the late 1980s.

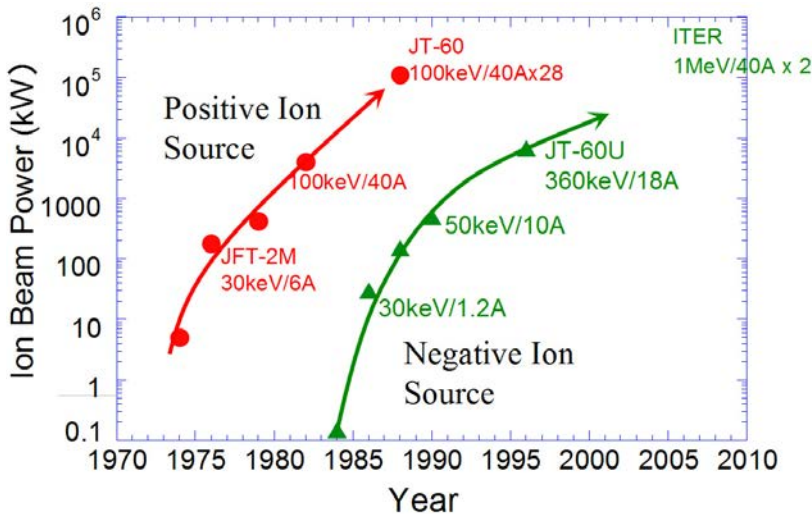


FIG. 5.28. History of the development of high current positive and negative ion sources.

In this chapter, the basic principles and technologies of positive and negative ion sources are reviewed and the typical positive and negative ion based NBIs are introduced.

### 5.2.2. Ion source

#### 5.2.2.1. Plasma generator

The ion source for NBI is required to produce a high power ion beam of more than several MW or several tens of MW. To produce such a high power ion beam with high beam quality at electrical efficiency, the plasma generator has to generate a dense, uniform, quiescent source plasma efficiently over a wide area at a low operating gas pressure. For the NBI experiments in the 1970s, various types of plasma generator were developed; they are the Duo-PIGatron developed in ORNL [5.81–5.83], a field-free source developed in LBL [5.84], and the Peri-plasmatron developed in Fontenay-aux-Roses [5.85, 5.86]. Figures 5.29–5.31 show schematics of these sources. It was difficult to keep a good uniformity of the source plasma both in the Duo-PIGatron and the Peri-plasmatron because of the existence of the longitudinal magnetic field for the plasma confinement. Although the field-free source could generate a uniform plasma over a wide area, the gas and the electrical efficiency were very bad since there was no magnetic plasma confinement. To overcome these difficulties, a new plasma generator called the “multicusp source” or “bucket source” had been developed [5.87, 5.88]. It utilizes a magnetic multicusp field for plasma confinement and there is a wide field-free region inside the multicusp field and thus a uniform plasma can be generated with high gas and electrical efficiencies. Almost all the existing NBIs are using the multicusp plasma generator.

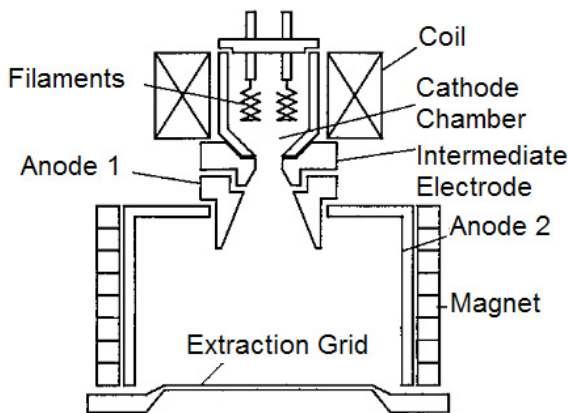


FIG. 5.29. Schematics of Duo-PIGatron source.

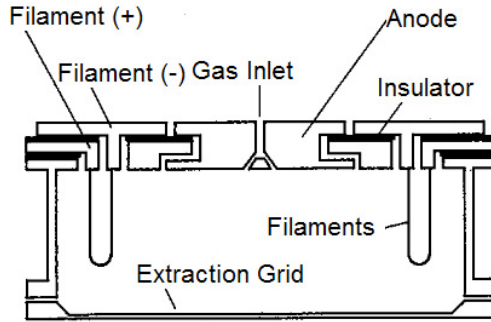


FIG. 5.30. Schematics of field-free source.

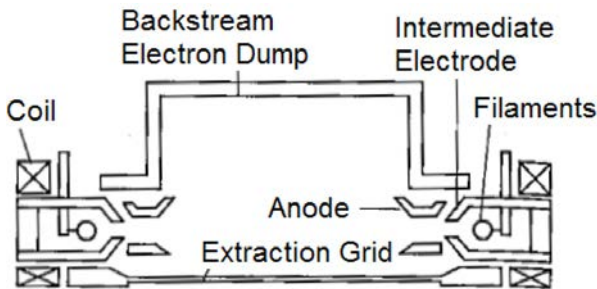


FIG. 5.31. Schematics of Peri-plasmatron.

5.2.2.2. Multicusp source

Figure 5.32 shows schematics of the multicusp plasma generator. All the walls except for an ion extractor are covered by permanent magnets forming the multicusp magnetic field. It is also called “bucket source”, since the source plasma is confined just like water inside a bucket.

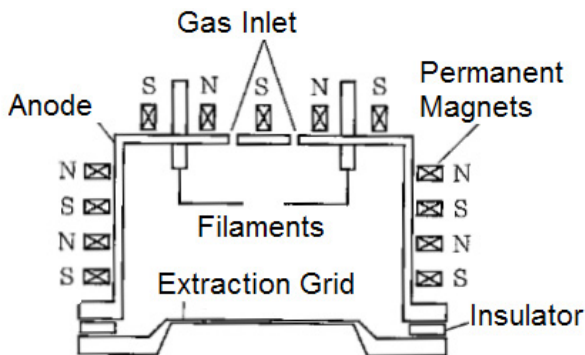


FIG. 5.32. Schematics of multicusp source or “bucket source”.

Figure 5.33 shows a typical magnetic configuration of a bucket source. The line cusp configuration parallel to the beam axis shown in Fig. 5.33(a) is normally used for cylindrical plasma generators. The line cusp configuration perpendicular to the beam axis shown in Fig. 5.33(b) is normally used for rectangular plasma generators. There is another multicusp configuration called the “checkerboard” configuration, where the neighbouring permanent magnets have opposite polarity forming a point cusp or very short line cusp configuration.

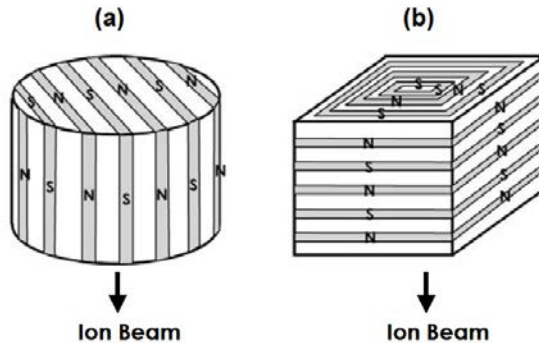


FIG. 5.33. Typical magnetic configuration of a “bucket source”.

Most of the existing multicusp plasma generators utilize a high current arc discharge to produce the source plasma. Cathodes such as tungsten filaments are installed in the field-free region and the wall acts as an anode. Energetic electrons emitted from the cathode having energies corresponding to the cathode sheath potential ionize the gas and are thermalized or lost to the loss cone of the multicusp field. Modelling of the plasma production has been studied in Refs [5.87, 5.89]. According to the modelling, a higher magnetic field is preferable to minimize the effective loss area (or effective anode area) at the wall and to enhance the electrical and gas efficiencies. Operating gas pressure is a function of the ratio of the total loss area to the plasma volume. Large volume plasma generators with minimized loss area can be operated at a very low operating gas pressure, which is preferable especially in a negative ion source to minimize the loss of the negative ions with the collision of the gas particles. The proton yield in the hydrogen ion source is also a function of the ratio of the total loss area to the plasma volume [5.90].

The magnetic field at the surface of the wall reaches 0.1–0.2 T to minimize the loss area and improve the efficiencies. However, it should be noted that there is a minimum value for the effective anode area to maintain an efficient arc discharge. When the effective anode area is smaller than this value, the sheath potential at the anode is converted to the opposite and the plasma potential becomes much lower than the anode voltage. Figure 5.34 shows the distribution of the plasma potential for both the normal discharge mode and the low efficiency

mode. In the low efficiency mode, the electrons emitted from the cathode have lower energy than the normal discharge mode, which decreases the efficiency of ionization. The arc impedance becomes very high and it is difficult to make a high current discharge. Therefore, the low efficiency mode is also called the “high impedance mode”. An electron trajectory calculation is effective in increasing the effective anode loss area and avoiding the high impedance mode.

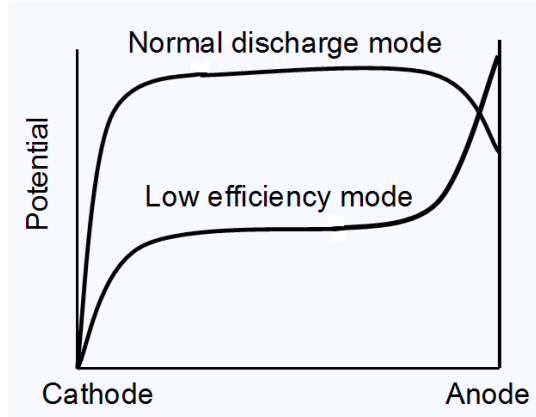


FIG. 5.34. Plasma potential profile for typical discharge mode.

### 5.2.2.3. Radiofrequency plasma source

Since the cathode is immersed in the dense plasma in a bucket source, it is easily damaged by ion backscattering. Because of the scattering and the evaporation of the cathode material, the cathode has a finite lifetime. It is about 100 to 300 hours for pure tungsten filaments, depending on the diameter of the filaments and the electron emission density. Tungsten filaments have to be replaced periodically in most of the ion sources for NBIs and the lifetime of the cathode material determines the maintenance frequency of the NBIs. Long life cathodes such as a hollow cathode or an indirectly heated cathode have been developed to decrease the maintenance frequency, but the cathode loss area increases in this cathode and decreases the gas and electrical efficiencies.

A radiofrequency (RF) plasma source has no filament and has a long life. An RF source has been developed in LBL and IPP Garching. Figure 5.35 shows a typical RF source developed for the AUG machine [5.91]. The plasma chamber is composed of a quartz vessel and back plate, where the line cusp magnet is arranged for plasma confinement. The quartz vessel is surrounded by an RF coil antenna, and RF power is coupled to produce a dense plasma for positive ion extraction.

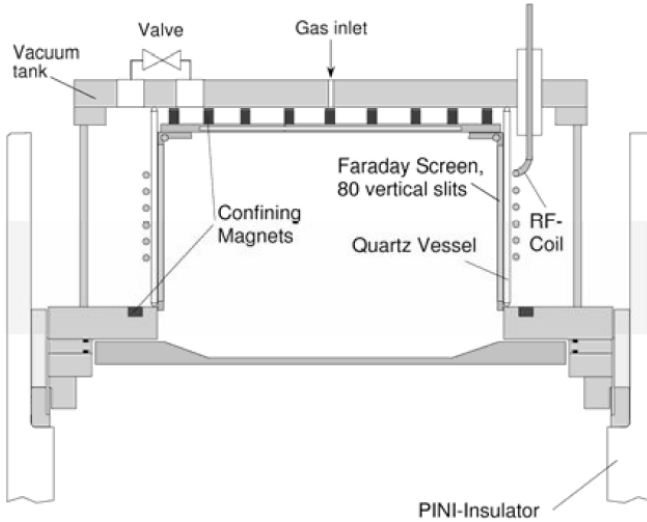


FIG. 5.35. A cross-sectional view of an RF driven source [5.91]. Reprinted from Ref. [5.91]. Copyright (2011), with permission from Elsevier.

An RF plasma source has been successfully developed at IPP Garching and applied to the negative ion source. It has been demonstrated that the RF plasma source has the capability to produce dense negative ions required for the NBI for ITER [5.92, 5.93].

### 5.2.3. Extraction and acceleration

#### 5.2.3.1. Child–Langmuir Law

Ions produced by the plasma generator are extracted and accelerated electrostatically. Extractable ion current density is determined by the electrical potential applied to the electrodes and the space charge of the ions between the electrodes. When the extraction voltage  $V_{ext}$  is applied between the two electrodes as shown in Fig. 5.36, Poisson’s equation is given by

$$\nabla^2 \phi = -\frac{\rho}{\epsilon_0} \quad (5.64)$$

where  $\epsilon_0$  is the dielectric constant, and  $\rho$  is the space charge of ions given by  $\rho = j_i / v_i$ . In this equation,  $j_i$  is the ion current density and  $v_i$  is the velocity of the ions.

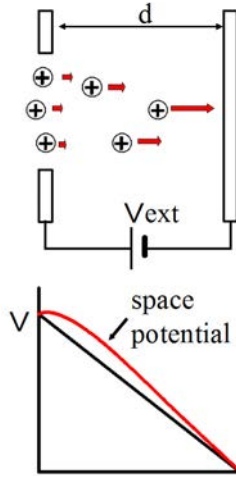


FIG. 5.36. Schematics of ion extraction by two electrodes.

By solving this equation, a basic equation called the Child–Langmuir Law is given as

$$j_i = \frac{4}{9} \epsilon_0 \left( \frac{2Ze}{M} \right)^{1/2} \frac{V_{ext}^{3/2}}{d^2} \quad (5.65)$$

where  $V_{ext}$  is the extraction voltage applied to the electrodes,  $d$  is the distance between the electrodes,  $Z$  is the ion charge number and  $M$  is the ion mass number. It should be noted that the ion current density  $j_i$  increases as a function of the extraction voltage as  $\sim V_{ext}^{3/2}$ .

Then the ion current extracted from a circular aperture of radius  $a$  is given by

$$I_i = \pi a^2 j_i = \frac{\pi \epsilon_0}{9} \left( \frac{2Ze}{M} \right)^{1/2} \left( \frac{2a}{d} \right)^2 V_{ext}^{3/2} \quad (5.66)$$

Equation (5.66) can be written as  $I_i = P V_{ext}^{-3/2}$ , where the coefficient  $P$  is called the “perveance” of the extraction system. Since the aspect ratio ( $2a/d$ ) of the apertures is chosen to be less than unity to keep a stable extraction surface and to optimize beam optics, the coefficient  $P$  (perveance) becomes almost constant for a circular aperture. For example, the maximum current extracted from a circular aperture is calculated to be around 0.5 A at 50 kV of extraction voltage.

In order to produce multi-ampere ion beams, the ion source for NBI utilizes multiple extraction apertures distributed over a wide extraction area. Since the optimum extraction current giving good beam optics is about 60% of the maximum current obtained from Eq. (5.66), it is necessary to distribute the multi-apertures over a rectangular area of 20 cm  $\times$  20 cm with a transparency of 50% to produce 60 A ion beams at 50 kV.

A rectangular extraction grid is normally employed in high current, long pulse ion sources for NBIs. This is because the cooling channels installed between the rows of apertures have the same length in the rectangular extraction grid, whereas the lengths are different in a circular extraction grid, which causes imbalanced cooling resulting in a burnout of the cooling channel at a high heat loading.

5.2.3.2. Multi-stage acceleration

The ion sources for NBIs use a simple accel-decel grid system or a single stage acceleration system for low acceleration energies (e.g. less than 50 kV). As the required energy increases, with single-stage acceleration it becomes difficult to produce high power density beams due to electrical breakdown problems among the extraction grids. For higher energy acceleration, a multi-stage acceleration system has been used. Compared with the single-stage acceleration system, a multi-stage system has additional grids called “gradient grids” or “intermediate grids”, which reduce the breakdown problems and provide the capability of electrostatic focusing. As for the heat loading, a multi-stage system has the merit of reducing the heat loading by dividing it between the stages.

Figure 5.37 shows an example of a two-stage acceleration system employed in the positive ion source for JT-60 [5.94]. It consists of four grids, called plasma, gradient, suppressor and exit grids. A negative bias voltage is applied in the suppressor grid to prevent the electrons produced in the downstream beam plasma from back-streaming to the plasma generator.

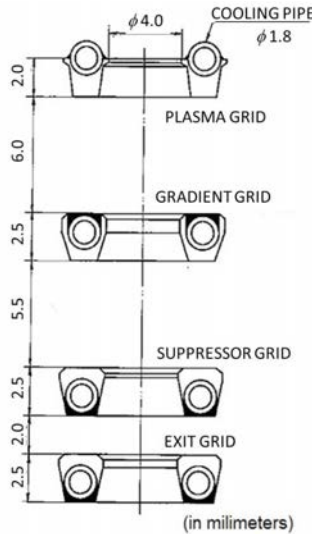


FIG. 5.37. Cross-sectional view of an aperture in two-stage acceleration system [5.94]. Reprinted from Ref. [5.94]. Copyright (2011), American Institute of Physics.

Figure 5.38 shows the various reactions causing the heat load to the grids in the two-stage acceleration system [5.95]. Roughly speaking, 1–2% of the power of the ion beam is deposited on each grid. Since the power density of the ion beam is typically  $10\text{--}20\text{ kW}\cdot\text{cm}^{-2}$ , it corresponds to a heat load of  $100\text{--}400\text{ W}\cdot\text{cm}^{-2}$  at the grid surface. Since the diameter of the cooling channel is limited in the acceleration grid, it is not easy to remove these levels of heat load. A lower operating gas pressure is preferable to reduce the collisions between the ion beam and the residual gas particles and to reduce the heat load in high power ion sources for NBIs.

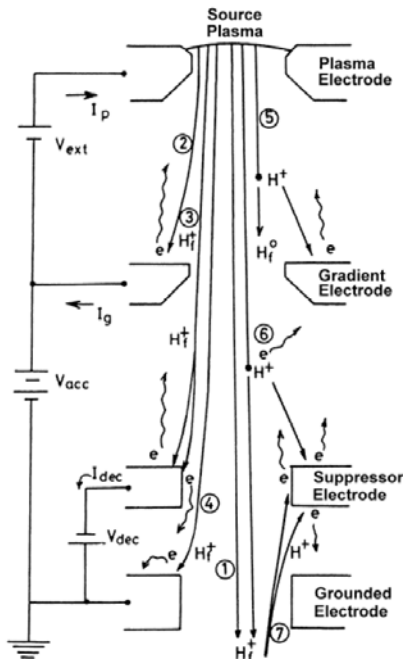


FIG. 5.38. Reactions causing heat loading to the grids in a two-stage acceleration system [5.95]. They are classified into three groups: direct interception of ions being accelerated (corresponding to 2, 3, 4), production of secondary particles in the grid gaps by beam-gas interactions (5, 6), and ions accelerated to the suppressor grid from the downstream beam plasma (7). Here  $V_{acc}$  is the acceleration voltage applied to the gradient electrode,  $I_g$  is the current flowing into the gradient electrode,  $V_{dec}$  is the negative bias voltage applied to the suppressor electrode,  $I_{dec}$  is the current flowing into the suppressor electrode and  $H_f^+$  means the fast ions extracted from the source plasma.

### 5.2.3.3. Beamlet steering

The ion beams extracted from multi-aperture grids consist of many small ion beams called “beamlets” extracted from each aperture. With a scale-up of the

extraction area, programmed steering of each beamlet towards the injection port is an attractive means to achieve high injection efficiency. There are two methods to steer the beamlet. One is a mechanical method using a curved grid and the other one is an electrostatic method using aperture displacement.

In aperture displacement, the steering angle  $q$  is given by

$$q[\text{rad}] = \delta / F \tag{5.67}$$

where  $\delta$  is the displacement distance with respect to the axis of the beamlet, and  $F$  is the focal distance of the electrostatic lens expressed by  $F = 4W_b / (E_1 - E_2)$  for a circular aperture and  $F = 2W_b / (E_1 - E_2)$  for a slot aperture, where  $W_b$  is the beam energy, and  $E_1$  and  $E_2$  are the electric field strengths in the upstream and in the downstream of the grid, respectively.

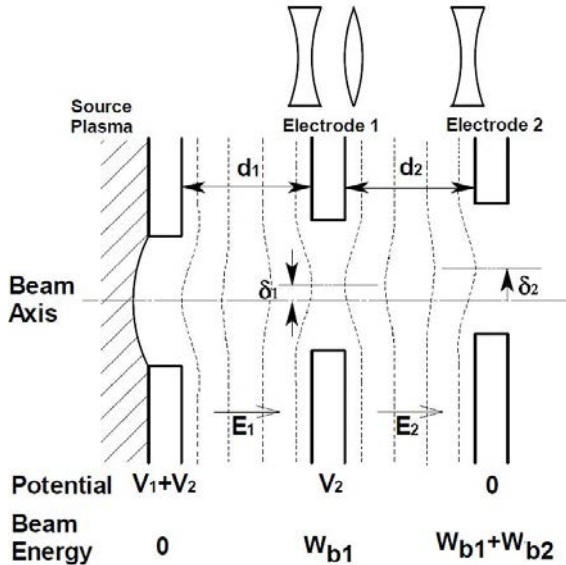


FIG. 5.39. Beamlet steering by aperture displacement.

The steering angle in a two-stage accelerator has been investigated theoretically [5.96, 5.97] and experimentally [5.98]. Considering a general case, where the gradient grid is displaced by distance  $d_1$  and the suppressor grid by a distance  $d_2$  with respect to the plasma grid as shown in Fig. 5.39, the steering angle  $q$  is expressed by

$$q = \frac{\delta_1}{F_1} + \frac{\delta_2}{F_2} - \frac{\delta_1 d_2}{F_1 F_2} \tag{5.68}$$

where  $F_1$  and  $F_2$  are the focal lengths of the lens for the gradient and suppressor grids, expressed by  $F_1 = 4W_{b1} / (E_2 - E_1)$  and  $F_2 = 4(W_{b1} + W_{b2} + W_{b3}) / (E_3 - E_2)$ ,

respectively. Here,  $eW_{b1}$  and  $e(W_{b1}+W_{b2}+W_{b3})$  are the energies of the ion beams that pass through the grids, and  $E_1$ ,  $E_2$  and  $E_3$  are the electric field intensities in the extraction, acceleration and deceleration gaps, expressed by  $E_1 = W_{b1}/d_1$ ,  $E_2 = (W_{b2}+W_{b3})/d_2$  and  $E_3 = W_{b3}/d_3$ , respectively.

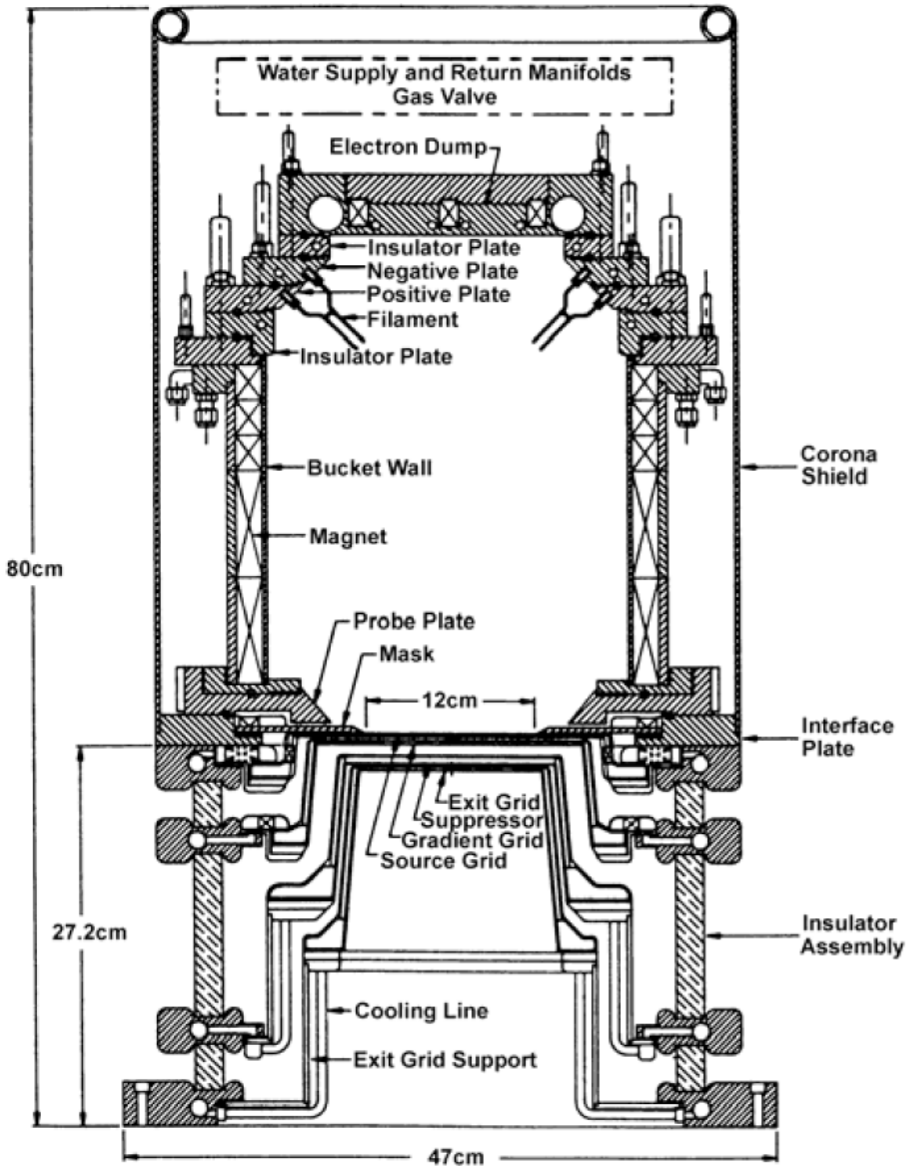
The effect of axial acceleration in the acceleration gap on the deflection angle should be considered [5.98]. Use of this effect in Eq. (6.68) yields

$$q = \left( \frac{W_{b1}}{W_{b1} + W_{b2} + W_{b3}} \right)^{1/2} \frac{\delta_1}{F_1} + \frac{\delta_2}{F_2} - \frac{2\{W_{b1}(W_{b1} + W_{b2} + W_{b3})\}^{1/2} - 2W_{b1}}{W_{b2} + W_{b3}} \left( \frac{\delta_1 \delta_2}{F_1 F_2} \right) \quad (5.69)$$

#### 5.2.4. Positive-ion-based NBI

Large positive ion sources were developed energetically in the 1970s and 1980s and used for high power neutral beam injection experiments in large fusion machines such as TFTR, JET and JT-60. In these ion sources, multicusp sources are used as the plasma generator and two-stage acceleration systems composed of four grids are used to extract and accelerate the positive ions up to 80–120 keV. The grids are actively water cooled and have multi-apertures within the rectangular extraction area to extract high current ion beams of several tens of amperes.

Figure 5.40 shows the positive ion source used for the TFTR and DIII-D [5.71]. The multicusp plasma generator has dimensions of 24 cm × 57 cm in width and 30 cm in depth. A deuterium positive ion beam of 73 A is accelerated up to 120 keV with a current density of 230 mA·cm<sup>-2</sup> using the two-stage accelerator. The arc efficiency is 0.6–0.7 A·kW<sup>-1</sup> and the proton yield is 80–85%. The grids have multi-slots within the area of 12 cm × 43 cm. The multi-slot grid has a higher transparency compared to the circular aperture grid. The transparency reaches 60%. Although the beam divergence perpendicular to the slot is 7 mrad, the divergence along the slot is 12 mrad. This is because the electrostatic focusing is weak along the direction parallel to the slot.



XBL 8511-4649

FIG. 5.40. Positive ion source developed for TFTR and DIII-D [5.71].

Figure 5.41 shows the positive ion source used for JET [5.72]. The multicusp plasma generator has a race-track shape with checkerboard configuration of the multicusp. A hydrogen positive ion beam of 60 A is accelerated up to 80 keV with a current density of  $200 \text{ mA} \cdot \text{cm}^{-2}$ . The two-stage acceleration system has

multiple circular apertures within the extraction area of  $45\text{ cm} \times 18\text{ cm}$ . An arc efficiency of  $0.34\text{ A}\cdot\text{kW}^{-1}$  is obtained at a low operation gas pressure of  $0.4\text{ Pa}$ .

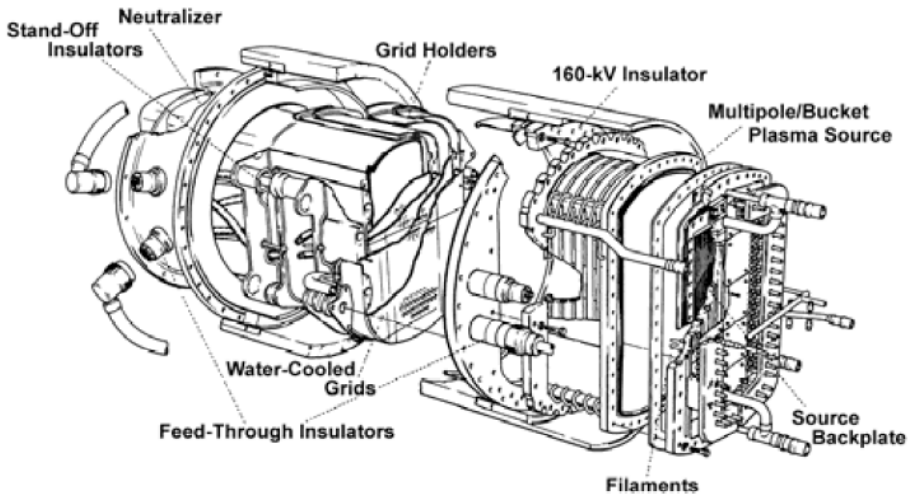


FIG. 5.41. Positive ion source developed for JET [5.72].

Figure 5.42 shows the positive ion source used for JT-60 [5.90]. The dimensions of the multicusp plasma generator are  $25\text{ cm} \times 40\text{ cm}$  width and  $34\text{ cm}$  in depth. By using strong magnetic configuration, the strength of the magnetic field at the inner surface of the chamber wall reaches  $0.27\text{ T}$ , which enables a high arc efficiency of  $0.7\text{ A}\cdot\text{kW}^{-1}$  and a high proton yield of  $90\%$  to be obtained [5.90]. The two-stage acceleration system has multiple circular apertures within the extraction area of  $12\text{ cm} \times 27\text{ cm}$ . A hydrogen positive ion beam of  $40\text{ A}$  is accelerated up to  $100\text{ keV}$  with a current density of  $270\text{ mA}\cdot\text{cm}^{-2}$ .

The injector unit of the positive-ion-based NBI for JT-60 consists of 14 injector units to deliver neutral beams up to  $20\text{ MW}$  at  $100\text{ keV}$ . Each injector is equipped with two positive ion sources, each producing  $4\text{ MW}$  hydrogen ion beams at  $100\text{ keV}$ . More than  $100\text{ MW}$  ion beams are produced by using 28 ion sources. The neutral beam power injected into the JT-60 plasma was only  $20\text{ MW}$ , because the neutralization efficiency is only  $20\%$  at  $100\text{ keV}$ . More than  $80\%$  of the ion beams are dumped in the beam dump in vain.

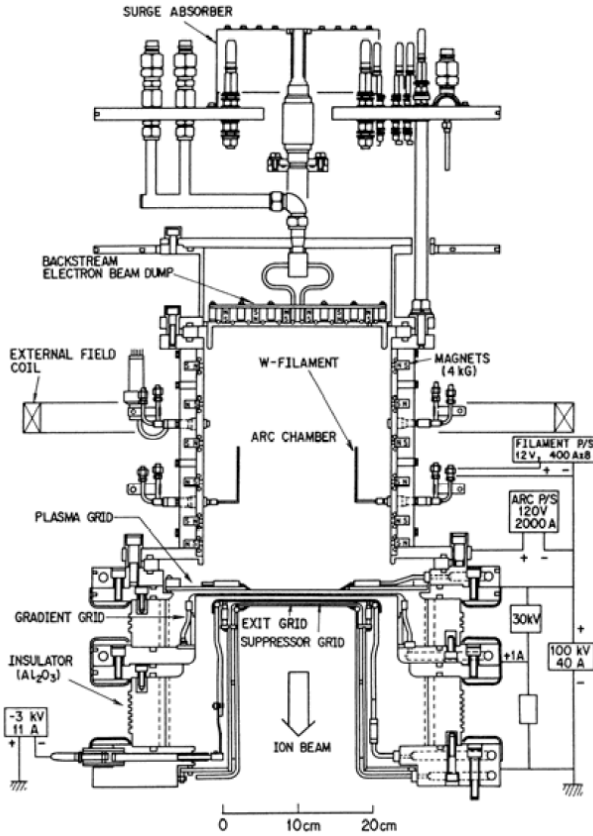


FIG. 5.42. Positive ion source developed for JT-60 [5.90].

### 5.2.5. Negative ion source

In order to achieve acceptable neutralization efficiency at beam energies in excess of 100 keV per nucleon, negative ions have to be used instead of positive ions. The development of negative ion sources for NBI also started in the 1970s in parallel with the development of the positive ion source. Negative ion sources have been used for high energy physics applications in tandem accelerators or as injectors for the cyclotron and synchrotron, but the beam current was of the order of milliamperes. For NBI application, multi-ampere negative ion beams are required. Development of high current negative ion sources with a reasonable current density and with good beam optics is essential to realize the NBI system for reactor grade machines. The beam energy of the negative-ion-based NBI is one order higher than the positive-ion-based NBI and the neutralization efficiency for negative ions is 60%, which is 2–3 times higher than the positive

ions at the energies used for TFTR, JET and JT-60. Therefore, the current density required for the negative ions becomes  $15\text{--}20\text{ mA}\cdot\text{cm}^{-2}$ , which is the target value of negative ion source development.

### 5.2.5.1. Negative ion production

There are three methods which have the possibility to produce multi-ampere negative ion beams required for NBI. Figure 5.43 shows the schematics of the principles of these three methods. They are:

- (1) Double charge exchange (DCX) (top);
- (2) Surface production (SP) (middle);
- (3) Volume production (VP) (bottom).

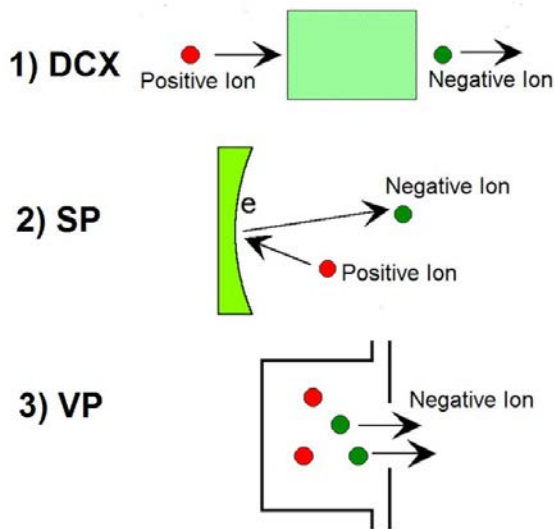


FIG. 5.43. Schematics of the principles of three methods to produce negative ions.

The double charge exchange method had been developed at the initial phase of development. In this method, a positive ion beam is converted into a negative ion beam by passage through an alkali metal vapour cell, where the positive ions get two electrons by a double charge exchange process. Although the principle is simple and it is easy to obtain ampere-class negative ion beams, it is difficult to handle a large amount of alkali metals. The system becomes too complicated to be used in a real NBI. In addition, beam quality is bad because of the divergence of the primary positive ions. It is reported that a 2.2 A, 10 keV hydrogen negative ion beam was obtained at LBL [5.99] and a 5.5 A, 80 keV negative ion beam for a short pulse length of 10 ms at  $26\text{ mA}\cdot\text{cm}^{-2}$  at the Kurchatov laboratory [5.100].

A negative helium ion source using the double charge exchange method is being developed for the diagnostic beam for ITER.

In the surface production method, a converter whose surface has a low work function is installed in a plasma generator. By biasing the converter negatively (100–200 V) with respect to the plasma potential, positive ions produced in the plasma generator are injected into the surface then converted to negative ions and reflected to the extractor. The work function of the converter surface is kept low by coating the surface with caesium vapour injection. Production of 1.1 A, 80 keV negative ion beams was successfully demonstrated with a long pulse length in LBL [5.101]. However, the negative ions have transverse energy at the reflection, resulting in large beam divergence in the accelerated ion beam. Other difficulties are stable control of the work function at the converter surface and the caesium flow in the downstream resulting in degradation of voltage holding in the accelerator.

In late 1970s it was found that there can be a copious amount of negative hydrogen ions in a hydrogen plasma. It was found that the negative ion density reaches more than 30% of the positive ion density by selecting the arc discharge condition and operating pressure [5.102, 5.103]. The negative ion ratio was two orders of magnitude higher than the density predicted by the negative ion production process known at that time. To explain the high density observed in the experiments, many hypotheses were proposed [5.104–5.106]. It is believed that the hydrogen negative ions are produced mainly by dissociative attachment of the vibrationally excited hydrogen molecules during collisions with low energy electrons as  $H_2(v)+e_{\text{slow}} (>1 \text{ eV}) \rightarrow H_2^- \rightarrow H^- + H^0$ , where  $e_{\text{slow}}$  corresponds to the low energy electrons produced in the plasma. The vibrationally excited hydrogen molecules, indicated by  $H_2(v)$ , are produced by the reactions listed in Table 5.4.

TABLE 5.4. REACTIONS PRODUCING VIBRATIONALLY EXCITED HYDROGEN MOLECULES

$H_2 + e_{\text{fast}} (>40\text{eV}) \rightarrow H_2 \rightarrow H_2^*(v) + h\nu$
$H_2^+ + H_3^+ \rightarrow \text{wall} \rightarrow H_2(v) + H^0$
$H_3^+ + e \rightarrow H_2(v) + H^0$
$H_2(v) + e \rightarrow H_2(v+1) + e$

The negative ions produced in the hydrogen plasma can be extracted as in the positive ion source, namely by reversing the extraction/acceleration voltage. Since the negative ions are produced in the plasma volume, this method is called volume production.

### 5.2.5.2. Advantages of volume production

The volume production method has big advantages over the other two methods. They are:

- (1) No use of caesium;
- (2) Simple structure of the source;
- (3) Low beam divergence;
- (4) Low impurity content;
- (5) Stable and reliable operation.

Another advantage is that the technologies developed for the positive ion source could be used for a volume production source. These advantages make the volume production method the most attractive one for use in negative-ion-based NBI.

However, two problems must be solved in this method. One is the problem of electron separation. Since the negative ions produced have no more than thermal energies (<1 eV), it is difficult to separate the negative ions from the plasma electrons. Another problem is the current density. The negative ion ratio decreases very rapidly as the arc discharge or the plasma density increases, because of the loss of negative ions with energetic electrons. The loss mechanisms of the negative ions are as listed in Table 5.5.

TABLE 5.5. LOSS MECHANISMS OF NEGATIVE IONS

$H^- + e, e_{\text{fast}} \rightarrow H^0 + e, e_{\text{fast}}$
$H^- + H^+ (H^{2+}, H^{3+}) \rightarrow H^0, H_2$
$H^- + H^0 \rightarrow H_2 + e$
$H^- + H_2 \rightarrow H^0 + H_2 + e$

To prevent the loss of negative ions by collisions with energetic electrons, the volume production source has a tandem plasma chamber [5.107], where the plasma chamber is divided into two regions, namely the driver region and the extraction region, by a transverse magnetic field called the “magnetic filter”. Figure 5.44 shows the concept of the tandem source. In the driver region, vibrationally excited hydrogen molecules are produced by collisions with energetic electrons. The magnetic filter prevents the energetic electrons from going into the extraction region, while the vibrationally excited molecules drift freely to the extraction region. The negative ions are produced in the extraction

region by the collision of vibrationally excited molecules with thermalized slow electrons.

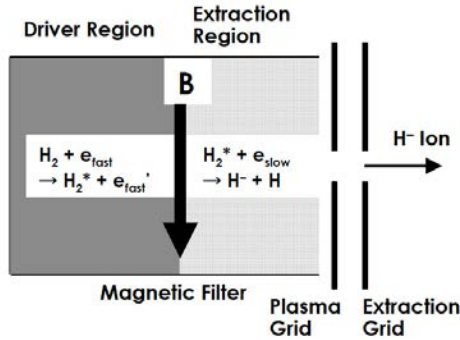


FIG. 5.44. Concept of tandem source to produce high density negative ions.

Various types of magnetic filter are illustrated in Fig. 5.45. The rod filter (Fig. 5.45(a)) uses multiple rods inserted into the plasma to create the transverse magnetic field by the small permanent magnets embedded in the rods [5.107], while the transverse magnetic field filter (Fig. 5.45(b)) is created by arranging a pair of strong permanent magnets outside the plasma chamber in the external filter. The plasma grid (PG) filter (Fig. 5.45(c)) is an electromagnetic filter where the transverse field is formed by the large electric current flowing into the plasma grid [5.108]. The configuration of the magnetic filter has been optimized to improve the beam uniformity produced by a large negative ion source [5.109, 5.110].

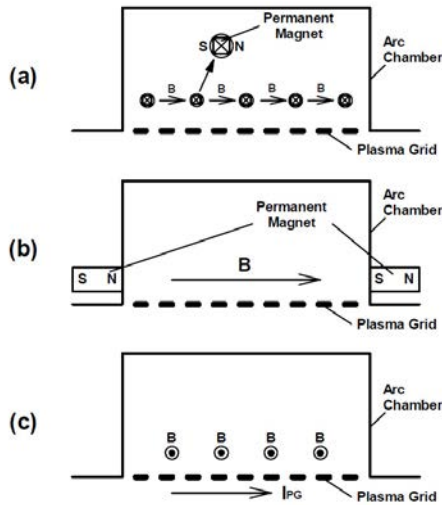


FIG. 5.45. Various types of magnetic filter in a volume source: rod filter (a), transverse magnetic field filter (b) and plasma grid filter (c).

There exists an optimum filter strength for negative ion production. Figure 5.46 shows the effect of the magnetic filter observed in a tandem volume source with electromagnetic filter [5.111]. The electron temperature in the extraction region decreases as the filter strength increases and the negative ion current density has a maximum when the electron temperature becomes almost 1 eV. It was also found that the optimum filter strength is higher in deuterium negative ion production than in hydrogen negative ion production.

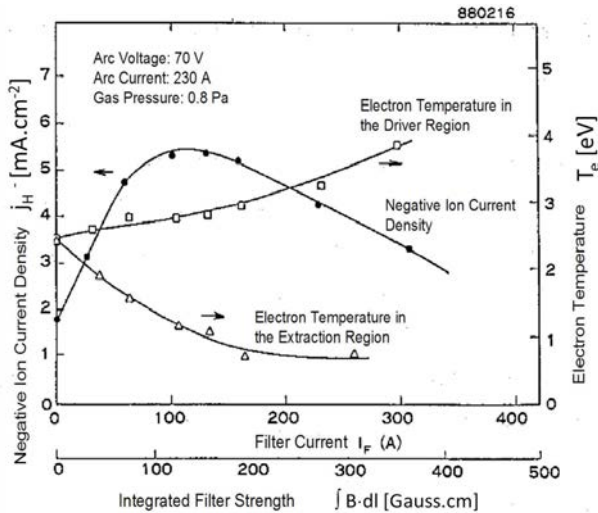


FIG. 5.46. Effect of the magnetic filter in a tandem volume source with electromagnetic filter [5.111].

### 5.2.5.3. Caesium seeding

In the tandem volume negative ion source, the negative ion current saturates at a level of less than  $10 \text{ mA}\cdot\text{cm}^{-2}$  even if the plasma density is increased by increasing the arc discharge current. The saturation current density tends to increase by increasing the operating gas pressure, but the gas pressure should be kept lower than  $0.5\text{--}1 \text{ Pa}$  in the plasma chamber, otherwise the extracted/accelerated negative ions are easily destroyed by collision with gas molecules.

Caesium seeding is the most effective method to overcome the difficulty. It was found that the negative ion production yield increases significantly by seeding a small amount of Cs into the volume production source [5.112, 5.113]. A big reduction in the extracted electron current and the operating gas pressure was also observed. Figure 5.47 shows the effect of Cs seeding obtained in a large volume production source [5.114]. The negative ion current increases

proportionally with the arc discharge current and reaches 10 A, while the current tends to saturate at a high arc discharge current without Cs. About 0.5 g of Cs was introduced into the source. The current density was  $37 \text{ mA}\cdot\text{cm}^{-2}$  and the operating gas pressure was 1.0 Pa. These parameters satisfy the values required for negative-ion-based NBIs.

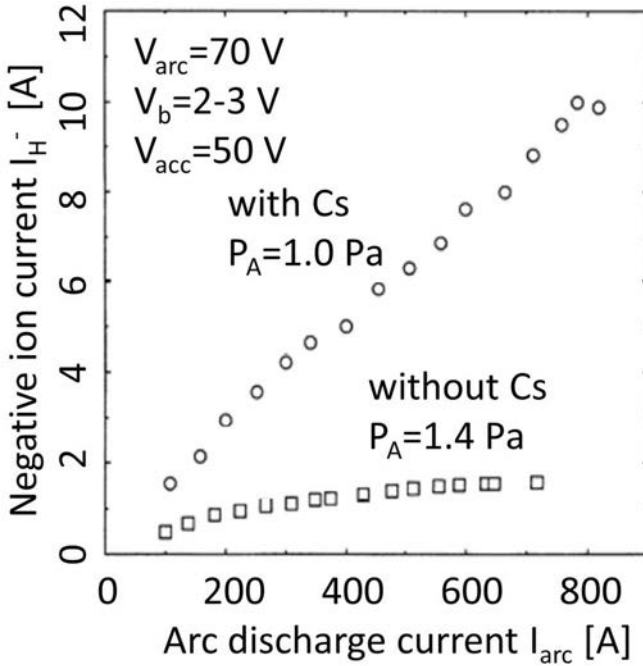


FIG. 5.47. Effect of caesium seeding in the JAERI 10 A negative ion source [5.114].  $V_{arc}$  and  $V_{acc}$  are the arc and the acceleration voltages, respectively, and  $V_b$  is the bias voltage of the plasma grid with respect to the arc discharge chamber.  $I_{arc}$  is the arc discharge current and  $P_A$  the working gas pressure.

It was observed that the Cs effect is a strong function of the temperature of the plasma grid [5.114, 5.115]. The negative ion current increases by a factor of 2–3 when the plasma grid temperature is kept at 200–400°C. In this temperature range the plasma grid surface is thought to be covered by half to one mono layer of Cs atoms, which offers minimum work function at the plasma grid surface. This strong temperature effect suggests the surface production of negative ions by Cs seeding.

The negative ion production rate was investigated by measuring the work function of the plasma grid surface by laser photo-detachment [5.116]. It was confirmed that the negative ion production increases when the work function of the plasma grid becomes 1 eV, which proved that the Cs effect is mainly due to the surface production.

Recently, it has been observed that high current density negative ion beams are produced in a caesium-free negative ion source developed for the J-PARC accelerator. An H-ion beam of 38 mA was extracted from a 9 mm diameter aperture [5.117] by using a lanthanum hexaboride ( $\text{LaB}_6$ ) cathode for arc discharge. This might be explained by the fact that the work function of the plasma grid is lowered by alkali metal impurities in the  $\text{LaB}_6$  cathode [5.118].

### 5.2.6. Negative ion extraction/acceleration

Since the electrons have the same charge as the negative ions and a lighter mass, electrons are extracted and accelerated with the negative ions. Effective suppression of the electrons is critical in negative ion extraction. Figure 5.48 shows a schematic of the extraction grid system developed for multi-ampere volume negative ion sources. Negative ions are extracted with electrons by applying an extraction voltage between the plasma and the extraction grids. Electrons are deflected by the dipole magnetic field produced by permanent magnets embedded in the extraction grid and deposited on the extraction grid. Negative ions are scarcely deflected and go through the extraction grid. The extraction voltage is selected up to 10 kV, because a higher voltage causes higher electron energy, resulting in a high heat load in the extraction grid.

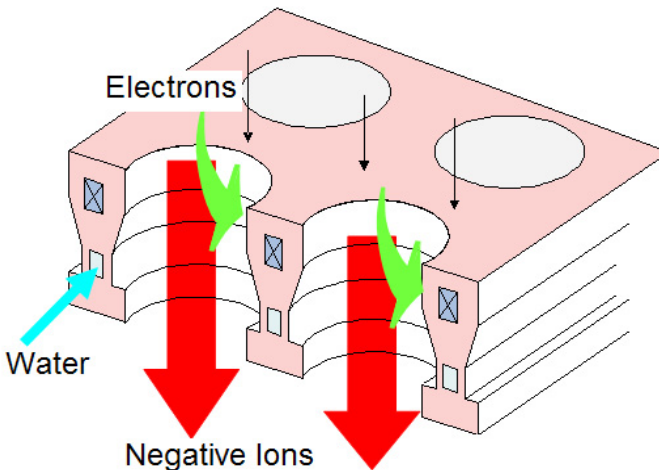


FIG. 5.48. Schematic of negative ion extractor.

The extracted negative ions are accelerated electrostatically in the multi-stage acceleration system. Figure 5.49 shows an example of a negative ion beam trajectory in a five stage acceleration system [5.119]. The electric field is increased step by step to the downstream accelerator gaps so that the beam is converged by the electrostatic lens between the stages.

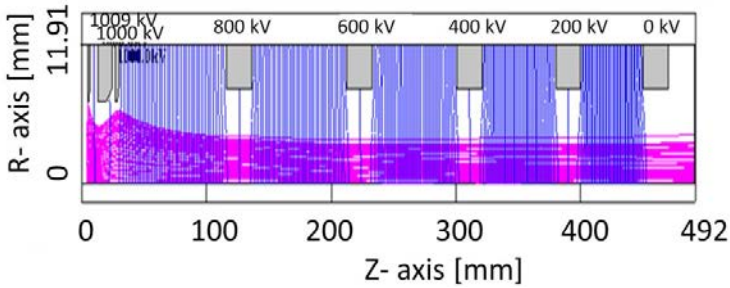


FIG. 5.49. Negative ion trajectory in a five stage acceleration system [5.119]. The electric field is shown in blue, while the ion beam trajectory is shown red. The electric potential applied in each grid is shown at the top.

Figure 5.50 left shows a picture of the negative ion beam extracted from a single aperture [5.120]. For comparison, a picture of the positive ion beam extracted from a single aperture is shown in Fig. 5.50 right. The beam divergence of the negative ion beam is as low as 2 mrad, while that of the positive ion beam is normally of the order of 10 mrad. The difference in the beam divergences is mainly due to the thermal temperature of the ions produced in the source plasma. The volume produced negative ions have very low thermal energies of less than 1 eV, while the positive ions have energies of more than several eV at the dissociation of molecules. The stable extraction surface and the good beam optics of the negative ion source contribute to the low beam divergence.

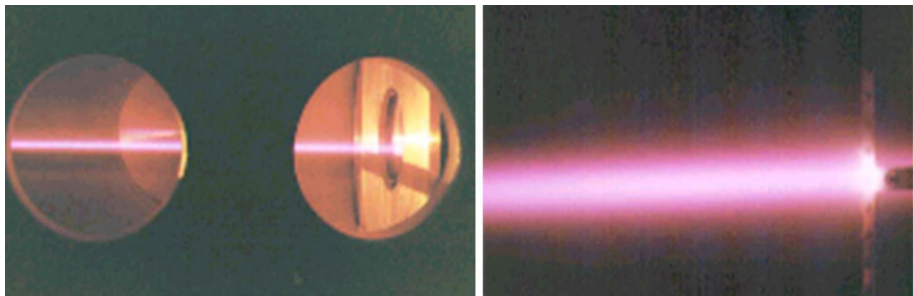


FIG. 5.50. Picture of negative ion beam (left) and positive ion beam (right) extracted from single aperture [5.120].

## 5.2.7. Negative-ion-based NBI

### 5.2.7.1. N-NBI for JT-60

After the successful demonstration of the high current negative ion production of 10 A with reasonable current density and negative ion extraction/

acceleration with good beam optics, the first negative-ion-based NBI was designed and applied in JT-60 in 1996 [5.75]. The good beam optics of the negative ion beam made it possible to install the ion source far from the tokamak and guide the neutral beam through a narrow neutralizer cell [5.121]. Figure 5.51 shows the cross-sectional view of the JT-60 negative ion source. Deuterium negative ions are produced in a Cs seeded volume production source. The source called “KAMABOKO source” has a semi-cylindrical chamber that has a large volume to surface ratio and the surface of the chamber is covered by strong magnetic line cusps. Because of the good confinement of the source plasma, the operating gas pressure is as low as 0.3 Pa. This low operating gas pressure is convenient to accelerate the negative ions at energies up to 500 keV without significant stripping loss of negative ions in the accelerator.

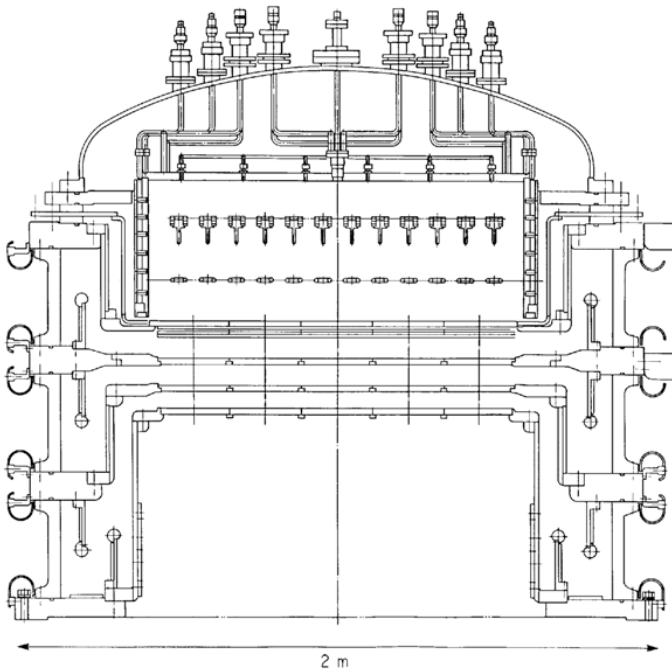


FIG. 5.51. Negative ion source developed for JT-60 N-NBI [5.75].

#### 5.2.7.2. N-NBI for LHD

Figure 5.52 shows the negative ion source for the negative-ion-based NBI for LHD [5.122]. The plasma generator has a dimension of 35 cm  $\times$  145 cm in width and 21 cm in depth and is covered by magnetic line cusps. A pair of strong line cusps are installed outside the chamber to create a transverse magnetic filter.

Three Cs ovens are installed on the top of the chamber to inject a small amount of Cs to enhance the negative ion production. The negative ions are extracted by a multi-aperture three-grid extractor and accelerated by a single acceleration system. There are 770 apertures over the extraction area of  $25\text{ cm} \times 125\text{ cm}$ . Hydrogen negative ion beams of 30 A and 180 keV were achieved with a good beam divergence of less than 10 mrad.

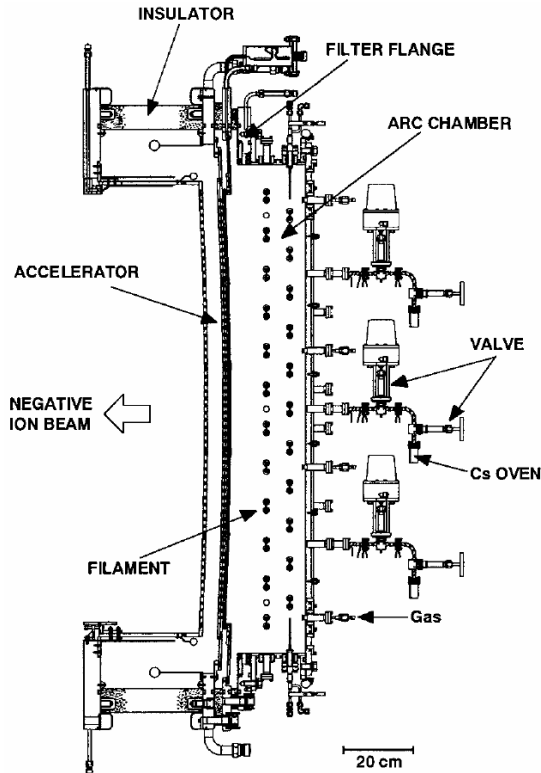


FIG. 5.52. Negative ion source developed for LHD N-NBI [5.122].

### 5.2.7.3. N-NBI for ITER

ITER will use two 1 MeV heating NBIs and one 100 keV diagnostic NBI. A third NBI for heating may be added later to increase the total neutral beam power from 33 MW to 50 MW.

Figure 5.53 shows the schematics of the 1 MeV negative-ion-based NBI for ITER [5.78, 5.79]. It is necessary to develop a negative ion source producing 1 MeV, 40 A (40 MW) D-ion beams. According to the reference design [5.79], D-ions are produced in an RF negative source which has a long life and no

filaments and simplifies the electric power supplies. The RF negative ion source developed in IPP Garching has been demonstrated to have a capability to generate the D-ions required for ITER. The D-ion beams produced are extracted from a multi-aperture three-grid extractor having 1300 extraction apertures of 14 mm in diameter over an area of  $60\text{ cm} \times 164\text{ cm}$  and accelerated by an accelerator with a current density of  $20\text{ mA}\cdot\text{cm}^{-2}$  at a gas pressure as low as 0.3 Pa.

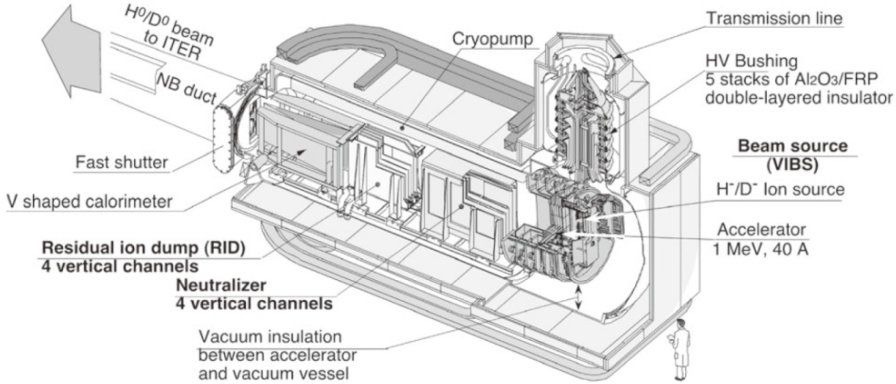


FIG. 5.53. Isometric illustration of the ITER NBI [5.79].

Since the H-/D-ions have an electron affinity of only 0.75 eV, they are easily neutralized by collisions with the residual gas in the accelerator before having their full energy. This is called “stripping” to distinguish it from the desired neutralization in the neutralizer. To minimize the stripping, the gas pressure in the accelerator has to be minimized, which leads to the requirement that the ion source, which is directly connected to the accelerator, operate at a low pressure of less than 0.3 Pa.

Two types of accelerator concept have been developed for ITER, namely SINGAP [5.123] by CEA Cadarache, and MAMuG [5.124] by JAEA in Naka. In the SINGAP accelerator the extracted and pre-accelerated negative ions are accelerated in one single step to 1 MeV, while the negative ions are accelerated in five stages (200 keV in each stage) in the MAMuG accelerator. The SINGAP accelerator has the advantage that the accelerator and the power supply are highly simplified because it does not require intermediate potential electrodes. However, it turned out that the voltage holding of the SINGAP accelerator is worse than that of the MAMuG accelerator, and that the power carried by electrons that exit the SINGAP accelerator is much higher than the power of electrons from MAMuG [5.124, 5.125]. For this reason the MAMuG accelerator is chosen in the reference design of ITER.

The ITER NBI is operated in a radiation environment. Neutrons from the tokamak will stream through the NB injection port, which has a large

opening about 1.4 m in height and 1.3 m in width, and activate all the beam line components, including the ion source/accelerator. A three-dimensional nuclear analysis has clarified that the neutron flux at the position of the negative ion source is as high as  $10^{10}$  neutrons/cm<sup>2</sup> [5.126] and a conventional insulation gas such as SF<sub>6</sub> is not applicable because of the radiation induced conductivity (RIC) [5.127]. The insulation gas is ionized by the radiation and the dark current produced by the ionization becomes huge and degrades the power efficiency. Therefore, the design of ITER NBI adopts vacuum insulation for the ion source with a high voltage bushing as a vacuum boundary between the ion source and insulation gas in the high voltage power supply.

### 5.2.8. MV power supply

To extract and accelerate high current density ion beams, the voltage applied between the electrodes in the ion source is close to the limit of vacuum insulation. In the positive ion source, for example, 100 kV is applied across a 10–14 mm gap. The electric field intensity reaches more than  $10 \text{ kV} \cdot \text{mm}^{-1}$ . High voltage breakdowns occur frequently at the beginning of the operation of a new ion source and then the voltage holding capability is improved step by step with the operation time. This is called “conditioning” of the ion source. Even after conditioning, breakdown is considered unavoidable in the operation of an ion source.

When breakdown occurs, the high voltage should be cut off immediately, otherwise the energies flowing to the electrode damage the electrode and degrade the voltage holding. After a certain period of interruption, the high voltage is turned on again to continue the beam injection. New technologies to regulate and to switch on/off electric powers of several tens of MW have been developed for the power supplies of positive-ion-based NBI.

In the negative-ion-based NBI, the voltage is much higher. Major issues of the 1 MV power supply for ITER NBI are high speed switching, regulation and transmission of DC ultra-high voltage (UHV) and suppression of surge energy input to the accelerator at breakdown. An inverter controlled high voltage power supply is proposed for ITER [5.128, 5.129]. Using a gate turn-off thyristor, regulation and control of the power supply is performed on the low voltage AC side. Figure 5.54 shows the schematics of the circuit diagram of the 1 MV power supply designed for ITER NBI. The power supply consists of a converter-inverter system and five sets of step-up transformer and rectifier. Each 200 kV DC output is connected in series to generate the DC 1 MV for the accelerator. A set of a filter capacitor and a resistor (CR filter) is supplied in each 200 kV line to reduce the voltage ripple. The capacitance value of the CR filter should be designed to be as small as possible, since such filter capacitors are sources of surge energy at breakdown.

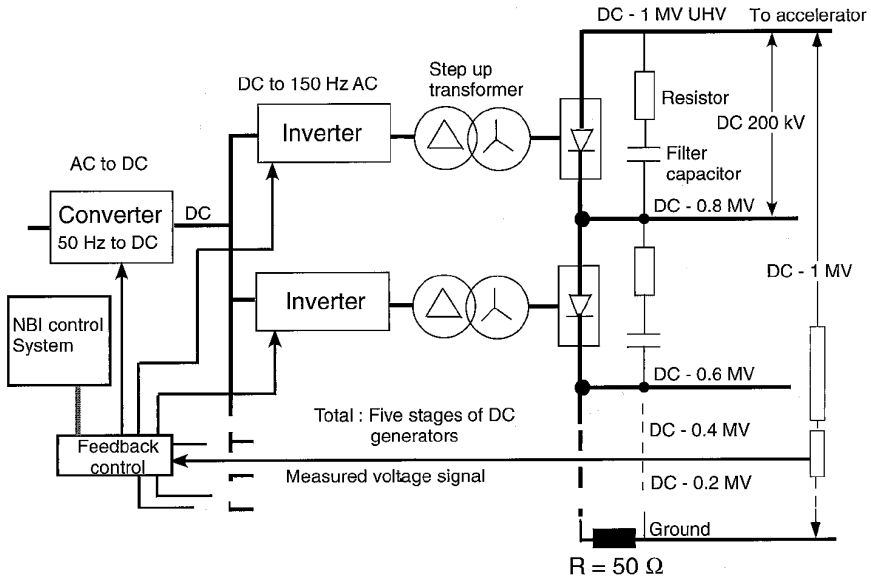


FIG. 5.54. Schematic diagram of the 1 MV power supply for ITER NBI [5.128].

The power supplies for the ion source and the ion extractor are at a 1 MV potential. The electric power is provided by a 1 MV insulating transformer and the high voltage parts of the power supplies are installed in the “HV deck” near the ion source. Transmission of this 1 MV potential to the HV deck and to the ion source requires high voltage insulators and careful design for DC UHV insulation.

### 5.2.9. Remarks on future NBI technology

Technologies for positive ion sources and positive-ion-based NBI are highly sophisticated and there is no large R&D item left. On the other hand, there exist many R&D items in the negative ion source and the negative-ion-based NBI. Out of the R&D items, the following seem to be crucial to realize the negative-ion-based NBI for ITER:

- (1) Development of maintenance-free negative ion source or RF source;
- (2) Improvement of uniformity and current density in negative ion production;
- (3) Demonstration of 1 MeV acceleration.

Not only the negative ion source but also the high voltage technologies such as a power supply and large diameter insulators are important.

A beam energy of 1 MeV seems to be close to the boundary of the electrostatic acceleration. According to clump theory [5.130], the voltage holding

capability in vacuum scales as  $d^{1/2}$  ( $d$  is the insulation distance) and is limited to 600–800 kV even if the distance becomes longer than 1 m. The theory shows good agreement with experiments predicting the voltage holding capability of the SINGAP accelerator [5.125]. The MuMAG accelerator has the advantage that the 1 MV is divided into five stages (200 V each stage), but it is inevitable to insulate the high voltage in vacuum because the ion source and accelerator are immersed in vacuum to prevent RIC [5.127].

In the future DEMO reactor, one of the difficulties is the large opening required for NBI. This causes neutron streaming to NBI and induces activation of the NBI components and also limits the flexibility of the DEMO reactor design. If higher beam energies above 2 MeV would be required for the future DEMO reactor, a drastic change of the ion source and the NBI system might be necessary. For example, an NBI design using RF acceleration was proposed for ITER [5.131] and for the ARIES-I tokamak reactor [5.132], where negative ions are accelerated to 2 MeV by a radiofrequency quadrupole (RFQ) and neutralized by a plasma neutralizer. A continuously operated, high current RFQ is being developed in the IFMIF/EVEDA (International Fusion Material Irradiation Facility/Engineering Validation and Engineering Design Activity) project [5.133] under the “Broader Approach” activities [5.134] to demonstrate stable production of 5 MeV, 125 mA deuterium ion beams, whose technology could be extended to the 1 A level by reducing the RFQ frequency. The ion beams accelerated by the RFQ could be bent to prevent direct neutron exposure and the smaller size of the beam might offer a possibility to reduce the size of the injection port, providing flexibility to the DEMO reactor design.

## REFERENCES

- [5.1] BERRY, L.A., et al., “Neutral beam injection experiments in ORMAK”, Proc. Int. Conf. Plasma Physics and Controlled Nuclear Fusion Research, Vol. **1**, Tokyo (1974), 113, IAEA Vienna (1975).
- [5.2] BOL, K., et al., “Neutral-beam heating in the adiabatic toroidal compressor”, *ibid.* 77.
- [5.3] USHIGUSA, K., et al., “Steady state operation research in JT-60U”, Proc. 16th IAEA Fusion Energy Conference, Montreal, Vol. 1 (1996) 37.
- [5.4] KIKUCHI, M., JT-60 Team, Plasma Phys. Control. Fusion **43** (2001) A217.
- [5.5] RIVIERE, A.C., Effect of the magnetic field ripple on diffusion in tokamak, Nucl. Fusion **11** (1971) 363.
- [5.6] JANEV, R.K., SMITH J.J., Atomic and plasma-material interaction data for fusion, Nucl. Fusion supplement **4** (1993).
- [5.7] OLSON, R.E., et al., Charge-state dependence of electron loss from H by collisions with heavy, highly stripped ions, Phys. Rev. Lett. **41** (1978) 163.
- [5.8] JANEV, R.K., BOLEY, C.D., POST, D.E., Penetration of energetic neutral beams into fusion plasmas, Nucl. Fusion **29** (1989) 2125.
- [5.9] JANEV, R.K., LANGER, W.D., EVANS, K. Jr., POST, D.E. Jr., “Elementary processes in hydrogen-helium plasmas, cross sections and reaction rate coefficients”, Springer Series on Atoms and Plasmas, Springer-Verlag, Berlin–Heidelberg, Vol. 4 (1987) 258.
- [5.10] BOREY, C.D., JANEV, R.K., POST, D.E., Enhancement of neutral-beam stopping cross section in fusion plasmas due to multistep collision processes, Phys. Rev. Lett. **52** (1984) 534
- [5.11] GORMEZANO, C., et al., Progress in the ITER Physics Basis, Chapter 6 on Steady State Operation, Nucl. Fusion **47** (2007) S285.
- [5.12] SUZUKI, S., et al., Attenuation of high-energy neutral hydrogen beams in high-density plasmas, Plasma Phys. Control. Fusion **40** (1998) 2097.
- [5.13] ITER PHYSICS EXPERT GROUP ON ENERGETIC PARTICLES, HEATING AND CURRENT DRIVE, Corrigendum, ITER physics basis, Chapter 6, Nucl. Fusion **40** (2000) 1429.

- [5.14] OIKAWA, T., et al., Heating and non-inductive current drive by negative ion based NBI in JT-60U, *Nucl. Fusion* **40** (2000) 435.
- [5.15] STIX, T.H., Heating of toroidal plasmas by neutral injection, *Plasma Phys.* **14** (1972) 367.
- [5.16] WESSON, J., Tokamaks, 2nd edn., Oxford Science Publications (1997).
- [5.17] MIYAMOTO, K., Plasma Physics for Nuclear Fusion, MIT Press (1980).
- [5.18] TOBITA, K., et al., Loss of fast tritons in JT-60U reversed magnetic shear discharges, *Nucl. Fusion* **37** (1997) 1583.
- [5.19] HEIDBRINK, W.W., SADLER, G.J., Review paper: The behaviour of fast ions in tokamak experiments, *Nucl. Fusion* **34** (1994) 535.
- [5.20] HEIDBRINK, W.W., et al., The diffusion of fast ions in ohmic TFTR discharges, *Phys. Fluids B* **3** (1991) 3167.
- [5.21] JET team, Fusion energy production from a deuterium-tritium plasma in the JET tokamak, *Nucl. Fusion* **32** (1992) 187.
- [5.22] ISHIDA, S., et al., "High performance experiments in JT-60U high current divertor discharges", Proc. 16th Int. Conf. Plasma Physics and Controlled Nuclear Fusion Research, Montreal, Canada, 1996, IAEA, Vienna, Vol. 1 (1997) 315.
- [5.23] KISHIMOTO, H., ISHIDA, S., KIKUCHI, M., NINOMIYA, H., Advanced tokamak research on JT-60, *Nucl. Fusion* **45** (2005) 986.
- [5.24] CONNOR, J.W., CORDEY, J.G., Effects of neutral injection heating upon toroidal equilibria, *Nucl. Fusion* **14** (1974) 185.
- [5.25] CORDEY, J., Effects of particle trapping on the slowing-down of fast ions in a toroidal plasma, *Nucl. Fusion* **16** (1976) 499.
- [5.26] GAFFEY, J.D., Jr., Energetic ion distribution resulting from neutral beam injection in tokamaks, *J. Plasma Phys.* **16** (1976) 149.
- [5.27] TANI, K., AZUMI, M., DEVOTE, R.S., Numerical analysis of 2D MHD equilibrium with non-inductive plasma current in tokamaks, *J. Comp. Phys.* **98** (1992) 332.
- [5.28] KIKUCHI, M., AZUMI, M., Review article: Experimental evidence for the bootstrap current in a tokamak, *Plasma Phys. Control. Fusion* **37** (1995) 1215.

- [5.29] KIKUCHI, M., "Frontier in Fusion Research - Physics and Fusion", Springer Verlag (2011).
- [5.30] START, D.F.H., CORDEY, J., Beam-induced currents in toroidal plasmas of arbitrary aspect ratio, *Phys. Fluids* **23** (7) (1980) 1477.
- [5.31] CLARK, W.H.M., et al., Measurements of the beam-driven current in the DITE tokamak, *Phys. Rev. Lett.* **45** (1980) 1101.
- [5.32] OIKAWA, T., et al., Reactor relevant current drive and heating by N-NBI on JT-60U, *Nucl. Fusion* **41** (2001) 1575.
- [5.33] PEREVERZEV, G.V., et al., "ASTRA, an automatic System of Transport Analysis in Tokamak, IPP 5/42, Garching (1991).
- [5.34] FOREST, C.B., et al., Determination of the noninductive current profile in tokamak plasmas, *Phys. Rev. Lett.* **73** (1994) 2444.
- [5.35] LAO, L.L., et al., Equilibrium analysis of current profiles in tokamaks, *Nucl. Fusion* **30** (1990) 1035.
- [5.36] GUENTER, S., et al., Interaction of energetic particles with large and small scale instabilities, *Nucl. Fusion* **47** (2007) 920.
- [5.37] STRINGER, T.E., et al., Effect of the magnetic field ripple on the diffusion in tokamaks, *Nucl. Fusion* **12** (1972) 689.
- [5.38] YUSHMANOV, P.N., Diffusive transport processes caused by the ripple in tokamaks, *Rev. Plasma Phys.* **16** (1987) 117.
- [5.39] TOBITA, K., et al., Ripple-trapped loss of neutral-beam-injected fast ions in JT-60U, *Phys. Rev. Lett.* **69** (1992) 3060.
- [5.40] TOBITA, K., et al., Energetic particle experiments in JT-60U and their implications for a fusion reactor, *Fusion Sci. Technol.* **42** (2002) 315.
- [5.41] TANI, K., AZUMI, M., KISHIMOTO, H., TAMURA, S., Effect of toroidal field ripple on fast ion behavior in a tokamak, *J. Phys. Soc. Jpn.* **50** (1981) 1726.
- [5.42] TURBUNIKOV, B.A., Particle interactions in a fully ionized plasma, *Rev. Plasma Phys.* **1** (1965) 105.
- [5.43] BOOZER, A., Physics of magnetically confined plasmas, *Rev. Mod. Phys.* **76** (2004) 1071.
- [5.44] TANI, K., et al., Ripple loss of alpha particles in a tokamak reactor with a non-circular plasma cross-section, *Nucl. Fusion* **33** (1993) 903.
- [5.45] GOLDSTON, R., et al., Confinement of high-energy trapped particles in tokamaks, *Phys. Rev. Lett.* **47** (1981) 647.

- [5.46] GLASSTONE, S., LOVBERG, R.H., Controlled Thermonuclear Reactions, D. Van Nostrand, Princeton, New Jersey (1960).
- [5.47] TAKIZUKA, T., YAMAGIWA, M., Reactivity for DT Plasma with Beam-induced Tail in Magnetic Confinement System, JAEARI-M 87-066 (1987).
- [5.48] MCKEE, G., et al., Confined alpha distribution measurements in a deuterium-tritium tokamak plasma, *Phys. Rev. Lett.* **75** (1995) 649.
- [5.49] FISHER, R.K., et al., Measurements of fast confined alphas on TFTR, *Phys. Rev. Lett.* **75** (1995) 846.
- [5.50] KEILHACKER, M., GIBSON, A., GORMEZANO, C., REBUT, P.H., Scientific success of JET, *Nucl. Fusion* **41** (2001) 1925.
- [5.51] HAWRYLUK, R.J., Results from deuterium-tritium tokamak confinement experiments, *Rev. Mod. Phys.* **70** (1998) 537.
- [5.52] ZWEBEN, S.J., et al., Special topic alpha particle physics experiments in the Tokamak Fusion Test Reactor, *Nucl. Fusion* **40** (2000) 91.
- [5.53] JET Team, Fusion energy production from a deuterium-tritium plasma in the JET tokamak, *Nucl. Fusion* **32** (1992) 187.
- [5.54] TAYLOR, G., et al., Fusion heating in a deuterium-tritium tokamak plasma, *Phys. Rev. Lett.* **76** (1996) 2722.
- [5.55] JET Team, prepared by THOMAS, P.H., Alpha particle studies during JET DT experiments, *Nucl. Fusion* **39** (1999) 1619.
- [5.56] MCGUIRE, K., et al., in Proc. 16th Int. Conf. Plasma Physics and Controlled Nuclear Fusion Research, Montreal, Canada, 1996, IAEA, Vienna, Vol. 1 (1997) 19.
- [5.57] POST, R.F., *Ann. Rev. Nuclear Sci.* **9** (1959) 367.
- [5.58] KUO, L.G., et al., *Phys. Fluids* **7** (1964) 988.
- [5.59] BERNSTEIN, W., et al., in Proc. Conf. on Plasma Physics and Controlled Fusion Research, Culham Vol. 2 (1966) 23.
- [5.60] DAM, C.C., et al., *Phys. Fluids* **8** (1965) 1472.
- [5.61] FURTH, H.P., *Nucl. Fusion* **15** (1975) 487.
- [5.62] JASSBY, D.L., *Nucl. Fusion* **17** (1977) 309.
- [5.63] CORDAY, J.G., et al., *Nucl. Fusion* **15** (1975), 441.
- [5.64] BERRY, L.A., et al., in Proc. 6th Int. Conf. on Plasma Physics and Controlled Nuclear Fusion Research, Berchtesgaden, Vol. 1 (1976), 49.

- [5.65] ELLIS, R.A., et al., Nucl. Fusion **16** (1976) 524.
- [5.66] EUBANK, H., et al., Phys. Rev. Lett. **43** (1979) 270.
- [5.67] TURNER, W.C., et al., Nucl. Fusion **19** (1979) 1011.
- [5.68] COENSGEN, F.H., et al., Phys. Rev. Lett. **44** (1980) 1132.
- [5.69] NODA, N., et al., Nucl. Fusion, **22** (1982) 1103.
- [5.70] GRIEGER, G., et al., Plasma Phys. Control. Fusion **28** (1986) 43.
- [5.71] VELLA, M.C., et al., Rev. Sci. Instrum. **59** (1988) 2357.
- [5.72] GREEN, T.S., et al., in Proc. 10th Int. Conf. on Plasma Physics and Controlled Nuclear Fusion Research, London, 1984, IAEA, Vienna Vol. 3 (1985) 319.
- [5.73] MATSUDA, S., et al., Fusion Eng. Des. **5** (1987) 85.
- [5.74] OKUMURA, Y., et al., Rev. Sci. Instrum. **67** (1996) 1092.
- [5.75] KURIYAMA, M., et al., Rev. Sci. Instrum. **71** (2000) 751.
- [5.76] IYOSHI, A., et al., Nucl. Fusion **39** (1999) 1245.
- [5.77] TAKEIRI, Y., et al., Nucl. Fusion **46** (2006) 199.
- [5.78] HEMSWORTH, R., et al., Rev. Sci. Instrum. **79** (2008) 02C109.
- [5.79] HEMSWORTH, R., et al., Nucl. Fusion **49** (2009) 045006.
- [5.80] BERKNER K.H. et al., Nucl. Fusion **15** (1975) 249.
- [5.81] TSAI, C.C., et al., Rev. Sci. Instrum. **48** (1977) 651.
- [5.82] GARDNER, W.L., et al., Rev. Sci. Instrum. **53** (1982) 424.
- [5.83] MENON, M.M., et al., Rev. Sci. Instrum. **56** (1985) 242.
- [5.84] EHLERS, K.W., in Proc. 7th Symp. on Engineering Problems of Fusion Research, Knoxville, TN, Volume 1 (1977) 291.
- [5.85] FUMELLI, M., Nucl. Instrum. Methods **118** (1974) 337.
- [5.86] BARIAUD, A., et al., in Proc. 6th Int. Conf. on Plasma Physics and Controlled Nuclear Fusion Research, Berchtesgaden, West Germany, Volume 3 (1976) 202.
- [5.87] GOEDE, A.P.H., et al., Phys. Fluids **25** (1982) 1797.
- [5.88] EHLERS, K.W., et al., Rev. Sci. Instrum. **50** (1979) 1353.
- [5.89] GOEBEL, D.M., Phys. Fluids **25** (1982) 1093.
- [5.90] OKUMURA, Y., et al., Rev. Sci. Instrum. **55** (1984) 1.

- [5.91] SPETH, E., et al., Fusion Eng. Des. **46** (1999) 383.
- [5.92] SPETH, E., et al., Nucl., Fusion **46** (2006) S220.
- [5.93] KRAUS, W., et al., Rev. Sci. Instrum. **79** (2008) 02C108.
- [5.94] OKUMURA, Y., et al., Rev. Sci. Instrum. **51** (1980) 728.
- [5.95] OKUMURA, Y., et al., Japan Atomic Energy Research Institute Report, JAERI-M 7696 (1978).
- [5.96] WHEALTON, J.H., Rev. Sci. Instrum. **48** (1977) 1428.
- [5.97] OHARA, Y., Jpn. J. Appl. Phys. **18** (1979) 351.
- [5.98] OKUMURA, Y., et al., Rev. Sci. Instrum. **51** (1980) 471.
- [5.99] HOOPER, E.B., et al., J. Appl. Phys. **52** (1981) 7027.
- [5.100] KRYLOV, A.I., et al., Sov. J. Plasma Phys. (Engl. Transl.) (United States) Journal Volume **13:4** (1987) 272.
- [5.101] KWAN, J.W., et al., Rev. Sci. Instrum. **57** (1986) 309.
- [5.102] NICOLOPOULOU, E., et al., J. Phys. **38** (1977) 1399.
- [5.103] BACAL, M., et al., Phys. Rev. Lett. **42** (1979) 1538.
- [5.104] HISKES, J.R., et al., J. Appl. Phys. **56** (1984) 1927.
- [5.105] HISKES, J.R., et al., J. Appl. Phys. **58** (1985) 1759.
- [5.106] FUKUMASA, O., et al., J. Jpn. Soc. Plasma Sci. Nucl. Fusion Res. **56** (1986) 409.
- [5.107] LEUNG, K.N., et al., Rev. Sci. Instrum. **54** (1983) 56.
- [5.108] HANADA, M., et al., Rev. Sci. Instrum. **61** (1990) 499.
- [5.109] HANADA, M., et al., Rev. Sci. Instrum. **77** (2006) 03A515.
- [5.110] KOJIMA, A., et al., Rev. Sci. Instrum. **81** (2010) 02B112.
- [5.111] OKUMURA Y., J. Jpn. Soc. Plasma Sci. Nucl. Fusion Res. **60** (1988) 329.
- [5.112] WALTHER, S.R., et al., J. Appl. Phys. **64** (1988) 3424.
- [5.113] LEUNG, K.N., et. al., Rev. Sci. Instrum. **60** (1989) 531.
- [5.114] OKUMURA, Y., et al., in Proc. 16th Symp. on Fusion Technology, London, Vol. 2 (1990) 1026.
- [5.115] TAKEIRI, Y., et al., Rev. Sci. Instrum. **71** (2000) 1379.
- [5.116] SHINTO, K., et. al, Jpn J. Appl. Phys. **35** (1996) 1894.

- [5.117] UENO, A., et al., Rev. Sci. Instrum. **81** (2010) 02A720.
- [5.118] DUDNIKOV, V., JOHNSON, R.P., Rev. Sci. Instrum. **81** (2010) 02A711.
- [5.119] KASHIWAGI, M., et al., Rev. Sci. Instrum. **81** (2010) 02B113.
- [5.120] OKUMURA, Y., et al., Rev. Sci. Instrum. **67** (1996) 1092.
- [5.121] HORIIKE, H., et al., Japan Atomic Energy Research Institute Report JAERI-M 86-064 (1986).
- [5.122] TAKEIRI, Y., et al., J. Plasma Fusion Res. **74** (1998) 1434.
- [5.123] DE ESCH, H.P.L., HEMSWORTH, R.S., MASSMANN, P., Fusion Eng. Des. **73** (2005) 329.
- [5.124] TANIGUCHI, M., et al., in Proc. 1st Int. Symposium on Negative Ions, Beams and Sources, Aix-en-Provence, AIP Conf. Proc. Volume 1097 (2009) 335.
- [5.125] DE ESCH, H.P.L., et al., 1st Int. Symposium on Negative Ions, Beams and Sources, Aix-en-Provence, AIP Conf. Proc. Vol. 1097 (2009), 353.
- [5.126] KRYLOV, K., INOUE, T., J. Plasma Fusion Res. **81** (2005) 779.
- [5.127] HODGSON, E., et al., Fusion Technol. **1** (1998) 295.
- [5.128] WATANABE, K., et al., Nucl. Fusion **46** (2006) S332.
- [5.129] WATANABE, K., et al., Nucl. Fusion **49** (2009) 055022.
- [5.130] CRANBERG, L., J. Appl. Phys **23** (1952) 518.
- [5.131] STIRLING, W.L., et al., "A Neutral Particle Beam System for ITER with RF Acceleration", Proc. 13th Symposium on Fusion Engineering (SOFE89), Knoxville, TN, Vol. 2 (1989) 1448.
- [5.132] MAU, T.K., et al., Fusion Eng. Des. **24** (1994) 205.
- [5.133] SUGIMOTO, M., GARIN, P., et al., Fusion Sci. Technol. **56** (2009) 259.
- [5.134] OKUMURA, Y., Fusion Sci. Technol. **56** (2009) 589.

## CHAPTER 6

# RADIOFREQUENCY WAVES, HEATING AND CURRENT DRIVE IN MAGNETICALLY CONFINED PLASMAS

**M. Porkolab, P.T. Bonoli**

Plasma Science and Fusion Center,  
MIT, Cambridge, Massachusetts

**R.I. Pinsky, R. Prater**

General Atomics,  
San Diego, California

**R.J. Temkin**

Plasma Science and Fusion Center,  
MIT, Cambridge, Massachusetts

**J.R. Wilson**

Princeton Plasma Physics Laboratory,  
Princeton, New Jersey

United States of America

### 6.1. INTRODUCTION

The need for supplementary heating of magnetically confined plasmas to fusion relevant temperatures ( $\sim 20$  keV) has been recognized from the beginning of modern fusion plasma research. Although in tokamaks the plasmas are formed initially by ohmic heating ( $P_\Omega \sim \eta_R j$ , where  $j$  is the current density and  $\eta_R$  is the resistivity) its effectiveness deteriorates with increasing temperature since the resistivity decreases as  $T_e^{-3/2}$ , and losses due to bremsstrahlung radiation increase as  $Z_{\text{eff}}^3 T_e^{1/2}$  (where  $Z_{\text{eff}}$  is the effective ion charge), and the plasma current cannot be raised to arbitrarily large values because of MHD stability limits. In addition, energy losses due to thermal conduction  $P_{\text{loss}}$  are typically anomalously large compared to neoclassical predictions and the dependence on temperature is not well understood. Thus, the simplest form of steady state power balance indicates that losses due to radiation and heat conduction must be balanced by auxiliary heating of some form,  $P_{\text{aux}}$ , which may simply be stated as  $P_\Omega + P_\alpha - P_{\text{loss}} = P_{\text{aux}}$ , where  $P_\alpha$  is the power input provided by alpha particles, which does not become significant until the temperature exceeds some tens of keV, depending on confinement and density.

In this chapter, we shall discuss forms of radiofrequency or microwave power (RF power) that may provide such heating to the point where alpha particle heating can maintain fusion conditions (ignition). Another important role for RF power that emerged over the last few decades is driving currents which may be necessary to maintain steady state plasma conditions. Additional currents due to the bootstrap effect are discussed in other chapters and they must supplement RF current drive to maintain steady state conditions, at least in tokamaks. Current drive may be due to direct momentum input by the RF waves, or asymmetric deformation of the electron distribution function either by quasi-linear diffusion of resonant particles, or asymmetric heating, or scattering of trapped particles into circulating ones. Absorption of RF waves in different regions of the plasma cross-section may be affected by special resonant layers (e.g. cyclotron resonance) or by local conditions which depend on the Landau resonance of particles with the waves with matching parallel phase velocity  $\omega / k_{\parallel}$  (determined by the index of refraction  $N_{\parallel} = ck_{\parallel} / \omega = c / v_{ph,\parallel}$ ). Such localized power deposition offers the possibility of current profile control, especially if the external antenna launching the waves has directionality relative to the toroidal magnetic field. Temperature profile control is rather difficult since it also depends on local heat conduction and convection, and it is discussed in Chapter 2. However, possible methods for RF current drive will be described in this chapter. A simple schematic of key components of an RF heating system is shown in Fig. 6.1.

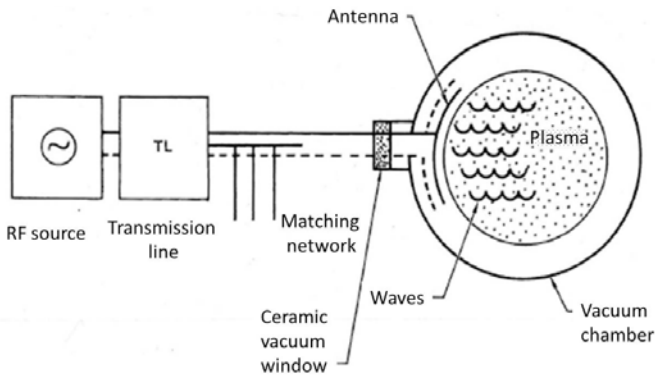


FIG. 6.1 Schematic layout of components of a typical RF heating system [6.1].

A high power RF source (typically MW size per unit) is necessary to generate the RF power, which is then transmitted by a coaxial transmission line (or waveguides in the case of a microwave source) to the confinement device (typically 10–50 m away). Since the transmission line is often pressurized with an inert gas, one or more vacuum breaks are needed (typically a ceramic or diamond window) before the transmission line is connected to an antenna inside the vacuum chamber. The antenna (often a rather complex structure, to be

described later in this chapter) will then launch waves in the plasma periphery that propagate to the plasma core, where they may be absorbed by collective plasma effects such as cyclotron or Landau damping.

A tuning circuit may be needed in the transmission system to prevent the reflected power coming back to the RF generator. The RF generator itself can be a rather complex system which consists of a high power vacuum tetrode (50 MHz, ~2 MW per tube), a klystron (2–10 GHz, ~0.5 MW per tube) or a gyrotron (110–170 GHz, ~1 MW per tube), which is then connected to a high voltage regulated DC power supply. In the first two cases, RF signal generators and intermediate power amplifiers (IPAs) are also required since tetrodes and klystrons are high power amplifiers (HPAs), whereas gyrotrons are high power oscillators (see Table 6.1).

The science behind RF heating and current drive is the physics of wave generation, propagation and absorption in an inhomogeneous plasma in a complex magnetic field geometry and may often require an understanding of quasi-linear and in some cases even non-linear plasma physics. Fortunately, over the last 40 years this field of plasma physics has progressed to an advanced level of scientific understanding and several excellent textbooks are available [6.2–6.5]. Wave propagation in an inhomogeneous plasma can be dealt with in the WKB formalism in many cases, at least for short (cm or mm) wavelengths. However, in special circumstances or at longer wavelengths in the low frequency regime, full wave treatment may be necessary and this has been developed only recently using large computer codes. Finally, absorption usually needs to be calculated by hot plasma kinetic theory, which often includes a self-consistent evolution of the velocity space deformation of the distribution function of one or more species of particles (quasi-linear effects and Fokker–Planck codes which include collisions). This usually implies an iterative technique with the wave fields that are obtained from WKB theory or full wave codes. This is by no means a trivial procedure, especially if the finite orbit of resonant particles is considered (in practice calling for a Monte Carlo code and iteration with a full wave code). Finally, coupling at the plasma–antenna interface presents additional problems since wave fields must be solved exactly, together with the plasma response, treating the antenna geometry as accurately as possible. This is a topic of continued research interest. Many of these problems will be addressed in the sections to follow. Finally, Table 6.1 summarizes types of waves of interest for RF heating and current drive, the relevant frequencies, types of antenna coupling structures, RF power sources and the status of their commercial availability.

## 6.2. THEORY OF RF WAVE PROPAGATION IN A MAGNETIZED PLASMA

The theory of wave propagation in magnetized plasmas has been developed by Stix in the late 1950s and early 1960s and his pioneering work

was summarized in his classic book [6.2] followed by an update in the 1980s [6.3]. Additional texts are also available, for example those by Brambilla [6.4] and Swanson [6.5]. We shall give a brief introduction to this work and will follow it up by works from others that lead to a basic understanding of the modern theory of wave propagation and absorption in hot magnetized plasmas. Due to the limited scope of this chapter, we shall not be able to discuss all the theoretical assumptions and intricate justifications that are needed to develop a fully rigorous theory. Nevertheless, such details can be found in the references given above. Here the approach will be to cover only elements of the theory that are needed to understand the theoretical foundations behind experiments on RF heating and non-inductive current drive in fusion relevant plasmas and be able to extrapolate to reactor applications.

TABLE 6.1. CLASSIFICATION OF RF REGIMES AND SOURCES FOR HEATING AND CURRENT DRIVE

(Here  $f_{ce}$  is the electron cyclotron frequency,  $f_{uh}$  is the upper hybrid frequency,  $f_{ci}$  is the ion cyclotron frequency,  $f_{LH}$  is the lower hybrid frequency and  $l$  is an integer)

Frequency regime and wave type	Characteristic frequency	Coupler (antenna)	Source	CW power per tube currently available
Electron cyclotron resonance (ECRH)	$f_{ce}, 2f_{ce}$ ~60–170 GHz (EBW, $lf_{ce}, f_{uh}$ for $l = 1, 2, 3$ )	Waveguide or horn or mirror (quasi-optical)	Gyrotron	1.0 MW
Lower-hybrid range of frequencies (LHRF)	$f_{LH}$ ~(2.5–8.0) GHz	Waveguide array (grill)	Klystron	0.3–0.7 MW
Ion cyclotron range of frequencies (ICRF)	$f_{ci}, 2f_{ci}, 3f_{ci}$ 30–120 MHz	Loop arrays	Tetrode	2.5 MW
Alfvén wave	$f < f_{ci}$ 10–30 MHz	Loop arrays	Tetrode	2.5 MW

The key to understanding wave propagation and absorption is to derive the wave equation and the dielectric tensor of a magnetized plasma, either in the cold plasma limit, suitable for electromagnetic wave propagation, or in a hot plasma,

necessary for calculating absorption and to describe certain short wavelength electrostatic waves, called Bernstein waves. This can be derived easily for a homogeneous plasma in the localized approximation by assuming small amplitude (linearized) waves. The equations can be generalized to inhomogeneous plasmas either in the WKB approximation for wavelengths short compared to the scale lengths of inhomogeneities, or for wavelengths comparable to the dimensions of the plasma cross-section the differential equations must be solved exactly to arrive at the full wave treatment. We start with Maxwell's equations (in the SI system of units where  $c^2 = 1/\mu_0\epsilon_0$  with  $\mu_0, \epsilon_0$  being the permeability and permittivity of vacuum respectively):

$$\nabla \times \vec{E}_1 = -\frac{\partial \vec{B}_1}{\partial t} \quad (6.1)$$

$$\nabla \times \vec{B}_1 = \frac{1}{c^2} \frac{\partial \vec{E}_1}{\partial t} + \mu_0 \vec{j}_1 \quad (6.2)$$

Here the subscript 1 designates perturbed (RF wave field) quantities. Taking the curl of Eq. (6.1) and using Eq. (6.2), one obtains

$$\nabla \times \nabla \times \vec{E}_1 = -\left( \frac{1}{c^2} \frac{\partial^2 \vec{E}_1}{\partial t^2} + \mu_0 \frac{\partial \vec{j}_1}{\partial t} \right) \quad (6.3)$$

Fourier decomposing and assuming field perturbations of the form  $\exp[i(\vec{k} \cdot \vec{x} - \omega t)]$ , Eq. (6.3) can be rewritten as

$$\vec{N} \times \vec{N} \times \vec{E}_1 + \vec{K} \cdot \vec{E}_1 = 0 \quad (6.4)$$

where  $\vec{N} = c\vec{k} / \omega$  is the index of refraction and  $\vec{K}$  is the dielectric tensor defined as

$$\vec{E}_1 + \frac{i\vec{j}_1}{\epsilon_0\omega} = \vec{K} \cdot \vec{E}_1 \quad (6.5)$$

Here  $j_1$  is the current that flows in the plasma in response to the electric and magnetic fields and in particular

$$\vec{j}_1 = \sum_j n_{0j} q_j \vec{v}_{1j} \quad (6.6)$$

where  $n_{0j}$  is the unperturbed density of particle species  $j$ ,  $q_j$  is the charge ( $q_i = Z_i e$  for ions and  $q_e = -e$  for electrons) and  $\vec{v}_{1j}$  is the perturbed plasma fluid velocity. In particular, the perturbed velocity may be calculated from cold plasma fluid motion or in a hot plasma from kinetic theory. Combining the above, the dispersion relationship may be written in the following matrix form:

$$\begin{Bmatrix} K_{xx} - N^2 \cos^2 \theta & K_{xy} & K_{xz} + N^2 \cos \theta \sin \theta \\ K_{yx} & K_{yy} - N^2 & K_{yz} \\ K_{zx} + N^2 \cos \theta \sin \theta & K_{zy} - N^2 & K_{zz} - N^2 \sin^2 \theta \end{Bmatrix} \begin{Bmatrix} E_x \\ E_y \\ E_z \end{Bmatrix} = 0 \quad (6.7)$$

where  $K_{ij}$  are the components of the dielectric tensor in a Cartesian coordinate system with  $\vec{B}_0$  pointing in the  $z$  direction (often designated as the subscript  $\parallel$ —direction parallel to the total magnetic field),  $N_z = ck_z / \omega$ , where  $k_z = k \cos \theta$ , with  $\theta$  being the angle between  $\vec{k}$  and  $\vec{B}_0$ . Without loss of generality, we orient the  $x$  axis such that  $\vec{k}$  lies in the  $x$ - $z$  plane and  $k_x = k \sin \theta$  and  $k_y = 0$ .

Because of the complexity of Eq. (6.7), to understand the various types of waves that may propagate in the plasma it is best to proceed first from cold plasma fluid theory. In that case the perturbed fluid velocity is obtained from the momentum equation, which in the limit of cold plasma and in the absence of collisions is given by

$$n_{0j} m_j \frac{\partial v_{1j}}{\partial t} = n_{0j} q_j (\vec{E}_1 + \vec{v}_{1j} \times \vec{B}_0) \quad (6.8)$$

which is essentially the Lorentz force equation since the species equilibrium density cancels out. Taking the partial derivative with respect to time equal to  $-i\omega t$ , and combining Eqs (6.5–6.8) in the cold plasma limit, we obtain the dispersion relationship

$$\begin{Bmatrix} S - N^2 \cos^2 \theta & -iD & N^2 \cos \theta \sin \theta \\ iD & S - N^2 & 0 \\ N^2 \cos \theta \sin \theta & 0 & P - N^2 \sin^2 \theta \end{Bmatrix} \begin{Bmatrix} E_x \\ E_y \\ E_z \end{Bmatrix} = 0 \quad (6.9)$$

which has been written in the so-called Stix parameters [6.2],  $S$ ,  $L$ ,  $R$  and  $D$ , where

$$R = 1 - \sum_j \frac{\omega_{pj}^2}{\omega^2} \frac{\omega}{\omega + \Omega_j} \quad (6.10)$$

$$L = 1 - \sum_j \frac{\omega_{pj}^2}{\omega^2} \frac{\omega}{\omega - \Omega_j} \quad (6.11)$$

$$S = 1 - \sum_j \frac{\omega_{pj}^2}{\omega^2 - \Omega_j^2} \quad (6.12)$$

$$D = 1 - \sum_j \frac{\Omega_j}{\omega} \frac{\omega_{pj}^2}{\omega^2 - \Omega_j^2} \quad (6.13)$$

$$P = 1 - \sum_j \frac{\omega_{pj}^2}{\omega^2} \quad (6.14)$$

Here, R(L) stands for right (left) hand polarized components; and  $S = (R + L)/2$  stands for the sum and  $D = (R - L)/2$  for the difference and  $S^2 - D^2 = RL$ . Note that were we to use hot plasma kinetic theory, in the above we would replace the tensor components in Eq. (6.7) as follows:  $K_{zz} = P$ ,  $K_{xx} = K_{yy} = S$ ,  $iK_{xy} = -iK_{yx} = D$  and we would calculate  $K_{ij}$  from kinetic theory. In the above relationships  $\omega_{pj} = 2\pi f_{pj}$  is the angular plasma frequency of particle species  $j$ , namely  $\omega_{pj}^2 = n_j q_j^2 / m_j \epsilon_0$ , and  $\Omega_j = 2\pi f_c = q_j B / m_j$  is the angular cyclotron (gyro) frequency of species  $j$  (with  $q$  carrying the sign of the charge as defined earlier and  $f_c$  the cyclotron frequency). Note that from the second row of Eq. (6.9) we can obtain the polarization of the electric field perpendicular to the magnetic field, namely the relationship between  $E_x$  and  $E_y$

$$\frac{iE_x}{E_y} = \frac{N^2 - S}{D} \quad (6.15)$$

and we note that  $iE_x / E_y = +1(-1)$  corresponds to right (left) hand circularly polarized waves (RHCP or LHCP), while a constant not equal to unity gives an elliptically polarized wave.

The dispersion relationship is obtained by setting the determinant of the above matrix equation to zero, as this is the condition for non-zero solution of the various electric field components. In general, this predicts an 8th order equation for  $\omega$  in terms of  $k$ . We shall instead write the equation for  $N$ , the index of refraction and after some algebra obtain the following compact equation:

$$AN^4 - BN^2 + C = 0 \quad (6.16)$$

where

$$A = S \sin^2 \theta + P \cos^2 \theta \quad (6.17)$$

$$B = RL \sin^2 \theta + PS(1 + P \cos^2 \theta) \quad (6.18)$$

$$C = PRL \quad (6.19)$$

We note that  $N = 0$  when  $C = 0$  (which occurs when  $P$  or  $R$  or  $L$  equal zero). We shall see that this condition corresponds to a ‘‘cut-off’’ condition in wave propagation, a plasma layer where the RF wave is reflected and the wave is

evanescent beyond the cut-off layer. By manipulating terms, it can be shown that the solution to Eq. (6.16) may be written as

$$N^2 = \frac{B \pm F}{2A} \quad (6.20)$$

where

$$F^2 = (RL - PS)^2 \sin^4 \theta + 4P^2 D^2 \cos^2 \theta \quad (6.21)$$

This result can be made more explicit by substituting the appropriate terms and further manipulating them, until one finally obtains the Appleton–Hartree equation for high frequency electron modes (namely when the contribution of ions can be ignored):

$$N^2 = 1 - \frac{2\alpha\omega^2(1-\alpha)}{2\omega^2(1-\alpha) - \omega_{ce}^2 \sin^2 \theta \pm \omega_{ce} \Lambda} \quad (6.22)$$

where  $\alpha = \omega_{pe}^2 / \omega^2$  and  $\Lambda = [\omega_{ce}^2 \sin^4 \theta + 4\omega^2(1-\alpha)^2 \cos^2 \theta]^{1/2}$

From Eq. (6.22) we see that two distinct modes of propagation will be obtained, depending on the plus or minus sign in front of  $\Lambda$ . We shall return to this complex equation later for a proper interpretation in different limits of plasma parameters, in particular high frequency electron modes of propagation (the Appleton–Hartree equation). Note that for ionospheric wave propagation problems, sometimes electron–neutral collisions are included by using an effective mass  $m_{eff} = m_e(1 + i\nu_e / \omega)$  with  $\nu_e$  being the electron–neutral collision frequency. In case of applications to ECRH in fusion plasmas, Eq. (6.22) may be implemented in ray tracing codes and it is supplemented with spatial absorption calculations from hot plasma theory, including cyclotron damping and relativistic effects.

Another important result can be obtained by manipulating the terms of Eqs (6.16–6.19), upon which the dispersion relation can be cast in the following transparent form:

$$\tan^2 \theta = \frac{-P(N^2 - R)(N^2 - L)}{S(N^2 - RL/S)(N^2 - P)} \quad (6.23)$$

We see that particularly simple results are obtained in the limit of perpendicular propagation, namely for  $\tan^2 \theta = \infty$  or  $\cos^2 \theta = 0$ , when we have:

$$N_{\perp}^2 = RL/S \quad (\text{X-mode or extraordinary mode of propagation}) \quad (6.24)$$

or

$$N_{\perp}^2 = P \quad (\text{O-mode or ordinary mode of propagation}) \quad (6.25)$$

We see that the X-mode, an elliptically polarized wave, has a cut-off for  $R = 0$  (right hand cut-off) or  $L = 0$  (left hand cut-off) and has a resonance at

$S = 0$  (hybrid resonances, a result of the perpendicular dielectric response as we shall see later in this chapter). The O-mode, a linearly polarized wave, has a cut-off at  $P = 0$ , which corresponds to electron plasma oscillations at the frequency  $\omega = \omega_{pe}$ , where the density  $n = n_{crit}$ . The wave does not penetrate the overdense region, where  $n > n_{crit}$ . For propagation at an angle, the cut-off densities are lower than that of perpendicular propagation, and by assuming a uniform magnetic field and density in one direction, say the  $z$  direction,  $N_z$  is conserved by Snell's Law and the modes obtained are called the QT-X (quasi-transverse X) or QT-O (quasi-transverse O) mode and the cut-offs can be readily estimated. In general, modern plasma physics often uses ray tracing codes to predict wave propagation in toroidal geometry.

In the limit of parallel propagation  $\tan^2 \theta = 0$  or  $\sin^2 \theta = 0$  and we have

$$N_{\parallel}^2 = R \quad (6.26)$$

or

$$N_{\parallel}^2 = L \quad (6.27)$$

From Eq. (6.15), we find that Eqs (6.26) and (6.27) correspond to the right and left hand circularly polarized wave, respectively. These waves have cut-offs if  $R = 0$  or  $L = 0$ , respectively. On the other hand, the waves have resonances at the appropriate cyclotron frequencies, namely  $N_{\parallel}^2 = \infty$  at  $\omega = \omega_{ci}$  for  $N_{\parallel}^2 = L$  and  $N_{\parallel}^2 = \infty$  at  $\omega = \omega_{ce}$  for  $N_{\parallel}^2 = R$ . Thus, these resonances occur when the circularly polarized wave fields rotate in the same direction as the appropriate resonant charged particles, and thus the perturbed fluid velocities  $v_{1x}$ ,  $v_{1y}$ . Here  $\omega_{ci}$  and  $\omega_{ce}$  designate the magnitudes of the cyclotron frequencies.

There is one more physically important limit of Eq. (6.23) and that is when the index of refraction approaches infinity or at least large values as compared to  $P$ ,  $R$ ,  $L$ , or  $RL/S$ , corresponding to short wavelengths. In that case Eq. (6.23) reduces to

$$\tan^2 \theta = -P / S \quad (6.28)$$

or

$$S \sin^2 \theta + P \cos^2 \theta = 0 \quad (6.29)$$

which is the condition for resonance for a general direction of wave propagation. This condition corresponds to excitation of nearly electrostatic (longitudinal) waves in the cold plasma limit, sometimes called resonance cones [6.6]. We shall discuss this in Section 6.2.2 in connection with the excitation of lower hybrid waves [6.7], which are a particular form of resonance cones and are most important for current drive applications.

Another important form of the wave equation is obtained by considering the typical experimental situation in toroidal geometry, with a dominant toroidal

magnetic field, such that we may consider the plasma to be approximately homogeneous in the toroidal direction, which we designate by the parallel ( $\parallel$ ) direction. Thus, waves may be launched by an antenna which fixes the index of refraction parallel to the magnetic field  $N_{\parallel}$  and wave propagation occurs in the radial and poloidal direction, which we designate by the perpendicular direction ( $\perp$ ), or the index of refraction  $N_{\perp}$ . Thus, we may rewrite Eq. (6.16) in the following form:

$$AN_{\perp}^4 + BN_{\perp}^2 + C = 0 \quad (6.30)$$

where  $A = S$ ,  $B = (N_{\parallel}^2 - S)(S + P) + D^2$  and  $C = P[(N_{\parallel}^2 - S^2) - D^2]$ . This dispersion relation has two solutions, corresponding to the slow and fast waves

$$N_{\perp}^2 = \frac{-B \pm (B^2 - 4AC)^{1/2}}{2A} \quad (6.31)$$

Let us now discuss the results obtained above in greater detail. In general, the best way to characterize cold plasma waves is with the help of the CMA diagram [6.2] (abbreviation for Clemmow, Mullay and Allis, who invented and perfected this diagram). A reduced form of the CMA diagram is displayed in Fig. 6.2. The vertical axis corresponds to the magnetic field normalized to the frequency, namely  $\omega_{ce} / \omega$ , and the horizontal axis corresponds to density, again normalized to frequency, namely  $\omega_{pe}^2 / \omega$ . The figure is subdivided into 13 regions (not all shown here), each separated by R and L cut-offs, the upper and lower hybrid resonances (in Eq. (6.12), set  $S = 0$ ), the  $P = 0$  cut-off ( $\omega = \omega_{pe}$ ) and the  $\omega_{ce}$ ,  $\omega_{ci} = \Omega_i$  lines ( $m_i / m_e$ , i.e.  $M / m$  line). In each of the 13 regions a small diagram is inserted (ellipse or figure "8") which corresponds to the tip of the phase velocity vector which rotates at an angle relative to the magnetic field, which is assumed to be pointing in the vertical direction. The magnitude of this vector is proportional to the magnitude of the phase velocity. Thus, when a figure is inside another, the outer wave corresponds to the fast wave (FW) solution of the typically fourth order equation (see Eq. (6.20) or Eq. (6.31), where we pointed out that solutions come in distinct pairs) and the inside figure corresponds to the slow wave (SW) solution. Furthermore, the figures show how the L or R waves propagating parallel to the magnetic field transform continuously into an X or O wave propagating perpendicular to the magnetic field, as the angle of propagation is varied. Waves of the figure "8" type do not propagate at right angles to the direction which corresponds to the top of the "8". Note that the O-mode propagates only at densities below the critical density  $n_{crit}$ . The left hand circularly polarized mode propagates only to the left of the L cut-off. One can think of this diagram as a plasma wave pond: a wave generator located at the centre of the phase front figures would send out waves with phase fronts corresponding to the shape of the little figures. Finally, it should

be noted that electrostatic (longitudinal) waves whose existence usually depends on finite temperature (e.g. acoustic waves, Bohm–Gross or Langmuir waves, and Bernstein waves [6.2] or cold lower hybrid waves [6.6, 6.7]), do not appear on this diagram.

The way this diagram can be used is to follow the ray path all the way from the edge of the plasma (vacuum region) to the interior, and vice-versa. One can also choose the appropriate magnetic field variation along the path of propagation, assuming slow variations (in the WKB sense), and check for accessibility to a resonance layer (cyclotron or hybrid, where the wave energy is expected to be absorbed for the appropriate waves (lower hybrid waves) propagating in the middle of the diagram (Fig. 6.2).

We shall now describe the waves of interest for heating and driving currents in a magnetized plasma. We shall take the appropriate limits of the above equations and then relate them to the CMA diagram, which can be used to understand accessibility, one of the most important applications of cold plasma wave theory. The absorption of each wave will be described later, using hot plasma wave theory. Beyond this point only waves of interest for applications to heating, or driving currents in fusion plasmas, will be described, starting with electron cyclotron waves used for electron cyclotron heating (ECH), the easiest regime to understand since the ion response can be neglected.

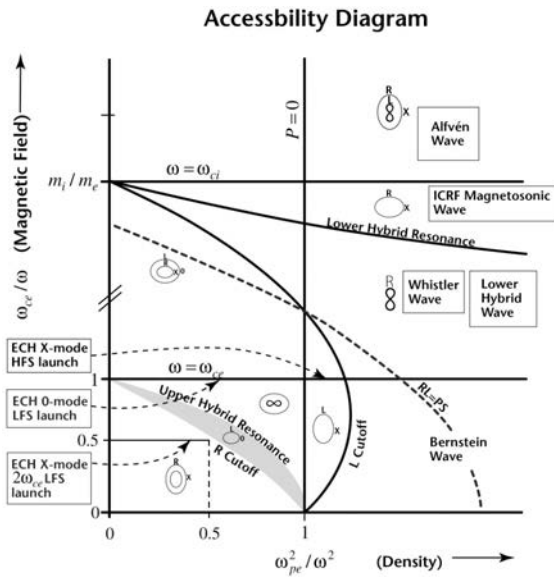


FIG. 6.2. Clemmow–Mullaly–Allis (CMA) diagram for electromagnetic wave propagation in a cold plasma (after Ref. [6.2]). Accessibility path of ECH waves, and location of the Alfvén, ion cyclotron (fast magnetosonic) and lower hybrid waves are shown on the reduced CMA diagram. Three dashed lines on the bottom left side with the arrows on the ends indicate the ray path.

### 6.2.1. Electron cyclotron waves

Electron cyclotron waves propagate at frequencies near the electron cyclotron frequency or its low order harmonics and they may be launched externally with a waveguide horn or mirror from outside the plasma. In general, wave propagation is at an angle to the magnetic field and may be determined by ray tracing using the Appleton–Hartree dispersion relationship Eq. (6.22). For near perpendicular launch or for electron cyclotron current drive, relativistic effects must be taken into account since the resonance condition is modified to

$$\omega - l\omega_{ce} / \gamma - k_{\parallel} v_{\parallel} = 0 \quad (6.32)$$

where  $\gamma$  is the relativistic mass correction factor  $\gamma = 1 / (1 - v^2 / c^2)^{1/2}$  and  $l$  is the harmonic number.

To understand wave propagation and accessibility to the cyclotron resonance layer or its harmonic, it is useful to examine wave propagation from the plasma edge to the plasma core using the CMA diagram. Since in general the wave is launched at an angle, it may be assumed that at the edge of the plasma the wave is characterized by a finite value of  $N \cos \theta$ , or  $N_{\parallel}$ , which remains approximately constant by Snell's Law. As the wave propagates towards the centre of the plasma column, its  $n_{\perp}$  varies according to the variation of the magnetic field and density, depending on the polarization of the injected wave at the edge of the plasma. Following a ray path on the CMA diagram, we see that for launching from the low field side of the torus, the X-mode is not accessible to the  $\omega = \omega_{ce}$  layer since it is reflected back from the R cut-off as long as  $\omega > \omega_{ce}$ . However, the wave would be accessible from the high field side (inside launch) as long as the density is not so high that the wave would be running into the L cut-off. Although studied in early tokamak experiments, inside launch is not practical in large fusion devices. Therefore, for all practical purposes, ECH and/or ECCD (electron cyclotron current drive) is usually carried out by the fundamental O-mode or second harmonic X-mode with outside (low field side) launch. Then for  $k_{\parallel} = 0$  the accessibility is given approximately by the following cut-off condition:

- (1) O-mode cut-off:  $\omega = \omega_{pe}$ , which corresponds to a density of  $n_e [10^{20} \text{ m}^{-3}] = 0.1 B[\text{T}]^2$ , if  $\omega_{pe} = \omega_{ce} = \omega$ , namely at 5.0 T, the accessible maximum density is  $2.5 \times 10^{20} \text{ m}^{-3}$  and the corresponding frequency is  $f_{ce} [\text{GHz}] = 28 B[\text{T}] = 140 \text{ GHz}$ .
- (2) X-mode second harmonic accessibility follows from Eq. (6.26), namely  $R = 0$ , which gives  $\omega_R$  from Eq. (6.10) as follows:

$$\omega_R^2 - \omega_R \omega_{ce} - \omega_{pe}^2 = 0 \quad (6.33)$$

and from Eq. (6.11),  $L = 0$  gives  $\omega_L$ :

$$\omega_L + \omega_L \omega_{ce} - \omega_{pe}^2 = 0 \quad (6.34)$$

so that at  $\omega = l\omega_{ce}$ , with  $l \leq 3$  the cut-off density is  $\omega_{pe}^2 / \omega_{ce}^2 = l!$ . Thus, at  $\omega = 2\omega_{ce}$  accessibility to  $\omega_{pe}^2 / \omega_{ce}^2 = 2$  is possible, but at the expense of higher frequency gyrotron power sources, which is practical only for lower magnetic fields ( $\leq 3$  T). For injection at an angle, we could use the formalism of Eq. (6.31) and the O- and X-modes could be modified and accessibility obtained (the QT-O and QT-X mode of propagation, see Ref. [6.2]). In general, finite values of  $N_{\parallel}$  reduce the maximum density for accessibility. However, unless the angle is large, the reduction is not serious. In modern work, ray tracing is used extensively and results will be presented later in the experimental section.

The wave energy absorption can be calculated from hot plasma kinetic theory [6.2–6.4]. While the real part of the dispersion relationship is obtained from cold plasma wave theory as presented above, the spatial damping rate is obtained by integrating in space the imaginary part  $k_{Im}$  as the wave propagates through the cyclotron frequency or its harmonics in the inhomogeneous magnetic field of a tokamak or a stellarator (here  $k_{Im} = \omega_{Im} / v_{gr}$  and  $\omega_{Im}$  is the imaginary part of the frequency and  $v_{gr}$  is the group velocity). The power transmission coefficient is  $T_r = \exp(-2\eta)$ , and the absorption is given by [6.2]

$$A_b = 1 - T_r = 1 - \exp(-2\eta) \quad (6.35)$$

where  $\eta = \int_{-\infty}^{\infty} k_{Im}(x) dx$ . We shall now give results of such absorption coefficients at propagation angles at an angle to the normal to the magnetic field, the angle of incidence being defined by the parallel component of the index of refraction  $N_{\parallel}$ . The optical depths predicted by the non-relativistic theory [6.8] for absorption at the fundamental resonance in a plane-stratified plasma are given by the formula

$$2\eta = \frac{4\pi^2 R T_e N_{\parallel}^2 \left[ (1 - \alpha/2 - N_{\parallel}^2)(1 - \alpha) - N_{\perp}^2 \right]^2}{\alpha \lambda mc^2 N_{\perp} \left[ (1 - \alpha - N_{\perp}^2)^2 + (1 - \alpha)N_{\parallel}^2 \right]} \quad (6.36)$$

where  $\alpha = \omega_p^2 / \omega^2$ ,  $T_e$  is the electron temperature,  $R$  is the scale length of the magnetic field (major radius in a tokamak),  $\lambda = 2\pi c / \omega$  is the free space wavelength of the incident radiation and  $mc^2$  is the rest energy of the electron. The perpendicular index of refraction is given by the Appleton–Hartree dispersion

$$N_{\perp}^2 = \left\{ 3 - 2\alpha - N_{\parallel}^2 \pm \left[ (1 + N_{\parallel}^2)^2 - 4\alpha N_{\parallel}^2 \right]^{1/2} \right\} / 2 \quad (6.37)$$

where the + (–) sign refers to the O-mode (X-mode). The plasma parameters are to be evaluated at resonance, since they have been expanded in a Taylor series

about the resonant surface and only the terms linear in the electron temperature are included. The strong coupling expansion used for this calculation was first formulated in Refs [6.9, 6.10]. For the calculation of the imaginary part of the wave vector for constant angle inside the plasma, see Refs [6.11–6.13].

For normal incidence, the relativistic line broadening is dominant. The region of validity of the theory is limited by the inequality  $\omega_p^2 / \omega^2 \gg 2^{3/4} N_{\parallel} (T_e / mc^2)^{1/2}$  and should not be applied to very low density plasmas. Simplified approximate formulas for absorption at the fundamental resonance can be derived from the above results and for  $\alpha < 1$  we obtain [6.14]

$$2\eta_{\text{O}} \approx \pi^2 \frac{R}{\lambda} \frac{T_e}{mc^2} \frac{\alpha(1-\alpha)^{1/2}}{1 + N_{\parallel}^2(0.5 - \alpha)} \quad (6.38)$$

and for the X-mode

$$2\eta_{\text{X}} \approx \pi^2 \frac{R}{\lambda} \frac{T_e}{mc^2} N_{\parallel}^2 \frac{(2-\alpha)^{3/2}(1+\alpha)^2}{\alpha} \quad (6.39)$$

We see that absorption for X-mode increases with the angle of incidence and it usually leads to a tail formation since injection only from the high field side is accessible. This method was tested in the 1970s on small tokamaks (Versator II, for example).

Because of good accessibility (i.e. right hand cut-off density  $n_{RHCO} = 2n_{crit}$ ) and strong absorption, of great interest in present day experiments is the second harmonic X-mode at magnetic fields less than 3 T, where high power gyrotrons are available now at frequencies up to 170 GHz. The absorption strength is comparable to that of fundamental O-mode (also finite Larmor radius absorption mechanism). Second harmonic ECH has been extensively tested in the 1970s on the T-10 tokamak by Alikaev et al. [6.15, 6.16]. More recent results will be discussed from DIII-D, ASDEX-Upgrade and TCV in the experimental section, to follow later. The absorption for the second harmonic O-mode is smaller than that of X-mode by a factor  $T_e/mc^2$  and in this case relativistic effects must be invoked for an accurate calculation of the absorption [6.17]. The second harmonic optical depth for the X-mode at normal incidence is [6.18, 6.19]

$$2\eta_{\text{X}} \approx 4\pi^2 \frac{R}{\lambda} \frac{T_e}{mc^2} \frac{\alpha(3-2\alpha)^{5/2}(1-2\alpha)^{1/2}}{(3-4\alpha)^{5/2}} \quad (6.40)$$

The O-mode at normal incidence is also of one higher order in  $(T_e^2 / m_e^2)c^2$  [6.18, 6.19]:

$$2\eta_{\text{O}} \approx 4\pi^2 \frac{R}{\lambda} \frac{T_e^2}{m^2 c^4} \alpha(1-\alpha)^{3/2} \quad (6.41)$$

The second harmonic X-mode absorption at normal incidence was verified in Refs [6.20–6.22]. More recent results will be summarized later. For

normal incidence of the O-mode, we need relativistic theory since relativistic broadening dominates Doppler broadening, namely  $v^2/2c^2 \geq k_{\parallel}v_{\parallel}/\omega$  or  $N_{\parallel} < (T_e/m_e c^2)^{1/2}$  [6.18, 6.23, 6.24]. The relativistic resonance condition Eq. (6.32) shows that there are no resonant particles on the low magnetic field side ( $\omega > \omega_{ce}(r)$ ) for near-perpendicular injection ( $N_{\parallel} \rightarrow 0$ ) [6.17]. Once the wave passes through the cyclotron resonance layer, absorption is expected to be complete in a very short distance. The absorption for fundamental O-mode can be estimated from the relativistic formula given by [6.23] (and references therein) for strong absorption

$$N_{\perp \text{Im}} = \frac{1}{2^{3/2}} \left(1 - \frac{\omega_p^2}{\omega_{ce}^2}\right)^{1/2} \left(\frac{\omega_p^2}{\omega_{ce}^2}\right) \frac{[-F''_{7/2}(Z_1)]}{|G_{7/2}|G'_{7/2} + |G_{7/2}|^{1/2}} \quad (6.42)$$

where

$$G_{7/2} = G'_{7/2} + G''_{7/2} = 1 + \frac{1}{2} \frac{\omega_p^2}{\omega_{ce}^2} F_{7/2}(Z_1) \quad (6.43)$$

$$Z_1 = \frac{(\omega - \omega_{ce}) m_e c^2}{\omega T_e} \quad (6.44)$$

and  $F_{7/2} = F'_{7/2} + F''_{7/2}$  is the relativistic form of the plasma dispersion function

$$F_q(Z) = -i \int_0^{\infty} \frac{\exp(izr)}{(1-ir)^q} dr \quad (6.45)$$

$$\text{Im}(z) > 0 \quad (6.46)$$

Prime and double prime quantities refer to the real and imaginary parts, respectively. For example, in a typical reactor regime, for  $T_e = 10$  keV, we get maximum damping at  $\Delta r \approx 5\text{--}10$  cm away from resonance (on the HFS) where  $Z_1 \approx -2.5$  and  $k_{\perp \text{Im}} \approx 2.8 \text{ cm}^{-1}$  for  $\omega_p^2/\Omega_e^2 = 0.8$ . Numerical plots of these functions can be found in Refs [6.23, 6.24].

However, it turns out that second harmonic X-mode absorption is due to finite Larmor radius effects (similar to the O-mode fundamental resonance absorption) and although the line shape would change, relativistic effects do not alter the total absorption per pass and Eq. (6.40) remains valid [6.25]. The O-mode optical depth is large enough for complete absorption at normal incidence with the parameters of present day tokamaks. Since the O-mode can be launched from the outboard side of tokamaks with much more convenient access, it is the preferred mode for bulk heating of electrons. In ITER it is envisaged that 170 GHz gyrotrons will provide heating and current drive at a magnetic field of 5–6 T using O-mode at the fundamental electron cyclotron resonance. Finally,

we note that predictions by quasi-linear theory (see below after the ion cyclotron resonance heating section) is more informative, and one finds that absorption and heating is almost completely in the perpendicular direction, even for the O-mode at perpendicular incidence, even though the wave electric field is parallel to the magnetic field. Nevertheless, it turns out that in practice, in large tokamaks at reactor relevant densities ( $n_e \approx 10^{20} \text{ m}^{-3}$ ) the distribution function remains nearly Maxwellian due to the strong collisional coupling of electrons and the relatively weak RF diffusion coefficient, except perhaps in relatively low density, high RF power density experiments.

There is one more possible scenario to heat and drive current in overdense plasmas such as in low field spherical tokamaks (STs) where  $1 \ll \omega_{pe}^2 / \omega_{ce}^2$  and that takes advantage of electron Bernstein waves (EBWs), which are quasi-electrostatic waves [6.26, 6.27]. These waves can be excited by conversion of O-mode propagation at an angle to the magnetic field, leading to mode conversion to the X-mode in the plasma interior, and then further mode conversion to EBW at the upper hybrid layer. In spite of the stringent launching geometry, there have been some initial promising results obtained in small devices. An excellent review article has been written on this topic by H.P. Laqua [6.28] and the interested reader is referred to this article for details.

### 6.2.2. Lower hybrid wave propagation and accessibility

The second frequency regime of interest is that of the so-called lower hybrid range of frequencies (see Fig. 6.3). In the usual case of  $\omega_{pi}^2 \gg \omega_{ci}^2$ ,  $\omega_{pe}^2 \approx \omega_{ce}^2$ , the lower hybrid frequency  $\omega_{LH}$  is near the ion plasma frequency  $\omega_{pi} = (m_e / m_i)^{1/2} \omega_{pe}$  and is a mixture of electron and ion contribution. Taking the limit  $\cos \theta = 0$  in Eq. (6.28) we get  $S = 0$  or

$$\omega_{LH}^2 = \frac{\omega_{pi}^2}{(1 + \omega_{pe}^2 / \omega_{ce}^2)} \quad (6.47)$$

where  $\omega_{ci}^2 = \omega_{ce}^2 (m_e / m_i)$  was neglected in comparison with  $\omega_{pi}^2$ . The dispersion relationship for lower hybrid waves in the cold plasma is obtained from Eq. (6.28), by multiplying the equation with  $k^2 = k_{\perp}^2 + k_{\parallel}^2$ , and in the present limit one obtains

$$\omega = \omega_{LH} \left( 1 + \frac{k_{\parallel}^2}{k^2} \frac{m_i}{m_e} \right)^{1/2} \quad (6.48)$$

where we also assumed  $k_{\parallel}^2 \ll k_{\perp}^2$ , valid in the plasma core but not at the plasma edge. This dispersion relation predicts that  $k \rightarrow k_{\perp} \rightarrow \infty$  at  $\omega = \omega_{LH}$  if  $k_{\parallel}$  is fixed at the surface by a slow-wave structure. This result has been verified in linear machine experiments in the 1970s by Bellan and Porkolab [6.7]. It was also

shown that the wave energy propagates along trajectories of the group velocity which define so-called “resonance cones” [6.6], emanating from the launching structure at the plasma edge (phase array waveguides, or “grill”, see Fig. 6.3).

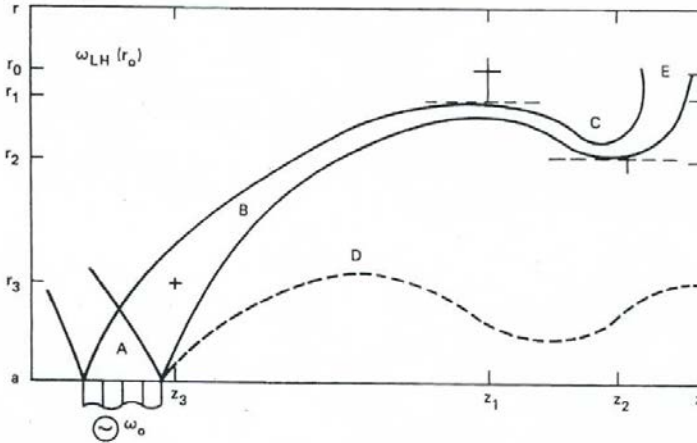


FIG. 6.3. Penetration of lower hybrid waves into an inhomogeneous plasma. Regions A, B, D correspond to the cold resonance cone regimes, region C to the mode conversion region, and E to mode converted (hot ion plasma or Bernstein) waves;  $\omega_0$  is the RF source frequency [6.1]. Reprinted from Ref. [6.1]. Copyright (2011), with permission from Ref. Elsevier.

The resonance cone angle is defined by the trajectory of the group velocity, and it is perpendicular to the phase velocity as given by Eq. (6.48). Thus, the cone angle is

$$\tan^2 \theta = (m_i / m_e)(\omega^2 - \omega_{\text{LH}}^2) / \omega_{\text{LH}}^2 \quad (6.49)$$

In Fig. 6.3 it is assumed that the plasma is uniform in the  $z$  direction and the density is increasing with radius from the edge ( $a$ ) to the plasma centre ( $r_0$ ) and  $k_{\parallel}$  (i.e.  $N_{\parallel}$ ) is fixed by the antenna array phasing. Note that the theory breaks down at  $r_1(z_1)$  where  $k_{\perp}^2$  approaches infinity and finite temperature effects must be taken into account. Owing to their low  $N_{\parallel}$ , rays D are not accessible (see Fig. 6.3) as explained below. Note that in the toroidal direction the path of the wave penetration is long, and in particular Eq. (6.49) shows that  $L_z \sim a(m_e / m_i)^{1/2}$  (where  $a$  is the plasma radius and  $L_z$  is the path length along the magnetic field). Since the electric field strengths are strong ( $E_x \approx 10 \text{ kV} \cdot \text{cm}^{-1}$ ), non-linear effects in the outer plasma layers could impact the lower hybrid or “slow wave” propagation. For example, parametric instabilities, soliton formation and scattering by drift-wave fluctuations may occur [6.29–6.32]. Although these processes have been observed in experiments, at present there is no clear understanding of these phenomena and therefore usually linear theory is assumed to hold as long as the frequency is well above the lower hybrid frequency.

To describe wave propagation, accessibility and mode conversion at the lower hybrid layer in an inhomogeneous plasma column, we must keep electromagnetic terms from Eq. (6.31). Then, in the lower hybrid regime for  $B^2 \ll 4AC$  we have

$$N_{\perp s}^2 \approx -\frac{P}{S}(N_{\parallel}^2 - S) - \frac{D^2}{S} \quad (6.50)$$

$$N_{\perp f}^2 \approx \frac{D^2 - (N_{\parallel}^2 - S)^2}{(N_{\parallel}^2 - S) + D^2 / P} \quad (6.51)$$

where the subscripts  $s$  and  $f$  refer to the slow and fast branches and  $P$ ,  $S$  and  $D$  were defined earlier. In particular, in the lower hybrid limit of plasma parameters, we have

$$S = 1 + \frac{\omega_{pe}^2}{\omega_{ce}^2} - \frac{\omega_{pi}^2}{\omega^2} \quad (6.52)$$

$$P = 1 - \frac{\omega_{pe}^2}{\omega^2} \quad (6.53)$$

$$D = \frac{\omega_{pe}^2}{\omega \omega_{ce}} \quad (6.54)$$

Resonance for the slow wave ( $n_{\perp s}^2 \rightarrow \infty$ ) exists at the location where  $S = 0$  or

$$\frac{\omega_{pe}^2}{\omega_{ce}^2} = \left( \frac{\omega_{ce} \omega_{ci}}{\omega^2} - 1 \right)^{-1} \quad (6.55)$$

that is  $\omega^2 = \omega_{LH}^2$ . In the limit  $n_{\parallel}^2 \gg 1 + 2\omega_{pe}^2 / \omega_{ce}^2 - \omega_{pi}^2 / \omega^2 \approx 0(1)$  the slow wave is nearly electrostatic and is referred to as the lower hybrid (Eq. (6.48)).

If  $B^2 > 4AC$ , the solution of the dispersion relation predicts two distinct branches, as shown in Eqs (6.50) and (6.51), and in Fig. 6.4: a slow wave and a fast wave. In general, these roots are distinct as long as  $B^2 > 4AC$ . However, for a sufficiently low value of  $N_{\parallel}$ , the condition  $B^2 = 4AC$  may be satisfied at two distinct values of the density,  $n_e^-$  and  $n_e^+$ , which are both lower than the density at the lower hybrid resonance layer. At these critical densities, the slow and fast modes coalesce, as illustrated in Fig. 6.4. The critical densities are given by the relationship

$$\omega_{pi} / \omega = N_{\parallel} g \pm \left[ 1 + N_{\parallel}^2 (g^2 - 1) \right]^{1/2} \quad (6.56)$$

where  $g^2 = \omega^2 / \omega_{ce} \omega_{ci}$ . Equation (6.56) specifies the minimum value of  $N_{\parallel}$  required for a wave packet to propagate to a density and magnetic field as specified by  $\omega_{pi}(n)$  and  $g(B)$ . The minus sign corresponds to the density  $n_e^-$  (see Fig. 6.4) and is relevant for electron Landau heating and thus current drive applications. The plus sign corresponds to  $n_e^+$ , the mode trapped in the plasma core, and is of relevance only for conversion to the finite temperature ion plasma wave and applications to ion heating. In particular, if we wish to have accessibility all the way to the lower hybrid resonance layer and heat ions, Eq. (6.56) reduces to  $N_{\parallel}^2 = 1 / (1 - g^2)$  and if the lower hybrid resonance layer is in the plasma, accessibility to it is given by

$$N_{\parallel}^2 > 1 + \omega_{pe}^2 / \omega_{ce}^2 \Big|_{\omega=\omega_{LH}} \quad (6.57)$$

This relation was first obtained in Ref. [6.33]. Since typically  $\omega_{pe}^2 \approx \omega_{ce}^2$ , we see that  $N_{\parallel crit} \approx 1.4$  and a slow wave structure is necessary to launch a wave from the surface of the plasma column [6.7, 6.34].

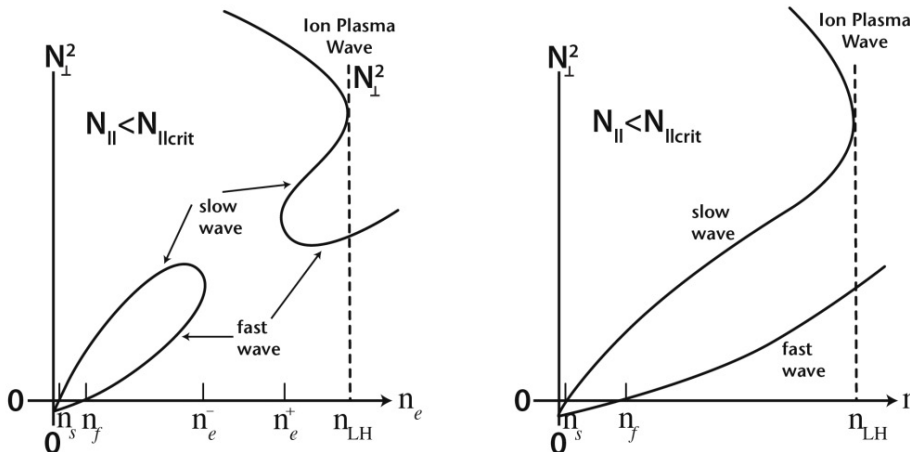


FIG. 6.4. Accessibility diagram of lower hybrid waves for two different values of  $N_{\parallel}$ . Left: The  $N_{\parallel}$  is too low for accessibility to the lower hybrid layer; however, accessibility to the slow-fast wave mode conversion layer ( $n_e^-$ ) is available for electron Landau absorption and thus current drive applications. The  $n_s$  is the critical density, where the slow wave is cut off, namely  $\omega = \omega_{pe}$ . Right: The  $N_{\parallel}$  is high enough to provide accessibility to the lower hybrid resonance layer and thus mode conversion to ion plasma waves and ion Landau absorption [6.35].

It is worth noting that near the edge of the plasma, Eq. (6.50) reduces to  $N_{\perp}^2 = (1 - \omega_{pe}^2 / \omega^2)(1 - N_{\parallel}^2)$  and since  $1 < N_{\parallel}^2$ , propagation is only possible if  $1 < \omega_{pe}^2 / \omega^2$ , or the plasma has to be “overdense” (see Fig. 6.4, density  $n_s$ ). This

can present difficulty in launching waves with low scrape-off layer densities, and will be discussed in Section 6.3.4.

When the lower hybrid resonance does not exist in the plasma ( $\omega > \omega_{\text{LH}}$ ), electron heating and/or current drive may still take place. In this case, the condition for wave penetration to the maximum density is still given by Eq. (6.56), if  $g^2 < 1$  and  $\omega_{pi}^2(0) / \omega^2 > g^2 / (1 - g^2)$ . Otherwise, accessibility is determined by the negative root of Eq. (6.56), and the critical value of  $n_{\parallel}$  needed for the slow wave to penetrate to a given density without mode conversion to the fast wave is

$$n_{\parallel}^2 = \omega_{pe}^2 / \omega_{ce}^2 + (1 + \omega_{pe}^2 / \omega_{ce}^2 - \omega_{pi}^2 / \omega^2)^{1/2} \quad (6.58)$$

For applications to RF current drive (which is of the greatest interest in connection with lower hybrid waves), absorption by electron Landau damping is of importance, which occurs due to interaction parallel to the confining magnetic field [6.36]. We note that Landau damping is the most important collisionless damping process occurring in high temperature plasmas and is due to collective effects associated with phase mixing of waves and interaction of waves with a distribution of particle velocities. Physically, Landau damping occurs since particles moving with velocities slightly less than the phase velocity of the wave are accelerated by the wave, and particles moving slightly faster than the wave are decelerated by the wave. Thus, if there are more particles moving slightly slower than the wave than faster, net energy is transferred from the wave to the particles, and the wave is damped [6.37]. Such is the case for the Maxwellian velocity distribution. In the presence of even rare collisions, the absorbed energy is thermalized (i.e. the plasma is heated). We also note that electron Landau damping of lower hybrid waves occurs when  $\omega / k_{\parallel} \sim 3v_{th,e}$  [6.38, 6.39]. Specifically, one relies on the fact that  $T_e$  peaks at the centre of the plasma column, and if the  $k_{\parallel}$  spectrum is such that in the outer layers of the plasma

$$3v_{th,e} \ll \omega / k_{\parallel} \quad (6.59)$$

and near the plasma core

$$\frac{\omega}{k_{\parallel} v_{th,e}} \leq 3 \quad (6.60)$$

then absorption by electron Landau damping occurs near the centre. The damping rate can be obtained by adding the imaginary part due to Landau damping to the electrostatic dispersion relationship Eq. (6.48), and is given by the finite  $T_e$  correction as

$$S \frac{k_{\perp}^2}{k^2} + P \frac{k_{\parallel}^2}{k^2} + i\epsilon_{\text{Im}} = 0 \quad (6.61)$$

where  $S = 1 + \omega_{pe}^2 / \omega_{ce}^2 - \omega_{pi}^2 / \omega^2$ ,  $P = 1 - \omega_{pe}^2 / \omega^2$ ,  $k_{\parallel}^2$  is fixed by the antenna,  $k_{\perp}^2$  is complex and its imaginary part (damping term) is obtained from [6.7, 6.39]

$$\varepsilon_{\text{Im}} = \frac{\pi^{1/2}}{k^2 \lambda_D^2} \frac{\omega}{k_{\parallel} v_{th,e}} \exp\left(-\frac{\omega^2}{k_{\parallel}^2 v_{th,e}^2}\right) \quad (6.62)$$

where  $\lambda_D^2 = v_{th,e}^2 / 2\omega_{pe}^2$  is the Debye length (squared) and  $v_{th,e} = (2T_e / m_e)^{1/2}$ .

One should note that for an accurate treatment of Landau damping one should include the so-called quasi-linear effects; namely, the deformation of the particle distribution function due to the expected strong electric fields must be considered in a self-consistent manner, balancing RF diffusion versus collisional drag, leading to net momentum input parallel to the magnetic field in the case of an asymmetrically launched wave spectrum [6.39]. Significant electron heating should take place if [6.38–6.40]

$$N_{\parallel} \approx \frac{\theta}{\sqrt{T_e}} \quad (6.63)$$

where  $T_e$  is the electron temperature in keV and  $\theta \approx 5$  for linear Landau damping and  $\theta \approx 7$  for quasi-linear damping. Subsequently, resonant electrons diffuse in velocity space to higher energies (as determined by the spectrum of waves) to create a suprathermal electron tail. Thus, we see that for a given value of  $N_{\parallel}$  (usually determined by accessibility) quasi-linear Landau damping allows wave penetration to higher temperatures than linear Landau damping due to the diffusion of resonant electrons by the RF waves. If the antenna launches a unidirectional spectrum with respect to the magnetic field, the suprathermal electron tail is preferentially populated in the direction of wave propagation, and an electron current may be generated in the toroidal direction; this is the principle of RF current drive [6.40].

Regarding the ion plasma wave, in high temperature plasmas it is not accessible and we shall not discuss it here. The interested reader is referred to the extensive literature describing the mode conversion process to such waves [6.2, 6.3, 6.7]. From a practical point of view, there is a competition between accessibility and Landau absorption and we find that for reactor grade plasmas for  $\omega_{pe}^2 \approx \omega_{ce}^2$ , the accessible  $N_{\parallel} \approx 1.8$  and the electron Landau absorption limit is about 12 keV, which limits LH wave penetration slightly beyond the top of the pedestal in an H mode plasma. This is fortuitous since alpha particles would absorb LH waves in the core of a burning plasma.

### 6.2.3. Ion cyclotron wave propagation and accessibility

The ion cyclotron wave, often called the “magnetosonic wave“, or simply the “fast wave” (FW) has been used successfully to heat plasmas for decades [6.2]. Note that on the CMA diagram (Fig. 6.2) this is the R-X wave, which propagates across the ion cyclotron resonance in a single ion species plasma without significant absorption. In contrast, the slow “ion cyclotron wave”, which is an extension of the shear Alfvén wave, is left hand circularly polarized and is absorbed at the ion cyclotron frequency as it propagates across the ion cyclotron frequency. In large machines at high densities it is not practical to launch such waves with external antennas and the waves would mainly propagate in the edge of the plasma. However, a version of ion cyclotron waves may be generated by mode conversion processes, and this will be discussed in subsequent sections.

The dispersion relationship of the fast magnetosonic wave in the ICRF (ion cyclotron range of frequencies) may be obtained from Eqs (6.30) and (6.31), and it is given by

$$N_{\perp}^2 = \frac{(N_{\parallel}^2 - R)(N_{\parallel}^2 - L)}{S - N_{\parallel}^2} \quad (6.64)$$

where the appropriate expressions for L, R and S in the ICRF are as follows:

$$R = 1 + \sum_i \frac{\omega_{pi}^2}{\omega_{ci}(\omega + \omega_{ci})} \quad (6.65)$$

$$L = 1 - \sum_i \frac{\omega_{pi}^2}{\omega_{ci}(\omega - \omega_{ci})} \quad (6.66)$$

$$S = 1 - \sum_i \frac{\omega_{pi}^2}{(\omega^2 - \omega_{ci}^2)} \quad (6.67)$$

Here  $\omega_{pi}$  is the angular ion plasma frequency and  $\omega_{ci}$  is the angular ion cyclotron frequency. Equation (6.64) predicts a rather complex behaviour for fast wave propagation and accessibility from the plasma edge, especially in the case of multi-ion species plasmas. In addition to Refs [6.41–6.43], an excellent summary of such phenomena can be found in Ref. [6.44]. Here we simply want to point out the salient features of Eq. (6.64).

The region of  $N_{\parallel}^2 = R$  corresponds to the right hand cut-off layer ( $N_{\perp}^2 = 0$ ), and the fast wave is evanescent at densities lower than this critical density,  $n_R$ . The right hand cut-off layer always exists in the plasma, regardless of the relative value of  $\omega / \omega_{ci}$ . Consequently, the wave has to “tunnel through” an evanescent layer in the plasma periphery and the reflected RF power must be prevented from

getting back into the RF source (usually a high power tetrode) by an external tuning (matching) network. The  $N_{\parallel}^2 = L$  layer is also a cut-off layer and in a single ion species plasma, this layer occurs only if  $\omega < \omega_{ci}$ . The critical densities are

$$n_R = (N_{\parallel}^2 - 1)\omega_{ci}(\omega + \omega_{ci}) / (q_i^2 / m_i \epsilon_0) \quad (6.68)$$

$$n_S = (N_{\parallel}^2 - 1)(\omega_{ci}^2 - \omega^2) / (q_i^2 / m_i \epsilon_0) \quad (6.69)$$

$$n_L = (N_{\parallel}^2 - 1)\omega_{ci}(\omega_{ci} - \omega) / (q_i^2 / m_i \epsilon_0) \quad (6.70)$$

where  $n_L$  and  $n_R$  are the densities corresponding to the left and right hand cut-off layers and  $n_S$  is the density corresponding to the resonance layer where  $N_{\parallel}^2 = S$  and  $N_{\perp}^2 \rightarrow \infty$ . For  $\omega < \omega_{ci}$  the relative densities are  $n_L < n_S < n_R$  and the three densities are called the cut-off-resonance-cut-off triplet [6.3]. At the resonance layer, finite temperature effects may have to be included and mode conversion into the surface wave, or the “kinetic shear Alfvén wave”, may take place [6.3]. The inhomogeneous magnetic field of a tokamak will only quantitatively change this picture. If  $\omega > \omega_{ci}$  everywhere in the plasma column, and if we consider regions of fast wave propagation well away from any cut-off or resonance layer, the fast wave dispersion can be approximated from Eq. (6.50) by the following simple relationship:

$$\omega \approx k_{\perp} v_A (1 + c^2 k_{\parallel}^2 / \omega_{pi}^2)^{1/2} \quad (6.71)$$

where  $v_A \approx c\omega_{ci} / \omega_{pi}$  is the Alfvén speed and where usually  $N_{\parallel}^2 \ll N_{\perp}^2$  so that  $\omega \approx k_{\perp} v_A$ . If  $\omega > \omega_{ci}$  everywhere in the plasma, one needs to be concerned only with the right hand cut-off layer, which is usually in the scrape-off layer, in front of the antenna, and around the plasma cross-section, at a density of  $n_R$  (see Fig. 6.5).

Next, we need to consider the importance of wave polarization here. In general, the fast wave is elliptically polarized, but at the majority ion cyclotron resonance it is purely right hand polarized in the cold plasma limit and thus we do not expect any absorption by ions. This can be obtained by inspecting the second row of Eq. (6.9), from which we can obtain the ratio of the left hand circularly polarized component of the electric field  $E_+$ , which in the ICRF regime reduces to

$$E_+ / E_y = (iE_x - E_y) / E_y = s \quad (6.72)$$

where  $s = 0, 1$  and  $1/9$  for  $\omega / \omega_{ci} = 1, 2$  and  $4/3$ , respectively. The first value corresponds to the fundamental majority cyclotron resonance frequency in a pure deuterium plasma, the second value corresponds to the harmonic of the deuterium cyclotron frequency (case of H minority cyclotron resonance in a majority deuterium plasma) and the third value corresponds to the cyclotron resonance of

a few per cent  $^3\text{He}$  minority species in a deuterium majority plasma (or second harmonic tritium minority in a deuterium–tritium plasma).

Since waves are absorbed mainly by the left hand circularly polarized component of an electromagnetic wave at its cyclotron frequency (unless the temperature of the plasma ions is very high, of the order of 100 keV or more), it will be necessary to seed the pure deuterium target plasma with a second ion species (minority species) for its cyclotron absorption by the wave. If a minority ion species (or a second majority ion species) is present in the plasma, the mode conversion layer will be affected by the second ion species. For example, if  $\omega \approx \omega_{cm}$  near the centre of the tokamak plasma column, then once more, the  $N_{\parallel}^2 = L$  and  $N_{\parallel}^2 = S$  layers will move into the plasma column and be located on the high field side of the lighter minority species cyclotron resonance layer. The  $N_{\parallel}^2 = R$  layer will remain near the plasma periphery, maintaining the presence of the evanescent layer. This is shown in Fig. 6.5 in the form of the plasma cross-section, and in Fig. 6.6 we show the various modes that can propagate and their relative perpendicular index of refraction. It should be noted that in a two ion species plasma corresponding to the above situation the  $N_{\parallel}^2 = S$  resonance layer may occur in the plasma core and approximately we have the so-called ion-ion hybrid resonance occurring, where we balance the two (or more) ion species, and in the cold plasma limit

$$\sum_i \frac{\omega_{pi}^2}{(\omega_{ii}^2 - \omega_{ci}^2)} \approx 0 \tag{6.73}$$

where  $\omega_{ii}$  stands for the ion-ion hybrid resonance frequency. This process was discovered early in fusion research and formed the basis of later experiments in TFR and PLT and others more recently, and the results will be discussed in Section 6.3.4. The efficiency of mode conversion processes in the absence of dissipation were discussed in the 1980s in Ref. [6.42].

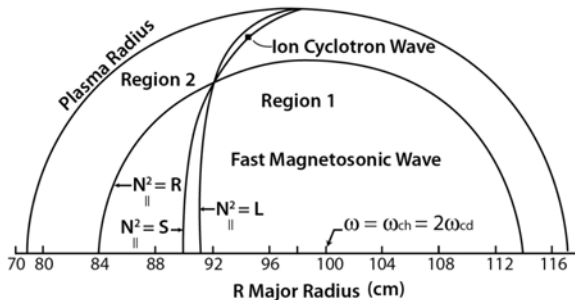


FIG. 6.5. Plasma cross-section in the ICRF regime showing the R and L cut-offs and the S resonance region and their relationship to the proton cyclotron resonance layer.  $\omega_{CD}$ ,  $\omega_{CH}$  are deuterium and hydrogen cyclotron frequencies [6.41]. Reprinted from Ref. [6.41]. Copyright (2011) by the American Physical Society.

By putting finite temperature into the equations, the mode conversion leads to a new hot ion plasma branch, that of ion Bernstein waves (see Fig. 6.6 left and Ref. [6.43]). Furthermore, if magnetic shear is taken into account off the midplane, a kinetic form of the slow ion cyclotron wave is excited by mode conversion (see Fig. 6.6 right and Ref. [6.44]). We see that in general, the fast wave propagates to the left hand cut-off layer, tunnels through the evanescent layer and, depending on plasma parameters, partially reflects, partially converts to the IBW just beyond the resonance layer, or to the ICW before the left hand cut-off layer, and partially continues its propagation as the fast wave (FW) branch. However, if the minority concentration is low (of the order of a few per cent), then the ion-ion hybrid resonance layer is near the minority ion cyclotron layer, and due to the finite value of  $k_{\parallel}$  and Doppler shift, dominant ion cyclotron absorption can take place [6.3, 6.4]. So the situation can be quite complicated and, in general, the Budden tunneling problem must be solved with dissipation taken into account (due to finite  $N_{\parallel}$  and cyclotron absorption), a process best handled by modern full wave codes (see Section 6.2.8).

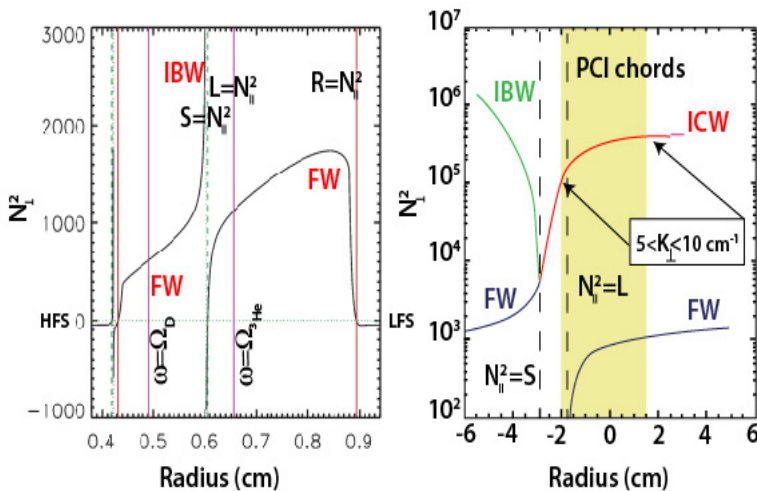


FIG. 6.6. Dispersion relationships with mode conversion in a multi-ion species plasma as a function of major radius. Left: Without shear. Indicates excitation of ion Bernstein waves (IBWs) [6.45]. Right: With shear. Note that shear introduces a new mode converted wave, the ion cyclotron wave (ICW), in addition to IBW [6.46].

#### 6.2.4. ICRF wave absorption in a hot plasma

As shown by Stix [6.3], the absorbed power in the plasma  $P_{abs}$  can be determined by calculating the dissipated wave power  $\text{Re}(\vec{j} \cdot \vec{E})$ , which can be written in the form

$$P_{abs} = \frac{-i\omega}{16\pi} \sum \vec{E} \cdot \left[ \vec{K} - \vec{I} \right] \cdot \vec{E} + \text{c.c.} \quad (6.74)$$

where the summation is over different modes,  $\vec{K}$  is the hot plasma dielectric tensor [6.3],  $\vec{I}$  is the unit diadic and c.c. represents the complex conjugate. Thus, the contribution will come from the anti-Hermitian part of  $\vec{K}$  and the Hermitian part will cancel.

#### 6.2.4.1. Absorption on electrons

Now we will be interested in Landau-type interactions with electrons, namely  $\omega \approx k_{\parallel} v_{th,e}$ . Examining the hot plasma dielectric tensor [6.3], we find that the following terms may contribute:  $K_{zz}$ ,  $K_{yy}$ ,  $K_{yz}$  and  $K_{zy}$ ; and after some lengthy algebra, we obtain the power absorbed per unit volume per unit time (in cgs-Gaussian units)

$$P_{abs} = \frac{\omega}{4\pi^{1/2}} \frac{\omega_{pe}^2}{\omega^2} \left[ k_{\perp}^2 N_{\parallel}^2 |E_y|^2 - \frac{\omega}{\omega_{ce}} \frac{k_{\perp}}{k_{\parallel}} |E_z| |E_y| + \frac{\omega^2}{k_{\parallel}^2 v_{th,e}^2} |E_z|^2 \right] \zeta_e e^{-\zeta_e^2} \quad (6.75)$$

In Eq. (6.75) we defined  $v_{th,e}^2 = 2T_e / m_e$ ,  $\omega_{pe}^2 = 4\pi n_e e^2 / m_e$ ,  $\zeta_e = \omega / k_{\parallel} v_{th,e}$  and  $\omega_{ce} = eB / cm_e$ . While Landau damping is the result of the force on a charge due to the parallel wave electric field ( $eE_z$ ), transit time magnetic pumping results from the force associated with the magnetic moment and the wave magnetic field ( $-\nabla_{\parallel}(\mu B)$  with  $\mu$  being magnetic moment).

The spatial damping decrement is given by the ratio of the absorbed power  $P_{abs}$  and the Poynting flux  $S_{\perp}$  [6.3]

$$2k_{\perp \text{Im}} = P_{abs} / S_{\perp} \quad (6.76)$$

where we take  $S \approx S_{\perp} \sim cN_x |E_y|^2 / 8\pi$  with  $N_x = ck_x / \omega$ , we assumed  $k_{\parallel}^2 \ll k_{\perp}^2$ , and  $k_{\perp} = k_x$ . Evaluating Eq. (6.76), and considering the polarization of the fields, we obtain the effective spatial damping rate [6.47, 6.48]

$$2k_{\perp \text{Im}} = k_{\perp \text{Re}} \left( \frac{\pi^{1/2}}{2} \right) \beta_e \zeta_e e^{-\zeta_e^2} \left[ 1 + \frac{1}{\alpha^2} \right] \quad (6.77)$$

where  $\beta_e = n_e T_e / (\epsilon_0 B^2)$  is the electron beta,  $k$  is in  $\text{cm}^{-1}$  and

$$\alpha = \frac{T_e}{m_i c^2} \left( \frac{(\omega^2 - \omega_{ci}^2)}{\omega_{pi}^2} \right) (S - N_{\parallel}^2) |K_{zz}| \quad (6.78)$$

In the cold plasma limit  $\zeta_e^2 \gg 1$ , Eq. (6.78) reduces to

$$\frac{1}{\alpha^2} \approx \left( \frac{m_e c^2}{T_e} \right)^2 \frac{\omega^4}{\omega_{pi}^4} \quad (6.79)$$

whereas in the hot plasma limit  $\zeta_e^2 \gg 1$  and Eq. (6.78) becomes

$$\frac{1}{\alpha^2} \approx \frac{m_e c^2}{T_e} \frac{\omega^4}{\omega_{pi}^4} \frac{1}{\zeta_e^4 (1 - 0.86 \zeta_e^2)} \frac{\omega^4}{\omega_{pi}^4} N_{\parallel}^4 \quad (6.80)$$

The term Eq. (6.79) has been noted previously by Moreau et al. [6.49]. For example, for  $\zeta_e \approx 0.7$  and the previously listed plasma parameters,  $1/\alpha^2 \approx 0.31$ . However, lowering the electron temperature from  $T_e \approx 6.0$  keV to  $T_e \approx 3.0$  keV increases  $\alpha^2$  to unity. At higher phase velocities ( $\zeta_e^2 \geq 1$ ),  $1/\alpha^2$  is less significant for  $T_e \geq 3.0$  keV. Replacing  $k_{\perp \text{Re}} \sim \omega/v_A$  and neglecting  $1/\alpha^2$  to lowest order we get the simple result

$$2k_{\perp \text{Im}} = \frac{\pi^{1/2}}{2} \frac{\omega^4}{\omega_{pi}^4} \frac{\omega_{pi}}{c} \beta_e \zeta_e \exp(-\zeta_e^2) \quad (6.81)$$

so that for  $\zeta_e \sim 1$ , single pass absorption is proportional to  $\omega$ ,  $n^{3/2}$ ,  $T_e$  and  $B^{-3}$ . Again,  $k$  is in  $\text{cm}^{-1}$ . Note that the maximum absorption occurs for  $\zeta_e \sim 0.7$ . For example, for present day machines,  $T_{e0} \approx 6.0$  keV,  $B_0 \approx 2.0$  T,  $n_{e0} \approx 5 \times 10^{19} \text{ m}^{-3}$ ,  $\beta_e \approx 0.03$ ,  $f = 76$  MHz in a D plasma,  $\zeta_e \sim 0.7$ ,  $\Delta r \sim a/2 \sim 0.50$  m,  $2k_{\perp} \Delta r \approx 0.62$  and the single pass absorption is  $[1 - \exp(-2k_{\perp \text{Im}} \Delta x)] \approx 0.47$ . For example, this may be an achievable value in the DIII-D tokamak. After a few bounces, most of the power would be absorbed by electron Landau damping. The required parallel wavelength at the antenna would be  $\lambda_{\parallel} \approx 60$  cm, which is very reasonable (toroidal wave propagation effects would reduce this to  $\lambda_{\parallel} \approx 44$  cm near the centre of the plasma where  $\zeta_e \sim 0.7$ ). For a phased array (typically 4 elements) with  $90^\circ$  or  $120^\circ$  phasing, a directional spectrum would result which would drive significant on-axis toroidal current, of magnitude  $n_e [10^{20} \text{ m}^{-3}] I [\text{MA}] R [\text{m}] / P [\text{MW}] \approx 0.1 T_e [10 \text{ keV}]$  [6.47]. Thus, for  $R = 2$  m,  $n_e = 1 \times 10^{20} \text{ m}^{-3}$ ,  $T_e = 10$  keV, a power  $P = 10$  MW would yield a current drive of  $I = 0.5$  MA. In summary, the fast wave Landau absorption condition  $\omega / k_{\parallel} v_{th,e} \sim 1$  is satisfied for

$$T_e [\text{keV}] \approx 50 / N_{\parallel}^2 \quad (6.82)$$

which follows from Eq. (6.63) for  $\theta = 7$  (quasi-linear Landau damping).

#### 6.2.4.2. Absorption of ICRF waves on ion cyclotron harmonics

One of the competing mechanisms for the absorption of fast magnetosonic waves is absorption on ions near the fundamental, or the harmonics of the ion cyclotron frequency [6.3, 6.43, 6.44, 6.47, 6.48]. This may occur on bulk ions or fast ions due to simultaneous neutral beam injection or even on alpha particles in a reactor grade plasma. Ion Landau damping can occur either directly or through

the intermediary of mode conversion into an BW and subsequent ion Landau damping of the IBW. The latter process may dominate if  $N_{\parallel} \approx 0$ . First, we shall assume that  $N_{\parallel}$  is finite (and in particular  $\omega / k_{\parallel} v_{th,e} \sim 1$  or  $N_{\parallel} \approx c / v_{th,e}$ ) and that the fast wave power density is not high enough to distort the initial Maxwellian distribution of ions. When this condition is violated the situation becomes considerably more complex [6.43] and we need to consider quasi-linear theory [6.50].

Ion cyclotron harmonic absorption in the limit of near-perpendicular propagation may be obtained from the general result Eq. (6.74). After a considerable amount of algebra, for  $b_i \ll 1$ , where  $b_i$  is the finite Larmor radius, and  $\omega \approx l / \omega_{ci}$ , Eq. (6.74) reduces to [6.47, 6.48]

$$P = \frac{\omega_{pi}^2}{16\pi^{1/2}} \frac{b_i(l-1)}{k_{\parallel} v_{th,i} (l-1)! 2^{(l-1)}} |E_+|^2 \exp \left[ -\frac{(\omega - l\omega_{ci})^2}{k_{\parallel}^2 v_{th,i}^2} \right] \quad (6.83)$$

where we considered absorption only by the left hand polarized field component  $E_+$ . Here  $l$  is harmonic number,  $E_+ = E_x + iE_y$  is the left hand polarized component of the wave electric field and  $b_i = k_{\perp}^2 r_{ci}^2$  is the finite ion Larmor radius (with  $r_{ci}^2 = v_{ti}^2 / 2^{1/2} \omega_{ci}$  and  $v_{th,i}$  being the ion thermal velocity). This formula is valid for  $b_i \ll 1$ , which is usually satisfied for not too high harmonics since  $k_{\perp} \sim \omega / v_A$  so that  $k_{\perp}^2 r_{ci}^2 \sim l^2 b_i / 2$ . We recall the result following Eq. (6.72), namely that at  $\omega = \omega_{ci}$ ,  $E_+ \rightarrow 0$  since the ions shield out the left hand polarized component of the electric field (i.e. the magnetosonic wave becomes purely right hand polarized for perpendicular propagation). As is well known [6.43, 6.44, 6.47, 6.48], if strong ion cyclotron absorption is desired, the polarization problem may be remedied by injecting a minority ion species into the plasma, typically a few per cent of H or  $^3\text{He}$  ions into a deuterium majority plasma. Thus ion cyclotron absorption becomes effective again at  $\omega = \omega_{cm}$ , where the subscript  $m$  designates the minority species, since  $E_+(\omega \neq \omega_{cM}) \neq 0$  (where  $M$  designates the usually heavier ion species). For  $\omega = 2\omega_{CD} = \omega_{CH}$  (where  $\omega_{CD}$ ,  $\omega_{CH}$  are deuterium and hydrogen cyclotron frequencies),  $|E_+ / E_y|^2 = 1$ , while for a  $^3\text{He}$  minority resonance in a deuterium plasma  $\omega = 4/3\omega_{CD}$  and  $|E_+ / E_y|^2 = 1/9$ . As a consequence, absorption is strongest in a deuterium plasma with H minority and  $^3\text{He}$  minority absorption is weaker by nearly an order of magnitude compared to D with H minority. However, in large tokamaks net absorption is sufficient as a result of multiple passes through the resonance layer. We can obtain the damping by integrating the power absorbed across a cyclotron harmonic resonance layer in a radially inhomogeneous magnetic field and divide the absorbed power by the Poynting flux  $S_{\perp} = (c/8\pi) N_{\perp} |E_y|^2$  (see Eq. (6.76)). The dominant factor in the integral comes from the exponential factor, and integrating through the resonance [6.47, 6.48] in a single ion species plasma at harmonics of the ion cyclotron frequency we obtain

$$2\eta = \frac{\pi}{2} \frac{\omega_{pi}}{c} R \left( \frac{l^2 \beta_i}{4} \right)^{(l-1)} \frac{(l-1)}{(l-2)!} \quad (6.84)$$

where  $\eta$  is the transmission coefficient and  $R$  is the major radius of the tokamak at the cyclotron resonance layer,  $\beta_i$  is the ion beta,  $l$  is the harmonic number and  $\omega_{pi}$  is the angular ion plasma frequency. This result shows that at  $l = 1$  the absorption is zero, at least when one uses cold plasma theory to calculate the polarization. It can be shown [6.47, 6.48] that if we were to improve on the polarization calculation, in a hot plasma at  $l = 1$  we would obtain a small but finite absorption given by

$$2\eta = \frac{\omega_{pi}}{c} R \frac{N_{\parallel}^2 T_i}{m_i c^2} \quad (6.85)$$

In present day plasmas this is negligibly small, but in a reactor grade plasma (ITER or DEMO) this absorption could be of the order of 0.1. For the simple situation assumed above, the power transmission is given by  $T_r = \exp(-2\eta)$ , and thus the absorption is given by

$$A_b = 1 - T_r = 1 - \exp(-2\eta) \quad (6.86)$$

where we neglected any reflection or mode conversion. This is a reasonable assumption as long as cyclotron Doppler broadening dominates over the distance between the cyclotron resonance layer and any kind of mode conversion layer, for example, for  $l = 2$ ,  $\beta_i R / 2 < k_{\parallel} v_{th,i} R / \omega$ . If this condition is violated the problem becomes significantly more complicated, leading to mode conversion into Bernstein waves and reflection and partial power transmission by fast waves [6.44]. In the Doppler regime, for  $l = 2$ , the absorption from Eq. (6.84) is

$$2\eta = \frac{\pi}{2} \frac{\omega_{pi}}{c} R \frac{l^2 \beta_i}{4} \quad (6.87)$$

which is proportional to the ion beta. We also see that absorption at the third harmonic would be reduced by a factor of  $\beta_i^2$ . It is easy to see that for  $\beta_i > 0.01$  at the second ion cyclotron harmonic in a JET or ITER size plasma a significant absorption can take place.

#### 6.2.4.3. Minority ion cyclotron absorption

In the presence of a minority ion component with a  $Z_i/m_i$  different than the majority species (for example,  $H^+$  or  $^3He^{++}$  in a majority  $D^+$  or  $T^+$  plasma), absorption at the ion cyclotron resonance can be significant even in a relatively cold (low beta) plasma, as long as cyclotron Doppler broadening dominates. Hence, this scenario is used most often in present day experiments, as well as

during startup in ITER plasmas. The absorption formula remains the same as given by Eq. (6.74), but the plasma parameters are calculated based on minority concentration. However, the polarization  $\left|E_+ / E_y\right|^2$  may still be calculated by the majority cold plasma parameters as previously. Since the wave frequency now is at the minority cyclotron frequency and not that of the majority species, the polarization term remains finite and significant absorption can result as indicated by the formula [6.44, 6.47]:

$$2\eta = \frac{\pi}{2} \frac{\omega_{pM}}{c} R \frac{n_m}{n_M} \frac{Z_m}{Z_M} \left| \frac{E_+}{E_y} \right|^2 \quad (6.88)$$

where subscripts  $m$  and  $M$  refer to the minority and majority species respectively and  $Z$  is the ion charge. The result for  $H^+$  minority in a  $D^+$  majority plasma is

$$2\eta = \frac{\pi}{2} \frac{\omega_{pD}}{c} R \frac{n_H}{n_D} \quad (6.89)$$

where subscript  $D$  refers to the majority  $D$  species and subscript  $H$  to the minority  $H$  species. Thus, we see that absorption is proportional to the fraction of minority density, which is typically 5%, and in present day experiments with  $R = 1$  m and a density of  $D$   $n_D = 5 \times 10^{19} \text{ m}^{-3}$ , we obtain  $2\eta = 1$  or we have an e-folding power loss through the resonance layer. At higher densities or in larger machines single pass absorption in excess of 90% is obtained, even in a relatively cold (say 1 keV) initially ohmically heated plasma, as long as Doppler broadening dominates, namely if  $n_H / n_D < k_{\parallel} v_{th,H} / \omega$ .

Additional complications from hot plasma contributions to the polarization calculation may have to be considered otherwise and absorption would be reduced. We note that absorption in  $D^+$  plasma with  ${}^3\text{He}^{++}$  minority would be reduced by a factor of 1/9 as compared to that predicted by Eq. (6.89), due to the polarization factor given by Eq. (6.72). It should be also noted that for  $D$  minority in a  $H$  majority plasma the absorption would be reduced again as compared to Fig. 6.5 and significant reflection may occur due to a reversal of the relative radial position of the cyclotron resonance layer and the left hand cut-off layer. Thus, scenarios in startup plasmas with  $H$  majority need careful examination, and modelling with modern full wave codes should be used for a quantitative prediction of absorption, reflection and transmission.

### 6.2.5. Quasi-linear absorption of ICRF waves on ions

As seen above, typically ICRF wave power is absorbed by a small fraction of minority ions, which then collisionally equilibrates with the bulk plasma (majority ion species) and this will automatically lead to a highly distorted non-Maxwellian distribution of the minority species. This means that while the

above absorption models may initially be quite accurate, ultimately we must consider a more accurate model based on quasi-linear theory [6.3, 6.43]. Similar processes may occur also for cyclotron harmonic absorption and since the power absorption is proportional to  $b_i^{(l-1)}$ , for  $l \geq 2$  the more energetic particles will preferentially absorb the RF power and hence become even more energetic, thus developing a perpendicular ion tail, balanced by collisions with the bulk. Again, quasi-linear theory is necessary for an accurate description of this process.

To obtain the true distribution function  $f$  of a species of charged particles, one must solve a Fokker–Planck equation, including quasi-linear (QL) diffusion and collisional drag and diffusion of the form [6.3, 6.43]:

$$\frac{\partial f}{\partial t} = \frac{\partial f}{\partial t} \Big|_{\text{QL}} - \nabla_{\mathbf{v}} \cdot (\langle \Delta \vec{v} \rangle f) + \frac{1}{2} \nabla_{\mathbf{v}} \cdot [\nabla_{\mathbf{v}} \cdot (\langle \Delta \vec{v} \Delta \vec{v} \rangle f)] \quad (6.90)$$

where the 2nd and 3rd terms on the RHS correspond to collisional terms and

$$\frac{\partial f}{\partial t} \Big|_{\text{QL}} = \frac{\partial}{\partial \vec{v}} \cdot \vec{D}_{\text{QL}} \cdot \frac{\partial f}{\partial \vec{v}} \quad (6.91)$$

is the wave induced quasi-linear term. Although the waves may be coherent, the transiting particles lose phase memory as they pass around the torus hundreds of times even if they experience only rare collisions. In general this is a difficult problem which has been solved analytically only in a few instances. For example, the case of a minority species distribution in the steady state in the presence of ICRF heating and collisional drag has been determined by Stix [6.3, 6.43]. In the steady state the result is the characterization of a high energy minority tail by an effective temperature

$$\frac{1}{T_{\text{eff}}} = \frac{1}{T_e(1+\zeta)} \left[ 1 + \frac{R_j(T_e - T_j + \zeta T_e)}{T_j(1+R_j+\zeta)} \frac{1}{1+(E/E_j)^{3/2}} \right] \quad (6.92)$$

where  $j$  stands for minority ion species and

$$R_j = \frac{n_j Z_j^2 v_{th,e}}{n_e v_{th,j}} \quad (6.93)$$

$$\zeta = \frac{m \langle P \rangle v_{th,e}}{8\pi^{1/2} n_e n Z^2 e^4 \ln \Lambda} \quad (6.94)$$

and  $\langle P \rangle$  is the average power per unit volume deposited. Here the majority ion species is characterized by density  $n_p$ , temperature  $T_p$ , charge  $eZ_j$  and thermal speed  $v_{th,j} = (2T_j / m_j)^{1/2}$ ; electrons are characterized by density  $n_e$  and thermal speed  $v_{th,e}$ ; the minority species being accelerated by cyclotron resonance are designated by  $n$ ,  $m$ ,  $v$ ,  $Z$  and  $E = mv^2 / 2$ . We note that for  $\zeta \approx 0$  the minority ion species

are characterized by a temperature close to that of the majority ion temperature, whereas for  $E \gg E_j(\zeta)$ ,  $T_{eff} \approx T_e(1 + \zeta)$  and ion acceleration is entirely balanced by electron drag. As will be shown below, the experimental verification of this theory has been one of the early triumphs of ICRF experiments on tokamaks. The results are summarized in Fig. 6.7 [6.3, 6.43].

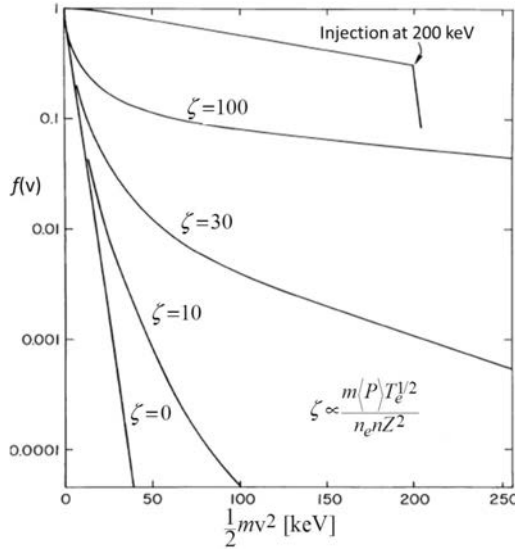


FIG. 6.7. Fokker-Planck energy distribution calculated for RF excitation at the minority cyclotron resonance for different normalized RF power densities [6.43].

Let us now ignore collisions and examine in more detail the quasi-linear diffusion term in the presence of RF waves. In particular, the power absorbed by charged particles can be calculated as follows:

$$P_{abs} = \int d^3v \frac{mv^2}{2} \left( \frac{\partial f_0}{\partial t} \right)_{QL} \tag{6.95}$$

The quasi-linear evolution of the distribution function in a magnetized plasma has been given by Kennel and Engelmann nearly three decades ago and the expression in 3-D is given in Ref. [6.50]. For simplicity, we shall skip details not applicable here and we readily deduce the following relevant expression for ion cyclotron resonance absorption [6.47]:

$$\frac{\partial f_0(\vec{v})}{\partial t} = \frac{\pi Z^2 e^2}{8m^2 |k_{\parallel}|} \sum_l |E_+|^2 \frac{1}{v_{\perp}} \frac{\partial}{\partial v_{\perp}} v_{\perp}^2 J_{l-1}^2 \left( \frac{k_{\perp} v_{\perp}}{\omega_{ci}} \right) \delta \left( v_{\parallel} - \frac{\omega - l\omega_{ci}}{k_{\parallel}} \right) \frac{1}{v_{\perp}} \frac{\partial f_0}{\partial v_{\perp}} \tag{6.96}$$

where  $J$  and  $\delta$  are Bessel and delta functions respectively, and the summation is over ion cyclotron harmonics. Using cylindrical coordinates and azimuthal symmetry, we may readily proceed with the integration in Eq. (6.96):

$$P_{abs} = \frac{\pi^2 Z^2 e^2}{4m |k_{\parallel}|} f_{0\parallel}(v_{\parallel res}) |E_+|^2 \int_0^{\infty} f_{0\perp} \frac{\partial}{\partial v_{\perp}} v_{\perp}^2 J_{l-1}^2 \left( \frac{k_{\perp} v_{\perp}}{\omega_{ci}} \right) dv_{\perp} \quad (6.97)$$

where  $v_{\parallel res} = (\omega - l\omega_{ci}) / k_{\parallel}$  is the resonant velocity determined by the  $\delta$  function vanishing argument. For a Maxwellian, Eq. (6.97) can be readily integrated for small arguments of the Bessel function and we obtain [6.47]

$$P_{abs} = \frac{\omega_{pi}^2 |E_+|^2}{16\pi^{1/2} k_{\parallel} v_{th,i}} b_i^{(l-1)} \frac{l}{(l-1)! 2^{(l-1)}} \exp \left[ -\frac{(\omega - l\omega_{ci})^2}{k_{\parallel}^2 v_{th,i}^2} \right] \quad (6.98)$$

which is exactly the same result as Eq. (6.83). We can now use Eq. (6.97) to integrate over a Maxwellian distribution to all orders of the finite ion Larmor radius. In particular, taking the derivative and integrating by parts, Eq. (6.97) can be integrated exactly and we obtain [6.47]

$$P_{abs} = \frac{\omega_{pi}^2 |E_+|^2 l}{16\pi^{1/2} k_{\parallel} v_{th,i}} \left[ I_{l-1}(b_i) + \frac{b_i}{l} (I_l(b_i) - I_{l-1}(b_i)) \right] \times \\ \times e^{-b_i} \exp \left[ -\frac{(\omega - l\omega_{ci})^2}{k_{\parallel}^2 v_{th,i}^2} \right] \quad (6.99)$$

where  $I_l$  is the modified Bessel function of order  $l$  and argument  $b_i$ . The small Larmor radius limit of Eq. (6.99) results from the first term of the square bracket (expand  $I_{l-1}(b_i)$ ) and it agrees with Eq. (6.98). It is easy to generalize Eq. (6.99) to include absorption on an energetic minority ion species. Using the bulk plasma to calculate the polarization and dividing  $P_{abs}$  with  $S$ , we can easily obtain the transmission coefficient  $2\eta$ , due to an energetic minority component or at a cyclotron harmonic. We note that in obtaining Eq. (6.99) we kept only the contribution from  $E_+$ . However, it was shown that for a tail or minority energy of the order of 100 keV or more, contributions from  $E_-$  can be just as important, especially for higher harmonics [6.51]. An evolution of the actual distribution function at harmonics is the topic of present day research using full wave codes and iterating them with a Fokker–Planck code [6.52].

Furthermore, for energetic ions of the order of 100 keV, finite-width banana orbits may be important and this is covered by Monte Carlo codes at the present time [6.53]. These examples show the power of using quasi-linear theory for calculating power absorption to all orders of the Larmor radius and for arbitrary distribution functions. In particular, larger values of  $b_i$  lead to stronger

absorption and the result is that cyclotron harmonic resonances in the plasma lead to energetic ion tail production due to quasi-linear diffusion.

We can also use Eq. (6.95) to calculate power absorption due to electron Landau damping and electron transit time magnetic pumping. It has been shown [6.47] that for a Maxwellian plasma the result for the quasi-linear power absorption is identical to Eq. (6.75), and the damping rates are identical to those obtained previously. In general, due to collisional drag, using the fast magnetosonic wave it is difficult to distort the distribution function from a Maxwellian for  $\omega / k_{\parallel} v_{\parallel} < 2$ , which is the usual region of interest for reasonable single pass damping (i.e. 10% per pass). Thus, for most cases of practical interest for fast wave electron absorption the results obtained earlier (Eqs (6.77–6.81)) usually suffice.

### 6.2.6. Quasi-linear absorption on electrons

#### 6.2.6.1. Lower hybrid current drive

Consider the quasi-linear deformation of the electron distribution from 1-D ( $v_{\parallel}$ ) analysis of the Fokker–Planck equation, with application to lower hybrid current drive (LHCD). Wave absorption may be computed assuming a Maxwellian distribution for the electrons where  $f_e \propto \exp[-(v_{\parallel} / v_{th,e})^2]$  and  $v_{th,e} = (2T_e / m_e)^{1/2}$ . However, it is well known that LH waves damping on “tail” electrons at  $v_{\parallel} \approx 3v_{th,e}$  (see Ref. [6.54]) will locally (in velocity space) modify the distribution function through acceleration by the RF electric field.

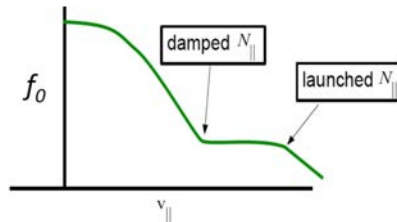


FIG. 6.8. Local modification of the electron distribution function as LH waves damp on “tail” electrons.

This modification of the electron distribution results in a “flattening” in velocity space which in turn can modify the local rate of Landau damping which is proportional to  $\partial f_e / \partial v_{\parallel}$  (see for example Fig. 6.8). Fisch [6.55, 6.56] recognized that it was possible to employ RF waves in the LHRF regime to create non-thermal particle distributions of the type shown in Fig. 6.8 which could be used to drive net toroidal current in a tokamak, thus making steady state operation feasible. Phased arrays of waveguides can be used to launch travelling LH waves (e.g.  $90^\circ$  phasing) that will impart momentum preferentially to electrons in one

direction. Furthermore, the process is highly efficient as the current carrying electrons are less collisional than the bulk electrons, being created at  $v_{\parallel} \geq 3v_{th,e}$ , so they would retain their momentum for a longer time than thermal electrons ( $v_{\parallel} = v_{th,e}$ ). It is possible to obtain quantitative estimates of the efficiency of this process by following the 1-D ( $v_{\parallel}$ ) solution method of Fisch [6.55]. Consider the 1-D ( $v_{\parallel}$ ) electron Fokker–Planck equation given by Eqs (6.100–6.103):

$$\frac{\partial f_e}{\partial t} = \frac{\partial}{\partial v_{\parallel}} D_{RF}(v_{\parallel}) \frac{\partial}{\partial v_{\parallel}} f_e(v_{\parallel}) + C(f_e) + \frac{eE_{\parallel}}{m_e} \frac{\partial}{\partial v_{\parallel}} f_e \quad (6.100)$$

$$C(f_e) = \frac{\partial}{\partial v_{\parallel}} \frac{2 + Z_{eff}}{2} \nu(v_{\parallel}) \frac{\partial}{\partial v_{\parallel}} \left[ v_{\parallel} f_e + \frac{1}{2} v_{th,e}^2 \frac{\partial f_e}{\partial v_{\parallel}} \right] \quad (6.101)$$

$$\nu(v_{\parallel}) = \nu_0 \left( v_{th,e} / v_{\parallel} \right)^3 \quad (6.102)$$

$$\nu_0 = \frac{\omega_{pe}^4 \log_e(\Lambda)}{2\pi n_e v_{th,e}^3} \quad (6.103)$$

where  $D_{RF}(v_{\parallel})$  is the RF or quasi-linear diffusion coefficient [6.50] due to the RF waves and is proportional to  $E_{RF}^2$ , and  $C(f_e)$  is the high velocity form of the Braginskii collision operator [6.57]. The third term on the right hand side of Eq. (6.100) corresponds to the Dreicer effect [6.58] whereby tail electrons in the presence of a DC electric field can be accelerated enough to overcome the electron collisional drag and “run away” to very high velocities. In deriving Eqs (6.100–6.103), a Maxwellian distribution was assumed in the perpendicular direction where  $f_e(v_{\perp}, v_{\parallel}) = f_0 \exp[-(v_{\perp} / v_{th,e})^2] f_e(v_{\parallel})$  in order to integrate the 2-D ( $v_{\perp}, v_{\parallel}$ ) Fokker–Planck equation over perpendicular velocities [6.55, 6.59]. Physically, Eqs (6.100–6.103) describe a competition between quasi-linear diffusion in parallel velocity space and collisions which tend to restore the distribution to a Maxwellian. A steady state solution of Eq. (6.101) can be found by assuming that  $D_{RF}(v_{\parallel})$  is non-zero within a finite region of parallel velocity space ( $v_1 \leq v_{\parallel} \leq v_2$ , where  $v_1$  and  $v_2$  are lower and upper parallel velocity plateau limits), neglecting the DC field term and taking  $f_e(v_{\parallel}) = 0$  and  $\partial f_e / \partial v_{\parallel} = 0$  at  $v_{\parallel} = \pm\infty$ :

$$f_e(w) = f_{e0} \exp \left[ \int_{v_1}^{v_2} \frac{wdw}{1/2 + D_{RF}(w)} \right] \quad (6.104)$$

$$\bar{D}_{RF}(w) = \frac{2}{2 + Z_{eff}} D_{RF}(w) / \left[ \nu(w) v_{th,e}^2 \right] \quad (6.105)$$

where  $w = v_{\parallel} / v_{th,e}$  is the normalized parallel phase speed. If  $D_{RF}(v_{\parallel}) / [v(v_{\parallel})v_{th,e}^2] \gg 1$ , that is, if the quasi-linear diffusion is strong compared to the collisional diffusion, then a plateau forms in the distribution function similar to what is depicted in Fig. 6.8. The normalization constant  $F_{e0}$  is chosen to conserve number density. Equations (6.104) and (6.105) can be used in the definitions of the driven RF current density ( $j_{RF}$ ) and RF power dissipation ( $S_{RF}$ ) given below (Eqs (6.106) and (6.107)) to derive a simple expression for the normalized current drive efficiency  $\tilde{\eta}$  [6.55]:

$$j_{RF}(v_{\parallel}) = n_e e \int_{-\infty}^{\infty} f_e(v_{\parallel}) dv_{\parallel} \quad (6.106)$$

$$S_{RF}(v_{\parallel}) = \frac{1}{2} n_e m_e \int_{-\infty}^{\infty} v_{\parallel}^2 \frac{\partial}{\partial v_{\parallel}} D(v_{\parallel}) \frac{\partial}{\partial v_{\parallel}} f_e(v_{\parallel}) dv_{\parallel} \quad (6.107)$$

$$\tilde{\eta} = \frac{j_{RF} / (n_e e v_{th,e})}{S_{RF} / (n_e m_e v_0 v_{th,e}^2)} = \frac{1}{2 + Z_{eff}} \left[ w_2^2 - w_1^2 \right] / \log_e(w_1 / w_2) \quad (6.108)$$

where  $w_1 = v_1 / v_{th,e}$  and  $w_2 = v_2 / v_{th,e}$ . For LH current drive the upper parallel velocity plateau limit  $v_2$  is typically determined by either wave accessibility or the extent of the launcher power spectrum and the lower parallel velocity limit  $v_1$  is determined by the condition for strong Landau damping, i.e.  $v_1 \approx 3v_{th,e}$ . Physically we see that efficiency of the current drive process is higher for higher phase velocity LH waves, which is intuitively consistent with the notion that these waves impart more momentum to electrons than slower waves. However, for higher phase velocities, accessibility (Eq. (6.58)) dictates lower values of  $\omega_{pe}^2 / \omega_{ce}^2$  or higher magnetic field for a given value of the density (which may be determined by the fusion power requirement  $\sim nT\tau_E$ ).

The physical picture of current drive described above turns out to be a simplified view of the actual process. Numerical solutions of the Fokker–Planck equation with a model diffusion operator [6.59] and an elegant analysis by Fisch and Boozer [6.60] revealed that 2-D ( $v_{\perp}$ ,  $v_{\parallel}$ ) velocity space effects are responsible for more than half of the driven current owing to the creation of an asymmetric resistivity from preferential heating of electrons. During LH current drive the asymmetry is driven by pitch angle scattering of electrons from the parallel to the perpendicular direction, while in electron cyclotron current drive (ECCD) the asymmetry arises from direct perpendicular heating of electrons. The resulting normalized efficiency is given by [6.60]:

$$\tilde{\eta} = \frac{j_{RF} / (n_e e v_{th,e})}{S_{RF} / (n_e m_e v_0 v_{th,e}^2)} = \frac{\vec{s} \cdot \nabla_s (w u^3)}{\vec{s} \cdot \nabla_s (u^2)} \frac{4}{5 + Z_{eff}} \quad (6.109)$$

where  $u^2 = w^2 + x^2$ ,  $x = v_{\perp} / v_{th,e}$  and  $\vec{s}$  is a velocity displacement vector. The enhancement in LH current drive efficiency that comes from including 2-D velocity space effects can be seen by evaluating Eqs (6.108) and (6.109) for a narrow spectrum of LH waves where  $\Delta = (w_2 - w_1)$ ,  $(\Delta / w_1) \ll 1$ ,  $\vec{s} = \vec{e}_z$  and parallel to  $\vec{B}$  is taken to be along the  $z$ -direction. Taking  $w_2 \approx w_1 \approx w$  yields  $\tilde{\eta}_{1D} \approx (2/3)w^2$  and  $\tilde{\eta}_{2D} \approx (4/3)w^2$ , so that 2-D effects result in an approximate factor of two increase in the current drive efficiency. Physically, this enhancement in efficiency occurs because of enhanced pitch angle scattering at high parallel phase speed that results in a large effective perpendicular temperature in the distribution function and a concomitant decrease in collisionality. This effect has been studied extensively using numerical models of varying detail [6.59, 6.61–6.63] and an example of this for a broad spectrum of LH waves is shown in Fig. 6.9 [6.64].

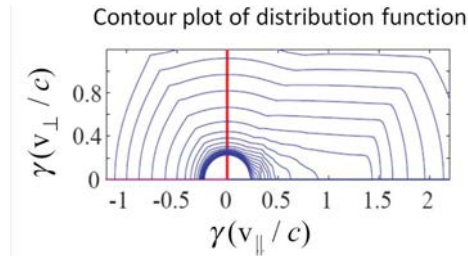


FIG. 6.9. 2-D Fokker–Planck simulation of the electron distribution function during LH current drive in Alcator C-Mod showing perpendicular broadening effect due to pitch angle scattering. Here  $\gamma$  is the relativistic factor defined as  $\gamma = [1 - (v/c)^2]^{-1/2}$ , where  $c$  is the speed of light, and  $v$  is the total velocity. Reprinted from Ref. [6.64]. Copyright (2011), American Institute of Physics.

### 6.2.6.2. Electron cyclotron current drive

From the discussion in the preceding section it can be seen that waves that preferentially heat electrons in the perpendicular direction can be used to drive current simply through the creation of an asymmetric plasma resistivity. Indeed this is the case with electron cyclotron current drive (ECCD). If one assumes that the velocity displacement vector ( $\vec{s}$ ) in Eq. (6.109) is in the direction perpendicular to  $\vec{B}$ , then it is straightforward to show that  $\eta_{2D}$  for ECCD is about  $3/4$  the value it is for LHCD [6.60].

However, this estimate omits the effects of particle trapping. EC waves accelerate electrons primarily in the direction perpendicular to the magnetic field, which increases their magnetic moment and hence their tendency to be trapped in the magnetic well. Ohkawa [6.65] exploited this effect to show that enhanced trapping of electrons travelling in one toroidal direction would result in a net

toroidal current. Unfortunately, this current is opposite in sign to the current due to the asymmetric resistivity that is generated by the same EC wave [6.66].

These trapping effects [6.67, 6.68], as well as other important physical effects like momentum conserving corrections to the background collision operator [6.61] have been investigated in detail through a Green's function treatment of the Fokker–Planck equation that takes advantage of the self-adjoint property of the collision operator [6.69]

$$\frac{j_{RF}}{S_{RF}} = \frac{\int \left( \frac{\partial \chi}{\partial \vec{p}} \cdot \vec{\Gamma}_{RF} \right) d^3 \vec{p}}{\int \left( \vec{\Gamma}_{RF} \cdot \vec{v} \right) d^3 \vec{p}} \quad (6.110)$$

$$\Gamma_{RF} = -\vec{D}_{QL} \cdot \frac{\partial f_e}{\partial \vec{p}} \quad (6.111)$$

Here  $\chi(\vec{p})$  is the Green's function that solves the Spitzer–Härm problem, namely  $C(f_m \chi) = -q v_{\parallel} f_m$ , where  $C$  is the high velocity collision operator and  $f_m$  is the perturbed distribution function. The advantage of this approach for treating ECCD [6.70] is that a full solution of the Fokker–Planck equation is not necessary in order to compute  $j_{RF}$  because the RF wave induced flux can be computed directly by taking  $f_e = f_{e0}$ , since there is very little distortion of the distribution function in ECCD. An example of this technique applied to estimate the effect of particle trapping on the EC current drive efficiency is shown in Fig. 6.10 left [6.67]. It can be seen that trapping significantly reduces the efficiency of ECCD at  $r/R > 0.1$  on the outside of the flux surfaces (LFS of tokamak). This is to be contrasted with methods that generate much faster electrons, such as LHCD, which is shown in Fig. 6.10 right.

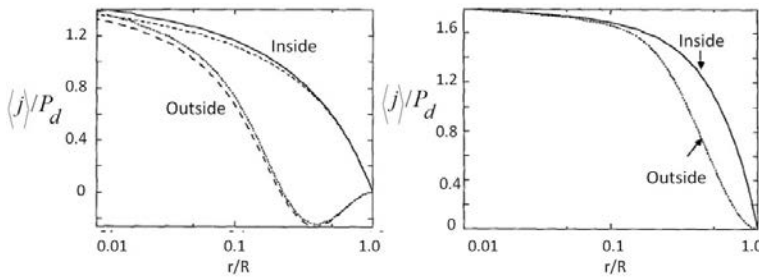


FIG. 6.10. Left: Non-relativistic ECCD current drive efficiency from an adjoint treatment versus inverse aspect ratio for the inside and outside extremes of a flux surface. Taken from Cohen [6.67]. Right: Non-relativistic LHCD current drive efficiency from an adjoint treatment vs. inverse aspect ratio for inside and outside extremes of flux surfaces. In this figure  $j$  is the driven EC current density normalized to its thermal value and  $P_d$  is the dissipated ECRF power density normalized to its thermal value following the definitions used in Eqs (6.108) and (6.109). Reprinted from Ref. [6.67]. Copyright (2011), American Institute of Physics.

A clear picture of the physics involved in ECCD can be obtained from Fokker–Planck code calculations. Figure 6.11 [6.66] shows the results of a calculation using the CQL3D Fokker–Planck code for ECCD applied at  $\rho = 0.4$  at a poloidal location directly above the discharge centre. The arrows in Fig. 6.11 show the net flux in velocity space due to a wave–plasma interaction in the region shaded white. These fluxes are the resultant of the flux due to the EC wave interaction combined with the collisional relaxation flux, forming convective cells in velocity space. Although the EC wave accelerates the electrons in the perpendicular direction in the interaction region, the net flux is along the resonance curve, with a significant parallel component. This figure shows that even though the interaction region is far from the trapping boundary, the interaction of electrons with the magnetic well can still be important. The total driven current can be found from the first moment of the distribution function associated with the fluxes of Fig. 6.11 and it will be shown later that the Fokker–Planck model is the best fit to the experiment.

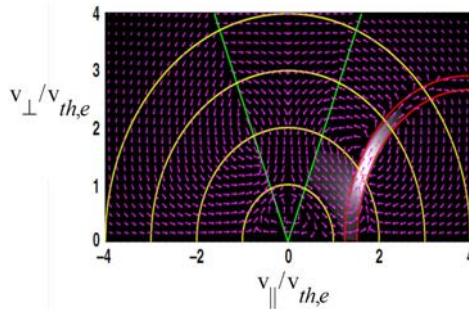


FIG. 6.11. Velocity space diagram for ECCD. The yellow circles are contours of constant  $v_{\perp}/v_{th,e}$ , the green lines separate the circulating particles below the lines from the trapped particles above the lines, and the red curves are the resonance condition at each side of a small range about the minor radius where the wave interaction is strongest. The white shading shows where the wave–particle interaction is strongest. The arrows indicate the direction of the flux in this velocity space due to the wave and to collisional relaxation. The length of the arrows is proportional to the logarithm of the local flux. Reprinted from Ref. [6.66]. Copyright (2011), American Institute of Physics.

### 6.2.6.3. Current drive by the fast ICRF waves

It is also possible to drive current with low frequency waves in the ICRF regime. Although these waves may have a low parallel phase speed  $\approx \omega/k_{\parallel}$ , they can be regarded as having a high momentum content, as measured by the parallel wavenumber ( $k_{\parallel}$ ) [6.71]. For example, fast magnetosonic waves at  $\omega \approx \Omega_{ci}$  can damp via direct electron Landau damping, transit time magnetic pumping or cyclotron damping.

Furthermore, since these waves cause minimal distortion to the distribution function when they damp, the adjoint treatment method of the previous section can also be used to estimate the current drive efficiency [6.61] as shown in Fig. 6.10. The right hand scale in Fig. 6.12 gives the CD efficiency for a plasma with  $n_e = 10^{20} \text{ m}^{-3}$ ,  $T_e = 10 \text{ keV}$  and  $R_0 = 1 \text{ m}$ . The dashed lines in Fig. 6.12 correspond to the normalized efficiency from an asymptotic analysis of the adjoint solution of the Fokker–Planck equation. For  $(v_{\parallel} / v_{th,e})^2 \gg 1$  the leading terms from this analysis given by Eqs (31) and (32a) from Ref. [6.61] for Landau damped and cyclotron damped waves respectively are:

$$\frac{j_{RF} / (n_e e v_{th,e})}{S_{RF} / (n_e m_e v_0 v_{th,e}^2)} = \frac{4(v_{\parallel} / v_{th,e})^2}{5 + Z_{eff}} + \dots \text{ (Landau damped waves)} \quad (6.112)$$

$$\frac{j_{RF} / (n_e e v_{th,e})}{S_{RF} / (n_e m_e v_0 v_{th,e}^2)} = \frac{3(v_{\parallel} / v_{th,e})^2}{5 + Z_{eff}} + \dots \text{ (cyclotron damped waves)} \quad (6.113)$$

It is interesting to note that these expressions are to leading order identical to the estimates given Ref. [6.60].

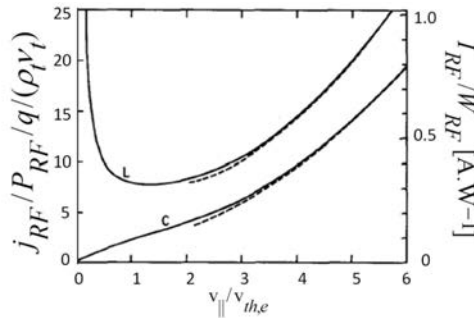


FIG. 6.12. Current drive efficiency obtained versus normalized parallel phase speed for low frequency waves damping via Landau (“L”) and cyclotron (“C”) damping (reproduced from Ref. [6.61]). Shown as dashed lines are asymptotic results for  $(v_{\parallel} / v_{th,e})^2 \gg 1$  using Eqs (31) and (32a) from Ref. [6.61]. On the left y-axis in this figure  $j_{RF} [A.m^{-2}]$  is the driven RF current density,  $P_{RF} [W.m^{-3}]$  is the dissipated RF power density,  $q [C]$  is the charge,  $\rho_i = m_e v_{th,e}$  is the thermal momentum value, and  $v_t$  is the thermal value of the collision frequency given by Eq. (6.103). On the right y-axis in this figure  $I_{RF} [A]$  is the integrated driven RF current and  $W_{RF} [W]$  is the integrated RF power dissipation. Reprinted from Ref. [6.61]. Copyright (2011), American Institute of Physics.

### 6.2.7. Wave propagation in toroidal geometry, geometric optics

The calculation of wave propagation and absorption of waves in the toroidal geometry of tokamak confinement systems has been an area of active research

in fusion plasmas for the past few decades. Considerable effort is required to formulate the wave propagation and absorption in toroidal geometry and computer implementation is almost always needed to arrive at a solution. Owing to the short wavelengths ( $\lambda_{\perp}$ ) relative to the device size ( $a$ ), in the lower hybrid range of frequencies (LHRF) and electron cyclotron range of frequencies (ECRF) ray tracing has been the preferred method. Here “ $\perp$ ” refers to the direction perpendicular to the applied magnetic field ( $\vec{B}$ ). In contrast, full-wave treatments have been used in the ion cyclotron range of frequencies (ICRF) where  $\lambda_{\perp} \leq a$ . These efforts allowed detailed comparisons between simulation and experiment, including simulation of non-thermal particle distributions that are ubiquitous to ICRF heating and LH current drive experiments. The remainder of this section discusses the use of ray tracing techniques to simulate LH wave propagation and quasi-linear electron Landau damping with an application to LH current drive given as an example. Full-wave solutions of wave propagation and absorption in the ICRF regime are then reviewed and examples of this technique applied to minority heating and mode conversion are given. Finally, we discuss recent developments in the use of full-wave techniques to treat LH wave propagation in order to include potentially important effects not included in the geometric optics limit such as focusing and diffraction of waves at caustic surfaces and proper reconstruction of wave fronts at plasma cut-offs.

#### 6.2.7.1. Geometric optics and the ray equations

An important property of plane waves is that their direction of propagation and their amplitude remain constant everywhere in space and time. In general, electromagnetic (EM) waves do not fit this description. Consider, however, a small region of space called a wave surface [6.72] on which the EM wave possesses the properties of a plane wave. On this wave surface the propagation direction and amplitude of the EM wave remain constant over the distance of a wavelength. Then a vector normal to this surface (the wave normal) would define the direction of propagation of the EM wave. The concept of a ray can then be introduced as a curve whose tangents at each point correspond to a wave normal, i.e. the direction of wave propagation. On each wave surface the electric and magnetic fields can be represented in terms of a phase function  $S(\vec{x}, t)$  known as the eikonal

$$\vec{E}(\vec{x}, t) = \vec{E}_0 \exp[iS(\vec{x}, t)] \quad (6.114)$$

$$\vec{B}(\vec{x}, t) = \vec{B}_0 \exp[iS(\vec{x}, t)] \quad (6.115)$$

where  $\vec{E}_0$  and  $\vec{B}_0$  are in general weakly varying functions of space and time with the eikonal function carrying the most important (zero-order) information

about the propagation direction. Some understanding of the eikonal function can be gained by assuming that over a small region of space and interval of time  $S(\vec{x}, t)$  can be expanded in a Taylor series as:

$$S(\vec{x}, t) = S_0 + \vec{x} \cdot \frac{\partial S}{\partial \vec{x}} + t \frac{\partial S}{\partial t} + \dots \quad (6.116)$$

By analogy with plane waves we can write  $S = S_0 + \vec{k} \cdot \vec{x} + \omega t$ , where

$$\vec{k} = \frac{\partial S}{\partial \vec{x}} = \nabla S \quad (6.117)$$

$$\omega = -\frac{\partial S}{\partial t} \quad (6.118)$$

The fact that  $\vec{k}$  can be expressed as the gradient of the eikonal is important since this also implies that  $\vec{k}$  is irrotational (i.e. that  $\vec{\nabla} \times \vec{k} = 0$ ). For wave propagation in a plasma which is not varying in time and for which there is a spatial inhomogeneity in only one direction, it can be shown that the local dispersion relation provides a unique mapping between the wave position and its wavenumber. Thus for a wave propagating in a plasma which is varying in only the  $x$ -direction, the propagation is uniquely determined from the local dispersion relation  $D_0(x, k_x(x), \omega) = 0$ , where  $k_y$  and  $k_z$  are constants. If however the plasma is varying in two or more spatial dimensions as is the case in a tokamak, then one must use the fact that  $\vec{k}$  is irrotational in addition to the local dispersion in order to determine  $\vec{k}(\vec{x})$  uniquely, i.e.

$$\nabla \times \vec{k} = 0 \quad (6.119)$$

$$D_0(\vec{x}, \vec{k}, \omega) = 0 \quad (6.120)$$

It was shown by Weinberg [6.73] that the solution in phase space for a wave that satisfies Eqs (6.119) and (6.120) is given by the ray equations

$$\frac{d\vec{x}}{dt} = -\frac{\partial D_0 / \partial \vec{k}}{\partial D_0 / \partial \omega} \quad (6.121)$$

$$\frac{d\vec{k}}{dt} = +\frac{\partial D_0 / \partial \vec{x}}{\partial D_0 / \partial \omega} \quad (6.122)$$

Equation (6.121) is the group velocity equation for a wave packet with wave vector  $\vec{k}$  and frequency  $\omega$ , while Eq. (6.122) can be viewed as the multi-dimensional analog of Snell's Law. The fact that more than a single component of  $\vec{k}$  will vary in a plasma with more than one dimension of inhomogeneity can be seen to follow immediately from Eq. (6.122).

## 6.2.7.2. Modifications to wave accessibility and absorption in toroidal geometry

We saw earlier that LH wave accessibility and absorption depends critically on the parallel wavenumber ( $k_{\parallel}$ ), which is typically imposed by the waveguide launcher at the plasma edge. Consider a toroidal geometry defined by the coordinates ( $r; \theta, \phi$ ), where  $r$  is the minor radial position,  $\theta$  is the poloidal angle and  $\phi$  is the toroidal angle. The choice of wave momenta that keeps the ray equations in canonically conjugate form are  $\vec{k} = (k_r, m, n)$ , where  $k_r$  is the radial wavenumber,  $m$  is the poloidal mode number and  $n$  is the toroidal mode number [6.74, 6.75]. The toroidal component of the magnetic field is assumed to vary as  $B_{\phi} = B_0 / [1 + (r / R_0) \cos \theta]$  and the density, temperature and poloidal magnetic field component are assumed only to be functions of  $r$ . The ray equations Eqs (6.121) and (6.122) have the straightforward consequence that  $k_{\parallel}$  now varies due to the non-conservation of the poloidal mode number since  $\partial D_0 / \partial \theta \neq 0$  and

$$k_{\parallel} = \vec{k} \cdot \vec{B} / |\vec{B}| = [e_r k_r B_r + e_{\theta} (m / r) B_{\theta} + e_{\phi} (n / R) B_{\phi}] / |\vec{B}| \quad (6.123)$$

This variation in parallel wavenumber makes a priori predictions of LH wave accessibility and absorption difficult in toroidal geometry and this effect was well documented numerically in early toroidal ray tracing calculations [6.75–6.77]. An example of the variation of the parallel refractive index ( $N_{\parallel} = k_{\parallel} c / \omega$ ) in toroidal geometry is shown in Fig. 6.13. These simulations were performed using the GENRAY ray tracing code [6.78] for parameters typical of the LH current drive experiment in Alcator C-Mod ( $f_0 = 4.6$  GHz,  $n_e(0) = 7 \times 10^{19} \text{ m}^{-3}$ ,  $B(0) = 5.3$  T and  $T_e(0) = 2.33$  keV) [6.79]. A group or “bundle” of ten rays was launched from the low field side of the tokamak near the plasma cut-off in a narrow range of parallel refractive index  $-1.58 \leq N_{\parallel} \leq -1.56$ . Linear electron Landau damping is computed along the ray paths and for these parameters the absorption is quite low on the first path of the rays into the plasma, since  $\omega / (k_{\parallel} v_{th,e}) > 6$  near the core for these parameters. Consequently the rays continue to propagate through a focal point or caustic near the plasma centre and then propagate back to the plasma periphery where they reflect from a cut-off. As the ray bundle approaches the cut-off, two interesting phenomena can be seen. First the trajectories start to spread spatially (Fig. 6.13 left). Second, the  $N_{\parallel}$  of the rays increases rapidly after reflection from the cut-off and the rays are strongly absorbed as they reach the hotter core plasma where the condition for strong electron Landau damping is satisfied, i.e.  $\omega / (k_{\parallel} v_{th,e}) \leq 3$  (see Eqs (6.62, 6.63)). This dramatic modification of the parallel wavenumber at reflection layers near the top and bottom of the tokamak cross-section was also observed in early ray tracing studies in circular plasmas [6.75].

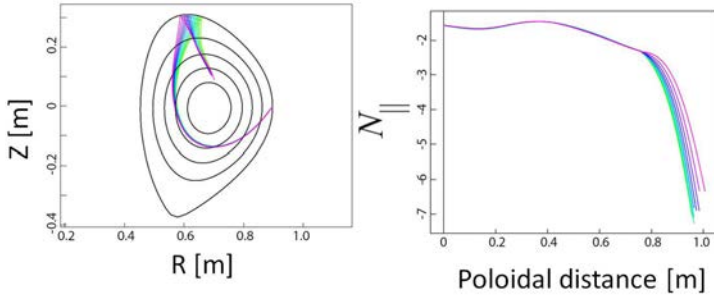


FIG. 6.13. Left: LH ray tracing calculation using the GENRAY code for Alcator C-Mod parameters – poloidal projection of rays. Right: Evolution of parallel refractive index versus poloidal distance along ray paths for rays shown in the left figure.

### 6.2.7.3. Numerical simulations of lower hybrid current drive using coupled Fokker–Planck and ray tracing calculations

As pointed out earlier, the distortion of the electron distribution as LH waves damp on tail electrons makes it necessary to solve the full 3-D  $(r, v_{\perp}, v_{\parallel})$  Fokker–Planck equation

$$\frac{\partial f_e}{\partial t} = \frac{\partial}{\partial v_{\parallel}} D_{RF}(v_{\parallel}) \frac{\partial f_e}{\partial v_{\parallel}} + C(f_e, v_{\parallel}, v_{\perp}) + \frac{eE_{\parallel}}{m_e} \frac{\partial f_e}{\partial v_{\parallel}} + \frac{1}{r} \frac{\partial}{\partial r} r \chi_F \frac{\partial f_e}{\partial r} \quad (6.124)$$

The fourth term on the right hand side of Eq. (6.124) is a diffusion operator with fast electron diffusivity ( $\chi_F$ ). Equation (6.124) has been solved with and without the radial diffusion operator by carrying out a non-linear iteration where the quasi-linear RF diffusion coefficient is evaluated using a toroidal ray tracing code [6.63, 6.80] and the diffusion coefficient is then used in a Fokker–Planck code to solve for the perturbed electron distribution. The new distribution function is then used in the ray tracing to recompute the RF diffusion coefficient, which is then used to resolve the Fokker–Planck equation for a new distribution function. This type of iterative computation was first carried out with 1-D  $(v_{\parallel})$  Fokker–Planck codes and toroidal ray tracing calculations [6.63, 6.81], but neglecting diffusion. Later, simulations were performed [6.82, 6.83] using a 1-D  $(v_{\parallel})$  Fokker–Planck code to evaluate the RF wave-induced flux and then convolving that with an adjoint solution of the Fokker–Planck equation (see Eqs (6.110) and (6.111)). More recently, 2-D  $(v_{\perp}, v_{\parallel})$  and 3-D  $(r, v_{\perp}, v_{\parallel})$  solutions have been obtained using the CQL3D/GENRAY codes [6.78, 6.80] and the DKE/LUKE model [6.84]. Indeed the distribution function shown in Fig. 6.9 is the result of iteration between the GENRAY ray tracing code and the CQL3D bounce averaged Fokker–Planck code. The non-thermal electron distribution shown in Fig. 6.9 has been used in a synthetic diagnostic code to simulate the

hard X ray spectra measured by a horizontally viewing hard X ray camera during LH current drive experiments on Alcator C-Mod [6.64].

## 6.2.8. Wave propagation in toroidal geometry, full-wave treatment

### 6.2.8.1. Full-wave simulations of minority heating in the ICRF

In order to simulate wave fields in the ICRF regime it is necessary to employ full-wave electromagnetic field solutions for several reasons. First, the wavelength of the fast magnetosonic wave can be of the order of the device size, which violates the conditions necessary for the validity of the geometric optics approach and ray tracing. Second, in the minority heating scheme that is often used to heat plasma with ICRF power, an incoming fast wave reaches a cyclotron resonance layer where it may be only partially absorbed. The wave can then propagate beyond this layer to a cut-off where the wave can tunnel to a mode conversion layer where it can convert to either a short wavelength ion Bernstein wave (IBW) or ion cyclotron wave (ICW). Ray tracing techniques are conceptually difficult to apply in these cases because it is not straightforward to match the incident fast wave fields to the short wavelength mode converted fields. Instead this process is described using Maxwell's equations combined with a conductivity relation to form a Helmholtz wave equation

$$-\nabla \times \nabla \times \vec{E} + \frac{\omega^2}{c^2} \left( \vec{E} + \frac{i}{\omega \epsilon_0} \vec{j}_p \right) = -i\omega \mu_0 \vec{j}_{ant} \quad (6.125)$$

where  $\vec{j}_{ant}$  is the externally driven antenna current and the plasma current density  $\vec{j}_p$  is in general a non-local, non-linear, integral operator on the electric field with a conductivity kernel that is given by

$$\vec{j}_p(\vec{r}, t) = \sum_s \int d\vec{r}' \int_{-\infty}^t dt' \sigma(f_{0s}(E), \vec{r}, \vec{r}', t, t') \cdot E(\vec{r}', t') \quad (6.126)$$

where  $s$  refers to the plasma species, either electrons  $e$  or ions  $i$ ,  $\sigma$  is the conductivity operator,  $r'$  is the position, and  $t'$  is time. Full-wave field solvers with varying levels of physics detail have been used to solve Eqs (6.125) and (6.126) [6.85–6.94]. One example of an advanced full-wave solver is the 2-D and 3-D “All Orders Spectral Algorithm” AORSA2D and AORSA3D [6.85], which is spectral in all three dimensions ( $R, Z, f$ ). Here ( $R, Z, f$ ) are cylindrical coordinates where ‘ $R$ ’ lies in the equatorial plane of the tokamak, ‘ $Z$ ’ is the vertical dimension, and ‘ $f$ ’ is the toroidal angle. The code includes all cyclotron harmonics in the evaluation of the plasma conductivity and no assumption is made about the perpendicular wavelength ( $\lambda_{\perp}$ ) relative to the ion gyroradius ( $\rho_i$ ). The plasma response formulated in this manner leads to an integral relation and the resulting

matrices that must be inverted are large, dense, non-symmetric, indefinite and complex [6.85]. Another sophisticated full-wave solver is the 2-D TORIC code [6.86, 6.87], which employs a mixed spectral, finite element representation for the electric field in  $(\rho, \theta, \phi)$ , where  $(\rho, \theta, \phi)$  are the usual pseudo-toroidal coordinates. The conductivity relation is truncated at second order in  $(\lambda_{\perp} / \rho_i)^2$  and at the second cyclotron harmonic. These assumptions result in a closed form for the plasma response and a matrix system to invert that is sparse and banded with large dense blocks. Both the AORSA and TORIC matrix inversion algorithms take advantage of the resulting dense block structures by using scalable libraries of parallelized linear algebra routines to efficiently invert their matrices. The semi-spectral basis set used in the TORIC solver has also been employed in the TASK-WM code [6.88, 6.93], which has been used to study ICRF wave propagation in 3-D configurations such as stellarators as well as in 2-D tokamak geometry. Finally, a relatively new approach has been employed by Dumont in the EVE code [6.89], which uses a Hamiltonian description for the particle dynamics in order to evaluate the conductivity operator in terms of action-angle variables. An example of minority hydrogen cyclotron damping simulated with the AORSA2D solver for Alcator C-Mod is shown in Fig. 6.14. The parameters used were  $B(0) = 5.4 \text{ T}$ ,  $n_H / n_e = 7\%$  and  $f_0 = 80 \text{ MHz}$ . This calculation would not be possible without the massively parallel architectures required for the global-wave solver. A spatial mesh of  $256 \times 256$  cells in  $(R, Z)$  was used in the solver. The need for high spectral resolution even in the case of ICRF heating at low minority concentration where mode conversion is weak can be seen upon examining the left circularly polarized electric field computed by AORSA in Fig. 6.14 left. Mode converted IBW can be seen clearly on the high field side near the midplane and mode converted ICW [6.44] can be seen propagating back towards the low field side above the midplane. Although very little power flows into mode converted waves during minority heating ( $<10\%$ ), the presence of these short wavelength modes does alter the polarization of the incoming fast wave in the mode conversion region. Although the minority cyclotron resonance layer passes through the plasma centre in this case, the ICRF power dissipation is clearly peaked off-axis. This feature can be seen more prominently in Fig. 6.14 right where the 2-D  $(R, Z)$  minority power dissipation has been plotted. There is a clear peak in the 2-D absorption along the resonance chord at about 0.07 m above the midplane. The ICRF wave fields shown in Fig. 6.14 left have been used to evaluate the RF quasi-linear diffusion coefficient in the bounce averaged Fokker-Planck code CQL3D [6.80]. In this way a non-thermal distribution for the minority ion species is evolved. The quasi-linear diffusion coefficient was then recomputed by the full-wave solver (AORSA) using the new minority ion distribution function in the plasma conductivity and the process was repeated until convergence was achieved [6.52, 6.95, 6.96].

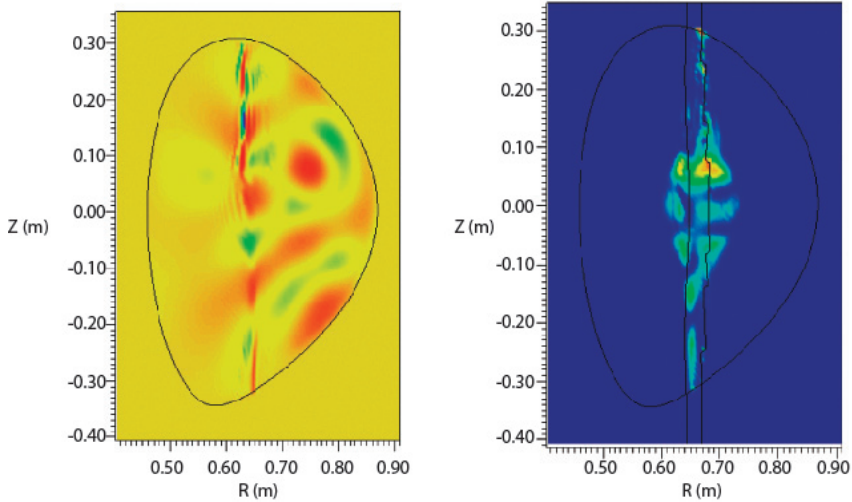


FIG. 6.14. Left: Electric field contours computed by the AORSA solver for minority hydrogen heating in Alcator C-Mod. Right: Power density contours of hydrogen ion cyclotron absorption from AORSA for the Alcator C-Mod minority heating case. Contour levels follow the rainbow, with red, orange and yellow being the highest values. Taken from Ref. [6.97].

One limitation with this approach is that when the ICRF generated minority ions are highly energetic or when the ICRF waves are interacting with energetic ions from neutral beam injection or fusion processes (alpha particles), the zero ion orbit width assumption used in the Fokker–Planck solver is no longer a valid approximation. A number of simulation models have been developed to address this problem. One such combined model, the SELFO code [6.98], has been used extensively to simulate finite ion orbit width effects during minority ICRF heating in the JET device. In this approach, electric fields from a full-wave solver (LION code [6.90]) were used to accelerate resonant particles in the FIDO Monte Carlo orbit code [6.99]. Non-thermal particle distributions were then reconstructed from the orbit code results and used in the full-wave solver. Finite ion orbit effects during ICRF heating have also been simulated in 3-D configurations such as the LHD stellarator using wave fields from the TASK WM solver [6.93] in the 5-D drift kinetic equation solver GNET [6.88]. More recently the AORSA solver [6.85] has been combined with the 5-D Monte Carlo code ORBIT RF [6.100] and with the Monte Carlo code sMC (Green [6.101]) to study ICRF minority heating in the Alcator C-Mod device and high harmonic fast wave heating in the DIII-D and NSTX devices. The coupling between AORSA and the sMC code is quite rigorous in the sense that particle “lists” or statistics from the Monte Carlo code are used to directly re-evaluate the plasma response in the full-wave solver. Also the 4D RF diffusion coefficient (two velocity and two spatial dimensions)

calculated from the electric fields in AORSA is used directly in the Monte Carlo code to accelerate resonant particles.

### 6.2.8.2. Full-wave simulations of mode conversion in the ICRF

Full-wave simulations of mode converted ion Bernstein waves (IBWs) and ion cyclotron waves (ICWs) in tokamak plasmas have also been performed using full-wave solvers [6.87, 6.102]. These calculations are especially challenging because of the disparate spatial scale lengths between the incoming fast wave and short wavelength mode converted waves. Mode converted ICRF waves are of particular interest for plasma profile control because they can be used to generate localized current and plasma rotation. Efficient mode conversion can be realized by increasing the minority ion concentration so that the cyclotron resonance is well separated spatially from the mode conversion layer. Furthermore, owing to the high minority ion concentration the maximum ion tail energies are not sufficient to overlap the mode conversion layer with the Doppler broadened cyclotron resonance layer. Figure 6.15 is an example of an ICRF mode conversion simulation in Alcator C-Mod.

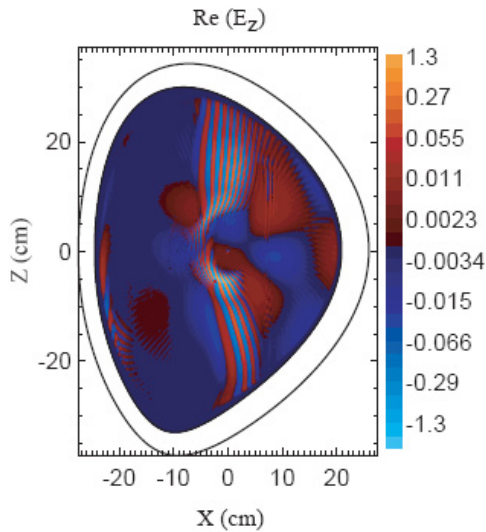


FIG. 6.15. TORIC simulation of ICRF mode conversion in the Alcator C-Mod device. Contours are plotted for the real part of the parallel electric field  $\text{Re}(E_z)$ . Contour levels shown on the right are logarithmic and in units of  $\text{kV}\cdot\text{m}^{-1}$ .  $B_0 = 5.8 \text{ T}$ , 33% H, 23%  $^3\text{He}$ , 21% D,  $T_e \approx T_i \approx 1.5 \text{ keV}$ . Reprinted from Ref. [6.79]. Copyright (2011), American Nuclear Society.

It can be seen that a short wavelength mode (the ICW) is excited to the low field side of the usual IBW mode conversion layer. Longer wavelength ICWs are also apparent in the simulation above and below the tokamak midplane and can

be seen propagating back to the low field side of the mode conversion layer at  $-0.02 \text{ cm} \leq X \leq 0 \text{ cm}$ . The TORIC simulation used 255 poloidal modes and 240 radial elements to represent the electric field in its semi-spectral basis set.

### 6.2.8.3. Full-wave simulations of lower hybrid waves

Because of the millimeter perpendicular wavelengths of LH waves, ray tracing techniques have long been the preferred method for treatment of wave propagation in this regime. It is well known, however, that the geometrical optics approximation breaks down at caustics or focal points as well as at layers where waves reflect, such as wave cut-offs. In particular, important effects such as focusing and diffraction are neglected in the lowest order geometrical optics approximation [6.103] at caustic surfaces. It is possible to capture these effects to some extent by using beam tracing techniques [6.104]. However, the advent of massively parallel computing architectures has made it possible to perform full-wave electromagnetic field simulations of LH waves in present day sized tokamak devices [6.105]. An example of such a simulation using the TORIC-LH solver is shown in Fig. 6.16. These simulations were performed for the Alcator C-Mod parameters of Section 6.6.3 ( $f_0 = 4.6 \text{ GHz}$ ,  $n_e(0) = 7 \times 10^{19} \text{ m}^{-3}$ ,  $B(0) = 5.3 \text{ T}$  and  $T_e(0) = 2.33 \text{ keV}$ ) and required 1023 poloidal modes and 980 radial elements in the TORIC spectral basis set. The electric field pattern in Fig. 6.16 left corresponds to a weak single pass damping regime where  $N_{\parallel} = -1.55$  initially and the field pattern on the right corresponds to a strong single pass case where  $N_{\parallel} = -3.6$  initially. A Maxwellian electron distribution was used in both cases to compute the electron absorption. The LH waves are coupled from four waveguides on the low field side (on the right of each figure). In both cases, focusing of the incident LH beam at a caustic surface near the centre is apparent. In the weak damping case these beams undergo multiple reflections from cut-offs at the plasma edge while in the strong damping case on the right the incident beam undergoes a single reflection from the edge before the wave undergoes strong spectral broadening in  $k_{\parallel}$ -space and damps. The full-wave fields shown above have also been employed to evaluate the RF diffusion coefficient in an iterative solution of the electron Fokker-Planck equation using CQL3D and TORIC-LH. A further exciting development in full-wave field analysis has been the application of a pure finite element method to solve the LH wave propagation problem from a waveguide launcher to the plasma core [6.106]. This approach benefits from the fact that in principle the waveguide fields, coupling at the plasma edge and propagation to the core can be treated simultaneously. Proper calculation of the dissipation of these waves in the different regions of the plasma is under development.

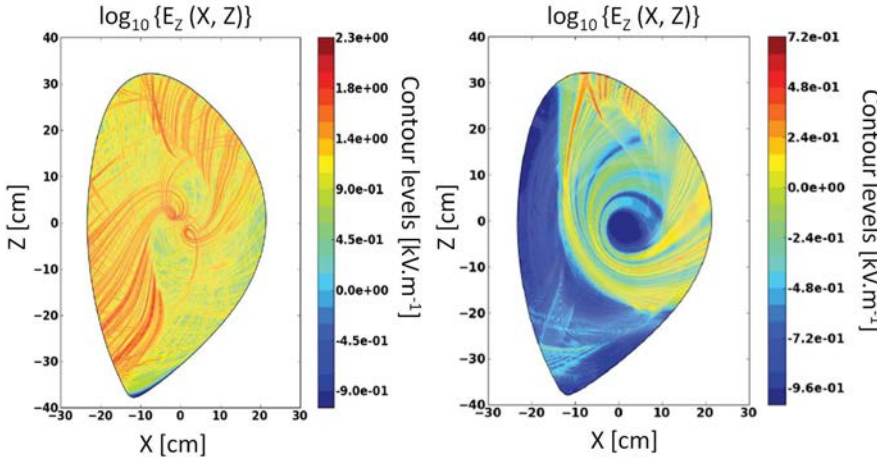


FIG. 6.16. Left: TORIC-LH simulation of LH waves in Alcator C-Mod in the weak damping regime ( $N_{\parallel} = -1.55$ ,  $T_e(0) = 2.33$  keV). Right: TORIC-LH simulation of LH waves in Alcator C-Mod in the strong damping regime ( $N_{\parallel} = -3.6$ ,  $T_e(0) = 2.33$  keV). Reprinted from Ref. [6.105]. Copyright (2011), American Institute of Physics.

### 6.3. EXPERIMENTAL RESULTS ON RF HEATING AND CURRENT DRIVE

A summary of RF heating and current drive results will be given in this section. Due to the extensive literature, we will confine our summary to toroidal devices, in particular tokamaks. There was a parallel evolution of applications of ECH and ICH in mirror machines in earlier years, but with the exception of a few cases, these machines have been shut down more than a decade ago. The interested reader may want to look up additional references on this topic elsewhere. Historically, in the ion cyclotron range of frequencies (ICRF) regime, heating results in the 1960s and early 1970s were limited by poor confinement of energetic minority species ions in both stellarators and tokamaks. However, this was followed by spectacular heating results in the 1980s at the multi-MW power levels in larger machines with excellent confinement, such as PLT, TFTR, JT-60 and JET. Rapid progress was obtained because of the availability of relatively low cost amplifier tubes (tetrodes) at the 1–2 MW level in this frequency regime. In the late 1970s and early to mid-1980s the theory of LHCD was developed (see previous section) and by the mid-1980s this drive was firmly established in experiments in the USA, in Europe and in Japan. Presently, multi-MW long pulse LHCD experiments are being carried out on Tore-Supra, JET and most recently Alcator C-Mod. Long pulse experiments are in preparation for the new superconducting tokamaks in China (EAST) and the Republic of Korea (KSTAR). Meanwhile, ECRH was progressing rapidly in the 1980s with the development of gyrotron tubes at 28–56 GHz at the 200 kW level, while in

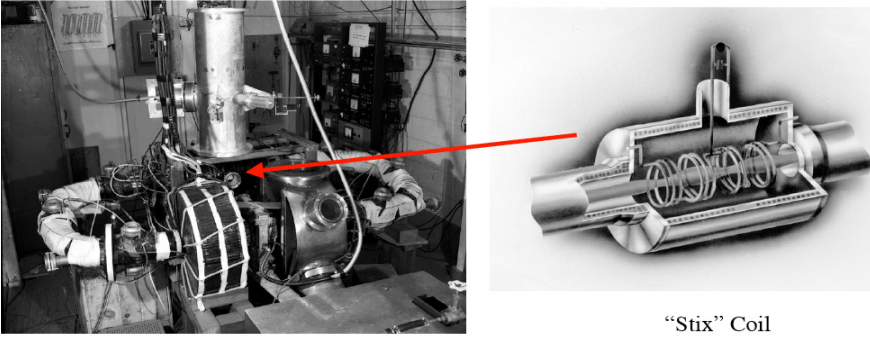
the late 1990s MW level gyrotrons were developed at frequencies in the range 110–140 GHz. Recent multi-MW experiments in T-3, DIII-D, ASDEX-U, TCV and JT-60 have yielded excellent heating and current drive results in good agreement with theory. Recent tube development at the 1 MW level has been achieved at frequencies up to 170 GHz, and development of 2 MW long pulse tubes is under way for ITER applications. While RF wave propagation in the plasma core is now well established, the coupling to high amplitude RF waves around metallic antennas in the ICRF and LH regimes is still an area of active research, including possible non-linear effects. Steady progress is being made to identify these interactions by both theory and experiment and development of realistic antenna codes to model these interactions is under way. We expect that reliable RF wave techniques in all three frequency regimes should be available for implementation in ITER during the next decade as needed. Reliability of antenna operations at high RF voltages and long pulses will need further attention and novel antenna design concepts are being developed and tested in ongoing experiments. Finally, we should mention that the development of new diagnostics, namely phase contrast imaging (PCI), offers ways to measure the injected RF waves and mode converted waves inside the hot plasma [6.46]. In the future, using synthetic diagnostics in full-wave codes, a quantitative determination of power flow inside hot fusion plasmas should be feasible. We shall now discuss some of the experimental results in some detail. Appropriate references will be given whenever appropriate.

### 6.3.1. ICRF heating and current drive experiments

The declassification of fusion research at the Geneva Conference in 1958 opened up information from the Princeton Stellarator RF heating programme of Stix and coworkers in the late 1950s (1958 and beyond). Simultaneously, Stix was preparing his famous text “The Theory of Plasma Waves”, which was published in 1962 [6.2]. This early work concentrated on understanding wave propagation and absorption in the “magnetic beach” geometry, which was then applied to some of the smaller stellarators (the B-65 device) in Princeton with various degrees of success by Stix and coworkers (Fig. 6.17).

The idea was that shear Alfvén waves with dispersion relationship  $\omega = k_{\parallel} v_A (1 - \omega / \omega_{ci})^{1/2}$  propagating at frequencies below the ion cyclotron frequency by a few tens of per cent would propagate into a region with lower magnetic field (the “magnetic beach”) and would dramatically increase their wavenumber, thus experiencing strong ion cyclotron absorption at  $1 - \omega / \omega_{ci} = 0$ , thereby transferring the wave energy to kinetic particle energy. This ingenious idea based on propagation of the left hand polarized slow Alfvén wave and its absorption at the ion cyclotron frequency (Fig. 6.18) was effective and produced a strong enhancement of neutrons at the resonant field [6.107]. This work was

### The B65 Stellarator



“Stix” Coil

FIG. 6.17. The B-65 stellarator and an early version of the Stix coil [6.107]. Reprinted from Ref. [6.107]. Copyright (2011), American Institute of Physics.

followed by more extensive studies by Hooke and coworkers on the B-66 device with longer scale lengths, better suited to basic studies of wave propagation and absorption satisfying the WKB conditions on wave propagation [6.108]. Here the dispersion relationship and wave damping decrement were verified in detail, laying a solid foundation to the theory of “slow wave” propagation in the Alfvén wave regime in relatively small plasma columns. However, this wave had to be abandoned in future larger tokamak plasmas that followed in the 1970s and 1980s, in particular PLT in Princeton and TFR in France, since launching the slow wave efficiently became impractical in higher density plasmas ( $n_e \geq 10^{19} \text{ m}^{-3}$ ) owing to the high values of  $N_{\parallel}$  required. Thus, exploration of fast wave heating started, initially at the deuterium harmonic cyclotron frequency, as well as at the ion-ion hybrid frequency.

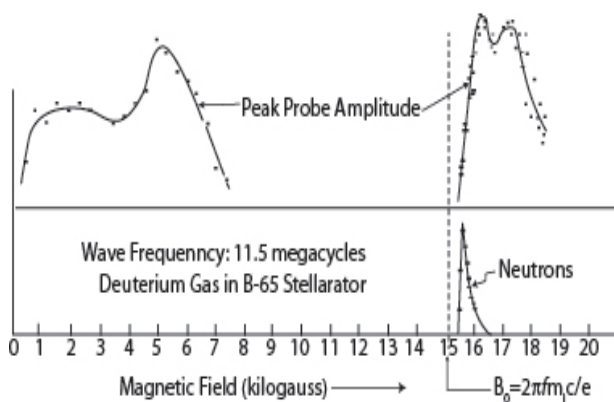


FIG. 6.18. Strong neutron enhancement followed the resonance condition as the magnetic field was varied. Taken from [6.107]. Reprinted from Ref. [6.107]. Copyright (2011), American Institute of Physics.

It was discovered early on by experiment and theory that ion cyclotron absorption in a single ion species plasma would not work due to the nearly complete right hand polarization of the fast wave at the fundamental cyclotron resonance, at least in the relatively cold ( $\sim 1$  keV) initially ohmically heated plasma. One of the earliest theoretical treatments of this picture discussed mode conversion of wave energy into IBWs, and electron heating, both for low and high field side launch, to explain the experiments in the early TFR tokamak and PLT results [6.41]. Some of the early results are depicted in Fig. 6.19 from the TFR tokamak, showing the effectiveness of heating and its spatial profile as a function of minority concentration. The heating is maximum around 25% minority concentration when the ion-ion hybrid (mode conversion) layer is located near the axis of the plasma radius at  $R = 98$  cm. This is in agreement with theoretical predictions given earlier. Unfortunately, only ions were measured and it is likely that electron heating was more substantial.

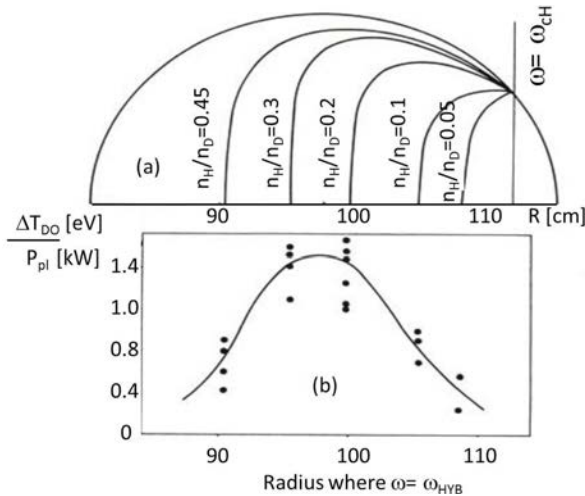


Fig. 6.19. (a) Profiles of the ion hybrid (mode conversion) layer in the TFR tokamak; (b) heating effectiveness as a function of  $n_H/n_D$  ratio and radius with  $B_\phi = 4.6$  T. Here  $\omega_{HYB}$  is the ion-ion hybrid frequency,  $P_{pl}$  is the RF power absorbed by the plasma and  $T_{DO}$  is the change in the central deuterium temperature. Taken from Ref. [6.109].

When carrying out experiments in “pure” deuterium plasmas at the deuterium cyclotron harmonic, better heating was achieved than one would have expected from theory. As it turns out, the actual absorption mechanism was minority absorption on the H minority species, since a few per cent of H is always present in deuterium plasmas. This was discovered by charge to mass resolved data from the escaping neutral atoms in the early TM-1-VCH device in the Soviet Union [6.110]. Energetic ion tails were also discovered in the early ATC experiments in the USA, but the H minority ion species was not

identified [6.111]. To optimize minority heating one has to reduce the minority species (H in this case) concentration to below 10% so as to move the mode conversion layer near the H minority resonance layer within the Doppler width  $\Delta r = k_{\parallel} v_{th,H} R / \omega_{cH}$ , where  $\omega_{cH}$  is the hydrogen cyclotron frequency. At higher concentrations the mode conversion layer moves far away from the cyclotron resonance layer and mode conversion into IBWs, and electron Landau absorption would dominate. However, because of reflection from the L cut-off layer, single pass absorption efficiency by mode conversion is not as efficient as minority absorption, which can be 90% or better in even medium size tokamaks. The kinetic theory of minority species absorption that was formulated by Stix [6.43] was verified first in the elegant PLT experiments with charge to mass discrimination by Hosea and co-workers [6.112] (see Fig. 6.20).

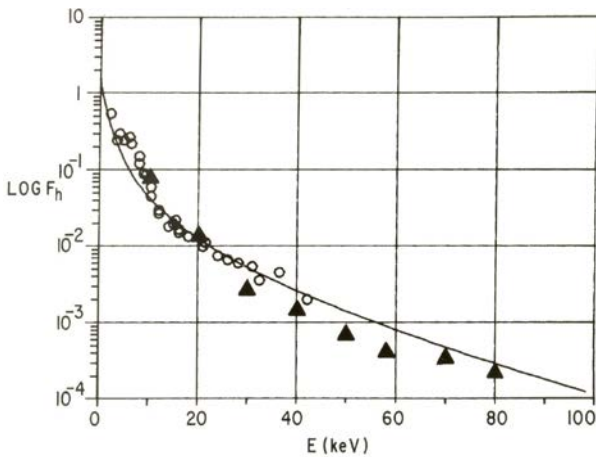


FIG. 6.20. Measured distribution of energetic minority ion species in the PLT tokamak and comparison with the Stix theory [6.112]. Here  $F_h$  is the hydrogen minority species distribution function.

It is clear that for efficient bulk plasma heating, the energetic ions have to be well confined until they slow down by collisions with the bulk plasma. Both ions and electrons are heated, and the slower particles heat ions while the faster ones heat electrons. While in the early experiments (C-stellarator, ST tokamak, etc.) energetic particle confinement was poor, in modern tokamaks (PLT, etc.) with at least 0.5 MA of plasma current the energetic particles were well confined, and therefore we would expect efficient heating of the plasma. This fundamental understanding was followed by impressive heating results in PLT and later TFTR, JT-60 and JET. One of the earliest multi-MW, multi-keV experiments was carried out on the PLT tokamak and the results are illustrated in Fig. 6.21 [6.113] and Fig. 6.22 [6.114] for the minority fundamental and majority second harmonic heating, respectively. Note the substantial second harmonic ion

tail in a pure H plasma in order to avoid mix up with minority heating in the earlier experiments [6.111]. A review of these early experiments has been given by Porkolab [6.1] and Colestock [6.115]. Because of the complexity of these heating regimes, historically the name ICRF or ion cyclotron resonance range of frequencies was adopted. Later, efficient beam ion acceleration was demonstrated in combined NBI and 2nd and 3rd harmonic ICRF injection experiments in JT-60 [6.116].

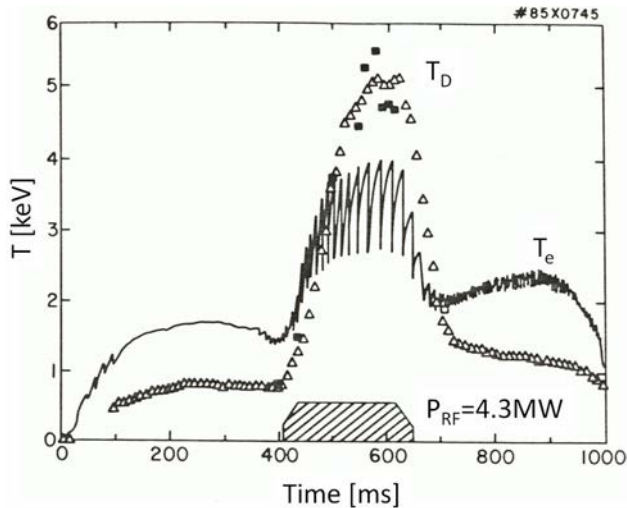


FIG. 6.21. Ion heating results from PLT with  $^3\text{He}$  minority heating in a D plasma with  $B = 3.2 \text{ T}$ ,  $I_p = 600 \text{ kA}$ ,  $n_e = 3.7 \times 10^{19} \text{ m}^{-3}$ ,  $P_{\text{RF}} = 4.3 \text{ MW}$  [6.113].

We should briefly mention here attempts to heat plasmas with directly launched IBWs in both PLT [6.117] and Alcator-C [6.118, 6.119]. While there was difficulty to inject large amounts of power owing to the parallel antenna straps required to launch  $E_{\parallel}$ , which ultimately resulted in significant impurity injection, there was clear evidence of particle confinement improvement (by factors up to 3 in Alcator-C) and peaking of density profiles. In today's terminology this may be interpreted as formation of a thermal barrier, at least for particles (which also led to impurity accumulation). While concomitant ion heating was also observed, this was typically limited at most to 30% of the initial temperature. The results were hard to understand and there was strong evidence that non-linear phenomena played an important role [6.120]. A large scale experiment at the MW level on DIII-D [6.121] failed to produce the expected core plasma heating and there was strong evidence of edge parametric decay phenomena, and these experiments were abandoned in the USA. However, there was a continuing programme on FT-U in Frascati at high frequencies (0.5 GHz) to reduce non-linear effects, with some success.

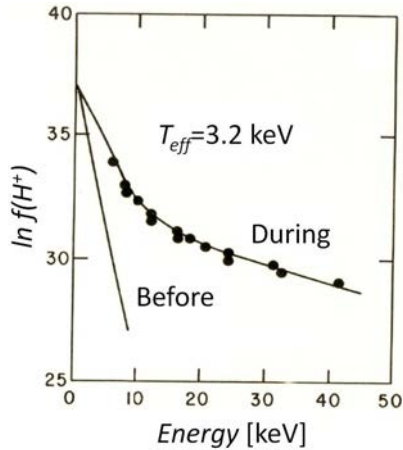


FIG. 6.22. Proton energy distribution in the presence of second harmonic heating in PLT. “Before” means before application of the ICRF power, and “During” means during application of the high power RF.  $B = 1.4 \text{ T}$ ,  $P_{RF} = 2.8 \text{ MW}$  [6.114]. Reprinted from Ref. [6.114]. Copyright (2011) by the American Physical Society.

Following the pioneering work in the 1980s, 1990s and 2000s, large amounts of ICRF power were installed in JET and TFTR, to test burning plasma relevant heating scenarios, including startup plasmas. The results were excellent and a large number of publications resulted (see Refs [6.122] for TFTR and [6.123, 6.124] for JET and related references). Some of these results included the following: second harmonic tritium heating was demonstrated in TFTR [6.122], and fundamental D minority,  $^3\text{He}$  minority, fundamental T minority and T majority second harmonic heating, were all demonstrated in JET [6.123] (see Fig. 6.23). At the same time it was shown that the RF driven fusion power with 6 MW of ICRF was comparable to that achieved with NBI power. Other references from recent research in JT-60U, ASDEX-Upgrade and Alcator C-Mod may be found in Refs [6.125, 6.126] and [6.79], respectively. For example, in JT-60, 5 MW of ICRF power was coupled successfully in a 4 MA hot ion H-mode plasma with 0.15 m antenna–separatrix gap, which meets ITER requirements [6.125]. We note that in a two ion species plasma mode conversion current drive up to 130 kA was demonstrated in TFTR [6.127]. Effective mode conversion heating was also found in ASDEX-Upgrade [6.126] and Alcator C-Mod [6.128]. While the heating was believed to be due to IBW mode conversion, as shown by theory off-axis, the magnetic shear significantly up-shifts the launched  $N_{\parallel}$  spectrum and coupling to kinetic ion cyclotron waves dominates IBW [6.44]. This effect was discovered in Alcator C-Mod by phase contrast imaging diagnostics that verified the dominant role played by the mode converted ICW, as opposed to the IBW [6.46, 6.129]. Recent experiments also confirmed mode conversion heating in ASDEX-Upgrade [6.126] and Alcator C-Mod [6.128].

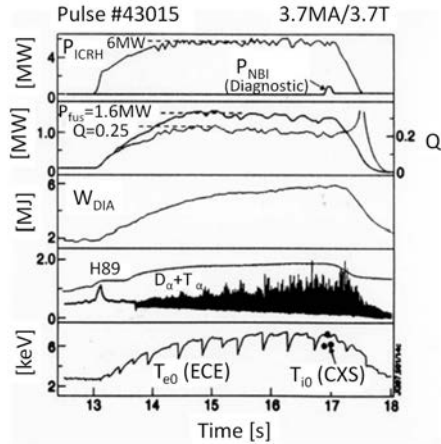


FIG. 6.23. Bulk ion heating was achieved on JET with D minority heating in T majority plasmas, yielding  $Q = 0.22$  [6.123].

Other exciting ICRF physics, besides various forms of heating, include fast wave current drive including ICCD, or ion cyclotron current drive, on the JET tokamak [6.130]. Another form of ICRF current drive is due to Landau absorption of the directionally launched fast wave (FW) as demonstrated in DIII-D and Tore-Supra. As shown in Fig. 6.24, in DIII-D the current drive efficiency is in good agreement with theoretical predictions when no other competing absorption mechanism is present [6.131].

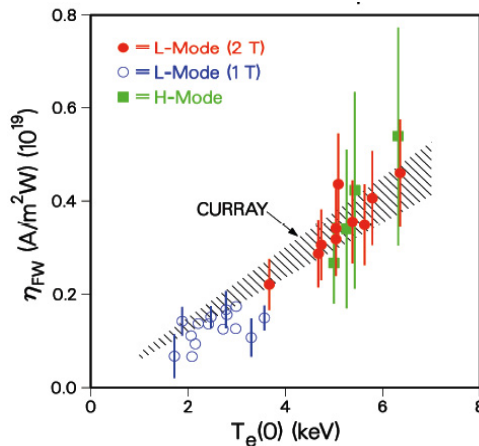


FIG. 6.24. The measured fast wave current drive efficiency  $\eta_{FW}$  in DIII-D is in excellent agreement with theoretical predictions [6.131]. CURRAY is the ray tracing and Fokker-Planck combined code that calculates the current drive efficiency. The symbols 1 T and 2 T are the magnetic fields where the experiments were carried out, and are distinguished by the red and blue colours. The green symbols correspond to H mode plasmas.

### 6.3.2. ICRF antenna and transmission line design

In this section we discuss the conversion of prime RF power to electromagnetic waves in the ICRF, including transmitters, transmission lines and the launchers (antennas) that excite plasma waves of the desired polarization and spectral characteristics in the edge of the plasma.

#### 6.3.2.1. ICRF transmission line architecture

A schematic layout of the simplest possible system with a single element antenna is shown in Fig. 6.25(a), while parts (b) and (c) of the figure show the topologies of configurations to drive a phased array of two elements.

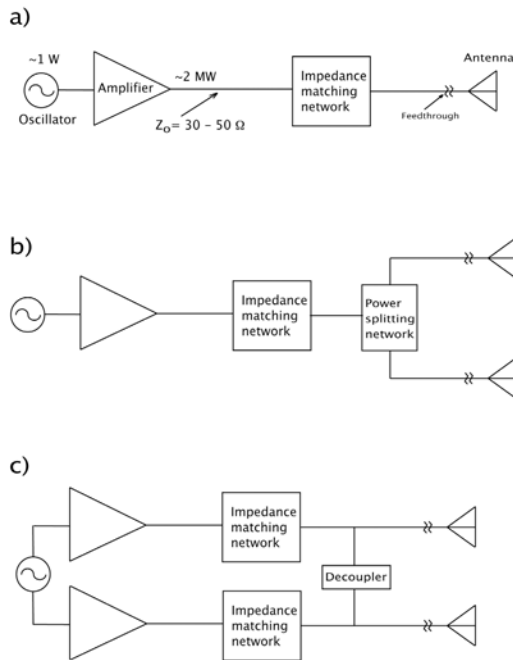


FIG. 6.25. Schematics of simple ICRF system configurations. (a) Single antenna, single source. Characteristic impedance of transmission line  $Z_0 = 30\text{--}50\ \Omega$ . (b) Feeding a pair of antenna elements with a single source. (c) Feeding a pair of antenna elements with two sources.

In Fig. 6.25(a) the feedthrough defines the boundary between the pressurized transmission line and the device vacuum. The antenna's input impedance is primarily reactive with only a small resistive part, in magnitude much smaller than the characteristic impedance of the transmission line  $Z_0 \sim 30\text{--}50\ \Omega$ . In Fig. 6.25(b), the power splitting may be inside the device vacuum and only a single feedthrough would be needed. In Fig. 6.25(c) a decoupler would be needed

if arbitrary phasing is desired to compensate for mutual reactance between the antenna elements.

### 6.3.2.2. ICRF source technology

An important advantage of heating and current drive systems in the ICRF over other auxiliary heating methods, particularly in future reactor applications, is the highly efficient continuous wave (CW) sources that are available. Prime electric power can be converted into electromagnetic wave energy in the ICRF at an overall efficiency of about 70%, which compares favourably with presently achievable efficiencies of other frequency regimes of interest for fusion applications, as well as both positive-ion- and negative-ion-based neutral beam sources. The reason that source efficiency is of importance in reactor applications is that reactors will operate in a high  $Q$  but not ignited regime, for reasons of controllability. The efficiency of the drivers directly feeds into the overall  $Q$  of the plant at fixed levels of confinement.

Sources with these high efficiencies and at high power levels have been available for many years because of the coincidence of the ICRF for hydrogenic plasmas at magnetic fields of 3–8 T with the VHF frequency band (30–300 MHz), which has been used for decades for radio and television broadcasting and other high power commercial applications. In essentially all experiments in the ICRF that have been carried out since the late 1950s, the RF sources have been based on modified high power broadcast transmitters. As early as 1964, a 4 MW transmitter at 25 MHz was in use for ICRF experiments on the C stellarator [6.132], though pulse lengths longer than 0.005 s were not needed in those experiments. The highest power ICRF transmitter that has been used in fusion experiments to date is the 32 MW system installed on JET [6.133], which is composed of sixteen 2 MW modules. This system was specified to be able to produce full power at a pulse length of at least 20 s. The highest power CW generator for fusion research that has been demonstrated to date is the 25–100 MHz 1.6 MW transmitter developed for the superconducting Large Helical Device. This module has been tested to 5000 s pulse length at full power into test load [6.134]. Each of these high power RF sources is built as a chain of two or three gridded-tube amplifiers, each stage having a power gain of ~13 dB, as illustrated in Fig. 6.26.

The final stage amplifier is built around a high power tetrode with a typical anode dissipation rating in steady state of up to 2.5 MW [6.135]. Figure 6.27 shows a photograph of such a tetrode made by EIMAC in the USA. At a typical anode efficiency of ~0.7, output power levels into a matched load of 5 MW from a single tetrode should be in principle possible. In practice, allowable maxima of anode current, of control and screen grid dissipation, and readily achievable drive power levels (at a gain of 13 dB) limit the achievable output power to somewhat lower than 3 MW from a single source. The remaining substantial

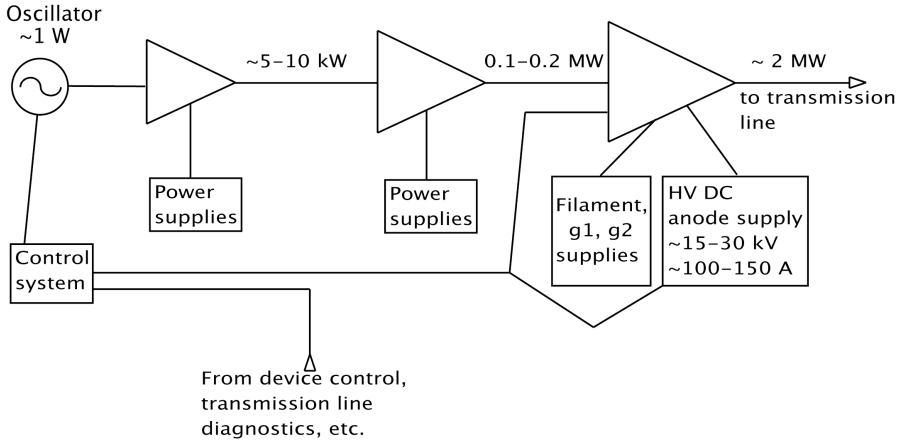


FIG. 6.26. Typical high power transmitter layout with three amplifier stages, the necessary power supplies and the control system.

margin of maximum power output relative to what is usually produced with a single amplifier has been used to permit operation with less than perfect matching, or to widen the available instantaneous bandwidth (when frequency is used as a tuning actuator), and to maximize tube lifetime and reliability. For high power long pulse operation in the VHF band, the circuit that matches the output impedance of the tetrode to the characteristic impedance of the transmission line (typically 30 or 50  $\Omega$ ) is implemented as a coaxial cavity. Such systems tend to have instantaneous bandwidths (without retuning) in the order of several hundred kHz and can be tuned between pulses in a matter of a few minutes to operating frequencies in the VHF band differing by a factor of two or more. Typical tunable frequency ranges are 25 to 50 MHz, 40 to 80 MHz, 25 to 100 MHz, or 30 to 120 MHz.

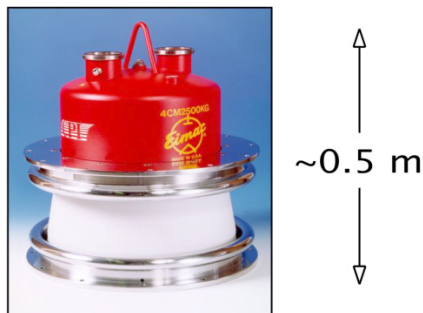


FIG. 6.27. Typical high power tetrode used in cavity amplifiers for ICRF systems in the VHF band (CPI Eimac 4CM2500KG). The structure at the top is the water jacket surrounding the anode; the cooling water inlet and outlet tubes are visible. Photograph courtesy of CPI EIMAC, Palo Alto, CA.

The needs of future devices in the area of ICRF transmitters will be able to be met with a relatively small amount of further development. In particular, extension of the power that is demonstrated in true steady state (no further evolution of the temperature of any of the components in the transmitter) up to 2 MW per unit and beyond should be carried out. It should be noted that requirements on the flexibility of the system, especially in the area of tunable frequency range, are likely to be maximum on ITER and decrease for subsequent, less experimental devices. The ultimate ICRF system is likely to operate only at a single, pre-chosen frequency, or at most in a narrow band around such a specific frequency. Removal of the need for a one or two octave wide tunable band should permit significant simplification of the transmitter and may be accompanied by gains in overall system efficiency and reliability.

### *6.3.2.3. ICRF transmission line design*

A significant advantage of RF heating methods over neutral beams is that the sources of RF energy can be located at a convenient distance from the plasma device with quite low levels of loss of power over long transmission lines. This is even more the case with waves in the ICRF than with the higher frequency ranges. In practice, distances of the sources from the plasma are measured in the hundreds of metres or even kilometres with losses of only a few per cent being typical. Since the transmission lines operate in the lowest order TEM mode, mode conversion at bends and resulting increased losses is not an issue, nor is alignment, etc. The wave launchers used in the ICRF usually involve a phased array of elements which present an impedance to their feedlines that is significantly different than the characteristic impedance of the transmission line. Furthermore, the elements in the array often have significant levels of mutual reactive coupling to each other, and the total number of elements often does not equal the number of RF sources being used to power them. Consequently, in addition to conveying the wave energy from source to plasma device, the transmission line must perform a number of additional functions. These functions include power splitting or combining, relative phase and amplitude control and impedance matching. A quite significant challenge is to deal with the fact that in the ICRF the coupling physics of the wave launchers is such (see the next section) that the input impedance of the coupler can vary strongly on a large range of timescales, from tens of microseconds (L/H transitions, ELMs) to very slow changes due to thermal expansion of the components of the system which may be hundreds to thousands of seconds. The impedance matching system must be capable of dealing with these changes to optimize power transfer from the source to the plasma and to minimize RF voltage in the tuned sections of the lines.

The development of both sources and transmission lines has been facilitated by the environment which is fully controllable (e.g. transmission lines can be pressurized with insulating gases, water and/or air cooling is readily introduced). Many developments in the transmission line area for the ICRF have been reviewed in Refs [6.136, 6.137], with a few of the highlights being listed here:

- Demonstration in existing experiments of multiple techniques of impedance matching that allow a significant range of coupler input impedance variation and yet present the transmitter with a well matched load at all times. This includes passive-lossy schemes involving 3 dB hybrid junctions, lossless systems such as the conjugate tee matching scheme, and fast-acting matching elements such as the ‘twin stub’ with narrow band frequency modulation, fast ferrite stubs and other devices.
- Successful methods of power division and phase control for large phased arrays of up to 12 elements, including significant development of necessary decoupling schemes that are needed to permit travelling wave phasings for current drive applications in the face of strong mutual reactance between elements in the arrays. The decouplers are also an integral part of the matching schemes listed above.
- Demonstration of actively cooled ICRF transmission lines operating in a thermal steady state at high CW power levels, as will be needed for ITER and steady state devices beyond ITER.

In summary, it can be asserted that the transmission line aspect of high power steady state ICRF systems is well in hand, with only minimal further development being needed for future systems.

An example of a transmission line system in present use is the tunerless system used on the DIII-D device to power a four-element phased array at a 90° phasing [6.138]. In this case, flexibility (in operation frequency and antenna phasing) is sacrificed to gain simplicity. This configuration uses a 3 dB 90° hybrid junction and a 2-port decoupler to provide complete isolation from reflected power to the transmitter in the face of rapidly changing antenna loading without adjustable tuning elements. Other transmission line configurations in present use employ external conjugate tees, such as on JET [6.139], to provide similar “load resilience”, or use conjugate tees internal to the antenna similarly with the added advantage of low electric fields in the vacuum coaxial feedlines (see next section and Ref. [6.140]) The latter system essentially moves part of the impedance matching system from its traditional location in the transmission line into the coupling structure, which is the topic of the next section.

## 6.3.2.4. ICRF wave launchers

The wave launcher (antenna) is the most critical component in a high power ICRF system for fusion applications (see Fig. 6.28). Once a propagating wave is successfully excited near the edge of the magnetically confined plasma, the fast Alfvén wave (fast wave) propagates to the core minority cyclotron resonance (or harmonic cyclotron resonance of the main species) without intervening cut-offs, as was discussed in previous sections. The launcher must efficiently excite the waves with the necessary polarization and the desired amplitude without introducing significant impurities or suffering from electrical breakdown. As discussed in previous sections, a wave of fixed wavelength along the static magnetic field (i.e. a fixed  $k_{\parallel}$ ) is evanescent in the low density region from the antenna face to the right hand cut-off density, which for typical parallel wavelengths and magnetic fields occurs at electron densities on the order of a few times  $10^{18} \text{ m}^{-3}$ . At lower densities, the wave is very nearly as evanescent as it is in vacuum (zero density), where  $N_{\perp} = i(N_{\parallel}^2 - 1)^{1/2}$ . The wave energy must tunnel through the evanescent layer from the antenna surface up to the cut-off density, and the wave amplitude therefore decreases exponentially in this region. The wave launcher must excite the appropriate polarization, which for a compressional (fast Alfvén) wave must have the RF magnetic field alternately parallel and anti-parallel to the static magnetic field, and the RF electric field perpendicular to the static magnetic field. In principle, this polarization could be excited by a capacitive coupler that imposes an RF electric field across the static magnetic field or by an inductive coupler that modulates the static magnetic field at the RF frequency. Of these two possibilities, for several reasons the inductive coupler has been used in all high power ICRF experiments.

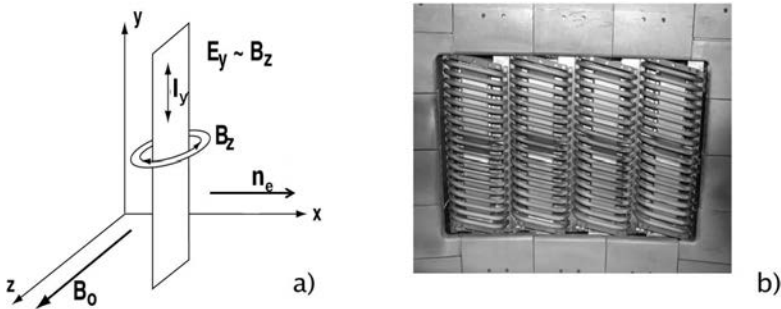


FIG. 6.28. (a) Approximative schematics of an idealized single element of a loop antenna to launch fast waves (the coordinate system shown here does not correspond to the right side of the figure); reproduced Fig. 3 from Ref. [6.141]. Reprinted from Ref. [6.141]. Copyright (2011), American Institute of Physics. (b) Practical phased array of four loop antennas, as viewed from the plasma, including slanted Faraday screen elements, double poloidal straps and surrounding graphite protection tiles, from DIII-D. The height and width of the array are 0.45 m by 0.70 m.

Energy that is carried away from the coupler by fast waves in the plasma looks like a loss to the exciting circuit, and hence can be modelled as a resistive component to the termination of the transmission lines that feed the coupler. This resistance is called the loading resistance and the larger the value of the loading resistance, the larger the amount of power that is coupled to the plasma per unit of antenna current. Figure 6.29 shows the simplest possible lumped-element antenna model, in which the feedline of characteristic impedance  $Z_0$  is terminated by a resistance  $R_L$  to ground in series with a reactance  $-iX$ , the net reactance  $X$  representing the parallel combination of the element's inductive reactance and capacitive reactance to ground. Such a lumped-element model is reasonable if one is not interested in the spatial dependence of fields along the radiating element. The loading resistance  $R_L$  is almost always much smaller than  $Z_0$ , so the current through the load resistance is a maximum, denoted by  $I_{max}$ . The total dissipated power is

$$P_{dis} = 1/2 I_{max}^2 R_L \quad (6.127)$$

where the factor of 1/2 is due to the use of peak amplitudes rather than root mean square and the maximum current  $I_{max}$  and the maximum voltage  $V_{max}$ , separated by a quarter of a wavelength in the feedline, are related by the characteristic impedance of the feedline

$$Z_0 = V_{max} / I_{max} \quad (6.128)$$

so

$$P_{dis} = (V_{max}^2 / 2Z_0^2) R_L \quad (6.129)$$

if the net reactance  $X$  is neglected.

Since the dissipated power can readily be measured with directional couplers in the transmission line and the voltage at a maximum in the transmission line can also be readily measured with capacitive voltage probes, this relation provides a simple way to measure the loading resistance without instrumentation inside the device vacuum. In typical applications, the antenna element is indeed electrically short, so that the antenna does not radiate electromagnetic waves into vacuum (i.e. in the absence of a plasma load.) Hence the loading resistance in the absence of plasma is almost entirely due to ohmic losses (skin-current losses) in the antenna and feedlines. If this ohmic loss is modelled as being lumped into the total load resistance  $R_L$ , i.e.  $R_L$  is taken to be the sum of ohmic losses in the antenna and feedline, denoted by  $R_{vac}$ , plus the power radiated into plasma,  $R_p$ , then  $R_L = R_{vac} + R_p$  (see Fig. 6.29). The power dissipated in the plasma (the power radiated from the antenna into the plasma) is

$$P_p = \frac{V_{max}^2}{2Z_0^2} R_p = \frac{V_{max}^2}{2Z_0^2} (R_L - R_{vac}) \quad (6.130)$$

and by comparing these equations we obtain the fraction of the total dissipated power that is coupled to plasma waves as  $P_p / P_{dis} = (R_L - R_{vac}) / R_L$ .

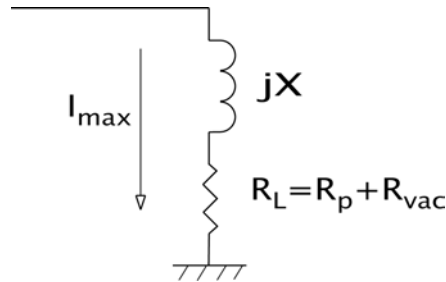


FIG. 6.29. Simple lumped-element equivalent circuit of antenna, viewed as a lumped-element termination of the feedline. The total loading resistance  $R_L$ , which is vacuum losses  $R_{vac}$  plus the plasma loading  $R_p$ , is much smaller than the characteristic impedance of the feedline.

Let us consider some typical numbers in this application. Suppose 0.5 MW is to be applied to a single antenna element, on which the loading resistance is  $1 \Omega$ . The peak antenna current would be 1 kA and if the feedline characteristic impedance is  $25 \Omega$ , then the peak voltage in the feedline, one quarter of a wavelength from the termination, is 25 kV. If the feedthrough is farther than one quarter of a wavelength from the termination, then this peak voltage occurs within the device vacuum, in the feedline. If the net reactance is not negligible compared with the characteristic impedance, the peak voltage is higher than in the case with  $X = 0$ ; for example, if  $X = Z_0$  in magnitude in this case the peak voltage becomes about 35.5 kV. One obtains in this simple model that the peak voltage is given by

$$|V|_{\max} = \sqrt{2Z_0 P_{dis} (1 + |\rho|) / (1 - |\rho|)} \quad (6.131)$$

and the reflection coefficient magnitude  $\rho$  is given by

$$|\rho|^2 = \frac{(Z_0 - R)^2 + X^2}{(Z_0 + R)^2 + X^2} \quad (6.132)$$

Since in decades of experience it has been found that high voltage electrical breakdown ('arcing') becomes probable if the RF electric field at any point within the device vacuum parallel to the static magnetic field exceeds a threshold value of about  $1.5 \text{ MV} \cdot \text{m}^{-1}$  [6.142] and often the coaxial feedlines have spacings between the inner and outer conductors on the order of centimetres, voltages of this order often cause a coupled power limit at low values of antenna loading resistance (compared with transmission line characteristic impedances). For this reason, the two important characteristics of the loading resistance in practice are that its absolute value is *low* (by comparison to a reasonable value of transmission

line characteristic impedance), and tends to be *highly sensitive* to edge plasma conditions and hence strongly varies in time. These characteristics stem from the exponential decrease in the wave amplitude in the tunnelling region. Since it is found experimentally that in ICRF heating a parallel wavenumber spectrum peaked at  $N_{\parallel}$  significantly larger than is needed for efficient absorption [6.47, 6.48, 6.143], the previous discussion indicates that the evanescence will be severe if the radial distance  $g$  from the antenna to the cut-off layer is such that  $k_{\parallel}g \sim 0.5$  or larger. A more sophisticated estimate [6.144] shows a less pessimistic number than 0.5, but of similar magnitude. To minimize deleterious plasma/wall interactions, in most high performance fusion devices the distance between the edge of the plasma and the antenna surface cannot be reduced to less than  $\sim 0.1$  m and therefore the evanescence tends to be strong and the loading resistance low, approximately  $1 \Omega$  per element. Nevertheless, for multiple antenna straps with optimized spectrum, JT-60 has obtained  $4 \Omega$  loading resistance with a 0.15 m antenna–separatrix gap, sufficient for present ITER requirements [6.145]. The combination of high antenna currents needed to couple large power levels and transmission lines terminated in an impedance much different (lower) than their characteristic impedance implies high electric fields within an electrical distance of  $1/4$  of a vacuum wavelength away from the region of high antenna current. Since in large devices this distance away from the current maximum is still within the torus vacuum region, these high electric fields can lead to electrical breakdown problems within the antenna structure, as discussed above.

Although the inductive launchers are designed to minimize the component of the RF electric field along the static magnetic field ( $E_{\parallel}$ ), the 3-D effects associated with current-carrying elements of finite poloidal length, radial currents from feeders, the effect of the housings in which the current carriers are located, and the impracticality of maintaining perfect alignment of the antenna elements with the perpendicular to the local static magnetic field all lead to non-zero  $E_{\parallel}$  in the vicinity of the coupler face. Furthermore, incomplete absorption of the RF energy in the core of the plasma on the first pass may lead to non-zero RF field amplitudes everywhere near the first wall in the device. The combination of static magnetic fields intersecting conducting surfaces, non-zero (albeit very low) electron density at those points, and non-zero RF field amplitudes parallel to the static magnetic field line at the contact points are the recipe for rectified RF sheaths to appear at those locations [6.146, 6.147]. These sheaths are categorized as near-field sheaths, such as the ones driven by the antenna currents directly, and far-field sheaths, which are the ones driven by the fields arising from incomplete first-pass absorption of the RF power. The acceleration of ions into conducting surfaces by the DC component of these rectified sheaths represents a power dissipation mechanism (with the power dissipated being the product of the sheath voltage drop and the ion current to the wall), and can cause localized heating of the surface ('hot spots'). The accelerated ions can sputter material from the

surface (both high  $Z$  materials such as the base material of the first wall and low  $Z$  materials from deposited Li, C, B, etc.); the sputtered material then contaminates the plasma [6.146].

Some of the difficulties that arise from non-zero  $E_{\parallel}$  were recognized very early, during the ICRF heating experiments on the C stellarator. The Faraday screen was introduced at that time in order to minimize the  $E_{\parallel}$  near the antenna [6.148]. The Faraday screen is essentially a polarizer to short-circuit the  $E_{\parallel}$  fields in the antenna near-field region. Over the next four decades of ICRF heating experiments, other functions have been attributed to the Faraday screen, such as reducing the plasma density in the vicinity of the current-carrying elements ('straps') and to reduce the effect of changing edge plasma conditions on the reactance of the antenna [6.149]. Nonetheless, several experiments have operated fast wave antennas without Faraday screens [6.149–6.152], with varying degrees of success. The motivation for these efforts is clear: the Faraday screen is probably the most difficult component of the FW antenna to engineer for steady state reactor-like conditions, with high heat and radiation fluxes to this plasma facing component, so that the antenna would be appreciably more attractive if the screen proved to be unnecessary.

The most straightforward path to both reducing deleterious effects associated with residual  $E_{\parallel}$  fields and raising the maximum power density on the antenna that can be achieved without high voltage breakdown would be to reduce the electric fields in the antenna without reducing the strap currents, namely by lowering the impedance of the antenna. It may be that a sufficient reduction of the electric fields near the plasma facing surface of the antenna in this way would permit reliable, efficient high power operation without a Faraday screen. Methods of lowering the impedance of the antenna that are being studied involve proliferation of current-carrying elements in both toroidal and poloidal directions — thereby reducing the peak electric field reached in any single element. It is an open question at this writing whether it is sufficient to minimize the electric fields only in the part of the antenna near the plasma surface, or whether it is necessary to reduce the electric fields everywhere in the coupler that is exposed to the torus vacuum. The answer to this question will determine whether an approach with reactive elements inside the torus vacuum is needed or external reactive elements will suffice.

Another avenue to increasing the power that can be coupled to the plasma with inductive wave launchers is to change the plasma conditions in the neighbourhood of the launcher to decrease the length of the evanescent zone, i.e. to reduce the distance from the face of the launcher to the layer at which the fast wave of the launched parallel wavelength begins to propagate. This is done most simply by reducing the gap between the edge of the plasma and the first wall, but in most devices the degree to which this is practical is determined by other considerations (heat loads to the plasma facing components, ripple losses,

etc.). In ITER, this gap must be in excess of 0.15 m, which is much larger than the values routinely used in present generation experiments. A technique under present study to address this issue is to puff deuterium gas into the scrape-off layer during fast wave injection. It is thought that either a fraction of the RF power goes into ionizing the gas in the near-field region of the antenna (analogous to an already established technique used in lower hybrid coupling experiments (see Section 6.3.4)) or the plasma radially diffusing across the field in the scrape-off layer ionizes the gas in a zone starting at the gas puffing orifice and extending more or less along the static magnetic field lines. Success in achieving substantial increases in fast wave antenna loading in this scenario has been reported from JET [6.153], and other experiments in this vein are being carried out on other devices at this writing. A potential difficulty with this technique is that raising the density near the first wall to increase the antenna coupling could increase the edge losses by sheath formation, for example, as cited in Ref. [6.154], while the edge losses due to far field sheaths scale with the far SOL density and inversely with the local electron temperature. The sensitivity of the core heating efficiency to these edge losses, in turn, may depend on the strength of the first-pass absorption in the core, and on the trajectories of the ray propagation as the wave energy leaves the antenna and propagates to the core. Hence, the results may be expected to be different with different frequencies, coupled wavenumber spectra, absorption mechanisms, details of geometry of the antenna and nearby limiting surfaces, etc.

In summary, the most difficult component of high power ICRF heating systems for fusion is the wave launching structure. The difficulties are due to the fact that waves that can propagate to the high density plasma core do not propagate at plasma densities lower than a particular cut-off value which is typically attained in the scrape-off layer at some distance from the surface of the antenna and the first wall. Therefore the wave launching structure must be near the plasma surface to avoid excessive wave evanescence and corresponding high electric fields in the launching structure in order to couple high power levels. The limit on coupled power manifests itself as a high probability of high voltage breakdown ('arcing') if the RF electric field in the direction parallel to the static magnetic field exceeds a value of  $\sim 1.5$  MV/m anywhere within the torus vacuum [6.142]. To enable high power levels to be coupled without exceeding this limit, the effective impedance of the antenna must be significantly reduced, the resistive loading must be increased, or the antenna's power density must be reduced. The consistency of these various approaches with good core heating efficiency and with other practical constraints on the wave launcher design, particularly for ITER and for future devices, is the topic of much present research.

The present frontier in this area is represented by the most complex and advanced ICRF antenna operated to date, the ITER-like antenna (ILA) on JET [6.155]. A cross-section of this antenna is displayed in Fig. 6.30. In this launcher, a number of the techniques discussed in the foregoing are simultaneously

employed, including a four-fold poloidal segmentation of the antenna strap to reduce the maximum electric field near the plasma, internal tuning elements to allow a wide range of loading resistances without presenting a mismatch to the RF sources and to take up much of the electric fields in private vacuum, and other ITER-relevant features. Operation has been achieved at peak RF electric fields thought to be adequate for ITER, with peak voltages of up to 42 kV. Due to the sensitivity of the loading to details of the density profile in the far scrape-off layer and the uncertainty of the profiles in that region of ITER, the projection of the loading results from the JET antenna to ITER is a topic of much recent work [6.155].

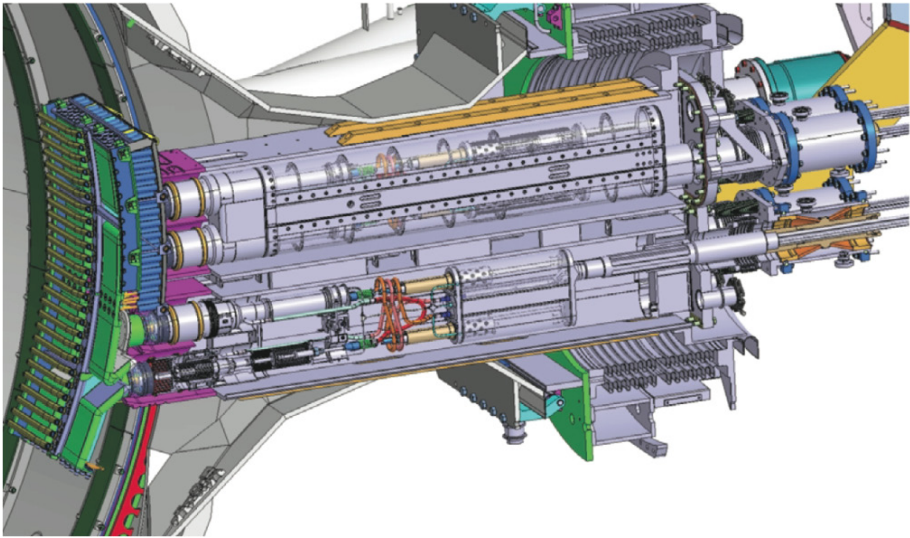


FIG. 6.30. Isometric cutaway view of JET ITER-Like antenna, with Faraday screen at left, resonant double-loop elements, internal conjugate tees, internal vacuum variable capacitors and other components (from Ref. [6.155]).

### 6.3.3. Lower hybrid heating and current drive experiments

After the early classic work of Golant, who worked out the accessibility of lower hybrid waves in an inhomogeneous plasma [6.33], Bellan and Porkolab proceeded to verify the dispersion characteristics of lower hybrid waves [6.7] (see Fig. 6.31). This work showed that lower hybrid waves can be launched effectively from the plasma edge with a phase array of loops surrounding a small plasma column, later to be replaced by a phase array of narrow waveguides in the  $TE_{10}$  mode of excitation in a tokamak plasma at the few GHz range of frequencies (see Ref. [6.156] and references therein), where  $TE_{10}$  stands for the

fundamental mode of excitation of a rectangular waveguide with the electric field pointing across the narrow dimension of the waveguide and the magnetic field perpendicular to it. While there were numerous attempts to use such waves in tokamaks to heat ions by mode conversion into hot ion plasma waves near the lower hybrid resonance layer in the plasma core (Fig. 6.3, region C), there was no convincing evidence ever of ion heating by mode converted waves. Instead, strong parametric decay instability (PDI) was observed in the plasma periphery as the density was raised so that the LH resonance condition would be satisfied and the so-called “density limit” was reached where strong PDI was observed near the plasma periphery [6.157]. Raising the source frequency well above the resonance layer greatly reduced the PDI and electron heating was observed by electron Landau absorption of the waves.

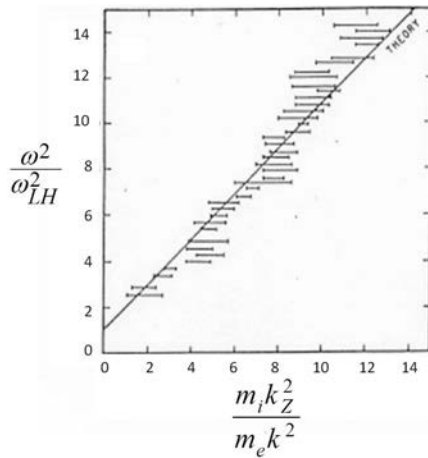


FIG. 6.31. Experimental verification of dispersion relationship of cold lower hybrid waves launched by a phased array of loops formed the basis for lower hybrid current drive experiments in tokamaks (after Ref. [6.7]). Plotted is the comparison of experimental data (horizontal lines) and theoretical predictions based on Eq. (6.48) (solid line).

The wave accessibility condition Eq. (6.58) and the Landau absorption Eq. (6.63) limit the minimum and maximum values of the slow wave index of refraction parallel to the magnetic field,  $N_{\parallel}$ , to the range:

$$\frac{\omega_{pe}}{\omega_{ce}} + \left[ 1 + \frac{\omega_{pe}^2}{\omega_{ce}^2} \left( 1 - \frac{\omega_{ce}\omega_{ci}}{\omega^2} \right) \right]^{1/2} < n_{\parallel} < \frac{7}{T_e^{1/2}} \quad (6.133)$$

where  $T_e$  is in keV.

Absorption is assumed to be due to the quasi-linear limit of Landau damping and is based on code results. It is typically at a phase velocity of about 2.4 times the thermal velocity (where the thermal velocity is defined as

$(2T_e / m_e)^{1/2}$ ). The interpretation of Eq. (6.133) is that in ITER type plasmas the wave penetrates with an index of refraction of about 1.8 and absorption is around 12 keV, which typically is at  $r/a = 0.8$ , which is the ideal distance for a reversed shear AT regime. Clearly, modelling of the edge pedestal height will be critical for assessing LH wave penetration in a reactor type plasma and as the density is increased in reactor regimes beyond ITER's values, wave penetration will be squeezed between accessibility and Landau absorption, unless the magnetic field is increased towards 8 T.

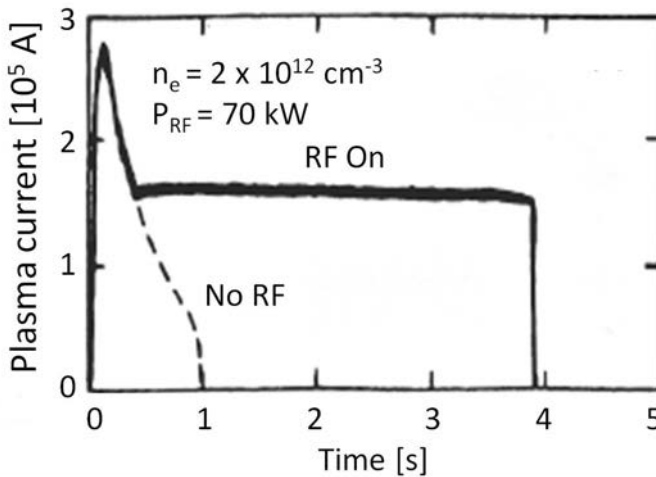


FIG. 6.32. Demonstration of the existence of LHCD in the PLT tokamak for a few skin times in the early 1980s. Copyright (2011) by the American Physical Society.

In the late 1970s the theory of current drive was worked out by Fisch and co-workers (Ref. [6.158] and earlier references therein) and a “feverish” experimental search began to find such currents which were expected to reach hundreds of kA at a few hundred kW of power in low density plasmas. Success followed in a number of experiments both in the USA and elsewhere. We show here only a few results owing to space limitation. Some of the early experiments included JFT-2 [6.159], WT-2 [6.160], Versator-II [6.161], PLT [6.162], Petula [6.163], ASDEX [6.164] and Alcator C [6.165]. Soon thereafter, further experimental results were obtained demonstrating ramping of currents and plasma startup without ohmic drive [6.166], and even transformer recharging [6.167]. Many of these experimental results were summarized in review papers at the Varenna RF workshop in 1985 [6.168, 6.169]. In Fig. 6.32, PLT demonstrated current drive for 3.5 s, exceeding resistive diffusion time,  $a/r_p$ , where  $a$  is the plasma minor radius and  $r_p$  is the plasma resistance due to collisions. In Fig. 6.33, current ramp and transformer recharge is demonstrated from ASDEX [6.167].

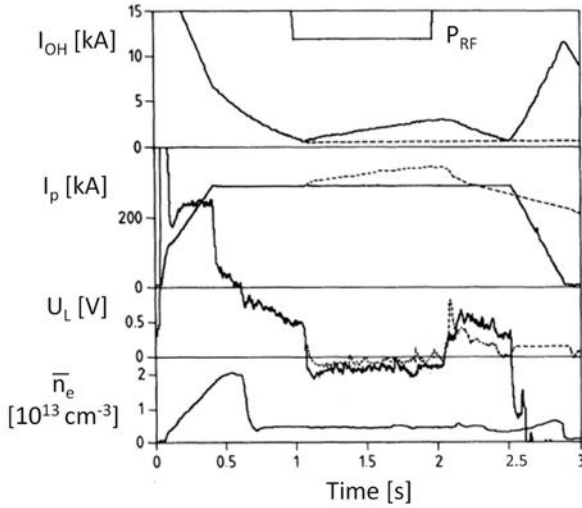


FIG. 6.33. Plasma current ramp up with LH current drive. Solid lines correspond to:  $I_p = \text{constant}$ ; dashed lines correspond to: ohmic current  $I_{OH} = \text{constant}$ ;  $P_{RF} = 675 \text{ kW}$ . Reprinted from Ref. [6.167]. Copyright (2011) by the American Physical Society.

In Fig. 6.34, currents have been demonstrated at ITER relevant densities in Alcator C [6.165]. The current drive efficiency increases with electron temperature and current as shown in Fig. 6.35 from JT-60 [6.170]. Depending on  $\omega_{pe}^2 / \omega_{ce}^2$ , Fokker–Planck code results indicate efficiencies  $\eta [10^{20} \text{ m}^{-3}] I [\text{MA}] R [\text{m}] / P [\text{MW}] = 0.1 T_e [10 \text{ keV}]$ . Many of the results were summarized in additional review papers [6.1, 6.156, 6.171] and references therein. More recent experimental results may be found in Refs [6.64, 6.79] (Alcator C-Mod) and [6.124] (JET).

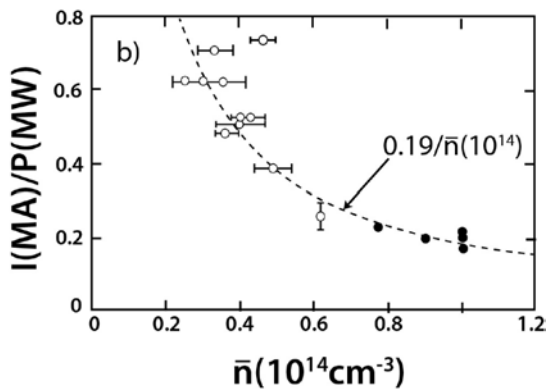


FIG. 6.34. Demonstration of LHCD efficiency in Alcator C at densities up to  $10^{20} \text{ m}^{-3}$  at a frequency of 4.6 GHz [6.165]. Reprinted from Ref. [6.165]. Copyright (2011) by the American Physical Society.

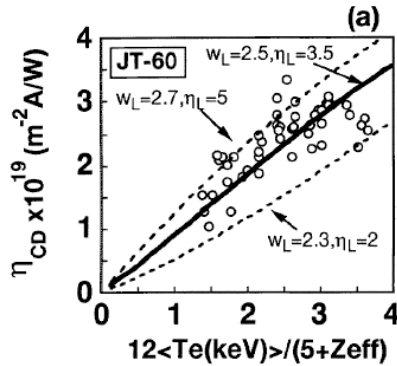


FIG. 6.35. Lower hybrid current drive efficiency increases with  $T_e$  in JT-60. Here  $\eta_{CD}$  is the current drive efficiency,  $w_L$  is the ratio of the minimum upshifted parallel phase velocity normalized to the electron thermal speed and  $\eta_L$  is the quasi-linear diffusion coefficient evaluated at  $w_L$ , and normalized to the collisional diffusion coefficient. For details see Ref. [6.170]. Reprinted from Ref. [6.170]. Copyright (2011), IOP Publishing Ltd.

Recently, lower hybrid wave power injection demonstrated current drive for minutes at the 1GJ level in Tore-Supra (TS). In Fig. 6.36 we show recent results demonstrating current drive with lower hybrid waves at the 500 kA level for 6 min. Finally, impressive coupling results were obtained in JET, where, using gas injection, LH waves were coupled efficiently through a 14 cm scrape-off layer [6.172].

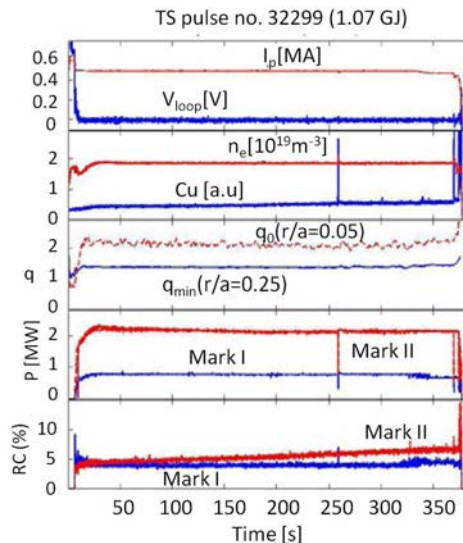


FIG. 6.36. Recent long pulse results from TS demonstrate non-inductive current drive for 7 min at 2.9 MW for 1 GJ [6.172]. Here, Cu is the relative copper impurity level and RC is the percentage of the radiated power due to impurities.

### 6.3.4. Lower hybrid wave launchers

RF waves in the lower hybrid range of frequencies ( $\omega_{ci} \ll \omega \ll \omega_{ce}$ ), and especially drive current, have been extensively used to heat in tokamak plasmas. In typical tokamaks this means utilizing frequencies in the range 1–10 GHz. Since the free space wavelength ( $2\pi c / \omega$ ) of such waves is 0.0–0.1 m, wave launching structures can be relatively compact. As shown previously, two possible polarizations of cold plasma waves exist in this frequency range — the fast (whistler) and the slow (cold lower hybrid or Trivelpiece–Gould) branches. In fusion applications the slow lower hybrid wave branch has been used since it is efficiently absorbed by Landau damping in present day tokamaks at temperatures from 1 to about 12 keV. More importantly, it is possible to construct a phase array of waveguides with  $N_{\parallel} > 1$  in vacuum with the  $TE_{10}$  polarization in each guide (the fundamental mode of propagation in a rectangular waveguide) so that at the plasma edge  $E_{RF}$  is parallel to the toroidal magnetic field. The individual waveguides are typically  $0.75\lambda_0$  (where  $\lambda_0$  is the free space wavelength) high in the poloidal direction and their individual widths in the toroidal direction are typically  $\lambda_0 / 8$  so that a stack of waveguides phased at  $90^\circ$  relative to their neighbours would produce a net wavelength in front of the guides of  $\lambda_0 / 2$  or  $N_{\parallel} = 2$  as required for good accessibility and efficient coupling to the slow wave in the edge of a tokamak plasma (called the “grill” or “grille”) [6.173]. The wave would then propagate into the plasma, where it could either damp on electrons via Landau damping or on ions after conversion to a hot ion wave. Because of the specific waveguide dimensions, each guide would remain in the fundamental mode of propagation. Higher order modes are cut off and no dielectric loading is necessary for mode propagation. On the contrary, to couple to the fast wave, the polarization of the wave at the edge is such that  $E_{RF}$  must be in the poloidal direction, and a phase array with  $N_{\parallel} > 1$  is not possible unless the individual waveguide is loaded with a dielectric so that its dimension can be reduced in the toroidal direction relative to  $\lambda_0 / 2$  without cutting off the fundamental mode of propagation. Such a dielectric loaded waveguide array experiment was carried out with some success [6.174]. Alternatively, a slotted slow wave structure was tested for fast wave launching in Versator II [6.175]. From the practical point of view, such experiments were abandoned after some initial trials due to technical difficulties. Instead, early experiments demonstrated the effectiveness of coupling to the slow wave with a “grill” and excellent coupling efficiencies (low reflectivity) were obtained without the use of tuning devices such as those required for lower frequency (ICRF) techniques. Consequently the standing wave ratio (SWR) in the launching structure is quite low. The practical power limit of such waveguide arrays is set by high voltage breakdown in the waveguides.

Referring back to Fig. 6.4 for  $N_{\parallel} < N_{\parallel}^{crit}$ , the fast and slow wave roots coalesce in the plasma core and the inward propagating slow wave converts to

an outward propagating fast wave before the centre of the plasma is reached. For typical applications of LHCD in tokamaks, this mode conversion region is placed in the core of the plasma, preferably at the plasma centre. Typically this means that  $N_{\parallel}$  is between  $\sim 1.3$  (high magnetic field and low density) and 3 (low magnetic field and high density). This accessibility condition places a lower bound on the  $N_{\parallel}$  coupled by the launching structure and the upper bound is determined by the desired location of wave absorption by electron Landau damping. As shown by Eq. (6.63), Landau absorption occurs when  $N_{\parallel} \sim \alpha / T_e^{1/2}$ , where  $\alpha = 5-7$  depending on whether linear or quasi-linear damping is assumed [6.176]. Therefore, we can summarize the spectral requirements placed on a lower hybrid launcher as follows: for RF current drive, the antenna must launch a directed spectrum with respect to the magnetic field such that the momentum transferred to the electrons is unidirectional. The  $N_{\parallel}$  values in the spectrum must exceed the critical value for accessibility but be below those at which absorption would take place in the plasma periphery. Note that for tokamaks with central temperatures less than  $\sim 5$  keV a window in  $N_{\parallel}$  values between the lower (accessibility) and upper (electron damping) limits of Eq. (6.133) can exist while for higher temperature tokamaks the lower hybrid wave will typically damp well before reaching the centre of the plasma. This is why LHCD can be very effective for driving current well off-axis. Because of the requirements on the  $N_{\parallel}$  spectrum for proper coupling and absorption, the slow wave antenna is typically a structure periodic in the toroidal direction. Adjacent elements in the array are phased such as to launch the preferred spectrum. The RF electric field polarization at the antenna-plasma interface must also be in the toroidal direction. The  $N_{\parallel}$  spectrum of the antenna can be estimated by Fourier transformation of the antenna fields; the representative or peak value of the spectrum is roughly  $N_{\parallel} \sim c\Delta\phi / \omega\Delta z$ , where  $\Delta z$  is the separation between radiating elements and  $\Delta\phi$  is the phase difference (in radians) between elements. Of course the actual launched spectrum is a combination of the applied spectrum and the plasma response. If significant parts of the launcher spectrum fall outside of the region of significant plasma response then there will be either RF energy in the plasma periphery, potentially leading to impurity production from the walls and limiters, or a large reflection of power into the launching structure, leading to large values of the RF electric field, in turn also leading to RF breakdown and damage. Other considerations for the antenna include the materials used, which must be compatible with the tokamak environment, and the necessity for an insulating vacuum window at some point between the RF source and the plasma.

Lower hybrid waves that satisfy the accessibility condition are evanescent in a thin layer near the waveguide mouth where  $\omega_{pe}^2 < \omega^2$ , which necessitates that the ends of the waveguides of the grill be close to the plasma edge. In fact, in modern tokamaks this layer may essentially be non-existent (note that for an RF frequency of 5 GHz this corresponds to a density of  $\sim 2.5 \times 10^{17} \text{ m}^{-3}$ ). For

conditions with sufficient density and proper density gradient, strong coupling to the plasma is achieved with little power reflected back along the waveguide towards the RF source. Such a waveguide array is shown in Fig. 6.37.

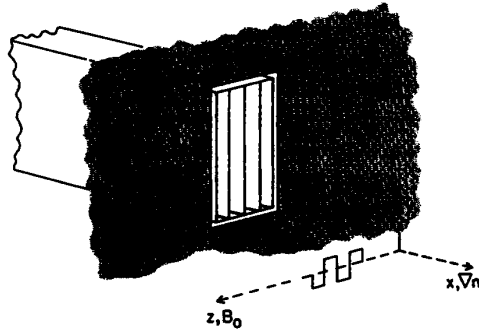


FIG. 6.37. Diagram of a waveguide grill launcher inserted through a port in the vacuum vessel wall [6.19].

Simple waveguide arrays grew from simple double waveguides to as many as 24 in a given row. Further growth has been by adding more rows and by more modern designs (see below). Each waveguide is oriented such that the fundamental  $TE_{10}$  mode carries the incident power, automatically aligning the applied electric field with the toroidal direction. The relative phase between guides is then set by phase shifters, either in the waveguide structure in the high power feed lines or in the low power RF drive preceding the (typically) klystron amplifiers (see Fig. 6.38). Thus the  $N_{\parallel}$  spectrum and directionality can be varied, even actively if electronic phase shifters are employed, allowing much greater flexibility than that of the longitudinal slow wave structure.

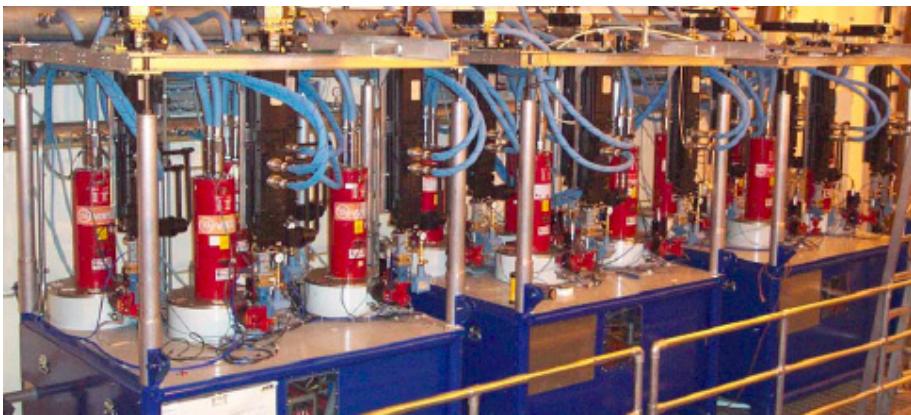


FIG. 6.38. The 4.6 GHz klystron amplifiers for the Alcator C-Mod LH system [6.79]. Reprinted from Ref. [6.79]. Copyright (2011), American Nuclear Society.

The major limitation on power in the waveguide grill antenna is RF breakdown in the vacuum portion of the waveguides. The location of the ceramic window used to isolate the machine vacuum is a compromise between placing them close to the plasma so as to ensure that electron cyclotron resonance is located in the pressured region of the waveguide array. This approach clearly requires brazing of a large number of ceramic windows into individual waveguides, a difficult technology which often prevents repair once the window has failed. However, the window is typically a sturdy ceramic block made of alumina ( $\text{Al}_2\text{O}_3$ ) or beryllium oxide ( $\text{BeO}$ ) of thickness  $\lambda_0/2$  and has been employed successfully in the Alcator C and C-Mod experiments for years. Placing the windows far away from the plasma introduces the cyclotron resonance in the waveguide in the vacuum region, and extra pumping of the waveguides must be provided to prevent RF breakdown. This makes it possible to combine guides and expand them to conventional sizes in externally accessible regions where commercial windows can be utilized. This approach has been deployed in the JET and TORE-Supra experiments, in particular with PAM launcher designs (see below).

#### 6.3.4.1. RF coupling theory

The general problem of coupling lower hybrid waves to the edge plasma has been approached in a variety of ways [6.33, 6.173, 6.177]. In general it is one of matching the impedance of the launching structure to that of the lower hybrid wave in the plasma. Typically a plane is defined at the waveguide mouth where the tangential components of the electric and magnetic fields are required to be continuous. A simple model for understanding coupling utilizes the density profile in Fig. 6.39.

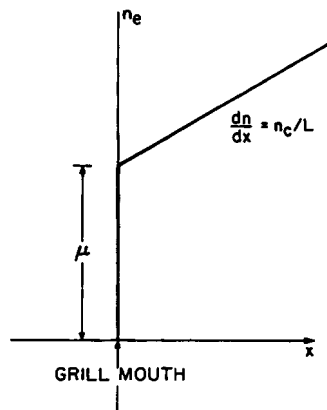


FIG. 6.39. Idealized density behaviour near the grill mouth, where  $\mu$  is a step in density at the grill mouth,  $n_c/L$  is the density gradient and  $x$  is the radial distance into the plasma [6.19].

The plasma density is assumed to be finite at the mouth of the waveguides and increase linearly away from the launcher. Since the perpendicular wavelength of the slow wave is significantly shorter than the density scale length in the edge plasma, coupling can be treated as a local problem independent of absorption or evanescence in the interior of the plasma. For cold lower hybrid waves with  $E_y = 0$ , the wave equation can be written (for  $K_{zz} = P \gg 1$ ) as:

$$\frac{\partial^2 E_z}{\partial^2 x^2} - \frac{\omega^2}{c^2} P (N_{\parallel}^2 - 1) E_z = 0 \quad (6.134)$$

where  $P$  is the cold plasma  $zz$  component of the dielectric tensor (Eq. (6.14)). For the density profile in Fig. 6.39,  $n(x) = n_0 + n_c x / L$ , where  $n_c = \epsilon_0 m_e \omega^2 / e^2$  (where  $n_c$  is coupling density and  $L$  is the density scale length) and with the substitution:

$$u(x) = \left[ \frac{\omega^2 N_{\parallel}^2 - 1}{c^2 L} \right]^{1/3} \left[ L \left( \frac{n_0}{n_c} - 1 \right) + x \right] \quad (6.135)$$

Eq. (6.134) becomes:

$$\frac{\partial^2 E_z}{\partial^2 u} - u E_z = 0 \quad (6.136)$$

The solutions to Eq. (6.136) are the Airy functions. A linear combination can be chosen which yields a wave radiating in the plus  $x$  direction. For  $|N_{\parallel}| < 1$  the evanescent solution is chosen and for  $|N_{\parallel}| > 1$  the oscillatory solution is chosen. Since the lower hybrid wave is backward in the direction perpendicular to the magnetic field the outgoing asymptotic solution should be proportional to  $\exp(-ik_x x)$ . For this general discussion we will consider only the propagating waves, as lower hybrid launchers are phased to avoid exciting  $|N_{\parallel}| < 1$ . However, the numerical coupling codes calculate the match over the entire range of  $N_{\parallel}$ . The propagating solution to Eq. (6.136) is:

$$E_z(u) = -i\text{Ai}(u) + \text{Bi}(u) \quad (6.137)$$

where Ai and Bi are the Airy functions of the first and second type. The RF magnetic field is obtained from Faraday's Law:

$$B_y(u) = i \frac{c}{\omega (N_{\parallel}^2 - 1)} \left[ \frac{\omega^2 N_{\parallel}^2 - 1}{c^2 L} \right]^{1/3} \left[ -i \frac{\partial \text{Ai}(u)}{\partial u} + \frac{\partial \text{Bi}(u)}{\partial u} \right] \quad (6.138)$$

The procedure for finding the reflection coefficient is to match  $E_z$  and  $B_y$  to the corresponding antenna components at  $x = 0$ :

$$E_z(u_0) = E_{zi}(0) + E_{zr}(0) \quad (6.139)$$

$$B_y(u_0) = B_{yi}(0) - B_{yr}(0) \quad (6.140)$$

where  $u_0 = u(x=0)$  and (0) means at  $x=0$ .  $E_{zi}$  and  $B_{yi}$  are the incident electric and magnetic fields imposed by the antenna, and  $E_{zr}$  and  $B_{yr}$  are the reflected fields of the antenna. The field reflection coefficient  $E_{zr}(0)/E_{zi}(0)$  is:

$$\Gamma = \frac{(Z_p / Z_0) - 1}{(Z_p / Z_0) + 1} \quad (6.141)$$

where  $Z_p = E_z(u)/B_y(u)$  is the wave impedance in the plasma and  $Z_0 = E_{zi}(x=0)/B_{yi}(x=0)$  is the wave impedance of the launcher. With  $Z_p / Z_0 = |Z|e^{i\phi}$  (with  $\phi$  being phase) the power reflection coefficient,  $|\Gamma|$ , is minimized for  $|Z|=1$ ,  $-\pi/2 < \phi < \pi/2$ .

#### 6.3.4.2. Numerical coupling codes

A variety of numerical codes have been written [6.176, 6.178, 6.179] to calculate coupling from an array of waveguides to lower hybrid waves. For illustrative purposes the initial approach used by Brambilla [6.173] for an array of  $N$  rectangular waveguides is given here. For infinitely high wave guides (an approximation of no great consequence since in a rectangular guide the field is sinusoidal in the vertical direction and the dimension is large compared to the horizontal) the waveguide fields can be written:

$$E_z^{\text{wg}}(x, z) = \sum_{p=1}^N e^{i\phi_p} \theta_p(z) \left[ \sum_{n=0}^{\infty} (\alpha_{np} e^{ik_n x} + \beta_{np} e^{-ik_n x}) \cos \frac{n\pi(z - z_p)}{b} \right] \quad (6.142)$$

$$B_y^{\text{wg}}(x, z) = \sum_{p=1}^N e^{i\phi_p} \theta_p(z) \cdot$$

$$\left[ \sum_{n=0}^{\infty} -\frac{\omega}{ck_n} (\alpha_{np} e^{ik_n x} - \beta_{np} e^{-ik_n x}) \cos \frac{n\pi(z - z_p)}{b} \right] \quad (6.143)$$

$$E_x^{\text{wg}}(x, z) = -i \frac{c}{\omega} \frac{\partial B_y^{\text{wg}}}{\partial z} \quad (6.144)$$

where wg stands for waveguide,  $b$  is the width of the guide,  $p$  is the waveguide number,  $z_p$  is the  $z$  coordinate of the edge of the  $p^{\text{th}}$  waveguide and  $\phi_p$  is the phase of the  $p^{\text{th}}$  waveguide. The function  $\theta_p(z)$  is a ‘‘window’’ function: it is equal to one for  $z_p \leq z \leq (z_p + b)$  and zero elsewhere. The sum over  $n$  waveguide modes includes both propagating and evanescent ones. The coefficients  $\alpha_{np}$

and  $\beta_{np}$  are the amplitudes of the incident and reflected  $n^{\text{th}}$  mode fields in the  $p^{\text{th}}$  waveguide respectively. The waveguide wave vector of the  $n^{\text{th}}$  mode is  $k_n = (\omega^2 / c^2 - n^2 \pi^2 / b^2)^{1/2}$ . The matching of the antenna fields to the plasma is performed by matching the forward and reflected waveguide fields at the array mouth to generalized vacuum fields in front of the array (written in terms of Fourier integrals):

$$E_z(x, z) = \int_{-\infty}^{\infty} \frac{\omega}{c} \left[ \sigma(N_{\parallel}) e^{ik_x x} + \rho(N_{\parallel}) e^{-ik_x x} \right] e^{i(\omega/x)N_{\parallel}z} dN_{\parallel} \quad (6.145)$$

$$B_y(x, z) = \int_{-\infty}^{\infty} \frac{i(\omega/c)}{(N_{\parallel}^2 - 1)^{1/2}} \left[ \sigma(N_{\parallel}) e^{ik_x x} - \rho(N_{\parallel}) e^{-ik_x x} \right] e^{i(\omega/c)N_{\parallel}z} dN_{\parallel} \quad (6.146)$$

Here  $\sigma(N_{\parallel})$  is the coefficient corresponding to the field incident on the plasma and  $\rho(N_{\parallel})$  is the coefficient of the reflected field from the plasma. For a given  $N_{\parallel}$  the field reflectivity of the plasma is  $Y(N_{\parallel}) = \rho(N_{\parallel}) / \sigma(N_{\parallel})$ . The vacuum region in front of the grill is employed as a mathematical convenience and is usually assumed to have zero width, although if close fitting guard limiters are present around a relatively narrow coupler it may be required to match the experimentally observed reflection coefficient. The vacuum fields (Eqs (6.142 and 6.143)) are matched to the plasma fields (Eqs (6.144) and (6.145)). The unknown quantities  $\sigma(N_{\parallel})$ ,  $\rho(N_{\parallel})$  and  $\beta_{np}$  are determined. The reflection in the  $p^{\text{th}}$  waveguide is  $|\beta_{0p}|^2 / |\alpha_{0p}|^2$ . The  $N_{\parallel}$  spectrum of the RF power launched into the plasma is obtained from the Poynting flux in the  $x$  direction at the plasma–vacuum boundary:

$$S_x(N_{\parallel}) = -\frac{c}{8\pi} \text{Re}(E_z B_y^*) = -\frac{c}{4\pi} \frac{|\sigma(N_{\parallel}^2)|^2}{(N_{\parallel}^2 - 1)^{1/2}} \text{Im}(Y(N_{\parallel})) \quad (6.147)$$

Note that the calculated power is zero for  $|N_{\parallel}| < 1$  since the waves are evanescent for overdense plasma. Actual spectra have been measured and compared with numerical codes. In Fig. 6.40 we show such measurements performed on the TdeV tokamak [6.180]. Additional confirmation has been provided by CO<sub>2</sub> laser scattering experiments in the plasma near the antenna in Alcator C, and the results were in good agreement with expectations (Ref. [6.181] and as shown in Fig. 6.41).

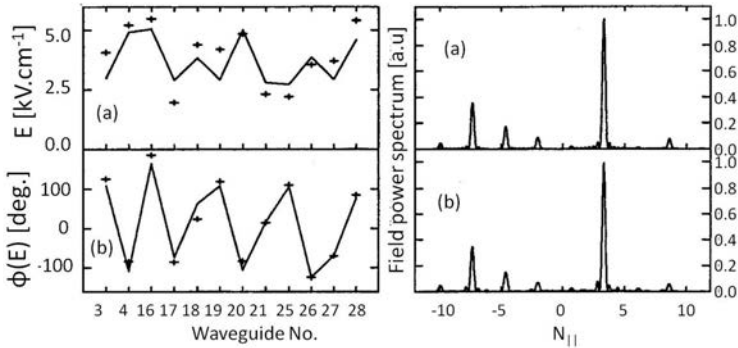


FIG. 6.40. Left: Amplitude and phase of RF fields at the mouth of the grill; crosses correspond to measured data and lines to the SWAN code [6.178] calculations.  $\phi$  is phase and  $E$  the electric field strength. Right: Reconstructions of the spectrum [6.180]. Reprinted from Ref. [6.180]. Copyright (2011), American Institute of Physics.

To provide some guidance for estimating the optimal density for coupling, note that for an overdense plasma,  $|u_0| \gg 1$ , asymptotic expressions for the Airy functions can be taken and

$$Z_p = - \left[ \frac{N_{||}^2 - 1}{\mu - 1} \right]^{1/2} \quad (6.148)$$

Optimal coupling is for  $Z_p / Z_0 = 1$  or  $\mu = n_0 / n_c = 1 + [1 - (c\pi / \omega h)^2] (N_{||}^2 - 1)$ , which yields the value of density  $n_0$  at the waveguide mouth for optimum coupling at a given  $N_{||}$ . Non-zero reflectivity in practice is due to the finite width of the  $N_{||}$  spectrum. The optimal density increases with increasing  $N_{||}$ .

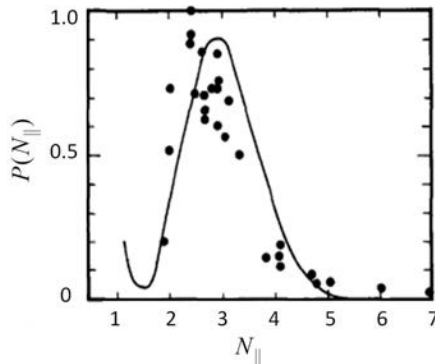


FIG. 6.41. Experimental verification of the Brambilla spectrum (solid curve) from Alcator-C for 90° phasing of adjacent waveguides. The dots are measurements with  $CO_2$  laser scattering. Reprinted from Ref. [6.181]. Copyright (2011), American Institute of Physics.

6.3.4.3. Evolution of LH launchers in tokamaks

Early launchers were arrays of simple waveguides starting with  $1 \times 2$  (1 row of 2 adjacent waveguides) such as Alcator A and later reaching up to as many as 4 rows and 24 columns. It was quickly found that the maximum power in a single waveguide was limited by voltage breakdown. This limit was found to be a strong function of materials and cleanliness in the vacuum portion of the launcher. Sources of the breakdown plasma are secondary electron emission (SEE), electron stimulated desorption (ESD) of contaminants on the waveguide walls and impact ionization of residual gas in the waveguides. If the vacuum window is located sufficiently far from the vacuum vessel the electron cyclotron resonance layer at the RF frequency due to the tokamak fields can exist within the vacuum guide. This allows resonant acceleration of free electrons to higher energies, increasing SEE and ESD. Proper choice of materials (those with low secondary emission coefficients) and cleaning of the guides (RF or glow discharge) was found to allow operation up to high power levels (up to  $50 \text{ MW}\cdot\text{m}^{-2}$  short pulse). The power per waveguide limit was found to be a function of both waveguide dimension (width) and RF frequency (see Fig. 6.42).

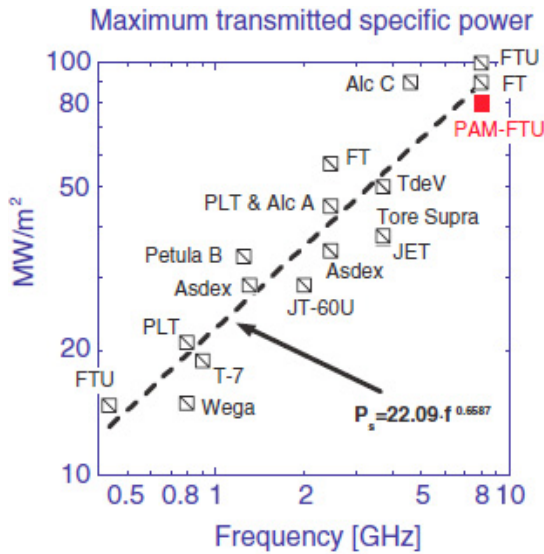


FIG. 6.42. Maximum power density delivered from lower hybrid phased grills (from Ref. [6.182]).  $P_s$  is the power density at the grill mouth transmitted without RF breakdown; it is shown as a linear fit to the data points, where  $f$  is frequency.

Because of the power per waveguide limit and the spectral purity requirements, the number of waveguides required for large high power experiments has grown to a level (hundreds of guides) where simple couplers

have become impractical. A fuller description of the basic couplers and their limitations is given in Ref. [6.183]. A new approach (the multi-junction grill) was proposed that would still have the plasma see  $TE_{10}$  wave fields but where the power is split by passive elements into waveguides in the evacuated region of the grill after the RF power has passed through the vacuum window [6.184] (see Fig. 6.43).

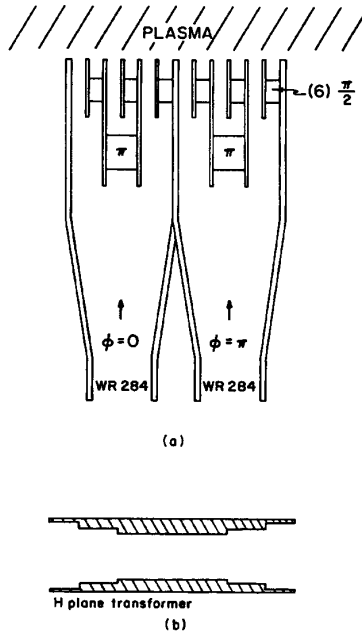


FIG. 6.43. (a) Top view of an eight-waveguide multi-junction grill designed to launch a travelling wave spectrum ( $\Delta\phi = \pi / 2$ ). The grill is fed by two standard waveguides. The labelled blocks represent passive phase shifters. (b) Sections of reduced height waveguide act as phase shifters to set the relative phase between adjacent waveguides. Taken from Ref. [6.184].

The advantages of such a design include:

- Reduces greatly the number of vacuum windows required (and increases their size to where commercially available ones can be used);
- Minimizes the number and complexity of transmission line components (also decreases the RF losses in the transmission system);
- Reduces the maximum power that can be reflected to the RF sources (the passive elements also act as tuning elements).

Drawbacks include a reduced flexibility of spectrum (Fig. 6.44) since the phase shifts are fixed, and a small reduction in power handling since the tuning

property of the elements (and the reduced dimensions of the guides) increases the RF electric fields for a given power.

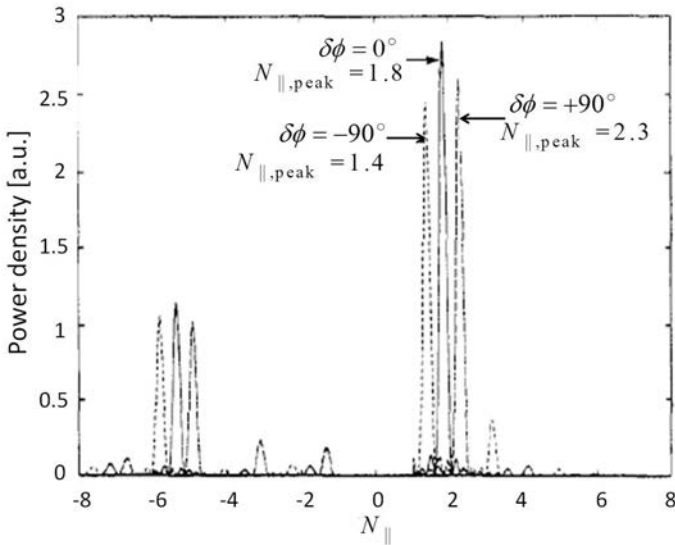


FIG. 6.44. Spectrum of the Tore-Supra multifunction grill. Taken from Ref. [6.178].

Most modern LH experiments in large machines with ample access, namely JET [6.185] (384 waveguides), Tore-Supra [6.186] and JT-60U [6.187] (212 waveguides) (see Fig. 6.45), utilize this approach.

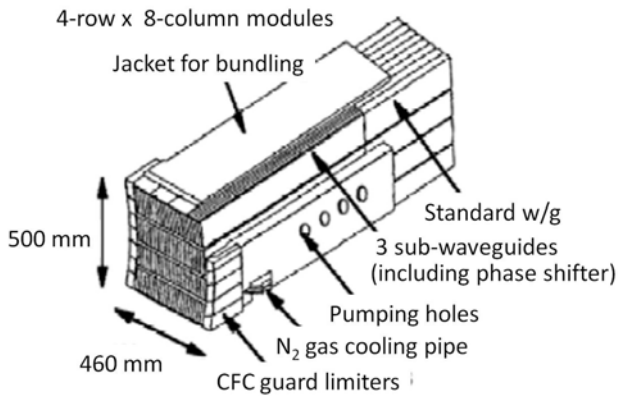


FIG. 6.45. Front internal section of the JT-60 divided multi-junction launcher for JT-60. Reprinted from Ref. [6.187]. Copyright (2011), American Nuclear Society.

However, Alcator C-Mod, a modern state-of-the-art compact high field device, still uses individually brazed windows. Such an approach allows great

flexibility and total control of the spectrum (see Fig. 6.46 for spectra for different phasings from Alcator C-Mod [6.188]). Further improvements of the Alcator C-Mod launcher design are evolving even now [6.189].

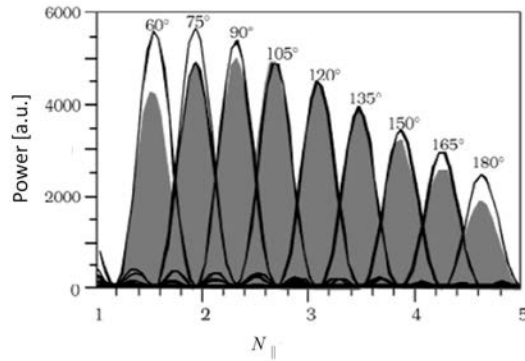


FIG. 6.46. Phase control of the of the Alcator C-Mod launcher power spectrum with alternate columns fixed phased at  $120^\circ$ . Shown are ideal (lines) and achieved (shaded) spectra. Reprinted from Ref. [6.188]. Copyright (2011), American Nuclear Society.

A challenge for continued use of lower hybrid waveguide launchers in future devices is the heat load to the launcher from the plasma and from RF losses in steady state. The multi-junction design has been extended to one in which every other waveguide is passive — the passive active multi-junction (PAM) approach [6.190]. In this approach the passive guides provide a path for cooling to be applied near the mouth of the grill. This is the approach foreseen for applying lower hybrid to ITER and beyond. For ITER (Fig. 6.47) a system with an  $N_{\parallel} = 2$  capable of coupling more than 16 MW at a power density of  $33 \text{ MW} \cdot \text{m}^{-2}$  has been proposed [6.190].

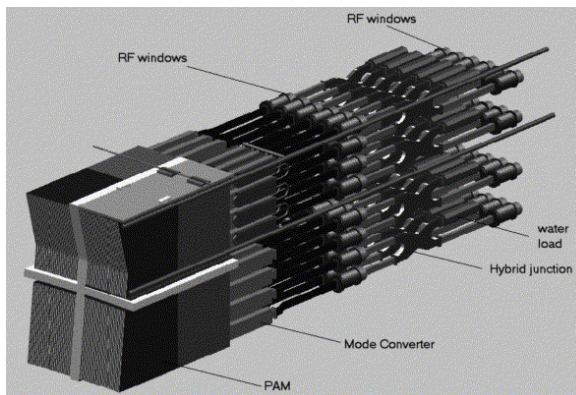


FIG. 6.47. Illustration of the proposed ITER PAM-LH launcher. Reprinted from Ref. [6.190]. Copyright (2011), with permission from Elsevier.

A prototype of this system was demonstrated on FT-U at  $75 \text{ MW}\cdot\text{m}^{-2}$  for short ( $<1 \text{ s}$ ) pulses confirming the properties of good coupling and insensitivity to edge plasma density [6.182]. A further demonstration is planned for Tore-Supra with 6 rows of 32 waveguides (half passive, half active), one quadrant of the ITER size. Figure 6.48 shows a photograph of the front face of this antenna. Testing commenced in 2010 with promising results for the future of this concept.



FIG. 6.48. Front face photograph of the Tore-Supra ITER prototype PAM launcher which is a quadrant of the proposed antenna for ITER.

### 6.3.5. Applications of electron cyclotron heating and current drive

Electron cyclotron heating (ECH) and electron cyclotron current drive (ECCD) have many practical applications due to their unique characteristics, especially the ability to deposit power and/or current in a highly localized, robustly controllable location in the plasma. Another important feature is that EC waves propagate in the vacuum between the launcher and the plasma, unlike other wave heating techniques which have an evanescent region between the launcher and the plasma, and this means that the launcher can be far from the plasma boundary. There is little sensitivity of the wave coupling to the plasma edge conditions and no tendency to introduce impurities. These characteristics have led to the use of ECH/ECCD for such diverse applications as plasma pre-ionization and discharge startup, plasma heating, support and maintenance

of the desired current profile in tokamaks and control of some MHD modes that otherwise limit performance.

The propagation, absorption and effect on the electron distribution of EC waves is well described by theory based on first principles as described in Section 6.2.1. This body of theoretical work has been encapsulated in practical predictive computer codes, so that experiments can provide the empirical validation of the models. The validation of these models Refs [6.66, 6.192, 6.193] and the references therein) supports the ability to predict with high confidence the EC power and current profile sources in plasma confinement devices.

#### *6.3.5.1. Wave propagation and absorption experiments*

In most situations of interest in fusion research, the propagation of EC plane waves is well described by the cold plasma dispersion relation as described in Section 6.1.1. The trajectory and wave vector evolution of the plane wave can be found, in the WKB approximation, as described in Section 6.2.7.1. In practical cases, however, plane waves are not applied; rather the power is launched as a narrow cone. There are two common ways of modelling the cone. One way is to propagate an array of independent, non-interacting rays with a power and angle distribution that simulates a Gaussian beam. This technique is relatively simple and in many cases is adequate, and it is embodied in codes like TORAY [6.194] and GENRAY [6.78, 6.195]. In cases where the EC beam is focused or has astigmatism, Gaussian beam codes must be used to address interference and diffraction effects. Representative Gaussian beam codes are TORBEAM [6.196], GRAY [6.197] and TRAVIS [6.198].

All ray tracing and beam codes make the approximations that the plasma is changing on a spatial scale large compared to the wavelength, that the imaginary part of the wavevector is small compared to the real part, and that a parallel wavenumber  $k_{\parallel}$  can be defined over each part of the wavefront for calculation of the resonance condition and the absorption. These conditions are usually but not always satisfied in fusion applications. In cases where these conditions are not met, the only alternative is the full wave approach. Given the very large ratio of plasma dimension to wavelength, this is very challenging [6.199].

The ray tracing and beam codes calculate the beam absorption and current drive along the wave trajectories. The contributions to the heating and current are summed in radial bins and provide a calculation of the heat and current profiles in practical cases. The ray tracing and beam codes have been benchmarked for a representative ITER case and found to produce very similar profiles of heating and current density [6.200]. An example of ray tracing using the TORAY-GA code in a DIII-D equilibrium is shown in Fig. 6.49 for three different densities. In the lowest density case the refraction is negligible, since the density is well below the cut-off density (that is satisfying the approximate condition for the

second harmonic X-mode  $\omega_{pe}^2 < \omega^2 / 2$ , which for 110 GHz requires a density below  $7.4 \times 10^{19} \text{ m}^{-3}$ ). Note that the effective density limit is usually smaller than cut-off density, sometimes significantly smaller, due to effects that affect how the beam approaches the resonance and the toroidal plasma geometry. A toroidal component to the beam, for example, enhances the tendency for the beam to glance off the plasma before it reaches the actual cut-off density, even after decreasing the cut-off density due to a non-zero value of  $k_{\parallel}$ . In the intermediate density case, refraction is significant enough to change the radial heating profile measurably and in the highest density case the rays are wildly refracted.

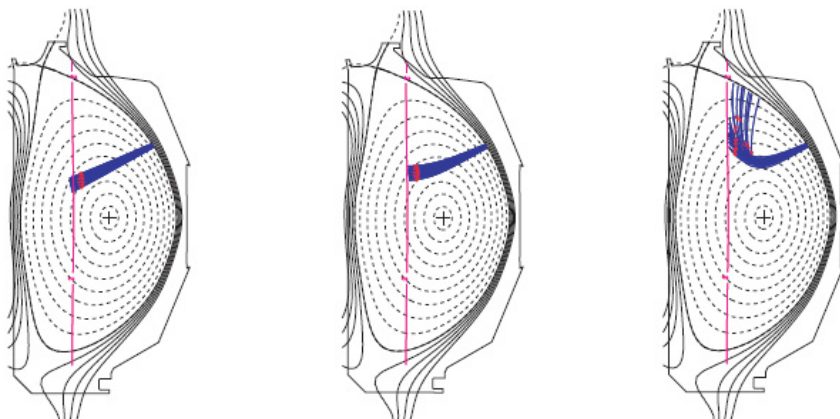


FIG. 6.49. Ray tracing calculations by the TORAY-GA code. The blue lines are ray trajectories for X-mode rays and the red crosses are where the absorption peaks for each ray. The vertical line is the second harmonic resonance for 110 GHz. The toroidal field is 1.7 T, the rather peaked density profile is scaled to a central density of (left)  $3 \times 10^{19} \text{ m}^{-3}$ , (centre)  $8 \times 10^{19} \text{ m}^{-3}$  and (right)  $11 \times 10^{19} \text{ m}^{-3}$ .

Wave absorption in the various regimes is discussed at length in Section 6.2.1 and the references there. Many code routines have been developed to calculate absorption; for a summary see Ref. [6.200]. These routines use either linear absorption models, for example the model by Mazzucato [6.201] used in the results shown in Fig. 6.49, or models that solve the Fokker–Planck equation in the quasi-linear limit (for an excellent review see Ref. [6.202]). The linear models may be either weakly relativistic or fully relativistic, depending on how the resonance condition is evaluated. The quasi-linear models are also fully relativistic in that sense, and they may have a more general model for the collision operator. In particular, the collision model in quasi-linear Fokker–Planck codes may avoid using the high speed limit of the collision operator and may use a model that conserves momentum in electron–electron collisions [6.203] Recently, works by Marushchenko [6.204, 6.205] and by Smirnov [6.179] have generalized the collision operator in linear codes as well.

The calculated absorption profile location and width are partly determined by the geometry of the intersection of the beam with the flux surfaces in the neighbourhood of the resonance, with the width also affected by the Doppler and relativistic broadening and the location by the Doppler shift. Under a representative condition of off-axis ECH in projected ITER conditions, the codes produced similar results [6.200]. An example is shown in Fig. 6.50.

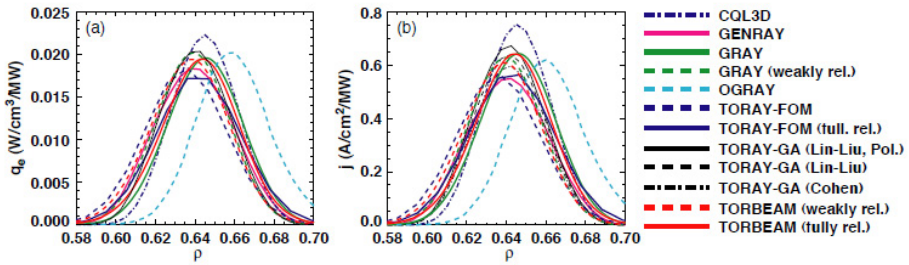


FIG. 6.50. (a) Profile of ECH power density deposited in electrons ( $q_e$ ), and (b) profile of ECCD current density  $j$  for some linear and quasi-linear (CQL3D, OGRAY) codes. Reprinted from Ref. [6.200].

In practice the absorption profile can be inferred by using the technique of modulating the EC power and measuring the changes in the electron temperature profile at the modulation frequency. The electron cyclotron emission (ECE) diagnostics has sufficiently low noise, high temporal response and high spatial resolution for this purpose. Such a measurement is shown in Fig. 6.51.

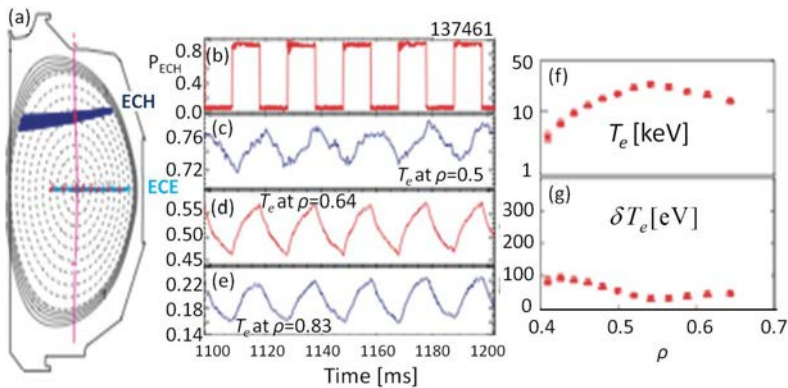


FIG. 6.51. Experiment to measure ECH location in DIII-D. (a) The blue lines represent the ECH beam and the vertical magenta line is the second harmonic resonance at 110 GHz. The ECE channels shown in light blue lie near the midplane. (b) ECH power (MW) modulated at 50 Hz. (c–e) Temperature response in keV of the ECE channels at  $\rho$  of 0.50, 0.64 and 0.83. (f) Fourier amplitude at 50 Hz of the ECE response. (g) Fourier phase of the ECE response relative to the ECH as a function of normalized radius.

The process illustrated in Fig. 6.51 can be applied to study systematic behaviour of the measured ECH location relative to the calculated location. The location can be measured with great precision using this technique, as shown in Fig. 6.52 [6.206] for the ASDEX Upgrade tokamak. This figure shows that by increasing the modulation frequency to 500 Hz the broadening of the response profile by transport on the timescale of the modulation period can be minimized, and extremely narrow profiles can be resolved and brought nearly into agreement with the TORBEAM calculations. Figure 6.52 shows that over a broad range of conditions the radial location is also well predicted by the TORBEAM code.

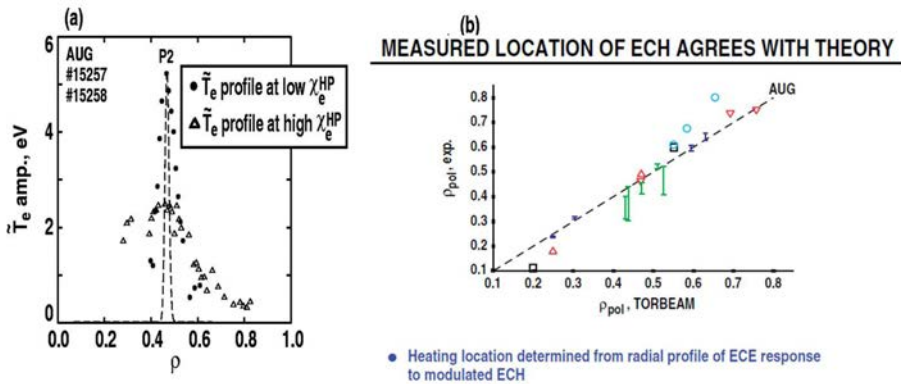


FIG. 6.52. (a) Fourier amplitude  $\tilde{T}_{e,amp}$  of the ECE measurements of  $T_e$  for ECH modulated at 500 Hz, as a function of normalized minor radius  $\rho_{pol0}$ , for high and low diffusivity  $\chi_e^{HP}$  cases in ASDEX Upgrade (where this is the diffusivity determined from heat pulse propagation). The high diffusivity is obtained by increasing the temperature gradient by applying additional ECH near the axis, while the low diffusivity case has ECH near  $\rho = 0.5$  in order to reduce the gradient. (b) Normalized minor radius of the peak plasma response  $\rho_{pol0} = (\rho_{pol} / a)$  versus the theoretical value from TORBEAM calculations for a variety of conditions. Reprinted from Ref. [6.206]. Copyright (2011), IOP Publishing Ltd.

For most applications to plasmas of interest in fusion research, the fundamental O-mode and the second harmonic X-mode are effectively fully absorbed in the plasma, so if the ray and beam codes get the location and width right, then the power density is also right. The high power density that results from the narrow deposition profile can be used for many purposes. An example is strong high central heating, which in the JT-60U tokamak has led to central temperatures of 23 keV [6.207], as shown in Fig. 6.53.

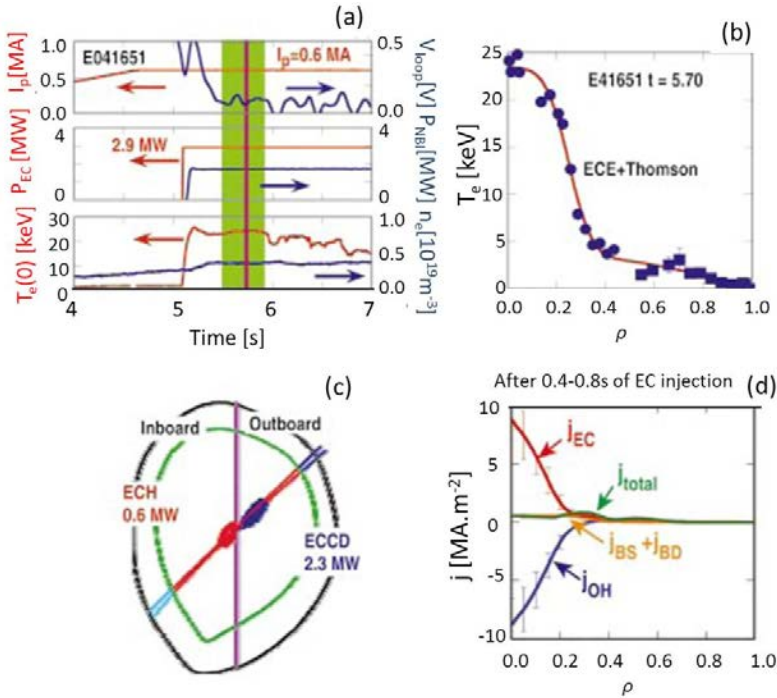


FIG. 6.53. Experiments on JT-60U showed that strong electron transport barriers, high central temperature and large ECCD could be generated by 0.6 MW of central ECH and 2.3 MW of central ECCD power, using fundamental O-mode and 110 GHz frequency. (a) Plasma current and edge loop voltage; ECH and neutral beam power; and central electron temperature and line-averaged electron density. (b) Electron temperature profile. (c) Deposition location for ECH (red) and co-ECCD (blue). (d) Components of the current density. Here,  $j_{BS}$  is the bootstrap current density,  $j_{BD}$  is the current density due to neutral beam injection, and  $j_{EC}$  is the current density due to ECCD. The negative  $j_{OH}$  is due to the induced electric field that arises to conserve the magnetic flux when the ECCD is applied. Taken from Ref. [6.207].

The internal transport barrier seen in the electron temperature profile of Fig. 6.53 was also found in the LHD, where it was shown that there is a power threshold for generation of the barrier [6.208], as shown in Fig. 6.54.

Another example of the application of the highly localized heating characteristic of ECH is control of the electron temperature gradient for studies of turbulence and validation of turbulence models. Figure 6.55 shows the ECH heating profile as a function of time for a case in which the modulated heating is out of phase at two nearby radial locations, one location of which is shown in Fig. 6.51. The contours of electron temperature from the ECE show periodic spatial modulation, resulting in a periodic modulation of the temperature gradient. The frequency and amplitude of the low level turbulence are modulated as well, and these characteristics can be compared with predictions of turbulence codes.

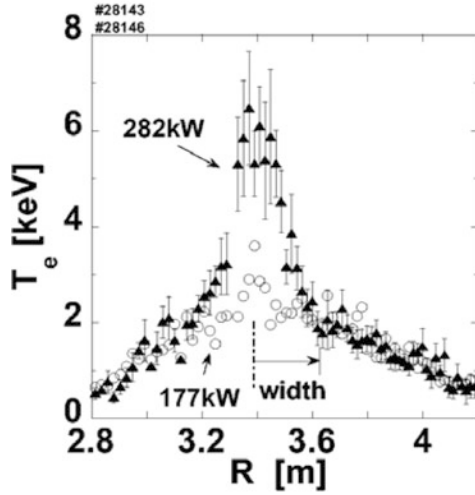


FIG. 6.54. Electron temperature profiles in LHD for 177 kW and 282 kW incident ECH power; showing creation of an electron transport barrier at the higher power. Reprinted from Ref. [6.208]. Copyright (2011), IOP Publishing Ltd.

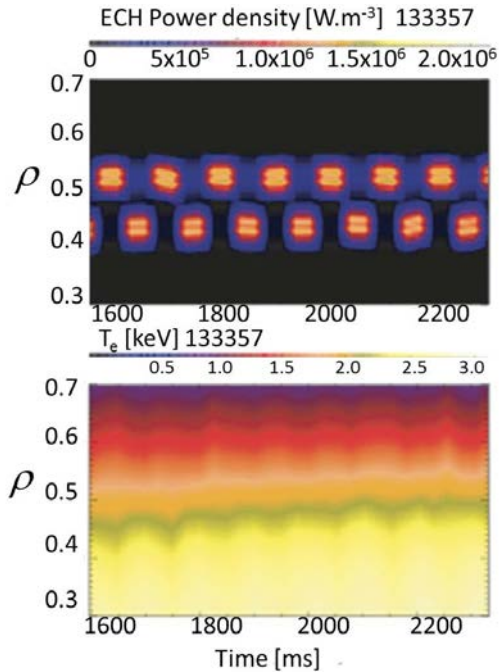


FIG. 6.55. Modulated ECH power density in two radial locations modulated out of phase for turbulence studies on DIII-D. (Top) Power density. (Bottom) Contours of electron temperature from the ECE diagnostics. As the contours become closer together, the  $T_e$  gradient increases.

The cut-off density may limit the role ECH may play in heating applications. In tokamaks, the density is empirically found to be limited to the Greenwald density,  $n_{GW}[10^{20} \text{ m}^{-3}] = I_p[\text{MA}] / \pi a^2[\text{m}]$ . From Section 6.1, propagation of EC waves is limited to  $\omega_{pe}^2 < \omega^2$  for the fundamental ordinary (O1) mode and by  $\omega_{pe}^2 < \omega^2 / 2$  for the second harmonic extraordinary (X2) mode, where  $\omega$  is the applied angular frequency. Then using  $q \propto \varepsilon^2 \kappa^2 RB_\phi / I_p[\text{MA}]$ , where  $q$  is the safety factor,  $\varepsilon$  is the inverse aspect ratio,  $\kappa$  is the elongation and  $R$  is the major radius, and  $B_\phi$  is the toroidal field, we get

$$\frac{n_{co}}{n_{GW}} \propto \frac{qRB_\phi}{\kappa^2} \quad (6.149)$$

where  $n_{co}$  is the EC cut-off density. This expression shows that the cut-off density becomes less restrictive for tokamaks with large major radius and large toroidal field.

Tokamaks of moderate size and field, like ASDEX Upgrade and DIII-D, have  $n_{co}/n_{GW}$  of order 0.3 to 0.5 for the O1-mode but of order unity for the X2-mode. For this reason, the X2-mode was implemented on those devices when high power gyrotrons with frequency above 100 GHz were developed. Then for the X2-mode, the cut-off density plays only a small role in limiting operating parameters. Larger, higher field tokamaks, like JT-60U and especially ITER, are not at all limited by the cut-off density. Small and/or low field tokamaks like TCV and spherical tokamaks like MAST are strongly limited in density range (see Ref. [6.209]). This limit has been circumvented in two different ways in these devices.

The limitation on density in TCV placed by the Greenwald limit has motivated installation of a higher frequency system that operates at the third harmonic of the extraordinary mode [6.210]. For harmonic numbers  $l \geq 2$  of the X-mode, the propagation limit is  $\omega_{pe}^2 < l(l-1)\omega_{ce}^2$  or using  $\omega = l\omega_{ce}$ ,  $\omega_{pe}^2 < [l(l-1)/l^2]\omega^2$  or

$$n[10^{19} \text{ m}^{-3}] < 0.00122 \frac{l(l-1)}{l^2} f^2[\text{GHz}] \quad (6.150)$$

From Eq. (6.150), by going from the X2-mode to the X3-mode by using 118 GHz power sources in place of 82.7 GHz sources, the limiting density was increased by a factor of 3.

Absorption is lower at higher harmonics, however. Generally, increasing the harmonic number of the X-mode by one introduces a factor  $T_e/mc^2$  in the absorption coefficient [6.66]. (The absorption of the O1-mode and the X2-mode are comparable as discussed earlier.) To counter the weaker absorption in TCV, the waves were launched from the top of the plasma nearly parallel to the resonance. By this means the waves were made to travel a relatively long

distance in the immediate vicinity of the resonance and thereby the net absorption is increased, typically to 70% in ohmic plasmas and to nearly full absorption in plasmas with pre-heating at lower density using the X2 power which generated a seed non-thermal component to the electron distribution function [6.211, 6.212]. The geometry of the TCV experiment is shown in Fig. 6.56.

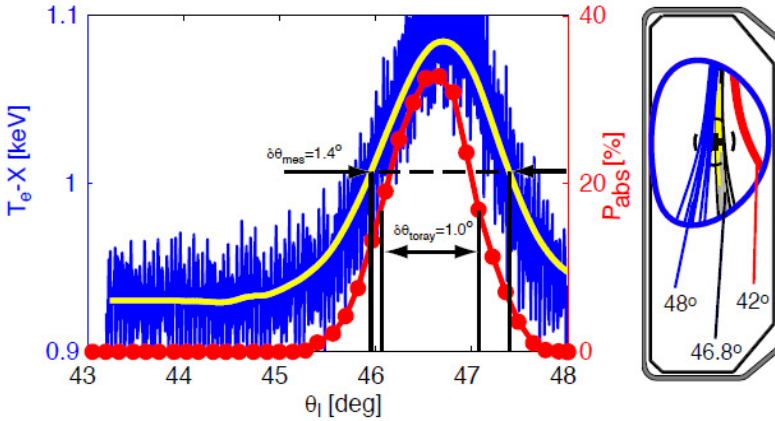


FIG. 6.56. Left: Electron temperature as a function of mirror steering angle for the X3 mode in TCV. Note the comparison between experimental measurements (blue curve) and predictions by the TORAY code (red). The yellow line is the average of the experimental signal for ease of comparison with the theoretically predicted value. Right: Ray bundles for three launch angles, illustrating typical trajectories. Taken from Ref. [6.211].

The second way to avoid the density limit, other than going to a higher harmonic, is to apply the electron Bernstein wave (EBW; see Fig. 6.2). This approach has been applied to stellarators, which are not subject to the Greenwald density limit and therefore often operate at high values of  $\omega_{pe}^2 / \omega_{ce}^2$ , and to spherical tokamaks, since they have very low field. The EBW, being an electrostatic wave, does not propagate in vacuum, so it cannot be excited directly by launchers outside the plasma. Instead, the ordinary-extraordinary-Bernstein wave (O-X-B) mode conversion approach [6.213] is used to launch the EBW. This work predicted that a critical window in the parallel index of refraction of the launched ordinary mode at the plasma boundary would result in effective mode conversion to the extraordinary mode at the surface where the ordinary mode is reflected. The outward travelling extraordinary mode is then converted to an inward propagating Bernstein wave at the upper hybrid layer. The dispersion relation of the EBW provides propagation to arbitrarily high density. Pioneering work on the Wendelstein 7-AS stellarator validated the theory of the O-X-B process [6.214]. Figure 6.57 shows the plasma heating as a function of the parallel index of refraction of the launched wave. In this experiment the magnetic field was set to have no cyclotron resonance in the plasma, so the wave

damping was non-resonant, and the central electron density was more than twice the O-mode cut-off density. Excellent agreement with theory of O-X and X-B mode conversion was found, as shown in the figure. Comparison to NBI heating showed that more than 70% of the launched EC wave power was found in the plasma core, showing that EBW heating can be quite efficient. These results were further confirmed by experiments on the MAST spherical tokamak [6.215]. A recent review of EBW heating has been given by Laqua [6.216].

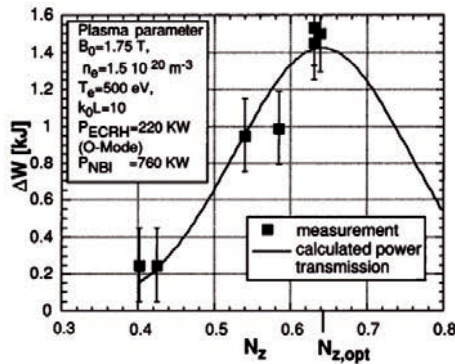


FIG. 6.57. Increase of the plasma energy content by O-X-B heating versus the longitudinal refractive index of the incident O-mode wave  $N_z$ . The solid line is the calculated transmission normalized to the maximum energy increase [6.214]. Here  $N_{z,opt}$  is the optimal value of  $N_z$ , the index of refraction parallel to the magnetic field, where maximum absorption takes place;  $k_0L = L / (\lambda_0 2\pi)$ , where  $L$  is the path length of the microwave beam and  $\lambda_0$  the free space wavelength. Reprinted from Ref. [6.214]. Copyright (2011) by the American Physical Society.

### 6.3.5.2. Electron cyclotron current drive (ECCD) experiments

Electron cyclotron waves can drive current in a toroidal plasma even without introducing significant toroidal angular momentum [6.60, 6.65]. Wave absorption can be highly localized in space near the intersection of the wave with the cyclotron resonance or its low harmonics, so the current may also be localized in a robustly controllable manner. This unique localization and controllability offer the opportunity to apply ECCD to applications like controlling the growth of MHD instabilities in the neighbourhood of rational surfaces or driving broad off-axis currents for optimizing the equilibrium for improved confinement and stability.

In experiments, the ECCD net current can be measured by comparing the plasma toroidal resistance (the loop voltage measured with a flux loop divided by the total plasma current measured with a Rogowski coil) with the neoclassical resistance calculated from measurements of the  $T_e$  and the  $Z_{eff}$  profiles. Plasma resistance below the calculated resistance is indicative of

ECCD. This determination of the driven current is subject to a rather high degree of uncertainty, particularly if MHD activity is present. Greater clarity can be obtained if the ECCD is larger than the total plasma current, so that the loop voltage goes negative. This was done in experiments on the TCV tokamak [6.217], in which over 80 kA of ECCD was driven by 1.0 MW of EC power, driving the loop voltage to or below zero for 4 s, which is many resistive times (Fig. 6.58). Such experiments may be done with great sensitivity in stellarator geometry since stellarators have little net plasma current to compete with the ECCD. Definitive ECCD experiments were reported from the Wendelstein 7-AS stellarator [6.218].

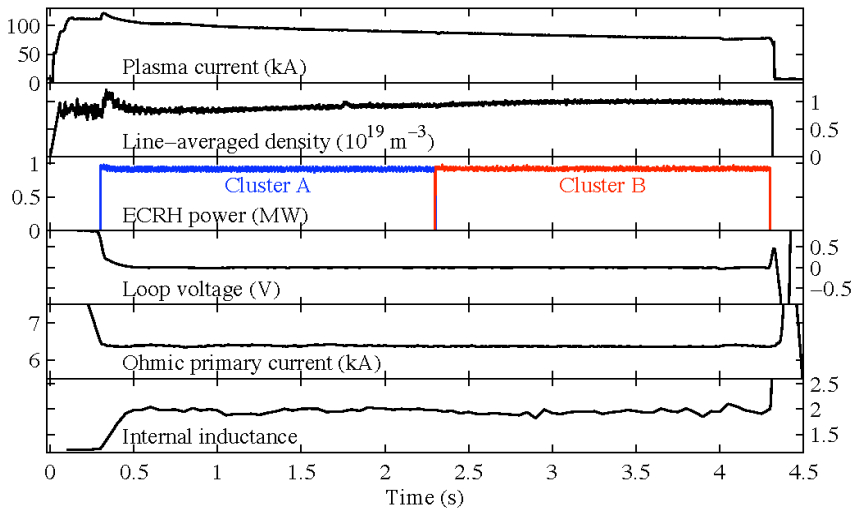


FIG. 6.58. Steady state current fully supported by ECCD using 1.0 MW of power distributed over the plasma cross-section. Reprinted from Ref. [6.217].

The loop voltage method can determine the total driven current but not the current profile. The profile of ECCD can be inferred from measurement of the local magnetic field inside the plasma, for example by the motional Stark effect (MSE) diagnostics (process developed by C.B. Forest [6.219]). The information from the internal magnetic measurements can be used to constrain the reconstruction of the equilibrium to obtain an accurate calculation of the flux surfaces in the plasma. Since the local toroidal electric field can be found from the time derivative of the local flux, the ohmic current density can be found by multiplying by the neoclassical resistivity. Subtracting the ohmic current density from the total current density yields the sum of the non-inductive currents (i.e. bootstrap current, ECCD and possibly neutral beam driven current) (see Ref. [6.219]). However, this method can have difficulty resolving the very narrow current profiles that ECCD can produce.

An alternate method is to compare the measured MSE pitch angles with simulations of the MSE evolution [6.220]. The current location, peak and width can be varied in the simulation until the differences between the simulation and the measured pitch angles are minimized, producing resolution up to the spatial separation of the measurement locations. An example from DIII-D of such a process is shown in Fig. 6.59. In this discharge the ECCD is fully contained between two adjacent MSE channels separated by about 5 cm.

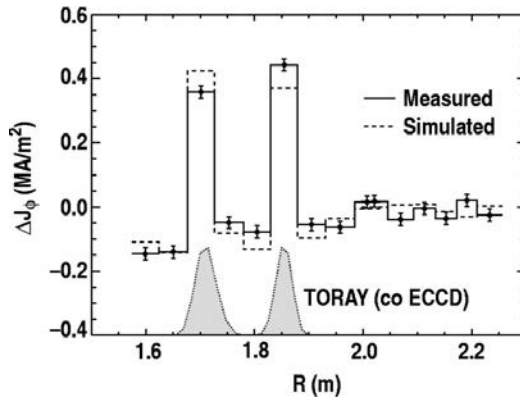


FIG. 6.59. Change in the measured (solid line) and simulated (dashed line) toroidal current density  $J_\phi$  as a function of major radius between a discharge with co-ECCD and one without EC power, taken from the DIII-D tokamak. The magnetic axis lies between the two peaks, so the peak at 1.7 m is on the high field side and the peak at 1.86 m is on the low field side of the magnetic axis, but both are on the same flux surface. The shaded curves are the location and width of the ECCD calculated by the TORAY code. Reprinted from Ref. [6.220].

Measurements of the location and magnitude of the ECCD can be systematically compared with models to validate the theory. Results of a large series of experiments on the DIII-D tokamak are shown in Fig. 6.60. This work shows that for a wide range of minor radius, poloidal location, plasma density and temperature, and EC power, the Fokker-Planck code CQL3D [6.203] predicts very accurately the total driven current. The linear TORAY-GA code also does well except at the largest driven currents. The CQL3D model includes the effects of the ohmic electric field on the quasi-linear distribution function and resistivity. Figure 6.60 shows that ECCD is well predicted by the models in the linear and quasilinear codes for the conditions of these experiments. Another example of similarity between the ECCD calculated by linear and Fokker-Planck codes was shown for a particular ITER case in Fig. 6.61. There are, however, important cases where the two approaches differ significantly. One example is when the power density per particle is high, which causes significant distortions of the distribution function. A criterion for the onset of significant quasi-linear effects was given by Harvey [6.221]:

$$2 \frac{q_e}{n_e^2} > 1 \quad (6.151)$$

where  $q_e$  is the heating power per unit volume in  $\text{MW} \cdot \text{m}^{-3}$  averaged over the flux surface and electron density  $n_e$  is given in  $10^{19} \text{m}^{-3}$ . A factor of two decrease from linear ECCD was attributed to quasi-linear effects in ECCD studies at high power per particle in experiments on Wendelstein 7-AS [6.222].

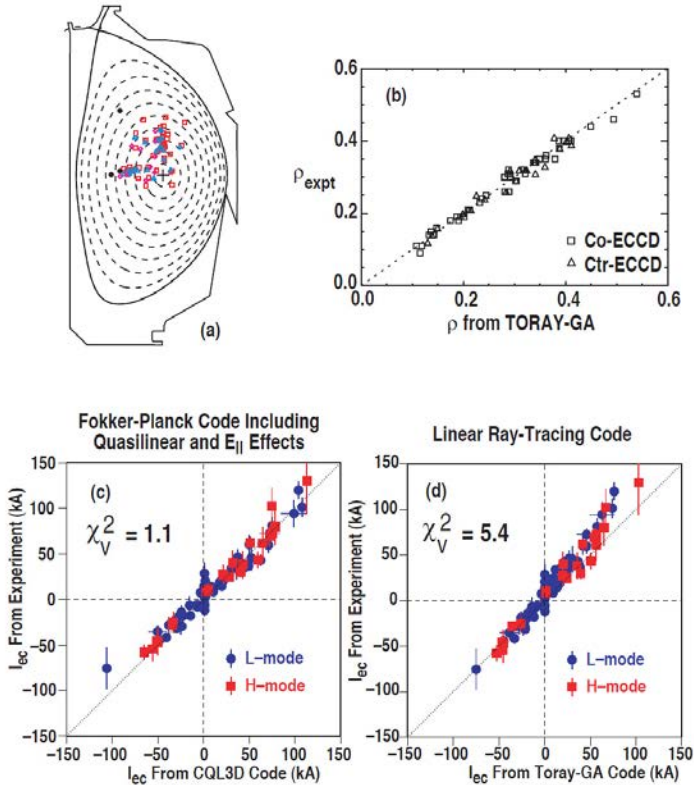


FIG. 6.60. ECCD measurements taken from the DIII-D tokamak. (a) Locations of the application of EC power on a plasma cross-section. The square points are for co-ECCD, the triangles are for counter-ECCD, and the diamond points are for radial ECH (no current drive). The solid circles are the locations of ECCD used in tests of stabilization of MHD activity where unambiguous results of current drive were found but no direct measurement of the driven current was made. (b) The normalized minor radius of the peak of the measured ECCD versus that calculated by TORAY-GA, for all the points of (a) except those with radial ECH. (c) Comparison of measured ECCD versus that calculated by the quasi-linear Fokker-Planck code CQL3D including the effects of the ohmic electric field. (d) Comparison of measured ECCD versus that calculated by the linear ray tracing code TORAY-GA. Here,  $\chi^2_{\text{v}}$  is the usual goodness-of-fit parameter, showing that the CQL3D model is better than the TORAY-GA model. Parts (a) and (b) are reprinted from Ref. [6.66]. Copyright (2011), American Institute of Physics. Parts (c) and (d) are reprinted from Ref. [6.65].

A second example is when particle transport is sufficiently strong that current-carrying electrons are moved to the plasma boundary before they fully slow down. This effect was found to be very strong in some experiments on TCV [6.223], reducing the ECCD from 550 kA calculated by CQL3D to 100 kA in the experiments. This effect is unmeasurably small in larger, higher current tokamaks [6.223]. A third example of the linear and quasi-linear codes differing in calculated ECCD is when momentum conservation in electron–electron collisions is important. For example, when applying ECCD near the magnetic axis of ITER, where the collisionality is very low and the trapped electron fraction is small, neglect of momentum conservation can cause a large decrease — nearly a factor of 3 in a representative case — in the calculated ECCD [6.200]. In this case, the results by CQL3D are much more valid than the linear calculations. This is illustrated in Fig. 6.61.

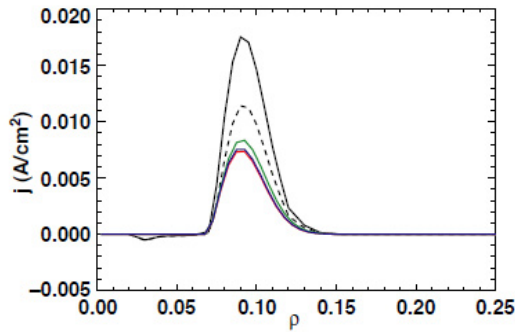


FIG. 6.61. Current density profile calculated by CQL3D using its standard collision operator (top solid line) and the non-momentum-conserving model (dashed line). Also shown are three TORAY models, the most sophisticated being the green curve. Reprinted from Ref. [6.200].

The codes can then be used to design experimental applications and to analyse the results. Applications include global current profile improvement for increased confinement and stability, control of MHD activity like neoclassical tearing modes and sawteeth, and for generating localized magnetic shear that can anchor electron transport barriers to a particular location in the plasma. An example of a high level of nearly central ECCD was shown in Fig. 6.53, in which 0.75 MA of ECCD was obtained in JT-60U.

The dimensionless theoretical ECCD can be characterized as [6.65, 6.224]

$$\frac{I_{ECCD}}{P_{EC}} = \frac{\epsilon_0^2}{e^3} \left( \frac{kT_e}{\ln \Lambda R n_e} \right) \zeta \left( Z, \epsilon, \theta, \frac{\omega}{k_{\parallel} v_{th,e}} \right) \quad (6.152)$$

where  $I_{ECCD}$  is the current driven by ECCD,  $P_{EC}$  is the electron cyclotron wave power,  $\epsilon_0$  is the permittivity of free space,  $e$  is the electron charge,  $k$  is the Boltzmann constant,  $T_e$  is the electron temperature (in K),  $\ln \Lambda$  is the Coulomb

logarithm and  $n_e$  is the electron density. The complications that come from the geometry, the magnetic well depth and the location in the electron distribution function of the interaction of the wave are in the function  $\zeta$ . The ion charge  $Z$  is related to the collisionality, while the inverse aspect ratio  $\varepsilon$  and the poloidal angle of the interaction  $\theta$  determine the magnetic well depth for purposes of determining the trapped fraction of electrons. The parameter  $\omega / k_{\parallel} v_{th,e}$ , where  $k_{\parallel}$  is the parallel wavenumber and  $v_{th,e}$  is the electron thermal velocity, is the relative wave parallel phase velocity where the EC power is absorbed. In practice,  $\omega / k_{\parallel} v_{th,e}$  may be affected by the wave trajectory as it approaches the resonance surface. The first two factors of Eq. (6.153) can be combined as the theoretical dimensionless figure of merit

$$\zeta \approx 33 \frac{n_e [10^{20} \text{ m}^{-3}] I_{ECCD} [\text{MA}] R [\text{m}]}{P_{EC} [\text{MW}] T_e [\text{keV}]} \quad (6.153)$$

For the discharge of Fig. 6.53, for example,  $\zeta \approx 0.04$ .

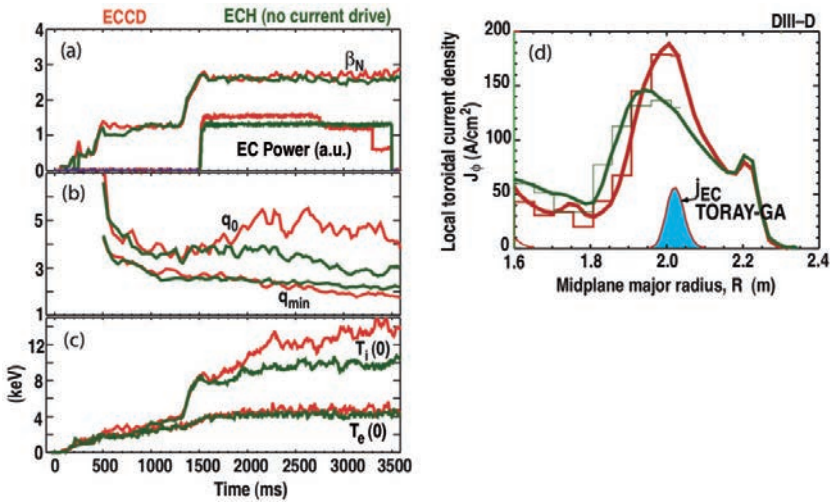


FIG. 6.62. Two similar discharges from DIII-D, one with off-axis ECCD (red) and one with ECH (green). (a)  $\beta_N$ , the plasma beta normalized by  $I_p [\text{MA}] / (a[\text{m}]B)$ , and the EC power. (b) Central value and minimum of the safety factor. (c) Central ion and electron temperatures, versus time. (d) Profile of equilibrium current and calculated ECCD. Reprinted from Ref. [6.225]. Copyright (2011) by the American Physical Society.

In addition to driving central current as in Fig. 6.53, ECCD may be used to alter or sustain a desired current profile. Tokamak discharges with negative central shear have been shown to have improved confinement and stability properties, and stellarators may obtain improved magnetic configuration by having the bootstrap current nullified. An example of discharge improvement by off-axis ECCD is shown in Fig. 6.62. This figure shows two nearly identical

discharges, one with ECH (no current drive) and one with ECCD. In both cases the power is deposited near  $\rho = 0.5$ . The discharge with ECCD shows stronger negative central shear, as seen in the rising behaviour of the central safety factor  $q_0$ . The increased negative central shear leads to increased core confinement, as seen in the rising core ion temperature. In this way, the plasma pressure is sustained stably above the no-wall beta limit for the duration of the EC pulses, and the non-inductive fraction is maintained above 85% with steady profiles. Thus, ECCD has significantly advanced this discharge towards a fully non-inductive high performance tokamak scenario.

ECCD has also been used to control MHD activity in a plasma. ECCD is highly suitable for this purpose because it is so localized and because the location can be well controlled. One example of control of the sawtooth period is shown in Fig. 6.63. In this case, the sawtooth period was varied over a factor 3 depending sensitively on whether the ECCD was placed within  $\delta\rho \approx 0.1$  inside the sawtooth inversion radius.

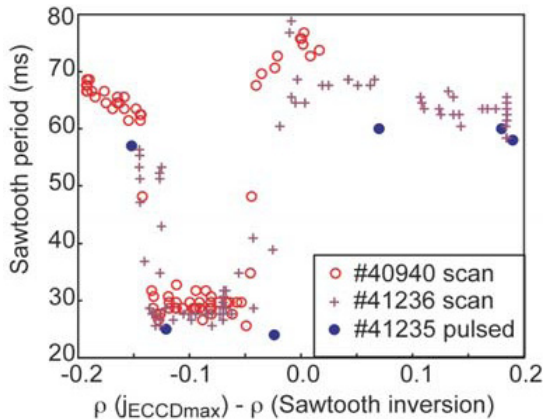


FIG. 6.63. Sawtooth period in a Tore-Supra discharge versus the location of the ECCD peak relative to the sawtooth inversion radius. Reprinted from Ref. [6.226]. Copyright (2011) by the World Scientific Publishing Company.

Another example of control of MHD activity by ECCD is the stabilization of the neoclassical tearing mode (NTM) by localized ECCD. Here, ECCD is used both to replace the missing bootstrap current in magnetic islands that may form on rational surfaces in high beta plasmas and to modify the current profile so that its classical stability to tearing modes is enhanced. An example of suppression of a fully grown NTM is shown in Fig. 6.64. In this experiment [6.227], an NTM with poloidal mode number 3 and toroidal mode number 2 starts with fully saturated amplitude. ECCD is modulated at the frequency of the NTM so that ECCD is applied only near the island centre. This approach to modulation has improved efficiency at stabilizing the mode. When the mode disappears, the normalized

beta  $\beta_N$  can be raised significantly, and the confinement H-factor also improves. NTMs can be avoided altogether by applying the ECCD at the rational surface before the mode appears; this approach requires less EC power and can allow the discharge to reach beta values that would otherwise be inaccessible [6.228].

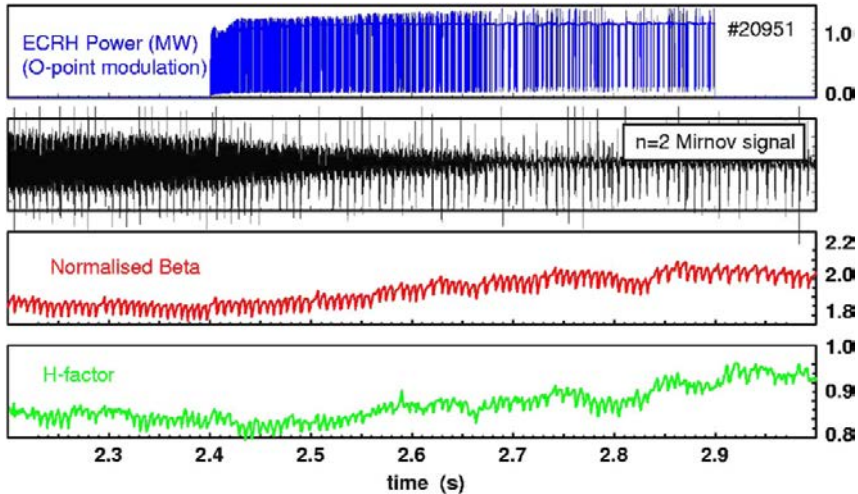


FIG. 6.64. Stabilization of an NTM by ECCD in a discharge in ASDEX Upgrade. Reprinted from Ref. [6.227]. Copyright (2011), IOP Publishing Ltd.

### 6.3.6. Electron cyclotron transmission line and antenna design

Power generated in the ECH frequency range, typically by gyrotrons, must be transmitted to the confinement device by transmission lines of typical length 50–100 m. The most common method is use of a waveguide. The fundamental mode of a waveguide in which the transverse dimensions are of the order of a half-wavelength (a few mm) is unsuitable for frequencies above a few tens of GHz due to excessive dissipation in the waveguide and likely breakdown caused by extremely high electric fields when operated at high power. Instead, a highly overmoded waveguide propagating a low order mode is used. Modern fusion related systems [6.229, 6.230] use circular waveguides with diameters 10–50 times the wavelength, propagating the very low loss  $HE_{11}$ -mode (see Ref. [6.229]) that propagates in waveguides with corrugated walls; for ITER conditions of 170 GHz and a 63.5 mm diameter corrugated waveguide, the theoretical loss is 0.02 dB/100 m. The dominant loss in waveguide transmission lines is at mitre bends, where 0.1–0.3% of the propagated power is ohmic loss on the mirrors and there is an additional mode conversion loss of 0.1–0.3%, depending on the design [6.231].

Transmission lines can suffer electrical breakdown, but the high frequencies of EC systems help to avoid it. The reliable power handling capability of corrugated waveguides, above  $10^5 \text{ W}\cdot\text{cm}^{-2}$  in practice, comes from the low energy excursion of a collisionless electron in a waveguide. The peak electric field at the centre of a waveguide propagating the  $\text{HE}_{11}$ -mode is  $E = [32P_{EC} / (\epsilon_0 c \pi d^2)]^{1/2} \approx 60P_{EC}^{1/2} / d$ , where  $c$  is the speed of light and  $d$  is the waveguide diameter. For the ITER waveguide diameter, the peak electric field is of order  $1 \text{ MV}\cdot\text{m}^{-1}$  for 1 MW of power. An unmagnetized electron in this field will oscillate with a peak energy  $W = (16e^2 / \pi \epsilon_0 m_e c) (P_{EC} / \omega^2 d^2)$ . Again for the ITER waveguide example, this energy is only about 0.1 eV, which is far below the ionization energy. The only way the electron can be accelerated to ionization energies is through a decorrelation process like collisions. Keeping the collision frequency either much smaller (evacuated waveguide) or much larger (pressurized waveguide) than the applied frequency will avoid this random walk in energy, which must take place in a time less than the time for the electron to drift to a waveguide wall or lose energy through excitation of the background gas. In practice, power at the MW level at 60 GHz and above has been robustly transmitted in waveguides of a few cm diameter, either evacuated or at atmospheric pressure.

The polarization of the electric field of the incident wave at the plasma boundary must be set in the transmission line to match the polarization of the desired mode, ordinary or extraordinary. This can be done using grooved mirrors in the bends of the transmission line [6.232]. In the local Stix coordinate system at the plasma boundary, the low density limit of the cold plasma dispersion relation provides the target polarization. An example diagram of a waveguide transmission line is shown in Fig. 6.65.

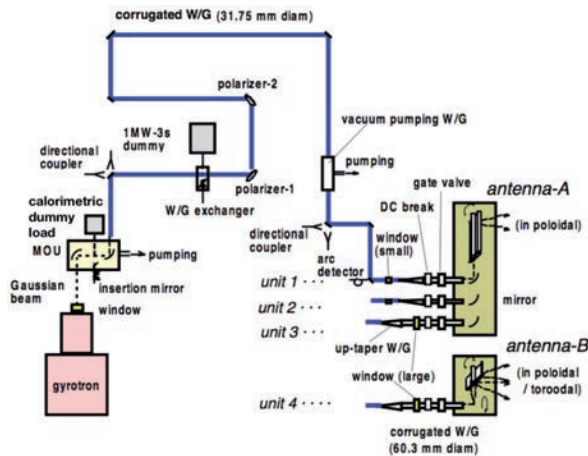


FIG. 6.65. Schematic drawing of the waveguide transmission line for the JT-60U tokamak [6.233]. Some components of the system are described in Ref. [6.231].

An alternative to the waveguide transmission line is the quasi-optical transmission line [6.234], which has been developed for the stellarator W-7X. This approach, shown in Fig. 6.66, uses free-space propagation of Gaussian beams with periodic focus mirrors in a confocal arrangement. Beams from up to seven 1 MW 140 GHz gyrotrons are transmitted to the stellarator by each of two such transmission systems. Each gyrotron beam has a pair of beam conditioning mirrors and a pair of polarizing mirrors before the beams enter the common mirror system (mirrors M5-M11 in Fig. 6.66(a)). This system has demonstrated robust alignment in tests with two gyrotrons operating each at 0.9 MW for 30 minutes. Overall efficiency is 90% for the Gaussian beam fraction of the power.

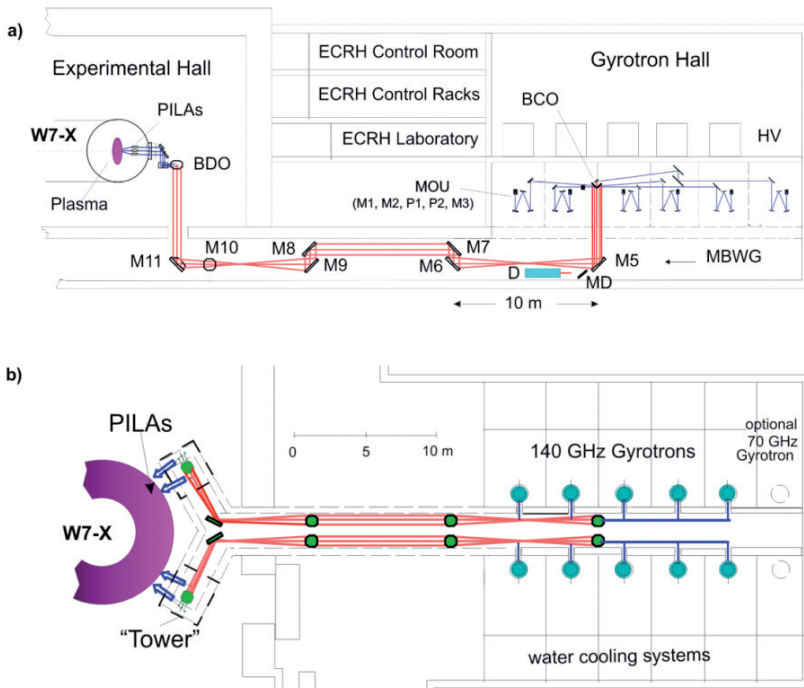


FIG. 6.66. Schematic design of the 140 GHz, 10 MW transmission system for ECH on W7-X. Shown is (a) a vertical cross-section and (b) a top view. Reprinted from Ref. [6.234]. Copyright (2011), American Nuclear Society.

Launchers for ECH systems are relatively simple, due to the feature that the EC wave propagates in vacuum. This means that the launcher need not be close to the plasma in order to have good coupling. And because the launching structure is many wavelengths in dimension, there are other advantages. First, where the wave exits a highly overmoded waveguide there is little reflected power, since the wave phase velocity is very nearly the same (namely  $c$ ) in the waveguide and outside it. Second, the beam emerging from a waveguide can have small

angular divergence even without additional focusing optics. For example, for the ITER case of the  $HE_{11}$ -mode at 170 GHz in a 63.5 mm diameter waveguide the radiation pattern from an open-ended waveguide is down 10 dB at  $\pm 1.8^\circ$ . Diffraction-limited divergence is of order  $1.6^\circ$ . The small angular divergence is very suitable for objectives requiring highly localized heating or current drive, like NTM control. Narrower deposition profiles may be obtained by using focusing mirrors, but diffraction is always a limit.

The simplest launcher is a terminated waveguide pointed at the plasma. This approach has been used successfully in many experiments. However, as the experiment objectives became more sophisticated, more flexible launchers were developed so that power could be directed with different poloidal and toroidal angles. Typically this has been done with articulating mirrors [6.233–6.235] so that aiming in the poloidal and toroidal directions can be accommodated. This front steering approach can launch very narrow beams over a wide range of angles. An alternative technique, which was developed to avoid the galling or seizing problems to which mirrors that move or slide in the high vacuum of tokamak vessels are subject, is the remote steering launcher [6.236, 6.237]. In this approach, waves are launched into a waveguide of tuned length such that the waveguide modes reconstruct at the end of the waveguide into a beam propagating at an angle to the axis of the waveguide. In this way, the steering mechanism can be relocated to the input end of the waveguide rather than the output end near the plasma, but the beam may not be as narrow as for the front steering system.

The ECH system for ITER will have the capability of 20 MW incident on the plasma from 24 gyrotrons of 170 GHz and 1 MW. Two front steering launcher systems are planned, an equatorial launch and a top launch [6.238]. These launchers are shown in Fig. 6.67. Extensive modelling has shown that this combination of launchers is capable of a wide range of physics objectives for the ITER scenarios.

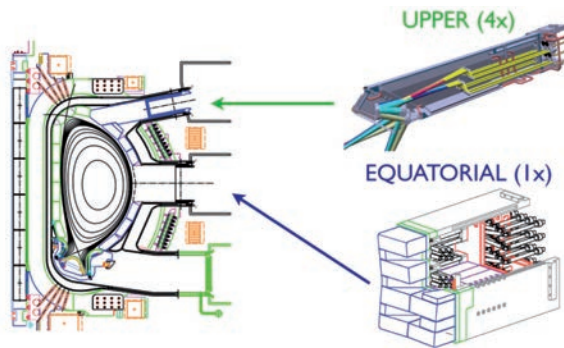


FIG. 6.67. Schematic diagram of the two types of ECH launchers designed for ITER. Reprinted from Ref. [6.238].

## 6.4. GYROTRONS FOR ECR HEATING AND CURRENT DRIVE

### 6.4.1. Introduction to gyrotrons

The gyrotron is a powerful source of coherent radiation capable of generating over 1 MW of continuous wave (CW) power at wavelengths in the millimeter wave range. For plasma heating at the electron cyclotron resonance frequency ( $\omega_{ce}$ ), the required frequency ( $\omega$ ) is given approximately by

$$\omega \approx s\omega_{ce} = s \frac{eB}{\gamma m_e} \quad (6.154)$$

where

$$\gamma = \frac{1}{\sqrt{(1 - v_e^2 / c^2)}} \quad (6.155)$$

and where  $e$  is the electron charge,  $B$  is the magnetic field strength,  $m_e$  is the electron mass,  $s$ , an integer, is the harmonic number (usually 1 or 2);  $\gamma$  is the Lorentz factor;  $v_e$  is the electron velocity, with axial component  $v_z$  and transverse component  $v_\perp$ ; and  $c$  is the speed of light. For a rough estimate, the required frequency in GHz is  $f = 28B$  when the Lorentz factor is taken as unity and the magnetic field is given in tesla. For plasma experiments operating in magnetic fields of  $B = 2\text{--}6$  T, the required heating frequency from the gyrotron is  $\omega / 2\pi = 56\text{--}168$  GHz for fundamental heating ( $s = 1$ ). These frequencies fall within the millimetre waveband.

This introduction to gyrotrons is intended to give the reader a brief overview of gyrotrons as a source of power for plasma heating. Gyrotron research is an exciting field and many excellent books and review papers have been written explaining the physics and engineering principles of the gyrotron in detail. The interested reader is strongly encouraged to consult these sources for more detailed information [6.239–6.246]. Since the gyrotron is by far the most powerful source of high average power in the millimetre waveband, it has been developed in the past few decades as a source for plasma heating at electron cyclotron resonance. Millimetre wave oscillators in the kilowatt to megawatt power level range and frequencies of up to 170 GHz are under intensive international development for plasma heating. The comparison of the gyrotron with other high power coherent sources is shown in Fig. 6.68. A more detailed comparison is given in a review article by Granatstein et al. [6.246]. Gyrotrons are the only source capable of meeting the power needs for ECH at millimetre wavelengths. Comparison of power capability shows that even at conventional microwave frequencies, down to about 10 GHz, the gyrotron is a more powerful source in long pulse or high average power operation than alternative sources like the klystron.

The gyrotron is a specific version of the electron cyclotron maser (ECM). The ECM instability was discovered in the late 1950s and was definitively demonstrated in the laboratory in 1964 [6.247–6.251]. In the ECM, energy can be extracted from the transverse component of the electron velocity of an electron beam. The gyrotron is a specific form of the ECM that was first invented and developed in the Soviet Union with the goal of achieving very high power from the ECM interaction [6.252]. Major features of the gyrotron, as opposed to the ECM, include a magnetron injection gun (MIG), capable of generating an annular beam with very high power, and an open resonator operating close to cut-off (where the transverse wavenumber  $k_{\perp}$  is much greater than the axial wavenumber  $k_z$ ) consisting of a section of overmoded waveguide with input and output tapers.

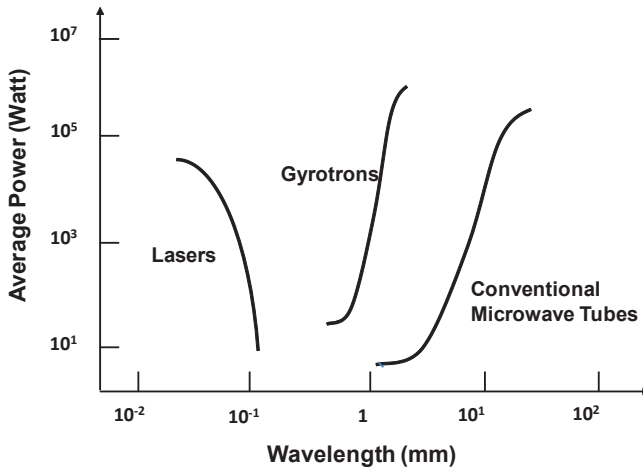


FIG. 6.68. Comparison of the gyrotron with alternative high power sources.

Figure 6.69 shows a schematic of a modern 1 MW gyrotron. The figure is based on the 1 MW, 110 GHz gyrotron tube designed by CPI for the purpose of plasma heating at the DIII-D tokamak. An annular electron beam generated by the MIG-type electron gun is formed in the gun region. As the electron beam propagates to the cavity region, it passes into a region of increasing magnetic field, where it is adiabatically compressed and the transverse velocity of the electrons is greatly increased. The required magnetic fields are generated by superconducting magnets. High power microwaves are generated in the cavity in a high order mode so as to reduce the heating per unit area of the cavity wall. The gyrotron shown in Fig. 6.69 operates in the  $TE_{22,6}$  circular waveguide mode. The output from the cavity is formed into a free space wave by a dimpled-wall launcher and is further corrected by a system of internal mirrors. The purpose of these mirrors is not only to guide the beam to the window, but also to shape the

beam into a Gaussian with the beam waist at the window of the gyrotron. The output window of megawatt power level gyrotrons is a single disk of chemical vapour deposition (CVD) diamond.

### 6.4.2. Physical principles of the gyrotron

The electromagnetic radiation in a gyrotron is produced by the interaction of a mildly relativistic gyrating electron beam and a TE wave close to cut-off in a cavity resonator. The oscillation frequency  $\omega$ , of the TE<sub>mnq</sub> mode (the transverse electric mode with radial index  $m$ , azimuthal index  $n$  and axial index  $q$ ) of a cylindrical cavity of length  $L$  and radius  $r_0$ , is given by

$$\omega^2 / c^2 = k^2 = k_{\perp}^2 + k_z^2 \tag{6.156}$$

where  $k_{\perp} (=v_{mn} / r_0)$  and  $k_z (=q\pi L \ll k_{\perp})$  are the transverse and longitudinal propagation constants of the TE<sub>mnq</sub> wave,  $c$  is the speed of light,  $v_{mn}$  is the  $n^{\text{th}}$  root of the derivative of  $J_m(x)$  (the Bessel function of order  $m$ ) and  $q$  is an integer (note that  $q$  is used here as the axial mode index and should not be confused with the safety factor). The resonance condition for the excitation of the cyclotron resonance maser instability is satisfied when beam conditions satisfy the cyclotron beam mode dispersion relation:

$$\omega - k_z v_z = s\omega_{ce} \tag{6.157}$$

where  $s$  is the cyclotron harmonic number and the cyclotron frequency  $\omega_{ce}$  is defined here to include the Lorentz factor as in Eqs (6.154) and (6.155). The

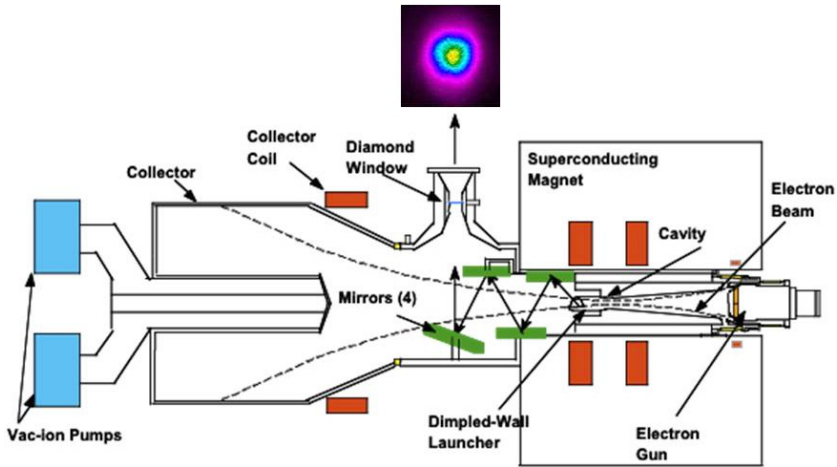


FIG. 6.69. Schematic of a megawatt power level gyrotron (110 GHz gyrotron schematic provided by CPI). An infrared camera image of a typical Gaussian-like output beam is shown [6.253].

resonance condition, which is a combination of these two relations, is displayed in an  $\omega - k$  relation, as shown in Fig. 6.70. The TE mode in the figure is given by Eq. (6.156) and the cyclotron mode by Eq. (6.157). The resonator TE<sub>mnp</sub> modes are also indicated, where values of  $k_z = q\pi L$  with  $q = 1, 2, 3$  and 4 are shown. In practice, the resonance condition may be achieved by tuning the magnetic field, so that the cyclotron mode is made to coincide with the TE mode cavity resonance. By tuning the magnetic field over a wide range, many different TE cavity modes may be excited. For convenience, most of the examples and illustrations used in the subsequent sections will be taken from the research programme at MIT on a 1–1.5 MW, 110 GHz gyrotron. Details of these results are published in journal articles and reports [6.254–6.259].

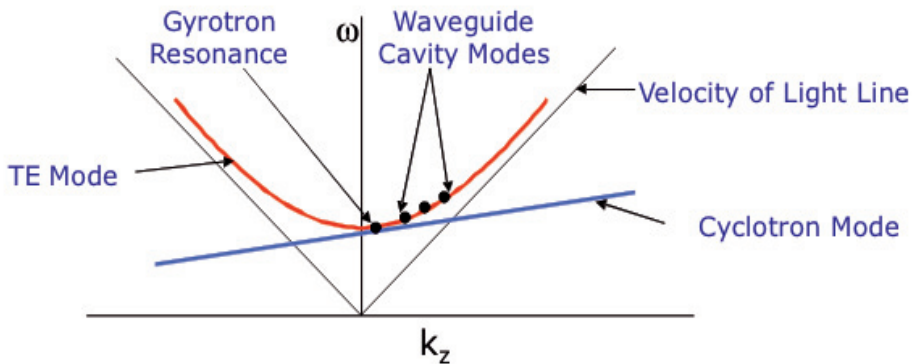


FIG. 6.70. The  $\omega - k$  diagram of the gyrotron interaction.

### 6.4.3. Overview of gyrotron theory

The electron cyclotron maser (ECM) instability results in bunching of the electron beam, as illustrated in Fig. 6.71. The electron beam consists of electrons arrayed in an annulus whose radius is much larger than the gyroradius  $\rho$  (also called the Larmor radius  $\rho_L$ ) of the cyclotron motion of the individual electrons. Initially, as seen on the left side of the figure, the electrons are randomly phased. As the electrons pass through the region of interaction with the transverse electric (TE) mode, the electrons become bunched in phase, as shown on the right side of the figure. The bunching is explained qualitatively as follows. The resonance condition, Eq. (6.157), is a function of energy through the Lorentz factor  $\gamma$ . Electron 1 in the figure is decelerated by the electric field, decreasing its energy and its Lorentz factor  $\gamma$ . This results in an effective increase of its cyclotron frequency. The conditions for electron 2, which is gaining energy, result in a decrease of its cyclotron frequency. The final result is a beam that is bunched in phase.

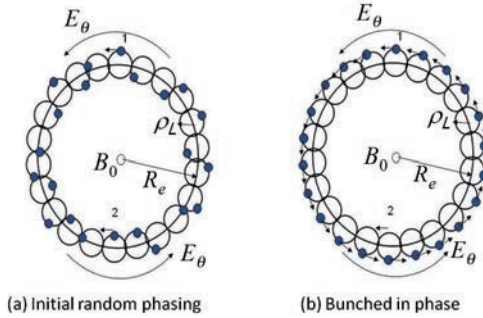


FIG. 6.71. Illustration of bunching in the annular beam of a gyrotron. The beam is passing along a static magnetic field of  $B_0$  and interacts with an RF electric field  $E$  (the field of the  $TE_{mpq}$  mode in the waveguide, in the poloidal direction, resonating with the electron's gyroradius). The annular beam radius  $R_e$  is much larger than the gyroradius  $\rho_L$ ; numbers 1 and 2 refer to two particular orbits locations relative to the electric field [6.258].

Figure 6.72 shows the result of a detailed calculation of bunching in an MW gyrotron. The sequential results are for the beam as it progresses along the  $z$  axis through the gyrotron cavity. The axial position is normalized in units of the parameter  $\mu$ , where

$$\mu = \pi v_{\perp}^2 L / v_z c \lambda \tag{6.158}$$

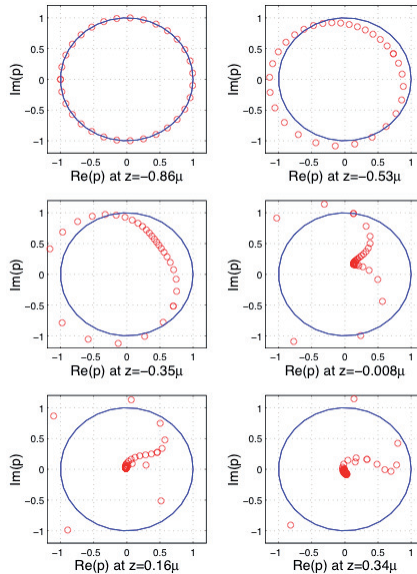


FIG. 6.72. Detailed calculation of the phase bunching in momentum space of a gyrotron electron beam [6.258]. The figure shows the Larmor radius of 32 electrons, initially equally spaced in phase, passing through the interaction region. The Larmor radius is given in complex notation so that  $Re(p)$  is the  $x$  position and  $Im(p)$  is the  $y$  position.

The calculation is for a 96 kV, 40 A electron beam with helicity factor  $\alpha(=v_{\perp}/v_z)$  equal to 1.3 and the magnetic field  $B = 4.47$  T. At the entrance to the cavity  $z = -0.86\mu$ , the 32 electrons are shown in Fig. 6.72 and are distributed randomly in phase. After a short travel in the cavity, at  $z = -0.53\mu$ , the electrons have been disturbed from their initial orbits by a sinusoidal perturbation of their momentum. This initial sinusoidal perturbation is predicted by linear theory. At later distances in the cavity, the electrons have given up energy to the TE wave. Their cyclotron orbits of radius  $\rho$  have decreased since  $\rho = v_{\perp}/\omega_{ce}$  and the decreasing energy of the particles reduces their transverse velocity. Figure 6.73 shows the efficiency achieved as a function of cavity length for the gyrotron electron beam. The final efficiency shown is the efficiency of energy extraction from the transverse energy component of the beam. Since energy is not extracted from the axial component of the electron beam by the ECM instability, it is important to achieve high values of  $\alpha$  in a gyrotron beam.

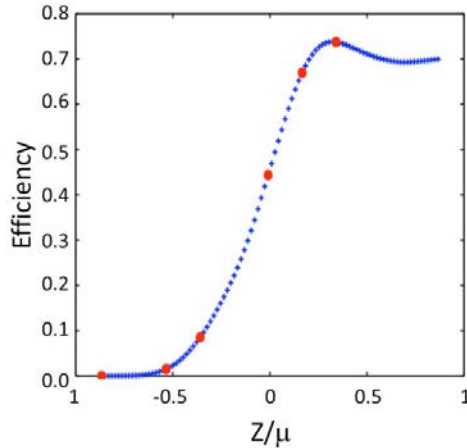


FIG. 6.73. Efficiency of extraction of energy from the transverse component of a gyrotron electron beam operating at 96 kV and 40 A [6.258].

The equations of motion of an electron in electric ( $\vec{E}$ ) and magnetic ( $\vec{B}$ ) fields are given by:

$$\frac{dU}{dt} = -e\vec{v} \cdot \vec{E} \quad (6.159)$$

$$\frac{d\vec{p}}{dt} = -e(\vec{E} - \vec{v} \times \vec{B} / c) \quad (6.160)$$

where  $U = \gamma mc^2$  and  $\vec{p}$  is the momentum. The solution of these equations has been studied extensively in both the linear and non-linear regimes. Linear theory is useful in predicting the threshold for the onset of oscillation of the desired

cavity mode. Figure 6.74 shows the threshold for oscillation of the modes of a cavity designed for operation at 1 MW and 110 GHz. The design cavity mode is the  $TE_{22,6,1}$  mode, which is predicted to start up at about 5 A of beam current in the calculation. In Figure 6.74 the axial mode number is assumed to be unity,  $q = 1$ , and has been dropped from the mode designations. Linear theory cannot predict the efficiency or the mode evolution in a gyrotron. However, Fig. 6.74 does provide clear evidence that gyrotrons operating in high order cavity modes, such as the  $TE_{22,6,1}$  mode, will be subject to mode competition. From Fig. 6.74, one can see that the  $TE_{19,7,1}$  mode is excited in the same region of magnetic field, voltage and current as the desired  $TE_{22,6,1}$  mode. This mode is in fact seen as a serious competitor in experimental research.

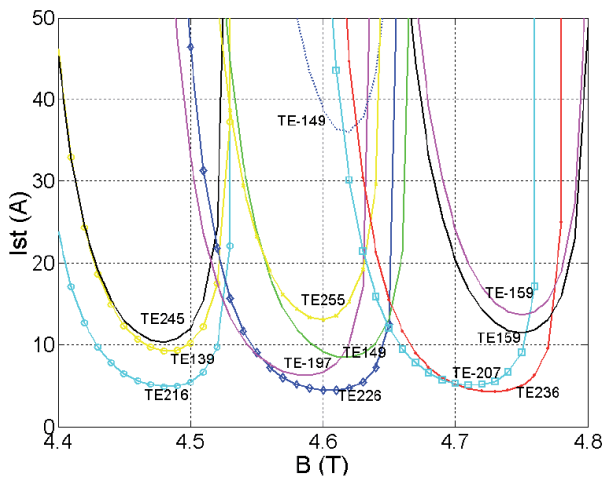


FIG. 6.74. Theoretical curves of start oscillation current  $I_{ST}$  as a function of magnetic field for a 1 MW, 110 GHz gyrotron [6.258].

Non-linear theory has been developed for estimating the efficiency of the gyrotron. Early work concentrated on developing a reduced set of equations averaged over a gyrotron orbit to yield efficiency estimates dependent only on the normalized cavity length and normalized power in the electron beam [6.260, 6.261]. These semi-analytic approaches are still useful for initial designs of gyrotrons. However, modern calculations of gyrotron operation are carried out with numerical simulation codes. An example of a non-linear calculation of mode excitation in a 1 MW, 110 GHz gyrotron under conditions of intense mode competition using the MAGY code is shown in Fig. 6.75 [6.262]. Figure 6.75 shows that the desired  $TE_{22,6,1}$  mode is excited but that during early portions of the pulse, competing modes are also excited. Mode competition is a continuing issue in gyrotron development but the use of modern codes has been very helpful in understanding and mitigating the effect.

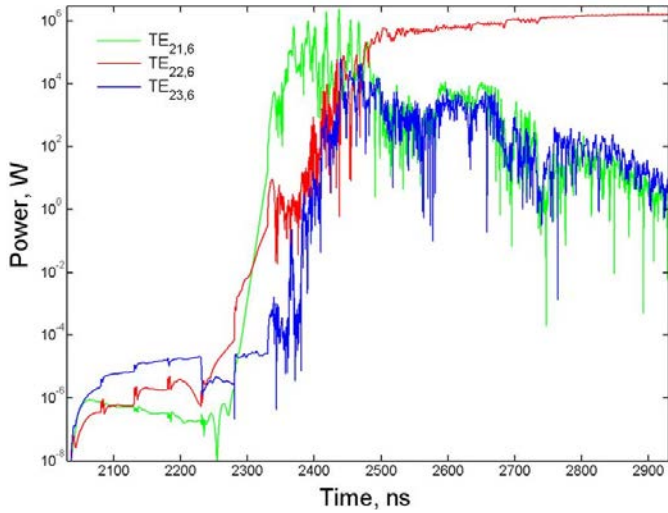


FIG. 6.75. Calculation of mode excitation in a 1 MW, 110 GHz gyrotron using the MAGY code [6.260]. Note that the desired  $TE_{22,6,1}$  mode is excited in equilibrium but that competing modes are present during early portions of the pulse.

Figure 6.76 shows results for a 1.5 MW, 110 GHz gyrotron operating in  $3 \mu\text{s}$  pulses at MIT. The  $TE_{22,6}$  mode was successfully excited over a wide range of magnetic fields with the highest power level of 1.5 MW being achieved at the operating point shown in the left hand figure by a red dot. The competing  $TE_{19,7}$  mode is also evident in the figure on the right, sometimes called a mode map, but did not prevent achievement of the high efficiency operating point.

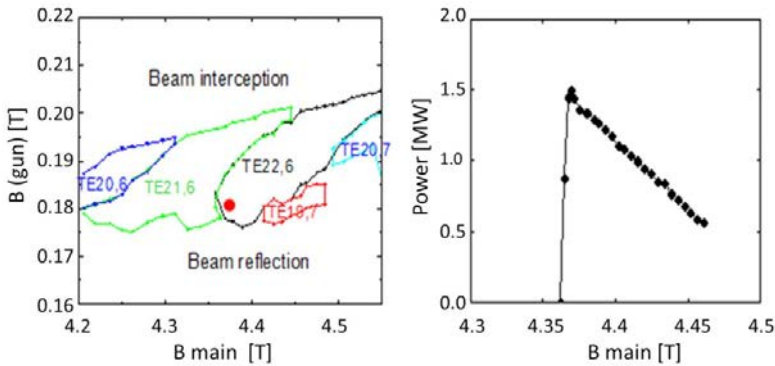


FIG. 6.76. Left: Mode map showing oscillations of modes as a function of the main magnetic field at the resonator (x-axis) and the electron gun magnetic field (y-axis). The  $TE_{22,6}$  mode has been successfully excited over a wide range of magnetic fields; the highest power was achieved at the operating point shown by a dot [6.255]. Right: Measured output power versus magnetic field for a 1.5 MW, 110 GHz gyrotron operating at 96 kV, 42 A in  $3 \mu\text{s}$  pulses. Reprinted from Ref. [6.255]. Copyright (2011), American Nuclear Society.

#### 6.4.4. Engineering features of the gyrotron

As can be seen from Fig. 6.69, the gyrotron has several major assemblies. The electron beam is created by the electron gun, transported through the vacuum tube by a magnetic field created by a superconducting magnet and deposited at the collector. Microwave radiation created in the cavity exits through an uptaper into a mode converting launcher. The microwave beam is radiated to a set of mirrors and exits the gyrotron through a dielectric window. A vacuum pump is also necessary in the gyrotron to help assure ultra high vacuum conditions.

##### 6.4.4.1. Electron gun and beam tunnel

The electron gun must supply the electron beam power for the gyrotron. If the overall output power is of the order of 1 MW and the efficiency of order 50%, the electron beam power must be in the 2–3 MW range. Typical voltages range from 70 to 100 kV with associated currents of 35–60 A to assure adequate electron beam power while maintaining space charge effects at a modest level. Electron gun designs are carried out with a variety of electrostatic codes. An example of an electron gun design for a 1 MW, 110 GHz gyrotron is shown in Fig. 6.77. The goal of the design is to produce an electron beam with the proper values of beam radius and beam helicity factor  $\alpha (= v_{\perp} / v_z)$  at the cavity. The design must also minimize the spread in the velocity of the electron beam. The electron beam tunnel, the region between the electron gun and the cavity, is shown in the simulation in Fig. 6.78 as a smooth wall. In fact, the beam tunnel cannot be a smooth wall since that would allow the onset of unwanted oscillations. The beam tunnel is often built of alternating rings of metal and dielectric to suppress instabilities.

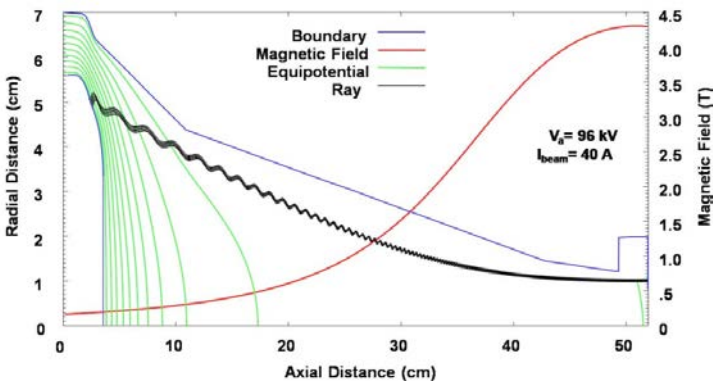


FIG. 6.77. Design of the electron gun for a 1 MW, 110 GHz gyrotron operating at a cathode voltage  $V_a$  of 96 kV and an electron beam current of 40 A [6.263]. Reprinted from Ref. [6.263]. Copyright (2011) by the IEEE.

#### 6.4.4.2. Gyrotron cavity

The gyrotron cavity must be an open resonator to permit the transit of the electron beam through the cavity. The simplest version of such a cavity is just a straight cylindrical pipe with a downtaper at the electron beam entrance end, to prevent power from passing out towards the electron gun, and an uptaper at the other end to permit passage of the microwaves out of the cavity. Figure 6.78 illustrates a simple cavity design for a 1 MW, 110 GHz gyrotron operating in the  $TE_{22,6,1}$  mode. Modern cavity designs are optimized to achieve high efficiency while limiting mode competition. For power levels above 1 MW, it may be useful to introduce a coaxial insert at the centre of the cavity to reduce space charge forces and possibly to reduce mode competition.

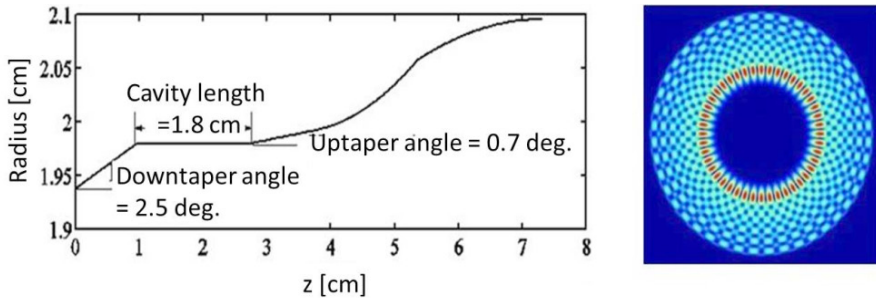


FIG. 6.78. Design of a tapered gyrotron cavity for a 1 MW, 110 GHz gyrotron. The mode pattern of the  $TE_{22,6,1}$  mode is shown to the right [6.256]. Reprinted from Ref. [6.256]. Copyright (2011), American Institute of Physics.

#### 6.4.4.3. Internal mode converter (IMC)

A major challenge of gyrotron design is to transform the cavity mode into a free space, Gaussian-like beam. Gyrotron modes such as the  $TE_{22,6,1}$  mode cannot be transported over long distances in waveguide because of losses due to both ohmic loss and mode conversion loss at bends. The free space Gaussian  $TEM_{00}$  mode (the fundamental transverse electromagnetic mode in free space) is generated inside the gyrotron by an internal mode converter (IMC). This mode can be coupled to a corrugated metallic transmission line with very high efficiency. The first approach to the IMC was suggested by Vlasov and coworkers in the form of a helically cut length of waveguide feeding power to a nearly parabolic collecting mirror. This concept is relatively easy to implement but is limited to an efficiency of about 80%. A major breakthrough was the invention of a dimpled wall launcher, which can achieve a mode conversion efficiency approaching 100% [6.264]. Further optimization of the mode launcher has been made possible

by improved optimization methods and improved codes [6.265]. An optimized launcher design with dimpled walls is shown in Fig. 6.79.

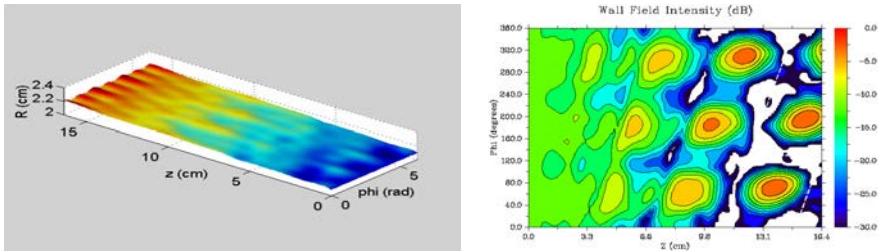


FIG. 6.79. Design of the internal mode converter for a 1 MW, 110 GHz gyrotron. The waveguide launcher wall ripples are shown at the left and the resulting field pattern on the waveguide wall is shown at the right. At the edge of the launcher, a nearly Gaussian beam has been created and is subsequently launched towards the first mirror [6.258].

#### 6.4.4.4. Phase correcting mirrors and output window

The microwave beam from the launcher is transported from the launcher to the output window by a set of mirrors. Figure 6.69 shows an example using four mirrors, but a smaller or larger number can be used. The mirror set can be used to correct phase and amplitude errors in the microwave beam from the launcher. In modern designs, the launcher output beam is of sufficient quality to be transmitted to the window by mirrors with smooth surfaces. Since the output window must transmit high power, a CVD diamond window is often used due to its very low microwave loss ( $\tan \delta \sim 2 \times 10^{-5}$ , where  $\tan \delta$  is defined as the imaginary part of the dielectric constant divided by the real part of the dielectric constant), high strength and excellent thermal conductivity. The diamond window can be edge cooled with water without a large temperature rise or stress in the window material.

#### 6.4.4.5. Depressed collector

The spent electron beam is guided to a collector which must be able to operate under conditions of very high average power. The tendency of the beam to strike a small area of the collector must be counteracted by use of small sweep coils that produce a local magnetic field in the collector region that oscillates in time at several hertz. The beam is then swept up and down the collector and also, in some cases, around azimuthally. A major advance in the development of gyrotrons was the successful demonstration of operation of the gyrotron with a depressed collector [6.266]. A gyrotron with a depressed collector is illustrated in Fig. 6.80.

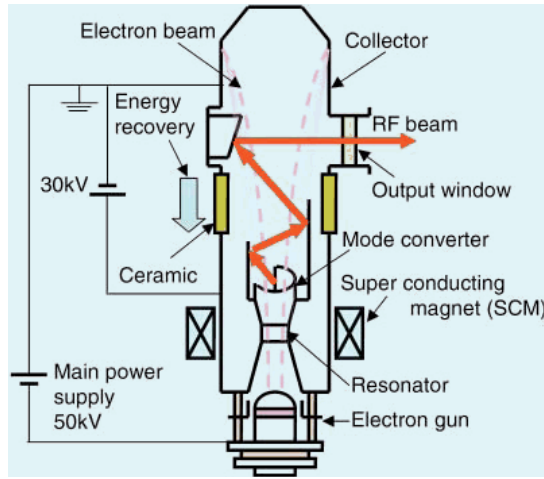


FIG. 6.80. Schematic of a gyrotron with a depressed collector. Reprinted from Ref. [6.267]. Copyright (2011), American Nuclear Society.

Megawatt power level gyrotrons typically have an efficiency of about 30 to 35% before application of the depression voltage. After application of the depression voltage, the efficiency can rise to well above 50%. The depression voltage is limited by the onset of beam interception on the body of the gyrotron. Experimental results on depressed collector operation of a short pulse gyrotron are illustrated in Fig. 6.81.

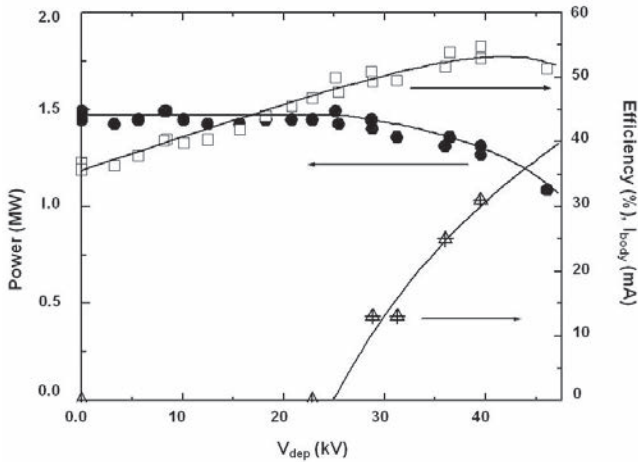


FIG. 6.81. The power and efficiency of the MIT 1.5 MW, 110 GHz gyrotron, operating at 96 kV and 42 A, are shown as a function of the depression voltage. The efficiency reaches 50% at a voltage depression of 25 kV.  $I_{body}$  is the current intercepted by the gyrotron internal parts; this current does not reach the collector. Reprinted from Ref. [6.254]. Copyright (2011), American Institute of Physics.

#### 6.4.4.6. Auxiliary components

The gyrotron output power must be coupled into a transmission line. Very low loss is achieved in evacuated metallic corrugated waveguide systems. Transmission by a set of mirrors is an alternative approach. A matching optics unit is used between the gyrotron and the transmission line to assure that the gyrotron beam couples efficiently to the waveguide and to remove stray radiation. The transmission line for the ECH system at DIII-D is illustrated in Fig. 6.82 [6.268]. A comprehensive review of the passive components needed for efficient operation of the transmission line has been given in Ref. [6.269].

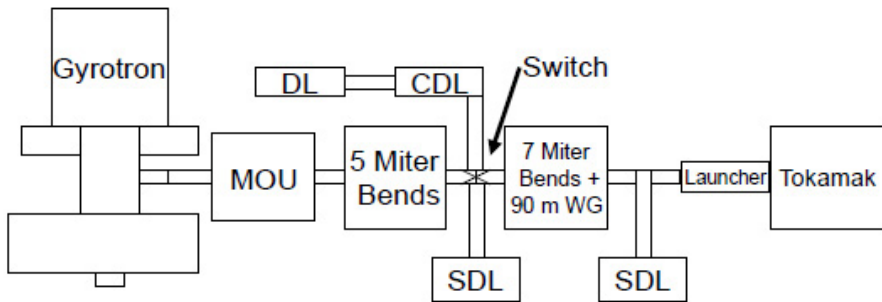


FIG. 6.82. Components of an ECH system, where MOU is a matching optics unit; DL is a dummy load; CDL is a compact DL; SDL is a small DL. Reprinted from Ref. [6.267]. Copyright (2011), American Nuclear Society.

#### 6.4.5. State of the art gyrotrons

The required power of ECH/ECCD systems will increase as future fusion devices will increase both in terms of size and in pulse length (CW). Table 6.2 presents the parameters of some of the major, multi-MW ECH systems that are currently in operation or planned in the near term. In order to meet the demands for high power plasma heating, present day gyrotrons are being designed, built and tested for operation at a power level of at least 1 MW and at frequencies in the 110–170 GHz range. The largest operating ECH system is the 6 MW, 110 GHz gyrotron system at General Atomics (GA) in San Diego.

TABLE 6.2. PARAMETERS OF MULTI-MW ECH SYSTEMS

Plasma device	Institution	ECH power [MW]	Frequency [GHz]	Pulse duration [s]	Gyrotron developer
ITER tokamak (under development)	ITER organization	24	170	1000	JAEA/ Toshiba, GYCOM, EU ITER TEAM
W7-X stellarator (under development)	IPP Greifswald	10 ( $10 \times 1.0$ )	140	CW	Thales (9), CPI (1)
DIII-D tokamak	GA	6 ( $6 \times 1.0$ )	110	10	CPI
JT-60 tokamak	JAEA	4 ( $4 \times 1.0$ )	110	5	JAEA/ Toshiba
LHD stellarator	NIFS	2 ( $2 \times 1.0$ ) 0.9 ( $2 \times 0.45$ ) 0.8/0.2 1 ( $2 \times 0.5$ )	77 82.7 84 168	5 2 3/CW 1	GYCOM, Toshiba
ASDEX-U tokamak	IPP Garching	4 ( $4 \times 1.0$ )	140/105	10	GYCOM
TCV tokamak	CRPP Lausanne	3 ( $6 \times 0.5$ ) 1.5 ( $3 \times 0.5$ )	82.7 110	2 2	GYCOM, Thales
T-10 tokamak	Kurchatov Institute, Moscow	1.5 ( $2 \times 0.75$ ) 1.5 ( $3 \times 0.5$ ) 0.5	129 140 158.5	0.5 0.5 0.5	GYCOM

Figure 6.83 shows one of the six operating 1 MW, 110 GHz gyrotrons installed at GA capable of 10 s pulse operation. The reliability of the ECH system has been high (about 84%). Research is also under way to develop a higher power gyrotron for DIII-D: a short pulse prototype gyrotron has operated at the 1.5 MW power level at MIT with 50% efficiency [6.255] and an industrial prototype of a 1.3 MW, 110 GHz gyrotron has operated in long pulse mode at CPI [6.270]. A comparable system of four 1 MW, 110 GHz, 5 s pulse length gyrotrons is operating at JT-60, while a 1.5 MW, 110 GHz gyrotron has also been demonstrated at JAEA [6.271].



FIG. 6.83. The CPI 1 MW, 110 GHz gyrotron installed at General Atomics for heating the DIII-D tokamak (photo courtesy of John Lohr, General Atomics, USA). See also Ref. [6.272].

Gyrotron development received a strong incentive and challenge in order to meet the needs of the W7-X and ITER projects, each of which requires CW operation of 1 MW gyrotrons. The status of the development of gyrotrons to meet these needs is summarized in Table 6.3, which is a modified version of a table presented in Ref. [6.273].

TABLE 6.3. PARAMETERS OF MW AND MULTI-MW GYROTRONS AT 140–170 GHz

Organization	Frequency (GHz)	Cavity Mode	Power (MW)	Efficiency (%)	Pulse Length
CPI	140	TE <sub>28,7</sub>	0.9	35	30 min
EU / TED	140	TE <sub>28,8</sub>	0.92	44	30 min
JAEA / Toshiba	170	TE <sub>31,8</sub>	1.0 0.8	55 57	13.3 min 60 min
IAP/GYCOM	170	TE <sub>25,10</sub>	0.95	53	1.7 min
EFDA / Fusion for Energy/TED	170	TE <sub>34,19</sub> coaxial	2	Under development	Under development
JAEA / Toshiba	170	TE <sub>31,12</sub>	1.5	27	0.1 s / under development
GYCOM / IAP	170	TE <sub>28,12</sub>	1.44	41	0.1 s / under development

All of the long pulse gyrotrons in the Table 6.3 operate with a single stage depressed collector, and the gyrotrons use diode electron guns, except for the JAEA gyrotrons, which have triode electron guns. The first of the gyrotrons to achieve the 1 MW power level was the CPI 140 GHz gyrotron for W7-X. It produced a 30 min pulse at 0.9 MW in 2005. This achievement was followed closely in time by a 140 GHz gyrotron developed by the EU gyrotron team and built by Thales TED [6.274]; this produced 0.92 MW at 140 GHz with a 30 min pulse length and is shown in Fig. 6.84. Nine Thales gyrotrons are currently in production, which, together with the CPI tube, will make up the 10 MW system for heating W7-X.

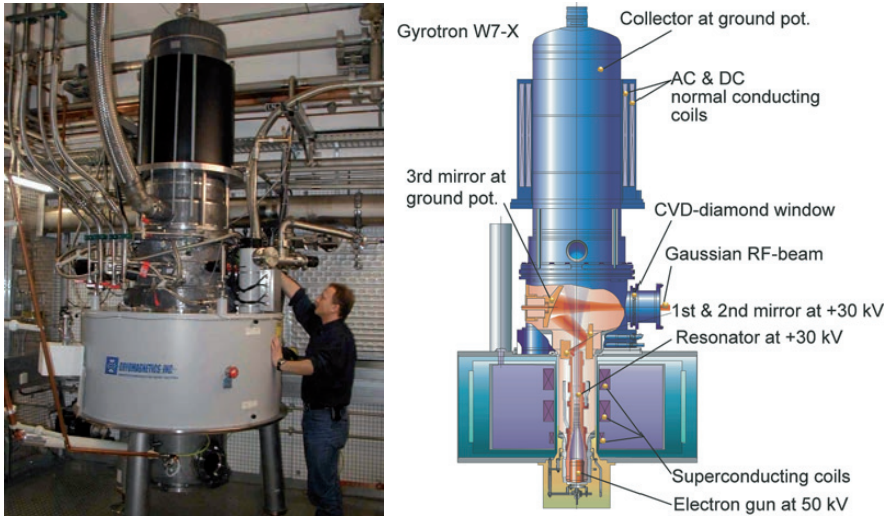


FIG. 6.84. The 1 MW, 140 GHz Thales gyrotron for W7-X. Reprinted from Ref. [6.274]. Copyright (2011) by the World Scientific Publishing Company.

Gyrotron development at a frequency of 170 GHz has been very successful. The feasibility of achieving 1–1.5 MW of gyrotron output power at 170 GHz was first demonstrated in short pulse experiments at MIT, where 1.5 MW at 170 GHz was achieved in the  $TE_{28,8}$  mode in  $3\mu s$  pulsed testing in 1997 [6.275]. Recently, JAEA has developed a 1 MW, 170 GHz gyrotron that has operated at a pulse length of 800 s (13.3 min) at over 50% efficiency [6.267]. This gyrotron meets the full ITER specification in terms of power, pulse length and efficiency — a remarkable achievement and a major breakthrough in gyrotron development. The ITER project will have 24 gyrotrons, with 8 gyrotrons supplied by each of three parties: Japan, the Russian Federation and the EU, assuming 1 MW per unit. The first prototype tube has been successfully developed in Japan and is now in use for component testing. The Institute of Applied Physics (IAP) and GYCOM have made excellent progress in developing a 170 GHz gyrotron, achieving a power

level of 1 MW with a 100 s pulse, despite being limited at present by the power supply [6.276]. The EU has chosen to supply 2 MW, 170 GHz gyrotrons utilizing a coaxial cavity. The 2 MW gyrotron will be tested at a new test stand that has been recently constructed at CRPP in Lausanne. A first gyrotron has been tested to confirm the basic features such as the correct operating mode. Successful demonstration of the 2 MW gyrotron will be another major breakthrough in gyrotron development. The gyrotrons under development for ITER are shown in Fig. 6.85. As shown in Table 6.3, both JAEA and IAP/GYCOM have initiated development of gyrotrons at the 1.5 MW power level for ITER. These gyrotrons would allow for higher levels of heating power or they could simply be operated at the 1 MW power level with an additional safety margin.

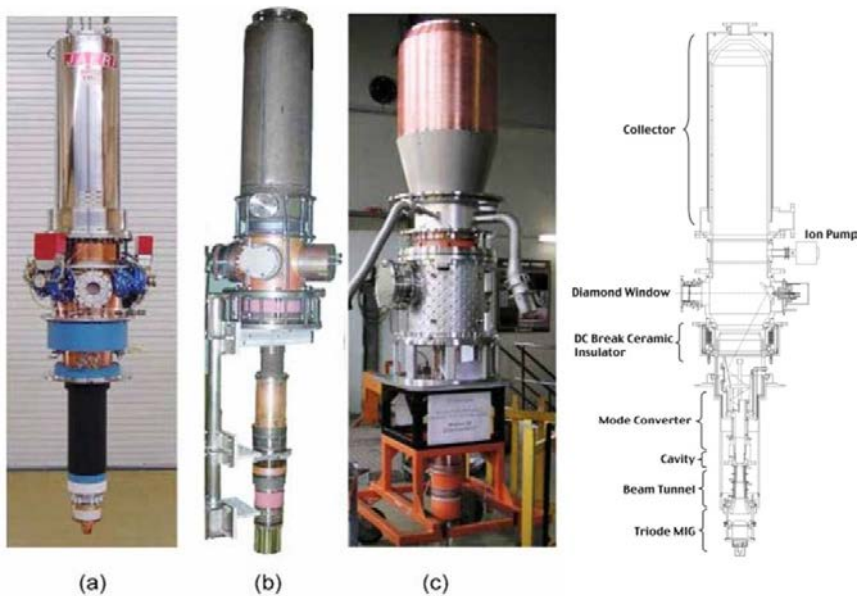


FIG. 6.85. Left: The 170 GHz gyrotrons for ITER: (a) Japan, (b) Russian Federation, and (c) EU coaxial gyrotron. The JAEA 1 MW, 170 GHz gyrotron has successfully met the ITER specifications by achieving 1 MW of output power for 800 s [6.267]. Right: A cross-sectional view of the JAEA 170 GHz gyrotron [6.271]. Reprinted from Ref. [6.267]. Copyright (2011), American Nuclear Society.

## 6.4.6. Prospects and future directions

### 6.4.6.1. Multi-megawatt gyrotrons

Multi-MW gyrotrons are attractive for heating systems that require tens of MW of power, such as the ITER ECH heating system. A major first step in

this direction has been taken by the EU team as shown in Table 6.3. The EU 2 MW gyrotron is also shown in Fig. 6.85(c). An additional incentive for the development of a 2 MW gyrotron for ITER is the possibility of expanding the power level of the ECH system from 24 MW to 48 MW in a second stage of the project. A separate effort is under way at CPI to develop a 2 MW, 95 GHz gyrotron oscillator [6.277]. The gyrotron is designed to minimize weight and size, while maximizing efficiency. The gyrotron, which is shown in Fig. 6.86, is under test. The gyrotron has a collector made of dispersion-hardened copper to permit power dissipation in a minimized volume. The design of a 4 MW, 170 GHz gyrotron has been recently developed at Forschungszentrum Karlsruhe (FZK) [6.278].



FIG. 6.86. A 2 MW, 95 GHz gyrotron at CPI. Reprinted from Ref. [6.277]. Copyright (2011) by the World Scientific Publishing Company.

#### 6.4.6.2. Frequency tuneable gyrotrons

High power gyrotrons are oscillators that are usually optimized for a single frequency of operation. Gyrotron amplifiers would have attractive features for plasma heating, such as control of power, phase and frequency, but gyrotron amplifiers have lower efficiency and lower average power capability. The ability to tune the frequency of a gyrotron over both small (tens of MHz) and large (several to tens of GHz) frequency intervals is of interest. Small frequency steps,

tens of MHz, may be used for a proposed fast switching application [6.279]. These small frequency steps, several tens of MHz, may be accomplished by voltage tuning of the gyrotron. Larger frequency steps are required when the magnetic field of the plasma is changed or the location of heating or current drive is changed. The possibility to step-tune in frequency by exciting the modes of the cavity sequentially was demonstrated in early experimental research [6.280]. A two-frequency gyrotron has been successfully developed by GYCOM for ASDEX-Upgrade with high power at the frequencies of 105 and 140 GHz. A four-frequency gyrotron is currently under development [6.281].

#### 6.4.6.3. *Improvement of gyrotron efficiency*

The required efficiency of modern gyrotrons operating with a depressed collector is in excess of 50%. The demonstration of a reliable 1 MW, 170 GHz CW gyrotron with 55% efficiency is a major advance in demonstrating high efficiency at high power [6.282]. The depressed collector is able to recover a large fraction of the axial energy of the gyrotron. The electron cyclotron maser interaction removes energy from the transverse portion of the electron beam; the parallel energy is not affected. In the non-relativistic limit, the fraction of transverse energy is simply  $(v_{\perp} / v)^2$ . For typical gyrotron beams with helicity  $\alpha = 1.3 - 1.5$ , about two thirds of the energy is in the transverse component and one third in the axial component. If the gyrotron can extract 70% of the transverse energy components and recover 90% of the axial component, an efficiency of about 75% can be achieved. In fact, a 0.8 MW, 75 GHz gyrotron has achieved 70% efficiency in 0.1 s pulsed operation [6.276]. The possible use of multi-stage depressed collectors could facilitate achievement of very high gyrotron efficiency. Since fusion requires a very high Q factor, defined as power out divided by power in, the achievement of 70% efficiency in gyrotron heating systems would provide an advantage in fusion energy development by significantly reducing the required wall plug input power for the auxiliary heating system.

#### 6.4.6.4. *Gyrotrons for DEMO*

With the completion of the ITER design and the need for rapid development of fusion energy, attention is now turning to the requirements of a demonstration fusion reactor or DEMO. Since there are several designs for a DEMO, it is premature to specify the ECH system. However, DEMO may well require a higher frequency heating system than the 170 GHz gyrotrons for ITER, possibly near 220 GHz. Basic research has shown that a gyrotron can achieve MW power levels in the 200–300 GHz frequency range [6.283]. Future development of gyrotrons operating at these higher frequencies will provide the sources needed for heating plasmas in the worldwide fusion energy programme.

REFERENCES

- [6.1] PORKOLAB, M., "Radio frequency heating of magnetically confined plasma", *Magnetic Confinement, Part B* (Edward Teller, Ed.), Academic Press, Chapter 13, (1981) 166.
- [6.2] STIX, T.H., *The Theory of Plasma Waves*, McGraw-Hill Book Co., Inc. (1962).
- [6.3] STIX, T.H., *Waves in Plasmas*, American Institute of Physics (1992).
- [6.4] BRAMBILLA, M., *Kinetic Theory of Plasma Waves, Homogeneous Plasmas*, Clarendon Press, Oxford, International Series of Monographs on Physics (1998).
- [6.5] SWANSON, D.G., *Plasma Waves*, 2nd edn., Institute of Physics Publishing, Bristol and Philadelphia (2003).
- [6.6] FISHER, R.K., GOULD, R.W., Resonance cones in the field pattern of a radio frequency probe in a warm anisotropic plasma, *Phys. Fluids* **14** (1971) 857.
- [6.7] BELLAN, P.M., PORKOLAB, M., Propagation and mode conversion of lower-hybrid waves generated by a finite source, *Phys. Fluids* **17** (1974) 1592.
- [6.8] ELDRIDGE, O., NAMKUNG, W., ENGLAND, A.C., Electron Cyclotron Heating in Tokamaks, ORNL/TM-6052, Oak Ridge Nation. Lab. (1977).
- [6.9] STEPANOV, K.N., PAKHOMOV, V.I., Magnetic Bremsstrahlung of a bounded plasma, *Zh. Eksp. Teir. Fiz.* **38** (1960) 1564; *Sov. Phys.-JETP* **11** (1960) 1126.
- [6.10] SITENKO, A.G., STEPANOV, K.N., On the oscillations of an electron plasma in a magnetic field, *Sov. Phys.-JETP* **4** (1957) 512.
- [6.11] LITVAK, A.G., PERMITIN, G.V., SUVOROV, E.V., FRAJMAN, A.A., Electron cyclotron heating of plasmas in toroidal systems, *Nucl. Fusion* **17** (1977) 659.
- [6.12] ALIKAEV, V.V., DNESTROVSKII, Yu.N., PARAIL, V.V., PEREVESEV, G.V., Perspectives for the use of electron-cyclotron waves to heat large tokamak plasmas, *Fiz. Plazmy* **3** (1977) 230; *Sov. J. Plasma Phys.* **3** (1977) 127.

- [6.13] AKHIEZER, A.I., AKHIEZER, I.A., POLOVIN, R.V., SITENKO, A.G., STEPANOV, K.N., Plasma Electrodynamics, Vol. 1, Pergamon Press, Oxford (1975).
- [6.14] PORKOLAB, M., FRIEDLAND, L., BERNSTEIN, I.B., Electron cyclotron resonance heating of plasmas in tandem mirrors, Nucl. Fusion **21** (1981), 1643.
- [6.15] ALIKAEV, V.V., AGAPOV, L.I., ARSEN'EV, Yu.I., BERLIZOV, A.B., BOBROVSKII, G.A., et al., Plasma heating in the T-10 at the second ECH harmonic, Fiz. Plazmy **9** (1983) 336; Sov. J. Plasma Phys. **9** (1983) 196.
- [6.16] ALIKAEV, V.V., PARAIL, V.V., "ECRH in T-10 tokamak", Heating in Toroidal Plasmas, Proc. 4th Int. Symp. Rome, 1984, International School of Plasma Physics and ENEA, Varenna (1984) 753.
- [6.17] ANTONSEN, T.M. Jr., MANHEIMER, W.M., Electromagnetic wave propagation in inhomogeneous plasmas, Phys. Fluids **21** (1978) 2295.
- [6.18] BORNATICI, M., Theory of electron cyclotron absorption of magnetized plasmas, Plasma Phys. **24** (1982) 629.
- [6.19] ENGLAND, A.C., ELDRIDGE, O.C., KNOWLTON, S.F., PORKOLAB, M., WILSON, J.R., Power transmission and coupling for radiofrequency heating of plasmas, Nucl. Fusion **29** (1989) 1527.
- [6.20] ARUNASALAM, V., MESERVEY, E.B., GURNEE, M.N., DAVIDSON, R.C., Absorption of a hot plasma near the second harmonic of the electron cyclotron frequency, Phys. Fluids **11** (1968) 1076.
- [6.21] TFR GROUP, "Emission and transmission measurements at the electron cyclotron frequency on TFR", Controlled Fusion and Plasma Physics, Proc. 9th Europ. Conf., Oxford, 1979, Vol. 1, Culham Laboratory, Abingdon (1979) 17.
- [6.22] McDERMOTT, F.S., et al., Wave absorption at the second harmonic of the electron-cyclotron frequency in a tokamak plasma, Phys. Fluids **28** (1985) 2625.
- [6.23] BORNATICI, M., CANO, R., DeBARBIERI, O., ENGELMANN, F., Electron cyclotron emission and absorption in fusion plasmas, Nucl. Fusion **23** (1983) 1153.
- [6.24] MYER, R.C., PORKOLAB, M., SMITH, G.R., KRITZ A.H., Electron cyclotron wave propagation and absorption in the compact ignition tokamak, Nucl. Fusion **29** (1989) 2155.

- [6.25] ANTONSEN, T.M., PORKOLAB, M., in Proc. Course, Varenna, Italy, 27 Aug – 8 Sept. 1979, Physics of Plasmas Close to Thermonuclear Conditions, Vol. I (1979), 315 (EUR FU BRU/XII/476/80).
- [6.26] BERNSTEIN, I.B., Waves in a plasma in a magnetic field, Phys. Rev. **109** (1958) 10.
- [6.27] CRAWFORD, F.W., KINO, G.S., WEISS, H.H., Excitation of cyclotron harmonic resonances in a mercury-vapor discharge, Phys. Rev. Lett. **3** (1964) 229.
- [6.28] LAQUA, P.H., Electron Bernstein wave heating and diagnostic, Plasma Phys. Control. Fusion **49** (2007) R1.
- [6.29] PORKOLAB, M., Parametric processes in magnetically confined CTR plasmas, Nucl. Fusion **18** (1978) 367.
- [6.30] PORKOLAB, M., Parametric instabilities due to lower-hybrid radio frequency heating of tokamak plasmas, Phys. Fluids **20** (1977) 2058.
- [6.31] BERGER, R.L., CHEN, L., KAW, P.K., PERKINS, F.W., Lower hybrid parametric instabilities – nonuniform pump waves and tokamak applications, Phys. Fluids **20** (1977) 1864.
- [6.32] ANDREWS, P.F., PERKINS, F.W., Scattering of lower hybrid waves by drift wave density fluctuations: Solution of the radiative transfer equation, Phys. Fluids **26** (1983) 2537.
- [6.33] GOLANT, V.E., Plasma penetration near the lower hybrid frequency, Sov. Phys. Tech. Phys. **16** (1972) 1980; Zhur. Tekh. Fiz. **41** (1971) 2492.
- [6.34] BRAMBILLA, M., Slow-wave launching at the lower hybrid frequency using a phased waveguide, Nucl. Fusion **16** (1976) 47.
- [6.35] PORKOLAB, M., “Lower hybrid heating experiments in tokamaks: An overview”, Course and Workshop on Applications of RF Waves to Tokamak Plasmas, Varenna, Italy Sept. 5 (1985) (Bernabei, S., Gaparino, U., Sindoni, E., Eds), EUR 10333 EN, **1** (1985) 288.
- [6.36] LANDAU, L.D., Vlasov equation and plasma dispersion relation, J. Phys. USSR **10** (1946) 25.
- [6.37] DAWSON, J., On Landau damping, Phys. Fluids **4** (1961) 869.
- [6.38] BELLAN, P.M., PORKOLAB, M., Experimental studies of lower hybrid wave propagation, Phys. Fluids **19** (1976) 995.

- [6.39] BRAMBILLA, M., Electron Landau damping of lower hybrid waves, Nucl. Fusion **18** (1978) 493.
- [6.40] FISCH, N.J., Confining a tokamak plasma with RF-driven currents, Phys. Rev. Letters **41** (1978) 873.
- [6.41] JACQUINOT, J., McVEY, B.D., SCHARER, J.E., Mode conversion at fast magnetosonic wave in a deuterium-hydrogen tokamak plasma, Phys. Rev. Lett. **39** (1977) 88.
- [6.42] BRAMBILLA, M., OTTAVIANI, M., Mode conversion near ion-ion hybrid and IC harmonic resonances in tokamaks, Plasma Phys. Control. Fusion **27** (1985) 1.
- [6.43] STIX, T.H., Fast-wave heating of a two-component plasma, Nucl. Fusion **15** (1975) 737.
- [6.44] PERKINS, F.W., Heating tokamaks via the ion-cyclotron and ion-ion hybrid resonances, Nucl. Fusion **17** (1977) 1197.
- [6.45] PORKOLAB, M., "RF heating and current drive in magnetically confined plasma: A historical perspective", Radiofrequency Power in Plasmas, Proc. 17th topical Conf., Clearwater, FL., 7-9 May, 2007, American Institute of Physics, **933** (2007) 3.
- [6.46] PORKOLAB, M., et al., Phase contrast imaging of waves and instabilities in high temperature magnetized plasmas, IEEE Trans. Plasma Sci. **34** (2006) 229.
- [6.47] PORKOLAB, M., "Plasma heating by fast magnetosonic waves in tokamaks", T.H. Stix Symp., Princeton, NJ, AIP Conf. Proc. **314** (1994) 99.
- [6.48] PORKOLAB, M., et al., Recent progress in ICRF physics, Plasma Phys. Control. Fusion **40** (1998) A35.
- 6.49] MOREAU, D., JACQUINOT, J., LALLIA, P.P., "Fast wave electron current drive", Proc. 13th Eur. Conf., Schliersee, 1986, Contr. Fusion and Plasma Heating, Vol. 10C (1986) 421.
- [6.50] KENNEL, C.F., ENGELMANN, F., Velocity space diffusion from weak plasma turbulence in a magnetic field, Phys. Fluids **9** (1966) 2377.
- [6.51] PINSKER, R.I. et al., Absorption of fast waves at moderate to high ion cyclotron harmonics on DIII-D, Nucl. Fusion **46** (2006) S416.

- [6.52] JAEGER, E.F., et al., Self-consistent full-wave and Fokker-Planck calculations for ion cyclotron heating in non-Maxwellian Plasmas, *Phys. Plasmas* **13** (2006) 056101.
- [6.53] CHOI, M., et al., Simulation of fast Alfvén wave interaction with beam ions over a range of cyclotron harmonics in DIII-D tokamak, *Nucl. Fusion* **46** (2006) S409.
- [6.54] BRAMBILLA, M., “Ignition with lower-hybrid heating”, *Proc. Physics of Plasmas Close to Thermonuclear Conditions, Varenna, Italy, 1979, Vol. I, CEC, Brussels* (1980) 291.
- [6.55] FISCH, N.J., Confining a tokamak plasma with RF-driven currents, *Phys. Rev. Lett.* **41** (1978) 873.
- [6.56] FISCH, N.J., Theory of RF current drive, *Rev. Mod. Phys.* **59** 175 (1987).
- [6.57] BRAGINSKII, S.I., *Reviews of Plasma Physics* (Leontovich, M.A., Ed.), Consultants Bureau, NY, Vol. I (1965) 205.
- [6.58] DREICER, H., Electron and ion runaway in a fully ionized gas, *Phys. Rev.* **115** (1959) 238.
- [6.59] KARNEY, C.F.F., FISCH, N.J., Numerical studies of current generation by radio-frequency traveling waves, *Phys. Fluids* **22** (1979) 1817.
- [6.60] FISCH, N.J., BOOZER, A.H., Creating an asymmetric plasma resistivity with waves, *Phys. Rev. Lett.* **45** (1980) 720.
- [6.61] KARNEY, C.F.F., FISCH, N.J., Efficiency of current drive by fast waves, *Phys. Fluids* **28** (1985) 116.
- [6.62] FUCHS, V., CAIRNS, R.A., SHOUCRI, M.M., HIZANIDIS, K., BERS, A., A one-dimensional model for lower-hybrid current drive including perpendicular dynamics, *Phys. Fluids* **28** (1985) 3619.
- [6.63] BONOLI, P.T., ENGLADE, R.C., Simulation model for lower-hybrid current drive, *Phys. Fluids* **29** (1986) 2937.
- [6.64] BONOLI, P.T., et al., Lower hybrid current drive experiments on Alcator C-Mod: Comparison with theory and experiment, *Phys. Plasmas* **15** (2008) 056117.
- [6.65] OHKAWA, T., Steady State Operation of Tokamaks by RF Heating, *General Atomics Report GA-A13847* (1976).
- [6.66] PRATER, R., Heating and current drive by electron cyclotron waves, *Phys. Plasmas* **11** (2004) 2349.

- [6.67] COHEN, R.H., Effect of trapped electrons on current drive, *Phys. Fluids* **30** (1987) 2442.
- [6.68] LIN-LIU, Y.R., CHAN, V.S., PRATER, R., Electron cyclotron current drive in general tokamak geometry, *Phys. Plasmas* **10** (2003) 4064.
- [6.69] ANTONSEN, T.M., CHU, K.R., Radio-frequency current generation by waves in toroidal geometry, *Phys. Fluids* **25** (1982) 1295.
- [6.70] GIRUZZI, G., Impact of electron trapping on RF current drive in tokamaks, *Nucl. Fusion* **27** (1987) 1934.
- [6.71] FISCH, N.J., KARNEY, C.F.F., Current generation with low frequency waves, *Phys. Fluids* **24** (1981) 27.
- [6.72] LANDAU, L.D., LIFSCHITZ, L.M., *The Classical Theory of Fields*, Vol. 2, Pergamon Press, New York (1974) 129–132.
- [6.73] WEINBERG, S., Eikonal method in magnetohydrodynamics, *Phys. Rev.* **126** (1962) 1899.
- [6.74] OTT, E., WERSINGER, J.M., BONOLI, P.T., Wave reflection from the lower hybrid surface: A toroidal effect, *Phys. Fluids* **22** (1979) 192.
- [6.75] BONOLI, P.T., OTT, E., Toroidal and scattering effects on lower hybrid wave propagation, *Phys. Fluids* **25** (1981) 359.
- [6.76] BARANOV, Yu.F., FEDEROV, V.I., Lower-hybrid wave propagation in tokamaks, *Nucl. Fusion* **20** (1980) 1111.
- [6.77] IGNAT, D.W., Toroidal effects on propagation, damping, and linear mode conversion of lower hybrid waves, *Phys. Fluids* **24** (1980) 1110.
- [6.78] SMIRNOV, A.P., HARVEY, R.W., Calculations of the current drive in DIII-D with the GENRAY ray tracing code, *Bull. Am. Phys. Soc.* **40** (1995) 1837; *The GENRAY Ray Tracing Code*, CompX Report CompX-2000–01 (2001).
- [6.79] BONOLI, P.T., et al., Wave-particle studies in the ion cyclotron and lower hybrid ranges of frequencies in the Alcator C-Mod tokamak, *Fusion Sci. Technol.* **51** (2007) 401.
- [6.80] HARVEY, R.W., MCCOY, M., “The CQL3D Fokker Planck Code”, *Proc. IAEA Tech. Comm. Meeting on Simulation and Modeling of Thermonuclear Plasmas*, Montreal, Canada, 1992 (USDOC NTIS Document No DE93002962).
- [6.81] VALEO, E.J., EDER, D.C., Numerical modeling of lower hybrid current drive and heating, *J. Comput. Phys.* **69** (1987) 341.

- [6.82] DEVOTO, R.S., et al., Modeling of lower hybrid current drive in self-consistent elongated tokamak equilibria, Nucl. Fusion **32** (1992) 773.
- [6.83] IGNAT, D.W., Dynamic modeling of lower hybrid current drive, Nucl. Fusion **34** (1994) 837.
- [6.84] DECKER, J., PEYSSON, Y., DKE: A Fast Numerical Solver for the 3D Drift Kinetic Equation, Report EUR-CEA-FC-1736, Euratom-CEA (2004).
- [6.85] JAEGER, E.F., et al., Advances in full-wave modeling of radio-frequency heated, multidimensional plasmas, Phys. Plasmas **9** (2002) 1873.
- [6.86] BRAMBILLA, M., Numerical simulation of ion cyclotron waves in tokamak plasmas, Plasma Phys. Control. Fusion **41** (1999) 1.
- [6.87] WRIGHT, J.C., et al., Full-wave simulations of fast wave mode conversion and lower hybrid wave propagation in tokamaks, Phys. Plasmas **11** (2004), 2473.
- [6.88] YAMAMOTO, T., MURAKAMI, S., FUKUYAMA, A., Simulation study of ICRF wave propagation and absorption in 3-D magnetic configurations, Plasma Fusion Res. **3** (2008) S1075.
- [6.89] DUMONT, R., ERIKSSON, L.-G., "Hamiltonian description of low frequency wave propagation and absorption in magnetically confined plasmas", Theory of Fusion Plasmas, Proc. Joint Varenna-Lausanne International Workshop, Varenna, Italy, 2006, Proc. of AIP Conference, Melville, NY, 871 (2006) 65.
- [6.90] VILLARD, L., APPERT, K., GRUBER, R., VACLAVIK, J., Global waves in cold plasmas, Comput. Phys. Rep. **4** (1986) 95.
- [6.91] LAMALLE, P.U., Nonlocal theoretical Generalisation and Tridimensional Numerical Study of the Coupling of an ICRH Antenna to a Tokamak Plasma, PhD thesis, Universite de Mons, 1994 and LPP-ERM/KMS Report nr. 101.
- [6.92] VAN EESTER, D., KOCH, R., A variational principle for studying fast wave mode conversion, Plasma Phys. Control. Fusion **40** (1998), 1949.
- [6.93] FUKUYAMA, A., YOKOTA, E., AKUTSU, T., "Global analysis of ICRF waves and Alfvén Eigenmodes in toroidal helical plasmas", Proc. 18th Int. Conf. on Fusion Energy 2000, Sorrento, Italy, 2000, IAEA, Vienna, CD-ROM THP2-26.

- [6.94] VDOVIN, V.L., “ICRF benchmarking modeling of ITER scenario #2”, Proc. 7th Steady State Operation ITPA Topical Group meeting, Como, Italy, May 4–6, 2005.
- [6.95] TSUJII, N., PORKOLAB, M., BONOLI, P.T., LIN, Y., WRIGHT, J.C., WUKITCH, S.J., JAEGER, E.F., HARVEY, R.W., “ICRF Mode Conversion Studies with Phase Contrast Imaging and Comparisons with Full Wave Simulations”, Proc. 19th Conf. on Radio Frequency Power in Plasmas, Newport, Rhode Island, June 1–3, 2011 (Proceedings to be published by IAP).
- [6.96] JAEGER, E.F., et al., Global wave solutions with self-consistent velocity distributions in ion cyclotron heated plasmas, Nucl. Fusion **46** (2006) S397.
- [6.97] BONOLI, P.T., et al., Evolution of non-thermal particle distributions in radiofrequency heating of fusion plasmas, J. Phys. Conf. Ser. **78** (2007) 012006
- [6.98] HELLSTEN, T., JOHNSON, T., CARLSSON, J., ERIKSSON, L.-G., HEDIN, J., LAXABACK, M., MANTSINEN, M., Effects of finite drift orbit width and RF-induced spatial transport on plasma heated by ICRH, Nucl. Fusion **44** (2004) 892.
- [6.99] CARLSSON, J., ERIKSSON, L.-G., HELLSTON, T., “FIDO, a code for calculating the velocity distribution of a toroidal plasma during ICRH”, Proc. Joint Varenna-Lausanne Workshop on Theory of Fusion Plasmas, Bologna, Bologna: Editrice Compositori (1994) 351.
- [6.100] CHOI, M., CHAN, V.S., JAEGER, E.F., GREEN, D.L., BONOLI, P., WRIGHT, J., RF SciDAC Team, Comparison of the Monte Carlo ion cyclotron heating model with the full-wave linear absorption model, Phys. Plasmas **16** (2009) 052512.
- [6.101] GREEN, D.L., CHOI, M., JAEGER, E.F., BERRY, L.A., RF-SciDAC Team, “Reconstruction in 3-D of the fast wave fields in ITER, DIII-D, C-Mod, and NSTX, including the coupling of full-wave and particle codes to resolve finite orbit effects”, Proc. 18th Topical Conf. on Radio-Frequency Power in Plasmas, Gent, Belgium, June 2009, Invited Paper I 15.
- [6.102] JAEGER, E.F., et al., Sheared poloidal flow driven by mode conversion in tokamak plasmas, Phys. Rev. Lett. **90** (2003) 155001.
- [6.103] PEREVERZEV, G., Use of the multi-dimensional WKB method to describe propagation of lower hybrid waves in tokamak plasma, Nucl. Fusion **32** (1992) 1091.

- [6.104] BERTELLI, N., A Beam Tracing Code for the Description of LH Wave Propagation in a Tokamak Plasma, PhD thesis, University of Pavia (2007) ISBN 978-8895767-04-8.
- [6.105] WRIGHT, J.C., et al., An assessment of full-wave effects on the propagation and absorption of lower hybrid waves, *Phys. Plasmas* **16** (2009) 072502.
- [6.106] MENEGHINI, O., SHIRAIWA, S., PARKER, R., Full-wave simulation of lower hybrid waves in Maxwellian plasma based on the finite element method, *Phys. Plasmas* **16** (2009) 090701.
- [6.107] STIX, T.H., PALLADINO, R.W., Observation of ion cyclotron waves, *Phys. Fluids* **3** (1960), 641.
- [6.108] HOOKE, W.M., et al., Experiments on ion cyclotron waves, *Nucl. Fusion*, Supplement Part 3 (1962) 1083.
- [6.109] ADAM, J., TFR Group, “ICRF heating in TFR at the ion-ion hybrid resonance”, Proc. 9th European Conf. on Controlled Fusion and Plasma Physics, Oxford, England, September 17–21 1979, Invited Papers A80-25771 09-75, Atomic Energy Research Establishment, Abingdon, Oxon, England, (1980) 355–369.
- [6.110] VDOVIN, V.L., SHAPOTKOVSKII, N.V., RUSANOV, V.D., “Wave generation and heating of ions at ion cyclotron frequencies in Tokamak-device TM-1-VCh”, Proc. 3rd Int. Meeting Theoret. Expt. Aspects of Heating in Toroidal Plasma, Grenoble (1976) 349.
- [6.111] TAKAHASHI, H., et al., Ion heating in ATC tokamak in the ion-cyclotron range of frequencies, *Phys. Rev. Lett.* **39** (1977) 31.
- [6.112] HOSEA, J., et al., Fast-wave heating of two-ion plasmas in the Princeton Large Torus, *Phys. Rev. Lett.* **43** (1979) 1802.
- [6.113] WILSON, R., et al., “ $T_e$  measurements using second harmonic electron cyclotron emission during high power ICRF in PLT”, Proc. AIP Conference, Callaway Gardens, CA (Swanson, D.G., Ed.) **129** (1985) 44.
- [6.114] HWANG D.Q., et al., Heating of plasma ions in a tokamak by the second-harmonic ion-cyclotron resonance interaction with radio-frequency waves, *Phys. Rev. Lett.* **51** (1983) 1865.
- [6.115] COLSTOCK, P.L., “An overview of ICRF experiments”, Wave Heating and Current Drive in Plasmas (Granatstein, V.L., Colestock, P.L., Eds) Gordon and Breach, New York (1985) 55.

- [6.116] KIMURA, H., et al., Higher harmonic ICRF heating experiments in JT-60, *Plasma Phys. Control. Fusion* **35** (1993) 845.
- [6.117] ONO, M., WURDEN, G.A., WOND, K.L., Efficient ion heating via finite-Larmor-radius ion-cyclotron waves in a plasma, *Phys. Rev. Lett.* **52** (1984) 37.
- [6.118] MOODY, J., et al., Ion-Bernstein-wave heating and improved confinement in the Alcator C tokamak, *Phys. Rev. Lett.* **60** (1988) 298.
- [6.119] MOODY, J.D., PORKOLAB, M., Power balance analysis of ion Bernstein wave heating experiments in the Alcator C tokamak, *Phys. Fluids* **B1** (1989) 1675.
- [6.120] PORKOLAB, M., Parametric instabilities in the tokamak edge plasma in the ion cyclotron heating regimes, *Fusion Eng. Des.* **12** (1990) 93.
- [6.121] PINSKER, R.I., PETTY, C.C., MAYBERRY, M.J., PORKOLAB, M., HEIDBRINK, M., Observation of parametric decay correlated with edge heating using an ion Bernstein wave antenna on DIII-D, *Nucl. Fusion* **33** (1993) 777.
- [6.122] HAWRYLUK, R.J., Results from deuterium-tritium tokamak confinement experiments, *Rev. Mod. Phys.* **70** (1998) 537.
- [6.123] JET Team, START, D.J., "Reactor relevant ICRF heating in JET- D-T plasmas", *Proc. 17th Fusion Energy Conf., Yokohama 1998*; *Nucl. Fusion* **39** (1999) 2025.
- [6.124] NOTREDAEME, J.M., Physics studies with the additional heating systems in JET, *Fusion Sci. Technol.* **53** (2008) 1103.
- [6.125] KIMURA, H., et al., "ICRF heating and TAE modes in reactor relevant JT-60U", *Proc. 16th IAEA Fusion Energy Conf., Montreal, 1996*, IAEA-CN-64/E-6, IAEA, Vienna, **3** (1997) 295.
- [6.126] NOTERDAEME, J.M., "ICRF heating results in ASDEX-Upgrade and W7-AS", *Proc. 16th IAEA Fusion Energy Conf., Montreal, 1996*, IAEA-CN-64/EP-4, IAEA Vienna, **3** (1997) 335.
- [6.127] MAJESKI, R.J., et al., Mode conversion heating and current drive experiments in TFTR, *Phys. Rev. Lett.* **76** (1996) 764.
- [6.128] BONOLI, P.T., et al., Electron heating via mode converted ion Bernstein waves in the Alcator C-Mod tokamak, *Phys. Plasmas* **4** (1997) 1774.

- [6.129] NELSON-MELBY, E., et al., Experimental observations of mode-converted ion cyclotron waves in a tokamak plasma by phase contrast imaging, *Phys. Rev. Lett.* **90** (2003) 155004.
- [6.130] MAYORAL, M.L., et al., Studies of burning plasma physics in the Joint European Torus, *Phys. Plasmas* **11** (2004) 2607.
- [6.131] PETTY, C.C., et al., Fast wave current drive in H-mode plasmas on the DIII-D tokamak, *Nucl. Fusion* **39** (1999), 1421; Fast wave and electron cyclotron current drive in DIII-D tokamak, *ibid.* **35** (1995) 773.
- [6.132] YOSHIKAWA, S., SINCLAIR, R.M., ROTHMAN, M.A., “Ion heating in the C Stellerator”, *Plasma Physics and Controlled Nuclear Fusion Research*, Vienna, 1966, Vol. II, IAEA, Vienna (1996) 925.
- [6.133] WADE, T.J., KAYE, A.S., JACQUINOT, J., Technology of the upgraded JET ICRF heating system, *Fusion Technol.*, **10, part 2B** (1986) 1398.
- [6.134] SEKI, T., et al., Steady-state amplifier at megawatt level for LHD ICRF heating, *Fusion Sci. Technol.* **40** (2001) 253.
- [6.135] <http://www.cpii.com/docs/datasheets/78/4CM2500KG%20June%202011.pdf>
- [6.136] PINSKER, R.I., Development of impedance matching technologies for ICRF antenna arrays, *Plasma Phys. Control. Fusion* **40** (1998) A215.
- [6.137] NOTERDAEME, J.M., et al., Matching to ELMy plasma in the ICRF domain, *Fusion Eng. Des.* **74** (2005) 191.
- [6.138] PINSKER, R.I., Development of next step relevant ICRF technology in the DIII-D program, *Fusion Sci. Technol.* **48** (2005) 1238.
- [6.139] MONAKOVH, I., GRAHAM, M., BLACKMAN, T., MAYORAL, M.L., “Operations of the external conjugate-T matching system for the A2 ICRH antennas at JET”, *Proc. 18th Top. Conf. RF Power in Plasmas*, Ghent, 2009, AIP Conference Proceedings 1187 (Melville, New York, 2009) 205.
- [6.140] CHAPPUIS, et al., Main design features and challenges of the ITER-like ICRF antenna for JET, *Fusion Eng. Design* **74** (2005) 223.
- [6.141] PINSKER, R.I., *Phys. Plasmas* **8** (2001) 1219.
- [6.142] KAYE, A., et al., Present and future JET ICRF antennae, *Fusion Eng. Design* **24** (1994) 1.

- [6.143] WEYNANTS, R.R., “ICRF review: From ERASMUS to ITER”, Proc. 18th Top. Conf. RF Power in Plasmas, Ghent, AIP Conference Proceedings 1187 (Melville, New York, 2009) 3.
- [6.144] BILATO, R., BRAMBILLA, M, HARTMANN, D.A., PARISOT, A., Influence of an evanescence layer in front of the antenna on the coupling efficiency of ion cyclotron waves, Nucl. Fusion **45** (2005) L5.
- [6.145] FUJII, T., et al., Performance of toroidally wide separation loop antenna for JT-60U ICRF experiments, Fusion Eng. Des. **26** (1995) 377.
- [6.146] NOTERDAEME, J.M., VAN OOST, G., The interaction between waves in the ion cyclotron range of frequencies and the plasma boundary, Plasma Phys. Control. Fusion **35** (1993) 1481.
- [6.147] MYRA, J.R., et al., Nonlinear ICRF-plasma interactions, Nucl. Fusion **46** (2006) S455.
- [6.148] ROTHMAN, M.A., SINCLAIR, R.M., YOSHIKAWA, S., ‘Non-resonant’ coupling of RF power to a plasma, J. Nucl. Energy, Part C, Plasma Physics, Accelerators, Thermonuclear Research **8** (1966) 241.
- [6.149] VAN NIEUWENHOVEN, R., et al., Comparison of the performance of ICRF antennas with and without Faraday shield on TEXTOR, Nucl. Fusion **32** (1992) 1913.
- [6.150] PINSKER, R.I., et al., “Direct electron heating with directional fast wave launch in DIII-D”, Proc. 11th Top. Conf. RF Power in Plasmas, Palm Springs, CA, 1995, AIP, NY (1996) 43.
- [6.151] NOTERDAEME, J.M., et al., “Achievement of the H-mode with a screenless ICRF antenna in ASDEX Upgrade”, Proc. 11th Top. Conf. RF Power in Plasmas, Palm Springs, CA, 1995, AIP, NY (1996) 47.
- [6.152] WUKITCH, S., et al., RF plasma edge interactions and their impact on ICRF antenna performance in Alcator C-Mod, J. Nucl. Mater. **363–365** (2007) 491.
- [6.153] MAYORAL, M.-L.I., et al., “Coupling of the JET ICRF antennas in ELMy H-mode plasma with ITER relevant plasma–straps distance”, Proc. 17th Top. Conf. RF Power in Plasmas, Clearwater, FL, 2007, AIP, NY (2007) 55.
- [6.154] PETTY, C.C., et al., Fast wave current drive in H mode plasmas on the DIII-D tokamak, Nucl. Fusion **39** (1999) 1421.

- [6.155] NIGHTINGALE, M.P.S., et al., "Overview on experiments on ITER-like antenna on JET and ICRF antenna design for ITER", Proc. 18th Top. Conf. RF Power in Plasmas, Ghent, AIP Conference Proceedings 1187 (Melville, New York, 2009) 213.
- [6.156] KNOWLTON, S.F., PORKOLAB, M., Lower hybrid wave launching antenna design, Nucl. Fusion **29** (1989) 1544.
- [6.157] PORKOLAB, M., Parametric instabilities due to lower-hybrid radio frequency heating of tokamak plasmas, Phys. Fluids **20** (1977) 2058; Parametric processes in magnetically confined CTR plasmas, Nucl. Fusion **18** (1978) 367.
- [6.158] FISCH, N.J., Theory of current drive in plasma, Rev. Mod. Phys. **59** (1987) 175.
- [6.159] YAMAMOTO, T., et al., Experimental observation of the RF-driven current by lower hybrid wave in a tokamak, Phys. Rev. Lett. **45** (1980) 716.
- [6.160] NAKAMURA, M., Toroidal plasma current sustainment by lower hybrid waves in the WT-2 tokamak, Phys. Rev. Lett. **47** (1981) 1902.
- [6.161] LUCKHARDT, S.C., et al., Generation of RF-driven currents by lower hybrid-wave injection in the Versator II tokamak, Phys. Rev. Lett. **48** (1982) 152.
- [6.162] BERNABEI, S., et al., Lower-hybrid current drive in the PLT tokamak, Phys. Rev. Lett. **49** (1982) 1255.
- [6.163] VAN HOUTTE, D., et al., "Lower hybrid heating and current drive on Petula-B", Proc. 4th Int. Symp., Heating in Toroidal Plasmas, Roma, Vol. 1 (1984) 554.
- [6.164] LEUTERER, F., et al., "Lower hybrid heating and current drive experiments in ASDEX", Proc. 10th Int. Conf., Plasma Physics and Controlled Nuclear Fusion Research, London, 1984, IAEA, Vienna, Paper F IV-3.
- [6.165] PORKOLAB, M., et al., Observation of lower-hybrid current drive at high densities in the Alcator C tokamak, Phys. Rev. Lett. **53** (1984) 450; *ibid.*, High-power electron landau heating experiments in the lower hybrid frequency range in a tokamak plasma, Phys. Rev. Lett. **53** (1984) 1229.
- [6.166] JOBES, F., et al., Formation of a 100-kA tokamak discharge in the Princeton large torus, Phys. Rev. Lett. **52** (1984) 1005.

- [6.167] LEUTERER, F., et al., Recharging of the ohmic transformer by means of lower hybrid current drive in the ASDEX tokamak, *Phys. Rev. Lett.* **55** (1985) 75.
- [6.168] De MARCO, F., “Review of current drive experiments at the lower hybrid frequency”, Course and Workshop on Applications of RF Waves to Tokamak Plasmas, Varenna, Italy Sept. 5 (1985) (Bernabei, S., Gaparino, U., Sindoni, E., Eds), EUR 10333 EN, Vol. 1 (1985) 316.
- [6.169] GORMEZANO, C., “Lower hybrid couplers”, Course and Workshop on Applications of RF Waves to Tokamak Plasmas, Varenna, Italy Sept. 5 (1985) (Bernabei, S., Gaparino, U., Sindoni, E., Eds), EUR 10333 EN, Vol. 1 (1985) 422.
- [6.170] USHIGUSA, K., Simple model to explain the temperature dependence of the lower hybrid current drive efficiency, *Plasma Phys. Control. Fusion* **38** (1996) 1825.
- [6.171] PORKOLAB, M., “RF heating and current drive in magnetically confined plasmas: a historical perspective”, Proc. 17th Topical Conference on Radio Frequency Power in Plasmas, Clearwater, FL (Ryan, P.M., Rasmussen, D.A., Eds) (2007) 3.
- [6.172] EKDAHL, A., et al., “Demonstration of ITER relevant LHCD operation large distance coupling in JET and long pulse operation in Tore-Supra”, Proc. 31st EPS Conf. on Plasma Physics, London 2004, Paper O-1.01, ECA, Vol. 28G (1971) 2492.
- [6.173] BRAMBILLA, M., Slow-wave launching at the lower hybrid frequency using a phased waveguide, *Nucl. Fusion* **16** (1976), 47.
- [6.174] PINSKER, R.I., COLESTOCK, P.L., Effect of surface modes on coupling to fast waves in the lower hybrid range of frequencies, *Nucl. Fusion* **32** (1992) 1789.
- [6.175] COLBURN, J.A., et al., “Fast wave slotted waveguide coupler on Versator II”, Proc. 7th Topical Conf. on Radio Frequency Power in Plasmas, Kissimmee, Florida, 1987, AIP Conference Proceedings **159** New York (1987) 123.
- [6.176] BRAMBILLA, M, Propagation and absorption of waves at the lower hybrid resonance, *Plasma Phys.* **18** (1976) 669.
- [6.177] PURI, S., TUTTER, M., Slow-wave coupling to the lower-hybrid resonance, *Nucl. Fusion* **14** (1974) 93.
- [6.178] LITAUDON, X., et al., Lower hybrid wave coupling in TORE-SUPRA through multi junction launchers, *Nucl. Fusion* **32** (1992) 1883.

- [6.179] MILANESIO, D., et al., “D. TOLPHA: an accurate and efficient numerical tool for analysis and design of LH antennas”, Proc. 17th Top. Conf. on RF Heating in Toroidal Plasmas, Clearwater, FL, AIP (2007) 301.
- [6.180] JACQUET, P., et al., Microwave probe diagnostic for the lower hybrid multijunction antenna on TdeV, Rev. Sci. Instrum. **68** (1997) 1176.
- [6.181] WATTERSON, R., et al., Spectrum and propagation of lower hybrid waves in a tokamak plasma, Phys. Fluids **28** (1985) 2622.
- [6.182] PERICOLI, V., et al., LHCD and coupling experiments with an ITER-like PAM launcher on the FTU tokamak, Nucl. Fusion **45** (2005) 1085.
- [6.183] ENGLAND, A.C, ELDRIDGE, O.C., KNOWLTON, S.F., PORKOLAB, M., WILSON, J.R., Power transmission and coupling for radiofrequency heating of plasmas, Nucl. Fusion **29** (1989) 1527.
- [6.184] GORMEZANO, C., et al., Lower-hybrid plasma heating via a new launcher – the multijunction grill, Nucl. Fusion **25** (1985) 419.
- [6.185] KAYE, A.S., et al., “The design of the JET lower hybrid antenna”, Proc. 15th Symp. on Fusion Technol., Rome, 1988, Fusion Technology 1998 (SOFT) Vol. 1 (1998) 449.
- [6.186] FROISSARD, F., et al., “Long pulse performance with the LHCD system on Tore-Supra”, Proc. 12th Conf. on RF Heating in Toroidal Plasmas Savannah (1997) 129.
- [6.187] SEKI, M., et al., Development and operation of the lower hybrid range of frequency system on JT-60U, Fusion Sci. Technol. **42** (2002) 452.
- [6.188] BERNABEI, S., et al., Design of a compact lower hybrid coupler for Alcator C-Mod, Fusion Sci. Technol. **43** (2003) 145.
- [6.189] PARKER, R., et al., “Modification of current profile, toroidal rotation and pedestal by lower hybrid waves in Alcator C-Mod”, Proc. 18th Topical Conf. on Radio Frequency Power in Plasmas, 24 June 2009, Gent, Belgium, AIP Conference Proceedings 1187, Melville, New York (2009) 319.
- [6.190] BIBET, P., et al., Overview of the ITER-FEAT LH system, Fusion Eng. Des. **66–68** (2003) 525.
- [6.191] BELO, J.H., ITER – like PAM launcher for Tore-Supra’s LHCD system, Fusion Eng. Des. **74** (3005) 283.

- [6.192] ERCKMANN, V., GASPARINO, U., Electron cyclotron resonance heating and current drive in toroidal fusion plasmas, *Plasma Phys. Control. Fusion* **36** (1994) 1869.
- [6.193] LUCE, T., Applications of high-power millimeter waves in fusion energy research, *IEEE Trans. Plasma Sci.* **30** (2002) 734.
- [6.194] KRITZ, A.H., HSUAN, H., GOLDFINGER, R.C., BATCHELOR, D.B., in Proc. 3rd Int. Symp. on Heating in Toroidal Plasmas, Grenoble, Italy, 1982, ECE, Brussels, Vol. 2 (1982) 707.
- [6.195] SMIRNOV, A.P., HARVEY, R.W., PRATER, R., “General linear RF-current drive calculation in toroidal plasma”, Proc. 15th Joint Workshop on Electron Cyclotron Emission and Electron Cyclotron Resonance Heating, Yosemite National Park, 2008, World Scientific, Singapore (2009) 301.
- [6.196] POLI, E., PEREVERZEV, G.V., PEETERS, A.G., TORBEAM, a beam tracing code for electron cyclotron waves in tokamak plasmas, *Phys. Plasmas* **6** (1999) 5.
- [6.197] FARINA, D., A quasi-optical beam tracing code for electron cyclotron absorption and current drive: GRAY, *Fusion Sci. Technol.* **52** (2007) 154.
- [6.198] MARUSHCHENKO, N.B., MAASSBERG, H., TURKIN, Y., Electron cyclotron current drive calculated for ITER conditions using different models, *Nucl. Fusion* **48** (2008) 054002.
- [6.199] VDOVIN, V., “Role of upper hybrid resonance and diffraction effects at electron cyclotron heating in tokamaks”, Proc. 14th Joint Workshop on Electron Cyclotron Emission and Electron Cyclotron Resonance Heating, Santorini, Greece 2006, Heliotopos Conferences Ltd., Athens (2006) 323.
- [6.200] PRATER, R., et al., Benchmarking of codes for electron cyclotron heating and electron cyclotron current drive under ITER conditions, *Nucl. Fusion* **48** (2008), 035006.
- [6.201] MAZZUCATO, E., FIDONE, I., GRANATA, G., Damping of electron cyclotron waves in dense plasmas of a compact ignition tokamak, *Phys. Fluids* **30** (1987) 3745.

- [6.202] WESTERHOF, E., “Fokker-Planck quasi-linear codes for the study of electron cyclotron resonance heating and electron cyclotron current drive”, Proc. 9th Joint Workshop on Electron Cyclotron Emission and Electron Cyclotron Heating, Borrego Springs, California, 1995, World Scientific, Singapore (1995) 3.
- [6.203] HARVEY, R.W., McCOY, M.G., “The CQL3D Fokker-Planck code”, Proc. IAEA TCM on Advances in Simulating and Modeling of Thermonuclear Plasmas, Montreal, Canada, 1992, IAEA, Vienna (1992) 527.
- [6.204] MARUSHCHENKO, N.B., MAASSBERG, H., TURKIN, YU., Electron cyclotron current drive calculated for ITER conditions using different models, Nucl. Fusion **48** (2008) 054002.
- [6.205] MARUSHCHENKO, N.B., BEIDLER, C.D., MAASSBERG, H., “Current drive calculations with an advanced adjoint approach”, Proc. 15th Joint Workshop on Electron Cyclotron Emission and Electron Cyclotron Resonance Heating, Yosemite National Park, California, 2008, World Scientific, Singapore (2009) 295.
- [6.206] KIROV, K.K., LEUTERER, F., PEREVERZEV, G.V., RYTER, F., SUTTROP, W., ECRH power deposition studies in ASDEX Upgrade, Plasma Phys. Control. Fusion **44** (2002) 2583.
- [6.207] SUZUKI, T., et al., Heating and current drive by electron cyclotron waves in JT-60U, Nucl. Fusion **44** (2004) 876.
- [6.208] SHIMOZUMA, T., et al., Formation of electron internal transport barriers by highly localized electron cyclotron resonance heating in the large helical device, Plasma Phys. Control. Fusion **45** (2003) 1183.
- [6.209] LLOYD, B., Plasma Phys. Control. Fusion **40** (1998) A119.
- [6.210] POCHELON, A., et al., “Physics studies with ECH/CD in the TCV tokamak”, Proc. 15th Topical Conference on Radio frequency Power in Plasmas, Moran, Wyoming, 2003; AIP, New York (2003) 297.
- [6.211] ALBERTI, S., ARNOUX G., PORTE L., BORTOLON A., KARPUSHOV A., MARTIN Y., NOWAK S., PITTS R., Third-harmonic X-mode, real-time controlled top-launch ECW experiments on TCV Tokamak, J. Phys. Conf. Series **25** (2005) 210–222.
- [6.212] ARNOUX, G., et al., “Third harmonic X-mode ECH top-launch on the TCV tokamak”, Proc. 16th Topical Conference on Radio Frequency Power in Plasmas, Park City, Utah, 2005; AIP, New York (2005) 387.

- [6.213] PREINHAELTER, J., KOPECKY, V.J., Penetration of high-frequency waves into a weakly inhomogeneous magnetized plasma at oblique incidence and their transformation to Bernstein modes, *J. Plasma Phys.* **10** (1973) 1.
- [6.214] LAQUA, H.P., ERCKMANN, V., HARTFUSS, H.J., LAQUA, H., W7-AS TEAM, Resonant and nonresonant electron cyclotron heating at densities above the plasma cut-off by O-X-B mode conversion at the W7-As stellarator, *Phys. Rev. Lett.* **78** (1997) 3467.
- [6.215] SHEVCHENKO, V., et al., "EBW heating experiments in MAST", Proc. 14th Joint Workshop on Electron Cyclotron Emission and Electron Cyclotron Resonance Heating, Santorini, Greece 2006; Heliotopos Conferences Ltd., Athens (2006) 54.
- [6.216] LAQUA, H.P., *Plasma Phys. Control. Fusion* **49** (2007) R1.
- [6.217] CODA, S. ALBERTI, S., BLANCHARD, P., GOODMAN, T.P., HENDERSON, M.A., et al., "Electron cyclotron current drive and suprathermal electron dynamics in the TCV tokamak", Proc. 19th Conf. Fusion Energy, Lyon, France, IAEA, Vienna (2002) paper EX/W-5.
- [6.218] ERCKMANN, V., et al., *Fusion Eng. Design* **53** (2001) 365.
- [6.219] FOREST, C.B., et al., Determination of the noninductive current profile in tokamak plasmas, *Phys. Rev. Lett.* **73** (1994) 2444.
- [6.220] PETTY, C.C., et al., Detailed measurements of the electron cyclotron current drive efficiency on DIII-D, *Nucl. Fusion* **42** (2002) 1366.
- [6.221] HARVEY, R.W., McCOY, M.G., KERBEL, G.D., Power dependence of electron-cyclotron current drive of low- and high-field absorption in tokamaks, *Phys. Rev. Lett.* **62** (1989) 426.
- [6.222] GEIGER, J., LAQUA, H.P., MAASSBERG, H., MARUSHCHENKO, N.B., WENDLAND, C., et al., "High power ECCD experiments at W7-AS", Proc. 18th IAEA Fusion Energy Conference, Sorrento, Italy, 2000; IAEA, Vienna (2000) paperEXP4/04;  
<http://www.iaea.org/programmes/ripc/physics/fec2000/html/node174.htm>.
- [6.223] HARVEY, R.W., SAUTER, O., PRATER, R., NIKKOLA, P., Radial transport and electron-cyclotron-current drive in the TCV and DIII-D tokamaks, *Phys. Rev. Lett.* **88** (2002) 205001
- [6.224] EHST, D.A., KARNEY, C.F.F., Approximate formula for radio-frequency current drive efficiency with magnetic trapping, *Nucl. Fusion* **31** (1991) 1933.

- [6.225] MURAKAMI, M., et al., Modification of the current profile in high-performance plasmas using off-axis electron-cyclotron-current drive in DIII-D, *Phys. Rev. Lett.* **90** (2003) 255001.
- [6.226] LENNHOLM, M., ERIKSSON, L.-G., TURCO, F., BOURQUEY, F., DARBOS, C., “Real time control of the sawtooth period on Tore-Supra using variable ECCD injection angles”, *Proc. 15th Joint Workshop on Electron Cyclotron Emission and Electron Cyclotron Resonance Heating*, Yosemite National Park, 2008, World Scientific, Singapore (2009) 74.
- [6.227] ZOHN, H., GANTENBEIN, G., LEUTERER, F., MARASCHEK, M., POLI, E., et al., Control of NTMs by ECCD on ASDEX Upgrade in view of ITER application, *Plasma Phys. Control. Fusion* **49** (2007) B341.
- [6.228] PRATER, R., LA HAYE, R.J., LUCE, T.C., PETTY, C.C., STRAIT, E.J., Stabilization and prevention of the 2/1 neoclassical tearing mode for improved performance in DIII-D, *Nucl. Fusion* **47** (2007) 371.
- [6.229] DOANE, J.L., Design of circular corrugated waveguides to transmit millimeter waves at ITER, *Fusion Sci. Technol.* **53** (2008) 159.
- [6.230] THUMM, M., KASPAREK, W., Passive high-power microwave components, *IEEE Trans. Plasma Sci.* **30** (2002) 755.
- [6.231] DOANE, J.L., OLSTAD, R.A., Transmission line technology for electron cyclotron heating, *Fusion Sci. Tech.* **53** (2008) 39.
- [6.232] NAGASAKI, K., ISAYAMA, A., EJIRI, A., Application of a grating polarizer to the 106.4 GHz ECH system on Heliotron-E, *Rev. Sci. Instrum.* **66** (1995) 3432.
- [6.233] IKEDA, Y., SEKI, M., MORIYAMA, S., KAJIWARA, K., ANNO, K., “Recent progress in the 110 GHz ECRF system on the JT-60U tokamak”, *Proc. 15th Joint Workshop on Electron Cyclotron Emission and Electron Cyclotron Resonance Heating*, Aix-en-Provence, 2003, World Scientific, Singapore (2003) 475.
- [6.234] ERCKMANN, V., et al., Electron cyclotron heating for W7-X: physics and technology, *Fusion Sci. Technol.* **52** (2007) 291.
- [6.235] ELLIS, R., HOSEA, J., WILSON, J., PRATER, R., CALLIS, R., “Design of a dual high-power, long pulse, steerable ECH launcher for DIII-D”, *Proc. 14th Topical Conf. on Radio Frequency Power in Plasmas*, Oxnard, California, 2001, AIP, Melville, New York (2001) 318.

- [6.236] PRATER, R., et al., “A design study for the ECH launcher for ITER”, Proc. 10th Joint Workshop on Electron Cyclotron Emission and Electron Cyclotron Resonance Heating, Ameland, The Netherlands, 1997; World Scientific, Singapore (1997) 531.
- [6.237] GANTENBEIN, G., et al., “High-power tests of a remote steering launcher mock-up at 140 GHz”, Proc. 13th Joint Workshop on Electron Cyclotron Emission and Electron Cyclotron Resonance Heating, Nizhny Novgorod, 2005, Institute of Applied Physics, Russian Academy of Sciences, Nizhny Novgorod (2005) 310.
- [6.238] HENDERSON, M.A., et al., “Synergy study of the equatorial and upper port ITER ECH launchers for an enhanced physics performance”, Proc. 14th Joint Workshop on Electron Cyclotron Emission and Electron Cyclotron Resonance Heating, Santorini, Greece 2006, Heliotopos Conferences Ltd., Athens (2006) 460.
- [6.239] NUSINOVICH, G.S., Introduction to the Physics of Gyrotrons, The Johns Hopkins University Press (2004).
- [6.240] KARTIKEYAN, M.V., BORIE, E., THUMM, M.K.A., Gyrotrons, High Power Microwave and Millimeter Wave Technology, Springer (2004).
- [6.241] BARKER, R.J., BOOSKE, J.H., LUHMANN, N.C., NUSINOVICH, G.S., Modern Microwave and Millimeter-Wave Power Electronics, IEEE Press (2005).
- [6.242] EDGCOMBE, C.J., Gyrotron Oscillators Their Principles and Practice, Taylor and Francis (1993).
- [6.243] TSIMRING, S.E. Electron Beams and Vacuum Microwave Electronics, Wiley Interscience (20[6.244] BARKER, R.J., SCHAMILOGLU, E., High-Power Microwave Sources and Technologies, IEEE Press (2001).
- [6.245] FELCH, K.L., DANLY, B.G., JORY, H.R., KREISCHER, K.E., LAWSON, W., LEVUSH, B. TEMKIN, R.J., Characteristics and applications of fast-wave gyrodevices, Proc. IEEE **87** (1999) 752–781.
- [6.246] GRANATSTEIN, V.L., PARKER, R.K., ARMSTRONG, C.M., Vacuum electronics at the dawn of the twenty-first century, Proc. IEEE **87** (1999) 702–716.
- [6.247] TWISS, R.D., Aust. J. Phys. **11** (1958) 564.
- [6.248] SCHNEIDER, J., Phys. Rev. Lett. **2** (1959) 504.
- [6.249] PANTELL, R.H., Proc. IRE **47** (1959) 1146.

- [6.250] GAPONOV, A.V., *Izv. VUZ Radiofizika* **2** (1959) 836.
- [6.251] HIRSHFIELD, J.L., WACHTEL, J.M., Electron cyclotron maser, *Phys. Rev. Lett.* **12** (1964) 533–536.
- [6.252] FLYAGIN, V.A., GAPONOV, A.V., PETELIN, M.I., et al., Gyrotron, *IEEE Trans. Microwave Theory Tech.* **25** (1977) 514–521.
- [6.253] FELCH, K., et al., Long-pulse and CW tests of a 110-GHz gyrotron with an internal, quasi-optical converter, *IEEE Trans. Plasma Sci.* **24**, Issue 3 (1996) 558–569
- [6.254] CHOI, E.M., SHAPIRO, M.A., SIRIGIRI, J.R., TEMKIN, R.J., Experimental observation of the effect of after-cavity interaction in a depressed collector gyrotron oscillator, *Phys. Plasmas* **14** (2007) 093302.
- [6.255] CHOI, E.M., et al., Efficiency enhancement of a 1.5 MW 110-GHz gyrotron with a single-stage depressed collector, *Fusion Sci. Technol.* **52** (2007) 334–339.
- [6.256] CHOI, E.M., et al., Experimental results for a 1.5 MW, 110 GHz gyrotron oscillator with reduced mode competition, *Phys. Plasmas* **13** (2006) 023103.
- [6.257] ANDERSON, J.P., et al., Studies of the 1.5-MW 110-GHz gyrotron experiment, *IEEE Trans. Plasma Sci.* **32** (2004) 877–883.
- [6.258] CHOI, E.M., Experimental Study of a High Efficiency Gyrotron Oscillator, PhD thesis, Dept. of Physics, MIT (2007).
- [6.259] ANDERSON, J.P., Experimental Study of a 1.5-MW, 110-GHz Gyrotron Oscillator, PhD thesis, Dept. of Elec. Eng. and Computer Sci., MIT (2005).
- [6.260] NUSINOVICH, G.S., ERM, R.E., Efficiency of a CRM MONOTRON with a Gaussian longitudinal distribution of high frequency fields, *Elektron. Tekh., Ser. 1, Elektron. SVCh* (1972) 55.
- [6.261] DANLY, B.G., TEMKIN, R.J., Generalized nonlinear harmonic gyrotron theory, *Phys. Fluids*, **29** (1986) 561–567.
- [6.262] BOTTON, M., ANTONSEN, T.M., LEVUSH, B., et al., MAGY: A time-dependent code for simulation of slow and fast microwave sources, *IEEE Trans. Plasma Sci.* **26** (1998) 882–892.
- [6.263] ANDERSON, J.P., et al., *IEEE Trans. Plasma Sci.* **30** 6 (2002) 2117–2123.

- [6.264] DENISOV, G.G., KUFTIN, A.N., MALYGIN, V.I., et al., 110 GHz Gyrotron with a built-in high-efficiency converter, *Int. J. Electron.* **72** (1992) 1079–1091.
- [6.265] NEILSON, J.M., Optimal synthesis of quasi-optical launchers for high-power gyrotrons, *IEEE Trans. Plasma Sci.* **34** (2006) 635–641.
- [6.266] SAKAMOTO, K., TSUNEOKA, M., KASUGAI, A., Major improvement of gyrotron efficiency with beam energy recovery, *Phys. Rev. Lett.* **73** (1994) 3532–3535.
- [6.267] SAKAMOTO, K., Progress of high-power-gyrotron development for fusion research, *Fusion Sci. Technol.* **52** (2007) 145–153.
- [6.268] CENGHER, M., et al., in *Proc. 15th Joint Workshop on ECE and ECRH (EC-15)*, World Scientific (2009) 483–489.
- [6.269] THUMM, M.K., KASPAREK, W., Passive high-power microwave components, *IEEE Trans. Plasma Sci.* **30** (2002) 755–786.
- [6.270] FELCH, K., et al., Operating experience on six 110 GHz, 1 MW gyrotrons for ECH applications, *Nucl. Fusion* **48** (2008) 054008.
- [6.271] MORIYAMA, S., et al., Steady-state operation of 170 GHz – 1 MW gyrotron for ITER, *Nucl. Fusion* **49** (2009) 085001.
- [6.272] LOHR, J., et al., The electron cyclotron resonant heating system on the DIII-D tokamak, *Fusion Sci. Technol.* **48**, 2 (2005) 1226–1237.
- [6.273] CIRANT, S., et al., Summary of the 4th IAEA Technical Meeting on ECRH Physics and Technology for ITER, *Nucl. Fusion* **48** (2008) 054001.
- [6.274] GANTENBEIN, G., et al., “The 140 GHz, 1 MW gyrotron – status and recent results”, *Proc. 15th Joint Workshop on ECE and ECRH (EC-15)*, World Scientific (2009) 529–534.
- [6.275] KREISCHER, K.E., et al., High power operation of a 170 GHz megawatt gyrotron, *Phys. Plasmas* **4** (1997) 1907–1914.
- [6.276] DENISOV, G.G., Development in Russia of high-power gyrotrons for fusion, *Nucl. Fusion* **48** (2008) 054007.
- [6.277] FELCH, K. et al., “Progress in increasing gyrotron output power beyond 1 MW”, *Proc. 15th Joint Workshop on ECE and ECRH (EC-15)*, World Scientific (2009) 422–426.

- [6.278] BERINGER, M.H., et al., “Towards a 4 MW, 170 GHz coaxial gyrotron resonator design”, Proc. 33rd Int. Conf. IR and MM Waves and THz Electron., IEEE Press. (2008) 466557.
- [6.279] ERCKMANN, V., et al., Power combination of two 140 GHz gyrotrons and fast switching of the combined beam, Fusion Sci. Technol. **55** (2009) 23.
- [6.280] KREISCHER, K.E., TEMKIN, R.J., Single mode operation of a high-power, step-tunable gyrotron, Phys. Rev. Lett. **59** (1987) 547–550.
- [6.281] WAGNER, D., et al., Progress and first results with the new multifrequency ECRH system for ASDEX upgrade, IEEE Trans. Plasma Sci. **37** (2009) 395–402.
- [6.282] SAKAMOTO, K., et al., Achievement of robust high-efficiency 1 MW oscillation in the hard-self-excitation region by a 170 GHz continuous-wave gyrotron, Nature Phys. **3** (2007) 411–414.
- [6.283] GRIMM, T., et al., Experimental study of a high frequency megawatt gyrotron oscillator, Phys. Fluids B. **2** (1990) 640–646.

# CHAPTER 7

## PLASMA–WALL INTERACTIONS

**J. Li**

Institute of Plasma Physics,  
Chinese Academy of Sciences,  
China

**H.Y. Guo**

Tri Alpha Energy, USA, and  
Institute of Plasma Physics,  
Chinese Academy of Sciences,  
China

**G.M. McCracken**

Culham Science Centre,  
UKAEA, Abingdon,  
United Kingdom

**J.L. Chen**

Institute of Plasma Physics,  
Chinese Academy of Sciences,  
China

### 7.1. INTRODUCTION

The problem of impurities in fusion plasmas has been recognized since the beginning of the fusion programme. Early experiments in glass vacuum vessels released gas from the wall to such an extent that the radiation from the impurities prevented the plasma from being heated above about 50 eV. The radiative power loss is principally due to line radiation from partially stripped ions, which is particularly a problem during the plasma startup phase. Another problem is fuel dilution, which arises because impurity atoms produce many electrons and, for a given plasma pressure, these electrons take the place of fuel particles. Impurities can also lead to disruptions, as a result of edge cooling and consequent current profile modification. The fractional impurity level which radiates 10% of the total thermonuclear power for a 10 keV plasma is 50% for helium, 7% for carbon, and less than 0.1% for molybdenum. Clearly, impurities of low atomic number are a much less serious problem than those of high atomic number.

Impurities originate either from the material surfaces facing the plasma due to a variety of plasma–surface interactions or from fusion reactions in a reactor,

i.e. helium ash. In addition, “external” impurities, such as Ne and Ar, may be used as an active means to control radiation. The impurities most easily released are those adsorbed on the surfaces with low binding energies, for example, water and carbon monoxide molecules. There are also bulk impurities in the solid materials, such as carbon, chlorine and sulphur, which can migrate to the surface. These species may be desorbed thermally or by the impact of ions, atoms, electrons or photons. They can normally be removed from the system by baking the vacuum vessel, or by cleaning with glow discharges (see Section 7.4.1.1). It is also possible for the wall material to be introduced into the plasma by such processes as sputtering, arcing and evaporation. Sputtering is a momentum transfer process which releases atoms when energetic ions, either hydrogen or impurities, strike solid surfaces. The walls can also be sputtered by neutrals arising from resonant charge exchange between hot ions in the plasma with cold neutrals. Arcing can occur between the plasma and the wall or limiter, driven by the sheath potential. Evaporation occurs when the power load is sufficient to heat the surfaces to temperatures near their melting point.

The impurities introduced from vacuum vessel containers were apparent in the earliest attempts to confine plasmas with magnetic and electric fields during the late 1940s and 1950s. One of the first papers to discuss some of these problems was presented at the 2nd “Atoms for Peace” conference in Geneva 50 years ago [7.1]. This was mainly concerned with arcing between the plasma and the vessel walls in the plasma boundary.

The problems of plasma-wall interaction were of two kinds: the contamination of the plasma preventing suitable conditions for fusion to take place, and damage to the components of the containment vessel leading to possible component failure. However, desorption of light impurities, such as carbon and oxygen, was the most serious problem in early experiments [7.2]. The Soviet tokamaks of the 1960s showed the importance of thorough baking and discharge cleaning of the vacuum vessel to reduce low  $Z$  impurities. They termed this process “training”, and it was largely due to their techniques that the first high temperature plasmas in tokamaks with good confinement were achieved.

The question of the protection of the containment vessel was initially solved by the use of mechanical limiters. Although a variety of geometries were used, they were frequently diaphragms with a central hole located at one or more points toroidally round the vessel. For magnetically confined plasma, the limiter is the first point of contact with a solid surface with the plasma which diffuses across field lines. It therefore protects the wall from structural damage by the plasma, particularly by disruptions, runaway electrons and other instabilities. It must therefore be able to withstand large thermal fluxes without melting or cracking. This led to the use of refractory metals such as molybdenum and tungsten.

The limiter has a further function, that by concentrating the plasma-surface interaction, the surface-adsorbed species are quickly removed and the plasma

impurity is improved. It was shown that the oxygen level decreased as the limiter to wall distance was increased. However, when the first neutral beam heating commenced on the PLT tokamak at Princeton, it was discovered that the resulting high edge temperatures led to an intolerable tungsten level [7.3]. Replacement of the tungsten with graphite resulted in a marked improvement in plasma performance and graphite became the material of choice in tokamaks for many years. It is now realized that in order to keep below the sputtering threshold, high Z materials can only be used with very low plasma edge temperatures, i.e. generally with high densities.

Subsequently, in the 1970s other wall conditioning treatments, such as gettering with titanium [7.4], zirconium, aluminium and chromium, were developed, which removed the light impurities chemically. Further developments of wall conditioning techniques were the processes of depositing a clean layer on to the wall by techniques known as carbonization and boronization. These involved the thermal or discharge induced decomposition of a carbon or boron molecule, to leave a fresh layer of carbon or boron surface on the walls.

A different approach to the problem of impurity control was the development of divertors. This involved diverting field lines outside the last closed flux surface to a target which was remote from the confined plasma. Divertors were an inherent part of the stellarator designs developed at Princeton by Spitzer during the 1950s [7.5]. Early experiments in the Japanese tokamak DIVA in the 1970s showed encouraging results [7.6] and later the poloidal divertor was further developed in the larger ASDEX and PDX tokamak devices. The poloidal field null is usually produced above or below the centre line of the plasma, so that the field lines are diverted onto a toroidally symmetric target.

In principle, these techniques were effective and plasmas with lower impurity levels were obtained. Moreover, critically for the fusion programme, the so called H-mode was first discovered on ASDEX in 1982 [7.7]. However, as power densities increased the divertor geometry resulted in very high power densities being deposited on the divertor target. Unplanned instabilities such as disruptions, rapid vertical displacement events (VDEs) and ELMs also caused serious threats to the vessel components. These problems are still a major consideration in current and future fusion machines.

## 7.2. BASIC PHYSICAL PROCESSES AND UNDERLYING THEORY

### 7.2.1. Basic concepts

#### 7.2.1.1. Boundary layer

In magnetic confinement devices the plasma is confined within closed magnetic flux surfaces, normally generated by a combination of fields due

to external conductors and by currents flowing in the plasma. Such fields can only be generated within a restricted volume, and there is therefore a boundary determined by the last closed flux surface (LCFS). The shape of the LCFS is determined by the magnetic fields. However, closed magnetic surfaces may be interrupted by a solid surface which then determines the position of the LCFS. Such a solid surface is called a limiter. Alternatively the closed surface may be determined entirely by the magnetic fields so that outside the LCFS, the plasma flows towards and eventually interacts with a solid surface. This is the basic geometry of a divertor. The two situations are compared in Fig. 7.1.

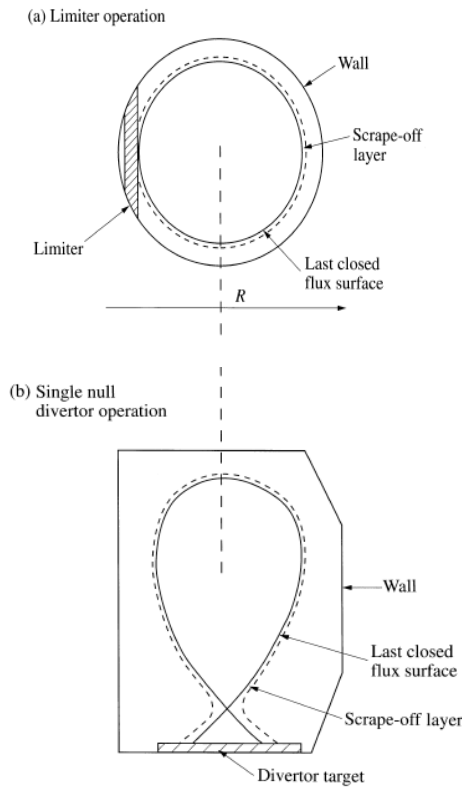


FIG. 7.1. Schematic diagram of poloidal flux surfaces in a tokamak (a) with a limiter and (b) with a divertor. The toroidal magnetic field is normal to the page.

The essential difference between the two is that with a limiter the LCFS is in contact with a solid surface, while with a divertor the solid surface is removed some distance from the LCFS, thus reducing the flux of impurities or recycling particles which get directly back inside the LCFS. The region outside the LCFS is known as the scrape-off layer (SOL). In this region the perpendicular flow across the magnetic field is balanced by parallel flow along the open field lines towards

the limiter or divertor target plate. The cross-field transport for both power and particles across the field is generally ‘anomalous’, being higher than predicted by neoclassical theory.

### 7.2.1.2. The plasma sheath

The sheath represents a thin plasma layer, about a few Debye lengths,  $\lambda_D$ , attached to the limiter or divertor target surface, providing shielding for the plasma. Because the electron thermal velocity is much larger than that of ions, an electric field is set up near the target surface to retard electrons and accelerate ions, so that both electrons and ions reach the ion sound speed at the sheath edge, i.e.  $v_{se} = c_s$ , with  $c_s = [(T_i + T_e) / m_i]^{1/2}$ . Note that temperature is always in [eV] unless stated differently.

The electric potential variation between the target surface and the sheath edge, i.e. the plasma–sheath interface or the floating potential, is

$$V_f = \frac{1}{2} \frac{T_e}{e} \ln \left[ \frac{2\pi}{(1-\delta)^2} \left( \frac{m_e}{m_i} \right) \left( 1 + \frac{T_i}{T_e} \right) \right] \quad (7.1)$$

as determined by the requirement that the total current to the target surface be zero.  $\delta$  is the total secondary electron emission coefficient due to ions and electrons. For a deuterium plasma with  $T_i = T_e$  and  $\delta = 0$ ,  $V_f \approx -3T_e / e$ . Figure 7.2 shows the spatial variation of electric potential, ion velocity and the ion and electron densities.

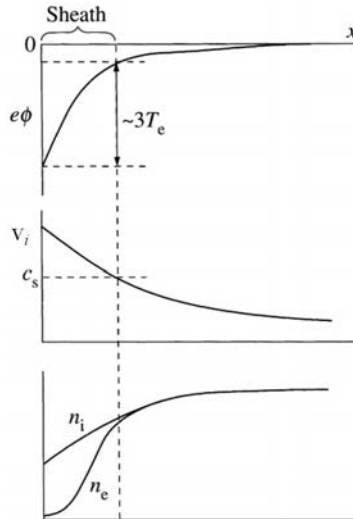


FIG. 7.2. Typical spatial variation of the electric potential, ion velocity and the ion and electron densities across the plasma sheath [7.8].

The energy of the plasma ions reaching the surface is determined by their thermal energy and the sheath potential through which they fall, given by Eq. (7.1). The ions are accelerated by the sheath, and when they reach the surface their energy distribution is very approximately an accelerated and truncated Maxwellian distribution. The electrons are decelerated by the sheath, their distribution remaining Maxwellian, but with a reduced density. The energy transported to a surface by a Maxwellian distribution of ions or electrons is  $2T$  per particle. Adding the energy due to the acceleration of ions in the sheath, the power flux to the surface  $q_{\parallel}$  is given by

$$q_{\parallel} \approx \gamma_{sh} \Gamma T_e \tag{7.2}$$

where  $\Gamma = n_{se} c_s$  is the incident particle flux, with  $n_{se}$  being the electron density at sheath edge, and  $\gamma_{sh}$  is the sheath heat transmission factor

$$\gamma_{sh} \approx \left( \frac{2T_i}{T_e} + \frac{2}{1-\delta} - \frac{eV_f}{T_e} \right) \tag{7.3}$$

taking into account the additional energy gained by ions due to acceleration in the sheath.  $\gamma_{sh} \approx 6.5$  with  $T_i = T_e$ , neglecting the secondary electron emission.

In practice the secondary electron emission coefficient  $\delta$  is often close to unity and the sheath heat transmission coefficient  $\gamma_{sh}$  can be significantly enhanced. Thus there is a large uncertainty in the sheath heat transmission coefficient, although the *effective* value of  $\delta$  cannot exceed 0.8 because of space charge effects.

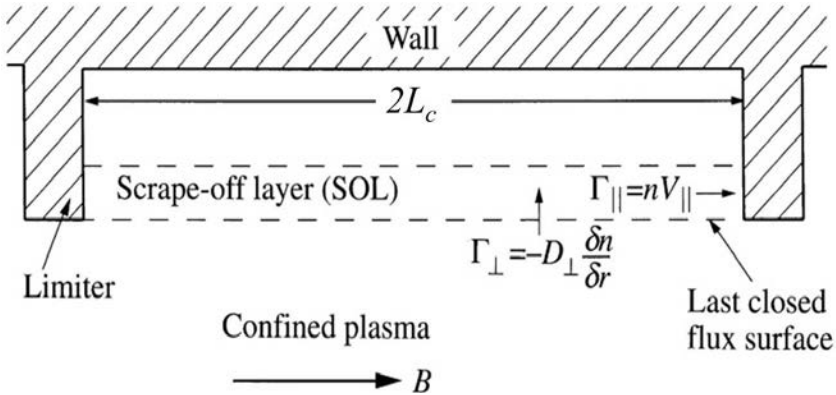


FIG. 7.3. Schematic diagram of the plasma flow from the confined plasma into the SOL by cross-field diffusion and along the field in the SOL to the limiters or divertor target [7.8]. Here,  $v_{\parallel}$  and  $\Gamma_{\parallel}$  represent the parallel particle flow and flux density along magnetic field lines, respectively, and  $\Gamma_{\perp}$  the particle flux density across the field lines.

### 7.2.1.3. The scrape-off layer

In the simple scrape-off layer (SOL) without other sources or sinks (such as ionization), the loss along the field from any given flux tube is balanced by the net flow across the field into the flux tube in steady state. These flows are illustrated schematically in Fig. 7.3.

If we assume that cross-field transport is diffusive, we can write

$$\frac{d}{dr} \left[ D_{\perp} \frac{dn}{dr} \right] = \frac{nc_s}{L_c} \quad (7.4)$$

where  $D_{\perp}$  is the cross-field diffusion coefficient and  $L_c$  is the connection length along the flux tube to the flow stagnation point. With the assumption that  $D_{\perp}$  and  $c_s$  are independent of radius, Eq. (7.4) is readily integrated to obtain

$$n(r) = n(a) \exp \left\{ -(r-a) / \lambda_n \right\} \quad (7.5)$$

where

$$\lambda_n = \left[ \frac{D_{\perp} L_c}{c_s} \right]^{\frac{1}{2}} \quad (7.6)$$

$a$  is the minor radius at the limiter or last closed flux surface and  $\lambda_n$  is the thickness of the SOL or e-folding length for density. The electron heat balance can be considered in an analogous way, leading to a temperature profile.

$$T_e(r) = T_e(a) \exp \left\{ -(r-a) \lambda_T \right\} \quad (7.7)$$

where approximately

$$1 + \frac{\lambda_n}{\lambda_T} = \frac{\delta}{5/2 + \chi_{\perp} \lambda_n / D_{\perp} \lambda_T} \quad (7.8)$$

$\lambda_T$  is the electron temperature e-folding length and  $\chi_{\perp}$  is the cross-field thermal diffusivity. Equations (7.5) and (7.7) lead to a radial distribution for the power flux similar to those for  $n_e$  and  $T_e$ .

Equations (7.6) and (7.8) give the e-folding lengths in the SOL in terms of the cross-field transport parameters. In practice, since the cross-field transport coefficients are not known, the measured values of  $\lambda_n$  and  $\lambda_T$  are used to deduce  $D_{\perp}$  and  $\chi_{\perp}$ . While for many years the assumption has been made that the cross-field transport is diffusive, this is increasingly being questioned. It is well known that there are large fluctuations of density and temperature which can be detected with probes. These fluctuation measurements of the radial e-folding length for  $n_e$  and  $T_e$  can be made with electrical probes by averaging, provided the impurity content is small. Typical values are  $\sim 10$  mm. If there are no sources in the SOL, this measurement, together with the assumption that  $T_e = T_i$ , enables  $c_s$

to be calculated and a value for  $D_{\perp}$  deduced. This is typically  $\sim 1 \text{ m}^2 \cdot \text{s}^{-1}$ . Absolute values of  $D_{\perp}$  comparable with the Bohm diffusion coefficient

$$D_B = T_e / 16eB \quad (7.9)$$

are frequently obtained, although the scaling with  $T_e$  and  $B$  is not. These inconsistencies have recently led to further study of the boundary layer with fast cameras. These show “blobs” and “filaments” in the boundary layer which are correlated with the fluctuations measured with probes, indicating a very turbulent region (see Section 7.5.2.2). The filaments have been observed to break away from the region near the LCFS and move outward radially so that significant particle fluxes reach the wall. These radial fluxes may account for the fact that the radial density profiles are not the simple exponentials that would be expected for a diffusive process.

The simplest model capable of reproducing the main features of transport along the magnetic field in the SOL is the isothermal fluid model. Steady-state, inviscid, isothermal one-dimensional flow is determined by conservation of particles and momentum:

$$\frac{d}{dx}(nv) = s_p(x) \quad (7.10)$$

where  $x$  is the distance to the surface along the magnetic field line, and  $s_p$  is the source rate of particles, for example due to cross-field transport or ionization, and

$$\frac{d}{dx} [nm_i v^2 + n(T_i + T_e)] = 0 \quad (7.11)$$

neglecting viscosity and ion-neutral collisions. Note that the first term in the bracket is the dynamic pressure and the second term is the static pressure. Thus,

$$\frac{n(M)}{n_0} = \frac{1}{1 + M^2} \quad (7.12)$$

where  $M = v/c_s$  is the Mach number and  $n_0$  is the density at the stagnation point with  $v = 0$ . At the sheath edge,  $M = 1$ , we have

$$n_{se} = \frac{1}{2} n_0 \quad (7.13)$$

and hence the particle flow is simply given by

$$\Gamma = \frac{1}{2} n_0 c_s \quad (7.14)$$

The electron density distribution is given by the Boltzmann relation and so using Eq. (7.12) the plasma potential  $V_p(M)$  is given by

$$V_p(M) = -\frac{T_e}{e} \ln(1 + M^2) \quad (7.15)$$

and  $V_p$  tends to  $-0.69T_e/e$  as  $M$  tends to 1 at the sheath edge.

Many other models, both fluid and kinetic, have been proposed for parallel flow. However, for the most important parameters the predictions of the different models are similar.

Impurities which are produced at surfaces in contact with the plasma and flow into the SOL are also subject to the presheath electric field and their own pressure gradient. Note that the presheath represents a finite-field region, where ions are accelerated to the sound speed before entering the sheath. In addition, they are subject to the frictional force of the ion flow towards the limiter. The flow velocity is difficult to calculate, and there is little experimental information.

### 7.2.2. Recycling

In most magnetic confinement devices, the pulse length is at least an order of magnitude longer than the particle replacement time. Thus on average, each plasma ion goes to the divertor target plate or limiter and returns to the plasma many times during the discharge. This process is called recycling. A global particle replacement time may be defined as the ratio of the total particle content within the last closed flux surface to the total particle influx (and therefore efflux) across this surface. This time should not be confused with the central particle confinement (or equilibration) time, which is the time for a particle to be lost from the centre of the plasma and is therefore of order  $a^2/D_{\perp}$ , where  $a$  is the plasma minor radius. For a limiter, the recycled particles enter the plasma predominantly as neutrals, but are ionized and then trapped by the magnetic field after traversing only a fraction of the plasma radius. The situation is more complicated in the case of the divertor, where most of the ionization may take place near the target. Under some conditions there may be no particle source in the core plasma, and the density at the LCFS is determined by the density gradient along the separatrix from the target. The global particle confinement, or replacement time, then has little meaning.

Although the recycling of particles involves processes both in the plasma and in the surface layer of the solid, the present section will concentrate primarily on the processes occurring in the solid. When a plasma ion or neutral arrives at a solid surface it undergoes a series of elastic and inelastic collisions with the atoms of the solid. It may be either backscattered after one or more collisions, or slowed down and finally trapped in the solid. The trapped atoms can subsequently reach the plasma again after diffusion back to the solid surface. The ratio of the flux returning to the plasma from the solid to the incident flux is known as the recycling

coefficient. In addition, the flux of plasma particles and radiation may release gas which was previously adsorbed on the wall. This additional influx of particles can lead temporarily to effective recycling coefficients which are significantly greater than unity. Large quantities of hydrogen can be built up in wall materials in contact with the plasma, the equilibrium concentration depending on the incident flux, the ion energy, and the wall material and temperature.

The backscattering of ions incident on a surface depends primarily on the ion energy and on the ratio of the masses of the surface atom and the incident ion. Scaling laws which depend on ion energy give an approximate value of the particle backscattering coefficient  $R_p$  for ions incident on all materials. A similar general law can be obtained for the energy reflection coefficient,  $R_E$ . Values of  $R_E$  and  $R_p$  as functions of reduced energy  $\epsilon$  are given in Fig. 7.4. For energy  $E$  in keV the reduced energy is defined as

$$\epsilon = \frac{32.5m_2E}{(m_1 + m_2)Z_1Z_2(Z_1^{2/3} + Z_2^{2/3})^{1/2}} \tag{7.16}$$

where  $m_1$  and  $m_2$  represent the masses of the incident and target atoms, respectively. The curves are derived from Monte Carlo calculations for a wide range of ion-target combinations. The scatter in experimental data is typically 25% and the Monte Carlo calculations generally agree with the available experimental data within these limits. It is seen that both particle and energy reflection coefficients increase with increasing mass ratio, as expected from simple conservation of momentum. The data in Fig. 7.4 are unreliable for energies below about 10 eV because at very low energies the use of sequential binary collisions in the calculations is no longer valid. The particles which are backscattered are predominantly neutral since an incident ion normally picks up an electron from the solid.

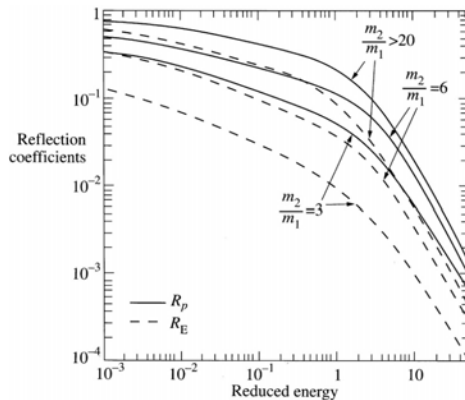


FIG. 7.4. Particle and energy reflection coefficients of ions backscattered from solid surfaces as a function of reduced energy,  $\epsilon$ , for three different ratios of the target to incident mass [7.9].

The average energy of the backscattered particles is determined by the ratio  $R_E/R_p$ , the mean energy being typically 30–50% of the incident energy. The energy distribution has been experimentally measured down to about 0.1 keV and calculated down to even lower energies. Some results are shown in Fig. 7.5. The distribution is continuous, typically having a maximum, the position of which depends on both the energy and the angle of incidence of the primary ion.

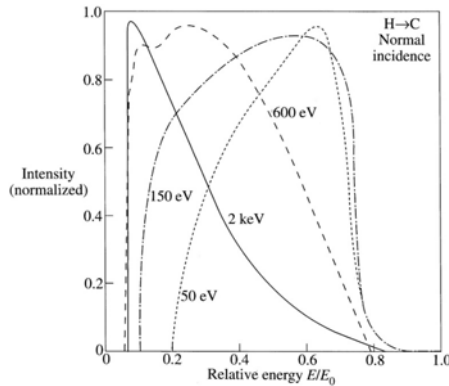


FIG. 7.5. Measured energy distribution of hydrogen atoms backscattered from carbon, for different incident ion energies,  $E_0$  [7.10]. The distributions are normalized at their maximum intensity.

The atoms which come to rest within the solid reside either in interstitial sites or in defects in the metal, such as vacancies. For hydrogen, however, diffusion readily occurs at temperatures above 300 K in many materials. Carbon, carbides and oxides are notable exceptions. When diffusion occurs, the behaviour of the hydrogen depends on the heat of solution of hydrogen in the material. In cases where hydrogen dissolves exothermically in the metal, such as titanium and zirconium, there is an effective potential barrier at the surface preventing hydrogen atoms being released. The hydrogen thus diffuses into the solid, eventually becoming distributed over the whole volume. In the endothermic case, hydrogen atoms diffuse to the surface and escape from it, after recombination to form molecules. Since the penetration range of the incident ions slowing down in the solid is small compared with the thickness of material, in most practical cases the concentration gradient, and hence the diffusive flow, is largest towards the surface facing the plasma. The hydrogen ions which have slowed down in the solid are usually released from the surface as molecules, having thermal energies characteristic of the solid surface.

The details of hydrogen diffusion in solids is a complex subject. In both metals and non-metals the diffusing atom can be trapped at lattice vacancies, interstitials or other imperfections with binding energies much larger than the activation energy for diffusion. In steady state, the ion flux to the solid is balanced

by the outflow, determined by the diffusive flow towards the surface and the molecular recombination rate at the surface. Depending on the materials and operating temperature, either may be the rate limiting process. In many practical cases a dynamic equilibrium is set up in which the recycled particles entering the plasma consist of 50% backscattered atoms with energies  $\sim 5T_e$  (taking into account the sheath potential accelerating the incident ions and the energy reflection coefficient  $R_E$ ) and 50% of slow molecules with energies  $\sim 0.03$  eV. With light element wall materials the proportion of the particles backscattered as atoms is lower,  $\sim 30\%$ .

While the recycling flux density is highest at the limiter or divertor target, recycling also occurs at the walls due to charge exchange neutral fluxes. Because charge exchange and ionization rate coefficients for hydrogen are roughly equal in the temperature range of interest, the integrated neutral recycling at the wall is of the same order as the integrated ion flux to the limiter or divertor target. The distribution of neutral flux can be calculated with Monte Carlo codes. Local measurements of the energy distribution of neutral fluxes to the wall indicate mean energies in the range 100–500 eV.

### 7.2.3. Atomic and molecular processes

In the processes of recycling and fuelling, many atomic and molecular reactions occur in the boundary layer as the incoming hydrogen isotopes meet the energetic ions and electrons of the plasma. Further reactions occur when impurities created by sputtering and by other plasma–surface interactions enter the plasma. In most cases the dominant atomic reactions are excitation and ionization. These lead to emission of radiation and cooling of the edge plasma. This is beneficial, since it lowers the incident ion energy and reduces the physical sputtering rate.

Considering first the recycling of hydrogen isotopes from the wall, the important atomic reactions are excitation, ionization, and charge exchange as shown in Table 7.1.

TABLE 7.1. IMPORTANT ATOMIC REACTIONS CONSIDERING FIRST THE RECYCLING OF HYDROGEN ISOTOPES FROM THE WALL	
Excitation	$H + e \rightarrow H^* + e$
Ionization	$H + e \rightarrow H^+ + e$
Charge exchange	$H^+ + H \rightarrow H + H^+$

The main molecular reactions are as listed in Table 7.2.

TABLE 7.2. MAIN MOLECULAR REACTIONS	
Dissociation	$\text{H}_2 + e \rightarrow \text{H} + \text{H} + e$
Dissociative ionization	$\text{H}_2 + e \rightarrow \text{H}^+ + \text{H} + 2e$
Molecular ionization	$\text{H}_2 + e \rightarrow \text{H}_2^+ + 2e$
Dissociative recombination	$\text{H}_2^+ + e \rightarrow \text{H} + \text{H}$
Dissociative ionization	$\text{H}_2^+ + e \rightarrow \text{H}^+ + \text{H}^+ + 2e$

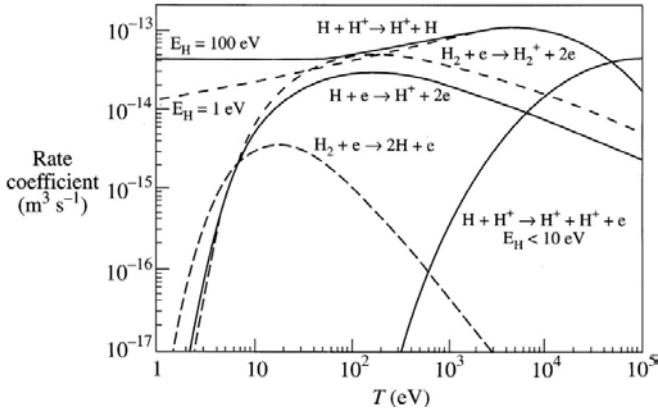


FIG. 7.6. Rate coefficients for hydrogen atoms and molecules for a number of common reactions [7.11]. The first symbol in the reactions indicated in the figure refers to the test particle and the second refers to the thermal species, the rate coefficient being integrated over the Maxwellian distribution of these species.  $E_H$  is the energy of the test particle.

The relative reaction rates for the different processes are functions of plasma temperature and density. Some rate coefficients are shown in Fig. 7.6. When atoms or molecules enter the plasma, the collision rate with the plasma species is  $nn_0 \langle \sigma v \rangle$ , where  $n$  is the plasma density,  $n_0$  the neutral density and  $\langle \sigma v \rangle$  is the reaction rate averaged over the electron velocity ( $v$ ) distribution. Considering a simple one-dimensional model with the source at the wall, the flux of neutrals as a function of radial position decreases due to ionization. The neutral flux  $F(r)$  at a given radius is given by

$$F(r) = F(a) \left( 1 - \int_r^a \frac{n_e(r') \langle \sigma v \rangle}{v_0} dr' \right) \quad (7.17)$$

where  $F(a)$  is the initial flux and  $\langle \sigma v \rangle$  is determined by the local electron temperature. The local ionization source function is  $dF(r)/dr$ . Thus, if the plasma density and temperature profiles are known, it is possible to determine

the penetration into the plasma of both the recycling species and impurity species. However, ionization in the boundary immediately modifies its density and temperature and more complex models usually have to be used to obtain a self-consistent solution. Charge exchange is a further complication which is particularly important in the case of hydrogen. Because the rate coefficient for charge exchange is greater than that for ionization (see Fig. 7.6), the penetration of neutral hydrogen is dominated by charge exchange. When the incoming particle undergoes charge exchange, an energetic plasma ion becomes a fast neutral, and subsequent charge exchange reactions between neutrals and plasma ion leads to a random walk and diffusion to the centre of the plasma. This can be analysed either by transport codes or by Monte Carlo methods [7.12].

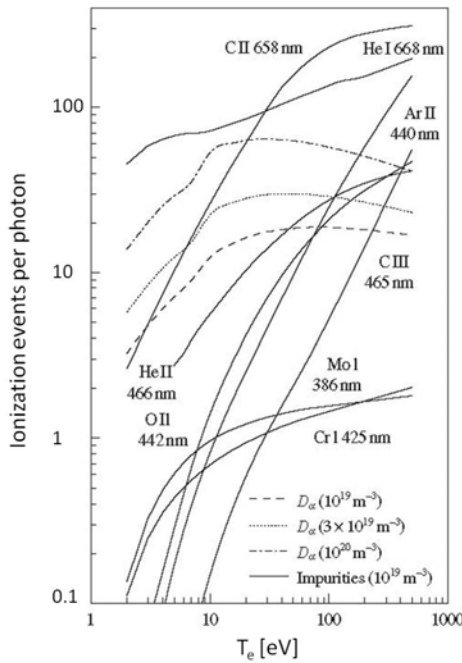


FIG. 7.7. Ionization events per emitted photon for some common impurity lines used for flux measurements, calculated as a function of local electron temperature. Data derived from the ADAS database at an electron density of  $1 \times 10^{19} \text{ m}^{-3}$  for the impurity lines and at the three densities indicated for deuterium atoms [7.8].

Ionization of impurities occurs in the same way as for hydrogen species, but charge exchange can be neglected in most cases. After the first ionization event the impurity ion is confined by the magnetic field, and it can then become multiply ionized in a series of collisions with electrons. The dominant charge state of the impurity ions at any position is determined by the local electron temperature, the electron density and the time for which the impurity is in the plasma. The ratio of

the excitation to ionization rate can be calculated for any given ionization state at a given electron temperature. This ratio gives rise to the useful concept of photon efficiency, i.e. the ratio of the number of photons emitted in a given transition per ionization event. The inverse photon efficiency (number of ionization events per photon emitted) is shown for a number of ions in Fig. 7.7. Knowledge of the photon efficiency together with absolute measurements of the radiation enables the influx of ions to be directly calculated.

By summing over all transitions, the average energy loss per ionization event can be obtained. For hydrogen atoms this varies from 150 eV for  $T_e = 2$  eV to 25–30 eV for  $T_e > 20$  eV. At low  $T_e$  it is also dependent on  $n_e$ . For impurities the situation is more complicated, as there are many possible charge states and excitation can occur in all of these until the ion is fully stripped of electrons. For a carbon atom entering a typical tokamak plasma, the energy lost in producing a fully stripped ion is in the range 1–10 keV per atom, depending on the electron temperature.

As an impurity particle enters the plasma and is raised into successively higher ionization states it is also heated by collisions with the background plasma, principally with the plasma ions. The classical thermalization time is

$$\tau_{th} = 2.2 \times 10^{17} \frac{m_I T_B^{3/2}}{m_B^{1/2} n_B Z_B^2 Z_I^2 \ln \Lambda} s \quad (7.18)$$

with  $T_B$  in keV, where  $m_I$  and  $m_B$ ,  $Z_I$  and  $Z_B$  are the masses and charge states of the impurity and plasma ions, and  $n_B$  and  $T_B$  are the density and temperature of the background plasma. The characteristic time for ionization is

$$\tau_{ion} = (n_e \langle \sigma v \rangle_{ion})^{-1} \quad (7.19)$$

The temperature which an ion reaches before being ionized to the next charge state is determined by  $\tau_{ion} / \tau_{th}$ , which is independent of density. The calculated temperature of some typical impurity ion species as a function of background plasma temperature is shown in Fig. 7.8. At low temperatures the collision rate is high, the ionization rate is low and the impurities are rapidly thermalized. For increased plasma temperature the ionization rate increases and the thermalization rate decreases, so that ionization occurs before thermalization is complete. In equilibrium, the charge state distribution of the ions is determined by the local electron temperature.

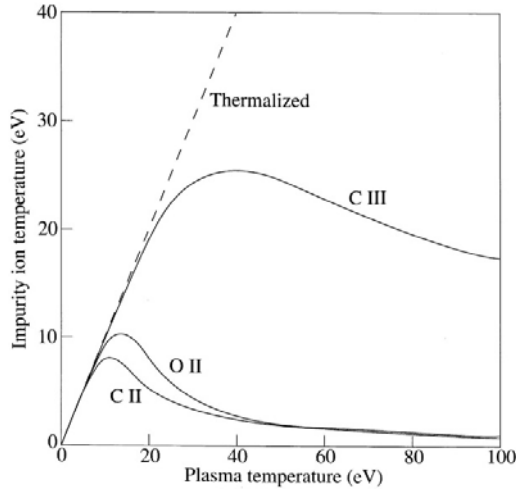


FIG. 7.8. Calculated temperature of CII, OII and CIII impurity ions as a function of background plasma temperature. The dashed line indicates the case where the impurity ion temperature reaches the bulk plasma temperature. ( $T_i = T_e$ , initial impurity ion temperature  $T_i(0) = 0$ ) [7.8].

Impurity ions moving out of the plasma and arriving at the plasma boundary are accelerated through the sheath potential and consequently the energy of an ion arriving at a material surface is a strong function of the ion charge state. The charge state calculated as a function of  $T_e$  is shown for oxygen in Fig. 7.9 for coronal equilibrium conditions. However, because of cross-field diffusion the charge states in the boundary can be significantly higher than the equilibrium values. The residence time can also be quite short ( $\sim 1$  ms) if the ions are ionized in the scrape-off layer and stream back along field lines into the divertor or limiter.

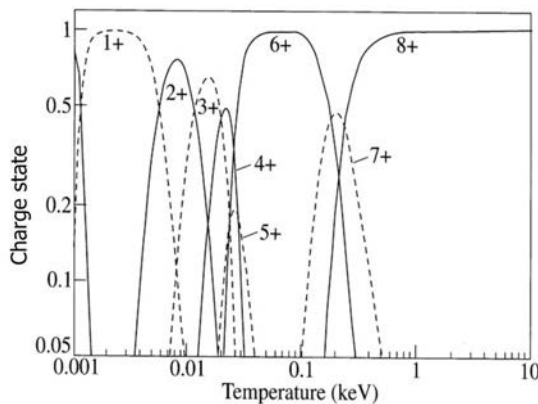


FIG. 7.9. The oxygen ionization state distribution in coronal equilibrium [7.13]. Reprinted from Ref. [7.13]. Copyright (2011), IOP Publishing Ltd.

## 7.2.4. Erosion processes

### 7.2.4.1. Physical sputtering

Sputtering is the removal of atoms from the surface of a solid as a result of momentum transfer by incident ions or atoms. It gives rise to impurities which cause power to be radiated from the plasma and make ignition more difficult to achieve. It also leads to erosion of surfaces at a rate which is expected to be a limiting factor in tokamak reactor design.

When an energetic ion or neutral atom is incident on a solid surface, it produces a collision cascade among the lattice atoms. Due to scattering, some momentum can be directed out of the surface. Physical sputtering takes place when this cascade results in a surface atom receiving sufficient energy to exceed the surface binding energy. Thus, sputter yields decrease with increasing sublimation energy of the solid, and increase with increasing energy transferred from the incident ion to the lattice atom. For light ions, such as hydrogen and helium, the sputter yields are small due to low energy transfer, the energy being dissipated mainly in inelastic processes.

There is in general a threshold energy,  $E_T$ , of the incident ion below which insufficient energy is transferred to the lattice atoms for sputtering to occur. Its theoretical value is

$$E_T = \frac{E_s}{\gamma_{sp}(1 - \gamma_{sp})} \quad (7.20)$$

where  $E_s$  is the sublimation energy of the target solid,  $\gamma_{sp} = 4m_1m_2 / (m_1 + m_2)^2$ . The energy necessary to transfer  $E_s$  to the target atom in a head-on collision is  $E_s = \gamma_{sp}$ . The additional fraction of  $(1 - \gamma_{sp})$  takes account of the reflection process, which is important for light ions.

Figure 7.10 gives some results for sputter yields obtained from Monte Carlo code calculations. These are generally in good agreement with experimental data except for carbon at low energy, where no threshold is found experimentally due to chemical effects. Above the energy threshold the sputter yield  $Y$  first increases approximately linearly, reaches a maximum and then decreases at high energies. The decrease in yield is due to the collision cascade taking place deeper in the solid so that there is a lower probability of atoms at the surface receiving sufficient energy to be sputtered. It is found that the position of the maximum yield moves to higher energy as the mass of the target atom increases. The dominant effect in determining the absolute magnitude of the sputter yield in different targets for the same incident ion is the surface binding energy. There is a considerable spread in the measured values of sputter yields for nominally the same system. This is due

to uncontrolled factors such as surface structure and impurity levels, which can effectively change the binding energy of the surface atoms.

The experimental results can be summarized by plotting the sputter yield against  $E/E_T$ . There is a general semi-empirical curve which describes the sputter yield of all ions over a wide range. This has the form

$$Y(E) = QS_n(E/E_{TF})g(E/E_T) \tag{7.21}$$

where  $Q$  is the yield factor, depending only on the incident ion and target atom combination,  $S_n(E/E_{TF})$  is the nuclear stopping cross-section,  $E_{TF}$  is a characteristic Thomas-Fermi energy and  $g(E/E_T)$  is a threshold function. Analytical forms are available for  $S_n(E/E_{TF})$  and  $g(E/E_T)$ . A prediction of sputtering yields at normal incidence can be obtained for any ion-solid combination from known values of  $Q$ ,  $E_T$  and  $E_{TF}$  using Eq. (7.21).

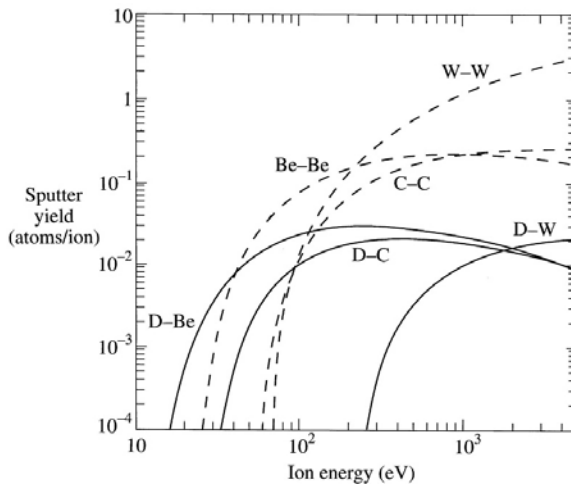


FIG. 7.10. Energy dependence of the physical sputtering yield for beryllium, carbon and tungsten by deuterium and self-sputter ions, calculated using the TRIM Monte Carlo code [7.14]. Reprinted from Ref. [7.14]. Copyright (2011) by the Max Planck Institut für Plasmaphysik.

The sputter yield increases as the angle of incidence,  $\theta$ , increases from the normal. To first order this increase varies as  $\cos(\theta)$ . However, for light ions incident on heavier substrates the yield  $S(\theta)$  increases faster than  $\cos(\theta)$  and  $dS(\theta)/d\theta$  increases with incident energy. This behaviour can be explained qualitatively by the increased probability of the incident ions being backscattered to the surface. Numerical codes based on both transport theory and Monte Carlo calculations give good agreement with laboratory experiments. At low energies,  $E \sim 300$  eV, the variation of yield with incident angle is negligible and this is the region of most interest in many plasma-surface interactions. In practice, it

is difficult to calculate the distribution in angle of incidence of ions arriving at a limiter or divertor target. The situation is complicated by the effects of the ion Larmor radius, the acceleration in the plasma sheath and the surface roughness. The surface roughness also varies with time during operation. Typically, when comparing code results with tokamak experiments it is found that the effective yield is about twice that predicted for normal incidence.

The angular distribution of atoms sputtered from randomly oriented target atoms is given to a good approximation by a simple  $\cos(\theta)$  distribution, though strong crystalline effects are observed in single crystal targets, leading to preferential directions of emission. The energy distribution of sputtered atoms has been quite extensively investigated. Theoretically it has a most probable energy of  $0.5E_s$  ( $\sim 2\text{--}5$  eV) with an energy distribution varying as  $E^{-2}$  at high energies as illustrated in Fig. 7.11 [7.15]. This result has been confirmed by experiments in tokamaks as well as in laboratory experiments using monoenergetic ion beams. Atoms sputtered by heavier ions have a higher mean energy due to the larger momentum transfer.

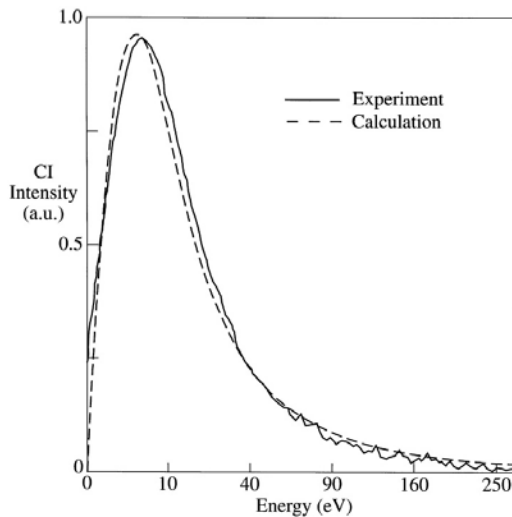


FIG. 7.11. Energy distribution of carbon atoms sputtered from the limiter of the TEXTOR tokamak,  $n_e = 1.7 \times 10^{19} \text{ m}^{-3}$ ,  $I_p = 350 \text{ kA}$ . A calculated distribution, assuming a surface binding energy of  $9.3 \text{ eV}$ , is shown for comparison [7.16].

#### 7.2.4.2. Chemical sputtering

Chemical reactions between incident ions or neutrals and a solid surface can also lead to erosion of surfaces. In fusion devices the most common of such reactions is that between hydrogen isotopes and carbon, for example  $4\text{H} + \text{C} \rightarrow \text{CH}_4$ .

Carbon is widely used as a limiter and divertor material because of its refractory qualities and the fact that it does not melt. However, it has chemical sputtering yields which are comparable and sometimes higher than physical sputtering yields in terms of atoms removed per incident ion or atom. The chemistry depends on hydrogen atoms, on or in the surface, combining with one or more carbon atoms to form a hydrocarbon molecule. Because the hydrocarbons have a low binding energy to the surface they may be thermally released at temperatures as low as 300 K. The chemical reaction rate depends on the surface temperature of the solid as well as the energy of the incident ions. The dependence on ion energy for a fixed surface temperature and on surface temperature for a fixed ion energy are illustrated in Fig. 7.12. During ion bombardment, methane is the primary hydrocarbon produced, but lesser amounts of heavier hydrocarbons, such as  $C_2H_4$  and  $C_3H_6$ , can also be formed as shown in Fig 7.12. Unlike physical sputtering, there is no well defined threshold energy below which the yield goes to zero, and so for carbon at low plasma temperatures chemical sputtering is frequently dominant.

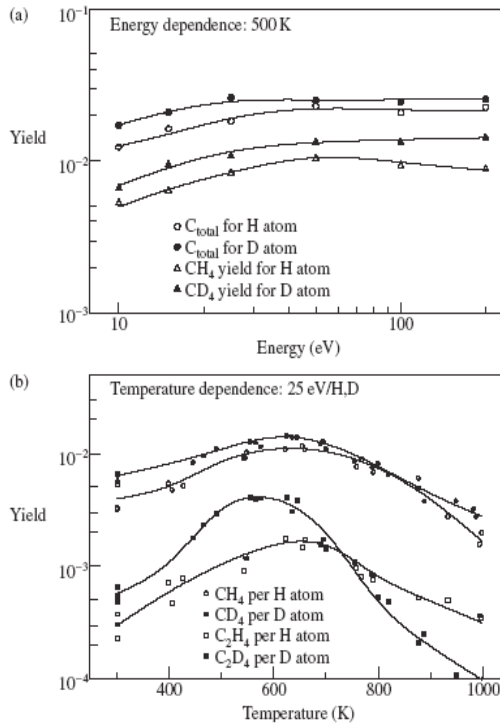


FIG. 7.12. Chemical erosion yield of pyrolytic graphite by energetic hydrogen and deuterium ions as a function of: (a) incident ion energy for a fixed surface temperature of 500 K; (b) surface temperature for an incident ion energy of 25 eV. In (a) the  $C_{total}$  curves refer to the total yield of  $CH_pC_2H_2$ ,  $C_2H_pC_2H_6$ ,  $C_3H_6$  and  $C_3H_8$  hydrocarbons due to hydrogen impact and equivalent deuterium yields [7.17].

The break-up reactions of the hydrocarbon molecules entering the plasma are complicated and not fully documented. However, it is known that the carbon atom or ion released in the molecular break-up has a significantly lower energy than the energy of the physically sputtered atoms. Thus the chemically sputtered species will penetrate less far into the plasma and consequently will have a shorter mean residence time. The prompt re-deposition of molecular fragments is not well documented, but may significantly reduce the effective chemical sputtering yield.

Chemical sputtering has an incident flux dependence due to competition between the rate of arrival of incident ions and the surface processes. This has been studied in considerable detail in recent years, and a summary of the results is shown in Fig. 7.13. It is advantageous that at the high fluxes expected in larger machines the yield per particle decreases.

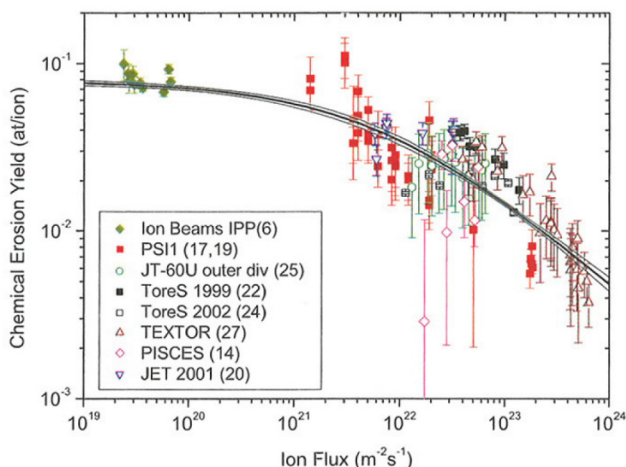


FIG. 7.13. Flux dependence of the chemical erosion yield measured at the temperature of maximum yield and for an ion energy of 30 eV, determined from spectroscopic measurements in different fusion devices and plasma simulators. The solid lines are fits using probability theory [7.18].

It is clear from the above discussion that sputtering processes can release impurities from the wall or limiter by an incident ion, whether hydrogenic or impurity. The energy of the incident ions is the sum of their thermal energy and their flow energy, including that due to acceleration through the sheath potential. Since impurity ions are usually multiply ionized, the acceleration through the sheath potential can result in energies greater than 100 eV. The possibility arises of impurity self-sputtering and a consequent runaway process. Since the physics of the physical sputtering process is well understood, it can be readily incorporated into numerical models of plasma confinement, and it is routinely included in most transport codes.

### 7.2.4.3. Arcing

An arc can strike between two electrodes in vacuum if a sufficiently large potential is applied between them. The essential feature of the arc is that material is evaporated from the cathode and is ionized, allowing the flow of current. Arc initiation often occurs at a sharp point or edge where the electric field due to the applied potential is enhanced. The voltage required to strike an arc is very dependent on the state of the surface, but once the arc has struck, the voltage between the two electrodes is in the range 10–20 V and is dependent only on the electrode material. A flow of current in the solid to a localized point in the surface causes Joule heating and electrons are produced at the surface by a combination of field emission and thermionic emission. The arc occurring as a result of an externally applied potential is known as a power arc.

The presence of a plasma can produce a “unipolar arc”, for which the required applied potential is produced by the plasma sheath [7.2]. Since the sheath potential is  $\sim 3T_e$ , a local electron temperature of only 5–10 eV is necessary to sustain an arc. When the arc is initiated, electrons from the cathode spot are accelerated away from the surface by the sheath potential. The flow of current locally reduces the sheath potential and, therefore, increases the flow of electrons in the tail of the Maxwellian distribution across the sheath in the area surrounding the arc. The circulating current can be derived by summing the electron flow towards and away from the solid surface. A minimum current of  $\sim 10$  A is required to sustain an arc, determined by the balance between energy deposition from the arc, Joule heating and thermal conduction; thus a minimum surface area is required.

Arcs give rise to erosion at the cathode spots. The material is released in the form of ions, neutral vapour, and molten and solid drops. The ion current is typically 7–10% of the total arc current. The ions are released with typical energies of 50–100 eV and in charge states up to 4 or 5. The higher charge states tend to occur for refractory high  $Z$  metals, such as Ti, Zr and Mo. It is not understood why the ion energies are significantly higher than the arc voltage drop. Erosion due to vapour emission and droplets is more probable for low melting point metals. The droplets range in size from 2 to 6  $\mu\text{m}$  and are ejected at low angles to the surface, typically 10–20°. They are thought to come from the molten rim of the arc crater. At higher surface temperatures, enhanced erosion due to ejection of large droplets is observed.

The erosion of surfaces by arcing in a vacuum diode has been measured for a wide range of materials and different conditions. It is found that the erosion is proportional to the total charge transmitted. The erosion rate varies from  $0.5 \times 10^7 \text{ kg} \cdot \text{C}^{-1}$  for molybdenum to  $2.2 \times 10^7 \text{ kg} \cdot \text{C}^{-1}$  for zinc. It is commonly assumed that because of the similarity of the cathode spot conditions, the erosion rates for bipolar and unipolar arcs are similar. Although this appears a reasonable

assumption, there is an absence of any reliable experimental data for unipolar arcs.

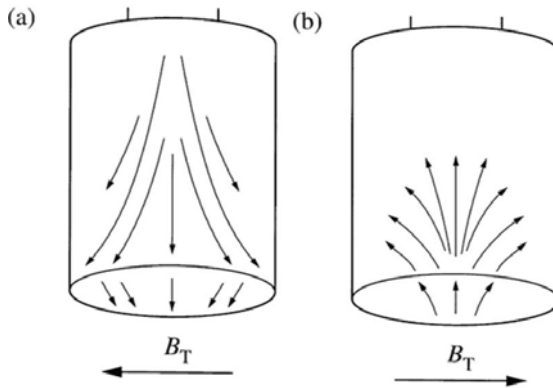


FIG. 7.14. Schematic representation of arc tracks observed on curved surfaces of a cylindrical probe exposed in the tokamak boundary. The direction of the arc depends on the direction of the magnetic field. Note that the direction of a unipolar arc is opposite to the  $\vec{j} \times \vec{B}$  force with  $\vec{j}$  being normal to the surface [7.8].

The presence of a magnetic field causes a force to be exerted on an arc column, although in the vacuum or unipolar arc the motion is, surprisingly, in the direction opposite to the  $\vec{j} \times \vec{B}$  force. This retrograde motion is seen on the limiters and walls of tokamaks. Two types of arc are observed, called type I and type II arcs. Type I arcs are formed on surfaces having some contamination, while type II occur on clean surfaces. The type I arc runs in the impurity vapour and causes comparatively little damage to the surface. Arcs are less likely to be initiated on a clean surface, but when they do form they result in deeper craters and more severe erosion of the surface. The occurrence of arcs removes contaminating layers from a surface, leading to a gradual transition from type I to type II arcs and an increase in the required breakdown potential. The arc current in a unipolar arc is normal to the surface and, if the surface is curved, the direction of the force changes as the arc moves across the surface. This results in a characteristic pattern frequently seen in tokamaks, as illustrated in Fig. 7.14. On a surface normal to a magnetic field, since the current and the magnetic field are in the same direction there is no net force and the arc moves about in a random manner.

Arcing is commonly observed in tokamaks, but normally occurs during the current rise phase, when the plasma is undergoing MHD instabilities. It is difficult to assess the impurity level produced by arcing, both because of the irregular nature of the arcing initiation process and because of the problem of measuring the current flow in the unipolar arc. Fortunately, since arcing usually takes place at the start of the discharge and the pulse lengths of tokamak discharges have

steadily increased, arcing has become relatively less important as an impurity production mechanism.

### 7.3. DEVELOPMENT OF PLASMA FACING MATERIALS

Plasma facing materials (PFMs) have been recognized as a key issue in the realization of practical fusion power since the beginning of magnetic fusion research. By the late 1970s, strong cooling of the central plasma was first observed in the PLT tokamak using tungsten limiters with NBI auxiliary heating [7.19]. For this reason, PLT switched the limiter material to graphite, which turned out to be very successful. By the mid-1980s, many tokamaks were operating with graphite limiters and/or divertor plates. But graphite's ability to trap hydrogenic species in co-deposited layers, along with poor physical properties in a neutron environment, led to the consideration of beryllium as a plasma facing material. Two small tokamaks successfully tested beryllium (ISX-B and UNITOR) and this led to extensive JET operation with beryllium limiters, divertor plates and evaporative gettering [7.20].

The success with graphite in limiter machines led to the use of graphite for divertor plates, although there are a number of cases where metals have been used, for example TiC coated Mo outside the X-point divertor in JT-60 [7.21]. The last decade of divertor research has seen a return of interest to metals, which had been largely put aside in favour of graphite. Divertor machines that have tried high-Z metal divertor plates in the low temperature/high-recycling mode (e.g. molybdenum in Alcator C-Mod [7.22] and tungsten in ASDEX-Upgrade [7.23]) and have indeed found very low levels of net erosion at the divertor target.

#### 7.3.1. Carbon containing materials

Carbon containing materials include graphite and carbon fiber composites (CFCs). After the first use of carbon in the PLT device (Princeton, USA), fine grain graphite was widely applied in fusion devices, such as in TFTR, JET and JT-60. Graphite is the most commonly used PFC material in the present devices because of its good outgassing property, low-Z character and capacity for handling high heat fluxes, good compatibility with a wide variety of plasma operations and the advantage that eroded carbon atoms are fully stripped in the plasma core, thus reducing core radiation. In addition, the surface does not melt if overheated — it simply undergoes sublimation. At present, graphite is the dominant material in the major tokamaks worldwide, with the exception of Alcator C-Mod, ASDEX-Upgrade and the JET ITER-like wall in the near future. Many machines have expanded graphite coverage to include virtually all of the vacuum vessel wall, in addition to the limiter/divertor plates (e.g. DIII-D) [7.24]. In some cases, the inner wall is used as a large area limiter and such structures,

if carefully constructed, are able to handle enormous power loads, greatly exceeding the power limits of divertor plates (e.g. TFTR [7.25]).

The wall materials, especially for limiters and divertor plates, have to fulfil several criteria. For removing the deposited energy, the materials must have an extremely high thermal conductivity as well as a high melting point, and for pulsed plasma operation, a large thermal shock resistance. Among the various different carbon based materials, the carbon fiber composites (CFCs) have been selected as reference divertor material. The main reasons are good mechanical strength, superior thermal shock resistance (the thermal stress parameter  $\sigma\lambda/aE$  for CFC is  $\sim 100$  times better than for Be), and high thermal conductivity (which gives the possibility to use thicker armour). The main efforts for the investigation and development of these materials are concentrated in the EU and Japan. The reference grades of the selected CFCs are presented in Ref. [7.26]. This selection was done because of the excellent properties of these materials, their availability in industry and the experience in using these materials for high heat flux components.

In comparison with Be and W, carbon materials have been widely used as armour in present tokamaks and their performance is well established. In addition, extensive laboratory tests/simulations on graphite began early, primarily aimed at understanding of the chemical reactions between graphite and hydrogenic plasmas, i.e. chemical erosion. Early laboratory results suggested that carbon would be eroded by hydrogenic ions with a chemical erosion yield of  $\approx 0.1 \text{ C/D}^+$ , a yield several times higher than the maximum physical sputtering yield. Another process, radiation enhanced sublimation (RES), was discovered at elevated temperatures, which further suggested high erosion rates for carbon.

The most serious issues with carbon PFC are lifetime restrictions on net erosion areas due to the large erosion yield of carbon, the associated buildup of carbon deposits and the subsequent tritium retention in these layers, which is the main mechanism of long term hydrogenic isotope retention in carbon clad fusion devices. While the mechanisms of physical sputtering are well understood, the chemical erosion of carbon, i.e. the release of volatile hydrocarbon molecules and radicals (e.g.  $\text{CH}_3$ ,  $\text{CH}_4$ ,  $\text{C}_2\text{H}_4$ ) caused by ionic and atomic hydrogen fluxes, continues to be an active area of research. Chemical erosion yield is measured on carbon clad devices using visible spectroscopy of highly dissociated hydrocarbon molecules ( $\text{CH}$ ,  $\text{C}_2$ ) interpreted through adequate modelling of the molecular processes. The yields measured for energetic ( $>10 \text{ eV}$ ) divertor plasmas span a range of 0.4–10%, corresponding to a large range of experimental conditions with surface temperatures  $T_{surf} = 350\text{--}600 \text{ K}$ , plasma fluxes of  $\Gamma_i = 0.1\text{--}1.0 \times 10^{23} \text{ m}^{-2}\cdot\text{s}^{-1}$  and, possibly, the enhanced erosion of co-deposited films under high power loads [7.27]. DIII-D reports a total suppression of hydrocarbon emission in detached plasmas ( $T_e < 2 \text{ eV}$ ), despite the modelled high photon efficiencies for CH in these conditions, which suggests a highly

suppressed chemical erosion yield  $<0.01\%$  [7.28]. The very large scatter in experimental measurements indicates that many plasma/surface parameters (such as ion impact energy, flux, surface temperature) play a major role in determining the magnitude of chemical erosion.

A database of chemical erosion yield obtained in different tokamaks, linear plasma devices and beam experiments has been recently compiled and used to normalize the yield data with respect to ion energy, target temperature and ion flux. The database suggests a weak dependence of the erosion yield on ion impact energy between 10 and 200 eV and a clear tendency for the yield to decrease with increasing flux density [7.29], implying a  $\sim 2.5$ -fold reduction in yield for the ITER strike-point conditions compared with previous assumptions ( $\sim 1\%$ ). Figure 7.15 illustrates the implications that such a yield reduction (taking into account realistic surface temperature, impact energy and flux dependences) has on the calculated gross erosion of the ITER divertor target [7.30], compared with previous estimates with a  $\sim 1\%$  fixed chemical erosion yield [7.31]. The reduction of the chemical gross erosion yield results in related improvements in target lifetime and expected tritium retention. This figure illustrates the complex coupling of target erosion and power load and associated tritium retention, which makes predictions to ITER uncertain. The carbon chemical erosion yield depends strongly on the target temperature, which is determined by the incident plasma power flux. The power flux at the divertor is determined by the radiative losses and the degree of detachment, which is strongly influenced by the release of carbon into the divertor by chemical erosion. On the other hand, changes in the plasma conditions at the divertor from quiescent to transient phases of the discharge (ELMs, disruptions) will most probably contribute more to carbon erosion than the uncertainties in the chemical erosion yield described above.

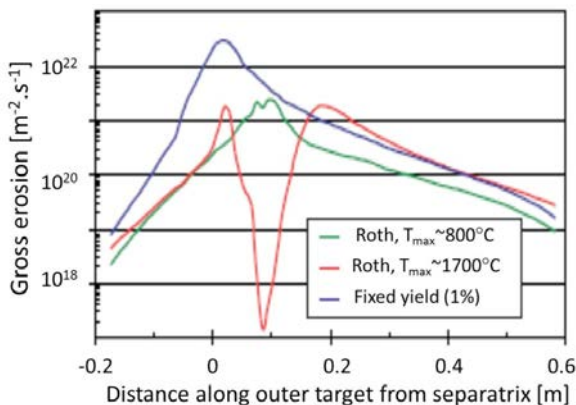


FIG. 7.15. Calculated chemical gross erosion of the outer ITER divertor target, assuming full erosion dependence on energy, surface temperature and particle flux [7.30] for the surface temperature at  $1700^{\circ}\text{C}$  (red) or  $800^{\circ}\text{C}$  (green), and a fixed erosion yield of  $1\%$  (blue) [7.31].

New results for brittle destruction have been obtained on the erosion of isotropic graphite and carbon fibre composites by explosive emission of small particulates occurring under rapid (~ms) heat loads. The so-called brittle destruction [7.32] leads to enhanced erosion and surface non-uniformities for carbon materials. This erosion mechanism has been observed to set in for graphite above an energy density threshold  $>100 \text{ MJ}\cdot\text{m}^{-2}\text{s}^{-1/2}$  (which is more than twice as large as the carbon sublimation limit) and at somewhat lower values for CFC. CFC erosion associated with local overheating and matrix-fibre detachment has been identified in experiments in electron beams/plasma guns and modelling [7.33]. Therefore, while carbon is chosen for its robustness in transient heating events like ELMs and disruptions in ITER, this resilience is limited and energy densities from transient events in ITER must be kept below the sublimation and brittle destruction thresholds for carbon, in order to prevent a severe limitation of the ITER divertor target lifetime even for CFC.

There is a lot of work going on at present investigating the influence of neutron irradiation on physical and mechanical properties of CFC, but usually the data are available for old CFC grades and only in limited cases for the new ones. Nevertheless, on the basis of available data, the following conclusions have been reached:

- Neutron irradiation leads to degradation of the thermal conductivity of carbon based materials even at neutron damage as low as  $10^{-3}$  dpa.
- The neutron induced degradation of thermal conductivity decreases with increasing irradiation temperature.
- Neutron irradiation induces an anisotropic shrinkage parallel to the direction of maximum thermal conductivity (fibers direction), while swelling occurs in the perpendicular direction.
- Neutron irradiation induces an increase of tritium retention with fluence.

A CFC divertor target will not be used before the ITER D-T phase due to the above mentioned reasons and also certainly will not be used in the future DEMO.

### 7.3.2. Beryllium

Chemical erosion and high hydrogenic species retention in co-deposited layers of carbon led to the consideration of beryllium as a plasma facing material, primarily promoted and implemented at JET [7.34]. Beryllium has the advantage of being a low-Z material, non-reactive with hydrogenic isotopes and a good thermal conductor. However, beryllium has several negative features, including a low melting temperature (1560 K), potential toxicity in manufacturing and relatively high physical sputtering rates. In fact, melting and evaporation of

the beryllium limiters was extensive in all three tokamak experiments cited. One immediate and clearly beneficial effect of beryllium operation was the observation of strong oxygen gettering by the evaporated beryllium.

The critical issues for the application of Be as an ITER PFC are:

- (1) Joining to heat sink structure;
- (2) Loss of melt layer during disruption;
- (3) Thermal fatigue resistance;
- (4) Tritium retention;
- (5) Neutron irradiation resistance.

Some of these issues in a first approach do not depend on the grades of materials (bonding, melting, etc.), but are very sensitive to the impurity levels, grain sizes, methods of production, thermo-mechanical treatment, etc., which usually differ for the Be grades. Selection of the Be reference grades was done mainly by the EU, US and Russian ITER parties, and was based on the experience of the development and application of Be in each individual country.

The major issue concerning the use of Be as a plasma facing material in next step devices, such as ITER, is related to its relatively low melting temperature (1560 K). Deposition of plasma energy during transients such as ELMs, VDEs and disruptions can bring the Be temperature to the melting point and, thus, cause extended melting. Furthermore, techniques that mitigate the effect of such events, such as massive impurity puffing to mitigate the thermal quench energy flux during disruptions, cause radiative fluxes leading to a deposition of energy of  $\sim 0.5 \text{ MJ}\cdot\text{m}^{-2}$  in timescales shorter than 1 ms, causing significant melting of the Be PFC (20–50  $\mu\text{m}$ ). The dynamics and loss of the layers of molten Be during transients, which are subject to forces associated with plasma impact, Lorentz forces, etc., remain to be studied in detail. The experience with Be in JET was recently reviewed [7.35] with emphasis on the behaviour and influence on the plasma of Be melting and molten Be. In JET, a single large ELM depositing  $\sim 1 \text{ MJ}$  in less than 1 ms led to substantial melting of the Be JET divertor target and terminated the high performance ELM-free phase of the discharge. However, the effects of Be melting on subsequent plasma operations were not catastrophic, due to the plasma's high tolerance to the low-Z Be. Therefore, the precise implications of significant Be first-wall melting on the lifetime of the wall in ITER and on the performance of a burning plasma experiment like ITER are still not clear and require further study. The ITER-like wall programme in JET will certainly play a very important role.

### 7.3.3. High-Z materials

In contrast to carbon, the erosion of high-Z materials by low energy hydrogen atoms is small. However, erosion of tungsten by fast particles plays an important role. Tungsten in the confined plasma is only partly ionized, even at reactor relevant temperatures in the range of 10–20 keV. The resulting strong radiation thus sets a lower limit for an acceptable tungsten concentration of only a few times  $10^{-5}$ . In connection with the pronounced neoclassical inward drift of high-Z ions, turbulent transport plays a beneficial role here.

One of the main advantages of tungsten is its low hydrogen retention at elevated temperatures. Due to the low expected erosion rates and the absence of a process similar to that of hydrocarbon formation, the H-retention by co-deposition does not play a significant role with tungsten. The implications of the formation of H bubbles, as well as blistering due to He, observed in laboratory experiments after irradiation with high fluences of H or He respectively, are still under discussion. Because of the higher atomic mass, substantial sputtering by deuterium occurs only at relatively high energies, (e.g. with a sputtering rate of the order of  $10^{-3}$  for 400 eV ions). Hence, sputtering does not lead to substantial erosion for sufficiently cold deuterium plasma in the SOL and in front of the target plates [7.36]. In addition, because of their low speed, W neutrals sputtered from the wall are ionized over distances small compared to their large gyroradius. This leads to a prompt re-deposition of a high fraction of sputtered particles.

In most present day devices, inertial cooling is sufficient due to the short pulse durations. The low particle fluences and consequent limited erosion enable the use of W coatings on a graphite substrate. In steady state devices, actively cooled components will be necessary, and for high heat flux components, the bonding between the W armour and the heat sink is of special concern. In the case of ITER, copper alloys are proposed as the heat sink material. Since copper exhibits a much larger thermal expansion than tungsten, castellated or ‘brush’-like structures may be used. In order to operate at higher cooling medium temperatures, concepts of actively cooled tungsten structures are under development for DEMO. Specific developments are aimed at suppressing the production of volatile tungsten oxide in the case of a loss of coolant accident with air ingress so as to reduce the risk of releasing radioactive material. The admixture of small amounts of silicon and chromium to tungsten leads to a glassy protection layer on the tungsten surface, which can reduce the tungsten oxidation rate by up to four orders of magnitude [7.37].

### 7.3.4. Mixed materials

Beryllium, carbon–carbon composites and tungsten are considered at present as candidate materials for ITER. The presence of various materials, as

divertor and first wall components, will unavoidably result in the formation of mixed layers on the surfaces of plasma facing components. If the plasma facing material in a device consists of more than a single element, there is a high probability that the composition of the plasma facing surfaces will evolve over time and may exhibit plasma interaction properties much different from the originally installed material.

Unfortunately, the properties of the materials used in design calculations are usually the values associated with the “as-received” material. In the proximity of high temperature plasma, material erodes from plasma facing materials in one location and is transported to other locations throughout the device. The transported material may then be deposited on, or implanted into, other materials. The term “mixed material” has recently been coined to describe the resultant, plasma-created surface. Even though the importance of this issue was recognized almost three decades ago, detailed investigations of plasma interactions with surfaces composed of more than a single element began only during the last decade or so.

JET has also spent considerable effort on understanding the behaviour of mixed material surfaces [7.38]. In the JET device both carbon and beryllium were used together as plasma facing materials, and the resultant surfaces show considerable mixing between the two elements. Compositional changes in the depth profiles of the mixed material surfaces can be correlated to the operational history of the machine [7.39]. The interrelated nature of the machine performance and the resultant plasma facing surfaces indicates the importance of predicting the behaviour of mixed material surfaces in ITER prior to operating the device, both for facility safety requirements, as well as from the point of view of plasma performance and the achievement of the goals of the overall ITER project.

The conclusions derived from many active areas of research are needed to be able to accurately predict which mixed material surfaces will form in which regions of the ITER plasma facing surfaces [7.40]. The creation of mixed material surfaces will depend on many factors that determine the arrival and loss rate of material from those surfaces. In order to know the arrival rate of an impurity species in the plasma at a given surface, one must understand the transport properties of the scrape-off layer (SOL) plasma. Edge plasma turbulence induces cross-field transport, resulting in both diffusive-like and convective plasma transport into and through the SOL region [7.41]. The magnitude of convectively transported flux to the first wall, commonly called blob transport [7.42], is actively being investigated. In addition, large SOL plasma flows have been measured but not yet explained in several plasma confinement machines. Finally, erosion terms due to asymmetries and off-normal events, such as ELMs [7.43], also contribute to the distribution of impurities throughout the ITER vessel. From the surface loss rate perspective, the surface temperature of the bombarded material is a critical factor in determining the chemical processes

acting in the surface and the resultant morphology of the exposed surface. The creation of mixed material compounds in the surface of plasma exposed materials can potentially alter the thermal conductivity of these surfaces and thereby make reliable predictions of the surface temperature doubtful.

It is clear that the mixing of materials in plasma facing surfaces can alter the hydrogenic retention properties of surfaces [7.44]. In the W/C case, the retention level seems to lie between those expected from the pure materials. In the Be/C case, retention is increased somewhat above that expected from pure carbon. However, the largest impact on the tritium accumulation inside the ITER vessel appears to be associated with changes in the hydrogenic inventory in co-deposited layers located in regions away from direct plasma contact, such as the pumping duct. The composition of co-deposited layers, and thereby their hydrogen retention properties, may be determined by the erosion properties of mixed materials, as has been seen in the PISCES experiments. Or the co-deposited materials containing W/C or Be/C mixes may react similarly to laboratory carbide formation measurements that observe the release of hydrogen when carbides form. Finally, the retention properties of the tungsten beryllides is still completely unknown, and it can only be hoped that the elevated temperature required for their formation may mitigate any adverse effects.

#### 7.4. PRESENT PROGRESS OF PLASMA–WALL INTERACTIONS IN TOKAMAKS

Significant progress has been achieved in plasma–wall interactions since the beginning of the tokamak research programme. It is well understood that the interactions between edge plasma and surrounding walls have a profound influence on the core plasma performance. The edge plasma provides a good thermal shielding, prevents impurity influx and offers a channel for releasing He ash in a fusion reactor. On the other hand, the wall surface plays a very important role in hydrogen isotopic recycling, fuelling, and particle and power handling. Efforts have been made in the last few decades for understanding the physics and mechanism of the major issues, such as wall conditioning, impurity migration, erosion and re-deposition, hydrogen isotope retention and removal, divertor physics and others.

##### 7.4.1. Wall conditioning

Wall conditioning provides an effective means for reducing both impurities and recycling from the plasma surrounding surface. Effective wall conditioning has turned out to be essential for achieving high plasma performance in present day fusion devices.

A wide variety of techniques have been developed during the last few decades. Baking of the internal components inside the vacuum vessel, glow discharge cleaning (GDC) [7.45, 7.46], and Taylor discharge cleaning (TDC) [7.47], which were developed in the early days of tokamak experiments, have been demonstrated to be effective and are still in use today.

Various surface conditioning techniques have been developed by applying a coating to the plasma facing surface, including metallic film gettering, carbonization, boronization, siliconization and lithium deposition. With the presence of magnetic fields, electron cyclotron resonant (ECR) and ion cyclotron resonant (ICR) discharge cleaning techniques have been explored, which could be used for next generation tokomaks such as ITER.

#### *7.4.1.1. Surface cleaning*

The principle of all the cleaning procedures using plasma discharges is to reduce metal or carbon oxides by hydrogenic plasma bombardment to form volatile species, thus depleting the contamination layers on the wall surfaces. These volatile substances, such as water vapour, methane and hydrocarbons, are then desorbed from the surface, both thermally and by particle impact, and ultimately evacuated from the device via the torus pumping system. Two key factors for achieving a large cleaning effect are the maximum volatile substance formation by plasma discharge, and the effective exhaust of the formed impurities before they are re-ionized, so that these impurity products are not re-ionized, dissociated and re-deposited on the surfaces in the cleaning plasma itself. This requires plasmas to have low  $T_e$  and a low ionization fraction. In addition, high wall temperatures are useful not only for increasing the rates of the reactions leading to the formation of the volatile species on the surface, but also for promoting their desorption from the surface. Furthermore, a large pumping speed is desired for efficient removal of the volatile species from the torus. The essential difference between various conditioning methods lies in the way the atomic hydrogen species are created and interact with the surface. Other effects such as charge exchange neutrals and sputtering due to high energy ion bombardment may also play a role.

The most effective method actually used for surface impurity cleaning is hydrogen or deuterium GDC. One or more anodes (normally two anodes are used for a uniform plasma discharge) are either located in portholes, or moved by a bellows assembly into the main volume of the vacuum vessel. The wall surfaces and limiters are at ground potential. Typical hydrogen pressures range from a few Pa to 0.1 Pa and the voltage between anode and cathode is of the order of a few hundred volts. Results from TEXTOR showed that a high wall temperature (over 350°C) is favourable for quick conditioning of the first wall during the GDC process. Oxygen contamination and water vapour of the vacuum

vessel can be very effectively removed by long glow discharges (~100 hours). Helium glow discharge conditioning for hydrogen removal has been optimized in DIII-D [7.48] and routinely used between each tokamak discharge. It has been instrumental in achieving high-performance H-mode plasmas and a wide operating space in DIII-D where major parts of the surface were covered by graphite.

However, due to the presence of high permanent magnetic fields, conditioning techniques based solely on glow discharges cannot be used. In future superconducting devices, such as ITER, which will be operated over long discharge durations and use deuterium/tritium mixtures, new techniques for wall conditioning are needed, firstly to obtain reproducible and controlled plasma discharges and secondly to reduce the tritium wall inventory after each discharge. ECR and ICR conditioning techniques have been carried out during the past ten years and very good results have been obtained.

The application of ECR conditioning in fusion devices was already studied in the 1980s in JFT-2, JIPPT-II, JFT-2M and the Gamma-10 tandem mirror [7.49]. A comprehensive review of ECR discharge cleaning in toroidal devices has been given by Sakamoto [7.50]. Due to its importance for future reactors, more experiments have been performed recently in Alcator C-Mod [7.51], LHD [7.52], TRIAM-1M [7.53], JT-60U [7.54] and HT-7. Comparisons of hydrogen-ECR and glow discharge cleaning have been made in TEXTOR and show similar cleaning effectiveness [7.55].

ICR conditioning is based on the presence of ion cyclotron resonant layers existing inside the vacuum chamber, which easily produce plasma breakdown with a suitable fuelling gas. Normally, ICR hardware is the same as that used for ICRF heating. With an RF power from 10 to 100 kW and toroidal magnetic field from 0.2 to 2 T, a wide range of breakdown gas fuelling pressures from 0.1 Pa to  $1 \times 10^{-3}$  Pa could be used. ICR experiments have been performed in Tore-Supra [7.56], TEXTOR [7.57], HT-7 [7.58, 7.59] and W7-AS [7.60] since 1996. Two kinds of ICR plasmas were used, continuous and pulsed modes. Extensive ICR conditioning has been routinely used in HT-7 for wall cleaning, recycling and isotopic control, by using helium and different working gases, and oxidation by using either pure oxygen, or a mixture of helium and oxygen. In HT-7, ICR conditioning techniques showed higher particle removal rates than GDC and ECR.

In the review paper [7.61], detailed comparisons are made between the IC and EC conditioning techniques, including the principal plasma parameters, cleaning efficiency and possible mechanisms. Table 7.3 lists the characteristics and discharge parameters of these two different techniques.

TABLE 7.3. ICC AND ECC DISCHARGE PARAMETERS IN DIFFERENT FUSION DEVICES [7.61]

	V [m <sup>3</sup> ]	B [T]	p [Pa]	P <sub>in</sub> [kW]	P <sub>in</sub> /N [kW.Pa <sup>-1</sup> m <sup>-3</sup> ]	n <sub>e</sub> [10 <sup>17</sup> m <sup>-3</sup> ]	T <sub>e</sub> [eV]	T <sub>i</sub> [eV]
ICC Tore Supra	50	4	10 <sup>-3</sup> -10 <sup>-1</sup>	20- 300	5-5x10 <sup>3</sup>	0.5-6	2-6	10- 1000
ICC Textor	10	0.1- 2.5	5x10 <sup>-3</sup> - 10 <sup>-1</sup>	30- 800	5x10 <sup>2</sup> -5x10 <sup>4</sup>	0.5-30		
ICC HT-7	2	03.- 1.2	10 <sup>-3</sup> - 5x10 <sup>-1</sup>	5-50	10-5x10 <sup>3</sup>	0.5-3	3-10	1000
ICC W7-AS	7	2	3x10 <sup>-3</sup> - 6x10 <sup>-2</sup>	10- 120	30-5x10 <sup>3</sup>	1-30	20	
ECC Textor	10	2	10 <sup>-2</sup> - 5x10 <sup>-2</sup>	100- 300	10 <sup>3</sup> -5x10 <sup>3</sup>	10-20		
ECC TRIAM-IM	0.5	0.08	1	1	2	0.2	6	
ECC TOMAS	1	0.1	2.5x10 <sup>-2</sup>	1	40	0.2-1.6	2-10	1-3
ECC Alcator-C	1	0.07- 0.1	4x10 <sup>-2</sup> - 2x10 <sup>-1</sup>	3	15-75	0.03-0.17	10-20	2-10

It is clearly shown in the table that for future application in ITER, ICR has more favourable features, since it can be run at full toroidal field without the need for extra hardware and with high conditioning efficiency at high density. The improved conditioning efficiency is attributed to a large symmetric flux of energetic CX neutrals of up to several keV, which desorbs molecular species from the entire first wall, and its low electron temperature of 2–5 eV, which avoids strong molecular breakup of the desorbed species from and subsequent re-deposition onto the walls, thus allowing the pumping of the molecules at high rates.

#### 7.4.1.2. Plasma assisted coating of thin films

Deposition of low-Z films, such as carbon, boron or silicon, is very effective at suppressing metal impurities and reducing oxygen content due to the gettering effect. High quality homogeneous thin films can be deposited on the first wall with plasma chemical vapour deposition. The plasma assisted coating techniques (carbonization [7.62], boronization [7.63], siliconization [7.64]) have been pioneered by the TEXTOR team. Thin film wall coating has been demonstrated in the past to be very efficient for impurity control. The hydrogen content is initially high but as it is reduced (e.g. with helium GDC), strong wall pumping and low recycling conditions can be achieved. Plasma performance has been significantly improved by applying these techniques. Among these techniques, boronization

provides a most effective means for improving plasma performance. The roles of the thin boron film have been identified experimentally as:

- (a) Suppression of oxygen contamination to core plasma;
- (b) Reduction in hydrogen recycling;
- (c) Suppression of contamination by wall material;
- (d) Action as a protecting layer against energetic charge exchange particles.

The equipment used for plasma assisted coating is almost the same as that normally used for glow discharge cleaning. One or more anodes are installed inside the tokamak vessel, with a continuous gas feed and the torus pumping system. Sometimes an RF system with 1 kW of power may be used to achieve a more stable glow discharge plasma if hazardous gases are introduced into the torus. In the presence of hazardous gases, such as  $B_2H_6$ ,  $SiH_4$ ,  $B_{10}H_{14}$ , or their deuterated equivalents, special vacuum components and operation procedures for gas injection and pumping systems are required to ensure safe handling. The molecules of the reactive gases are partly ionized in the glow plasma and accelerated in the sheath onto walls, limiters or divertor plates, which act as the discharge cathode. By using different working gases, different films, such as C, B or Si, can be deposited on the wall with a mean thickness of about 50–100 nm. In addition, ‘solid target’ boronization has been developed by Boucher et al. [7.65]. The uniformity of the film coated along the toroidal and poloidal directions by using glow discharges varied by a factor of 3–5, depending on how many anodes were used. Using high flow rates, toroidally distributed multiple gas injectors, more anodes and “pulsed glow” has improved the homogeneity.

In the presence of the toroidal magnetic field, ECR and ICR plasmas have been used for thin film coating. Boronization with low pressure ECR discharges has been performed in Heliotron E [7.66] and some laboratory work [7.67]. The plasma was produced at a pressure of  $10^{-2}$  Pa by injection of  $\sim 1$  kW of microwave power at 2.45 GHz, with a toroidal field of about 0.08 T, producing a boron layer about 100–200 nm thick. Analysis showed that the deposition process in ECR discharges is mainly due to neutral hydrocarbon bombardment. In most cases, the layer formation is inhomogeneous and the films are limited in thickness.

ICR boronization using the less hazardous carboranes  $C_2B_{10}H_{12}$  was fully developed in HT-7 [7.68] and became a routinely used coating process. Carborane is solid and needs to be heated to over 100°C before introduction into the torus, with a much simpler exhausting system. Pulsed RF plasmas with a magnetic field of 2 T and 20 kW of RF power were produced by using a mixture of 50% of carborane ( $C_2B_{10}H_{12}$ ) with 50% of helium. The boronization process lasted a few hours and was followed by an He ICR plasma for removing the high hydrogen content in the film. A fine homogeneous and hard a-B/C:H film was produced by a pulsed ICRF plasma. The film shows stronger adhesion,

greater thickness and longer lifetime compared with those produced by the GDC method. Good uniformity of the film in both toroidal and poloidal directions has been obtained by using a long antenna on the high-field side of the vessel. The re-emission of hydrogen was easily controlled by using a helium ICR discharge after boronization, leading to very strong wall pumping. The plasma performance was significantly improved after boronization, with a higher density limit and wider operation space being obtained. In addition, the hard X rays accompanied by high power lower hybrid current drive were dramatically suppressed. This gives direct evidence that the thin boron film serves as a protecting layer against the energetic particles, which is very important for future long-pulse operation.

RF siliconization was also performed in HT-7 and EAST by using a silane ( $\text{SiH}_4$ ) gas mixture (10%) with helium (90%) to facilitate gas handling. The RF discharge was operated in pulsed mode with a 1 s on, 1 s off cycle, and by using the long ICRF antenna side of the vessel. This results in a homogeneous coating in the toroidal and poloidal directions with a film thickness of 50–80 nm. The promising results obtained from ICR plasma assisted deposition have shown that such techniques are applicable to future superconducting fusion devices with a fully W wall after disruption or quick startup of plasma discharge even if the coating techniques are not foreseen in ITER.

## 7.4.2. Impurities and dusts

### 7.4.2.1. Impurities

Generally speaking, plasma impurities have two main effects on plasma performance: the radiation of power and the dilution of the hydrogenic species. The power loss by line radiation increases strongly with  $Z$ . Total radiative power is  $P_r = n_e \sum n_z R(T_e)$ , where  $R$  is the radiation parameter for different atoms. The radiation parameter for some impurities is shown in Fig. 7.16. The energy loss by bremsstrahlung radiation is proportional to  $Z^2$ . Plasma impurities also lead to the dilution of hydrogenic fuel. Plasmas, once contaminated, tend to be further polluted at an enhanced rate. Upon approach to the surface, impurity ions are accelerated in the sheath up to a total impact energy,  $E \sim qV_{sh} + 2T_i$ , where the sheath potential  $V_{sh} \sim 3.8T_e / e$ . These multiply charged impurity ions lead to enhanced erosion by sputtering.

The mechanism of impurity generation is very complex. Several mechanisms have been identified and well studied in the last few decades, such as backscattering, thermal desorption, physical sputtering, chemical sputtering and radiation enhanced sublimation. In addition, a plasma disruption always leads to impurity generation, which seriously affects plasma performance of the subsequent discharges.

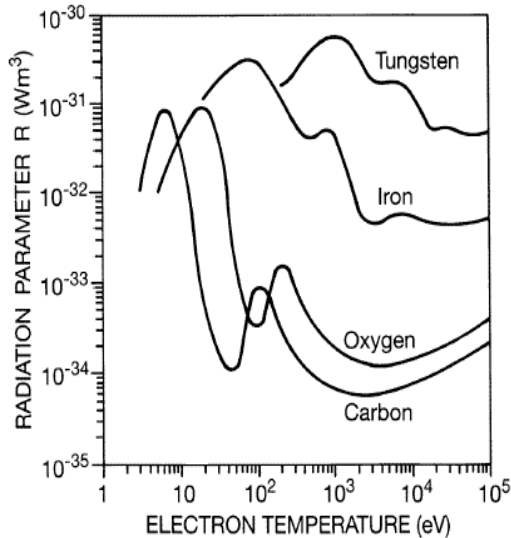


FIG. 7.16. Radiation parameter  $R$  of various plasma impurities as a function of  $T_e$ .

Among most impurities, oxygen plays a particular role, especially in devices with graphite covered walls. Oxygen chemical sputtering forms  $\text{CO}$  and  $\text{CO}_2$  with an elevated yield close to unity, even at room temperature. Under graphite wall conditions, chemical sputtering is much stronger than physical sputtering, especially at the graphite divertor target. Thus, chemical sputtering due to D/T, oxygen and carbon offers an additional, important erosion mechanism [7.69].

With the use of a divertor, particle and power loads can be relatively easily controlled by choosing a proper divertor configuration. High plasma density in the divertor results in a very good shielding to the impurities originated from the target plates. Divertor targets are exposed to strong power and particle fluxes, which can lead to erosion by sputtering, as well as macroscopic erosion processes, such as melting, evaporation or sublimation due to large transient heat loads, for example an ELM or disruption. For high- $Z$  target materials, impurity-induced physical sputtering has been identified as the dominant cause of material erosion [7.70]. In particular, self-sputtering of high- $Z$  impurities can contribute significantly to impurity-induced sputtering processes [7.71].

In contrast to the divertor, erosion rates at the first wall are predicted to be sufficiently low, so that the tiles do not need replacement. However, because of the large wall area, the total amount of eroded material is significant. This is the main reason for choosing beryllium as the first wall material for ITER, which has a very large first wall surface area,  $\sim 700 \text{ m}^2$ . It is to be noted that impurities produced in the main chamber are more efficient in contaminating the core plasma, especially those from the first wall surfaces physically close to the core, which receive considerable ion fluxes. These impurity sources may be

concentrated near the main-chamber components such as protection limiters, RF antenna and the baffles near the divertor entrance. In addition, neutrals, including impurities, originating from the divertor may leak into the main chamber and interact directly with the walls, contributing to the overall wall source.

#### 7.4.2.2. *Dusts*

Dust is produced inside the vacuum vessel of a tokamak by the interaction of the plasma with the components of the first wall and the divertor. Dust has received little attention for the past few decades, mainly because it is neither a safety nor an operational problem in existing tokamaks. However, ITER design has highlighted the fundamental need for an understanding of the production of dust in next generation burning plasma devices, since it is regarded as a potential safety hazard, which may be toxic, radioactive and/or chemically reactive. The hazard of dust depends on the dust composition, how much dust is produced and how well the dust is confined. Since small carbon particles can retain large amounts of hydrogen, dust will also influence the T inventory. It is likely that dust formation in and transport from the divertor region can play an important role in core plasma contamination.

Measurements of dust concentration, diameter, surface area, porosity, chemical composition and activity have been carried out during the maintenance periods of several tokamaks. Winter [7.72] reviewed dust in magnetic confinement fusion devices and its impact on plasma operation, mainly based on TEXTOR-94 experimental data. More comprehensive data were reviewed in Ref. [7.73], which includes many different machines, especially JET and TFTR, where T was used. The INEEL Fusion Safety Program has collected dust data from major world tokamaks, such as DIII-D, Alcator C-Mod, Tore-Supra, ASDEX-Upgrade and TFTR following typical run periods, and extensively analysed the collected dust to determine the composition, particle size distribution and specific surface area [7.74–7.77].

The concentration of dust in a tokamak varies with location and wall material. Normally, the size distribution of the identified particles extends from about 100 nm up to the mm range. In TEXTOR, about 15% of the particles are ferromagnetic, independent of the size. It is very likely that these particles were completely molten and that the phase separation occurred during resolidification. Even though the mechanism of dust formation and distribution is still not fully understood, it is clear that dust is usually induced by erosion, co-deposition arc, melt layer and wall conditioning processes (such as siliconization, boronization, Li coating). By properly aligning and shaping target tiles on the divertor and limiter, dust formation can be reduced significantly. In JET, many millimetres were eroded from some tile edges by the plasma, which was most likely responsible for the light dusting of carbon based materials observed

over the interior of JET at the time. The divertor of JET was modified in 1992 to avoid exposed divertor tile edges. As a result, discharges could be run at high power levels for longer periods without impurity problems, and the amount of dust observed in JET since 1994 has been greatly reduced. Similar results were obtained in TFTR [7.78].

### 7.4.3. Erosion and re-deposition

Erosion and re-deposition of wall materials are key issues in tokamak research, especially for next-step burning plasma experiments such as ITER. Net erosion can severely limit the lifetime of divertor target plates, and subsequent material re-deposition and trapping of tritium fuel is of economic and safety concern. However, data are limited by restricted access to machines and the lack of experimental methods which provide real time erosion information. Furthermore, comparison between erosion/deposition processes depends strongly on local plasma conditions in various machines that in most cases are not well known. However, dedicated experiments, notably in DIII-D and ASDEX-Upgrade, with good near surface plasma diagnostics, and in situ and ex situ erosion measurements have verified erosion/deposition models for several materials and plasma regimes. However, the present database on net erosion is still in a preliminary state and much more experimental work is needed.

#### 7.4.3.1. Divertor erosion and re-deposition

In a tokamak with a divertor configuration, the most intense interaction occurs at the strike point of the separatrix, between the plasma and the divertor target plate. Erosion studies have been carried out on a large number of tokamaks, such as JET [7.39, 7.79] and DIII-D [7.80]. In spite of the differences in divertor plasma parameters and between long term exposure and single discharge erosion, the data are in good agreement and show a strong decrease of the erosion rate with the atomic mass of the target material.

The balance between carbon erosion and re-deposition depends strongly on the plasma temperature and divertor geometry. For most of the current divertor experiments, the electron temperature at the inner divertor strike point is lower than at the outer divertor strike point, usually leading to detachment in the inner divertor. This results in deposition at the inner strike point and erosion at the outer strike point.

Federici et al. [7.73] reviewed the co-deposition processes in many tokamaks. It is found that the intense co-deposition of carbon and deuterium occurs in the regions which are shaded from direct ion bombardment, but near the carbon surfaces exposed to high ion fluxes. Since ions cannot reach these shaded surfaces, the observed carbon deposition can only be due to neutral

carbon atoms or molecules. Note that physically sputtered atoms are unlikely to return to the surface as neutrals; instead, they will be ionized and return to surfaces intersecting field lines. However, carbon surfaces exposed to large fluxes of hydrogenic ions, such as divertor strike points, may be a strong source of hydrocarbon molecules produced by chemical sputtering. A large fraction of these carbon impurities can promptly return to the nearby surfaces as energetic neutral carbon or hydrocarbon radicals. Chemical erosion followed by molecular dissociation will, therefore, result in intense recycling of neutral carbon and hydrogen back and forth between the plasma and the surface, thus leading to the carbon deposition on the surfaces shaded from the plasma. Beryllium and carbon can both be eroded from the plasma contacting regions, but only the carbon can be deposited as neutrals into the shaded regions. This process might be used as an active means to localize the deposition of carbon in the regions where it can be readily removed or heated, to thermally release co-deposited tritium.

#### *7.4.3.2. Limiter erosion and re-deposition*

Long-term erosion and deposition studies on limiters have been carried out in JET, TEXTOR [7.81], TFTR [7.82] and HT-7 [7.83]. Both net erosion of the order of a micrometre and net deposition were observed, depending on the tile shaping. Theoretical and experimental simulations indicate that sputtered carbon can be transported deep into the scrape-off layer by diffusion and into the gap between tiles by multiple reflections off the faces of the gap. Deposition in the gaps was more pronounced between the tiles which were erosion dominated on their plasma facing surfaces, indicating local re-deposition. Net erosion on the fine grain graphite tiles used in HT-7, which is a long pulse (~100 s) operating machine, was much greater than that in TEXTOR and TFTR. The net erosion rates dropped by a factor of 5–10 with the use of doped graphite tiles with 50–100  $\mu\text{m}$  SiC gradient coatings in HT-7, which have much lower chemical sputtering at high temperatures and exhibit superior surface characteristics for a sufficiently long life. Under long term plasma operation, the doped graphite tiles with SiC coating showed high resistance to physical and chemical sputtering.

For divertor tokamaks such as ASDEX-Upgrade and Alcator C-Mod, investigations have shown that, even at several decay lengths outside the separatrix, moderate ion fluxes can reach limiter structures, and lead to characteristic erosion/deposition patterns.

#### *7.4.3.3. Main chamber wall erosion and re-deposition*

The first wall of a tokamak is not a homogenous surface. Typically, the inner wall is covered by well aligned tiles, while the outer wall houses different components, such as antennas, passive stabilization coils, protection limiters.

The large areas of the vessel wall behind the protection limiters are subject to charge exchange neutral bombardment. Therefore, erosion and re-deposition at the main chamber wall have a strong correlation with charge exchange fluxes. When erosion in the divertor is suppressed, for example during operation with detached divertor plasmas, the main chamber wall can become the dominant source of impurities.

Theoretical modelling of the ITER first wall [7.84] showed that the erosion rate is about 0.3 nm/s for beryllium, which would lead to significant tritium co-deposition in re-deposited beryllium (~1–6 g (of tritium)/400 s pulse), but very low (~0.002 nm/s) for tungsten. This clearly shows that a beryllium first wall does not extrapolate to a demonstration or commercial fusion reactor, due to its short lifetime limited by erosion, coupled with the non-trivial tritium co-deposition issues. In contrast, there is no erosion, and hence no tritium co-deposition problems foreseen, for tungsten, because of its very low sputtering yields for D-T. Therefore, it would be prudent to consider a tungsten wall for ITER, at least at some point in the experimental programme.

#### 7.4.4. Hydrogen isotope retention and removal

Hydrogen isotope retention is one of the critical issues for future D-T tokamaks. For present-day tokamaks, hydrogen retention and re-emission from PFCs affects neutral recycling in the plasma boundary and the overall plasma density control. For next-step burning plasma experiments, such as ITER, most of the tritium is likely to be retained in the deposited carbon layers in the divertor region, particularly in the plasma shadowed area; this which is hard to remove and could become a safety issue. Tritium retention poses serious challenges for ITER operation. Even with a much more modest duty cycle than DEMO, the ITER tritium inventory limit could be reached in a few weeks of D-T plasma operations with a CFC divertor. However, there is not yet an effective means available for removing tritium to ensure continued D-T operation for ITER. It is absolutely necessary to understand the short-term and long-term hydrogen isotope retention characteristics of the individual materials used for the first wall and divertor.

For graphite or other carbon based materials, four essential mechanisms have been identified for the uptake and retention of hydrogen:

- (1) Buildup of a saturated surface layer;
- (2) Chemisorption on inner porosity surfaces;
- (3) Intergranular diffusion and trapping;
- (4) Co-deposition of hydrogen with carbon on plasma exposed surfaces.

Co-deposition is foreseen to be the dominant mechanism for hydrogenic retention in ITER. Retention by other mechanisms such as implantation and

surface adsorption, which may be significant for small short-pulse machines, is expected to rapidly reach saturation in ITER. A major advantage of the use of tungsten as the PFC is that its retention of hydrogen is negligibly low at the ITER operating temperatures. This has been measured in various beam experiments, and confirmed in the tungsten experiments in present machines, mainly in ASDEX-Upgrade.

For ITER, tritium removal is still a major unsolved development task if carbon plasma facing components are going to be used for the divertor. Efforts have been made during past decades for meeting the requirements for ITER, including both laboratory work and tokamak experiments. The presently envisioned methods for the removal of tritium from ITER are reviewed in Refs [7.85, 7.86] and can be roughly divided into the following categories:

- **Oxidation methods:** Remove the C deposits by oxidation, which transforms carbon into CO and CO<sub>2</sub> and thereby releases the incorporated T, mainly in the form of tritiated water. Baking and glow discharge cleaning (GDC) with oxygen gas has been investigated in TEXTOR and HT-7. Oxygen GDC showed a much higher H removal rate than oxygen baking; the latter only exhibits a transient effect.
- **Conditioning methods:** Control wall tritium retention during tokamak discharges through various wall conditioning techniques, as described in Section 7.4.1. In particular, a further advance has been made recently in wall conditioning with ICR plasmas in the presence of the toroidal magnetic field. Oxygen ICR has been extensively carried out in HT-7 and recently in the fully superconducting divertor tokamak EAST. Using a mixture of O/He working gas, very high H removal rates can be readily obtained. By using boronization after oxygen ICR, very good plasma discharges can be achieved. These techniques have been shown to be effective at removing the retained fuel from the plasma facing components and may be applied routinely in ITER, to release tritium from the surrounding walls.
- **Surface heating:** Thermally release tritium from the re-deposited hydrocarbon film or ablate the film itself by the external heating, for example using a laser or flash lamp. White has proposed using the end of plasma discharges in ITER for tritium removal by inducing a radiative collapse [7.87].

None of the methods mentioned above are sufficient to meet the ITER tritium removal requirements at the present time. Further development is required. CFC will be replaced with W when ITER starts D-T operation; the T removal issue for ITER would be much easier when a full W divertor is used.

## 7.5. CONTROL OF PLASMA–WALL INTERACTIONS

### 7.5.1. Divertors

#### 7.5.1.1. Introduction

The original divertor concept was proposed by Spitzer [7.88] in the early 1950s to deal with two intrinsic deficiencies of conventional limiters. First, because the limiter is in direct contact with the main plasma, impurities produced by the impact of the plasma on the limiter can penetrate straight into the core and degrade plasma performance. Second, limiters provide only limited opportunities for achieving efficient edge pumping, which is essential for density control and the exhaust of helium “ash” in a fusion reactor. Various divertor configurations have been explored, but the axisymmetric poloidal field divertor configuration has proved to be most successful. It is produced by using additional poloidal field coils to create, typically, one or two nulls in the poloidal field. In this case, the separatrix, i.e. last closed magnetic flux surface, is determined entirely by the magnetic field, in contrast to the limiter configuration, where the separatrix is determined by the position of the limiter. As an example, Fig. 7.17 shows the limiter and divertor configurations employed in JET. The use of divertors moves the location of the principal plasma–surface interaction away from the confined plasma, thus facilitating impurity control. In addition, by guiding the plasma exhaust stream into the divertor region, the neutralization at the divertor target plates can result in a high neutral gas pressure, allowing efficient pumping. Furthermore, divertor operation allows the possibility of achieving low plasma temperature at the target plate, accompanied by strong volume losses, such as

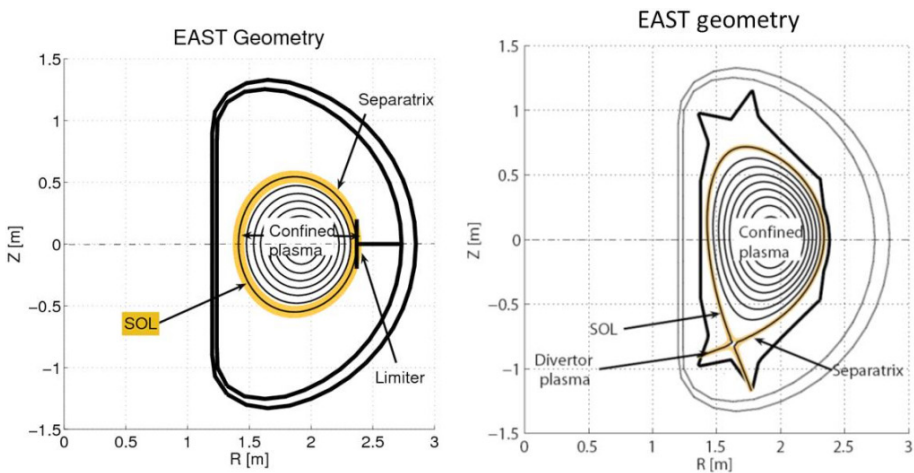


FIG. 7.17. Limiter and divertor configurations employed in EAST.

radiation, charge exchange and recombination. This not only reduces impurity production and erosion at the target plate, but also provides an effective means for controlling the power reaching the divertor plate, which is one of the major concerns for high power and long pulse operation.

7.5.1.2. Divertor operation regimes

Figure 7.18 shows a sketch of a single null poloidal divertor configuration produced simply by using an additional poloidal field coil with current flowing in the same direction as the main plasma current. The SOL surrounds the confined plasma outside the separatrix, intercepted by the divertor targets at both ends. Power and particle fluxes enter the SOL and exit from it either along the magnetic field lines directly to the divertor target plates, or across the magnetic field lines to the vacuum chamber walls. In contrast to the confined region, the plasma in the SOL is not confined and its parameters change drastically both parallel and perpendicular to the magnetic field  $\vec{B}$ . Parallel energy transport is determined by classical conduction and convection, with kinetic corrections to heat diffusivities at low collisionalities, but perpendicular transport is turbulent in nature.

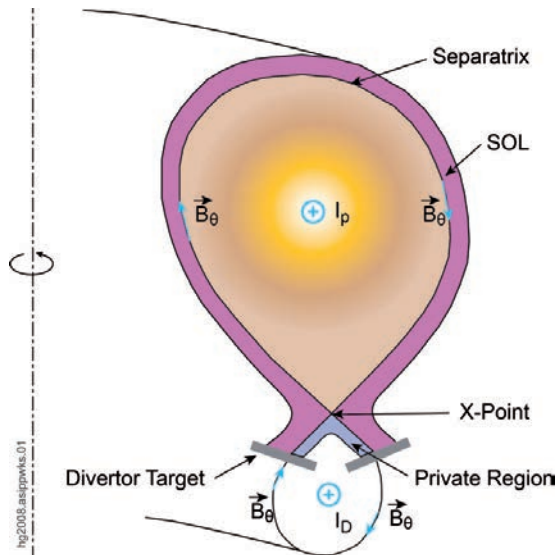


FIG. 7.18. Sketch of a simple, single null poloidal divertor configuration, produced by driving the current  $I_D$  in a poloidal field  $B_\theta$  coil in the same direction as the main plasma current  $I_p$ , forming an X-point at the bottom.

Experimental investigations have shown that turbulent transport in the SOL region is highly intermittent and dominated by radial motion of plasma filaments,

manifested as blobs in the plane perpendicular to the magnetic field. Such intermittent “transport events”, with radial velocities well exceeding  $500 \text{ m}\cdot\text{s}^{-1}$ , may significantly influence plasma interaction with main chamber walls in future long pulse devices.

The divertor SOL exhibits three distinct regimes, as described below, and can be characterized by the collisionality, i.e. the number of collisions that particles undergo in the SOL before reaching the divertor target along the field lines:

$$\nu^* \equiv L_c / \lambda \quad (7.22)$$

where  $L_c$  is the connection length being  $L_c = \pi R q$  for a single-null divertor configuration, and  $\lambda$  is the Coulomb collision mean free path being  $\lambda = \lambda_i - \lambda_e \approx 10 \times 10^{16} T_e^2 / n_e$  for  $T_i = T_e$  [7.8]. Since the parallel (along  $\vec{B}$ ) plasma transport is largely understood, the basic features of the divertor SOL can be determined by a fluid model based on the classical laws of conservation of particles, momentum and energy.

#### 7.5.1.2.1. Sheath-limited regime

At low collisionality, the divertor SOL is in the so-called “sheath-limited” regime, as characterized by  $\nu^* < 10$  [7.89]. In this regime, the plasma is essentially isothermal along  $\vec{B}$ , the energy losses are predominantly limited by the heat transmission property of the sheath. Thus, energy loss is governed by the heat transmission properties of the sheath at the boundary, i.e. the divertor target plates, as described in Sections 7.2.1.2 and 7.2.1.3. The major characteristics of the sheath-limited plasma regime are summarized as follows:

- (1)  $T = T_t = T_u = \text{constant}$  along  $\vec{B}$  and  $n_t = 0.5n_u$ ; here  $n_u$ ,  $T_u$  and  $n_t$ ,  $T_t$  are the density and temperature at the upstream far away from the target, and divertor target respectively, and thus

$$n_t T_t = \frac{1}{2} n_u T_u \quad (7.23)$$

- (2) Particle flux to the target surface is:

$$\Gamma_t = n_t c_{st} = \frac{1}{2} n_u c_{st} \quad (7.24)$$

where  $c_{st}$  is the ion sound speed at the target plate, i.e.

$$c_{st} = \sqrt{\frac{(T_i + T_e)_t}{m_i}} \quad (7.25)$$

with subscript  $t$  standing for target.

(3) Power flux to the target surface is

$$q_{\parallel} \approx \gamma_{sh} \Gamma_t T_t \tag{7.26}$$

where  $\gamma_{sh}$  is the sheath heat transmission factor, given by Eq. (7.3).

Note that in the sheath-limited regime, due to the acceleration of the ions by the pre-sheath electric field, as given by Eq. (7.15), the static pressure drops along  $\hat{B}$ , reduced to half of the upstream value, as given by Eq. (7.23). However, the total pressure including both static and dynamic pressure remains unchanged, i.e.  $p_t = n_t (T_i + T_e)_t + n_i m_i c_{st}^2 = n_u (T_i + T_e)_u = p_u$ . Here,  $p_u$  represents the pressure at the upstream where  $v_{th,i} = 0$ , usually close to the top of the machine for a single-null divertor located at the bottom of the machine. Note, however, that the actual flow pattern in the SOL is complex, and will be further discussed in Section 7.5.2.1.

The sheath-limited regime is representative of typical limiter SOL conditions. The plasma density is low and the temperature is high, leading to the erosion of the target plates and strong impurity production, as both physical and chemical sputtering yields increase with ion impact energy, and the latter also exhibits an enhanced yield at low incident fluxes.

7.5.1.2.2. Conduction-limited regime

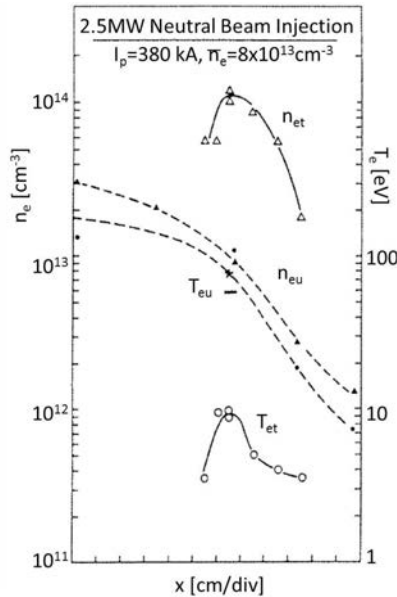


FIG. 7.19. Comparison of electron density and temperature profiles between upstream ( $n_{eu}$ ,  $T_{eu}$ ) and target ( $n_{et}$ ,  $T_{et}$ ), mapped to the divertor; in ASDEX [7.90].

Low plasma temperatures at the target can be readily achieved by simply raising the plasma density. As the collisionality increases, for  $\nu^* \geq 10$ , the plasma enters the “conduction-limited”, or “high-recycling” regime. In this regime, parallel (electron) conduction is limiting and temperature drops along  $\vec{B}$  are substantial, with the plasma temperature at the target significantly lower than that at the upstream. This was demonstrated in the earliest divertor experiments, for example in ASDEX [7.90], as shown in Fig. 7.19.

Since convection is not important, the basic relationship between the upstream plasma parameters and those at the target plates can be obtained using the “two-point model”, based on momentum and energy conservation, taking into account the sheath heat transmission properties and the boundary conditions on plasma flow at the sheath edge, as described above. Assuming particle recycling and ionization occur in a small region near the target, the energy and momentum sources or sinks can be neglected in the SOL. Momentum balance (see Eq. (7.11)) along the magnetic field leads to

$$n(T_i + T_e)(1 + M^2) = \text{constant} \quad (7.27)$$

or

$$nT(1 + M^2) = \text{constant} \quad (7.28)$$

for  $T = T_i = T_e$ . With  $M = 0$  at the upstream stagnation point and  $M = 1$  at the target, this leads to the same relationship between the upstream and the target pressure as for the sheath-limited regime as given by Eq. (7.23), which is rewritten here as

$$n_u T_u = 2n_t T_t \quad (7.29)$$

Note, however, that the simple relationship between the upstream and target density for the sheath-limited regime, i.e.  $n_t = 0.5n_u$ , does not hold for the conduction-limited plasma, as discussed later.

Due to  $v_i = 0$  over most of the SOL, except for a small region near the target, and poor ion thermal conductivity, heat transport along the SOL is predominantly by electron conduction, i.e.

$$q_{\parallel} = -\kappa_{0e} T_e^{5/2} \frac{dT_e}{dx} = \text{constant} \quad (7.30)$$

where  $\kappa_{0e} \sim 2000 \text{ W} \cdot \text{m}^{-1} \cdot \text{s}^{-1} \cdot \text{eV}^{-5/2}$  is the electron parallel heat conductivity coefficient,  $q_{\parallel}$  is the energy flow from the confined plasma across the separatrix, and is balanced by the heat flux across the sheath at the target, i.e.  $q_{\parallel} = \gamma_{sh} n_t T_t c_{st}$ , where  $c_{st} = (2T_t/m_i)^{1/2}$  is the ion sound speed at the target. Thus, we obtain the following relation between the upstream and target temperatures:

$$T_u^{7/2} = T_t^{7/2} + \frac{7q_{\parallel}L_c}{2\kappa_{0e}} \quad (7.31)$$

where  $L_c$  is the connection length between the upstream stagnation point and the target.

A close examination of the above simple model reveals the following key points:

- (1) The target temperature  $T_t$  is strongly influenced by the upstream density  $n_u$ . Thus raising the upstream density for a given input power and magnetic configuration provides an effective means for reducing  $T_t$ :

$$T_t \propto \frac{q_{\parallel}^{10/7}}{L_c^{4/7} n_u^2} \quad (7.32)$$

- (2) Raising  $n_u$  is also very effective for achieving the high target density  $n_t$ :

$$n_t \propto n_u^3 q_{\parallel}^{-8/7} L_c^{6/7} \quad (7.33)$$

- (3) The particle flux  $\Gamma_t$  exhibits a quadratic dependence on  $n_u$  in this conduction-limited regime, which is thus also named “high-recycling” regime:

$$\Gamma_t \propto n_u^2 \quad (7.34)$$

It is beneficial to achieve low temperature, and high density and particle flux at the target. First, operation at a low target temperature reduces sputtering, and hence erosion of the divertor target. Second, the divertor screening for impurities is strong at low temperature, high density, as discussed in Section 7.5.2.1, thus further reducing contamination to the confined plasma. In addition, achievement of high particle flux at the target is desirable for efficient pumping. However, the heat flux to the target remains an issue.

#### 7.5.1.2.3. Detached plasma regime

At low temperature and high density, the physics of the divertor is largely influenced by the presence of neutrals. The birth, history and annihilation of a neutral are controlled by recombination (target and volume recombination), ion-neutral interaction (charge exchange and elastic collisions) and electron impact ionization. Figure 7.20 gives the effective rates for volume recombination, charge exchange reactions and ionization. Figure 7.21 illustrates the following processes occurring in the divertor region:

- (1) Impurity radiation in the SOL and in the divertor;
- (2) Momentum and energy transfer by charge exchange (and elastic ion-neutral collisions) neutrals to the divertor chamber wall;
- (3) Volume recombination by three-body recombination, which becomes effective at low plasma temperature ( $<1$  eV);
- (4) Ionization and hydrogen radiation near the targets.

Impurity radiation mainly occurs in regions where the electron temperature is about 10 eV and higher, hydrogen ionization occurs near 5 eV and plasma recombination at 1 eV and lower.

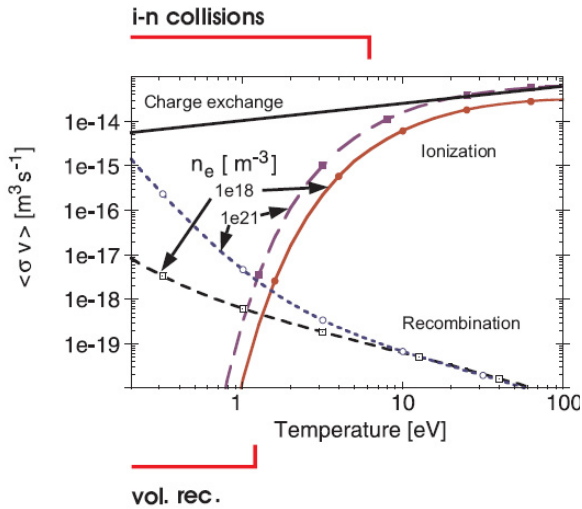


FIG. 7.20. Charge exchange, ionization and recombination rate coefficients for hydrogen.

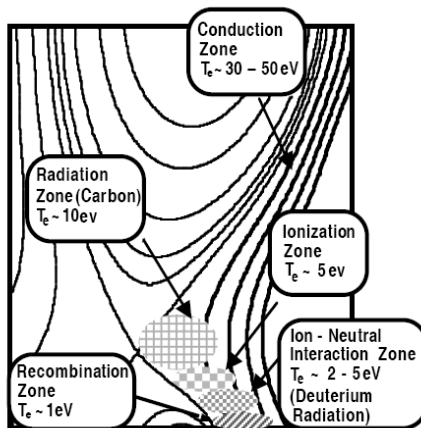


FIG. 7.21. Elementary processes in the divertor region.

At sufficiently low temperature, i.e.  $T_t \leq 1$  eV, and high density, volume recombination and charge-charge losses become important, and plasma pressure balance no longer holds. The plasma enters into the detached regime as a natural extension of the conduction limited regime at higher plasma density and/or lower power into the divertor (lower separatrix power or higher radiation). The transition from the conduction-limited regime to the detached regime occurs at  $\nu^* \sim 100$ . Detachment is characterized experimentally by the following main features:

- A reduction of ion fluxes to the target, possibly due to synergistic effects of recombination and ion-neutral friction;
- A reduction of plasma pressure near the target, possibly due to ion-neutral friction;
- A reduction in heat flux reaching the target plate by volume losses including radiation, recombination and charge-exchange.

Although the plasma detachment process is complex and is not fully understood, it can be readily achieved experimentally, for example by operating at sufficiently high plasma densities for a given input power. As an example, Fig. 7.22 shows the measurements from Langmuir probes at the upstream and the target for the different SOL operation regimes achieved in Alcator C-Mod [7.91]. As expected, for the low density, sheath-limited regime, the plasma is nearly isothermal and the total plasma pressure is essentially conserved between the upstream and the target. For the intermediate density, conduction-limited regime, the temperature at the target is significantly lower than that at the upstream, but the pressure balance is maintained, as predicted by the simple two-point model, i.e.  $2n_u T_u = 2n_t T_t$ . Note that the plasma pressure at the divertor target includes the contribution from the dynamic pressure. As the density is further increased to  $1.8 \times 10^{20} \text{ m}^{-3}$ , the plasma enters the detachment state, as manifested by a substantial drop in pressure between the upstream and the target. The plasma detachment is also influenced by divertor geometry, as discussed in Section 7.5.1.3.

Detached plasma offers a very attractive operation regime for fusion reactors in terms of power exhaust, erosion and impurity production at the target plates. However, the drop in particle flux renders it more difficult to pump helium ash produced by the fusion reactions. It is therefore desirable to achieve partial detachment, predominantly near the strike point, to reduce peak heat flux and maintain sufficient pumping. In most present tokamaks, the neutral mean free path is larger or comparable to the dimensions of the divertor plasma in detached conditions. This leads to the leakage of neutrals from the divertor, and hence the saturation or slower increase of neutral pressure in the divertor. For next-step

devices, such as ITER, it is expected that the divertor plasma will be sufficiently opaque to neutrals in partially detached conditions [7.92].

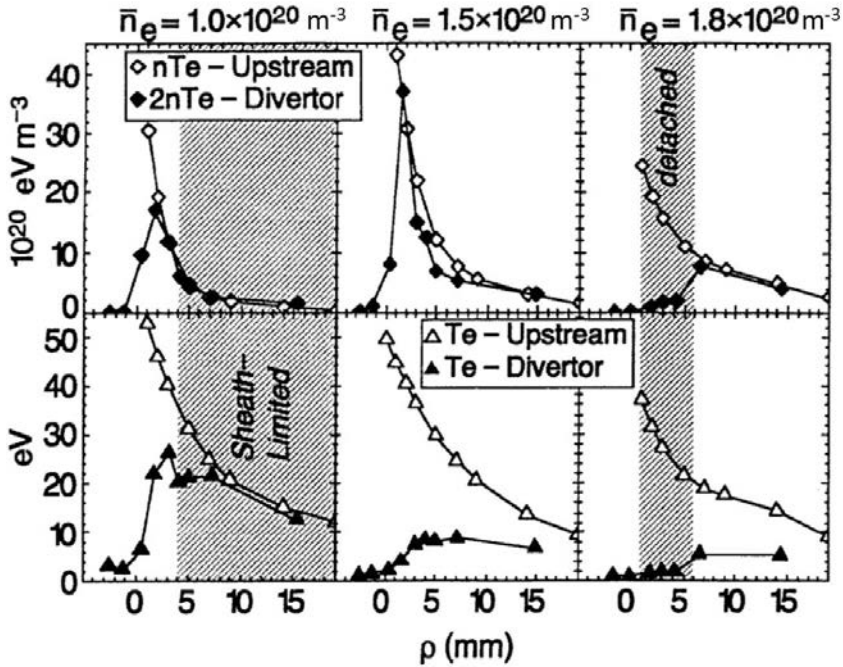


FIG. 7.22. Profiles of electron pressure and temperature (mapped to the midplane) at the upstream and the target for sheath-limited, conduction-limited and detached regimes, as measured by Langmuir probes in C-Mode [7.91]. Reprinted from Ref. [7.91]. Copyright (2011), American Institute of Physics.

### 7.5.1.3. Effect of divertor geometry

The fully closed poloidal divertor configuration with a separate chamber to place the divertor targets was investigated in early divertor experiments, for example in ASDEX, as shown in Fig. 7.23, which demonstrated the following key features:

- (1) Cold and dense plasmas at the divertor target plates;
- (2) Strong neutral compression in the divertor region;
- (3) Effective shielding for impurities.

As a consequence of divertor operation, a high-confinement H-mode was discovered by Wagner and his colleagues in ASDEX [7.93].

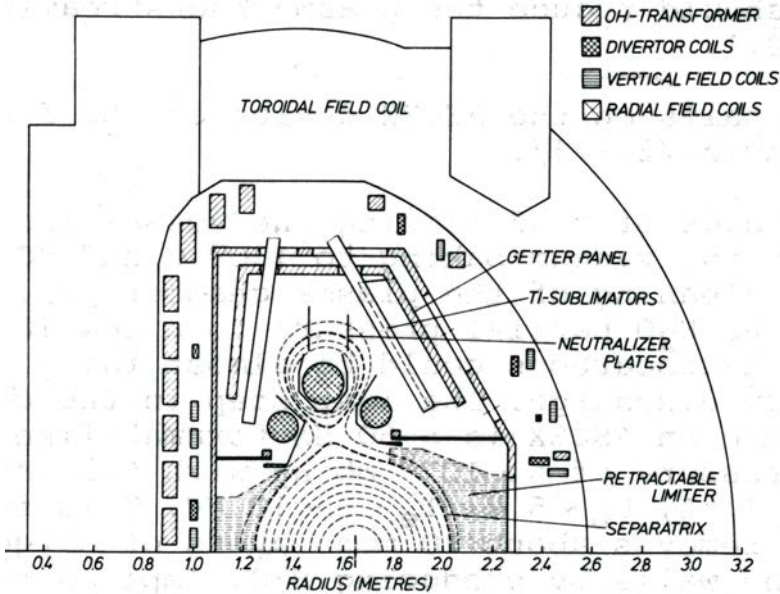


FIG. 7.23. Closed divertor geometry in ASDEX ([7.90] and references therein).

However, for a reactor, the closed divertor requires an additional superconducting coil installed within the toroidal coil cage, which is technically not realistic. Instead, an “open” divertor configuration was suggested by Ohya [7.94]. The first experimental tests of this concept were conducted in DIII and achieved similar results as with the closed divertor, albeit with less neutral compression in the divertor. The geometry of the open divertor concept is also compatible with high-elongation and high-triangularity plasma configurations that are beneficial in achieving high confinement and high  $\beta$ .

Extensive variations of divertor geometries have been evaluated since the 1990s, for example in ASDEX-Upgrade, JET, JT-60U, and Alcator C-Mod, ranging from simple, flat (horizontal) target configurations to more closed vertical or W-shaped target configurations, with/without the septum and with/without dome, etc. [7.95]. The basic consideration for optimizing divertor geometry lies in enhancing divertor closure and thus increasing neutral pressure in the divertor. First, it is essential to achieve significant pumping for helium ash removal and control of edge recycling. Second, the neutrals escaping from the divertor can cause charge exchange losses in the plasma and erosion of the main chamber wall, either directly by chemical sputtering or via charge exchange, which reduces the lifetime of the wall and leads to core plasma contamination, as divertor screening for impurities produced at the main chamber wall is poor, compared to those originated from the divertor target. Divertor closure is also influenced by magnetic configuration, as well as divertor plasma parameters. As

expected, increasing divertor closure enhances divertor neutral compression and thus pumping. To illustrate this, Fig. 7.24 shows the evolution of the divertor geometry in JET going from Mark I, Mark IIA/P to Mark IIGB with increased closure, and the corresponding divertor neutral pressures [7.96].

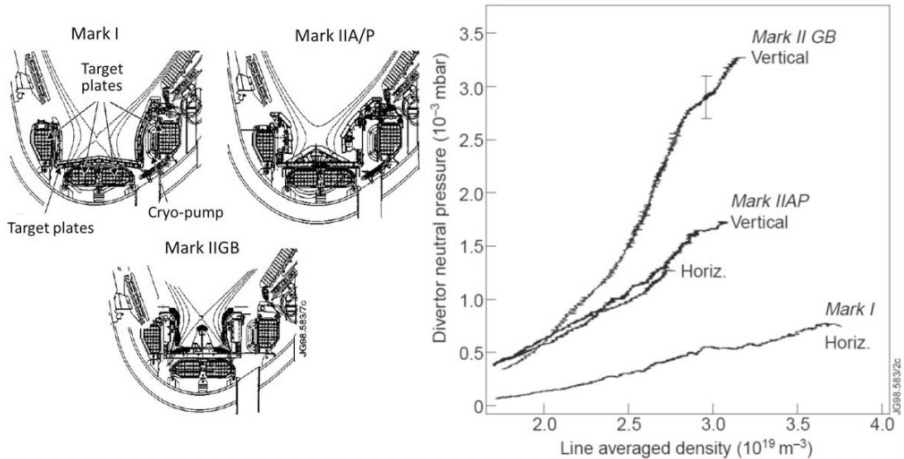


FIG. 7.24. Sketch of the three divertor geometries in JET, i.e., Mark I, Mark IIA/P and Mark IIGB with increasing divertor closure (left), and measurements of corresponding divertor neutral pressures for similar L-mode discharges (right) [7.96].

The principal objective of optimizing divertor geometry is to minimize the power load on the divertor target, which is a key issue for next-step burning plasma experiments. For ITER, it is required that up to 60% power flow across the separatrix be lost via volume losses, such as radiation, charge exchange and recombination, before reaching the target plate. This can only be achieved by operating in the detached regime, preferably with partial detachment near the separatrix strike point which is subject to the largest power loads, while maintaining attachment in the outer SOL region to ensure adequate pumping, as discussed in Section 7.5.1.2. This favours the vertical target configuration, which was first developed and applied on Alcator C-Mod [7.97]. With such a vertical divertor configuration, the recycling neutrals are emitted towards the separatrix, which becomes a region of preferential ionization, decreasing the temperature and increasing the density in its vicinity, thus promoting detachment near the strike point, as desired. On the other hand, for the horizontal target configuration, neutrals produced at the separatrix strike point are recycled in the outer part of the SOL, with detachment initiating at the corner of the divertor. The different neutral re-ionization patterns for the horizontal and vertical target configurations are shown schematically in Fig. 7.25.

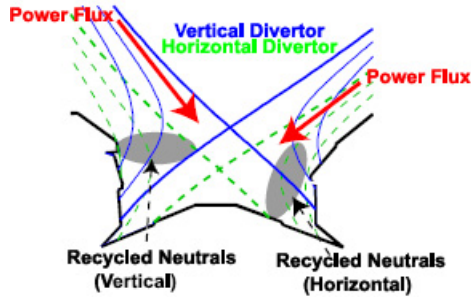


FIG. 7.25. Sketch of ionization patterns for recycling neutrals from horizontal and vertical target plates [7.98]. Reprinted from Ref. [7.95]. Copyright (2011), IOP Publishing Ltd.

It has been demonstrated that divertor operation with increased closure reduces the power load on divertor target plates by increased volume power losses and results in divertor detachment at up to ~20% lower main plasma densities, without affecting overall plasma performance.

The most commonly used divertor configuration is the single-null poloidal divertor configuration. The double-null configuration, i.e. with an X-point at both top and bottom, has also been explored in various divertor tokamaks, such as ASDEX, ASDEX-Upgrade, DIII-D, Alcator C-Mod and EAST (Fig. 7.26). The double-null configuration increases the divertor target area and accommodates significantly higher triangularity. The latter plays an important role in improving confinement and stability for the main plasma, as mentioned above. However, operation with the double-null may exacerbate divertor asymmetry in power loading due to physical isolation of the inboard and outboard SOLs. Further, it involves additional poloidal field coils and decreases the volume available for the confined plasma.

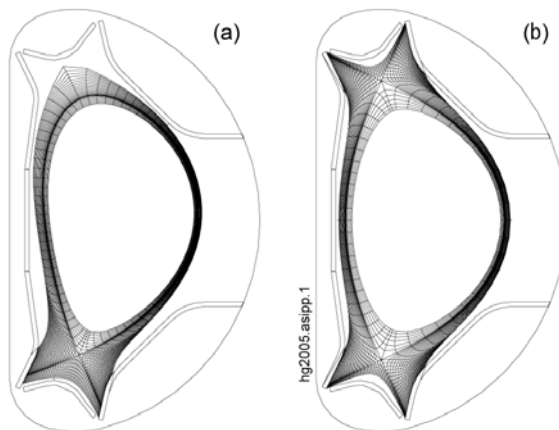


FIG. 7.26. Comparison of single-null and double-null divertor configurations in EAST [7.99].

## 7.5.2. Particle transport in the divertor SOL

### 7.5.2.1. Plasma flow and drift effects

#### 7.5.2.1.1. Basic divertor flows and impurity screening

The principal functions of divertors are to provide sufficient particle and heat exhaust and to simultaneously maintain efficient screening for the impurities produced at the target plates. Plasma flow in the divertor SOL affects the neutral compression, pumping and impurity shielding of divertors, as well as divertor tokamak material migration [7.100], thus playing an important role in divertor operation. In the simple picture, a small plasma flow is present in the SOL far from the divertor target due to acceleration by the small but finite pre-sheath electric field, which extends far beyond the sheath because of imperfection of sheath shielding. This flow is then further accelerated, towards the divertor target, by the presence of plasma sources, for example due to ionization or cross-field transport across the separatrix from the confined plasma, ultimately reaching the sonic speed with  $M_{\parallel} = v_{\parallel}/c_s = 1$  at the sheath edge near the target, as described in Section 7.5.1.2.

Strong plasma flows are naturally present in the divertor, resulting from local flux amplification due to recycled neutrals. The detailed flow pattern in the divertor plasma is determined by the spatial distribution of ionization sources, and can be strongly affected by the presence of drifts. Under typical high recycling conditions, both density and temperature profiles peak at the separatrix, thus resulting in a high ionization rate near the separatrix. Therefore, neutrals recycling from the target near the separatrix will be re-ionized locally near the separatrix. For vertical divertor configurations, most recycling neutrals from the other part of the target also tend to be re-ionized near the separatrix (see Fig. 7.25). Consequently, this may lead to a reverse flow directed away from the target near the separatrix. It should be noted that such reverse flows due to localized excess ionization sources are usually small compared with the sonic flow at the target [7.89]. On the other hand, significant flow reversal has been observed in a number of tokamaks [7.101, 7.102], usually above the X-point in the main SOL, and exhibits a strong dependence on the ion  $\nabla B$  drift direction, suggesting that drifts may play an important role in determining parallel flows in the divertor SOL. The drift flow is also suspected to be a contributing physics mechanism for in-out divertor asymmetries, as discussed later.

Divertor screening for impurities relies predominantly on the strong plasma flow naturally present in the divertor. In the divertor SOL, impurity ions are subject to two major forces, i.e. frictional drag imposed by the bulk plasma flow towards the target (in the absence of flow reversal) and the opposite ion temperature gradient force that tends to drive impurity ions along the temperature

gradient towards the main confinement chamber [7.89]. The efficiency of impurity screening is dependent on the impurity production mechanism and source distribution, background plasma conditions and divertor geometries:

- (a) **Physical sputtering and chemical sputtering:** Physically sputtered atoms exhibit typically a Thompson velocity distribution [7.103], with a most probable energy of  $1/2E_s$ , falling off at high energy as  $E^{-2}$ , for example  $E_s = 7.4$  eV for C and 8.8 eV for W (see Section 7.2.4.1). In contrast, chemically sputtered impurities such as  $CD_4$  are released with relatively low energy characteristic of the surface temperature. Therefore, the divertor screening efficiency for chemically sputtered impurities is relatively strong because those impurities can be re-ionized near the target where a large flow is present and frictional force drag is strong, in contrast to physical sputtering. This not only reduces the leakage of the impurities to the main chamber, but also mitigates the erosion of the target due to prompt re-deposition, as discussed in Section 7.4.3.1.
- (b) **Impurity source distribution:** Strong flows are present in the divertor, directed towards the target, at least in the region close to the target. Flow reversal may occur, but usually in the main SOL between the X-point and the outer midplane (for example, see Ref. [7.101]). As a result, the divertor screening is much stronger for the impurities originated from the target than those produced at the main confinement chamber walls.
- (c) **Divertor operation regimes:** As temperature decreases, the frictional force increases because of increasing collision frequencies of impurity ions with bulk plasma ions, while the temperature gradient force drops, thus improving impurity screening efficiency. It is therefore beneficial to achieve low temperature, high density divertor plasma conditions, for example by operating at the high recycling, or partially detached regimes. In addition, operation at low divertor temperatures reduces physical sputtering yields, which have a strong dependence on ion impact energy  $E_0 = 2T_i + 3T_e$  for  $D^+$  ions. At sufficiently low temperature  $E_0 < E_T$  (the threshold energy for physical sputtering), physical sputtering can be completely eliminated. Chemical sputtering yields also exhibit a significant reduction at low ion impact energy, in particular at relatively high surface temperatures, i.e. around 700 K for hydrocarbon production [7.104]. In contrast, for the high temperature sheath-limited regime, divertor screening is poor, which leads to significant impurity leakage to the main confinement chamber and compromising confinement of the core [7.105, 7.106].

- (d) Divertor geometry:** Increasing divertor closure was expected to also result in a reduction in impurity contamination to the confined plasma because of increased neutral compression and improved divertor pumping. This was observed in some L-mode plasmas, for example in JET [7.95, 7.105], as shown in Fig. 7.27, when moving from the Mark IIA/P divertor to the more closed Mark IIGB divertor (Fig. 7.24). Improvement in plasma purity leads to lower impurity radiation, increasing the density limit achieved in these L-mode discharges. However, no obvious changes were seen in H-mode discharges, possibly due to stronger impurity sputtering at the components forming the narrower entrance of the more closed divertor, thus offsetting possible improvements of divertor closure.
- (e) Divertor pumping:** Pumping in the divertor provides an active means of controlling impurities and hydrogenic recycling at the target plate, and is essential for helium ash removal in a D-T fusion reactor. The efficiency of divertor pumping is dependent on divertor geometry and the relative location of the strike point to the pumping slot [7.95, 7.107]. Increasing divertor closure increases divertor neutral pressure, facilitating neutral particle and impurity removal. Placing the strike point close to the pumping slot enhances ballistic scattering of neutrals into the pumping plenum and reduces the neutral backflow from the pump. In addition, strong divertor pumping, when combined with  $D_2$  puffing into the upstream SOL, may induce a significant SOL flow directed towards the divertor [7.108], increasing the divertor screening for impurities. Significant improvements in Ne/Ar enrichment in the divertor were obtained by using such a ‘puff and pump’ technique in DIII-D [7.108, 7.109] and JT-60U [7.110]. Improvement in helium exhaust was also seen in JT-60U with inner-leg divertor pumping [7.111].

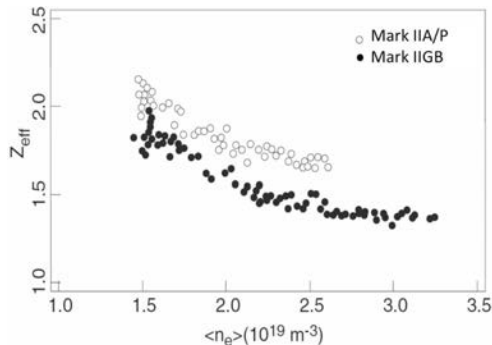


FIG. 7.27. Comparison of  $Z_{\text{eff}}$  in JET L-mode plasmas between the Mark IIA/P and more closed Mark IIGB divertors, showing improvement in plasma purity with increased divertor closure [7.105].

### 7.5.2.1.2. Divertor in-out asymmetries and drift effects

Strong in-out divertor asymmetries in the power and particle fluxes have been observed in many tokamaks [7.107], favouring the outer divertor. As a result, the plasma at the inner target tends to have a lower electron temperature and a higher density, leading to stronger radiation and earlier divertor detachment than at the outer divertor. It is important to reduce this asymmetry to distribute the power load evenly for high power, long-pulse operation. The divertor asymmetry appears to be largely attributed to:

- (1) Geometric effects, i.e. the larger surface area on the outboard side with more power flow across the separatrix entering the outer divertor SOL, and the compression of the magnetic flux surfaces on the outboard side due to the Shafranov shift, which would lead to stronger radial gradients and promote cross-field transport in the outside of the plasma, further favouring power flow into the outer divertor SOL;
- (2) Classical drift effects, as described below;
- (3) Enhanced transport on the outboard low field side (LFS), due to unfavourable magnetic curvature.

The details of LFS enhanced transport will be discussed in Section 7.5.2.2.

Divertor asymmetry is further exacerbated by divertor radiation that has a strong dependence on local plasma parameters. As discussed in Ref. [7.104], localized radiation may lead to a positive feedback effect: as radiation increases, temperature decreases, and through pressure balance, local plasma density will rise. This further increases radiation, as both hydrogenic and low- $Z$  impurity radiation increase in efficiency with decreasing density and increase in absolute intensity with increasing density, thus further increasing local radiation and producing the asymmetry in heat loading on the target. Such a positive feedback effect is more pronounced in the conduction-limited, high recycling regime [7.112].

Divertor asymmetry is strongly influenced by classical drifts, as evidenced by its dependence on the relative direction of the toroidal field  $\vec{B}_\phi$ . For example, the in-out ratios of radiated power and particle fluxes on JET significantly exceed unity with the ion  $\nabla B$  drift towards the divertor targets, reducing significantly, or reversing when the toroidal field is reversed [7.113]. The basic single particle guiding-centre drifts in the presence of steady electric and magnetic fields are the  $\vec{E} \times \vec{B}$ ,  $\nabla B$  and curvature drifts [7.114]. The  $\vec{E} \times \vec{B}$  drift

$$\vec{v}_E = \frac{\vec{E} \times \vec{B}}{B^2} \quad (7.35)$$

is independent of species, charge or mass, so that both ions and electrons drift together across the electric and magnetic fields at the same speed. In contrast, both  $\nabla B$  and curvature drifts depend on the charge of the particle, and therefore give rise to a net current. In a curl-free magnetic field, the curvature drift, which is driven by the centrifugal force due to particle motion along the curved magnetic field, has the same form as the  $\nabla B$  drift, with the combined  $\nabla B$  and curvature drifts

$$\vec{v}_{\vec{B} \times \nabla B} = \frac{T_{\parallel} + T_{\perp}}{q} \frac{\vec{B} \times \nabla B}{B^3} \quad (7.36)$$

For simplicity, both  $\nabla B$  and curvature drifts will be referred to as  $\vec{B} \times \nabla B$  drifts without distinction.

In a plasma where both temperature and density gradients exist, the diamagnetic drift arises naturally, simply due to *inhomogeneous* distribution of guiding centres, in addition to the basic  $\vec{E} \times \vec{B}$  and  $\vec{B} \times \vec{\nabla} B$  guiding-centre drifts. The diamagnetic drift can be readily obtained from the momentum balance equation of the fluid model as

$$\vec{v}_{\nabla p} = \frac{\vec{B} \times \nabla p}{nqB^2} \quad (7.37)$$

The diamagnetic drift also depends on the sign of the charge and gives rise to a diamagnetic current, which tends to reduce the magnetic field in the plasma. It should be noted that in magnetic fields with gradients and curvature, diamagnetic drifts, given by Eq. (7.37), include contributions from the  $\nabla B$  and curvature guiding-centre drifts.

The total flux density for steady state conditions obtained in fluid approximations can be written as

$$\vec{v} = v_{\parallel} \vec{b} + \vec{v}_E + \vec{v}_{\nabla p} - \frac{1}{neB} \vec{b} \times \vec{R} + \frac{(p_{\parallel} - p_{\perp} + nmv_{\parallel}^2)}{neB} \vec{b} \times \kappa \quad (7.38)$$

where  $\vec{b} = \vec{B}/B$  is a unit vector, and  $\kappa = (\vec{b} \cdot \nabla) \vec{b}$  is the curvature vector. Both electric fields and gradients of plasma pressure arise spontaneously in the divertor and edge plasmas, thus giving rise to  $\vec{E} \times \vec{B}$  and diamagnetic drifts. Simple estimates [7.89, 7.113] show that the relative contributions of  $\vec{E} \times \vec{B}$  and diamagnetic drifts to both poloidal and radial particle transport scale as  $\rho_{s\theta}/\lambda_{SOL}$ , where  $\lambda_{SOL}$  is the width of the SOL, and  $\rho_{s\theta} = c_s/\omega_{i\theta}$  is the ion poloidal Larmor radius with  $\omega_{i\theta} = eB_{\theta}/m_i$ . This ratio may reach unity in the region near the separatrix where strong gradients are present. The fourth term on the right hand side of Eq. (7.38) is only of the order of  $\lambda_p/R$  of the diamagnetic drift, where  $\lambda_p$  is the pressure decay length, while the last term is of a higher order. It is worth noting that the flux due to the diamagnetic drift

$$\Gamma_{\nabla p} = n\vec{v}_{\nabla p} = \frac{\vec{B} \times \nabla p}{qB^2} \quad (7.39)$$

is largely divergence-free, i.e. particles flow within the plasma, forming closed circuits, without intercepting divertor targets or walls; only the non-divergence-free part of the diamagnetic drift, which is of the same order as the  $\nabla B$  and curvature guiding-centre drifts, contributes to the overall particle transport. The  $\nabla B$  and curvature drifts are only of the order of  $\lambda_{SOL}/R$ , i.e. the ratio of the SOL width to the major radius of the diamagnetic drift, which is of the same order as the  $\vec{E} \times \vec{B}$  drift. In contrast, the flux arising from the  $\vec{E} \times \vec{B}$  drift

$$\Gamma_E = n\vec{v}_E = n \frac{\vec{B} \times \nabla V}{B^2} \quad (7.40)$$

where  $V$  is electric potential, is not divergence-free, due to density variations, and the non divergence-free part of the  $\vec{E} \times \vec{B}$  flow contributes to the overall plasma transport.

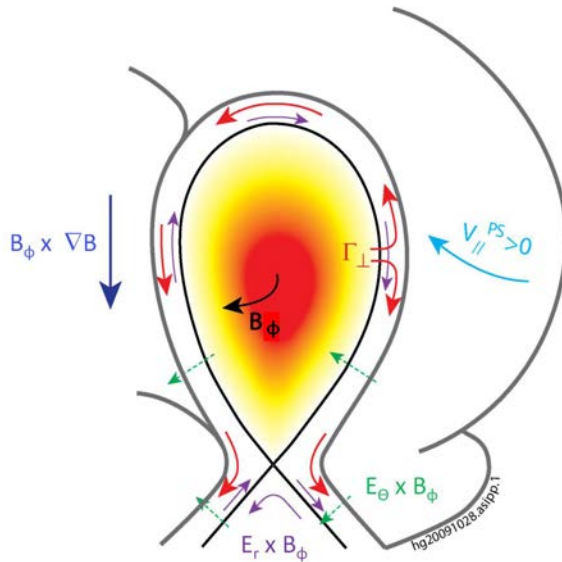


FIG. 7.28. Sketch of cross-field  $\vec{E} \times \vec{B}$  and  $\vec{B} \times \nabla \vec{B}$  drifts, as well as parallel Pfirsch–Schlüter (PS) flow,  $v_{\parallel}^{PS}$ , in the divertor and edge plasmas for normal direction of toroidal magnetic field  $B_{\phi}$ , along with turbulence-induced flow,  $\Gamma_{\perp}$ , on the outboard side.

Figure 7.28 shows the major guiding-centre drifts in the divertor SOL plasma for a single-null divertor configuration with the toroidal field  $\vec{B}_{\phi}$ , in the ‘normal’ direction, for which the ion  $\nabla B$  drift is towards the X-point at the

bottom, which is the preferred mode of operation because it has a lower power threshold for H-modes. The direction of all the drifts is reversed when the direction of  $\vec{B}_\phi$  is reversed.  $\vec{E} \times \vec{B}$  drifts are manifested as the poloidal  $\vec{E}_r \times \vec{B}$  drift due to the radial electric field  $\vec{E}_r$ , and the radial  $\vec{E}_\theta \times \vec{B}$  drift due to the poloidal electric field  $\vec{E}_\theta$ . As can be seen,  $\vec{E} \times \vec{B}$  drifts can directly affect in-out divertor asymmetries. By contrast, the smaller  $\vec{B} \times \nabla B$  drifts are up-down, and do not directly contribute to in-out divertor asymmetries.

Classical drifts, in particular  $\vec{E} \times \vec{B}$  drifts, can significantly affect the radial and poloidal particle transport, i.e. perpendicular to  $\vec{B}$ , in the SOL and affect divertor asymmetries. For normal  $\vec{B}_\phi$ , the poloidal  $\vec{E} \times \vec{B}$  drift in the main SOL tends to raise the pressure in the outer divertor, while the poloidal drift in the private plasma is from outside to inside and tends to raise the pressure in the inner divertor. The latter may be more important than the poloidal drift in the main SOL due to the presence of a large radial electric field  $\vec{E}_r$ , in the private plasma, which arises from the rapid drop in the electron temperature near the separatrix [7.115]. There is strong experimental evidence [7.99, 7.101] that poloidal  $\vec{E} \times \vec{B}$  drift in the private plasma plays a dominant role in influencing the in-out divertor asymmetry for usual attached divertor conditions. Detailed 2-D modelling using the UEDGE fluid code shows that plasma potential and pressure peak at the X-point, driving a clockwise circulation of  $\vec{E} \times \vec{B}$  flux around the X-point through the private plasma [7.116]. The radial  $\vec{E} \times \vec{B}$  drift also tends to raise the pressure at the outside divertor. As discussed in Ref. [7.89], there should be a positive feedback effect since higher pressure at the inner divertor, either due to radial  $\vec{E} \times \vec{B}$  drifts or due to poloidal  $\vec{E} \times \vec{B}$  drifts in the private plasma, will, in turn, lead to an increase in radiation and hence a decrease in temperature, further enhancing the in-out asymmetry.

Such drift effects are substantially reduced and even reversed under detached plasma conditions [7.101]. However, for partial plasma detachment, as envisioned for ITER, the divertor detachment is localized near the strike points with the private plasma being still attached, so drifts could have significant implications.

#### 7.5.2.1.3. Parallel particle transport and possible contributions of drifts

The presence of plasma flow in the SOL plays an important role in plasma transport and may affect the properties of the confined plasma by imposing the flowing boundary conditions [7.117]. Contrary to expectations, strong flows have been observed in the SOL with Mach number  $M_\parallel$  up to unity, well away from the target plate. The mechanisms for driving such a large parallel flow are not fully understood, but a number of contributing physics processes have been identified, including (1) ion source, (2) Pfirsch–Schlüter (PS) flows arising from

the poloidal asymmetry of the neo-classical drifts [7.101, 7.116, 7.118–7.121] and (3) enhanced outboard ballooning-like particle transport [7.117].

The SOL plasma flow is mainly induced by the LFS-induced asymmetry in transport (Section 7.5.2.2) and classical drifts. The overall flow pattern in the SOL has been shown to be similar in many tokamaks, and exhibits a strong dependence on the direction of the magnetic fields [7.92, 7.122], as shown in Fig. 7.29. For the normal field direction, i.e. with ion  $\nabla B$  drift towards the X-point, a stagnation point in the flow is observed usually between the outer midplane and the X-point, with a strong inboard flow in the rest of the SOL, peaking at the inner midplane [7.117]. For the reversed field, the stagnation point moves to the top of the machine for the lower single-null divertor configuration with flow towards both inner and outer divertors. As plasma density increases, the flow speed tends to decrease at the outer midplane, but increase at the inner midplane, for both normal and reversed  $\vec{B}$  directions. The strong dependence of the SOL flow pattern on the sign of the magnetic fields suggests that classical drifts should also play a role in parallel particle transport.

According to the neo-classical transport theory, a parallel flow, i.e. the Pfirsch–Schlüter (PS) return flow, arises naturally in the SOL due to the poloidal asymmetry of  $\vec{E} \times \vec{B}$  and  $\vec{B} \times \nabla B$  drifts in toroidal geometry, and plays an essential role in parallel (along  $\vec{B}$ ) plasma transport. It has long been recognized that the PS current is the direct consequence of the  $\vec{B} \times \nabla B$  and curvature drifts (including both  $\nabla B$  and curvature effects), which corresponds to the non-divergence-free part of the diamagnetic drifts. For normal  $\vec{B}_\phi$  (Fig. 5.12), the  $\vec{B} \times \nabla B$  drifts lead to charge separation, with electrons moving towards the top of the torus and ions towards the bottom, which, in turn, gives rise to the PS return current along the magnetic fields. Such PS currents were detected directly by Langmuir probes at the divertor target in JET [7.123]. By contrast, the  $\vec{E} \times \vec{B}$  drifts are the same for both ions and electrons, and thus do not generate currents. However, they do contribute to the PS ion flow due to the non-divergence-free part of the poloidal  $\vec{E} \times \vec{B}$  drifts. In the large aspect ratio, circular cross-section approximation, a simple analytic expression for the PS flow can be calculated as [7.107]

$$v_{\parallel}^{PS} = 2q \cos\theta \left( \vec{E}_r - \frac{\nabla p_r}{en_e} \right) \times \frac{\vec{B}_0}{B^2} \quad (7.41)$$

where  $q$  is the safety factor,  $\vec{B}_0$  is the magnetic field at the midplane plasma centre ( $R = R_0$ ), and  $\theta$  is the poloidal angle. Here,  $\theta = 0$  is defined at the outboard midplane. The ion flows are along the magnetic field in the anticlockwise direction on the outboard side for normal  $\vec{B}_\phi$  direction, reach maximum speeds at the outer midplane, a negative minimum at the inner midplane, and vanish at top and bottom. Note that  $\vec{E}_r$  and  $(-\nabla p_r)$  are usually in the same directions

in the SOL, reinforcing each other. The PS flow is also present in the confined plasma, but is much smaller than in the SOL because  $\vec{E}_r$  and  $(-\nabla p_r)$  are in opposite directions and pressure gradients are much smaller in the main plasma.

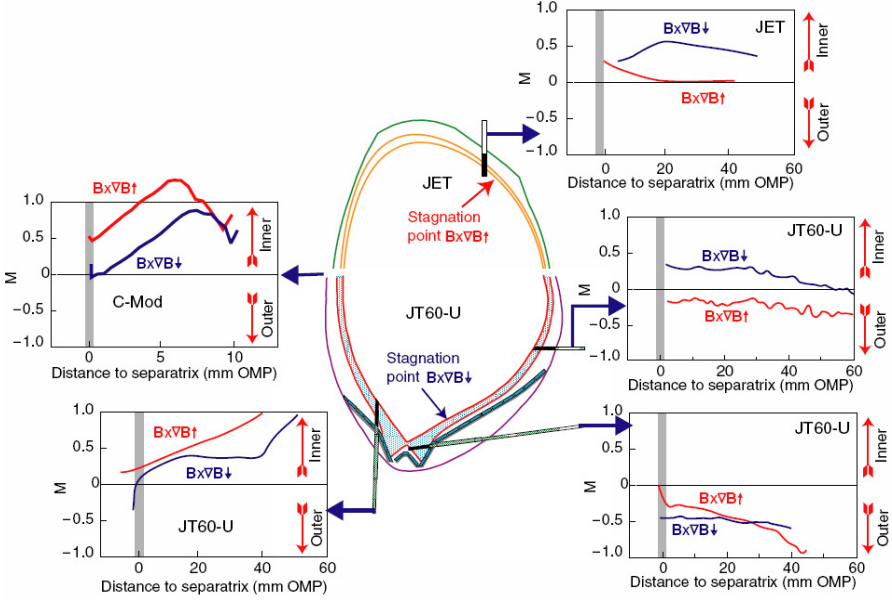


FIG. 7.29. Parallel Mach number profiles measured by Mach probes for L-mode plasmas in JT-60U, JET and C-mode (compiled by Matthews [7.116]). Note that ‘omp’ stands for the outer midplane. Reprinted from Ref. [7.100]. Copyright (2011), with permission from Elsevier.

The ion PS flows are sustained by an up-down pressure asymmetry, and this, in turn, gives rise to a surface averaged radial current [7.124]

$$\bar{j}_r = \left\langle \frac{1}{rB} \frac{\partial p}{\partial \theta} \right\rangle \quad (7.42)$$

in the SOL due to toroidal effects, which does not exist in the confined plasma because all the field lines are closed. The resulting  $\bar{j}_r \times B_\theta$  force drives a net parallel ion flow from the outer target to the inner target, for the normal  $\vec{B}_\phi$  direction, in addition to the basic PS flow. This force can also lead to in-out pressure asymmetry, favouring the inner divertor for the normal  $\vec{B}_\phi$  direction, which reverses with toroidal field reversal, thus providing another potential explanation for observed divertor in-out asymmetries, as discussed earlier.

The classical drift effects have been implemented in 2-D fluid code packages such as EDGE2D, UEDGE and SOLPS/B2-Eirene to model the SOL flow. However, these codes can only qualitatively reproduce the observed flow pattern, for example flow direction, but significantly underestimate the

magnitudes of the flow. Attempts have been made recently to explore other potential drive mechanisms for the SOL flow, such as enhanced outboard ballooning particle transport and outward plasma filaments (blobs) [7.117, 7.121], as will be discussed in the next section.

### 7.5.2.2. Recent advances on cross-field particle transport

Cross-field transport plays a key role in determining power and particle deposition on the plasma facing components, in particular, the energy deposition profile on the divertor target, and the long range particle transport that might govern main chamber recycling, which are two key issues in the ITER design. In the simple divertor SOL, power and particle fluxes across the magnetic field are balanced by parallel transport along the open field lines towards the divertor target, which represents the dominant sink for particles and energy. In this case, the characteristic particle lifetime in the SOL is approximately given by

$$\tau_{SOL} \approx L_c / c_s \quad (7.43)$$

where  $L_c = \pi Rq$  is the connection length for the single-null divertor configuration. Since the cross-field transport is not well understood, it is usually described in terms of anomalous diffusion, with an ad-hoc diffusion coefficient  $D_{\perp}$ . Thus, the width of the SOL for particles is

$$\lambda_n \approx \sqrt{D_{\perp} \tau_{SOL}} = \sqrt{D_{\perp} L_c / c_s} \quad (7.44)$$

$\lambda_n$  and hence  $D_{\perp}$  can be readily deduced from density and temperature measurements, for example by Langmuir probes, assuming  $T_i = T_e$ . For typical SOL plasma conditions,  $D_{\perp} \sim 1 \text{ m}^2 \cdot \text{s}^{-1}$ , of the order of magnitude of the Bohm diffusion coefficient,  $D_B$ , see Eq. (7.9), albeit without the  $T_e/B$  scaling.

It has become increasingly evident that the simple diffusive transport paradigm is inadequate to describe the edge transport, which is turbulent in nature and exhibits intermittent macroscopic events such as blobs and ELMs. Although the underlying physics of cross-field transport is not yet fully resolved, significant progress has been made in recent years in both experimental and theoretical/computational studies. Data assembled from many magnetic fusion experiments reveal a common two-zone SOL structure with strong variations in density and temperature gradients, as well as transport dynamics: (1) A steep gradient region near the separatrix, called *near* SOL, followed by (2) a *far* SOL region with flatter radial profiles extending onto the wall, which is characterized as an outer ‘shoulder’, although the degree of relative flatness varies in different experimental devices, as shown in Fig. 7.30(a) [7.125].

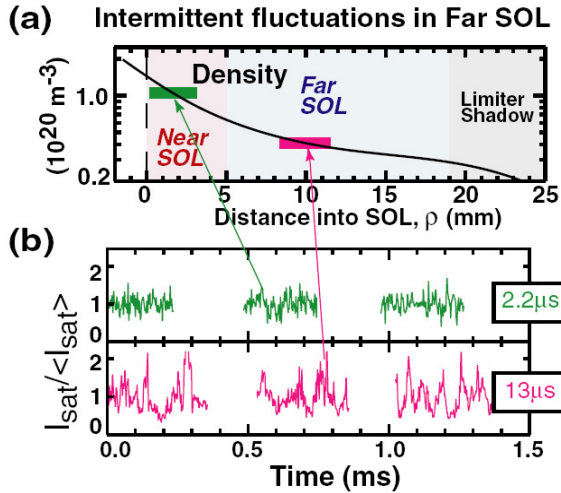


FIG. 7.30. (a) Density profile and (b) fluctuations of SOL in ohmic L-Mode discharges on C-Mod, showing strong variations in density gradient and fluctuation structure across the SOL [7.125].

Detailed analysis of fluctuation structure and direct visualization of edge turbulence with imaging systems reveal strong variations in transport dynamics in the edge and across the SOL. The near SOL exhibits relatively small amplitude, random fluctuations, as shown in Fig. 7.30(b), with a largely Gaussian probability distribution function (PDF), while the fluctuations in the far SOL are characterized by larger scale, lower-frequency ‘bursts’ with a highly skewed PDF fluctuation structure, favouring an enhanced probability of large positive-amplitude events [7.126].

#### 7.5.2.2.1. Far SOL

Turbulence imaging systems show that plasma appears to intermittently ‘peel away’ in clumps from the near SOL region and propagate quasi-ballistically across the far SOL region towards the main chamber wall, as manifested by field-aligned filaments or ‘blobs’ with velocities well above 100 m/s. Such blob-like transport is seen in both L- and H-mode plasmas [7.127, 7.128] and accounts for a large fraction of the total particle flux. Although ELM-induced blobs exhibit larger amplitudes than those seen in the L-modes, the time-averaged fluxes tend to be lower, which is consistent with a global improvement in particle confinement for the H-modes. The transport dynamics in the far SOL are reminiscent of avalanches in a self-organized critical system [7.129, 7.130]. The blobs, which originated from the near SOL region due to such avalanche-like effects, contain a large number of particles, and this, coupled with a large

outward speed, results in a large, time-averaged particle flux to the main-chamber wall. As a result, the overall cross-field transport is largely convective rather than diffusive. This is clearly incompatible with a Bohm-like diffusion paradigm.

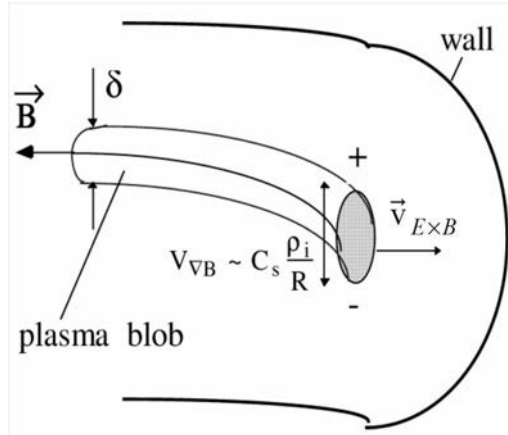


FIG. 7.31. Sketch of blob transport in the far SOL, driven by  $\nabla B$  plasma polarization and associated  $\vec{E} \times \vec{B}$  drift [7.131]. Here  $\delta$  indicates the finite extension of the blob across the magnetic field lines. Reprinted from Ref. [7.131]. Copyright (2011) by the American Physical Society.

The detailed dynamics of blob formation are still unclear. However, the basic physics mechanism for propagation of the blobs is well established [7.131], which is the basic interchange instability due to field curvature. The blob represents a coherent structure ejected from the near SOL region with a density of the order of that at separatrix, much higher than the background plasma in the far SOL, which extends along  $\vec{B}$ , but is of finite dimension perpendicular to  $\vec{B}$ . The combined  $\nabla B$  and curvature (or centrifugal) drifts, as given by Eq. (7.36), can be rewritten as

$$v_{\vec{B} \times \nabla B} = \frac{2kT}{q} \frac{\vec{R}_c \times \vec{B}}{R_c^2 B^2} \tag{7.45}$$

for a low- $\beta$ , isotropic Maxwellian plasma, where  $\vec{R}_c$  is the vector radius of the field line curvature. The  $\vec{B} \times \nabla B$  drifts cause charge separation, and hence polarization of the blobs, like a dipole; the associated electric field leads to rapid  $\vec{E} \times \vec{B}$  convection along  $\vec{R}_c$  towards the main chamber wall, as illustrated in Fig. 7.31, thus enhancing particle recycling at the wall. There is a synergy between blob transport and main chamber recycling since local ionization sources in the far SOL due to recycled neutrals can, in turn, sustain the blob transport [7.132]. This can lead to a ‘main chamber recycling’ regime with flat density profiles where cross-field transport fluxes compete against particle

losses along the field lines, as observed in C-Mod [7.133]. At sufficiently high densities (or more generally, collisionalities), this leads to a dramatic increase in heat convection across the SOL due to an explosive increase in transport fluxes, rendering high density operation regimes energetically inaccessible, and thus may set a fundamental transport limit [7.134].

Note that the basic interchange mode occurs only in the *bad* curvature region where  $\nabla p$  and  $\vec{R}_c$  are oppositely directed, i.e. in the outboard SOL. This simple picture is consistent with a number of experimental observations. For example, the transport and fluctuation levels are observed to be significantly (up to 10 times) higher in the outboard SOL than in the inboard SOL for the single null divertor configuration in C-Mod [7.127] and no coherent fluctuations were observed on the inboard SOL for the double-null configurations in ASDEX [7.135]. Such ballooning-like cross-field transport asymmetry appears to drive strong plasma flow along field lines in the SOL, as discussed in Section 7.5.2.1.

#### 7.5.2.2.2. Near SOL

As aforementioned, the blobs appear to originate from the near SOL region, and propagate *freely* through the far SOL. Therefore, the overall level of cross-field transport in the SOL may ultimately be set by the conditions in the near SOL. Since the near SOL exhibits relatively small, random fluctuations, one might expect that the transport should conform to a diffusive-like, gradient-driven paradigm, with the time-averaged flux given by

$$\Gamma_{\perp} = -D_{\perp} \nabla n \quad (7.46)$$

where  $D_{\perp}$  is the effective cross-field diffusivity. However, the most recent results from C-Mod have clearly demonstrated this is not the case [7.136]. To illustrate this, Fig. 7.32 shows density gradients and  $\Gamma_{\perp}$  as a function of line-averaged density for various L-mode plasma conditions. It appears that as density (and hence collisionality) increases, cross-field fluxes increase non-linearly without appreciable changes in density gradients — a factor of 20 increase in  $\Gamma_{\perp}$  while  $\nabla n$  changes by only about a factor of 2 (for normal  $\vec{B}_{\phi}$  direction) or not at all (for reversed  $\vec{B}_{\phi}$ ). Thus, the simple diffusive transport described by Eq. (7.46) is inadequate to represent the time-averaged edge transport and the system appears to be clamped near a ‘critical gradient’.

Transport in the near SOL region may involve highly non-linear electromagnetic turbulences, which cannot be treated by simple linear or secondary instability analysis. A prevailing theoretical treatment is based on low frequency electromagnetic fluid drift turbulences, which provide a basis for a number of first-principle 3-D turbulence simulations, using transcollisional fluid-like models with extension to the state-of-art gyrofluid models. More advanced tools are being developed using gyrokinetic models with a similar treatment [7.137].

These models predict that the fluctuations and resultant transport are dependent on collisionality, poloidal  $\beta$ -gradient and magnetic shear. As collisionality or density increases, fluctuation amplitudes and particle transport increase dramatically (see, for example Ref. [7.138]), consistent with experimental observations (Fig. 7.32). In addition, cross-field transport is found to increase strongly with poloidal  $\beta$ -gradient,  $\alpha_{\text{MHD}}$ , and exhibits an explosive growth when  $\alpha_{\text{MHD}}$  exceeds a critical value, accompanied by a spontaneous change in the mode structure from drift wave to ideal ballooning [7.139]. This, along with recent experimental evidence [7.125, 7.136, 7.140], points to a marginally-stable system controlled by poloidal  $\beta$ -gradient and possibly regulated by the plasma flow, where small changes in such a gradient would lead to a large change in transport fluxes in the near SOL region.

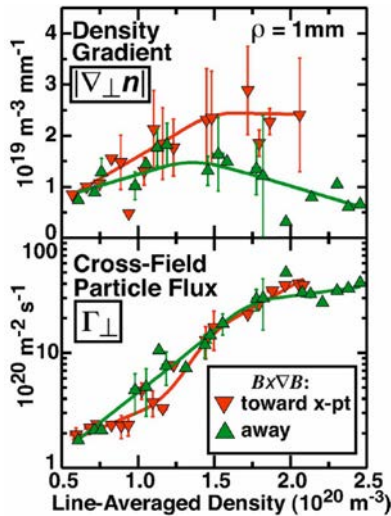


FIG. 7.32. Density gradients and cross-field particle fluxes in the near SOL as a function of line-averaged density for L-mode plasmas in C-Mod [7.136]. Reprinted from Ref. [7.136]. Copyright (2011), American Institute of Physics.

### 7.5.3. Energy deposition

#### 7.5.3.1. Steady state power load on the divertor

In steady state operation, the total input power from the ohmic and additional heating, as well as fusion power, must be balanced by power losses to the surrounding plasma-facing components (PFC), i.e. via radiation, conduction, convection, charge exchange, etc. While significant particle fluxes can reach main chamber walls due to turbulent transport processes as described

in Section 7.5.2.2, energy transport mainly occurs in the near SOL region. As a result, most of the power loss from the confined plasmas is predominately deposited onto the divertor during steady state, with a typical scale  $\lambda_q \sim 5$  mm. As an example, Fig. 7.33 shows the radial profiles of the time-averaged heat fluxes at the divertor target, mapped to the flux surfaces at the midplane, for typical ELMy H-mode plasmas in JET [7.141]. This poses a serious challenge for high power, steady-state burning plasma experiments, such as ITER, as excessive localized power fluxes not only cause impurity sputtering, but may result in evaporation and melting (for metal) of the solid materials, limiting the lifetime of plasma facing components.

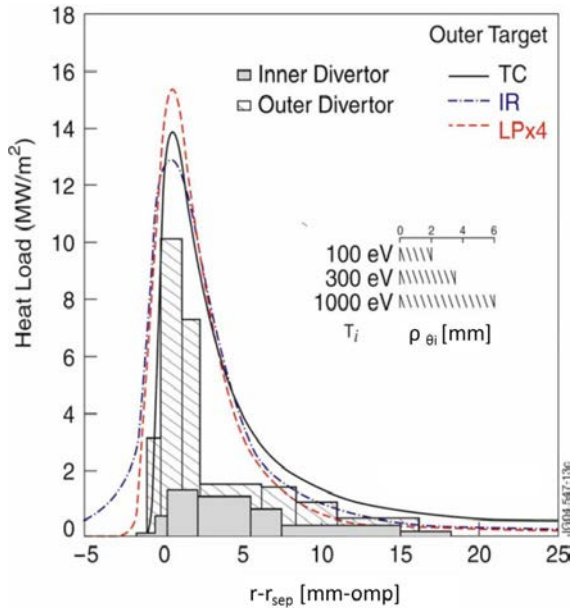


FIG. 7.33. Radial profiles of time-averaged heat fluxes to the divertor targets, mapped to the outer midplane (omp), derived from various diagnostics for typical H-mode plasmas in JET, with  $\vec{B} \times \nabla B$  drifts towards the X-point [7.141].

Power deposition on the divertor target is governed by competition between rapid parallel heat transport along the field lines and much slower cross-field transport and also affected by radiation and recycling-related losses, i.e. ionization, recombination and charge exchange in the divertor, as well as the presence of drifts. Parallel energy transport is largely classical, but the cross-field energy transport in the SOL is largely anomalous. Experimental evidence shows that the cross-field electron and ion transport may be controlled by different underlying transport mechanisms, i.e. possibly drift wave turbulences for electrons and collisional heat diffusion for ions [7.141].

The basic energy transport scales can be estimated assuming classical (collisional) energy transport in both the parallel ( $\parallel \vec{B}$ ) and radial directions ( $\perp \vec{B}$ ) for electrons. For simple, classical energy transport, the cross-field (radial) heat conduction can be approximated as a random diffusion process, assuming that the Larmor radius and collision time represent the characteristic radial step and the associated step time, i.e.

$$\chi_{\perp} \sim \rho_{\sigma}^2 \nu_{\sigma} \quad (7.47)$$

where  $\sigma \in \{i, e\}$ . The associated radial power deposition width can be estimated as [7.141]

$$\lambda_q = (\chi_{\perp} \tau_{\parallel})^{1/2} \quad (7.48)$$

where  $\tau_{\parallel}$  is the effective energy loss time due to convection and conduction along field lines.

For electron energy transport,  $\chi_{e\perp} \approx \rho_e^2 \nu_e = \rho_e^2 v_e / \lambda_e$  and  $\tau_{e\parallel} \approx L_c^2 / \chi_{e\parallel} = L_c^2 / (v_e \lambda_e)$ , where the connection length  $L_c$  represents the characteristic scale for parallel transport. Hence, we obtain

$$\lambda_{qe}^c = \rho_e \nu_e^* \quad (7.49)$$

where  $c$  stands for classical,  $\nu_e^* = L_c / \lambda_e$  is the electron collisionality, or the number of collisions that electrons undergo in the SOL before reaching the target. For typical steady-state ELMy H-mode SOL conditions,  $\nu_e^* \sim 10$  and  $\rho_e \sim 10^{-5}$  m for  $T_e \sim 50$  eV and  $B \sim 2$  T,  $\lambda_{qe}^c \sim 1 \times 10^{-4}$  m, which is over an order of magnitude smaller than experimental observations (Fig. 7.33). This suggests that electron energy transport is not governed by classical diffusion, possibly by turbulence transport processes.

In contrast, classical energy transport is much faster for ions than for electrons, due to their much larger ion Larmor radius  $\rho_i \sim (m_i / m_e)^{1/2} \rho_e$  for  $T_i = T_e$ , as readily seen from the following simple estimation. Due to bad conductivity, ion energy transport along the field line is dominated by convection with a characteristic time  $\tau_{i\parallel} \approx L_c / c_s \sim M L_c / v_i$ , where  $M$  is the Mach number. This, along with  $\chi_{i\perp} \approx \rho_i^2 \nu_i = \rho_i^2 v_i / \lambda_i$ , yields

$$\lambda_{qi}^c = \rho_i (M \nu_i^*)^{1/2} \quad (7.50)$$

In toroidal geometry, this takes the *neo-classical* form

$$\lambda_{qi}^{nc} = \rho_{\theta i} (M \nu_i^*)^{1/2} \quad (7.51)$$

where  $nc$  stands for neo-classical and  $\rho_{\theta i}$  is the poloidal ion Larmor radius. With  $\nu_i^* \sim \nu_e^* \sim 10$ ,  $M \sim 0.5$  and  $\rho_{\theta i} \sim (B/B_{\theta}) \rho_i \sim 2 \times 10^{-3}$  m assuming  $B/B_{\theta} \sim 3$

at the outer midplane, we obtain  $\lambda_{qi}^{nc} \sim 4 \times 10^{-3} \text{ m}$ , consistent with experimental observations.

Finally, assuming that the radial transport is controlled by collisionless direct ion orbit losses, the width simply scales as  $\rho_{\theta i}$ , which represents the smallest radial scale length for ion dynamics.

At low ion collisionality, ion and electron energy channels are decoupled with  $T_i > T_e$  due to much worse ion conductivity along the magnetic field lines. This leads to an increased contribution from the ion channel to the power deposition, as illustrated in Fig. 7.33. The data shown in the figure were obtained from low density, natural H-modes in JET during steady state, which were sustained entirely by recycling without additional gas fuelling. As can be seen, the total heat load from infrared (IR) thermography and embedded thermocouples greatly exceeds the electron energy deposition, obtained from embedded target Langmuir probes at the outer target. This implies a contribution from hot  $D^+$  ions with  $T_i \sim 300 \text{ eV}$  at the separatrix, consistent with the measurements from charge exchange recombination spectroscopy (CXRS). In the figure are also indicated poloidal ion Larmor radii for various ion temperatures: 100, 300 and 1000 eV, with the highest temperature corresponding to that at the top of the pedestal. It appears that the width of the power deposition  $\lambda_q \sim 3 \text{ mm}$  is consistent with the ion poloidal Larmor radius  $\rho_{\theta i}$  evaluated at the separatrix, but smaller than that at the pedestal.

Due to lack of a quantitatively accurate, first-principle description of the underlying transport process, cross-field energy transport is usually characterized by an effective heat diffusivity  $\chi_{\perp}$ , which can be reconstructed from measured profiles of density and temperature at the target and the upstream and target power deposition, along with spectroscopic measurements for recycling neutrals and impurities, using 2-D fluid codes. It is found that  $\chi_{\perp} \sim 0.1\text{--}1.0 \text{ m}^2 \cdot \text{s}^{-1}$  for typical divertor SOL conditions [7.110].

The classical drifts do not directly affect the (radial) distribution of the heat load at the target, which is predominantly controlled by the parallel and radial energy transport discussed above, but mainly affect the divertor asymmetry in power deposition, as manifested by its strong dependence on the  $\vec{B} \times \nabla B$  direction [7.141, 7.142]. It should be noted that power flows preferentially into the outboard SOL irrespective of the  $\vec{B} \times \nabla B$  direction, largely arising from the larger outboard area, stronger magnetic compression on the outboard side due to the Shafranov-shift and enhanced transport rates due to bad magnetic curvature on the low field side. Thus, the drifts merely redistribute the power deposition between the inner and outer divertors. The asymmetry is most marked for normal  $\vec{B}$  operation, i.e. with the  $\vec{B} \times \nabla B$  direction towards the X-point, and with significantly more power flux to the outer divertor. Reversing  $\vec{B}$  increases the power flux into the inner divertor, reducing the in-out asymmetry. For example,

detailed power balance analysis for matched normal (forward)  $\vec{B}$  and reversed  $\vec{B}$  L-mode discharges in JET showed that the ratio of power entering into the outer and inner divertors  $P_{outer} / P_{inner} \sim 2.3$  for normal  $\vec{B}$ , reducing to  $\sim 1.3$  for reversed  $\vec{B}$  [7.141].

The total heat flux including classical drifts is given by [7.113]

$$q = \frac{5}{2} p \vec{v} + \frac{5}{2} \frac{k}{eB^2} p \vec{B} \times \nabla T \quad (7.52)$$

where the first term on the right-hand side is the fluid convection heat flux with the flow speed  $\vec{v}$  given by Eq. (7.38), while the last term represents the conductive heat flux arising from the temperature gradient  $\nabla T$ . The dominant heat flux drifts present in the SOL are associated with the diamagnetic drifts and  $\vec{E} \times \vec{B}$  drifts. The diamagnetic drift heat fluxes include both the convective heat flux associated with the  $\nabla p$  drift

$$q_{\nabla p} = \frac{5}{2} \frac{kT}{eB^2} \vec{B} \times \nabla p \quad (7.53)$$

and the conductive heat flux associated with  $\nabla T$

$$q_{\nabla T} = \frac{5}{2} \frac{kp}{eB^2} \vec{B} \times \nabla T \quad (7.54)$$

Similar to the diamagnetic particle fluxes, these diamagnetic heat fluxes are largely divergence-free, i.e. predominantly affecting power circulation within the plasma, not depositing power on the target plates.

In contrast, the  $\vec{E} \times \vec{B}$  drifts do lead to power load onto the target plates, with

$$q_{E \times B} = \frac{5}{2} \frac{p}{B^2} \vec{E} \times \vec{B} \quad (7.55)$$

The dominant role of the classical drifts, mainly the  $\vec{E} \times \vec{B}$  drifts, in the SOL energy transport has been confirmed, for example, recently in detailed analysis of well matched normal and reversed  $\vec{B}$  experiments in JET [7.141].

### 7.5.3.2. Transient energy deposition during ELMs

Energy deposition during transient events, such as ELMs and disruptions, poses a serious threat to the lifetime of the plasma facing components in the next-step burning plasma facilities. The peak values of instantaneous power fluxes of typical Type I ELMs, which are envisioned as the primary operation regime for ITER, exceed the inter-ELM levels by up to two orders of magnitude, despite the time averaged ELM energy being comparable to or smaller than the inter-ELM component [7.141]. Disruptions occur less frequently than ELMs,

but generate even greater peak power fluxes onto PFCs, typically one order of magnitude higher than ELMs. In contrast to the steady-state power load, transient energy deposition not only causes localized evaporation/melting and large scale erosion at the PFC surfaces, but may result in the structural damage of the PFCs arising from thermal shock, thus affecting the integrity of the solid materials.

ELMs act to expel periodically particles and energy that build up in the pedestal region during the improved confinement phase between the ELMs. Power flow into the SOL during an ELM involves both conductive and convective energy transport from the pedestal region. The ELM energy losses from the confined plasma exhibit a strong dependence on pedestal collisionality. As the collisionality increases, the conductive energy losses tend to decrease, while the convective losses remain largely unchanged [7.6, 7.143]. Figure 7.34 shows the total ELM energy losses  $\Delta W_{ELM}$  normalized to the pedestal energy  $W_{ped}$  for ELMy plasmas obtained in various tokamaks, as well as the projection for ITER [7.143].

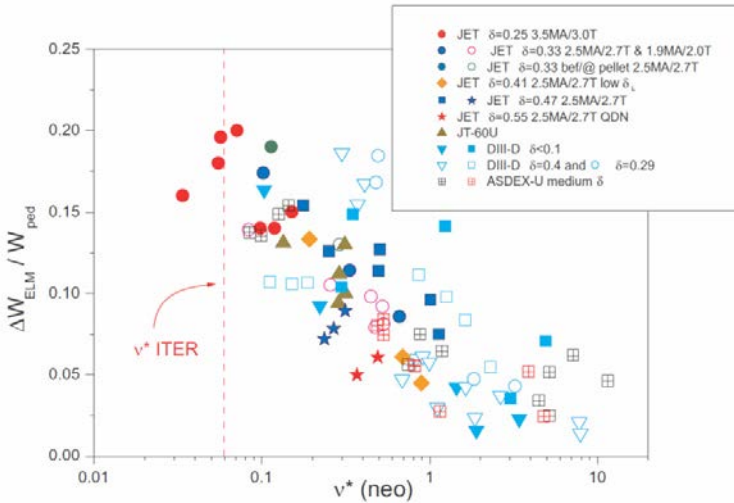


FIG. 7.34. Ratio of energy expelled by an ELM  $\Delta W_{ELM}$  to pedestal energy  $W_{ped}$  versus pedestal collisionality. Data obtained from a large number of tokamaks with various magnetic configurations [7.143]. Projection for ITER also indicated. Reprinted from Ref. [7.143]. Copyright (2011), IOP Publishing Ltd.

ELM energy deposition on the divertor target is characterized by a fast impulse with a timescale of  $\sim 0.1$ – $1$  ms (phase I), followed by a slower energy flux lasting over a few ms (phase II). As an example, Fig. 7.35 shows the time evolution of ELM power deposition on the inner and outer divertor targets, obtained from IR measurements for typical Type I ELMs in ASDEX-Upgrade and JET [7.144]. Phase I exhibits strong broadband MHD activities. During this

phase, high energy electrons reach the divertor target almost instantaneously, as seen by soft X ray cameras. It is expected that electron conduction should play a dominant role in energy transport from the pedestal to the target. However, the characteristic timescale of phase I is usually longer than the strong MHD period, but correlates well with the transient time of fast ions from the pedestal to the divertor target along the field line in various tokamaks. This suggests that the energy transport during this initial phase is either limited by the formation of a high energy sheath so that the ELM energy is predominantly transported with an effective velocity of the order of the ion sound speed [7.145], or dominated by convection associated with fast ions originated from the pedestal region. In contrast, phase II exhibits an increased particle flux, without the presence of high energy electron fluxes, and energy transport to the divertor is dominated by convection [7.143].

ELM energy enters preferentially into the outboard SOL, in agreement with the peeling-ballooning modes as a driving mechanism for ELMs [7.146, 7.147]. It was observed on MAST that most of the power (>93%) was deposited on the outboard divertor targets during Type III ELMs, evenly distributed between the upper and lower divertor regions, for the connected double-null divertor configuration [7.148, 7.149]. However, for the single-null configuration, a larger fraction of the ELM energy deposits onto the inner divertor, as shown in Fig. 7.35; this is opposite to the inter-ELM phase, where the inner divertor receives little power with plasma usually in the detached state. The asymmetry in ELM energy deposition appears to be dependent on the ELM size and divertor plasma conditions. Stronger asymmetry is observed in the H-mode plasmas at high densities with small ELMs and increased degree of detachment at the inner divertor [7.144].

Despite enhanced radial transport during ELMs, the power deposition profiles at the outer divertor remain largely unchanged compared to those between ELMs, due to rapid parallel heat transport along the SOL. In contrast, the particle parallel transport time tends to be longer than the ELM duration, and this, coupled with ELM-enhanced recycling, leads to significant broadening of the SOL density profile during and even between ELMs, as shown in Fig. 7.36. The radial propagation velocity of ELMs is typically of the order of  $v_r \sim 1 \text{ km} \cdot \text{s}^{-1}$ , with radial time scale  $\tau_r \sim 100 \mu\text{s}$  comparable to the timescale for parallel transport  $\tau_{\parallel}$  [7.92]. The density perturbation caused by ELMs exhibits the characteristics of peeling-ballooning modes with an approximate toroidal mode number  $n \sim 10\text{--}15$ . This leads to significant particle fluxes to the main chamber wall, similar to blobs (Section 7.5.2.2). The associated *convective* radial energy transport to the wall increases with ELM sizes, and accounts for up to 50% of the total ELM energy losses from the pedestal for Type I ELMs in the present experiments. This could have significant implications for the lifetime of main chamber components in next-step fusion devices such as ITER.

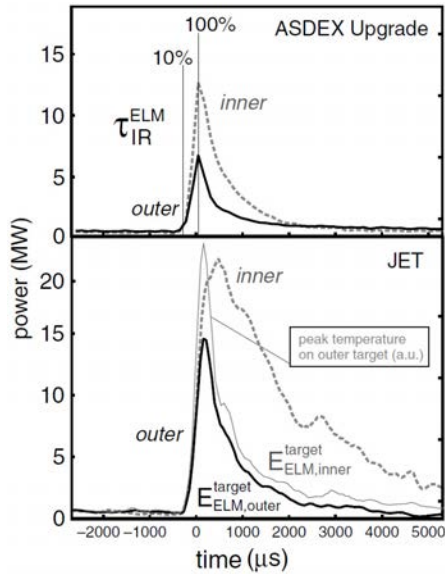


FIG. 7.35. Time evolution of ELM power deposition on the inner and outer divertors during type I ELMs in ASDEX Upgrade and JET [7.144]. Reprinted from Ref. [7.144]. Copyright (2011), with permission from Elsevier.

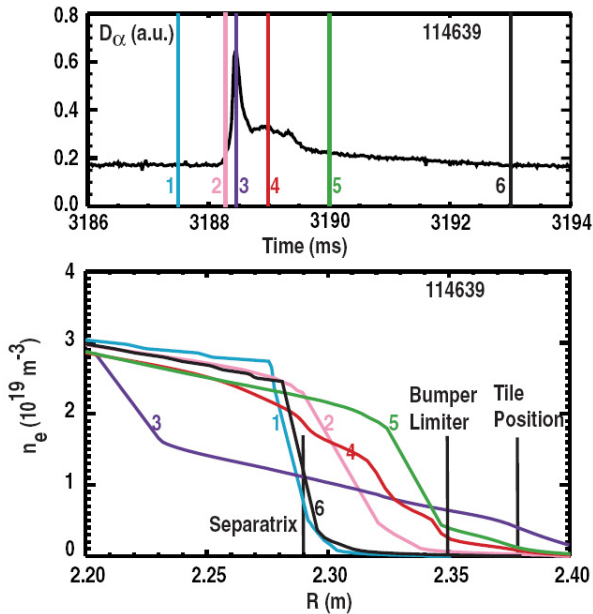


FIG. 7.36. Time evolution of  $D_\alpha$  emissions during a Type I ELM in DIII-D (top), and radial profiles of electron density at the outer midplane at various times during the ELM (bottom) [7.92]. Reprinted from Ref. [7.150]. Copyright (2011), IOP Publishing Ltd.

### 7.5.3.3. Active control of peak heat fluxes

As discussed in Section 7.5.1.2, partial detachment near the strike points offers a preferred solution to the problems of reducing the peak heat flux and erosion of divertor target plates. Gas puffing of various impurities such as neon (Ne), argon (Ar) and nitrogen ( $N_2$ ) has been used in the present tokamaks, and has achieved partial or complete divertor detachment with radiated power fraction,  $f_{rad} > 80\%$ . Gas puffing has proved to be very effective for Type III ELMy H-mode plasmas. However, such regimes usually exhibit reduced confinement quality and/or unacceptable impurity content in the confined plasma [7.92]. Recently, highly radiative plasmas ( $f_{rad} \sim 100\%$ ) with good confinement ( $H_{H98(y,2)} = 0.96$ ) have been achieved in JT-60U high  $\beta_\theta$  H-mode plasmas using HFS pellets and Ar injection. These plasmas are sustained at high density ( $\bar{n}_e/n_{GW} = 0.92$ ) with acceptable core Ar accumulation [7.151].

Extrinsic impurity injection has also been considered by the ITER design team as a means of achieving the desired radiated power fraction (over 50%) for the control of target heat load to acceptable levels [7.152]. For ITER-relevant Type I ELMy H-modes, while a large radiation fraction can be achieved in steady state, i.e. averaging over ELMs and inter-ELM periods, the energy deposited during the ELM pulse itself remains largely unaffected. For example, radiative plasmas with  $f_{rad} \sim 55\%$  were achieved in the Type I ELMy H-modes in JET, using nitrogen or argon puffing, but the power deposition on the divertor target during ELMs was only marginally reduced compared to the non-seeded discharges [7.153].

A potential issue with impurity injection is the accumulation of injected high- $Z$  impurities in the confined plasma. It has been recently demonstrated that central power deposition, for example by ICRH and ECRH, may be used as an effective tool for the control of core impurity accumulation [7.154, 7.155]. In addition, HFS pellet injection has recently been used in ASDEX-Upgrade to actively trigger ELMs to control power flux and prevent impurity accumulation caused by ELM-free operation [7.156].

## 7.6. ISSUES OF PLASMA–WALL INTERACTIONS FOR NEXT STEP TOKAMAKS

Recent experimental and modelling results have indicated four key issues that will greatly affect the plasma–wall interaction (PWI) design for the next-step devices [7.157]:

- Exhaust of the power and particles to facilitate long pulse operation;
- Mitigation of off-normal events such as disruptions to ensure the integrity of PFCs;

- Control of impurity and dust production, and associated materials mitigation, to achieve adequate PFC lifetimes and tolerable plasma contamination ( $Z_{eff} \leq 1.5$ );
- Control of tritium inventory.

It is to be noted that most of the PWI studies have been focused on carbon PFCs, and thus plasma interaction properties of mixed materials, in particular, Be, C and W, which are presently foreseen for ITER, remain an open issue. Furthermore, extending plasma fusion regimes from the pulse to steady-state scenarios poses a great challenge for the operation of the next-step devices from both physics and technology points of view [7.158]. With the ITER construction being started, addressing this issue is becoming a worldwide effort.

### 7.6.1. Power handling and particle exhaust

For a future D-T long pulse burning plasma device, the thermal power, including fusion power, auxiliary heating power and ohmic heating power, must be dissipated, and the helium ash must be exhausted from the confined fusion plasma. This has a strong impact on the machine engineering design (impurity control, material selection, safety, etc.). Two major PWI issues have been identified for long pulse operation:

- (1) Steady state and transient heat loads, especially the localized heat load associated with fast particle losses, must be effectively removed before the PFC reaches an intolerable high temperature.
- (2) Uncontrolled density rise, arising from the thermal outgassing of PFC, instead of deuterium saturation, which usually leads to the termination of the discharge in most experiments.

It is found that the improved PFC cooling leads to better plasma performance and facilitates long pulse operation. In particular, with active cooling of the whole vessel including remote parts, as implemented in Tore-Supra, density control has been demonstrated for up to 6 minutes [7.159] and reaching 400 s in HT-7 [7.160].

Operation of next-step tokamak experiments will require effective means to disperse the thermal power and attain a significant reduction in divertor heat flux to an acceptable level dictated by the engineering design limit, i.e. about  $5\text{--}10 \text{ MW}\cdot\text{m}^{-2}$ , without compromising fusion performance.

The current strategy to achieve power dissipation is to convert most of the heat flux to impurity radiation in the so-called “core-mantle” region, i.e. the outer periphery of the core plasma, and in the divertor scrape-off layer (SOL) by redistributing the heat flux over the relatively large side-wall area of the

divertor region. This could be achieved, for example, by introducing highly radiative noble gases, such as neon, argon or krypton (via feedback control). Furthermore, the so-called “vertical target” configuration, as adopted in the ITER design, can be used to preferentially reduce the peak heat load near the strike point by directing the neutrals reflected off the divertor plate towards the separatrix, decreasing the temperature and increasing the density in its vicinity and promoting plasma detachment.

A serious limitation encountered on all machines aiming at long pulse operation is density control [7.161]. After a given duration, depending on the coupled power and the plasma density, an uncontrolled density rise often takes place, and despite cutting the plasma fuelling, terminates the discharge. Plasma performance is also affected by the loss of density and recycling control, with a progressive confinement degradation as the density rises, as observed in JT-60U long H-mode discharges [7.162]. This density rise seems to be associated with outgassing from heated components, rather than wall saturation by deuterium. Indeed, it was also observed in the helium discharges in LHD and correlated with toroidally localized H $\alpha$  emission from the components heated by local ICRF losses [7.163]. Results from long pulse machines with actively cooled PFCs, such as in Tore-Supra, show that the retention does not saturate but maintains a constant rate throughout the discharge.

In most machines, when operating in hydrogen or deuterium, wall pumping dominates the particle balance and allows efficient particle control for many particle confinement times. However, the wall will eventually saturate, and lose its pumping capability for hydrogen, and moreover the wall cannot pump helium. Therefore, strong external pumping devices have been installed in the modern divertor tokamaks to facilitate density control [7.164] and helium exhaust [7.165]. It is still not clear whether wall saturation will happen or not in the ITER steady-state operation scenario (>3000 s) with full W divertor, and how to control plasma density after wall saturation is still an unsolved issue. Further investigation is needed.

### 7.6.2. Transient heat loads

Estimated steady state heat loads in ITER are within the requirement of materials for the detached divertor or “radiation-mantle” operation scenarios. Extrapolation from present day devices shows that, although erosion under steady state conditions is acceptable, transient heat loads, such as ELMs and disruptions, pose the most serious challenge to PFC integrity and lifetime. The main power load to material surfaces during ELMs will occur at the divertor plates. The magnitude of the ELM energy deposition on the divertor plates in ITER relevant conditions (high density, high confinement H-modes) under a physics-based scaling has been formulated. Experimental studies of PFCs

exposed to ELM-like transient loads have shown that significant erosion can occur if the surface temperature is such that sublimation (CFC) or melting (W) is approached [7.166]. This would reduce the divertor lifetime to a few full performance discharges with uncontrolled ELMs in ITER [7.167].

It has been found that a significant fraction of the ELM energy (20% or more for very large uncontrolled ELMs) could be deposited on main chamber PFCs, not only in the divertor. ELMs lead to a fast radial expulsion of ions and electrons from the core, in essence carrying plasma energy from the pedestal directly to main chamber PFC. The radial transit time of the ELM is similar to the ion energy parallel loss time, such that ELM fluxes to the main chamber are of similar magnitude to those reaching the divertor. This raises concerns regarding the lifetime of ITER Be wall and upper divertor.

This heavy erosion threshold corresponds to energy densities in the range of 0.7–1.0 MJ·m<sup>-2</sup>, while for energy densities of ~0.5 MJ·m<sup>-2</sup>, the erosion is found to be negligible [7.166]. On this basis, requirements have been derived for ELM control in ITER consistent with negligible ELM erosion of the divertor targets resulting in a required maximum plasma energy loss for controlled ELMs in ITER of  $\Delta W_{ELM}$  controlled  $\leq 1$  MJ. The expected frequency for such controlled ELMs is  $f_{ELM}$  controlled = 20–40 Hz [7.168]. These requirements have been taken into account for the incorporation/detailed specification of ELM control strategy and schemes in ITER.

The plasma facing components in ITER will also be subjected to a number of short transient events, with extremely high energy densities [7.169]. These incidents are partially off-normal events, i.e. plasma disruptions with energy densities of a few, up to several tens of MJ·m<sup>-2</sup>, plasma instabilities, and so called VDEs (vertical displacement events) with energy densities of  $\leq 60$  MJ·m<sup>-2</sup>. The energy deposition during disruptions is in the millisecond timescale range, while the VDEs occur on a much longer timescale ( $\Delta t \approx 100$ –300 ms). In ITER, both events can result in substantial material erosion due to melting and/or evaporation processes. Hence, the number of these lifetime limiting events has to be kept within specified limits (less than 10% and 1% of all plasma discharges for disruptions and VDEs, respectively).

Other transient heat loads, such as position excursion, attached plasma and sudden transition from H-phase to L-phase and runaway electrons could also produce unacceptable heat load on PFCs. According to recent assessment in the ITER design review, some of these heat loads can be over 100 MW·m<sup>-2</sup> in a short period (1–3 s) and could induce significant erosion. Control and mitigation tools for these transient events are underdeveloped and a solution will be provided by modelling and experimental efforts.

### 7.6.3. Material migration

Erosion of plasma facing materials, impurity transport through the plasma and its deposition define the topic of material migration [7.170], which affects the lifetime of PFCs, degrades core plasma performance due to impurity contamination and leads to tritium retention in the migrated materials in a fusion reactor. Thus, material migration is a pivotal issue both for ITER and for the longer term economic and technological viability of fusion power. Furthermore, erosion, co-deposition along with melt layer and wall conditioning processes also lead to macroscopic dust production, which is regarded as a potential safety hazard. Material migration does not present any significant operational issues for current tokamaks, but it will become increasingly important, moving to ITER and then onwards to a demonstration fusion power plant.

To minimize impurity migration, it is essential to optimize both plasma behaviours and properties of the plasma facing components. An important recent example is the choice of the so-called “partially-detached divertor plasma” as the most promising and favourable operation regime for an ITER-class tokamak [7.171]. A detached or partially detached plasma allows for a large heat flux reduction at the divertor plate near the strike point, sufficient helium exhaust, and greatly reduces the incident particle energy at the divertor ( $T_e < 5$  eV), thus reducing or eliminating physical sputtering of even low- $Z$  materials. However, in this case, chemical processes are expected to dominate carbon erosion, and the complex transport/dissociation of hydrocarbon molecules in the plasma must be understood to predict erosion and deposition rates.

Control of the tritium retention in the migrated materials will also be critical, as further discussed in the next section. Because of the complexity of the problem, predictions for next step devices such as ITER will remain uncertain, and it is difficult to develop tritium control techniques without full wall material tests in the current tokamaks, combined with components of relevant geometry.

### 7.6.4. Control of in-vessel tritium inventory

Tritium retention in plasma facing materials (PFMs) and control of the in-vessel tritium inventory have emerged as the primary concerns for ITER and future fusion reactors fuelled with D-T mixtures, which have critical implications for in-vessel component design, materials selection, operational schedule and safety. The initial material selection for ITER PFCs is as follows: beryllium on the main vessel walls, tungsten on the divertor upper baffle and dome, and CFC around the strike points on the divertor plates. The most critical issues are the lifetime for PFCs and the extent of tritium retention in the vessel. Tritium retention in PFMs consists of implantation, trapping and diffusion as well as surface erosion and co-deposition of tritium with eroded material.

Recent experimental and modelling results indicate that as long as C-based materials are used, even in very limited regions of the in-vessel components, the dominant mechanism for tritium retention will be co-deposition of tritium with eroded carbon in the colder regions of the divertor system, with a limit of T inventory level of 700 g. This limit could be reached within a few hundred full performance discharges [7.172]. The specific property of carbon to retain large quantities of tritium in deposited layers has led to the decision of ITER to propose a change from CFC divertor strike point tiles to a full W divertor in the D-T phase, with Be as vessel first wall.

Tritium removal from a next-step machine using carbon is a major unsolved problem. A promising means for the removal of T-rich co-deposited layers involves exposure to oxygen (e.g. by thermo-oxidative erosion at temperatures above 570 K or using oxygen plasma discharges), which has been found to be most effective in laboratory experiments to remove T from a carbon surface (by removing the T-containing films). However, the major drawbacks of such techniques include collateral effects on other in-vessel components, especially at elevated temperatures and recovery time for normal plasma operation. As discussed in Section 7.4, many other techniques for post-discharge T removal have been proposed and none of them could meet ITER operation requirements. Some other solutions for T retention mitigation are also proposed. A regime of controlled operations (the so-called “good housekeeping” [7.173]) with a spectrum of recovery techniques is likely to be the best strategy for managing the tritium inventory. For example, careful attention to optimizing the tritium fuelling efficiency (minimizing the tritium introduced), tailoring the isotope ratio [7.174] and ending every shot in a deuterium-only phase with sweeping of the divertor strike points [7.175] have all been proposed. Further experimental efforts are needed in present tokamaks, especially in long pulse divertor plasma configurations such as EAST and KSTAR. Some of them can be tested only during ITER operation to have a clearer solution.

The W divertor/Be first wall option, presently foreseen for the D-T phase of ITER, will make the T retention issue considerably less problematic, extending the number of discharges until the tritium limit is reached to about 3000. Still, removal methods for co-deposited Be layers must be developed and tested unless a full W wall could be used, which is expected to allow about 15 000 discharges before the tritium limit is reached.

### **7.6.5. Integrated PWI issues for steady state operation**

Achieving long-duration (>3000 s), high-performance ( $Q = 10$ ) discharges in ITER is one of the greatest challenges towards a fusion reactor. This requires integrating many physical concepts and technological achievements that hitherto have been considered as separate issues. Long pulse operation involves a

sequence of progressively increasing characteristic timescales, ranging from milliseconds for MHD events, seconds for energy and particle transport times, tens of seconds for current diffusion times, and up to hundreds of seconds for wall processes, such as saturation and erosion, to reach equilibrium. Although many present-day experiments have pulse lengths long enough to allow studies of the MHD and transport issues in conditions that are effectively quasi-steady-state, most experiments have pulse lengths that are marginal for studying current diffusion phenomena and, generally, all are too short to study wall saturation and erosion.

Further extension of the discharge duration will bring experiments into the range of wall saturation timescales. The present database consists of limited shots from TRIAM-1M, HT-7, Tore-Supra and LHD. In consequence, even the simple determination of the wall saturation timescale remains to be studied. The only experimental evidence is that the gas feed has to be stopped on Tore-Supra after 1 minute [7.176] and on TRIAM-1M after 30 minutes [7.177], and that on LHD the wall remains unsaturated after 1 minute [7.178]. Clearly, the wall saturation time is longer than these values, but how much longer is still to be determined. Consequently, the possible impact of the wall saturation state on the overall plasma behaviour remains an open issue. In particular, very long pulses will be required to address particle balance issues in the presence of a saturated wall, which is essential for steady state operation. For instance, an important issue to be resolved is whether a satisfactory particle balance can be achieved relying only on the external pumping capability that is presently foreseen.

The relevance of present experiments to the PWI issues for ITER is somewhat restricted by the fact that there is no device combining an adequate plasma regime (semi-detached at low  $T_e$ ), a realistic PFC material mix (nearly all present results are related to carbon PFCs only) and steady-state PFC temperature ensured by active cooling. For example, attempts have been made to study erosion and re-deposition problems by analysing the final state of PFCs after a long campaign of short pulses. However, this not only integrates over a wide range of different plasma conditions used during the experimental campaign, but even within a single shot, the surface temperature of inertially-cooled plasma facing components is constantly evolving. Consequently, it is difficult to provide a realistic simulation of erosion and re-deposition processes during the long pulse operation of a magnetic fusion reactor.

Active cooling of the plasma facing components holds the prospect of steady state operation, but at the expense of a constraint on the injected power level, which is limited by the exhaust capability of the most heavily loaded part of the plasma facing components. For this reason a strong R&D development programme is presently under way in the domain of actively cooled plasma facing components.

Many PWI issues for steady state operation will be addressed in a new generation of superconducting, actively cooled divertor devices, such as EAST and KSTAR, which could partly fill the gap towards ITER. However, the main open issues related to mixed materials effects (including localized heat loads on Be and W, formation of Be/W alloys, properties of mixed re-deposited layers, co-deposition and bulk diffusion of T with Be, etc.) will not be addressed in these machines, which still largely rely on carbon PFCs. Projects such as the ITER-like Be/W/C wall in JET and the full W divertor in ASDEX-Upgrade, along with dedicated PSI experiments including PISCES and MAGNUM, should allow for progress on these topics, albeit not in a fully steady state perspective.

For the DEMO fusion power plants following ITER with long D-T operations and strong radiation damage from neutrons and charged particles, W offers a preferable candidate for PFM, as compared to Be and C [7.179, 7.180]. For a DEMO-type fusion power reactor, Be will not be suitable due to neutron damage, which leads to gas production and excessive increase of T inventory. In addition, Be would not provide sufficient lifetime due to excessive erosion, which is intrinsic to low-Z materials. C will be subject to even stronger erosion than Be, due to both physical and chemical sputtering, and potential for large T retention. The latter has recently led ITER to completely abandon C from its planning for the nuclear operation phase. Furthermore, C is also subject to neutron damage resulting in dimensional instability and reduction of thermal conductivity. Neutron damage at levels above 5–10 dpa would lead to the exclusion of both Be and C [7.179]. Note that ITER's planned neutron fluence is  $\sim 0.5$  dpa/year, while DEMO's first wall components should experience a neutron fluence of  $\sim 100$  dpa/year.

With the expectation that the aforementioned transient, off-normal events will be well controlled before DEMO is able to be built, the issue with melt layer loss during disruptions and Type I ELMs for W will largely disappear in DEMO. In this case, the sputtering of PFMs during normal operation will determine the component lifetime. W seems to be the only choice for DEMO PFMs. However, W offers a far lower tolerable limit for plasma contamination [7.73] than the low-Z materials. Recently, operation with a fully W-covered wall in ASDEX-Upgrade [7.181] has demonstrated low D retention, and acceptable W concentration in the plasmas, i.e.  $\sim (1-3) \times 10^{-5}$ , within the tolerable range for ignition, in ITER-relevant operational scenarios. Unfortunately, although its thermal conductivity does not degrade significantly under neutron irradiation compared to Be and C, W could suffer significant radiation damage from high He ion fluencies. Further efforts are needed in developing W-based PFMs [7.180] and pursuing other advanced material concepts for DEMO, which should involve the broad fusion and materials research community and ultimately ITER.

## REFERENCES

- [7.1] CRASTON, J.L. et al., Peaceful uses of Atomic Energy, Proc. 2nd Int. Conf. Geneva, 1956; **32** (1958) 414.
- [7.2] McCracken, G.M., STOTT, P.E., Nucl. Fusion **19** (1979) 889.
- [7.3] ARUNSALAM, V., et al., Control. Fusion Plasma Phys. (Proc. 8th European Conference, Prague) **2** (1977) 17.
- [7.4] STOTT, P.E., et al., Nucl. Fusion **15** (1975) 431.
- [7.5] PRINCETON PLASMA PHYSICS LABORATORY, Annual Report MATT-Q-23 (1965) 73.
- [7.6] NAGAMI, M., et al., J. Nucl. Mater. **76/77** (1978) 521.
- [7.7] ASDEX TEAM, Nucl. Fusion **29** (1989) 1959.
- [7.8] WESSON, J., Tokamaks, 3rd edn, Chapters 9, 14, Oxford University Press, Oxford (2004).
- [7.9] THOMAS, E.W., et al., Nucl. Instrum. Methods **B69** (1992) 427.
- [7.10] ARATARI, R., et al., J. Nucl. Mater. **91** (1989) 162.
- [7.11] JANEV, R.K., et al., Elementary Processes in Hydrogen-Helium Plasmas, Cross-Sections and Reaction Rate Coefficients, Springer Verlag, Berlin (1987).
- [7.12] STANGEBY, P.C., McCracken, G.M., Nucl. Fusion **30** (1990) 1225.
- [7.13] CAROLAN, P.G., PIOTROWICZ, V.A., Plasma Phys. **25** (1983) 1065.
- [7.14] ECKSTEIN, W., Sputtering Data Report PP9/82, Max Planck Institut für Plasmaphysik, Garching (1993).
- [7.15] THOMPSON, M.W., Phil. Mag **18** (1968) 377.
- [7.16] BOGEN, P., RUSBULDT, D.J., Nucl. Mater. **179** (1992) 196.
- [7.17] MECH, B.V., et al., J. Nucl. Mater. **255** (1998) 153.
- [7.18] ROTH, J., et al., Nucl. Fusion **44** (2004) L21.
- [7.19] ARUNASALAM, V., BARNES, C., BOL, K., et al., "Recent results from the PLT tokamak", Proc. 8th EPS Conf. on EPS, Vol. 2, Prague (1977) p. 17.
- [7.20] MILLS, B.E., BUCHENAUER, D.A., PONTAU, A.E., ULRICKSON, M., J. Nucl. Mater. **162-164** (1989) 343.
- [7.21] KISHIMOTO, H., JT-60 TEAM, Nucl. Fusion supplement **1** (1989) 67.

- [7.22] SHIMIZU, K., TAKIZUKA, T., SAKASAI, A., *J. Nucl. Mater.* **241–243** (1997) 167.
- [7.23] NEU, R., DUX, R., KALLENBACH, A., et al., *Nucl. Fusion* **45** (2005) 2009.
- [7.24] JACKSON, G.L., et al., *J. Nucl. Mater.* **220** (1995) 173.
- [7.25] STRACHAN, J.D., et al., *J. Nucl. Mater.* **196–198** (1992) 28.
- [7.26] BARABASH, V., AKIBA, M., MAZUL, I., et al., *J. Nucl. Mater.* **233–237** (1996) 718.
- [7.27] PUGNO, R., et al., in Proc. 30th EPS Conf. on Controlled Fusion and Plasma Physics, St. Petersburg, Russia, 2003, Vol. 27A (ECA) (2003) P-1.153.
- [7.28] WHYTE, D.G., *Phys. Scr.* **T111** (2004) 34.
- [7.29] ROTH, J., et al., *Nucl. Fusion* **44** (2004) L21.
- [7.30] ROTH, J., et al., *J. Nucl. Mater.* **337–339** (2005) 970.
- [7.31] BROOKS, J.N., et al., *J. Nucl. Mater.* **266–269** (1999) 58.
- [7.32] WUERZ, H., et al., *J. Nucl. Mater.* **307–311** (2002) 60.
- [7.33] LANDMAN, I.S., et al., *Phys. Scr.* **T111** (2004) 206.
- [7.34] THOMAS, P.R., et al., *J. Nucl. Mater.* **176–177** (1990) 3.
- [7.35] LOARTE, A., et al., *J. Nucl. Mater.* **337–339** (2005) 816.
- [7.36] KAUFMANN, M., NEU, R., *Fusion Eng. Des.* **82** (2007) 521.
- [7.37] KOCH, F., BOLT, H., *Phys. Scri.* **T128** (2007) 100.
- [7.38] RUBEL, M., et al., *J. Nucl. Mater.* **313–316** (2003) 321.
- [7.39] COAD, J.P., ANDREW, P., HOLE, D.E., et al., *J. Nucl. Mater.* **313–316** (2003) 419.
- [7.40] DOERNER, R.P., *J. Nucl. Mater.* **363–365** (2007) 32–40.
- [7.41] CARRERAS, B.A., *J. Nucl. Mater.* **337–339** (2005) 315.
- [7.42] ZWEBEN, S.J., GOULD, R.W., *Nucl. Fusion* **25** (1985) 171.
- [7.43] LOARTE, A., SAIBENE, G., SATORI, R., et al., *Phys. Plasmas* **11 (5)** (2004) 2668.
- [7.44] GUSEVA, M.I., SUVOROV, A.L., KORSHUNOV, S.N., et al., *J. Nucl. Mater.* **266–269** (1999) 222–227.
- [7.45] DYLLA, H.F., et al., *J. Vac. Sci. Technol.* **17** (1980) 286.

- [7.46] WAELBROECK, F.G., WINTER, J., WIENHOLD, P., J. Vac. Sci. Technol. **A2** (1984) 1521.
- [7.47] OREN, L., TAYLOR, R., J. Nucl. Fusion **17** (1977 ) 1143.
- [7.48] JACKSON, G.L., TAYLOR, T.S., TAYLOR P.L., Nucl. Fusion **30** (1990) 2305.
- [7.49] SAKAMOTO, Y., et al., J. Nucl. Mater. **93–94** (1996) 333.
- [7.50] SAKAMOTO, Y., in Proc. 9th Int. Vac. Congress – 5th Int. Conf. Solid Surfaces, Madrid (1983) 716.
- [7.51] NACHTRIEB, R.T., et al., J. Nucl. Mater. **266–269** (1999) 896.
- [7.52] KOMORI, A., et al., in Proc. 12th Int. Stellarator Workshop, Madison, USA (1999) P2.
- [7.53] HANADA, K., et al., Fusion Eng. Des. **54** (2001) 79.
- [7.54] USHIGUSA, K., et al., Fusion Eng. Des. **45** (1999) 137.
- [7.55] SAKAMOTO, Y., ISHII, S., YANO, K., et al., Fusion Technology, Vol. 1, Pergamon, New York (1982) 347.
- [7.56] DE LA CAL, E., GAUTHIER, E., Plasma Phys. Control. Fusion **39** (1997) 1083.
- [7.57] ESSER, H.G., et al., J. Nucl. Mater. **241–243** (1997) 861.
- [7.58] ZHAO, Y.P., et al., Chin. Phys. Lett. **14** (1997) 916.
- [7.59] LI, J., et al., Nucl. Fusion **39** (1999) 973.
- [7.60] BRAKEL, R., et al., J. Nucl. Mater. **290–293** (2001) 1160.
- [7.61] DE LA CAL, E., GAUTHIER, E., Plasma Phys. Control. Fusion **47** (2005) 197–218.
- [7.62] WINTER, J., J. Nucl. Mater. **145–147** (1987) 131.
- [7.63] WINTER, J., ESSER, H.G., KONEN, L., et al., J. Nucl. Mater. **162–164** (1989) 713.
- [7.64] SAMM, U., BOGEN, P., ESSER, H.G., et al., J. Nucl. Mater. **220–222** (1995) 25.
- [7.65] BOUCHER, C., MARTIN, F., STOMSFIELD, B.L., et al., J. Nucl. Mater. **196–198** (1992) 587.
- [7.66] NODA, N., et al., J. Nucl. Mater. **176–177** (1990) 640.

- [7.67] YOSHIFUMI, I., et al., *Plasma Sources Sci. Technol.* **5** (1996) 305–310.
- [7.68] XIE, J.K., et al., *J. Nucl. Mater.* **290–293** (2001) 1155.
- [7.69] HIGASHIJIMA, S., et al., *J. Nucl. Mater.* **266–269** (1999) 1078.
- [7.70] LIPSCHULTZ, B., et al., *Nucl. Fusion* **41** (2001) 585.
- [7.71] GEIER, A., et al., *J. Nucl. Mater.* **313–316** (2003) 1216.
- [7.72] WINTER, J., *Plasma Phys. Control. Fusion* **40** (1998) 1201.
- [7.73] FEDERICI, G., SKINNER, C.H., BROOKS, J.N., et al., *Nucl. Fusion* **41** (2001) 1967.
- [7.74] CARMACK, W.J., MCCARTHY, K.A., PETTI, D.A., et al., *Fusion Eng. Des.* **39&40**, part A (1998) 477.
- [7.75] GORMAN, S.V., CARMACK, W.J., HEMBREE, P.B., *Fusion Technol.* **34** (1998) 745.
- [7.76] MCCARTHY, K.A., et al., *Fusion Technol.* **34** (1998) 728.
- [7.77] CHAPPUIS, Ph., et al., *J. Nucl. Mater.* **290-293** (2001) 245.
- [7.78] McSMITH, M.D., et al., *Fusion Technol.* **26** (1994) 498.
- [7.79] GUO, H.Y., et al., *J. Nucl. Mater.* **241-243** (1997) 385.
- [7.80] WHYTE, D., et al., *J. Nucl. Mater.* **290-293** (2001) 356.
- [7.81] KRETER, A., et al., *Phys. Scr.* **T128** (2007) 35.
- [7.82] WAMPLER, W.R., et al., *J. Vac. Sci. Technol.* **A 6 (3)** (1988) 2111.
- [7.83] HU, J.S., et al., in *Proc. 32nd EPS Conf. on Plasma Phys.* **72** (2005) 377.
- [7.84] BROOKS, J.N. *Fusion Eng. Des.* **60** (2002) 515.
- [7.85] ANDREW, P., et al., *Fusion Eng. Des.* **47** (1999) 233.
- [7.86] SKINNER, C.H., et al., *J. Nucl. Mater.* **290–293** (2001) 486.
- [7.87] WHYTE, D.G., DAVIS, J.W., *J. Nucl. Mater.* **337–339** (2005) 560.
- [7.88] SPITZER, L., *Phys. Fluids* **1** (1958) 253.
- [7.89] STANGEBY, P.C., *The Plasma Boundary of Magnetic Fusion Devices*, Institute of Physics, Bristol (2000).
- [7.90] SHIMOMURA, Y., KEILHACKER, M., LACKER, K., MURMANN, H., *Nucl. Fusion* **23** (1983) 869.

- [7.91] LaBOMBARD, B., et al., Phys. Plasmas **2** (1995) 2242.
- [7.92] LOARTE, A., et al., Nucl. Fusion **47** (2007) S203.
- [7.93] WAGNER, F., BECKER, G., BEHRINGER, K., et al., Phys. Rev. Lett. **49** (1982) 1408.
- [7.94] OHYABU, N., et al., Nucl. Fusion **34** (1994) 387.
- [7.95] LOARTE, A., Plasma Phys. Control. Fusion **43** (2001) R183.
- [7.96] JET TEAM (prepared by MONK, R.D.) Nucl. Fusion **39** (1999) 1751.
- [7.97] HUTCHINSON, I., et al., Phys. Plasmas **1** (1994) 1511.
- [7.98] GUO, H.Y., ZHU, S., LI, J., J. Nucl. Mater. **363-365** (2007) 162.
- [7.99] GUO, H.Y., ZHU, S. and LI, J., J. Nucl. Mater. **363-365** (2007), 162.
- [7.100] MATTHEWS, G.F., J. Nucl. Mater. **337-339** (2005) 1.
- [7.101] ASAKURA, N., et al., Nucl. Fusion **44** (2004) 503.
- [7.102] LaBOMBARD, B., et al., J. Nucl. Mater. **241-243** (1997) 149.
- [7.103] BOHDANSKY, J., Nucl. Fusion, Special Suppl. **61** (1984) 61.
- [7.104] MECH, B.V., et al., J. Nucl. Mater. **255** (1998) 153.
- [7.105] GUO, H.Y., et al., Nucl. Fusion **40** (2000) 379.
- [7.106] GUO, H.Y., et al., Nucl. Fusion **40** (2000) 69.
- [7.107] PITCHER, C.S., STANGEBY, P.C., Plasma Phys. Control. Fusion **39** (1997) 779.
- [7.108] SCHAFFER, M.J., WADE, M.R., MAINGI, R., et al., J. Nucl. Mater. **241-243** (1997) 585.
- [7.109] WADE, M.R., et al., Nucl. Fusion **38** (1998) 1839.
- [7.110] ITAMI, K., et al., J. Nucl. Mater. **266-269** (1999) 1097.
- [7.111] SAKASAI, A., et al., J. Nucl. Mater. **266-269** (1999) 312.
- [7.112] ASAKURA, N., et al., Nucl. Fusion **36** (1996) 795.
- [7.113] CHANKIN, A.V., J. Nucl. Mater. **241-243** (1997) 199.
- [7.114] GOLDSTON, R.J., RUTHERFORD, P.H., Introduction to Plasma Physics, Institute of Physics, Bristol (2000).
- [7.115] ROGNLIEN, T.D., PORTER, G.D., RYUTOV, D.D., J. Nucl. Mater. **266-269** (1999) 654.
- [7.116] PORTER, G.D., et al., J. Nucl. Mater. **313-316** (2003) 1085.

- [7.117] LaBOMBARD, B., et al., Nucl. Fusion **44** (2004) 1047.
- [7.118] ASAKURA, N., et al., Nucl. Fusion **39** (1999) 1983.
- [7.119] ASAKURA, N., et al., Phys. Rev. Lett. **84** (2000) 3093.
- [7.120] ERENTS, S.K., et al., Plasma Phys. Control. Fusion **46** (2004) 349.
- [7.121] PITTS, R.A., et al., J. Nucl. Mater. **363–365** (2007) 505.
- [7.122] ASAKURA, N., J. Nucl. Mater. **363–365** (2007) 41.
- [7.123] SCHAFFER, M.J., CHANKIN A.V., GUO, H.Y., et al., Nucl. Fusion **37** (1997) 83.
- [7.124] CHANKIN A.V., STANGEBY, P.C., Nucl. Fusion **42** (2001) 421.
- [7.125] LaBOMBARD, B., et al., Nucl. Fusion **45** (2005) 1658.
- [7.126] CARRERAS, B.A., J. Nucl. Mater. **337–339** (2005) 315.
- [7.127] TERRY, J.L., et al., Phys. Plasmas **10** (2003) 1739.
- [7.128] ENDLER, M., et al., Plasma Phys. Control. Fusion **47** (2005) 219.
- [7.129] CARRERAS, B.A., et al., Phys. Rev. Lett. **80** (1998) 4438.
- [7.130] SARAZIN, Y., GHENDRIH, Ph., Phys. Plasmas **5** (1998) 4214.
- [7.131] KRASHENINNIKOV, S.I., Phys. Lett. A **283** (2001) 368.
- [7.132] D'IPPOLITO, D.A., et al., Phys. Plasmas **9** (2002) 222.
- [7.133] LaBOMBARD, B., et al., Nucl. Fusion **40** (2000) 2041.
- [7.134] GREENWALD, M., Plasma Phys. Control. Fusion **44** (2002) R27.
- [7.135] ENDLER, M., et al., Nucl. Fusion **35** (1995) 1307.
- [7.136] LaBOMBARD, B., et al., Phys. Plasmas **15** (2008) 056106.
- [7.137] SUTTROP, W., et al., J. Nucl. Mater. **266–269** (1999) 118.
- [7.138] SCOTT, B.D., Plasma Phys. Control. Fusion **49** (2007) S25.
- [7.139] XU, X.Q., COHEN, R.H., Contrib. Plasma Phys. **36** (1998) 158.
- [7.140] SCOTT, B.D., Phys. Plasmas **12** (2005) 062314.
- [7.141] FUNDAMENSKI, W., et al., Nucl. Fusion **45** (2005) 950.
- [7.142] PITTS, R.A., et al., J. Nucl. Mater. **337–339** (2005) 146.
- [7.143] LOARTE, A., et al., Plasma Phys. Control. Fusion **45** (2003) 1549.
- [7.144] EICH, T., et al., J. Nucl. Mater. **337–339** (2005) 669.

- [7.145] BERGMANN, A., Nucl. Fusion **42** (2002) 1162.
- [7.146] CONNOR, J.W., et al., Phys. Plasmas **7** (1998) 2678.
- [7.147] SNYDER, P.B., et al., Phys. Plasmas **9** (2002) 2037.
- [7.148] COUNSELL, G.F., et al., Plasma Phys. Control. Fusion **44** (2002) B23.
- [7.149] COUNSELL, G.F., et al., J. Nucl. Mater. **313–316** (2003) 804.
- [7.150] ZHANG, L., et al., Plasma Phys. Control. Fusion **46** (2004) A121.
- [7.151] TAKENAGA, H., et al., Nucl. Fusion **45** (2005) 1618.
- [7.152] ITER TECHNICAL BASIS, ITER EDA Documentation Series No 24. IAEA, Vienna, 2002.
- [7.153] MONIER-GARBET, P., et al., in Proc. 30th EPS Conf. on Control. Fusion and Plasma Phys., St. Petersburg, Russia, Vol. 27A (2003) P-1.095.
- [7.154] RICE, J.E., et al., Nucl. Fusion **42** (2002) 510.
- [7.155] NEU, R., et al., J. Nucl. Mater. **313–316** (2003) 116.
- [7.156] LANG, P.T., et al., Nucl. Fusion **43** (2003) 1110.
- [7.157] FEDERICI, G., COAD, J.P., HAASZ, A.A., et al., J. Nucl. Mater. **283–287** (2000) 110–119.
- [7.158] SAOUTIC, B., Plasma Phys. Control. Fusion **44** (2002) B11–B22.
- [7.159] HOUTTE, D.V., MARTIN, G., BÉCOULET, A., et al., Nucl. Fusion **44** (2004) L11.
- [7.160] GONG, X.Z., et al., in Proc. 18th PSI, Toledo, Spain, 25–30 May 2008, O-9.
- [7.161] ASAKURA, N., Plasma Phys. Control. Fus. **46** (2004) B335.
- [7.162] TAKENAGA, H., ASAKURA, N., HIGAHIJIMA, S., et al., J. Nucl. Mater. **337–339** (2005) 802.
- [7.163] SAITO, K., KUMAZAWA, R., MUTOH, T., et al., J. Nucl. Mater. **337–339** (2005) 995.
- [7.164] WATKINS, J.G., et al., Bull. Am. Phys. Soc. **46** (2001) 225.
- [7.165] SAKASAI, A., et al., in Proc. 18th Int. Conf. on Fusion Energy, Sorrento, 2000, EX5/5.
- [7.166] KLIMOV, N., et al., J. Nucl. Mater. **390–391** (2009) 721.
- [7.167] FEDERICI, G., et al., Plasma Phys. Control. Fusion **43** (2003) 1523.

- [7.168] LOARTE, A., et al., Plasma Phys. Control. Fusion **43** (2003) 1549.
- [7.169] LINKE, J., ESCOURBIAC, F., MAZUL, I.V., et al., J. Nucl. Mater. **367–370** (2007) 1422.
- [7.170] MATTHEWS, G.F., J. Nucl. Mater., **337–339** (2005) 1.
- [7.171] KUKUSHKIN, A.S., et al., Control. Plasma Phys. **38** (1998) 20.
- [7.172] ROTH, J., TSITRONE, E., LOARER, T., et al., Plasma Phys. Control. Fusion **50** (2008) 103001.
- [7.173] COUNSELL, G.F., et al., Plasma Phys. Control. Fusion **B48** (2006) 89.
- [7.174] GOUGE, M., et al., Fusion Technol. **28** (1995) 1644.
- [7.175] ANDREW, P., BRENNAN, P.D., COAD, J.P., Fusion Eng. Des. **47** (1999) 233.
- [7.176] ZUSHI, H., et al., in Proc. 19th Int. Conf. on Fusion Energy, Lyon, France, 2002, IAEA, Vienna OV/4–6.
- [7.177] NAKAMURA, Y., et al., J. Nucl. Mater. **290–293** (2001) 1040.
- [7.178] BRUSATI, M., et al., in Proc. 19th EPS Conf. on Control. Fusion and Plasma Phys., Innsbruck, Austria, Vol 16C (ECA) (1992) I-307.
- [7.179] BOLT, H., et al., J. Nucl. Mater. **307–311** (2002) 43.
- [7.180] WONG, C.P.C., et al., J. Nucl. Mater. **390–391** (2009) 1026.
- [7.181] ZOHM, H., et al., Nucl. Fusion **49** (2009) 104009.

# CHAPTER 8

## HELICAL CONFINEMENT CONCEPTS

**C. Beidler, R. Brakel, R. Burhenn, A. Dinklage, V. Erckmann, Y. Feng,  
J. Geiger, D. Hartmann, M. Hirsch, R. Jaenicke, R. Koenig, H.P. Laqua,  
H. Maassberg, F. Wagner, A. Weller, H. Wobig<sup>†1</sup>**  
Max-Planck Institut für Plasmaphysik,  
EURATOM Association,  
Greifswald, Germany

### 8.1. INTRODUCTION

Stellarators, conceived 1951 by Lyman Spitzer in Princeton [8.1], are toroidal devices that confine a plasma in a magnetic field which originates from currents in coils outside the plasma. A plasma current driven by external means, for example by an ohmic transformer, is not required for confinement. Supplying the desired poloidal field component by external coils leads to a helically structured plasma topology. Thus stellarators — or helical confinement devices<sup>2</sup> — are fully three-dimensional in contrast to the toroidal (rotational) symmetry of tokamaks.

As stellarators can be free of an inductive current, whose radial distribution depends on the plasma parameters, their equilibrium must not be established via the evolving plasma itself, but to a first order already given by the vacuum magnetic field. They do not need an active control (like positional feedback) and therefore cannot suffer from its failure. The outstanding conceptual advantage of stellarators is the potential of steady state plasma operation without current drive. As there is no need for current drive, the recirculating power is expected to be smaller than in equivalent tokamaks. The lack of a net current avoids current driven instabilities; specifically, no disruptions, no resistive wall modes and no conventional or neoclassical tearing modes appear. Second order pressure-driven currents (Pfirsch–Schlüter, bootstrap) exist but they can be modified and even minimized by the magnetic design. The magnetic configuration of helical devices naturally possesses a separatrix, which allows the implementation of a helically structured divertor for exhaust and impurity control.

---

<sup>†1</sup> Deceased 18 March 2011.

<sup>2</sup> In this chapter helical confinement devices and stellarators are taken as synonyms as is common in most literature. In a more strict sense the term stellarator covers the concept where the external currents flow in opposite directions in adjacent helical coils and thus balance, in contrast to heliotrons/torsatrons and heliacs, where a net toroidal current exists in the coil system (see Section 8.2.2).

The three-dimensionality of stellarators, which allows for these advantages, gives also rise to their drawbacks. Due to the missing toroidal symmetry: (1) particle drift orbits can strongly deviate from the magnetic flux surfaces with the corollary of large neo-classical fluxes; (2) trapped energetic particles are not necessarily confined; and (3) the helical windings used in classical helical devices result in large aspect ratio devices, but the equilibrium  $\beta$  is low for large aspect ratios and low values of the rotational transform.

A variety of stellarator configurations are possible and several concepts have emerged as described in Section 8.2 — the classical stellarator, the heliotron/torsatron, the heliac and the optimized stellarators based on quasi-symmetry and drift optimization. The concepts differ by the magnetic parameters chosen, like rotational transform, magnetic shear, well depth, aspect ratio and the symmetry properties of the magnetic field strength  $|B|$  on the magnetic surfaces. Today, helical devices are operated in Australia, Germany, Japan, Spain, Ukraine and the USA. The largest device in operation is the Large Helical Device (LHD) [8.2] operated in Toki-City, Japan. In Germany, the stellarator Wendelstein 7-X is under construction and will start operation in 2014.

To gain reactor relevance, helical devices need to overcome the drawbacks of three-dimensionality. The concepts of stellarator optimization are summarized in Section 8.5. Their theoretical background is (1) that the deviation of particles from the flux surface as well as equilibrium and stability properties depend on the variation of the magnetic field strength  $|B|$  in the flux surface, and (2) that  $|B|$  can be made (nearly) two-dimensional in an otherwise three-dimensional toroidal geometry (expressed in proper magnetic coordinates). Systems with these properties are called quasi-symmetric systems and meanwhile several smaller stellarators are operated or designed according to these concepts (in particular the quasi-helically symmetric stellarator HSX in Wisconsin [8.3], the quasi-axisymmetric device NCSX in Princeton [8.4], and the quasi-poloidally symmetric design QPS in Oak Ridge [8.5]). The design of Wendelstein 7-X [8.6] follows the quasi-isodynamic principle [8.7], which achieves the desired optimization criteria by a minimization of the geodesic curvature of the flux surfaces. An additional degree of freedom is used for a strong reduction of the bootstrap current with the goal to obtain a largely pressure independent magnetic field configuration. The Heliotron-J device operated in Kyoto is based on a related concept [8.8].

Helical devices are an independent reactor line as outlined in Section 8.6, but they share the basic technology with tokamaks. A helical reactor, based on the classical concepts, has the technical disadvantage of large forces between the bulky helical coils. This can be alleviated by the modular concept as introduced in Section 8.2.2 or in the so-called force-free approaches of the heliotron line (Section 8.6.1). An advantage of a stellarator reactor is that some concepts can be based on conventional NbTi as superconductor for the coils, which will have a cost-saving impact on the power reactor. As in tokamaks, the reactor size is firstly

determined by the scaling of the energy confinement time, which roughly grows with the plasma volume, which must be large enough to ensure ignition and self-sustained burn. However, the dimensions of a stellarator reactor must also be large enough to accommodate a blanket and neutron shield everywhere between plasma and the complex 3-D coil system. Thus the three-dimensionality as an engineering issue adds substantial complexity in comparison to a 2-D system.

## 8.2. HELICAL CONFINEMENT CONCEPTS

### 8.2.1. Production of 3-D toroidal flux surfaces

Nested magnetic flux surfaces are the key element in confinement. In the frame of an ideal MHD-model the plasma pressure is constant on magnetic field lines and in order to achieve a system of closed pressure surfaces, the existence of closed magnetic surfaces is required. In a helical device, current-carrying coils provide the confining field and magnetic surfaces exist already in the vacuum. A magnetic surface is a toroidal surface enclosing a certain flux  $\psi(x, y, z) = \text{constant}$ , which is densely covered by magnetic field lines ( $\vec{B} \cdot \nabla \psi = 0$ ) as illustrated in Fig. 8.1 (top). Furthermore, the surface should be smooth and the derivatives of the flux function  $\psi$  should be continuous up to second order  $\psi \in C^2$ . On every toroidally closed surface one can introduce a coordinate system: a toroidal angular coordinate  $\phi$  and a poloidal coordinate  $\theta$ . A pair of functions  $\theta(s), \phi(s)$ , where  $s$  is the coordinate along the field line, describes the orbit of the field line on the surface  $\psi = \text{constant}$ . The coordinate system  $\psi, \phi, \theta$  is a convenient and powerful system to describe plasma properties. For comparison with experiment it is often useful to assign to each flux surface  $\psi = \text{constant}$  an average effective minor radius  $r_{\text{eff}}$ .

Three issues must be discussed:

- (1) When do closed magnetic surfaces exist?
- (2) How to generate them?
- (3) What are their properties?

The idea of magnetic surfaces and their basic properties have been described by Spitzer in his fundamental paper on the stellarator concept [8.1]. A magnetic field line on a toroidal surface is either closed after a finite number of toroidal transitions or it covers the surface ergodically. Ergodic means that the field line comes arbitrarily close to every point on the surface. Field lines cannot cross each other; this implies that once the field on the surface proceeds in the toroidal direction it also must proceed in the poloidal direction, thus encircling the surface helically. The ratio between poloidal turns and toroidal turns is called the *rotational transform*  $\iota$ , which is a rational number if the field

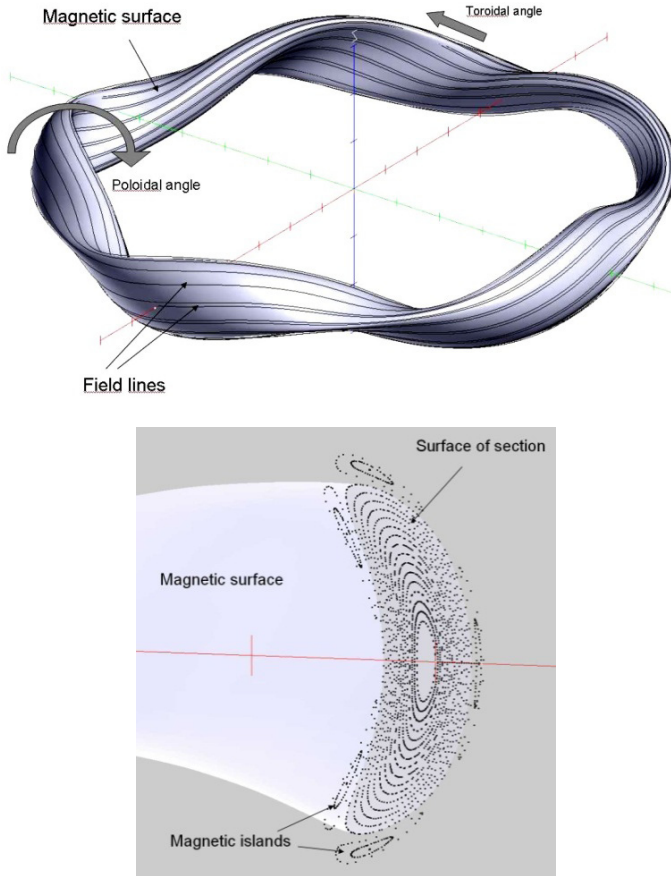


FIG. 8.1. Top: Magnetic surface and magnetic field lines of a stellarator configuration with 5-fold toroidal symmetry. Bottom: The intersections of magnetic field lines with a poloidal surface, the so called Poincaré-plot, display the existence of nested flux surfaces. In the outer region five resonant islands exist forming separate confinement regions.

line closes upon itself<sup>3</sup>. If one field line closes on a surface so do all field lines. If a field line covers the surface ergodically the rotational transform is an irrational number. In general, the rotational transform is not constant but varies with  $\psi$  in the radial direction,  $\iota = \iota(\psi)$ . The radial derivative is called the magnetic shear and plays an important role in plasma stability. Another important requirement

<sup>3</sup> The original quantity — the rotational transform  $\iota$  — is defined as the change of the poloidal angle of a field line  $\theta_n$  after the field line has passed  $n$  toroidal turns:  $\iota = \lim_{n \rightarrow \infty} [\theta_n / 2\pi n]$ , thus its unit is radians. In the simplest approximation of a stellarator with large aspect ratio this  $\iota$  can be regarded as the pitch of the field line on the flux surface. However, throughout this chapter we use the normalized rotational transform  $\iota = \iota / 2\pi = 1/q$ , where  $q$  is the safety factor used for tokamaks.

is that magnetic surfaces must be nested as shown in Fig. 8.1 (bottom), which means that there is always a finite distance between two distinct surfaces. This implies  $|\nabla\psi| \neq 0$  except on the magnetic axis, which is the innermost surface degenerated to a single closed field line; on the axis the gradient of  $\psi$  is zero:  $|\nabla\psi| = 0$ . However, it cannot be excluded that several magnetic axes exist and these axes are surrounded by small closed magnetic surfaces forming so-called magnetic islands (see Fig. 8.1 for an example). This may occur on surfaces where  $\iota$  is a rational number such that the field lines close and already small error fields in resonance with the rational field line result in finite island structures. Magnetic islands provide a shortcut to plasma transport as particles following a field line encircle the island thereby connecting plasma volumes at different minor radii. Islands therefore should be minimized in the interior of the confinement region. However, at the plasma boundary they can be utilized for divertor action guiding particles to divertor plates.

The topology of magnetic surfaces has been extensively discussed in the literature. Magnetic surfaces are akin to the integral surfaces of mechanical systems, and indeed, the theory of magnetic surfaces can be formulated in terms of Hamiltonian mechanics showing all the properties of Hamiltonian systems: existence of surfaces in cases of continuous symmetry, destruction by island formation and ergodicity, existence of KAM-surfaces [8.9] and more. Island overlapping makes the field lines in between chaotic. Analytic computation of magnetic surfaces is only possible in cases of symmetry like toroidal symmetry or helical symmetry. For details the reader is referred to the excellent review paper by Morozov and Solov'ev [8.10]. Three-dimensional helical devices, however, do not exhibit a toroidal invariance, and therefore the existence of closed magnetic surfaces can only be proved under certain conditions. This is the subject of the celebrated KAM-theorem, which says that a magnetic surface of a toroidally invariant magnetic field remains toroidally closed and undestroyed if the deviation from symmetry, i.e. the perturbation, is not too large. However, the existence of magnetic surfaces on every scale — even very small ones — might be too rigorous a requirement, since Coulomb collisions and finite Larmor radius effects introduce a smoothing effect on a small radial scale and thus decouple pressure surfaces, density surfaces, etc. from magnetic surfaces. An integrated theory of plasma equilibrium including all dissipative effects and the structure of magnetic surfaces does still not exist.

The helical structure of field lines also requires some kind of helicity in the coil system. Different paths for their realization are outlined in the next chapter. Due to the periodic boundary conditions the helicity of the coils and thus of the resulting flux surfaces is characterized by toroidal and poloidal mode numbers as is illustrated by Fig. 8.2 (top), where a poloidal mode number of 9 is evident.

A common issue of all coil systems is the accuracy with respect to deviations from the design value. Since magnetic island formation is a resonance

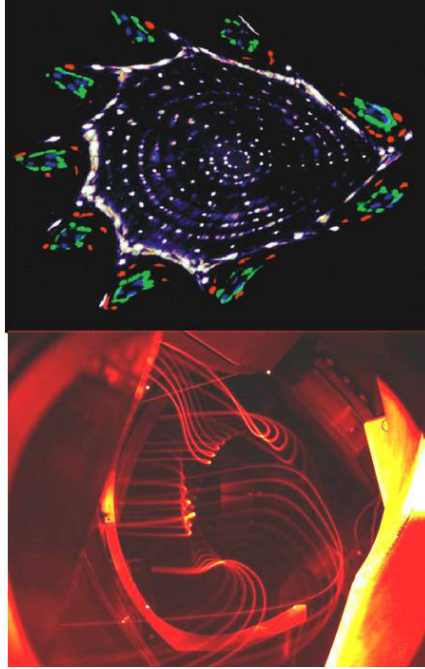


*FIG. 8.2. In a stellarator the confining magnetic field that already exists in vacuum can be measured accurately by an electron beam technique. Top: A poloidal cut (Poincaré-plot) obtained with a fluorescent rod moving in a poloidal cross-section of W7-AS. Different measurements superimposed in false colour show field lines remaining in the nine island structures which enclose the confinement region. Bottom: With low pressure hydrogen gas filled in the device the 3-D structure of the magnetic field lines can be visualized. Courtesy of M. Otte, IPP, Greifswald, Germany.*

effect caused by symmetry-breaking error fields, small production errors or misalignment of coils can lead to large islands and thus destroy the plasma confinement. However, together with a careful assembly of the coil system this problem can be minimized to a tolerable level by choosing a proper range of the rotational transform and the shear: The value of the rotational transform may be chosen in a range where low order rational values sensitive to external perturbations are absent. Alternatively, if low order rationals are allowed to exist in the confinement region, the shear may be chosen strong enough such that the radial width of perturbing islands and thus the associated shortcut of transport is minimized.

### 8.2.2. Helical confinement devices

In his fundamental paper [8.1] Spitzer mentioned two methods for producing rotational transform  $\iota$  on nested flux surfaces. The first one, illustrated

in Fig. 8.3, arranges circular toroidal field coils into a “figure-8”; rotational transform is produced by the geometry. The B-1 stellarator operated at Princeton [8.11] was an example of such a figure-8 stellarator. In modern stellarators, the helical twist of the magnetic axis remained as a geometrical feature.

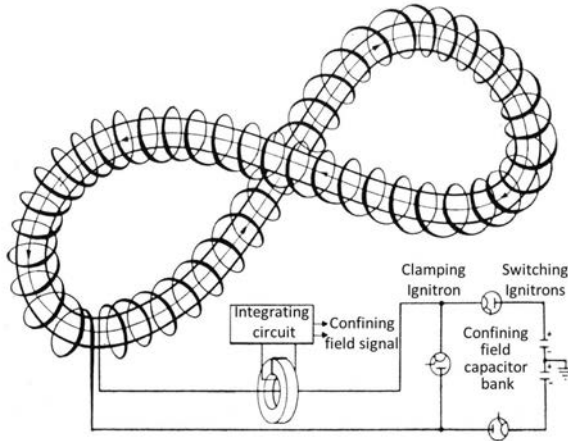


FIG. 8.3. Bending of a torus into “figure-8” geometry leading to rotational transform [8.11]. Reprinted from Ref. [8.11]. Copyright (2011), American Institute of Physics.

The second method is to produce a rotational transform by “the use of a transverse magnetic field, whose direction rotates with distance along the magnetic axis” [8.1]. The transverse radial and poloidal field components  $B_r$  and  $B_\theta$  can be generated by  $2l$  ( $l = 1, 2, 3, \dots$ ) helical conductors, wound on the outside of a regular torus vessel with currents flowing oppositely in adjacent conductors. Additional toroidal field coils provide the toroidal field component. A schematic is shown in Fig. 8.4.

### 8.2.2.1. Classical stellarators

In early experiments of this type straight sections were introduced in the torus mainly because of practical reasons forming a racetrack-type stellarator. The largest stellarator of this type was the Model C Stellarator at Princeton [8.12]. Its experimental results did not satisfy the expectations because the observed plasma confinement time was close to the so-called Bohm-diffusion [8.13]. It was suspected that especially for the racetrack configurations [8.14] error fields leading to magnetic islands spoiled the confinement properties due to the deviations from axisymmetry. Experimentally this was verified at IPP, Garching, using “classical” stellarators with a circular magnetic axis. Great emphasis was laid on the fabrication of the coil systems to avoid error fields causing deviation from the ideal symmetry. It could be shown that for low temperature plasmas

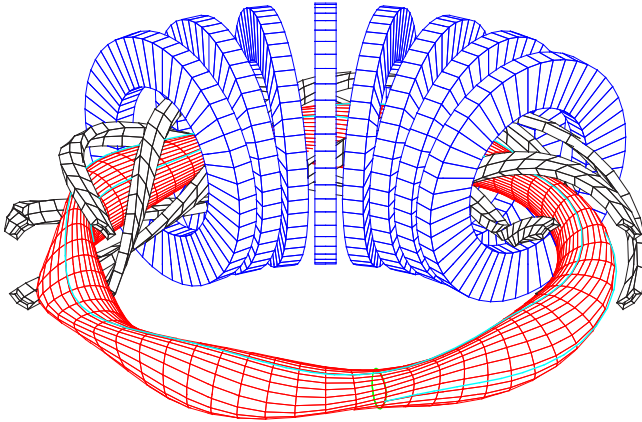


FIG. 8.4. Schematic of a classical  $l=2$  stellarator with toroidal field coils (blue) and helical windings (black). A magnetic surface is shown in red. Courtesy of J. Kisslinger, IPP, Garching.

under stationary conditions classical confinement of the Pfirsch–Schlüter type [8.15] could be reached, where transport is determined by collisions between plasma particles only [8.16] (see Section 8.3.5).

Stellarators of type  $l=2$  and  $l=3$  were mostly realized. Basic differences with different multipolarity  $l$  are the shape of the last closed flux surface/separatrix and the  $\tau$  profiles. Stellarators with  $l=1$  or  $l=2$  have a roughly constant, low-shear  $\tau$  profile if the number of periods is not too large. Stellarators with  $l>2$  are without rotational transform in the plasma core but introduce magnetic shear with  $\tau$  rising towards the edge. The major advantage of an  $l=2$  low-shear configuration is that low order rational  $\tau$  values can be avoided in the  $\tau$  profile thus excluding the formation of islands due to resonant error fields. Also resonant unstable modes can be prevented to develop. Though shear leads to rational values in the  $\tau$  profile, shear limits the island size and can contribute to the stabilization of ideal MHD-modes. On the other hand, the low central  $\tau$  values of pure  $l=3$  configurations lead to large pressure induced flux surface deformations at finite  $\beta$  which limits their performance (see Section 8.3.2).

An advantage of the classical stellarator design is the possibility to vary the helical and toroidal field components independently. This provides an easy variation of the externally generated rotational transform in a single experimental device. In cases where the stellarator is equipped with an ohmic transformer, the transition from tokamak-like configurations (rotational transform produced almost entirely or partly by a toroidal plasma current) to pure stellarator configurations (with no net toroidal plasma current) can be studied.

A technical disadvantage of the classical stellarator design arises from the interaction forces between the toroidal field coils and the helical windings. Helices embedded in large toroidal magnetic fields experience large radial forces

alternating in direction from one helix to the next. Thus, it becomes a serious problem to support the helices of large devices with significant toroidal fields, as relatively little space is available for supporting mechanical structures. Furthermore, the interlinkage of helical windings and toroidal field coils would make disassembly and maintenance in a fusion reactor rather difficult.

Examples of classical stellarators [8.17–8.19] are CLEO at Culham (United Kingdom), L-2 at Moscow (Russian Federation), JIPPT-II at Nagoya (Japan), Wendelstein 7-A (W7-A) at Garching (Germany) and other smaller ones. W7-A was the largest ever constructed of these classical stellarators ( $R_0 = 2$  m, minor radius  $a = 0.1$  m,  $l = 2$  helical windings, five-fold toroidal symmetry, i.e. number of periods  $N_p = 5$ , magnetic field strength  $B_0 < 3.4$  T). With accurately fabricated helical windings and minimized field errors, a confinement comparable to that of similarly sized tokamaks was demonstrated. Being equipped with an OH-transformer, tokamak-like operation was possible. With NBI and ECRH, W7-A demonstrated in 1980 for the first time stellarator operation without net toroidal current [8.20].

#### 8.2.2.2. Torsatrons/Heliotrons

Torsatrons and heliotrons create poloidal and toroidal field components from one helical winding energized by unidirectional current. The basic concept was proposed by Gourdon [8.21] and Uo [8.22]. A field with  $l$ -fold poloidal symmetry is generated by  $l$  helical windings, generating also an average vertical field compensated by an additional set of vertical field coils. Figure 8.5 gives an example with  $l = 2$  and 10 toroidal periods. In contrast to the classical stellarator the complication with two sets of interlinked coil systems is avoided and the reduced number of coils gives better access to the plasma. More flexibility can be obtained by adding toroidal field coils, allowing the rotational transform to vary.

Examples of torsatrons are Uragan III at Charkov (Ukraine) [8.23] and ATF at Oak Ridge (USA) [8.24] ( $R_0 = 2.1$  m,  $a = 0.27$  m,  $l = 2$ ,  $N_p = 12$ , medium shear,  $B_0 \leq 2$  T). At ATF additional flexibility of controlling the magnetic configuration was provided by three independently driven pairs of axisymmetric coils which allowed varying the dipole and quadrupole moments of the poloidal magnetic field. In this way it has been proved that in helical devices the bootstrap current (see Section 8.3.5) can be minimized or even inverted [8.25].

Several heliotrons were built in Japan such as Heliotron-E (for results see the review [8.26]), Heliotron-J, Compact Helical System (CHS) and LHD. In 1984 Heliotron-E ( $R_0 = 2.2$  m,  $a = 0.2$  m,  $l = 2$ , additional toroidal field coils, high shear,  $B_0 \leq 2$  T) obtained the first high energy currentless plasma in a helical device initiated and heated solely by ECRH and NBI [8.27].

Heliotron-J is a helical-axis heliotron ( $l = 1$ ,  $N_p = 4$  helical coil) with a very flexible magnetic field configuration. Two types of eight toroidal field coils with

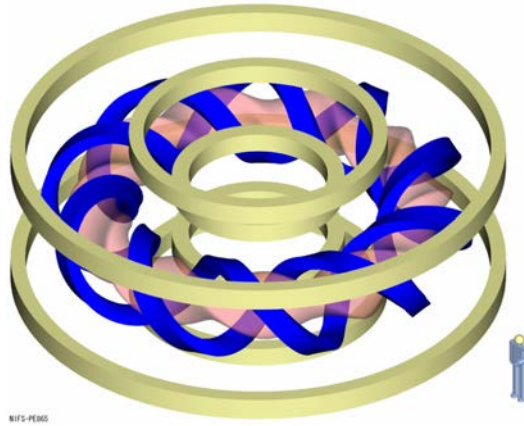


FIG. 8.5. Heliotron (example shown: LHD) with unidirectional helical windings (blue) and vertical field coils (yellow) together with a magnetic surface shown in pink. Courtesy of National Institute for Fusion Science, Japan.

different coil currents make it possible to modify the magnetic field strength along the magnetic axis (degree of “bumpiness”, see Section 8.3.5). The reduction of trapped particle transport (neoclassical  $1/\nu$ -transport, see Section 8.3.5) is one of the key research issues [8.28]. The low aspect ratio CHS ( $l = 2$ ,  $m = 8$  helical coil,  $R_0 = 1.0$  m,  $a = 0.2$  m) has an edge magnetic field structure, which allowed first “local island divertor” (LID) experiments that served as guidance for the design of the LID for the LHD [8.29].

LHD [8.2], a heliotron, is the largest helical device at present and the first one with superconducting coils. The dependence of energy confinement and plasma stability can be varied by shifting the magnetic axis radially. Inward shifted configurations ( $R_0 = 3.55$ – $3.6$  m) have low toroidal field ripple, they are advantageous in terms of reduced neoclassical transport losses (see Section 8.3.5) and show optimum plasma confinement [8.30]. The associated magnetic hill (see Section 8.3.3) was expected to lead to poor MHD stability but turned out less critical than expected. The outward shifted configurations ( $R_0 = 3.75$ – $3.9$  m) have a rather large field ripple and correspondingly high ripple losses under collisionless conditions. LHD is equipped with two different divertor systems (see Section 8.3.7):

- (1) The open and unpumped “helical divertor” (HD) has a shape similar to the double-null open divertor in tokamaks except for its helically twisted structure.
- (2) The closed and pumped LID uses an  $m/n = 1/1$  magnetic island controlled by an externally applied resonant field to guide particle and heat fluxes to the divertor plates [8.31].

HELICAL CONFINEMENT CONCEPTS

TABLE 8.1. GEOMETRY DATA AND ACHIEVED PLASMA PARAMETERS (IN DIFFERENT DISCHARGES) OF W7-AS [8.33] AND LHD (Courtesy of H. Yamada, NIFS, Japan; see also Ref. [8.32])

	W7-AS	LHD
Major radius $R_0$ [m]	2.0	3.5–4.15
Plasma radius $a$ [m]	$\leq 0.18$	0.5–0.65
Material of coils	copper coils	superconducting coils
Rotational transform $\iota$	0.3–0.6 (range)	$\approx 0.4 \sim 1.3$ (profile)
Shear	low	medium to high
Central electron temperature $T_e(0)$	6.8 keV with $P = 2$ MW, $B_0 = 2.5$ T, $\bar{n}_e = 2 \times 10^{19} \text{ m}^{-3}$	10 keV with $P_{ECRH} = 1.2$ MW, $\bar{n}_e = 0.6 \times 10^{19} \text{ m}^{-3}$ , $B_0 = 2.9$ T
Central ion temperature $T_i(0)$	1.7 keV with $P = 1.8$ MW, $B_0 = 2.5$ T, $\bar{n}_e = 5 \times 10^{19} \text{ m}^{-3}$	5.6 keV with $P = 19$ MW, $B_0 = 2.9$ T, $\bar{n}_e = 1.6 \times 10^{19} \text{ m}^{-3}$ , in hydrogen
Electron density	$\bar{n}_e = 4 \times 10^{20} \text{ m}^{-3}$ , $P = 2.8$ MW, $B_0 = 2.5$ T, $T_i(0) \approx T_e(0) \approx 0.35$ keV	$n_e(0) = 1.2 \times 10^{21} \text{ m}^{-3}$ , $P = 21$ MW, $B_0 = 2.5$ T, $T_i(0) \approx T_e(0) \approx 0.22$ keV
Average $\beta$ $\langle \beta \rangle = 2\mu_0 \langle p/B^2 \rangle$	3.4% with $P = 2.8$ MW, $B_0 = 0.9$ T, $\bar{n}_e = 2 \times 10^{20} \text{ m}^{-3}$	5.1% with $P = 12$ MW, $B_0 = 0.425$ T, $\bar{n}_e = 2.3 \times 10^{19} \text{ m}^{-3}$
Energy confinement time $\tau_E$	0.06 s with $P = 0.33$ MW, $B_0 = 2.5$ T, $n_e(0) = 1.1 \times 10^{20} \text{ m}^{-3}$ , $n_e(0)\tau_E T_i(0) = 5 \times 10^{18} \text{ m}^{-3} \cdot \text{s} \cdot \text{keV}$	0.22 s with $P = 3.3$ MW, $B_0 = 2.8$ T, $n_e(0) = 5.5 \times 10^{20} \text{ m}^{-3}$ , $n_e(0)\tau_E T_i(0) = 5.2 \times 10^{19} \text{ m}^{-3} \cdot \text{s} \cdot \text{keV}$
Pulse length	restricted to $< 1.5$ s (copper coils)	up to 54 min with $P = 0.5$ MW, $n_e(0) = 0.4 \times 10^{19} \text{ m}^{-3}$ , $T_e(0) \approx T_i(0) \approx 1$ keV

With the superconducting coils of LHD the potential of helical devices for steady state operation was explored [8.32]. By the end of 2009, discharges with a pulse length up to 54 min at  $P = 0.5$  MW, with  $n_e(0) = 0.4 \times 10^{19} \text{ m}^{-3}$ ,  $T_e(0) \approx T_i(0) \approx 1$  keV had been obtained. The major parameters achieved with LHD up to 2009 are summarized in Table 8.1. The most important results of LHD are presented in Ref. [8.30].

### 8.2.2.3. Heliacs

A rotational transform can be created quite efficiently if the magnetic axis itself has a helical structure in space. The figure-8 device by Spitzer already employed this idea for two periods. The heliac concept (HELical Axis Configuration) shown in Fig. 8.6 utilizes circular coils, which are placed helically around a circular central coil, which produces a part of the poloidal field and allows additional flexibility in the setting of  $\iota$ . The resulting bean-shape plasma column has a helical magnetic axis that spirals around the circular conductor. Unlike in the figure-8 configuration, a magnetic well is realized, ensuring good MHD stability properties. The heliac offers a high degree of flexibility so that important equilibrium, stability and transport issues can be addressed. Representatives of this concept are H-1 at Canberra (Australia) (see, for example, Ref. [8.34]) and TJ-II at Madrid (Spain) (see, for example, Ref. [8.35]). For a reactor design, the interlinked coil system of a classical HELIAC may be not acceptable and would have to be replaced by a modular one [8.17] (see Section 8.2.2.4).

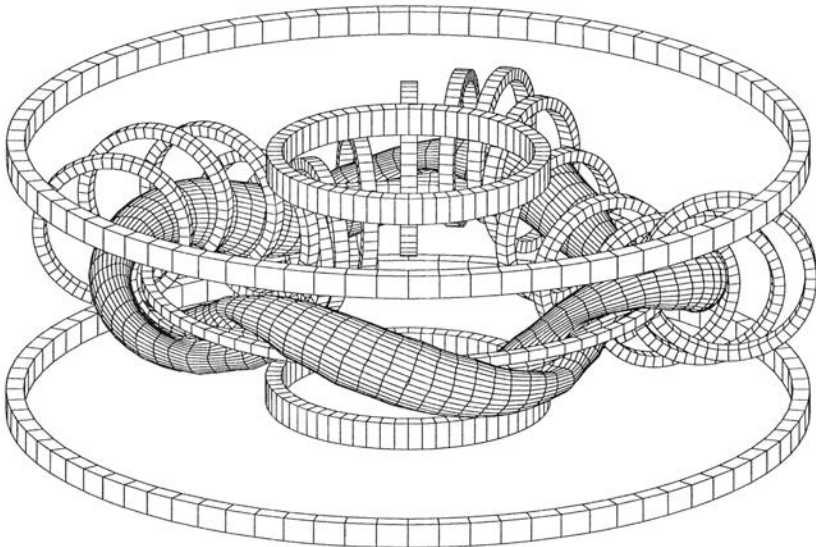


FIG. 8.6. Typical heliac coil set together with vertical field coils and a magnetic surface.

## 8.2.2.4. Modular stellarators

Modular stellarators do not separate between toroidal and poloidal field coils. Instead, a generalized stellarator configuration of nested magnetic surfaces with multiple helicity is achieved by a system of discrete modular coils which provides both toroidal and poloidal fields. The principal idea is illustrated in Fig. 8.7. A schematic of a modular stellarator is depicted in Fig. 8.8. The helical coils (in blue in Fig. 8.7, left) are unfolded in the  $\theta$ - $\phi$  plane, where  $\theta$ ,  $\phi$  are poloidal and toroidal angles, respectively. Superimposing the toroidal field coils (shown as black arrows), both coil systems can be combined to result in meander-like coils following alternately the helical and toroidal coil paths (shown in red). For real coils, the resulting edges need some smoothing (Fig. 8.7, right). Since there is no net toroidal current in the coils, no vertical field coils are needed and a modular stellarator can be built without any toroidally closed windings with the confinement provided solely by the modular coils. However, as the modular coil system realizes a fixed configuration with fixed rotational transform  $\iota(r)$ , additional coils have to be added if experimental flexibility is required.

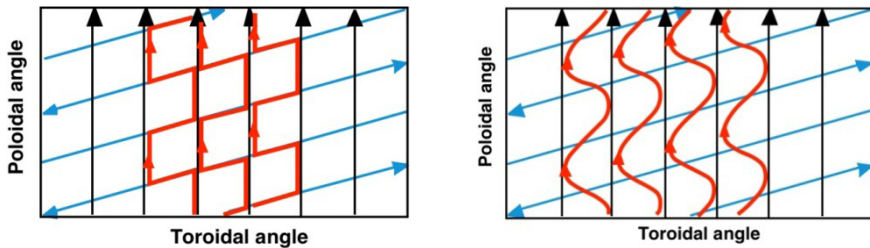


FIG. 8.7. Left: Superposition of helical windings (blue) and the TF-coils (black) and mapped into the  $\theta$ - $\phi$  plane. The meander-like coils (in red) represent the combined system. A case is considered where the currents in the helical windings and in the TF-coils are equal. Right: For realization of the system some smoothing of the coil shape is necessary.

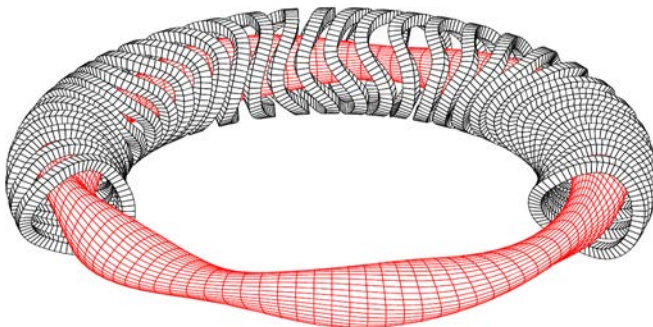


FIG. 8.8. Scheme of a classical  $l = 2$  stellarator with five toroidal field periods with a modular coil system [8.33]. Reprinted from Ref. [8.33]. Copyright (2011), IOP Publishing Ltd.

Historically the development of the modular coil concept by Wobig and Rehker [8.36] was initiated by the excessively large forces between the toroidal field coils and the helical windings. With modular coils the required mechanical support structures are feasible because they can be located outside and between the coils.

Most importantly, however, modular coils offer the chance to realize a large variety of configurations, which can hardly be achieved by continuous coils. In particular, this refers to the superposition of helical fields with different helicities and the incorporation of toroidal mirror fields. These are desirable field characteristics in the realization of optimum configurations. With modular coils a magnetic field configuration can be tailored according to desired properties with regard to equilibrium, stability and transport (see Section 8.5).

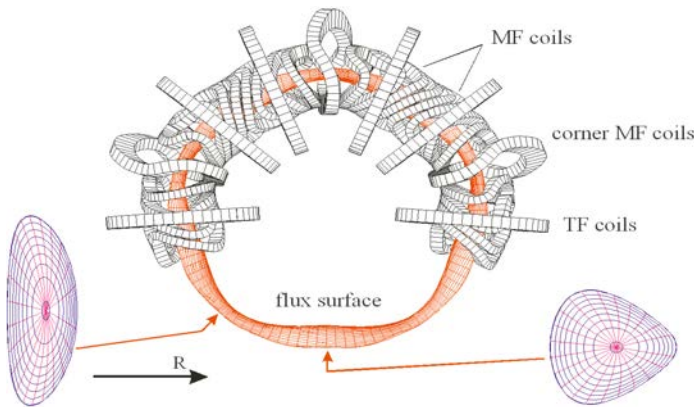


FIG. 8.9. W7-AS: Top view of an outer 3-D flux surface and cross-sections. Besides the modular field (MF) coils (nine for each of the five periods) additional toroidal field (TF) coils provided the flexibility to modify the magnetic configuration. The plasma cross-section, which varies from almost elliptical at the corners of the pentagon to more triangular in between, reflects the capability of a modular stellarator to combine elements of different helicity in a single device as an option for its optimization [8.33]. Reprinted from Ref. [8.33]. Copyright (2011), IOP Publishing Ltd.

Examples of modular stellarators built so far are Wendelstein 7-AS (W7-AS, see Fig. 8.9) in Garching (Germany) and the smaller HSX device at the University of Wisconsin (USA).

The modular coil system of W7-AS designed in the early 1980s was the first example in which a desired magnetic configuration was the starting point of the coil design. At that time a full optimization of the coils was beyond numerical possibilities; instead a semi-numerical procedure was followed (see Section 1 of Ref. [8.33]). The experiment was realized as an upgrade of W7-A to provide an early experimental check of the theoretical predictions of stellarator optimization. Due to the resulting restrictions W7-AS was considered as a “partly

optimized” stellarator, which, however, successfully demonstrated some basic elements of the optimization strategy (see Section 8.5). Moreover, first tests of the island divertor concept (see Section 8.3.7) were performed. W7-AS operation was terminated in 2002; the major results have been published in a review paper [8.33]. Geometry data and achieved plasma parameters are given in Table 8.1.

The second example, the Helically Symmetric Experiment (HSX,  $R = 1.2$  m,  $a = 0.15$  m, 4 periods), is the first stellarator to possess a quasi-helically symmetric magnetic field configuration where the neoclassical transport can be reduced to a level similar to axisymmetric tokamak configurations [8.37] (see Section 8.3.5). There have been other proposed modular devices which followed different optimization criteria, the Quasi-Poloidal Stellarator (QPS) in Oak Ridge (USA) [8.5] and the quasi-axisymmetric NCSX, PPPL, Princeton (USA) [8.4] (project stopped prior to completion).

The concept of modular coils, the principle of optimization and the capability for high power steady state operation are combined in Wendelstein 7-X, a superconducting device ( $R_0 = 5.5$  m,  $a = 0.5$  m, number of field periods  $N_p = 5$ ) which is being built in Greifswald, Germany. W7-X is designed to demonstrate the reactor capability of the advanced stellarator line [8.6] (see Section 8.6).

## 8.3. THE PHYSICS OF HELICAL SYSTEMS

### 8.3.1. Heating and particle–wave interaction

#### 8.3.1.1. *Electron cyclotron heating and current drive*

The interaction of RF waves with magnetically confined plasma particles is strongly dependent on the distribution function as discussed in Chapter 6. That chapter also describes the conventional heating by electron cyclotron waves. Here, we concentrate on two characteristics where stellarators significantly differ from tokamaks: (1) consequences of the complex phase-space structures on current drive and (2) the capability to operate at densities much above the tokamak Greenwald limit (see Chapter 2) necessitating heating schemes which operate below the plasma frequency (electron Bernstein wave heating). Apart from basic physics interests, current drive by electron cyclotron (EC) waves is of relevance for compensating the bootstrap current.

We start with the simplest case from both the theoretical and experimental point of view, which is the propagation and absorption of electromagnetic waves in the electron cyclotron range of frequencies. The wave propagation can be treated by ray tracing methods, because the wavelength is in general short compared to all plasma inhomogeneities. The dominant interaction takes place near the resonance in both real and velocity space, and interaction with

ions is due to Coulomb collisions only. Wave propagation at different angles of incidence in the 3-D stellarator magnetic field configuration introduces a rich field of physics such as Doppler shifted absorption and current drive in the presence of complex interaction with trapped and passing particles [8.38]. The experimental arrangements for such investigations are simple, i.e. a well collimated EC-wave-beam has to be launched from an external antenna structure while scanning the angle of incidence with respect to the direction of the magnetic field and measuring the heating effect by diamagnetic loops and deducing the CD effects from the loop voltage response.

From simple considerations one may conclude that only such external sources are useful for current drive which act on the parallel momentum of electrons. Furthermore, if we assume that the driven current increases with increasing net input of parallel momentum it would be most efficient to push slow electrons. This follows simply from the input of parallel momentum  $\Delta v_{\parallel}$  by a given energy  $\Delta W_{\parallel} = mv_{\parallel}\Delta v_{\parallel}$  which scales as  $\Delta v_{\parallel} / \Delta W_{\parallel} = (mv_{\parallel})^{-1}$ . If the kinetic response of the heated electrons is analysed in a more appropriate form it follows that both conclusions are incorrect [8.39]. The main reason is a consequence of the nature of Coulomb collisions, whose cross-section becomes smaller with increasing relative speed of the colliding particles. Under usual experimental conditions, most particles reside in the bulk of the distribution function with velocities close to the thermal one. Due to the small relative speed, thermal particles experience a strong collisional coupling, thus preserving the Maxwellian character in the bulk of the distribution function. Suprathermal electrons, however, from their frames of reference, will see most other particles as having high relative speeds and reduced collisional coupling, allowing for a deviation from the Maxwellian equilibrium in the tail of the distribution function. In most cases of experimental interest a steady state situation between heating, collisions and losses (e.g. radiation, radial transport) is reached. The driven current will then be proportional to the anisotropy with respect to  $v_{\parallel}$  of the steady state electron distribution function (due to  $m_i \gg m_e$  the ion contribution is usually negligible). From a quantitative estimation of the efficiency for steady state current drive it was found that it could be advantageous to heat fast electrons to maintain a steady state tail anisotropy of the distribution function. More energy has to be invested to accelerate them, but the reduction in the collisional coupling guarantees that the induced perturbation will resist the collisional isotropization for longer times, thus making the investment profitable.

Current drive is, however, also possible by generating an “asymmetric plasma resistivity” [8.39] without injecting parallel momentum. Let us analyse the effects of the wave–particle interaction in velocity space to understand this electron cyclotron current drive (ECCD) mechanism, where the contribution from the finite parallel momentum inferred by the wave with finite  $k_{\parallel}$  can usually be neglected. In the frame of quasi-linear theory the heating is described

as a diffusion along lines of constant  $v_{\parallel}$ . In cases when the  $k_{\parallel}$ -spectrum of the ECRH beam is not symmetric, the resonance region will not be symmetric in  $v_{\parallel}$ . The interaction of an obliquely propagating wave in X-mode polarization with electrons having a loss-cone distribution is shown in Fig. 8.10, where the quasi-linear diffusion term  $(\partial f / \partial t)_{ECRH}$  is also shown. The perpendicular energy of the resonant electrons is increased by ECRH which creates a deviation from the Maxwellian target  $(\partial f / \partial t)_{ECRH} < 0$  at velocities below and  $(\partial f / \partial t)_{ECRH} > 0$  at velocities above the resonant values.

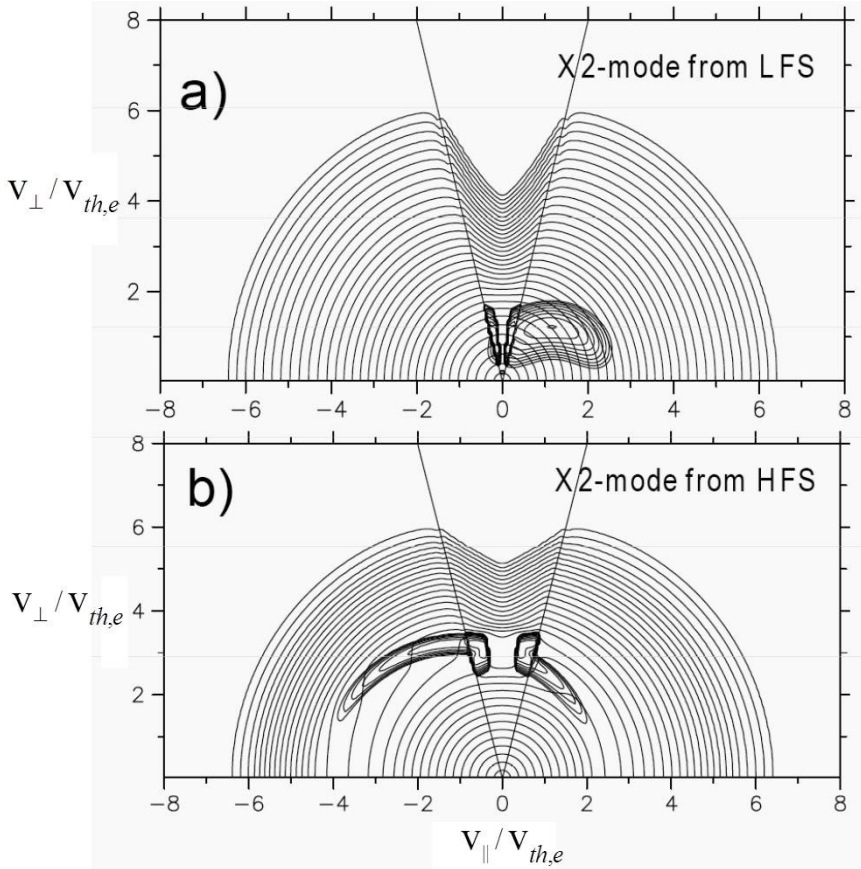


FIG. 8.10. Contours of the electron distribution function,  $f_e(v_{\parallel}, v_{\perp})$ , together with the quasi-linear diffusion coefficient,  $D_{\perp}(v_{\parallel}, v_{\perp})$ , as a function of the parallel and perpendicular velocities,  $v_{\parallel}$ ,  $v_{\perp}$  (normalized to the thermal velocity  $v_{th,e}$ ) for a non-symmetric  $k_{\parallel}$ -spectrum of the microwave beam. The absorbed power density is  $10 \text{ W}\cdot\text{cm}^{-3}$ . The straight lines indicate the loss-cone (trapped electrons). (a) low field side launch with X2-mode; (b) high field side launch with X2-mode,  $N_{\parallel,HFS} = -N_{\parallel,LFS}$  (see Ref. [8.40] for more details). Reprinted from Ref. [8.40]. Copyright (2011), IOP Publishing Ltd.

Wave–particle interaction with either bulk or tail electrons was investigated at W7-AS by comparing microwave launch from either the high field side (HFS) or low field side (LFS). Basic features of the deformation of the electron distribution function by wave coupling (X2-mode) from HFS and LFS are seen in Fig. 8.10. Only a small deformation of the distribution function is seen (Fig. 8.10(a)) for LFS launch, where the wave couples mainly to bulk electrons. A much stronger deformation is seen (Fig. 8.10(b)) for HFS launch, where the wave, interacts preferentially with fewer collisional suprathermal electrons. Note that no current is directly driven because only the perpendicular energy is increased by the wave, leaving the parallel momentum unaffected. As, however, Coulomb collisions are more efficient at lower energies the anisotropy at energies lower than the resonant one,  $W_{\perp res}$  is smoothed out more efficiently than the one for larger energies  $W_{\perp} > W_{\perp res}$ . This difference in the isotropization causes the appearance of a net current, which is known as “asymmetric plasma resistivity”. The total toroidal momentum is, of course, conserved. The collisional redistribution of the ECRH driven anisotropy in  $W_{\perp}$  causes some parallel momentum to flow from the electron to the ion component. In steady state, the ions and the electrons will drift in opposite directions with vanishing net parallel momentum.

For the W7-AS experimental conditions the current drive efficiency for HFS is, however, less than for LFS launch because some power is lost by momentum transfer to the trapped particles and even some current is driven into the reverse direction. Two independent 140 GHz beams with up to 0.4 MW power each were launched from both the HFS and the LFS [8.40] with an almost optimum launch angle of  $\pm 19^\circ$ . The bulk temperature and the integrated line density are comparable in both scenarios ( $T_e = 2$  keV,  $\bar{n}_e = 3 \times 10^{19} \text{ m}^{-3}$ ). The experimental results confirm the theoretical expectations showing a slightly lower ECCD efficiency in the HFS case as compared to the LFS case with  $I_{CD}^{HFS} / I_{CD}^{LFS} \cong \Delta U_{loop}^{HFS} / \Delta U_{loop}^{LFS} \cong 0.8$ .

ECCD is very sensitive to trapped particle effects once banana orbits can be collisionlessly completed (i.e. the effective collision frequency of trapped particles is lower than their bounce frequency within a magnetic mirror). Qualitatively speaking, three mechanisms related to the presence of a trapped particle population influence the ECCD efficiency in this collisionality regime. Which mechanism will be the dominant one depends on the position in velocity space where the ECRH power is deposited:

- (a) Due to their very fast bounce motion, trapped particles cannot possess any privileged parallel velocity, thus any parallel momentum transferred to trapped particles will be “instantaneously isotropized” by the fast bouncing motion. As a consequence, no current can be driven by direct heating of trapped electrons.

- (b) Heating in close vicinity of the trapped particle region causes a current of opposite sign compared to the one expected by the usual “asymmetric plasma resistivity” mechanism. The momentum isotropization due to the bounce motion of trapped electrons is faster than that related to Coulomb collisions. The “surplus” of electrons at  $W_{\perp} > W_{\perp res}$  (related to bouncing trapped particles) will be isotropized on a faster timescale than the “depletion” of electrons at energies  $W_{\perp} < W_{\perp res}$  (but related now to barely passing particles).
- (c) Electrons which are heated far from the trapped particle region will experience the classical “anisotropic resistivity” mechanism. The CD efficiency is, however, still affected by a trapped particle population and decreases with increasing amount of trapped particles. Any  $v_{\parallel}$  anisotropy in the passing particle population will be damped by collisional friction with the population of trapped particles which can annihilate their parallel momentum within a bounce period.

In axisymmetric configurations, conservation of the canonical angular momentum will connect the annihilation of parallel momentum with an inward drift of the trapped particles. In principle this parallel momentum could be recovered (under the form of an increment in bootstrap current) when, due to radial transport, the trapped particle diffuses outward again [8.41]. However, in the case of ECCD, where the direct input of parallel momentum is generally negligible, only marginal effects are expected.

The different effects were investigated in basic experiments at W7-AS with 0.2 (0.4) MW RF-power in the X2-mode ( $B_{res} = 1.25$  T). The toroidal launch angle was scanned from co- to counter-current drive direction in two different magnetic mirror configurations with resonance on the axis. The EC-driven current was compensated by an inductively driven current, the measured quantity was the loop voltage required for full current compensation. The experimental results are compared with ray tracing calculations using the measured profiles of  $n_e$  and  $T_e$  in both magnetic mirror configurations. Here co- (counter-) CD denotes the current direction which increases (decreases) the rotational transform, respectively. In W7-AS co-CD thus corresponds to ECCD in the direction of the bootstrap current [8.42]. Representative results are shown in Fig. 8.11 for two cases.

*Case 1:* The maximum of the magnetic mirror was placed in the ECRH launching plane; results are shown in Fig. 8.11(a). Mainly passing particles are directly heated and the impact of trapped particles on the driven current is due to friction.

*Case 2:* The minimum of the magnetic mirror was placed in the ECRH plane; the results are shown in Fig. 8.11(b). The wave absorption in this case is dominated by trapped and barely passing particles. For perpendicular launch with no ECCD, the loop voltage is non-zero for both cases and represents the voltage

for bootstrap current compensation. In case 1 the maximum of the loop voltage and thus the driven current is much larger ( $\pm 13 \text{ A} \cdot \text{kW}^{-1}$ , note the different scales) as compared to case 2, where the EC-driven current is only about  $0.8 \text{ A} \cdot \text{kW}^{-1}$  and has opposite sign. In the latter case a large fraction of ECCD power is absorbed directly by trapped particles, which do not contribute to current drive, the change of sign is a consequence of the ECRH induced trapping of otherwise barely passing particles.

The experimental results shown in Figs 8.11(a) and (b) are well represented by the theoretical modelling shown for both cases in Figs 8.11(c) and (d), respectively.

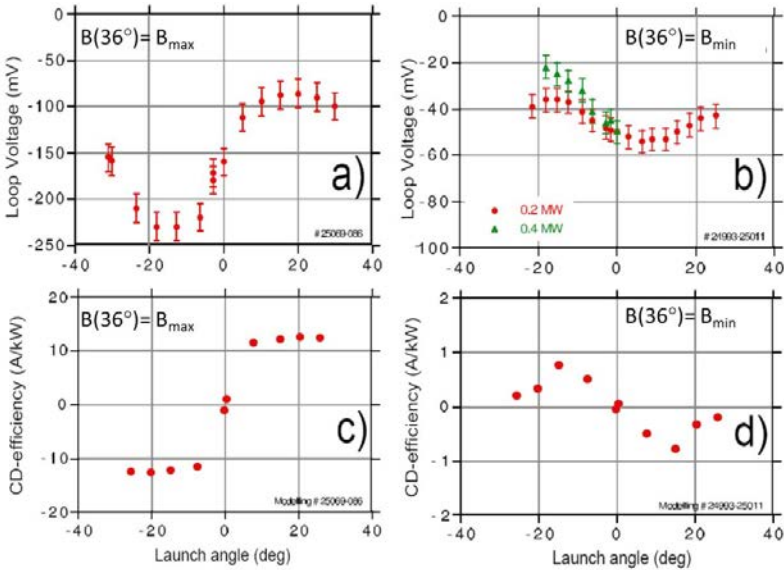


FIG. 8.11. Effect of trapped particles on ECCD. Top: Measured loop voltage versus launch angle with plasma net current  $I_p = 0$  for magnetic field configurations with the maximum (a) and the minimum (b) of  $B$  located in the EC-launching plane. The ECCD power is 0.4 (green triangles) and 0.2 MW (red dots). Bottom: CD-efficiency calculated from linear theoretical modelling for both cases (c, d) [8.42].

### 8.3.1.2. Electron Bernstein wave heating in stellarators

High density operation is a quite attractive option for a stellarator reactor (see Section 8.6). However, heating a high density plasma by ECRH with electromagnetic waves is limited by the cut-off density of the electron cyclotron frequency. Overdense plasma heating can only be performed by mode conversion from the electromagnetic wave into electrostatic waves, the electron Bernstein waves (EBWs). The propagation of these waves is not restricted by an upper

density limit. They are also highly absorbed by strong cyclotron interaction with electrons even at high harmonics and low temperature. The most favourite mode conversion process is the double-step conversion from an ordinary into a slow extraordinary wave and in a second step into an EBW. The crucial point in achieving this so called OXB-mode conversion is to create a proper target plasma with a density well above the O-mode cut-off density  $n_e = (2\pi f)^2 \epsilon_0 m_e / e^2$  and with a density scale length  $L_n$ , which satisfies  $2 < k_0 L_n < 20$ . Here  $k_0$  is the vacuum wavenumber. The three-dimensional stellarator geometry allows choosing launching positions, favourable for the mode conversion. Best conditions are found if the local density gradient is maximal, for example at the low field side of a toroidal position where the plasma cross-section is mostly elongated. Clear indication of OXB-mode conversion had been found in the W7-AS stellarator [8.43]. Furthermore, the propagation of the EBW is highly sensitive to the magnetic configuration. The  $N_{||}$  component is changed by field curvature, shear and  $\nabla \vec{B}$  along  $\vec{B}$ . This was demonstrated by the reversal of the EBW-driven current at W7-AS in a maximum  $B$  configuration in comparison with the standard configuration with a local minimum of  $B$  at the antenna position [8.44].

One key issue for commercial fusion reactors is the stability at high beta values. High beta experiments are mostly performed at low magnetic field. For a fixed ECRH-frequency (140 GHz) this requires heating at a higher harmonic resonance. The plasma is usually optically thick for even higher harmonic EBWs. Nevertheless the density has to surpass the threshold for OXB conversion. The accessibility of the plasma core can further be restricted by the appearance of the next resonance at the plasma edge. Therefore, the experiments at W7-AS have mainly concentrated on the third and fourth harmonic heating at a magnetic field of 1.5–1.6 T and 1.0–1.2 T respectively. At least 3 MW of NBI heating was necessary to sustain the OXB threshold density at that low magnetic field. Due to the confinement degradation with heating power ( $\sim P^{-0.6}$ ) only small effects on the plasma parameters could be expected by additional EBW-heating with 1.1 MW heating power. Clear resonance effects with magnetic field could be shown and the value of the average  $\beta$  could be increased by  $\Delta\beta / \beta = 5\%$  in the best case. The power was mainly deposited at half the plasma radius. This was confirmed by the tomographic reconstruction of the change of the soft X ray (SX) emission at the ECRH switch-off. Central power deposition was not possible due to the appearance of the next harmonic resonance at the plasma edge. With the ECRH stray radiation diagnostic a total efficiency of OX-coupling of up to 80% could be estimated. The OXB heating efficiency is at least as good as that of NBI. This was shown for the second harmonic OXB heating with 140 GHz of the high density H-mode (HDH) plasma at W7-AS (see Section 8.3.6 and Fig. 8.12). Here 1 MW NBI was replaced by 1.1 MW EBWs with an improvement of plasma energy.

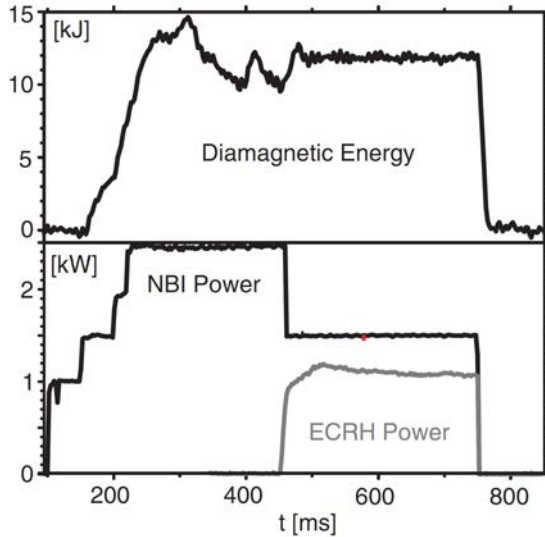


FIG. 8.12. Comparison between NBI and OXB-heating. A constant density of  $3.5 \times 10^{20} \text{ m}^{-3}$  was reached at 380 ms.

### 8.3.1.3. Ion cyclotron heating in helical systems

Ion cyclotron range of frequency (ICRF) heating is a well established plasma heating method in tokamaks and was also the first heating method employed in the Model C stellarator at Princeton [8.45]. Since then experiments have been conducted on numerous helical devices, among them ATF [8.46], CHS [8.47], Heliotron-E [8.48], LHD [8.49], Heliotron-J [8.50] and W7-AS [8.51]. The heating schemes that had successfully been employed on tokamaks were also introduced to stellarators and, in general, the applicability of these schemes to helical devices could be confirmed. In particular, minority heating of hydrogen in deuterium or helium, mode conversion heating and second harmonic hydrogen heating experiments were conducted. Fast hydrogen tails were observed, yet in most cases the heating efficiency decreased with increased power and saturation of the hydrogen tail temperature was measured.

Due to the 3-D nature of the magnetic fields in stellarators the tools needed for a full theoretical understanding are more complicated and always require massive computational support since the toroidal wavenumber cannot be separated out [8.52]. However, wave absorption of those stellarators with a quasi-symmetric magnetic field can be approximately treated with 2-D numerical codes for ICRF wave propagation. In addition, the particle dynamics is more complicated since the missing constant of motion associated with the toroidal symmetry allows for new classes of trapped particles with complicated drift motions. The advent of faster computers provides means to also treat these

situations either by full-wave calculation or by Fourier decomposition in all three coordinates.

Experimentally the 3-D nature of the magnetic field allows for heating scenarios not directly obtainable under conditions of toroidal symmetry. An example is magnetic beach heating where the heating frequency and magnetic field topology are chosen such that the magnetic field in the toroidal region of the antenna is too high for the absorbing resonance to be inside of the plasma but changes such that the resonance enters the plasma at some toroidal distance. In the original experiments the slow wave was directly excited at the periphery of a pure hydrogen plasma because of the low density [8.53] and then damped at some toroidal distance at the hydrogen resonance.

The magnetic topology of magnetic beach heating was again investigated in W7-AS [8.54]. For this magnetic configuration Fig. 8.13 shows the horizontal cross-section of the vacuum magnetic field in a half module of W7-AS as it is characterized by mod B contours, i.e. lines of constant value of B. The location of the hydrogen resonance is inside of the plasma only in a region at some toroidal distance from the high field side antenna. Shown are also the two-ion hybrid resonance (labelled MC) and the fast wave cut-off. For hydrogen concentrations less than about 40% the two-ion hybrid resonance is inside the plasma. As long as the hydrogen concentration was sufficiently low for the two-ion hybrid resonance to be still inside of the plasma and as long as the magnetic configuration was such that the hydrogen resonance was inside of the plasma at some toroidal distance both significant ion and electron heating and the evolution of a high energetic hydrogen tail were observed. Since the group velocity perpendicular to the mode conversion layer approaches zero the fast wave can propagate toroidally towards decreasing magnetic field. Approaching the hydrogen resonance the fast wave is converted into a slow wave (shear Alfvén wave). The slow wave finally is strongly damped on hydrogen via cyclotron damping.

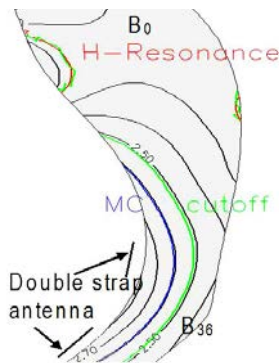


FIG. 8.13. Magnetic beach heating in W7-AS: horizontal cross-section of the vacuum mod B contour lines in a half module, hydrogen resonance (red), two-ion hybrid resonance (blue) and fast wave cut-off (green)[8.54].

### 8.3.2. Plasma equilibrium

#### 8.3.2.1. Basic equilibrium properties

The MHD equilibrium of a magnetically confined plasma is determined by the radial force balance between the gradient of the plasma pressure  $p$  and the Lorentz force of the current density  $\vec{j}_\perp$  perpendicular to the magnetic field  $\vec{B}$ . In the simplest form, it is given by  $\nabla p = \vec{j} \times \vec{B}$  determining the current density  $\vec{j}_\perp = (\vec{B} \times \nabla p) / B^2$  flowing perpendicularly to the magnetic field, also called “diamagnetic” since it reduces the magnetic field inside the plasma. Magnetic field and current density are connected by Ampere’s Law  $\vec{\nabla} \times \vec{B} = \mu_0 \vec{j}$  and are subject to the constraints  $\vec{\nabla} \cdot \vec{B} = 0$  and  $\vec{\nabla} \cdot \vec{j} = 0$ . In toroidal geometry, the latter condition causes non-zero components of the equilibrium current density along the magnetic field, the so-called Pfirsch–Schlüter (PS) currents [8.15], to ensure the total current densities to be divergence-free. In the case of net current-free stellarators (no toroidal plasma current within each flux surface), the current flows along poloidally closed current lines (Fig. 8.14). The divergence of the diamagnetic current and hence the existence of the PS current is associated with the variation of the magnetic field strength perpendicular to the magnetic field as follows from decomposing  $\vec{\nabla} \cdot \vec{j} = 0$  into parallel and perpendicular components with respect to the magnetic field direction,  $\vec{\nabla} \cdot \vec{j}_\parallel = -\vec{\nabla} \times \vec{j}_\perp = (2/B) \vec{j}_\perp \cdot \vec{\nabla} B$ .

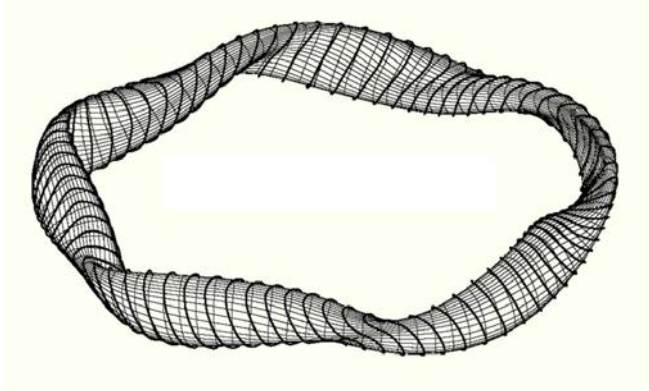


FIG. 8.14. Magnetic surface of an optimized (quasi-isodynamic) stellarator configuration (Wendelstein 7-X, Helias). The current lines (thick) are poloidally closed. The current lines are most inclined to the field lines (thin lines in toroidal direction) in the straight sections where the curvature is reduced [8.55].

It should be noted that the two components, the diamagnetic ( $\vec{j}_\perp$ ) and PS ( $\vec{j}_\parallel$ ) currents, are no real currents because each of them is not divergence-free. The condition for the special net current-free case  $\vec{\nabla} \cdot \vec{j}_\perp = 0$ , which implies  $\vec{j}_\parallel = 0$  (zero PS currents), is given by  $(\vec{B} \times \nabla p) \cdot \nabla p = 0$ , the so-called Palumbo

condition [8.56]. At the same time this condition also ensures that particle drift trajectories stay within the magnetic surface resulting in zero neoclassical transport. Magnetic configurations with such properties are referred to as isodynamic systems. However, the Palumbo condition cannot be met in toroidal confinement systems.

The parallel current densities were first computed by Pfirsch and Schlüter [8.15], who found the relation  $j_{\parallel} \approx (2j_{\perp}/\tau)\cos\theta$  for the case of an axisymmetric magnetic field  $\vec{B}$  in the large aspect ratio approximation. Here, the rotational transform  $\tau \equiv t/2\pi = d\psi_{\theta}/d\psi_{\phi} = 1/q$  is a measure for the twist of the field lines ( $\psi_{\theta}, \psi_{\phi}$  are the poloidal and toroidal flux functions). In stellarators, the computation of the Pfirsch–Schlüter currents is more complex due to the non-axisymmetric field configurations required for the generation of the rotational transform. Pfirsch–Schlüter currents are desired to be kept small, since they lead to pressure induced changes of the magnetic field configuration and eventually to an equilibrium pressure limit by destruction of flux surfaces. In particular, just like in tokamaks, their dipole structure gives rise to a vertical field causing a horizontal outward shift of the plasma axis relative to the outermost flux surface, the so-called Shafranov shift.

### 8.3.2.2. Optimized stellarators

Assuming the existence of nested flux surfaces, it can be shown that a plasma equilibrium is determined by the shape of the outermost plasma surface, the toroidal flux enclosed by this surface, the profiles of the plasma pressure and the rotational transform [8.57]. Hence, configurations can be optimized by 3-D plasma shaping. Reducing the PS currents is one key element resulting in increased pressure limits, reduced collisional and neoclassical plateau diffusion and increased MHD stability at the same time.

In particular, this is achieved by reducing the field inhomogeneities on the flux surfaces, in particular those along trajectories orthogonal to the field lines. The 3-D magnetic field is usually represented by a Fourier expansion in magnetic coordinates, in which the field lines are described by straight lines:

$$|B| = \bar{B} \cdot \left[ 1 + \sum_{\mu\nu} \varepsilon_B^{\mu\nu}(r) \cos(\mu\theta - \nu N_p \phi) \right] \quad (8.1)$$

Here,  $N_p$  is the number of field periods,  $\varepsilon_B^{\mu\nu}$  describe the Fourier harmonics of the equilibrium field inhomogeneities with the poloidal and toroidal indices<sup>4</sup>

---

<sup>4</sup> In Sections 8.3.2 and 8.3.3 the Fourier indices for the equilibrium field inhomogeneities are assigned with  $\mu, \nu$  in order to distinguish them from the mode numbers of perturbations  $m, n$  generally used in MHD theory. Note that in kinetic theory it is common to use the characters  $\mu$  and  $\nu$  for the magnetic moment and the collision frequency respectively.

$\mu, \nu$ , and  $\theta, \phi$  are the respective angles. The particular labelling used here is chosen to distinguish from that of the MHD mode perturbations treated in the MHD stability section. Most relevant for the PS current is the axisymmetric  $(\mu, \nu) = (1, 0)$  field harmonic which describes the fundamental toroidal curvature. This component gives rise to the dipole part of the PS currents and can be somewhat reduced by vertical elongation of the plasma, which may be considered as a reduction of the poloidal variation of  $B$  on a flux surface in a  $(1/R)$ -magnetic field while its volume is kept fixed.

Strong 3-D shaping of stellarators makes it possible to reduce the toroidal curvature term to much smaller values than achieved in tokamaks. In W7-X,  $\varepsilon_B^{10}$  is reduced by a factor of 2.2–2.6 and an equivalent tokamak would need a vertical elongation  $\kappa$  of 5–7 for the same reduction (values of 2 are causing vertical stability problems), as inferred from the relation  $\varepsilon_B^{10}(r) = -\varepsilon_t / \sqrt{\kappa}$ . Here,  $\varepsilon_t = r/R$  is the inverse aspect ratio and  $\kappa = b/a$  is the elongation, with  $b$  and  $a$  being the respective semi-major and semi-minor axes of an ellipse. Therefore, in stellarator optimization the reduction of the average toroidal curvature term  $\varepsilon_B^{10}$  in magnetic coordinates directly acts on the dipole part of the equilibrium currents (PS currents) and thus on the Shafranov shift, thereby improving the stiffness of the equilibrium with respect to  $\beta$ .

Stellarator optimization (see Section 8.5), which goes beyond the properties of equilibrium and stability, also considers the effect of the field harmonics on particle drifts leading to more elaborate concepts. Note that already a reduced  $\varepsilon_B^{10}$  also influences the neoclassical transport properties (see Sections 8.3.4 and 8.3.5) for which, however, other Fourier harmonics are important too. W7-X can access “quasi-isodynamic” configurations in which the great majority of the collisionless trapped particle orbits are confined. Other concepts aiming at configurations with favourable neoclassical transport properties use 3-D shaping to eliminate specific field harmonics  $\varepsilon_B^{\mu\nu}$  to make the field strength appear to the particle motion as if a special symmetry was present. In toroidal systems this reduced symmetry notion can be achieved quite perfectly for quasi-axisymmetry and quasi-helical symmetry but not for poloidal symmetry, which is replaced by the concept of isodynamicity.

Hence, critical issues associated with plasma equilibria in stellarators are the Shafranov shift, island formation and stochasticity (near rational surfaces and in the presence of field errors), and the structure of magnetic fields outside the last magnetic surface. The Shafranov shift must be sufficiently small so that under reactor conditions the plasma is not distorted too much. Islands should be minimized since enhanced plasma losses may occur and the structure of the magnetic field outside the last surface is decisive with respect to a given divertor geometry. An optimization criterion based on reducing the field harmonics

to only a few dominant ones as applied in W7-X turns out to be beneficial for minimizing field stochastization effects.

### 8.3.2.3. Computation of 3-D equilibria

The equilibrium equation  $\nabla p = \vec{j} \times \vec{B}$  is much more difficult to solve for non-axisymmetric or 3-D configurations than for the axisymmetric case since the existence of magnetic surfaces is not guaranteed. On the level of equilibrium description this is a fundamental difference between stellarators and axisymmetric tokamaks. In the latter case, axisymmetry makes it possible to generally define a poloidal flux function, and the equilibrium problem can then be cast into the Grad–Shafranov equation, which is elliptic and hence provides a well posed boundary value problem for a scalar flux function (see Chapter 3). In three dimensions the problem cannot be reduced to such a differential equation for only one scalar function. Several numerical equilibrium codes have been developed based on different approaches which attempt to solve the equilibrium equation by iterative or variational methods.

A simplification of the problem is achieved by assuming the existence of nested flux surfaces. The 3-D equilibrium problem can then be cast into an energy principle. The VMEC code [8.58], in particular, computes a minimum of the plasma potential energy functional

$$W = \int \left( \frac{B^2}{2\mu_0} + \frac{p}{\gamma - 1} \right) dV \quad (8.2)$$

by variation of the Fourier coefficients for  $R$  and  $Z$  representing the magnetic surface geometry, while two profile quantities are prescribed — pressure and toroidal net current. Here  $\gamma$  is the ratio of specific heats. The boundary may be kept fixed or be varied (fixed- versus free-boundary) under the constraint of a fixed enclosed toroidal magnetic flux. The basic assumption of nested flux surfaces excludes the treatment of internal magnetic islands and ergodic regions and thus also the adjustment of the plasma volume due to ergodization of the plasma boundary.

The MFBE code [8.59] addresses the external field structure by using the VMEC code iteratively. For every VMEC solution, the magnetic field structure outside the VMEC boundary is computed using the virtual casing principle. The plasma volume for the next VMEC run is adjusted in order to finally reach a volume consistent with the magnetic field structure outside the VMEC boundary. However, even with MFBE islands inside the plasma cannot be treated because of their influence on confinement and thus the plasma shape.

For a full treatment of MHD-equilibria with islands and ergodization, the assumption of nested flux surfaces as a basis for the numerical scheme has to be abandoned. Already Spitzer proposed to solve the equilibrium condition

$\nabla p = \vec{j} \times \vec{B}$  by a Picard iteration, i.e.  $\nabla \times \vec{B}^{n+1} = \mu_0 \vec{j}(\vec{B}^n)$ . This scheme has been implemented in the PIES code (Princeton Iterative Equilibrium Solver), which makes no a priori assumption about the existence of nested flux surfaces [8.60]. Field line tracing is used to investigate the evolving magnetic configuration on the existence of flux surfaces. The pressure is set constant on flux surfaces, if existent, according to  $\vec{B} \cdot \nabla p = 0$  and according to a specified pressure profile. If islands or ergodic regions are detected, the pressure gradient is flattened. The numerical effort is considerably larger than for the VMEC code. Figure 8.15 shows the Poincaré plots of a W7-X vacuum field configuration in comparison with an equilibrium calculation with PIES.

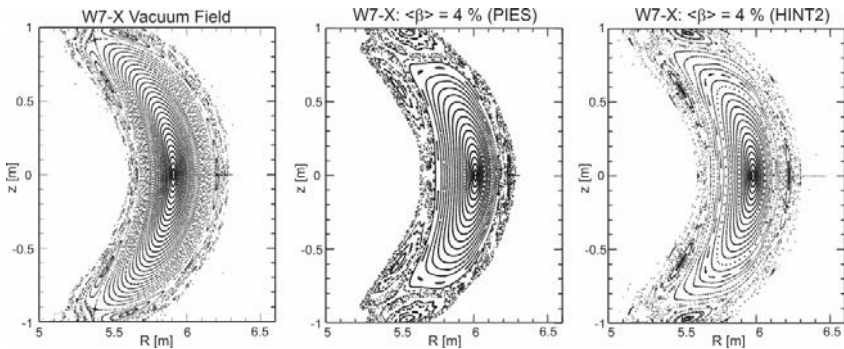


FIG. 8.15. Comparison of vacuum surfaces with finite  $\beta$  equilibrium in W7-X (PIES and HINT2). Courtesy of M. Drevlak, IPP, Greifswald, Germany, and Y. Suzuki, NIFS, Toki, Japan.

In the right part of Fig. 8.15, the result of another equilibrium code, the HINT2 code [8.61], is shown for comparison. The numerics in HINT does also not rely on the existence of nested flux surfaces. HINT2 and its predecessor HINT [8.62] solve the time evolution of the resistive MHD equations [8.63] to arrive at an equilibrium state of the plasma on an Eulerian grid. In order to separate timescales the iteration is done in an alternating procedure by first calculating a new pressure distribution with a fixed magnetic field according to  $\vec{B} \cdot \nabla p = 0$ , and then solving the time dependent force balance and Faraday's Law with a fixed pressure distribution. The employed numerical scheme allows, like in PIES, for island formation and for the treatment of ergodic regions.

#### 8.3.2.4. Experimental equilibrium identification

Experimental verification of calculated finite  $\beta$  3-D equilibria is an issue of particular importance in stellarators given the complexity and uncertainties of analytical and numerical equilibrium models. Accurate equilibrium reconstruction is required for stability and transport analysis, in particular. The most prominent

finite  $\beta$  equilibrium effect in toroidal magnetic confinement is the Shafranov shift, which leads to a horizontal outward shift of the magnetic axis relative to the centre of the outermost flux surface as a result of the Pfirsch–Schlüter current. In addition, the plasma is shifted radially outward as a whole (“free-boundary shift”), which can be controlled by a vertical field. In a low  $\beta$ , large aspect ratio approximation, the Shafranov shift can roughly be represented by [8.55].

$$\frac{\Delta}{a} \approx \frac{R}{a} \left( \frac{\varepsilon_B^{10}}{\varepsilon_t} \right)^2 \frac{\langle \beta \rangle}{2\tau^2} \quad (8.3)$$

where  $R$  and  $a$  are the major and minor radius, respectively, and  $\langle \beta \rangle$  is the volume averaged  $\beta$ . This equation describes the main dependences, but a quantitative analysis requires full 3-D equilibrium calculations. In axisymmetric devices and classical stellarators the factor  $\varepsilon_B^{10}/\varepsilon_t = 1$ , whereas in optimized stellarators with reduced Pfirsch–Schlüter currents  $\varepsilon_B^{10}/\varepsilon_t < 1$  is achieved. Actually, extensively optimized stellarators such as of the Helias type may not require additional vertical field coil systems for plasma position control. If the Shafranov shift exceeds a critical value, it will eventually give rise to an equilibrium  $\beta$  limit due to a progressive deterioration of flux surfaces. This effect is expected to become significant for  $\Delta/a \approx 1/2$  so that the equilibrium  $\beta$  limit is roughly given by

$$\langle \beta \rangle_{\text{eq}} \approx (a/R) \left( \varepsilon_t / \varepsilon_B^{10} \right)^2 \tau^2 \quad (8.4)$$

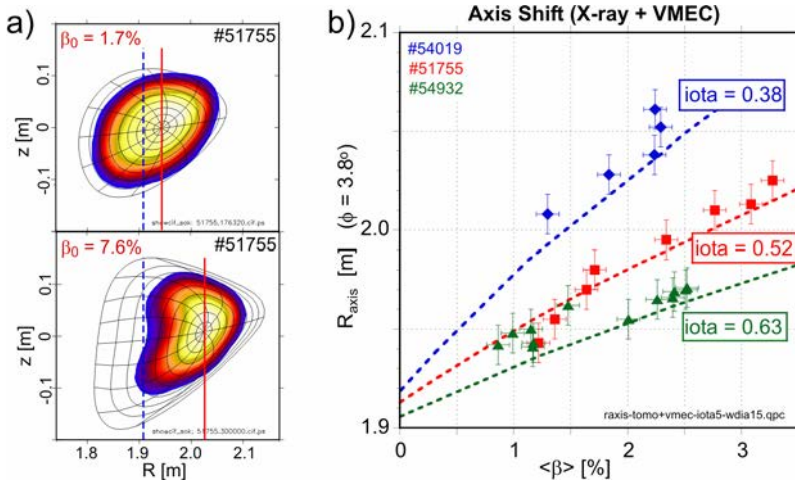


FIG. 8.16. (a) Tomographic reconstructions of X ray emissivity distributions in W7-AS (low and high  $\beta$ ). Comparison with free-boundary VMEC calculations (black solid contours) are included in the plots. The dashed lines mark the locations of the magnetic axis of the vacuum configuration. (b) The experimental data points represent the radial plasma axis positions as deduced from the peak position of the X ray distributions for three configurations of different  $\iota$ . Dashed lines: predictions by VMEC.

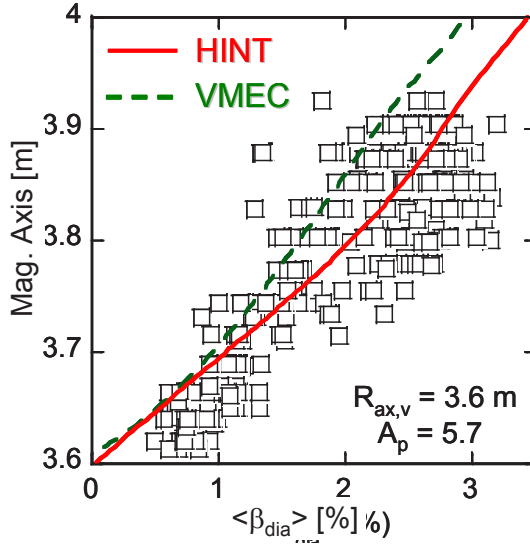


FIG. 8.17. Axis shift in the Large Helical Device. The data points were determined from the peak positions of the electron pressure profiles measured by Thomson scattering. The data points are compared with HINT and VMEC equilibrium code calculations. Axis shift in the Large Helical Device with aspect ratio of  $A_p = R_{\text{ax,v}}/a = 5.7$  and axis position of vacuum magnetic field configuration at  $R_{\text{ax,v}} = 3.6 \text{ m}$ . Courtesy of K.Y. Watanabe, NIFS, Toki, Japan.

The Shafranov shift is deduced experimentally from radial electron and ion temperature profiles in the horizontal midplane of the plasma or from 2-D soft X ray emission measurements assuming constant plasma parameters on flux surfaces (Figs 8.16 and 8.17). The X ray emissivity contours in a poloidal plane are reconstructed by tomographic analysis of line integrated data from linear X ray detector arrays viewing the plasma from different poloidal angles.

Another method is to view the plasma along a tangential direction with a 2-D X ray imaging camera. The images correspond to flux surfaces averaged in the toroidal direction, but they can be deconvoluted exploiting the calculated field line geometry and assuming constant emissivity along field lines. In addition, Pfirsch–Schlüter currents are measured by magnetic flux loops at the top/bottom side of the plasma detecting their vertical field component.

Investigations of the Shafranov shift have been made on several stellarators, heliotrons and other helical devices including Wendelstein W7-A and W7-AS, Heliotron-E, LHD and the Compact Helical System CHS [8.64]. In general, the experimental findings and the predictions of ideal MHD 3-D equilibrium calculations are in reasonable agreement.

In particular, the predicted reduction of the Shafranov shift by a factor of about two compared with an equivalent classical stellarator could be verified in W7-AS [8.33] by X ray tomography analysis (Fig. 8.16). Nevertheless, the

Shafranov shift approaches the critical value  $\Delta/a \approx 1/2$  in high  $\beta$  discharges ( $\langle\beta\rangle \approx 3\%$ ), particularly in the case of reduced rotational transform causing a saturation of the stored plasma energy with increasing heating power. In CHS, the observed Shafranov shift reached values of about 60% of the critical value, depending on the magnetic configuration. In LHD beta as large as  $\langle\beta\rangle \approx 5\%$  has been obtained in configurations optimized for reduced Shafranov shift [8.32]. In heliotron-type devices the rotational transform depends on the aspect ratio according to  $\tau \propto R/a$ , so that the Shafranov shift in the linear (low  $\beta$ ) regime can be given by  $\Delta/a \approx (a/R)\langle\beta\rangle$ . A key element was, therefore, to increase the aspect ratio.

Although fairly good agreement between experiments and equilibrium code predictions could be achieved, there remain a few issues connected with uncertainties regarding internal plasma current densities, experimental identification of the plasma edge, effects of non-isotropic plasma pressure (e.g. during strong NBI heating) and formation of islands or ergodic regions. In most cases, the diagnostic tools and predictive capabilities are not yet precise enough to clarify these issues.

### 8.3.3. Plasma stability

#### 8.3.3.1. Introduction and theoretical background

MHD instabilities are magnetic perturbations connected with plasma displacements, which are growing exponentially and which are subject to boundary conditions imposed by the periodicity of the magnetic field configuration and the plasma/vacuum coupling. Avoiding MHD instabilities is a basic requirement in fusion plasmas because of their deleterious effect on the plasma confinement. The sources of free energy available for driving MHD perturbations are associated with gradients in the plasma pressure and in the parallel current densities. The theory typically examines the stability of the equilibrium plasma against small perturbations. The energy principle [8.65, 8.66] based on the ideal linearized MHD equations and the conservation of energy in ideal MHD is widely used to assess the basic MHD stability properties. To easily identify the various physical mechanisms determining the ideal MHD stability we adopt a representation from Freidberg [8.67] and Bateman [8.68]:

$$\delta W_p = \int d\vec{r} \left[ \frac{1}{\mu_0} |\tilde{\vec{B}}_{\perp}|^2 + \mu_0 \left| \frac{1}{\mu_0} \tilde{B}_{\parallel} - \frac{\vec{B}}{B^2} \cdot \nabla p \right|^2 \dots \right. \\ \left. + \gamma p |\nabla \cdot \tilde{\xi}|^2 - 2(\tilde{\xi} \cdot \nabla p)(\kappa \cdot \tilde{\xi}) - \vec{j} \cdot \frac{\vec{B}}{B^2} (\tilde{\xi} \times \vec{B}) \cdot \tilde{\vec{B}}_{\perp} \right] \quad (8.5)$$

Here,  $\delta W_p$  is the change of the plasma potential energy inside the plasma volume associated with an arbitrary perturbation characterized by a fluid displacement  $\xi$  and the corresponding field perturbation  $\vec{B} = \nabla \times (\xi \times \vec{B})$ . The three first terms are stabilizing associated with effects of field line bending, magnetic field and plasma compression giving rise to shear Alfvén waves, fast magneto-acoustic waves and sound waves, respectively. In stellarators the most important MHD instabilities are pressure driven interchange and ballooning modes, which are potentially caused by the fourth term, depending on the sign of the pressure gradient relative to the averaged or local field line curvature,  $\kappa = \vec{B}/B \cdot \nabla (\vec{B}/B)$  for which  $\kappa = 1/2B^4 [\vec{B} \times \nabla (2\mu_0 p + B^2)] \times \vec{B}$  follows for a finite  $\beta$  equilibrium. The last term contains the energy reservoir due to the parallel current to kink the plasma. In contrast to tokamaks, current driven instabilities are usually absent in stellarators since no strong current drive is applied and bootstrap currents are small in most cases.

Hence, the MHD stability behaviour of stellarators without net toroidal current through each magnetic surface is completely different from that in tokamaks, since potentially dangerous classes of MHD instabilities, such as the current driven kink modes and their resistive counterparts, in particular tearing modes, are eliminated. Consequently, plasma disruptions can be completely avoided in stellarators. Moreover, the presence of vacuum magnetic surfaces and the possibility to generate favourable profiles of shear and magnetic well for stability by proper 3-D surface shaping results in much better external control of the plasma stability.

The basic properties necessary for a stable stellarator configuration can be inferred from the Mercier stability criterion for ideal interchange modes. This evolves from the energy principle by assuming perturbations being highly localized in the radial direction, so that stability can be explored by an investigation of periodic perturbations on a single flux surface (“local stability analysis”). The Mercier criterion is a necessary condition for the linear ideal MHD stability in 3-D configurations [8.69, 8.70]. The most dangerous perturbations result if their mode topology is aligned to the magnetic field, i.e. if they are resonant to the local rotational transform value. In this case, the energy required for field line bending is minimized. The resulting stability criteria can be written as [8.71]:

$$D_M = D_S + D_W + D_{J.B} + D_G > 0 \quad (8.6)$$

where  $D_S = (\epsilon')^2/4 > 0$  reflects the stabilizing influence of global magnetic shear.

$$D_W = \left( p'V'' - p'^2 \left\langle \frac{1}{B^2} \right\rangle \right) \left\langle \frac{B^2}{|\nabla \psi_\phi|^2} \right\rangle \quad (8.7)$$

is the contribution due to the magnetic well (both vacuum and finite  $\beta$ ), where  $\psi_\phi$  is the normalized toroidal flux and  $V$  is the volume enclosed by the flux surface. The derivative is with respect to  $\psi_\phi$ , i.e. ( $' = d / d\psi_\phi$ );  $\langle \rangle$  stands for flux surfaces averages. The correction by the diamagnetic effect is included:

$$D_{j \cdot B} = \left\langle \frac{I'_\phi B^2 - j_{\parallel} B}{|\nabla \psi_\phi|^2} \right\rangle \quad (8.8)$$

is the contribution of the toroidal current  $I_\phi$  and

$$D_G = \left\langle \frac{j_{\parallel} B}{|\nabla \psi_\phi|^2} \right\rangle^2 - \left\langle \frac{j_{\parallel}^2}{|\nabla \psi_\phi|^2} \right\rangle \left\langle \frac{B^2}{|\nabla \psi_\phi|^2} \right\rangle \leq 0 \quad (8.9)$$

accounts for the geodesic curvature driven instability potential, namely the PS currents. For non-optimized stellarators or for configurations with considerable shear or toroidal net currents, for example torsatrons/heliotrons or quasi-axisymmetric configurations, the full criterion has to be investigated, whereas for optimized stellarators with low shear and vanishing toroidal net currents a reduced criterion containing only the magnetic well and the geodesic curvature term  $D_M \approx D_W + D_G > 0$  is a good approximation. Figure 8.18 contains an example for the analysis of the Mercier criterion for a case of W7-AS. This figure also shows a feature inherent to 3-D systems, namely the locally narrow unstable regions. These are caused by resonances in the driving term of the PS currents, which lead them to diverge at rational surfaces in the presence of a pressure gradient. Pressure flattening in the vicinity of rational surfaces removes these formal instabilities.

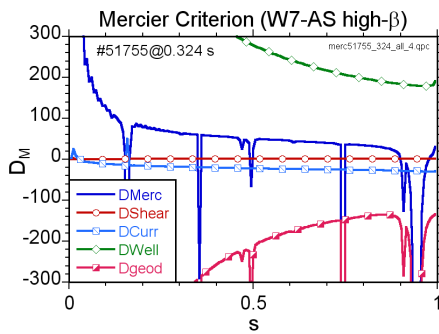


FIG. 8.18. Local ideal MHD stability analysis for a Wendelstein W7-AS high- $\beta$  case ( $\langle \beta \rangle = 3.2\%$ ). The plasma is stable ( $D_M > 0$ ) across the whole plasma ( $s$  is the toroidal flux label defined by  $s = \sqrt{\psi_\phi}$ ) apart from local narrow unstable regions at rational surfaces. The stabilization is mainly due to the magnetic well (green symbols), whereas the dominating destabilizing effect is due to the interchange term (magenta symbols) depending on the geodesic curvature.

The elements to design stable reactor-relevant stellarator experiments are magnetic well, magnetic shear and the connection length between regions of opposite curvature of field lines. The term “magnetic well” describes an average minimum  $B$  property of a magnetic configuration, i.e. the average magnetic field strength on the flux surfaces increases with the enclosed volume. The value is derived from  $V'' \equiv d^2V/d\psi_\phi^2$ . A magnetic well corresponds to  $V'' < 0$ , which is stabilizing, whereas a “magnetic hill” ( $V'' > 0$ ) has a destabilizing effect. The magnetic well of a configuration is defined as a dimensionless parameter on each flux surface by

$$\hat{f}(V) = 2 \frac{V}{\langle B^2 \rangle} \frac{d}{dV} \left\langle \frac{B^2}{2} \right\rangle \quad (8.10)$$

where the flux surface average for any function  $f$  is defined by

$$\langle f \rangle = \int_0^L \frac{f}{B} dl \bigg/ \int_0^L \frac{dl}{B} \quad (8.11)$$

Here,  $L$  denotes the length of the line of force over the magnetic surface ( $L \rightarrow \infty$  on irrational surfaces). A magnetic well corresponds to a configuration with surface averaged favourable curvature and is realized in most stellarators. The average or global magnetic shear is defined on each surface by the dimensionless parameter

$$s(V) = 2 \frac{V}{\tau} \frac{d\tau}{dV} \quad (8.12)$$

where  $\tau$  is the rotational transform.

High shear also provides an important method to stabilize MHD modes, but the effect is reduced by resistivity which allows the plasma to slip through the magnetic field, thus reducing the restoring magnetic force. In stellarators, shear usually increases from the plasma axis to the edge due to its generation by external coils. This property corresponds to “reversed shear” in advanced tokamak scenarios, and hence is favourable for suppressing ballooning modes and neoclassical tearing modes.

In recent experiments at LHD it was found that the Mercier criterion can be exceeded substantially [8.72]. Similarly, in W7-AS no or mostly benign mode activity was found in Mercier unstable regions [8.73]. Mostly the observed global MHD modes saturate at a low level which is subcritical for affecting the plasma confinement. By comparison of ideal MHD calculations with experimental data of LHD a more relevant stability index was proposed defined by the threshold  $\gamma/\omega_A \approx 10^{-2}$  of the linear growth rate  $\gamma$  of ideal low  $n$  modes normalized to the poloidal Alfvén frequency  $\omega_A = R/v_A$ , where  $v_A$  is the Alfvén speed at the mode location. According to the numerical stability analysis the threshold corresponds

to a ratio  $\delta/a \approx 0.05$  of the width  $\delta$  of the mode eigenfunction to the plasma radius  $a$ .

### 8.3.3.2. Ballooning modes

Whereas surface averaged configuration parameters are used to assess the local interchange stability by the Mercier criterion, ballooning modes can be regarded as a special class of interchange modes, characterized by a short wavelength across the field lines in a constant pressure surface (modes with high toroidal mode numbers) and a large but finite wavelength along the field line. Hence, unstable perturbations tend to develop locally on the magnetic surface where the local magnetic field line curvature is most unfavourable. As in the case of interchange modes the most unstable modes have a long wavelength along the field line minimizing the stabilization due to field line bending (shear Alfvén stabilization). The large difference of the perpendicular and parallel wavenumbers described by the conditions  $k_{\parallel}/k_{\perp} \ll 1$ ,  $k_{\perp}a \gg 1$ , where  $a$  is the plasma radius, reduces the ballooning stability problem to the solution of a 1-D differential equation for each field line. The ideal ballooning stability boundary deduced from the field line ballooning equation is correlated with the Mercier criterion if sufficient field periods along the field line are included. In cases of pronounced violation of the local ballooning criterion, corresponding unstable localized perturbations have been found by 3-D global stability codes such as CAS3D (see Section 8.3.3.3) which have been set up for high radial resolution and a large number of perturbation harmonics (Fig. 8.19).

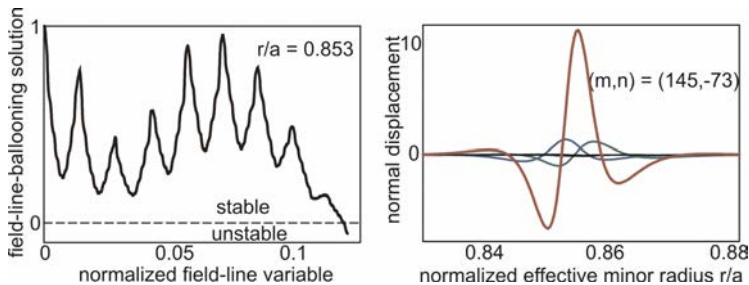


FIG. 8.19. Left: Solution of the field line ballooning equation for the W7-AS discharge 51382 with  $\langle \beta \rangle \approx 0.9\%$  in the Mercier unstable region at  $r/a = 0.853$ . Right: Unstable global, but high- $n$  perturbation corresponding to the field line ballooning solution on the left. The variable along the field line is normalized with respect to field-line closure; for this particular case 0.1 corresponds to 14.5 times around the torus. Courtesy of C. Nührenberg, IPP, Greifswald, Germany.

The stability depends crucially on the local shear in the region of bad curvature, where the local shear is a measure for the amount a field line has to

be stretched by the perturbation in order to interchange with a neighbouring field line [8.66]. In a tokamak the bad curvature region is at the horizontal outboard side in circular plasmas or at the tips of elongated plasmas. Each field line on a magnetic surface of a tokamak has the same local stability properties. In a stellarator the ballooning stability is more complex due to the 3-D distribution of local field line curvature and local shear on the magnetic surfaces. Therefore, the local ballooning stability also depends on the field line label within a magnetic surface. Note that non-axisymmetry gives rise to two branches in the solution space of the ballooning equation instead of only one as in the tokamak case. They are termed “interchange branch” relating to the ballooning solutions in the axisymmetric case and the “ballooning branch” which appears only in 3-D systems with a higher localization in the toroidal and poloidal directions [8.74]. In a low- $\beta$  approximation, the global magnetic shear in stellarators is always positive in the stellarator definition, i.e.  $\iota(r)$  increases from the magnetic axis to the boundary corresponding to reversed tokamak shear, which is favourable to suppress ballooning instabilities in the Mercier stable regime. The ballooning stability criterion is more restrictive than the Mercier criterion so that ballooning modes can typically occur in Mercier stable configurations. In 3-D configurations, effects of reversed shear, decoupling of local and global shear, reduced geodesic curvature and reduced connection lengths between regions with opposite curvature can have a strong impact on the ballooning stability [8.75] and even in Mercier unstable configurations unstable ballooning modes may not appear.

Experimentally it is difficult to identify ballooning modes as they constitute a local perturbation with relatively high mode numbers. So far, no direct evidence exists in stellarators.

### 8.3.3.3. Global pressure driven modes

The study of global (non-local) MHD instabilities in 3-D toroidal plasmas requires advanced computational tools such as the CAS3D code [8.76] or the Terpsichore code [8.77]. These codes are based on the formulation of the ideal MHD energy principle in magnetic coordinates and solve the full linear eigenmode problem in 3-D geometry:

$$\lambda K - \delta W_p = \text{minimum} \quad (8.13)$$

where

$$K = \frac{1}{2} \int d\vec{r} \rho |\xi|^2 \quad (8.14)$$

is the kinetic energy functional associated with the displacement  $\xi$  of the mass density  $\rho$  and  $\lambda = \omega^2$  are the eigenvalues of the equation, where  $\xi(\vec{r}, t) = \xi(\vec{r}) e^{i\omega t}$  is used to represent exponentially growing modes. The calculations of the energy functionals start from 3-D MHD equilibria computed

by VMEC, i.e. with the assumption of nested flux surfaces and the plasma without mass flow/rotation. Realistic equilibria with magnetic islands or with inclusion of plasma rotation have not yet been treated by linear stability theory. Recently, anisotropic pressure effects have been included in Terpsichore and VMEC for studies of high  $\beta$  NBI cases in LHD [8.78].

The non-axisymmetric field and flux geometry in stellarators result in mode structural properties which differ from the tokamak case. Like the equilibrium field (Eq. (8.1)) the spatial mode structure on each flux surface is usually represented by a Fourier expansion in the poloidal and toroidal angle coordinates  $\theta$  and  $\phi$ . In a tokamak,  $\phi$  is an ignorable parameter of the equilibrium, and therefore modes with different toroidal periodicity (denoted by their toroidal mode numbers  $n$ ) are independent. The poloidal mode structure, however, consists of a spectrum of Fourier components due to sideband coupling via the poloidal field inhomogenities. In stellarators, the toroidal periodicity of the equilibrium configuration causes also sideband couplings between different toroidal mode numbers. Basically, the sideband effects originate due to non-vanishing products between mode components among each other and in addition with components of the equilibrium components occurring in the evaluation of the potential energy (Eq. (8.5)). Depending on the number of field periods  $N_p$ , only a few independent “mode families” appear in stellarators [8.76]. The conditions for coupling between two mode perturbations with poloidal mode numbers  $m_1$  and  $m_2$  and toroidal mode numbers  $n_1$  and  $n_2$  are given by

$$m_1 \pm m_2 = \mu \quad (8.15)$$

$$n_1 \pm n_2 = \nu N \quad (8.16)$$

where  $\mu, \nu = 0, 1, 2, \dots$  are the Fourier indices of the equilibrium harmonics according to Eq. (8.1). This means that for a stellarator with five field periods like Wendelstein W7-X three toroidal mode families based on  $n = 0, 1, 2$  exist, termed  $N = 0, 1, 2$  families [8.79]. All the modes with  $n > 2$  can be constructed by 3-D coupling.

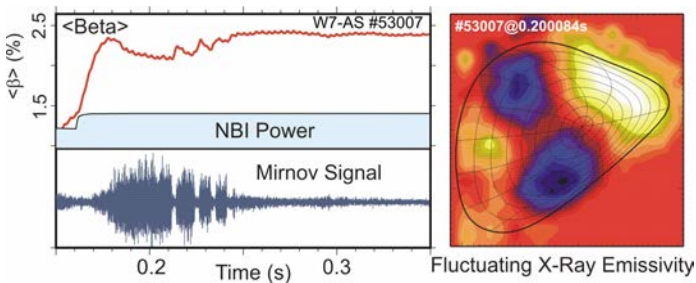


FIG. 8.20. Left: Transient low frequency (10 kHz) MHD mode activity during NBI heating in W7-AS at  $\langle \beta \rangle \approx 2\%$ . Right: A dominating  $m = 2$  structure is seen in the tomographic reconstruction of the fluctuating X ray emissivity.

Experimentally, global pressure driven modes have been studied in stellarator and heliotron configurations, both in plasmas without toroidal net current and with residual currents due to unbalanced NBI heating and bootstrap currents (see Section 8.3.5). Typically, low  $n$  resonant mode structures are observed rotating in the electron diamagnetic drift direction. Figure 8.20 shows data from W7-AS for a case with  $\langle\beta\rangle \approx 2\%$  where the  $m = 2$  component dominates in the X ray tomogram. The result of a corresponding numerical analysis with the CAS3D code is given in Fig. 8.21. The  $m = 2$  harmonic is predicted to dominate in the inner region, whereas higher harmonics are expected to contribute significantly at the plasma edge. A typical feature of these global modes is their self-stabilization at higher plasma  $\beta$  due to the increase of the magnetic well depth and the global shear induced by the Shafranov shift. In the case of optimized stellarators with strongly reduced PS currents this effect is small, and therefore a sufficiently deep magnetic well has to be provided in the vacuum configuration. A low shear stellarator helps to stabilize low  $n$  global modes by excluding low order rational surfaces from the confinement region.

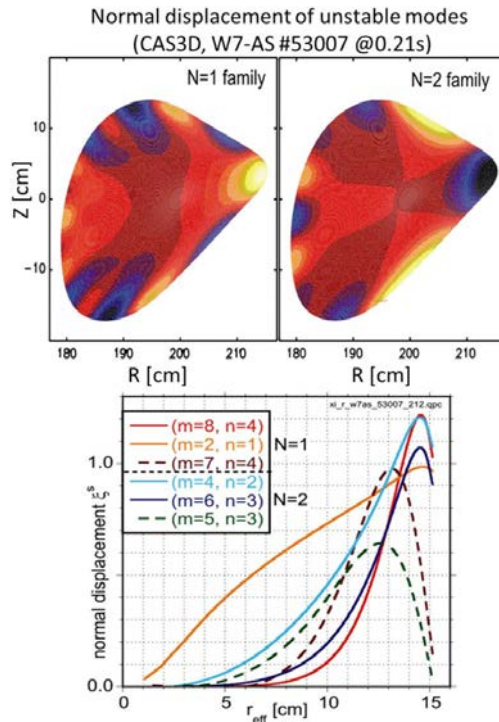


FIG. 8.21. Global ideal MHD stability analysis with the CAS3D code for the W7-AS high  $\beta$  case shown in Fig. 8.20. Top: Normal displacement contours of unstable modes are shown for two mode families separately in the poloidal plane of the X ray measurements. Bottom: Radial eigenfunctions of the most important harmonics are plotted.

### 8.3.3.4. Energetic particle driven Alfvén instabilities

#### 8.3.3.4.1. Introduction

A plasma supported by a magnetic field is subject to fundamental electromagnetic-hydrodynamic waves [8.80] such as shear and compressional Alfvén waves and fast magneto-acoustic waves. Alfvén instabilities driven by resonant energetic ions were observed in tokamaks, stellarators and spherical tori [8.81]. These instabilities can have very different forms and consequences. They are not necessarily harmful and can be used for plasma diagnostics. Shear Alfvén waves — basic oscillations between perpendicular plasma kinetic energy and perpendicular field line bending energy — are the most common Alfvén perturbations. They are incompressible and essentially connected with a twist of the field lines due to their transverse polarization ( $\vec{B}_\perp \gg \vec{B}_\parallel$ ,  $\vec{E}_\perp \gg \vec{E}_\parallel$ ). Their dispersion relation in a cylindrical plasma geometry and in the case of frequencies  $\omega$  well below the ion cyclotron frequency is given by

$$\left(\vec{k} \cdot \vec{B}\right)^2 - \omega^2 \rho = 0 \quad (8.17)$$

or equivalently by

$$\omega^2 = \left(k_\parallel \cdot v_A\right)^2 \quad (8.18)$$

Here, the Alfvén velocity  $v_A = \sqrt{B^2/\mu_0\rho}$  is the speed of the perturbations propagating along the magnetic field lines,  $\rho$  is the plasma mass density,  $k_\parallel = (m\tau - n)/R$  is the wave vector parallel to the magnetic field, and  $m$ ,  $n$  are the poloidal and toroidal wavenumbers of the perturbation in the usual Fourier representation. The dispersion relation (Eq. (8.18)) gives rise to a continuous spectrum (Alfvén continuum, AC), since the Alfvén velocity and the rotational transform are in general non-uniform across the plasma radius in practical magnetic confinement systems. Actually, the quadratic form of the dispersion relation describes two branches of counter-propagating modes. Alfvén waves of the continuum are strongly damped by magnetic shear and by the variation of the Alfvén velocity due to phase mixing preventing spatially extended modes of equal phase velocity (continuum damping). Whereas shear Alfvén modes in axisymmetric systems are perturbations extended over flux surfaces, in the case of strong non-axisymmetric field geometries they become progressively localized along single magnetic field lines, turning into ballooning-like perturbations and a particular  $(m,n)$  mode does not exist anymore [8.82].

## 8.3.3.4.2. Frequency gaps, gap modes

The Alfvén spectrum in toroidal magnetic fusion devices exhibits characteristic frequency gaps, inside which weakly damped discrete so called gap modes or global Alfvén eigenmodes (AEs) exist. Hence, these gap modes are susceptible to being destabilized by suprathermal particle distributions via particle–wave resonances in the range of the Alfvén speed such as neutral beam injected ions, tail ions produced during ion cyclotron heating and fusion born fast particles.

These gaps of the continuous Alfvén spectrum are caused by different effects:

- (i) In the case of the so-called global Alfvén eigenmode (GAE) [8.83], the relevant continuum branch with certain mode numbers  $(m, n)$  stays above a finite low-frequency limit across the entire plasma, i.e.  $\omega_A^2(m, n) = (k_{\parallel} \cdot v_A)^2$ . Conventional GAEs are predicted to reside in the “natural” gaps just underneath the low frequency extremum  $\omega_{A, \min}^2(m, n)$ . Since the GAE gap is the only one which occurs in cylindrical geometry, the mode is also dubbed cylindrical GAE. In high shear tokamaks and helical systems, relevant GAE gaps do not exist or they are closed by other continuum branches where the GAEs can suffer strong continuum damping via sideband couplings. However, in the case of low shear stellarators the formation of GAE gaps and the excitation of GAE modes take place commonly due to a reduced frequency range of the continuum branches and a larger separation between them [8.84]. Figure 8.22 shows an example of the characteristics of GAE activity in the W7-AS stellarator which are well in agreement with the modelling results of the 3-D MHD stability code AE3D [8.85]. Essential properties of GAEs are the almost monochromatic wave structure (i.e. a single Fourier harmonic is dominating) and the non-resonant behaviour (in the sense that  $\tau = m/n$  or  $k_{\parallel}(m, n) = 0$  does not exist in the plasma).
- (ii) Similarly, in the low frequency range so-called beta induced Alfvén eigenmodes (BAE) [8.81] may occur in respective BAE gaps. Here, the gaps and the corresponding BAEs owe their existence to effects of geodesic curvature and finite plasma compressibility in the presence of significant plasma pressure. The original continuum resonances at low frequencies, present in the incompressible plasma limit, are removed by couplings between Alfvén and sound continuum branches. The BAE frequency does not scale with the Alfvén speed but with the ion thermal velocity, indicating its hybrid wave characteristic.
- (iii) The presence of non-uniform magnetic fields along the field lines and of magnetic shear leads to a breakup of the continuous cylindrical Alfvén

spectrum with formation of gaps and discrete global modes inside the gaps. This is the most important effect in the intermediate frequency range caused by couplings among the different continuum branches. The characteristic frequencies of the gaps and of the respective global modes are determined by the crossing points of two or more branches of counter-propagating cylindrical AC modes. In cylindrical geometry the modes are independent and do not interact. In the presence of parallel field ripple and plasma shaping, however, the degeneracy of the frequencies is removed. The participating cylindrical branches coalesce in the vicinity of the intersection point forming new branches of mixed modes, which are separated by a gap. The width of the gap is determined by the relative magnitude of the non-uniformity of the field and of the plasma geometry. The harmonic composition of the discrete global modes inside the gap is similar to that of the adjacent mixed continuum modes below and above the gap. In a more general context, the gap formation can be regarded as an “avoided crossing” phenomenon, being caused by destructive interference of counter-propagating waves or by resonant reflection of waves by a periodic potential associated with the modulation of the field and hence of the Alfvén velocity along the field lines.

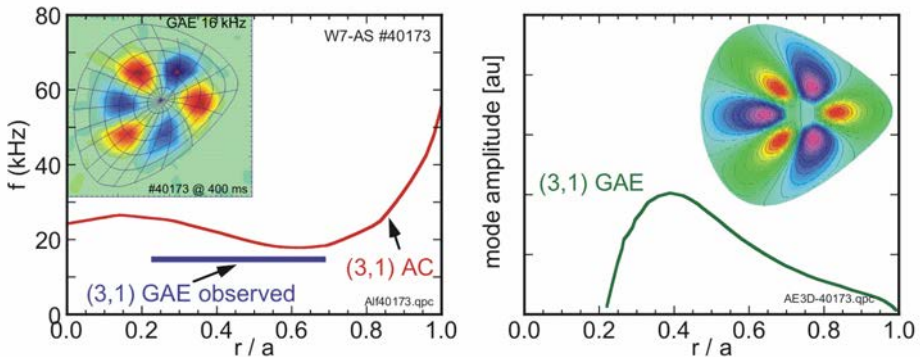


FIG. 8.22. Left: The red solid curve represents the  $(m,n) = (3,1)$  shear Alfvén continuum for a case of NBI driven GAE activity in the W7-AS stellarator. The dark blue horizontal bar at the top of the GAE gap marks the radial extent of the mode and the observed GAE frequency (16 kHz). The 2-D mode structure (inset), dominated by  $m = 3$ , was obtained from a tomographic reconstruction of the fluctuating X ray emissivity. Right: Radial eigenfunction (green solid line) and 2-D mode structure as predicted by a numerical MHD stability calculation (AE3D). Courtesy of D.A. Spong, ORNL, Oak Ridge, Tennessee, USA.

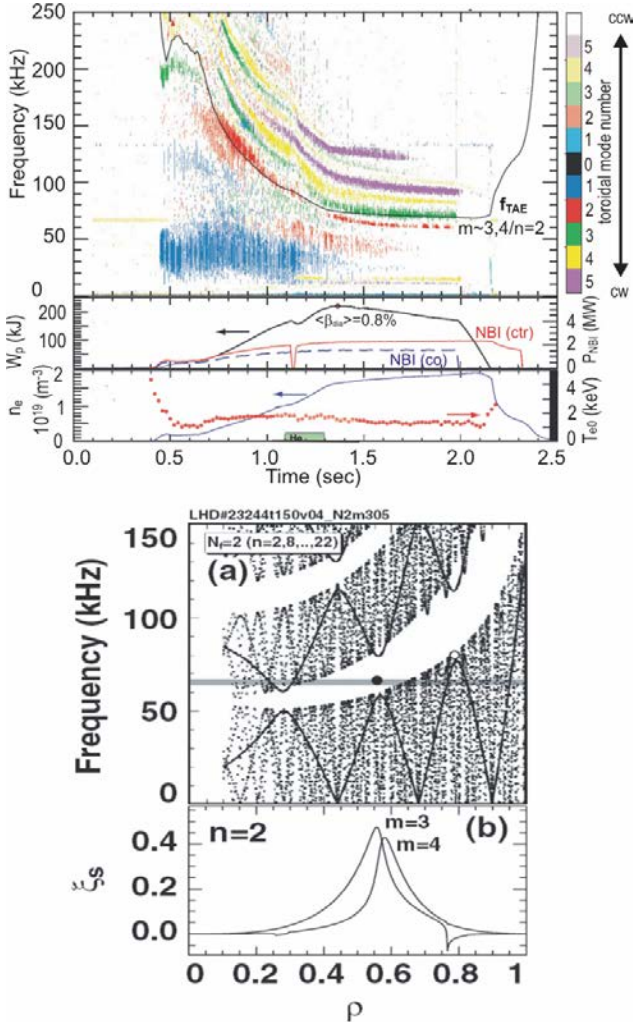


FIG. 8.23. Top: Typical TAE activity during NBI heating in LHD. Just below the spectrogram the waveforms of plasma energy ( $W_p$  – black), power  $P_{NBI}$  of the co- (blue) and counter-NBI (red) are shown and below this the time traces of electron density ( $n_e$  – blue) and electron temperature ( $T_{e0}$  – red). A green block in the density/temperature time trace denotes a He-gas puff to increase the electron density. The time evolution of the frequencies seen in the spectrogram of the magnetic fluctuations is closely related to the change of the Alfvén speed (density – blue). The different lines correspond to Doppler shifted modes of different toroidal mode numbers. The predicted frequency for  $n = 2$  (black line in spectrogram) agrees with the measurement. Bottom: Predicted gap structure showing the TAE and EAE (ellipticity induced Alfvén eigenmode) gaps. The observed mode agrees with the predicted TAE inside the gap (marked by the horizontal line and the dot) whose mode structure is shown in the bottom part of the figure by the component  $\xi_s$  of the plasma displacement normal to the flux surface. Courtesy of K. Toi, NIFS, Toki, Japan; S. Yamamoto, Institute of Advanced Energy, Kyoto, Japan; Fig. 3 from Ref. [8.86].

The toroidicity induced Alfvén eigenmode (TAE) is the most important gap mode in tokamaks but also in helical systems with significant shear (Fig. 8.23). It results from coupling of  $m$  and  $m+1$  AC branches in consequence of toroidal curvature, which is given by the parameter  $\varepsilon_B^{10}$  introduced in Section 8.3.2. Actually, taking the magnetic field representation (Eq. (8.1)) and the selection rules for mode coupling (Eqs (8.15) and (8.16)) into account, the Fourier coefficients  $\varepsilon_B^{\mu\nu}$  of the equilibrium field strength can be regarded as coupling parameters where the coupling indices  $(\mu, \nu)$  characterize the type of the different gap modes. It should be noted that besides the magnetic coupling parameters, additional geometrical coupling parameters describing the 3-D shape of the flux surfaces have to be taken into account. Using the condition for the intersection point of counter-propagating  $(m, n)$  and  $(m+\mu, n+\nu N_p)$  modes, i.e.  $k_{\parallel}(m, n) = -k_{\parallel}(m+\mu, n+\nu N_p)$ , the characteristic gap frequencies, generalized by including the non-axisymmetric stellarator term  $\nu N_p$ , are given by

$$\omega_{\times} = \left| \frac{\mu \tau_{\times} - \nu N_p}{2R} \right| \cdot v_{A\times} \equiv \left| k_{\parallel\times}(\mu \nu) \right| \cdot v_{A\times} \quad (8.19)$$

with

$$\tau_{\times} \equiv \frac{2n + \nu N_p}{2m + \mu} \quad (8.20)$$

Here, local values at the intersection point are denoted with a cross. Equation (8.20) describes a global multiharmonic gap, since the frequency is determined by the coupling indices  $(\mu, \nu)$  rather than by local mode numbers  $(m, n)$ . Due to the non-axisymmetry, new types of Alfvén eigenmodes such as helicity and mirror induced Alfvén eigenmodes (HAEs and MAEs) appear. Some characteristics of the most important AEs are summarized in Table 8.2.

TABLE 8.2. NOMENCLATURE AND CHARACTERISTICS OF ALFVÉN GAP MODES INDUCED BY MAGNETIC AND GEOMETRIC NON-UNIFORMITIES			
<i>(The subscript 'x' denotes values at the crossover point)</i>			
Acronym	Coupling indices ( $\mu, \nu$ )	Non-uniformity (equilibrium)	Norm. gap frequency $\Omega = \omega_x \cdot R/v_{A,x}$
TAE	(1,0)	toroidal curvature	$\frac{1}{2} t_x$
EAE	(2,0)	ellipticity	$t_x$
NAE	(3,0)	triangularity (or higher shape non-uniformities)	$\frac{3}{2} t_x$
HAE $_{\mu\nu}$	( $\mu, \nu$ ) $\mu, \nu > 0$	helicity (non-axisymmetric)	$\frac{1}{2} \nu N_p \left  1 - \frac{\mu}{\nu N_p} t_x \right $
MAE $_{0\nu}$	(0, $\nu$ ) $\nu > 0$	mirror field (non-axisymmetric)	$\frac{1}{2} \nu N_p$

Based on Eq. (8.19), the normalized frequencies in the centre of the gaps are plotted in Fig. 8.24 as a function of the rotational transform for the case of a five period device such as W7-AS and W7-X. In LHD, the stellarator modes are at higher frequencies because of the higher number of field periods ( $N_p = 10$ ). The relatively large rotational transform in W7-X compared to W7-AS gives rise to a novel feature of the Alfvén spectrum, namely the possibility of crossings between helical and axisymmetric gaps, which can lead to ‘gap annihilation’ and combination gaps [8.87].

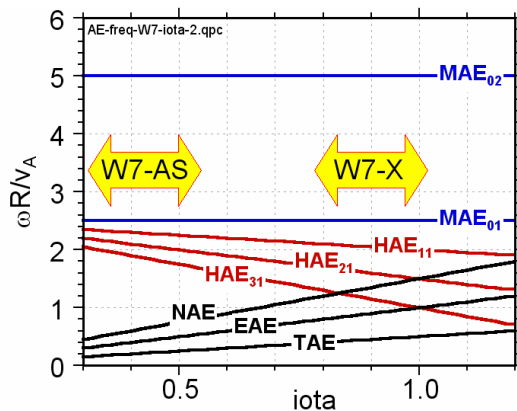


FIG. 8.24. Normalized characteristic AE frequencies in the five-periodic Wendelstein stellarators W7-AS and W7-X.

Another interaction between gaps can occur if the widths of individual gaps would exceed the frequency distance in between them due to large coupling parameters. In this case, the Alfvén continua can be squeezed into narrow bands surrounded by wide gaps. These peculiarities of 3-D configurations can lead to rather complex Alfvén spectra. In Fig. 8.25, results from W7-AS are shown [8.88], which confirm the existence of Alfvén modes induced by non-axisymmetric couplings. In particular, the HAE modes were also found in the Large Helical Device [8.89].

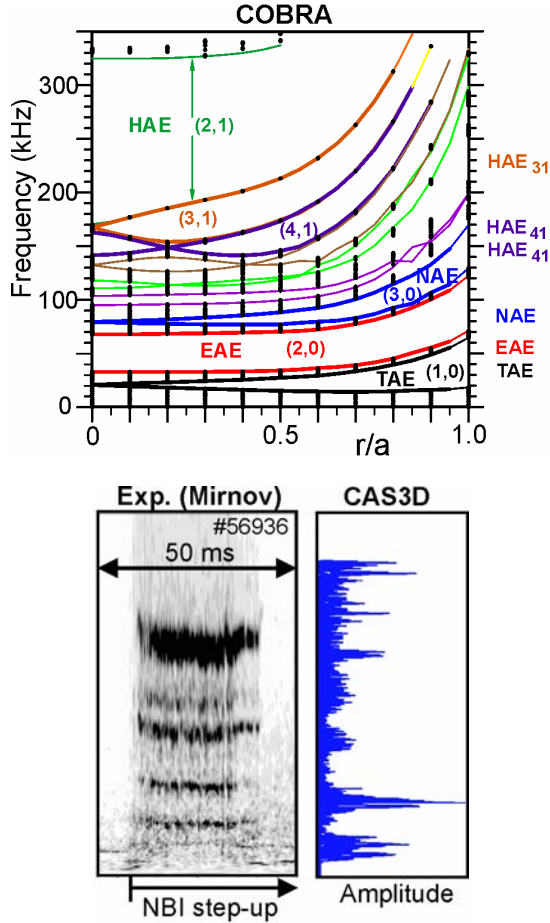


FIG. 8.25. Top: Gap structure predicted for an NBI heated discharge in W7-AS. The dots represent the continuum resonances found by the COBRA code [8.90], the lines mark the gap boundaries. At high frequencies wide gaps are found with narrow bands of AC modes in between. In the experiment, several modes up to 250 kHz were seen transiently (lower left), which are consistent with expected gap modes. The high frequency modes are attributed to helicity induced AEs. Lower right: The modes show up also in the spectrum computed by CAS3D.

## 8.3.3.4.3. Particle–wave interaction

Likewise, there are also peculiarities concerning the particle–wave interaction due to a number of non-axisymmetric resonances [8.91]. The energy transfer between energetic ions and Alfvén waves via Landau or inverse Landau damping is approximately given by  $q\vec{v}_D \cdot \vec{E}_\perp$ , where  $q$  and  $\vec{v}_D$  are the charge and the drift velocity of the particle, respectively, and  $\vec{E}_\perp(m, n)$  is the fluctuating electric field of the wave. The corresponding basic resonance conditions including sideband resonances are given by

$$\omega - \left[ (m + j\mu_r)\tau + (n + j\nu_r N_p) \right] \frac{v_\parallel}{R} = 0, \quad (j = 0, \pm 1) \quad (8.21)$$

where  $(\mu_r, \nu_r)$  are the magnetic coupling numbers characterizing the type of the sideband resonance (not to confuse with the coefficients  $(\mu, \nu)$  used to label the type of the AE) and  $v_\parallel$  is the particle velocity parallel to the magnetic field. Setting  $k_\parallel(m, n) \approx k_{\parallel, \times}(\mu, \nu)$  (see Eq. (8.19)), the particle resonances can be expressed by

$$|v_\parallel| = v_{A, \times} \cdot \left| 1 + 2j \frac{\mu_r \tau_\times - \nu_r N_p}{\mu \tau_\times - \nu N_p} \right|^{-1} \quad (8.22)$$

There is always the fundamental resonance  $|v_\parallel| = v_{A, \times}$ . For the TAE  $((\mu, \nu) = (1, 0))$ , the well known toroidicity induced sideband resonance  $|v_\parallel| = (1/3) \cdot v_{A, \times}$  is recovered with  $(\mu_r, \nu_r) = (1, 0)$ , which describes a (1,0) modulation of the particle orbits. Besides the resonance condition, the energetic ion pressure has to be sufficiently large and the fast ion diamagnetic drift frequency has to exceed the mode frequency in order to excite the Alfvén eigenmodes. Actually, realistic particle distributions are mostly stabilizing (velocity space damping). The excitation energy is tapped from the free expansion energy associated with the spatial gradient of the fast particle pressure (represented by the diamagnetic fast particle drift frequency) via the particle drift motion. The complex structure of eigenmodes, particle orbits and wave–particle resonances in stellarators and helical systems requires hybrid 3-D MHD codes coupled with gyrokinetic or gyrofluid models for the fast ions, for example CAS3D-K [8.92] or AE3D-K [8.85] are required to predict the stability of Alfvén modes and to assess their non-linear evolution and the related fast ion transport.

A variety of effects related to the interplay of energetic particles and Alfvénic modes have been found in experiments on stellarators and helical systems [8.93–8.98]. These data are very important for benchmarking with results from numerical codes in order to assess the role of these instabilities in the presence of strong alpha-particle heating in a fusion device. In tokamaks, a high degree of understanding and modelling has already been reached.

## 8.3.3.4.4. Current induced instabilities

In stellarators, any deleterious current driven instabilities are absent during “currentless” operation. Thus, two major issues of tokamaks are inherently resolved in stellarators: (i) disruption-free operation is ensured, and (ii) at the same time there is no need of non-inductive current drive to achieve steady state operation. Quasi-axisymmetric stellarators [8.99] like the NCSX device (Section 8.5) are actually advanced tokamak–stellarator hybrids in which the bootstrap current (Section 8.3.5) provides a significant contribution to the total rotational transform. Here, current-driven instabilities can play a role.

The first fusion relevant stellarator plasmas were started and heated by inductive currents (ohmic heating, OH) as in tokamaks. Current driven instabilities in stellarators and their potential stabilization by the external transform were investigated in Heliotron-E [8.100], in CHS [8.101], and in the W7-A and W7-AS stellarators [8.102, 8.103] by using OH current drive. A key element of disruption avoidance in current-carrying stellarators is the possibility of influencing the existence and position of low order rational surfaces independently from the current profile. Moreover, the plasma equilibrium is maintained during disruptive events by the external field, whereas disruptions in tokamaks are associated with a complete loss of the plasma equilibrium. Therefore, the thermal collapse and the current disruption are much more benign (Fig. 8.26).

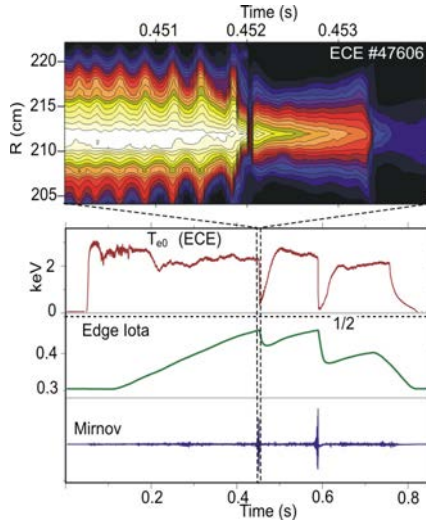


FIG. 8.26. OH-current ramp during an ECRH heated discharge in W7-AS. When the total rotational transform at the edge approaches  $\iota(a) = 1/2$ , disruption-like events occur (see  $T_{e0}$  (ECE) and signal from Mirnov-coil) preceded by growing  $(m,n) = (2,1)$  tearing modes as seen in the expanded view of ECE  $T_e$ -contours (top). The modes stop rotating just prior to the thermal collapses. In spite of the almost complete crash of the electron temperature, the current persists, and the discharge recovers.

Sawtooth oscillations were observed in different stellarators, for example in W7-A during OH operation [8.104], in W7-AS with OH and electron cyclotron current drive [8.95], and in LHD in the case of significant uncompensated NBI driven currents [8.105]. In the latter case, the relaxations were associated with different rational surfaces. It could be shown that pressure driven modes and the modification of their stability thresholds by net plasma currents (as described by the Mercier criterion) play an important role in helical systems. Sawtooth-like relaxations were even observed during currentless discharges in Heliotron-E around  $t = q = 1$  [8.106], indicating that the internal kink can be dominated by interchange modes. In particular, it was found in Heliotron-E that the location of the rational surface in a magnetic hill region and resistive effects reducing shear stabilization are important ingredients resulting in the destabilization of resistive interchange modes causing the observed internal disruptions.

### 8.3.4. Bounce-averaged particle orbits

In an ideal axisymmetric configuration, the collisionless particle orbits are periodic in the poloidal cross-section. This feature is completely absent without strict symmetry. Whereas passing particles in 3-D stellarator configurations are much less affected, particles trapped in local ripples can have a significant radial drift and escape from the plasma without collisions. These ripple-trapped particles dominate the neoclassical transport in the stellarator long-mean-free-path (*lmfp*) regime. Consequently, either a significant reduction of this radial drift (*drift-optimization*) or a minimization of the fraction of ripple-trapped particles (as in *quasi-symmetric* configurations) is essential for the improvement of the neoclassical confinement in stellarators.

In general the guiding-centre drift velocity in spherical velocity coordinates  $v, \zeta = v_{\parallel}/v$  is

$$\vec{v}_D = \frac{1}{B^2} \vec{B} \times \nabla \Phi + \frac{m(1 + \zeta^2)v^2}{q 2B^3} \vec{B} \times \nabla B \quad (8.23)$$

It can be written in a more compact form based on the (adiabatic) invariants  $E$  and  $\mu$ , i.e. with  $v_{\parallel}(E, \mu)$ ,  $v_D$  is given by

$$\vec{v}_D = -v_{\parallel} \vec{e}_B \times \nabla \frac{v_{\parallel}}{\omega_c} \quad (8.24)$$

with the cyclotron frequency,  $\omega_c = qB/m$ , and the unit vector along the field line,  $\vec{e}_B = \vec{B}/B$ .

In the ripple of the stellarator magnetic field, i.e. a (local) minimum of the field strength, particles can be reflected by the “mirror term”  $\propto \vec{B} \cdot \nabla B$ . For sufficiently small drift velocity compared to  $v_{\parallel}$ , the quasi-periodic bounce motion (“banana” orbit) allows a further time averaging (in addition to the

gyroaveraging). For small collision frequencies compared with the bounce frequency of these trapped particles, the bounce-averaged equations of motion describe the drift of the *banana centre* (equivalent to the *guiding centre* in the drift kinetic equation). Here, the bounce-averaging is obtained by the time-averaging over a bounce period along the field line between the reflection points (defined by  $v_{\parallel} = 0$ ). Bounce-averaging of the guiding-centre drift velocity in the form of Eq. (8.24) yields

$$\langle \vec{v}_D \rangle_{ba} := \frac{1}{\tau_b} \oint \vec{v}_D \frac{ds}{v_{\parallel}} = -\frac{1}{\omega_c^0 \tau_b} \vec{e}_B \times \nabla \oint v_{\parallel} \frac{ds}{b} \equiv -\frac{1}{\omega_c^0 \tau_b} \vec{e}_B \times \nabla J \quad (8.25)$$

where  $J = \oint v_{\parallel} \cdot ds/b$  is the bounce invariant (also called the second adiabatic invariant or longitudinal invariant),  $\tau_b = \oint ds/v_{\parallel}$  is the bounce time,  $b = B/B_0$  is the magnetic field normalized to its mean value on the magnetic axis,  $\omega_c^0 = qB_0/m$ , and  $s$  the coordinate along the field line.  $J$  can be approximated for small  $\pm/N_p$  by integrating only in the toroidal direction (and is then referred to as  $J^*$ ) leading to a simple analytic expression for a classical stellarator configuration. This “ $J^*$  approach” is the basis for the traditional *lmfp* transport theory, the analytical neoclassical theory; see, for example, Refs [8.107–8.109].

For a cylindrical (magnetic) coordinate system in real space,  $r$ ,  $\theta$ ,  $\phi$ , where  $r$  is the (effective) flux surface radius,  $\theta$  the poloidal and  $\phi$  the toroidal angle, the bounce-averaging eliminates the toroidal angle and reduces the phase space to 4 dimensions: 2 velocity and 2 real space coordinates. With respect to  $r$ ,  $\theta$ , Eq. (8.25) defines the equations of motion of the “bounce-averaged orbits”, i.e. the *banana centres* of ripple-trapped particles, in Hamiltonian form:

$$\dot{r} = \frac{1}{\omega_c^0 \tau_b} \frac{1}{r} \frac{\partial J}{\partial \theta} \quad (8.26)$$

and

$$\dot{\theta} = -\frac{1}{\omega_c^0 \tau_b} \frac{1}{r} \frac{\partial J}{\partial r} \quad (8.27)$$

$J(r, \theta) = \text{constant}$  solves Eq. (8.27), i.e.  $J$  is actually an invariant of the bounce-averaged equations of motion.

In a complex stellarator configuration, quite different classes of trapped particles can exist. For a single class,  $J(r, \theta) = \text{constant}$  describes the motion of the banana orbits. In the case of collisionless trapping or detrapping, i.e. a transition between different classes,  $J$  jumps at the boundary. In this way bounce-averaging reduces the phase-space dimension, for example by eliminating the toroidal angle in the equations of motion, but introduces an *index* for the classification of the different types of ripple-trapped particles.

For the axisymmetric field in a tokamak, bounce-averaging eliminates the poloidal angle. Thus,  $J$  is independent of  $\theta$  and the tokamak bananas have no

average radial drift (they drift only toroidally). Consequently, bounce-averaging is not applicable for estimating the radial transport for axisymmetric (or helically symmetric, see below) configurations.

### 8.3.5. Neoclassical transport models

In stellarators, neoclassical transport becomes particularly important at high temperatures, i.e. in the long mean free path (*lmfp*) regime. The reason is that the radial  $\nabla B$  drift of ripple-trapped particles leads to a very unfavourable scaling of the radial heat flux with  $T^{9/2}$  if radial electric fields  $E_r$  are small [8.107–8.109]. In the *lmfp* the stellarator neoclassical transport coefficients at equivalent collisionalities are much higher than in the tokamak banana regime, where the radial neoclassical heat flux scales only with  $T^{1/2}$ . Radial electric fields limiting the radial displacement of ripple-trapped particles (in particular the ions) can significantly improve the stellarator neoclassical confinement. At higher collision frequencies, however, the neoclassical transport regimes, i.e. the plateau and the Pfirsch–Schlüter regime, are nearly equivalent in stellarators and tokamaks.

Improving neoclassical confinement in the *lmfp* regime is one of the major goals for stellarator optimization. The 3-D shaping of magnetic configurations in real space is equivalent to the structure of  $B = |\vec{B}|$  on the flux-surfaces which completely determines the particle orbits [8.110, 8.111] and, consequently, the neoclassical confinement properties. For example, a quasi-axisymmetric configuration has a very strong and complex 3-D topology in real space, but in magnetic coordinates the toroidal variations of  $B$  can be strongly reduced.

#### 8.3.5.1. Neoclassical modelling

The starting point for the neoclassical theory is the linearized drift (or bounce-averaged) kinetic equation where the source term is neglected. With the Maxwellian,  $f_M$ , used as the 0th order distribution function (note that for the collision term  $C(f_M) \equiv 0$ ), and assuming that the density  $n$ , the temperature  $T$  and the electrostatic potential  $\Phi$  are constant on the flux surfaces, the 1st order (stationary) drift kinetic equation with respect to the deviation from the Maxwellian,  $f_1$ , is obtained. In the neoclassical ordering, both terms with  $\partial f_1 / \partial r$  and  $\partial f_1 / \partial v$  are neglected with respect to the corresponding 0th order terms:

$$\begin{aligned} & \left( \vec{v}_{\parallel} + \vec{v}_{E \times B} + \vec{v}_{\nabla B} \right) \cdot \nabla_{\theta, \phi} f_1 + \zeta \frac{\partial f_1}{\partial \zeta} - C(f_1) = \\ & = - \left( \vec{v}_{\nabla B} \right)_r \left\{ \frac{n'}{n} + \frac{q\Phi'}{T} + \left( \frac{mv^2}{2T} - \frac{3}{2} \right) \frac{T'}{T} \right\} f_M \end{aligned} \quad (8.28)$$

with the pitch  $\zeta = v_{\parallel}/v$ . Here,  $\nabla_{\theta,\phi}$  is the gradient within the flux surface and  $(\vec{v}_{\nabla B})_r$  is the radial component of the drift velocity and  $\nu$  the pitch collision frequency. The  $\vec{v}_{\nabla B}$  and  $\vec{v}_{E \times B}$  are  $\nabla B$  and  $\vec{E} \times \vec{B}$  drift velocity, respectively. Furthermore, only the ‘‘mirror term’’,  $\propto \vec{B} \cdot \nabla B$ , is taken into account in  $\zeta$ , the poloidal component of  $\vec{v}_{\nabla B}$  is often neglected and the simplified Lorentz (pitch angle) collision term is used

$$C(f_1) = \frac{\nu}{2} \frac{\partial}{\partial \zeta} (1 - \zeta^2) \frac{\partial}{\partial \zeta} f_1 \quad (8.29)$$

This collision term does not conserve momentum, however, as ripple-trapped particles (with a symmetric distribution in  $\zeta = v_{\parallel}/v$ ) dominate the stellarator transport in the *lmfp* regime, momentum conservation is negligible for the radial transport in stellarators. In addition, for the parallel flows, the ripple-trapped particles represent a significant momentum sink due to friction with the passing particles. Consequently, an *intrinsic ambipolarity* ensured by particle collisions does not exist in stellarators in contrast to ideal axisymmetric tokamak configurations.

An additional approximation in Eq. (8.28) is needed in order to keep the conservative properties of the linearized drift-kinetic equation in 3-D phase space:  $\vec{v}_{E \times B} \approx \vec{B} \times \nabla \Phi / \langle B^2 \rangle$  (with the flux-surface average  $\langle \dots \rangle$ ), i.e. the incompressible form of the  $\vec{E} \times \vec{B}$  flow. The compressible formulation leads to an additional term  $\sim (\vec{B} \times \nabla B) \cdot \nabla \Phi$  in both acceleration terms with  $\dot{\zeta}$  and  $\dot{v}$  which become important for large radial electric fields leading to density variations on the flux surface, a Pfirsch–Schlüter-like parallel flow and a pressure anisotropy. In the incompressible form,  $r$  and  $v$  are only parameters in Eq. (8.28), which is now a local (on a flux surface) and monoenergetic drift kinetic equation.

The radial gradients of density, temperature and potential in Eq. (8.28) appear as (thermodynamic) forces driving the deviation from the Maxwellian,  $f_1$ . By solving this equation, the monoenergetic neoclassical particle and energy flux densities  $\Gamma^{me}$  and  $Q^{me}$  are obtained by flux-surface averaging:

$$\begin{Bmatrix} \Gamma^{me} \\ Q^{me} \end{Bmatrix} = \frac{1}{4\pi^2} \int_0^{2\pi} \int_0^{2\pi} \int_{-1}^1 \begin{Bmatrix} 1 \\ \frac{m}{2} v^2 \end{Bmatrix} (\vec{v}_{\nabla B})_r f_1 d\zeta d\theta d\phi \quad (8.30)$$

By convolution, the thermal transport matrix is defined. With  $f_1$  being proportional to  $(\vec{v}_{\nabla B})_r \sim v^2$ , the neoclassical transport in the stellarator *lmfp* regime has a strong and unfavourable temperature dependence compared to a tokamak.

## 8.3.5.2. Classical and advanced stellarator configurations

In the simplest approximation, a classical stellarator can be described by the superposition of a toroidal and a helical magnetic field, with magnitude

$$B/B_0 = 1 - \varepsilon \cos \theta - \varepsilon_h \cos(m\theta - N_p \phi) \quad (8.31)$$

where  $\varepsilon, \varepsilon_h$  is the poloidal or helical modulation of  $B$  respectively ( $\varepsilon$  need not be equal to  $\varepsilon_t = r/R$ , the inverse aspect ratio) and  $m, N_p$  is the helical field multipolarity or period number respectively. In the *lmfp* regime particles localized in the helical ripple may experience significant radial drifts and are generally expected to provide the dominant contribution to the overall neoclassical transport. Within the traditional analytic theory (for example, see Ref. [8.112]), the form this contribution takes is determined by the relative magnitudes of the effective collision frequency,  $\nu_{eff} = \nu / 2\varepsilon_h$ , and the  $\vec{E} \times \vec{B}$  precessional frequency,  $\Omega_E = E_r / rB_0$  with  $E_r = -\Phi'$ . For the simple model field of a classical stellarator, the results may be summarized by the “monoenergetic” diffusion coefficients in the  $1/\nu$ ,  $\sqrt{\nu}$  and  $\nu$  collisionality regimes

$$D_{1/\nu} = \frac{4}{9\pi} \left( v_d \frac{\varepsilon}{\varepsilon_t} \right)^2 \frac{(2\varepsilon_h)^{3/2}}{\nu} \quad (8.32)$$

$$D_{\sqrt{\nu}} = \frac{4\sqrt{2}}{9\pi} \left( v_d \frac{\varepsilon}{\varepsilon_t} \right)^2 \frac{\nu^{1/2}}{|\Omega_E|^{3/2}} \quad (8.33)$$

$$D_\nu = \left( \frac{v_d}{\Omega_E} \frac{\varepsilon}{\varepsilon_t} \right)^2 \frac{\nu}{2F_{bl}} \quad (8.34)$$

for weak radial electric fields, with the effective collision frequency  $\nu_{eff} \gg \Omega_E$ , for the  $\vec{E} \times \vec{B}$  precessional frequency about the effective collision frequency  $\nu_{eff} \approx \Omega_E$  and for strong  $E_r$  such that  $\nu_{eff} \ll \Omega_E$ , respectively. In the  $\nu$  regime,  $F_{bl}$  results as  $F_{bl} = \sqrt{\varepsilon + 2\varepsilon_h} - \sqrt{2\varepsilon_h}$ . In these expressions,  $v_d = mv^2 / 2qB_0R$  is the averaged radial component of the  $\nabla B$  drift. It is decreased by the factor  $\varepsilon / \varepsilon_t$ , which corresponds to the reduction of the averaged toroidal curvature in an advanced stellarator.

The neoclassical transport scaling of the  $1/\nu$  regime where the radial electric field is small is crucial for stellarator confinement. Due to the poloidal variation of  $B$  on a flux surface, trapped particles can drift radially. In classical stellarators, this poloidal variation of  $B$  is a result of the torus effect and is roughly given by  $r/R$ , the ratio of the minor to the major radius. The averaged radial component of the  $\nabla B$  drift is decreased by the factor  $\varepsilon / \varepsilon_t$  corresponding to the reduction of the averaged toroidal curvature in an advanced stellarator. The related diffusion coefficient of Eq. (8.32), for example, can be easily obtained

from a simple diffusion step-size argument:  $D \approx f_d v_d^2 \tau_d$  with  $f_d$  the number of particles being involved in the diffusion process,  $v_d$  their velocity and  $\tau_d$  the related time step. For the classical stellarator  $1/\nu$  regime,  $f_d \equiv \sqrt{\varepsilon_h}$  is the fraction of trapped particles,  $v_d = (\vec{v}_{\nabla B})_r$  and  $\tau_d = 1/\nu_{eff} = \varepsilon_h/\nu$  is the detrapping time. This approach yields directly the dependence of Eq. (8.32).

For classical stellarator configurations, which can be reasonably well represented by the simple model field, the predictions of the bounce-averaged analytic theory in Eqs (8.32) to (8.34) have been compared with numerical solutions of the monoenergetic drift kinetic Eq. (8.28) by Monte Carlo techniques (for example, Ref. [8.112]) or by Fourier–Legendre decomposition (e.g. the DKES code [8.113]); good agreement was found.

For a more complex magnetic field geometry, however, the analytic approach cannot be used. The magnetic field strength on flux surfaces is represented by the  $(m, n)$  Fourier modes with respect to the poloidal ( $\theta$ ) and toroidal angle ( $\phi$ ) in magnetic (Boozer) coordinates as given in Eq. (8.1). The coefficients of the classical stellarators (see Eq. (8.31)) are given by  $\varepsilon \equiv -b_{10}$  (torus effect) and  $\varepsilon_h \equiv -b_{m1}$  (helical effect).

Numerical computations of the monoenergetic transport coefficient in the *lmfp* regime for quite different stellarator configurations (even in the case of a fairly broad  $b_{mn}$  Fourier spectrum) showed that the  $1/\nu$ ,  $\sqrt{\nu}$  and  $\nu$  collisionality regimes (Eqs (8.32) to (8.34)) are always clearly present. Furthermore, the different dependences on the radial electric field for each regime could also be identified corresponding to the traditional analytic theory. The figure of merit for the radial transport in complex stellarator configurations is the *effective helical ripple*,  $\varepsilon_{eff}$ . For the transport in the  $1/\nu$  regime with  $E_r = 0$  according to Eq. (8.32),  $\varepsilon_{eff}$  is defined by the same radial transport coefficient as in an equivalent classical configuration with a single helical component  $\varepsilon_h$ . In general,  $\varepsilon_{eff}$  depends on the full  $b_{mn}$  Fourier spectrum, but cannot be given in an analytic form. In stellarator optimization,  $\varepsilon_{eff}$  is minimized within the constraints of the other physical goals. With minimization of the  $D_{1/\nu}$  coefficient, also the other coefficients for  $E_r \neq 0$  are reduced.

### 8.3.5.3. Radial electric field

The impact of the radial electric field on the radial transport coefficients scales with  $E_r/\nu B$ , i.e. the ion coefficients (with much smaller  $\nu$ ) are much more strongly affected than the electron ones. The radial electric field is determined from the solutions (*roots*) of the ambipolarity condition of the thermal fluxes (with energy convolution),  $\Gamma_e \equiv Z_i \Gamma_i$ , where impurity fluxes are disregarded. The transport coefficients depend only on the absolute value of  $E_r$ , and with  $E_r$  part of the thermodynamic force, only an odd number of roots can exist. For

the case of  $\Gamma_e(E_r = 0) \ll Z_i \Gamma_i(E_r = 0)$ , the ambipolar  $E_r$  can be estimated from the approximation  $\Gamma_i(E_r) = 0$  (*ion-root*), and the ambipolar particle flux is given by  $\Gamma_e(E_r)$ . If  $\Gamma_e$  exceeds significantly the ion-plateau flux, a strongly positive  $E_r$ , the *electron-root*, reduces the electron fluxes to the ion level whereas at higher collision frequencies, the *ion-root* with strongly negative  $E_r$  appears. The feature of multiple roots appears only in the very *lmfp* regime. If multiple roots can exist, only the odd roots are stable (the others are unstable), and a thermodynamic principle (the energy dissipation of the poloidal plasma rotation must be minimized) determines which root is realized [8.114].

#### 8.3.5.4. Bootstrap current

The solution of Eq. (8.28) has also an asymmetric part with respect to  $\zeta$  which determines the bootstrap current (in Eq. (8.30),  $(v_{\nabla B})_r$  is replaced by  $v_{\parallel}$ ). The transport coefficients in a helically-symmetric configuration are equivalent to the tokamak ones, but the bootstrap coefficient is negative, reducing the rotational transform, in contrast to tokamaks, where the bootstrap current increases the poloidal field component and thus supports the toroidal current. This feature allows for a minimization of the bootstrap current in stellarator configurations with a large helical Fourier mode in the  $b_{mn}$  spectrum of Eq. (8.1). Bootstrap current minimization was one of the optimization criteria of the W7-X stellarator. It makes it possible to maintain a low-order rational  $\iota$  at the separatrix weakly dependent on the pressure such that the associated islands can be used for an island divertor concept. On the other hand, a quasi-axisymmetric configuration like NCSX has a tokamak-like bootstrap current nearly independent of  $E_r$  (i.e. increasing the rotational transform, but unfavourable for an island divertor). For *ion-root* scenarios the ion contribution to the bootstrap current is significantly decreased whereas the electron contribution is increased, leading to a fairly weak dependence of the total bootstrap current density on  $E_r$ .

#### 8.3.5.5. Parallel resistivity

In the following the parallel transport coefficients related to a parallel thermodynamic force are briefly discussed. In principle, a parallel electric field (loop voltage) is less important for stellarators than for tokamaks, but this parallel thermodynamic force can be replaced by any other parallel source such as tangential NBI or electron cyclotron current drive (in the formalism of the adjoint approach). Then, the drift kinetic equation equivalent to Eq. (8.28) for the first order distribution function  $g_1$  is given by

$$\left( \vec{v}_{\parallel} + \vec{v}_{E \times B} + \vec{v}_{\nabla B} \right) \cdot \nabla_{\theta, \phi} g_1 + \zeta \frac{\partial g_1}{\partial \zeta} - C(g_1) = -v \zeta B \frac{q}{T} \frac{\langle \vec{E} \cdot \vec{B} \rangle}{\langle B^2 \rangle} f_M \quad (8.35)$$

and the monoenergetic inductive current is defined by replacing in Eq. (8.30)  $(v_{\nabla B})_r f_1$  by  $v_{\parallel} g_1$ . Equation (8.35) has also a symmetric solution with respect to  $\zeta$  leading to the Ware pinch term ( $g_1$  replaces  $f_1$ ). Both the bootstrap current and the Ware pinch coefficient are non-diagonal terms in the neoclassical transport matrix (without a direct drive) and, in accordance to Onsager symmetry, both coefficients have the same absolute value, but different signs.

Since trapped particles (also the tokamak bananas) do not contribute to the inductive current, Eq. (8.35) can be solved analytically in the collisionless limit by neglecting the  $v_{E \times B}$  and  $v_{\nabla B}$  terms. Then, the parallel electric conductivity is simply reduced by the *passing particle fraction*,  $F_{pp}$ , compared to the collisional limit

$$F_{pp} = \frac{3}{4} \langle b_{\max}^2 \rangle \int_0^1 \frac{\mu d\mu}{\sqrt{1 - \mu b_{\max}}} \quad (8.36)$$

where the integration variable  $\mu$  corresponds to the normalized magnetic moment and  $b_{\max} = B/B_{\max}$  with  $B_{\max}$  being the maximum of  $B$  on the flux surface. In this formulation, the parallel electric conductivity in both stellarators and tokamaks is equivalent. The main difference with respect to finite collision frequencies is related to the quite different bounce time,  $\tau_b$ , of the ripple-trapped particles in stellarators and the tokamak bananas.

The impact of momentum conservation on the parallel and radial fluxes is quite different. Momentum conservation is important for the parallel electric conductivity: it is a 100% effect equivalent to the collisional limit, i.e. the classical Spitzer problem [8.115]. In the stellarator *lmfp* regime, the symmetric component (with respect to  $v_{\parallel}$ ) of the ripple-trapped particle distribution function dominates the radial transport, and momentum conservation in estimating the radial fluxes becomes negligible. For the bootstrap current, there is a fairly strong impact on the parallel ion flow (due to the parallel momentum balance), but the electron flow is coupled to the ion flow by friction. Consequently, the bootstrap current is less affected by momentum conservation than the inductive current. Both for the bootstrap current and the inductive current, parallel momentum correction techniques have been developed [8.116, 8.117] which are based only on the monoenergetic transport coefficients.

### 8.3.5.6. Optimization of neoclassical transport

For classical stellarator configurations, the neoclassical *lmfp* confinement is very poor and can be improved only by a significantly increased magnetic field strength or by configurations at a very large aspect ratio (reduced average toroidal curvature). However, the fully 3-D stellarator configuration space has sufficient freedom to allow for a fairly general realization of physical goals

[8.118], at least with a modular coil system. A reduced toroidal curvature is also obtained in optimized configurations with high average elongation, resulting in a reduction of the Pfirsch–Schlüter currents and, consequently, a small Shafranov shift. In this sense, such magnetic configurations become stiff against the plasma pressure. A high elongation contributes significantly to the reduction of the *effective helical ripple*,  $\varepsilon_{\text{eff}}$ .

A first approach to *drift-optimization*, the analytical so called “ $\sigma$ -optimization” [8.119] eliminates the variation of  $B_{\text{min}}$  in the (helical) direction of this minimum thus cancelling the radial drift of the deeply ripple-trapped particles (see Eq. (8.25)). This scenario can be realized in inward-shifted LHD configurations ( $R_0 = 3.60$  m), but is counteracted there by the Shafranov shift. In general, the reduction of the  $B_{\text{min}}$  in the helical or poloidal direction of the minima is an essential part of drift-optimization at least of the deeply trapped particles. This concept is realized for example in the drift-optimized W7-X configurations.

In contrast to drift-optimization, the confinement optimization in *quasi-symmetric configurations* is based on the minimization of the fraction of localized particles and a drift-optimization is not essential.

The concepts of optimizing the neoclassical confinement have quite different constraints for the bootstrap current. Both quasi-axisymmetric and quasi-helically symmetric configurations have bootstrap currents very close to the ideal symmetric ones. For the quasi-axisymmetric configurations, the

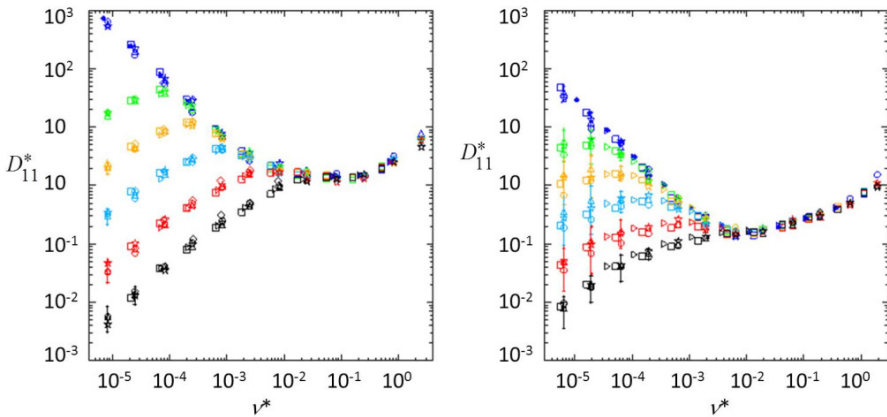


FIG. 8.27. Monoenergetic radial transport coefficients  $D_{11}^*$ , i.e. diagonal elements of the transport matrix (normalized to the plateau value of an equivalent tokamak with circular cross-section) versus the normalized collisionality  $\nu^* = \nu \cdot R / (\pm v)$ . Left: The (classical) LHD configuration with  $R = 3.75$  m. Right: The drift-optimized W7-X (standard) configuration; both at half the plasma radius. Colours indicate different normalized radial electric fields,  $E_r/\nu B$ , increasing from blue to black. The different symbols correspond to different codes indicating the benchmarking of these versus each other. For more details see the topical review [8.120].

bootstrap current is positive (tokamak-like) and supports the rotational transform whereas in the quasi-helically symmetric case the bootstrap current counteracts the rotational transform generated by the external coils (an unfavourable scenario as it requires stronger external poloidal field components). For these quasi-symmetries, the confinement optimization restricts the degree of freedom for minimizing the bootstrap current. Bootstrap current minimization, as for example needed for an island divertor concept (with both the edge  $\pm$  and shear controlled), can be achieved both for quasi-poloidal symmetry (the neoclassical transport vanishes for ideal poloidal symmetry) and for a drift-optimized configuration. A high degree of drift-optimization (see Fig. 8.27) together with minimization of the bootstrap current (see Fig. 8.28) in a fairly stiff magnetic configuration (with respect to the plasma pressure) is the essential goal of the W7-X design.

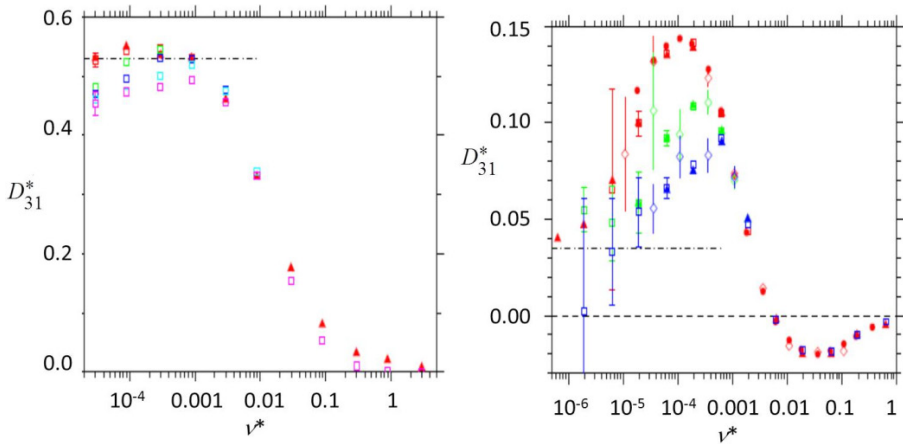


FIG. 8.28. Monoenergetic bootstrap current coefficients  $D_{31}^*$ , i.e. non-diagonal elements of the transport matrix (normalized to the collisionless limit of an equivalent tokamak with circular cross-section) versus the normalized collisionality  $\nu^* = \nu \cdot R / (\pm v)$ . For the quasi-axisymmetric NCSX configuration (left) and the drift-optimized W7-X (standard) configuration (right), both at half the plasma radius. Colours refer to different normalized radial electric fields,  $E_r / \nu B$  and symbols indicate different codes; see Fig. 8.27. The collisionless limit is given for reference (dot-dashed line at the left side of each figure) and the equivalent axisymmetric  $D_{31}^*$  by the dotted line (right figure only).

### 8.3.6. 3-D features of transport and confinement

Cross-field transport of energy, particles and impurities can be derived by power and particle balance analysis under stationary conditions using the measured profiles of  $T_e$ ,  $T_i$  and  $n_e$  and the respective sources and sinks. Alternatively, transport coefficients are deduced from the profile response to perturbations such as changes or modulation of heating power or the gas input. An

example is shown in Fig. 8.29(d–f), which shows experimental profiles (a–c) and particle and energy fluxes (d–f) derived from them compared with expectations from neoclassical theory (c–f).

### 8.3.6.1. Role of neoclassical transport

If the core temperatures are sufficiently high, the neoclassical transport in the  $lmfp$  regime prevails owing to its strong and unfavourable temperature scaling. For the discharge shown in Fig. 8.29 one finds agreement between experimentally derived fluxes and neoclassically expected ones up to a radius  $r/a = 2/3$ . This is, however, not a virtue because, scaled to reactor conditions, neoclassical transport is in the  $1/\nu$  regime preventing the classical stellarator plasma to ignite, necessitating therefore rigorous optimization (see Section 8.5). At the plasma edge, where the collisionality is high and the gradients steep, the experimentally obtained particle and energy diffusivities exceed those calculated from neoclassical theory by more than an order of magnitude. In this region, transport is anomalous — mostly dominated by the observed turbulence.

In the neoclassical plasma core of stellarators the electron-root or the ion-root develops under conditions as predicted by theory. Electron-root conditions result if the electron flux  $\Gamma_e$  exceeds the ion flux such that ambipolarity is ensured by strongly positive  $E_r$ , reducing the electron flux down to the level of  $\Gamma_e \cong Z_i \Gamma_i$ . These conditions are generally reached in the plasma core when  $T_e \gg T_i$ , viz. in ECRH discharges at high power per particle,  $P_{ECRH}/n_e$ . Highly peaked  $T_e$  profiles develop in the central electron-root region whereas the ions show fairly flat  $T_i$  profiles.  $E_r$  measured in the plasma centre can become strongly positive with values up to several hundred  $\text{V}\cdot\text{cm}^{-1}$  in agreement with neoclassical calculations. For an inter-machine survey see Ref. [8.121].

For  $T_e \approx T_i$  as obtained at higher densities, ambipolarity is sustained by ion-root conditions reducing the large diffusivities of the ion  $1/\nu$  regime down to the level of the neoclassical electron fluxes. In the plasma interior where  $\nabla T_i$  is small this is achieved by moderate values of  $E_r$ . Towards the plasma edge with larger  $\nabla T_i$  values, ion-root conditions with moderate to strongly negative  $E_r$  are established to reduce the large ion fluxes. At the edge, ion-root conditions are normally realized even if in the centre electron-root conditions prevail, resulting in a strongly sheared  $E_r$  at the interlayer. It may additionally reduce possible anomalous fluxes by shear flow decorrelation of turbulent eddies too and thus may support the strong  $T_e$ -gradients of the core electron-root confinement [8.122].

If  $P_{ECRH}/n_e$  is ramped down, a sudden transition from the electron- to the ion-root occurs in the core showing a threshold behaviour and a hysteresis. This is expected from neoclassical transport theory as a corollary of a thermodynamically forbidden zone between the electron- and ion-root branch. Limit cycle oscillations have also been observed. For a summary see Ref. [8.123].

In the scrape-off layer  $E_r$  is positive due to the rapid electron parallel transport along open field lines. Strong  $\nabla E_r$  evolves at the plasma edge (see Fig. 8.29(c)) with the potential to serve as a seed for an edge transport barrier improving confinement.

The measured  $E_r(r)$  are in general consistent with the solutions of the ambipolarity condition for the neoclassical particle fluxes (see Fig. 8.29(d), dotted line). This implies that the anomalous particle fluxes, which exceed the neoclassical ones by about an order of magnitude in the gradient region, are to a high degree of electrostatic nature and intrinsically ambipolar.

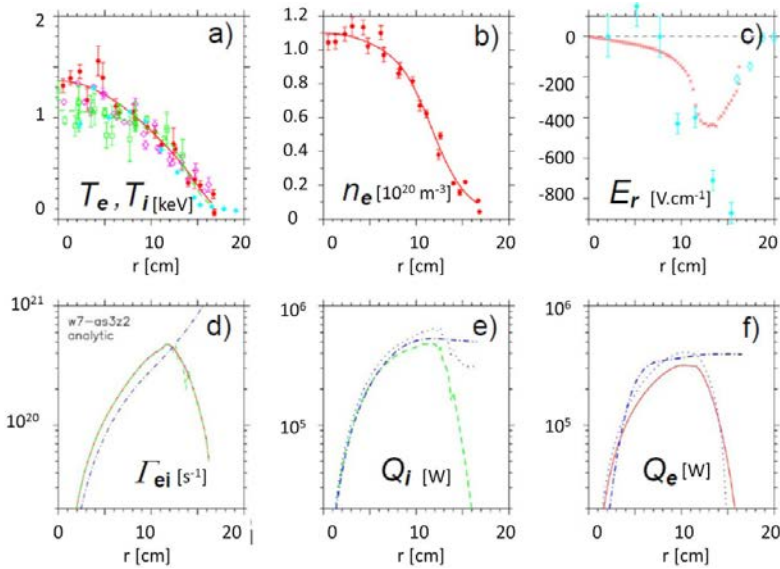


FIG. 8.29. Top: Profiles for a W7-AS discharge (#34609,  $P_{\text{NBI}} = 1.35 \text{ MW}$ ,  $P_{\text{ECRH}} = 0.35 \text{ MW}$ ,  $n_e(0) = 1.1 \times 10^{20} \text{ m}^{-3}$ ) with good confinement properties and ion-root conditions  $T_i \approx T_e$  for all radii: (a)  $T_e$  from Thomson scattering (red full circles),  $T_e$  from ECE (magenta open diamonds),  $T_i$  from CXRS (full blue diamonds),  $T_i$  from NPA (open green squares),  $T_e$  fit (red line),  $T_i$  fit (broken green line). (b)  $n_e$  from Thomson scattering (red full circles),  $n_e$  fit (red line). (c)  $E_r$  from neoclassical calculations (red crosses),  $E_r$  from CXRS (full blue diamonds),  $E_r$  from passive rotation measurements (boron spectroscopy) (open blue diamonds). Bottom line: Particle and power balance analysis respectively: (d) Experimental particle fluxes (blue dot dashed line), electron particle flux from neoclassical calculations (red dashed line), ion particle flux from neoclassical calculations (green dashed line – almost coincides with red dashed line). (e) Ion heat flux from neoclassical calculations (green dashed line), experimentally determined ion heat flux (blue dot dashed line), ion heat flux from neoclassical calculation with correction of  $\gamma E_r$ . (f) Electron heat flux from neoclassical calculations (red), experimentally determined electron heat flux (blue dot dashed line), electron heat flux from neoclassical calculation with correction of  $\gamma E_r$ . The neoclassical transport coefficients decrease in the outer radial region due to their temperature dependence. In this region, the experimentally found transport is anomalously high [8.33]. Reprinted from Ref. [8.33]. Copyright (2011), IOP Publishing Ltd.

In the core of a stellarator reactor with  $T_e \sim T_i$ , ion-root conditions with only moderate  $E_r$ , are expected. The reduction of neoclassical transport in the *lmfp* relies on the conditions leading to the  $\sqrt{\nu}$  regime (which requires finite  $E_r$ , see Section 8.3.5) but critically needs a further reduction of neoclassical fluxes by stellarator optimization targeting for a low effective ripple  $\varepsilon_{eff}$  (see Section 8.3.5). Alternatively, operation at extremely high densities as suggested by LHD may allow avoiding the *lmfp* regime at all.

### 8.3.6.2. Characterization of turbulent transport

The outer plasma zone, whose properties largely determine the energy confinement time, is generally governed by electrostatic turbulence driven by the constituents of the pressure gradient. Turbulence shows to a large extent the same features as known from tokamaks [8.124] (see Chapter 2). In the scrape-off layer the signatures of fluctuations are in agreement with drift-interchange turbulence with amplitudes and phases able to explain at least a significant part of the anomalous transport. Inside the last closed flux surface the fluctuations of  $n_e$  and also  $T_e$  (whenever measured) strongly correlate with magnetic configuration and plasma scenario. Obvious examples are the LH-transition and the  $\tau$ -dependence of turbulence and confinement in low shear devices. Modelling of turbulence in 3-D geometry is, due to its complexity, still a matter of ongoing research. The optimization of neoclassical transport is expected to affect the interplay between equilibrium flow, turbulence and turbulence induced flows [8.125, 8.126].

The confinement time observed in helical systems is comparable to that of tokamaks reproducing with power degradation its main feature. Also bifurcations emerging from anomalous transport appear. W7-AS was the first “non-tokamak” to operate in the H-mode [8.127], reproducing basically all characteristic features of this confinement regime.

Figure 8.30 compares experimental  $\tau_E$  (global energy confinement time) values from W7-AS with those expected from different stellarator and tokamak scalings: the International Stellarator Scaling (ISS 95 [8.128]), the W7-AS scaling (AS [8.129]), the Lackner–Gottardi scaling (L-G [8.130]) and the tokamak ELMy H-mode scaling (IPB98(y,2) [8.131]). The data of Fig. 8.30 are taken from discharges at operational limits: highest electron and ion temperatures, density, beta, confinement time, at detachment and for the best steady-state discharge. To allow comparison with tokamak confinement,  $\iota$ ,  $B$  and the geometry are rephrased into an effective plasma current. Despite the obvious differences in magnetic features, there is an obvious similarity in tokamak and stellarator confinement because the experimental data are nearly equally well described by either tokamak or stellarator scalings. This is only correct, however, for a global parameter like  $\tau_E$  considered as scaling parameter over several orders

of magnitude. In the following, circumstances are described where the magnetic topology affects features which themselves determine the confinement.

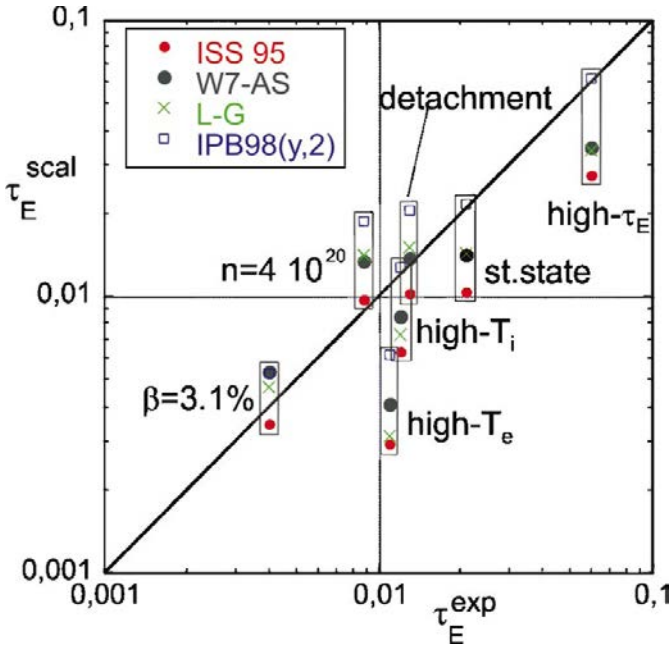


FIG. 8.30. The  $\tau_E$  values from different scaling relations against experimental values at operational boundaries in W7-AS (high  $\beta$ ,  $n_e$ ,  $T_e$ ,  $T_i$ ,  $\tau_E$ , under detached conditions, and for a quasi-steady-state discharge). The W7-AS data are with hydrogen; the tokamak H-mode scaling (blue squares) is applied assuming deuterium as plasma species [8.132]. Reprinted from Ref. [8.132]. Copyright (2011), American Institute of Physics.

Highest global energy confinement times in stellarators/heliotrons are comparable to tokamak H-mode confinement up to devices as large as LHD. This is shown in Fig. 8.31, summarizing the experimental energy confinement time from major 3-D devices. These data are plotted against the scaling ISS04  $\tau_E^{\text{ISS04}}$  derived with a non-linear regression to confinement data from stellarators and torsatrons/heliotrons [8.133]:

$$\tau_E^{\text{ISS04}} = f \times 0.134 a^{2.28} R^{0.64} P^{-0.61} \bar{n}_e^{0.54} B^{0.84} \tau_{2/3}^{0.41} \quad (8.37)$$

where  $f$  is a configuration factor discussed below. ISS04 is close to ion plateau (Lackner–Gottardi) scaling. The confinement time degrades with the heating power  $P$ . The power dependence is the same for electron cyclotron resonance or neutral beam heating. The confinement time increases with density  $\bar{n}_e$  but is experimentally found to saturate (differently from Eq. (8.37)) at highest densities. The confinement time increases with the magnetic field  $B$  and the rotational transform  $\iota$  (apart from a subtle dependence as described below).

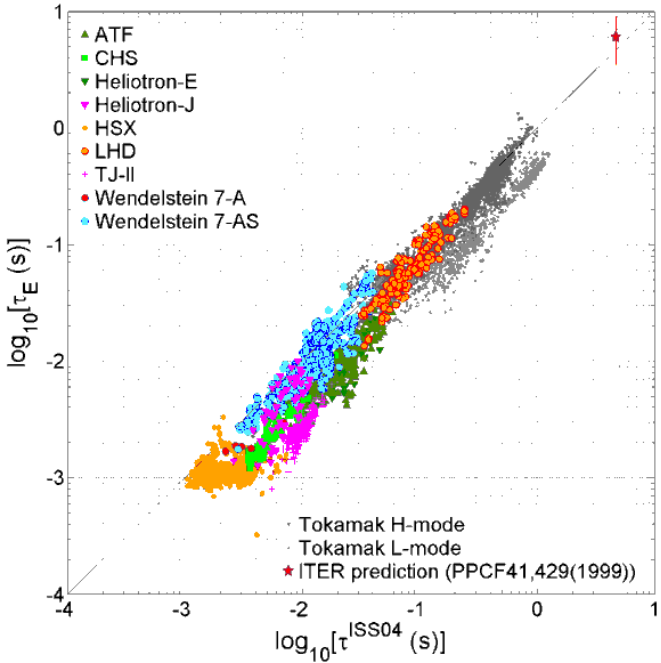


FIG. 8.31. Energy confinement data of stellarators/heliотrons versus ISS04 confinement time scaling. To allow comparison with tokamak confinement, the plasma current is rephrased by  $\iota$ ,  $B$  and the geometry. The expected confinement time for ITER is also shown in the upper right corner. (Data from International Stellarator/Heliотron Confinement Database [www.ipp.mpg.de/ISS](http://www.ipp.mpg.de/ISS) and [ishcdb.nifs.ac.jp](http://ishcdb.nifs.ac.jp)).

Stellarator and torsatron/heliотron confinement seem to differ somewhat, pointing to a subtle role of the details of the magnetic configuration (magnetic shear and ripple, geometry). In  $\tau_E^{ISS04}$  this dependence is reflected by a configuration factor  $f$  summarizing configuration and device specific effects; the largest  $f$  being 1, representing best confinement. In tokamaks, similar dependences on elongation and triangularity exist. For 3-D geometry, however, the configuration dependency is more involved and a full first-principle description of  $f$  has not been attained. The configuration factor varies from  $f = 0.25$  to 1. Largest values are attained for W7-AS at low rotational transform ( $f = 1$ ) and inward shifted LHD plasmas ( $f = 0.93$ ).

Furthermore, there is experimental evidence that magnetic field optimization from the neoclassical transport point of view — roughly the orbit deviation from the flux surface — has also a beneficial effect on the level of turbulent transport [8.31]. Inward shifted LHD plasmas with lower magnetic ripple as necessary to reduce neoclassical losses are characterized by a confinement time which clearly exceeds the expectations from scaling even if the confinement is largely determined by anomalous fluxes [8.134].

Rephrasing the ISS04 scaling into a dimensionless scaling gives

$$\frac{\tau_E^{ISS04}}{\tau_{Bohm}} \propto \rho^{*-0.79} \beta^{-0.19} \nu^{*0.00} \quad (8.38)$$

where  $\tau_{Bohm}$  is the Bohm time,  $\rho^*$  the minor-radius normalized ion gyroradius,  $\beta$  the plasma beta and  $\nu^*$  the collisionality. This scaling is close to gyroBohm scaling ( $\rho^{*-1}$ ). The dimensionless expression of ISS04 (International Stellarator Scaling 2004) is also very close to the tokamak scaling IPB98(y,2) (ITER Physics Basic Scaling) expressed in dimensionless parameters but exhibits a more favourable  $\beta$  dependence ( $\tau_E^{IPB98(y,2)} \propto \beta^{-0.90}$ ).

First-principle heat transport simulations incorporating all transport mechanisms in helical devices have been initiated recently (see Ref. [8.135]). Nevertheless, data sets of global confinement can be statistically tested to obey scaling constraints complying with fundamental scaling invariances [8.136] or dimensional correctness [8.137, 8.138]. Specific constraints for scaling laws follow from transformation invariances of the kinetic equation occasionally supplemented by the laws of electromagnetism. Employing methods from Bayesian probability theory, the tests of invariance allow calculating the probability of one distinct scaling model among others if the errors in all variables were provided [8.139].

These studies reveal that the heat transport in stellarator plasmas is fundamentally different in different regimes of the dimensionless parameters. For low  $\beta$  discharges in W7-AS, this approach showed the confinement data to comply with a “collisional, low  $\beta$ ” model [8.140], i.e. the confinement is governed by high-collisionality transport. Since low beta models do not include electromagnetic effects, the global energy confinement time reflects the underlying transport to be electrostatic being supported by 1-D transport analyses. For high  $\beta$  confinement in W7-AS, however, electromagnetic effects have to be incorporated [8.141]. An extension to intermachine comparison with LHD data showed that the experimental findings are best described by transport models without collisions [8.142]. These findings are fundamental for the comparison of sophisticated transport models and indicate the validity of the empirical scaling laws to be restricted to the collisionality and beta regime of present day helical devices [8.143].

### 8.3.6.3. Particle transport

Density profiles of stellarators are expected to be flat in cases without central particle source, because there is no Ware pinch (no external momentum input). This is in agreement with observation. The density gradients reside at the plasma edge in the range of the recycling source. With strong central ECRF heating and peaked  $T_e$  profiles, the flat density profile becomes even slightly

hollow. With core fuelling (NBI or pellets [8.144]), density profiles peak in the core. With off-axis ECRF heating resulting in flat central temperature profiles the core density profile is observed to peak even without a central source (see Fig. 8.32).

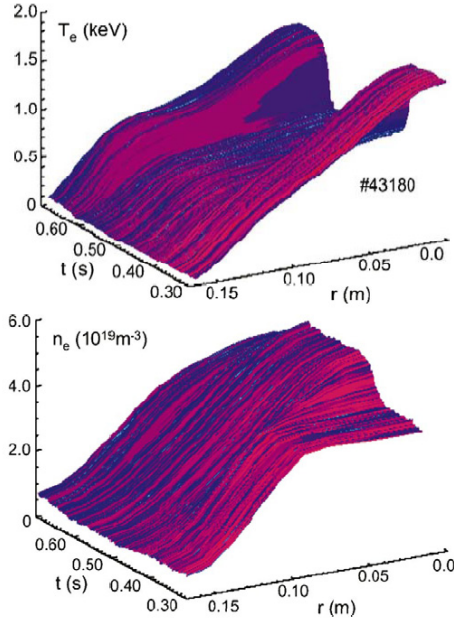


FIG. 8.32. Top:  $T_e$  profiles of an ECRH heated discharge in W7-AS with on- and off-axis heating phases. Off-axis heating occurs from 0.45 to 0.65 s; the power deposition occurs at  $r = 0.12$  m. Bottom: Density profile during ECRH in the on-axis/off-axis scenario [8.132]. Reprinted from Ref. [8.132]. Copyright (2011), American Institute of Physics.

These observations elucidate the mechanisms which govern particle transport: particle diffusion, thermal diffusion and a convective particle inward term play a role. Thermal diffusion causes flat or even hollow density profiles at peaked  $T_e$  profiles. The experimental analysis shows that the thermally driven ( $\Gamma \approx -\nabla T_e$ ) neoclassical flux component, which is outward directed in stellarators, can explain the hollow  $n_e$  profiles with strong central ECRF heating. The convective inward term, caused by an  $E_r/T_e$  term in the neoclassical transport equation or resulting from the background turbulence, causes the density profile to peak when the central  $T_e$  gradient is flat (e.g. in the case of off-axis heating); in this case, thermal diffusion does not enter. Figure 8.32 shows a case where the heating power location has been switched during the discharge — at constant power — from central to mid-radius and back to central heating. The  $T_e$  profile follows the power deposition and the density profile shape changes opposite to that of  $T_e$ .

In the following, we summarize major confinement characteristics, which indicate distinct differences between tokamaks and helical systems.

### 8.3.6.4. Electron temperature evolution

A distinct difference to the electron transport as observed in tokamaks [8.145] seems to be the orthodox response of the stellarator  $T_e$  profile to changes of the heating power and the power deposition [8.146]. On W7-AS, off-axis heating with ECRH leads to flat (or hollow)  $T_e$  profiles inside the deposition radius (see as an example Figs 8.32 and 8.34(b)). The concept of profile resilience does not seem to apply to helical systems.

Figure 8.33(a) shows  $T_e$  profiles in log-representation for ECRH core heated electron transport dominated discharges with heating powers varying in a large power range from 0.25 to 2 MW at  $\bar{n}_e = 4.8 \times 10^{19} \text{m}^{-3}$ . Figure 8.33(b) shows the  $T_e$  gradient (mid-radius) and the parameter  $R/L_{Te}$ , the major radius divided by the profile fall-off length,  $T_e/\nabla T_e$ , for two densities  $2.4$  and  $4.8 \times 10^{19} \text{m}^{-3}$ . The  $T_e$  gradient increases with heating power (note the negative values);  $R/L_{Te}$  is larger than in tokamaks (note the aspect ratio of W7-AS being 11) and falls with increasing power because of a strong  $T_e$  rise in the plasma periphery. For the 2 MW case, the power flux through the mid-radius flux surface is about  $0.25 \text{ MW} \cdot \text{m}^{-2}$ .

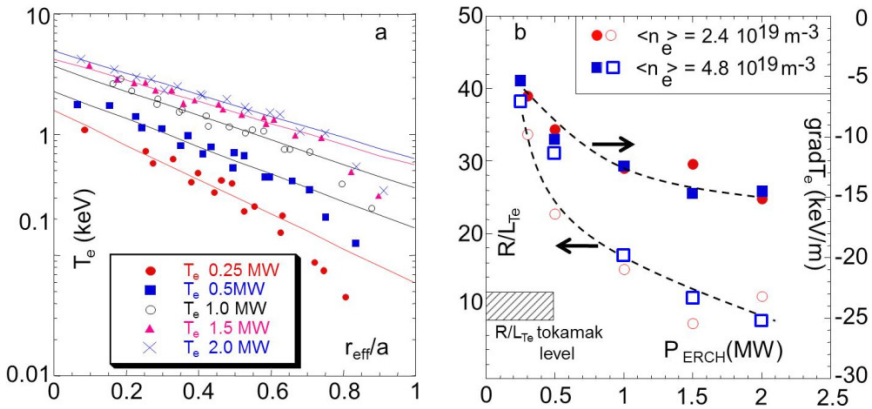


FIG. 8.33. (a) Log-lin plot of  $T_e$  profiles for an ECRH power scan ranging from 0.25 to 2 MW; (b)  $T_e$  gradient (empty symbols) and  $R/L_{Te}$  values (full symbols) versus ECRH power; the  $R/L_{Te}$  range typical for tokamaks is indicated [8.132]. Reprinted from Ref. [8.132]. Copyright (2011), American Institute of Physics.

The electron heat diffusivities measured via heat pulse propagation  $\chi_{HP}$  are similar to those obtained from a conventional power balance analysis:  $\chi_{HP} \approx \chi_{PB}$ . Figure 8.34 shows the results from on- and off-axis power modulation. The phase

of the  $T_e$  wave drops symmetrically to the inside and the outside of the off-axis deposition radius  $r/a = 0.45$  (Fig. 8.34(a)). The  $T_e$  profile is flat inside but steep outside (Fig. 8.34(b)). In a mixed case with on- and off-axis heating (at the same total power of 1.2 MW),  $\chi_{HP}$  and  $\chi_{PB}$  could be analysed (Fig. 8.34(c)). Outside ECRH deposition both  $\chi_e$  values are unchanged (see  $T_e$  gradients in Fig. 8.34(b)). For  $r/a < 0.45$  only  $\chi_{HP}$  could be estimated. It rises from  $1 < \chi_{HP} < 2.5 \text{ m}^2 \cdot \text{s}^{-1}$  with off-axis heating to  $4 < \chi_{HP} < 12 \text{ m}^2 \cdot \text{s}^{-1}$  for 0.6 MW central ECRH power.

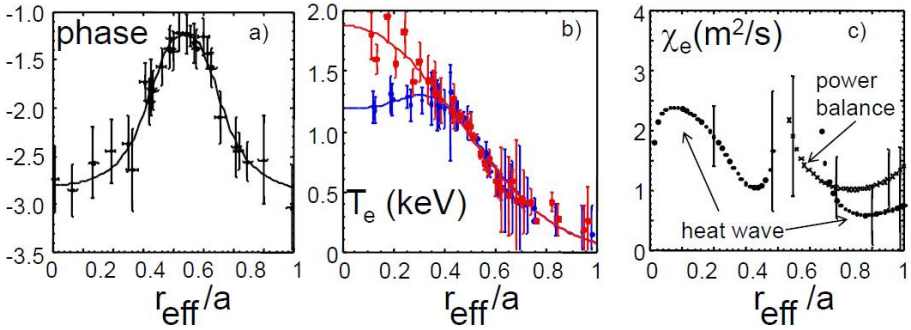


FIG. 8.34. (a) Radial variation of the heat wave phase (off-axis deposition at  $r_{\text{eff}}/a = 0.45$ ); (b)  $T_e$  profiles (peaked profile (red): on-axis power 0.6 MW + off-axis power 0.6 MW; flat profile (blue): off-axis power 1.2 MW); (c) heat-wave and power balance  $\chi_e$  for the case with 0.6 MW on-axis + 0.6 MW off-axis heating [8.132]. Reprinted from Ref. [8.132]. Copyright (2011), American Institute of Physics.

As the critical onset condition is provided by  $R/L_{T_e, \text{crit}}$  in toroidal systems, the inherent turbulence physics seems to cause a sharp onset condition in the case of low aspect ratio configurations and — to the extent turbulence is involved — to a soft one for higher aspect ratios. Otherwise, the results — lack of profile resilience and agreement between  $\chi_{HP}$  and  $\chi_{PB}$  — point to a transport mechanism not depending on gradients. These results corroborate the fact that for  $T_e > 1$  keV, the plasma core is predominantly governed by neoclassical transport. Similar studies considering ion transport are not yet available.

### 8.3.6.5. Isotopic effect

Tokamaks have a strong isotopic dependence in several confinement characteristics and specifically the one of the H-mode power threshold ( $P_{LH} \sim A_i^{-1}$  with  $A_i$  being isotope mass number) is of scientific and programmatic significance. No distinct confinement difference is, however, observed between hydrogen and deuterium stellarator discharges (in all collisionality- and  $\beta$ -ranges, with  $T_e/T_i$  large or close to 1). There is also no obvious isotopic dependence in the required conditions to transit into the H-mode.

8.3.6.6. *Magnetic configuration effects on confinement*

The leading magnetic configuration parameters which influence plasma confinement in stellarators are the rotational transform  $\iota$ , the magnetic shear  $d\iota/dr$ , magnetic mirrors and magnetic well. Magnetic mirrors, including local field ripples, affect the particle orbits and manifest themselves in the confinement under collisionless conditions. Flux surfaces are susceptible to external perturbation fields with Fourier components  $(m, n)$  being in resonance with the rotational transform. Such error fields induce the formation of magnetic islands at resonant surfaces with  $\iota(r) = n/m$ , which short-circuit radial transport and thus reduce the confinement. The radial extent of such islands scales inversely with the magnetic shear, i.e. magnetic islands become large with low shear. Therefore, magnetic effects play a larger role in low shear stellarators and heliacs. With high shear, the radial island width is kept small, but the radial distance of islands decreases and a larger number of overlapping islands may exist, which — when shear becomes too large — may lead to ergodic regions with poor confinement. In addition to these topological effects, rotational transform and magnetic shear may directly affect radial anomalous transport.

In low shear devices like W7-AS or TJ-II the  $\iota$  and shear dependence of transport can be separately probed in discharges with small and large net plasma currents, the currents resulting from the internal bootstrap current and from currents imposed inductively (with an OH system) or from the heating systems. Figure 8.35 shows the sensitive dependence of plasma energy on the boundary value of the rotational transform in the W7-AS stellarator for net-current-free ECRF heated plasmas at electron densities of  $\bar{n}_e = 2.3 \times 10^{19} \text{ m}^{-3}$  and moderate  $\beta < 1\%$  [8.147]. The central electron temperature reaches up to 2.5 keV. At these conditions magnetic shear is low and confinement is dominated by electron heating and anomalous electron transport. In the following, effects of the magnetic topology on turbulent electron transport are described. Pronounced maxima of plasma confinement are observed when the rotational transform is close to a low order rational number, i.e. at  $\iota_a = \{1/3, 2/5, 1/2\}$ . It has further been observed that the strong  $\iota$  dependence is lost and confinement increases to a high level when sufficient magnetic shear is introduced by externally driven plasma currents, this being independent on the direction of current, i.e. on the sign of magnetic shear [8.148]. Similar results have been found in the TJ-II stellarator, where the electron heat conductivity is observed to decrease with increasing negative shear. For positive shear a similar tendency is indicated, but the database does not yet allow a firm conclusion [8.149]. Further on at high  $\beta$ , the sensitivity of confinement on the low order rationals is lost by magnetic shear from the pressure driven equilibrium currents [8.150].

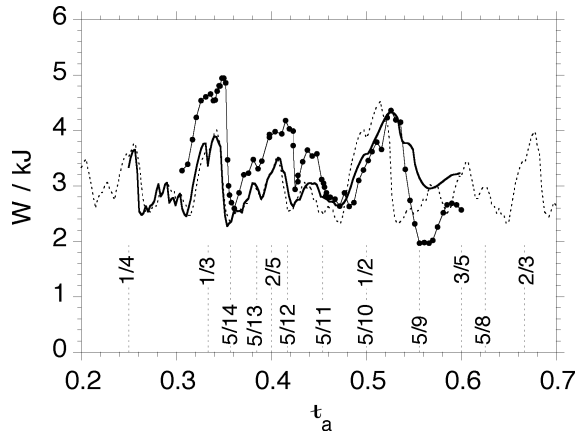


FIG. 8.35. Variation of the plasma energy (symbols) with the boundary value of the rotational transform  $\tau_a$  in net current free discharges of W7-AS with  $P_{\text{ECRH}} \leq 350 \text{ kW}$ ,  $\bar{n}_e \cong 2.3 \times 10^{19} \text{ m}^{-3}$ . Continuous and dashed lines show the calculated electron kinetic energy content obtained from the empirical transport model with the small shear in the vacuum field taken into account (full line) or not (dashed line). Taken from Ref. [8.147].

The observations are consistent with the assumption that electron energy transport is enhanced at rational magnetic surfaces, but reduced by magnetic shear. The rarefaction of density of higher order rational numbers in the vicinity of the low order rationals then explains the observed confinement maxima. A heuristic model of the electron heat conductivity which accounts for these features reproduces the very details of the  $\tau$  dependence of electron confinement in W7-AS (see Fig. 8.35), but it is left open which physical processes are involved in transport at rational surfaces [8.147]. It may be suggested that resonant modes are responsible which do not exist close to low order rational values of the rotational transform if an upper limit is claimed for the relevant mode numbers. The damping role of shear as observed experimentally may be explained by a stabilization of modes or a radial decorrelation of turbulent structures.

Evidence of sheared electric fields and formation of local electron heat transport barriers in the proximity of low order rationals has been reported from LHD [8.151] and TJ-II [8.152]. In tokamaks, electron heat transport barriers have successfully been described by a heuristic model [8.153] which postulates a reduction of transport near low order rational surfaces and strongly resembles the W7-AS model. As a consequence of the subtle  $\tau$  dependence of confinement, the database of W7-AS is established in the  $\tau$ -windows of good confinement in the vicinity of  $\tau = 0.3$  and  $\tau = 0.5$  (e.g. for the international scaling efforts).

### 8.3.6.7. Improved confinement regimes

#### 8.3.6.7.1. Optimum confinement mode

With sufficient ion heating the core region with high temperatures and dominating neoclassical transport can extend up to  $r/a = 2/3$ . These good confinement cases are characterized by a narrow density profile with low edge densities and concomitant high  $T_i$ . The outward shifted steep  $\nabla T_i$  and associated strongly sheared  $E_r$  at the plasma edge seem to lead to a reduction of the anomalous ion heat transport which, in turn, increases core temperatures. Such a scenario indicates an edge–core coupling mediated by neoclassical transport rather than by a concept like profile resilience. The discharge of Fig. 8.29 is an example of such conditions, which in W7-AS were called “optimum confinement” as the highest ion temperatures in this device ( $T_i = 1.5$  keV), maximum energy confinement times ( $\tau_E = 60$  ms) and maximum values of  $n \cdot \tau_E \cdot T_i = 5 \times 10^{21}$  eV·s·m<sup>-3</sup> have been obtained [8.33]. However, due to the low edge densities required, this scenario does not seem compatible with successful divertor operation and it is prone to impurity accumulation.

#### 8.3.6.7.2. Classical H-mode

In the experiment a fairly complex manifestation of the H-mode is observed, depending on the magnetic configuration, on density and heating power.

The H-mode of W7-AS shares with the tokamak H-mode the following characteristics:

- The H-mode develops most easily (low power) with separatrix edge;
- It can develop with grassy edge localized modes (ELMs), solitary large ELMs, with dithering and quiescent phases;
- The edge fluctuation level strongly decreases at the transition;
- Steep parameter gradients develop at the plasma edge;
- The H-mode correlates well with the development of an electric field at the plasma edge with  $E_r$  and  $\nabla E_r$  values similar to those of tokamaks;
- The H-mode remains typically for a confinement time after the heating pulse has been terminated; then an L-mode back-transition occurs;
- The H-mode transition or back-transition and the appearance of ELMs are, like in tokamaks, marked by the  $H_\alpha$ -traces and readily seen in all turbulence monitors;
- ELMs originate from the plasma edge with a pivot point which resides about 1–3 cm inside the separatrix;
- ELMs expel particles and energy and they last for about 200  $\mu$ s;

- The energy and particle content losses from larger, distinct ELMs are typically 5%;
- Quiescent H-phases are prone to impurity accumulation despite broad density profiles.

The following differences to typical tokamak H-mode characteristics seem to be of relevance:

- Judged by the presence of grassy ELMs, the H-mode can develop right at the beginning of the discharge without noticeable transition;
- The transition into the quiescent H-mode occurs at a critical (power dependent) density and has an upper power limit. Because of the critical role of the density, a delay between the heating pulse and the H-transition cannot clearly be concluded;
- The quiescent H-mode develops in small  $\nu$  windows in the neighbourhood of  $\nu \sim 0.5$  when the plasma edge is bounded by an island separatrix;
- At high density, the H-mode can develop in the form of the high-density H-mode (HDH) with good energy confinement and — opposite to the conventional H-mode — low impurity confinement [8.33, 8.154].

The observations of the peculiarities of the H-mode in W7-AS are not in gross contradiction to the understanding of the H-mode physics as described in other chapters of this book. The details of the H-mode of helical systems are described in Ref. [8.123].

#### 8.3.6.7.3. The high density H-mode

A transition into the high density H-mode (HDH) occurs at high density  $\bar{n}_e > 10^{20} \text{ m}^{-3}$  [8.33, 8.154] where the critical density depends on the heating power. At the transition, the impurity confinement time rapidly drops (see Fig. 8.36), the plasma purifies itself, the impurity radiation moves to the plasma edge and the power flux to the target plates rises. Compared with other high density operational regimes, the HDH  $\tau_i / \tau_E$  ratio would excellently meet ignition conditions [8.155].

The HDH-regime is accessible from the L-mode, the ELMy or quiescent H-mode (H\*), which implies that the transition into the HDH-mode can occur from a state with peaked (e.g. with core NBI heating) or broad (H\*) density profiles. It always ends in a state with very broad density profiles.

The transition from H\* to HDH is initiated by gas-puffing to increase the density. With beam fuelling, the preceding phases are prone to impurity accumulation, increase of core radiation and discharge collapse irrespective of the density profile form.

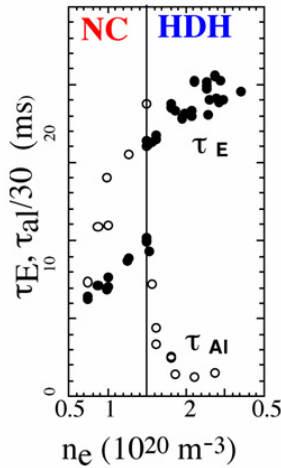


FIG. 8.36. Increase of  $\tau_E$  (full circles) and decrease of  $\tau_{Al}$  (empty circles), the impurity confinement time of injected Al-tracers, at the HDH transition of W7-AS. The vertical line represents the separation between neoclassical (NC) and high density H-mode (HDH) regimes.

The most startling aspect of the HDH regime is that the canonical collinearity between energy and impurity confinement is lost but not due to the transport effect of large MHD instabilities as is the case with ELMy H-modes. The HDH-mode does not show ELMs and this is one of its attractions.

The HDH regime is similar to the Enhanced D-Alpha (EDA)-mode of C-mod, and the ELM-free, quasi-stationary H-mode of DIII-D. All these cases show the presence of a quasi-coherent instability inside the edge pedestal. The above mentioned confinement collinearity seems to be broken by MHD, however in these cases on a small scale level. The high density H-modes show that the MHD, which limits the edge gradients, does not necessarily have to be global with disastrous impact on the plasma-wall interaction. The limitation of the edge pressure gradient by fine-scale quasi-coherent activity may not be the typical case but is still rather generic as the mechanism seems to apply to tokamaks as well as to stellarators in spite of the large differences in the magnetic characteristics of the edge.

The HDH regime allows steady plasma operation and it is rather robust. This mode can easily be established for all powers above 0.7 MW (power flux across the separatrix:  $0.06 \text{ MW}\cdot\text{m}^{-2}$ ) and it is established for the highest  $\beta$  values achieved in W7-AS (see Section 8.4.2). Considering the advantages of high densities for divertor operation, the HDH-mode may be the preferred operational mode for W7-X (depending on the necessary transition power and the accessibility of the critical density). Then the role of the collisionality in the transition conditions along with further characteristics of the HDH-mode can be explored.

### 8.3.6.8. Impurity transport

The impurity behaviour is basically determined by transport processes in three plasma regions: (a) the direct interaction zone between plasma and the surfaces of plasma-facing components responsible for the impurity sources caused by erosion of wall material, (b) the scrape-off layer (SOL) controlling the impurity influx across the separatrix, and (c) the core plasma. Each of these regions has its own relevance for the global impurity behaviour and only their simultaneous treatment enables one to assess the final role of intrinsic impurity ions in fusion plasmas. However, the complexity of the underlying physical processes requires elaborate models for each zone, so that — for simplicity — the transport studies often have to be restricted to one of these regions and the results have to be matched at the end.

Neoclassical impurity fluxes in the bulk plasma can be expressed in the general form (see Section 8.3.5) [8.156]

$$\Gamma_Z = -n_Z D_Z \left\{ \frac{n'_Z}{n_Z} + \gamma_Z \frac{T'_i}{T_i} - Z \left( \frac{n'_i}{n_i} + \gamma_i \frac{T'_i}{T_i} \right) \right\} = -D_Z n'_Z + n_Z v_{pinch} \quad (8.39)$$

with the ionic charge of impurity ions  $Z$ , ion and impurity density  $n_i$  and  $n_Z$ , ion temperature  $T_i$ , impurity temperature  $T_Z \approx T_i$ , impurity diffusion coefficient  $D_Z$  and convective impurity velocity (inward pinch)  $v_{pinch}$ . The coefficient  $\gamma_i$ , an off-diagonal coefficient in the transport matrix, will be discussed below. Equation (8.39) describes the impurity fluxes as long as the impurity concentration is low and does not affect the background plasma properties. In a simplified picture,  $-D_Z n'_Z$  represents all fluxes connected with the impurity density gradient as a driving mechanism (diffusive part) and  $v_{pinch} n_Z$  all convective fluxes (e.g. fluxes driven by the ion temperature gradient of the background plasma).

Impurity transport studies were performed on different helical devices, analysing the temporal and spatial evolution of impurity radiation in response to non-recycling [8.157] transient impurity sources. For this purpose short pulses of impurity ions were injected into the plasma either by gas puff [8.158], the injection of solid pellets [8.159] or by laser blow-off [8.160]. The temporal evolution of the spectral line radiation of different ionization states after the pulse allows the determination of the transport parameters  $D_Z$  and  $v_{pinch}$ . The decay times of the spectral line emission of the highest observable ionization states were taken as a measure for the impurity confinement time  $\tau_i$ .

For neoclassical transport, impurity concentrations can be predicted. However, many of the existing impurity transport codes are based on simplified neoclassical models, which are well suited for interpretation of symmetric tokamak plasmas but do not correctly consider stellarator specific transport features. With increasing  $Z$  the third term inside the brackets of Eq. (8.39) becomes dominant and the impurity transport depends nearly exclusively on the

properties (density and temperature profiles) of the background plasma. Equation (8.39) makes clear that in the case of peaked proton density profiles and positive  $\gamma_i$ , impurities are drawn towards the plasma centre, where they dilute the fusion mixture and reduce the plasma temperature by radiating off a fraction of the plasma energy. Opposite to tokamaks where the coefficient  $\gamma_i$  in front of the thermal gradient can also be negative (“impurity screening” if the bulk ions are in the so-called “banana” transport regime), it is predicted to be always positive for 3-D devices and aggravates impurity accumulation in the presence of peaked ion temperature profiles. At low density the “electron-root” can develop, which is able to keep the impurity ions back from the core plasma.

In many cases the neoclassical transport coefficients  $D_Z$  and  $v_{pinch}$  are not sufficient to describe the experimental data. Therefore, “anomalous” coefficients from turbulent transport have to be evoked to reproduce the experimental results. In W7-AS both impurity and energy confinement time obey quite similar dependences on global parameters (density, heating power, etc.), suggesting common driving mechanisms: for the aluminium confinement time  $\tau_{Al} \propto a^{2.4} \cdot \hat{n}_e^{1.2} \cdot B^{0.3} / P^{0.8}$  (ECRF heating) is obtained. Turbulent transport usually causes flattened density profiles and generally goes along with degraded global confinement leading to low contamination levels.

In W7-A the main features of impurity transport in medium to high density NBI plasmas were in fact nearly consistent with neoclassical transport [8.161]. This is no longer the case in medium-sized devices. At low density generally poor impurity confinement is observed [8.162–8.164], which is attributed to either strong turbulent transport [8.165, 8.166] or the appearance of the electron root at low collisionality [8.167]. Accumulation of intrinsic impurities is not observed. At higher density, however, a clear positive density dependence of the impurity confinement develops [8.162, 8.164, 8.168]. This is due to an increasing ratio of inward convection  $v_{pinch}$  to diffusion coefficient  $D_Z$  in the bulk plasma causing longer confinement times as summarized in Fig. 8.37 [8.162, 8.164]. In W7-AS and Heliotron E, the diffusion coefficient decreases with increasing density. This is in contrast to conventional neoclassical scaling, which predicts an increase of  $D_Z$  with density for both cases. Transport simulations for LHD [8.165, 8.166] plasmas reveal diffusion coefficients being one order of magnitude enhanced over the neoclassical level for low and medium density. Nevertheless, the impact of a changing ambipolar radial electric field on impurity confinement was clearly demonstrated in LHD [8.167, 8.169]. The radial electric field evolved gradually from positive to negative values, with growing density causing the outward flow of impurities to flip to an inward flow.

We conclude that in the low to medium density range, impurity transport is determined largely by turbulent contributions giving rise to the observed density scaling. Details of this scaling depend also on the size of the device. The turbulent

contributions become weaker towards highest densities, where again neoclassical features are observed.

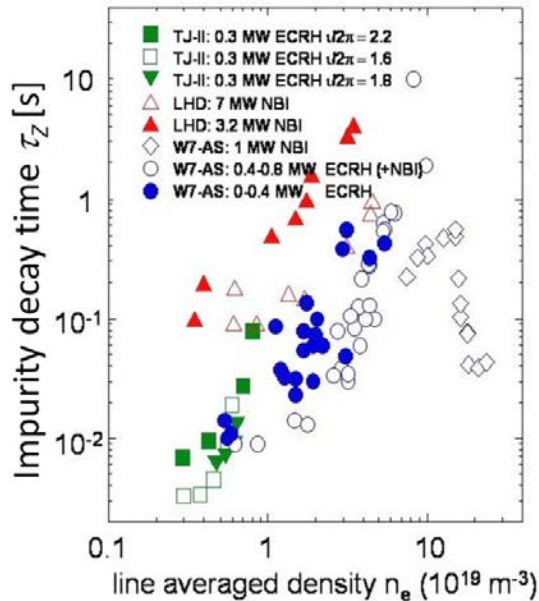


FIG. 8.37. Impurity confinement time  $\tau_z$  versus density in TJ-II, LHD, W7-AS. Open blue diamonds on the right side show W7-AS data at transition to HDH indicated by the decrease of  $\tau_z$  towards higher densities by about an order of magnitude [8.156].

The consequences of the unfavourable impurity confinement at high density manifest themselves in radiation losses that steadily rise throughout the pulse duration by accumulating impurity ions [8.162, 8.167]. The core radiation reduces the effective heating power and at a radiation fraction  $>50\%$  to  $60\%$  the plasma energy degrades in W7-AS and the discharge terminates by radiative instability (Fig. 8.38). Hence, the radiation losses determine the pulse length and the “density limit” (see Section 8.4.1).

For steady state operation, impurity accumulation has to be avoided. Whether this can be achieved under relevant conditions will be one of the most crucial tests for present and future helical systems with steady state operational capability. Impurity accumulation in quasi-neoclassical plasmas can be avoided in regimes with flat instead of peaked ion density profiles. This can be achieved for example by adding central ECRH power additionally to the main operating heating system. Unlike NBI, ECRH does not introduce a central particle source into the plasma but rather induces peaked electron temperature profiles which drive particle fluxes outwards by thermodiffusion, resulting in a flattening of density profiles [8.171]. Increasing ECRH power also degrades impurity

confinement and contributes to avoiding impurity accumulation [8.168]. On the other hand, reduced confinement can hardly be seen as the favoured solution.

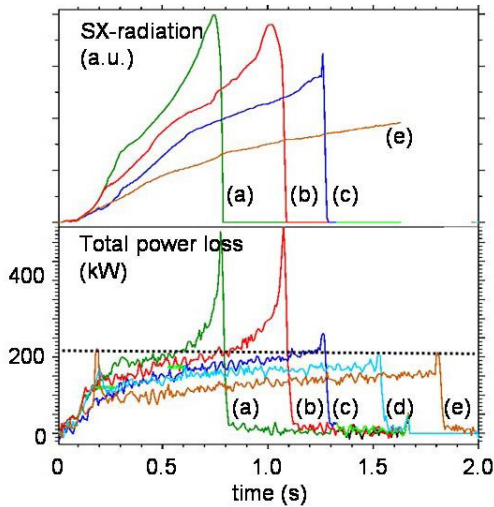


FIG. 8.38. Impurity radiation in 0.5 MW NBI-heated W7-AS plasmas at constant density of  $0.87 \times 10^{19} \text{ m}^{-3}$  (e,d),  $1.05 \times 10^{19} \text{ m}^{-3}$  (c),  $1.15 \times 10^{19} \text{ m}^{-3}$  (b),  $1.25 \times 10^{19} \text{ m}^{-3}$  (a). The dashed line indicates 40% of heating power [8.33] using data from Ref. [8.170].

Another important aspect in the prevention of impurity accumulation is impurity shielding inside the SOL. Since the stationary level is linked to the net impurity influx into the plasma core, shielding of the impurity sources in plasmas with long impurity confinement might allow successful sustainment of the plasma at a reasonable core radiation level. Such a retention of the impurity influx can be achieved by direct shielding mechanisms via friction in the SOL or by periodic particle exhaust into the SOL, for example by ELMs in the H-mode.

Both the helical divertor in LHD and the island divertor in W7-AS demonstrate effective impurity retention [8.172, 8.173]. The parallel ion temperature gradient along the separatrix (“upstream” position) to the lower temperature in front of the divertor plates (“downstream”) causes a competition between downstream directed frictional plasma flow flushing the impurity ions back to the divertor plates and parallel upstream directed impurity flux induced by thermal forces on the impurity ions. The latter depends on the temperature gradient ( $\nabla T_i$ ) and, via the collision frequency, quite sensitively on  $T_i$  ( $\sim T_i^{3/2}$ ). A reduction of the impurity influx can be achieved by reduction of  $\nabla T_i$  or the upstream  $T_i$ .

Non-axisymmetric divertors based on edge islands have the potential to decrease  $\nabla T_i$  and the upstream  $T_i$  simultaneously by additional cross-field heat transport through the islands which grows with SOL collisionality (high

density with low  $T_i$ ) and acts like a supplementary bypass between up- and down-stream positions. This causes a strong reduction of the parallel conductive heat flux ( $\sim T_i^{5/2}$ ) and finally of the thermal impurity influx. As a consequence, the impurity density at the separatrix as well as the impurity influx into the core region [8.173] are decreased (see Section 8.3.7).

This impurity screening mechanism plays a role in the SOL of W7-AS during the HDH-mode [8.173] and also in the stochastic (magnetic) edge and surface layer of LHD [8.172]. With the onset of the HDH-mode in W7-AS with extremely flat density profiles, strong gradients at the plasma edge and edge densities above  $1$  to  $2 \times 10^{19} \text{ m}^{-3}$ , the impurity influx is remarkably reduced. Simultaneously, in the HDH mode of W7-AS the core impurity confinement is strongly degraded, both enabling stationary operation at high density up to  $4 \times 10^{20} \text{ m}^{-3}$  without accumulation. Increase of impurity confinement neoclassically inferred by the large edge density gradients in HDH was not observed and seems to be counteracted by enhanced transport processes in the edge gradient region. The simultaneous appearance of a quasi-coherent mode at the plasma edge supports this assumption [8.174].

In LHD, the trend for accumulation in long pulse experiments starting at densities of  $1 \times 10^{19} \text{ m}^{-3}$  was stopped beyond a power dependent line averaged density of  $2.7 \times 10^{19} \text{ m}^{-3}$  [8.167] and an actual reduction of contamination was observed. However, impurity pellet injection experiments have shown that the impurity confinement still remains long, indicating that the observed onset of purification is predominantly determined by edge shielding processes. Likewise, Super Dense Core (SDC) plasmas of LHD ( $n_e(0) = 5$  to  $6 \times 10^{20} \text{ m}^{-3}$ ) with internal diffusion barriers (ITBs) obtained by frequent pellet injection in the presence of a helical divertor or the local island divertor (LID) do not suffer from enhanced radiation [8.144, 8.175], although good impurity confinement is given and accumulation is indicated [8.176]. Obviously, all three divertor concepts — the edge island divertor, the helical divertor as well as the LID — seem to provide very effective shielding of the impurity influx.

With respect to impurity core confinement, recently even hollow impurity profiles were found at LHD [8.177] in plasmas with internal transport barrier (ITB) and strong ion temperature gradients. Transport analysis reveals low diffusion coefficients for both bulk and carbon ions but large outward convection of carbon impurities. This favourable outward flow is related to the ion temperature gradient but is opposite to neoclassical predictions and therefore considered to be driven by turbulence.

### 8.3.7. Boundary layer and divertor physics

Two significant problems that need to be solved for any future fusion device are heat removal and particle control. A very promising method to attack these problems in tokamaks as well as in helical devices is the use of a divertor, providing a controlled interaction zone between plasma and wall. By carefully designing a divertor, conditions can be created in front of the divertor targets which lead to a sufficient reduction of the power load on the targets by strong radiation redistribution, a significant increase in neutral gas pressure for particle pumping and a strong decrease of the energy of the particles hitting solid surfaces to reduce the impurity sources resulting from physical sputtering processes. Any solution of course needs to allow for an energy confinement which is at least sufficient for the realization of a fusion reactor. Since energy confinement has been found to be strongly related to edge anomalous transport and edge plasma profiles, the ultimate aim is to find an integral solution which is optimum with respect to exhaust and confinement. The development of adequate divertor solutions is one of the key issues for present and next step larger stellarators. However, in contrast to the extensive experience gained with divertors in tokamaks over the past decades (see Chapter 7), related research on stellarators is still in its infancy. An overview of the present status is given in Refs [8.33, 8.178–8.180].

#### 8.3.7.1. Island divertor concepts

Depending on the type of helical device, divertors are realized in two different ways, though in the end both of them are making use of island structures inherent to the respective magnetic field configurations. In low to moderate shear advanced stellarators like W7-AS and W7-X, magnetic islands at the edge provide a natural separatrix configuration. Since the field perturbations associated with the islands are very small,  $\Delta B_r / B_\phi \sim 10^{-3} - 10^{-4}$ , additional resonant perturbations of the same magnitude created by control coils are sufficient to modify the island geometry, thereby giving an external control over key parameters for the creation of an effective divertor plasma, such as island size, connection length and distance from X-point to the target. The low shear in W7-AS and W7-X allows the existence of single island chains at the edge. In contrast, heliotron type devices like LHD have a much larger shear, especially at the edge. The rotational transform in the edge region of LHD covers several low order resonances which overlap each other, forming a stochastic layer of several cm thickness. In the outermost region close to the wall, the increased poloidal field components of the two helical coils create four divertor legs which are cut by graphite targets positioned just in front of the wall (Fig. 8.39), forming a helical divertor configuration similar to the double-null

configuration in tokamaks. However, the resulting short connection lengths between the ‘X’-points and the targets ( $\sim 2$  m on average) make the divertor legs transparent for the recycling neutrals, at least for the present open divertor configuration. Instead, the pre-X-point stochastic layer is optically thick and is expected to largely determine the performance of the helical divertor in LHD. Thus, low-order magnetic islands are the basic elements forming the helical SOLs in both the island and helical divertor concepts.

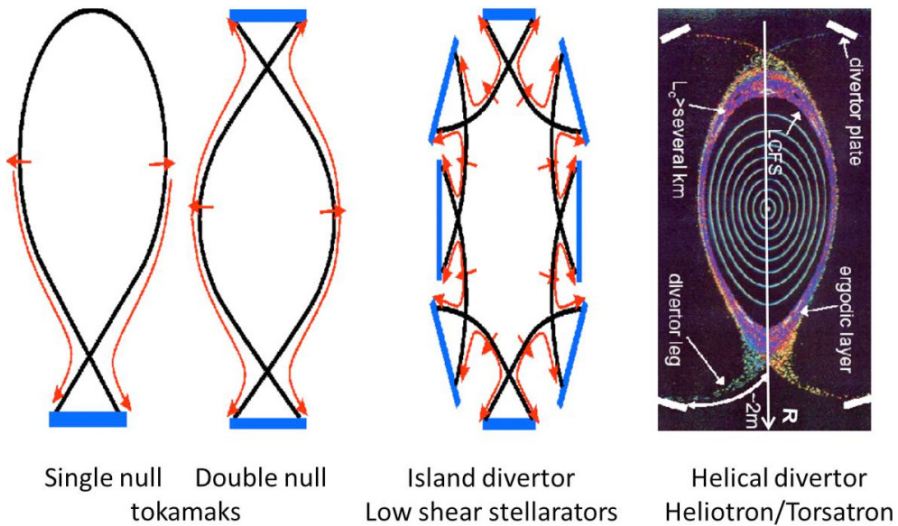


FIG. 8.39. Schematics of single-null and double-null tokamak divertors and of two types of intrinsic island divertors typical for W7-AS and W7-X as well as for LHD. Projections of energy and particle flow directions to targets (thick red solid lines) are indicated by arrows. The helical divertor in the heliotron-type device LHD has 4 divertor legs (right), reminiscent of the double null configuration in tokamaks. Mode numbers of boundary islands in stellarators vary from machine to machine, for example in W7-AS the poloidal mode number  $m$  can be changed from 8 to 10, with 9 being the standard case; in W7-X,  $m$  can be chosen from 4 to 6, with  $m = 5$  being the standard case. The stochastic layer of the helical divertor in LHD consists of multiple low-order island chains [8.173, 8.181].

With respect to the symmetry of the different devices, divertor targets and baffles in tokamaks are axisymmetric, while those in stellarators have to be toroidally finite and three-dimensionally shaped in order to avoid leading edges.

### 8.3.7.2. Transport features of helical SOLs

The island divertor (ID) in W7-AS [8.182] and W7-X [8.183] and the helical divertor (HD) in LHD [8.181] follow the same principle as the tokamak poloidal field divertor, subjected also to the same basic atomic and plasma surface interaction processes. However, significant differences in divertor geometry and

magnetic configuration exist between helical and axisymmetric devices, which influence the plasma, neutral and impurity transport in the SOL. This section focuses on some helical SOL specific transport effects, therefore serving as a supplement to the tokamak divertor physics (see Chapter 7).

In both the ID and the HD concepts, a topological target–core separation is realized by means of magnetic islands. Associated with the small radial field component  $B_r$  forming the islands, both divertors have small diversion field line pitches,  $\Theta = B_r / B (\sim \Delta x / L_c)$ , where  $\Delta x$  is the perpendicular distance from the X-point to the target, in comparison with  $\Theta = B_\theta / B$  in tokamaks. The small field line pitches significantly increase the weight of cross-field transport which, under certain conditions, can even short-circuit the parallel ones. Helical SOLs are fully three-dimensional and plasma transport is strongly modulated by the helical structures of the island chains. As a consequence, multi-parallel transport channels exist with varying shape and locations in helical directions, resulting in rather complex transport patterns, in particular for the parallel plasma flows. Counter-flows reside on different parts of helical SOLs and cross-field transport can transfer momentum from one channel into another, causing momentum loss of counter-streaming ions. The geometry-induced effects can make the essential transport features of the helical SOLs deviate from the standard transport picture as emerged from tokamaks. This can well be illustrated by extending the tokamak two-point (2P) model to cover the helical SOLs by including cross-field transport contributions [8.173]:

$$T_u^{7/2} = T_d^{7/2} + \frac{7q_{\parallel}L_c}{2\kappa_e} - \frac{7\chi(n_{es} + n_{ed})}{4\kappa_e\Theta^2}(T_u - T_d) \quad (8.40)$$

$$p_u = 2p_d(1 + f_m) \quad (8.41)$$

$$n_{ed}c_{sd}\gamma T_d = q_{\parallel} \quad (8.42)$$

where the subscripts ‘ $d$ ’ and ‘ $u$ ’ indicate down- and upstream, respectively;  $c_{sd}$  is the sound speed at the targets;  $\kappa_e$  is the electron parallel conductivity coefficient;  $q_{\parallel}$  is the parallel heat flux;  $p_u$  and  $p_d$  are the respective upstream and downstream plasma thermal pressure;  $\gamma$  is the sheath heat transmission factor; and  $n_{es}$  is the average electron density at the inner separatrix (last closed flux surface). In view of the complexity of the 3-D island geometry, all the upstream quantities resulting from the 3-D simulations shown in this section are evaluated in this way, while the downstream ones are weighted by the plasma thermal pressure profiles on the targets. The  $f_m$  in Eq. (8.41) represents the momentum loss resulting from viscous transport between counterflows residing on different parts of the helical SOLs. Here, the CX-induced momentum losses [8.184] are not taken into account. The last term in Eq. (8.40) is the cross-field heat conduction contributed from both

ions and electrons. This term is only relevant for small  $\Theta$  like that in helical SOLs and disappears if  $\Theta$  is increased to the tokamak level. Then, in the absence of  $f_m$ , Eqs (8.40) to (8.42) reduce to a standard 2P model for tokamaks.

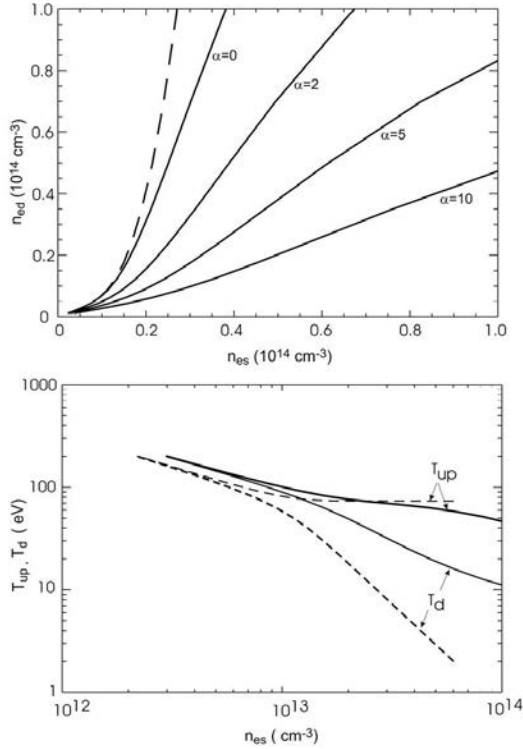


FIG. 8.40. Comparison between the standard (dashed) and the extended 2P model (solid). Top: Downstream density versus separatrix density for different  $\alpha$ -values assumed in the extended 2P model. Bottom: Upstream and downstream temperatures versus separatrix density, where  $\alpha = 5$  is assumed in the extended 2P model [8.173].

The geometry-related momentum loss processes are associated with the complex 3-D geometry of individual SOLs and the determination of  $f_m$  needs a 3-D transport code. For a qualitative understanding of the leading physics, we, without loss of generality, parameterize the momentum loss term as  $f_m = \alpha / T_d^{1/2}$ , where  $\alpha$  is introduced as a free parameter to represent the strength of the momentum loss [8.173]. Results from the standard and the extended 2P models are compared in Fig. 8.40. With increasing  $n_{es}$  above a certain value, the standard 2P model shows sudden departures of  $n_{ed}$  from  $n_{es}$  and  $T_d$  from  $T_u$ , indicating transition from low to high recycling regime as is well known from tokamaks. Increasing the momentum loss in the extended 2P model suppresses the increment in  $n_{ed}$  with respect to  $n_{es}$  and moderates the decrease in  $T_d$ . The

transition to a high recycling regime becomes softer and eventually vanishes. For strong momentum losses ( $\alpha \geq 5$  in Fig. 8.40, top),  $n_{ed}$  is almost linearly coupled with  $n_{es}$  and remains below  $n_{es}$ . The role of the cross-field heat conduction is reflected by the drop in  $T_u$  in the high  $n_{es}$  range where a constant  $T_u$  is expected from the standard 2P model. The significant contributions of the cross-field heat conduction to the energy transport in the islands have an important consequence on impurity transport. Cross-field transport smoothes the parallel temperature gradients and thereby reduces the related thermal forces which tend to drive impurities inwards (see Section 8.3.6.8). The impurity retention potential of the edge magnetic islands in helical devices is presently under intensive experimental investigation [8.172].

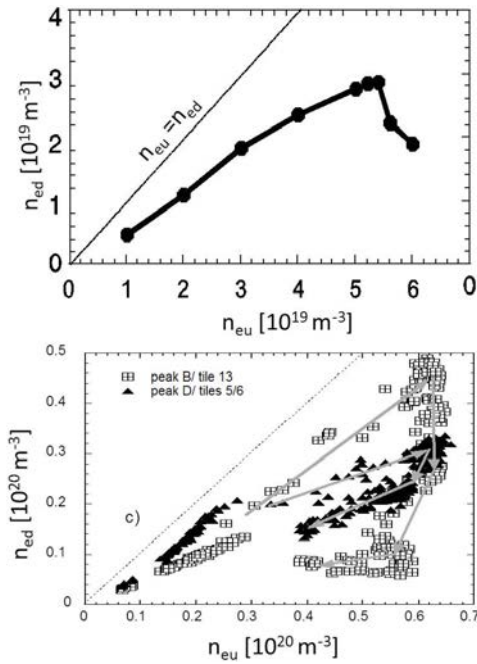


FIG. 8.41. Top: A density scan at W7-AS taking the intrinsic carbon impurity into account.  $n_{ed}$  increases almost linearly with  $n_{eu}$  until the ionization front detaches from targets, leading to a roll-over of  $n_{ed}$  [8.173]. Bottom: Peak  $n_{ed}$  values from target-integrated Langmuir probes at different locations versus the upstream density  $n_{eu}$ . The AS divertor target is covered by 17 graphite tiles arranged sequentially in the toroidal direction. Two groups of Langmuir probe arrays are flush-mounted in tiles 5/6 (data with filled triangles) and tiles 13/14 (data with open squares), detecting particle fluxes coming from opposite toroidal directions.  $H^0 \rightarrow H^+$  injection,  $P_{NBI}^{abs} = 1.4 \text{ MW}$ . Grey arrows indicate the directions of increasing  $\bar{n}_e$  [8.33]. Reprinted from Ref. [8.33]. Copyright (2011), IOP Publishing Ltd.

A more quantitative and strict description of the divertor transport in helical devices needs a 3-D code. EMC3/EIRENE has been developed for this

purpose [8.185, 8.186]. The code is capable of self-consistently treating plasma, neutral and impurity transport in general 3-D SOLs of arbitrary geometry. It was initially developed for W7-AS, recently having found worldwide applications to 3-D edge transport problems encountered not only in stellarators but also in tokamaks. Figure 8.41 (top) shows an example of 3-D simulation results based on the W7-AS island divertor geometry and physics parameters, compared with experimental results in Fig. 8.41 (bottom). Neither simulations nor experiments show any indication of a transition to a high recycling regime. Similar results have also been found for the HD in LHD, where both 3-D simulations and experiments consistently show that the momentum loss in the stochastic layer of LHD is even stronger than in the island divertor of W7-AS [8.187, 8.188].

W7-X will be equipped with the same type island divertor as tested on W7-AS. Nevertheless, the larger size and the lower poloidal number of the edge magnetic islands in W7-X significantly reduce the viscous transport between counterflows residing on adjacent island fans. Preliminary 3-D code simulations have predicted that the W7-X islands should allow a significant rise of the downstream density.

### 8.3.7.3. *Detachment regime*

In view of its large radiation fraction, the detachment regime found in tokamaks is also attractive for stellarators. Nevertheless, the concept of removing thermal power via radiation works only if the radiation layer can be controlled and kept away from the confinement zone to avoid a severe degradation of energy confinement. In tokamaks, it has been shown that the X-point geometry favours impurity radiation and an intensive radiation belt around the X-point, termed X-point MARFE, is usually observed in detached plasmas. The island chains in helical SOLs provide a multi-null divertor configuration where the number, location and geometry of the X-points can be adjusted externally, thus having the potential of more flexible control of the radiation location for an optimum power removal. Indeed, a geometric parameter window has been experimentally identified for W7-AS within which more than 90% of the power entering the island SOL can be radiated by light impurities and the radiation layer can be stabilized outside the confinement region without remarkable loss of any global energy confinement. Outside this window, MARFE-like radiation instabilities drive detached plasmas unstable [8.189, 8.190].

Stabilizing the detached plasmas in W7-AS needs sufficiently large islands and field line pitches. For these configurations, 3-D code (EMC3-EIRENE) simulations show that the radiation layer is located around the inboard X-points outside the separatrix (see Fig. 8.42). This in/out asymmetric radiation pattern makes the radiative power removal imperfect in the sense that a certain power fraction flows still from the low-field side onto the targets, implying that the

detachment is only partial. On the other hand, however, the existence of such a radiation-less power channel is considered to be essential for the stability of the detached plasmas because it transports energy into the divertor region to sustain the ionization processes of the recycling neutrals. For configurations outside the stable partial detachment window, the 3-D code shows intensive radiation originating in the divertor region and a strong degradation of neutral screening. Theory suggests that the recycling neutrals are a potential trigger for the observed detachment instability [8.191].

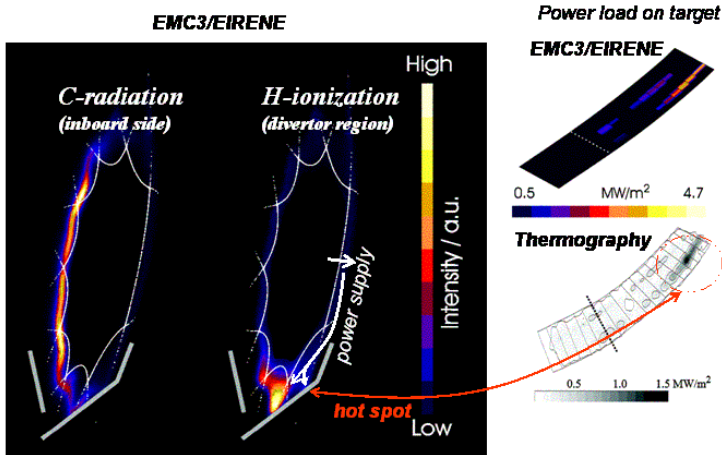


FIG. 8.42. Typical distribution pattern of carbon radiation and hydrogen ionization in a stable partial detachment for the W7-AS standard divertor configuration. A radiation-free power channel on the low field side transporting energy down to the recycling regions is detected by the target surface thermography, in good agreement with the code results [8.173].

No stable detachment can be established in the HD of LHD so far [8.180], where the X-point geometry of the multi-island chains is strongly destroyed by the stochastic fields. Simulations show that the impurity radiation prefers the remnant islands in this case and the radiation level exceeds 90% of the SOL power after onset of detachment. A partial detachment associated with a poloidally asymmetric radiation distribution as in W7-AS is not observed in the HD of LHD and also not predicted by modelling.

As an outlook, significant progress in the development of the two divertor concepts presently being investigated, the HD in LHD and the ID in W7-AS, shows rather promising results, with sustained detachment having been reached in both devices and stable partial detachment, with sufficiently high sub-divertor neutral gas pressures for efficient particle exhaust in W7-AS. Preliminary 3-D transport modelling with EMC3/EIRENE [8.192], as well as earlier 2-D approximations [8.193], indicate that W7-X will be the first helical device which will have a high recycling regime. This will allow an onset of detachment already

at lower  $n_{es}$  than previously observed in W7-AS. The island screening potential for intrinsic impurities under high SOL collisionalities, which was predicted for W7-AS and LHD and recently confirmed in LHD experiments [8.194], has been predicted also for W7-X.

Of course only the very first steps in the understanding of the physics of the two divertor concepts have been taken and much work still needs to be done. For example, while the EMC3/EIRENE code made it possible to well model the main features of partially detached plasmas in W7-AS, it did not yet reproduce the observed volume recombination of deeply detached plasmas [8.195]. Furthermore, since drift effects still need to be included self-consistently in the modelling, the observed power load asymmetries between upper and lower divertor, which are presently attributed to drift effects (since experimentally the load asymmetries could be inversed by reverting the magnetic field direction), can presently only be explained qualitatively. A further critical point is that the SOL scenarios and hence the divertor performance are considerably influenced by details of the edge magnetic field configuration. For this reason, exact knowledge and control of the actual equilibrium edge configuration — a deficit in the present studies — are essential for future applications. In contrast to tokamaks, this is a challenge at least for low shear stellarators. As large boundary islands can be introduced by relatively small superimposed resonant fields, their structure is very sensitive to perturbations due to plasma currents and/or error fields. Progress regarding these specific problems of island divertors is expected from future island divertor studies on the W7-X stellarator together with further extension of the 3-D edge code.

## 8.4. OPERATIONAL LIMITS

The commercial and technical attractiveness of a fusion reactor based on toroidal magnetic confinement is closely linked to the achievement of high density and high plasma  $\beta$ . For a given plasma  $\beta$ , high density operation (along with comparably low plasma temperature) yields several favourable aspects: a minimum excess electron pressure due to  $T_e \approx T_i$ , a higher energy confinement time scaling  $\propto \sqrt{n}$  and a lower fast particle contribution to  $\beta$ . High density operation reduces engineering demands, for example by a reduced heat flux to the targets. Likewise, it is desirable to operate at sufficiently high  $\beta$ , since the D-T fusion power increases approximately  $\propto \beta^2$  in the plasma temperature range of interest.

### 8.4.1. Density limit

The density limit is defined as the maximum achievable density for given experimental conditions. At still higher densities the energy content of the

plasma starts to decrease. In tokamaks, the discharge quite often collapses by a disruptive instability (see Chapter 3). In contrast, the density limit in stellarators is determined by heating power and radiation resulting in modest timescales of plasma decay. The density limit results of tokamaks are conventionally represented in a Hugill diagram [8.196], where the plasma current  $I_p$  is plotted against a normalized average density  $\bar{n}_e R_0 / B_0$ . The density limit is described by the empirically determined Greenwald limit [8.196] defined as

$$n_G [10^{20} \text{m}^{-3}] = \frac{I_p [\text{MA}]}{\pi a^2 [\text{m}^2]} \tag{8.43}$$

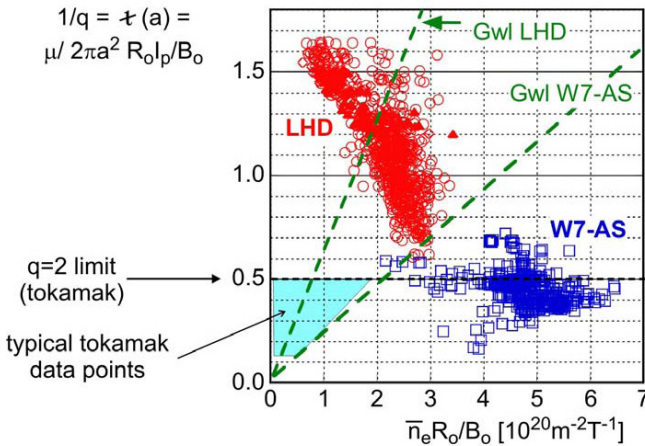


FIG. 8.43. Stellarator/heliotron data (high- $\beta$  subset) from LHD and W7-AS have been included in a Hugill diagram for typical tokamak density limit data. In addition an equivalent density limit for LHD and W7-AS is indicated with appropriate shape factors taken into account.

Figure 8.43 plots the high density results from LHD and W7-AS into a Hugill diagram. The respective Greenwald limits are given. The vertical axis is the rotational transform at the plasma boundary  $\tau(a)$ . To compare with tokamaks it may be expressed by an equivalent toroidal current as  $\tau(a) = 1/q = [\mu / (2\pi a^2)] R_0 I_p / B_0$ , where  $q$  is the so called safety factor. The space typically accessible for tokamaks is indicated bounded by the  $q = 2$  limit. In order to apply the Greenwald limit to stellarator experiments the (average) rotational transform as produced by the stellarator coils has to be converted to an equivalent plasma current that produces the same rotational transform. For both LHD and W7-AS,  $\tau(a)$  was used as the relevant rotational transform (note that W7-AS is nearly shear-free whereas LHD has strong shear). The plasma shape of LHD and W7-AS (elongation and triangularity of the plasma cross-section) has been taken into account when rephrasing  $\tau(a)$  into  $I_p$ . In both cases the stellarator

data points clearly exceed the Greenwald limit, pointing towards different inherent physics processes determining the density limit in the two confinement concepts. On the other hand, also the formal translation of the external rotational transform into a tokamak current may not reflect the underlying physics correctly.

Generally, density limit experiments in currentless stellarators do not show indications for an “absolute” limit. Instead, the limit is determined by radiation losses essentially from the bulk plasma which are proportional to the electron density  $\bar{n}_e$  for constant impurity density and constant electron temperature. If with increasing density the total core radiation level exceeds about 50–60% of the heating power, degradation of the plasma energy is observed, leading to reduced electron temperatures and thus typically to further enhanced radiation losses. Finally, this thermally unstable phase of the discharge is terminated by a radiative collapse (see Section 8.3.7). If the heating power remains, the plasma may recover. The density for the radiative collapse depends on the impurity species (and hence on machine conditions), on the available heating power  $P$  (or power density) and on the transport losses depending on the toroidal field  $B_0$  (see Section 8.3.6). These dependences are reflected in scaling laws for the critical density  $n_c$  published by Sudo and Giannone [8.197]. The Sudo scaling for the density limit [8.198] is given by

$$n_c^{Sudo} \left[ 10^{20} \text{ m}^{-3} \right] = 1.11 (PB_0/V)^{0.5} \quad (8.44)$$

where the deposited heating power  $P$  is given in [MW] and the plasma volume  $V$  in  $\text{m}^{-3}$ . To describe recent LHD results the Sudo scaling has been reinterpreted as an “edge” density limit scaling [8.199]. For the density limit of edge radiation dominated discharges with island divertor on W7-AS the following rather similar scaling law was derived [8.197]:

$$n_c^{W7} \left[ 10^{20} \text{ m}^{-3} \right] = 1.5 (P[\text{MW}]/V[\text{m}^3])^{0.4} B_0 [\text{T}]^{0.32} \quad (8.45)$$

The standard high density scenarios of stellarators as achieved by strong gas feed suffer from impurity accumulation (see Section 8.3.6). Quasi-steady-state operation with no measurable impurity accumulation was achieved in W7-AS in the HDH-mode with averaged electron densities up to  $\bar{n}_e = 4 \times 10^{20} \text{ m}^{-3}$  in stationary HDH mode discharges with very broad density profiles.

In LHD, another high density scenario was found, the superdense core (SDC) regime [8.200]. Here, very high central densities reaching  $n_e(0) = 1 \times 10^{21} \text{ m}^{-3}$  are obtained with central fuelling by repetitive pellet injection whilst the edge is strongly pumped using the LID or the helical divertor respectively. The SDC regime could be maintained for  $> 1$  s, being limited by the cooling capability of the divertor. Since the energy confinement time increases with electron density in stellarators (see Section 8.3.6), discharges with densities close to the density

limit usually have the highest energy content or plasma pressure. Therefore, the highest  $\beta$  values are obtained at lower field close to the density limit.

### 8.4.2. Beta limit

Volume averaged  $\beta$  values of up to  $\langle\beta\rangle = 5\%$  were realized in the LHD device and of  $\langle\beta\rangle \leq 3.4\%$  in the W7-AS stellarator, respectively. The highest  $\beta$  values in optimized configurations of LHD and W7-AS are largely determined by transport and hence by limitations of the available heating power rather than by MHD limits induced by the destruction of equilibrium flux surfaces or by MHD instabilities at high  $\beta$ . However, the properties of the magnetic configuration with respect to the equilibrium flux surface topology (see Section 8.3.2) and of MHD stability (see Section 8.3.3) will eventually give rise to an ultimate beta limit.

In tokamaks, the linear ideal MHD stability determines the operational limits. Examples are the inevitable onset of a major disruption whenever the safety factor at the edge falls below  $q = 2$ , or whenever the plasma  $\beta$  exceeds the Troyon limit [8.201, 8.202]. Here, the semi-empirical Troyon beta limit scaling is given by  $\langle\beta\rangle_{max} = \beta_{N,max} (I/aB)$  with a value of  $\beta_{N,max} \approx 3.5 \text{ MA}^{-1} \text{ mT}$  depending on the type of the  $\beta$  limiting instability [8.202]. This limit to  $\beta_N \equiv \langle\beta\rangle/(I/aB)$ , referred to as normalized plasma  $\beta$ , is equivalent with the ideal ‘no-wall’ stability limit effective in the absence of wall stabilization of external kink modes. Under conditions of particularly shaped current density and pressure profiles, the Troyon limit has been exceeded in experiments but still in accordance with advanced ideal stability predictions [8.203].

In stellarators and helical systems, the equilibrium and stability beta limits are rather soft similarly as in the case of the density limit. Deleterious consequences such as current disruptions causing an abrupt loss of the plasma equilibrium are absent. The beta limits manifest themselves rather by gradually increasing local transport associated with (i) the invasion of pressure induced stochastic field regions from the plasma boundary towards the interior plasma region, (ii) increasing amplitudes of unstable MHD modes, or (iii) confinement degradation effects at high collisionality at the density limit.

As far as the breaking of equilibrium flux surfaces is concerned, experiments in LHD and W7-AS have shown that finite pressure gradients can still be maintained where stochastic field regions are predicted. Numerical studies of high  $\beta$  equilibria [8.204, 8.205] suggest that the soft equilibrium beta limit is reached when the stochastic region at the edge expands towards the inside and steep pressure gradients can no longer be maintained. The breaking of the force balance causes a decrease of the pressure gradient and a subsequent saturation of the plasma beta. Figure 8.44 shows a numerical study of pressure induced field perturbations appearing in high  $\beta$  LHD equilibria calculated with HINT2 (see

Section 8.3.1). A complete plasma collapse is expected in the case of a very large Shafranov shift inducing a separatrix near the plasma axis.

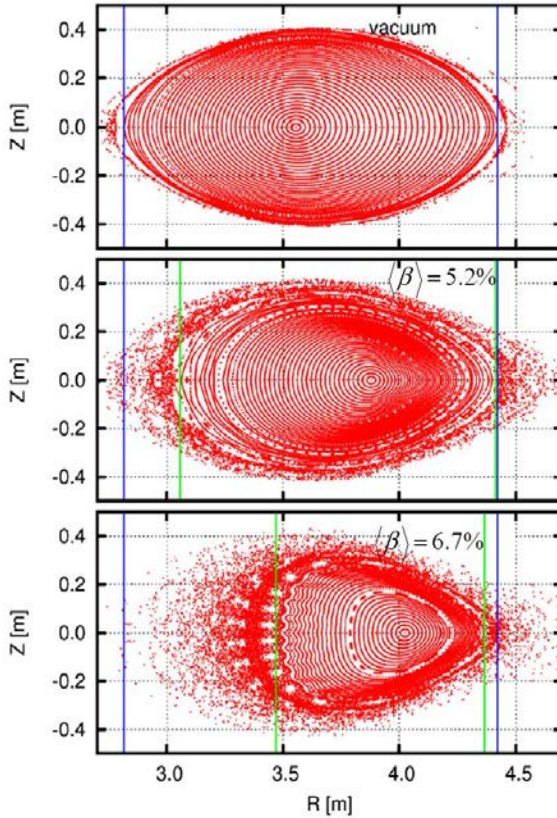


FIG. 8.44. Numerical  $\beta$  limit studies of high  $\beta$  LHD equilibria with the HINT2 code. Top: Vacuum surfaces. Middle: Case with  $\langle\beta\rangle \approx 5\%$  (around the maximum  $\beta$  reached experimentally) where the stochastic region invades the volume inside the vacuum boundary. Bottom: The case of  $\beta$  beyond the experimentally achieved value. The blue lines indicate the separatrix location of the vacuum configuration; the green lines highlight the last closed flux surface of the high  $\beta$  equilibrium [8.206].

Concerning the stability limits, the MHD activity observed in stellarators/heliotrons saturates mostly on a harmless level. This applies even to high  $\beta$  configurations in LHD, where a trade-off in favour of configurations with improved confinement properties and heating conditions results in unfavourable ideal MHD stability properties at high  $\beta$ . Also in W7-AS, regions of ideally unstable pressure profiles do not prevent access to higher  $\beta$ , where the plasma is more stable due to the formation of increased magnetic well depth and shear, or the expulsion of low order rational surfaces from the confinement zone. This self-stabilization due to beta induced changes of the equilibrium configuration

may be enforced by a local flattening of the pressure profile around the mode perturbation at the corresponding resonant values of the rotational transform so that critical pressure gradients are not exceeded.

In LHD a comprehensive comparison of mode saturation amplitudes and experimentally achieved values of beta and local beta gradients with numerical stability calculations was made [8.72]. As mentioned in Section 8.3.3, the critical values, where low  $n$  ideal MHD-modes start to cause significant radial transport reaching a limit to the local pressure gradient, are clearly beyond the Mercier stability boundary. The linear growth rate of low  $n$  ideal modes can be used as a more relevant stability index. In particular, values of  $\gamma/\omega_A \approx 10^{-2}$  (Fig. 8.45) corresponding to a radial mode width of about 5% of the plasma radius yield a boundary which is consistent with the experimental data. In the plasma core, the limit of  $d\beta/dr$  can be circumvented with increasing beta so that the stability limit in conventional LHD high  $\beta$  configurations is expected to be determined by edge MHD activity. However, there is an alternative approach to achieve high central  $\beta$  [8.207] based on the SDC plasmas introduced in the previous section. In these outward shifted configurations with peaked pressure profiles, the stability properties are improved. Central  $\beta$  values comparable with the standard case could be achieved at higher magnetic fields. A different operational limit in a particular configuration space can occur, which is forced by a fast collapse of the core density within several hundred microseconds. It is conjectured that this effect is due to the large Shafranov shift causing a fast reconnection of flux surfaces at the outboard side of the plasma.

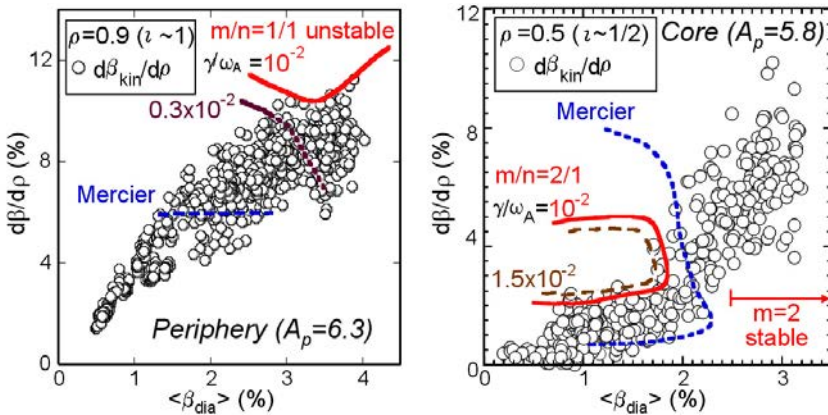


FIG. 8.45. Local  $\beta$  gradients derived from profile measurements ( $d\beta_{kin}/d\rho$ ) versus the volume averaged  $\langle\beta\rangle$  from diamagnetic loop in high- $\beta$  LHD discharges; (left) at the periphery ( $r/a \equiv \rho = 0.9$ ) and (right) in the core ( $\bar{n} = 0.5$ ). The Mercier boundaries (blue dashed lines) are clearly exceeded. The red lines give contours of growth rates for low  $m,n$  modes around  $\gamma/\omega_A \approx 10^{-2}$ . Mode induced local limits of the pressure gradients coincide with growth rates of  $\gamma/\omega_A \approx 10^{-2}$  (continuous red line) [8.72].

In Wendelstein type stellarators the stability benefits from a magnetic well across the whole plasma allowing for the very quiescent discharges in W7-AS up to the maximal achieved  $\beta$  values.

## 8.5. STELLARATOR OPTIMIZATION

Depending on the objective, the optimization of a helical system targets at different criteria and proceeds along different strategies. For the sake of flexibility the coil system of *experimental devices* often consists of several independent components, main field coils and helical windings, while in a *reactor device* mechanical issues and structural problems dominate. Common to both approaches is the desire to optimize the plasma confinement with respect to equilibrium and stability and to reduce collisional and anomalous plasma losses.

### 8.5.1. Equilibrium

The equilibrium  $\beta$  of stellarators is limited by a beginning destruction of flux surfaces and increasing ergodization of the plasma boundary if the plasma core is shifted outward relative to the outermost flux surface. A too large Shafranov shift also may cause an asymmetric load to the wall (radiation and neutrons). As discussed in Section 8.3.2 the desired reduction of the Shafranov shift corresponds to a reduction of the parallel current density  $\vec{j}_{\parallel}$ . The ideal case  $\vec{j}_{\parallel} = 0$ , which implies  $\vec{\nabla} \cdot \vec{j}_{\perp} = 0$ , is equivalent to the so called Palumbo condition [8.56]  $\lambda = (\vec{B} \times \nabla B) \cdot \nabla p = 0$  (see Section 8.3.2). Since the pressure is constant on flux surfaces and  $\nabla p$  always points in the radial direction, the ideal case  $\lambda = 0$  (zero Pfirsch–Schlüter currents) would be a configuration with constant magnetic field strength on magnetic surfaces, which cannot be fulfilled in toroidal geometry. However, for a minimization of  $\lambda = (\vec{B} \times \nabla B) \cdot \nabla p$  it is already sufficient to reduce the gradient of the magnetic field strength on a flux surface in the direction perpendicular to the field lines. From a geometric point of view the factor  $\lambda$  is proportional to the geodesic curvature of magnetic field lines, which is the projection of the curvature vector onto the magnetic surface. Magnetic configurations where the geodesic curvature is minimized are called quasi-isodynamic systems [8.7] where the prefix “quasi” means that due to the inherent toroidicity the geodesic curvature cannot be zero everywhere on a flux surface. Quasi-isodynamicity relies on the poloidal closure of contours of the second adiabatic invariant  $J$  by minimizing the *poloidal* variation of  $|B|$ .

### 8.5.2. Particle drift

The  $\nabla B$  drift of charged particles across magnetic surfaces, which determines the step width of collisionless transport, is proportional to

$(\vec{B} \times \nabla B) / B^2$  and thus also proportional to  $\lambda = (\vec{B} \times \nabla B) \cdot \nabla p$ . Reducing the geodesic curvature of a flux surface therefore has beneficial effects on the particle orbits as well and reduces both the neoclassical transport of the thermal bulk and the losses of fast heating ions such as the alpha particles in a reactor. As first approach, in the analytical  $\sigma$ -optimization [8.119] the variation of the  $B$  minima in helical or poloidal direction can be reduced such that at least the radial drift of the *deeply* trapped particles is minimized.

However, the radial losses of charged particles in the *lmfp* can already effectively be reduced if inward and outward drift of a particle remain finite but balance each other (see Section 8.3.4). This is the case for the banana orbits in a tokamak, where for a full orbit inward and outward drift balance such that in this limit the particles are absolutely confined. The banana orbits rely on the toroidal symmetry of the magnetic field strength which means that on a flux surface the magnetic field strength depends on the poloidal coordinate only, i.e.  $B = B(\theta)$ . More generally, the condition of confined orbits in the *lmfp* is fulfilled if the magnetic field strength has continuous symmetry properties on a flux surface. This requires that a coordinate system can be found where  $B$  on the flux surface and thus also the Hamiltonian of the particle drift depend only on one instead of two angular variables and the associated generalized momentum is conserved. A tokamak with  $B = B(\theta)$  for example yields *toroidal* momentum conservation. Despite the fact that the flux surfaces of stellarators have a three dimensional geometric shape, the decisive quantity is the *magnitude* of the magnetic field strength expressed in Boozer coordinates  $B = B(r, \theta, \phi)$ , where  $r$  is the flux surface label [8.110]. Due to the inherent torodicity the desired symmetry properties of  $B$  on a flux surface can only be approximated and are addressed as quasi-symmetries [8.208]. In general on three dimensional flux surfaces quasi-axisymmetry with  $B = B(\theta)$  [8.99], quasi-helical symmetry  $B = B(\theta - \phi)$  [8.209] and quasi-poloidal symmetry  $B = B(\phi)$  [8.5] are possible (see Fig. 8.46). Quasi-toroidal symmetry approximates a tokamak, quasi-helical symmetry, where the free coordinate is a linear combination of  $\theta$  and  $\phi$ , approaches a straight stellarator. Strictly speaking quasi-poloidal symmetry is a contradiction to a toroidal magnetic field. However, it can be realized in a weak sense by equilibria using toroidal magnetic mirror components, which for all flux surfaces, including the magnetic axis, yield a large fraction of trapped particles that experience a slow poloidal drift motion only thereby approaching the condition of isodynamicity. Transport optimization concepts in stellarators are summarized in Ref. [8.125].

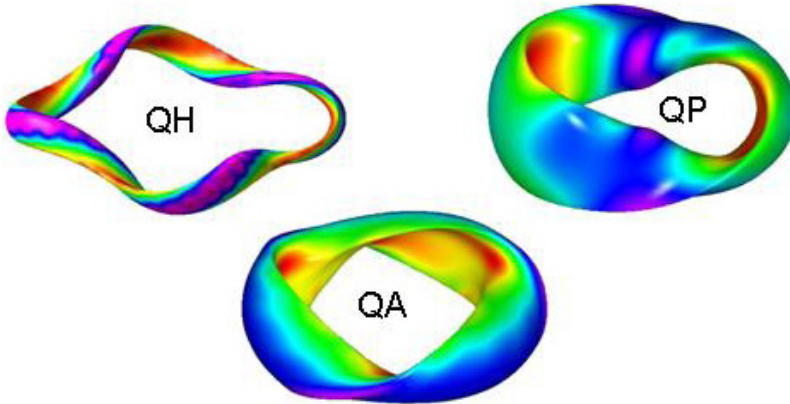


FIG. 8.46.  $|B|$  plots on a flux surface for realizations of a quasi-helical (QH), a quasi-poloidal (QP) and a quasi-axisymmetric (QA) system; HSX, Quasi Poloidal Stellarator (QPS) and NCSX are the associated experimental devices. Blue corresponds to low  $|B|$  and red to high  $|B|$ . Courtesy of D. Spong, Princeton Plasma Physics Laboratory, PPPL, USA.

### 8.5.3. Stability

As already discussed in Section 8.3.3, a reduction of the parallel Pfirsch-Schlüter currents  $\vec{j}_{\parallel}$ , which constitute the geodesic curvature driven instability potential, is beneficial for stability. In a fusion device the plasma should be stable up to about  $\langle\beta\rangle \approx 5\%$  but already the vacuum field should possess a magnetic well which provides MHD stability at low plasma pressure. It is, however, still in question to what extent a magnetic well is necessary already for the vacuum configuration if with rising  $\beta$  the plasma equilibrium reaches stabilizing properties as discussed in Section 8.4.2. A strong reduction of the Shafranov shift also strongly reduces its contribution to the finite  $\beta$  deepening of the magnetic well. Thus, the vacuum magnetic well may be of higher importance in optimization schemes relying strongly on PS current reduction.

### 8.5.4. Integrated optimization concepts

In summary, the properties to be optimized for a reactor relevant design are:

- Good magnetic surfaces of the vacuum field without large islands and stochastic regions in the bulk plasma. This implies *either* low shear (as possible in stellarators or heliacs) at an  $\iota$  value which avoids major resonances *or* a sufficiently large amount of shear (as realized in heliotrons) such that the island size at major rationals is minimized.

- A plasma edge configuration which allows for successful and reliable divertor operation. In a low shear configuration large islands in the boundary region may be used for a divertor. In heliotrons the stochastic region of the helical edge enables a helical divertor.
- Sufficiently low Shafranov shift and a stiff equilibrium configuration up to  $\langle \beta \rangle \approx 5\%$ . A stiff configuration corresponding to minimum toroidal currents requires a minimization of the bootstrap current also. It eases divertor control in particular for low shear configurations where the island divertor configuration sensitively depends on the edge rotational transform.
- MHD-stability up to  $\langle \beta \rangle \approx 5\%$ .
- Sufficiently small neoclassical plasma losses to satisfy the ignition condition together with a low level of turbulence.
- Good confinement of fast alpha particles for at least one slowing down time in order to provide sufficient heating of the thermal plasma and to avoid wall erosion by energetic particles.
- Additional technical conditions such as the feasibility of the coil system, tolerable mechanical forces on the coil system and sufficiently large space between coils and plasma for blanket and shield.

It is not difficult to fulfil one or two of these requirements. Decisive for successful reactor design, however, is the extent to which the different optimization criteria can be fulfilled simultaneously.

In the helical device based on the heliotron concept (see Section 8.2.2) some of the technical difficulties of a classical stellarator are alleviated or removed. In particular, mechanical forces on the helical windings can be significantly reduced. If the magnetic surfaces are inward shifted by a superimposed vertical field neoclassical transport can be reduced along the concept of  $\sigma$  optimization as a first approach to drift optimization (see Section 8.3.5). The resulting low  $\beta$  instability can be stabilized — or at least kept at a tolerable level — in the second stability regime. Although the finite Shafranov shift counteracts this optimization, a maximum  $\langle \beta \rangle \approx 5\%$  could be reached in LHD (see Table 8.1).

In quasi-axisymmetry and quasi-helical symmetry the optimization of neoclassical transport and alpha particle confinement are achieved at the expense of an optimized bootstrap current.

In quasi-axisymmetry [8.99] trapped particles drift toroidally (like tokamak bananas) and a bootstrap current occurs, which *increases* the rotational transform as in a tokamak. Therefore hybrid systems between a tokamak and stellarator can be realized [8.210]. The quasi-axisymmetric National Compact Stellarator Experiment (NCSX) in Princeton is an example [8.4]. An important issue for quasi-axisymmetric configurations is the level of bootstrap current to be tolerated

and how much of the rotational transform has to be applied externally to allow steady state operation without global current driven instabilities.

In quasi-helical symmetry [8.209] trapped particles drift helically and a considerable bootstrap current occurs in the direction which *reduces* the rotational transform. To compensate the reduction of  $\iota$  the poloidal field supplied by the external field coils must be increased, for example by a stronger shaping of the modular coils — an undesired feature for a reactor. Basic properties of this concept are tested in the Helical Symmetric Experiment (HSX) at the University of Wisconsin [8.3].

In contrast, the concept of drift optimization which reduces the radial component of the  $\nabla B$  drift and simultaneously minimizes the Pfirsch–Schlüter currents — both by minimizing the geodesic curvature — allows for an additional optimization of the bootstrap current [8.7]. Minimization of the bootstrap current by balanced helical and toroidal magnetic field components is predicted by neoclassical theory and has experimentally already been demonstrated by the ATF torsatron in Oak Ridge, USA [8.25]. The *bootstrap current* in the *lmfp*-regime vanishes for an MHD equilibrium if the contours of  $|B|$  are poloidally closed and for all trapped particles the 2nd adiabatic invariant  $J$  becomes a function of the magnetic flux only [8.211]. Such a concept minimizes the free energy in the magnetic field by minimizing *all* parallel currents and maintains the optimized field structure largely independent of  $\beta$ .

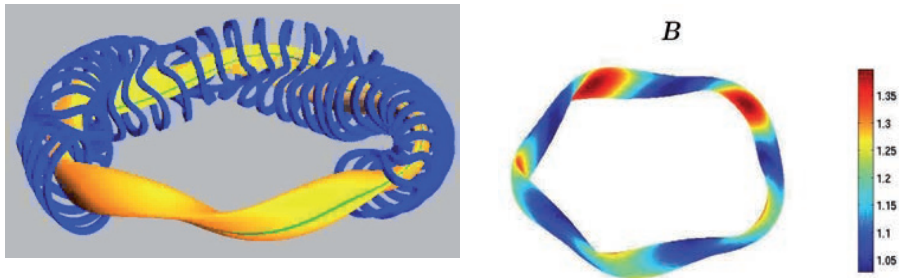


FIG. 8.47. Wendelstein 7-X, a realization of the helias concept. Coil system (left) and (right)  $|B|$ -contours on a flux surface at half radius  $r/a=0.5$ . Courtesy of R. Kleiber, IPP, Greifswald, Germany.

The integration of drift optimization together with a minimization of pressure driven Pfirsch–Schlüter and bootstrap currents resulting in a rather stiff magnetic configuration has led to the helias concept [8.212] developed at IPP in Garching. Following the philosophy of the Wendelstein line a low shear device is chosen which uses boundary islands to limit the plasma by a separatrix and to provide the magnetic islands for a divertor (see Section 8.3.7). The Wendelstein 7-X device (see Fig. 8.47) under construction in Greifswald, Germany, is a

realization of this concept supplied with the capabilities (superconducting coils, steady state heating, actively cooled steady state compatible in-vessel components) to explore steady state high performance operation in all reactor relevant aspects (apart from those connected to internal alpha particle heating).

## 8.6. HELICAL REACTOR CONCEPTS

Extrapolating the classical stellarator to a reactor results in the particular disadvantage that the helices imbedded in a large toroidal magnetic field experience large radial forces, which alternate in direction from one helix to the next. For large devices with significant confining fields mechanical support of the helices becomes a major difficulty as relatively little space is available. Therefore the overall coil performance represents a major element in the reactor design and systems analyses of helical devices. The heliotron [8.213, 8.214] and modular coil configurations [8.36, 8.215], however, show a strong promise in alleviating these mechanical problems.

Another critical design constraint is the small distance between plasma edge and coil inboard side where it is necessary to accommodate a breeding blanket and a sufficient shielding blanket for the coils. For helical devices, constrictions result on the inner side of the torus at those locations where — due to the helical shape of the outermost flux surface — the plasma edge comes particularly close to the coils.

### 8.6.1. Heliotron reactors

In a heliotron the complication with two sets of interwoven windings is eliminated. By a proper choice of the helicity and the number of field periods the forces on the helical windings can be significantly reduced even down to zero (force-free heliotron concept). Furthermore, residual forces tend to point radially outward, so that the support structure is no longer a severe problem. Since one set of windings is used (rather than the winding pairs of a classical stellarator), good access to the plasma vessel is provided.

Helical reactor design studies are based on the LHD concept [8.216] with its natural divertor with two X-points, which helically encircle the plasma. Apart from this helical structure it has many features in common with the tokamak divertor. Two versions of the LHD-type reactor concepts exist: the Force-Free Helical Reactor (FFHR [8.217]) and the Modular Helical Reactor (MHR) [8.218]. The main feature of the FFHR [8.219] is the arrangement of the helical windings in such a way that the forces on them are minimized. This makes it possible to use high magnetic fields of  $B = 12$  T where the required confinement can be achieved already for a moderate  $\langle\beta\rangle$  at which undesirable effects on equilibrium and MHD activity remain tolerable. The FFHR requirements lead to

an  $l = 3$  system with 18 periods, the space required for a blanket sets the major radius to 20 m. A more compact version of the reactor, FFHR2 with  $R = 10$  m,  $l = 2$ ,  $n = 10$  may be considered as an increased version of LHD towards an ignition experiment. In Table 8.3 the major parameters of FFHR1 and FFHR2 are summarized and compared with those of LHD.

In FFHR design, molten salt FLIBE ( $\text{LiF-BeF}_2$ ) has been selected as a self-cooling tritium breeder. There are safety aspects which favour this choice: low tritium solubility, low chemical reactivity with water and air, and low pressure operation. The space available for a blanket is rather narrow, not more than 1 m radial distance is left for blanket and shield, therefore shielding of the superconducting coils against neutron radiation is a critical issue. Large gaps between helical windings are an advantage of the heliotron systems; access to the blanket is easy, and removal and replacement of blanket elements in the reactor should not be difficult.

Parameters	LHD	FFHR	FFHR2
Major radius $R$ [m]	3.9	20	10
Average minor radius $a$ [m]	0.65	2	1.2
Plasma volume $V$ [m <sup>3</sup> ]	32.5	1579	284
Magnetic field $B$ [T]	4	12	10
Average beta $\langle\beta\rangle$ [%]	5	0.7	1.6
Central density $n_e(0)$ [m <sup>-3</sup> ]	$1 \times 10^{20}$	$2 \times 10^{20}$	$2.75 \times 10^{20}$
Temperature $T_e(0)=T_i(0)$ [keV]	10	22	27
Fusion power $P$ [MW]		3000	1000
Polarity $l$	2	3	2
Field periods $N_p$	10	18	10
Stored magnetic energy $W_B$ [GJ]	1.64	1290	147

### 8.6.2. Modular stellarator reactors

In modular stellarators no vertical field coils are required. Therefore the system can be built without any toroidally closed windings, with the confinement

provided solely by the modular coils. Furthermore, there is no force directed inward towards the minor axis. Thus the required mechanical support structures can be located outside and on the sides of the coils. Access for maintenance is complicated due to the strongly shaped coils.

Modular coils offer the chance to realize a large variety of configurations — even those which cannot be achieved by continuous ones — which is desirable in the search for an optimum configuration as described above. As size and weight of modular coils are small enough for shipping, the modular coils do not need to be manufactured on the site of the reactor. Moreover, they can be tested before assembly thus minimizing the risk of failure during operation — a procedure which has been applied to all coils of W7-X.

#### 8.6.2.1. *US compact stellarator power plant study (SPPS)*

The stellarator power plant study SPPS is the first attempt of an integrated design of a stellarator reactor addressing all major components of the plant: the physics base, the coil system, the blanket, maintenance, the power balance and last but not least, the costs. The magnetic configuration of the first study basically is a heliac configuration including elements of optimization as developed for this concept. The MHH (Modular Helias-like Heliac) is a 4-period modular stellarator reactor which has been designed in a joint effort by a group of fusion laboratories in the USA [8.220].

Minimization of the dimensions required for the breeding blanket results for compact stellarators in a blanket concept with liquid lithium as breeder and coolant. To reduce MHD losses of the liquid flowing across the magnetic field the cooling channels are coated with CaO. Low activation vanadium alloys are envisaged as structural material. Although the thermal fusion power is only 2200 MW, the high temperature in the cooling channels (610°C) results in a high thermal efficiency of 46%.

Due to the radiation damage of first wall and blanket components periodic replacement of these parts is necessary. The peak neutron wall loading in the MHH is about  $2 \text{ MW}\cdot\text{m}^{-2}$ , which means that for a maximum acceptable load of  $15 \text{ MW}\cdot\text{a}\cdot\text{m}^{-2}$  the lifetime of the first wall is 7.7 full power years or, at 70% availability, 11 calendar years. In the SPPS study a maintenance scheme is proposed which is based on the horizontal extraction of a sector with coils and blanket through large ports in the cryostat. This maintenance concept makes use of the modular structure of the coil system. However, detailed engineering studies are missing; in particular the process of opening and closing the large ports for extracting the whole sector needs to be clarified. Furthermore, the issues of mechanical stresses in the coils and the support structure of the coils have not been addressed in detail. Since the magnetic field in the coils is rather large, 14.5 T, a Nb<sub>3</sub>Sn superconductor must be used. Blanket and shield in the MHH were

studied in a one-dimensional approximation. Using liquid lithium as breeder and coolant requires a minimum breeding zone of 35 cm and a shield of 80 cm thickness.

The expertise of the MHH studies has been extended to the ARIES-CS concept, which is a compact stellarator reactor with three periods and 7.75 m major radius [8.221], i.e. the size of tokamak reactors. This variant is based on a 3-period quasi-axisymmetric configuration of the NCSX-class, where under ideal conditions charged particles are absolutely confined and neoclassical transport is reduced to a tokamak-like level. A finite bootstrap current is desired (see Section 8.5). The compact structure of the device requires a new approach for the blanket design, as for those regions where the coil–plasma distance is a minimum, a breeding blanket cannot be realized. Instead a tungsten carbide shield keeps energy and neutron fluxes to the coils sufficiently low. The large magnetic field up to 16 T requires Nb<sub>3</sub>Sn superconductors with inorganic insulators, since a heat treatment of the complex coil system is not possible. The support system consists of a massive steel shell with grooves for the superconducting winding packs. Due to this technique the problem of strong forces and stresses can be coped with. Elaborate cost analysis has shown that the cost of electricity of a compact stellarator reactor is competitive with that of an ARIES tokamak reactor [8.222].

#### 8.6.2.2. *The Helias reactor*

The Helias reactor (HSR5/22) [8.223] is an upgraded version of the Wendelstein 7-X experiment [8.6]. Again the dimensions are determined from the necessity to accommodate a blanket and a shield between coils and plasma. The distance between plasma and coils needed for this purpose is of the order of 1.3 m. Furthermore, the ignition condition, based on presently known confinement scaling laws, requires a plasma minor radius of at least 1.8 m. To meet these requirements all dimensions of Wendelstein 7-X must be scaled up by a factor of 4, leading to a major radius of  $R = 22$  m (HSR5/22). The modular coil system comprises 50 coils, which are constructed in a conservative approach using NbTi superconducting cables. Efforts have been made to reduce the magnetic field in the coils by a proper shape of the winding pack. Technical studies have concentrated on the optimization of the coil system with respect to the magnetic field distribution, forces and stresses. Furthermore, the size of the reactor can be decreased by reducing the number of field periods to 4 and the major radius to 18 m, which also reduces the number of modular coils to 40 (HSR4/18) [8.224]. The basic stellarator optimization is maintained. A list of the main parameters of these two devices is given in Table 8.4. HSR4/18 and HSR5/22 are designed as power reactors with a fusion power of 3000 MW. In contrast, the first column in Table 8.4 describes a helias ignition experiment [8.225], HSR 4/18/i (comparable with the first ITER proposal, ITER-FDR) where the fusion power has been

## HELICAL CONFINEMENT CONCEPTS

limited to 1500 MW, the magnetic field on the coils is only 8.5 T; in this case one can operate the cooling cycle at 4.2 K, while in the other cases 1.8 K is required.

TABLE 8.4. MAIN DATA OF HELIAS REACTOR CONFIGURATIONS			
	<b>HSR 4/18/i</b>	<b>HSR4/18</b>	<b>HSR 5/22</b>
Major radius $R$ [m]	18	18	22
Av. minor radius $a$ [m]	2.1	2.1	1.8
Plasma volume $V$ [m <sup>3</sup> ]	1524	1524	1407
Average beta $\langle\beta\rangle$ [%]	3.4	4.2	4.24
Density $n(0)$ [m <sup>-3</sup> ]	2.1	$2.84 \times 10^{20}$	$3.0 \times 10^{20}$
Temperature $T(0)$ [keV]	15	15	15
$\iota(0)$	0.86	0.83	0.84
$\iota(a)$	0.97	0.96	1.00
Av. field on axis [T]	4.4	5	4.75
Max. field on coils [T]	8.5	10.3	10.0
Number of coils	40	40	50
Magnetic energy [GJ]	76	98	100
Fusion power [MW]	1500	3000	3000

### 8.6.3. Concluding remarks

Helical reactor systems offer an alternative to the tokamak approach to magnetic fusion power. Their outstanding advantage is the potential to be operated in steady state without current drive. Helical systems can operate free of net toroidal current and therefore do not suffer from the free energy associated with it.

- Steady state operation would simplify blanket design, since fatigue problems resulting from pulsed thermal loads will be eliminated. As there is no need for current drive the recirculating power in a reactor can be kept small. Plasma confinement during startup is facilitated by the presence of a magnetic confinement right from the beginning.

- Steady state operation implies a need for continuous refuelling, impurity control and ash removal. Several options exist. The magnetic configuration of helical devices possesses a natural separatrix with no need for additional divertor coils. In heliotrons a helical divertor can be used favourably for impurity control. In low shear stellarators the same goal can be achieved by the island divertor.
- These advantages are gained at the expense of a high degree of physics and engineering complexity originating from the three dimensionality of the magnetic field. The concept of stellarator optimization, which, in a first step, has been preferentially applied to physics rather than to engineering issues, points the path to overcome these challenges and obtain a reliable reactor design.

The large spectrum of possible stellarator configurations has not yet allowed identification of a favourite reactor candidate. However, the possible advantages justify further intense research on this alternative path guided by the experimental results from LHD and W7-X.

## ACKNOWLEDGEMENT

The authors of this chapter are most familiar with the results of W7-AS and the features of W7-X. But others also contributed with data and information or by reading chapters of this contribution, which is gratefully acknowledged.

## REFERENCES

- [8.1] SPITZER, L. Jr., *Phys. Fluids* **1** (1958) 253.
- [8.2] MOTOJIMA, O., et al., *Nucl. Fusion* **40** (2000) 599.
- [8.3] CANIK, J.M., et al., *Phys. Plasmas* **14** (2007) 056107.
- [8.4] ZARNSTORFF, M.C., et al., *Plasma Phys. Control. Fusion* **43** (2001) A237–A249.
- [8.5] NELSON, B.E., et al., *Fusion Eng. Des.* **66–68** (2003) 205–210.
- [8.6] BEIDLER, C., et al., *Fusion Technol.* **17** (1990) 148; GRIEGER, G., et al., *Phys. Fluids* **B4** (7) (1992) 2081.
- [8.7] NÜHRENBERG, J., *Plasma Control. Fusion* **52** (2010) 124003; WOBIG, H., *Plasma Phys. Control. Fusion* **41** (1999) A159–73.
- [8.8] WAKATANI, M., et al., *Nucl. Fusion* **40** (2000) 569.
- [8.9] CARY, J.R., LITTLEJOHN, R.G., *Ann. Phys.* **151** (1983) 1.
- [8.10] MOROZOV, A.I., SOLOV'EV, L.S., "The structure of magnetic fields", *Review of Plasma Physics*, Vol. 2 1–110 (LEONTOVICH, M.A., Ed) Consultants Bureau, New York (1963).
- [8.11] COOR, T., et al., *Phys. Fluids* **1** (1958) 411.
- [8.12] YOUNG, K.M., *Plasma Phys.* **16** (1974) 119.
- [8.13] BISHOP, A.S., et al., in *Proc. 2nd Conf. on Plasma Physics and Controlled Nuclear Fusion Research*, Culham, Vol. I (1966), IAEA, Vienna (1966) 479.
- [8.14] SINCLAIR, R.M., et al., *Rev. Sci. Instrum.* **41** (1970) 1552.
- [8.15] PFIRSCH, D., SCHLÜTER, A. *Der Einfluß der elektrischen Leitfähigkeit auf das Gleichgewichtsverhalten von Plasmen niedrigen Drucks in Stellaratoren*, MPI-report MPI/PA/7/62, Garching, Germany (1962).
- [8.16] BERKL, E., et al., in *Proc. 3rd IAEA Int. Conf. Plasma Physics and Controlled Nuclear Fusion Research*, Novosibirsk, Vol. 1 (1969) 513.
- [8.17] CARRERAS, B.A., et al., *Nucl. Fusion* **28** (1988) 1613–1694.
- [8.18] MIYAMOTO, K., *Nucl. Fusion* **18** (1978) 243.
- [8.19] GRIEGER, G., et al., *Nucl. Fusion* **25** (1985) 1231–1242.

## HELICAL CONFINEMENT CONCEPTS

- [8.20] TEAM W7–A, NB GROUP, in Proc, 8th IAEA Conf. on Plasma Physics and Controlled Nuclear Fusion Research, Vienna, Austria, 1980, p.185.
- [8.21] GOURDON, C., et al., in Proc. 3rd IAEA Int. Conf. Plasma Physics and Controlled Nuclear Fusion Research Novosibirsk, Vol. 1 (1968) 847.
- [8.22] UO, K., et al., in Proc. 4th IAEA Int. Conf. Plasma Physics and Controlled Nuclear Fusion Research Madison, Vol. 3 (1971) 109.
- [8.23] BEREZHNYJ, L., et al., in Proc. 12th IAEA Int. Conf. Plasma Physics and Controlled Nuclear Fusion Research Nice, Vol. 2 (1989) 599.
- [8.24] MURAKAMI, M., et al., Recent results from the ATF torsatron, Phys. Fluids **B3** (1991) 2261.
- [8.25] MURAKAMI, M., et al., Phys. Rev. Lett. **66**(6) (1991) 707.
- [8.26] WAKATANI, M., SUDO, S., Plasma Phys. Control Fusion **38** (1996) 937–988.
- [8.27] UO, K., et al., in Proc. 10th Conf. on Plasma Phys. and Controlled Nuclear Fusion Research, London, Vol. 2, IAEA, Vienna (1985) 383.
- [8.28] SANO, F., in Proc. 21st IAEA Fusion Energy Conf., Chengdu, Peoples Republic of China (2006) EX/5–5Ra.
- [8.29] MORISAKI, T., et al., J. Nucl. Mater **241–243** (1997) 977.
- [8.30] LHD TEAM, Fusion Sci. Technol., Special Issue **58** (2010).
- [8.31] KOMORI, A., et al., Nucl. Fusion **45** (2005) 837.
- [8.32] MOTOJIMA, O., et al., Nucl. Fusion **47** (2007) S668.
- [8.33] HIRSCH, M., et al., Plasma Phys. Control. Fusion. **50** (2008) 053001.
- [8.34] BLACKWELL, B.D., et al., in Proc. 21st IAEA Fusion Energy Conf., Chengdu, (2006), EX/P6–3.
- [8.35] SANCHEZ, J., et al., Nucl. Fusion **47** (2007) S668.
- [8.36] WOBIG, H., REHKER, S., in Proc. 7th Symp. on Fusion Technology, Grenoble, France (1972) 333–343.
- [8.37] CANIK, J.M., in Proc. 21st IAEA Fusion Energy Conf., Chengdu, Peoples Rep. of China (2006) EX5/2.
- [8.38] MAASSBERG, H., et al., Plasma Phys. Control. Fusion **47** (2005) 1137.

- [8.39] FISCH, N.J., BOOZER, A.H., Phys. Rev. Lett. **45** (1980) 720.
- [8.40] ROME, M., et al., Plasma Phys. Control. Fusion **45** (2003) 783–792.
- [8.41] HARVEY, R.W., DENDY, R., Phys. Fluids **B4** (1992) 902.
- [8.42] ERCKMANN, V., et al., Fusion Eng. Des. **26** (1995) 141.
- [8.43] LAQUA, H.P., et al., Phys. Rev. Lett. **78** (1997) 3467.
- [8.44] LAQUA, H.P., et al., Phys. Rev. Lett. **90** (2003) 075003.
- [8.45] HOOKE, W.M., et al., Nucl. Fusion Suppl. Part **3** (1962) 1083.
- [8.46] KWON, M., et al., Nucl. Fusion **7** (1992) 1225.
- [8.47] MASUDA, S., et al., Nucl. Fus. **37** (1997) 53.
- [8.48] OKADA, H., et al., Nucl. Fus. **36** (1996) 465.
- [8.49] SAITO, K., et al., Plasma Phys. Control. Fusion **44** (2002) 103.
- [8.50] OKADA, H., et al., Nucl. Fusion **47** (2007) 1346.
- [8.51] HARTMANN, D.A., CATTANEI, G., BRAUN, F., et al., Radiofrequency power in plasmas, in Proc. 12th Topical Conf. AIP, Savannah, GA, USA, **403** (1998) 49–56.
- [8.52] WATARI, T., Plasma Phys. Control. Fusion **40** (1998) A13.
- [8.53] STIX, T., et al., Phys. Fluids **1** (1958) 446.
- [8.54] HARTMANN, D.A., et al., in Proc. 12th Int. Stellarator Workshop, Madison, Wisconsin, (1999), publication available on CD only.
- [8.55] WOBIG, H., Plasma Phys. Control. Fusion **35** (1993) 903–917.
- [8.56] PALUMBO, D., Nuovo Cimento X **53** (1968) 507.
- [8.57] BOOZER, A.H., Rev. Mod. Phys. **76** (2004) 1071–1141.
- [8.58] HIRSHMAN, S.P., VAN RIJ, W.I., MERKEL, P., Three-dimensional free boundary calculations using a spectral Green's function method, Comput. Phys. Commun. **43** (1986) 143–155.
- [8.59] STRUMBERGER, E., Finite- $\beta$  magnetic field line tracing for Helias configurations, Nucl. Fusion **37** (1997) 19–27.
- [8.60] REIMAN, A., GREENSIDE, H., Comp. Phys. Commun. **43** (1986) 157–167.
- [8.61] SUZUKI, Y., et al., Nucl. Fusion **46** (2006) L19–L24.
- [8.62] HARAFUJI, K., et al., J. Comput. Phys. **81** (1989) 169–192.

- [8.63] PARK, W. MONTICELLO, D.A., STRAUSS, H., MANICKAM, J., Three-dimensional stellarator equilibrium as an ohmic steady state, *Phys. Fluids* **29** (1986) 1171–1175.
- [8.64] YAMADA, H., et al., *Nucl. Fusion* **32** (1992) 25–32.
- [8.65] BERNSTEIN, I.B. et al., *Proc. R. Soc.* **A244** (1958) 17;  
*http://rspa.royalsocietypublishing.org*
- [8.66] GREENE, J.M., JOHNSON, J.L., *Plasma Phys.* **10** (1968) 729–745.
- [8.67] FREIDBERG, J.P., *Ideal Magneto-hydrodynamics*, Plenum Press, New York and London (1987).
- [8.68] BATEMAN, G., *MHD Instabilities*, The MIT Press, Cambridge, Massachusetts and London (1978).
- [8.69] GREENE, J.M., JOHNSON, J.L., *Phys. Fluids* **5**(5) (1962) 510–517.
- [8.70] MERCIER, C., *Nucl. Fusion Suppl.* **2** (1962) 801.
- [8.71] ICHIGUCHI, K., et al., *Nucl. Fusion* **33**(3) (1993) 481–492.
- [8.72] WATANABE, K.Y., et al., *Nucl. Fusion* **45** (2005) 1247–125.
- [8.73] WELLER, A., et al., *Fusion Sci. Technol.* **50** (2006) 158–70.
- [8.74] CUTHBERT, P., et al., *Phys. Plasmas* **5** (1998) 2921–2931.
- [8.75] NAKAJIMA, N., et al., *Phys. Fluids* **B4** (1992) 1115–1121.
- [8.76] SCHWAB, C., *Phys. Fluids* **B5** (1993) 3195–3206.
- [8.77] ANDERSON, D.V., et al., *Int. J. Supercomput. Appl.* **4**(3) (1990) 34–47.
- [8.78] COOPER, W.A., et al., *Nucl. Fusion* **46** (2006) 683–698 ; COOPER, W.A., et al., *Plasma Phys. Control. Fusion* **49** (2007) 1177–1191.
- [8.79] NÜHRENBERG, C., *Phys. Plasmas* **3**(6) (1996) 2401–2410.
- [8.80] ALFVEN, H., *Nature* **150** (1942) 405–406.
- [8.81] HEIDBRINK, W.W., et al., *Physics of Plasmas* **6** (1999) 1147–1161.
- [8.82] SALAT, A., *Plasma Phys. Control. Fusion* **34** (1992) 1339–1357.
- [8.83] APPERT, K., et al., *Plasma Phy.* **24** (1982) 1147–1159.
- [8.84] WELLER, A., et al., *Phys. Rev. Lett.* **72** (1994) 1220–1223.
- [8.85] SPONG, D.A., et al., in *Proc. 22nd IAEA Fusion Energy Conference*, Geneva, Switzerland IAEA, (2008) CN-165 TH/3–4.
- [8.86] YAMAMOTO, S., *Nucl. Fusion* **45** (2005) 326–336.

- [8.87] YAKOVENKO, Y., et al., *Plasma Phys. Control. Fusion* **49** (2007) 535–558.
- [8.88] WELLER, A., et al., *Plasma Phys. Control. Fusion* **45** (2003) A285–A308.
- [8.89] YAMAMOTO, S., et al., *Nucl. Fusion* **45** (2005) 326–336.
- [8.90] KOLESNICHENKO, Y.I., et al., *Nucl. Fusion* **42** (2002) 949–958.
- [8.91] KOLESNICHENKO, Y.I., et al., *Phys. Plasmas* **11** (2004) 158–170.
- [8.92] KONIES, A., *Phys. Plasmas* **7** (2000) 1139–1147.
- [8.93] ISOBE, M., et al., *Nucl. Fusion* **46** S9 (2006) 18–S925.
- [8.94] LUTSENKO, V.V., et al., in *Proc. 19th IAEA Fusion Energy Conference Lyon IAEA, (2002) CN–94 TH/P3–16*.
- [8.95] WELLER, A., et al., *Phys. Plasmas* **8** (2001) 931–956.
- [8.96] TOI, K., et al., *Plasma Phys. Control. Fusion* **46** (2004) S1–S13.
- [8.97] OSAKABE, M., et al., *Plasma Phys. Control. Fusion* **46** (2006) S911–S917.
- [8.98] YAMAMOTO, S., et al., *Fusion Sci. Technol.* **51** (2007) 92–96.
- [8.99] NÜHRENBERG, J.N., et al., *Theory of Fusion Plasma*, Editrice Compositori, Bologna, 1994, Varenna, Italy (1994) p. 3–12.
- [8.100] ZUSHI, H., et al., *J. Phys. Soc. Jpn.* **57** (1988) 3009–3019.
- [8.101] SAKAKIBARA, S., et al., *Jpn. J. Appl. Phys.* **34** (1995) L252–L255.
- [8.102] JAENICKE, R., et al., *Nucl. Fusion* **20** (1980) 1093–1100.
- [8.103] SALLANDER, E., et al., *Nucl. Fusion* **40** (2000) 1499–1509.
- [8.104] BLAUMOSER, M., et al., in *Proc. 6th Int. Conf. on Plasma Physics and Controlled Nuclear Fusion Research Berchtesgaden, West Germany Vol. 2 (1976) CN–35/D2 81–92*.
- [8.105] NAGAYAMA, Y., et al., *Phys. Rev. Lett.* **90** (2003) 205001.
- [8.106] HARRIS, J.H., et al. *Phys. Rev. Lett.* **53** (1984) 2242–224.
- [8.107] GALEEV, A.A., et al., *Phys. Rev. Lett.* **22** (1969) 511.
- [8.108] GALEEV, A.A., SAGDEEV, R.Z., *Rev. Plasma Phys.* **7** (1977) 307.
- [8.109] KOVRIZHNYKH, L.M., *Nucl. Fusion* **24** (1984) 851.
- [8.110] BOOZER, A.H., *Phys. Fluids* **23** (1980) 904.

- [8.111] FOWLER, R.H., ROME, J.A., LYON, J.F., *Phys. Fluids* **28** (1985) 338.
- [8.112] BOOZER, A.H., KUO-PETRAVIC, G., *Phys. Fluids* **24** (1981) 851.
- [8.113] VAN RIJ, W.I., HIRSHMAN, S.P., *Phys. Fluids B* **1**(3) (1989) 563–569.
- [8.114] MAASSBERG, H., et al., *Phys. Fluids B* **5** (10) (1993) 3627.
- [8.115] SPITZER, L., HÄRM, R., *Phys. Rev.* **89** (1953) 977.
- [8.116] SUGAMA, H., NISHIMURA, S., *Phys. Plasmas* **15** (2008) 042502.
- [8.117] MAASSBERG, H., BEIDLER, C.D., TURKIN, Y., *Phys. Plasmas* **16** (2009) 072504.
- [8.118] NÜHRENBERG, J., ZILLE, R., *Theory of Fusion Plasmas*, Varenna, Editrice Compositori, 3. 1987.
- [8.119] MYNICK, H.E., et al., *Phys. Rev. Lett.* **48** (1982) 322.
- [8.120] BEIDLER, C.D., et al., *Nucl. Fusion* **51** (2011) to be published.
- [8.121] YOKOYAMA, M., et al., *Nucl. Fusion* **47** (2007) 1213.
- [8.122] ITOH, K., et al., *Phys. Plasmas* **14** (2007) 020702.
- [8.123] WAGNER, F., et al., *Plasma Phys. and Control. Fusion.* **48** (2006) A217–A239.
- [8.124] ENDLER, M., et al., *J. Nucl. Mater.* **266–269** (1999) 84–90.
- [8.125] MYNICK, H.E., *Phys. Plasmas* **13** (2006) 058102.
- [8.126] WATANABE, T.H., et al., *Phys. Rev. Lett.* **100** (2008) 195002.
- [8.127] ERCKMANN, V., et al., *Phys. Rev. Lett.* **70** (1993) 2086.
- [8.128] STROTH, U., et al., *Nucl. Fusion* **36** (1996) 1063.
- [8.129] STROTH, U., et al., *Phys. Scri.* **51** (1995) 655.
- [8.130] LACKNER, K., GOTTARDI, N., *Nucl. Fusion* **30** (1990) 767.
- [8.131] ITER Physics Expert Groups, ITER Physics Basis Editors, ITER EDA, Physics Basis Document, *Nucl. Fusion* **39** (1999) 2232.
- [8.132] WAGNER, F., et al., *Phys. Plasmas* **12** (2005) 072509.
- [8.133] YAMADA, H., et al., *Nucl. Fusion* **45** (2005) 1684–1693.
- [8.134] YAMADA, H., et al., *Nucl. Fusion* **41** (2001) 901.
- [8.135] XANTHOPOULOS, P., et al., *Phys. Rev. Lett.* **99** (2007) 035002.
- [8.136] CONNOR, J.W., TAYLOR, J.B., *Nucl. Fusion* **17** (1977) 1048.

- [8.137] KADOMTSEV, B.B., *Sov. J. Plasma Phys.* **1** (1975) 295.
- [8.138] LUCE, T.C., et al., *Plasma Phys. Control. Fusion* **50** (2008) 043001.
- [8.139] PREUSS, R., et al., *Nucl. Fusion* **39** (1999) 849.
- [8.140] DOSE, V., et al., *Phys. Rev. Lett.* **81** (1989) 3407.
- [8.141] PREUSS, R., et al., *Phys. Rev. Lett.* **99** (2007) 245001.
- [8.142] WELLER, A., et al., *Nucl. Fusion* **49** (2009) 065016.
- [8.143] DINKLAGE, A., et al., *Nucl. Fusion* **47** (2007) 1265.
- [8.144] YAMADA, H., *Plasma Phys. Control. Fusion* **49** (2007) B487–B49.
- [8.145] RYTER, F., et al., *Plasma Phys. Control. Fusion* **43** (2001) A323.
- [8.146] WAGNER, F., et al., *Phys. Rev. Lett.* **56** (1986) 2187.
- [8.147] BRAKEL, R., et al., *Nucl. Fusion* **42** (2002) 903.
- [8.148] BRAKEL, R., et al., *Plasma Phys. Control. Fusion* **39** (1997) B273.
- [8.149] ASCASIBAR, H., et al., *Plasma Fusion Res.* **3** (2008) S1004.
- [8.150] RENNER, H., et al., in *Proc. 19th Int. Conf. on Controlled Fusion and Plasma Physics*, Innsbruck, (Geneva: European Physical Society) **16C** part I (1992) 501.
- [8.151] IDA, K., et al., *Phys. Rev. Lett.* **88** (2002) 015002.
- [8.152] ESTRADA, T., et al., *Plasma Phys. Control. Fusion* **47** (2005) L57;  
ESTRADA, T., et al., *Nucl. Fusion* **47** (2007) 305.
- [8.153] De BAAR, M.R., et al., *Phys. Rev. Lett.* **78** (1987) 4573.
- [8.154] McCORMICK, K., et al., *Phys. Rev. Lett.* **89** (2002) 15001.
- [8.155] REITER, D., et al., *Nucl. Fusion* **30** (1990) 2141.
- [8.156] BURHENN, R., et al., *Nucl. Fusion* **49** (2009) 065005.
- [8.157] NOZATO, H., et al., *Rev. Sci. Instrum.* **76** (2005) 073503.
- [8.158] MUTO, S., et al., *Plasma Fusion Res.* **2** (2007) S1069.
- [8.159] SUDO, S., et al., *Plasma Phys. Control. Fusion* **44**(3) (2002) 129.
- [8.160] BURHENN, R., et al., *Rev. Sci. Instrum.* **70** (1999) 603.
- [8.161] W7–A TEAM, NI GROUP, *Nucl. Fusion* **25**(11) (1985) 1593.
- [8.162] BURHENN, R., et al., *Fus. Sci. Technol.* **46** (2004) 115.
- [8.163] HIDALGO, C., et al., *Nucl. Fus.* **45** (2005) S266.

- [8.164] TAMURA, N., et al., Plasma Phys. Control. Fusion **45**(1) (2003) 27.
- [8.165] MORITA, S., et al., Plasma Sci. Technol. **8**(1) (2006) 55.
- [8.166] NOZATO, H., et al., Phys. Plasmas **13**(5) (2006) 092502.
- [8.167] NAKAMURA, Y., et al., Nucl. Fusion **43** (2003) 219.
- [8.168] KANEKO, H., et al., Nucl. Fusion **27**(7) (1987) 1075.
- [8.169] IDA, K., et al., Nucl. Fus. **45** (2005) 391.
- [8.170] GIANNONE, L., et al., Plasma Phys. Control. Fusion **42** (2000) 603.
- [8.171] ERCKMANN, V., et al., Plasma Phys. Control. Fusion **36**(12) (1994) 1869.
- [8.172] KOBAYASHI, M., Contrib. Plasma Phys. **48**(1–3) (2008) 255.
- [8.173] FENG, Y., et al., Nucl. Fusion **46** (2006) 807.
- [8.174] BELONOHY, E., et al., in Proc. 34th EPS Conf., Warsaw, Poland (2007) P2.046.
- [8.175] MORISAKI, T., et al., Phys. Plasmas **14** (2007) 056113–1.
- [8.176] TAMURA, N., et al., in Proc. Joint Conf. 17th Int. Toki Conf. and 16th Int. Stellarator/Heliotron Workshop, Toki, Japan, 2007, paper P1–069.
- [8.177] IDA, K., et al., Phys. Plasmas **16** (2009) 056111.
- [8.178] KÖNIG, R., et al., Fus. Sci. Technol. **46** (2004) 152.
- [8.179] MORISAKI, T., et al., Plasma Sci. Technol. **8** (2006) 14.
- [8.180] MIYAZAWA, J., et al., Nucl. Fusion **46** (2006) 532.
- [8.181] OHYABU, N., et al., Nucl. Fusion **34** (1994) 387.
- [8.182] GRIGULL, P., et al., Plasma Phys. Control. Fusion **43** (2001) A175.
- [8.183] RENNER, H., et al., Nucl. Fusion **40** (2000) 1083.
- [8.184] STANGEBY, P.C., et al., Nucl. Fusion **33** (1993) 1695.
- [8.185] FENG, Y., et al., J. Nucl. Mat. **266–269** (1999) 812.
- [8.186] REITER, D., Technical Report Jül–1947, KFA Jülich, Germany, 1984.
- [8.187] KOBAYASHI, M., et al., 2007 J. Nucl. Mater. 363–365 294
- [8.188] FENG, Y., et al., Nucl. Fusion **48** (2008) 024102.
- [8.189] WENZEL, U., et al., Plasma Phys. Control. Fusion **44** (2002) L57.
- [8.190] THOMSEN, H., et al., Nucl. Fusion **44** (2004) 820.

- [8.191] FENG, Y., et al., Nucl. Fusion **45** (2005) 89.
- [8.192] FENG, Y., et al., Nucl. Fusion **49** (2009) 095002.
- [8.193] KISSLINGER, J., et al., in Proc. 22nd EPS Conf. on Controlled Fusion and Plasma Physics, Bournemouth, UK **19C** II (1995) 149.
- [8.194] CHOWDHURI, M.B., et al., Phys. Plasmas **16** (2009) 062502.
- [8.195] RAMASUBRAMANIAN, N., et al., Nucl. Fusion **44** (2004) 992.
- [8.196] GREENWALD, M., et al., Nucl. Fusion **28** (1988) 2199.
- [8.197] GIANNONE, L., et al., Plasma Phys. Control. Fusion **45**(9) (2003) 1713–1731.
- [8.198] SUDO, S., et al., Nucl. Fusion **30** (1990) 11–21.
- [8.199] MIYAZAWA, J., et al., Nucl. Fusion **48** (2008) 015003.
- [8.200] OHYABU, N., et al., Phys. Rev. Lett. **97** (2006) 05502.
- [8.201] ITER Physics Expert Groups, ITER Physics Basis Editors, ITER EDA, Physics Basis Document, Chapter 3: "MHD stability, operational limits and disruptions", Nucl. Fusion **39** (1999) 2251–2389.
- [8.202] TROYON, F., et al., Plasma Phys. Control. Fusion **26** (1984) 209–215.
- [8.203] STRAIT, E.J., Phys. Plasmas **1** (1994) 1415–1431.
- [8.204] SUZUKI, Y., et al., in Proc. 22nd IAEA Fusion Energy Conference, Geneva, Switzerland IAEA, (2008) CN–165 TH/P9–19.
- [8.205] REIMAN, A., et al., Nucl. Fusion **47** (2007) 572–578.
- [8.206] SUZUKI, Y. WATANABE, K.Y., SAKAKIBARA, S., NAKAJIMA, N., OHYABU, N., Theoretical studies of equilibrium beta limit in heliotron plasmas, National Institute for Fusion Science, Toki, Japan, 22nd IAEA FEC conference, Geneva, Switzerland, 2008, TH/P9–19.
- [8.207] OHDACHI, S., et al., in Proc. 22nd IAEA Fusion Energy Conference, Geneva, Switzerland, 2008, EX/8–1Rb.
- [8.208] GARREN, D.A., BOOZER, A.H., Phys. Fluids B **3** (1991) 2822.
- [8.209] NÜHRENBERG, J., ZILLE, R., Phys. Lett. **A129** (1992) 113–117; LOTZ, W., et al., Plasma Phys. Control. Fusion **34** (1992) 1034.
- [8.210] BOOZER, A.H., Plasma Phys. Control. Fusion **50** (2008) 124005.
- [8.211] SUBBOTIN, A., et al., Nucl. Fusion **46** (2006) 921–927.
- [8.212] NÜHRENBERG, J., ZILLE, R., Phys. Lett. **A 114** (1986) 129–136.

- [8.213] GOURDON, C., et al., Nucl. Fusion **11** (1971) 161–166.
- [8.214] POLITZER, P.A., et al., Massachusetts Institute of Technology Report PFC/TR–79–1, 1979.
- [8.215] MILLER, R.L., KRAKOWSKI, R.A., Los Alamos National Laboratory Report, June 1983, LA–97–37–MS.
- [8.216] IIYOSHI, A., et al., Fusion Technol. **17** (1990) 169.
- [8.217] SAGARA, A., et al., Fusion Eng. Des. **41** (1998) 349.
- [8.218] YAMAZAKI, K., WATANABE, K.Y., Nucl. Fusion **35**(10) (1995) 1289.
- [8.219] SAGARA, A., et al., Fusion Eng. Des. **81** (2006) 2703–2712.
- [8.220] Stellarator power plant study (1997) UCSD–ENG–004.
- [8.221] NAJMABADI, F., et al., Fusion Sci. Technol. **54**(3) (2008) 655–672.
- [8.222] The Aries I Tokamak Reactor Study, Final report, University of California, 1991, UCLA–PPG–1323 Volume II.
- [8.223] KISSLINGER, J., et al., in Proc. 17th Int. Conf. on Plasma Physics and Controlled Nuclear Fusion Research, Yokohama **IV** (1998) 1239–42.
- [8.224] BEIDLER, C., et al., Nucl. Fusion **41** (2001) 1759.
- [8.225] WOBIG, H., et al., Nucl. Fusion **43** (2003) 889–898.

## CHAPTER 9

# THE BROADER SPECTRUM OF MAGNETIC CONFIGURATIONS FOR FUSION

**S.C. Prager**

Princeton Plasma Physics Laboratory,  
Princeton, New Jersey

**D.D. Ryutov**

Lawrence Livermore National Laboratory,  
Livermore, California

United States of America

### 9.1. INTRODUCTION

The development of magnetic configurations to confine plasmas for fusion energy is a challenge that is a mixture of basic physics, engineering and invention. To optimize a configuration one has to examine effects on a wide range of physical features including single particle behaviour, equilibrium, stability, pressure, turbulent transport and sustainment. These features can be considered as outputs of an optimization. These outputs are affected by many aspects of the magnetic field (or inputs to the optimization), including spatial symmetries, curvature, shear, pitch and spatial gradients. In addition, plasma behaviour is affected by the spatial dependence of other quantities (such as temperature and density), as well as velocity-space effects. Thus, the number of degrees of freedom in magnetic confinement science is very large and the evolution of configurations attractive for fusion energy is a rich scientific endeavour. The study of multiple configurations is an invaluable tool to develop fusion plasma physics. By investigating multiple configurations, physics of general use to the fusion programme can be learned that is not accessible through the study of one configuration only.

The set of fusion configurations that have been studied form an almost continuous spectrum of magnetic geometries. The practice of assigning a name to many points on the spectrum, while useful, eclipses the physics links between the different configurations. An axisymmetric torus with helical field lines that are loosely wrapped around the torus (with safety factor  $q > 1$ ) and with moderate aspect ratio (major to minor radii about 3 or above) defines the tokamak. If the aspect ratio is reduced, to about 2 or below, it is sometimes known as the spherical tokamak. If the toroidal field of a tokamak is reduced by a factor of 10, the configuration is known as a reversed field pinch. If the aspect ratio of the reversed field pinch is reduced to unity (the hole in the

centre vanishes), one arrives at a spheromak. And if the toroidal field of the spheromak is set to zero, the configuration turns into a field reversed configuration.

A similar sequence can be described for open systems. A simple mirror configuration is a linear configuration in which the two ends are bounded by regions of strong magnetic field (mirrors) that prevent plasma from escaping out the ends. If the field at the end is allowed to expand over a relatively large distance, the configuration is known as a gas dynamic trap. However, if extra plugs containing hot plasma are attached to the end, beyond the mirrors, the configuration is known as a tandem mirror.

These sometimes odd names have some physics and historical relevance, but they give the appearance of a plethora of unrelated concepts, obscuring the grand challenge that they present — to develop a predictive understanding of fusion plasmas confined by magnetic fields. The tokamak is the most highly developed point on the spectrum and is the vehicle by which we will demonstrate and investigate the science of burning plasmas. The stellarator is the next most highly developed configuration, offering the potential advantages of steady-state and disruption-free operation. This chapter is devoted to the remainder of magnetic configurations, some highly developed, some just now emerging, but all less developed than the stellarator. Each has its own potential advantages and disadvantages in terms of fusion and complementary physics features.

We have chosen to emphasize configurations roughly in proportion to their level of development. Some of the configurations are actively being developed today, some have reached, at least for now, the end of their evolution. Our purpose is to introduce the rudimentary physics of each configuration so that the reader can appreciate the present state of knowledge of magnetic configurations and hopefully be stimulated to continue the evolution of configurations towards fusion application.

In Section 9.2 we describe the reversed field pinch, the configuration most heavily studied (after the tokamak and stellarator) at the time of this writing. Compact tori (spheromaks and field reversed configurations) are assessed in Section 9.3. The class of open confinement systems is considered in Section 9.4. A range of other inventive configurations, much less developed, are described in Section 9.5. We give a brief summary in Section 9.6.

### 9.2. REVERSED FIELD PINCH: TOROIDAL CONFINEMENT AT WEAK MAGNETIC FIELD

The reversed field pinch (RFP) is a toroidal configuration with helical magnetic field lines that is confined by a very weak toroidal magnetic field [9.1] Roughly speaking, if one considers a tokamak and then reduces the toroidal field by a factor of 10, the plasma will assume the configuration of a reversed field pinch. It is similar to a tokamak, but the field lines are much more strongly

wrapped around the torus and the applied toroidal field is between 10 and 100 times weaker than that of a tokamak. The name derives from the feature that the toroidal field decreases with radius from the plasma centre and reverses direction near the plasma edge. All of the interest in the RFP stems from the weak toroidal magnetic field. This leads to a string of potential engineering advantages (if physics challenges can be overcome) and it extends our understanding of toroidal magnetic confinement by confronting phenomena in the weak field limit.

The RFP offers the potential for high engineering beta, the use of normal (rather than superconducting) coils, high mass power density, efficient assembly and disassembly and possibly free choice of aspect ratio, as indicated below.

- *High engineering beta:* The physics beta of the RFP (in which the volume-averaged pressure is normalized to the magnetic pressure at the plasma surface) is automatically high since the toroidal field is weak. But a more germane measure for fusion energy application is the engineering beta, in which the magnetic field pressure is measured at the coils. For a tokamak, the distinction is small since the dominant field varies weakly with radius. For the RFP, the poloidal field is dominant, and decays inversely with radius. For typical reactor designs the engineering beta can be roughly twice the physics beta.
- *Normal magnets:* Superconducting magnets are not necessary, eliminating the need for neutron shielding of the magnets.
- *High mass power density:* The high engineering beta and normal coils lead to a reactor system with a high ratio of fusion power to the reactor system mass (relative to other toroidal systems with aspect ratios greater than unity). This is a favourable economic indicator.
- *Single piece maintenance:* The high mass power density yields a compact design (relative to other toroidal systems) that enables the fusion power core to be removed from the plant as a single piece. This facilitates system maintenance, a significant factor in reactor reliability and the cost of electricity.
- *Possibly free choice of aspect ratio:* To date, the physics of the RFP does not depend strongly on aspect ratio. Thus, the choice of aspect ratio can be made on engineering grounds. There might be some physics advantage to lower aspect ratio (where the number of unstable tearing modes decrease), but this feature has not yet been explored in detail.

These advantages have been validated through the relatively comprehensive TITAN system study [9.2] that was completed around 1990. However, the study was predicated on a set of physics assumptions. It is the understanding and achievement of these physics assumptions, combined with new approaches to RFP development, that is the main subject of this section.

A comprehensive understanding of toroidal magnetic confinement would imply that plasma behaviour would be predictable over a wide range of magnetic field strengths (or safety factors). Generally, the RFP (with  $q < 1$ ) provides new information since it extends our understanding to low field strength, testing the understanding derived at high field. Since the safety factor is less than unity (a result of the weak field), the RFP is vulnerable to resistive MHD instabilities that enhance transport and alter the large-scale field (and other quantities) in the plasma. The RFP is sometimes described as undergoing strong magnetic self-organization [9.3]. In the first part of this section we describe our understanding of the rather intriguing process of magnetic self-organization in the “standard RFP”. We first describe the ideal MHD equilibrium and stability of the RFP (Section 9.2.1). The self-organization process (Section 9.2.2) requires the influence of resistivity. The MHD model of self-organization is highly developed, and provides an explanation of why the magnetic field reverses. We describe a heuristic view of the process (based on a minimum energy state argument) and summarize the key points of the full non-linear MHD dynamical process that rearranges the field (sometimes known as the “dynamo effect”). The instabilities that cause the field rearrangement also cause the magnetic field lines to develop a level of stochastic wandering. In Section 9.2.3 we describe the origin of magnetic stochasticity and its harmful effect on plasma confinement. The description to this point characterizes what we refer to as the standard RFP.

For much of the history of RFP research, the RFP was plagued by magnetic field stochasticity and poor confinement. However, understanding of these processes has led to the development of techniques to suppress the stochasticity and improve confinement, such that the standard RFP can now be considered obsolete. The remainder of this section reflects the emerging view of the RFP subjected to these new techniques. In Section 9.2.4 we describe the physical basis and results of improving confinement to the extent that the residual transport is likely dominated by electrostatic fluctuations (with magnetic fluctuations playing only a minor role). While beta limits are already at reactor levels for the RFP, the ultimate beta limit is not yet known. The physics of the RFP beta limit is given in Section 9.2.5. The RFP experiences substantial instabilities that would occur in the absence of a surrounding conducting shell. The appearance and feedback stabilization of these “resistive wall instabilities” is described in Section 9.2.6. Finally, remaining is the thorny issue of sustainment of the RFP configuration. Techniques for sustainment are discussed in Section 9.2.7.

### 9.2.1. The configuration: ideal MHD equilibrium and stability

The ideal MHD RFP equilibrium differs from that of a tokamak only in the toroidal magnetic field — its magnitude and variation with radius. Like the tokamak, the RFP equilibrium magnetic field is axisymmetric and helical. The

field is produced by helical currents consisting of a component parallel to the magnetic field and a perpendicular diamagnetic current. The equilibrium fields are shown in Fig. 9.1. The poloidal field is produced by toroidal currents, and has the same form as for a tokamak. However, the toroidal field monotonically decreases with radius, passes through zero near the plasma edge, and thereafter reverses direction (hence the name RFP). The toroidal field decreases with radius due to the poloidal current flowing in the plasma. The central value of the toroidal field is about ten times weaker than that of a tokamak with a similar current.

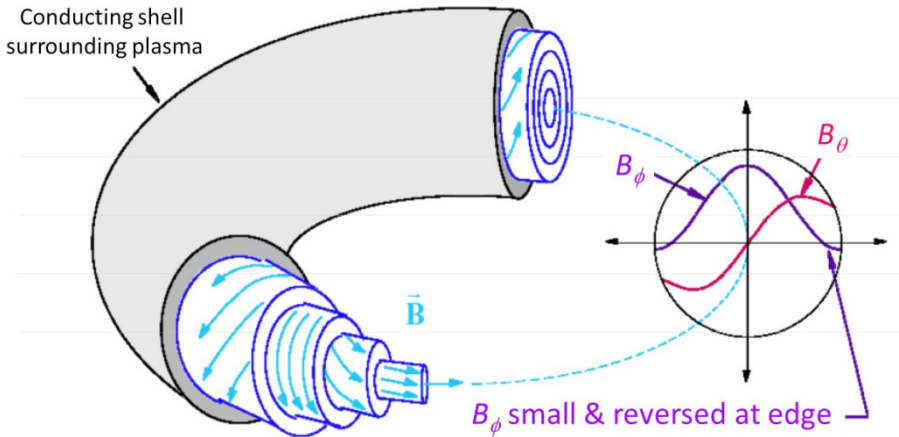


FIG. 9.1. Schematic of magnetic field lines in the RFP, and radial dependence of toroidal and poloidal magnetic fields.

A simple analytic expression can be derived which approximately describes the RFP equilibrium in a cylinder. For a plasma satisfying MHD force balance

$$\vec{j} \times \vec{B} = \nabla p \tag{9.1}$$

The pressure gradient term affects the magnetic field structure through the perpendicular diamagnetic current. For most RFP plasmas, the diamagnetic current is smaller than the parallel current, so that an approximate solution for magnetic field can be obtained by neglecting the pressure gradient. In this case the current flows parallel to the magnetic field ( $\vec{j} \times \vec{B} = 0$ ) or

$$\nabla \times \vec{B} = \lambda(r)\vec{B} \tag{9.2}$$

where we have considered a cylindrical equilibrium in which the magnetic field depends on radius only, but has components in the  $\theta$  (“poloidal”) and  $z$  (“toroidal”) directions. For analytic simplicity we assume that the arbitrary

function  $\lambda$  is constant in radius (a case discussed further below). This special case results in two coupled equations:

$$\frac{dB_z}{dr} = -\lambda B_\theta \quad (9.3)$$

$$\frac{1}{r} \frac{d(rB_\theta)}{dr} = \lambda B_z \quad (9.4)$$

These equations combine to yield Bessel's equation with the solution

$$B_\theta(r) = B_0 J_1(\lambda r) \quad (9.5)$$

$$B_z(r) = B_0 J_0(\lambda r) \quad (9.6)$$

where  $J_0$  and  $J_1$  are Bessel functions (zero and first order) and  $B_0$  and  $\lambda$  are constants. These functions are oscillatory in radius. If we consider that the surface of the plasma resides just beyond the first zero of  $J_0$ , then the fields very well resemble those of the RFP (Fig. 9.1). The main deviation of these fields from the experimental profiles is the edge toroidal field, which in experiment is of smaller magnitude (less deeply reversed) than the Bessel function. This reflects the fact that the current density (and  $\lambda$ ) tends towards zero near the plasma surface.

Relative to the tokamak, the weak toroidal magnetic field of the RFP has three consequences for ideal MHD stability — two negative and one positive. The two negative features arise when  $q$  falls below unity. First, the RFP plasma does not satisfy the Kruskal–Shafranov stability criterion ( $q > 1$ ) for current driven kink instabilities; when the plasma boundary is free to move, spatially global instabilities can develop. Second, if  $q < 1$  the magnetic curvature is dominated by the poloidal field and is unfavourable (“bad curvature”) at all points along the field line. This is in contrast to a tokamak for which  $q > 1$  and the curvature, dominated by the toroidal field, is on-average favourable. This feature of the RFP can encourage pressure driven instabilities to develop. However, the unfavourable curvature can be somewhat offset by the third consequence of low toroidal field: strong magnetic shear — the magnetic field direction rotates from toroidal in the core to dominantly poloidal at the edge. With strong magnetic shear, bending of field lines by perturbations induces a strong restoring force.

Linear ideal MHD stability for the RFP has been studied extensively, from both the MHD energy principle (which determines whether the plasma is stable or unstable) [9.4, 9.5] and from solving the full linear equations for the spatial profile and growth rates of instabilities. Approximate analytic expressions have been obtained for special cases; however, expressions of broad utility are not generally available. Rather detailed properties have been evaluated from computational solutions. Thus, here we only summarize the dominant results that

have arisen mostly from computational solutions. Within MHD the sources for instability are the plasma current and pressure.

9.2.1.1. *Current driven instability*

With a perfectly conducting boundary, the RFP can be stable to current driven ideal MHD instabilities. A conducting shell provides a stabilizing restoring force from the current induced in the shell by the motion of the current carrying plasma. In addition, the shell prevents motion of the plasma at the surface of the shell. Without a stabilizing conducting shell, numerous global, free-boundary instabilities arise. These modes are similar to the  $m = 1, n = 1$  external kink mode that occurs in a tokamak if  $q$  at the boundary falls below unity (where  $m$  and  $n$  are poloidal and toroidal mode numbers — the number of wavelengths fitting in the poloidal and toroidal circumference). For the RFP a spectrum of modes with  $m = 1, n > 1/q$  arises (where  $q$  is the safety factor at the plasma centre). As discussed later, these modes can simultaneously be feedback stabilized; this establishes that a conducting shell is not needed.

9.2.1.2. *Pressure driven instability*

Since the RFP has bad curvature it is susceptible to the interchange instability. The pressure at which the instability is excited is determined by the competition between the destabilizing pressure gradient and the stabilizing magnetic shear. The shear forces field lines to be bent in the presence of an instability, providing a restoring force due to field line tension. There is one wavelength for which the field line would not be bent — that for which the wavelength parallel to a field line is infinite (or the parallel wavenumber  $k_{\parallel} = 0$ ). In this case, a field line is equally displaced at all points along the line. Because of magnetic shear, for given poloidal and toroidal wavelengths this condition can only be satisfied at one radius. That radius is given by  $k_{\parallel} = (m/r)B_{\theta} - (n/R)B_z = 0$ , or

$$q = \frac{m}{n} \tag{9.7}$$

where  $q = rB_z / (RB_{\theta})$ . These “mode-resonant” surfaces constitute a resonance between the perturbation (represented by  $m, n$ ) and the equilibrium field (represented by  $q$ ). Interchange modes will be localized to mode-resonant surfaces. Treating the RFP as a cylinder, the following stability criterion had long ago been derived by Suydam for interchange modes [9.6]:

$$\frac{dp}{dr} < -\frac{rB_z^2}{8\mu_0} \left( \frac{1}{q} \frac{dq}{dr} \right)^2 \tag{9.8}$$

where each quantity is evaluated on the mode-resonant surface. Magnetic shear is sufficiently strong so that pressure profiles can be produced with rather high plasma pressure (measured relative to the confining magnetic field pressure).

While ideal MHD instability generally must be satisfied to sustain a plasma, for the RFP the added effect of non-zero electrical resistivity (even if very small) provides a more severe constraint. It also introduces instabilities that greatly determine behaviour in the RFP, including why the toroidal magnetic field reverses.

### 9.2.2. Reversal of magnetic field: minimum energy state and reconnection

There are two complementary views of why the plasma, under the condition of a weak applied magnetic field, adopts a reversed field state. The first is based on a conjecture that the plasma assumes a minimum energy state, subject to a particular assumption. This view provides useful insight and perspective. The second view reveals the detailed dynamics through which instability drives the plasma towards field reversal. It also reveals the extent to which the energy argument applies. Below we describe both views.

#### 9.2.2.1. Minimum energy state

The experimental observation that the magnetic field is reversed received a heuristic explanation in 1974. Taylor put forth an argument, or conjecture, that the RFP is described as a state of minimum magnetic energy, subject to a particular topological constraint that the magnetic helicity is conserved [9.7]. This argument provides an interesting perspective on the RFP equilibrium, although subsequent comprehensive investigation of the underlying three-dimensional dynamics reveals a comprehensive understanding. Taylor conjectured that the RFP evolves or relaxes to a preferred state in which the magnetic energy is minimized. Obviously, if the problem statement ended here, the minimum energy state would be the trivial one with zero field. Taylor applied the constraint that magnetic helicity is held constant. Magnetic helicity ( $H$ ) is a measure of the knottedness, or entanglement, of the magnetic field, and is given by

$$H = \int (\vec{A} \cdot \vec{B}) dV \quad (9.9)$$

where  $\vec{A}$  is the magnetic vector potential, related to the magnetic field through  $\vec{B} = \nabla \times \vec{A}$ , and the volume of integration ( $V$ ) is extended over a magnetic flux tube. A flux tube is any volume containing magnetic flux for which the magnetic field is tangent to the surface of the domain. It is not obvious that the integral measures the knottedness of field lines. However, this is easily illustrated by

considering a simple case of two linked flux tubes, as shown in Fig. 9.2. The first tube contains flux  $\Phi_1$  and the second tube contains flux  $\Phi_2$ .

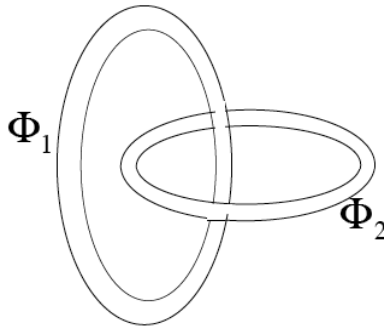


FIG. 9.2. Two linked flux tubes, one carrying flux  $\Phi_1$  and the other carrying flux  $\Phi_2$ .

Let us consider that the tubes are thin and evaluate the helicity contained within flux tube 1,

$$H = \int_1 (\vec{A} \cdot \vec{B}) dV = \int_1 (A_{\parallel} B) dS dl \tag{9.10}$$

where the integral extends over the volume of tube 1,  $A_{\parallel}$  is the vector potential parallel to the magnetic field (or the flux tube surface, since the flux tube is considered to be infinitesimally thin), and  $dS$  and  $dl$  are differential surface and length elements. If the tube is thin, we can separate the surface and length integrals,

$$H = \int B dS \int A_{\parallel} dl = \Phi_1 \Phi_2 \tag{9.11}$$

recognizing that  $\Phi_1 = \int B dS$  (the definition of magnetic flux) and  $\Phi_2 = \int A_{\parallel} dl$  (through Faraday's Law). Thus, we see that the helicity is the product of flux in the two linked tubes. Interestingly, the flux in tube 2 enters the expression even though the integration was carried out only over the volume of flux tube 1. If the tubes were not linked, the helicity would be zero. One can extend the argument to show that if tube 1 linked to  $N$  tubes, each with flux  $\Phi_2$ , then  $H = N\Phi_1\Phi_2$ . For a plasma with continuous helical magnetic field, such as an RFP or tokamak, the helicity is not so simply evaluated, but still represents the flux linkage contained between the poloidal and toroidal fields.

The utility of helicity is that it is a conserved quantity in an ideal plasma. It can be shown that helicity is invariant within a moving flux tube that satisfies ideal MHD. This is not surprising. In an ideal MHD plasma, magnetic flux is frozen into the plasma fluid. One might then expect that helicity would also be

fixed as the plasma evolves. The shapes of the field lines can change as they are dragged by a moving, ideal plasma, but their linkages cannot change. That is, field lines cannot be torn.

Taylor considered the helicity contained within the entire plasma (bounded by a conducting shell), and assumed that the helicity is conserved within the plasma, even if the plasma is slightly resistive. One can then invoke helicity conservation as a constraint for the minimization of magnetic energy. Applying the Lagrange multiplier technique to minimize magnetic energy ( $\int B^2 dV$ ) within the plasma, subject to the constraint of constant helicity, the resulting solution is  $\nabla \times \vec{B} = \lambda \vec{B}$ , where  $\lambda$  is a constant which entered the minimization problem as the Lagrange multiplier. Note that this is the simple equilibrium equation we used earlier to illustrate the RFP state. Hence, the minimum energy state is one which is reversed for a range of  $\lambda$  values.

The Taylor minimum energy state ignores pressure and plasma flow. It has proved to be a useful concept because it later was found that the resistive MHD process that drives the plasma towards a state with reversed field approximately conserves helicity, even though the process locally breaks field lines. These processes, based upon the action of multiple non-linearly coupled instabilities, that cause magnetic reconnection, constitute a standard model for understanding the magnetic fluctuations and equilibrium fields of the RFP. We turn our attention to this model in the next section.

#### *9.2.2.2. Standard model of RFP dynamics: non-linear tearing modes and magnetic reconnection*

Magnetic field fluctuations that arise spontaneously have a strong influence on RFP behaviour — the shape of the equilibrium magnetic field and confinement. The origin of the magnetic fluctuations is a resistive MHD instability that causes magnetic reconnection (the tearing instability or cousins of the tearing mode). Even though the resistivity is extremely small, at specific locations in the plasma it can cause the field lines to tear and reconnect. This produces a large effect on the global structure of the field. The energy source for the instability is the gradient in the plasma current density.

In a simple picture of reconnection, one considers a magnetic field structure as shown in Fig. 9.3(a). Field lines alter direction about the dotted line, along which the magnetic field vanishes. If a perturbation is imposed with wavelength in the horizontal direction (Fig. 9.3(b)), the presence of resistivity can cause the field lines to tear and reconnect, producing the field structure of Fig. 9.3(c). In the absence of resistivity, the frozen flux constraint prevents reconnection. Now consider that a uniform magnetic field out of the page is added to Fig. 9.3. The plots would then represent the field component in the plane of the page only. Reconnection will still occur at the location of the dotted line. However, at that

location the field no longer vanishes (the out of plane component is non-zero). Rather, that location is identified by the vanishing of  $k_{\parallel}$ . The horizontal component of the field vanishes; hence at this location only the wavelength is in the perpendicular direction. Reconnection can occur at mode-resonant surfaces where  $k_{\parallel} = 0$ , or  $q = m/n$  (where  $m$  and  $n$  are the mode numbers of the tearing instability).

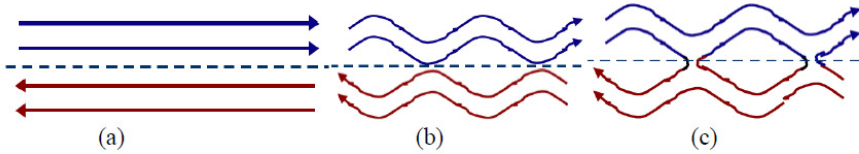


FIG. 9.3. Field line structure (a) before perturbation, (b) with perturbation in an ideal plasma, (c) with perturbation in a resistive plasma undergoing reconnection.

Derivation of the linear properties of the tearing mode has been accomplished analytically [9.8]. It involves a separation of the plasma into a region localized about the mode-resonant surface, where tearing occurs, and the rest of the plasma, within which magnetic flux is frozen. Resistivity is included in the thin boundary layer about the mode-resonant surface, whereas the remainder of the plasma is described by ideal MHD. Matching of the separate solutions yields the growth rate and spatial structure of the mode. It is found that the energy source of the mode is the current density gradient (or, more precisely,  $d\lambda/dr$ , where  $\lambda = j_{\parallel}/B$  is a normalized current density). The mode grows on a timescale which is intermediate between the Alfvén transit time  $\tau_A = a/v_A$  (where  $a$  is the plasma radius and  $v_A$  is the Alfvén speed) and the resistive diffusion time  $\tau_R = \mu_0 a^2/\eta$ . The mode growth time is  $\tau_A^{2/5}\tau_R^{3/5}$ . The mode grows more slowly than an ideal MHD mode (which grows on an Alfvén timescale), but more rapidly than field diffusing classically through the plasma. For experimental parameters the growth time is short (typically less than 1 ms), so the mode quickly approaches a non-linear state.

Typically, the long wavelength modes (low  $m$ ,  $n$ ) are the most unstable, because the stabilizing effect of field line bending is weak. For the RFP,  $q < 1$ , so that there are multiple unstable modes, each resonant at a different radius, as shown in Fig. 9.4. The occurrence of a large group of rather closely spaced modes is in contrast to the tokamak, for which there are only a few tearing modes that appear and are more widely separated.

Our focus here is not on the detailed properties of the linear instability, but rather on the effect of the instability on plasma behaviour. One curious effect is that the equilibrium magnetic field is altered by the instability, a phenomenon captured by MHD [9.3]. The origin of this effect can be seen in a simple Ohm's Law,  $\vec{E} + \vec{v} \times \vec{B} = \eta \vec{j}$ . Let us now decompose each quantity into its equilibrium

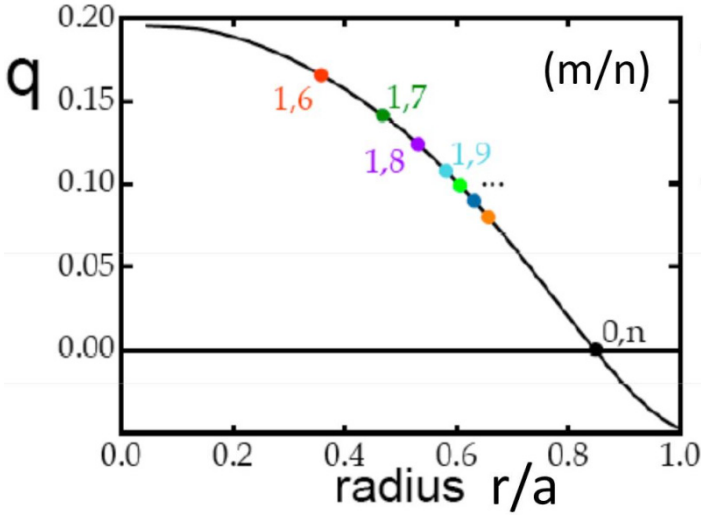


FIG. 9.4. RFP safety factor profile, showing location of resonant modes satisfying the relation  $q = m/n$ .

and fluctuating components, for example  $B = \langle B \rangle + \tilde{B}$ , where  $\langle \rangle$  denotes an average over the poloidal and toroidal directions, and is a function of radius only. If we take an average of Ohm's Law, and select the component in the direction parallel to  $\langle B \rangle$ , we obtain

$$\langle \vec{E} \rangle_{\parallel} + \langle \vec{v} \times \tilde{\vec{B}} \rangle_{\parallel} = \eta \langle \vec{j} \rangle_{\parallel} \tag{9.12}$$

Since the fluctuations are periodic in the poloidal and toroidal directions, their average vanishes (e.g.  $\langle \tilde{B} \rangle = 0$ ). However, the average of a product of fluctuations survives. Thus, we note that there are now two sources of parallel equilibrium current: the equilibrium electric field and the fluctuation induced electromotive force ( $\langle \vec{v} \times \tilde{\vec{B}} \rangle_{\parallel}$ ). Information about this term can be obtained by solving for the linear tearing mode eigenfunctions ( $\tilde{v}, \tilde{B}$ ) and then taking the product. The result of this exercise (known as quasi-linear theory) is [9.9]

$$\langle \tilde{v} \times \tilde{B} \rangle_{\parallel} \approx D \frac{d\lambda}{dr} \tag{9.13}$$

where  $D$  is proportional to  $|\tilde{B}|^2$  and  $\lambda = \langle j \rangle_{\parallel} / \langle B \rangle_{\parallel}$ . Thus, this term is diffusive, tending to flatten the current density gradient (normalized to the magnetic field). This effect reflects the tendency of instabilities to reduce the energy source that drives them, which for a tearing mode is the normalized current density gradient.

The situation is made more interesting by the presence of many unstable tearing modes, each resonant at a different radius. As the tearing modes grow,

they interact with each other through three-wave non-linear coupling [9.3]. This can occur if three modes satisfy a wave-beating relationship (a wavenumber sum rule) given by  $m_3 = m_1 + m_2$ ,  $n_3 = n_1 + n_2$ , where the subscripts denote three different modes. For example, the  $(m, n) = (1, 6)$  mode can couple to the  $(1, 7)$  and  $(0, 1)$  modes through this process. It turns out that the  $(1, 6)$  and  $(1, 7)$  modes are unstable and the  $(0, 1)$  mode is often stable. Thus, the  $(0, 1)$  mode, which resonates at the reversal surface (where the equilibrium toroidal magnetic field vanishes), is purely driven by the non-linear coupling. Through the  $(0, 1)$  mode, other unstable modes are coupled, such as the  $(1, 7)$  and  $(1, 8)$ , the  $(1, 8)$  and  $(1, 9)$ , etc. In this way, we have a group of non-linearly coupled modes, whose coupling is mediated by the  $m = 0$  mode. The modes do not grow without bound; rather they saturate through two mechanisms: relaxation of the current density profile and energy transfer to stable modes, such as the  $m = 0$ . The  $n$  value of the  $m = 1$  modes that are most active depend upon the aspect ratio; the examples given here apply to an aspect ratio of 3.

The MHD description of the full dynamics of the magnetic fluctuations has been extensively studied, aided by computational solution of the MHD equations.

This “standard model” of the RFP predicts a spectrum of magnetic fluctuations (Fig. 9.5 left) that is consistent with experiment (Fig. 9.5 right).

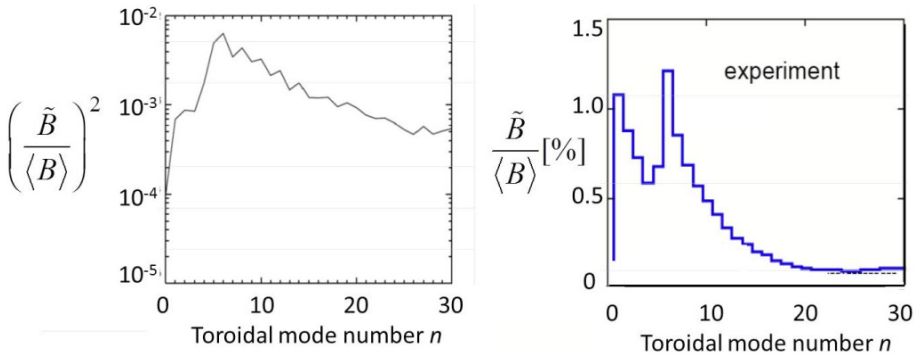


FIG. 9.5. Toroidal mode number spectrum of magnetic fluctuations, predicted by MHD computation (left) by the DEBS code and measured in experiment (right). Courtesy of MST group.

MHD also predicts a strong modification of the current profile by the fluctuations. For example, in experiment the current density is not accounted for by the measured electric field (Fig. 9.6). There must be an additional large source of current. MHD provides the explanation — the fluctuation induced electromotive force — as shown in Fig 9.6 [9.10]. This extra generation of current, or magnetic field, is often referred to as a “dynamo” effect, in analogy with the astrophysical dynamo which denotes the spontaneous generation of a magnetic field in astrophysical plasmas. Without the dynamo effect the toroidal

magnetic field would decrease with radius, but it would not reverse. The redistribution of the current profile by the dynamo, needed to saturate the modes, corresponds to a toroidal magnetic field that reverses near the plasma boundary.

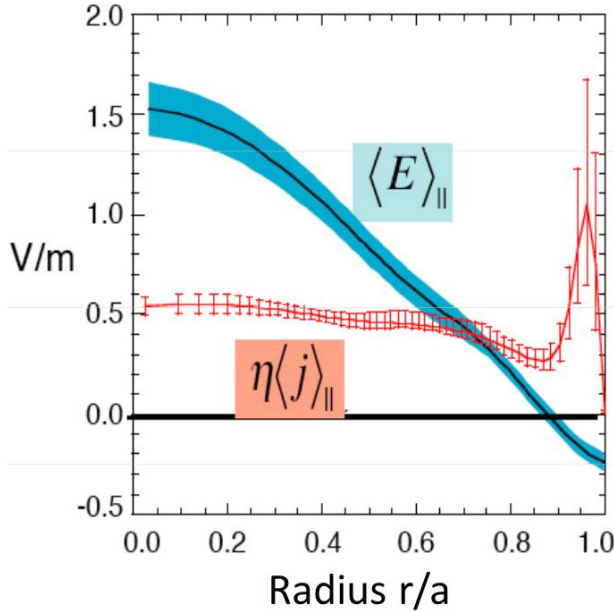


FIG. 9.6. Experimental measurement of parallel electric field and current density terms in mean-field Ohm's Law. Reprinted from Ref. [9.10]. Copyright (2011), American Institute of Physics.

The MHD dynamo term ( $\langle \tilde{\mathbf{v}} \times \tilde{\mathbf{B}} \rangle_{\parallel}$ ) has been measured in experiment and found to be significant. However, it has also been discovered that effects beyond MHD are important. For example, one can examine a more complete Ohm's Law for additional dynamo effects. Adding only the Hall term to Ohm's Law yields a new term, as follows:

$$\langle \vec{E} \rangle_{\parallel} + \langle \tilde{\mathbf{v}} \times \tilde{\mathbf{B}} \rangle_{\parallel} + \langle \tilde{\mathbf{j}} \times \tilde{\mathbf{B}} \rangle_{\parallel} = \eta \langle \vec{j} \rangle_{\parallel} \quad (9.14)$$

We now see from the third term that if the current density fluctuations are correlated with magnetic fluctuations, this can be a source of parallel equilibrium current. This two-fluid effect is expected theoretically to be present, and is experimentally measured. Experiments show that both MHD and Hall dynamo effects [9.11] are important. Additional mechanisms beyond MHD are also under study. A full understanding of the conditions at which various dynamo effects dominate is a current topic of research, linked to the ongoing investigation of reconnection effects beyond MHD.

### 9.2.3. Confinement: effects of magnetic stochasticity

The influence of multiple tearing modes on the magnetic field has a strong effect on plasma confinement. This is not evident from the evaluation of the effect on the mean field, discussed above, but from its effect on the full 3-D magnetic field pattern (mean plus fluctuations field). In the absence of tearing modes, helical magnetic field lines lie on nested concentric tori, called magnetic surfaces. Let us consider the effect of a single tearing mode on the trajectory of magnetic field lines in the vicinity of its mode-resonant surface. The component of the perturbed field that is most consequential is the radial component, which adds a radial excursion to the field line. If it is small ( $\tilde{B}_r \ll \langle B \rangle$ ), then one would expect that the effect of the field line will be small — a slight wiggle in the line. This is true everywhere in the plasma except near the mode-resonant surface. At that location  $k_{\parallel} = 0$ . That is, the amplitude of the perturbed field is constant along a field line. Thus, even though small, a radial perturbation field can produce a large radial excursion of the field line at that radial location. The field line trajectory is easily derived. Consider a coordinate system near the resonant surface ( $r = r_0$ ) where  $x = r - r_0$  is the radial distance from the resonant surface and  $\chi_{\perp} = m\theta - n\phi$  (with  $\theta$  and  $\phi$  being poloidal and toroidal angles respectively) is an angle perpendicular to the field line (but within a magnetic surface) at the resonant surface (the field line is described by  $\chi_{\perp} = \text{constant}$ ). The equation for the field line is then

$$\frac{dx}{\tilde{B}_x} = \frac{h_{\chi} d\chi_{\perp}}{\langle B_{\chi} \rangle} \quad (9.15)$$

where  $h_{\chi}$  is the scale factor,  $\tilde{B}_x = b_x \sin \chi_{\perp}$ ,  $b_x$  is a constant, and  $\langle B_{\chi} \rangle$  is zero at the resonant surface, but non-zero elsewhere because of the shear in the magnetic field line. Near the resonant surface we can expand the equilibrium field component as  $\langle B_{\chi} \rangle \approx \langle B_{\chi} \rangle' x$  where the constant  $\langle B_{\chi} \rangle' = d\langle B_{\chi} \rangle / dx$  is evaluated at the resonant radius. Equation (9.15) then becomes

$$\frac{dx}{d\chi_{\perp}} = \frac{h_{\chi} \tilde{B}_x \sin \chi_{\perp}}{\langle B_{\chi} \rangle' x} \quad (9.16)$$

We then obtain the equation for the field line trajectory in the  $r - \chi_{\perp}$  plane,

$$x = \pm \sqrt{(C + A \cos \chi_{\perp})} \quad (9.17)$$

where

$$A = \frac{h_\chi}{4} \frac{\tilde{B}_x}{\langle B_\chi \rangle'} \tag{9.18}$$

and  $C$  is the constant of integration.

The field line trajectories in the  $(x, \chi_\perp)$  plane are as shown in Fig. 9.3(c), if the horizontal axis represents  $\chi_\perp$  and the vertical axis represents  $x$ . In a torus, the projection of field lines onto the poloidal plane is as shown in Fig 9.7 left for an  $m = 1$  instability. The structure is referred to as a magnetic island. The width of the magnetic island (separatrix to separatrix) is  $w = 2\sqrt{2A}$ . Evaluating the scale factor,  $h_\chi$ , and expressing  $\langle B_\chi \rangle'$  in terms of the safety factor  $q$ , yields the island width [9.12]

$$w = 4 \sqrt{\frac{\tilde{B}_r}{\langle B_\theta \rangle} \frac{r_0}{nq'}} \tag{9.19}$$

Even if the instability amplitude is small (e.g.  $\tilde{B}_r / \langle B_\theta \rangle \approx 0.01$ ) the island width can be substantial (e.g.  $w \approx 0.1a$ , where  $a$  is the plasma surface radius). Islands have been observed through their effect on soft X ray emission, as shown in Fig. 9.7 right. Contours of constant soft X ray emission can be interpreted as contours of constant electron temperature, which in turn can be viewed as magnetic field lines since we expect the field lines to be isothermal.

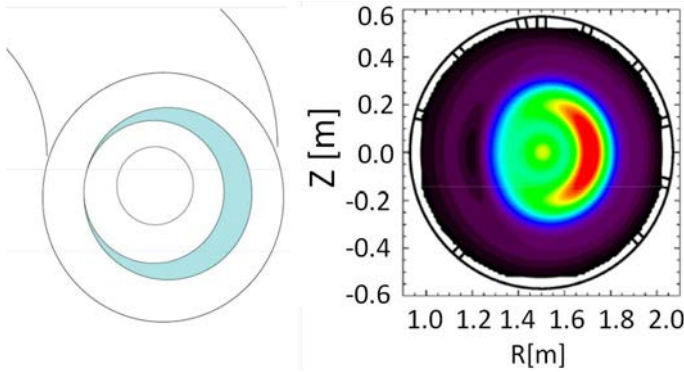


FIG. 9.7. Sketch of projection of field lines (left) onto the poloidal plane (blue shaded region is the interior of the magnetic island) and contours of constant soft X ray emission (right, [9.13]) measured in experiment to image the magnetic field lines.

The RFP experiences multiple tearing modes, each producing a magnetic island centred about its resonant surface. If the magnetic islands overlap, the magnetic field lines develop trajectories that wander chaotically (or stochastically). Magnetic field line trajectories have been computed from the computational solution of the MHD equations that evolve multiple tearing modes

for the RFP [9.14]. To model the experiments, the edge values of each Fourier mode ( $m, n$  component) are forced to match the experimental values. The field line trajectories are often characterized by puncture plots, such as shown in Fig. 9.8 top. Each point represents the piercing of a toroidal plane (horizontal slice of the torus) by a field line. In the absence of instability, the puncture plot displays straight lines, each lying on a nested toroidal surface. In the presence of multiple instabilities, the magnetic field becomes stochastic, as seen in the figure, and an individual field line will wander radially. Magnetic stochasticity is not as severe as it appears, since a field line has to circumnavigate the torus many times before it wanders a significant radial distance. Nonetheless, the magnetic stochasticity substantially enhances energy and particle transport. Particles follow the field lines; thus, as the field lines wander radially, the particles follow.

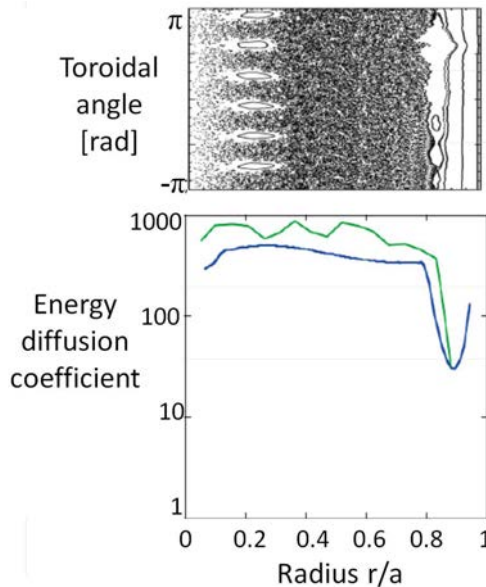


FIG. 9.8. Top: field line puncture plot obtained from MHD computation (with edge field values normalized to experiment); Bottom: measurement of energy diffusion coefficient (blue) and theoretical prediction from Eq. (9.21). Reprinted from Ref. [9.14]. Copyright (2011) by the American Physical Society.

A full theory of plasma transport in the presence of magnetic stochasticity is not yet in hand. However, a heuristic treatment provided a useful physics perspective. The field lines are assumed to wander diffusively and to be characterized by a field line diffusion coefficient  $D_M$  defined as

$$D_M = \frac{(\Delta r)^2}{\Delta L} \quad (9.20)$$

where  $\Delta r$  denotes the radial excursion of a field line as it travels a complete distance (mainly along the magnetic surface)  $\Delta L$ . Since the particles roughly stream parallel to a field line, the particles will diffuse similarly to the field. Thus, the particle (or energy) diffusion coefficient (for either electrons or ions) is given simply by [9.15]

$$D = v_{th} D_M \quad (9.21)$$

where  $v_{th}$  is the thermal velocity. A diffusively wandering trajectory can be described by a correlation length,  $L_c$ . For a random walk process, we let  $\Delta L = L_c$ . The radial excursion is then  $\Delta r = L_c \tilde{B}_r / \langle B_\theta \rangle$ , such that  $D_M = L_c (\tilde{B}_r / \langle B_\theta \rangle)^2$ . There are subtleties in the meaning of  $L_c$  for a field line which it is not profitable to consider here. Its introduction here is only to establish that diffusion might scale as  $\tilde{B}_r^2$ .

These intuitive estimates for transport in the RFP do indeed roughly capture the magnitude of transport within the core of the RFP. For example, Fig. 9.8 (bottom) shows a comparison of the measured electron energy diffusion coefficient and the theoretical estimate based on Eq. (9.21). The experimental diffusion coefficient is obtained by measurement of the electron temperature gradient and the input ohmic power ( $\vec{j} \cdot \vec{E}$ ). The theoretical diffusion coefficient employs Eq. (9.21). The magnetic diffusion coefficient is obtained from the puncture plot shown. We see from Fig. 9.8 top that the theoretical estimate is comparable to the experimental value in the plasma core, where the field is stochastic.

The resulting global energy confinement time of present experiments is about 1 ms. This value is low compared to a tokamak of comparable size and plasma current. Extrapolation to a fusion energy system of the “standard” RFP depends upon how plasma transport scales as the plasma parameters approach that of a reactor. Since the dominant instabilities that drive the transport are resistive tearing modes, a key control parameter is the Lundquist number,  $S = \tau_R / \tau_A$ , a dimensionless measure of the electrical resistivity. As the resistivity decreases ( $S$  increases) one might expect the amplitude of resistive tearing fluctuations to decrease. Since  $S \sim T^{3/2} a B / n^{1/2}$ , its value increases substantially as the plasma temperature and current increase. Scaling of fluctuations and transport remains an open issue. However, a very limited scaling has been obtained through MHD computation and current experiments. In both cases, the magnetic fluctuations decrease with Lundquist number very roughly as  $\tilde{B} / \langle B \rangle \sim S^{-0.2}$ . While the fluctuations decrease with  $S$ , the rate of decrease is rather slow and would extrapolate to a reactor with very high current and likely relatively high cost.

As a result, development of the RFP no longer depends on reliance on scaling as a means to achieve favourable confinement. New routes to improved

confinement have been developed, such that the RFP has been somewhat redefined, as discussed in the next section.

#### 9.2.4. Improved confinement

Confinement in the RFP as of about a decade ago conformed to the picture described in the previous section: the free energy contained in the plasma current density gradient excites multiple tearing instabilities; the overlapping magnetic islands from each tearing mode yield a magnetic field that wanders stochastically; particles follow the field lines in their radial wander, thereby enhancing transport of particles and energy. This simple picture ignores many unknown fundamental features of RFP transport that are presently under study, including momentum transport by fluid stresses, non-ambipolar transport leading to charge buildup and flow generation, and electrostatic fluctuation induced transport in the edge region. Nonetheless, the picture captures much of RFP transport physics.

Understanding the tearing mode physics responsible for transport has led to two approaches to reduce anomalous transport in the RFP. The first approach suppresses multiple tearing instabilities by reducing the free energy source — the current density gradient. The second approach aims to produce a state in which all the fluctuation energy condenses to a single large tearing mode, thereby reducing the plasma to a helical state, free of the stochasticity that requires multiple modes. This state appears to be the preferred configuration at high plasma current. We describe the principle and experimental status of each of these approaches below.

##### 9.2.4.1. Eliminating the free energy source

Stability to tearing instabilities in the RFP is determined by the radial profile of the normalized parallel current density  $\lambda = \langle j \rangle_{\parallel} / \langle B \rangle$ . For a standard RFP, the  $\lambda$  profile is as shown in Fig. 9.9. A significant gradient develops in the outer half. This occurs because of the peakedness of the profile of the parallel electric field. In the steady state  $\langle E_{\phi} \rangle$  is constant (ignoring toroidal effects). Thus,  $\langle E \rangle_{\parallel}$  reflects the peakedness of the toroidal magnetic field. The resulting centrally peaked  $\lambda$  profile is unstable. If a parallel current profile were produced in which the current profile were less peaked, one would expect the instabilities to be reduced [9.16]. This can be accomplished by driving extra current in the outer region. The stabilizing effect of a flatter current density profile is evident from linear MHD stability. However, the idea has been explored more thoroughly through MHD computation.

For example, consider that the additional current drive were applied after the RFP reached its usual state with a saturated level of magnetic fluctuations. Fluctuations would then decrease in response to the reduced free energy source. However, the fluctuation induced dynamo effect would then be altered, which

would further alter the current profile, which would then change the fluctuations level. A full non-linear MHD treatment is necessary to capture the self-consistent physics of the interaction between the current profile and the fluctuations. This has been accomplished by including extra current drive through an ad hoc force term  $F(r)$  in Ohm's Law [9.17]

$$\vec{E} + \vec{v} \times \vec{B} + \vec{F}(r) = \eta \vec{j} \tag{9.22}$$

The physics of the production of the ad hoc force (e.g. electron acceleration by an RF wave) is not of interest here — only the effect of the force on the MHD dynamics. Choosing the force  $F(r)$  to be localized to the outer region (guided by linear theory), the  $\lambda$  profile evolves to a non-linear steady state that has additional current in the outer region (Fig. 9.9). The magnetic fluctuations are reduced across the full spectrum of toroidal modes and the magnetic puncture plot evolves from the stochastic one of Fig. 9.9 to one for which much of the cross-section contains well ordered magnetic surfaces. Thus, we would expect significant improvement in confinement.

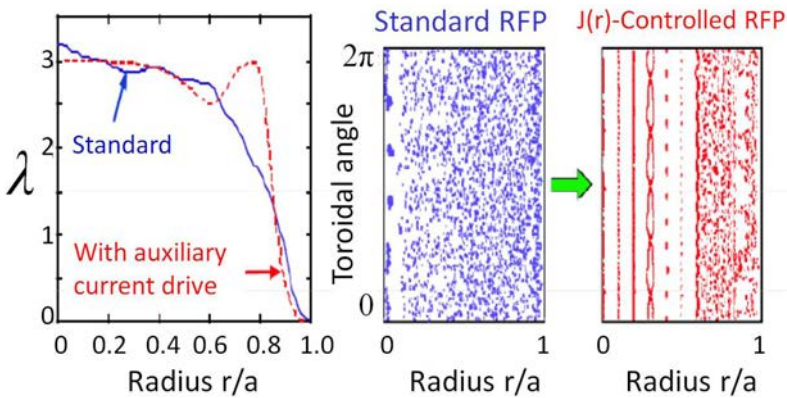


FIG. 9.9. Results from non-linear MHD computation for the profile of  $\lambda = \langle j \rangle_{\parallel} / \langle B \rangle$ , with (blue) and without (red) added current drive, and the corresponding magnetic field line puncture plots [9.18].

This approach has been developed experimentally, with very large gains in confinement [9.19]. The current profile is made flatter by programming the applied ohmic electric field. After the plasma is fully formed, a poloidal surface voltage is applied to drive current in the outer region, producing a modest reduction in the gradient in the outer region (Fig. 9.10). As a result, the magnetic fluctuations are observed to decrease substantially (Fig. 9.11) [9.20], corresponding to reduction of all the dominant tearing instabilities. The best estimate for the magnetic field puncture plot in the experiment (using the measured edge fluctuation levels) is shown in Fig. 9.12 top. The stochasticity is very much reduced from the

standard case of Fig. 9.8. The measured energy diffusion coefficient is reduced by over an order of magnitude (Fig. 9.12, comparing to Fig. 9.8). The stochastic transport theory is comparable to experiment only where the field is stochastic, and disagrees outside that region, where the theory should not apply. As a result of the decreased diffusion, the electron temperature increases about threefold. The net result is that the energy confinement time increases tenfold. In this state the confinement in the RFP is comparable to that of a tokamak of similar size and plasma current. Since tokamak transport is driven mainly by electrostatic fluctuations (arising from  $\vec{E} \times \vec{B}$  drifts from electrostatic fields), this similarity raises the question of whether magnetic fluctuation induced transport has been sufficiently reduced in the RFP so that electrostatic fluctuations are becoming dominant.

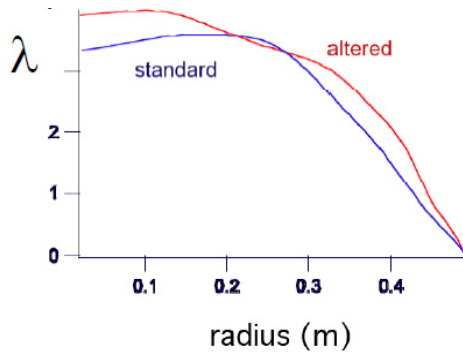


FIG. 9.10. Measured  $\lambda$  profiles in the standard RFP and with the profile altered by programming the applied electric field. Reprinted from Ref. [9.21]. Copyright (2011) IOP Publishing Ltd.

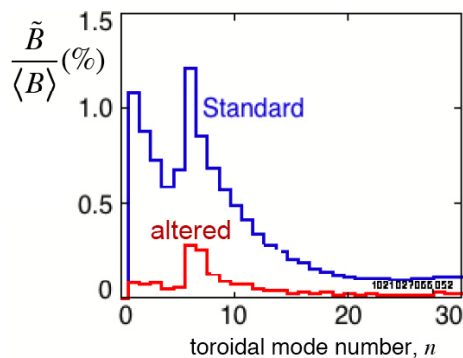


FIG. 9.11. Magnetic fluctuations (versus toroidal mode number) measured in experiment for the standard RFP (blue) and for the RFP with the current profile altered (red) [9.22]. Courtesy of J.S. Sarff.

Some indication can be given by measuring the dependence of electron diffusion on particle speed. If driven by magnetic fluctuations, we might expect diffusion to scale with electron speed (see Eq. (9.19)). If driven by electrostatic fluctuations (and resulting  $\vec{E} \times \vec{B}$  drifts), diffusion might be independent of electron speed. In the improved confinement state, energetic electrons are observed (through their bremsstrahlung hard X ray emission) at energies up to 100 keV. The diffusion coefficient (after substantial modelling) appears to transition from one proportional to electron velocity to one independent of velocity, providing evidence that electrostatic fluctuations might now be dominating transport [9.23]. In this sense, this state might constitute a new physics regime: a  $q < 1$  plasma dominated by electrostatic fluctuations.

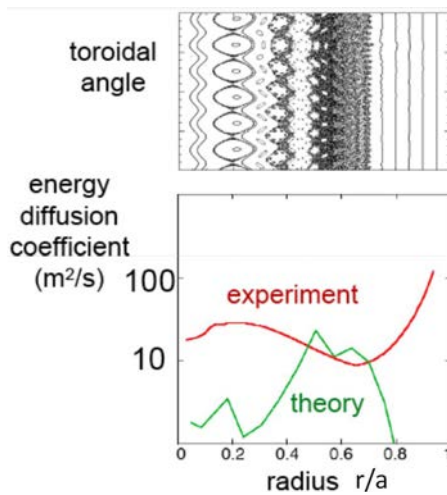


FIG. 9.12. Top: Field line puncture plot produced by MHD computation (normalized to experimental edge fluctuation amplitudes) for an RFP with current profile altered). Bottom: Measured energy diffusion coefficient (red) and theoretical expectation (green) based on Eq. (9.21). A comparison with Fig. 9.8 indicates a large reduction in diffusion [9.24].

#### 9.2.4.2. Single helicity states

In the above approach to improved confinement, all tearing modes are reduced with the aim that the magnetic surfaces in the poloidal cross-section become non-stochastic and nearly circular. A complementary approach is to eliminate all Fourier tearing components except one [9.25]. That is, that the  $m = 1$  wavenumber spectrum condenses into one toroidal mode. If this occurs the plasma is no longer axisymmetric, but in the limit of large aspect ratio is helically symmetric (the magnetic field is constant along the helical trajectory  $m\theta - n\phi = \text{constant}$ , where  $m$  and  $n$  are the mode numbers of the one remaining

helical mode). The plasma shape becomes helical — the magnetic surfaces become nested tori that possess a helical distortion, as in Fig. 9.13. This state is a helical RFP equilibrium (somewhat resembling a stellarator equilibrium), where the dynamo is produced by one large  $m = 1$  mode. Magnetic stochasticity is absent and confinement would be expected to be determined by other mechanisms.

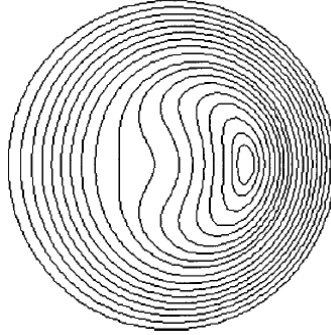


FIG. 9.13. Magnetic surface of a quasi-single helicity state, produced by MHD computation. Reprinted from Ref. [9.26]. Copyright (2011) American Institute of Physics.

MHD computation has shown that for sufficiently high dissipation, the RFP plasma will spontaneously evolve to a single helicity state. The dissipation is usefully characterized by the Hartmann number,  $H = av_A(\eta\nu)^{-1/2}$ , where  $\nu$  is the plasma viscosity. The Hartmann number functions as a control parameter for access to the single helicity (SH) state. Its role is indicated by writing the MHD equations using rescaled variables for time and velocity [9.27]:

$$t' = \sqrt{\frac{\eta}{\nu}} t \tag{9.23}$$

$$\vec{v}' = \sqrt{\frac{\nu}{\eta}} \vec{v} \tag{9.24}$$

which yields

$$\frac{\partial \vec{B}}{\partial t'} = \nabla \times (\vec{v}' \times \vec{B} - \nabla \times (H^{-1} \vec{j}')) \tag{9.25}$$

$$P^{-1} \left[ \frac{\partial \vec{v}'}{\partial t'} + (\vec{v}' \cdot \nabla) \vec{v}' \right] = \vec{j} \times \vec{B} + \nabla^2 (H^{-1} \vec{v}') \tag{9.26}$$

where the Prandtl number  $P = \tau_R / \tau_\nu$ , where  $\tau_R$  is the resistive diffusion time and  $\tau_\nu = a^2 / \nu$  is the viscous diffusion time determined by the plasma viscosity  $\nu$ .

If we ignore the inertial term (the left hand side of Eq. (9.26)), then the rescaled equations depend only on the Hartmann number. Ignoring the first term is justified for tearing modes that grow or vary slowly compared to an Alfvén time. It is not obvious that the non-linear inertial term (which contains mode coupling) would be small. However, MHD computation shows that  $H$  determines the multiplicity of helical modes in the plasma. The spectral spread, or effective number of  $m=1$  modes,  $N_s$ , can be characterized by  $N_s = [\sum_n (W_n^2 / W^2)]^{-1}$ , where  $W_n$  is the energy in the  $(m, n) = (1, n)$  mode and  $W = \sum_n W_n$  is the total energy in  $m=1$  modes. If all the energy resides in one mode, then  $N_s = 1$ , whereas if all  $N$  modes have equal energy then  $N_s = N$ .

Computation solving the MHD equations indicates that the final state of the plasma contains one mode — a state of single helicity — if  $H$  is less than about  $3 \times 10^3$ . As seen in Fig. 9.14, the transition from multiple helical modes (MH) (about ten modes for this particular case) to a single helical mode (SH) is rather abrupt.

In a hot fusion plasma, collisions between particles are relatively rare and dissipation, both resistive and viscous, is relatively weak. Viscosity in an RFP is characterized by a tensor, not the simple scalar form assumed in computation. However, if one takes a characteristic value for the collisional viscosity, and considers neoclassical resistivity (measured to be applicable to RFP experiments), then the Hartmann number is larger than the transition value. Thus, we would expect that a fusion plasma would evolve to a state of multiple helicity, unless the viscosity is anomalously high (as might occur from electrostatic turbulence). A complementary approach to an SH state might be actively to drive the plasma towards the state, such as by applying a helical magnetic boundary condition.

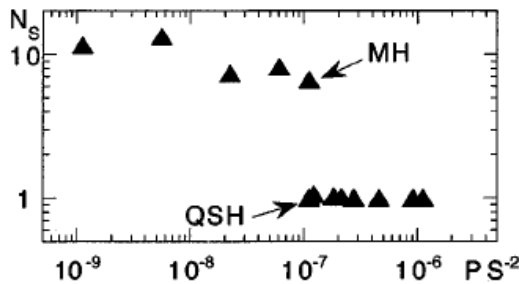


FIG. 9.14. Width of  $m = 1$  spectrum,  $N_s$ , versus  $H^{-2} (= P/S^2)$  showing the transition from a multiple-helicity (MH) state to a quasi-single-helicity (QSH) state at small Hartmann number;  $H$  (corresponding to strong dissipation). Reprinted from Ref. [9.26]. Copyright (2011) American Institute of Physics.

Encouragement can be extracted from current experiments in which, under some operating conditions, the plasma achieves a state in which one mode is much larger than all others [9.26, 9.28, 9.29]. It is not a perfect SH state since

the dominant mode is not sufficiently large and the other modes, although small, are non-zero. In experiment, these “quasi-single helicity” (QSH) plasmas exhibit a large magnetic island within which confinement is markedly improved. The magnetic structure is inferred from soft X ray tomography. The interior of the island is substantially hotter than its surrounding, suggesting improved confinement within the island. Interestingly, it has recently been observed that at high plasma current ( $>1$  MA) the QSH is preferred. The QSH persistence (the fractional time that the plasma resides in the QSH state during one discharge) increases significantly with current, as seen in Fig. 9.15. The thermal energy content also increases with current, due to the larger volume occupied by the helical structure and the particularly low value of the secondary mode amplitudes. Future research will aim to extend these results to a full SH state.

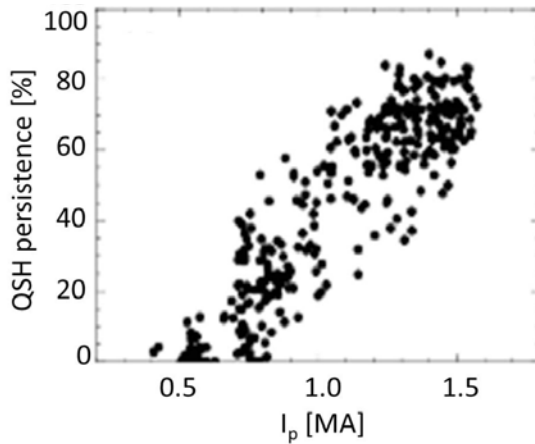


FIG. 9.15. Persistence of QSH states (fractional time that the plasma resides in the QSH state) versus plasma current. Data courtesy of Ref. [9.30].

### 9.2.5. Beta limits in the RFP

All RFP experiments operate at relatively high beta values, typically 5–10%. Some early experiments reached about 20%. Here we define beta as the ratio of the volume-average plasma pressure to the surface-average magnetic pressure ( $\beta = \langle p \rangle_V / (\langle B^2 \rangle_S / 2\mu_0)$ ). A related measure of reactor relevance considers an “engineering beta,” in which the magnetic pressure is evaluated at the coil surface, rather than the plasma surface. This is relevant since the field at the coil determines forces on the coils. For an RFP, since the poloidal magnetic field is dominant at the surface, the magnetic pressure falls off from the surface as  $1/r^2$ . Hence, this effect is significant. Another measure, sometimes employed, takes the magnetic pressure driven by the coils in vacuum (before plasma

startup), which is the vacuum toroidal magnetic field. For the RFP this quantity is very large (100% or larger), but less significant as a figure of merit for a reactor.

Despite the high beta values achieved in the RFP, the beta stability limit is not yet determined experimentally (or theoretically, since the non-linear consequences of exceeding linear stability limits are not yet known, as discussed below). That is, it is not clear whether the beta values achieved are limited by energy transport from current-driven tearing modes or from a finite pressure effect. Heating and current drive are both produced by the same input ohmic power. To determine the beta limit requires separation of current drive and heating through non-ohmic heating, not yet accomplished in the RFP.

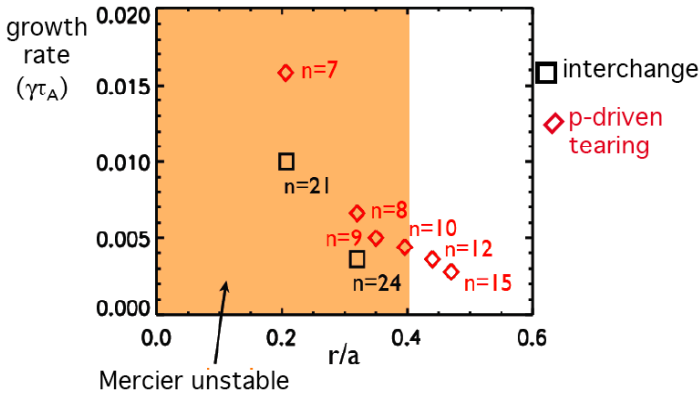


Fig. 9.16. Growth rates (normalized to Alfvén times) calculated for linear MHD instabilities for an equilibrium obtained in experiment. The horizontal location of the points indicates the mode-resonant surface. Both localized interchange and global pressure driven tearing modes are predicted to be unstable. Reprinted from Ref. [9.31]. Copyright (2011) American Institute of Physics.

The beta values achieved in standard RFP plasmas do not appear to be a stability limit. As confinement is improved, beta increases from about 9% to 15%. To increase beta further, solid hydrogen pellets were injected into the plasma — a common technique to increase plasma density. Beta then increases further to 26%, without being confronted with an apparent stability limit [9.31]. For these plasmas, linear stability has been evaluated for localized and global modes. The theoretical growth rates of the unstable modes are shown in Fig. 9.16, as well as the location of their resonant surfaces. Linear theory predicts that these modes should be unstable to localized interchange modes (according to the Suydam criterion, Eq. (9.8)). Moreover, they are predicted to be unstable to pressure driven, global tearing instabilities. Tearing modes have long been studied as current driven instabilities. However, in the RFP, as beta rises to the range of 20% the pressure becomes a dominant contributor. Despite the predicted presence of these instabilities, no dramatic effects are observed. It is possible

that the instabilities have a softer effect on transport; understanding the beta limit requires study of the non-linear evolution of the modes and further elevation of beta in experiment.

### 9.2.6. Resistive wall instabilities and their control

In many RFP experiments the plasma is surrounded by a highly conducting, close-fitting wall that stabilizes the plasma to all ideal, free-boundary instabilities. A perfectly conducting wall forces the radial component of the magnetic field at the boundary to vanish. For an ideal plasma, in which the plasma is frozen to the field, the radial velocity is also zero at the boundary. Hence, the boundary is fixed. Instabilities that require the boundary to move are stable with a conducting boundary. As a result, existing experiments that operate with a highly conducting shell avoid free-boundary instabilities. However, if the plasma duration is sufficiently long, the effect of any wall with finite electrical conductivity will eventually disappear, as the plasma duration exceeds the electrical penetration time of the shell. For a wall of thickness  $d$  and electrical conductivity  $\eta_w$ , the wall time, typically measured as the time for a vertical field to diffuse through the surrounding shell, is  $\tau_w = \mu_0 a d / 2\eta$ . Instabilities that are stable with a conducting shell, but become unstable in the absence of a shell, are called resistive wall instabilities [9.32].

#### 9.2.6.1. Characteristics of resistive wall instabilities in the RFP

The growth rate of resistive wall modes (RWMs) is of the order of the wall time. The instability grows as the perturbed magnetic field penetrates through the resistive wall. Many present and past RFP experiments have included walls (metal toroidal shells) for which the resistive wall penetration time is 0.1–1 s, chosen to be significantly longer than the plasma duration. Thus, resistive wall instabilities have been suppressed for the experimental time and the focus has been on studying the internal (fixed boundary) resistive MHD tearing modes and their effect on confinement.

Resistive wall instabilities are also a major issue for tokamak research. However, the influence of a resistive wall is perhaps even more important for the RFP, for three reasons. First, RWMs occur at zero beta in the RFP, whereas for the tokamak their occurrence mostly onsets above a critical beta value. In the RFP, current-driven, global ideal instabilities occur as indicated in Section 9.2.1. Second, the RFP has a larger number of unstable resistive wall modes, discussed below. Third, in the RFP the resistive tearing modes grow to larger amplitude with a resistive wall. These are not RWMs since the tearing modes are unstable even with a conducting shell. However, when the conducting wall boundary condition is removed, tearing modes are more unstable.

RWMs have been observed in experiment to be in agreement with theoretical expectation [9.33]. We see in Fig. 9.17 that with a surrounding wall with a penetration time less than the possible plasma duration, multiple modes grow. Fortunately, techniques have also been devised and shown to be able to stabilize RWMs in the absence of a perfectly conducting wall.

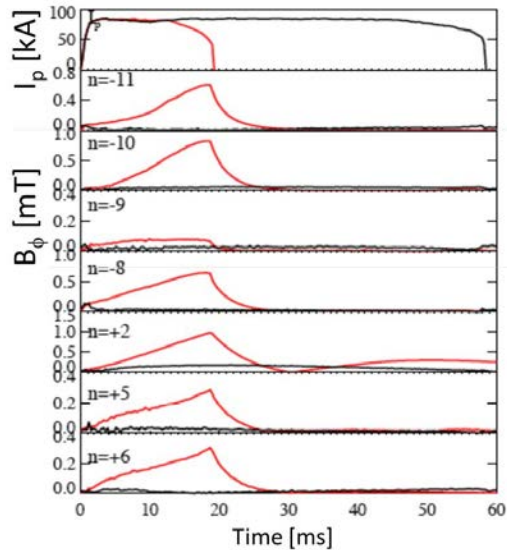


FIG. 9.17. Red curves: After the top plot, radial magnetic field of growing instabilities in the presence of a resistive wall. Black curves: Radial magnetic field with feedback stabilization. At  $t \sim 20$  ms, the plasma current (top plot) terminates from the instabilities. Black curves are with feedback stabilization [9.33].

#### 9.2.6.2. Feedback suppression of resistive wall instabilities

In concept, suppression of RWMs by feedback control is straightforward. The influence of a perfectly conducting boundary can be simulated electrically by a network of coils that forces the radial magnetic field to vanish at the plasma surface. Implementation could be challenging since many modes must be stabilized simultaneously. Fortunately, complete feedback stabilization has been demonstrated recently [9.34, 9.35]. In experiments, the entire surface of the resistive shell is covered with nearly 200 feedback coils, each capable of independently controlling the radial magnetic flux within its area (Fig. 9.18). The result (Fig. 9.19 and Fig. 9.17, black curves) is that all relevant modes are suppressed: the ideal RWMs that are stable with a perfectly conducting boundary and the resistive tearing modes that are unstable even with a perfectly conducting boundary (but rise to larger amplitude with a resistive shell).

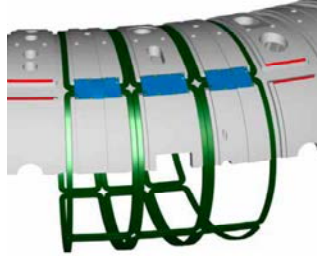


FIG. 9.18. Schematic of a portion of the 192 feedback coils that cover the vacuum vessel of the RFX experiment.

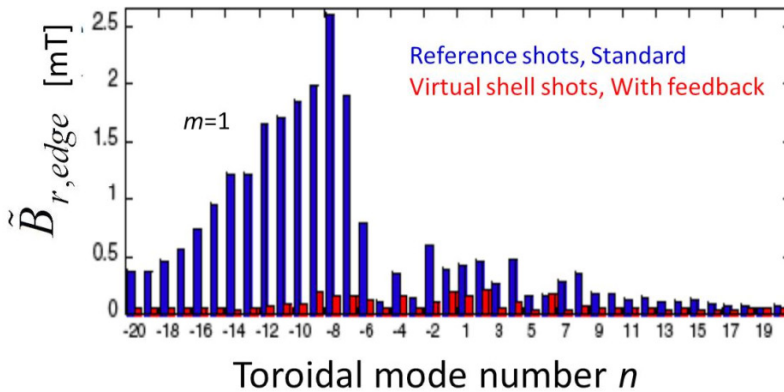


FIG. 9.19. Feedback suppression of instabilities with a resistive wall. The radial magnetic field is shown after 60 ms of growth (about equal to the wall time), showing the modes for a discharge without feedback (blue) and with feedback (red). Reprinted from Ref. [9.35]. Copyright (2011) American Physical Society.

### 9.2.7. Sustaining the plasma

Sustainment of fusion in the steady state is a desirable feature for a fusion reactor. Under some conditions, the tokamak can achieve a steady state through the neoclassical bootstrap current (supplemented with a small amount of auxiliary current drive). The bootstrap current in the RFP is very small. Since the safety factor  $q < 1$  (the toroidal field is weak), many neoclassical effects are small (except possibly at small aspect ratio with very strong plasma pressure gradients). Thus, for the RFP other solutions have to be sought if steady state is desired.

Several techniques have been conceived to produce plasma current in fusion configurations employing the concept of injection of magnetic helicity. Magnetic helicity is resistively dissipated, as is also true for the plasma current. In the steady state the magnetic helicity in the plasma must be maintained at a

constant value. An evolution equation for helicity is easily derived using only Maxwell's equations and Ohm's Law to yield

$$\frac{dH}{dt} = 2\Phi_\phi V_\phi - 2 \int (\eta \vec{j} \cdot \vec{B}) dV \quad (9.27)$$

where  $V$  is plasma volume,  $\Phi_\phi$  is the toroidal magnetic flux within the plasma and  $V_\phi$  is the toroidal surface (loop) voltage. The second term, an integral over the plasma volume, represents ohmic dissipation of helicity. The first term represents a source (or injection) of helicity. If a toroidal loop voltage is maintained in the presence of toroidal flux, helicity is injected into the plasma. In the steady state, the injection and dissipation terms are equal. We have assumed that the magnetic field is parallel to the plasma boundary. If this is not the case, a second source term arises when the magnetic field intersects a charged surface. This is the basis for electrostatic helicity injection methods, not discussed here.

The source term,  $\Phi_\phi V_\phi$ , includes the standard ohmic current drive of the tokamak and RFP, where in the steady state both the toroidal flux and loop voltage are constant in time. However, a true steady state is not possible since the loop voltage is produced by magnetic flux threading the hole in the torus increasing in time. This cannot continue indefinitely. But, consider that both  $\Phi_\phi$  and  $V_\phi$  vary sinusoidally in time, and in phase, such that  $\Phi_\phi, V_\phi \sim \sin(\omega t)$ . Averaging over a period, the first term in Eq. (9.27) is non-zero and there is a non-zero average helicity input to the plasma. The toroidal flux oscillation is induced by applying a sinusoidal poloidal surface loop voltage,  $V_\theta$ , since  $V_\theta = d\Phi_\phi / dt$ . Since the  $V_\phi$  and  $\Phi_\phi$  are 90 degrees out of phase, maximal helicity injection is achieved by applying oscillating toroidal and poloidal loop voltages, with a 90 degree phase difference (shown schematically in Fig. 9.20). As initially proposed [9.36], the oscillating voltages served to inject helicity into the plasma and the current profile was considered to automatically adjust to the RFP state by relaxing to the minimum energy state described in Section 9.2.2.1. It is intriguing that this is an ohmic current drive technique, which is steady state. Since it is ohmic, the current drive efficiency is expected to be high.

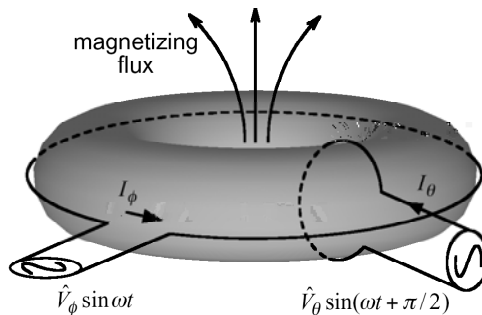


FIG. 9.20. Schematic of surface loop voltages applied for oscillating field current drive.

The helicity injection perspective provides little information on the physical mechanism by which current is driven. A full 3-D MHD study of the dynamics of the technique (sometimes called “oscillating field current drive” or OFCD) has been undertaken to confirm the current drive expectation and to examine its effect on plasma stability (magnetic fluctuations) [9.37]. OFCD can be viewed to operate in two steps. First, the oscillating fields drive plasma current in the outer region of the plasma. This is understood easily as a classical effect through Ohm’s Law. The oscillating poloidal magnetic field induced by the oscillating toroidal voltage corresponds to an oscillation in the radial velocity oscillation,  $\delta v_r$ , where  $\delta$  denotes an oscillation which is sinusoidal at the OFCD frequency  $\omega$  and is axisymmetric (and, in the cylindrical approximation of the RFP, poloidally symmetric). The oscillating poloidal voltage produces an oscillating toroidal field in the plasma,  $\delta B_\phi$ . Then through the electromotive force,  $\delta v_r \delta B_\phi$ , a steady, poloidal current is driven. The current is localized to the outer region of the plasma because the oscillating electric fields decay from the surface, where the loop voltage drive resides. The edge current drive is similar to the dynamo described earlier, in that it depends on the MHD electromotive force in Ohm’s Law. However, it is quite different in that the OFCD effect is classical, with the oscillations axisymmetric and driven by applied voltages. The tearing mode dynamo is non-classical, with helical fluctuations arising spontaneously by instability.

A complementary view of the OFCD classical “dynamo” effect is obtained by considering that  $\delta \vec{v} = \delta \vec{E} \times \vec{B} / B^2$ . Inserting this expression into the electromotive force term shows that its component parallel to the equilibrium field is  $(\delta \vec{v} \times \delta \vec{B})_{\parallel} = \delta \vec{E} \cdot \delta \vec{B}$ . This expression makes explicit that OFCD in the plasma edge is simply ohmic drive, but involving projection of the oscillating electric field along the oscillating magnetic field.

The above classical effect drives current in the outer region of the RFP, which decays spatially towards the centre. The second step in the total current drive process is that instabilities arise to produce a dynamo effect that drives current in the plasma core. That is, the fluctuation induced dynamo effect causes diffusion of the edge current into the core. The physics of this inward diffusion process is as described in Section 9.2.2.2. However, whereas the tearing instabilities without OFCD are produced by current density gradients associated with a centrally peaked profile, in OFCD the driven current profile is initially edge peaked. In addition, the change of the tearing mode behaviour through an OFCD cycle produces a time dependent dynamics that is quite complex.

The dynamics have been captured through MHD computation, which demonstrates that OFCD can indeed sustain the plasma current. It also shows that, averaged over an OFCD cycle, magnetic fluctuations from the requisite instabilities are not higher than in the standard RFP. However, the fluctuations vary greatly throughout a cycle and the effect on confinement remains an open question.

## BROADER SPECTRUM OF MAGNETIC CONFIGURATIONS

To date, experiments have demonstrated OFCD at a power level small compared to that needed for full current sustainment. About 10% of the plasma current has been driven by OFCD. An early result, demonstrating 5% current drive, is shown in Fig. 9.21 top [9.38]. More recent work has extended this result to 10%, as shown in Fig. 9.21 bottom [9.39]. Confinement remains unchanged. However, the viability of the technique awaits examination at higher power levels.

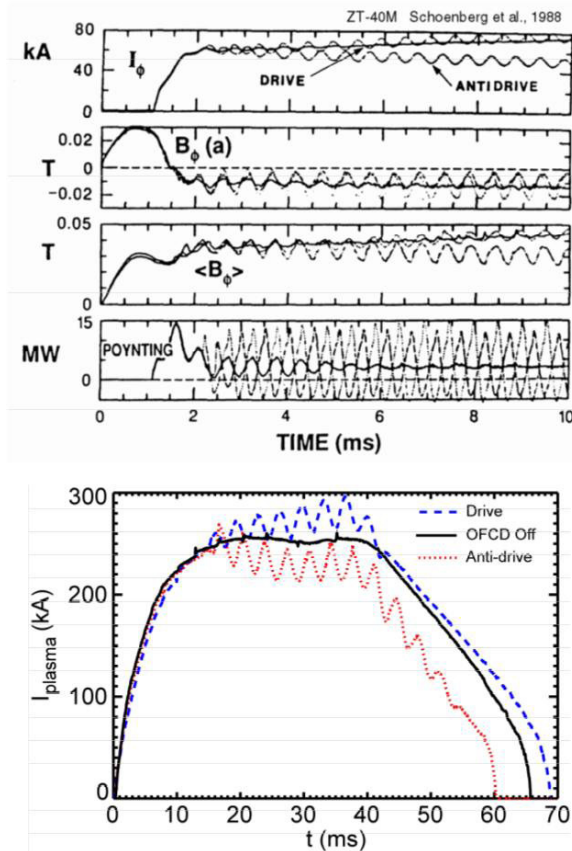


FIG. 9.21. Top: Early result showing current drive of 5% with OFCD on (labelled “drive”), compared to the case of OFCD off, and with the case (labelled “anti-drive”) for the phases set to drive current in a direction opposite to the overall current. Reprinted from Ref. [9.38]. Copyright (2011) American Physical Society. Also shown are the oscillating toroidal field, toroidal flux, and Poynting flux into the plasma volume. Bottom: More recent study with 10% current drive (dashed red curve) compared to OFCD off (solid black curve) and anti-drive (red dotted curve). Reprinted from Ref. [9.39]. Copyright (2011) American Institute of Physics.

Should OFCD prove deleterious to confinement, a hybrid scenario has been considered in which the plasma is sustained in a quasi-steady-state consisting of

two stages that repeat indefinitely in time. In one stage the plasma is confined in an improved confinement regime of operation, during which the plasma current is slowly decaying in time, to perhaps about 80% of its initial value. This stage could be the current-profile controlled regime described in Section 9.2.5. It could also be a closely related regime, introduced theoretically, in which the plasma experiences a self-similar decay. In such a decay the magnetic field spatial profile is fixed, but the magnitude decays exponentially in time. These states have been shown theoretically to have a stable current density profile; thus, tearing modes are suppressed. In the second stage of the quasi-steady-state, the plasma current is rebuilt through OFCD. If the rebuild time (of poor confinement) is much shorter than the slowly decaying stage (of good confinement), this might prove a viable approach to sustainment.

### 9.3. COMPACT TORI: ELIMINATING THE HOLE IN THE TORUS

Compact tori is the term used to describe toroidal configurations without toroidal field coils interlocking with a plasma. Their distinctive feature is the possibility of using a simply-connected vacuum vessel, this being a considerable engineering advantage. In the case where poloidal and toroidal field in a confinement zone are of the same order of magnitude, the configuration is called a “spheromak”. It was first studied in the 1970s by Rosenbluth et al. [9.40]; a detailed review of the earlier work can be found in Ref. [9.41].

If toroidal magnetic field is absent, one obtains a so-called field-reversed configuration (FRC). It is more difficult to trace the origin of this configuration; for review of the earlier work see Ref. [9.42]. Typically (but not always), FRC has a significant length-to-radius ratio. Recently, FRCs with a small toroidal field have drawn attention. We will discuss the differences between spheromaks and FRCs with a weak toroidal field later, in Section 9.3.2.

#### 9.3.1. Spheromaks

##### 9.3.1.1. Magnetic surfaces

The magnetic field of an ideal axisymmetric spheromak forms a set of nested magnetic flux surfaces, as schematically shown in Fig. 9.22. It is thought that, to be globally stable with respect to MHD modes, the spheromak, as well as RFP, must be near the Taylor state [9.7] (see Section 9.2.2.1), where the current is nearly parallel to the magnetic field lines (see Eq. (9.2)) with the parameter  $\lambda$  in this equation being almost constant. The presence of the nested flux surfaces should provide good thermal insulation from the walls. The presence of magnetic field perturbations can lead to stochastization of the field lines and the loss of good confinement. Such effects are discussed later in this section.

Note that Fig. 9.22 is an idealized picture that merely illustrates the concept of a spheromak, without providing information about the shape of a confining vessel. More realistic equilibria will be presented later.

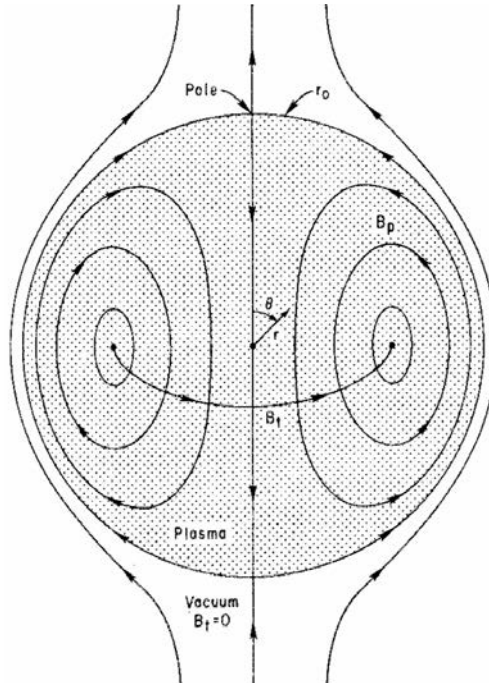


FIG. 9.22. The structure of the spheromak magnetic field as shown in the original paper [9.40].

### 9.3.1.2. Spheromak formation

Spheromaks can be formed by several techniques. We present some details of the so-called gun-injection technique that was used in several projects, including the largest spheromak experiment to date, the SSPX (Sustained Spheromak Physics Experiment) at Livermore [9.43, 9.44] (see Fig. 9.23). Two coaxial electrodes, inner (cathode) and outer (anode, grounded) form a plasma gun with a gap much smaller than the radius of the outer electrode (50 cm). A set of coils, shown in yellow, produce an initial (“bias”) poloidal magnetic field. Some of these coils are situated inside the cathode and create the bias magnetic field localized essentially inside the gun, with very little bias field present in the main vacuum chamber. The timescale of the bias field is much longer than the skin time of the electrodes. The timescale of the spheromak formation and sustainment is, on the other hand, much shorter than the skin time, so that the normal component of the magnetic field at the surface of the conducting vessel

(which is called for this reason “flux conserver”) remains constant during the pulse. Before providing further details related to the formation process, we mention that shown in the main confinement volume are nested flux surfaces corresponding to a quasi-steady-state equilibrium reached sometime *after* the spheromak formation. This equilibrium is reconstructed by means of the CORSICA code [9.45] with the input from the magnetic probe measurements. The separatrix (red line in Fig. 9.23) bounds the region of closed flux surfaces. The field lines outside the separatrix are connected to the electrodes.

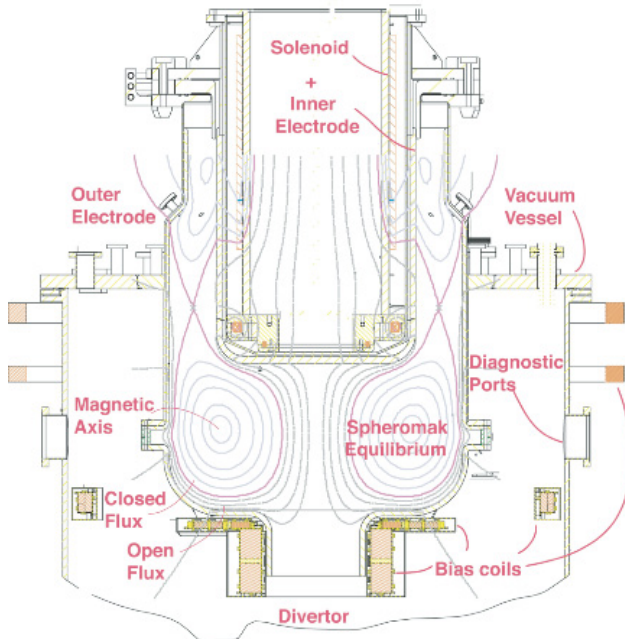


FIG. 9.23. Layout of the SSPX experiment. Shown in orange are poloidal field coils. Note the presence of a solenoid inside the cathode. Reprinted from Ref. [9.44]. Copyright (2011) American Institute of Physics. Eight pulsed gas valves are evenly distributed over the azimuth at the level of a characteristic “knee” in the plasma gun. A set of nested flux surfaces or the toroidally symmetric equilibrium is limited by the separatrix shown in red. The flux surfaces are reconstructed on the basis of the magnetic probe measurements by the CORSICA code [9.45]. The inner diameter of the flux conserver is approximately 1 m.

Returning to the formation process itself, we describe one of the possible modes of spheromak formation in the gun geometry, a so-called “bubble-burst” mode. It is illustrated schematically by Fig. 9.24 for the situation where the initial magnetic field in the main vacuum chamber is almost zero [9.46] (note a strong divergence of the field lines in the main part of the flux conserver). The shot starts with the gas (typically hydrogen or deuterium) puffed into the gun by several pulsed valves situated on the outer electrode (see Fig. 9.23). This forms

## BROADER SPECTRUM OF MAGNETIC CONFIGURATIONS

a gas cloud that is broken down when a high enough voltage is applied between the electrodes, forming the current path 1 in Fig. 9.24, with the current flowing predominantly along the bias magnetic field. A toroidal magnetic field is then formed in the gun, above the current layer. It pushes the current layer in the outward direction. The plasma resistivity is small enough that the bias magnetic field is pulled down during this motion, as shown for the instants 1 and 2 (see numbers on the left side of Fig. 9.24), and a plasma bubble containing toroidal magnetic field gradually emerges into the main vacuum volume. The equilibrium is a result of the balance of the hoop force of the curved poloidal field against the downward directed pressure of the toroidal field. At a certain instant of time (3 in Fig. 9.24), when the bubble becomes large enough, the hoop force can no longer balance the pressure of the toroidal field, the equilibrium is lost, and the bubble, together with magnetic fields frozen into the bubble plasma, bursts into the main volume, forming a spheromak. This is accompanied by reconnection near the gun muzzle. After a few hundred microseconds, the spheromak settles down and the confinement/sustainment phase begins. A possible axisymmetric (and thereby idealized, see below) equilibrium at this stage is shown in Fig. 9.23.

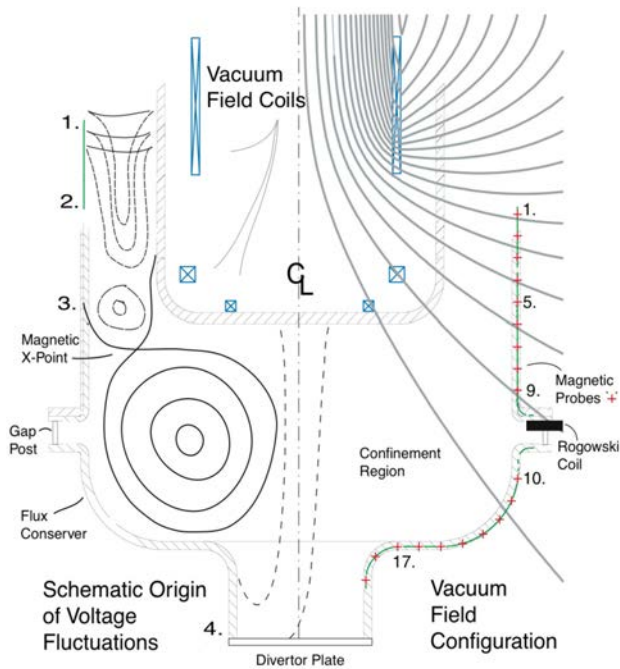


FIG. 9.24. Illustration of the bubble-burst model. Right-hand side: initial poloidal field for one of possible settings of the currents in poloidal field coils. Numbers are used to identify locations of magnetic probes. Left-hand side: an illustration of the bubble-burst model. The numbers on the left indicate the time sequence. Reprinted from Ref. [9.46]. Copyright (2011) American Physical Society.

During the violent bubble-burst phase, there are no good flux surfaces, and field lines are wandering over the whole volume of the flux conserver, making only a few turns around the geometrical axis before striking the walls or getting into a cold plasma region near the walls [9.47]. At this (formation) phase the parallel electron heat conduction is the dominant heat loss mechanism, and the plasma temperature is low.

9.3.1.3. Sustainment phase and helicity injection

In the sustainment phase, the spheromak equilibrium is close to the Taylor force-free state (Eq. (9.2)). At this stage, good flux surfaces can be formed and plasma confinement may become determined by cross-field heat losses. As was shown with the SSPX device, the cross-field thermal diffusivity in good confinement regimes may become quite low: only a few times higher than the classical ion thermal diffusivity [9.44]. It is not quite clear what type of plasma fluctuations determines the magnitude of cross-field anomalous transport at this stage. The maximum electron temperature obtained in the SSPX device was 500 eV, at the plasma density  $\sim 10^{20} \text{ m}^{-3}$  and the confining magnetic field  $\sim 0.6 \text{ T}$  [9.48]. A typical set of time histories of various plasma parameters is shown in Fig. 9.25.

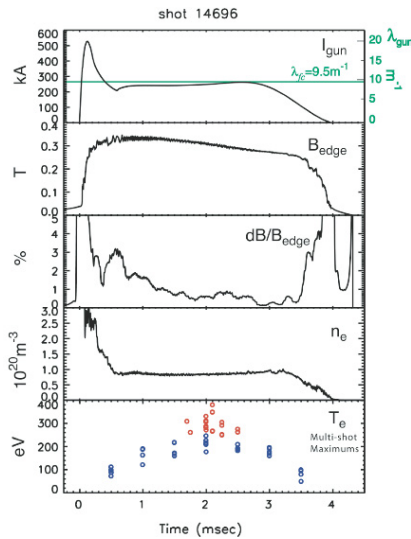


FIG. 9.25. Time histories of plasma parameters. (a) gun current with a characteristic initial spike and a long flat-top;  $\lambda$  is a parameter introduced in Eq. (9.2); (b) poloidal field at the plasma edge near the equatorial plane; (c) relative magnitude of the magnetic field perturbations at the edge; (d) chord-averaged plasma density; (e) electron temperature from Thomson scattering. Reprinted from Ref. [9.44]. Copyright (2011) American Institute of Physics.

At the quiescent stage, ohmic dissipation causes redistribution of the current, leading to some deviation of the system from the exact Taylor state. Typically, the poloidal current that flows closer to the walls decays faster than the toroidal current that occupies a relatively warm plasma region around the magnetic axis. To avoid a gross deviation from the Taylor state and rapid decay of the spheromak, one has to sustain current on the open field lines linked to the plasma gun. Still, as there is no loop voltage applied to the spheromak, the toroidal current inside the separatrix would be decaying, if not sustained by some continuous “helicity injection” process (see Section 9.2.2.1 for discussion of helicity).

The concept of helicity injection was discussed in Section 9.2.7 in conjunction with RFP physics. In gun-produced spheromaks a different technique can be used based on the possibility of indefinitely sustaining a voltage across the gun. This technique is called “coaxial helicity injection” (CHI). We mention here two specific models of CHI. One model attributes sustainment of the spheromak current to a continuing quasi-periodic ejection of the spheromak-like objects (filaments carrying both toroidal and poloidal current) from the plasma gun and their merging with the existing spheromak [9.46]. The other model associates the sustainment with a kink instability of the central column, which stirs perturbations in the whole spheromak and drives the toroidal current. Such a mechanism is thought to be responsible for the current sustainment in the British spheromak SPHEX [9.49, 9.50]. The structure of this “dough-hook”-like central column is shown in Fig. 10 of Ref. [9.50].

In its extreme case, a very strong kinking of the plasma column, with subsequent reconnection, may occur. The column may curl so strongly that it reconnects on itself [9.51], generating a spheromak with a central hole that accommodates the restored (after reconnection) central column (Fig. 9.26). Such events have apparently been observed in the experiments with current-carrying plasma jets at Caltech [9.52].

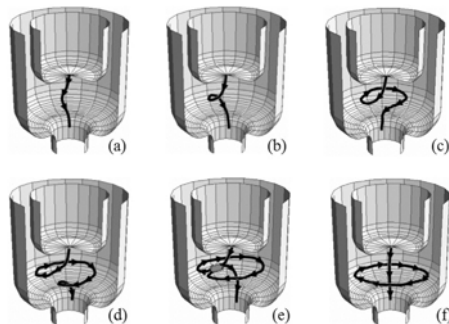


FIG. 9.26. The time sequence for the varying current pattern in an extreme case of non-linear kinking of the central column leading to formation of the spheromak configuration (toroidal current ring with embedded toroidal field). Arrows indicate the direction of the current. Reprinted from Ref. [9.51]. Copyright (2011) American Institute of Physics.

All these mechanisms can operate in the same experiment, with their relative role depending on a particular shape of the initial bias (poloidal) magnetic field and the temporal dependence of the gun current. What is common in them is that the sustainment of the toroidal current is inseparable from the presence of non-axisymmetric magnetic perturbations. This, in turn, leads to a question of distortion of the flux surfaces and confinement degradation by CHI. As a general observation, one can say that, in a hot plasma needed for fusion applications ( $T > 5$  keV), the Joule dissipation is quite a slow process, so that required fluctuations could have a small amplitude and the intrinsic loss channel associated with CHI would probably be small. Here we discuss the effect of fluctuations for present day devices with modest temperatures.

As we have already mentioned, among the modes that are thought to be most important is the kinking of the central current column, which stirs perturbations in the whole spheromak. If these perturbations are resonant at some flux surfaces inside the confinement region, one can expect a stronger detrimental effect on the confinement. As the resonances are directly related to the radial profile of the safety factor  $q$ , it was realized that the  $q$  profiles may have significant effect on the mode activity. This is illustrated by Fig. 9.27 (from Ref. [9.44]), where the presence of strong fluctuations (detected by the array of magnetic probes situated at the walls) correlates clearly with the appearance of the resonances. Other modes of current driven instabilities may also be present and lead to similar results.

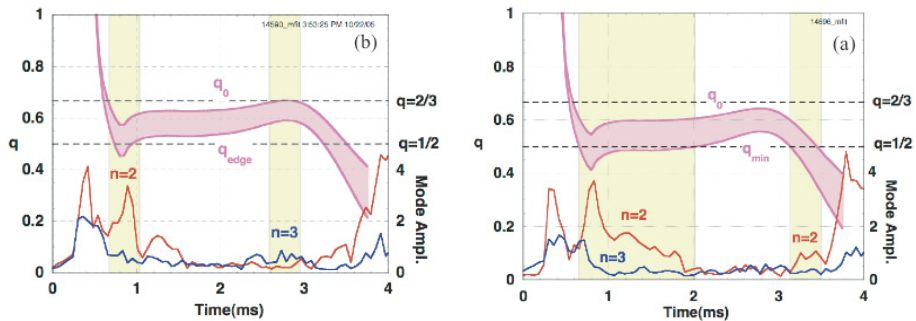


FIG. 9.27. Correlation of the mode activity with the presence of resonant surfaces in the confinement region. A pink band shows the range of the safety factors reached between the magnetic axis ( $q_0$ ) and a minimum ( $q_{min}$ ) that is typically reached not far from the separatrix. When the low-mode resonances are absent (i.e. outside the vertical yellow bands), the plasma is relatively quiet. However, when a resonance surface enters the plasma, the corresponding mode significantly increases in the probe signals ( $m$  and  $n$  are poloidal and toroidal mode numbers, respectively). In (a) the  $n = 2$  mode is excited at the beginning and end of the shot. In (b)  $q$  becomes high enough at the end to excite the  $n = 3$  mode. The  $q$  profile is obtained by CORSICA reconstruction [9.45]. Reprinted from Ref. [9.44]. Copyright (2011) American Institute of Physics.

#### 9.3.1.4. Current amplification

An important issue for reactor applications of spheromaks is that of the achievable value of the “current amplification” parameter, by which one usually means the ratio of the toroidal current inside the separatrix to the drive current on the open field lines. As in any plausible steady state reactor based on a spheromak, the toroidal current will be in the range of 10 MA or more, the current multiplication must exceed 20–30, as otherwise the energy loss on the open field lines would weigh too heavily on the power balance, and the engineering issues related to the damage to electrodes by high currents and associated heat loads would become hard to solve.

Several approaches to the current amplification, all related to the control over the temporal dependence of the drive current, have been tried on the SSPX facility. Some of them used a large spike of the current at the initial stage, with a relatively low value of the sustainment current at the subsequent long lasting sustainment phase. The other relied on applying a sequence of partially overlapping current pulses. Various bias flux configurations have been tried. It turned out that the best results are obtained when the ratio  $j / B_{bias}$  (where  $j$  is current density and  $B_{bias}$  is the bias magnetic field) in the gun corresponds to the eigen solution of the Taylor problem for the gun [9.53]. Thus far, the maximum current amplification reached with SSPX has not exceeded a factor of 2–3. Potentially better results could be achieved by programming the bias flux in an optimum way [9.54].

For the steady state system based on a spheromak, one could use also various non-inductive current drive techniques developed for tokamaks, in particular, RF current drive or neutral beam injection (NBI) current drive. As spheromaks usually have a relatively weak magnetic field, with a complex spatial structure, it is somewhat difficult to use the former set of techniques. The NBI technique is conceptually more straightforward. In principle, by the proper aiming of the neutral beams, one can have a significant degree of control over the current distribution — exactly what is needed to keep the plasma close to the Taylor state and thereby avoid excitation of large fluctuations. The main difficulty is that the Taylor state implies the presence of a significant current density in the vicinity of the separatrix, where the plasma is already relatively cold and the Joule dissipation is large. This would reduce the energy efficiency of the whole system. Therefore, it is important to search for the stable states with zero or low current density near the walls. Some encouraging results in this direction have been reported in Ref. [9.55].

Strictly speaking, the exact Taylor state (Eq. (9.2)) cannot sustain a pressure gradient. On the other hand, it is hard to expect that for small enough pressure gradient the MHD stable configuration would fall apart. It is thought that the onset of pressure driven instabilities can be associated with the Mercier limit.

Experimentally, the plasma beta in the regimes of a good plasma confinement was in the range of 5–10%. This fact could be interpreted as an indication of the existence of the pressure limit, but the nature of this limit remains unclear: it may be associated not with the onset of some destructive instability, but rather with the balance between the heating and cross-field losses. For a given heating power, such an equilibrium would limit the beta. For a recent discussion of the pressure limit see Ref. [9.56].

### 9.3.1.5. Regular versus stochastic magnetic field

The formation and the subsequent confinement of plasma in the SSPX facility have been simulated [9.57] by the 3-D MHD code NIMROD [9.58]. Most interesting is a possibility to directly simulate the magnetic field line structure in specific regimes of plasma confinement. The structure is visualized by a field line puncture plot in a poloidal cross-section. For a low fluctuation level, a set of nested surfaces was revealed, whereas at higher fluctuation levels stochastization of the magnetic field lines could occur. In the case of a low fluctuation level, one could have good flux surfaces near the magnetic axis and complete stochasticity at the periphery (Fig. 9.28). A generally good agreement with the observed macroscopic features of the plasma behaviour was obtained. One of the persistent (and not yet quite understood) discrepancies between the code and experimental results was a consistently lower (than in the experiment) electron temperature.

This discrepancy may be related to the fact that the version of the code used in these simulations did not contain the physics responsible for the onset of plasma rotation, which was almost certainly present in the SSPX facility, although not measured directly (see Ref. [9.47] for explanations). Most probably, the rotation is caused by two-fluid effects. In particular, in Ref. [9.59], it has been pointed out that magnetic field imperfections and the associated finite, albeit large, length of magnetic field lines connecting the plasma core and the plasma periphery lead to a rapid establishment of the parallel electron momentum balance, which, by virtue of the quasi-neutrality constraint, determines the electric field distribution across the average flux surfaces. The  $\vec{E} \times \vec{B}$  rotation velocity predicted by this model is in the range suggested by SSPX experiments.

### 9.3.1.6. Spheromak: a flexible configuration

In addition to the two spheromak facilities mentioned above (SSPX and SPHEX), there have been several other spheromak experiments, some of them ongoing. Specially mentioned should be the CTX experiment in Los Alamos National Laboratory (Ref. [9.60] and references therein), where many important results related to formation and sustainment of a gun-driven spheromak were

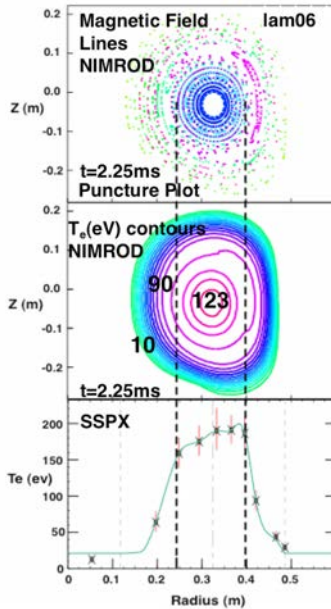


FIG. 9.28. The results from NIMROD simulation (lam06 is a designation of the code run) of a characteristic SSPX shot [9.57]. Upper: magnetic field line puncture plot. There is a region with good flux surfaces in the plasma core (between the vertical dashed lines); at the plasma periphery, field lines are stochastic. Middle: iso-contours of electron temperature from NIMROD. Lower: experimentally measured radial temperature profile whose shape agrees well with the simulation; the maximum temperature in the simulation is roughly a factor of two lower than in the experiment. Reprinted from Ref. [9.57]. Copyright (2011) American Institute of Physics.

obtained in the late 1980s and early 1990s. With a flux conserver radius of  $\sim 0.3$  m and a gun current up to 600 kA, a spheromak configuration with an electron temperature up to 400 eV and a maximum magnetic field strength of 3 T was obtained. The onset of pressure driven instabilities near the Mercier limit was observed. This facility played a large role in establishing the conceptual base for the later SSPX experiment at Livermore.

The Swarthmore spheromak (SSX) [9.61] uses high resolution Doppler spectroscopy and large probe arrays to find plasma flows associated with reconnection processes, and relates the results to the processes in the Earth's magnetosphere and solar chromosphere.

The Princeton spheromak MRX [9.62, 9.63] uses a formation technique based on the toroidal inductive core. The plasma is initially formed around this core and therefore traps both toroidal and poloidal magnetic flux, and later is pushed towards the axis of symmetry by the increased poloidal field, thereby forming a spheromak not contacting material surfaces. An interesting feature of the MRX facility is its capability to form and then merge two spheromaks, with

various signs of helicity, and study reconnection processes by a large array of magnetic and electrostatic probes. These studies are of interest for astrophysics and geophysics.

An important feature of the HIST device in Japan is the possibility of inserting a central, current carrying rod, thereby transitioning from a simply connected spheromak configuration to a configuration of a spherical tokamak. In the experiments with a rapid reversal of the current in the rod, it was observed that both toroidal and poloidal fields in a plasma reverse [9.64].

A novel approach to spheromak formation and helicity injection is studied at the HIT-SI facility in Seattle [9.65, 9.66]. This facility employs a bow-tie confinement volume connected through slots with two inductive helicity injectors, which are segments of a reversed field pinch. By proper phasing of the oscillating toroidal flux and loop voltage in each segment, one can reach a situation where continuous helicity flow is formed to the spheromak sitting in the confinement zone.

One of the interesting applications of pulsed spheromaks in fusion research is using them for fuelling large tokamak devices. It is envisaged that a spheromak moving with a high enough velocity will penetrate deep into the plasma of the reactor tokamak and deliver fusion fuel to the plasma core. Experiments of this type have been carried out with several tokamaks, most recently with the JFT-2M tokamak in Japan [9.67]. Spheromaks with a velocity of  $180 \text{ km} \cdot \text{s}^{-1}$  were generated. They penetrated to the plasma core of a tokamak with a minor radius of 35 cm, in a toroidal field  $\sim 1 \text{ T}$ . Reference [9.67] contains references to earlier experiments of this type.

### 9.3.2. Field reversed configuration (FRC)

#### 9.3.2.1. Field geometry

The magnetic field structure of a typical FRC is shown in Fig. 9.29. It is characterized by the presence of a null-point of the O-type inside the confinement domain. Also characteristic are two nulls of the X-type at the ends of the plasma confinement zone. Outside the separatrix, the field lines are open. This configuration is very attractive for many versions of fusion reactors, because it combines a closed field line confinement zone with a simple geometry of a linear device; in addition, it possesses a natural channel for the heat exhaust along the field lines, very much like in mirror machines (Section 9.4). Despite the fact that the configuration shown in Fig. 9.29 is theoretically strongly unstable with respect to several MHD modes (see below), real FRCs demonstrate a remarkable cohesion; they can be translated along the axis of a linear configuration, reflected from the mirrors, and adiabatically compressed. This versatility allows using FRCs both in pulsed, high density approaches to fusion, and in steady state

magnetic confinement approaches. A review of FRC research until 1987 can be found in Ref. [9.42].

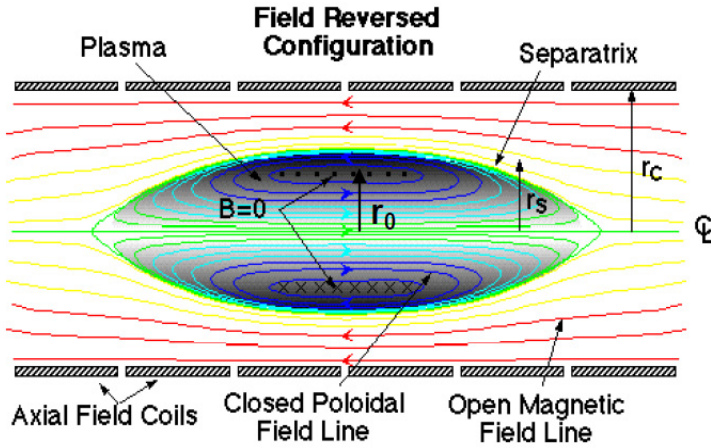


FIG. 9.29. Typical FRC equilibrium. The dots and crosses show the current direction at the field-reversal surface. The outermost green line represents the separatrix with two X-points at the ends of the confinement zone;  $r_c$  is the radius of the magnetic flux conserver;  $r_s$  is the separatrix radius in the equatorial plane,  $r_0$  is the radius of the field reversal. The figure depicts a figure of revolution, with the central horizontal line being the rotation axis; in the further discussion this is the  $z$  axis. Taken from Ref. [9.68].

The ratio of the plasma length  $L$  to plasma diameter  $D$  is called “plasma elongation”  $E = L / 2r_s$ , and is typically rather large, 2–3 and more. The radial pressure balance for an elongated FRC reads as

$$p + \frac{B_z^2}{2\mu_0} = \frac{B_c^2}{2\mu_0} \tag{9.28}$$

where  $B_c$  is the magnetic field on the flux conserver. In highly elongated FRCs the field reversal can be considered as occurring at an elongated reversal surface. Obviously, the plasma pressure on the reversal surface is equal to the magnetic pressure of the confining field just outside the separatrix. In other words, the FRC is a high-beta configuration — an additional advantage. In the regimes of a good plasma confinement the pressure must be constant along the flux surfaces. At the plasma periphery near the separatrix, where the field lines become open, the pressure is small compared to its value at the null point. As the outer and inner radius of an FRC are connected by field lines, there is also a zone of a low pressure near the axis.

The radial size of an FRC is usually characterized by a dimensionless parameter  $S$  which is the average number of ion gyroradii that can be accommodated between the reversal surface and the separatrix:

$$S \equiv \int_{r_0}^{r_s} \frac{r dr}{r_s \rho_i} \quad (9.29)$$

with  $\rho_i$  being the ion gyroradius. Experimentally, FRCs with  $S$  between 1 and  $\sim 10$  have been studied.

### 9.3.2.2. FRC formation

One of the ways of forming an FRC is creating a preliminary plasma in a solenoidal magnetic field and then using a pulsed coil that would reverse the direction of the magnetic field outside the plasma. We present here some details of these processes based on the ongoing FRX-L experiment at Los Alamos [9.69, 9.70] (see Fig. 9.30). The preliminary plasma was formed in a bias magnetic field  $\sim 0.2$  T. To facilitate the reconnection at the ends of the device, cusp field coils were used at the ends [9.71]. The pulsed field of the opposite polarity was 3T, with a rise-time of  $\sim 3$   $\mu$ s. After reconnection occurred at the ends of the device,

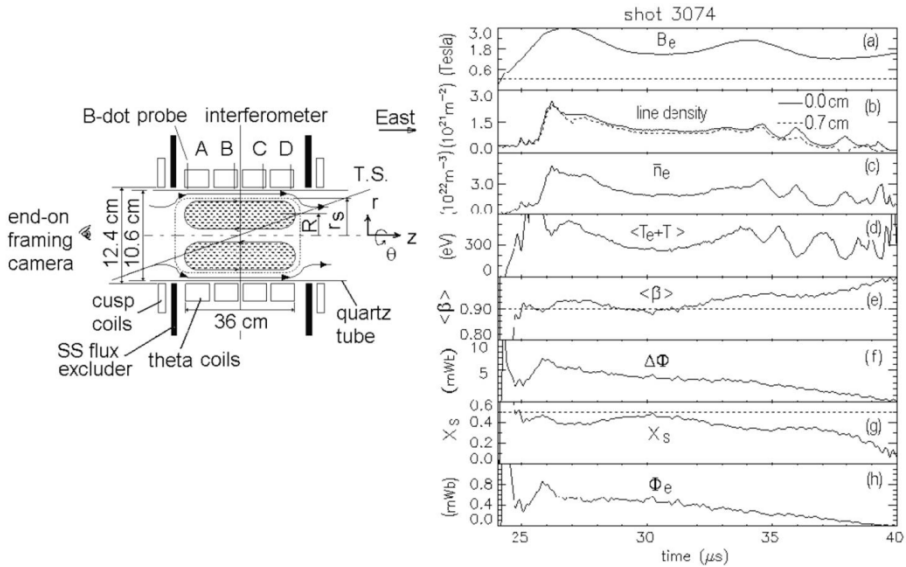


FIG. 9.30. FRX-L experiment at Los Alamos. Left: geometry of the experiment. Shaded is the zone occupied by the FRC plasma. Note the presence of quasi-steady cusp coils near the ends of the device. Right: typical time histories of plasma parameters: (a) external magnetic field in the midplane; (b) line integrated density along two chords; (c) volume averaged density; (d) total averaged temperature; (e) normalized separatrix radius  $X_s = r_s/6.2$  cm, at the midplane; (f) trapped poloidal flux. Reprinted from Ref. [9.70]. Copyright (2011) American Institute of Physics.

the FRC experienced some shrinking in the axial direction and then settled into the long-lived equilibrium state. The reversed field was sustained at the level of 2 T for times exceeding the decay time of the FRC. The plasma density in this state was  $\sim 4 \times 10^{16} \text{ cm}^{-3}$  and the sum of the electron and ion temperatures,  $T_e + T_i$ , was  $\sim 400 \text{ eV}$ . After approximately 10  $\mu\text{s}$ , significant plasma rotation developed, with a frequency  $\omega_{rot} \sim 2 \times 10^6 \text{ s}^{-1}$  and an  $n = 2$  rotational instability developed that led to a loss of the FRC. We return to FRC instabilities later and now consider some equilibrium properties of prolate FRCs.

### 9.3.2.3. FRC equilibrium

There exists a very useful analysis of the elongated equilibrium presented in Ref. [9.72]. The magnetic flux can be defined as

$$\psi(r) = 2\pi \int_0^r B_z(r) r dr \quad (9.30)$$

with  $\psi$  becoming zero at the axis and at the separatrix. Obviously,

$$d\psi = 2\pi B_z r dr \quad (9.31)$$

In the equilibrium state, the pressure is constant along the flux surfaces. Assume that  $p$  is a linear function of the flux,  $p = (B_c^2 / 2\mu_0)(\psi / \psi_0)$ , where  $\psi_0$  is the flux at the reversal surface (the linearity assumption is not critical, just allows making the analysis simpler). Combined with the equilibrium constraint (Eq. (9.28)), this equation shows that  $B_z = B_c \sqrt{1 - (\psi / \psi_0)}$ . Substituting this relation into Eq. (9.31) and integrating the resulting differential equation from  $r_0$  to  $r_s$ , one obtains

$$r_0 = r_s / \sqrt{2} \quad (9.32)$$

Consider now the axial component of the stress tensor and impose a condition of axial equilibrium. To do that, one can consider two cross-sections, the equatorial plane, and the plane a few  $r_s$  away from the ends of an FRC. In both planes, the magnetic field has essentially only a  $z$ -component. As the segment of the system situated between these two planes is in equilibrium, the integral of the parallel component of the stress tensor over the cross-section must be the same for both planes.

At a surface situated outside the FRC, the axial component of the stress tensor is uniform and equal to  $-(B_c^2 / 2\mu_0)(r_c^2 - r_s^2)^2 / r_c^4$ . On the other hand, the axial component of the stress tensor in the equatorial plane is  $p - B_z^2 / 2\mu_0 = 2p - B_c^2 / 2\mu_0$  (we have used the equilibrium condition Eq. (9.28)). Integrating this component over the equatorial cross-section from

$r = 0$  to  $r = r_c$ , and equating this to the integral over the distant cross-section, one obtains:

$$2\pi \int_0^{r_s} pr dr - \pi r_c^2 (B_c^2 / 2\mu_0) = -\pi r_c^2 (B_c^2 / 2\mu_0) (r_c^2 - r_s^2)^2 / r_c^4 \quad (9.33)$$

this yielding

$$\bar{\beta} \equiv \frac{2\pi \int_0^{r_s} pr dr}{\pi r_s^2 (B_c^2 / 2\mu_0)} = (1 - \frac{r_s^2}{2r_c^2}) \quad (9.34)$$

If the flux conserver is situated very close to the separatrix, one has  $\bar{\beta} \approx 1/2$ . This parameter relates the plasma thermal energy to the magnetic field energy of the external confining magnetic field. Locally, the ratio of the plasma energy density to the magnetic field energy density (the parameter that determines, in particular, plasma microstability) varies across the plasma and is infinite on the reversal surface.

This result has very interesting consequences for the problem of FRCs adiabatically compressed in the radial direction. They can be compressed by the moving wall of the flux conserver (the liner), or by the injection of a rapidly moving FRC into the conical duct, with a gradually decreasing cross-section. The first mode of operation will be realized in the FRX-L experiment [9.73], whereas the second one will be tried as described in Ref. [9.74].

Consider a tightly fitted flux conserver, so that  $r_c \approx r_s$ . For the radial compression by a factor of  $C > 1$  ( $C$  is sometimes called "convergence"), one has  $r_s = r_{s0} / C$ . Here and below in this section, the subscript "0" refers to the initial (pre-compression) state. The conservation of the magnetic flux then means that the magnetic field increases as  $C^2$ , and the plasma pressure  $p$ , according to the condition  $\bar{\beta} \approx 1/2$ , increases as  $C^4$ . On the other hand, the pressure for the adiabatic compression scales as  $V^{-5/3}$  where  $V$  is the plasma volume  $V \propto Lr_s^2$ . In other words,  $p(Lr_s^2)^{5/3} = p_0(L_0r_{s0}^2)^{5/3}$ . Then, since  $r_s = r_{s0} / C$  and  $p = p_0C^4$ , we find that

$$L = L_0 / C^{2/5} \quad (9.35)$$

So, somewhat unexpectedly, the radial compression of an FRC leads to its shortening. This effect is due to the increase of the axial force acting on the ends of the FRC due to the magnetic field curvature. The particle density and temperature scale, obviously, as

$$n = n_0 C^{12/5} \quad (9.36)$$

$$T = T_0 C^{8/5} \quad (9.37)$$

The elongation  $E = L / 2r_s$  increases as  $E = E_0 C^{3/5}$ . These equations are built on the assumption that the FRC is compressed purely radially. A different approach is possible if a stronger compression is needed, an approach based on geometrically self-similar compression. This regime can be reached if the ends of the FRC are pushed towards the equatorial plane in concert with the radial compression,  $r = r_0 / C$ ,  $L = L_0 / C$ , so that the elongation stays constant,  $E = E_0$ . Such a regime can be achieved by using a shaped liner as discussed in Ref. [9.75].

#### 9.3.2.4. Plasma rotation and stability

We return now to the problem of plasma rotation. The exact mechanism that causes FRC rotation is not known yet. We mention here three plausible explanations, with the first two nicely summarized in Ref. [9.42], where further references can be found. The first explanation is based on the observation that the ions lost via some diffusive process through the separatrix remove momentum from the plasma. This is related to the observation that there is an azimuthal flow associated with the radial pressure gradient. An ion just lost through the separatrix moves preferentially in the ion diamagnetic direction. This determines the sign of the momentum imparted to the plasma remaining inside the separatrix.

The second mechanism attributes rotation to electrical contact with the conducting end-plates on the open field lines outside the separatrix. This is the same mechanism that causes plasma rotation in mirror devices (see Section 9.4). The rotation is initially generated outside the separatrix and is then transferred to the confined plasma by viscosity.

Recently, a third mechanism has been proposed [9.76], relating rotation to the possibility that flux surfaces in the FRC may not be perfect, but are rather “fuzzy” due to the presence of random magnetic fluctuations. The mechanism is similar to that described in Ref. [9.59] in conjunction with rotation in spheromaks (see Section 9.3.1). Detailed comparison with the existing experimental data presented in Ref. [9.76] seems to support this model.

In all these models the rotation frequency is in the range of the ion diamagnetic drift frequency. Such a rotation in long enough systems is known to cause  $n = 2$  rotational instability [9.77]. As has already been mentioned, the rotational instability has often been observed in FRC experiments. A universal cure that has been found quite efficient is the introduction of a stabilizing multipole magnetic field [9.42]. The other large scale FRC instability is that of the internal tilt. The structure of perturbations is illustrated in Fig. 9.31, reproduced from Ref. [9.78]. An intuitive explanation of this instability is based on the observation that the current running in the FRC and peaked near the field

reversal surface is opposite to the current in the external field coil. These two currents possess anti-parallel magnetic moments. Such a configuration has a larger energy than the one where the magnetic moments are parallel. Accordingly, the plasma “magnet” tries to turn over, thereby producing the instability. Actual description of this instability is quite complex, due to the complex initial geometry and steep variation of the unperturbed parameters. MHD stability analyses, summarized in Ref. [9.79], shows that the tilt instability is strong, with the characteristic e-folding time of order of the Alfvén transit time  $L/v_A$ , with  $v_A$  being a characteristic Alfvén velocity. On the other hand, as has already been mentioned, experimentally, FRCs demonstrate a remarkable resilience and can exist in a relatively quiescent state for more than 100 Alfvén transit times (see, for example, Ref. [9.80]).

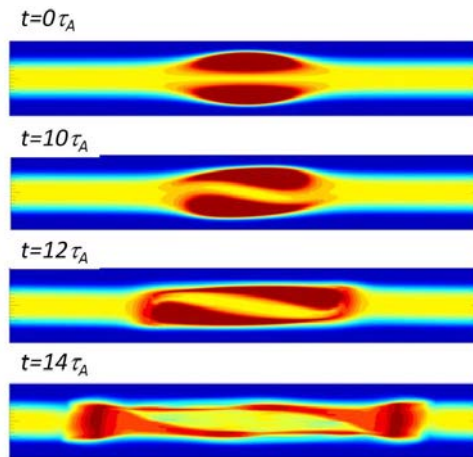


FIG. 9.31. Evolution of the tilt instability (pressure contours) in the  $r$ - $z$  plane, with  $z$  directed horizontally. Time is measured in Alfvén transit times. Initial elongation is 4. Reprinted from Ref. [9.78]. Copyright (2011) American Institute of Physics.

It has long been thought that kinetic effects play a significant role in FRC stability. Indeed, the presence of a field reversal surface leads to the appearance of the orbits that encompass a significant part of the FRC even if the parameter  $S$  is relatively large, say, 10. Another important parameter is the elongation  $E$ . One can expect that larger elongation reduces, in relative terms, the contribution of curved field regions near the ends. Empirically, instability usually showed up when the parameter  $S/E$  was below, roughly, 2–3 [9.42].

#### 9.3.2.5. Steady state FRCs

Thus far, we have been considering FRCs of the pulsed type. A significant effort has also been spent on the quasi-steady-state (and, eventually, steady-state)

FRCs. Historically, the first attempt in this direction was led by N. Cristofilos with the ASTRON facility [9.81]. The field reversed configuration was supposed to be produced by a cylindrical shell of high energy charged particles rotating around the axis in an external magnetic field. At a high enough current of energetic electrons, a field reversal would occur. Then, one could generate a fusion temperature plasma in the closed field line region; this plasma would have a long lifetime as there would be no end losses. Later, it was proposed to use MeV range protons to reach the field reversal [9.82]. Field reversal with energetic electrons was achieved in the 1970s [9.83]. An expectation was that the “stiffness” of the ring of the energetic electrons or ions would provide good MHD stability of the system. However, none of these attempts have been quite successful, for a variety of reasons, ranging from the difficulty of creating a field reversing ring in a strong enough external field to a variety of virulent instabilities which did still exist in the system.

One more attempt of creating the steady state FRC that was tried in the 1970s was by the off-axis injection of neutral beams into the mirror trap [9.84]. It was expected that ion orbits would be such as to produce azimuthal current in the direction needed for the field reversal. An off-axis neutral beam injection was used, with the beams positioned in such a way as to impart a torque to the plasma, with the torque direction corresponding to the field reversal. Experiments with the 2XIIB facility at Livermore [9.84] have produced a high beta plasma, and the on-axis magnetic field has dropped to  $\sim 0.1$  of its vacuum value, but reversal was not reached. The average ion energy was in the range of 12 keV, the plasma density was as high as  $10^{14} \text{ cm}^{-3}$ , and the plasma diameter was  $\sim 15 \text{ cm}$ . Ion confinement time was somewhat shorter than the ion drag time against electrons, which were relatively cold,  $\sim 150 \text{ eV}$ . The authors attributed this fact to the presence of ion cyclotron fluctuations.

More recently, experiments on sustaining the plasma current by means of RF drive have been tried [9.85]. A low frequency rotating magnetic field (RMF) was applied, in the range of 100 kHz in an external magnetic field of  $\sim 0.3 \text{ kG}$ . The rotating field entrained electrons and sustained the azimuthal current that caused field reversal. The reversed state was sustained for more than 2 ms, with the sum of electron and ion temperatures  $\sim 200 \text{ eV}$ , and the density  $\sim 10^{13} \text{ cm}^{-3}$ . The amplitude of the RF magnetic field, which had a significant component normal to the FRC field, was quite high, in the range of 10% of the external field. It was pointed out in Ref. [9.86] that FRCs and other plasma configurations where only a poloidal field is present are very sensitive to even minor non-axisymmetric perturbations which lead to the opening of the majority of field lines. Although this effect should have been present in the experiment under consideration, it might be mitigated by the presence of a divertor-like configuration of the magnetic field beyond the separatrix [9.85]. A possible way of reducing the effect

of the RF drive on heat loss is to switch to an odd-parity field distribution along the magnetic axis [9.87].

Another possibility of increasing the “stiffness” of the flux surfaces is by introducing a weak toroidal magnetic field [9.86, 9.88]. It turns out [9.88] that, in order to have a significant favourable effect on a prolate FRC,  $E > 4-5$ , this field ( $B_\phi$ ) can be quite small, in the range of 10% of  $B_z$ . Therefore, it does not have any direct effect on the plasma equilibrium: the toroidal field pressure remains at the level of a few per cent of the poloidal field pressure. Therefore, FRCs with a weak toroidal field are distinctly different from spheromaks, which are, to the first order, force-free structures. Note that toroidal field may be spontaneously generated in FRCs [9.42, 9.89].

## 9.4. OPEN CONFINEMENT SYSTEMS

### 9.4.1. Confining a plasma on the open field lines

In a general sense, open confinement systems are those for which every point in the plasma confinement volume is directly connected along the magnetic field line with the walls of a vessel surrounding the plasma. In a more narrow sense, however, the open confinement systems are identified with mirror machines and their variations. We will use below this narrow definition.

The attractiveness of mirror machines as the basis for a future fusion reactor is related to the following features: the main energy producing element in mirror machines is a simple straight solenoid — a great engineering advantage; the plasma beta (demonstrated experimentally) can be as high as  $\sim 0.5$ ; there exists a natural channel for the heat and fusion ash removal through the ends of the machine, where large expansion tanks can be placed; mirror geometry is amenable to the use of direct energy convertors — a feature important for the use of advanced fuel, where most of the reaction products will be charged particles. All this supported an interest in mirrors through the decades of fusion research, although at present the scale of mirror research, worldwide, is rather limited.

### 9.4.2. Mirror confinement

The concept of mirror confinement was proposed independently by Post in the USA [9.90] and Budker in the USSR [9.91] in the early 1950s. Over the years, a number of modifications of the original concept have been suggested and there exist several review papers summarizing various stages of mirror research [9.92–9.96]. We, however, start discussion from the simplest (original) version of a mirror machine and only after that consider various modifications, which can lead to more attractive fusion reactors than those based on a simple mirror.

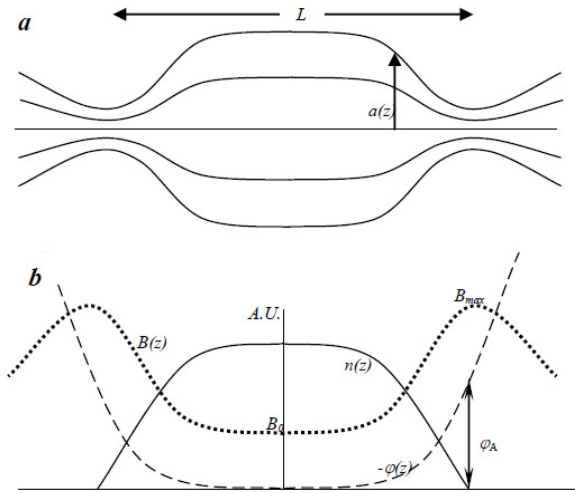


FIG. 9.32. (a) Magnetic field lines in an axisymmetric mirror machine;  $L$  — mirror-to-mirror length;  $a(z)$  — outer radius of the plasma, with  $z$  being a distance along the axis. (b) Distribution of various parameters along the axis: magnetic field strength  $B(z)$  (dotted line); plasma density  $n(z)$ , which becomes very small in the mirror throat and continues to decrease beyond the throat (solid line); ambipolar potential  $\varphi(z)$  (with “minus” sign) (dashed line); the zero is taken to be in the midplane; potential difference between the equatorial plane and the mirror throat  $\varphi_A$  (positive). The midplane corresponds to  $z = 0$ .

Mirror confinement utilizes the fact that, for magnetic fields varying at the spatial scale much greater than the ion gyroradius  $\rho_i$ , the particle magnetic moment  $\mu \equiv mv_{\perp}^2 / 2B$  is an adiabatic invariant and, for the purpose of our discussion, can be considered as a constant of motion. Consider a magnetic field with the field lines shown in Fig. 9.32a, i.e. a field that increases both ways from the midplane. For reasons that will become clear shortly, the zones of a strong magnetic field are called “magnetic mirrors”. Consider then a particle that starts its motion from the equatorial plane of the device. The constancy of the particle energy  $E \equiv m(v_{\parallel}^2 + v_{\perp}^2) / 2$ , in combination with the constancy of the magnetic moment  $\mu$ , means that the parallel energy of the particle decreases when the particle moves towards the region of the stronger magnetic field at the end of the device,  $mv_{\parallel}^2 / 2 = E - \mu B$ .

Expressing the energy and the magnetic moment in terms of the quantities corresponding to the initial position of the particle (which we mark by a subscript “0”), one can rewrite the expression for the parallel velocity as

$$v_{\parallel}^2 = v_{\parallel 0}^2 - v_{\perp 0}^2 \left( \frac{B}{B_0} - 1 \right) \quad (9.38)$$

One sees that, on the way from the midplane towards the regions of a high magnetic field, the parallel velocity decreases and, for a large enough value of

TABLE 9.1. PARAMETERS OF A GENERIC MIRROR MACHINE WITH A FUSION-GRADE PLASMA

Parameter	Notation and units	Numerical value
Ion average energy	$\overline{W}_i$ [keV]	100
Electron temperature	$T_e$ [keV]	20
Plasma density	$n$ [m <sup>-3</sup> ]	10 <sup>20</sup>
Vacuum magnetic field in the midplane	$B_0$ [T]	4
Mirror magnetic field	$B_M$ [T]	10
Mirror-to-mirror length	$L$ [m]	10
Plasma radius in the midplane	$a$ [m]	1
Ion collision time	$\tau_{ii}$ [s]	1
Ion mean free path	$\lambda_{ii}$ [m]	3 × 10 <sup>6</sup>
Electron collision time	$\tau_{ee}$ [s]	10 <sup>-3</sup>
Fusion gain factor	$Q$	1.2
Ion gyroradius in the midplane (deuterons)	$\rho_i$ [cm]	1.5

the initial perpendicular velocity, the particle is reflected back from the mirror and starts oscillating between two turning points. It is therefore confined in a finite volume. Introducing a quantity called “pitch angle”,  $\vartheta_0$ , according to the equation  $\sin \vartheta_0 = v_{\perp 0} / v_0$ , one can write a condition for the particle confinement in a mirror machine as

$$\sin \vartheta_0 > \sqrt{\frac{B_0}{B_{\max}}} \equiv \frac{1}{\sqrt{R_M}} \quad (9.39)$$

where the quantity  $R_M \equiv B_{\max} / B_0$  is called a “mirror ratio”. Particles with smaller (than in Eq. (9.39)) pitch angles are not confined between the magnetic mirrors and are lost through the ends. In the velocity space the zone of unconfined particles forms a cone with an opening angle equal to  $\vartheta_0$ , which is usually called the “loss cone”. Table 9.1 provides a set of parameters for some generic mirror device with a fusion grade plasma.

### 9.4.3. Role of ion collisions

Particle collisions lead to particle scattering over the pitch angle, so that the ions whose velocity vectors have initially been outside the loss cone, within

the time of order of the ion collision time  $\tau_{ii}$ , are scattered into the loss cone and are lost from the system. So, the ion confinement time  $\tau_i$  will be of the order of the ion scattering time  $\tau_{ii}$ . Later we discuss additional effects which have to be taken into consideration to assess the confinement in a mirror device.

As Table 9.1 shows, the ion average energy  $\bar{W}_i$  is assumed to be quite high, a factor of 20 higher than the value of 5 keV at which the D-T reaction rate becomes significant. This is due exactly to the observation that the confinement time  $\tau_i$  is of order of the ion scattering time  $\tau_{ii}$ : the latter scales as  $\bar{W}_i^{3/2}$  and at lower energies becomes too short to provide any significant fusion gain. Even at the assumed value of the average ion energy  $\bar{W}_i \sim 100$  keV the fusion gain barely exceeds unity. One can also see that the ion mean free path exceeds by many orders of magnitude the device length — a property that was tacitly assumed when the ion confinement time was identified with the ion scattering time into the loss cone.

The stationary state of the plasma in mirror devices can be sustained by the cross-field injection of energetic atomic beams. Fast neutrals are trapped by ionization and charge exchange and form a source of high energy ions. Subsequent slowing down of these ions and their scattering into the loss cone determines steady state of the ion population in the mirror trap. Detailed kinetic calculations of the fusion gain were made in Ref. [9.97]. They show that the dependence of the confinement time on the mirror ratio  $R_M$  for  $R_M > 2$  is relatively weak,  $\tau_i \sim \tau_{ii} \ln R_M$ .

One can also use continuous gas puff combined with RF heating of the ions to sustain the steady state.

#### 9.4.4. Electron axial confinement

Electron collisions are much more frequent than ion collisions. On the other hand, due to plasma neutrality, the electron particle lifetime in the trap must be comparable with the ion confinement time, so that the “average” electron would experience many collisions before it leaves the device. This, in turn, means that electrons are close to Maxwellian distribution and are, in particular, almost isotropic. As those of them that occupy the loss cone area in the phase space are not confined by the mirrors, an ambipolar potential confining the electrons will be inevitably formed (Fig. 9.32b). Electron leak over this potential barrier will be due to a tail of the Maxwellian distribution. The height of the barrier will be established in such a way as to ensure equal ion and electron particle lifetime in the mirror trap. The electron loss rate can be evaluated by using the so-called Pastukhov formula [9.98]. We present it here in the form of a rough estimate:

$$\tau_e \sim R_M \tau_{ee} \left( \frac{e\varphi_A}{T_e} \right)^{3/2} \exp \left( \frac{e\varphi_A}{T_e} \right) \quad (9.40)$$

where  $\varphi_A$  is an ambipolar potential confining the electrons; we have taken the potential in the midplane as zero (Fig. 9.32b). As  $\tau_{ee}$  is orders of magnitude shorter than  $\tau_{ii}$ , the condition of equal particle loss rate,  $\tau_e \sim \tau_i \sim \tau_{ii}$ , shows that the ambipolar potential exceeds the electron temperature by a small factor.

The fact that the electrons are lost from the trap at energies greatly exceeding their average (thermal) energy is one of the factors that keeps the electron temperature at a level significantly lower than the ion energy  $\bar{W}_i$ . An exact value of the electron temperature is determined by the electron heating rate. The value presented in Table 9.1 corresponds to the situation where the heating is entirely determined by the collisional energy transfer from the ions. If additional heating sources are present, the electron temperature can be somewhat higher. As  $T_e < \bar{W}_i$ , one has to include the ion energy loss via electron drag when assessing the ion energy confinement time. This reduces the ion lifetime. Another factor that reduces it is the presence of the ambipolar potential, which forms a potential hill for the ions. Taken together, these factors make the simple mirror device not attractive as a fusion reactor prototype. The main problem is associated with a relatively poor axial plasma confinement. This is why subsequent suggestions have been focusing on reducing end losses (see Sections 9.4.7–9.4.9).

There may be another and more severe constraint on the achievable electron temperature associated with the possible effect of secondary electron emission from the end plates. The presence of a large amount of cold secondary electrons could reduce the electrostatic potential confining plasma electrons and lead to enhanced electron heat loss. This effect can be almost entirely eliminated by using suppression grids near the end surfaces. The presence of a strong magnetic flux expansion also acts in a favourable direction. A similar cooling mechanism will appear if there is a significant pressure of a neutral gas in the end tanks. The ionization of the gas particles creates cold electrons that can replace the hot ones and open up a channel for fast heat loss. This problem can be cured by providing sufficient pumping in the end tanks.

#### 9.4.5. Velocity-space microinstabilities

As was shown in Section 9.4.2, the ion distribution function is significantly anisotropic due to the presence of a loss cone in the velocity space. This anisotropy may serve as a source of free energy for a variety of instabilities with scales of the order of the ion gyroradius and shorter. Development of such microfluctuations will cause enhanced (compared to purely Coulomb collisions) scattering of the ions and further degrade the ion confinement time.

One of the most potent instabilities of this type is the so-called drift cyclotron loss cone instability (DCLC), predicted by Post and Rosenbluth [9.99]. The perturbations have the form of flutes, aligned with the field lines and

having azimuthal phase velocity in the direction of the ion diamagnetic drift. The perturbation frequency is of the order of the ion cyclotron frequency. This instability causes a rapid scattering of the ions into the loss cone and significant degradation of the plasma confinement. It was observed experimentally in the 1960s and 1970s.

The presence of some small population of isotropic warm ions with average energy significantly less than  $\bar{W}_i$ , leads to stabilization of DCLC modes. Such a population can be, in particular, created in the form of continuous flow of a relatively cold plasma through the device. This stabilizing technique was successfully implemented with the 2XIIB mirror device at Livermore [9.100] where plasma guns and “gas boxes” were attached to the ends of the device and generated the necessary amount of stabilizing plasma. With the DCLC instability suppressed, a plasma with very impressive parameters was obtained: ion average energy  $\sim 10$  keV, plasma density  $\sim 10^{14}$  cm $^{-3}$  and plasma beta  $\sim 0.5$ . The ion confinement time was determined by the electron drag and charge exchange, with the anomalous scattering being completely suppressed.

An alternative solution could consist of injecting the neutral beams not perpendicularly to the magnetic field, but at an angle of  $\sim 45$  degrees. In this case the mirror ratio has to be at least a couple of times higher than  $1 / \sin^2 45^\circ = 2$ ; for example, it can be  $R_M = 5$ . Then, the initially produced ions will be bouncing between the mirrors and will have a significant parallel velocity near the midplane. Such an ion distribution is called “sloshing ion distribution”. The ions get scattered and, at the same time, slowed down by the electron drag. The sloshing ion distribution is much more stable with respect to velocity space microinstabilities. A qualitative explanation of this improved stability is given in Ref. [9.96]. The stability of a sloshing ion population was demonstrated in quite a spectacular way on the GDT facility (see below in Section 9.4.9).

At high plasma pressure the modes associated with the pressure anisotropy ( $p_\perp > p_\parallel$ ) may show up, in particular the so-called “mirror mode”. It is unstable if the condition

$$-\frac{2\mu_0}{B} \frac{\partial p_\perp}{\partial B} > p_\perp \quad (9.41)$$

holds; here the derivative is taken along the field line. Note that, for the perpendicular pressure to vary along the field line, there must be a pressure anisotropy, so that the large absolute value of the derivative corresponds to a large anisotropy. The modes are non-electrostatic and cause significant magnetic field perturbations. In the short-wavelength limit, with the length scale of perturbations approaching the ion gyroradius, they become so-called Alfvén ion cyclotron (AIC) modes.

### 9.4.6. MHD stability

Among the large scale configurational instabilities (which can be reasonably well described by MHD equations) of particular concern is a flute instability of a low beta plasma: this instability has typically a growth time of order of one ion transit time between the mirrors, i.e. orders of magnitude shorter than the plasma confinement time (see Table 9.1). Therefore, if the instability is present, one just cannot create a plasma with any reasonable density in the mirror device. The flute instability is driven by unfavourable curvature of the field lines in the plasma confinement zone near the midplane in Fig. 9.32a, where the field lines are convex.

In a “long–thin” (paraxial) approximation the criterion for the flute stability for an axisymmetric plasma with a sharp radial boundary can be presented as (see Ref. [9.101]):

$$\int \frac{p_{\parallel} + p_{\perp}}{B(z)^{3/2}} \frac{d^2 a}{dz^2} dz > 0 \quad (9.42)$$

where  $a(z)$  is the radius of the plasma edge (coinciding with one of the magnetic surfaces) and  $B(z)$  is the on-axis magnetic field. In a long–thin approximation, one has  $a(z) = \text{constant} / \sqrt{B(z)}$ . The integration is extended to the magnetic field maximum (the mirror throat) where the plasma pressure, for  $\lambda_{ii} \gg L$ , becomes negligible [9.102] (note that in the regime of small mean free path this conclusion loses its validity, see Section 9.4.9). In the equilibrium, the pressure varies along the field line and can be considered as a function of  $B$ ,  $p_{\parallel} = p_{\parallel}(B)$ ,  $p_{\perp} = p_{\perp}(B)$ . With these observations made, one can integrate Eq. (9.42) by parts to obtain the following stability criterion:

$$\int \frac{dz}{B(z)^{3/2}} \left( \frac{dB}{dz} \right)^2 \frac{d}{dB} \left( \frac{p_{\parallel} + p_{\perp}}{B(z)^{3/2}} \right) > 0 \quad (9.43)$$

In a typical situation, the sum  $p_{\parallel} + p_{\perp}$  is a decreasing function of  $B$ , and the integral is manifestly negative, this meaning that axisymmetric mirrors are unstable with respect to flute perturbations. We will discuss later the possibility of reversing the sign of this integral by making the pressure distribution strongly peaked in the zone of a favourable curvature by using sloshing ions.

To ensure stability, one can introduce a magnetic field whose field lines will be concave on the plasma boundary. This can be done by abandoning the axial symmetry. The most common configuration of this type is a quadrupolar field (Fig. 9.33). As was shown both theoretically and experimentally, this configuration is stable with respect to flute modes (see references in Ref. [9.92]). Fields of quadrupole structure have been successfully used in several experimental facilities, in particular 2XIIB at Livermore [9.100].

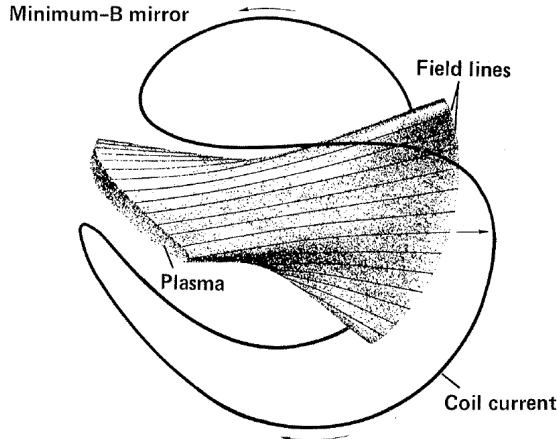


FIG. 9.33. The quadrupole magnetic field generated by a “baseball” coil. Note that magnetic field lines are concave [9.92].

### 9.4.7. Suppression of end losses

#### 9.4.7.1. Tandem mirrors

An elegant solution to the problem of too large end losses was suggested in the 1970s by Dimov, Zakaidakov and Kishinevski [9.103], and Fowler and Logan [9.104]. It is based on the use of the aforementioned ambipolar potential. Consider a long solenoid (a “central cell”) with mirror machines (“end cells”) attached at its both ends (see Fig. 9.34a). Assume that, by very intense injection of neutral beams, we create a high density plasma in each of the end cells. Then a large ambipolar potential will be formed that would electrostatically confine an ion of the central cell, irrespective of its pitch angle, if the ion velocity is not too high. This effect will exist not only for single ions, but also for a plasma in the central cell, provided its density is significantly less than that in the end cells. For a given density ratio, the electrostatic potential confining the central cell ions will be

$$e\phi_e = T_e \ln \frac{n_{end}}{n_{central}} \tag{9.44}$$

For  $n_{end}$  much greater than  $n_{central}$ , the depth of the ion potential well,  $e\phi_e$ , may significantly exceed the ion temperature. The plasma in the central cell will then be confined electrostatically, will have an essentially isotropic distribution function and will not be affected by velocity-space microinstabilities.

If the ion temperature of this central-cell plasma exceeds, roughly, 10 keV, the fusion reactions will produce significant power. By increasing the length

of the central cell, one could, in principle, increase this power as much as one wants. On the other hand, the power required to sustain dense plasma in the end cells (where the confinement is a simple mirror confinement and energy gain is small) does not depend on the length of the central cell. Therefore, by making the central cell long enough, one can always achieve a positive energy balance.

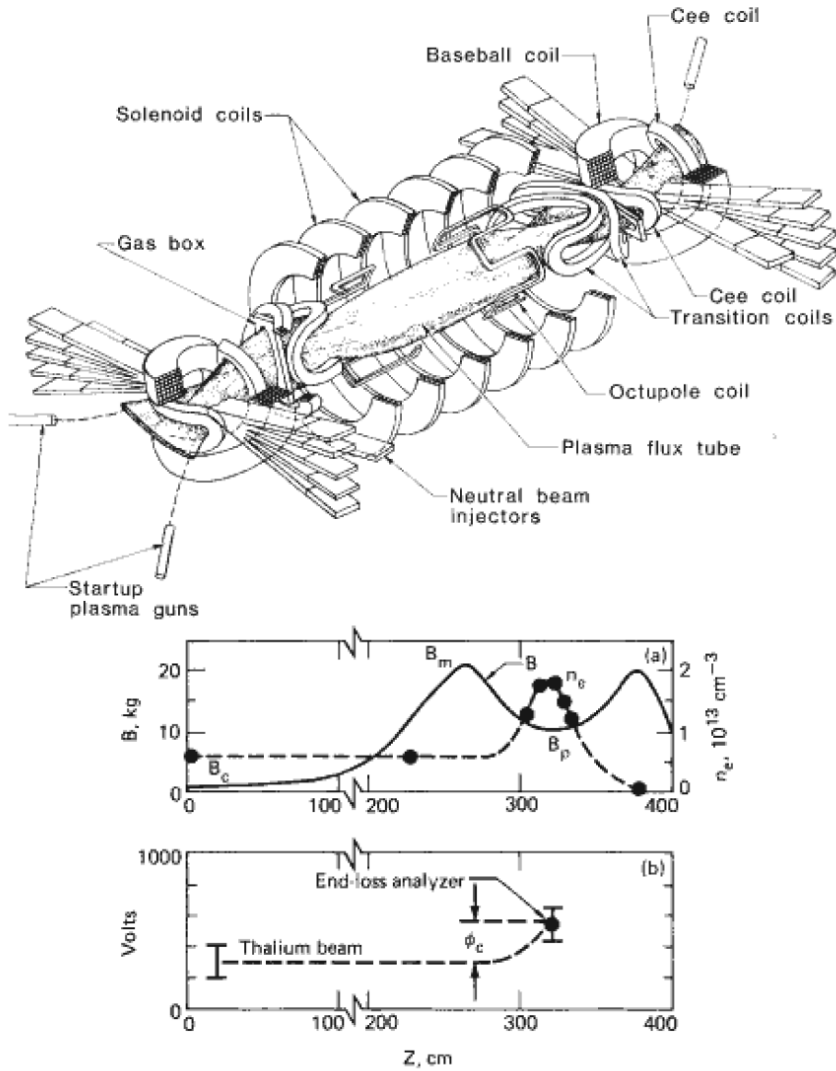


FIG. 9.34. TMX experiment: Upper: Schematic of the facility. Lower: (a) axial distribution of the magnetic field (solid line) and density (dashed line); (b) axial distribution of the electrostatic potential with the experimental points in the central cell and in the middle of the end cell. The potential difference between the two agrees well with Eq. (9.44). Reprinted from Ref. [9.105]. Copyright (2011) American Physical Society.

The ion lifetime in the central cell will be described by an equation similar to Eq. (9.39), with obvious substitutions of the ion quantities instead of electron quantities:

$$\tau_i \sim \tau_{ii} \left( \frac{e\varphi_e}{T_i} \right)^{3/2} \exp \left( \frac{e\varphi_e}{T_i} \right) \sim \tau_{ii} \left( \frac{T_e}{T_i} \ln \frac{n_{end}}{n_{central}} \right)^{3/2} \left( \frac{n_{end}}{n_{central}} \right)^{T_e/T_i} \quad (9.45)$$

This idea has been tested experimentally on several facilities in the USA and Japan, including TMX [9.105] in Livermore, Tara [9.106] at MIT and Phaedrus [9.107] in Wisconsin. Figure 9.34a shows a schematic of the TMX facility. The plasma in the end cells was sustained by neutral beam injection. The ambipolar confinement of the ions in the central cell was indeed successfully demonstrated. Figure 9.34b illustrates the axial density and potential distribution characteristic of tandem mirrors.

When applied to fusion reactor conditions, Eq. (9.45) indicates that, in order to have a really strong suppression of the end losses, with fusion gains  $Q$  of the order of 20, one would have to create a plasma with quite a high density in the end cells. This requirement is severe in terms of the injection power, neutral beam quality and the magnetic field strength needed for confinement of hot dense end cell plasmas. To overcome this difficulty, an idea of thermal barriers was suggested by Baldwin and Logan [9.108]. The idea is based on the ambipolar separation of the electron population in the central cell and that in the additional “barrier” cell. As the ambipolar potential (Eq. (9.44)) is proportional to the electron temperature, the requirements on the ion density in the plug cell are reduced, and the system becomes much more reactor-relevant.

Creating thermal barriers requires a high level of control over the particle distribution functions and is complex in its experimental realization. The use of several sets of neutral beams and ECH systems was envisioned in the original idea. The thermal barrier potential distribution was experimentally created with the TMX-U facility in Livermore [9.109] at modest plasma densities of less than  $10^{13} \text{ cm}^{-3}$  in the central cell. However, this work has not been developed any further in the USA, where the mirror programme was terminated in the late 1980s. The work continued on the Gamma-10 facility in Japan, where details of the ambipolar potential distribution have been studied by a variety of diagnostics [9.110].

MHD stability in most of the tandem mirror facilities was provided by the use of a non-axisymmetric magnetic field. Particle drift motion in such fields may be quite complex, leading to large deviations of the particle guiding centres from the flux surfaces. This, in turn, may lead to neoclassical transport, somewhat similar to that encountered in stellarators. Detailed analyses of this effect have been carried out (see review [9.111]) and ways of reducing the neoclassical losses by means similar to those later applied to stellarators have

been assessed (see Refs [9.112, 9.113]). Still, the geometry of magnetic coils and magnetic surfaces remained quite complex. This makes it important to find ways of providing MHD stability in the axisymmetric configuration.

Techniques potentially suitable for reaching the axisymmetric stability in tandem mirrors have been reviewed in Ref. [9.114]. One possibility consists of injecting sloshing ions with a very narrow angular distribution and strong peaking of their pressure near the turning points [9.115]. This would allow reversing the sign of the stability integral (9.43) as now the ratio  $(p_{\parallel} + p_{\perp})/B^{3/2}$  would become a non-monotonic function of  $B$ . It has recently been suggested to inject the ion beams from the end surfaces of the mirror facility; the beams would be reflected back before entering the mirror throat and would thereby stay in the favourable curvature of the magnetic field [9.116]. In this case, the integration limits in Eq. (9.43) have to be extended beyond the mirrors, as the ion pressure there would be artificially made non-vanishing. Other approaches, in particular using cusp stabilizers and non-paraxial stabilizers, are described in Ref. [9.114], where further references are given. This area remains, however, largely an area of theoretical investigations, without much experimental work being done.

#### 9.4.7.2. Plasma rotation

Plasma axial confinement can be improved also in a simple mirror configuration by setting the plasma into a fast enough rotational motion. Indeed, if in the geometry of a simple mirror shown in Fig. 9.32 a plasma rotates around the magnetic axis with a frequency  $\omega$ , there appears a centrifugal force that pushes the plasma towards the equatorial plane. The confinement condition, instead of Eq. (9.39), becomes

$$\sin^2 \vartheta_0 + \frac{\omega^2 a^2}{v^2} \left( 1 - \frac{1}{R_M} \right) > \frac{1}{R_M} \quad (9.46)$$

where  $a$  and  $v$  are the radius of the magnetic surface and particle velocity, both in the midplane. Clearly, the particles with not too high velocities are confined irrespectively of their pitch angle. With large enough rotation frequency, a fusion grade plasma can be confined without problems associated with the loss cone. The frequency can vary from one flux surface to another, thereby creating velocity shear.

This technique has been tested in experiments with the PSP-2 facility at Novosibirsk [9.117]. In order to bring the plasma into rotation, a 400 kV voltage was applied across the plasma. The mirror-to-mirror length was 1.5 m, the plasma radius in the midplane was 40 cm, and the magnetic field in the midplane was 15 kG. A set of ring electrodes situated at the ends of the device and having independent power supplies allowed control of the rotation velocity and rotation

shear. A plasma with ion temperature of 10 keV and density of  $10^{12} \text{ cm}^{-3}$  was obtained; the confinement time was limited by charge exchange losses. No gross flute instability was detected; this seems to be in agreement with the possibility of shear stabilization of the flute instability [9.117]. Recently, experiments with rotating plasmas have started at the University of Maryland [9.118].

Sheared plasma rotation may be also used to suppress drift-type instabilities responsible for cross-field transport in solenoidal sections of tandem mirrors [9.119]. In general, mirrors provide a relatively simple way of controlling the radial potential distribution since their end plates can be segmented and biased independently from each other to obtain the desired potential distribution.

#### 9.4.7.3. Gas-dynamic trap

One more way of reducing the end loss is to increase the mirror ratio  $R_M$  and the mirror-to-mirror length  $L$  so as to make the mean free path with respect to the scattering over the loss cone angle,  $\lambda_{eff}$ , shorter than  $L$ . The possibility of reaching this condition is related to the fact that, for  $R_M \gg 1$ ,  $\lambda_{eff}$  scales as  $\lambda_{eff} \sim \lambda_{ii} / R_M$ , due to the Fokker–Planck nature of Coulomb collisions. So, for a very high mirror ratio and a not exceedingly high ion temperature, the condition  $\lambda_{eff} < L$  can be satisfied for a modest plasma density and device length. For example, for an ion temperature of 5 keV, plasma density of  $10^{14} \text{ cm}^{-3}$  and mirror ratio of 50 it is satisfied for  $L > 200 \text{ m}$ . If the condition  $\lambda_{eff} < L$  holds, the concept of the loss cone loses its relevance, as the distribution function in the trap is now isotropic. The plasma loss rate is determined by the gas-dynamic plasma outflow from the mirror (whence the name of the device), and the lifetime, instead of being of the order of  $\lambda_{ii} / v_{th,i}$ , as was in the case of a standard simple mirror, becomes of the order of  $LR_M / v_{th,i}$ , i.e. much longer.

Transition to the gas-dynamic regime of axial confinement has additional benefits. The first is that velocity-space microinstabilities cannot have any effect on the confinement time, as the plasma is locally Maxwellian. The second is that the system can be made MHD stable within the axisymmetric geometry, due to the presence of non-negligible plasma density in the region of the flaring magnetic field outside the mirrors. As the field line curvature in this region can be made favourable and large, the stability integral (9.42) becomes positive.

This analysis was presented in Ref. [9.120] and has been verified in a series of detailed experiments on the GDT device at Novosibirsk [9.121]. A schematic of the device is shown in Fig. 9.35. The mirror-to-mirror length was 7 m, the magnetic field was 0.2 T in the equatorial plane and up to 15 T in the mirrors. The plasma radius in the midplane was 15 cm and the plasma density  $\sim (2-3) \times 10^{13} \text{ cm}^{-3}$ . The plasma was heated by neutral beam injection, with an injection angle of 45 degrees with respect to the device axis. The electron temperature reached a value of 150 eV, in close agreement with classical

predictions. The plasma was MHD stable over a broad range of parameters, in good agreement with theory.

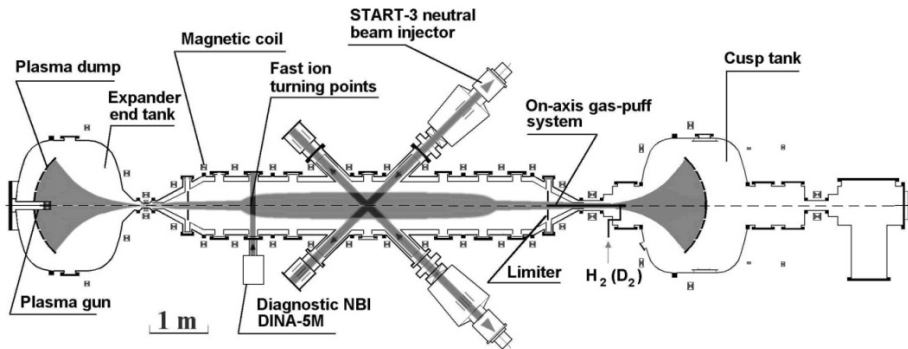


FIG. 9.35. The GDT facility. The ion beams for plasma heating are injected at 45 degrees and demonstrate a classical behaviour, without any sign of velocity-space instabilities. Near the turning points, the beta of the sloshing ions was as high as 0.5. The areas with favourable curvature of the magnetic field in the end tanks serve for MHD stabilization of the whole device.

In general, the physics of stability and confinement in GDT is very robust and suitable for extrapolation to the larger scale devices. One such device could be a volumetric neutron source for materials and subcomponent testing for future fusion reactors [9.122]. The idea of the source is based on the properties of the “sloshing ions” created by skewed neutral beam injection. If the angular spread of these ions is small, they produce strong density peaks near their turning points. These regions become a source of intense neutron radiation. Neutron sources based on a simple mirror were analysed in Ref. [9.123]. Another potential application of the GDT is its use as an actinide burner. In this version the neutron flux would be used for transmutation of the most hazardous materials produced in fission power plants. Recent assessment of this possibility can be found in Ref. [9.124].

## 9.5. OTHER FUSION CONFIGURATIONS: A BROAD RANGE OF IDEAS

### 9.5.1. Levitated dipoles

The magnetic field of a current ring can be used for plasma confinement. The field lines form a set of nested flux surfaces around the current-carrying conductor. If one wants to eliminate plasma losses to the mechanical support structures one can use the magnetic levitation of the superconducting ring. As, at large distances, a ring magnetic field is close to a dipole field, this configuration is sometimes called “the levitated dipole.” It is studied at the LDX

facility (Levitated Dipole Experiment) at MIT [9.125], see Fig. 9.36. A similar configuration on a much larger scale exists in the Earth’s magnetosphere.

The difference is that geomagnetic field lines have “ends” at their intersections with the Earth’s atmosphere. So, the magnetospheric field does not have closed flux surfaces and acts as a giant mirror, with a plasma and fast particles being mirror-confined in the equatorial region of the field. Some smaller scale experiments directed to studies of the mirror aspect of the dipole confinement have been carried out at Columbia University [9.126].

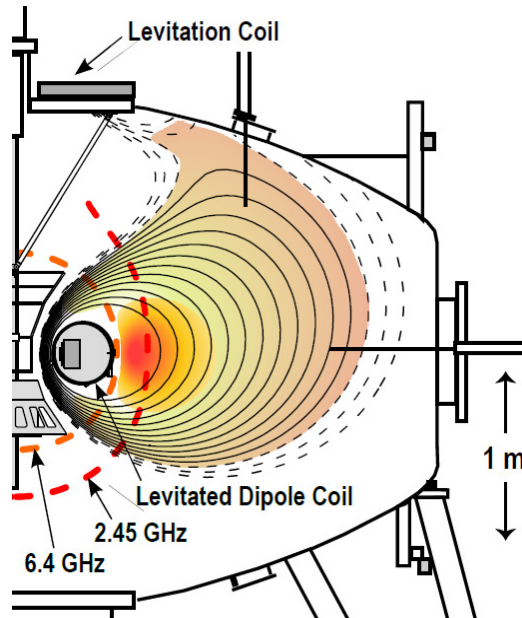


FIG. 9.36. Schematic of the LDX experiment at MIT [9.125]. The superconducting levitated dipole coil with a mass of 680 kg is energized to 1.2 MA of current and links the magnetic flux confining the plasma. The copper levitation coil provides the force that balances the gravity force on the levitating coil. The magnetic field is purely poloidal. A set of nested magnetic flux surfaces is shown. The electrons are heated by gyrotron microwave sources. Shown in orange and red dashed lines are resonant surfaces for two frequencies. Reprinted from Ref. [9.125]. Copyright (2011) with permission from Elsevier.

An interesting feature of this system is that, despite the apparently unfavourable field line curvature, it can be MHD stable for quite steep pressure gradients. The reason for this is that the system is intrinsically non-paraxial (see Sections 9.4.6 and 9.4.7), introducing significant stabilizing terms due to plasma compressibility. Speaking of the fusion applications, the levitated dipole may be a basis for a reactor burning aneutronic or weakly neutronic fuel (like D-<sup>3</sup>He) [9.127]. The use of D-T fuel is somewhat problematic because of the need to protect the superconducting coil from the neutron irradiation.

### 9.5.2. Cusps

Cusp geometry can be created by two axisymmetric coils with opposite currents (Fig. 9.37a). The plasma is supposed to be confined near the null-point (the origin of the coordinate system (0) in Fig. 9.37a), with the spatial scale of the plasma object being  $a$  (a fraction of the coil size). The attractiveness of this configuration is related to the fact that the magnetic field grows in all directions from the plasma confinement zone or, stated differently, the magnetic field has a favourable curvature. Therefore, the plasma should be MHD stable. A disadvantage of the cusp geometry is the presence of the magnetic field null in the central point. So, the particle gyroradii in the vicinity of this point are larger than the magnetic field scale length. This, in turn, leads to a loss of conservation of the magnetic moment  $\mu$ , rapid change of the pitch angle and particle loss through a ring and point cusps. After the central part of the cusp is emptied, the interface between this zone and surrounding plasma becomes MHD unstable, and the plasma from the outer flux surfaces rapidly fills this zone again. This new plasma is again lost along the field lines, the central zone gets emptied, etc. Still, the cusp geometry, due to its simplicity, is of a significant interest for basic research. It can be also used as a stabilizer for mirror devices [9.128, 9.129].

The cusp research prior to 1984 was summarized in Ref. [9.130].

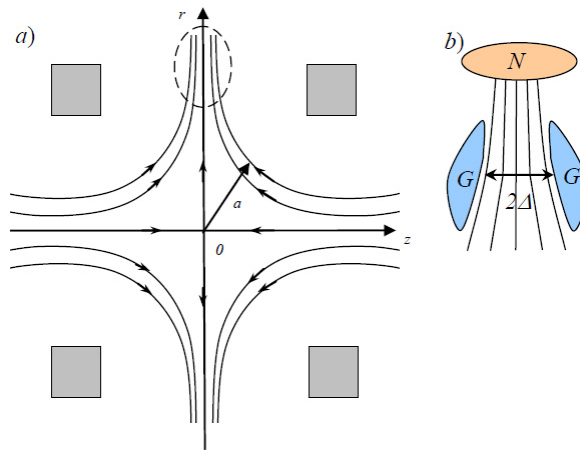


FIG. 9.37. Magnetic cusp. (a) Magnetic field structure. It is axisymmetric with respect to the  $z$ -axis (a “spindle cusp”). Small arrows indicate the magnetic field direction. Cross-sections of the coils are shown in grey. Plasma fills a zone of characteristic dimension ‘ $a$ ’ around the origin. Plasma confinement time is  $\sim 10$ – $30$  ion transit times over the distance ‘ $a$ ’; the exact number depends on the details of the geometry. The dashed ellipse shows a zone enlarged in panel (b), but without electrodes that have to be added to provide electrostatic plugging. (b) Towards the concept of electrostatic plugging of the ring cusp (see Section 9.5.3). Electrodes  $G$  are grounded, whereas electrode  $N$  is biased strongly negatively. The half-width  $\Delta$  is smaller than the Debye radius.

### 9.5.3. Magneto-electrostatic confinement and electrostatic confinement

If the plasma half-width  $\Delta$  in the ring cusp is smaller than the plasma Debye radius, the cusp can be plugged electrostatically, by a simple electrode system, as shown in Fig. 9.37b. A high negative potential is applied to electrode  $N$  with respect to the grounded electrode  $G$ . Due to the smallness of  $\Delta$ , the plasma potential in the middle of the gap is not significantly different from that of the grounded electrodes. Then, the plasma electrons cannot reach the electrode  $N$  and are perfectly confined along the field lines. As the bulk plasma is quasi-neutral, the bulk plasma potential adjusts itself in such a way as to confine the ions.

For a large enough radius  $R$  of the ring cusp, the gap  $\Delta$  can indeed be made quite small,  $\Delta \sim a^3 / R^2$ . This equation stems directly from magnetic flux conservation arguments and the fact that the magnetic field in a cusp geometry grows linearly with radius. It is, however, virtually impossible to make the radius of the point cusp (the one situated on the rotation axis) to be smaller than the Debye radius. Indeed, the same flux conservation arguments show that the plasma width (diameter) in the point cusp is  $\sim a(a/R)^{1/2}$ , i.e. much larger than the thickness  $\Delta$  of the point cusp. For any reasonable set of plasma parameters the plasma diameter in the point cusp is significantly greater than the Debye radius.

To mitigate this problem, one can use the geometry of multiple linked cusp cells, with electrostatic plugging of ring cusps. Then, even if the axial losses are not suppressed, the plasma lifetime could increase significantly due to the increased plasma volume. Yet another approach is based on the toroidal cusp [9.131], where all four gaps would have approximately the same thickness and could be electrostatically plugged.

The electrostatic plasma confinement can, in principle, be used without any magnetic field present. Two spherical concentric mesh spheres of high transparency could play a role identical to the electrodes  $N$  and  $G$  in Fig. 9.37b. The confinement properties in this case depend significantly on the transparency of the mesh electrodes. A review of both electrostatic and magneto-electrostatic systems can be found in Ref. [9.132].

### 9.5.4. Pinches

This is, perhaps, one of the earliest fusion concepts. It is based on self-constricted plasma configurations, of which the simplest is the so-called  $Z$ -pinch. In this configuration a plasma current driven along the axis of a plasma column (whence the term “ $Z$ ” in the name of the configuration) produces an azimuthal ( $\theta$ ) magnetic field that causes radial compression of the column due to the  $\vec{j} \times \vec{B}$  force. The plasma compression leads to plasma adiabatic heating. Reaching a steady state in which the plasma pressure would be balanced by the

radial pinch force was thought to be possible at the beginning of fusion research. A significant effort was spent on this approach, only to find that the Z-pinch is strongly unstable with respect to sausage and kink instabilities, which lead to a quick radial loss of the plasma [9.90].

One more self-constricted configuration is the  $\theta$ -pinch, where the interaction of the rapidly increasing axial magnetic field with the azimuthal ( $\theta$ ) current leads to plasma compression. To eliminate axial losses of the plasma along the field lines, it was suggested to use a toroidal  $\theta$ -pinch. A large experimental programme based on toroidal  $\theta$ -pinches existed at Los Alamos until 1976 [9.133]. These experiments have also identified a large group of plasma instabilities.

More recently, Z-pinch implosions have experienced a new revival, related to the development of modern pulse-power generators. Unlike the older experiments, where a quasi-steady-plasma confinement in the compressed stage was the main goal, these new experiments focused on the fast implosion phase, culminating in forming a short lived, dense and hot plasma column on the axis. This column, before it disassembles within the inertial time, produces a copious radiation that can be used for many purposes, including inertial confinement fusion [9.134]. These aspects of Z-pinch research are covered in Chapter 10.

### 9.5.5. Magnetized target fusion

Magnetized target fusion, MTF (sometimes also called “magneto-inertial fusion”, MIF), covers the density domain between  $10^{18} \text{ cm}^{-3}$  and  $10^{22} \text{ cm}^{-3}$ , i.e. the domain lying above the typical density of magnetic confinement, but below the density of inertial confinement. The plasma object (“target”, see specific examples below) is supposed to be magnetized, so as to suppress heat losses from the plasma, and to be compressed by a heavier shell (a “liner”) that would perform the compression work and thereby heat the plasma. After reaching the stagnation point, the liner rebounds, so that the plasma confinement time is eventually determined by the liner inertia. The plasma beta in the state of maximum compression is greater than 1; in other words, the presence of the liner provides the “inertial confinement” of the plasma. The momentum is transferred to the wall by the strong magnetic field that is formed in a narrow near-wall layer; in some cases the momentum can be transferred directly by the pressure of a very dense and relatively cold near-wall gas. The success of this approach depends strongly on the solution of such issues as gross MHD stability of a magnetized plasma configuration and anomalous transport of heat in a high-beta, strongly collisional plasma. Discussion of these issues as well as references to the earlier works can be found in Refs [9.75, 9.135, 9.136].

A target of choice for MTF is at present the FRC, although many other configurations are possible. An experiment in which an integrated test of the whole concept will be performed is planned with the use of the pulsed power

facility “Shiva-Star” [9.137]. An FRC with parameters similar to those obtained in the FRX-L experiment (Section 9.3.4.2) will be injected into a thin-wall aluminium liner, which will be imploded by a strong axial current (in the Z-pinch configuration). The FRC will be confined in the axial direction due to the faster liner implosion at the end sections, which, in turn, will be achieved by thinning the liner near the ends. The expected ion temperature and plasma temperature in the compressed state are of the order of 2–3 keV and  $10^{19} \text{ cm}^{-3}$ , respectively.

For fusion reactor concepts based on MTF, one of the key problems is that of operating these implosions in a repetitive regime, with a frequency between 10 and 0.1 Hz. Several ideas have been discussed in the literature (for a summary see Ref. [9.138]), including assembling a target and then compressing it by an array of plasma jets injected from the walls of the reaction chamber. Other, more conservative and lower frequency approaches assume that the target will be lowered into the chamber by a disposable set of electrodes, connected to an energy source shielded from debris and neutron irradiation.

### 9.5.6. Other concepts

In addition to the concepts described above, there have been several other concepts suggested and tried experimentally at some level during the 50-year history of fusion research. Space limitations allow us just to briefly mention these concepts with one or two characteristic references which could guide an interested reader to other publications.

The Elmo Bumpy Torus (EBT) system was pursued in the USA in the 1970s [9.139]. It consists of a set of toroidally linked mirrors, with a population of hot (often relativistic) electrons confined in each cell. These electrons provide MHD stability, very much like in the ASTRON concept [9.81]. They provide also plasma equilibrium. The isotropic fusion plasma fills all the mirrors and is toroidally confined.

The Levitron is a toroidal device with a toroidal levitating ring (as in the levitated dipole) but immersed into a toroidal magnetic field. This would create a tokamak-like equilibrium with nested magnetic surfaces and improved stability, because the plasma would not have to carry significant toroidal current [9.140]. As a curiosity, one can mention that it was the levitron that was considered by Sakharov in his 1951 report [9.141] as a prime candidate for a toroidal fusion reactor; the system where the toroidal current would be carried by the plasma itself (and later named “tokamak”) was considered as an alternative.

The toroidal multipole [9.142] used the field of several (typically four) toroidal coils generating a multipole poloidal magnetic field. In the most advanced version of this device, the toroidal rings could be suspended in a transiently levitating mode. The presence of the multipole field provides an MHD stable equilibrium plasma configuration for a current-less plasma. In the absence

of the toroidal field, the magnetic field of a toroidal multipole was shear-less and thereby very sensitive to the magnetic field errors. Introduction of the toroidal field allowed for a significant reduction of plasma losses in this geometry.

The plasma focus is a close cousin of the Z-pinch, but with a significantly different geometry of the electrodes. In the plasma focus the discharge is initiated in an annular plasma disc between two coaxial cylindrical electrodes. The  $\vec{j} \times \vec{B}$  force accelerates the disc axially. At the end of the coaxial electrodes, the plasma shell bends and converges on the geometrical axis, somewhat similarly to the Z-pinch. It ends up in a highly compressed and hot structure near the axis [9.143]. This structure is a source of intense particle beams, X ray radiation and, for a D-D plasma, of neutron emission.

## 9.6. SUMMARY

Over the decades, a large array of magnetic configurations has been studied, producing a huge amount of fusion plasma science. As configurations are developed, information and techniques learned through one configuration influence the development of other configurations. In this way, configurations evolve unexpectedly in response to new information. Configurations that were at a pause can become unstuck by new discoveries, and configurations that appeared promising for fusion energy can become unattractive as new limits are uncovered. The plasma science of fusion energy is sufficiently complex that, as we approach ever closer to practical fusion power, the need for potential contributions of broad research of multiple magnetic configurations remains strong.

**ACKNOWLEDGEMENTS**

The authors are grateful to E.B. Hooper, P. Martin and S. Woodruff for helpful comments. The work of D. Ryutov was performed at Lawrence Livermore National Laboratory under Contract DE-52-07NA27344.

## REFERENCES

- [9.1] BODIN, H.A., NEWTON, A.A., Reversed field pinch research, Nucl. Fusion **20** (1980) 1255.
- [9.2] NAJMABADI, F., et al., The TITAN Reversed-Field-Pinch Fusion Reactor Study, University of California, Los Angeles Report UCLA-PPG-1200 (1990).
- [9.3] ORTOLANI, S., SCHNACK, D.D., Magnetohydrodynamics of Plasma Relaxation, World Scientific, Singapore (1993).
- [9.4] ROBINSON, D.C., High beta diffuse pinch configurations, Plasma Phys. **13** (1971) 439; ROBINSON, D.C., Tearing-mode-stable diffuse-pinch configurations, Nucl. Fusion **18** (1978) 939.
- [9.5] FREIDBERG, J.P., Ideal magnetohydrodynamic theory of magnetic fusion systems, Rev. Mod. Phys. **54** (1982) 801.
- [9.6] SUYDAM, B.R., in Proc. 2nd United Nations Int. Conf. on the Peaceful Uses of Atomic Energy, United Nations, Geneva, 1958, Vol. 81 (1958) 157; FREIDBERG, J.P., Ideal magnetohydrodynamic theory of magnetic fusion systems, Rev. Mod. Phys. **54** (1982) 869.
- [9.7] TAYLOR J.B., Relaxation of toroidal plasma and generation of reverse magnetic fields, Phys. Rev. Lett. **33** (1974) 1139; TAYLOR, J.B., Relaxation and magnetic reconnection in plasmas, Rev. Mod. Phys. **58** (1986) 741.
- [9.8] FURTH, H.P., KILLEEN, J., ROSENBLUTH, M.N., Finite resistivity instabilities of a sheet pinch, Phys. Fluids **6** (1963) 459; GOLDSTON, R.J., RUTHERFORD, P.H., Introduction to Plasma Physics, Institute of Physics Publishing (1995) 337.
- [9.9] BHATTACHARJEE, A., HAMEIRI, E., Self-consistent dynamo-like activity in turbulent plasmas, Phys. Rev. Lett. **57** (1986) 206.
- [9.10] ANDERSON, J.K., BIEWER, T.M., FOREST, C.B., O'CONNELL, R., PRAGER, S.C., SARFF, J.S., Dynamo-free plasma in the reversed field pinch, Phys. Plasmas **11** (2004) L9.
- [9.11] DING, W.X., BROWER, D.L., CRAIG, D., DENG, B.H., FIKSEL, G., MIRNOV, V, PRAGER, S.C., SARFF, J.S., SVIDZINSKI, V., Measurement of the hall dynamo effect during magnetic reconnection in a high-temperature plasma, Phys. Rev. Lett. **93** (2004) 045002.
- [9.12] GOLDSTON, R.J., RUTHERFORD, P.H., Introduction to Plasma Physics, Institute of Physics Publishing (1995) 357.

## BROADER SPECTRUM OF MAGNETIC CONFIGURATIONS

- [9.13] MARTIN, P., et al., Overview of quasi-single helicity experiments in reversed field pinches, *Nucl. Fusion* **43** (2003) 1855.
- [9.14] BIEWER, T.M., FOREST, C.B., et al., Electron heat transport measured in stochastic magnetic field, *Phys. Rev. Lett.* **91** (2003) 045004.
- [9.15] RECHESTER, A.B., ROSENBLUTH, M.N., Electron heat transport in a tokamak with destroyed magnetic surfaces, *Phys. Rev. Lett.* **40** (1978) 38.
- [9.16] SOVINEC, C., PRAGER, S.C., Magnetohydrodynamic effects of current profile Control in reversed field pinches, *Nucl. Fusion* **39** (1999) 777.
- [9.17] UCHIMOTO, E., CEKIC, M., HARVEY, R.W., LITWIN, C., PRAGER, S.C., SARFF, J.S., SOVINEC, C.R., Lower hybrid poloidal current drive for Fluctuation reduction in a reversed field pinch, *Phys. Plasmas* **1** (1994) 3517.
- [9.18] SOVINEC, C., PRAGER, S.C., Magnetohydrodynamic effects of current profile control in reversed field pinches, *Nuclear Fusion* **39** (1999) 777.
- [9.19] SARFF, J.S., HOKIN, S.A., JI, H., PRAGER, S.C.; SOVINEC, C.R., Fluctuation and transport reduction in a reversed field pinch by inductive poloidal current drive, *Phys. Rev. Lett.* **72** (1994) 3670; CHAPMAN, B.E., et al., Reduced edge instability and improved confinement in the MST reversed field pinch, *Phys. Rev. Lett.* **87** (2001) 205001; SARFF, J.S., et al., Tokamak-like confinement at high beta and low toroidal field in the reversed field pinch, *Plasma Phys. Control. Fusion* **45** (2003) A457.
- [9.20] DING, W., BROWER, D.L., TERRY, S.D., PRAGER, S.C., SARFF, J.S., WRIGHT, J.C., Measurement of internal magnetic fluctuations in a reversed field pinch by Faraday rotation, *Phys. Rev. Lett.* **90** (2003) 035002.
- [9.21] SARFF, J.S., et al., Tokamak-like confinement at high beta and low field in the reversed field pinch, *Plasma Phys. Control. Fusion* **45** (2003) A457.
- [9.22] STONEKING, M.R., et al., Fivefold confinement time increase in the Madison Symmetric Torus using inductive poloidal current drive, *Phys. Plasmas* **4** (1997) 1632.

- [9.23] O'CONNELL, R., DEN HARTOG, D.J., FOREST, C.B, ANDERSON, J.K., BIEWER, T.M., CHAPMAN, B.E., CRAIG, D., FIKSEL, G., PRAGER, S.C., SARFF, J.S., TERRY, S.D., HARVEY, R.W., Observation of velocity-independent electron transport in the reversed field pinch, *Phys. Rev. Lett.* **91** (2003) 045002.
- [9.24] SARFF, J.S. et al., "Tokamak-like Confinement at a High Beta and Low Toroidal Field in the MST Reversed Field Pinch." *Nucl. Fusion* **43** (2003)1684.
- [9.25] FINN, J.M., NEBEL, R.A., BATHKE, C., Single and multiple helicity Ohmic states in reversed-field pinches, *Phys. Fluids* **B4** (1992) 1262; CAPELLO, S., PACCAGNELLA, R., Nonlinear plasma evolution and sustainment in the reversed field pinch, *Phys. Fluids* **B4** (1992) 611.
- [9.26] MARTIN, P., et al., Quasi-single helicity states in the reversed field pinch: beyond the standard paradigm, *Phys. Plasmas* **7** (2000) 1984.
- [9.27] CAPELLO, S., ESCANDE, D.F., Bifurcation in viscoresitive MHD: the Hartmann number and the reversed field pinch, *Phys. Rev. Lett.* **85** (2000) 3838.
- [9.28] ESCANDE, D.F., et al., Quasi-single-helicity reversed-field-pinch plasmas, *Phys. Rev. Lett.* **85** (2000) 1662.
- [9.29] MARTIN, P., et al., Overview of quasi-single-helicity experiments in reversed field pinches, *Nucl. Fusion* **43** (2003) 1855.
- [9.30] MARTIN, P., et al., Overview of RFX-Mod Results, *Nucl. Fusion* **49** (2009) 104019.
- [9.31] WYMAN, M.D., CHAPMAN, B.E., et al., High beta, improved confinement reversed-field-pinch plasmas at high density, *Phys. Plasmas* **15** (2008) 010701.
- [9.32] FRIEDBERG, J., *Plasma Physics and Fusion Energy*, Section 13.5, Cambridge University Press (2007).
- [9.33] BRUNSELL, P.R., et al., "Reversed field pinch operation with intelligent shell feedback control in EXTRAP T2R", *Nucl. Fusion* **46** (2006) 904.
- [9.34] BRUNSELL, P.R. et al., Feedback stabilization of multiple resistive wall modes, *Phys. Rev. Lett.* **93** (2004) 225001.
- [9.35] PACCAGNELLA, R., et al., Active-feedback control of the magnetic boundary for magnetohydrodynamics stabilization of a fusion plasma, *Phys. Rev. Lett.* **97** (2006) 075001.

- [9.36] BEVIR, M., GRAY, J.W., Proc. Reverse Field Pinch Theory Workshop, Los Alamos Report LA-8944-LC; Los Alamos National Laboratory, Los Alamos, New Mexico (1981) 176; BEVIR, M.K., GIMBLETT, C.G., MILLER, G., Quasi-steady-state toroidal discharges, *Phys. Fluids* **28** (1986) 1826.
- [9.37] EBRHIAMI, F., PRAGER, S.C., SARFF, J.S., WRIGHT, J.C., The three-dimensional magnetohydrodynamics of AC helicity injection in the reversed field pinch, *Phys. Plasmas* **10** (2003) 999.
- [9.38] SCHOENBERG, K.F., INGRAHAM, J.C., MUNSON, C.P., WEBER, P.G., BAKER, D.A., GRIBBLE, R.F., HOWELL, R.B., MILLER, G., REASS, W.A., SCHOFIELD, A.E., SHINOHARA, S., WURDEN, G.A., Oscillating field current drive experiments in a reversed field pinch, *Phys. Plasmas* **31** (1988) 2285.
- [9.39] MCCOLLAM, K.J., BLAIR, A.P., PRAGER, S.C., SARFF, J.S., Oscillating-field current-drive experiments in a reversed field pinch, *Phys. Rev. Lett.* **96** (2006) 035003.
- [9.40] ROSENBLUTH, M.N., BUSSAC, M.N., MHD stability of spheromak, *Nucl. Fusion* **19** (1979) 489–498; BUSSAC, M.N., FURTH, H.P., OKABAYASHI, M., ROSENBLUTH, M.N., TODD, A.M.M., Low-aspect-ratio limit of the toroidal reactor: the spheromak, *Nucl. Fusion, Suppl.*, **3** (1979) 249–264.
- [9.41] JARBOE, T.R., Review of spheromak research, *Plasma Phys. Control. Fusion* **36** (1994) 945.
- [9.42] TUSZHEWSKI, M., Field reversed configurations, *Nucl. Fusion* **28** (1988) 2033.
- [9.43] HOOPER, E.B., PEARLSTEIN, L.D., BULMER, R.H., MHD equilibria in a spheromak sustained by coaxial helicity injection, *Nucl. Fusion*, **39** 863 (1999).
- [9.44] MCLEAN, H.S., WOOD, R.D., COHEN, B.I., HOOPER, E.B., HILL, D.N., MOLLER, J.M., ROMERO-TALAMAS, C., WOODRUFF, S., Transport and fluctuations in high temperature spheromak plasmas, *Phys. Plasmas* **13** (2006) 56105.
- [9.45] PEARLSTEIN, L.D., BULMER, R.H., JONG, R.A., KAISER, T.B., LODESTRO, L.L., BERK, H.L., Predictive modeling of axisymmetric toroidal configurations, in Proc. 28th EPS, June, 2001, Funchal, Madeira, P5.034.

- [9.46] WOODRUFF, S., HILL, D.N., STALLARD, B.W., BULMER, R., COHEN, B., HOLCOMB, C.T., HOOPER, E.B., MCLEAN, H.S., MOLLER, J., WOOD, R.D., New mode of operating a magnetized coaxial plasma gun for injecting magnetic helicity into a spheromak, *Phys. Rev. Lett.* **90** (2003) 095001.
- [9.47] HOOPER, E.B., KOPRIVA, T.A., COHEN, B.I., HILL, D.N., MCLEAN, H.S., WOOD, R.D., WOODRUFF, S., SOVINEC, C.R., Magnetic reconnection during flux conversion in a driven spheromak, *Phys. Plasmas* **12** (2005) 92503.
- [9.48] HUDSON, B., WOOD, R.D., MCLEAN, H.S., HOOPER, E.B., HILL, D.N., JAYAKUMAR, J., MOLLER, J., MONTEZ, D., ROMERO-TALAMAS, C.A., CASPER, T.A., JOHNSON III, J.A., LODESTRO, L.L., MEZONLIN, E., PEARLSTEIN, L.D., Energy confinement and magnetic field generation in the SSPX spheromak, *Phys. Plasmas* **15** (2008) 056112.
- [9.49] RUSBRIDGE, M.G., GEE, S.J., BROWNING, P.K. BROWNING, CUNNINGHAM, G., DUCK, R.C. AL-KARKHY, A. MARTIN, R., BRADLEY, J.W., The design and operation of the SPHEX spheromak, *Plasma Phys. Control. Fusion* **39** (1997) 683.
- [9.50] DUCK, R.C., BROWNING, P.K., CUNNINGHAM, G., GEE, S.J., AL-KARKHY, A., MARTIN, R., RUSHBRIDGE, M.G., Structure of the  $n=1$  mode responsible for relaxation and current drive during sustainment of the SPHEX spheromak, *Plasma Phys. Control. Fusion* **39** (1997) 715.
- [9.51] ROMERO-TALAMAS, C.A., HOLCOMB, C., BELLAN, P.M., HILL, D.N., Spheromak formation and sustainment studies at the sustained spheromak physics experiment using high-speed imaging and magnetic diagnostics, *Phys. Plasmas* **13** (2006) 022502.
- [9.52] BELLAN, P.M, YOU, S., YUN, G.S., Measurements of plasma jets and collimated flux tubes that are the precursors of spheromak self-organization, *J. Fusion Energy* **26** (2007) 25
- [9.53] WOOD, R.D., HILL, D.N., MCLEAN, H.S., et al., Improved magnetic field generation efficiency and higher-temperature spheromak plasmas, *Nucl. Fusion* **49** (2009) 025001.
- [9.54] HOOPER, E.B., HILL, D.N., MCLEAN, H.S., ROMERO-TALAMAS, C.A., WOOD, R.D., Achieving high flux amplification in a gun-driven, flux-core spheromak, *Nucl. Fusion* **47** (2007) 1064.

## BROADER SPECTRUM OF MAGNETIC CONFIGURATIONS

- [9.55] FOWLER, T.K., JAYAKUMAR, R., Stable Spheromaks with Profile Control, Lawrence Livermore National Laboratory, LLNL-TR-400902, January 2008.
- [9.56] WOODRUF IOP Publishing Ltd, HOOPER, E.B., PEARLSTEIN, L.D., BULMER, R., HILL, D.N., HOLCOMB, C.T., MCLEAN, H., MOLLER, J., STALLARD, B.W., WOOD, R.D., Observation of a pressure limit in a gun-driven spheromak, *Phys. Plasmas* **13** (2006) 44506.
- [9.57] COHEN, B.I., HOOPER, COHEN, R.H., HILL, D.N., MCLEAN, H.S., WOOD, R.D., WOODRUFF, S. SOVINEC, S.R., CONE, G.A., Simulation of spheromak evolution and energy confinement, *Phys. Plasmas* **12** (2005) 056106.
- [9.58] SOVINEC, C.R., GIANAKON, T.A., HELD, E.D., KRUGER, S.E., SCHNACK, D.D., NIMROD: a computational laboratory for studying nonlinear fusion magnetohydrodynamics, *Phys. Plasmas* **10** (2003) 1727.
- [9.59] RYUTOV, D.D., A model of plasma rotation in the Livermore spheromak for the regimes of large connection lengths, *Phys. Plasmas* **14** (2007) 022506.
- [9.60] WYSOCKI, F.J., FERNANDEZ, J.C., HENINS, I., MARKLIN, G.J., Progress with energy confinement time in CTX spheromak, *Phys. Fluids* **B2** (1990) 1342.
- [9.61] BROWN, M.R., COTHRAN, C.D., FUNG, J., CHANG, M., HORWITZ, J., SCHAFFER, M.J., LEUER, J., BELOVA, E.V., Dipole trapped spheromak in a prolate flux conserver, *Phys. Plasmas* **13** (2006) 102503; BROWN, M.R., COTHRAN, C.D., FUNG, J., Two fluid effects on three-dimensional reconnection in the Swarthmore spheromak experiment with comparisons to space data, *Phys. Plasmas* **13** (2006) 056503.
- [9.62] YAMADA, M., FURTH, H.P., HSU, W., JANOS, A., JARDIN, S., OKABAYASHI, M., SINNIS, J., STIX, T.H., YAMAZAKI, K., Quasistatic formation of the spheromak plasma configuration, *Phys. Rev. Lett.* **46** (1981) 188.
- [9.63] JI, H., BELOVA, E., GERHARDT, S.P., YAMADA, M., Recent advances in the SPIRIT (self-organized plasma with induction, reconnection, and injection techniques) concept, *J. Fusion Energy* **26** (2007) 93.

- [9.64] NAGATA, M., OGURO, T., KAGEI, Y, KAWAMI, K., HASEGAWA, H., FUKUMOTO, N, LIDA, M., MASAMUNE, S., KATSURAI, M., UYAMA, T., Self-reversal phenomena of toroidal current by reversing the external toroidal field in helicity-driven toroidal plasmas, *Phys. Rev. Lett.* **90** (2003) 225001.
- [9.65] JARBOE, T.R., HAMP, W.T., MARKLIN, G.J., NELSON, B.A., O'NEILL, R. LG., REDD, A.J., SIECK, P.E, SMITH, R.J., WROBEL, J.S., Spheromak formation by steady inductive helicity injection, *Phys. Rev. Lett.* **97** (2006) 115003/1–4.
- [9.66] SIECK, P.E., JARBOE, T.R, IZZO, V.A., HAMP, W.T., NELSON, B.A, O'NEILL, R.G., REDD, A.J., SMITH, R.J., Demonstration of steady inductive helicity injection, *Nucl. Fusion* **46** (2006) 254.
- [9.67] FUKUMOTO, N., OGAWA, H. NAGATA, M., UYAMA, T., SHIBATA, T., KASHIWA, Y., SUZUKI, S., KUSAMA, Y., J-M GROUP, Compact toroid injection system for JFT-2M, *Fusion Eng. Des.* **81** (2006) 2849.
- [9.68] Redmond Plasma Physics Laboratory, Seattle, WA, USA;  
*[http://depts.washington.edu/rppl/programs/frc\\_intro.html](http://depts.washington.edu/rppl/programs/frc_intro.html)*
- [9.69] ZHANG, SHOUYIN, WURDEN, G.A., INTRATOR, T.P, RUDEN, E.L., WAGANAAR, W.J., GRABOWSKI, C.T., RENNEKE, R.M., DEGNAN, J.H., High-density field-reversed configuration plasma for magnetized target fusion, *IEEE Trans. Plasma Sci.* **34** (2006) 223.
- [9.70] ZHANG, SHOUYIN, INTRATOR, T.P, WURDEN, G.A, WAGANAAR, W.J, TACCETTI, J.M., RENNEKE, R.M, GRABOWSKI, C.T., RUDEN, E.L., Confinement analyses of the high-density field-reversed configuration plasma in the field-reversed configuration experiment with a liner, *Phys. Plasmas* **12** (2005) 52513.
- [9.71] ESKOV, A.G., KURTMULLAEV, R.H., KRESHCHUK, A.P, LAUKHIN, Ya.N., MALYUTIN, A.I., MARKIN, A.I., MARYUSHOV, Yu.S., MIRONOV, B.N, ORLOV, M.M., PROSHLETOV, A.P., SEMENOV, V.N., SOSUNOV, Yu.B., “Principles of plasma heating and confinement in a compact toroidal configuration”, *Proc. 7th IAEA Conf. on Plasma Physics and Controlled Nuclear Fusion Research, Vienna, Austria, 1979, Vol. II, IAEA, Vienna (1979)* 187.
- [9.72] BARNES, D.C., SEYLER, C.E., ANDERSON, D.V., “On compact toruses and energetic particle injection”, *Proc. 1st US–Japan Joint Symp., Princeton, NJ, 1970.*

## BROADER SPECTRUM OF MAGNETIC CONFIGURATIONS

- [9.73] DEGNAN, J.H., AMDAHL, D.J., BROWN, A., et al., Experimental and computational progress on liner implosions for compression of FRCs, *IEEE Trans. Plasma Sci.* **36** (2008) 80.
- [9.74] SLOUGH, J., ANDREASON, S., GOTA, H., PHIL, C., VOTROUBEK, G., The pulsed high density experiment: concept, design, and initial results, *J. Fusion Energy* **26** (2007) 199.
- [9.75] DRAKE, R.P., HAMMER, J., HARTMAN, C., PERKINS, J., RYUTOV, D.D., Submegajoule liner implosion of a closed field line configuration, *Fusion Technol.* **30** (1996) 310.
- [9.76] STEINHAEUER, L., Equilibrium rotation in field-reversed configurations, *Phys. Plasmas* **15** (2008) 012505.
- [9.77] FREIDBERG, J.P., PEARLSTEIN, L.D., Rotational instabilities in a theta pinch, *Phys. Fluids* **21** (1978) 1207.
- [9.78] BELOVA, E.V., JARDIN, S.C., JI, H., YAMADA, M., KULSRUD, R., Numerical study of tilt stability of prolate field-reversed configurations, *Phys. Plasmas* **7** (2000) 4996.
- [9.79] BELOVA, E.V., DAVIDSON, R.C., YAMADA, H., Advances in the numerical modeling of field-reversed configurations, *Phys. Plasmas* **13** (2006) 056115.
- [9.80] TUSZEWSKI, M., TAGGART, D.P., CHRIEN, R.E., REJ, D.J., SIEMON, R.E., WRIGHT, B.L., Axial dynamics in field-reversed theta pinches. II: Stability, *Phys. Fluids* **B3** (1991) 2856.
- [9.81] CHRISTOFILOS, N.C., Astron, in *Proc. 2nd United Nations Conference on the Peaceful Uses of Atomic Energy*, United Nations, Geneva, 1958, Vol. 32 (1958) 279–290.
- [9.82] FLEISCHMANN, H.H., KAMMASH, T., System analysis of the ion-ring-compressor approach to fusion, *Nucl. Fusion* **15** (1975) 1143.
- [9.83] DAVIES, H.A., REJ, D.J., FLEISCHMANN, H., Production of field-reversing electron rings by ring stacking, *Phys. Rev. Lett.* **39** (1977) 744.
- [9.84] TURNER, W.C., CLAUSER, J.F., COENSGEN, F.H., CORRELL, D.L., CUMMINS, W.F., FREIS, R.P., GOODMAN, R.K., HUNT, A.L., KAISER, T.B., MELLIN, G.M., NEXEN, W.E., SIMONEN, T.C., STALLARD, B.W., Field-reversal experiments in a neutral-beam-injected mirror machine, *Nucl. Fusion* **19** (1979) 1011.

- [9.85] GUO, H.Y., HOFFMAN, A.L., MILROY, R.D., STEINHAEUER, L.C., BROOKS, R.D., DEARDS, C.L., GROSSNICKLE, J.A., MELNIK, P., MILLER, K.E., VLASES, G.C., Improved confinement and current drive of high temperature field reversed configurations in the new translation, confinement, and sustainment upgrade device, *Phys. Plasmas* **15** (2008) 056101.
- [9.86] RYUTOV, D.D., KESNER, J., MAUEL, M.E., Magnetic field perturbations in closed-field-line systems with zero toroidal magnetic field, *Phys. Plasmas* **11** (2004) 2318.
- [9.87] STEINHAEUER, L.C., GUO, H.Y., HOFFMAN, A.L., ISHIDA, A., RYUTOV, D.D., Modeling of field-reversed configuration experiment with large safety factor, *Phys. Plasmas* **13** (2006) 056119.
- [9.88] COHEN, S.A., MILROY, R.D., Maintaining the closed magnetic-field-line topology of a field-reversed configuration with the addition of static transverse magnetic fields, *Phys. Plasmas* **7** (2000) 2539.
- [9.89] GUO, H.Y., HOFFMAN, A.L., STEINHAEUER, L.C., MILLER, K.E., Observations of improved stability and confinement in a high-beta self-organized spherical-torus-like field-reversed configuration, *Phys. Rev. Lett.* **95** (2005) 175001.
- [9.90] BISHOP, A., Project Sherwood, Addison-Wesley, Reading, MA (1958).
- [9.91] BUDKER, G.I., "Thermonuclear reactions in a system with magnetic stoppers, and the problem of direct transformation of thermonuclear energy into electrical energy", in: *Plasma Physics and the Problem of Controlled Thermonuclear Reactions*, Pergamon Press, New York-Oxford-London-Paris, Vol. 3 (1961), 1 (translation from the Russian 1958 edition).
- [9.92] POST, R.F., The magnetic mirror approach to fusion, *Nucl. Fusion* **27** (1987) 1579.
- [9.93] RYUTOV, D.D., Open-ended traps, *Sov. Phys. Uspekhi* **31** (1988) 300.
- [9.94] RYUTOV, D.D., Mirror devices, *Plasma Dev. Oper.* **1** (1990) 79.
- [9.95] HERSHKOWITZ, N., MIYOSHI, S., RYUTOV, D.D., Mirror devices, *Nucl. Fusion* **30** (1990) 1761.
- [9.96] POST, R.F., RYUTOV, D.D., Mirror fusion research: update and prospects, *Comments Plasma Phys.* **16** (1995) 375.

## BROADER SPECTRUM OF MAGNETIC CONFIGURATIONS

- [9.97] FUTCH, A.H. Jr, HOLDREN, J.P., KILLEEN, J., MIRIN, A.A., Multi-species Fokker-Planck calculations for D-T and D-3He mirror reactors, *Plasma Phys.* **14** (1972) 211.
- [9.98] PASTUKHOV, V.P., Collisional losses of electron from an adiabatic trap in a plasma with a positive potential, *Nucl. Fusion* **14** (1974) 3.
- [9.99] ROSENBLUTH, M.N., POST, R.F., High-frequency electrostatic plasma instability inherent to “loss-cone” particle distributions, *Phys. Fluids* **8** (1965) 547; POST, R.F., ROSENBLUTH, M.N., Electrostatic instabilities in finite mirror-confined plasmas, *Phys. Fluids* **9** (1966) 730.
- [9.100] CORRELL, D.L., CLAUSER, J.H., COENSGEN, F.H., CUMMINS, W.F., DRAKE, R.P., FOOTE, J.H., FUTCH, A.H., GOODMAN, R.K., GRUBB, D.P., MELIN, G.M., NEXSEN, W.E., SIMONEN, T.C., STALLARD, B.W., TURNER, W.C., Production of large-radius, high-beta, confined mirror plasmas, *Nucl. Fusion* **20** (1980) 655.
- [9.101] ROSENBLUTH, M.N., LONGMIRE, C.L., Stability of plasmas confined by magnetic fields, *Ann. Phys.* **1** (1957) 120.
- [9.102] BALDWIN, D.E., End-loss processes from mirror machines, *Rev. Mod. Phys.* **49** (1977) 317.
- [9.103] DIMOV, G.I., ZAKAIDAKOV, V.V., KISHINEVSKII, M.E., A thermonuclear trap with double mirrors, *Fizika Plazmy* **2** (1976) 597.
- [9.104] FOWLER, T.K., LOGAN, B.G., The tandem mirror reactor, *Comments Plasma Phys. Control. Fusion* **2** (1977) 167.
- [9.105] COENSGEN, F.H., ANDERSON, C.A., CASPER, T.A., CLAUSER, J.F., CONDIT, W.C., CORRELL, D.L., et al., Electrostatic plasma-confinement experiments in a tandem mirror system, *Phys. Rev. Lett.* **44** (1980) 1132.
- [9.106] MCVEY, B.D., POST, R.S., BLACKFIELD, D.T., GERVER, M., IRBY, J., KESNER, J., KLINKOWSTEIN, R.E., LANE, B., MAUEL, M E., MONTGOMERY, D.B., POTOK, R., SMITH, D.K., YANG, T.F., TARA tandem mirror, Proc. 11th European Conf. on Controlled Fusion and Plasma Physics; European Physical Society, Petit-Lancy, Switzerland (1983) 263–266.

- [9.107] HERSHKOWITZ, N., BREUN, R.A., BROOKER, P., BROWNING, J., BROUCHOUS, D., CONRAD, J.R., CUI, B.S., FERRON, J., GOULDING, R.H., INTRATOR, T., KEIL, D., LITWIN, C., MAJESKI, R., MEASSICK, S., NELSON, B., PERSING, H., PROBERT, P., ROBERTS, D., TATARONIS, J.A., YUNJIAN, W., YASAKA, Y., Improved MHD stabilization in the Phaedrus-B tandem mirror obtained by using ICRF excited by rotating field antennas and measurements of a model antenna near fields, Plasma Physics and Controlled Nuclear Fusion Research 1988, Proc. 12th Int. Conf. International Atomic Energy Agency. IAEA, Vienna, Austria (1988) 487.
- [9.108] BALDWIN, D.E., LOGAN, B.G., Improved tandem mirror fusion reactor, Phys. Rev. Lett. **43** (1979) 1318.
- [9.109] GRUBB, D.P., ALLEN, S.L., CASPER, T.A., CLAUSER, J.F. COENSGEN, F.H., CORRELL, D.L., et al., Thermal-barrier production and identification in a tandem mirror, Phys. Rev. Lett. **53** (1984) 783.
- [9.110] INUTAKE, M., CHO, T., ICHIMURA, M., ISHII, K., ITAKURA, A., KATANUMA, I., KIWAMOTO, Y., KUSAMA, Y., MASE, A., MIYOSHI, S., NAKASHIMA, Y., SAITO, T., SAKASAI, A., SAWADA, K., WAKAIDA, I., YAMAGUCHI, N., YATSU, K., Thermal barrier formation and plasma confinement in the axisymmetrized tandem mirror GAMMA 10, Phys. Rev. Lett. **55** (1985) 939; CHO, T., HIGAKI, H., HIRATA, M., HOJO, H., ICHIMURA, M., ISHII, K., et al., Overview of recent progress in the GAMMA 10 tandem mirror, Fusion Sci. Technol. **51** (2007) 11.
- [9.111] RYUTOV, D.D., STUPAKOV, G.V., Transport processes in non-axisymmetric open traps, Rev. Plasma Phys. **13** (1987) 93 (KADOMTSEV, B.B., ED.), Consultants Bureau (1987).
- [9.112] STUPAKOV, G.V., One method of reducing transverse losses of plasma from ambipolar trap, Fizika Plazmy **5** (1979) 958.
- [9.113] SKOVORODA, A.A., SHAFRANOV, V.D., Magnetic surfaces and flux coordinates for omnigenous open confinement systems, Plasma Phys. Rep. **20** (1994) 221.
- [9.114] RYUTOV, D.D., "Axisymmetric MHD-stable mirrors", Physics of Mirrors, Reversed Field Pinches and Compact Tori, Proc. Intern. School of Plasma Physics Piero Caldirola, 1–11 September 1987 (ORTOLANI, S., SINDONI, E., Eds), Vol. 2, Editrice Compositori, Bologna (1987) 791.

- [9.115] HINTON, F.L., ROSENBLUTH, M.N., Stabilization of axisymmetric mirror plasmas by energetic ion injection, *Nucl. Fusion* **22** (1982) 1547.
- [9.116] POST, R.F., FOWLER, T.K., BULMER, R., BYERS, J., HUA, D., TUNG, L., Axisymmetric tandem mirrors: stabilization and confinement studies, *Fusion Sci. Technol.* **47** (2005) 49.
- [9.117] ABDRAHIMOV, G.F., BAJBORODIN, S.I., BEKHTENEV, A.A., VOLOSOV, V.I., KUBAREV, V.V., PAL'CHIKOV, V.E., YUDIN, Yu.N., Experiments on the stabilization of a rotating plasma, *Nucl. Fusion Suppl.* **1** (1981) 539; ABDRAHIMOV, G.F., BELOBORODOV, A.V., VOLOSOV, V.I., KUBAREV, V.V., POPOV, Yu.S., YUDIN, Yu.N., Hot rotating plasma in the PSP-2 experiment, *Nucl. Fusion* **31** (1991), 1275.
- [9.118] ELLIS, R.F., CASE, A., ELTON, R., GHOSH, J., GRIEM, H., HASSAM, A., LUNSFORD, R., MESSER, S., TEODORESCU, C., Steady supersonically rotating plasmas in the Maryland centrifugal experiment, *Phys. Plasmas* **12** (2005) 55704.
- [9.119] NUMAKURA, T., CHO, T., KOHAGURA, J., HIRATA, M., MIYATA, Y., MINAMI, R., KIMINAMI, S., SHIMIZU, K., MORIMOTO, N., ITOU, M., IKUNO, T., NAMIKI, S., YAMAGISHI, T., HIRAI, K., OGURA, K., KARIYA, T., IMAI, T., MIYOSHI, S., Effects of plasma confining potentials and the associated radially sheared electric fields on the plasma energy confinement, *Fusion Sci. Technol.* **51** (2007) 343.
- [9.120] MIRNOV, V.V., RYUTOV, D.D., Linear gasdynamic system for plasma confinement, *Sov. Tech. Phys. Lett.* **5** (1979) 279.
- [9.121] ABDRAHIMOV, A., ABDRAHIMOV, G., ANIKEEV, A., BAGRYANSKY, P., BEKLEMISHEV, A., DEICHULI, P., et al., Status of the GDT experiment and future plans, *Fusion Sci. Technol.*, **47**, Issue 1T (2005) 27–35.
- [9.122] RYUTOV, D.D., Mirror type neutron source, *Plasma Phys. Control. Fusion* **32** (1990) 999.
- [9.123] COENSGEN, F.H., CASPER, T.A., CORRELL, D.L., DAMM, C.C., FUTCH, A.H., LOGAN, B.G., MOLVIK, A.W., High-performance beam-plasma neutron sources for fusion materials development, *Nucl. Sci. Eng.* **106** (1990) 138.
- [9.124] NOACK, K., ROGOV, A., ANIKEEV, A.V., IVANOV, A.A., KRUGLYAKOV, E.P., TSIDULKO, Yu.A., The GDT-based fusion neutron source as driver of a minor actinides burner, *Ann. Nucl. Energy* **35** (2008) 1216.

- [9.125] GARNIER, D.T., BOXER, A.C., ELLSWORTH, J.L., KESNER, J., MAUEL, M.E., Confinement improvement with magnetic levitation of a superconductive dipole, *Nucl. Fusion* **49** (2009) 055023.
- [9.126] LEVITT, B., MASLOVSKY, D., MAUEL, M.E., Measurement of the global structure of interchange modes driven by energetic electrons trapped in a magnetic dipole, *Phys. Plasmas* **9** (2002) 2507.
- [9.127] MAUEL, M.E., “The D-3He dipole fusion reactor”, *Current Trends in International Fusion Research, Proc. 1st Int. Symp. on Evaluation of Current Trends in Fusion Research, Plenum* (1997) 149–151.
- [9.128] BAGRYANSKY, P.A., ANIKEEV, A.V., COLLATZ, S., DEICHULY, P.P., IVANOV, A.A., KARPUSHOV, A.N., KOREPANOV, S.A., et al., Recent results of experiments on the gas dynamic trap, *Fusion Sci. Technol.* **35** (1999) T79.
- [9.129] KATANUMA, I., SASAGAWA, Y., TATEMATSU, Y., NAKASHIMA, Y., CHO, T., PASTUKHOV, V.P., Magnetic divertor design in GAMMA10 central cell, *Nucl. Fusion* **46** (2006) 608.
- [9.130] HAINES, M.G., Plasma containment in cusp-shaped magnetic-fields, *Nucl. Fusion* **17** (1977) 811.
- [9.131] IOFFE, M.S., KANAEV, B.I., PITERSKII, V.V., YUSHMANOV, E.E., Plasma confinement in the Atoll electrostatically plugged magnetic cusp I., *Soviet J. Plasma Phys.* **10** (1984) 261.
- [9.132] DOLAN, T.J., Magnetic electrostatic plasma confinement, *Plasma Phys. Control. Fusion* **36** (1994) 1539.
- [9.133] CANTRELL, E.L., ELLIS, W.R., HARRIS, H.W., JAHODA, F.C., KRISTAL, R., MACHALEK, M.D, MCCONNELL, J.R., QUINN, W.E., RIBE, F.L., SAWYER, G.A., SEIBEL, F.T., SIEMON, R.E., Plasma experiments in the Scyllac toroidal theta pinch, *Proc. 5th Int. Conf. on Plasma Physics and Controlled Nuclear Fusion Research, 1975, Part III, IAEA, Vienna* (1975) 13–21.
- [9.134] MATZEN, M.K., SWEENEY, M.A., ADAMS, R.G., ASAY, J.R., BAILEY, J.E., et al., Pulsed-power-driven high energy density physics and inertial confinement fusion research, *Phys. Plasmas* **12** (2005) 55503.

- [9.135] RYUTOV, D.D., BARNES, D., BAUER, B., HAMMER, J.H., HARTMAN, C.W., KIRKPATRICK, R.C., LINDEMUTH, I.R., MAKHIN, V., PARKS, P.B., REISMAN, D.B., SHEEHEY, P.T., SIEMON, R.E., Particle and heat transport in a dense wall-confined MTF plasma (theory and simulations), *Nucl. Fusion* **43** (2003) 955–960.
- [9.136] RYUTOV, D.D., SIEMON, R.E., Magnetized plasma configurations for fast liner implosions: a variety of possibilities, *Comments Mod. Phys.* **2**, 5 (2001) 185.
- [9.137] DEGNAN, J.H., AMDAHL, D.J., BROWN, A., CAVAZOS, T., COFFEY, S.K., DOMONKOS, M.T., FRESE, M.H., FRESE, S.D., GALE, D.G. GRABOWSKI, T.C., INTRATOR, T.P., KIRKPATRICK, R.C., KIUTTU, G.F., LEHR, F.M., LETTERIO, J.D., PARKER, J.V., PETERKIN Jr, R.E., RODERICK, N.F., RUDEN, E.L., SIEMON, R.E., SOMMARS, W., TUCKER, W., TURCHI, P.J., WURDEN, G.A., Experimental and computational progress on liner implosions for compression of FRCs, *IEEE Trans. Plasma Sci.* **36** (2008) 80.
- [9.138] THIO, Y.C.F., Status of the US program in magneto-inertial fusion, *J. Phys. Conf. Ser.* **112** (2008) 042084.
- [9.139] UCKAN, N.A., SANTORO, R.T., EBT reactor characteristics consistent with stability and power balance requirements, *Nucl. Technol. Fusion* **4** (1983) 1326.
- [9.140] AINSWORTH, N.R., ALCOCK, M.W., BRADFORD, R.E., COLLINS, P.R., CORDEY, J.G., EDLINGTON, T., FLETCHER, W.H.W, JONES, E.M., PAYNE, M.F., RIVIERE, A.C., “Fluctuations, diffusion and beam-induced currents in Culham Levitron”, *Plasma Physics and Controlled Nuclear Fusion Research* (1978), Proc. 7th Int. Conf., Innsbruck, Austria, August 23–30, 1978, Vol. 1, Vienna, IAEA (1979) 745–761.
- [9.141] SAKHAROV, A.D., “Theory of magnetic thermonuclear reactor (Part II)”, *Plasma Physics and the Problem of Controlled Thermonuclear Reactions* (LEONTOVICH, M.A., Ed.), Pergamon Press, Vol. 1 (1961) 21.

- [9.142] KERST, D.W., FORSEN, H.K., MEADE, D.M., LENCIONI, D.E., SPROTT, J.C., DE LA FUENTE, H.V., MOLVIK, A.W., BREUN, R.A., CAVALLO, A.J., DRAKE, J.R., GREENWOOD, J.R., JERNIGAN, T.C., PRATER, R., RUDMIN, J.W., Plasma injection, heating, confinement, and losses in multipole structures, Proc. 4th Conf. on Plasma Physics and Controlled Thermonuclear Fusion, IAEA, Vienna, Austria, Vol. 1 (1971) 3–14.
- [9.143] MAISONNIER, C., PECORELLA, F., RAGER, J.P., SAMUELLI, M., STRANGIO, C., MESSINA, A., “Comparative studies of plasma focus devices”, Proc. 5th Int. Conf. on Plasma Physics and Controlled Nuclear Fusion Research, IAEA, Vienna, Austria, Vol. 3 (1975) 99–108; MAISONNIER, C., RAGER, J.P., GOURLAN, C., GALANTI, M., MORGAN, P.D., Preliminary results of the 1-MJ plasma focus experiment, Nucl. Fusion, Suppl. **3** (1977) 447–453.

# CHAPTER 10

## INERTIAL FUSION ENERGY

**K. Mima**  
Japan

### 10.1. BRIEF HISTORY

In 1917, Albert Einstein suggested the theory of stimulated emission of light that led to the development of the laser. The first laser, based on Einstein's theory, was demonstrated by the Maiman experiment in 1960 [10.1]. In association with the invention and developments of the laser, N.G. Basov, A. Prokorov and C.H. Towns received the Nobel prize for physics in 1963. On the other hand, it had been recognized that nuclear fusion energy is the energy source of our universe. It is the origin of the energy in our sun [10.2] and in the stars [10.3–10.8].

Right after the laser oscillation experiment, it was suggested by J. Nuckolls, E. Teller and S. Colgate in the USA and A. Sakharov in the USSR that nuclear fusion induced by lasers be used to solve the energy problem. Following the suggestion, the pioneering works for heating plasmas to a thermonuclear temperature with a laser were published by N. Basov, O.N. Krohin [10.9, 10.10], J.M. Dawson [10.11], C.R. Kastler [10.12], H. Hora [10.13], F. Floux [10.14] and S. Eliezer [10.15]. The new concept of fusion ignition and burn by laser “implosion” was proposed by J. Nuckolls [10.16], which extended the spherically imploding shock concept discovered by G. Guderley [10.17] to the laser fusion concept. Since then, laser fusion research has started all over the world. For example, many inertial fusion energy (IFE) facilities have been constructed for investigating implosion physics:

*Lasers:* GEKKO I, GEKKO II, GEKKO IV, GEKKO MII and GEKKO XII at ILE, Osaka University, Japan; JANUS, CYCLOPS, ARUGUS, SHIVA and NOVA at Lawrence Livermore National Laboratory (LLNL), USA; OMEGA at the Laboratory for Laser Energetics (LLE), University of Rochester, USA; PHEBUS at Limeil, Paris, France; the ASTERIX iodine laser at the Max-Planck-Institut für Plasmaphysik (IPP), Garching, Germany; MPI, GLECO at the Laboratoire d'Utilisation des Lasers Intenses (LULI), École Polytechnique, France; HELIOS at Los Alamos National Laboratory, USA; Shengan II at the Shanghai Institute of Optics and Fine Mechanics, China; VULCAN at the Rutherford Appleton Laboratory, UK; PHAROS and NIKE at the Naval Research Laboratory (NRL) in Washington, DC, USA; and so on.

*Pulse power facilities:* the PBFA/Z-Machine at Sandia National Laboratories (SNL), New Mexico, USA; AngaraV at the Kurchatov Institute, Moscow, Russian Federation; and so on.

At present, ignition and burn of imploded fusion fuel are expected to be demonstrated within a few years by the National Ignition Facility (NIF) at LLNL, USA [10.18], [10.19] and the Laser Megajoule Facility (LMJ) at Bordeaux, France [10.20]. However, commercial application is still more than two decades away. This is a brief history of research and development on inertial fusion energy science and technology.

## 10.2. INTRODUCTION

In this overview, the science and technology related to inertial fusion energy (IFE) are described. Inertial fusion will be achieved with multiple choices of energy drivers, ignition schemes and burn scenarios such as implosion and hot spark formation. The “direct drive” describes a scenario where many high intensity laser beams irradiate uniformly a spherical shell containing the nuclear fuel. At stagnation, the nuclear fuel is highly compressed and heated to induce nuclear fusion. The “indirect drive” scenario starts with the conversion of the laser or heavy ion beams into soft X rays in a cylindrical cavity of a few mm size. The spherical shell with the nuclear fuel is imploded by the X ray photons in the cavity. In both schemes, the direct and indirect drive, the shell must be stable to hydrodynamic instabilities, such as Rayleigh–Taylor (R–T), in order to obtain the high compression necessary for ignition. Hydrodynamic instabilities are initiated by all spherical symmetry imperfections in the shell surface and non-uniformity of the pellet irradiation.

The severe requirement of hydrodynamic stability has been relaxed in the “fast ignition” scheme. In this case, the compression is achieved by “direct drive” or “indirect drive” but the necessary heating for the nuclear ignition is derived from another laser which heats a segment of the fuel.

In the last part of this overview, the critical issues of science and technology on the path towards an inertial fusion energy reactor are discussed. The final goal is to obtain an economical electric power plant based on inertial fusion energy.

## 10.3. BASIC CONCEPT OF INERTIAL FUSION ENERGY

The idea of IFE to fuse deuterium-tritium was published by N.G. Basov and O.N. Krokhin [10.9]. This idea was directly related to the laser experiment by T.H. Maiman in 1960 [10.1]. In the early publications on IFE [10.9, 10.11], it was required to use short laser pulses to realize high gain fusion. Fusion neutrons from laser irradiation of lithium-deuterium targets had been detected [10.10].

## INERTIAL FUSION ENERGY

A national research centre for laser fusion was established in the USA at the Lawrence Livermore Laboratory, followed by other centres. In 1972 a paper was published by J. Nuckolls [10.16] stating that it is necessary to compress the fusion fuel to a very high density. There are two main schemes for pellet implosion, i.e. direct and indirect drives. The concepts are shown schematically in Fig. 10.1. In direct drive implosion, the surface of the fuel pellet is directly irradiated by driver beams. In contrast, in indirect drive implosion, the driver energy is converted into soft X rays, which fill a cavity as quasi-black-body radiation. The soft X rays are then absorbed on the surface of the pellet to generate ablation pressure to drive the implosion. There is another scheme called “hybrid” [10.21] which combines the direct and indirect concepts.

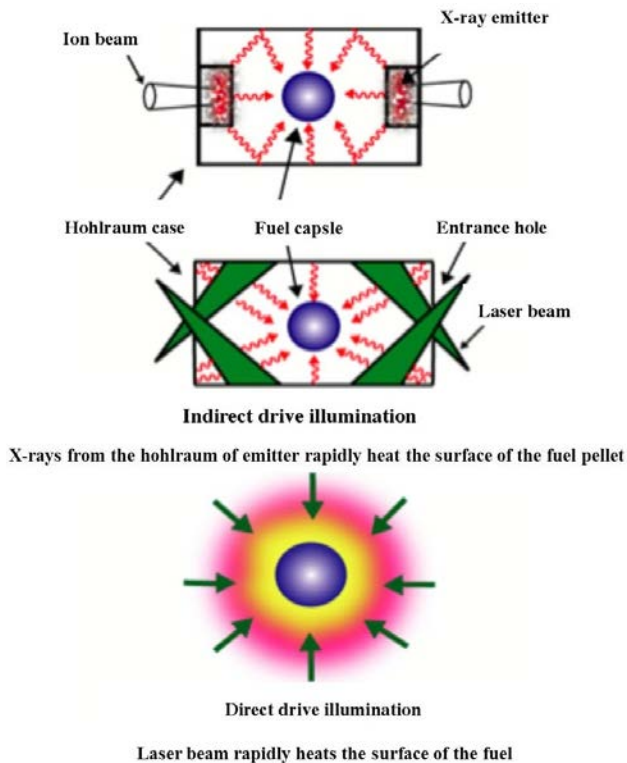


FIG. 10.1. Implosion schemes. (a) Ion beam indirect implosion; (b) laser indirect drive implosion; (c) laser direct drive implosion. Reprinted from Ref. [10.28]. Copyright (2011), IOP Publishing Ltd.

As for ignition of the imploded fuel, there are basically two concepts, i.e. central ignition [10.16] and fast ignition [10.22–10.24]. The corresponding ignition processes are illustrated in Fig. 10.2. When the implosion is spherically symmetric, the central hot spark is formed as shown in Fig. 10.2(a) for the

isobaric model [10.25]. If the implosion produces a compressed fuel of uniform density, we can ignite it with local heating by introducing an intense laser with pulse length much shorter than the expansion time of the compressed core. It is called fast ignition, where the hot spark is formed on the edge of a high density core plasma as shown in Fig. 10.2(b). So, fast ignition is sometimes called “off-centre ignition”.

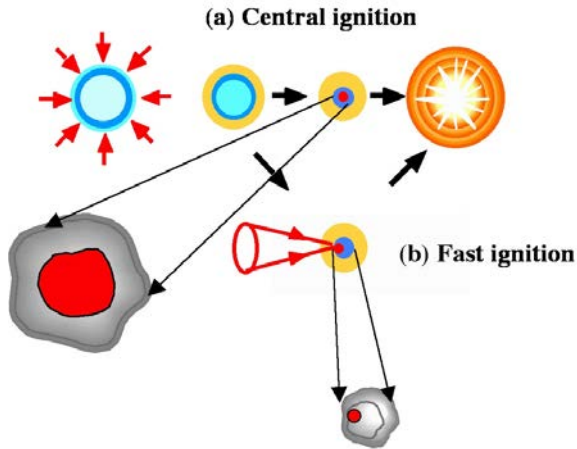


FIG. 10.2. Central ignition and fast ignition. The plasma density of the hot spark in fast ignition is expected to be 3–5 times higher than that for central ignition. Therefore, the hot spark size indicated by the red area is much smaller in fast ignition. So, the required laser energy for ignition and high gain will be smaller by one order of magnitude.

In Fig. 10.3, NIF and LMJ are the ignition demonstration machines under construction with central ignition. FIREX-II is the planned ignition facility for fast ignition in Japan. KOKYO and KOYO-F are conceptual designs for commercial reactors in central and fast ignition respectively.

#### 10.4. REQUIREMENT ON FUSION GAIN

The fusion energy gain (target gain) is defined as  $Q = E_f / E_d$ , where  $E_f$  is the fusion energy output from a fuel pellet and  $E_d$  is the laser energy irradiated onto the fuel pellet (driver energy). In the case of a D-T fusion reaction,



where  $\alpha$  and  $n$  are the helium nucleon and neutron respectively. In this reaction, the self-burning of the fusion reaction occurs when the self-heating by  $\alpha$  overcomes the bremsstrahlung losses at temperatures greater than 4 keV. When the burning plasma is uniformly heated to 4 keV and uniformly ignited, the maximum theoretical gain is given by the expression

$Q_{max} = 17.6 \text{ MeV} / (4 \times (3/2) \times 4) \text{ keV} \approx 730$ , where  $E_d$  (driver energy) is converted into  $E_p$  (imploded plasma thermal energy) with 100% efficiency and the plasma is totally burned. Here, in the denominator, the ideal equation of state (EOS), with an average energy of  $E = (3/2)k_B T$ , was used for the two ions and the two electrons, i.e.  $D + T + 2e$  with a temperature  $k_B T = 4 \text{ keV}$ , where  $k_B$  is the Boltzmann constant [10.26]. Note that four particles contribute to one fusion reaction.

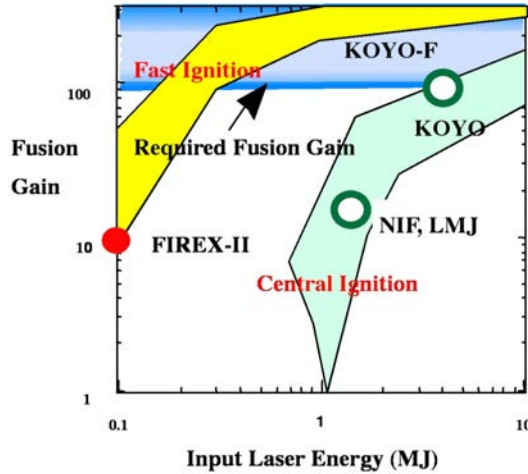


FIG. 10.3. Predicted fusion gain for central ignition and fast ignition as a function of input laser energy  $E_d$

Another interesting fusion reaction is the  $D-^3\text{He}$  reaction, since this is a neutron-free fusion reaction:



where the temperature is required to be higher than 30 keV. So, the maximum gain for uniform ignition is

$$G_{max} = 18.4 \text{ MeV} / (5 \times (3/2) \times 30) \text{ keV} \sim 73 \quad (10.3)$$

However, in a real situation, the gain is much smaller than  $G_{max}$ , since the burn fraction  $\Phi$  is significantly smaller than unity and the imploded plasma thermal energy is a small fraction of the incident driver energy, where  $\Phi = [\text{burned fuel mass}]/[\text{initial total fuel mass}]$ . Thus,  $E_f$  depends upon the various processes related to the production of burning plasmas, such as implosion, ignition and burn [10.27, 10.28].  $E_f$  and  $E_d$  are given as follows:

$$E_f = W\Phi \quad (10.4)$$

and

$$E_d = E_p / (\eta_{abs} / \eta_h) \quad (10.5)$$

where  $W$  is the fusion energy (= 17.6 MeV for D-T and 18.4 MeV for D-<sup>3</sup>He),  $E_p$  is the plasma thermal energy,  $\eta_{abs}$  is the absorption coefficient of the driver incident on the fuel pellet, and  $\eta_h$  is the hydrodynamic efficiency, which is the ratio of the internal energy of the burning plasma to the absorbed driver energy. Using those relations, we obtain the realistic gain as follows:

$$Q = 730 \eta_{abs} \eta_h \Phi \quad (\text{for D-T}); \quad Q = 73 \eta_{abs} \eta_h \Phi \quad (\text{for D-}^3\text{He}) \quad (10.6)$$

Here, the plasma is uniformly heated and ignited. Usually,  $\eta_{abs} \eta_h \Phi \sim 3\%$ . So,  $Q$  cannot be higher than 22 (2.2) for D-T (D-<sup>3</sup>He).

Since a realistic driver efficiency is typically 0.1 for a laser, the conversion efficiency of thermal energy to electricity is 0.4 and the fraction of circulation energy to the generated total electric power in the reactor system is required to be less than 0.25. Also,  $Q$  for an IFE reactor is required to be greater than 100 in a fusion reactor. Therefore, the fusion gain of uniform ignition is not enough and hot spark ignition (where the fusion burn starts locally) is necessary. The ignition conditions and gains for the two methods of ignition are shown in Fig. 10.3.

## 10.5. IMPLOSION CONCEPT

### 10.5.1. Why compression?

The burning fraction is evaluated as follows. Let us assume fuel that consists of 50% T and 50% D, and the fusion cross-section is  $\sigma$ . Then the fuel number density  $n$  is depleted due to the nuclear reaction as follows:

$$\frac{dn}{dt} = -n^2 \langle \sigma v \rangle / 2 \quad (10.7)$$

Here  $\langle \sigma v \rangle$  is the average over the energy distribution of D and T. When  $\langle \sigma v \rangle$  is constant in time, the equation can be integrated to obtain

$$n = n_0 / (1 + n_0 \langle \sigma v \rangle t / 2) \quad (10.8)$$

Therefore the burning fraction  $\Phi$  is given by

$$\Phi = 1 - n / n_0 = (n_0 \langle \sigma v \rangle t / 2) / (1 + n_0 \langle \sigma v \rangle t / 2) \quad (10.9)$$

The fusion reaction time  $t$  is given by the time the plasma is sustained. In the case of IFE,  $t \sim R / 4c_s$ , where  $R$  is the plasma radius and  $c_s$  is the sound speed. Then, the burning fraction is given by the following function of  $\rho R$ :

$$\Phi = \rho R / (A + \rho R) \quad (10.10)$$

where  $A$  is a function of temperature and approximately  $A [\text{g}\cdot\text{cm}^{-2}] = 10 / (T / 10 \text{ keV})^2$  for the D-T reaction. In ICF, the name of the game is compression. The pellet fuel mass  $M_f$  of the nuclear fuel is

$$M_f [\text{g}] = 4\pi R^3 \rho / 3 = 4.19 (\rho R^3) / \rho^2 \sim 33 / \rho^2 \quad (10.11)$$

where  $\rho R = 2 \text{ g}\cdot\text{cm}^{-2}$  was used. Without compression ( $\rho R = 0.2 \text{ g}\cdot\text{cm}^{-2}$ ) and the above equation implies a nuclear D-T mass of about 0.8 kg, an undesirable value for a controlled fusion reactor. However, a compressed fuel with density  $\rho = 400 \text{ g}\cdot\text{cm}^{-3}$  needs a pellet with only 4.5 mg D-T fuel. The driver energy  $E_d$  that heats the D-T fuel within a sphere of radius  $R$  and particle density  $n$  is given by

$$\eta_{abs} \eta_h E_d = 3nT(4\pi R^3 / 3) \quad (10.12)$$

Namely,

$$E_d = T \left( \frac{1}{\eta_a \eta_h} \right) (4\pi 2.5 m_p \rho_0^2) (\rho R)^3 (\rho_0 / \rho)^2 \quad (10.13)$$

where the ideal gas equation of state (EOS) has been used,  $m_p$  is the proton mass,  $\rho_0 = 0.2 \text{ g}\cdot\text{cm}^{-3}$  is the initial D-T density, and the temperature  $T$  is in [eV]. Taking a laser energy that heats the plasma to a temperature of 10 keV (alpha particle heating is much larger than bremsstrahlung loss) and inducing a 20% burn of the nuclear fuel (namely  $\rho R \sim 2 \text{ g}\cdot\text{cm}^{-2}$ ), we get

$$E_d [\text{J}] = \left( \frac{4 \times 10^{11}}{\eta_a \eta_h} \right) \left( \frac{\rho_0}{\rho} \right)^2 \quad (10.14)$$

Taking typical values of  $\eta_h = 0.1$  and  $\eta_a = 0.8$ , ICF ignition and nuclear burn require a pulsed (few nanoseconds) laser system with an energy

$$E_d [\text{J}] = 5 \times 10^{12} \left( \frac{\rho_0}{\rho} \right)^2 \quad (10.15)$$

It is evident from this result that without compression one requires an unrealistic pulse laser with energy of 5 TJ, while a 2000 times compression (i.e.  $400 \text{ g}\cdot\text{cm}^{-3}$ ) reduces the laser energy to 1.25 MJ. Compressing a plastic shell with an initial density of  $1 \text{ g}\cdot\text{cm}^{-3}$  and a density of  $600 \text{ g}\cdot\text{cm}^{-3}$  has been already achieved experimentally at Osaka University in Japan [10.29]. Therefore, it is not surprising that the largest laser system operated at LLNL (the National Ignition Facility) in the USA and the megajoule laser under construction in France will demonstrate ignition and burn with about  $1.5 \text{ MJ} / 3\omega$  input, where  $\omega$  means the fundamental frequency of the Nd-glass laser.

From a famous paper in Nature [10.16], the ICF philosophy is based on plasma compression by implosion. The limitations of compression are plasma instabilities and hydrodynamic instabilities (Rayleigh–Taylor, etc.). In the next

section it is shown that there is an optimum compression, i.e. the gain  $G$  is a maximum for a given compression. The value for a given density, fuel mass and particular ICF scheme depends on the EOS. We calculate the gain  $Q$  for fast ignition (FI) and compare it with the central spark ignition (CSI). Since we do not know the exact EOS, we shall assume the ideal gas EOS for the ions and the Thomas–Fermi EOS [10.30–10.32] for the electrons, with a multiplier, the so-called isentrope parameter,  $\alpha$ . In particular, the pressure  $p_e$  (in megabars) and the fuel specific energy  $\varepsilon_F$  [ $\text{J}\cdot\text{g}^{-1}$ ] are given in terms of the density  $\rho$  [ $\text{g}\cdot\text{cm}^{-3}$ ]

$$p_e = \alpha p_{FD}; \quad p_{FD} [\text{Mbar}] = 2\rho^{5/3} \quad (10.16)$$

$$\varepsilon_F = \alpha\varepsilon_{FD}; \quad \varepsilon_{FD} [\text{J}\cdot\text{g}^{-1}] = 3.3 \times 10^5 \rho^{2/3} \quad (10.17)$$

where  $p_{FD}$  is the Fermi–Dirac pressure and  $\varepsilon_{FD}$  the Fermi–Dirac specific energy. For D-T fuel with a mass of a few mg, one finds that the optimum fuel plasma density is a few hundred  $\text{g}\cdot\text{cm}^{-3}$ . With greater compression, the gain goes down; there is an optimum compression for achieving the maximum gain for a given isentrope parameter  $\alpha$ .

### 10.5.2. Gain scaling of implosion ignition

Figure 10.4 shows the fusion energy gain scaling with incident laser energy. The gain scaling curve for indirect drive by Lindl and direct drive with central ignition [10.25], and the gain curve from ILE, are shown for fast ignition with  $\rho = 300 \text{ g}\cdot\text{cm}^{-3}$ . In central ignition, the driver energy is given by the sum of the internal energy of the hot spark with mass  $M_h$  and internal energy of the cold main fuel with mass  $M_c$ . So,  $E_d = M_c\alpha\varepsilon_{FD} + M_h\varepsilon_h$  where  $\varepsilon_h > 6 \times 10^8 \text{ J}\cdot\text{g}^{-1}$ . Since the fusion burning fraction  $\Phi$  is roughly proportional to  $\rho\Delta R + \rho_h R_h$  and  $M_c$  is roughly  $\rho(\Delta R + R_h)^3 = [\rho(\Delta R + R_h)]^3 / \rho^2$ , the burning fraction is proportional to the cube root of the driver energy,  $E_d^{1/3}$  when  $\rho\Delta R$  is much larger than  $\rho_h R_h$ . Here,  $\rho_h R_h$  is the area density of the hot spark at the centre, where  $R_h$  is the radius of the hot spark, and  $\Delta R$  is the main fuel layer thickness as shown in the density profile in Fig. 10.1. This is the reason why the gain increases as the 1/3 power of the driver energy for the large driver energy region of Fig. 10.4. The asymptotic scaling laws for imploding thin shells have been investigated more precisely by M.M. Basko et al. [10.33]. The central hot spark ignition target design and driver pulse shape and requirement on the driver have been reviewed by J. Lindl [10.34] and M. Rosen [10.35].

It should be noted that the NIF completed in May 2009 will demonstrate fusion ignition and burning and energy gain. The credibility of the gain by the direct drive central ignition target is discussed in the next section. It is believed that the uniform irradiation configuration of NIF's 192 beams will be able to achieve fusion ignition and burning and an energy gain of 30. If fast ignition

works well, we can achieve a higher gain of 100–200 with less than 1 MJ laser energy. The recent progress in fast ignition and its credibility and uncertainty are described in Section 10.8.

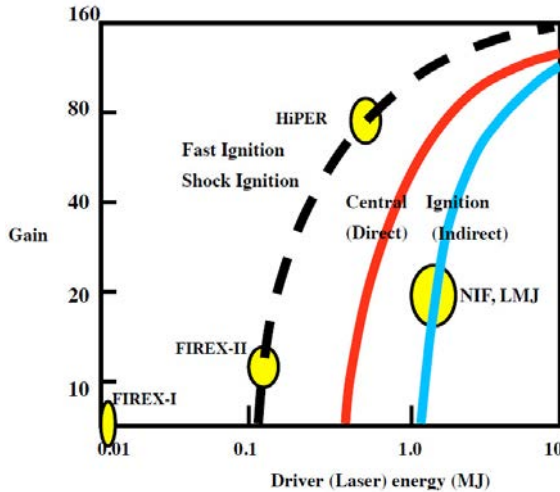


FIG. 10. 4. Fusion gain scaling for central spark ignition and fast ignition.

## 10.6. IMPLOSION PHYSICS

As was indicated in the previous section, high density compression and hot spark formation are crucial issues in IFE research. In high density compression, efficient plasma compression by implosion has to be achieved. A high efficiency implosion is characterized by efficiencies in the laser absorption ( $\eta_a$ ) and the hydrodynamics ( $\eta_h$ ), the isentrope ( $\alpha$ ) and the uniformity of the implosion velocity  $\rho v$ . So, the important plasma physics for high efficiency implosion are the laser plasma interaction, heat conduction and radiation hydrodynamics. As for the formation of the hot spark, dense plasma radiation hydrodynamics and relativistic laser plasma interactions are crucial.

In direct drive implosion and ignition by laser, the critical physics issues are laser absorption, plasma instability and the stability of the implosion [10.36]. The relation of issues to implosion processes are shown schematically in Fig. 10.5. When multi-laser beams irradiate the surface of a pellet (which is usually a plastic capsule containing a D-T ice layer), the pellet surface is ablated and forms a corona plasma by laser heating, field ionization and electron impact ionization. Laser beams penetrate into the corona plasma up to the cut-off region, as shown in Fig. 10.5. The laser beams are absorbed and scattered in the corona plasma by classical processes and various non-linear collective processes. In

those processes, the absorption efficiency, heating uniformity and hot electron production are important from the standpoint of implosion efficiency. Through those processes, the corona plasma is heated to a few keV and the pellet surface is further ablated by the electron and radiation heat conduction from the cut-off region to the pellet surface. In laser plasma interactions, resonance absorption, self-focusing, parametric instabilities, stimulated Raman scattering and stimulated Brillouin scattering have been important subjects. In the heat conduction, the kinetic effects (so-called non-local heat transport) and thermal smoothing have been widely investigated. The pressure of the hot dense ablation plasma drives a shock wave and then accelerates the fuel shell towards the centre of the pellet. This is called “laser implosion”. If the implosion is spherically uniform and the accelerated fuel shell shrinks and stagnates at the centre, then a strong spherical shock (Guderly shock) is generated to form a hot spark at the centre of an ultra-dense plasma. However, the implosion becomes non-spherical due to the hydrodynamic instabilities. The hydrodynamic instabilities grow from initial perturbations on the target and non-uniformity of the laser irradiation and lead to breakup of the shell and quenching of the hot spark at the centre as schematically shown in Fig. 10.5. Some details of the hydrodynamic instabilities are described below.

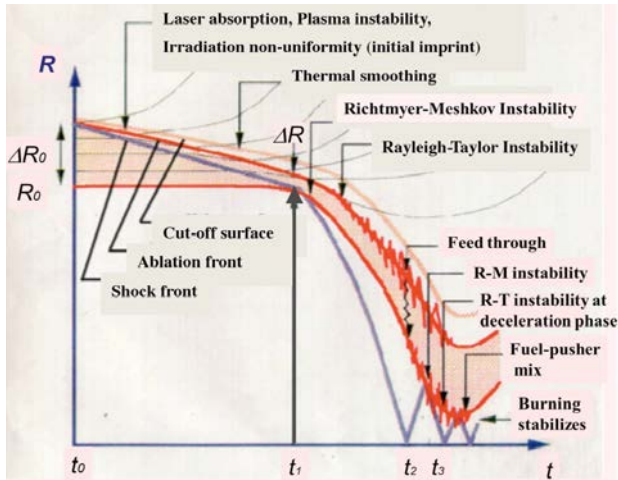


FIG. 10.5. Laser plasma interaction physics and hydrodynamics in direct drive implosion.  $R$  is the radius of the plasma and  $t_0$ ,  $t_1$ ,  $t_2$  and  $t_3$  are initial, shock break out, first shock colliding and stagnation times, respectively. The orange curve indicates the cut-off surface and the red curves indicate the ablation surface (outer) and inner surface of a fuel pellet. The relevant physics at various stages are indicated by labels. Note here that  $t_0$ – $t_1$  is the “initial phase” where the first shock wave propagates through the shell,  $t_1$ – $t_2$  is the “acceleration phase”,  $t_2$ – $t_3$  is the “deceleration phase” where the reflected shock wave pushes the imploding shell outwards, and after  $t_3$  until the maximum compression is the “stagnation phase”. Reprinted from Ref. [10.28]. Copyright (2011), IOP Publishing Ltd.

At the initial phase of irradiation, the separation of the absorption region (cut-off region) from the ablation front on the solid target is small. Therefore, the non-uniformity of the laser irradiation is strongly imprinted on the target surface (initial imprint). Then, the shock wave driven by the main pulse can excite the Richtmyer–Meshkov (R–M) instability, being coupled with the original target roughness and the initial imprint. The ablation pressure non-uniformity is relaxed from the laser non-uniformity at a later time due to the thermal smoothing during the energy transport from the absorption region to the ablation surface. In the main pulse acceleration phase, the Rayleigh–Taylor (R–T) instability grows. Even if the non-uniformity of the accelerated shell is small, mixing of the hot spark and surrounding dense cold fuel will take place due to an explosive growth of R–T instability in the stagnation phase.

In such a situation, the spark is cooled down and no fusion ignition takes place. Therefore, the mixing layer thickness should be sufficiently smaller than the hot spark radius. If we can manage to keep spherical symmetry and ignite the fuel, then the fine polishing by  $\alpha$  particle heating can smooth the burning wave front. The elementary processes mentioned above such as initial imprint, R–M instability, thermal smoothing, R–T instability, non-linear saturation and turbulent mixing have been independently and separately investigated with adequately modelled experiments on plane targets of various structures and laser irradiation conditions.

### **10.6.1. Ablative acceleration and laser–throughout plasma interaction in direct drive implosion**

The implosion is initiated by producing hot dense plasmas on a fuel pellet surface. The leading edge of the intense laser pulse evaporates and ionizes the pellet surface to produce corona plasmas as shown in Figs 10.6(a) and (b). The laser propagates in the corona plasma to be absorbed and scattered and then deposit the energy. When the laser beam reaches the turning point where the electron density is  $n_t = n_c \cos^2 \theta$  for an incident angle  $\theta$  and the cut-off density  $n_c$  (this is sometimes called the “critical density”), it is reflected back into the vacuum.

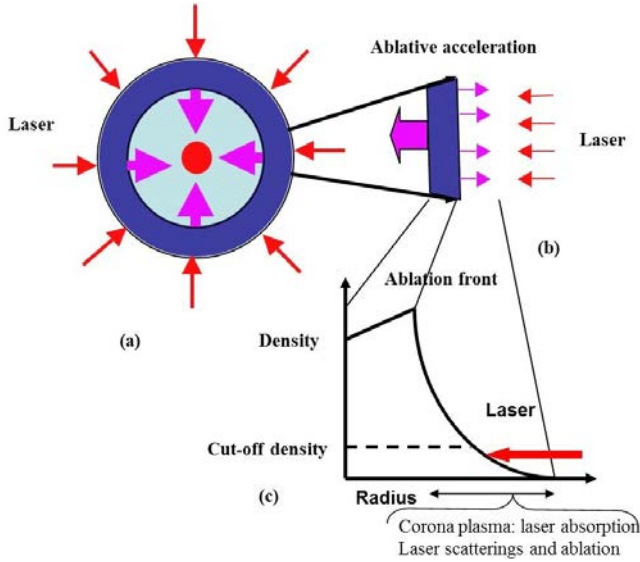


FIG. 10.6. Ablative acceleration and implosion. (a) Direct drive scheme: a dark blue ring indicates the fuel shell, the pink arrows indicate the imploding motion of the shell, the red spot at the centre indicates the compressed plasma and the red arrows indicate laser beams; (b) ablative acceleration process, where the pressure of the laser-produced hot dense plasma accelerates the shell; (c) density profile and the laser plasma interaction region. Taken from Ref. [10.37].

### 10.6.2. Classical absorption

During the propagation of the laser in the plasma, it is absorbed by electron–ion collisions and the excitation of electron plasma waves. The absorption through e–i collisions is called classical absorption and the absorption through plasma wave excitation is called collective absorption. When the laser wavelength is short, as with the third harmonics of an Nd:glass laser, which is currently used for implosion experiments, and the laser intensity is not very high, the classical absorption is dominant. When the collision frequency is  $\nu_e$  at the cut-off density and the plasma scale length is  $L$  around the cut-off surface, the absorption efficiency  $\eta_a$  is approximately given by

$$\eta_a = 1 - \exp(-32L\nu_e / 15c) \quad (10.18)$$

where  $c$  is the speed of light. This indicates that  $L\nu_e / c$  is larger than unity for high  $\eta_a$ . It will be satisfied for a plastic ablator plasma, when the scale length of  $L$  is longer than  $10 \mu\text{m}$  and the plasma electron temperature  $T_e$  is lower than  $5 \text{ keV}$  for a laser with wavelength  $\lambda = 0.35 \mu\text{m}$ , since  $\nu_e$  is proportional to  $1/T_e^{3/2}$ . Thus, the laser intensity is required to be less than  $10^{15} \text{ W}\cdot\text{cm}^{-2}$  since

the expanding plasma energy flux is about  $4T_e n_e c_s \sim 10^{15} \text{ W}\cdot\text{cm}^{-2}$ . Note here that  $Lv_e/c$ , that is, the absorption efficiency, becomes smaller for a longer wavelength laser, since  $v_e \propto n_e/T^{3/2} \propto 1/(\lambda^2 T^{3/2})$ .

So, in the case of a longer wavelength laser, the laser intensity should be lower to make the temperature lower for keeping the absorption efficiency constant. Actually, for the second harmonic  $\lambda = 0.53 \mu\text{m}$ , the laser intensity  $I_L$  should be as low as  $2 \times 10^{14} \text{ W}\cdot\text{cm}^{-2}$  and  $T_e$  is proportional to  $(I_L \lambda^2)^{2/3}$  when the plasma scale length is fixed. This means that  $T_e n_e$ , namely the corona plasma pressure, is lower for a long wavelength laser when the heating process is classical.

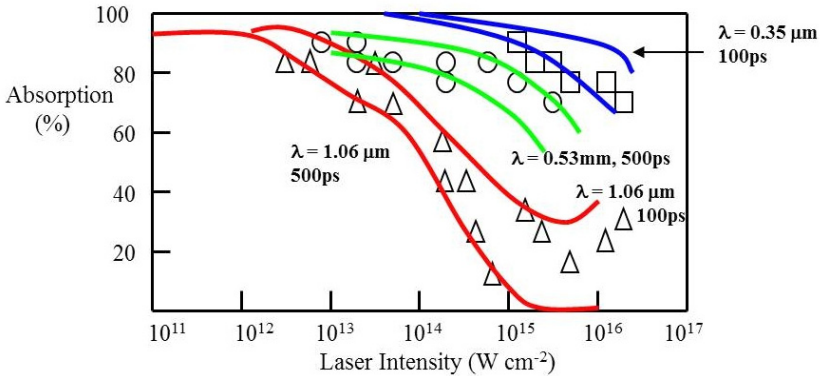


FIG. 10.7. Intensity and wavelength dependence of absorption rate [10.38]. Triangles represent data for  $\lambda = 1.06 \mu\text{m}$ ; circles for  $\lambda = 0.53 \mu\text{m}$  and squares for  $\lambda = 0.35 \mu\text{m}$ . Two absorption curves for each laser wavelength correspond to 500 ps (lower) and 100 ps (up) laser pulse duration.

Laser intensity dependent absorption has been explored in many experiments. Figure 10.7 shows a summary of the experimental results. As discussed in this section, the classical absorption decreases with the laser intensity. In the case of an  $\lambda = 1.06 \mu\text{m}$  laser, the absorption efficiency increases when the laser intensity is higher than  $10^5 \text{ W}\cdot\text{cm}^{-2}$ . It is an indication of the collective absorption which is discussed in the following section.

### 10.6.3. Collective laser plasma interactions

When collisions are not dominant, the incident laser interacts with collective modes in corona plasmas, i.e. electron plasma waves, ion acoustic waves and electromagnetic waves. Collective laser plasma interactions include “collective absorption” and “stimulated scattering”. As for collective absorption, the resonant mode conversion and/or Brillouin absorption, parametric instabilities, which are

“phonon–plasmon decay” and “two plasmon decay”, are important absorption mechanisms. Through these processes, the laser energy is mainly converted into high energy electrons. The energy absorption processes are shown schematically in Fig. 10.8.

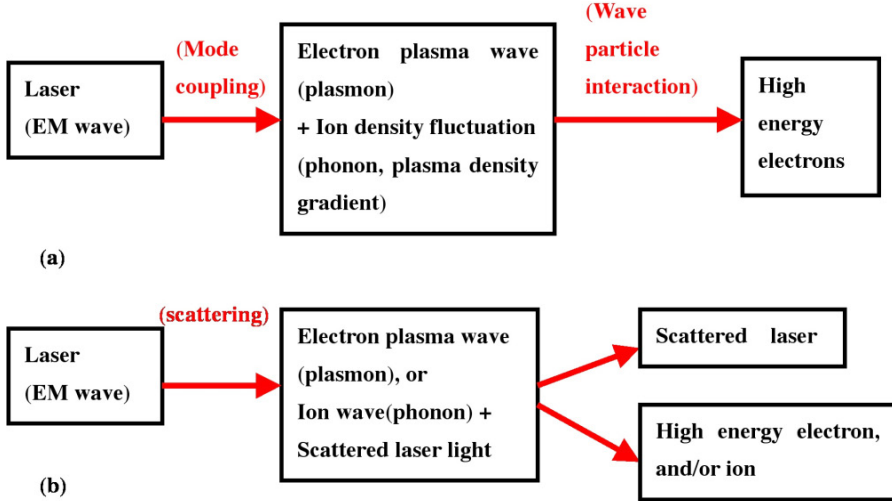


FIG. 10.8. (a) Collective absorption processes; (b) stimulated scatterings.

In the above processes, frequency and wavenumber are conserved as frequency matching,  $\omega_L = \omega_e + \Omega_i$ , or wavenumber matching,  $k_L = k_e + k_i$ , where  $\omega_L$ ,  $\omega_e$  and  $\Omega_i$  are the laser, electron plasma wave and ion wave frequencies, respectively, and  $k_L$ ,  $k_e$  and  $k_i$  are the corresponding wavenumbers.

#### 10.6.3.1. Resonant mode conversion

In this process, the frequency and wavenumber matching conditions  $\omega_e = \omega_L$ ,  $\Omega_i = 0$  and  $k_i \sim 1/L$  are met. When a P-polarized obliquely incident laser is reflected at a turning point in a non-uniform plasma where the density is  $n_t = n_c \cos^2 \theta$  for an incident angle  $\theta$ , the laser field tunnels into the critical point where the electron plasma wave frequency is equal to the laser frequency. Therefore, the electromagnetic wave (incident laser) is resonantly converted into electron plasma waves. These electron plasma waves excited at the critical surface propagate down the density gradient and then the phase velocity slows down. Then the electron plasma wave is dissipated by linear and non-linear wave particle interactions [10.39–10.43].

Resonant mode conversion is described schematically in Fig. 10.9. The absorption efficiency of the resonant absorption depends upon the density scale

length and the incident angle. The absorption efficiency is given approximately by

$$\zeta(\omega_L L / c)^{-1/3} \exp\left(\frac{-2\zeta^{3/2}}{3(\omega_L L / c)^{1/2}}\right) \quad (10.19)$$

where  $\zeta = \sin^2 \theta \cdot \omega_L L / c$ . The exact formula for the conversion efficiency is given in the textbooks of Gintzburug and Kruer [10.40, 10.45]. The maximum absorption efficiency is about 0.5, when  $\zeta = (\omega_L L / 4c)^{1/3}$ ; i.e. the incident angle satisfies  $\sin \theta = (c / 2\omega_L L)^{1/3}$ . Note that when  $L$  is the hydrodynamic scale length for a nanosecond laser pulse,  $L$  is of the order of 100  $\mu\text{m}$ , so  $\sin \theta < 0.1$ . In such a case, a very small fraction of the laser energy can be absorbed by resonance absorption. However, the ponderomotive force of the laser field is comparable to the plasma pressure to steepen the density profile near the turning point as shown in Fig. 10.9. As a result, the resonant absorption plays an important role as a collective absorption process [10.41, 10.43, 10.44]. Since the Maxwellian tail electrons are accelerated by large amplitude electron plasma waves, “hot electrons” (which are also called suprathermal electrons) are generated. The slope temperature of hot electrons  $T_h$  is empirically scaled to the laser intensity as follows:

$$T_h \sim 13T_e^{1/4} (I_L \lambda_L^2)^{0.39} \quad (\text{from Refs [10.41, 10.45]}) \quad (10.20)$$

$$T_h \sim 7T_e^{1/3} (I_L \lambda_L^2)^{0.33} \quad (\text{from Refs [10.42, 10.46]}) \quad (10.21)$$

where  $T_h, T_e$  are in keV and  $I_L \lambda_L^2$  in  $10^{15} \text{W} \cdot \mu\text{m}^2 \cdot \text{cm}^{-2}$ . When  $T_h$  is higher than a few tens of keV, the ablatively accelerated fuel layer is preheated by hot electrons and the preheating will prevent compression. So,  $I_L \lambda_L^2$  is required to be lower than  $0.5 \times 10^{15} \text{W} \cdot \mu\text{m}^2 \cdot \text{cm}^{-2}$ .

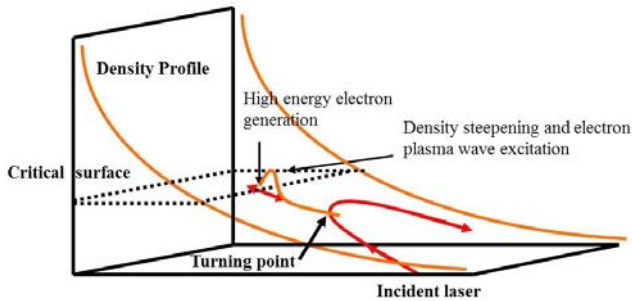


FIG 10.9. Resonant absorption near the critical density surface: density profile and laser propagation. The vertical axis is for plasma density and the orange curves indicate density; the red curves are the incident laser ray trace and the propagation of an electron plasma wave around the critical density; the x-axis is the plasma expansion direction and the y-axis is along the target surface. Reproduced from Ref. [10.37].

10.6.3.2. Density profile modifications

The ablating plasma is pushed by the ponderomotive force. The laser intensity and averaged density of the ablating plasma at the interface between underdense plasma and overdense plasma are shown in Fig. 10.10.

The density jumps around the cut-off surface from the upper shelf density  $n_2$  to the lower shelf density  $n_1$  and the sonic point ( $n_s$ ) is in between this density jump. The  $n_1$  and  $n_2$  are related to  $n_s$  by the pressure balance

$$n_s^2 / n^2 + 2 \ln(n / n_s) + v_0^2 / 2v_e^2 \tag{10.22}$$

where  $v_0$  and  $v_{\max}$  are the quiver velocity and that corresponding to the maximum laser intensity. We set  $v_0 = 0$  and  $n > n_s$  to obtain  $n_2 / n_s \sim 1 + v_{\max} / 2v_e$ , and set  $v_0 = v_{inc}$  (which corresponds to the incident laser amplitude) and  $n > n_s$  to obtain  $n_1 / n_s \sim 1 - (v_{\max}^2 - v_0^2)^{1/2} / 2v_e$ . Since the width of the density jump is about the skin depth, the density scale length  $L$  of the steepening density profile is given by  $(c / \omega)n_c / (n_2 - n_1) \sim (c / \omega)v_e / v_{\max}$ , which is a few micrometres and will enhance the resonant absorption but suppress the parametric instabilities discussed in the following.

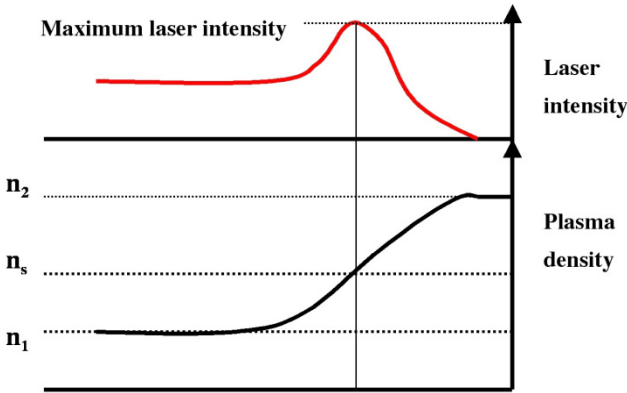


FIG. 10.10. Density profile steepening around the cut-off surface due to ponderomotive force; the x-axis is along the plasma expansion [10.45].

10.6.3.3. Electron–ion decay and oscillating two stream instabilities

The frequency matching condition is  $\omega_e = \omega_L - \Omega_i$ , and  $\Omega_i = kc_s$ . Here, the incident laser with a frequency  $\omega_L$  decays into an electron plasma wave and an ion acoustic wave. Since  $\omega_e \gg \Omega_i$ ,  $\omega_e \sim \omega_L$ , so that this instability takes place near the cut-off (sometimes called the critical surface). Through this instability, the electron plasma wave turbulence generates hot electrons whose energy is a few

tens of keV [10.47–10.52]. However, this parametric instability is suppressed due to the density profile steepening since this parametric instability is a convective instability. Thus the threshold of the instability is given by [10.53],

$$\gamma_0 > \frac{\pi (v_{ge} c_s)^{1/2}}{2L} \quad (10.23)$$

Here  $v_{ge}$  and  $c_s$  are the electron plasma wave group velocity and the ion sound velocity, and  $\gamma_0$ , the maximum growth rate of the instability, is given in Ref. [10.45] as follows

$$\gamma_0 = \left(\frac{3}{4}\right)^{1/2} \omega_L \left(\frac{Zm_e (kv_0)^2}{m_i 16\omega_L^2}\right)^{1/3} \quad (10.24)$$

when the laser intensity is high enough and the growth rate is higher than the ion wave frequency. Here,  $v_0$  is the electron quiver velocity in the laser field,  $v_e$  is the electron thermal velocity,  $m_e$ ,  $m_i$  and  $Z$  are the electron mass, ion mass and ion charge number, and  $k$  is the wavenumber of the unstable mode. Equations (10.23) and (10.24) lead to the threshold of the parametric decay instability:

$$\left(\frac{v_0}{v_e}\right)^2 > \left(\frac{k_D}{k}\right)^{1/2} \left(\frac{m_i}{Zm_e}\right)^{1/4} \left(\frac{2\pi}{k_D L}\right)^3 \quad (10.25)$$

where  $k_D$  is the Debye wavenumber. This indicates that the instability threshold depends strongly on the density scale length. For example, with  $T_e \sim 5$  keV and a laser intensity  $10^{15}$  W·cm<sup>-2</sup> at 0.35  $\mu$ m wavelength,  $(v_0/v_e)^2$  is about 0.01. Then  $k_D L$  is required to be greater than 200. This is not satisfied when density steepening occurs. So, in the laser implosion, the parametric instabilities near the cut-off are very weak and the effect of those instabilities is small in comparison with the resonance absorption and two-plasmon decay instability and stimulated Raman scattering which are discussed in the following section.

#### 10.6.3.4. Two-plasmon decay instability

The frequency matching conditions are

$$\omega_L = \omega_{e1} + \omega_{e2} \sim 2\omega_p \quad (10.26)$$

where  $\omega_p$  is the electron plasma frequency and

$$k_{e1} = -k_{e2} \quad (10.27)$$

This instability represents a resonant decay of a light wave into two electron plasma waves [10.54–10.56]. So, two-plasmon decay occurs near the quarter of the surface where the electron density is  $n_c/4$ . Since the two-plasmon decay instability is localized in a narrow region, the localized  $\vec{E}$  field and local

heating causes density profile steepening which suppresses the instability. So the instability occurs in bursts. Although the instability is intermittent, a significant number of 100 keV hot electrons are generated to cause preheating of an imploding shell. The instability thresholds are given for collisional dumping of the electron plasma wave  $v_e$  or for the plasma non-uniformity,

$$\omega_L v_0 / c > 2v_e \text{ or } (v_0 / v_e)^2 > 12c / (\omega_L L) \quad (10.28)$$

where  $L$  is the density scale length at the quarter critical density. This threshold is lower than that for the Raman instability at the quarter critical region unless the plasma is quite hot [10.45].

#### 10.6.3.5. Stimulated Raman scattering

The Raman instability is the decay of an incident laser into a scattered electromagnetic wave and an electron plasma wave. The frequency and the wavenumber matching conditions are

$$\omega_L = \omega_s + \omega_e \quad (10.29)$$

and

$$k_L = k_s + k_e \quad (10.30)$$

where  $\omega_L(\omega_s)$  and  $k_L(k_s)$  are the frequency and wavenumber of the incident (scattered) light, and  $\omega_e$  and  $k_e$  are the frequency and wavenumber of the electron plasma wave [10.46, 10.57]. The growth rate of the stimulated Raman scattering (SRS),  $\gamma$ , is given as follows:

$$\gamma = \left( \frac{\omega_p}{(\omega_L - \omega_p)} \right)^{1/2} \frac{kv_0}{2} \quad (10.31)$$

where  $k$  is the number of the excited plasma wave. Since

$$k^2 = k_L^2 + k_s^2 - 2k_L k_s \cos \theta \quad (10.32)$$

and

$$k_s^2 = \frac{(\omega_L - \omega_p)^2 - \omega_p^2}{c^2} \quad (10.33)$$

the growth rate is maximum for backscattering:  $\theta = \pi$  and

$$\gamma = \left( \left( \omega_L^2 + (\omega_L - \omega_p)^2 - 2\omega_p^2 \right) \left( \frac{\omega_p}{\omega_L - \omega_p} \right) \right)^{1/2} \frac{v_0}{c^2} \quad (10.34)$$

The growth rate is maximum

$$\gamma = 3^{1/2} \omega_L v_0 / 2c \text{ at } \omega_p = 0.5\omega_L \quad (10.35)$$

Thus the SRS is localized near the quarter critical surface. Two-plasmon decay and the SRS compete in this region. Although the threshold of the two-plasmon decay is lower when the electron temperature is low, the SRS will dominate if the electron temperature is higher than 10 keV, since the electron plasma waves of the two-plasmon decay will be highly damped modes. The threshold of the SRS is

$$\gamma^2 > \nu_e \nu_s \text{ (collisional)} \quad (10.36)$$

or

$$\left(\frac{v_0}{c}\right)^2 > \frac{2c}{\omega L} \text{ (non-uniformity)} \quad (10.37)$$

By particle in cell (PIC) simulation, the electron energy spectrum in the SRS is typically as shown in Fig. 10.11.

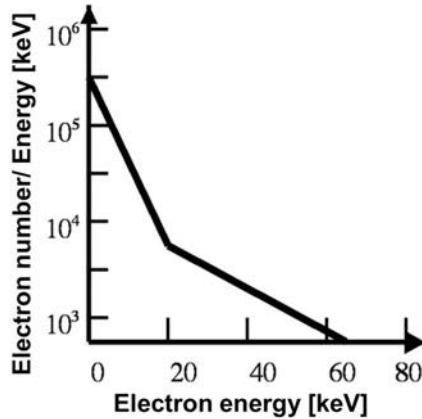


FIG. 10.11. Hot electron spectrum of a PIC simulation [10.45].

#### 10.6.3.6. Stimulated Brillouin scattering

In the underdense plasma, the incident laser is also scattered by the density fluctuations associated with ion acoustic waves. Thus, the incident laser decays into a scattered electromagnetic wave ( $\omega_s, k_s$ ) and an ion acoustic wave ( $\omega_i, k_i$ ). The frequency and wavenumber matching conditions for resonant decay are as follows [10.57, 10.58]:

$$\omega_L = \omega_s + \omega_i \quad (10.38)$$

and

$$k_L = k_s + k_i \quad (10.39)$$

The growth rate is  $\gamma = (1/8)^{1/2} (k_L v_0 \omega_{pi} / (\omega_L k_L c_s)^{1/2})$  (where  $\omega_{pi}$  is the ion plasma frequency) when the scattering is backwards and

$$\gamma < \omega_{pi}, \text{ namely, } \left(\frac{v_0}{c}\right)^2 < \frac{8v_e}{c} \left(\frac{Zm}{M}\right)^{1/2} \sim 0.01 \tag{10.40}$$

which corresponds to  $I\lambda^2 \sim 10^{16} \lambda^2 [\text{W}\cdot\text{cm}^{-2}]$ , where  $I$  is the laser intensity. The threshold of the instability is  $(v_0 / v_e)^2 > 8 / k_L L$ , for a non-uniform plasma. When  $I\lambda^2 \sim 10^{14} \lambda^2 [\text{W}\cdot\text{cm}^{-2}]$ , the threshold scale length is  $k_L L > 10\,000$ , which is not the case for the directly driven ablation plasmas.

10.6.3.7. Filamentation instability: self-focusing

Filamentation instability is laser intensity modulation due to the modulation of the plasma refractive index which is induced by the density fluctuation. The mechanism of this instability is illustrated in Fig. 10.12 [10.53, 10.59, 10.60]. This instability plays an important role in uniform laser irradiation in both indirect and direct drive implosion.

The growth rate of the instability is given by

$$\gamma / \omega_L = \frac{n}{8n_c} \left(\frac{v_0}{v_e}\right)^2 \text{ for the modulation wavenumber } \frac{k}{k_D} = \frac{v_0}{2c} \tag{10.41}$$

Therefore, for moderate intensity, the filament size  $1/k$  is relatively large and may be stabilized by the plasma non-uniformity,  $L \ll c/\gamma$ , a random phase plate (RPP) [10.61] and other smoothing techniques [10.62].

As shown in Fig. 10.12, the laser intensity is modulated transversely by the plasma density modulation due to the laser ponderomotive force. This instability leads to irradiation uniformity in laser fusion.

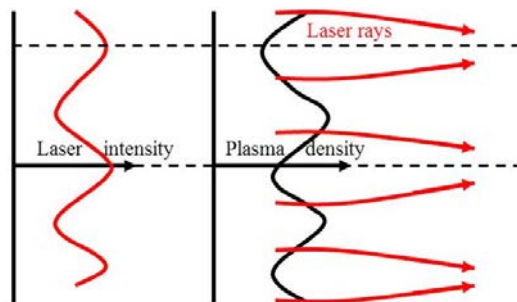


FIG. 10.12. Mechanism of filamentation instability in plasmas. The red arrows indicate the laser propagation direction (rays); the red curve indicates laser intensity modulation and the black curve indicates modulation of the plasma density. Black arrows are the axis for laser intensity and plasma density.

## 10.7. ABLATION PRESSURE AND DIRECT DRIVE IMPLOSION HYDRODYNAMICS

As shown in Fig. 10.6, hot dense plasmas are produced by the absorbed laser energy to drive the implosion of the fuel capsule. The critical issues of the ablative acceleration of the spherical shell are:

- Ablation pressure;
- Hydrodynamic efficiency;
- Preheating;
- Uniformity.

In this section, these four issues are described.

### 10.7.1. Ablation pressure

When a low- $Z$  material of the pellet surface of Fig. 10.6 is irradiated by laser beams, the absorbed laser energy is transported from the cut-off region to the ablation front mainly by electron heat conduction to ablate the fuel shell. Initially, the heat wave propagation velocity is supersonic. However, after a short time of less than a nanosecond, the heat wave velocity becomes lower than the sonic velocity and ablative acceleration starts. In quasi-stationary ablation, the ablative plasma expands with the plasma sound velocity at the cut-off density. When the plasma pressure is  $p_a$  at the ablation front and the plasma is stationary between the ablation front and the cut-off surface, pressure balance requires that

$$p_a = \rho_c (c_s^2 + v_c^2) \quad (10.42)$$

where  $\rho_c$ ,  $c_s$  and  $v_c$  are the mass density, sound velocity and plasma expansion velocity on the cut-off surface, respectively. Since the cut-off surface is approximately the sonic point,  $v_c \sim c_s$ , then

$$p_a = 2\rho_c c_s^2 \quad (10.43)$$

From energy conservation, the total ablated plasma energy is equal to the absorbed laser energy. Therefore, we obtain for ideal EOS:

$$\eta_{abs} I_L = \left( \frac{3}{2} \rho_c c_s^2 + \frac{1}{2} \rho_c v_c^2 \right) v_c + 2\rho_c c_s^2 v_c \sim 4\rho_c c_s^2 v_c \sim 4 \frac{c_s dM}{dt} \quad (10.44)$$

where the first term on the right hand side is the convection loss and the last term is the  $p.dV$  work;  $M$  stands for the areal mass density of the planer plasma. Since  $v_e = c_s$ , the plasma flow velocity is  $v_e \sim c_s \sim (\eta_{abs} I_L / 4\rho_c)^{1/3}$ . So the ablation pressure is given as follows:

$$P_a = 2\rho_c^{1/3} \left( \frac{\eta_{abs} I_L}{4} \right)^{2/3} \quad (10.45)$$

This formula shows that the ablation pressure is higher for a short wavelength laser because  $\rho_c$  is proportional to  $1/\lambda^2$  and the classical absorption of  $\eta_a$  decreases with laser wavelength. The scaling law of the ablation pressure on laser intensity and laser wavelength has been widely investigated by experiment as shown in Fig. 10.13.

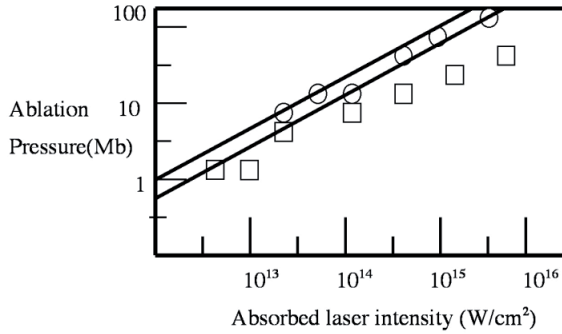


FIG. 10.13. Ablation pressure as a function of absorbed laser intensity: squares — Rutherford ( $\lambda = 1.06 \mu\text{m}$ ); circles — Rutherford ( $\lambda = 0.53 \mu\text{m}$ ) [10.63].

The mass ablation rate  $-dM/dt$ , which is the ablated mass per unit area, was also measured by the ion charge collector and compared with the scaling law

$$-\frac{dM}{dt} = \rho_c \left( \frac{\eta_{abs} I_L}{4\rho_c} \right)^{1/3} \quad (10.46)$$

as shown in Fig. 10.14.

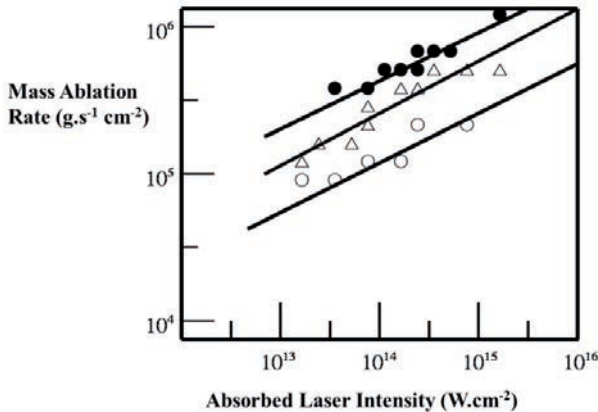


FIG. 10.14. Ablation pressure and mass ablation rate. Experimental data are symbolically marked after Ref. [10.63]. Solid circles, open triangles and open circles are for laser wavelengths of  $0.35 \mu\text{m}$ ,  $0.53 \mu\text{m}$  and  $1.06 \mu\text{m}$ . Reprinted from Ref. [10.63]. Copyright (2011), American IOP Publishing Ltd.

### 10.7.2. Rocket model and hydrodynamic efficiency

Let assume that a shell of area density  $M(t)$  is accelerated by the ablation pressure  $p_a$ , as shown in Fig. 10.6. When the accelerated shell velocity at time  $t$  is  $v(t)$ , the equation of motion, the so-called rocket equation, is as follows:

$$M(t) \frac{dv(t)}{dt} = p_a \quad (10.47)$$

Here  $M(t) = M_0 + \int_0^t (dM/dt) dt$ , where  $M_0$  is the initial area mass of the accelerated shell and  $dM/dt$  is the mass ablation rate, and

$$p_a = -c_{ex} \frac{dM(t)}{dt} \quad (10.48)$$

for an exhaust velocity  $c_{ex}$ . When  $c_{ex}$  is constant, Eq. (10.47) can be integrated to obtain

$$v(t) = c_{ex} \ln \frac{M_0}{M(t)} \quad (10.49)$$

The hydrodynamic efficiency  $\eta_h$  is the ratio of the kinetic energy of the accelerated shell to the absorbed laser energy. With

$$\eta_{abs} I_L = -\frac{1}{2} c_{ex}^2 \frac{dM}{dt} \quad (10.50)$$

$\eta_h$  is given as follows:

$$\eta_h = \frac{1}{2} M(t) \frac{v(t)^2}{\int_0^t \eta_{abs} I_L dt} = \psi \frac{(\ln \psi)^2}{1 - \psi} \quad (10.51)$$

where  $\psi$  denotes  $M(t)/M_0$ . The hydrodynamic efficiency is a maximum at about  $\psi \sim 1/3$  and  $\eta_h \sim 0.7$ . This efficiency is for the ‘‘ideal rocket model’’, where the exhaust is assumed cold. In reality, the exhaust, the ablated plasma, is hot and thermal energy is lost. Actually

$$\eta_{abs} I_L = -2c_{ex}^2 \frac{dM}{dt} \quad (10.52)$$

instead of Eq. (10.50). Therefore, the hydrodynamic efficiency is about 0.2 at maximum. Because of the other effects, such as irradiation non-uniformity, hot electron effects and so on,  $M(t)/M_0$  is designed to be greater than 0.5, so the expected hydrodynamic efficiency is usually assumed to be 0.1.

### 10.7.3. Implosion non-uniformity and stability

In direct drive implosion by laser, the most serious physical issue is the stability of the implosion [10.64]. Instability grows from the initial perturbation on the target and the non-uniformity of the laser irradiation and leads to breakup

of the shell and quenching of the hot spark at the centre as shown schematically in Fig. 10.15.

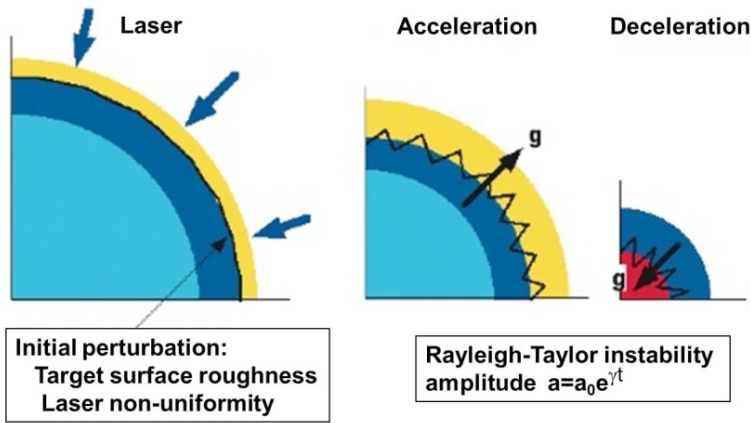


FIG. 10.15. During the implosion, the pellet shell is perturbed and the perturbations grow due to Richtmyer–Meshkov instability and Rayleigh–Taylor instability. The yellow and blue areas are the ablated plasmas and compressing fuel shell. The red area is the hot spark [10.28]. Reproduced from Ref. [10.65].

Concerning the stability of implosion, the experimental data on various parameters of the compressed core have been compared with a 1-D simulation. Typical examples are shown in Fig. 10.16 [10.27, 10.29, 10.66], where the areal densities agree with the 1-D prediction up to a convergence ratio (CR: initial target radius divided by the final radius) of about 30, when the irradiation uniformity is improved by using an RPP [10.61]. The neutron yield, however, decreased faster as CR increased, as shown in Fig. 10.16(b), and about  $10^{-3}$  of the 1-D calculations at CR = 30, where high density compression was achieved. The estimated radius of the hot spark with the simulations at the same CR was calculated to be about  $5 \mu\text{m}$  (hot spark CR  $\sim 50$ ). A possible explanation for the discrepancy in the yield would be that the remaining irradiation and target non-uniformities might cause a collapse of the hot spark, from where most of the neutrons are generated in the 1-D simulation.

Recently, significant progress in direct drive implosions has been demonstrated at LLE [10.67]. The LLE experiments shown in Fig. 10.16(b) were conducted on the OMEGA 60-beam, 30 kJ, UV laser system. The improvements in irradiation uniformity have significantly improved the implosion performance. A single-beam non-uniformity of 3% (averaged over 300 ps within the laser pulse) was achieved with full implementation of 1 THz bandwidth 2-D smoothing by spectral dispersion (SSD) [10.68] and polarization smoothing with birefringence wedges [10.69]. This corresponds to an on-target non-uniformity of less than 1% rms due to beam overlap.

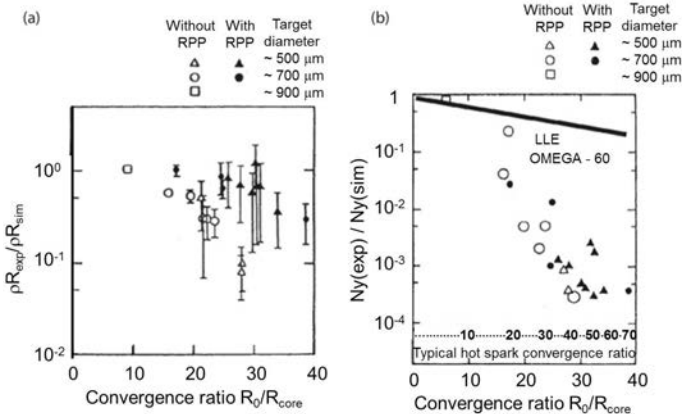


FIG. 10.16. Area density (a) and neutron yield (b) normalized by 1-D implosion simulation results [10.27]. In (b), the thick line indicates data from the 60-beam OMEGA laser at LLE, Rochester, and the typical hot spark convergence ratio is indicated on the horizontal axis. Reprinted from Ref. [10.27]. Copyright (2011), IOP Publishing Ltd.

With these conditions, moderate CR targets ( $\sim 15$ ) produce  $\sim 30\%$  of the neutron yield predicted by 1-D simulation and nearly 100% of the predicted fuel and shell areal densities. As predicted for CR values close to 40, the primary neutron yield is  $\sim 20\%$  of the 1-D prediction. These results are also plotted in Fig. 10.16(b). The remarkable progress of implosion performance shows the validation of indirect drive inertial fusion heading towards high gain laser IFE for power plants. It is also reasonable to be increasingly confident about achieving ignition, burning and energy gain at the reactor scale, because the size of the hot spark and surrounding cold fuel becomes larger with higher laser energy. The thickness of the mixed region and the loss of the hot spark region will become less serious and once ignition occurs at the centre, all the fuel will be burned to produce fusion energy. Recent simulations of high gain implosion include the mixing effect due to Rayleigh–Taylor (R–T) instability. The effect is included in predicting the gain curve in Fig. 10.4.

There are still several stabilizing schemes for implosion that can be expected to be effective in achieving a high gain with a mitigated requirement for target fabrication and irradiation uniformity. They can be categorized as:

- (a) Shock preheating of the shell with a tailored pulse such as a picket-fence pre-pulse or a sharp rise front edge before the main pulse for compression [10.70];
- (b) Radiation preheating with a high  $Z$  doped foam coat or high  $Z$  thin layer coat on the fuel pellet [10.71–10.73];
- (c) Multicolour irradiation [10.74] using non-local heat transport by hot electrons.

The physical processes of implosion related to the stability issue are illustrated schematically in Fig. 10.5. Due to laser intensity non-uniformity, the target surface is non-uniformly ablated. At the initial phase of the implosion, the separation of the absorption region (cut-off region) from the ablation front on the solid target is short. Therefore, the initial non-uniformity of the laser irradiation can be strongly imprinted on the target surface (initial imprint). The shock wave driven by the main pulse can excite the Richtmeyer–Meshkov (R–M) instability, being coupled with the original target roughness and the initial imprint. The non-uniformity of the ablation pressure is relaxed from the laser non-uniformity at later times due to thermal smoothing during the energy transport from the absorption region to the ablation surface. In the main pulse acceleration phase, the R–T instability grows. However, shorter wavelength perturbations are stabilized owing to the ablation stabilization [10.75]. If the in-flight aspect ratio is too large, the accelerated shell breaks easily (shell breakup). Even when the inward acceleration is sufficiently symmetric, mixing of the hot spark and main cold fuel will take place due to an explosive growth of R–T instability in the stagnation phase. In such a situation, the spark is cooled down and no fusion ignition will take place. In general, the R–T instability is not generated as a single mode, but many modes grow simultaneously, finally inducing turbulent mixing. The growth rate of the mixing layer thickness would be smaller than the linear growth rate due to the non-linear saturation and the mode-mode coupling in the non-linear phase. If one can manage to keep a spherically symmetric implosion, fire polishing by  $\alpha$  particle heating can smooth the burning wave even with some level of non-uniform structure in the main fuel. Such elementary processes mentioned above as initial imprint, R–M instability, thermal smoothing, non-linear saturation and turbulent mixing have been independently and separately investigated with adequately modelled experiments on planar targets of various structures and laser irradiation conditions.

#### 10.7.4. Implosion instabilities

The key that governs the stability of the direct drive implosion was identified as being R–T instability, which leads to the non-uniformity requirement of laser irradiation and the fuel pellet. The growth rate of the R–T instability at the ablation front [10.34, 10.75, 10.76] is given by

$$\gamma = \alpha \left( \frac{k \cdot g}{(1 + k \cdot L)^{1/2}} \right) - \beta \cdot k \cdot v_a \quad (10.53)$$

where  $k$  is the wavenumber of the growing mode,  $g$  is the acceleration,  $v_a$  is the ablation velocity and  $L$  is the density scale length at the ablation front. Empirical values of  $\alpha = 0.9$  and  $\beta = 3\text{--}4$  are given from comparison of numerical and

experimental results for direct drive implosions. The concepts of stabilizing implosions aim to enlarge the characteristic scale length,  $L$ , and to increase the ablation velocity  $v_a$ , with the reduced density  $\rho_a$ , keeping the ablation pressure,  $\rho_a v_a^2$ , constant. They are: (a) shock preheating, (b) radiation energy transport and (c) non-local heat transport by hot electrons, as previously mentioned. The gain estimations of recent numerical simulations for direct drive implosions include consideration of these physical processes involved in the instability and stabilizing mechanisms. Together with progress in fuel pellet fabrication and laser control technology, it can be reasonably expected that fusion ignition, burn and energy gain can be demonstrated by direct drive implosions with multi-beam MJ lasers if the beams are properly arranged for direct drive.

## 10.8. FAST IGNITION: PRESENT STATUS AND FUTURE PROSPECTS

### 10.8.1. Why fast ignition?

Fast ignition is the new scheme for igniting compressed fuel plasmas by using an ultra-intense laser pulse, called a petawatt laser [10.24]. E.R. Harrison [10.77], C. Maisonnier [10.78], T. Yamanaka [10.22] and N. Basov's group [10.23] proposed this independently before the proposal by M. Tabak. Fast ignition became realistic after the breakthrough of high power laser technology by G. Mourou et al. [10.79]. This scheme has potential advantages over central hot-spark ignition since the compression and the ignition can be separated. As shown in Fig. 10.2, the fuel  $\rho R$  can be significantly higher in fast ignition than in central hot spark ignition for the same implosion laser energy because of the lack of a central low density hot region (hot spark). When the plasma is assumed isobaric, the hot spark density is 10 times lower than the main fuel density. Therefore, the radius of a hot spark of  $\rho R_h \approx 0.4 \text{ g}\cdot\text{cm}^{-2}$  is two times larger than the high gain fuel radius, where  $\rho R > 2 \text{ g}\cdot\text{cm}^{-2}$ . This means that the total mass of the fast ignition, high gain core is about ten times smaller than that of the central ignition core. In other words, the required implosion laser energy can be ten times smaller in the fast ignition case. So the fast ignition fusion reactor can be small and allows the freedom of choosing the output power and driver efficiency. Although short pulse laser plasma interactions have been widely investigated, imploded plasma heating mechanisms are still an open question. Several heating schemes have been proposed, using highly energetic particles such as electrons [10.80–10.85], protons [10.86] and macroparticles [10.77, 10.78].

In contrast with the above mentioned schemes using electrons and ions, different ideas for fast ignition using plasma momentum have been proposed by other authors [10.87–10.89]. A new ignition scheme, impact ignition [10.90, 10.91], has also been proposed. The target is composed of two portions, a spherical pellet made of a D-T shell coated with an ablator and a hollow conical

target which is stuck to the spherical pellet. The conical component has a fragmental spherical shell (the impactor) also made of D-T and an ablator which is accelerated to a very high velocity to heat the imploded shell.

In this section, fast ignition conditions are reviewed: the requirements of the heating laser and the present status of experimental and theoretical research on heating.

### 10.8.2. Ignition conditions

As shown in Fig. 10.17, when a fuel pellet is compressed by laser implosion, the core plasma is surrounded by a large scale coronal plasma. In order to inject a short pulse laser into the core, the laser pulse should penetrate into an overdense region by hole boring or cone laser guiding. When the ultra-intense laser energy reaches near the core, the laser energy is converted into high energy electrons or ions that carry the energy and heat the core plasma. The required short pulse energy for ignition depends upon the heating spot diameter, the heating depth, the transport and absorption efficiencies, the electron and ion energy spectra and so on. The fast ignition hot spark is isochoric between the spark and main fuel and off-centre. First of all, we will compare the ignition condition for an isochoric spark with that for an isobaric spark. One-dimensional burning plasma simulations are carried out to determine the ignition boundaries in  $\rho R$  and temperature  $T$  space, of which the hot spark geometry is shown in Fig. 10.17(a) [10.92].

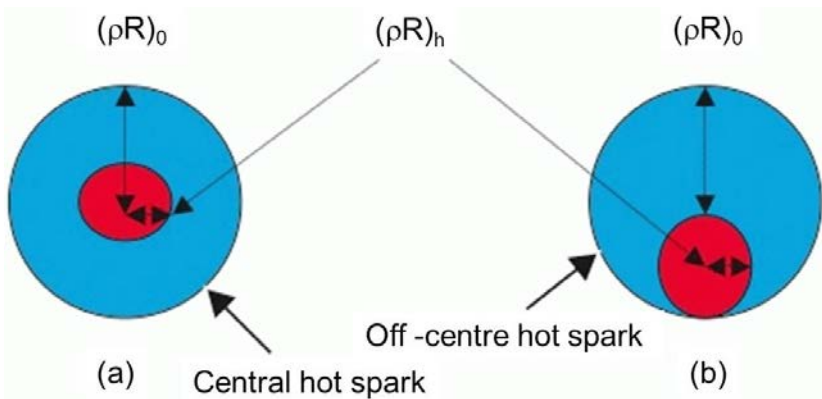


FIG. 10.17. Assumed geometry of central isochoric hot spark (a) and off-centre spark (b) for fast ignition [10.92].

Figure 10.18 shows that the ignition boundary for an isochoric hot spark is higher with respect to  $\rho_h R_h$  than that for an isobaric hot spark since the main fuel layer acts as a tamper layer to suppress the expansion of the hot spark. Fast

ignition is relevant to the isochoric hot spark case. In this case, the approximated ignition condition is given as

$$T(\rho_h R_h)^3 = 1.0 \quad (10.54)$$

where  $\rho R$  and  $T$  are in units of  $\text{g}\cdot\text{cm}^{-2}$  and keV, respectively, and the above numerical factor on the right-hand side of Eq. (10.54) is valid for temperatures around 10 keV. Since the hot spark energy is given by

$$W_h [\text{GJ}] = 10.6(\rho_h R_h)^3 T \left( \frac{\rho}{\rho_0} \right)^{-2} \quad (10.55)$$

for the solid density  $\rho_0$  and the hot spark density  $\rho$ , the required spark energy from Eqs (53) and (54) is approximately given by

$$W_h [\text{kJ}] = 40 \left( \frac{\rho}{100} [\text{g}\cdot\text{cm}^{-3}] \right)^{-2} \quad (10.56)$$

when  $T$  is 10 keV. For an off-centre isochoric hot spark, 2-D burning simulations have been carried out for the initial geometry of Fig. 10.17(b) [10.92]. As indicated by the triangles in Fig. 10.18, the ignition condition is the same as that for the central isochoric spark in Fig. 10.17(a).

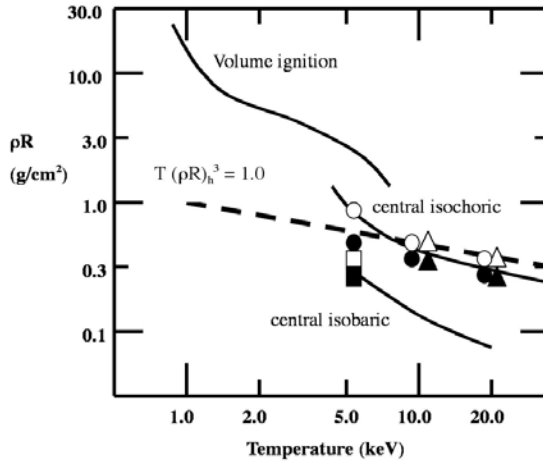


FIG. 10.18. Ignition conditions for: (a) volume ignition (top, solid line); (b) central isobaric spark (open and solid squares); (c) central isochoric spark (open and solid triangles) and off-centre round isochoric spark (open and solid circles);  $T(\rho R)_h^3 = 1.0$  is the dotted line [10.92].

However, the cylindrical heat deposition geometry and finite heating time effects change the ignition condition significantly; the hot spark is produced at the edge of the main fuel by relativistic electron heating. The heated area radius and depth are  $r_b$  and  $d$ , respectively, and the fuel density and radius are  $\rho$  and  $R$

as shown in Fig. 10.19. Note here that the stopping range of the intense electron beam ( $d$ ) is shorter than the “thin” electron beam as discussed in Ref. [10.93]. Thus when the mean distance between beam electrons is shorter than the Debye shielding distance of the plasma, the collective interactions between beam electrons and the plasma become important and enhance the stopping power. Furthermore, the self-generated magnetic field may play an important role in the heat deposition of the intense relativistic electron beam. Since the magnetic field effects on the heat deposition processes have not yet been clarified, the following discussions include only the shortening of the stopping range [10.93].

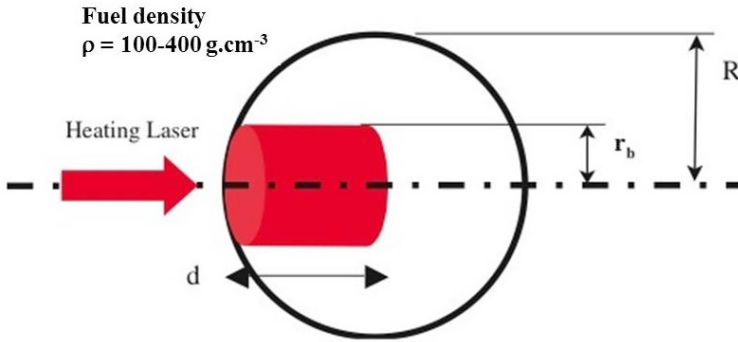


FIG. 10.19. Geometry of 2-D simulation of fast ignition. The heating relativistic electron pulse is injected from the left,  $d$  is the stopping range (depth of heated area), and  $r_b$  is the heated area radius [10.81].

In the geometry of Fig. 10.19, the ignition conditions have been investigated with 2-D burning simulations in Ref. [10.81]. The off-centre ignition burning process is shown in Fig. 10.20 [10.94], where the temperature and density contours of the burning wave are illustrated. Once the ignition condition is met, the burning fraction is more or less the same as the central ignition.

With the heating parameter survey of 2-D simulations, the ignition conditions for the heating energy, power and radius, the energy deposition range and the fuel density have been explored in many papers. According to the comprehensive work in Ref. [10.81], the optimized ignition conditions are given by the following relations:

$$W_h \text{ [kJ]} = 140\rho_{100}^{1.85} \quad (10.57)$$

$$P_h \text{ [PW]} = 12.6\rho_{100}^{1.85} \quad (10.58)$$

$$I_h \text{ [W}\cdot\text{cm}^{-2}] = 2.4 \times 10^{19} \rho_{100}^{0.95} \quad (10.59)$$

$$r_b \text{ [\mu m]} = 60\rho_{100}^{0.975} \quad (10.60)$$

where  $r_b$  is the heating beam radius,  $P_h$  is the heating power,  $I_h$  is the heating energy flux density,  $\rho_{100}$  represents  $\rho[\text{g}\cdot\text{cm}^{-3}]/100$ , and the beam stopping range,  $\rho d$ , is assumed to be  $0.6 \text{ g}\cdot\text{cm}^{-2}$ . Note that the required energy for ignition in Eq. (10.57) is three times higher than that of Eq. (10.56). This is due to the difference of hot spark size, which depends on the electron stopping range and the heating geometry. However, the fuel density dependence of the ignition energy is essentially the same in both cases. In the actual ignition, the beam radius  $r_b$  and the range  $\rho d$  depend upon the PW laser–plasma interaction physics; and  $r_b$  depends upon the laser propagation, the electron heat transport and the heat deposition process. The stopping range  $\rho d$  depends on the plasma resistivity and the collision processes of the relativistic electrons. The experimental and theoretical works related to those issues are reviewed in the following subsection.

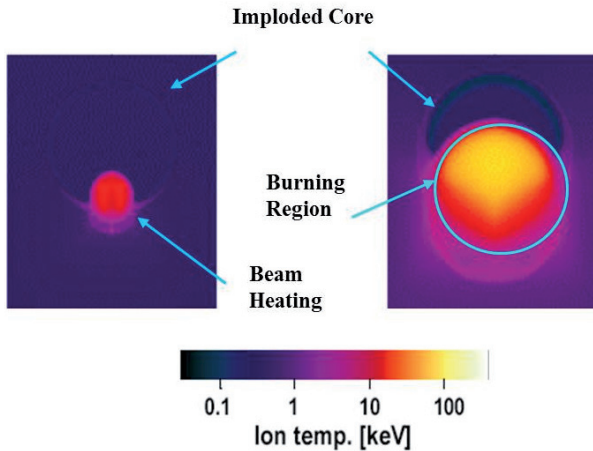


FIG. 10.20. Burning simulation of fast ignition core plasma [10.94].

As shown in Eqs (10.57)–(10.60), the optimum compressed plasma density decreases with the increase of hot spark radius and the heating laser energy and the pulse width  $\tau_p$  increase as  $\rho_{100} = (r_b / 60 \mu\text{m})^{-1.025}$ ,  $\tau_p = 55 \rho_{100}^{-0.85}$  [ps],  $W_h = 140 (r_b / 60 \mu\text{m})^{1.9}$  [kJ]. For example, when  $r_b = 10 \mu\text{m}$ ,  $\tau_p = 10$  ps,  $W_h = 4$  kJ and  $\rho = 600 \text{ g}\cdot\text{cm}^{-3}$ , which is 3000 times the solid density of D-T. This means that a 10–20 kJ heating pulse ignites the core plasma. Those conditions may be violated because an MeV electron beam generated by the laser spreads wider than a  $10 \mu\text{m}$  radius and/or the compressed density is not as high as 3000 times the solid density. According to experiments at Osaka, LLNL [10.95] and elsewhere,  $r_b$  could be  $30 \mu\text{m}$  and the required laser energy will be higher than 70 kJ. So the heating spot size and coupling efficiency of the short pulse laser energy to the core plasma are the most important critical issues in fast ignition research. The heating beam pulse energy, power and intensity are shown

for various fuel densities in Fig. 10.21. From this figure, the required laser pulse energy and power can be roughly predicted.

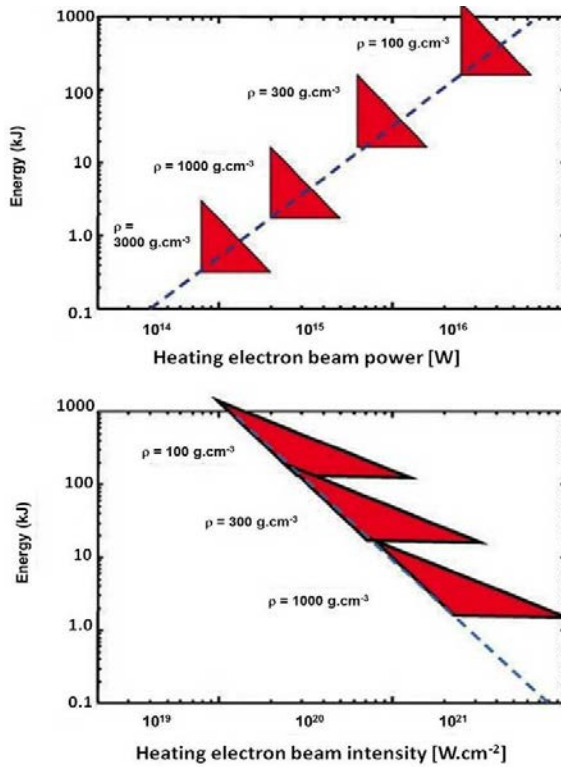


FIG. 10.21. Ignition conditions on beam energy, power and intensity for various fuel densities. The red areas indicate the ignition regions. The blue broken lines are the minimum heating energy and power (upper) and the minimum heating energy and intensity required for ignition. Reproduced from Ref. [10.81].

### 10.8.3. Fast ignition integrated experiments

Significant experimental research has been carried out at Osaka, LLNL (USA), Rutherford (UK) and so on. In particular, this has included relativistic electron generation and imploded plasma heating. In the following, we will discuss the implosion and heating research on fast ignition at ILE, Osaka University.

#### 10.8.3.1. Direct plasma heating

In the case of injection of a heating laser beam into a corona plasma of spherical implosion, the coupling efficiency of a petawatt module (PWM) laser

pulse to a core plasma is sensitive to the focus position of the heating laser, because of the strong laser interaction with the long scale corona plasma [10.96–10.98]. When the focus position is near the critical surface of coronal plasmas, the PWM laser pulse penetrates into the overdense region and the neutron yield is significantly enhanced. However, the neutron energy spectra measured in experiments [10.97] are broad and not isotropic, as shown in Fig. 10.22(a). The width of the spectral peak around 2.45 MeV indicates that the reacting ion energy is of the order of 100 keV. Furthermore, the neutron spectral shape depends upon the direction of the neutron spectrometer, as shown in Fig. 10.22(a). These results can be interpreted in terms of the enhanced fusion reaction around the critical surface. According to PIC simulations, electrons are expelled from laser channels and solitons by strong laser heating and/or ponderomotive force. As a result, ions in the laser-produced bubbles are accelerated by Coulomb explosions to high energy [10.99]. Since the fusion reaction enhancement is dominated by those high energy ions, thermal neutron enhancement was not observed and the effect of core plasma heating was not clear in PWM direct heating [10.100]. However, when the short pulse laser energy increases to the 1 kJ level in the PW laser, the laser pulse penetrates the higher density region since non-linear scattering may be saturated because of the strong plasma heating. Therefore, in PW laser experiments, the thermal neutrons also may increase and core plasma heating may take place also in a cone-less target.

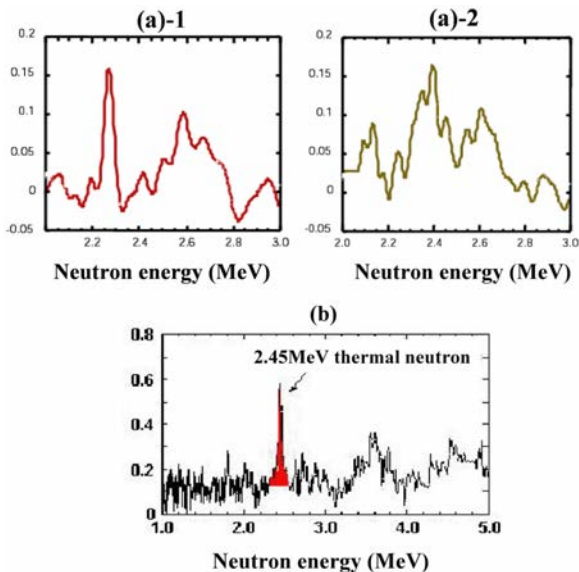


FIG. 10.22. (a) Neutron spectrum for direct heating of imploded CD plastic (deuterated plastic) targets. The vertical axis is the neutron number per unit energy. (a) –1 and –2 are for the different observation directions, which are normal to and along the laser injection direction, respectively. (b) Neutron spectrum for the cone target. Taken from Ref. [10.84].

### 10.8.3.2. Cone-shell target

In a cone guide target, the neutron spectral peak at 2.45 MeV is narrow, as shown in Fig. 10.22(b). The neutron yield in this experiment is of the order of  $10^5$  with 50 J heating laser input, which is 10 times higher than that for non-heating. This indicates that the thermonuclear fusion is enhanced by the temperature increase of the core plasma due to the heating with the PWM laser at ILE. The temperature was estimated from the neutron yield, the observed  $\rho$  and the core plasma radius. In the best shot, the temperature increased by 130 eV. We found from these results that 25% of the input PWM laser pulse energy is transported to the core plasma [10.97].

In the petawatt laser experiment, two kinds of cone targets are imploded and heated. The cone angles are 30 and 60 degrees. The heating efficiency is higher in the 30 degree cone than in the 60 degree cone. When the 300 J/0.6 ps chirped pulse amplification (CPA) laser pulse is injected, the neutron yield reaches  $10^7$ , while the neutron yield was  $10^5$  without heating, as shown in Fig. 10.23 [10.85]. This indicates that the core plasma temperature increased by 500 eV and the energy coupling between heating laser and core plasma is 20–25%. Since the focused laser energy included in the 50  $\mu\text{m}$  diameter is less than 40%, a 20–25% coupling efficiency means that actual coupling is higher than 50%. Otherwise, laser energy in the halo of the spot is collected by the cone guide. In Fig. 10.23, a simple scaling curve is shown, where the temperature increase is assumed to be proportional to the input short pulse laser energy and the coupling efficiency

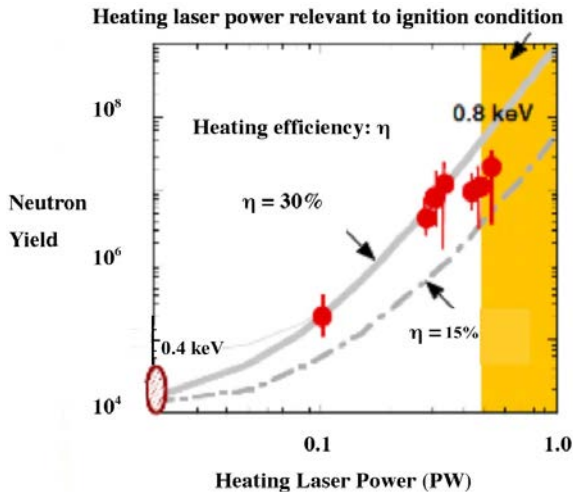


FIG. 10.23. Integrated experiment on implosion and heating of cone target. The neutron yield without heating is shown in the left hand corner. The red circles are the neutron yields with heating. A solid curve and the dash-dot curve represent simulation predictions for 30% and 15% coupling efficiency [10.84, 10.85].

is assumed to be the same as that of the cone guide PWM experimental results. This indicates that the coupling efficiency for the 300 J case is almost the same as for an 80 J case. This scaling law has been used for planning the Fast Ignition Realization Experiment (FIREX) project. Further analysis of the experiments has been done by developing an integrated code FI3 (Fast Ignition Integrated Interconnected Simulation Code), which consists of codes describing implosion, heating and fusion reaction. The FI3 code includes the radiation hydrodynamic code, the Fokker–Planck code and the PIC simulation code. It is found that the ion temperature of the experiment is sensitive to the X ray radiation heating of the cone, the cone angle and the pre-plasma. When a reasonable pre-plasma scale and transverse profile of the relativistic electron beam are assumed, the FI3 simulation could explain the experimental results. However, for predicting the neutron yield of future experiments with a higher heating laser energy, further improvements of the simulation modelling are necessary.

#### **10.8.4. Fast ignition simulation**

##### *10.8.4.1. Integrated simulation*

Since the fast ignition is two steps — implosion and heating — and the kinetic effects are important in the heating process, the integrated simulation has to describe hydrodynamics on a long time scale and the laser–plasma interactions on a short time scale. Integrated simulations have been carried out by two approaches which are hybrid simulation codes like LSP [10.101] and EU group [10.102], and an interconnected simulation system like the FI3 code [10.103]. Recently, a very aggressive proposal was made in Ref. [10.104], which is an integrated simulation by a collisional PIC code. In this section, the FI3 code simulation is described. As shown in Fig. 10.24, the FI3 code connects three different codes by exchange of the simulation input and output data through a proto-call. The overall implosion hydrodynamics is simulated by a 2-D radiation hydrodynamic code, which includes laser absorption, atomic processes, electron and radiation heat transport, the equation of state and hydrodynamics. The plasma density and temperature profiles at the injection of the short pulse heating laser is given to the PIC code and the Fokker–Planck code for simulating high energy electron generation, transport and plasma heating. The PIC code simulates the relativistic laser–plasma interactions, which include laser hole boring, filamentation, the generation of high energy electrons in target surface plasmas and the quasi-static electric field and magnetic field generation associated with intense high energy electron beams, the high energy ion acceleration and so on. Some results of PIC simulations of fast ignition will be discussed later.

The momentum distribution of the high energy electron beam, which is dependent on space and time and obtained by the PIC simulation is transferred to

the Fokker–Planck simulation code coupled with the burning plasma simulation code, of which initial conditions are provided by the implosion radiation-hydro-simulation. The Fokker–Planck and burning plasma simulation code [10.105] includes space-time evolutions of the electric field and magnetic field induced by the high energy electron beam propagation, the return current dynamics, collisional energy deposition of the electron beam into high density plasmas, and fusion reaction and ignition processes.

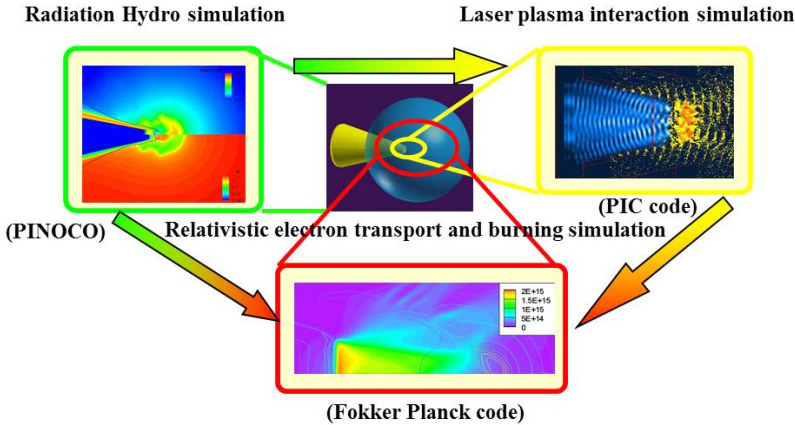


FIG. 10.24. Structure of Fast Ignition Integrated Interconnected Simulation (FI3) code. From left to right at the top of the figure, hydro simulation, target geometry, and electron energy density distribution of PIC simulation are shown. At the bottom, the electron energy density in a high density region obtained by the Fokker–Planck simulation is shown. Taken from Refs [10.105, 10.106].

#### 10.8.4.2. Radiation hydrodynamic simulation

The radiation hydro simulation code is called PINOCO [10.106], which is the ALE (arbitrary Lagrange Eulerian) code based upon the CIP scheme [10.107]. An example of the simulation of a cone-shell target is shown in Fig. 10.25, where the initial geometry of the cone shell simulation is described in part (a). It is found that the implosion of the fuel capsule of the cone-shell target is significantly different from the spherical fuel capsule as shown in Fig. 10.25 [10.106].

Thus, no strong spherical reflection shock wave is generated. So a hot spark (in other words a high isentropic region) is not generated at the target centre. It is also found by comparing Figs 10.25(b) and (c) that the imploding fuel shell interacts with the plasma on the radiatively ablated gold cone surface and the compression is degraded when the gold cone surface is not coated with plastic. In Fig. 10.25(d), the time dependence of area mass density of the compressed deuterium plasma is shown. The broken and solid lines are for with and without

## INERTIAL FUSION ENERGY

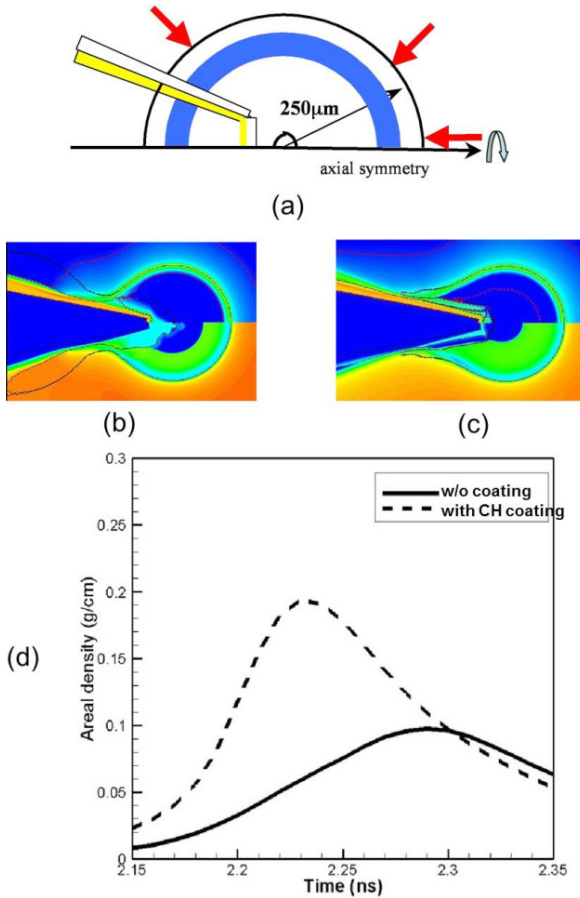


FIG. 10.25. Radiation hydro simulations of the cone-shell target. (a) The initial geometry of the 2-D PINOCO simulation (red arrows represent the laser beams); (b) density (top) and temperature contours (bottom) of the cone-shell target without coating of plastic on the outside of the cone; (c) same for the target with coating; (d) time dependent  $\rho R$ . Taken from Ref. [10.108].

plastic coating. The area density with the coating is 1.5 times higher than that without coating.

The PINOCO simulation of the cone target is validated by comparing the X ray images of a simulation (top of Fig. 10.26) with those of the Gekko XII experiment (bottom of Fig. 10.26). The experimental X ray images show that the centre of the imploded plasma moves from the left to the right. The motion of the core plasma agrees qualitatively with the PINOCO simulation. Similar 2-D cone target simulations have also been carried out by the simulation code LASNEX [10.109] and the results were compared with the X ray shadow graph obtained by the OMEGA experiments [10.110].

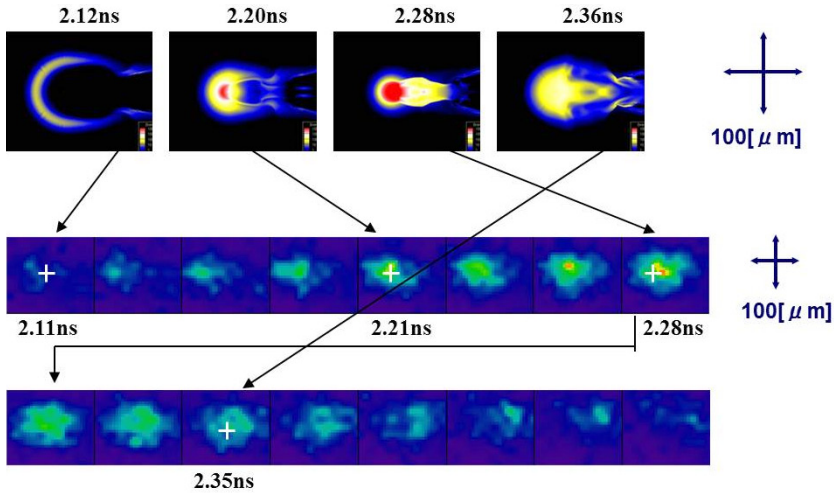


FIG. 10.26. Validation of the PINOCO simulations. X ray images from the simulations (top) are compared with those from the Gekko XII experiment (bottom), indicating the location of the centre of the pellet. 100 [ $\mu\text{m}$ ] on the right hand side indicates the scale of the figures. Taken from Ref. [10.111].

### 10.8.5. Relativistic electron generation, transport and heating physics

Recent 3-D PIC simulation results for the focused ultra-intense laser interaction with a solid plane target show that the relativistic electron current profile in the target is self-organized and confined to a small radius as shown in Fig. 10.27. This indicates that a small hot spark could be generated by relativistic electron heating [10.112].

In the cone target, an ultra-intense laser light is partially reflected on the cone surface wall and focused onto the top of the cone, while the relativistic electrons are generated on the side wall of the cone and on the top wall. Since the electrons are accelerated along the laser propagation direction, a strong current is driven along the cone axis and the relativistic electron flow is pinched to the top of the cone by the magnetic fields as shown in Fig. 10.28.

Electron energy spectra for a plane target and a conical target are compared in Fig. 10.29. This result shows that the electron energy and the number of high energy electrons increase significantly in the conical target. These characterizations of the laser interactions with the cone target contribute to enhancing the coupling efficiency between a short pulse laser and a small core plasma, as was indicated by the enhancement of the neutron yield discussed in the previous section. The PIC simulations have been limited to the small scale and short time durations. Therefore it is necessary for carrying out longer space and timescale simulations to introduce Fokker–Planck and/or hybrid simulations.

INERTIAL FUSION ENERGY

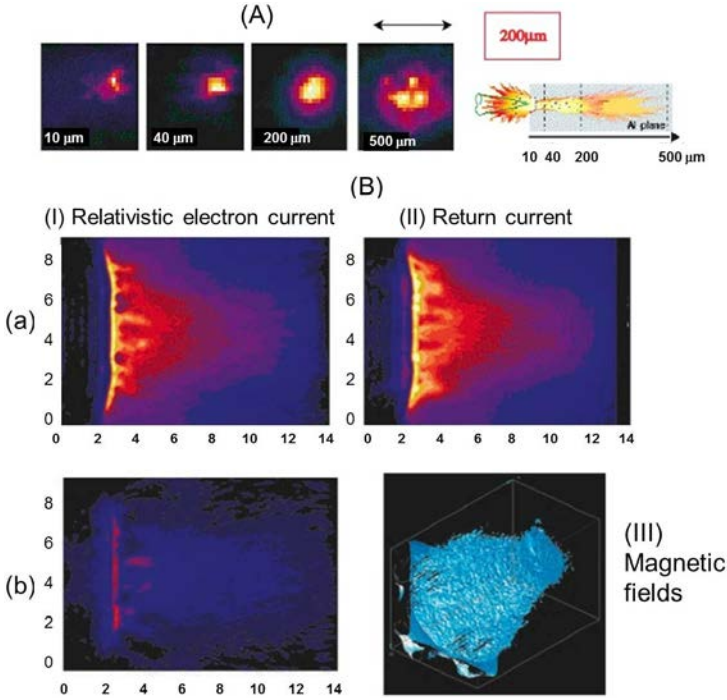


FIG. 10.27. Relativistic electron current self-organization (self-pinch): (A) transport experiment; (B)(I)-(a) current profile of hot electrons with energy lower than 1 MeV; (I)-(b) current profile of hot electrons with energy higher than 1 MeV; (II) return current profile; (III) magnetic field iso-intensity surface. Taken from Refs [10.84, 10.112].

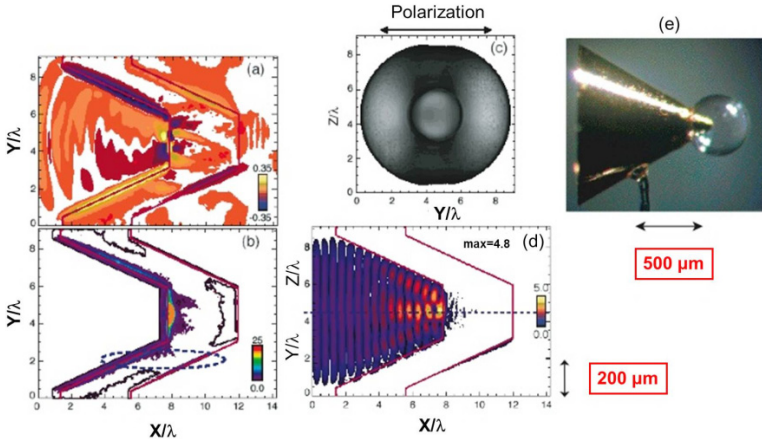


FIG. 10.28. Photograph of a cone shell target (top right) and PIC simulation results for cone-laser interactions; (a) magnetic field structure; (b) electron energy density distributions on the side wall; (c) electron energy density distribution at the top of the cone; (d) laser intensity distribution in the cone. Here,  $X$  is along the cone axis and  $Y$  and  $Z$  are the coordinates of the plane perpendicular to the cone axis. Taken from Ref. [10.114].

In the Fokker–Planck simulation, the electron energy spectrum as in Fig. 10.29 is taken from the PIC simulation. Then, one can calculate the ion temperature of the dense core plasma to compare the ion temperature of the heating experiment [10.85] with that of the simulation [10.105, 10.113].

An enhanced coupling efficiency of the heating laser energy to a small core plasma is essential for achieving ignition with relatively little laser energy. Because of this, the relativistic electron transport and energy deposition in the cone guide target and/or in the corona of the imploded plasma are the most critical issues in the fundamental physics of fast ignition, though extensive experimental and theoretical works have been conducted in an attempt to understand and control dense plasma heating by using an ultra-intense laser.

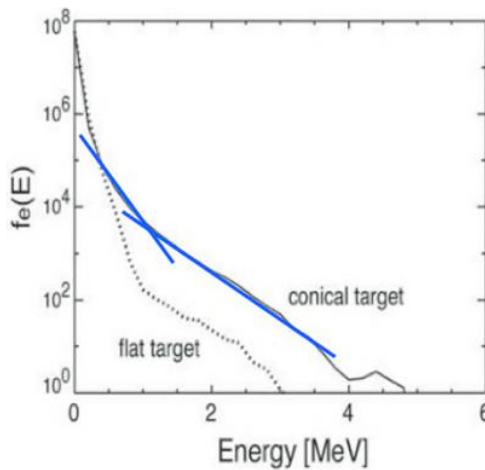


FIG. 10.29. The number of hot electrons for a conical target is enhanced by more than one order of magnitude above that of a flat target.  $f_e(E)$  is the electron energy distribution function. The blue lines indicate that there are multi-acceleration mechanisms of high energy electrons. Taken from Ref. [10.114].

### 10.8.6. Petawatt laser and future Fast Ignition Facility

A PW laser at Osaka University was recently completed; this delivers 500 J/0.5 ps [10.115]. In PW laser experiments, the imploded plasma has been heated up to about 1 keV [10.85]. PW laser target experiments at Osaka University, Rutherford Appleton Laboratory and elsewhere are clarifying the heating scaling law that determines the relations between heating laser energy, hot spark temperature and neutron yield. Using the Fokker–Planck code, cone shell target experiments at Osaka were simulated. When the relativistic electron spectrum of the cone target is assumed to be the double Maxwellian spectrum as shown in Fig. 10.29, the predicted neutron yield correlates with the experimental

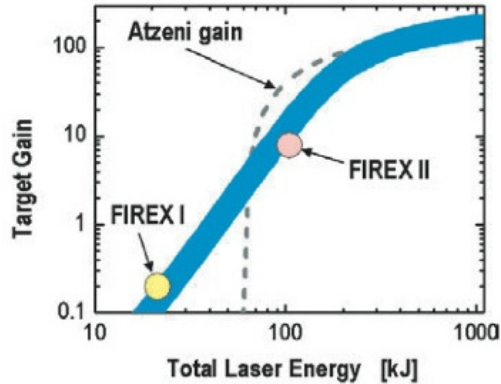


FIG. 10.30. The laser energy scaling law of neutron yields for fast ignition. The broken line is the gain predicted by Refs [10.113, 10.116, 10.117].

results as shown in Fig. 10.23 [10.113]. The results have been extended to the larger laser energy case; the gain for the multi 10 kJ heating pulse is predicted to be as shown in Fig. 10.30. If the coupling efficiency is higher than 30%, the required heating laser energy for the experiment (Fast Ignition Realization Experiment I: FIREX-I) is estimated to be 10 kJ for 1500 times solid density D-T plasmas and 30  $\mu\text{m}$  spot diameter as shown in Fig. 10.30 [10.113, 10.116]. For ignition, the most critical parameter is the hot spot radius,  $r_b$ , which strongly depends upon the relativistic electron transport. According to simulation and fundamental experimental results, the relativistic electron heat flow is well confined by self-generated magnetic fields. In particular, in the cone shell target, the deposited laser energy is concentrated at the top of the cone. Therefore, the hot spark radius could be controlled by the cone top radius and the distance between the cone top and the core plasma. From the present understanding of the heating processes, ignition can be achieved with a pulse energy of less than



FIG. 10.31. (a) 10 kJ/10 ps LFEX laser; (b) 5 kJ/10 ps OMEGA-EP laser. Taken from Ref. [10.118].

50 kJ/10 ps for an imploded plasma  $\rho R$  higher than  $1.0 \text{ g}\cdot\text{cm}^{-2}$ . The second phase of the FIREX project at Osaka University (FIREX-II) is aiming to demonstrate ignition such as shown in Fig. 10.30.

For demonstrating the feasibility of fast ignition, two major high energy short pulse lasers have been completed at Osaka university (Laser for Fast ignition Experiment: LFEX) (see Fig. 10.31(a)) and the University of Rochester (OMEGA-EP) (see Fig. 10.31(b)). The LFEX is coupled with the Gekko XII implosion laser and the OMEGA-EP is coupled with the OMEGA implosion laser.

For the FIREX-I, an advanced target is proposed for achieving better performance. The target design is shown in Fig. 10.32 [10.119]. Here, the double cone, low  $Z$  (plastic) coating of the inner and the outer wall of the cone, and the Br doped ablator are introduced for better high energy electron transport, higher implosion  $\rho R$  (as indicated in Fig. 10.23), low scattering of high energy electrons along the inner cone surface, and stabilization of the R-T instability in the implosion.

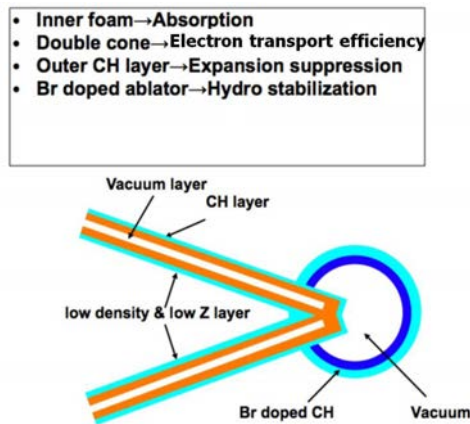


FIG. 10.32. Advanced target design for FIREX-I. Orange layers indicate gold foils. The advantages of this target are listed at the top of the figure. Taken from Ref. [10.119].

The effect of the double cone has been investigated by the 2-D PIC simulation (Fig. 10.33) [10.120, 10.121]. As shown in Fig. 10.33(a), the double cone target has a vacuum layer between the inside cone wall and the corona plasmas. When electrons emitted from the inner cone fill the vacuum, the negative space charge and the negative potential build up to reflect back the high energy electrons and confine them inside the cone as shown in Fig. 10.33(c). Figures 10.33(b) and (d) show the single cone geometry and the energy density of high energy electrons. The electron flux into the cone tip is 1.5 times higher for the double cone (Fig. 10.33(c)) than for the single cone.

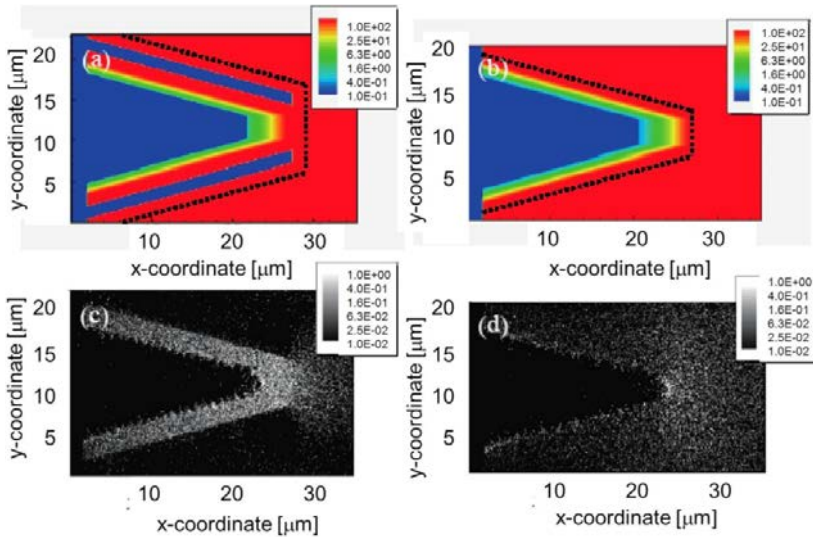


FIG. 10.33. A PIC simulation of the effects of double cone geometry. (a), (c) High energy electron transport. (b), (d) Corresponding single cone simulation. (a), (b) Initial electron density profiles. (c), (d) High energy electron distributions where the density is normalized by the cut-off density. Reprinted from Ref. [10.120]. Copyright (2011), American Institute of Physics.

## 10.9. INDIRECT DRIVE FUSION

### 10.9.1. Concept of indirect drive implosion

Direct drive implosion has a higher coupling efficiency between the input laser energy and the compressed plasma energy, and the numerical calculations indicate lower input energy for ignition and burn. However, numerical simulations using the LASNEX code [10.122] indicated that the direct drive implosion has much higher Rayleigh–Taylor (R–T) instability growth and the laser plasma instabilities produce hot electrons under high intensity irradiation by a  $1 \mu\text{m}$  Nd:glass laser to degrade the quality of the implosion. In the 1980s, those problems were partly solved by using a shorter wavelength laser and various smoothing techniques [10.61, 10.62, 10.68].

On the other hand, the indirect drive has intrinsic advantages in those difficulties. Calculations carried out in 1975 showed that it is possible to achieve high gain with radiation driven indirect targets. The fuel capsules are similar to those for direct drive capsules, except that the ablator material must be properly matched to the driving X ray spectrum in order to ensure that the compression can be kept in a near Fermi degenerate state to generate high ablation pressure and to control the R–T instability.

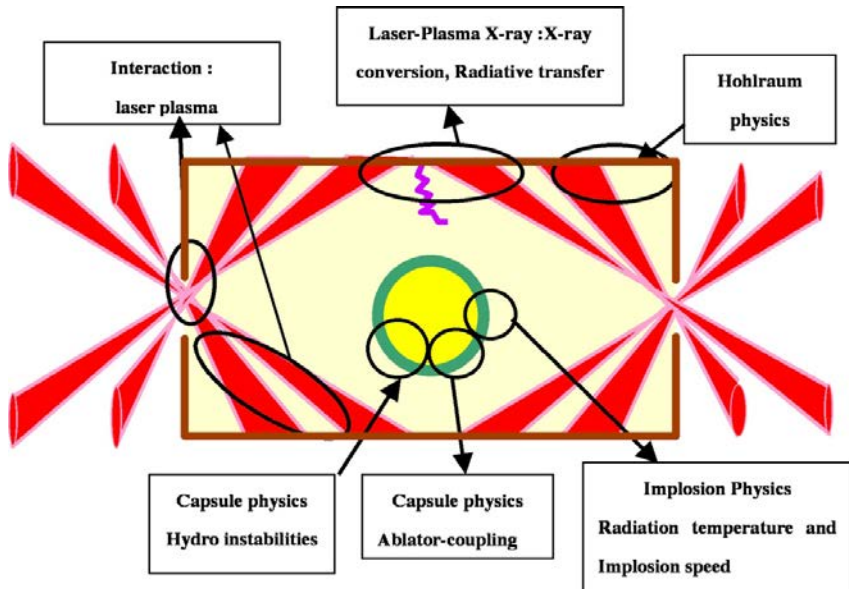


FIG. 10.34. Physics of indirect drive implosion.

In indirect drive implosion, as shown in Fig. 10.34, the injected laser beams are absorbed on the wall inside the cavity and X ray radiation is generated. The cavity is designed to generate X rays efficiently and confine these through the albedo effect, which means that X rays absorbed on the inner cavity surface are re-emitted from hot dense high- $Z$  plasmas. The coupling efficiencies from the input laser energy to the X rays and to implosion kinetic energy are related to the X ray energy loss to the cavity wall. When the X ray heat wave penetrates faster, more laser energy is lost. In order to slow down the heat wave penetration, high opacity materials such as Au are chosen as the cavity wall material. In order to eliminate opacity windows which are related to X ray absorption edges, it is usually necessary to blend materials for the cavity. When the X ray confinement is high, the X ray energy spectrum approaches that of black body radiation. The radiation temperature  $T_r$  is an important parameter for the radiation driven implosion, as discussed later.

As for the laser-plasma interaction in the cavity, non-linear plasma instabilities are an issue, as described in Sections 10.6.2 and 10.6.3. In the cavity, the plasma scale length is longer than that for the corona plasma, and the plasma has low density and high  $Z$ . Stimulated Brillouin scattering and self-focusing and filamentation instabilities have been considered to be difficulties. In order to suppress those instabilities, the cavity is filled with a low- $Z$  gas in which Landau damping of ion acoustic waves is enhanced by light ions.

Radiation driven implosion is similar to direct drive implosion except that the energy deposition process is different. The X ray driven ablation pressure and

mass ablation rate corresponding to those for the direct drive in Eqs (10.45) and (10.46) of Section 10.7.1 are given in Ref. [10.34] as follows:

$$p \text{ [Mbar]} = 3 \left( \frac{T_r}{100 \text{ eV}} \right)^{3.5} = 170 \left( \frac{I_X}{10^{15} \text{ W}\cdot\text{cm}^{-2}} \right)^{7/8} \quad (10.61)$$

and

$$\frac{dm_i}{dt} [\text{g}\cdot\text{cm}^{-2}\cdot\text{s}^{-1}] = 3 \times 10^5 \left( \frac{T_r}{100 \text{ eV}} \right)^3 = 10^7 \left( \frac{I_X}{10^{15} \text{ W}\cdot\text{cm}^{-2}} \right)^{3/4} \quad (10.62)$$

where  $I_X$  is the X ray intensity. From these results with the rocket equation, we get the implosion velocity

$$v_{imp} [\text{cm}\cdot\text{s}^{-1}] = 1.8 \times 10^7 \left( \frac{I_X}{10^{15} \text{ W}\cdot\text{cm}^{-2}} \right)^{1/8} \ln \left( \frac{m_0}{m_0 - \Delta m_0} \right) \quad (10.63)$$

$$v_a [\text{cm}\cdot\text{s}^{-1}] = 6.6 \times 10^5 \beta^{3/5} \left( \frac{I_X}{10^{15} \text{ W}\cdot\text{cm}^{-2}} \right)^{9/40} \quad (10.64)$$

The implosion velocity  $v_{imp}$  is proportional to  $T_r^{1/2}$  and dependent on the ablated mass fraction,  $\Delta m_0$ , which increases with increase of radiation temperature  $T_r$ . Since the central hot spark temperature is high enough for ignition, the implosion velocity is required to be higher than  $3 \times 10^7 \text{ cm}\cdot\text{s}^{-1}$ . Thus,  $T_r$  should be about 300 eV for  $\Delta m_0 / m_0 > 0.7$ . So, it is very important to achieve a high radiation temperature.

In comparison with direct drive, LASNEX calculations for the indirect drive showed a dramatically reduced growth of perturbations due to the R–T instability. Because the mass ablation rate, namely  $v_a$  in the Takabe formula (Eq. (10.31)), is larger in the indirect X ray drive, the R–T instability growth rate is lower and the capsule shell is thicker for radiation drive. Furthermore, the laser beams are absorbed far from the capsule, as indicated schematically in Fig. 10.1 (middle) and Fig. 10.34, and thus the indirect drive implosion is not affected by small scale perturbations induced by the laser irradiation non-uniformities. A potential disadvantage of indirect laser driven implosion other than the low energy coupling efficiency is the plasma instabilities associated with the longer propagation of the laser beams from the laser entrance hole to the hohlraum inner wall where the laser beams are absorbed. This may result in the generation of hot electrons which cause preheating of the capsule.

For the indirect drive, the implosion depends only upon the X ray radiation in the hohlraum. Therefore, indirect drive is essentially independent of the driver. So, much of the physics of indirect drive by lasers carries over to other drivers such as heavy ion beams. Indirect drive laser experiments provide a key element of the database required to ensure that the heavy ion beam driven implosion will work when accelerators are available.

### 10.9.2. Status of indirect drive implosion experiments

Between 1986 and 1990, LLNL made rapid progress in indirect drive target physics: Nova experiments were devoted to X ray irradiation symmetry control [10.123, 10.124], the first X ray drive R–T instability quantitative experiments [10.125, 10.126], the expected benefits of pulse shaping and radiation temperature scaling of implosions [10.127]. Figure 10.35 shows the scaling law of the radiation temperature inside a hohlraum. The 2-D LASNEX simulations reproduce the experimental results. The solid lines indicate the analytical scaling for a given laser radiation conversion efficiency. The figure shows that the radiation is well confined in the hohlraum, since the black body radiation energy in a fixed cavity is proportional to  $T^4$ .

The relation of neutron yield and hohlraum radiation temperature from the Nova experiments is shown in Fig. 10.36. The neutron yield predicted by the LASNEX simulation shown by the solid squares in Fig. 10.37 is consistent with the Nova experiments.

Based on these Nova experiments and a series of underground nuclear experiments (Halite/Centurion (H/C) project), the development of the NIF (National Ignition Facility) conceptual design was authorized in 1993. The gain scaling and the point target design for the NIF were successfully investigated by using the Nova experiments and the related analysis, as shown in Fig. 10.37. The prediction of Fig. 10.37 indicates that the gain of NIF can be higher than 10. The goal of NIF is the demonstration of ignition and burn propagation; this would complete inertial confinement fusion physics and open the door for the application to fusion energy production. The outlook for the NIF laser is shown in Fig. 10.38; the laser is now completed and under operation. The NIF ignition campaign started in 2010. A typical hohlraum target for the NIF experiment is shown in Fig. 10.39.

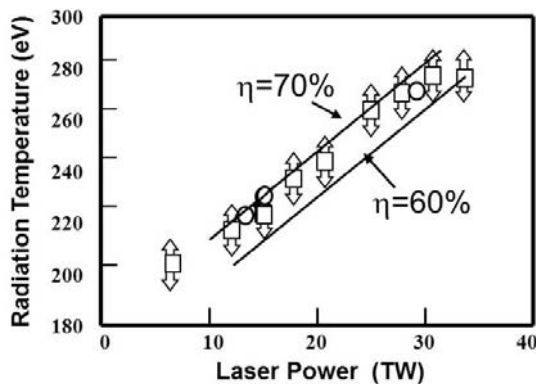


FIG. 10.35. Radiation temperature of Nova experiments (squares) and LASNEX simulations (circles). Reprinted from Ref. [10.128]. Copyright (2011), American Institute of Physics.

## INERTIAL FUSION ENERGY

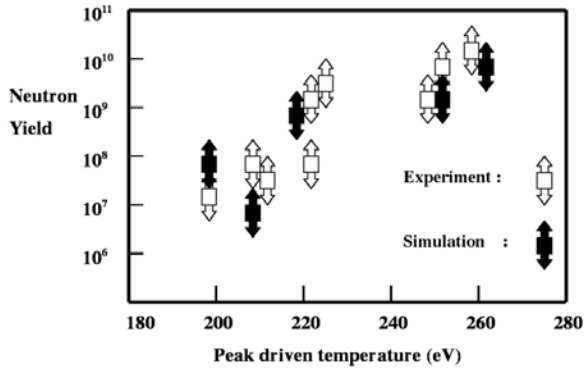


FIG. 10.36. Neutron yields of Nova experiments and LASNEX simulations. The correlation of radiation temperature and neutron yield is consistent between experiments and simulations. Reprinted from Ref. [10.128]. Copyright (2011), American Institute of Physics.

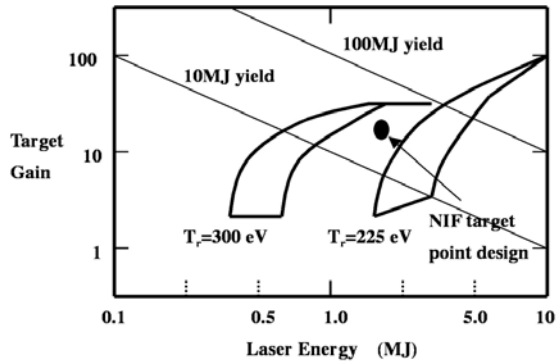


FIG. 10.37. Gain versus hohlraum radiation temperature, and laser energy and NIF point design. The point design is done by LASNEX, which is validated by the Nova experiments. The two straight lines stand for target gain = 10 MJ/laser energy and target gain = 100 MJ/laser energy. Reprinted from Ref. [10.128]. Copyright (2011), American Institute of Physics.



FIG. 10.38. NIF main amplifier. Taken from Refs [10.129, 10.130].

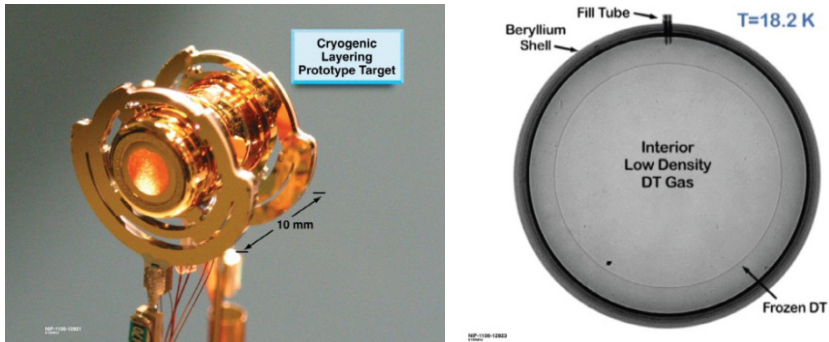


FIG. 10.39. (a) Hohlräum of the NIF target and (b) an up-to-date fabricated fuel capsule. Taken from Ref. [10.130].

### 10.9.3. Recent progress in indirect drive experiments

Currently, two megajoule UV laser facilities are progressing towards ignition demonstration within the indirect drive approach. One of them is the NIF, where a National Ignition Campaign (NIC) is being carried out at Lawrence Livermore National Laboratory (LLNL) in the USA. Another is the LMJ project in the CEA/CESTA research centre in France.

The NIF was formally commissioned in May 2009. The hohlraum energetics campaign with all 192 beams began shortly thereafter and ran until early December 2009. These experiments explored hohlraum operating regimes in preparation for ignition experiments with layered cryogenic targets in the second half of the fiscal year 2010. The first stage of the NIC culminated with an experiment in which an ignition scale hohlraum was irradiated with 1.05 MJ, approximately thirty times the energy that any hohlraum had been irradiated with previously. The results demonstrated the capability to produce a 285 eV radiation environment in an ignition scale hohlraum, while meeting ignition requirements for symmetry, backscatter and preheat. Complementary scaling experiments indicate that with 1.3 MJ drive, the radiation temperature increases to more than 300 eV, which is the design temperature for the first cryogenic layered implosion experiments [10.130, 10.131].

At the second stage of the ignition campaign, this hohlraum will be used to achieve the fuel conditions required for ignition. Computer models of the implosion, developed in the framework of the NIC programme, were extensively used for point design of the target, and the experiment strategy has been developed for optimization of the implosion. The fundamental input variables of an ICF implosion are the implosion velocity ( $v_{imp}$ ) and fuel entropy ( $S$ ) or adiabat ( $\alpha$ ) and ablator on the outer surface of the dense fuel. A comparison of the computer models with preliminary experiments permitted identification of

the 14 laser and 3 target parameters which must be set precisely in experiments in order to optimize the imploded fuel assembly as required for ignition. It was demonstrated in the 2009 NIC experiments that more than 90% of the incident energy is absorbed and the implosion symmetry was controlled by changing the difference of wavelengths of the inner and outer cone laser beams as shown in Fig. 10.40 [10.130, 10.131].

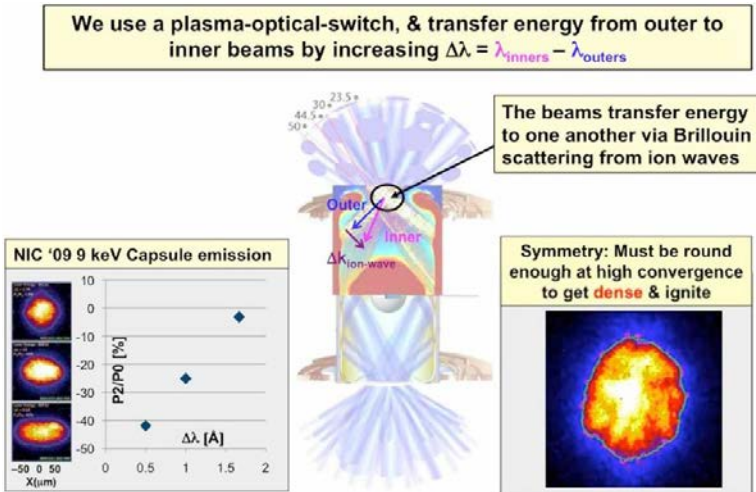


FIG. 10.40. Symmetry control is successful by plasma-optical switching and transfer of energy from outer to inner beam.  $P_2/P_0$  indicates the amplitude of the spherical harmonics of mode 2 divided by the average radius of the imploded core plasma. This asymmetry depends on the laser wavelength difference between the outer and inner beams. Taken from Ref. [10.131].

The second stage of integrated NIC experiments was carried out in late 2010. Laser operation, all diagnostics channels, cryogenic target fabrication and injection were organized to produce a full set of data. With the aim of eliminating premature chamber activation, cryogenic targets of THD (mixture of tritium, deuterium and hydrogen) were imploded. Such targets have the same fuel mass but a smaller neutron yield. Figure 10.41 shows an image of an imploded cryogenic target. This experiment indicates that fabrication imperfections in the fuel capsule cause a serious asymmetry of implosion. Thus, a jet of material passing through the hot spot from the bottom cools the fuel at the moment of the peak implosion, as shown in Fig. 10.41. However, a radial convergence ratio higher than 20 is achieved. In the second stage of the NIC in 2011, the target symmetry, shock timing and mix were controlled to optimize the fuel assembly, and 50/50 D-T target experiments have started to achieve a neutron yield of  $10^{15}$ . However, in order to approach ignition, it is expected that a 10 times higher yield is required. In 2012, the NIF beam energy will be increased to 1.8 MJ to demonstrate ignition and an energy gain of 30.

The full scale LMJ has 240 beams in 60 quads capable of delivering 2 MJ and 600 TW pulses of the third harmonics of  $1.06\ \mu\text{m}$  light (Fig. 10.42). At the first stage to be commissioned in 2014, the facility will be operating with 160 beams combined in 40 quads delivering an energy of 1.2 MJ and a power of 330 TW in two cones from each side of the hohlraum. The building was completed in 2009. Actually, two out of the four laser bays are completed, as shown in Fig. 10.42(a), and the target chamber is equipped as shown in Fig. 10.42 (b). The first stage of the ignition experimental campaign will start in 2015.

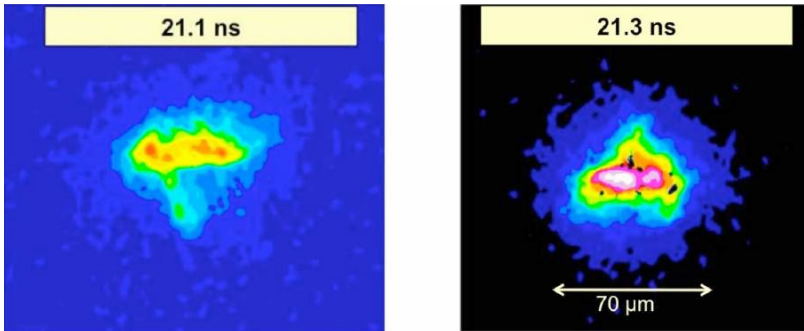


FIG. 10.41. X ray framing images of the NIC. A sequence of frames from the gated X ray detector (GXD) shows a jet of material passing through and cooling the hot spot as the implosion reaches peak emission. The left frame is at 0.2 ns before the maximum compression (the right frame). Taken from Ref. [10.130].

New high efficiency hohlraum targets for ignition experiments have been proposed and designed for the LMJ experiments. The target design includes: (1) a cocktail hohlraum wall (75% U + 25% Au) for better radiation confinement; (2) a rugby ball shaped hohlraum for X ray drive efficiency enhancement; (3) a gradually doped ablator to reduce the risk of hydrodynamic instabilities and control radiation preheat (see Fig. 10.42) [10.132]. In order to control plasma instability inside the hohlraum, laser-plasma interactions in large scale plasmas



LMJ laser hall n°1 completed.

(a)

(b)

FIG. 10.42. Current view of LMJ and the chamber [10.132].

were also investigated at the LIL facility (4 beams of 30 kJ) at the CEA/CESTA and at the LULI2000 facility (2 beams of 1 kJ) at the LULI, École Polytechnique, France, to provide confidence in the effectiveness of the implemented optical smoothing techniques and laser energy absorption.

**10.9.4. Other drivers for indirect drive implosion**

The driver for indirect implosion is either a laser, or a pulse power (Fig. 10.43(a)) or particle accelerator (Fig. 10.43(b)) which converts electric power into short pulses of X rays delivered to the fuel pellet in the proper spatial

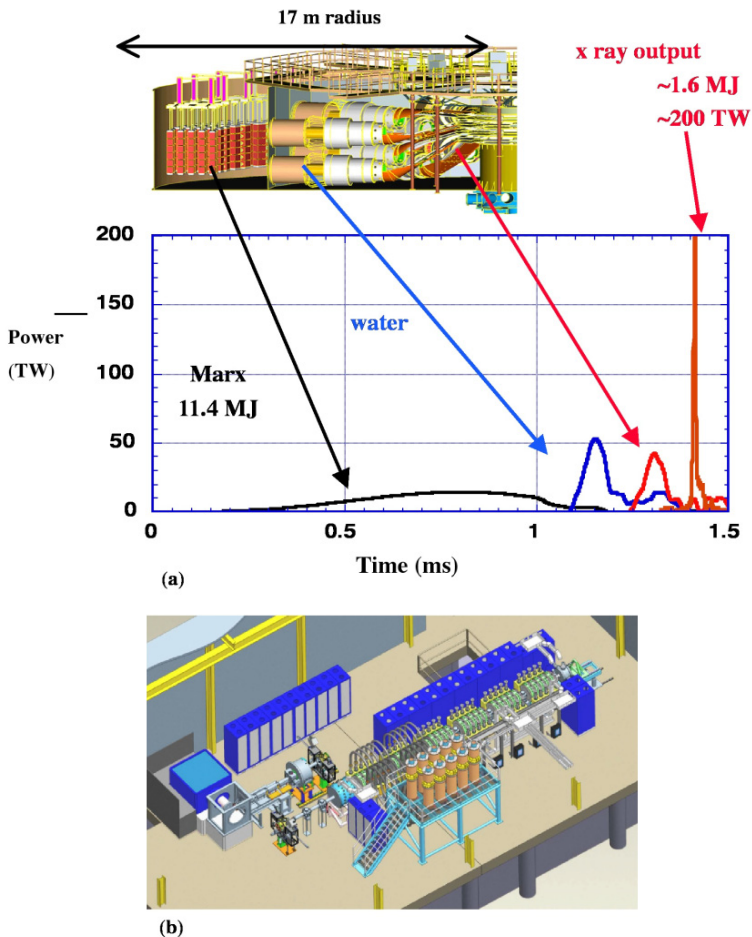


FIG. 10.43. (a) Pulse power driver (Z-machine at Sandia National Laboratories): X ray power and pulse form wire array implosion. (b) Heavy ion beam driver developed at LBNL, HIBF virtual laboratory. This is the test bed of the high power heavy ion beam accelerator. Taken from Ref. [10.135].

and temporal form to cause implosion, ignition and thermonuclear burn. Recently, the Z-Machine at SANL demonstrated generation of 200 TW high power X rays for indirect drive [10.133]. As shown in Fig. 10.43(a), an 11.4 MJ pulse power from Marx with 0.5 ms is compressed into a pulse forming line to 0.1 ms. A pulse is fed into a wire array as shown in Fig. 10.44; the wire array is ablated and imploded by the  $J_z \times B_\theta$  force to stagnate (where z is along the axis of the fibre array cylindrical target). In the stagnation, the imploded kinetic energy is converted into a nanosecond X ray pulse as shown in Fig. 10.43(a). The X ray pulse power reaches 200 TW over 8 ns; thus a 1.6 MJ X ray pulse is generated, which is 15% of the input pulse power energy. The radiation temperature of the X rays is higher than 200 eV. The radiation was applied to imploding a fusion capsule to generate neutrons. As the high gain implosion scheme, for example, a double pinch hohlraum with 1.3–2.6 MJ X ray input has been designed [10.134] to yield 400–3000 MJ (see Fig. 10.45).

As for heavy ion beam fusion, a beam of heavy ions (such as Bi) is accelerated to the order of 10 GeV and injected into a hohlraum target as shown in Fig. 10.1 top. The peak current of the heavy ion beam is a few tens of kA and the beam power and energy are about a few hundred TW and a few MJ with a few nanoseconds. The high current heavy ion beam acceleration is the issue of this scheme and test machines are operated and planned at LBNL, as shown in Fig. 10.43(b).

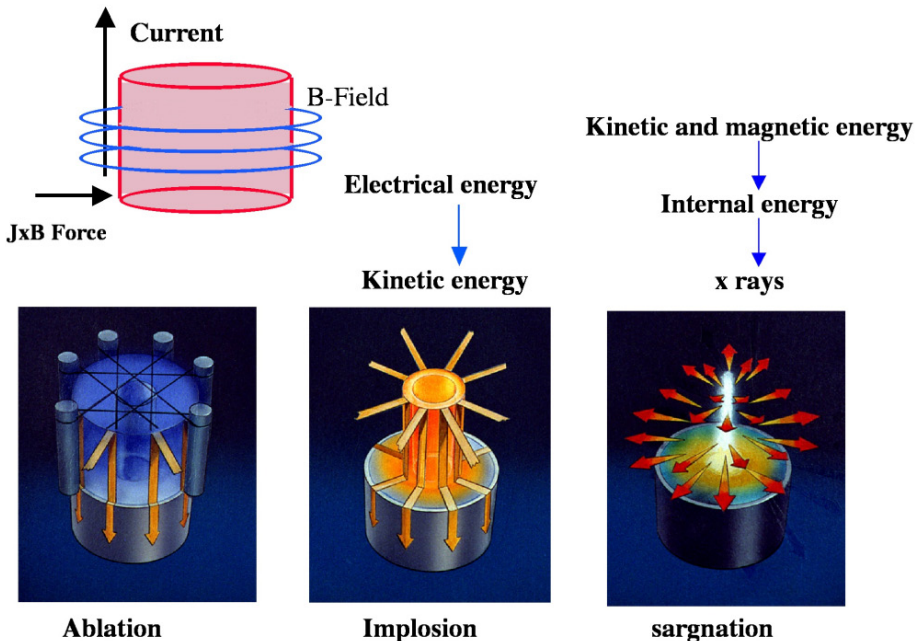


FIG. 10.44. Wire array Z-pinch implosion for strong X ray emission [10.133, 10.136].

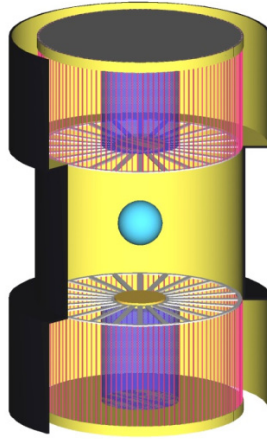


FIG. 10.45. Double pinch hohlraum 1.3–2.6 MJ X ray to yield 400–3000 MJ. Produced according to Ref. [10.134].

## 10.10. IFE POWER PLANT DEVELOPMENT

### 10.10.1. IFE power plant systems

An IFE power plant consists of four major, separate but interconnected subsystems (elements of a power plant), as shown in Fig. 10.46, the functions of which are as follows:

- (a) The driver, usually either a laser or particle accelerator, converts electric power into short pulses of light or particles and delivers them to the fuel pellet in the proper spatial and temporal form to cause implosion, ignition and thermonuclear burn, i.e. fusion.
- (b) In the pellet factory, fuel pellets are manufactured, filled with D-T fuel and sent to the reactor, and then injected into the reaction chamber.
- (c) In the reaction chamber, the injected fuel pellet (target) is tracked, i.e. its position, flight direction and velocity are measured precisely. Driver beams are directed to the target to implode it and to produce thermonuclear energy with a repetition rate of a few times per second. The thermonuclear emissions are captured in a surrounding structure called a blanket and their energy is converted into thermal energy (heat). Tritium is also produced in the blanket.
- (d) In the remainder of the plant, two major processes for material and energy are performed. Tritium and some other target materials are extracted from the recirculating blanket fluid material and from the reaction chamber exhaust gases. Then these extracted materials are recycled to

the target factory. The thermal energy in the blanket fluid is converted into electricity, a portion of which is conditioned and recirculated to power the driver.

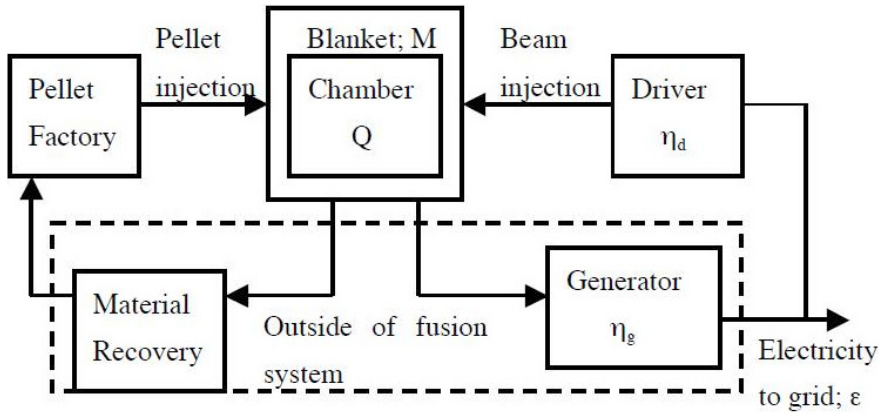


FIG. 10.46. Energy and material flow diagram in a laser fusion power reactor [10.137].

Corresponding to the major processes, two cycles are formed in a power reactor as shown in Fig. 10.46: the target material cycle and the power cycle. In the material cycle, the entire target disintegrates due to implosion fusion in the reaction chamber and a portion of the D-T fuel is burned. Target debris is deposited in the chamber gas and/or in the chamber wall. Tritium fuel is manufactured from Li in the blanket. Tritium and other target materials are extracted, conditioned and returned to the target factory for use in new target fabrication. In the power cycle, a series of energy conversion processes occurs, each with a characteristic efficiency and/or multiplication as shown in Fig. 10.46. Electric energy is converted to laser light or particle beam energy in the driver with an efficiency  $\eta_d$ . The driver energy produces thermonuclear energy by fuel pellet implosion with a target gain  $Q$ . Neutron energy from the fusion reaction is converted into thermal energy in the blanket. Neutrons in the blanket also breed tritium and induce nuclear reactions leading to energy multiplication with a factor  $M$ . Finally, the heat energy is converted into electricity with an efficiency  $\eta_g$ . A portion  $\varepsilon$  of the gross electricity produced must be recirculated to the power driver, completing the power cycle. In the power cycle, the basic condition for power balance is

$$\eta_d Q M \eta_g \varepsilon = 1 \quad (10.65)$$

The recirculation power fraction  $\varepsilon$  should be less than 25% for economic reasons. If  $\varepsilon$  is too large, then the cost of electricity (CoE) sold rises rapidly because much of the plant equipment is used simply to generate electricity for the driver itself. The blanket gain  $M$  is about 1.05–1.25, depending on the design

of the blanket material and structure. The efficiency of the turbine generator  $\eta_g$  ranges from 30 to 40%. Therefore, the product  $\eta_d Q$  should be

$$\eta_d Q \geq 10 \quad (10.66)$$

This product determines the minimum target gain necessary for any given driver efficiency. The estimated target gain is shown in Fig. 10.3. Typical values predicted are  $Q \approx 30$  for indirect drive,  $Q \approx 100$  for direct drive and  $Q \approx 200$  for fast ignition.

Corresponding to each gain value, the necessary condition for driver efficiency is given for an indirect drive with heavy ion beam accelerator (HIB) to be 30–40%, for a direct driver with laser to be 10% and for fast ignition, if it works well, 5%. A higher driver efficiency  $\eta_d$  with a higher target gain  $Q$  at smaller driver energy provides the condition for a smaller recirculation power fraction  $\varepsilon$  and a lower driver cost, which gives a competitive CoE. An IFE power plant must be safe and must have minimum impact on the environment. Ensuring these features requires that all the system components of the plant and materials used must be examined carefully for their potential negative impacts. The economic, safety and environment (ESE) aspects should be examined in the technical design of each specific type of power plant. It should be noted that these aspects can be evaluated reasonably quantitatively with recent developments in physics and technology related to the elements of IFE power plants.

### 10.10.2. Driver development

The specifications of the laser driver for a commercial power plant are: (1) total energy (MJ/pulse); (2) intensity ( $10^{14}$ – $10^{15}$  W·cm<sup>-2</sup> on target); (3) pulse shape (tailored in 20–40 ns pulses); (4) wavelength (0.3–0.5  $\mu$ m); (5) spatial uniformity of irradiation (<1%); (6) efficiency (>10% for direct implosions, >5% for fast ignition); (7) repetitive operation (~10 Hz); (8) cost (capital and operating costs, including life and maintainability); and (9) reliability or availability [10.137].

In the above specifications, items (1) to (5) are those required for the research phase to demonstrate ignition and fusion gain. Items (6) to (9) are those required for a driver for a laser fusion power plant. An advanced solid state laser [10.138] has demonstrated a breakthrough in diode laser pumping and feasible prospects of a power plant driver [10.139, 10.140]. Figure 10.47 shows the progress of flash lamp pumped glass lasers on the left-hand side, which are basically single-shot lasers, and the expected development of diode pumped solid state lasers (DPPSLs) on the right-hand side.

The important requirement of solid-state lasers as reactor drivers is the capability of achieving uniform irradiation on the surface of the fuel pellet for uniform implosion. Several important concepts and technologies for better

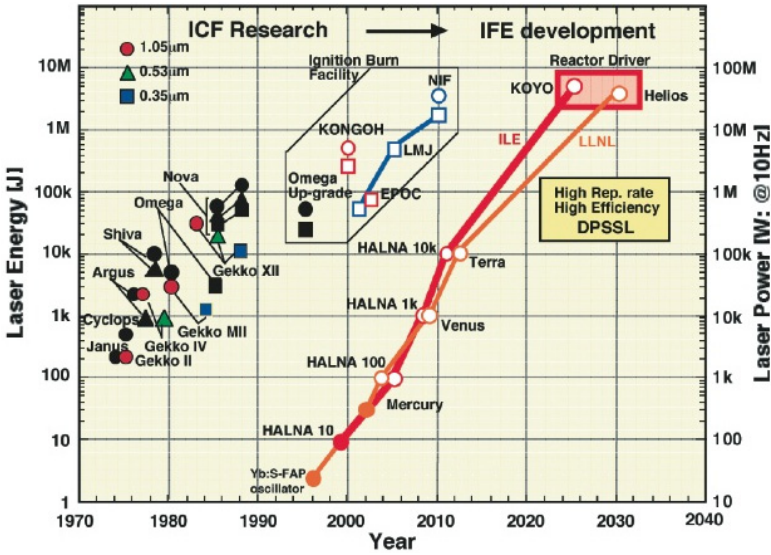


FIG. 10.47. Laser driver development [10.141].

irradiation have been developed. They are: (a) RPP (random phase plate) to obtain a smooth envelope distribution in a far field pattern even with a beam of non-uniform intensity distribution in the near field; (b) smoothing by SSD to obtain time-averaged uniformity of intensity even with a speckle structure of the instantaneous pattern; and (c) pulse tailoring in intensity (picket fence to control the shock heating of the fuel shell), in wavelength (two-colour irradiation to control non-local heat transport) or in coherency (partially coherent light (PCL) at the foot to reduce the perturbation by the initial imprint). It should be noted

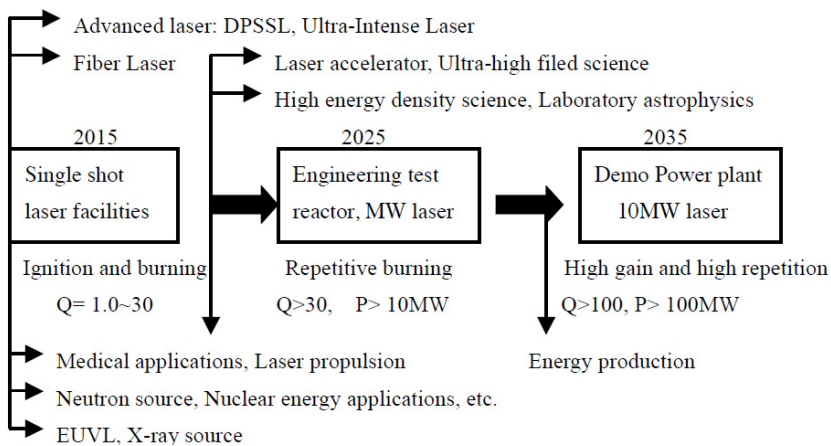


FIG. 10.48. Stepwise development of laser fusion driver and possible spin-off applications. Taken from Ref. [10.141].

that the Omega 60 beam achieved an on-target uniformity better than 1% rms with an improved power balance of 60 beams below 5% rms and implementation of several smoothing techniques [10.67–10.69].

For better and more practical drivers of diode pumped solid state lasers (DPSSLs) for laser fusion power plants in commercial use, there are two major key issues. The first is high power laser diodes for pumping and the other is solid state laser material. Laser diodes have progressed and achieved the required specifications for pumping. A cost reduction in the diode laser of 10–100 times below the present level is required, and this is expected to be possible with the increase in demand for application of laser diodes and/or DPSSLs to industry and science as shown in Fig. 10.48, along with increased laser fusion power plant development.

### 10.10.3. Reaction chamber

In a laser fusion power plant, small fusion targets of 5–6 mm diameter are successively injected and shot by laser beams. Following the implosion and fusion explosion of a fuel pellet, successive pulses of different energy species hit the first wall of the chamber. They are reflected or scattered laser light, X rays from the fusion plasma, neutrons and plasma debris. The energy spectrum and pulse shape of each energy species for typical high gain implosions are estimated with burning simulation codes. The unique feature of the IFE reaction chamber is the technical possibility of utilizing the wetted surface for the plasma-facing wall. This comes from the mitigated requirement for a vacuum in the chamber for IFE, in contrast with MFE chambers, where a high vacuum is important for better energy confinement. The use of a liquid wall gives flexibility in designing various kinds of chamber concepts such as a thin liquid layer on porous solid [10.142] or a woven fabric wall [10.143] or a thick liquid layer of 30–50 cm that is flowing down, forming a cavity for the fusion reaction [10.144, 10.145].

On the other hand, the use of a dry wall for an IFE reaction chamber needs special care because of the high peak intensity of wall loading due to the pulsed energy release of X rays and various species of ion from the implosion fusion. The dynamic responses of the dry wall have been analysed to examine the possibility of its use as the first wall of a reaction chamber [10.146]. The dry wall seems to survive against the pulsed energy fluxes of laser light, X rays and neutrons that are emitted from moderate fusion explosions with reasonable separation of the first wall from the fusion reaction point [10.147, 10.148]. The heating and the sputtering of the wall surface by the plasma debris need more investigation in order to clarify the damage and the lifespan of the chamber first wall. It should be noted, however, that a distributed magnetic field on the surface or low pressure gas in the cavity could mitigate the plasma flow hitting the wall surface, which could lead to a longer life of the wall [10.148, 10.149]. In the

thick liquid wall chamber design, most of the fusion energy including neutrons is absorbed in the flowing liquid. The conceptual design of the KOYO [10.143, 10.145] power plant is shown in Fig. 10.49 with the technology and issues when utilizing a thin liquid layer for first wall protection.

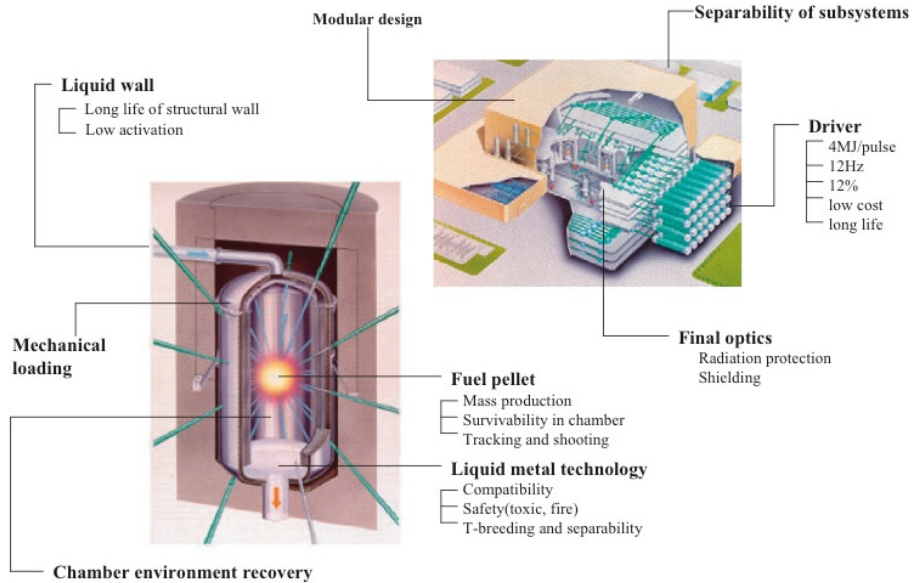


FIG. 10.49. KOYO, a conceptual design of a laser fusion reactor. Left: reactor chamber; right: bird's-eye view of the system. Taken from Ref. [10.141].

A fast ignition fusion reactor was also designed conceptually by the ILE, Osaka University group (see Fig. 10.50). This reactor design discloses the possibility of a relatively compact laser fusion power plant [10.146].

The reaction chamber of a laser fusion power plant involves several important issues, other than the first wall protection described above, that must be examined carefully during design. They can be summarized as follows:

- (1) Mechanical and thermal responses of the reaction chamber, such as the dynamics of the surface of the first wall, which includes absorption of X ray and plasma debris, evaporation and re-condensation of the surface, shock formation from the surface inwards and fatigue of the structural material under repeated stress;
- (2) Radiation damage, neutron activation and shielding;
- (3) Restoration of the chamber environment for driver beam propagation and pellet injection;
- (4) Damage protection of the final elements to guide the driver beams;
- (5) Tritium breeding in the blanket and extraction.

These technical issues span a wide field of physics and engineering and have many engineering problems in common with an MFE reactor. Collaboration and cooperation with reactor technology developments in industry and the MFE community are important for the progress of IFE reactor technology.

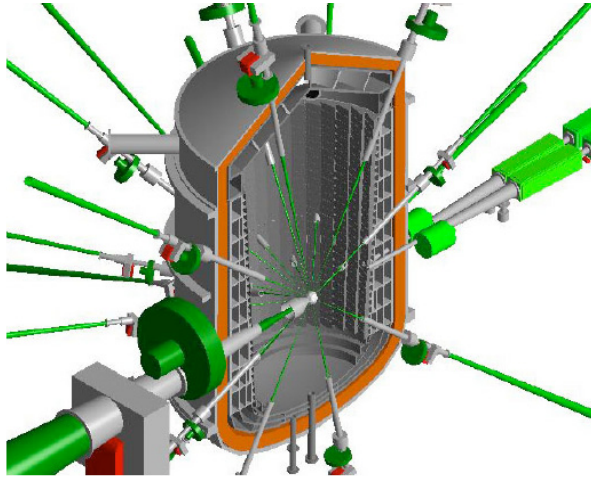


FIG. 10.50. Laser fusion reactor chamber for fast ignition: KOYO-F [10.146].

#### 10.10.4. Fuel pellet

The precise fabrication of structured fuel pellets and targets for laser implosion and related physics experiments has been well developed. Recent progress in micromachining, fine coating and characterizing techniques for microstructures in industry has interacted well with the target technology for laser fusion, and vice versa. The next step towards a power plant is to demonstrate repetitive injection, tracking and shooting with a high repetition rate laser [10.150]. This is a very challenging development for industry also. Mass production of fuel pellets at low cost is also an important issue for realistic IFE power plant development. The tritium handling technology is common with MFE and the development process can be shared except for the precision cryogenic fuel technology. The effects of the residual gas in the chamber on the flying cryogenic pellet have been evaluated. These include the condensation effect of the chamber gas on low temperature fuel pellets, the heat flow through the gas and radiation, and disturbance of the flight trajectory by the fluctuating condition of the chamber. It can be concluded that 3–5 Hz operation of a liquid wall chamber is acceptable. The pressure of the protecting gas for the dry wall chamber could be optimized to compromise the protection effect on the first wall with the fuel pellet flight and the laser beam propagation in the chamber.

Finally, the fuel pellet design and the chamber wall design are interconnected, in particular for the dry wall reactor. The sputtering of the chamber wall and final optics is sensitive to clusters and ion species of the fusion target materials. Actually, ions bombard the wall in the energy range of 100 keV to a few MeV (see Ref. [10.151]). In particular, medium and high  $Z$  ions with several 100 keV will sputter a few atoms/single ions even on a tungsten wall. So it is necessary to choose light elements for the ablator and to reduce the ablator thickness and the total amount of the heavy metal cone (for fast ignition) and cavity (for indirect drive target). Further research is required on the impacts of high energy particle sputtering on chamber wall and optics.

### 10.10.5. Recent progress in inertial fusion technologies

#### 10.10.5.1. LIFE project at LLNL

The demonstration of ignition at NIF and the technology development undertaken by the NIC team are expected to provide a solid basis for future scientific and technological development in support of IFE. A Laser Inertial Fusion Energy (LIFE) engine concept would have a similar footprint to NIF and is actively being pursued at LLNL [10.19] (see Fig. 10.51). It is looking at further detail at specific driver, target and other issues required to implement a 1 GW commercialization demonstration in approximately 2030, with widespread fusion based power production in the 2050 time frame. Examples of specific issues

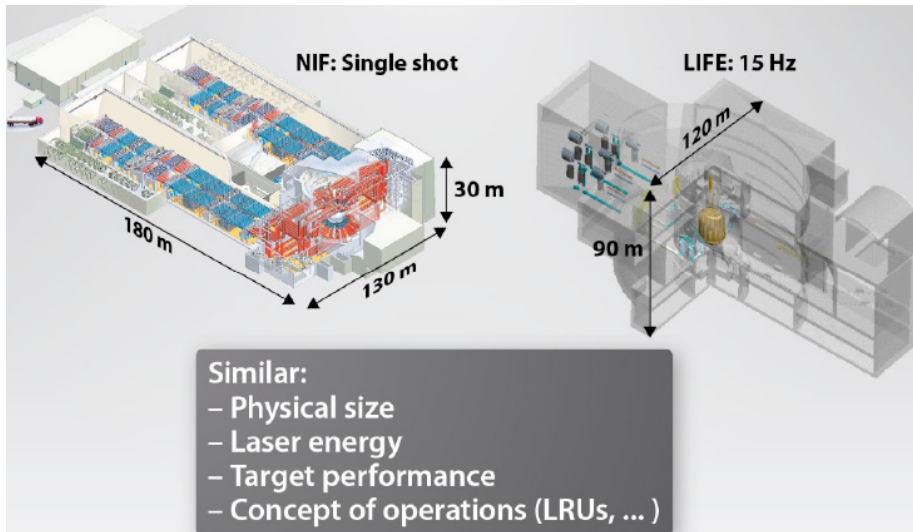


FIG. 10.51. Laser Inertial Fusion Energy (LIFE) Engine. A LIFE would have a similar footprint to NIF while generating 1 GW(e). Taken from Ref. [10.19].

being considered include the use of second harmonic versus third harmonic laser light and comparison of pure fusion and fusion–fission hybrid schemes. The requirements based approach being undertaken is defining key areas in which further research and technology development are required. NIC results coupled with a robust IFE programme could lead to a prototype IFE demonstration plant in the 10–15 year time frame.

*10.10.5.2. HiPER project in the EU*

High Power Laser Energy Research (HiPER) is the European strategic forum on the research infrastructure (ESFRI) programme for developing an approach to a European Laser Driven Fusion Energy Facility. The preparatory phase started in 2011 [10.152, 10.153]. The key objectives of this phase concern the organization of international collaboration and development of common knowledge on energy generation by inertial fusion. A key decision to be taken is the definition of the ignition scheme (fast or shock ignition) and the design of an Engineering Test Bed Facility operating a burst mode of hundreds to a thousand shots at a few Hz rate. The HiPER facility will operate with a minimum of 48 compression beams delivering 400 kJ in 10–20 ns and possibly a PW beam-line of 100 kJ in 10–20 ps. The choice of ignition scheme will be tested on the existing single shot systems, NIF and LMJ. Energy yields from 40 to 100 MJ per shot are expected.

The HiPER facility will demonstrate, with the lowest risk, a design of target manufacturing and injection systems and a repetitive laser system, and accommodate experiments in technology for reliable power production. The HiPER chamber area design is significantly different from single shot systems (NIF and LMJ) in terms of laser requirements, optics protection, activation of walls and structural materials. It considers such aspects as: (i) resistance of the first wall to debris, radiation, shrapnel and neutrons; (ii) maintenance of deep vacuum and cryogenic environments required for experiments; (iii) accommodation of the many diagnostic instruments, beam lines and associated optics equipment; (iv) minimization of activation of the chamber components together with a low radioactivity and ease of operation, maintenance and chamber disposal; (v) tritium handling.

The shielding structure is shown schematically in Fig. 10.52 [10.151, 10.154]. The chamber has an inner wall radius of 500 cm, and the thickness is 10 cm. For the facing and structural materials a combination of tungsten with steels (EUROFER97) and aluminium respectively is being considered [10.155]. The study was performed using the codes MCNPX (particle transport) and ACAB (activation and radiological responses) for characterization of radiological effects on the chamber and its environment. The chamber design accounts for the thermo-mechanical effects on the first wall and final optics by  $\alpha$  particles and

X rays as well as bigger particles (debris and shrapnel) in the repetitive operation regime. The energy fluence deposited on the first wall was calculated for all species of particles (except neutrons), accounting for their time deposition on the wall. For a 50 MJ target energy release, the energy fluence on the first wall is about 3–4 J·cm<sup>-2</sup>. The debris (microparticles, shrapnel with tens of microns) and clusters (nanoparticles) produce sputtering one or two orders of magnitude higher than their independent constituents. Their effect has to be studied in more detail accounting for their energy and size distribution (at the moment available only in a few experiments).

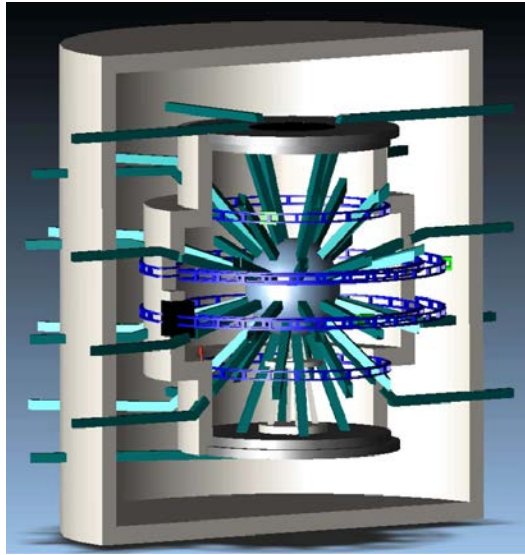


FIG. 10.52. Chamber concept of HiPER. Light green, green, blue and red indicate vehicles for remote handling, laser beam ducts, remote handling stage and a person. Taken from Refs [10.151, 10.154].

#### 10.10.5.3. Recent progress in laser technology

The development of high repetition rate driver lasers has four steps: (1) lasers in operation, delivering 10 J in a few nanoseconds with a repetition rate of 10 Hz, (2) short term projects, 100 J, a few nanoseconds, 10 Hz, (3) intermediate scale system, 1 kJ, a few nanoseconds, 10 Hz, (4) prototype system, 10 kJ, a few nanoseconds, 10 Hz, which will be one beam of the IFE reactor driver of a few MJ total size. Associated with the laser driver R&D of the HiPER project, four diode pumped solid state laser (DPSSL) programmes are ongoing in the EU. These are POLARIS (achievement: 12 J/0.003 Hz, goal 150 J/0.1 Hz) in Germany; LUCIA (achievement: 7 J/2 Hz, goal: 100 J/10 Hz)

in France; DIPOLE (planned goal: 1 kJ/10 Hz) in the UK and HILASE (planned goal: 100 J/10 Hz, 10 J/100 Hz) in the Czech Republic.

In Japan, Osaka University and Hamamatsu Photonics have proposed a cryogenic Yb:YAG ceramic as a novel reactor laser material instead of the conventional Nd:glass [10.156]. The stimulated emission cross-section and the thermal conductivity for this ceramic can be tuned by controlling the material temperature. Also, using a diode-pumped oscillator with a cryogenic Yb:YAG disk, the highest optical-optical slope (conversion efficiency from LD light to Yb:YAG laser energy) efficiency of 90% has been demonstrated. The heating of the laser material is one third of that in the conventional Nd:glass. Based upon the laser parameters obtained, a new diode-pumped reactor laser system has been conceptually designed with cryogenic Yb:YAG ceramics. A 1.1 MJ compression laser and a 0.1 MJ heating laser will be operated at a 16 Hz repetition rate. The overall electrical-optical conversion efficiency is numerically calculated to be as high as 12%. The compact main amplifier of less than 3000 m<sup>3</sup> volume size would be realized by using an active mirror architecture.

The Korea Advanced Institute of Science and Technology (KAIST) and the Korea Atomic Energy Research Institute (KAERI) are developing a laser driver technology based on stimulated Brillouin scattering (SBS) phase conjugate mirrors (PCMs) [10.157]. At KAIST, a coherent beam combination of small output energy lasers is operating at a repetition rate of 10 Hz using an innovative phase controlled technique. It makes it possible to lock/control the phases of SBS waves of each PCM independently with a simple optical composition [10.157]. This new approach can be up-scaled by the number of combined beams of small output energy lasers with a high repetition rate. Actually, a coherent tiled four beam combination provides stable phase correlation, even if the amplifiers are inserted in the system and operated without special fine tuning.

#### *10.10.5.4. Recent progress of target fabrication and injection technology*

The scientists of General Atomics have developed a robotic target assembly station, a target injection system and a very accurate target tracking system. The status of that R&D was presented at an IFE technology satellite meeting [10.158].

The scientists of ILE, Osaka, have developed a fabrication process for low density plastic capsules and its scaling to the future mass production method by using a microfluid technology. For the FIREX-I project, a foam cryogenic target is designed where low density foam shells with a conical light guide will be cooled down to cryogenic temperatures and will be fuelled through a capillary. The required diameter and thickness of the capsule are 500 μm and 20 μm, respectively. New materials have been investigated for low density plastic capsules. By employing a new high viscosity polymer, ILE scientists

have succeeded in preparing capsules that are matched to FIREX-I requirements without cross-linking. The fuelling test was started in 2010 [10.159].

The scientists of the Czech Technical University of Prague reported a new approach for navigating laser beams to an injected pellet by using the SBS PCM [10.150]. By illuminating an injected pellet with seed laser beams, reflected seeding laser pulses are collected by the focusing optics, amplified, reflected by the SBS PCM, amplified once again on return and converted to a higher harmonic. The beams are automatically aimed at a moving pellet by a special target displacement compensation system, which is a completely passive system having its optical components appropriately designed for every individual beam.

## ACKNOWLEDGEMENT

The author of this chapter is very grateful to J.M. Perlado, Y. Kato and S. Nakai for their continuous support for preparing this manuscript. He also thanks J. Alvarez for his critical reading of the technology part. Finally, he is grateful to B. Gulejova and K. Lackner for their great assistance.

## REFERENCES

- [10.1] MAIMAN, T.H., *Nature* **187** (1960) 493.
- [10.2] ATKINSON, R. d'E., HOUTERMANS, F.G., Zur Frage der Aufbau-Möglichkeit der Elemente in Sternen, *Z. Phys.* **54** (1929) 656.
- [10.3] BETHE, H.A., PEIERLS, R., The neutrino, *Nature* **133** (1934) 689.
- [10.4] BETHE, H.A., *Rev. Mod. Phys.* **9** (1937) 167.
- [10.5] BETHE, H.A., Energy production in stars, *Phys. Rev.* **55** (1939) 434.
- [10.6] GAMOW, G., TELLER, E., *Phys. Rev.* **53** (1938) 608.
- [10.7] TELLER, E., *Fusion*, Academic Press, New York (1981).
- [10.8] LANDAU, L., *Nature* **141** (1938) 333.
- [10.9] BASOV, N.G., KROKHIN, O.N., Condition for heating up of a plasma by the radiation from an optical generator, *Soviet Physics - JETP* **19** (1964) 123.
- [10.10] BASOV, N.G., et al., *IEEE J. Quant. Electron.* **4** (1968) 864.
- [10.11] DAWSON, J.M., On the production of plasma by giant pulse lasers, *Phys. Fluids* **7** (1964) 981.
- [10.12] KASTLER, C.R., *Acad. Sci. Paris* **285** (1964) 489.
- [10.13] HORA, H., in *Proc. of Laser Interaction and Related Plasma Phenomena*, June 9–13, 1969, Graduate Center in Hartford, Conn., USA, Plenum Press (1969) 365.
- [10.14] FLOUX, F., *Laser Interaction and Related Plasma Phenomena* (SCHWARZ, H., HORA, H., Eds), Plenum Press, New York (1969) 409.
- [10.15] ELIEZER, S., *Laser Fusion for Pedestrians*, Israel Atomic Energy Commission Report 1A-1374 (1992).
- [10.16] NUCKOLLS, J., WOOD, L., THIESSEN, A., ZIMMERMAN, G., Laser compression of matter to superhigh densities: Thermonuclear applications, *Nature* **239** (1972) 139.
- [10.17] GUDERLEY, G., *Luftfahrtforschung* **19** (1942) 302.
- [10.18] HAYNAM, C.A., WEGNER, P.J., AUERBACH, J.M., et al., National Ignition Facility laser performance status, *Appl. Opt.* **46** (2007) 3276.
- [10.19] MOSES, E., et al., in *Proc. 22nd IAEA Fusion Energy Conf.*, Geneva, Switzerland, 2008; *Nucl. Fusion* **49** (2009) 104022.

- [10.20] BIGOT, B., Inertial fusion science in Europe, *J. Phys. IV France* **133** (2006) 3.
- [10.21] NISHIMURA, H., et al., in Proc. 17th IAEA Fusion Energy Conf., Yokohama, Japan, 19–24 October 1998; IAEA-CN-69/IF/04.
- [10.22] YAMANAKA, T., Internal Report of Institute of Laser Engineering, Institute of Laser Engineering, Osaka University, 1986.
- [10.23] BASOV, N.G., GUS'KOV, S.Yu., FEOKISTOV, L.P., Thermonuclear gain of ICF targets with direct heating of ignitor, *J. Sov. Laser Res.* **13** (1992) 396.
- [10.24] TABAK, M., HAMMER, J., GLINSKY, M.E., KRUEER, W.L., WILKS, S.C., WOODWORTH, J., CAMPBELL, E.M., PERRY, M.D., MASON, R.J., Ignition and high gain with ultrapowerful lasers, *Phys. Plasmas* **1** (1994) 1626.
- [10.25] MEYER-TER-VHEN, J., On the energy gain of fusion targets: The model of Kidder and Bodner improved, *Nucl. Fusion* **22** (1982) 561.
- [10.26] ELIEZER, S., MIMA, K., Eds, *The Applications of Laser Plasmas*, Taylor and Francis Publisher 2008.
- [10.27] NAKAI, S., TAKABE, H., *Rep. Prog. Phys.* **59** (1996) 1071.
- [10.28] NAKAI, S., MIMA, K., *Rep. Prog. Phys.* **67** (2004) 321–349.
- [10.29] AZECHI, H., JITSUNO, T., KANABE, T., et al., High density compression experiments at ILE, Osaka, *Laser Part. Beams* **9** (1991) 193.
- [10.30] ELIEZER, S., *The Interaction of High Power Lasers with Plasmas*, Institute of Physics Publishing, Bristol (2002).
- [10.31] ELIEZER, S., MURAKAMI, M., MARTINEZ-VAL, J.M., Equation of state and optimum compression in inertial fusion energy, *Laser Part. Beams* **25** (2007) 585.
- [10.32] MORE, R.M., in Proc. 29th Scottish Universities Summer School in Physics, Camelot, Southampton, 1986, in the section on “Laser-Plasma Interactions 3” (HOOPER, M.B., Ed.) (1986) 157.
- [10.33] BASKO, M.M., MEYER-TER-VEHN, J., Asymptotic scaling laws for imploding thin fluid shells, *Phys. Rev. Lett.* **88** (2002) 244502.
- [10.34] LINDL, J.D., *Inertial Confinement Fusion*, Springer, New York (1998).

- [10.35] ROSEN, M.D., The physics issues that determine inertial confinement fusion target gain and driver requirement: A tutorial, *Phys. Plasmas* **6** (1999) 1690.
- [10.36] BODNER, S.E., Rayleigh-Taylor instability and laser-pellet fusion, *Phys. Rev. Lett.* **33** (1974) 761.
- [10.37] NISHIGUCHI, A., MIMA, K., BALDIS, H., *Laser Plasma Theory and Simulation*, (LETOKHOV, V.S., SHANK, C.V., SHEN, Y.R., WALTHER, H., Eds), Harwood Academic Publisher (1994).
- [10.38] YAMANAKA, C., *Introduction to Laser Fusion* (LETOKHOV, V.S., SHANK, Y.R., SHEN, Y.R., WALTHER, H., Eds), Harwood, London (1991).
- [10.39] DENISOV, N.G., *JETP* **4** (1957) 544.
- [10.40] GINTZBURG, V.L., *Propagation of Electromagnetic Waves in Plasmas*, Pergamon, New York (1964).
- [10.41] ESTABROOK, K.G., *Phys. Fluids* **18** (1975) 1151.
- [10.42] FORSLUND, D., *Phys. Rev. A* **11** (1975) 679.
- [10.43] TAKABE, H., MULSER, P., *Phys. Fluids* **25** (1982) 2304.
- [10.44] UENEOYAMA, T., *J. Phys. Soc. Jpn.* **50** (1981) 3107.
- [10.45] KRUER, W., et al., "Laser Plasma Interactions", *Frontier of Physics* (KRUER, W., Ed.), Addison Wesley Publisher (1989).
- [10.46] FORSLAND, D.W., et al., *Phys. Fluids* **18** (1975) 1002.
- [10.47] SILIN, V.P., *Zh. Eksp. Teor. Fiz.* **48** (1965) 1676.
- [10.48] DUBOIS, D.F., GOLDMAN, M.V., *Phys. Rev. Lett.* **14** (1965) 544.
- [10.49] NISHIKAWA, K., *J. Phys. Soc. Jpn.* **24** (1968) 916 and 1152.
- [10.50] VALEO, E., et al., *Phys. Rev. Lett.* **28** (1972) 340.
- [10.51] YAMANAKA, C., et al., *Phys. Rev. A* **6** (1972) 2335.
- [10.52] MIMA, K., NISHIKAWA, K., *Basic Plasma Physics II* (GALEEV, A.A., SUDAN, R.N., Eds), Chapter 6 (1984) 452.
- [10.53] PERKINS, F., et al., *PRL* **32** (1974) 1234.
- [10.54] GOLDMAN, M.V., *Ann. Phys.* **38** (1966) 117.
- [10.55] LIU, C.S., ROSENBLUTH, M.N., *Phys. Fluids* **19** (1976) 967.
- [10.56] SIMON, A., SHORT, R.W., *Phys. Fluids* **26** (1983) 3107.

- [10.57] DRAKE, J.F., KAW, P.K., LEE, Y.C., *Phys. Fluids* **17** (1974) 778.
- [10.58] LIU, C.S., *Adv. Plasma Phys.* (1976) 121–177.
- [10.59] KAW, P.K., et al., *Phys. Fluids* **16** (1973) 1522.
- [10.60] COHEN, B.I., et al., *Phys. Fluids* **22** (1979) 1115.
- [10.61] KATO, Y., MIMA, K., et al., *Phys. Rev. Lett.* **53** (1984) 1057.
- [10.62] OBENSCHAIN, S.P., et al., *Phys. Rev. Lett.* **56** (1986) 2807.
- [10.63] KEY, M.K., et al., *Phys. Fluid* **26** (1983) 2011.
- [10.64] BODNER, S.E., et al., Naval Research Laboratory (1998) NRL/MR/6730-98-8113.
- [10.65] RICHTMYER, R.D., Taylor instability in shock acceleration of compressible fluids, *Commun. Pure Appl. Math.* **13** (1960) 297–319.
- [10.66] NISHIGUCHI, A., MIMA, K., AZECHI, H., MIYANAGA, N., NAKAI, S., Kinetic effects of electron thermal conduction on implosion hydrodynamics, *Phys. Fluids B4* (1992) 417; doi:10.1063/1.860292.
- [10.67] McCRORY, R.L., et al., in *Proc. 19th IAEA Fusion Energy Conf.*, Lyon, France, 14–19 October 2002, IAEA-CN-94/IF-1.
- [10.68] SKUPSKY, S., SHORT, R.W., KESSLER, T., et al., Improved laser-beam uniformity using the angular dispersion of frequency-modulated light, *J. Appl. Phys.* **66** (1989) 3456.
- [10.69] REGAN, S.P., MAROZAS, J.A., KELLY, J.H., et al., Experimental investigation of smoothing by spectral dispersion, *J. Opt. Soc. Am.* **B17** (2000) 1483.
- [10.70] McKENTY, P.W., GONCHAROV, V.N., TOWN, R.P.J., et al., Analysis of a direct drive ignition capsule designed for the National Ignition Facility, *Phys. Plasmas* **8** (2001) 2315.
- [10.71] BODNER, S.E., COLOMBANT, D.G., SCHMITT, A.J., et al., High gain direct drive target design for laser fusion, *Phys. Plasmas* **7** (2000) 2298.
- [10.72] AZECHI, H., SHIRAGA, H., NAKAI, M., et al., Suppression of the Rayleigh-Taylor instability and its implication for the impact ignition, *Plasma Phys. Control. Fusion* **46** (2004) B245.
- [10.73] FUJIOKA, S., SUNAHARA, A., NISHIHARA, K., et al., Suppression of the Rayleigh-Taylor instability due to self-radiation in a multiablation target, *Phys. Rev. Lett.* **92** (2004) 195001.

- [10.74] SHIGEMORI, K., et al., Bull. Am. Phys. Soc. **46** (2001) 286.
- [10.75] TAKABE, H., MIMA, K., MONTIERTH, L., MORSE, R.L., Self-consistent growth rate of the Rayleigh-Taylor instability in an ablatively accelerating plasma, Phys. Fluids **28** (1985) 3676.
- [10.76] BETTI, R., GONCHAROV, V.N., McCRORY, R.L., VERDON, C.P., Growth rates of the ablative Rayleigh-Taylor instability in inertial confinement fusion, Phys. Plasmas **5** (1998) 1446.
- [10.77] HARRISON, E.R., Alternative approach to the problem of producing controlled thermonuclear power, Phys. Rev. Lett. **11** (1963) 535.
- [10.78] MAISONNIER, C., Macroparticle accelerators and thermonuclear fusion, Nuovo Cimento **42** (1966) 332.
- [10.79] STRICKLAND, D., MOUROU, G., Opt. Commun. **56** (1985) 219.
- [10.80] PUHKOV, A., MEYER-TER-VEHN, J., Laser hole boring into overdense plasma and relativistic electron currents for fast ignition of ICF targets, Phys. Rev. Letters **79** (1997) 2686.
- [10.81] ATZENI, S., Inertial fusion fast ignitor: Igniting pulse parameter window vs. the penetration depth of the heating particles and the density of the precompressed fuel, Phys. Plasmas **6** (1999) 3316.
- [10.82] KEY, M.K., KABLE, M.D., COWAN, T.E., et al., Hot electron production and heating by hot electrons in fast ignitor research, Phys. Plasmas **5** (1998) 1966.
- [10.83] NORREYS, P.A., ALLOTT, R., CLARKE, J., et al., Experimental studies of the advanced fast ignitor scheme, Phys. Plasmas **7** (2000) 3721.
- [10.84] KODAMA, R., NORREYS, P.A., MIMA, K., et al., Fast heating of super solid density matter as a step toward laser fusion ignition, Nature **412** (2001) 798.
- [10.85] KODAMA, R., SHIRAGA, H., SHIGEMORI, K., et al., Fast heating scalable to laser fusion ignition, Nature **418** (2002) 933.
- [10.86] ROTH, M., COWAN, T.E., KEY, M.H., et al., Fast ignition by intense laser-accelerated proton beams, Phys. Rev. Letters **86** (2001) 436.
- [10.87] CARUSO, A., PAIS, V.A., The ignition of dense DT fuel by injected triggers, Nucl. Fusion **36** (1996) 745.
- [10.88] GUS'KOV, S.Yu., Direct ignition of inertial fusion targets by a laser-plasma ion stream, Quantum Electron. **N31** (10) (2001) 885.

- [10.89] MARTINEZ-VAL, J.M., ELIEZER, S., PIERA, M., VERALDE, P.M., in Proc. AIP Conf. Vol. 406 (1997) 208.
- [10.90] MURAKAMI, M., NAGATOMO, H., A new twist for inertial fusion energy: Impact ignition, Nucl. Instrum. Methods Phys. Res. A **544** (2005) 67.
- [10.91] MURAKAMI, M., NAGATOMO, H., AZECHI, A., OGANDO, F., ELIEZER, S., Innovative ignition scheme for ICF- impact fast ignition, Nucl. Fusion **46** (2006) 99.
- [10.92] MAHADY, A.I., TAKABE, H., MIMA, K., Pulse heating and ignition for off-centre ignited targets, Nucl. Fusion **39** (1999) 467.
- [10.93] DEUTSCH, C., Inertial confinement fusion driven by intense ion beams, Ann. Phys. **11** (1986) 1–111.
- [10.94] JOHZAKI, T., NAKAO, Y., MIMA, K., Implosion and core heating requirements in sub-ignition experiments FIREX-I, Phys. Plasmas **15** (2008) 0627021.
- [10.95] GREEN, J.S., et al., Phys. Rev. Lett. **100** (2008) 015003.
- [10.96] TANAKA, K.A., KODAMA, R., FUJITA, H., et al., Studies of ultra-intense laser plasma interactions for fast ignition, Phys. Plasmas **7** (2000) 2014.
- [10.97] KODAMA, R., et al., “Super-penetration of ultra-intense laser light in long scale-length plasmas relevant to fast ignitor”, Proc. 18th IAEA Fusion Energy Conf., Sorrento, Italy (2000); IAEA-CN-77/IFP/09.
- [10.98] TAJIMA, K., MIMA, K., BALDIS, H., High Field Science, Kluwer Academic/Plenum Publishers, New York (2000).
- [10.99] SENTOKU, Y., et al., Appl. Phys. **B74** (2002) 207.
- [10.100] KITAGAWA, Y., SENTOKU, Y., AKAMATSU, S., et al., Progress of fast ignitor studies and Petawatt laser construction at Osaka University, Phys. Plasmas **9** (2002) 2202.
- [10.101] WELCH, D.R., CAMPBELL, R.B., et al., Phys. Plasmas **13** (2006) 063105.
- [10.102] HONRUBIA, J.J., MEYERTER, V., Nucl. Fusion **46** (2006) L25.
- [10.103] SAKAGAMI, H., JOHZAKI, T., NAGATOMO, H., MIMA, K., Fast ignition integrated interconnecting code project for cone-guided targets, Laser Part. Beams **24** (2006) 191.

- [10.104] SENTOKU, Y., KEMP, A.J., Numerical methods for particle simulations at extreme densities and temperatures: Weighted particles, relativistic collisions and reduced currents, *J. Comput. Phys.* **227** (2008) 6846.
- [10.105] JOHZAKI, T., SAKAGAMI, H., NAGATOMO, H., MIMA, K., *Laser Part. Beams* **25** (2007) 621.
- [10.106] NAGATOMO, H., et al., *Phys. Plasmas* **14** (2007) 056303.
- [10.107] YABE, T., MOCHIZUKI, T., Impact radiative fusion concept, *Jpn. J. Appl. Phys.* **22** (1984) L261.
- [10.108] NAGATOMO, H., et al., *J. Phys. Conf. Series* **244** (2010) 022050.
- [10.109] HATCHETT, S., et al., *Fusion Sci. Technol.* **49** (2006) 327.
- [10.110] STOCKEL, C., et al., *Phys. Plasmas* **9** (2002), 2195–2201.
- [10.111] ZHONG, J.Y., SHIRAGA, H., et al., *J. Phys. Conf. Series* **112** (2008) 022064.
- [10.112] SENTOKU, Y., MIMA, K., KAW, P., NISHIKAWA, K., Anomalous resistivity resulting from MeV-electron transport in overdense plasma, *Phys. Rev. Letters* **90** (2003) 155001.
- [10.113] MIMA, K., et al., “Fast ignition experimental and theoretical researches toward FIREX”, *Proc. 19th Fusion Energy Conf.*, Lyon, France, 14–19 October 2002; IAEA-CN-94/IF3.
- [10.114] SENTOKU, Y., MIMA, K., et al., *Phys. Review E* **65** (2002) 046408-1.
- [10.115] KODAMA, R., IZAWA, Y., et al., *Nucl. Fusion* **44S** (2004) 276; doi:10.1088/0029-5515/44/12/S19
- [10.116] YAMANAKA, T., et al., in *Proc. 19th IAEA Fusion Energy Conf.*, Lyon, France, 14–19 October 2002; IAEA-CN-94/OV/3-1.
- [10.117] ATZENI, S., Thermonuclear burn performance of volume-ignited and centrally ignited bare deuterium-tritium microspheres, *Jpn. J. Appl. Phys.* **34** (1995) 1980.
- [10.118] McCRORY, R.L., et al., in *Proc. 22nd Int. Conf. on Fusion Energy*, Geneva, Switzerland, 2008, IAEA, Vienna CD-ROM file IF/1-1.
- [10.119] NAGATOMO, H., et al., *Nucl. Fusion* **49** (2009) 075028.
- [10.120] NAKAMURA, T., SAKAGAMI, H., JOHZAKI, T., NAGATOMO, H., MIMA, K., KOGA, J., *Phys. Plasmas* **14** (2007) 103105.

- [10.121] CAI, H.B., et al., Phys. Rev. Lett. **192** (2009) 245001.
- [10.122] ZIMMERMAN, G.B., KRUEER, W., Comments Plasma Phys. **2** (1975) 51.
- [10.123] KAUFMANN, R.L., et al., Laser Program Annual Report: Laser Driven Hohlräume, LLNL, California, UCRL-50055-86/87, p. 4-2.
- [10.124] TURNER, R.E., et al., “Results from the symmetry-I”, Experimental Series on Nova, LLNL, California, UCRL-50055-86/87, p. 4-25.
- [10.125] KILKENY, J., et al., Preliminary R-T Instability Experiments on Nova, LLNL, California, UCRL-50055-86/87, p. 4-64.
- [10.126] MUNRO, D.H., et al., LASNEX Shell Instability Modelling of the Nova R-T Experiments, LLNL, California, UCRL-50055-86/87, p. 4-82.
- [10.127] SUTER, L.J., et al., Analysis of Pulse Shaped Nova Experiments, LLNL, California, UCRL-50055-88/89, p. 2-8.
- [10.128] LINDL, J.D., Inertial Confinement Fusion: The Quest for Ignition and Gain Using Indirect Drive, AIP Press (1997).
- [10.129] MOSES, E.I., Nucl. Fusion **49** (2009) 104022.
- [10.130] LINDL, J.D., et al., in Proc. 23rd Fusion Energy Conf., Daejeon, Korea (2010), IAEA, Vienna, CD-ROM file OV/2-1 and <http://www-naweb.iaea.org/naweb/physics/FEC/FEC2010/html/index.htm>
- [10.131] GLENZER, S.H., et al., Science **327** (2010) 1228.
- [10.132] JACQUEMOT, S., et al., in Proc. 23rd Fusion Energy Conf., Daejeon, Korea (2010), IAEA, Vienna, CD-ROM file IFE/2-3 and <http://www-naweb.iaea.org/naweb/physics/FEC/FEC2010/html/index.htm>
- [10.133] MATZEN, K., “Overview of Recent ICF and HEDP related experiments on the Z-machine”, in Proc. 32nd EPS, Taragona, Spain (2005), Plenary Talk II.003.
- [10.134] MEHLHORN, T.A., Plasma Phys. Control. Fusion **45** (2003) 1-11.
- [10.135] LOGAN, B.G., in Proc. 22nd Int. Conf. on Fusion Energy, Geneva, Switzerland, 2008, IAEA, Vienna, CD-ROM file IFE/p6-06.
- [10.136] SANFORD, T.W.L., et al., Phys. Rev. Lett. **77** (1996) 5063.
- [10.137] HOGAN, W.J., COUTANT, J., NAKAI, S., ROZANOV, V.B., VELARDE, G., Energy from Inertial Fusion, IAEA, Vienna (1995) ISBN 92-0-100794-9.

- [10.138] KRUPKE, W.F., *Fusion Technol.* **15** (1989) 377.
- [10.139] NAITO, K., et al., *Jpn. J. Appl. Phys.* **31** (1992) 259.
- [10.140] ORTH, C.D., et al., *Nucl. Fusion* **44** (1996) 75.
- [10.141] NAKAI, S., MIMA, K., *Rep. Progr. Phys.* **67** (2004) 321.
- [10.142] BOOTH, L.A., *Central Station Power Generation by Laser Driven Fusion*, Report LA- 4858-MS, Los Alamos, NM: Los Alamos National Laboratory, Vol. 1 (1972).
- [10.143] MIMA, K., et al., in *Proc. 14th IAEA Fusion Energy Conf.*, Wurzburg, Germany, 30 September – 1 October 1992; IAEA-CN-56/G-2-3.
- [10.144] YAMANAKA, C., Report ILE-8127P, Inst. of Laser Engineering, Osaka, Japan (1981).
- [10.145] MOIR, R.W., et al., *Fusion Technol.* **25** (1994) 5.
- [10.146] KOZAKI, Y., et al., in *Proc. 19th IAEA Fusion Energy Conf.*, Lyon, France, 14–19 October 2002; IAEA-CN-94/FT/P-1-25.
- [10.147] GOTO, T., SOMEYA, Y., OGAWA, Y., HIWATARI, R., ASAOKA, Y., OKANO, K., SUNAHARA, A., JOHZAKI, T., *Nucl. Fusion* **49** (2009) 075006.
- [10.148] RAFFRAY, A.R., BLANCHARD, J., LATKOWSKI, J., NAJMABADI, F., RENK, T., SETHIAN, J., SHARAFAT, S., SNEAD, L., *Fusion Eng. Des.* **81** (2006) 1627–1638.
- [10.149] BLANCHARDL, J.P., RAFFRAY, R.A., *Fusion Sci. Technol.* **52** (2007) 440.
- [10.150] KALAL, M., et al., *J. Korean Phys. Soc.* **56** (2010) 184–189.
- [10.151] PERLADO, J.M., et al., in *Proc. 23rd IAEA Fusion Energy Conf.*, Daejeon, Korea, 11–16 October, 2010, paper IFE 1-5.
- [10.152] DUNNE, M., *Nature Phys.* **2** (2006) 2.
- [10.153] EDWARDS, C.,  
*<http://www.hiper-laser.org/index.asp>*
- [10.154] JUAREZ, R., SANZ, J., PERLADO, J.M., in *Proc. 23rd Fusion Energy Conf.*, Daejeon, Korea, 2010, IAEA, Vienna, CD-ROM file IFE/P6-22 and  
*<http://www-naweb.iaea.org/napc/physics/FEC/FEC2010/html/index.htm>*

## INERTIAL FUSION ENERGY

- [10.155] JUAREZ, R., et al., Fusion Eng. Des. (2011), FUSENGDES-D-10-00575,SOFT 2010,OPORTO; doi:10.1016/j.fusengdes.2011.02.026
- [10.156] KAWANAKA, J., et al., Laser Phys. **15** (2005) 1306.
- [10.157] KONG, H.J., et al., Laser Part. Beams **27** (2009) 179.
- [10.158] BERNAT, T.P., STEPHENS, R.B., et al., Ignition Target Fabrication and Fielding for the National Ignition Facility, March (2005), <https://e-reports-ext.llnl.gov/pdf/325960.pdf>
- [10.159] NAGAI, K., et al., Nucl. Fusion **49** (2009) 095028.



# INDEX

## A

---

active charge exchange 438, 445  
active diagnostic methods 426  
advanced stellarator 898  
advanced tokamak 29, 74, 322, 880  
advanced tokamak scenarios 322, 880  
Alfvén continuum 307, 887  
Alfvén eigenmodes 337, 886  
Alfvén modes 337  
Alfvén waves 337, 885  
alpha particle heating 610, 892  
alpha particles 17, 535, 569, 609  
anomalous transport 64, 75, 83, 176  
aspect ratio 66  
axisymmetric magnetic surfaces 546  
AXUV detectors 382–384

## B

---

ballooning modes 246, 263, 881  
ballooning representation 106  
banana drift 560  
basic microinstabilities 86  
beam emission spectroscopy 182, 435  
beamlet steering 582  
beta limit 344, 933, 982  
beta value 29, 325  
blanket 25, 50, 941, 1095  
bolometer equation 380  
bolometry 378

## INDEX

Boltzmann equation 71  
bootstrap current 75, 900  
boronization 758, 789  
Braginskii equations 64  
bremsstrahlung 17, 400, 401  
burning plasma 376, 394, 423–425, 433, 464, 466, 629, 664, 783, 793, 794, 796

## C

---

charge exchange 183, 438, 445, 538  
charged fusion products 412, 416  
chemical erosion 780, 782  
Child–Langmuir law 579  
chirping modes 341  
classical tearing modes 322  
coaxial helicity injection 995  
collisionality 73, 99–101, 113, 114, 123, 137, 159, 176, 192, 799, 800, 822, 904  
collisionless trapped electron mode 100  
confinement 59, 849, 959  
confinement degradation 326, 344, 833, 867, 933, 996  
confinement scaling 123  
confinement trends 124, 128  
core transport 62, 138  
core turbulence 194  
correlated electron cyclotron emission 183  
correlation length 59, 100, 186  
cost comparison 42  
Cotton–Mouton polarimetry 470  
counter injection 536  
cross-field transport 59, 72, 760, 819, 903, 927  
current density 65  
current drive 150, 551, 554, 609, 861  
current profile control 610  
current quench 347

## INDEX

cyclotron frequency 63, 67, 93, 179, 304, 305, 384, 428, 474, 475, 612, 615, 617, 620, 621, 630–632, 635, 636, 638, 659, 660, 662, 716, 717, 866, 885, 894, 1013

cyclotron radius 63

## D

---

damage potential 349

Debye length 629

density control 832

density fluctuation measurements 482

density fluctuations 61, 84, 91, 93, 114, 170, 171, 178, 191, 428, 476, 479, 481, 482, 1061

density limit 343, 678, 696, 702, 867, 930

density limit disruptions 343

density scale length 59

detachment 805, 828

diagnostic neutral beams 435

diagnostics 360

diffusion coefficient 73, 762, 898, 918

dimensional parameters 124

dimensionless analysis 136

dimensionless parameters 239

dispersion interferometers 468

disruption 342

disruptive instabilities 342

dissipative trapped electron mode 101

distribution function 63

divertor operation regimes 799

drift kinetic equation 71

drift wave turbulence 109, 112, 175

drift waves 86

D–T experiments 568

**E**

---

edge localized modes (ELMs) 327  
edge pedestal 169  
electrical probes 368  
electromagnetic turbulence 60  
electron Bernstein waves (EBWs) 392, 612  
electron cyclotron current drive (ECCD) 620, 703  
electron cyclotron emission 183, 384  
electron cyclotron resonance heating (ECRH) 612  
electron drift instabilities 86  
electron dynamics 99  
electron heat transport 114, 914  
electron temperature gradient instability 99  
electron thermal transport 113  
electron transport 113  
ELMy H-mode 328, 906  
energetic particle modes 311, 337  
energy confinement 18, 123, 230  
energy scenarios 11  
energy transfer 543  
ergodization 285  
error analysis 133

**F**

---

fast ignition 1069, 1074, 1077, 1082  
fast ion diffusion coefficient 549  
fast ion distribution function 551  
fast particle effects 313  
feedback control 489  
field reversed configuration (FRC) 1000  
filamentation instability 1062  
first wall 756  
fishbones 321  
frequency spectra 187

## INDEX

fusion power gain 17  
fusion power production 42, 45  
fusion reactions 20

## G

---

gas puffing 831  
geodesic acoustic modes (GAMs) 192  
global Alfvén eigenmodes 176, 886  
global MHD modes 306  
Greenwald density 143  
Greenwald limit 931

## H

---

hard X rays 412  
heat load 327, 831–833  
heat pulse 349  
heat transport 114, 909  
heavy ion beam probe 181  
helical system 861  
helicity injection 987, 994  
heliotron 855, 941  
high beta 982, 1024  
H-mode 120, 128, 915  
H-mode confinement trends 128  
H-mode pedestal 265  
H-mode threshold 123

## I

---

ion Bernstein waves (IBWs) 653, 656  
ion cyclotron resonance heating (ICRH, ICRF) 630  
ideal MHD stability 246  
ignition 19, 36, 1043  
implosion physics 1051  
improved confinement regimes 32, 915

## INDEX

impurity control 758, 789, 798, 832  
impurity transport 375, 378, 918  
inertial confinement fusion (ICF) 27, 35, 38, 1043  
instabilities 86, 95, 246, 342, 877, 984, 1012, 1058, 1068  
interchange mode 246, 247, 262  
interferometry 452  
internal inductance 236  
internal kink modes 317  
internal transport barrier (ITB) 128, 163, 265, 699, 922  
International Thermonuclear Experimental Reactor (ITER) 2, 360, 574, 597,  
727, 730  
ion source 437, 575, 584  
ion temperature gradient (ITG) 85, 89, 96  
ion transport 148, 175, 904  
island divertor 923

## K

---

kinetic MHD 302  
kinetic models 299  
kink modes 317

## L

---

Langmuir probes 368  
large aspect ratio approximation 234  
laser fusion power plant 1095  
L-H threshold scalings 140  
L-H transition 140  
limiter plasmas 758  
linear stability of global modes 269  
local transport 145  
long pulse operation 836  
Lorenz ionization 540  
lower hybrid current drive (LHCD) 642

---

**M**

---

Mach probes 372  
magnetic configuration 65, 847, 913, 958  
magnetic confinement fusion 27  
magnetic field ripple 78  
magnetic measurements 362  
magnetic reconnection 317, 967  
magnetic shear 98, 104, 850  
magnetized plasma 611, 1024  
magnetized target 1024  
MHD energy principle 248  
MHD model 246, 287  
MHD modes 316, 334  
MHD stability 246  
microturbulence 103  
microwave interferometry 459  
mirror machine 1008  
mirrors 1105  
momentum transport 116  
multi-stage acceleration 581

---

**N**

---

negative ion based NBI 595  
negative ion extraction 594  
negative ion production 588, 595  
negative ion source 571, 587  
neoclassical tearing modes (NTMs) 317, 322, 325  
neoclassical theory 152  
neoclassical transport 59, 64, 901, 904, 906, 919, 937  
neutral beam injection (NBI) 535  
neutral transport 149  
non-ideal effects 313, 336  
non-linear gyrokinetic simulations 114, 191  
non-local effects 195

## INDEX

### O

---

one dimensional equilibria 253  
operational limits 930

### P

---

particle drifts 63, 563  
particle transport 114, 810, 909  
passive neutral particle analysis 394  
pedestal 133, 169, 173, 192, 265, 328  
pellet injection 467, 831  
Peri-plasmatron 575  
petawatt laser 1069, 1075  
phase contrast imaging 181  
plasma confinement 30, 59, 63, 124, 136, 853, 1008  
plasma elongation 126, 1001  
plasma equilibrium 232, 239, 870  
plasma facing components (PFCs) 349, 364, 796, 797, 834, 835, 837  
plasma focus 1026  
plasma generator 575, 576, 582, 584  
plasma heating 535, 536, 1074  
plasma length 230, 1001  
plasma rotation 116, 336, 440, 1003, 1005  
polarimetry 452, 454  
positive ion based NBI 574  
power balance 17, 160  
power flows 60  
profile stiffness 160, 161, 163, 176

### Q

---

Q factor 17

### R

---

radial fluxes 59  
radial profiles 189–191

## INDEX

radio frequency (RF) heating 150, 658  
reconnection 285  
recycling 47, 759, 764, 767, 802, 803  
re-deposition 794  
reduced (low frequency) MHD 291  
reflectometry 179, 452  
resistive bolometers 380  
resistive instabilities 276  
resistive wall mode (RWM) 270, 278, 281, 335  
reversed field pinch (RFP) 959  
reversed magnetic shear 122, 164  
reversed shear Alfvén eigenmodes 338  
runaway electrons 353, 364, 391, 419, 757

## S

---

safety factor 65  
sawtooth, sawteeth 317  
scrape-off layer (SOL) 765, 932  
sheared flow 61, 122  
spectroscopy 182, 183, 404, 438  
spherical tokamak 50, 175, 1000  
spherical torus 113, 190  
spheromak 990  
sputtering 486, 772, 774  
stability 85, 89, 225, 984, 1059, 1062  
steady state operation 823, 836  
steady state tokamak 324, 333  
stellarator 871, 936  
stochastic field 64, 82  
straight tokamak model 258, 272  
structural materials 40, 486  
superconductor 848, 944  
suprathermal electrons 390, 864, 1057

---

**T**

---

target design 1092  
tearing modes 272  
temperature fluctuations 191  
temperature gradient 75, 85, 89, 96, 99  
temperature gradient mode 85, 96  
thermal quench 345  
Thomson scattering 426, 429, 431  
tokamak 32, 91, 225, 246, 568, 831  
tokamak configuration 226, 227  
tokamak dynamics 228  
tokamak equilibrium 230, 232  
tokamak plasma geometry 536  
tokamak turbulence 91  
toroidal angular momentum 59  
toroidal current 27, 997  
toroidal field coils 854, 855, 859  
toroidal geometry 106, 306, 648, 651, 653, 825, 870  
transport barriers 118, 163  
trapped electrons 99, 551  
trapped ion mode 100, 102, 103  
trapped particle instabilities 95  
triangularity 30, 138  
tritium handling 1101, 1103  
tritium inventory 41, 832, 835  
tritium retention 780, 797, 835  
turbulence measurements 176  
turbulent transport 176, 784, 906, 958  
two-fluid effects 300

---

**U**

---

UV spectroscopy 375

## INDEX

### V

---

vacuum vessel 376, 459, 465, 468, 756, 779  
vertical displacement events 758  
Vlasov equation 63, 92, 94, 95  
volume recombination 803  
vorticity 293, 297

### W

---

wall conditioning 786  
wall modes in rotating plasmas 278  
wall pumping 789, 833  
wall stabilization 334  
waste 40, 41, 47  
wavenumber spectra 185, 188

### X

---

X ray radiation 400, 1077, 1086

### Z

---

zonal flow 100, 108, 192, 211  
zonal flow shear 108





# IAEA

International Atomic Energy Agency

No. 22

## Where to order IAEA publications

In the following countries IAEA publications may be purchased from the sources listed below, or from major local booksellers. Payment may be made in local currency or with UNESCO coupons.

### AUSTRALIA

DA Information Services, 648 Whitehorse Road, MITCHAM 3132  
Telephone: +61 3 9210 7777 • Fax: +61 3 9210 7788  
Email: [service@dadirect.com.au](mailto:service@dadirect.com.au) • Web site: <http://www.dadirect.com.au>

### BELGIUM

Jean de Lannoy, avenue du Roi 202, B-1190 Brussels  
Telephone: +32 2 538 43 08 • Fax: +32 2 538 08 41  
Email: [jean.de.lannoy@infoboard.be](mailto:jean.de.lannoy@infoboard.be) • Web site: <http://www.jean-de-lannoy.be>

### CANADA

Bernan Associates, 4501 Forbes Blvd, Suite 200, Lanham, MD 20706-4346, USA  
Telephone: 1-800-865-3457 • Fax: 1-800-865-3450  
Email: [customer-care@bernan.com](mailto:customer-care@bernan.com) • Web site: <http://www.bernan.com>

Renouf Publishing Company Ltd., 1-5369 Canotek Rd., Ottawa, Ontario, K1J 9J3  
Telephone: +613 745 2665 • Fax: +613 745 7660  
Email: [order.dept@renoufbooks.com](mailto:order.dept@renoufbooks.com) • Web site: <http://www.renoufbooks.com>

### CHINA

IAEA Publications in Chinese: China Nuclear Energy Industry Corporation, Translation Section, P.O. Box 2103, Beijing

### CZECH REPUBLIC

Suweco CZ, S.R.O., Klecakova 347, 180 21 Praha 9  
Telephone: +420 26603 5364 • Fax: +420 28482 1646  
Email: [nakup@suweco.cz](mailto:nakup@suweco.cz) • Web site: <http://www.suweco.cz>

### FINLAND

Akateeminen Kirjakauppa, PO BOX 128 (Keskuskatu 1), FIN-00101 Helsinki  
Telephone: +358 9 121 41 • Fax: +358 9 121 4450  
Email: [akatilau@akateeminen.com](mailto:akatilau@akateeminen.com) • Web site: <http://www.akateeminen.com>

### FRANCE

Form-Edit, 5, rue Janssen, P.O. Box 25, F-75921 Paris Cedex 19  
Telephone: +33 1 42 01 49 49 • Fax: +33 1 42 01 90 90  
Email: [formedit@formedit.fr](mailto:formedit@formedit.fr) • Web site: <http://www.formedit.fr>

Lavoisier SAS, 145 rue de Provigny, 94236 Cachan Cedex  
Telephone: + 33 1 47 40 67 02 • Fax +33 1 47 40 67 02  
Email: [romuald.verrier@lavoisier.fr](mailto:romuald.verrier@lavoisier.fr) • Web site: <http://www.lavoisier.fr>

### GERMANY

UNO-Verlag, Vertriebs- und Verlags GmbH, Am Hofgarten 10, D-53113 Bonn  
Telephone: + 49 228 94 90 20 • Fax: +49 228 94 90 20 or +49 228 94 90 222  
Email: [bestellung@uno-verlag.de](mailto:bestellung@uno-verlag.de) • Web site: <http://www.uno-verlag.de>

### HUNGARY

Librotrade Ltd., Book Import, P.O. Box 126, H-1656 Budapest  
Telephone: +36 1 257 7777 • Fax: +36 1 257 7472 • Email: [books@librotrade.hu](mailto:books@librotrade.hu)

### INDIA

Allied Publishers Group, 1st Floor, Dubash House, 15, J. N. Heredia Marg, Ballard Estate, Mumbai 400 001,  
Telephone: +91 22 22617926/27 • Fax: +91 22 22617928  
Email: [alliedpl@vsnl.com](mailto:alliedpl@vsnl.com) • Web site: <http://www.alliedpublishers.com>

Bookwell, 2/72, Nirankari Colony, Delhi 110009  
Telephone: +91 11 23268786, +91 11 23257264 • Fax: +91 11 23281315  
Email: [bookwell@vsnl.net](mailto:bookwell@vsnl.net)

### ITALY

Libreria Scientifica Dott. Lucio di Biasio "AEIOU", Via Coronelli 6, I-20146 Milan  
Telephone: +39 02 48 95 45 52 or 48 95 45 62 • Fax: +39 02 48 95 45 48  
Email: [info@libreriaaeiou.eu](mailto:info@libreriaaeiou.eu) • Website: [www.libreriaaeiou.eu](http://www.libreriaaeiou.eu)

## **JAPAN**

Maruzen Company, Ltd., 13-6 Nihonbashi, 3 chome, Chuo-ku, Tokyo 103-0027  
Telephone: +81 3 3275 8582 • Fax: +81 3 3275 9072  
Email: journal@maruzen.co.jp • Web site: <http://www.maruzen.co.jp>

## **REPUBLIC OF KOREA**

KINS Inc., Information Business Dept. Samho Bldg. 2nd Floor, 275-1 Yang Jae-dong SeoCho-G, Seoul 137-130  
Telephone: +02 589 1740 • Fax: +02 589 1746 • Web site: <http://www.kins.re.kr>

## **NETHERLANDS**

De Lindeboom Internationale Publicaties B.V., M.A. de Ruyterstraat 20A, NL-7482 BZ Haaksbergen  
Telephone: +31 (0) 53 5740004 • Fax: +31 (0) 53 5729296  
Email: books@delindeboom.com • Web site: <http://www.delindeboom.com>

Martinus Nijhoff International, Koraalrood 50, P.O. Box 1853, 2700 CZ Zoetermeer  
Telephone: +31 793 684 400 • Fax: +31 793 615 698  
Email: info@nijhoff.nl • Web site: <http://www.nijhoff.nl>

Swets and Zeitlinger b.v., P.O. Box 830, 2160 SZ Lisse  
Telephone: +31 252 435 111 • Fax: +31 252 415 888  
Email: info@swets.nl • Web site: <http://www.swets.nl>

## **NEW ZEALAND**

DA Information Services, 648 Whitehorse Road, MITCHAM 3132, Australia  
Telephone: +61 3 9210 7777 • Fax: +61 3 9210 7788  
Email: service@dadirect.com.au • Web site: <http://www.dadirect.com.au>

## **SLOVENIA**

Cankarjeva Zalozba d.d., Kopitarjeva 2, SI-1512 Ljubljana  
Telephone: +386 1 432 31 44 • Fax: +386 1 230 14 35  
Email: import.books@cankarjeva-z.si • Web site: <http://www.cankarjeva-z.si/uvvoz>

## **SPAIN**

Díaz de Santos, S.A., c/ Juan Bravo, 3A, E-28006 Madrid  
Telephone: +34 91 781 94 80 • Fax: +34 91 575 55 63  
Email: compras@diazdesantos.es, carmela@diazdesantos.es, barcelona@diazdesantos.es, julio@diazdesantos.es  
Web site: <http://www.diazdesantos.es>

## **UNITED KINGDOM**

The Stationery Office Ltd, International Sales Agency, PO Box 29, Norwich, NR3 1 GN  
Telephone (orders): +44 870 600 5552 • (enquiries): +44 207 873 8372 • Fax: +44 207 873 8203  
Email (orders): book.orders@tso.co.uk • (enquiries): book.enquiries@tso.co.uk • Web site: <http://www.tso.co.uk>

### **On-line orders**

DELTA Int. Book Wholesalers Ltd., 39 Alexandra Road, Addlestone, Surrey, KT15 2PQ  
Email: info@profbooks.com • Web site: <http://www.profbooks.com>

### **Books on the Environment**

Earthprint Ltd., P.O. Box 119, Stevenage SG1 4TP  
Telephone: +44 1438748111 • Fax: +44 1438748844  
Email: orders@earthprint.com • Web site: <http://www.earthprint.com>

## **UNITED NATIONS**

Dept. I004, Room DC2-0853, First Avenue at 46th Street, New York, N.Y. 10017, USA  
(UN) Telephone: +800 253-9646 or +212 963-8302 • Fax: +212 963-3489  
Email: publications@un.org • Web site: <http://www.un.org>

## **UNITED STATES OF AMERICA**

Bernan Associates, 4501 Forbes Blvd., Suite 200, Lanham, MD 20706-4346  
Telephone: 1-800-865-3457 • Fax: 1-800-865-3450  
Email: customercare@bernan.com • Web site: <http://www.bernan.com>

Renouf Publishing Company Ltd., 812 Proctor Ave., Ogdensburg, NY, 13669  
Telephone: +888 551 7470 (toll-free) • Fax: +888 568 8546 (toll-free)  
Email: order.dept@renoufbooks.com • Web site: <http://www.renoufbooks.com>

**Orders and requests for information may also be addressed directly to:**

### **Marketing and Sales Unit, International Atomic Energy Agency**

Vienna International Centre, PO Box 100, 1400 Vienna, Austria  
Telephone: +43 1 2600 22529 (or 22530) • Fax: +43 1 2600 29302  
Email: sales.publications@iaea.org • Web site: <http://www.iaea.org/books>





This publication is a comprehensive reference book for graduate students and an invaluable guide for more experienced researchers. It provides an introduction to nuclear fusion and its status and prospects, and features specialized chapters written by leaders in the field, presenting the main research and development concepts in fusion physics. It starts with an introduction to the case for the development of fusion as an energy source. Magnetic and inertial confinement are addressed. Dedicated chapters focus on the physics of confinement, the equilibrium and stability of tokamaks, diagnostics, heating and current drive by neutral beam and radiofrequency waves, and plasma-wall interactions. While the tokamak is a leading concept for the realization of fusion, other concepts (helical confinement and, in a broader sense, other magnetic and inertial configurations) are also addressed in the book. At over 1100 pages, this publication provides an unparalleled resource for fusion physicists and engineers.

INTERNATIONAL ATOMIC ENERGY AGENCY  
VIENNA  
ISBN 978-92-0-130410-0